R-13-40

The impact of concrete degradation on the BMA barrier functions

Lars Olof Höglund, Kemakta Konsult AB

August 2014

Svensk Kärnbränslehantering AB
Swedish Nuclear Fuel
and Waste Management Co

Box 3091, SE-169 03 Solna
Phone +46 8 459 84 00

SKB

ISSN 1402-3091
SKB R-13-40
ID 1427016
Updated 2018-03

The impact of concrete degradation on the BMA barrier functions

Lars Olof Höglund, Kemakta Konsult AB

August 2014

Update notice

The original report, dated August 2014, was found to contain factual errors which have been corrected in this updated version. The corrected factual errors are presented below.

Updated 2018-03

Location	Original text	Corrected text
Page 68, paragraph above Figure 5-5, last sentence.	The results suggest that a mean leaching depth of 0.4 m would be reached after ~ 3,000–4,000 years, cf. the numerical calculations for case Large 7 in Section 8.9.	Sentence deleted.
Page 223, paragraph above heading Conclusions.	Calculations presented in Section 5.1 considering the diffusion of dissolved calcium from the concrete into the passing groundwater in the macadam backfill show comparable results with a predicted mean leaching depth of 0.4 m within 3,000–4,000 years.	Paragraph deleted.

Acknowledgment

The author wishes to thank the two reviewers Andrés Idiart, Amphos[21], and Russell Alexander, Bedrock Geosciences, for valuable and constructive comments and criticism received during the factual review of this report. It is my hope that the handling of the comments may be considered respectful in view of the efforts made reviewing this report.

I also wish to thank my colleagues Miranda Keith-Roach, Magnus Sidborn, Magdalena Ericsson and Håkan Yesilova at Kemakta for their endless patience and valuable contributions during the revision of the report.

Summary

This report presents a series of analytical models and numerical reactive transport models focussed on investigating physical and chemical processes that cause fractures and chemical degradation in concrete barriers, and the impact of fractures on the long term performance of SFR. The report also provides data on hydraulic conductivities, effective diffusivities and porosities of the concrete barriers for the Safety Assessment PSU, and addresses the issue of fractures in SFR barriers explicitly for the first time.

Strålsäkerhetsmyndigheten (SSM) requested that SKB carry out further investigations of the physical and chemical concrete degradation processes that impact the concrete throughout the lifetime of the barriers. Additionally, fractures have been observed in the 1BMA barriers during two site inspections. Fractures may affect several of the key parameters used in the groundwater flow modelling (hydraulic conductivity) and radionuclide transport modelling (hydraulic conductivity, effective diffusivity and sorption capability) for the SFR site. This means they have a direct bearing on the safety assessment. There is a plan to repair the 1BMA barriers, but there are clearly important questions remaining over the extent to which these fractures would impact on performance, as well as any further fractures that form during the operational or post closure periods.

Simple mathematical models have been applied in this report in order to generate transparent results for the impact of different physical and chemical degradation processes in the concrete barriers in 1BMA and 2BMA. Within reasonable limits, these results may also be interpreted in terms of the likely impact on the barriers in other parts of SFR. The results may also be of relevance to metal waste and packaging in SFR, since many wastes are stabilised in concrete or cement, and the majority of vaults will be grouted. This means that the waste and the barrier system form a monolithic structure, thus surrounding mechanical disturbances due to the corrosion of any steel component within the structure may also affect the surrounding concrete barriers. The mathematical approach also maintains direct links to the theoretical understanding of the mechanisms involved. For the reactive transport modelling, the results from two geochemical databases have been compared to indicate the sensitivity of the output to the chemical species included and the associated thermodynamic constants.

The results presented here indicate that:

- Fractures increase the hydraulic conductivity and effective diffusivity of the barriers.
- Shrinkage of the concrete, as it dries during the operational phase and cools during resaturation with cold groundwater, will induce fractures.
- Fractures increase the leaching of calcium and other important chemical components from the concrete, thereby increasing the porosity of the adjacent concrete, and ultimately leading to a widening of the fractures.
- Leaching of CSH-gels is well conceptualised, as shown by good agreement using two different geochemical databases in the reactive transport.
- A reactive front of the potentially deleterious minerals ettringite and thaumasite that can lead to gradual deterioration of the concrete will propagate through the different concrete barriers in the period between 2,000 years and 10,000 years after closure.
- Chloride intrusion will cause depassivation of steel components of the barriers (reinforcement bars and form ties) and result in corrosion.
- Corrosion of reinforcement will lead to fracture formation in the concrete and spalling of the surface layer, the fractures will gradually become wider as corrosion progresses.
- Corrosion of form ties that fully penetrate the concrete walls leads to fracture formation and will eventually result in fully penetrating fractures that may extend to the edges of the concrete walls and floors.
- The barrier function will decrease with time, but the new 2BMA design will degrade much more slowly than the current 1BMA.

The new design of the 2BMA concrete barriers was found to perform significantly better in the longer term than the 1BMA concrete barriers in an unrepaired state. However, the performance of the 1BMA barrier in the repair scenario studied suggested that further improvement of the repair measures would be required to obtain the desired barrier function. The major reasons for the advantageous performance of the new design of 2BMA are the presumption that large fractures will be observed and repaired prior to closure and the absence of reinforcement bars, which means that corrosion processes will not induce fracture formation. In line with this, the values selected to represent the barrier properties over time reflect good long-term performance. Tentatively, the results of the simulations suggest that the thin fractures assumed to exist in the concrete may have limited impact on the chemical degradation of the concrete barriers.

It is clear that the uncertainties are large at a conceptual level, in the model applications, and in the interpretation of the model results over long time. Therefore the set of parameters recommended as a basis for the safety assessments was selected cautiously.

Sammanfattning

Denna rapport presenterar ett antal analytiska modeller och modellering av reaktiv transport med fokus på att undersöka fysikaliska och kemiska processer som orsakar sprickbildning i betongbarriärer, och vilken inverkan sprickor har på den långsiktiga barriärfunktionen i SKBs slutförvar SFR. Rapporten ger också förslag till val av data avseende hydrauliska konduktiviteter, effektiva diffusiviteter och porositeter för betongbarriärer till säkerhetsanalysen SR-PSU, och behandlar för första gången explicit olika frågeställningar kopplade till sprickor i SFRs betongbarriärer.

Strålsäkerhetsmyndigheten (SSM) har i ett föreläggande krävt att SKB ska genomföra kompletterande utredningar av fysikaliska och kemiska degraderingsprocesser i betong som påverkar barriärernas hela livslängd. Sprickor har även observerats i förvarsdelen 1BMA vid två olika inspektioner. Sprickor kan ha en väsentlig inverkan på flera viktiga parametrar som används för att beskriva barriärfunktionerna vid modellering av grundvattenflöde (hydrauliska konduktiviteter) och radionuklidtransport i SFR-förvaret (hydrauliska konduktiviteter, effektiva diffusiviteter och sorptionsförmåga). Detta betyder att förekomst av sprickor har en direkt påverkan på säkerhetsanalysen. En plan för reparation av betongbarriärerna i 1BMA har utarbetats, men viktiga frågor återstår rörande i vilken grad förekomsten av sprickor, liksom hur eventuella nya sprickor som kan bildas under resterande driftstid eller efter tillslutning, påverkar barriärfunktionen.

Enkla matematiska modeller har använts i denna utredning för att ta fram tydliga och transparenta resultat för inverkan av olika fysikaliska och kemiska degraderingsprocesser i betongbarriärerna i 1BMA och 2BMA. Inom rimliga gränser kan resultaten även utnyttjas för att bedöma möjlig påverkan på andra förvarsdelar i SFR. De modeller och resultat som tagits fram för inverkan av armeringskorrosion för sprickbildning kan även ha relevans för metallförpackningar och metallskrot i avfallet eftersom planerad kringgjutning i många förvarsdelar ger en monolitisk struktur. Detta medför att mekaniska spänningar, som uppkommer då korrosion av stål sker, kan fortplantas och påverka även omslutande betongbarriärer. Det matematiska angreppssättet ger även en direkt anknytning till teoretisk förståelse av de grundläggande mekanismerna. För modelleringen av reaktiv transport har två olika termodynamiska databaser använts och resultaten jämförs för att visa på resultatens känslighet för vilka lösta och fasta ämnen som ingår i de olika databaserna.

Resultaten som presenteras i rapporten indikerar att:

- Sprickor ökar den hydrauliska konduktiviteten och effektiva diffusiviteten hos barriärerna.
- Krympning av betongen, till följd av uttorkning under driftsfasen och avkylning under återmättnad med kallt grundvatten, leder till sprickbildning.
- Sprickor ökar utlakningen av kalcium och andra viktiga kemiska komponenter i betongen, vilket ökar porositeten hos betongen runt sprickorna, och leder till att sprickorna vidgas.
- Lakningen av CSH-geler bygger på en rimligt god konceptuell förståelse, vilket visas av en god överensstämmelse i resultaten då olika termodynamiska databaser används.
- En reaktionsfront, där de två potentiellt skadliga mineralen ettringit och thaumasit bildas, vandrar genom betongbarriärerna under perioden 2 000 till 10 000 år efter tillslutning.
- Kloridinträngning leder till depassivering av stålkomponenter i betongbarriärerna (armeringsjärn, formstag, mm.) varvid korrosion initieras.
- Korrosion av armeringsjärn leder till sprickbildning i betongen och avspaltning av täckskikt över armeringen. Sprickorna vidgas gradvis i takt med att korrosionen fortskrider.
- Korrosion av genomgående formstag leder till sprickbildning och kommer på sikt att resultera i genomgående sprickor som sträcker sig till kanten på betongväggen/golvet.
- Funktionen hos betongbarriärerna kommer att minska med tiden, men med den nya designen för 2BMA förväntas betongdegraderingen ske mycket långsammare än för den nuvarande utformningen i 1BMA.

Den nya barriärutformningen för 2BMA bedöms ha en avsevärt förbättrad långtidsfunktion jämfört med betongbarriärerna i1BMA i sitt nuvarande skick (före reparation). De genomförda undersökningarna av ett reparationsscenario för betongbarriärerna i 1BMA visar att långtgående förbättringar krävs för att nå de eftersträvade barriärfunktionerna. Avgörande faktorer för den förbättrade barriärfunktionen hos den nya designen för 2BMA är att större sprickor antas kunna observeras och repareras före tillslutning och att frånvaron av armering medför att korrosionsprocesser inte ger upphov till sprickbildning. Med detta som utgångspunkt har parametervärden för olika tidsperioder valts som representerar betongbarriärer med god långtidsfunktion. Resultaten från genomförda simuleringar ger preliminära indikationer att de tunna sprickor som antagits förekomma kan ha en begränsad inverkan på den kemiska degraderingen av betongbarriärerna.

Det är uppenbart att det finns stora osäkerheter på en konceptuell nivå, i modelltillämpningar, och i tolkning av modellresultaten över långa tider. De föreslagna parametervärdena för säkerhetsanalysen har därför valts på försiktig grund.

Contents

Notation

A	area	(m^2)
a	area fraction	(−)
B	geometric width (in direction perpendicular to main flow direction)	(m)
b	fracture aperture width	(m)
C	amount of cement	(kg/m^3)
C_m	property function in the Carman-Kozeny relation for material m	(m/s)
c or c_i	aqueous concentration of species i	(M)
c_{init}	initial aqueous concentration	(M)
c_0	aqueous concentration at the external surface of the concrete	(M)
$c_s^{(i)}$ or c^i_{sol}	aqueous solubility of species i	(M)
D	diffusivity	(m^2/year)
D_e	effective diffusivity	(m^2/year)
d	diameter or distance	(m)
E	modulus of elasticity, Hooke's law	(Pa)
f_a	leaching depth	(m)
f_t	tensile strength	(Pa)
g	gravitational constant	(m/s^2)
H	geometric height	(m)
h_a	leaching depth	(m)
i	hydraulic head gradient	(−)
i_{corr}	corrosion current	($\mu A/cm^2$)
j	molar flux	(mol/m^2/year)
K	hydraulic conductivity	(m/s)
k	permeability	(m^2)
k_{RH}	correction factor for final drying shrinkage at relative humidity RH in relation to drying shrinkage at 50% relative humidity	(–)
L	geometric length (distance along main flow or transport direction)	(m)
l	geometric length (distance normal to main flow or transport direction)	(m)
M_i	molar weight of species i	(kg/kmol)
N_{cs}	hydraulic conductivity contrast	(−)
N_i	molar dissolution rate for phase i	(mol/year)
n	count, number of features	(−)
n_i	molar amount of species i	(mol)
p	corrosion depth	(m)
P	pressure	(Pa)
P_i	internal pressure	(Pa)
Q	flow rate	(m^3/year)
q^i_0	initial solid phase concentration of phase i	(kmol/m^3)
q_{gw}	Darcy flux of groundwater	(m^3/m^2/year)
r_0	corrosion rate	(m/year)
r	radius (or denoting radial direction)	(m)
R	ideal gas constant	(m^3Pa/K/mol)
R_D	diffusion resistance	(s/m)
R_F	flow resistance	(s)
R_i	volumetric rate for phase i	(m^3/year)
RH	relative humidity	(%)

T	temperature	(K)
t	time	(year)
u_{cor}	increase in radius due to corrosion (tensile expansion)	(m)
u_p	increase in radius due to internal pressure	(m)
v_x	velocity in x-direction	(m/year)
V	volume	(m^3)
V_m	molar volume	(m^3/kmol)
W	amount of water	(kg/m^3)
w_r	mass of corrosion products	(kg)
X_i	degree of leaching of phase i	(m)
x	distance in x-direction (or denoting the x-axis)	(m)
y	distance in y-direction (or denoting the y-axis)	(m)

Greek symbols

α_r	steel to corrosion product density ratio (Equation 4-23, Equation 4-38)	(−)
α_s	stiffness reduction factor (Equation 4-30)	(−)
γ	coefficient relating corrosion depth and resulting crack aperture width	(−)
δ	surface layer thickness	(m)
δ_D	constrictivity factor of the pore system	(−)
σ	tensile stress	(Pa)
ε	strain, or shrinkage	(−, m)
μ	dynamic viscosity	(kg/m/s)
v	volume ratio	(m^3/m^3)
v_C	Poisson's ratio of concrete	(−)
ρ	density	(kg/m^3)
τ	tortuosity factor	(−)
ϕ	porosity	(−)
ξ or ξ_D	roughness correction factor	(−)
κ	inner to outer coaxial cylinder ratio	(−)

1 Introduction

Concrete barriers are used in many nuclear waste repositories for low and intermediate level radioactive waste, including the Swedish SFR repository. Concrete is used for construction purposes, as a waste conditioning material and as a grout material and has an important role in limiting water flow through repository parts, restricting diffusion and sorbing radionuclides. Processes that affect the ability of the concrete barriers to provide these functions, i.e. that lower the pH of the pore water or increase the hydraulic conductivity or diffusivity of the barrier, are particularly important to address in the safety case for a cementitious repository.

When modelling water flow in a repository over time, the hydraulic conductivities of system components are estimated for different time periods. Both the hydraulic conductivity and diffusivity in concrete are considered when calculating radionuclide release from a repository and the rates and patterns of barrier degradation. Since degradation processes such as leaching may lead to depletion of different chemical components of the concrete, gradually reducing the pH of the cement pore water, they may also affect the hydraulic conductivity and the diffusivity of the barriers. Therefore, there is likely to be a positive feedback mechanism between the degradation state of the barrier and the rate of degradation. However, the interaction between groundwater and leachate from the concrete barriers may also result in precipitation blocking the porosity. Fractures that are present in the barrier at closure or form early in the lifetime of the repository will increase the hydraulic conductivity and diffusivity of the barriers and may enhance the rate of local degradation processes. This means they have a direct bearing on the safety assessment for SFR.

Strålsäkerhetsmyndigheten (SSM) has requested that SKB investigate all aspects of physical and chemical concrete degradation throughout the lifetime of the concrete, including the role of fractures and fracturing processes. Fractures have also been observed in the existing 1BMA barriers during two inspections. Therefore the original purposes of this work were: a) to provide data for SKB to respond to SSM; and, b) to supply data on hydraulic conductivities, effective diffusivities and porosities of the concrete barriers for the Safety Assessment PSU. This report therefore assesses the impact of fractures on barrier degradation and on the function of the barriers. Selected physical and chemical processes that may cause degradation are studied and quantitative estimates of their importance are made. Special emphasis has been made to address the impact of corrosion processes on the integrity of concrete barriers, due to the presence of steel reinforcement and form rods in the 1BMA barriers. The fractures observed during the inspections of the barriers and the early results of this work suggested that the performance of the 1BMA barrier would deviate significantly from the design criteria. Therefore, the decisions were made to a) avoid steel reinforcement and form rods in the, as yet unbuilt, 2BMA and b) extensively repair the 1BMA barriers, so that their performance will meet the design criteria.

Therefore, the objectives of this report are to:

- Assess the influence of the physical processes on fracture formation, including shrinkage during drying, contraction due to cooling by groundwater and the corrosion of steel reinforcement and form rods.
- Evaluate the effect of fractures on concrete degradation and barrier function, focussing on the hydraulic conductivity and diffusivity arising from fractures of varying size and frequency.
- Investigate the chemical evolution of the barriers using reactive transport modelling and the resultant changes in the porosity, effective diffusivity and hydraulic conductivity of the concrete.
- Determine porosity, effective diffusivity and hydraulic conductivity data for application in the Safety Assessment PSU, for the 1BMA, 2BMA, and Silo barriers.

The early chapters in this report describe the systems that will be analysed. Chapter 2 details the physical structure, functions and properties of the 1BMA and 2BMA vaults and Chapter 3 describes the chemical composition of the groundwater and the likely changes in its composition over time. The current understanding of concrete degradation mechanisms is then reviewed in Chapter 4 and the key processes that need to be investigated in the modelling are defined. Chapters 4–8 describe

the models used to assess these processes and present the results for selected cases. Table 1-1 summarises the large number of models applied in this report, briefly stating the approach used in each, the assumptions and other relevant information.

The first stages of the modelling involved the application of simple mathematical models to explore concrete fracturing processes, diffusion- and advection-controlled leaching in concrete, and the impact of fractures on leaching processes, in a transparent, step-wise manner (Chapters 4, 5 and 6). This approach introduces a quantitative understanding of each relevant process based on the theoretical understanding of the mechanisms involved, and for the effects to be defined for a range of conditions. The results of these simple mathematical models can therefore be interpreted in terms of the likely impact on the barriers in other SFR vaults. They were therefore used to inform the selection of input parameters for the reactive transport modelling (Chapter 7) and for SR-PSU (Chapter 9). More generally, the results may also inform future studies of the effect of metal waste and packaging in SFR on concrete degradation, since many wastes are stabilised in concrete or cement, and the majority of vaults will be grouted. This means that the waste and the barrier system form a monolithic structure, thus mechanical disturbances due to the corrosion of any steel component within the structure may also affect the concrete barriers. The results of the simple mathematical models were therefore used as follows, to:

- Assist when selecting the input parameters for the reactive transport modelling (i.e. 4.2.2, 6.3, 6.4).
- Evaluate the formation (4.2.2) and effect of different types of fracture/disturbance in the concrete (6.3–6.14) to inform the selection of diffusivity and hydraulic conductivity values for SR-PSU, and to inform design developments.
- Assess the diffusivity and hydraulic conductivity of the current 1BMA barriers (6.15).
- Compare with the reactive transport modelling in Chapter 7 (4.2.2, 5.1.1, 5.1.2, 5.1.3, 5.2) or the converted results in Chapter 8 (6.3, 6.4), to assess the suitability of these simple models for quick, conservative assessments relating to concrete degradation.

Reactive transport modelling of the BMA barrier systems was then carried out using PHAST (Parkhurst et al. 2010) (Chapter 7) to examine the chemical changes in the cement minerals over time due to chemical reactions with groundwater components. A number of scenarios were addressed to examine the impact of the concrete's initial condition on its degradation, and the validity of selected simplifications. The results from two geochemical databases were also compared to indicate the sensitivity of the output to the dissolved chemical species and solid minerals included, and the associated thermodynamic constants.

Chapter 8 translates the results from the reactive transport modelling into spatial changes in porosity, effective diffusivity and hydraulic conductivity over time. Chapter 9 compares the data from the different chapters and combines the estimated effects of physical fracture-forming processes with the results of the reactive transport modelling to provide overall conclusions. Finally, Chapter 9 presents the data selected for inclusion in the Safety Assessment SR-PSU.

Alkali-silica reactions were not included in any of the analyses, since the cement used in SFR concrete is of a low-alkali type and the ballast is assumed to comply with the requirements to avoid alkali-silica reactions according to Swedish standard SS 13 42 03. The inflow water chemistry was based on the likely groundwater composition, and thus the study did not address the impact of dissolved waste components, which may also have deleterious effects on the concrete. However, the dissolution/degradation of waste form components is outside the scope of this study, but has been studied by Cronstrand (2013). Equally, the effect of cement additives is out of the scope of this stage of the investigation. Variations in the redox state of the barrier were not taken into consideration, since the conditions are likely to be reducing at least until glacial meltwaters reach SFR (possibly also then buffered by the host rock). Additionally, the effects of permafrost, rock fall out and other potentially damaging physical or climatic phenomena were considered to be outside the scope of the present study.

Table 1-1 Summary of the models applied.

Chapter/ Section	Process modelled	Approach used	Assumptions	Comments
4.2.2	Concrete shrinkage as a result of drying in the repository's operational phase, and the aperture width of the resultant fractures.	Analytical solution based on Möller et al. (1980).	70% relative humidity.	
4.2.2	Concrete shrinkage due to cooling during the resaturation phase and its effect on the hydraulic conductivity.	Analytical solution based on Möller et al. (1980).	Temperature change of –7°C.	The counter effect of swelling during resaturation due to diminished capillary suction in the partly dried concrete is not considered.
4.2.2	Chloride intrusion into concrete and initiation of steel corrosion.	Analytical solution based on Möller et al. (1980).	Groundwater [Cl^-] 0.10–0.14 M. Effective diffusivity in the concrete of $3.5 \cdot 10^{-12}$ m^2/s. [OH^-] 0.038–0.067 M	Chemical interactions between Cl^- and the concrete are neglected (see 5.2).
4.2.2	Effect of the formation of steel corrosion products on concrete fracturing.	Analytical solution based on Möller et al. (1980) and Li et al. (2005).	Corrosion product is either a) solid magnetite with no porosity or b) a generic compressible porous rust. Constant corrosion rate ($5 \cdot 10^{-8}$ m/year, 6 mm bar radius and maximum tensile strength in the concrete of 1.5 MPa.	
5.1.1	Rate of diffusion-controlled leaching from portlandite, weathered portlandite and CSH gels over time.	Analytical solution based on a shrinking core model (e.g. Levenspiel 1972) and diffusion into the groundwater flowing around the concrete structure according to Bird et al. (1960).	Concrete diffusivity: $3.0 \cdot 10^{-11}$ m^2/s (weakly weathered), $5.0 \cdot 10^{-11}$ m^2/s (strongly weathered).	Simple chemistry, with an approximate correction to couple the leaching of Ca^{2+} and OH^-. Simplified concrete matrix.
5.1.2	Rate of advection-controlled leaching in portlandite and CSH gels over time.	Analytical solution applying the time dependent groundwater flux through the cavern of Holmén and Stigsson (2001).	All water flows through the concrete barrier.	Water flow assumption is pessimistic.
5.1.3	Impact of fractures on diffusion- and advection-controlled leaching.	Analytical solutions for three limiting cases, applying the time dependent groundwater flux through the cavern of Holmén and Stigsson (2001).	Thin fractures have formed through the barrier. Advective flow converges to the fractures.	
5.1.3	Limiting fracture aperture for the assumed flow convergence (in 5.1.3).	Analytical solution.		Confirms that the assumption in 5.1.3 that water converges to the fractures is reasonable.
5.2	Intrusion of Cl^-, CO_3^{2-} and SO_4^{2+}.	Analytical solution based on a shrinking core model (e.g. Levenspiel 1972).	The reactions between Cl^-, CO_3^{2-} and SO_4^{2+} with calcium aluminate/ferrite minerals are additive.	Simplified chemistry. Influence of steel corrosion not included.

Chapter/ Section	Process modelled	Approach used	Assumptions	Comments
6.3	Overall hydraulic conductivity of concrete with fully penetrating fractures.	Analytical solution with fracture conductivities as defined by Höglund and Bengtsson (1991), Walton et al. (1990) and US DOE (2009).	Hydraulic conductivity of $1 \cdot 10^{-11}$ m/s in intact concrete and a 0.4 m thick concrete barrier. The fracture surfaces are smooth.	Calculated for a range of fracture widths and spacings. In real fractures, the surface roughness is important and infilling material may be present (Walton et al. 1990).
6.4	Overall diffusivity of concrete with fully penetrating fractures.	Analytical solution.	Effective diffusivity of the fracture equals that of water. Effective diffusivity of intact concrete is $3 \cdot 10^{-12}$ m^2/s. Ideal process between two parallel plates with smooth surfaces.	In real fractures, the surface roughness may be important and infilling material may be present.
6.5	Overall hydraulic conductivity of concrete with fully penetrating fractures of distributed fracture width and length.	Analytical solution that builds on 6.3.	Finite number of plane fractures that can be grouped into size-classes, i.e. width and length.	The approach for summing the contribution from each size-class of fractures is an analogy with (Braester and Thunvik 1988, Walton et al. 1990).
6.6	Overall diffusivity of concrete with fully penetrating fractures of distributed fracture width and length.	Analytical solution that builds on 6.4.	As for 6.5.	Applies the same summing approach as in 6.5.
6.7	Overall conductivity of concrete penetrated by circular holes caused by completely corroded form ties.	Analytical solution based on Bird et al. (1960) and Abramowitz and Stegun (1972).	12 form ties per m^2 of 0.01 m radius.	Calculated for porous holes of varying permeability, and open holes with viscous flow.
6.8	Overall diffusivity of concrete penetrated by circular holes caused by completely corroded form ties.		As for 6.7.	Calculated for holes of varying diameter.
6.9	Overall conductivity of concrete penetrated by an annular shaped space between two coaxial cylinders caused by incompletely corroded form ties.	Analytical solution based on Bird et al. (1960).	12 form ties per m^2 with an outer radius of 0.01 m.	
6.10	Overall diffusivity of concrete penetrated by an annular shaped space between two coaxial cylinders caused by incompletely corroded form ties.	Calculation of the average values over the cross-section.	As for 6.9.	
6.11	Impact on conductivity by disturbed zones around form ties.	Analytical solution.	Tiny fractures form around 10% of the form ties.	
6.12	Impact on diffusivity by disturbed zones around form ties.	Calculation of the average values over the cross-section.		

Chapter/ Section	Process modelled	Approach used	Assumptions	Comments
6.13	Overall conductivity of concrete penetrated by cylindrical injection holes.	As in 6.7.	Injection holes have a diameter of 0.1 m and are backfilled with concrete.	These holes are for the injection of grout.
6.14	Overall diffusivity of concrete penetrated by cylindrical injection holes.	As in 6.8.	As for 6.13.	As for 6.13.
6.15	Application to the 1BMA vault in SFR: hydraulic conductivity, diffusivity and change in porosity as a function of fracture width and fracture spacing.	Analytical solutions using the approach in 6.5 for hydraulic conductivity, 6.6 for diffusivity. Porosity was also calculated using an analytical solution.	Surface roughness factor of 0.5–1 for hydraulic conductivity calculations and 1 for diffusivity calculations. Concrete has fully penetrating fractures.	Based on the current observed state of 1BMA. Compared with an estimated change in porosity arising from chemical leaching. The porosity assumed in the reactive transport modelling can be regarded to include increase of the overall porosity due to observed fractures in the concrete.
7	Reactive transport modelling of concrete barrier degradation in BMA as a function of their initial state.	Reactive transport modelling in PHAST. Uses a 2-D cross-section perpendicular to the main axis of each vault with simplified 1 and 2 BMA barrier systems.	Fully penetrating fractures with an aperture of 100 µm and spacing of 1 m that are present in 2BMA barriers due to drying shrinkage (4.2.2). Fully penetrating fractures in 1BMA are 1 mm thick. Inclusion of the major minerals in the geochemical database is adequate. Hydraulic cage is present. Fixed inflowing groundwater composition, with a change after 2,000 years due to the anticipated change in the type of groundwater. Pure advective outflow of dissolved components. 3 time periods define the changes in total inflow. The presence of iron in the waste, in waste packaging and in reinforcement bars and other steel construction component, which is a source of iron have not been considered in the modelling of the reactive transport.	Seven cases modelling concrete degradation in: 2BMA, 1BMA in its current state, 1BMA following repair of the barriers, and 1BMA in its current state, using some model simplifications. Two geochemical databases (MinteqCem-2001 and Cemdata07) were applied to 1BMA and 1BMA repair scenarios. Scaled barrier geometry although actual barrier thickness used. Modelled over 100,000 years.
8	Effect of barrier degradation on diffusivity and hydraulic conductivity over time.	Analytical solutions that convert the data from Chapter 7 into diffusivities, based on Bentz and Garboczi (1992) and modified Archie's Law; and hydraulic conductivities, based on the Kozeny-Carman relation and a modified version as proposed by Benbow et al. (2005).	Impact on internal pore structure is not taken into account.	Calculated for 1-D pathways through the barrier system defined in Chapter 7 (intact concrete, fracture), and the entire 2-D cross-section for the 2BMA case. For 1BMA, data were calculated for a position in a thin fracture and a position in intact concrete over time, since the simplified model system does not due to the fractures and steel bars present result in high heterogeneity.

2 Description of 1BMA and 2BMA repositories

2.1 Overview – 1BMA

1BMA is an operational vault in the SFR repository for low and intermediate level radioactive waste at Forsmark. It is used for storage of waste with lower activity level than the waste stored in the Silo repository and for waste packages that are unsuitable for deposition in the Silo due to the geometry of the packages, their mechanical properties (e.g. swelling), or their chemical composition. The vault consists of a concrete structure divided into 13 large compartments and two small compartments, see Figure 2-1. The vault is built like a large box with separating walls creating the compartments. The concrete walls and floor structures are made of in-situ cast reinforced concrete. To keep the moulds in place during casting penetrating form rods made out of steel were used, see Figure 2-2. The supporting concrete structures rest on solid rock and the bottom of the compartments rests on a gravel layer on the excavated bottom. The walls and roof of the vault are lined with shotcrete to stabilise the rock during the operating phase.

The waste packages (concrete/steel moulds or steel drums) are emplaced in the compartments in such a way that each compartment will have at least two rows of concrete moulds that act as a support for pre-fabricated reinforced concrete lids. The lids are put in position as soon as a compartment is filled and after that a thin concrete layer is cast on top of the lid in order to prevent water intrusion during the operating phase. When the operating phase is complete, an additional reinforced concrete lid will be cast on top of the compartments. In addition, the space between the waste packages inside the compartments is planned to be filled with a concrete grout that is similar to the type used to grout the shafts inside the silo.

The 1BMA vault is located about 60 meters below the seabed in Öregrundsgrepen. The current plan is to build a complementary vault, 2BMA, in the same rock formation but slightly deeper than 1BMA, at a depth of about 117–137 m below the seabed (Figure 2-3). For further information of the design of the SFR repository (see SKB 2014c).

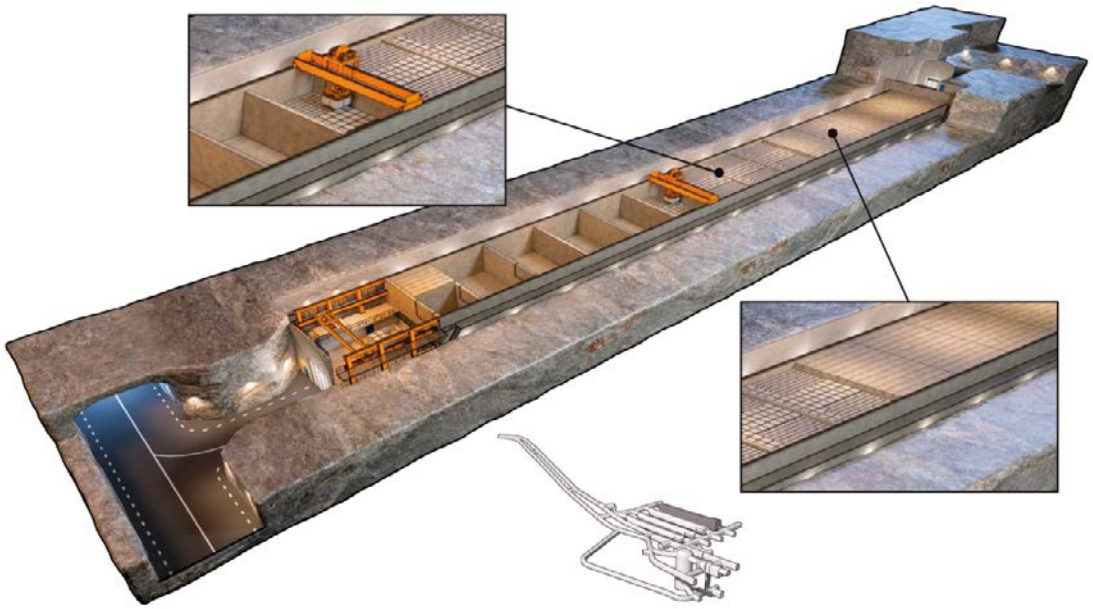

Figure 2-1. *Illustration of 1BMA during the operating phase. The upper detail shows the emplacement of waste packages with the over head crane, the lower detail shows the concrete lid. In addition there is a view of SFR 1 with the position of 1BMA highlighted. (SKB 2014c).*

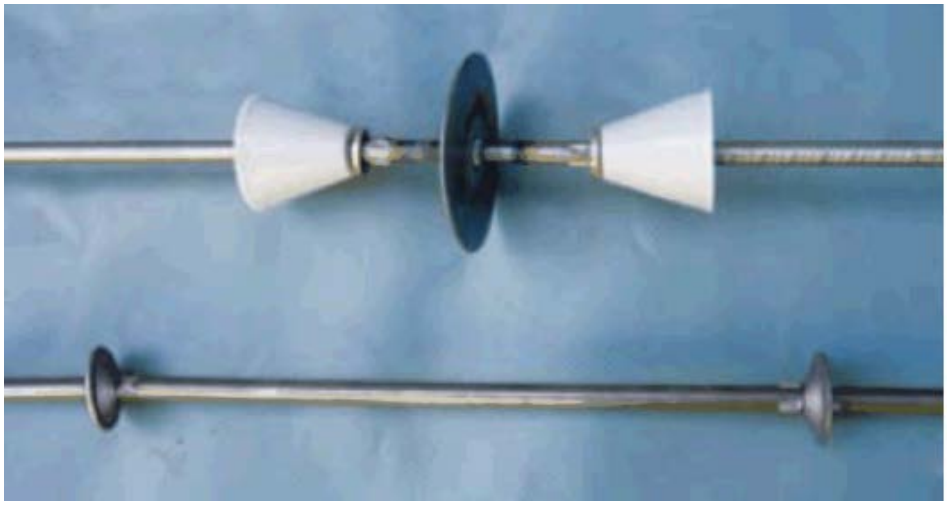

Figure 2-2. *Example of form rods.*

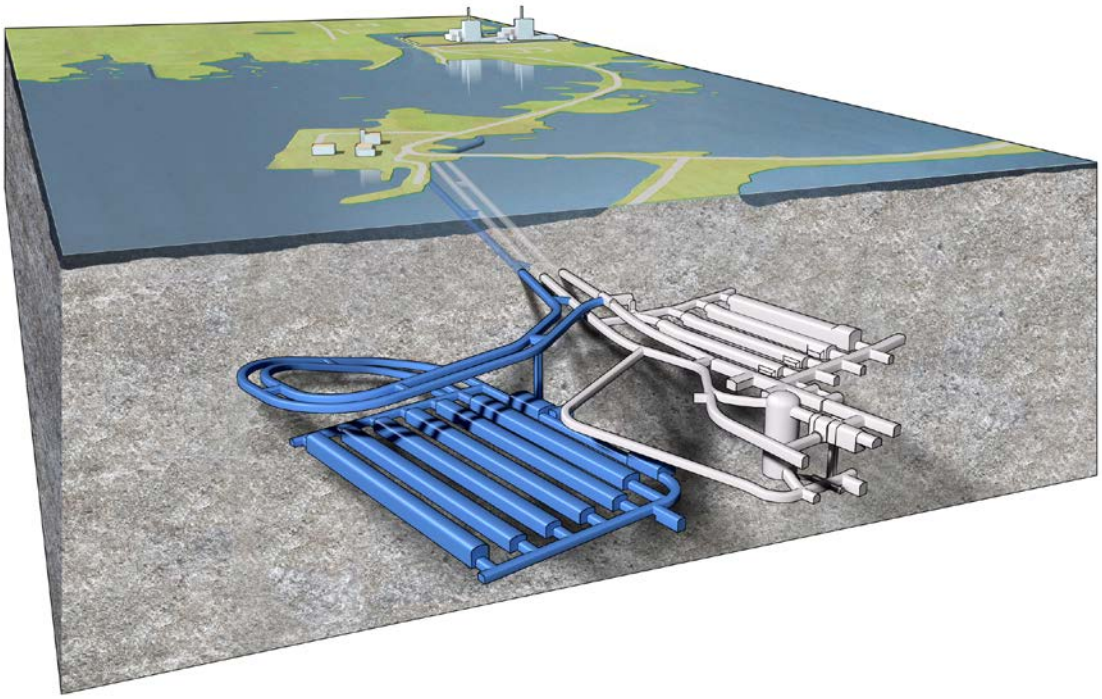

Figure 2-3. *Illustration of the SFR repository including the planned new vaults (in blue) situated slightly below the existing vaults (in grey).*

The waste intended for the BMA vaults is contained in different types of waste packaging, as shown in Figure 2-4. The waste packaging types used for 1BMA wastes are concrete moulds and steel drums. The present waste storage capacity of the 1BMA vault is:

- 576 concrete- or steel moulds per compartment, or
- 2,596 steel drums per compartment, or
- 288 moulds and 1,536 steel drums per compartment when mixed.

Figure 2-5 shows a schematic view of the concrete barriers, the concrete moulds containing the waste and the concrete grout around the concrete constructions in the 1BMA vault. During closure, the empty voids outside the concrete barriers in the 1BMA vault will be backfilled with sand or gravel. Ninety percent of the volume above the concrete constructions, under the rock ceiling, will be filled with macadam (crushed rock that has been sieved to the size fraction 16–32 mm (SKB 2014c). Dimensions of the 1BMA vault and concrete constructions are presented in Table 2-1.

Figure 2-4. *Illustration of the various types of waste packages stored in the SFR repository. The picture shows the steel drums (A), the steel mould (B) and the concrete mould (C) used for storing waste in the BMA vault.*

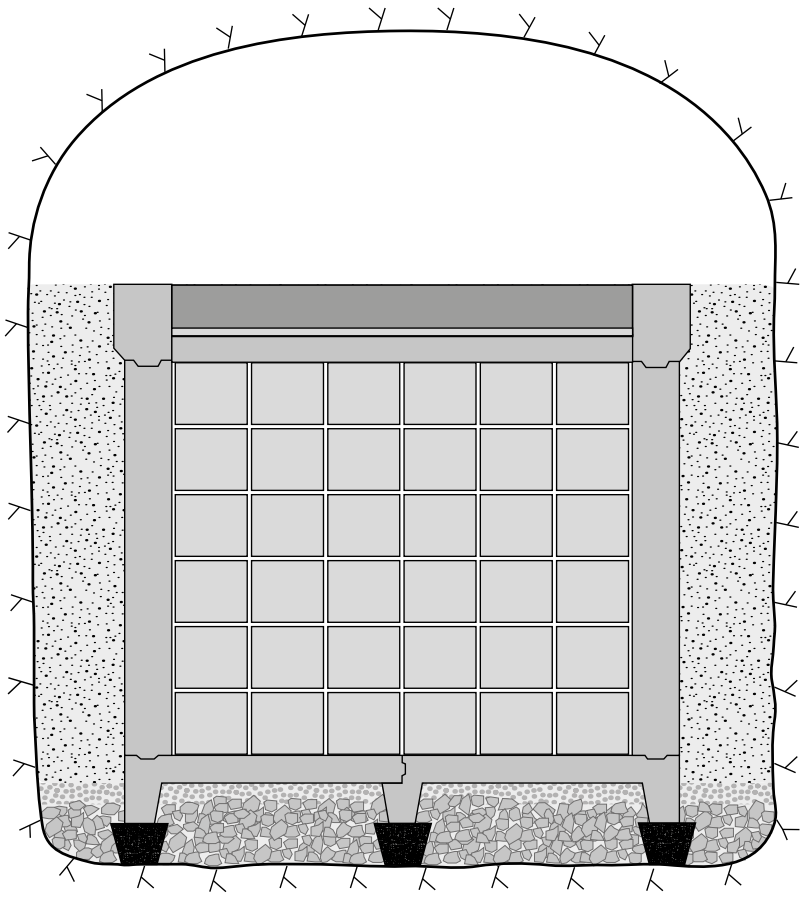

Figure 2-5. *Illustration of the different concrete barriers, concrete moulds and macadam backfill in the 1BMA vault. Figure is not to scale.*

Table 2-1. Approximate dimensions of the 1BMA vault and concrete constructions.

1BMA vault	Dimensions
Vault	
Length	160 m
Rock wall height	16.5 m
Width	19.6 m
Concrete structures	
Length	140 m
Height	8.915 m
Width	15.62 m
Empty void or sand filled slot	1–2 m
Reinforced concrete lid[1]	0.5 m
Cast concrete lid[1]	0.05 m
Concrete plank[1]	0.4 m
Side walls	0.4 m
Concrete bottom	0.25 m
Compartment wall	0.4 m
Macadam	0.15 m
Rock fill	0.3 m
Large compartments	
Number	13
Inner length	9.9 m
Inner width	14.82 m
Small compartments	
Number	2
Inner length	4.95 m
Inner width	7.2 m

[1] Total thickness of the lid should be 0.915 m (i.e. the sum of reinforced lid + cast concrete + concrete plank).

2.2 Functions considered for the system components in 1BMA

A detailed investigation of the 1BMA concrete structure has been carried out and this showed that extensive repair and reinforcement measures need to be adopted to achieve the desired barrier properties at closure. The Closure Plan for SFR (SKBdoc 1358612) describes the planned measures for the closure of 1BMA and it is assumed in the SR-PSU safety assessment that the 1BMA concrete barriers will be in good condition at closure.

The functions considered for the system components are the following:

Limited advective flow – Water flow in the concrete walls and through the waste packages should be limited. In 1BMA, the hydraulic contrast between the permeable crushed rock/macadam backfill surrounding the concrete structures and the less permeable concrete walls diverts water flow away from the compartments to the more permeable surrounding materials. In addition, the concrete grout surrounding the waste packages (except for bituminised waste) inside the concrete walls will limit the potential flow through the waste packages.

Mechanical stability – The stability of the rock vault and the concrete structure (for example in the case of rock fall) is enhanced by the concrete grout around the waste packages and the backfilling of the rock vault with macadam.

Retention – The radionuclides released from the waste packages are retained by sorption on the concrete grout surrounding the waste packages, concrete walls and the crushed rock/macadam outside the concrete structures.

Favourable water chemistry – The water chemistry in the rock vault will be influenced by the large amounts of cementitious materials in waste packaging, structures and grout. The resulting alkaline

environment will limit the rates of corrosion and microbial degradation. In addition, the creation of anaerobic conditions in the vault caused by the consumption of oxygen during aerobic corrosion and microbial respiration will favour the sorption of many radionuclides e.g. technetium and the actinides.

2.3 Overview – 2BMA

As part of the planned extension of SFR, the 2BMA rock vault will be built to receive intermediate level waste arising from the decommissioning of Sweden's nuclear sites. The concrete barriers will consist of 14 detached caissons, made of non-reinforced concrete. The floor and walls will be cast in one step to minimise joints in the constructions. The waste packages (mainly steel moulds and 4K steel moulds[1]) will be emplaced in caissons using an over head crane, see Figure 2-6. The caissons will be grouted at regular intervals using a similar type of grout to that used for the silo shafts (SKB 2014c), to minimise the mechanical stress on the non-reinforced concrete walls. The grout will form a 0.1 m layer between every set of four waste packages.

When each caisson is full, a 0.5 m thick concrete lid will be placed on top of the waste, to protect it. The concrete constructions are supported from the inside by the waste packages and the concrete grout and on the outside by crushed rock/macadam. The concrete floor rests on a bed of packed gravel (grain size 6–20 mm) which also serves the purpose as a part of a hydraulic cage around the caissons. Descriptions adapted from SKB (2014c).

A schematic view of the concrete constructions in the 2BMA vault is presented in Figure 2-7 *(note that the numbers in the figure refer to the design Layout 2.0, whereas the calculations will be based on Layout 1.5)*. At repository closure, the space between the concrete caissons and the rock walls and the space above the concrete lid are planned to be backfilled with crushed rock/macadam, see Figure 2-7.

Dimensions of the 2BMA vault and concrete constructions have been collected from SKB (2014c) and are summarised in Table 2-2.

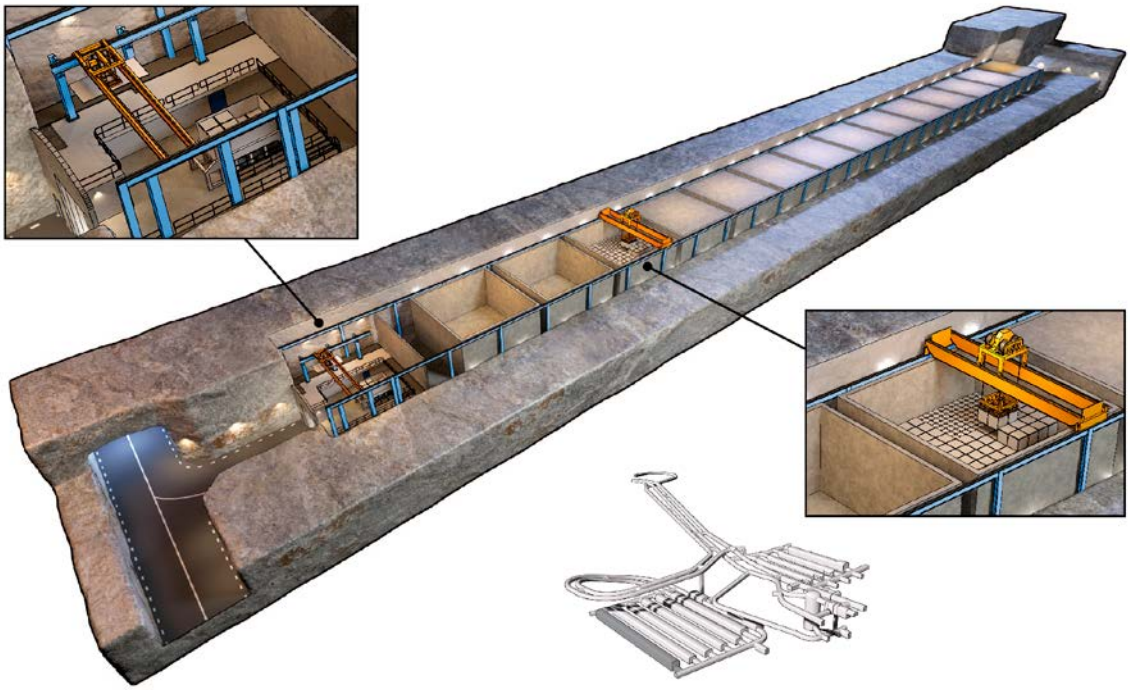

Figure 2-6. *Illustration of 2BMA during the operational phase. The inserted details show the emplacement of waste packages with the over head crane. The position of 2BMA in SFR is shown in the miniature inset (SKB 2014c).*

[1] Tetramould waste packages used for storage of trash and scrap metal (SKB 2014d).

Table 2-2. Approximate dimensions of the 2BMA vault and concrete constructions (SKB 2014c, Layout 1.5). An illustration is given in Figure 2-7.

2BMA vault	Dimensions
Vault	
Length	275 m
Height	16.8 m
Width	19.2 m
Cross-section area	310 m^2
Excavated volume	85,250 m^3
Concrete structures and rock fill	
Length	246.3 m
Height	8.4 m
Width	16.2 m
Crushed rock/gravel/macadam fill outside walls	1.5 m
Crushed rock/gravel/macadam fill above the caissons	7.35 m (average)
Concrete lid	0.5 m
Concrete walls	0.5 m
Concrete floor	0.5 m
Crushed rock/gravel/macadam fill bottom	0.4 m
Caissons	
Number	14
Inner length	15.2 m
Inner width	15. 2 m
Inner volume (one caisson)	1,710 m^3

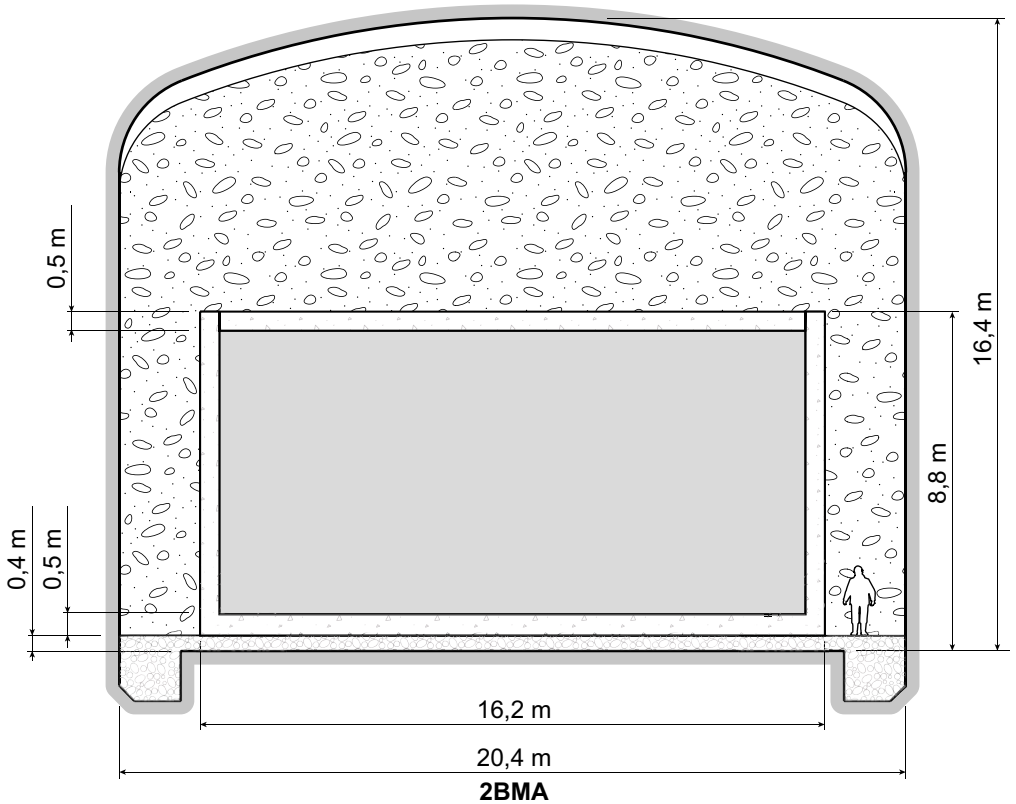

Figure 2-7. *Schematic cross section of 2BMA with macadam backfill. (Please note that the numbers in the figure refer to the design Layout 2.0, whereas the calculations will be based on Layout 1.5). (SKBdoc 1358612, Figure 4-10).*

2.4 Functions considered for the system components in 2BMA

The functions considered for the system components are the following:

Limited advective flow – Water flow in the interior of the caissons and through the waste packages should be limited. In 2BMA, the hydraulic contrast between the permeable crushed rock/gravel/macadam backfill surrounding the concrete structures and the less permeable concrete caissons will divert water flow away from the compartments to the more permeable surrounding materials. In addition, the concrete grout surrounding the waste packages in the interior of the caissons will limit the potential flow through the waste packages.

Mechanical stability – The stability of the rock vault and the concrete structure (for example to rock falls) is enhanced by the concrete grout around waste packages and the backfilling of the rock vault with macadam.

Retention – The radionuclides released from the waste packages are retained by sorption in the concrete grout surrounding the waste packages, concrete caissons and the crushed rock/gravel/macadam outside the concrete structures.

Favourable water chemistry – The water chemistry in the rock vault will be influenced by the large amounts of cementitious materials in waste packaging, structures and grout. The resulting alkaline environment will limit the rates of corrosion and microbial degradation. In addition, the creation of anaerobic conditions in the vault caused by the consumption of oxygen by aerobic corrosion and microbial degradation will favour the sorption of many radionuclides e.g. technetium and the actinides.

2.5 Properties of the concrete barriers

Concrete consists of hydrated cement clinker minerals mixed with different filler and ballast materials such as sand and gravel. Steel reinforcement bars and form rods used during construction are embedded in the concrete (1BMA only).

The concrete is manufactured from unhydrated cement, sand, gravel and possible additives. Water is added to initiate the hydration of the cement clinker minerals which leads to hardening of the concrete, as described below. Additives can be used in concrete, e.g. to improve flow properties and workability of the freshly mixed concrete slurry. In some cases significant amounts of filler materials, such as slag or fly ash, are added to change the mechanical or chemical properties of the concrete.

Composition of the cement used in SFR

The unhydrated cement clinker minerals are formed during manufacture of the cement at high temperature in cement kilns. Typical unhydrated cement clinker minerals[2] and components are:

- Tricalcium silicate, C_3S.
- Dicalcium silicate, C_2S.
- Tricalcium aluminate, C_3A.
- Tetracalcium aluminate ferrite, C_4AF.
- Calcium sulphate (gypsum), $C\hat{s}H_2$ *(added as a retardant to the cement)*.
- Alkali hydroxides, $N + K$.

The cement used for concrete constructions in 1BMA, such as the concrete walls etc, is Degerhamn Anläggningscement. The chemical composition of this cement is presented in Table 2-3 (from Höglund 2001 and SKB 2014c). The assumption for this study is that the same concrete is used for the 2BMA constructions.

[2] Abbreviations commonly used in cement science for the clinker components:
C=CaO, S=SiO_2, A=Al_2O_3, F=Fe_2O_3, H=H_2O, $C\hat{s}H_2$=$CaSO_4 \cdot 2H_2O$, N=Na_2O, K=K_2O

Table 2-3. Chemical composition of Degerhamn Anläggningscement, including both the oxide composition and the corresponding clinker mineral composition (SKB 2014c).

Component	Content % by weight
Ca	64
SiO_2	21
Al_2O_3	3.5
Fe_2O_3	4.6
MgO	0.7
K_2O	0.62
Na_2O	0.07
SO_3	2.2
Cl	< 0.1
Free $CaCO_3$	0.9
Corresponding clinker components	
Tricalcium silicate, C_3S	64.4
Dicalcium silicate, C_2S	10.9
Tricalcium aluminate, C_3A	2.0
Tetracalcium aluminate ferrite, C_4AF	13.9
Calcium sulphate (gypsum), $C\hat{s}H_2$	3.7
Alkali hydroxides, $N + K$	0.7

Degerhamn Anläggningscement satisfies the requirements of EN 197-1 Cement-Part 1: Composition, specifications and conformity criteria for common cements and is in accordance with SS 13 42 02–03 for MH/LA. Anläggningscement has a low C3A content and satisfies the requirements (i) for sulphate resistance of SR 3 type cement in EN 197-1, for low alkali cement in accordance with SS 13 42 03 and (ii) for cement with moderate heat development in accordance with SS 13 42 02. (Heidelberg Cement 2013). The specification "low alkali cement" stated in this report complies with the current standards for cement and concrete. However, this should not be confused with low-pH cements (sometimes also referred to as low alkali cements) currently being studied in connection with such radioactive waste storage facilities where hyperalkaline conditions are not desired.

Mixing proportions for concrete in SFR

The mixing proportions used for concrete components and concrete grout in SFR are presented in Table 2-4 (from Höglund 2001).

The ballast material is selected to comply with Swedish standards on resistance to alkali-silica reactions. The chemical composition of the ballast material is presented in Table 2-5.

Table 2-4. Mixing proportions for concrete structures in 1BMA in SFR, amounts given in kg/m^3.

Component	Construction concrete (Jacobsen and Gjörv 1987, SKB 2014c)	Concrete grout (SKB 2014c)
Degerhamn anläggningscement	350	325
Water	164.5	366
Ballast	1,829 (total) 0–8 mm 920 kg/m^3 8–16 mm 374 kg/m^3 16–32 mm 535 kg/m^3	1,302
Additives (anti-foaming, cellulose)	0.5% Sika Plastiment BV-40 0.05–0.2% Sika Retarder	6.5
Air	–	2.5% by volume
W/*C* ratio	0.47 (0.46–0.49)	1.125

Table 2-5. Chemical composition of the ballast material, Baskarpsand, used in the 1BMA concrete (SKB 2014c).

Component	Content % by weight
SiO_2	78.8
Al_2O_3	11.6
Fe_2O_3	1.21
CaO	1.12
MgO	0.28
K_2O	3.86
Na_2O	3.09
Loss on ignition at 1,000°C (LOI)	0.48
Proportion of free quartz	43
Sintering temperature	1,250°C

2.6 Cement hydration

Unhydrated cement clinker minerals are highly reactive in contact with water and undergo hydration reactions to form new hydrated solid compounds that give the cement its mechanical strength. The amount of water added to the cement will influence the properties of the hardened cement. The balance between the water and cement added to the mixture is termed the *W*/*C*-ratio. Since water is consumed as the hydrated minerals form, the cement clinker minerals will not be completely hydrated at low *W*/*C*-ratios (less than ~ 0.3), due to lack of water. At high *W*/*C*-ratios, water will remain in the cement after full hydration and contribute to an increased porosity. In general terms, a low *W*/*C*-ratio would give denser and stronger cement than cement with high *W*/*C*-ratio. The choice of mixing proportions is, however, a compromise between factors such as strength; degree of hydration requirements, workability of the fresh paste, special demands on the permeability etc. Commonly, a *W*/*C*-ratio between 0.3 and 0.6 is used for normal construction work. In the 1BMA vault in SFR, the construction concrete has a *W*/*C*-ratio of 0.47.

The porosity of the concrete barriers in 1BMA has been calculated from the mixing proportions in Table 2-4 and a simple hydration model presented by Höglund (1992). The results are presented in Table 2-6 (from Höglund 2001). The stated porosity refers to the total porosity of the concrete, taking into the account the presence of significant amounts of ballast that has been assumed to be non-porous.

The composition of the hydrated cement minerals in the concrete as a result of the initial hardening of the concrete has been calculated and is presented in Table 2-7 (from Höglund 2001).

Table 2-6. Porosity of the 1BMA construction concrete calculated using the hydration model by Höglund (1992).

Type of pores	Porosity (m^3/m^3)
Capillary pores	0.03
Gel pores	0.047
Contraction pores	0.022
Total porosity	0.099

Table 2-7. Composition of hydrated cement used in SFR. Composition calculated using the hydration model by Höglund (1992) from the chemical composition of the SFR cement and the mixing proportions stated in Table 2-4.

Hydrate	Amount kmol/m³ concrete	Fictive concentration kmol/m³ pore water
C_3FH_6	0.1008	1.020
C_3AH_6	0.02397	0.2424
Monosulphate	0.09613	0.9722
Ettringite	0	0
CSH-gel (Ca/Si=1.8)	1.225	12.39
Portlandite	1.036	10.48
Brucite	0.06079	0.6149
KOH	0.04607	0.4660
NaOH	0.007903	0.07993
$CaCO_3$	0.06295	0.6367
Porosity	0.099	m^3/m^3 concrete

Recent analyses of concrete sample from 1BMA indicate a somewhat higher porosity than the calculated results shown in Table 2-6. The experimental values are in the range 16.5–16.9% with a variation of +/– 2% (SKBdoc 1432256). The reason for such discrepancy between calculated and experimental values could result from the assumed W/C-ratio and the assumed density of the ballast material (which constitutes ~70% of the material).

Hydrated cement

The main binding phases of hydrated cement are calcium silicate hydrates (CSH) and calcium hydroxide (CH). In addition, two other major hydration products are produced from reactions involving calcium aluminate, calcium alumino-ferrite, and calcium sulphate, which are complex calcium sulpho ferri-aluminates[3] known as AF_t and AF_m.

The interstitial solution of an ordinary Portland-cement-based concrete will reach chemical equilibrium with the cement constituents. Since the hydrated cement minerals are alkaline, this results in a hyper-alkaline pore water (pH around 13) with high concentrations of Na^+, K^+, Ca^{2+} and OH^- ions.

[3] AF_t= $C_6(A,F)X_3H_y$ and AF_m= $C_4(A,F)XH_y$, where X=$CaSO_4$; y= 32 for ettringite and y= 12 for monosulphate.

3 Groundwater composition

The calculations in this investigation are based on the groundwater composition defined by Höglund (2001) for the salt-water period, see Table 3-1, and the fresh water period, see Table 3-2. Revised groundwater data (Auqué et al. 2013) have been made available during the study. However, the differences compared with the previous data are not major; hence the present calculations have not been updated with the more recent data. In the calculations the concentrations have been assumed to change in a stepwise manner after 2,000 years, whereas a more gradual transition would be expected to take place in reality. For further detail on the composition of groundwater assumed in the reactive transport calculations see Appendix H.

Table 3-1. Chemistry data proposed for the salt-water period (i.e. the coming 1,000–5,000 years) and the associated variation interval (Höglund 2001).

Parameter	Salt-water period		
(mg/l)	Proposed	Min	Max
HCO_3^- (alkalinity)	100	40	110
SO_4^{2-}	500	20	600
Cl^-	5,000	3,000	6,000
Na^+	2,500	1,000	2,600
K^+	20	6	30
Ca^{2+}	430	200	1,600
Mg^{2+}	270	100	300
pH	7.3	6.5	7.8
Eh* (mV)	Reducing	–400	–100
Si as SiO_2(aq)	5.66	–	–
Electrical balance %	–0.04%		

* –400 to –100 = proposed interval in Wikberg (1999).

Table 3-2. Chemistry data proposed for the fresh water period (i.e. following the salt water period presented in Table 3-1) and the associated variation interval (Höglund 2001).

Parameter	Fresh water period		
(mg/l)	Proposed	Min	Max
HCO_3^- (alkalinity)	300	170	540
SO_4^{2-}	50	3	110
Cl^-	45	5	1,000
Na^+	100	20	200
K^+*	4	0.2	10
Ca^{2+}	35	25	140
Mg^{2+}	9	3	10
pH	7.49	6.7	8.7
Eh (mV)	Reducing	–400	–100
Si as SiO_2(aq)	5.9		
Electrical balance %	–0.08%		

* Proposed value= rounded “Allard standard water” (Höglund et al. 1997). Min and max values are taken from measurements made by SGU in Swedish groundwater “SGUs grundvattennät” and “PMK-grundvatten”; (Bertills 1995).

4 Degradation processes for concrete

This chapter reviews the current understanding of chemical and then mechanical/physical concrete degradation mechanisms. A simplified modelling approach is used to investigate the impact of drying shrinkage during the operation, of contraction due to cooling by inflowing groundwater after closure, and of the corrosion of steel reinforcement on the rate and mechanism of concrete degradation. The sections relating to chemical degradation are based on SKB (2014a), but further information is provided where appropriate. The information in this section is used to identify the processes and mechanisms most likely to affect barrier function.

4.1 Relevance of chemical degradation processes

Concrete degradation may occur as a result of different chemical processes such as dissolution, precipitation and recrystallisation. These processes may occur as a result of interactions between the concrete barrier materials, the groundwater, the waste and the host rock. In addition to chemical degradation processes, different physical and mechanical effects can affect the integrity of the concrete barriers; of particular importance are processes leading to formation of fractures in the concrete barriers.

The chemical degradation of the concrete barriers includes the leaching of soluble chemical components, which gradually leads to the depletion of the components that bind the cement. Therefore, the mechanical strength and the stiffness of the concrete will decrease as result of leaching. Leaching may also increase the porosity of the barriers thereby increasing their diffusivity and hydraulic conductivity (Ekström 2003). Leaching will also deplete the most alkaline components of the concrete first, which results in a gradual reduction of the pH in the repository. This may affect the retention of radionuclides in the barriers. Other chemical processes may occur due to interactions with certain chemical components in the groundwater or in the waste, e.g. sulphate that can affect the cement mineral assemblage, potentially leading to fracture formation. Occurrence of fractures would significantly reduce the ability of the concrete barriers to supply the desired safety function as a hydraulic barrier.

This description focuses on the degradation of concrete barriers in the BMA vaults. Where appropriate, other components of the vault and the concrete grout are also included in the descriptions. Dissolution, precipitation and recrystallisation reactions are of great importance, as they affect the hydraulic and chemical properties of the cementitious barriers. These reactions therefore affect the safety functions of the BMA barriers over time.

4.1.1 Dissolution, Precipitation and Recrystallisation

Precipitation occurs when a solution becomes supersaturated with respect to a solid phase. Dissolution occurs when a solid chemical compound is undersaturated with respect to the solution it is in contact with. Congruent dissolution means a complete disintegration of the solid compound and the formation of dissolved species that enter the solution phase. Incongruent dissolution means a dissolution process where one of the solid phase chemical components is preferentially dissolved and released, followed by a corresponding change in the solid phase composition. Net dissolution can continue as long as any mass of the solid phase remains and the solubility limit of the solution is not reached. Net precipitation can take place as long as the solution remains oversaturated. The dissolution and precipitation processes continue also when saturation is reached, however the two processes proceed at equal rates which means that the concentrations in solution and the amount of the solid compound remain unchanged.

The rate and extent of dissolution and precipitation processes in the concrete barriers is influenced by:

- The rate of advective water transport carrying dissolved species.
- The rate of diffusive transport of dissolved species.
- The composition of the concrete barriers including the assemblage of hydrated cement clinker minerals.

- Any changes in the chemical composition of the concrete barriers induced by chemical reactions with surrounding rock/groundwater, waste packaging, porewater or conditioned waste. This may in turn influence the microstructure of the concrete which would affect its transport properties.
- The composition of concrete barrier pore water. This is in turn determined by local thermodynamic equilibria between the pore water and the solid hydrated cement minerals.
- Kinetic factors causing metastable equilibria or slow establishment of equilibria.

During recrystallisation, the structure of a precipitated compound gradually becomes more ordered, i.e. achieves a higher degree of crystallinity, while maintaining the same chemical composition. The driving force for recrystallisation is the higher thermodynamic stability (lower solubility) of more crystalline structures. The general tendency in a static chemical system, i.e. in a system with invariant ambient conditions, is therefore to form compounds of increasing crystallinity over time.

In reactive systems, such as in cement during hydration, kinetic factors will have an impact on the compounds that are precipitated. The interfacial free energy (solid mineral – solution) is higher for more crystalline phases, which have a lower solubility, of a certain mineral. Hence, according to the Ostwald step rule, see e.g. Stumm (1992), kinetics will favour precipitation of the least supersaturated compounds from the pore water solution, thereby creating a solid phase that may be metastable compared to more crystalline phases. According to the Ostwald principle, the recrystallisation processes may therefore proceed in many small steps, which over time results in increased crystallinity, interfacial free energy and size of crystals.

Recrystallisation processes may be of importance for understanding the long-term properties of e.g. CSH-gels in concrete. Recrystallisation may have an impact on the pore geometry since the very fine-structured amorphous and/or microcrystalline tobermorite-like and jennite-like mineral phases may gradually change in shape. The pore geometry may have a significant impact on the hydraulic conductivity and the diffusivity.

4.1.2 Leaching and interaction with groundwater/waste

A good understanding of cement hydration processes, see previous chapter, is an essential starting point for the description of dissolution/precipitation/recrystallisation processes that result from leaching by groundwater.

Leaching by groundwater

Hydrated cement minerals are fairly soluble in comparison with many rock forming silicate minerals, which means that they are more susceptible to dissolution and degradation. The contact of the alkaline concrete porewater with dilute groundwater (pH lower than 9) at the exterior of the repository creates large concentration gradients which induce diffusive mass transport (of mainly Na^+, K^+, Ca^{2+} and OH^- ions) in the concrete porewater.

Inflow of ambient groundwater by advection will gradually drive away the concrete porewater components and enhance the diffusion of ions and the degradation of cement. However, in many cases the dissolution of one mineral may result in the precipitation of another. The high pH created by dissolution of the hydrated cement minerals in the concrete may also increase the reactivity of other minerals present in the concrete (e.g. ballast, filler materials or other additives), in the waste packaging, waste, macadam backfill material, or host rock.

During the initial stage of cement degradation, the pore water will be dominated by alkali metal hydroxides (composed of K^+, Na^+ and OH^- ions) which give hyper alkaline conditions with a pH of ~ 13. Generally, the alkali metal hydroxides are soluble, and would therefore be easily leached from the concrete. Studies of the composition of concrete solid phases and porewater show, however, that the leaching of alkali metal hydroxides is retarded due to some type of chemical interaction with the solid phases, likely the CSH-gel phases or the ballast (Lagerblad and Trägårdh 1994). Leaching of alkali metal hydroxides ions will therefore decrease gradually, rather than in a stepwise manner. As the pH decreases, the solubility of the calcium hydroxide (portlandite) and of the CSH-gel will

gradually increase. During the portlandite leaching phase, the pH is buffered to ~12.5. This is followed by the pH gradually decreasing to ~ 10 as incongruent leaching of CSH-gel occurs (SKB 2008). As a result, the Calcium to Silica ratio (Ca/Si-ratio) of the CSH-gel gradually decreases due to leaching.

The durability of cement is affected by the decalcification process, since calcium is the main component of hydrated cement. The continuous outwards diffusion of dissolved calcium and/or hydroxide ions alters the original chemical equilibrium, and induces dissolution of calcium compounds to restore chemical equilibrium. The dissolution of calcium hydroxide (portlandite) and CSH-gels leads to an increase in the porosity of the concrete, which at the same time enhances the diffusion rate and the hydraulic conductivity (Ekström 2003). Loss of calcium also reduces the mechanical strength that may result in fracture formation and, ultimately, in collapse of the barriers.

The dissolution of CSH-gels needs special consideration. The reason is that the CSH-gels will preferentially leach calcium hydroxide, leading to an incongruent dissolution of the gels. This has the effect that the remaining gels will become gradually enriched in silica. Simplified, this can be seen as a dissolution/precipitation reaction where a calcium hydroxide-rich phase dissolves and a new phase with slightly lower calcium hydroxide content precipitates immediately afterwards. A more correct conceptualisation may be that calcium is released from the CSH-gel into solution followed by a rearrangement of the partly calcium-depleted solid silicate phase. Experimental evidence shows an increased length of the silicate anion chains in leached CSH-gels (Haga et al. 2002). The solubility of the CSH-gel is complex due to its amorphous to semi crystalline structure, which might be described in terms of a mixture of tobermorite- and jennite-like phases (Chen et al. 2004). Detailed investigations have shown that CSH-gels have a large variability in their composition, nanostructure and morphology (Richardson 2004). Significant efforts have been made to understand the processes and structure of CSH-gels formed during cement hydration. Different attempts have been made to determine the relationship between solid phase composition and the composition of the porewater in CSH-gels, and a comprehensive overview and compilation of experimental data from earlier studies is presented by Chen et al. (2004). Based on interpretations of these earlier data and new experiments, Chen et al. (2004) suggest that the observed variability of the solubility of CSH-gels, especially at high Ca/Si-ratios, can be explained by different experimental approaches that may cause differences in the silicate structure, in particular the occurrence of Ca-OH bonds in CSH-gels with jennite-like structure. The results also suggest that CSH solids are present in different metastable phases that are susceptible to transforming/recrystallising into one another in the long term. Experimental studies by Baur et al. (2004), using radioisotopes to determine the dissolution-precipitation rates of ettringite, monosulphate and CSH under equilibrium conditions, show evidence that a complete reconstruction can be achieved during 1–4 years. Experimental investigations using combined small-angle neutron and X-ray scattering data have generated data on the density of CSH-gels that differ from previous estimates that were based on different drying techniques (Allen et al. 2007).

The dissolution of calcium silicate hydrates is accompanied by the leaching of other minerals in the cement. AF_m dissolution releases $Al(OH)_4^-$, which will also diffuse out and could induce precipitation of either secondary AF_m or ettringite in the presence of excess sulphate. The large molar volumes and crystalline morphologies of these minerals may reduce the porosity and mechanical strength of the cement by producing micro-cracks (Lagerblad 2001).

Chemical interactions with groundwater

The reactions between certain hydrated minerals and dissolved compounds transported in the pore water are important in concrete. The chemical composition of groundwater and the porewaters of the waste and waste packaging affect the rate of concrete barrier degradation. Laboratory experiments have shown that the degradation depth is highly dependent on the carbonate concentration of the external solution. If the external groundwater contains dissolved carbon dioxide, precipitation of calcite might be expected. This has been found to reduce the degradation rate by sealing the pore network on the exposed surface of cement (Pfingsten 2001). A study by Moranville et al. (2004) showed that leaching depth decreases by a factor of 5 when the external water is in equilibrium with atmospheric CO_2, due to the sealing produced by calcite precipitation at the cement-water interface. Brucite may also be prone to precipitation at the cement-groundwater interface, due to its low solubility at high pH (Lagerblad 2001). Also the availability of concrete mineral surfaces as sorption sites may be affected by such sealing processes.

An external groundwater containing dissolved sulphate could also have a large impact on the longevity of concrete material (Höglund 2001) due to reaction with calcium aluminates causing ettringite precipitation. Ettringite has the ability to bind large amounts of water as waters of crystallisation, resulting in this mineral phase having a large molar volume. Unless sufficient pore volume is available to accommodate the mineral formed, this could result in cracking and mechanical deterioration of the concrete. The porosity of the concrete affects the rate of ettringite formation and concrete deterioration, as it controls the inwards migration of sulphate (e.g. Marchand et al. 2002). It has also been argued that gypsum formation can be expansive and cause deterioration (Tian and Cohen 2000). Gypsum is typically only found at high sulphate concentrations, higher than those encountered in most natural groundwaters.

The chloride concentration of the groundwater can also affect the long-term behaviour of the cement due to the precipitation of Friedel's salts (i.e. calcium-aluminium chlorides). It has been suggested that chloride can reduce the impacts of sulphate attack; since the chloride ion has a higher diffusion rate than SO_4^{2-}, its reaction with calcium aluminate and calcium hydroxide has been seen to block the formation of ettringite (Zhang et al. 2013). However, in experiments simulating a radioactive liquid waste with high Cl^- and SO_4^{2-} (0.5 M), liquid/solid ratio = 22), the converse was seen; with SO_4^{2-} reacting preferentially with calcium aluminate hydrates (Guerrero et al. 2009). A combined attack by sulphate and carbonate at low temperature may lead to precipitation of thaumasite ($Ca_3Si(OH)_6(SO_4)(CO_3)\cdot 12H_2O$) by reaction with AF_m/AF_t phases where silica from CSH-gel has replaced aluminate. This could cause the concrete to deteriorate (Justnes 2003). Different routes have been described for the formation of thaumasite, e.g., i) where ettringite reacts with CSH and calcite, or ii) where CSH reacts with gypsum and calcite as suggested by Bellmann (2004). Damidot et al. (2004) have modelled the complex system of $CaO\text{-}Al_2O_3\text{-}SiO_2\text{-}CaSO_4\text{-}CaCO_3$ and suggest that thaumasite is stable at lower pH than ettringite but requires higher sulphate concentrations. Model exercises by Glasser and Matschei (2007) show a complex reaction sequence involving in the initial stages AF_m, hemi-carbo aluminate, ettringite, mono-carbo aluminate, portlandite and calcite, whereas the later stages involves mono-carbo aluminate, calcite, strätlingite, ettringite, CSH-gel, thaumasite, aluminium hydroxide, gypsum and amorphous silica.

Local supersaturation of minerals in the pore water may occur in response to any rapid changes of the external chemical conditions, such as release of dissolved compounds from the waste or sudden changes of the groundwater composition. This could result in the formation of colloidal material in the pore water. However, studies of the alkaline springs in Maqarin, Jordan (Smellie 1998) support the expectation that the colloid concentration would be low due to the high concentration of calcium ions in the vicinity of cement and concrete. A review of colloids in the near-field of cementitious repositories is given in Swanton et al. (2009). Since colloid formation is not expected to have an impact on the barrier degradation, colloids are not treated further in this study.

Under hyper-alkaline conditions there is a risk of alkali-silica reactions between the hydroxyl ions leached from the cement and reactive silica in ballast material. This causes formation of alkali-silica gels that increase in volume by uptake of water and exert an expansive pressure, eventually leading to fracture formation. This reaction is known to be deleterious for the mechanical strength of cement and concrete. The cements and ballast materials used for construction concretes in SFR are selected to avoid this type of reaction.

Minor amounts of special chemicals may be used as additives to the concrete, including lignosulphonate-based plasticisers (used to increase flow properties and workability of the fresh concrete mix before hardening) and retarders (used to slow down the early hydration) that may include sugar, sucrose, sodium gluconate, glucose, citric acid, and tartaric acid. Typical amounts of additives are on the order of less than 1 to 2% of the amount of cement in the concrete. Concrete additives are not known to cause degradation of the hardened concrete, whereas the macromolecular additives tend to be strongly sorbed to the concrete minerals (Hakanen and Ervanne 2006). The chemical stability of concrete additives is described in SKB (2014d). Aspects of the organic compounds that may be used as additives to the concrete as a substrate for microbial metabolism are treated in SKB (2014a).

Chemical interactions with compounds leached from the waste

Initially, the concrete barriers will protect the waste packaging and the cement waste matrices from the direct influence of groundwater as the groundwater passes through the barriers first. However

over time this buffering capacity will be depleted and the concrete barriers will, to some extent, be influenced by the leaching and transport of soluble cement minerals from the waste packaging and cement waste matrices.

The migration of chemical species from the waste may initiate chemical reactions that could affect the integrity of the concrete barriers. Of particular importance is the presence of waste containing significant amounts of soluble salts or degradable materials such as ion exchange resins that may expel sulphate, and cellulose and plastics that may form organic acids, including iso-saccharinic acid, see SKB (2014d).

Exposure to increased concentrations of dissolved species released from the waste may induce dissolution – precipitation such as: the formation of ettringite from monosulphate and/or calcium aluminates/ferrites following increased exposure to sulphate; the formation of Friedel's salt as result of increased chloride concentrations; or the precipitation of thaumasite as a result of increased exposure to carbon dioxide/dissolved carbonate species and sulphate. Further description of possible effects of different components in the waste that may affect cement based materials is given in SKB (2014d).

The chemical interactions between the macadam backfill material and the alkaline leachate from the concrete barriers will depend on the properties of the macadam backfill used. If the macadam backfill material resembles the ballast material used in the construction concrete, with low reactive silica content, deleterious reactions with the leachate would be unlikely.

4.1.3 Overview of previous model studies/experimental studies

A large amount of research has been reported in the scientific literature involving accelerated laboratory leaching tests of relevance for dissolution, precipitation and recrystallisation processes in concrete; examples of important papers are those of Carde et al. (1996), Faucon et al. (1998), Catinaud et al. (2000), Saito and Deguchi (2000), Moranville et al. (2004) and Maltais et al. (2004). The influence of the cement particle size for the performance of Portland cement has been studied by Bentz et al. (1999). Different cement hydration models have been evaluated by Bentz (2010).

Reactive transport-based models of concrete degradation require that geochemical species and processes are selected for inclusion. Maltais et al. (2004) suggest that the inclusion of potassium, sodium, magnesium, calcium, sulphate, hydroxide, aluminium and chloride is sufficient to describe most degradation processes. However other sets of chemical components have also been proposed, e.g. the addition of silica (Höglund 2001, Moranville et al. 2004, Hidalgo et al. 2007), iron (Möschner 2007), carbonate (Höglund 2001) and fluoride (Savage et al. 2011).

An additional challenge in modelling arises from the sensitivity of the results to small differences in thermodynamic data. For example, Damidot et al. (2011) noted differences in the mineralogy calculated using two cement databases, despite the thermodynamic data lying well within the reported literature data ranges. They recommended sensitivity analysis as a tool for addressing uncertainties, and the use of experimental evidence to back up the results where possible.

In their review, Lagerblad and Trägårdh (1994) have pointed out that the early models used to describe the leaching of alkali and calcium hydroxides in the SFR safety assessment were oversimplified. The criticism reflects the simplifications made when calculating the leaching of alkali hydroxides as dissolved substances, and the fact that the counter effect of alkali metals ions in the groundwater was neglected, leading to a rapid depletion of alkali metal ions in the concrete material. Furthermore, the leaching of calcium hydroxide and calcium silicate hydrates (CSH-gel) was represented as being independent of the alkali metal leaching. Experimental studies by Glasser et al. (1985) indicate retention of sodium and potassium by hydrated cement minerals. Modelling of cement degradation by Berner (1990) addressed the alkali metal retention by assuming that 5% of the remaining inventory of sodium and potassium is released in each pore water exchange cycle. In the model study by Höglund (2001) the leaching of alkali hydroxides was represented by ion exchange processes, also taking into account the counter ion effect of the surrounding groundwater. The model for the ion exchange processes was calibrated against experimental data by Lagerblad and Trägårdh (1994). The modelling results showed a significantly different leaching behaviour for the alkali metal hydroxides compared to the previous estimates. A similar modelling approach has been reported by Savage et al. (2011).

Further, in modelling studies by Höglund (2001) and Moranville et al. (2004) the leaching of different calcium compounds, e.g. portlandite, CSH-gel and AF_m/AF_t-phases, was coupled to the leaching of alkali hydroxides. This has the effect that during the early period, the leaching of calcium compounds is suppressed by the high pH maintained by the alkali hydroxides in the pore water. The available data for thermodynamic calculations have significantly improved since the early studies for SFR, especially regarding the preferential leaching of calcium from CSH-gels with variable Ca/Si-ratio. Extensive experimental data have also been provided, combined with modelling, for different chemical systems including different combinations of calcium, silica, aluminium, sulphate, carbonate, sodium, potassium and chloride (Stronach and Glasser 1997, Perkins and Palmer 1999, Baur et al. 2004, Barbarulo et al. 2007, Birnin-Yauri and Glasser 1998, Damidot et al. 1992, 1994a, b, Damidot and Glasser 1993, 1995, de Silva and Glasser 1993, Glasser et al. 1999). Faucon et al. (1998) used a combination of experimental studies and modelling to investigate the re-precipitation of secondary minerals including AF_m, ettringite and calcite in a cement exposed to demineralised water. The impact of temperature on the stability of ettringite and its consequences for delayed ettringite formation is discussed by e.g. Höglund (1992) and Glasser (1996). Detailed studies of solid-solutions between Al- and Fe-ettringite minerals have been presented by Möschner (2007), with experimental data presented also for Fe-monosulphate and Fe-monocarbonate. The formation of Fe-ettringite phases is slower than the corresponding Al-ettringite, with time constants on the order of a few months and few weeks respectively (Möschner 2007). It was also found that Al-ettringite is more stable than Fe-ettringite at high pH, Fe-ettringite being gradually replaced by Fe-monosulphate at pH > 13.1 (Möschner 2007).

In early studies for SFR the limiting Ca/Si-ratio for the CSH-gel was assumed to be 2.5, and this has been shown to be too high (Stronach and Glasser 1997). The CSH-gels are commonly represented by a solid solution series that varies in composition roughly between $C_{1.8}SH$ and $C_{0.8}SH$. Berner (1990) modelled the incongruent dissolution, assuming CaH_2SiO_4 and $Ca(OH)_2$, and SiO_2 and CaH_2SiO_4, respectively as end-members for calcium-rich and calcium-depleted CSH-gels, and adjusting the apparent solubility product as a function of the Ca/Si-ratio. In the study by Höglund (2001), the CSH-gel was represented by three discrete CSH mineral phases: $C_{1.8}SH$, $C_{1.1}SH$ and $C_{0.8}SH$. The $C_{1.8}SH$-phase may coexist with portlandite in the more alkaline regime, whereas $C_{0.8}SH$ may coexist with amorphous SiO_2 in highly leached concrete. In the intermediate regime, between highly alkaline and highly leached conditions, $C_{1.1}SH$ coexists with either $C_{1.8}SH$ or $C_{0.8}SH$ depending on the Ca/Si-ratio. The model applied by Höglund (2001) accounts for the gradual transformation of portlandite and CSH-gel between these different mineral phases. Moranville et al. (2004) and Gaucher et al. (2005) used a similar approach. Kulik and Kersten (2002) report an upper end-member composition corresponding to $C_{1.7}SH$. In a modelling exercise of the early hydration reactions of Portland cement, a limiting composition of the CSH-phase corresponding to $C_{1.67}SH$ was used (Savage et al. 2011).

It has been concluded by Benbow et al. (2007) that modelling of cement degradation is complex, and the process will be controlled by the incongruent dissolution of the CSH gel over long periods. Benbow et al. (2007) have compared three different models representing the gradual degradation of CSH, developed by Börjesson et al. (1997), Walker (2003) and Sugiyama and Fujita (2005). The models by Börjesson et al. (1997) and Walker (2003) use calculations of the excess energy of the solid solution as a function of its composition as a method for determining the solid phase activity coefficients. Sugiyama and Fujita (2005), on the other hand, applied conditional equilibrium constants related to the solid phase activity coefficients. The models also differ with respect to the selection of solid-solution end-members; Börjesson et al. (1997) and Walker (2003) consider portlandite and a CSH gel, whereas Sugiyama and Fujita (2005) consider portlandite and SiO_2(s). A comprehensive literature review of different approaches to represent the CSH-gel in models is given in Soler (2007). In a recent comparative study, different model approaches have been applied to mimic experimental data on the early hydration processes in Portland cement (Savage et al. 2011).

Recent efforts have been made to improve the modelling capabilities with respect to the incongruent dissolution-precipitation of CSH-gel phases in the cement (Grandia et al. 2010). Some criticism is given to earlier modelling attempts where modelling of the incongruent dissolution-precipitation of the CSH-gels was attempted as a solid solution process. The main criticism is that the CSH-gels are in fact not crystalline phases and hence are not solid solutions. Grandia et al. (2010) have nevertheless used two different methods to estimate equilibrium constants for discrete mineral compositions in the assumed solid solution series to represent the CSH-gels. The approach resembles those used by Höglund (2001) and Gaucher et al. (2005), although it is more detailed with up to 21–30 discrete mineral phases representing the CSH-gels.

The long-term leaching of concrete has been reported to follow a dissolution and precipitation sequence involving the following steps (Hidalgo et al. 2007):

- Dissolution of portlandite.
- Decalcification of CSH-gel.
- Silicate polymerisation.
- Incorporation of tetrahedral and/or hexagonal aluminium in the silica structure to give an aluminosilicate gel.

Model studies of cement degradation have also been used to estimate the impact of leaching on the physical properties (i.e. porosity, diffusivity) and how these changes affect the leaching process. Some of the models involve adjusting parameters to fit curves derived from experimental data (Yokozeki et al. 2004) and some others are either "pure" random models (Bentz and Garboczi 1992) or "hybrid" models, where randomness is constrained by appropriate user-defined probability distributions (Marchand et al. 2001). A pure mechanistic approach for cement degradation modelling requires the coupling of multi-component solute diffusion and chemical reactions taking place in the system, as well as a model of the microstructure of cement and concrete and how it evolves over time. Dimensionless analyses of diffusion and reaction rates demonstrate the adequacy of a local equilibrium assumption for coupled reactive transport modelling of cement leaching (Barbarulo et al. 2000). By this approach, a mixed non-linear set of equations can be solved numerically. The domain of the problem could be represented either as a homogeneous medium, obtained by averaging the variables of interest over a representative elementary volume, or a pore structure modelled on the basis of microstructural information, such as that provided by mercury intrusion porosimetry, or on the reconstruction of the microstructure by means of random models (Bentz 1999). The latter has been addressed by Moranville et al. (2004). Model studies of the long-term stability of concrete barriers in the SFR repository have addressed the impact of leaching processes on changes in porosity and diffusivity over time (Cronstrand 2007). The model calculates the porosity change due to precipitation – dissolution processes and applies the relationship suggested by Bentz and Garboczi (1992) to describe the effect on diffusivity.

The possible impacts of the release of different salts from evaporator concentrates intended for disposal in SFR on cement and concrete have been studied by geochemical and reactive transport modelling (SKBdoc 1417785). The importance of sodium, potassium, magnesium, chloride, sulphate, carbonate, nitrate, phosphate, sulphide and ionic strength was evaluated, as well as the effect of pre-treatment of the salt concentrates with lime. Model results indicate the presence of halite (NaCl), hydroxiapatite ($Ca_5(PO_4)_3OH$), magnesite ($MgCO_3$), thenardite (Na_2SO_4) and thermonatrite ($Na_2CO_3 \cdot H_2O$) in the evaporator concentrates.

Experimental investigations have been performed to study the impact of salts on concrete stability, mimicking the composition of evaporator concentrates in SFR (SKBdoc 1032170). Different cement mixtures were tested and the mechanical strength, weight increase and swelling of test specimens were measured. No deleterious effects were seen over a period of one year.

Studies of the leaching of portlandite and CSH-gel have shown that the depletion of portlandite is responsible for ~ 70% of the loss of concrete strength, whereas only a minor part of the loss can be attributed to leaching of CSH-gel (Carde et al. 1996).

Experimental evidence has also been reported on long-term concrete leaching through the analysis of old, man-made, cementitious structures (Álvarez et al. 2000, Lagerblad 2001, Yokozeki et al. 2004). Calcium leaching and concrete degradation was observed to a depth of approximately 100 mm following 100 years exposure to water (Yokozeki et al. 2004).

Sulphate attack has been investigated in several studies, and expansion due to ettringite and gypsum formation has been identified in concretes exposed to high concentration (5% i.e. 50 g/L) sulphate solutions (Ramezanianpour and Hooton 2013, Kunther et al. 2013, Sahmaran et al. 2007). Gypsum formation is of greatest importance at either high sulphate concentration (> 8,000 ppm) or below pH 11.5–12 (Santhanam et al. 2001). However, it has also been predicted to form when concretes are in contact with weak sodium sulphate solutions at pH ~12.5 (Marchand et al. 2002). Cements with a high C_3S/C_2S ratio produce greater amounts of portlandite ($Ca(OH)_2$) during hydration, making them vulnerable to gypsum and ettringite formation under sulphate attack (Sahmaran et al. 2007).

Ettringite formation has also been found to have induced expansion and spalling on the surface of a 45 year old concrete lining of a tunnel ventilation shaft[4], and thaumasite was found in cracks created by the ettringite-triggered expansion. Calcite and portlandite dissolution were sources of carbonate and calcium respectively for thaumasite formation, and the transformation of the cement paste to thaumasite led to its near complete disintegration (Leeman and Loser 2011). Gypsum was only detected in severely deteriorated areas very close to the rock face, with sulphate above 20 mass%. The results were reported to be in general agreement with laboratory leach tests and thermodynamic data, with the suggestion that the zones of gypsum formation also had a low alkalinity. Schmidt et al. (2009) found that exposure of cement to a 0.4% sulphate solution resulted in the formation of ettringite and then, in limestone-containing cements and after the cement had cracked, thaumasite. Also, while thaumasite was seen when the experiments were carried out at 8ºC, virtually none was seen at 20°C. Gypsum formed when 4.4% Na_2SO_4 was used, but again in pre-formed cracks. In all experiments, the rate of expansion accelerated rapidly once cracks reached a pivotal thickness. Although modelling showed that gypsum formation was dependent on the solution phase sulphate concentration, it did not show the sensitivity of thaumasite formation to temperature. Ramezanianpour and Hooton (2013) also found that cracking, which resulted from gypsum and ettringite formation in their laboratory study using 5% Na_2SO_4, was a prerequisite for thaumasite formation.

Limestone-containing concretes are clearly at greater risk of thaumasite formation due to their carbonate content, and this has been demonstrated in the laboratory by Torres et al. (2004). Low temperatures may enhance thaumasite formation, therefore laboratory studies are often carried out at 5°C, including those of Torres et al. (2004) and Ramezanianpour and Hooton (2013). Therefore field observations of thaumasite may be important indicators that thaumasite formation does not only occur at low temperatures (Santhanam et al. 2001). Matschei and Glasser (2010) conclude that C_3AH_6 is destabilised in the presence of carbonate and/or low temperatures < 8°C and is unlikely to form in calcite saturate Portland cement at temperatures < 40°C. Since calcite has been observed in the ballast of the 1BMA concrete this may be relevant (SKBdoc 1432256 ver 1.0).

In terms of modelling sulphate attack, Sun et al. (2013) showed that inclusion of damage evolution in the concrete samples improved the model fit to experimental data, due to the enhanced access of sulphate into the concrete. Sorption of aggressive species can be an important removal mechanism; Florea and Brouwers (2012) showed that differentiation between the Cl^- binding abilities of different hydrated cement phases improved their model fit to experimental data over a wide range of Cl^- concentrations.

New experimental studies have been initialised within the Äspö-project as well as by Ringhals nuclear power station. The emphases of these studies are on reactions and degradation processes in concrete materials. The Äspö experiments are expected to run for up to 40 years (SKB 2010).

The chemical degradation of cement conditioned ion exchange resins may potentially be a source of chemical compounds that could affect the concrete barriers. Examples include the release of sulphate ions from sulphonic acid-type ion exchange resins, which may lead to ettringite formation, and the release of carbonate ions from carboxylate-type ion exchange resins that may form carbohydrate minerals. The risk of thermal and chemical degradation of carboxylate-type ion exchange resins has been investigated by literature survey and experiments by Allard et al. (2002). It was concluded that the ion exchange resins are very stable under alkaline conditions and that the main form of degradation that may occur is likely to involve decarboxylation.

4.1.4 Natural analogues/observations in nature

Natural analogues to alkaline cements have been extensively studied at the hyperalkaline springs in Maqarin in northern Jordan (Pitty and Alexander 2011, Smellie 1998). The Maqarin natural analogue site is considered to be a good representation of the processes occurring in a cementitious repository during portlandite and CSH-gel phase dissolution. Three different stages of concrete degradation have been identified:

1. An early, hyperalkaline stage dominated by leaching of sodium and potassium hydroxides.
2. An intermediate stage with a slightly lower pH determined by dissolution of portlandite.
3. A late and less active stage with a lower pH, dominated by dissolution of silica.

[4] Here the concrete was produced using a low C3A-cement and aggregates that contained calcite and the local groundwater contained ~2,000 mg/L sulphate.

Tobermorite is a naturally occurring mineral (roughly with the composition $Ca_5Si_6O_{16}(OH)_2 \cdot nH_2O$) that can be seen as a crystalline analogue to CSH-gels in cements. Tobermorite can also be obtained as a crystalline product by gently heating CSH-gels in cement (Parsons 2010), thus indicating the importance of changes in temperature for long-term recrystallisation processes. The natural cement clinker and concretes in Jordan are generally highly stable and the impervious material only leach when fractured (Pitty and Alexander 2011).

CSH-gel has been reported to be persistent in nature over periods of 10,000 years, despite it being metastable with respect to crystalline phases such as tobermorite and jennite (Stronach and Glasser 1997). Very old gels have been reported in natural cements from Scawt Hill, Northern Ireland and Maqarin, Jordan (Milodowski et al. 1989, 1998). These are up to 2 Ma old in Jordan (Pitty and Alexander 2011) and possibly more than 100 Ma old in N.Ireland and appear to have survived as they have been isolated from groundwaters.

Mineral characterisation at Scawt Hill and Carneal Plug indicate also the presence of ettringite (Milodowski et al. 2009). The occurrence of different ettringite-group minerals in natural alkaline environments are reviewed by Möschner (2007) including Al- and Fe-ettringites.

4.1.5 Time perspective

Chemical reactions related to hydration can occur for as long as unhydrated clinker minerals remain in the concrete barriers. Hydration of clinker minerals may continue over extended periods of time, most commonly in concretes with a low *W*/*C*-mixing ratio. The *W*/*C*-mixing ratio is therefore usually chosen to ensure full hydration, and this would be expected to be complete within the first year post-mixing, i.e. long before repository closure. Over time, the barrier function relevant for the safety analysis shifts in the following way:

- For the initial period – short-term, the chemical conditions established by the initial hydration reactions dominate, which create a hyper-alkaline porewater of alkali metal hydroxides and calcium hydroxide. The mechanical strength may be relatively high and may be of significant importance for the repository performance. The physical barrier properties may be of relatively high importance, e.g. low hydraulic conductivity and low diffusivity.
- For the short-term – mid-term, e.g. a few hundred years from closure, the mechanical strength and the physical barrier function may be reduced, e.g. by fractures and leaching, whereas the alkaline conditions would still be expected to prevail.
- In the long-term, e.g. a few thousand years from closure, the mechanical and physical barrier functions are expected to gradually deteriorate, and the chemical buffering will gradually decrease as calcium is depleted by leaching and by precipitation of calcite.
- In the very long-term, e.g. after tens of thousands of years from closure, the concrete barrier is likely to approach a completely degraded stage and exert a gradually decreasing impact even on the chemical conditions.

Since concrete leaching is mainly a coupled diffusion-reaction phenomenon, the time needed for complete degradation of concrete barriers will be highly dependent on the relative surface area of the concrete where diffusion exchange with the adjacent waste/waste packaging and/or groundwater can take place and is related to the geometrical dimensions of the concrete barriers. The increase in porosity and permeability due to concrete degradation need to be taken into account since this could mean a change of the flow conditions and the calculated degradation times. It is also emphasised that the conditions may be different due to varying amounts of concrete present in the different parts of the SFR repository.

Long-term climate change will influence the temperature at repository depth. Estimates of the change in temperature at the SFR repository are presented in SKB (2006). Temperature changes will affect thermodynamic equilibria and may lead to a gradual transformation and recrystallisation of the concrete minerals, which has been studied by e.g. Cronstrand (2007). One example is the change of stability field of AF_m versus AF_t with temperature, which could affect the porosity. This may impact the mechanical, hydraulic and chemical properties of the concrete barriers.

During permafrost conditions the likelihood of any dissolution, precipitation or recrystallisation processes in the concrete is negligible. Freezing may have significant impact on the mechanical integrity of the concrete barriers, but this is not within the scope of the present study.

4.1.6 Summary of chemical processes judged important

Based on the description above, the following processes are judged to be of potential importance for the barrier degradation in the 1BMA and 2BMA vaults in SFR:

- Leaching by groundwater.
  - Alkali hydroxides (effect on pH).
  - Portlandite (effect on pH, impact on mechanical strength, porosity, diffusivity, hydraulic conductivity).
  - CSH-gels (effect on pH, impact on mechanical strength, porosity, diffusivity, hydraulic conductivity).
- Interaction with dissolved substances in the groundwater.
  - Sulphate – ettringite formation, thaumasite formation.
  - Chloride – induce steel corrosion, formation of Friedel's salts.
  - Carbonate – carbonation, lowering of pH, reduced corrosion passivation, formation of calcite and carboaluminates, thaumasite formation.
  - Magnesium – formation of brucite and hydrotalcites.
- Alkali-silica reaction between ballast material and alkaline leachate (this process is important in general terms, however the type of cement used and the quality of ballast material selected for the BMA vault are such that alkali-silica reactions are unlikely to occur).
- Chemical effects of cement additives.

4.2 Mechanical/Physical degradation processes

This section describes different physical processes that may lead to the degradation of the concrete barriers in the BMA vault. A number of physical processes can be categorised as accidents or global events, e.g. rock fallout, earthquakes or permafrost, as they are a consequence of specific external processes e.g. rock mechanics or climate change. These processes are difficult to assess from the perspective of concrete barrier degradation and are therefore only mentioned here without any attempt to describe their evolution over time or to quantify their impact. Certain other processes listed below are either considered in other studies or have been judged out of scope for the present study.

4.2.1 Causes of fracture formation

Fractures may be formed in concrete for different reasons and the most likely causes and mechanisms are listed below. Factors that are difficult to quantify, such as those arising from accidents and external events, are not considered further in the report.

- Fracture formation at an early stage due to shrinkage during hydration and curing.
- Inadequate mixing or curing conditions (early stage) (unlikely due to QA processes, not considered here).
- Inadequate reinforcement (early stage) (considered in the assessment of 1BMA, not of concern for 2BMA since there is no reinforcement).
- Fractures due to heating or cooling.
- Excessive heating due to quick hydration (early stage) (included in the considerations for 1BMA).
- External factors such as fire (early stage) (not considered here).
- Heat generation in waste, e.g. due to radioactive decay (negligible in SFR, not considered here).
- Cooling due to inflow of groundwater at closure (considered for BMA).
- Fractures formed due to subsidence.
- Inadequate foundation for structures (likely short term, may be observed as increasing amounts of waste are loaded into the concrete structures) (integral part of the considerations for BMA).
- Rock movements (at any time) (not considered here).

- Fractures due to excessive mechanical load.
- Accidents, e.g. collision during transport (early stage) (not considered here).
- Dropped waste packages during emplacement (early stage) (not considered here).
- Excessive load due to inadequate stacking (early stage) (not considered here).
- Increased mechanical load due to failure of supporting backfill material (any time) (not considered here).
- Fractures due to earthquakes (any time) (not considered here).
- Fractures due to the impact of the host rock caving in (any time) (not considered here).
- Fractures due to freezing (expected to occur at a relatively advanced stage of the repository evolution; not considered here).
- Fractures due to gas pressurisation (not considered here).
- Excessive gas formation in certain waste collies (early stage – short term).
- Inadequate function of gas vents (short term – long term).
- Fractures due to corrosion of reinforcement bars (short term – long term, considered for 1BMA only, not applicable to 2BMA since there is no reinforcement).
- Heterogeneities/cavities caused by corrosion of reinforcement bars or form ties (considered for 1BMA only, not applicable to 2BMA since there is no reinforcement).
- Disturbed zones depleted in cement around form ties (considered for 1BMA only, not applicable to 2BMA since there are no form rods).
- Fractures due to delayed hydration (early stage – short term) (unlikely due to QA processes, not considered here).
- Fractures due to swelling of certain types of waste in waste packages (early stage – short term) (not considered here).
- Fractures due to alkali-silica reaction between alkaline components and unsatisfactory ballast material (early stage – short term) (judged unlikely for the type of cement used and the quality of selected ballast material in BMA).
- Fractures due to other types of chemical attack (short term – long term) (considered).

Although indicative time frames are given for the different fracture forming processes in the list above, it is difficult to make more exact predictions of when fractures may occur. An in-depth review of mechanisms for the initiation and propagation of fractures in concrete are given in Walton et al. (1990) and US DOE (2009). In the US DOE report (2009), the current understanding of the basic phenomena, the present basis for predicting the occurrence of fractures, and the need for further research are also discussed. Different methods for estimating the impact of degradation processes that may limit the functional lifetime of concrete structures are described in Edvardsen et al. (2000) and in Betongföreningen (2007).

4.2.2 Scoping calculations for selected mechanical/physical processes

In this section, simple models are presented for a selection of mechanical and physical processes that may contribute to degradation of the concrete barriers in the BMA vaults. The selection was based on processes judged to be important for the BMA concrete structures as identified is Section 4.2.1. Other mechanical/physical processes may also affect the long-term performance of the BMA barriers, e.g. freezing during permafrost, rock fallout etc., but are out of the scope of the present work and/or are covered by other studies. The considered processes comprise fracture formation due to: drying shrinkage during construction and during operation; thermal contraction due to cooling by inflowing groundwater after closure; and corrosion of different steel components used as construction elements in the concrete barriers. It is noted that the same approach would be applicable also for waste drums and steel components in the waste.

Some material properties that will be used in the calculations have been summarised in Table 4-1.

Table 4-1. Selected parameter data used in the scoping calculations.

Parameter	Value	Unit	Reference
Tensile strength of concrete	1.5	MPa	Selected characteristic value for concrete class C 20/25 (Boverket 2004)
Compressive strength of concrete	19	MPa	Selected characteristic value for concrete class C 20/25 (Boverket 2004)
Elastic modulus of concrete	30	GPa	Selected characteristic value for concrete class C 20/25 (Boverket 2004)
Density of concrete	2,450	kg/m^3	Estimated from composition and mineral densities
Final drying shrinkage of concrete	$0.4 \cdot 10^{-3}$ $0.25 \cdot 10^{-3}$ $0.1 \cdot 10^{-3}$	unitless	(Boverket 2004) 55% relative humidity 75% relative humidity > 95% relative humidity
Coefficient of thermal expansion/ contraction of concrete	$1 \cdot 10^{-5}$	per °C	(Boverket 2004)
Poisson's ratio	0.15	unitless	(Trafikverket 2012)

Fracture formation due to drying and temperature variation

This section focuses on 2BMA, since it represents the condition of the barriers assumed for the Safety Assessment SR-PSU. The condition of the 1BMA barriers will be improved considerably before repository closure, given the extensive repairs planned for 1BMA. However, the processes discussed are also applicable for the concrete barriers in 1BMA. An assessment of the effect of drying and temperature variation in the Silo is included in Appendix B.

Drying shrinkage

During the operational phase, the concrete barriers will be exposed to the environmental conditions in the repository. The concrete will be in direct contact with air. Since the concrete is sensitive to variations in moisture content, the relative humidity of the air in the vault during operation may affect the properties of the concrete. When concrete is in contact with air over long periods, an equilibrium will be established between the moisture content of the concrete and the humid air. Concrete has its maximum volume when saturated with water and shrinks as it dries, in response to the loss of water and the accompanying increase in capillary suction that causes the concrete to contract. Concrete equilibrated with air of 50% relative humidity shrinks by ~ 0.5‰. Some simple estimates can be made using a model for shrinkage presented in Möller et al. (1980). The final shrinkage (ε_{csu}) is given by:

$$\varepsilon_{csu} = \varepsilon_g \cdot k_{RH} \qquad \text{Equation 4-1}$$

where:

k_{RH} = a correction factor for the final shrinkage in relation to the shrinkage at 50% relative humidity

ε_g = final shrinkage at 50% relative humidity which is given by:

$$\varepsilon_g = 3.75 \cdot 10^{-6} \cdot (W_0 - 50) \qquad \text{Equation 4-2}$$

W_0= initial amount of water in the concrete (mixing water)

Using the W_0 value of 164.5 kg/m^3 concrete for the construction concrete in BMA, ε_g = 0.43‰ can be calculated. The exact environmental conditions in the 2BMA vault are not known at present. However, it may be desired to keep the relative humidity at a level below ~ 80% to avoid condensation of water vapour, e.g. on metal surfaces in the vault. Measured data on relative humidity and air temperature for 1BMA during 2012–2013 are presented in Figure 4-1.

For a reasonable average of the relative humidity of 70%, the value of k_{RH} = 0.82 can be estimated from data given in Möller et al. (1980, p 323, Figure 6). The final shrinkage at 70% relative humidity is estimated to 0.35‰. The threshold strain for concrete is in the range 0.1–0.2‰. For strains above the threshold, fractures will form. Hence, shrinkage due to drying to 70% relative humidity is likely to result in fracture formation in the concrete. Even if new fractures did not form, it is likely that thin fractures present in the concrete would dilate in response to drying shrinkage.

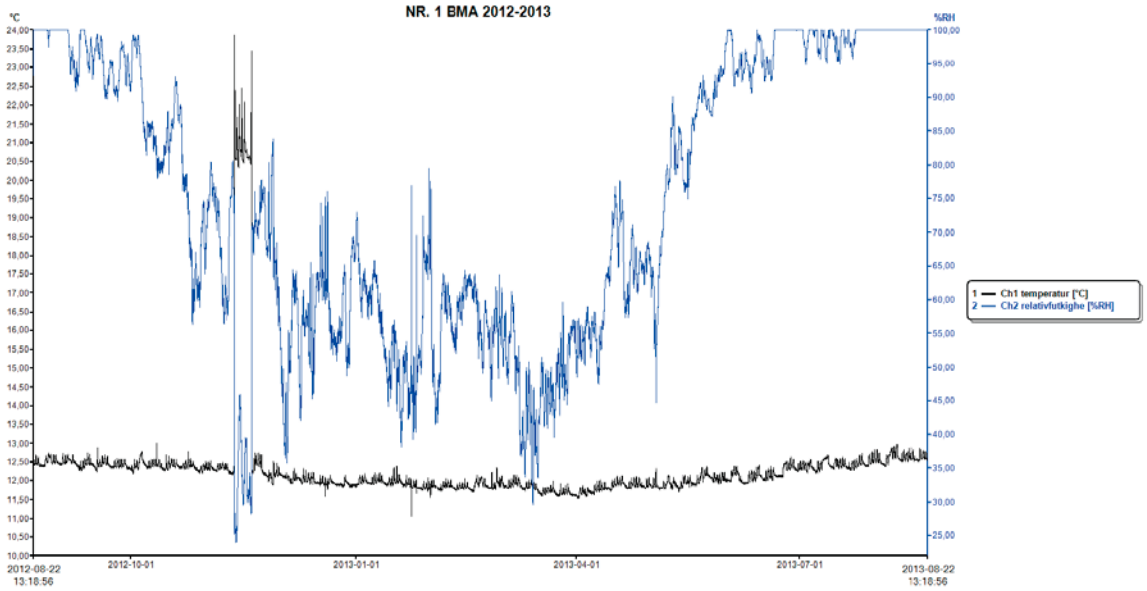

Figure 4-1. *Measured relative humidities and air temperatures in the 1BMA vault during 2012–2013.*

The total shrinkage of the 15 m long 2BMA caissons calculated for various values of relative humidity is presented in Figure 4-2. Estimates of the potential fracture apertures in the 2BMA concrete caissons as a result of the total shrinkage for different assumed fractured densities are presented in Figure 4-3. The fracture aperture is calculated from the final shrinkage (ε_{csu}) and the fracture spacing (d):

$b = \varepsilon_{csu} \cdot d$

Drying shrinkage fracture aperture widths are commonly on the order of a few tens of micrometers.

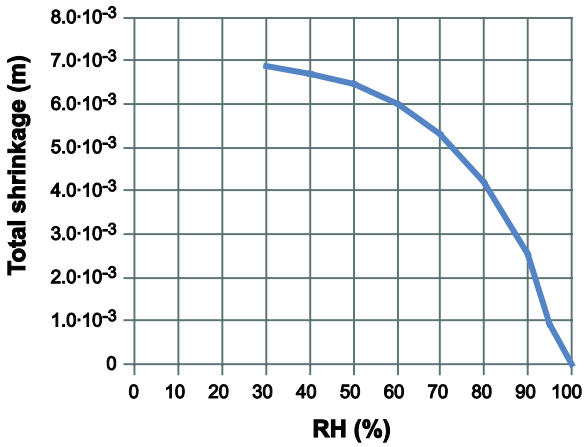

Figure 4-2. *Calculated total shrinkage of a 15 m long concrete caisson in 2BMA versus relative humidity.*

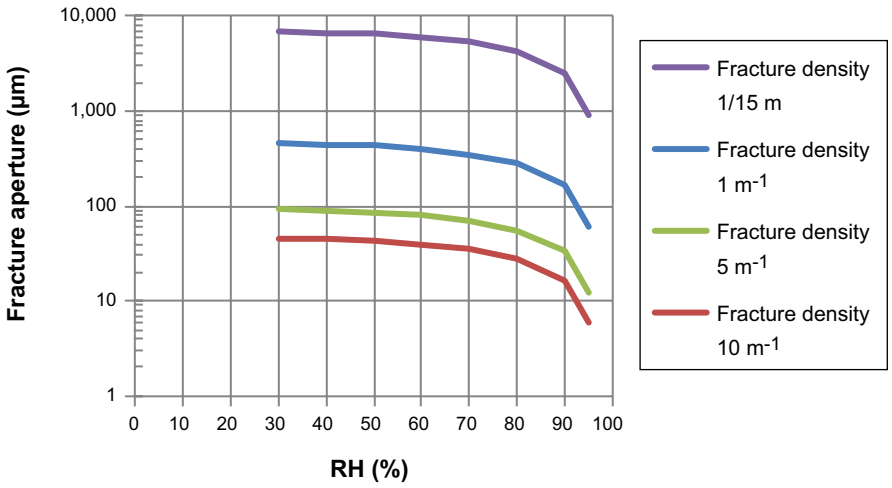

Figure 4-3. *Estimated fracture apertures for different assumed fracture densities resulting from shrinkage of concrete when exposed to different relative humidities.*

Temperature variations

Temperature variation may cause the concrete barriers to expand or contract. The coefficient of thermal expansion of concrete is in the range $5–15 \cdot 10^{-6}$ (1/°C).

During the early hardening of the concrete, the heat released from the cement hydration reactions may increase the temperature. However, this effect is not considered in this report.

During the operational period, the temperature variation is likely to be limited, c.f. Figure 4-1, and is not investigated here.

However, at closure, the temperature of the concrete barriers and the air in the vault will be in equilibrium. The temperature in the 2BMA constructions at the time of closure is assumed to be 12°C (based on measurements during operation in 1BMA, see Figure 4-1) and the temperature in the groundwater has been assumed to 5–7°C (SKB 2014c). This means that the concrete barriers will re-equilibrate in response to a temperature change $\Delta T = –7$°C. The dimensional change due to this can be estimated to be $–70 \cdot 10^{-6}$ m/m. This falls within the range of threshold strains for concrete, i.e. 0.1–0.2‰. However, it is doubtful that this strain can be disregarded in the safety assessment. It is also reasonable to assume that any small fractures present in the concrete at the time of closure will dilate as the caissons contract, particularly since the concrete walls will not be reinforced. Scaling the dimensional changes to the full 15 m length of a caisson results in a temperature contraction of the order 1.05 mm. If this was to result in one single fracture, the fracture aperture width would be 1.05 mm. If more than one fracture would form or if thin fractures already present dilated, the total contraction would be distributed over several fractures and the aperture width of each fracture would be smaller. The estimated impact of the post-closure temperature contraction on the overall hydraulic conductivity of the 2BMA concrete barriers is presented in Figure 4-4.

The time that temperature-induced dimensional changes occur depends on the rate of groundwater flow into the vault and is beyond the scope of this investigation. However, it is likely that new temperature equilibrium will be established during the first few years – 100 years after closure.

The resaturation process will also diminish the capillary suction in the partly dried concrete barriers. This may cause a small swelling that could counteract the contraction caused by cooling. However, it may be difficult to take credit for this possible swelling process in the safety assessment.

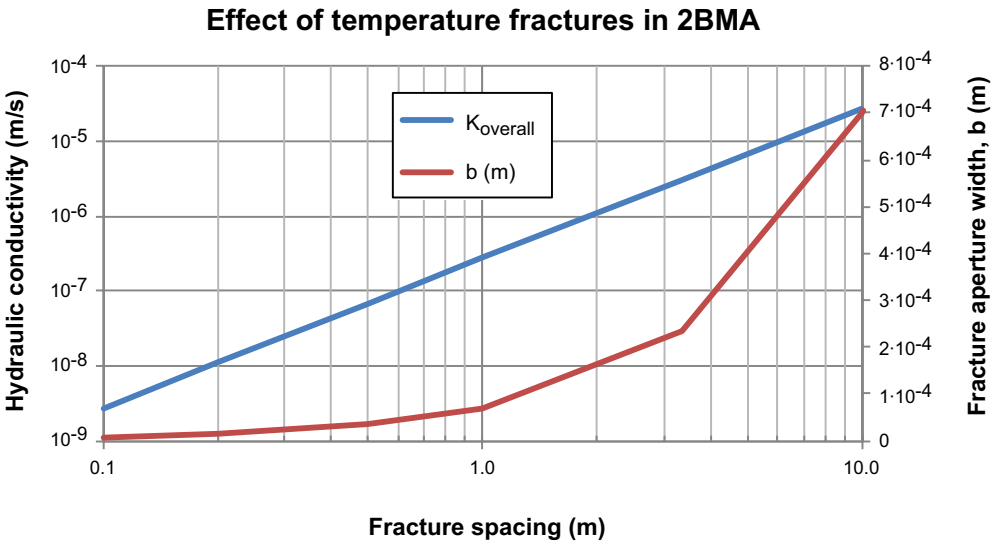

Figure 4-4. *Estimated impact on the overall hydraulic conductivity of concrete barriers in 2BMA caused by temperature contraction when groundwater resaturates the repository after closure. The figure also shows the predicted fracture aperture width (b) as a function of the fracture spacing.*

Corrosion of reinforcement bars and other steel components

Corrosion of reinforcement bars and other construction components of steel (e.g. form rods, grid plates, grouting pipes) present in the concrete is judged to be of relevance for the 1BMA vault. However, the concrete barriers of the 2BMA vault are designed without reinforcement bars and the descriptions presented in this section will therefore not be applicable. Fracture formation due to the corrosion of reinforcement bars in concrete proceeds through different phases; see also illustration in Figure 4-5:

- The initiation phase – ingress of chloride and/or carbonation in the concrete leads to depassivation of the steel bars.
- The propagation phase.
  - Corrosion occurs at the surface of the steel bars. A layer of corrosion products, which have larger molar volumes than the non-corroded steel, accumulates at the interface between the steel bar and the concrete, initially filling available pores near the surface of the steel bar, and thereafter gradually increasing the mechanical stress in the cover concrete as the volume of corrosion products increases.
  - Fracture formation is initiated when the mechanical stress exceeds the tensile strength of the cover concrete.
  - The continued accumulation of corrosion products leads to increasing fracture width and eventually the spalling of layers of the cover concrete layer.
  - Continued corrosion, and fracturing and spalling of concrete may eventually result in loss of the mechanical strength to such a degree that the structure collapses.

If depassivation occurs during the operational phase, the iron will react with oxygen in the air, which may result in fairly rapid corrosion. Later, during the post-closure phase, oxygen will become depleted and the corrosion processes will be anaerobic causing the iron to react with water, and generate hydrogen gas.

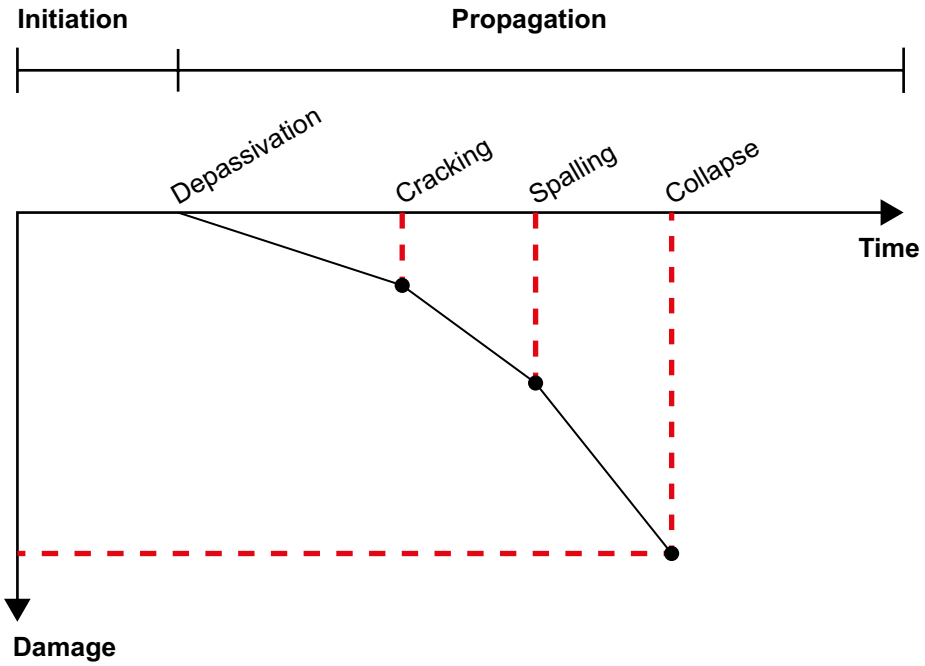

Figure 4-5. *Different phases in the deterioration of concrete constructions due to corrosion of reinforcement bars, modified from Edvardsen et al. (2000).*

As a result of the corrosion processes, a layer of corrosion products will form on the corroding metal surface. These corrosion products will be mainly iron oxides/hydroxides and their molar volume is larger than the volume of corroded iron. This means that a gradual volume expansion will take place at the interface between concrete and metal. Hence, corrosion will induce a mechanical stress in the concrete covering the reinforcement bars. When the stress becomes too large, a fracture will form in the concrete. A schematic illustration is given i Figure 4-6.

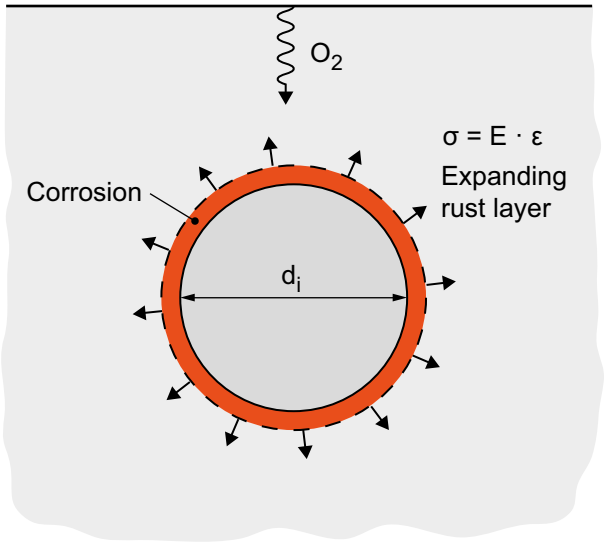

Figure 4-6. *Illustration of corrosion of reinforcement bars during oxidising conditions causing fracture formation in concrete constructions.*

Chloride initiation of steel corrosion

It is well known that chloride can initiate the corrosion of steel in concrete (e.g. Tuutti 1982). Experimental investigations have shown that the chloride concentration necessary to depassivate steel embedded in concrete is dependent on the hydroxide concentration in the concrete pore water. Tuutti (1982) reported threshold concentrations based on measurements in Portland cement and slag cement, see Table 4-2, and applied a generic relationship for chloride-induced corrosion under alkaline conditions:

$$\frac{c_{Cl^-}}{c_{OH^-}} \leq 0.6 \qquad \text{[Criterion 1]}$$

where the concentrations of chloride and hydroxide ions respectively are given in equivalents/litre. Since the charges of both species are unity, the relationship can also be applied for molar units.

A model to describe the intrusion of chloride ions in concrete based on transient diffusion of dissolved species in porous media is given in Betongföreningen (2007):

$$c(x,t) = c_{init} + (c_0 - c_{init}) \cdot \left(1 - \text{erf}\left(\frac{x}{2 \cdot \sqrt{D_e \cdot t}}\right)\right) \qquad \text{Equation 4-3}$$

$$\text{erf}(\xi) = \frac{2}{\sqrt{\pi}} \int_0^{\xi} e^{-t^2}\, dt \qquad \text{Equation 4-4}$$

where:

c_{init} = initial concentration of chloride in the concrete (M)

c_0 = ambient chloride concentration at the external surface of the concrete in contact with the groundwater (M)

x = the distance (depth) from the concrete surface (m)

D_e = the effective diffusivity of chloride ions in concrete (m^2/year)

t = time (years)

Chloride intrusion has been calculated assuming an initial chloride concentration in concrete of zero and a groundwater concentration in the range of 3,500–5,000 mg/l, equivalent to 0.1–0.14 M (Figure 4-7). An effective diffusivity of $3.5 \cdot 10^{-12}$ m^2/s has been assumed in the calculations. The model of the chemical conditions in the concrete barriers (Chapter 8) shows that the pH drops to ~ 12.75–12.5 after only a few decades, corresponding to a hydroxide ion concentration in the range of 0.038–0.067 M. Applying criterion 1, the threshold chloride concentration for steel corrosion will be in the range of 0.023–0.04 M. Figure 4-3 clearly shows that the chloride concentrations are expected to reach this threshold early on in the evolution of the repository, initiating corrosion of reinforcement bars, form rods and other steel components in the concrete barriers. However, steel components that penetrate through the central parts of the walls (thickness 0.4 m) may be protected from exposure to threshold concentrations of chloride for ~ 100–200 years. In these estimates, any chemical reactions between chloride ions and the concrete have been neglected, and these would increase the times, see further discussion on this in Section 5.2.

Table 4-2. Threshold chloride concentrations for depassivation of steel embedded in different types of cement, based on Tuutti (1982).

Cement type	Hydroxide ion concentration (M)	Threshold concentration of chloride
Portland cement *W/C* = 0.4	1.1	0.7 M / 25 g/L
Portland cement *W/C* = 0.6	0.4	0.25 M / 9 g/L
Slag cement *W/C* = 0.4	0.3	0.22 M / 8 g/L
Slag cement *W/C* = 0.6	0.1	0.056 M / 2 g/L

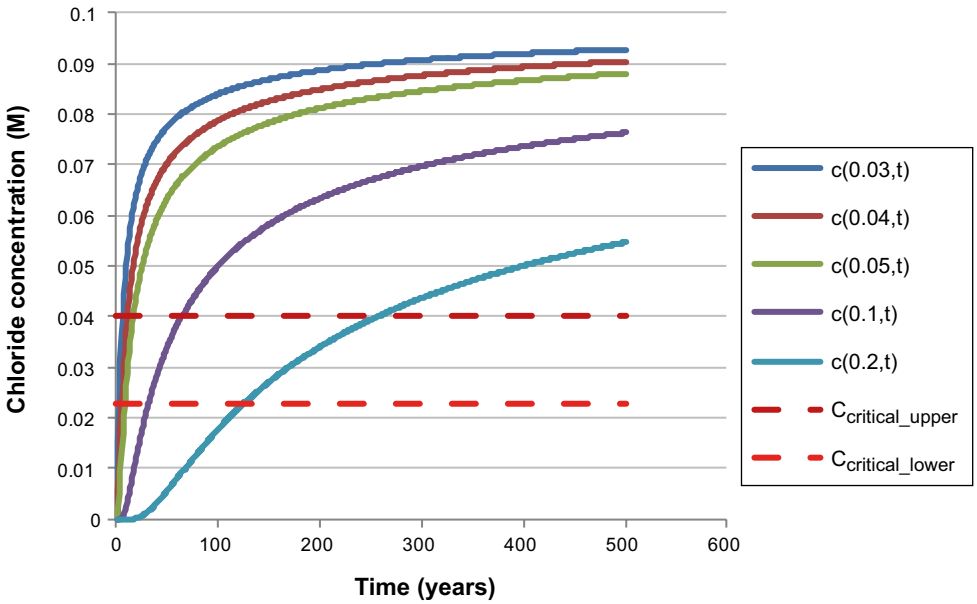

Figure 4-7. *Calculated chloride intrusion in concrete. Concentration profiles c(x,t) are given at different distances x (m) from the concrete external surface. The range of threshold chloride concentrations (labelled C_{crit} in the figure) considered causing depassivation of reinforcement bars and other steel parts in concrete are shown for comparison. The chloride concentration in the groundwater has been assumed to be 0.1 M (3,500 mg/l).*

Corrosion processes

During the operational phase of the SFR repository, corrosion may proceed by reaction with oxygen, as exemplified by:

$$2\ Fe(s) + O_2 + 2\ H_2O \Leftrightarrow 2\ Fe(OH)_2(s) \qquad \text{Equation 4-5}$$

which may further oxidise:

$$2\ Fe(OH)_2(s) + ½\ O_2 + H_2O \Leftrightarrow 2\ Fe(OH)_3(s) \qquad \text{Equation 4-6}$$

The iron(III)hydroxide formed may later dehydrate to yield $Fe_2O_3 \cdot nH_2O$.

During a later stage, when oxygen has been depleted by various oxygen consuming processes (e.g. corrosion and microbial activity) corrosion will take place by a hydrogen evolving reaction:

$$3\ Fe(s) + 4\ H_2O \Leftrightarrow Fe_3O_4 + 4\ H_2(g) \qquad \text{Equation 4-7}$$

Impact of corrosion products on the integrity of the concrete

The corrosion of reinforcement bars and other steel components in concrete leads to consumption of iron and the formation of a solid corrosion product with a larger volume. It may therefore have the following effects that reduce the ability of the concrete structures to carry a mechanical load (Andrade et al. 2011):

- Reduction of the cross-section area of the steel bars.
- Loss of ductile strength of the steel bars due to reduced area.
- Reduction of the bond strength between the concrete and the reinforcement bars.
- Accumulation of corrosion products (rust) at the interface between reinforcement bars and concrete, giving rise to mechanical forces that may lead to cracking of the concrete cover.

Factors of importance for the first appearance of fractures in concrete are the quotient between the thickness of the concrete cover and the diameter of the reinforcement bars, the quality and strength of the concrete, and the corrosion rate (Andrade et al. 2011). The rust layer that forms consists of iron oxides/hydroxides of varying porosity. For the more porous oxides, the density has been determined to be ~ 3,000 kg/m^3, whereas the low-porous oxides have a density of ~ 3,700 kg/m^3 (Tuutti 1982). Li et al. (2005) give the value 3,600 kg/m^3 for the density of a corrosion product consisting mainly of ferrous and ferric hydroxides. Assuming that magnetite is the predominant low-porous corrosion product, the measured bulk density would correspond to a porosity of ~ 28%. In the following, some examples show the effect of different assumptions regarding the properties of the corrosion products.

Formation of solid magnetite with no porosity

This describes the case where the densest possible corrosion product is formed, hence the smallest impact on the concrete is calculated for a given corrosion rate.

If a uniform corrosion rate r_0 (m/a) is assumed, the volumetric corrosion rate of iron can be estimated from the initial diameter d_i and the length of reinforcement bars L:

$$R_{Fe} = \pi \cdot d_i \cdot L \cdot r_0 \text{ (m}^3\text{/a)} \qquad \text{Equation 4-8}$$

The volumetric rate of the corrosion product formed (formation of magnetite Fe_3O_4 is assumed) is given by:

$$R_{Fe3O4} = \frac{V_{m,Fe3O4}}{3 \cdot V_{m,Fe}} \cdot R_{Fe} = \frac{V_{m,Fe3O4}}{3 \cdot V_{m,Fe}} \cdot \pi \cdot d_i \cdot L \cdot r_0 \text{ (m}^3\text{/a)} \qquad \text{Equation 4-9}$$

Hence, the actual volume change after time t can be estimated by integrating the difference in volumetric rates of iron depletion by corrosion and product formation over time:

$$\Delta V_{Fe \rightarrow Fe3O4} = \int_0^t (R_{Fe3O4} - R_{Fe}) dt = \pi \cdot d_i \cdot L \cdot r_0 \cdot t \cdot \left(\frac{V_{m,Fe3O4}}{3 \cdot V_{m,Fe}} - 1 \right) \text{(m}^3\text{)} \qquad \text{Equation 4-10}$$

This integration is approximate and may be inaccurate for large amounts of magnetite formation. In such cases it is necessary to account for the effects of radial symmetry.

In order to estimate the stress, the change of the diameter of the reinforcement bar due to the corrosion and magnetite formation processes over time t can be calculated:

$$\Delta d_i = \frac{\Delta V_{Fe \rightarrow Fe3O4}}{\pi \cdot d_i \cdot L} = r_0 \cdot t \cdot \left(\frac{V_{m,Fe3O4}}{3 \cdot V_{m,Fe}} - 1 \right) \text{(m)} \qquad \text{Equation 4-11}$$

Assuming that the expansion will take place in the concrete around the reinforcement bar/form tie, the strain after time t can be estimated to:

$$\varepsilon = \frac{\Delta d_i}{d_i} = \frac{r_0 \cdot t}{d_i} \cdot \left(\frac{V_{m,Fe3O4}}{3 \cdot V_{m,Fe}} - 1 \right) (-) \qquad \text{Equation 4-12}$$

The tensile stress σ after time t can be calculated by means of Hooke's law:

$$\sigma = E \cdot \varepsilon = E \cdot \frac{\Delta d_i}{d_i} = E \cdot \frac{r_0 \cdot t}{d_i} \cdot \left(\frac{V_{m,Fe3O4}}{3 \cdot V_{m,Fe}} - 1 \right) \text{(Pa)} \qquad \text{Equation 4-13}$$

A stress condition for when fracturing will initiate can be expressed, based on the tensile strength of the concrete f_t:

$$\sigma > f_t \quad \text{(Pa)} \qquad \text{Equation 4-14}$$

By combining these expressions (Equations 4-11 and 4-12), the time t_b, when the first fractures will form can be estimated:

$$t_b = \frac{f_t}{E \cdot r_0} \cdot \frac{d_i}{\left(\frac{V_{m,Fe3O4}}{3 \cdot V_{m,Fe}} - 1 \right)} \text{(a)} \qquad \text{Equation 4-15}$$

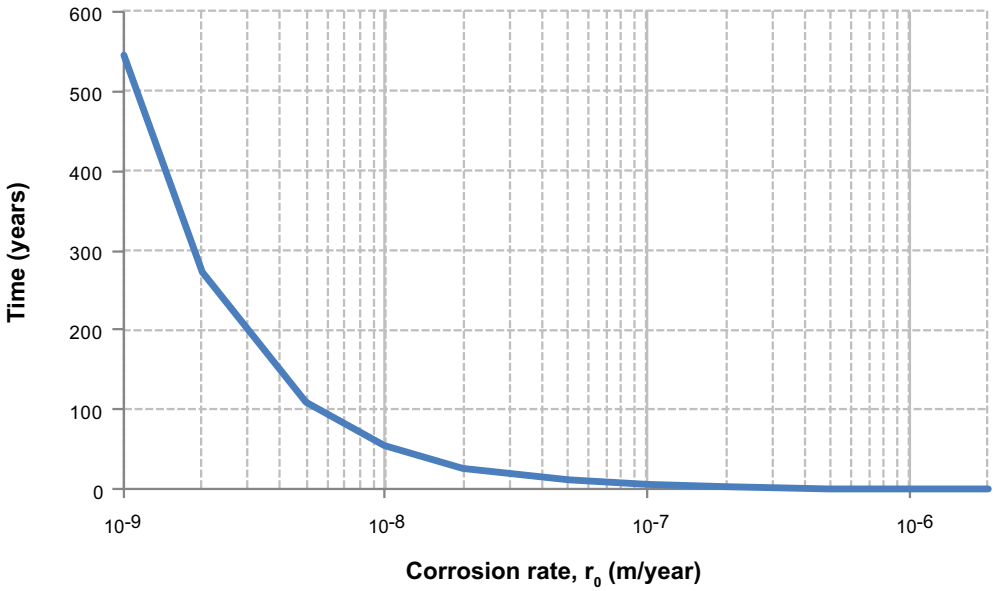

Figure 4-8. *Calculated time to reach the critical stress that may initiate fracturing in the concrete cover due to corrosion of reinforcement bar for a range of corrosion rates r_0. Solid, non-porous magnetite is assumed to form in this case. Initially the steel bars may be passivated; hence the time to initiate corrosion should be added to these estimates.*

Assuming:

f_t = the tensile strength of the concrete = $1.5 \cdot 10^6$ Pa

E = the elastic modulus of concrete = $30 \cdot 10^9$ Pa

$V_{m,Fe3O4}$ = molar volume of the corrosion product, here assumed to be magnetite = 0.045 m^3/kmol

$V_{m,Fe}$ = molar volume of the steel (iron) = 0.007 m^3/kmol

d_i = diameter of the reinforcement bar = 0.012 m assumed in the example.

The corrosion time required for the reinforcement bars to generate a tensile stress in the concrete cover that may initiate fracture formation is shown in Figure 4-8 for different corrosion rates.

Formation of a porous corrosion product

This case considers the formation of a porous corrosion product that precipitates at the surface of corroding reinforcement bars. This means that for a given corrosion rate, the corrosion products will occupy a larger volume than in the previous case, basically resulting in a more rapid fracturing of the concrete. These corrosion products may consist of a mixture of iron hydroxides and iron oxides. Since the porous corrosion products will be compacted in the confined pore space of the concrete, a mechanical pressure will gradually develop as they form (e.g. Balafas and Burgoyne 2010). The degree of compaction of the corrosion product depends on the pressure and can be characterised by the bulk modulus. A model to describe this process is given in Betongföreningen (2007), see illustration in Figure 4-9.

For a given corrosion depth, p, and a quotient ν describing the volume of rust to the volume of steel, an expression for the increase of the radius of the rust layer when allowed free expansion without tension is given by:

$$\Delta r_a = -r_i + \sqrt{r_i^2 + (\nu - 1) \cdot (2 \cdot r_i \cdot p - p^2)} \ \text{(m)} \qquad \text{Equation 4-16}$$

Assuming the corrosion depth is given by $p = r_0 \cdot t$ gives:

$$\Delta r_a = -r_i + \sqrt{r_i^2 + (\nu - 1) \cdot (2 \cdot r_i \cdot r_0 \cdot t - (r_0 \cdot t)^2)} \ \text{(m)} \qquad \text{Equation 4-17}$$

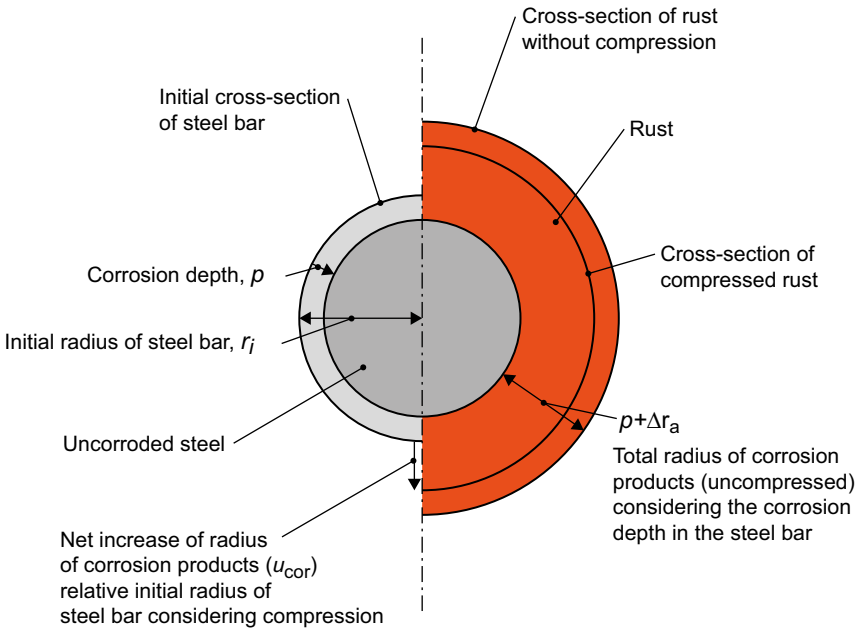

Figure 4-9. *Volume increase of corrosion products (rust) with and without correction for compression caused by the tension exerted at the interface between the steel, rust and concrete. Modified from Betongföreningen (2007).*

Taking into consideration the tension caused by formation of a rust layer, the actual increase of the radius of the rust layer is u_{cor}. From this the strain in the rust layer is calculated from:

$$\varepsilon_{cor} = \frac{u_{cor} - \Delta r_a}{p + \Delta r_a} \; (-) \qquad \text{Equation 4-18}$$

$$u_{cor} = \varepsilon_{cor} \cdot (p + \Delta r_a) + \Delta r_a = \varepsilon_{cor} \cdot (r_0 \cdot t + \Delta r_a) + \Delta r_a \;\; (\text{m}) \qquad \text{Equation 4-19}$$

The mechanical properties of the porous corrosion products have been experimentally investigated where the tension has been determined as a function of the strain. An approximation giving a graphical relationship between the tension and the strain has been proposed by Betongföreningen (2007). Using this graphical relationship a mathematical expression has been derived in the present study as shown in Figure 4-10.

A simplistic model for the fracture aperture width can be derived assuming that the perimeter of the concrete enclosing the reinforcement bar at the time the concrete is hardened will remain constant (since concrete is a brittle material), and that the expansion of the rust layer will cause a fracture to open up to accommodate the increasing radius. This means that when a fracture has formed, the perimeter of the concrete around the steel bar is no longer a closed circle, see illustration in Figure 4-11. From these assumptions follows that the fracture aperture width, b, can be estimated as:

$$b = 2 \cdot \pi \cdot u_{cor} \; (\text{m}) \qquad \text{Equation 4-20}$$

As an example, assuming a corrosion rate $r_0 = 1 \cdot 10^{-6}$ m/year, a bar radius $r_i = 0.006$ m, and a maximum tensile stress in the concrete of 1.5 MPa, which corresponds to a strain of –0.26 using the equations shown in Figure 4-10, the expansion of the rust layer can be calculated as shown in Figure 4-12.

Calculated results using the simplistic model presented in Equation 4-20 are also shown in Figure 4-12.

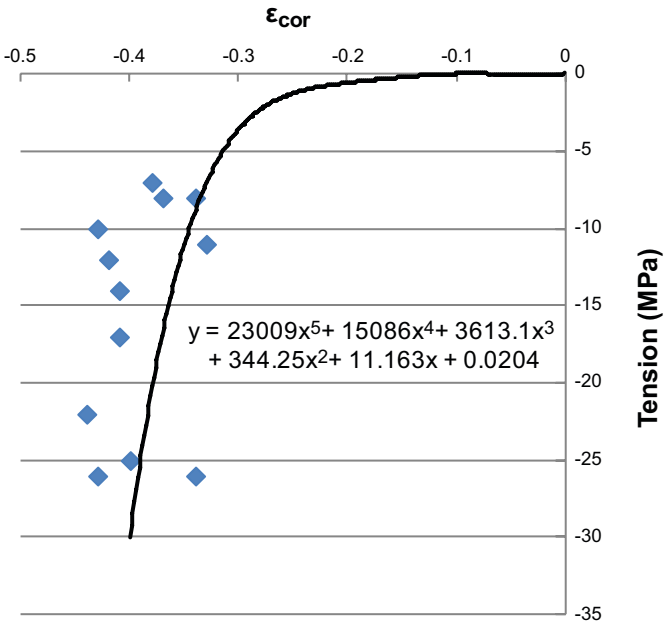

Figure 4-10. *Approximate relationship between tension and strain in porous corrosion product during the corrosion of reinforcement bars in concrete. Solid line determined by fitting to the experimental data compiled in the reference (figure modified from Betongföreningen 2007).*

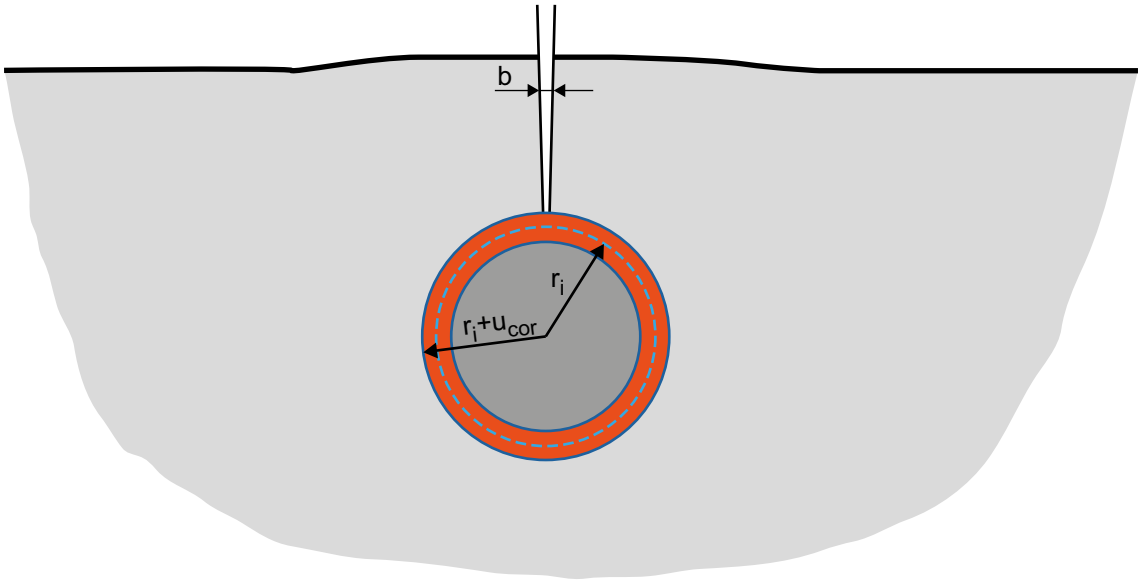

Figure 4-11. *Illustration to simple model for estimation of the fracture width caused by an expanding rust layer on the reinforcement bars.*

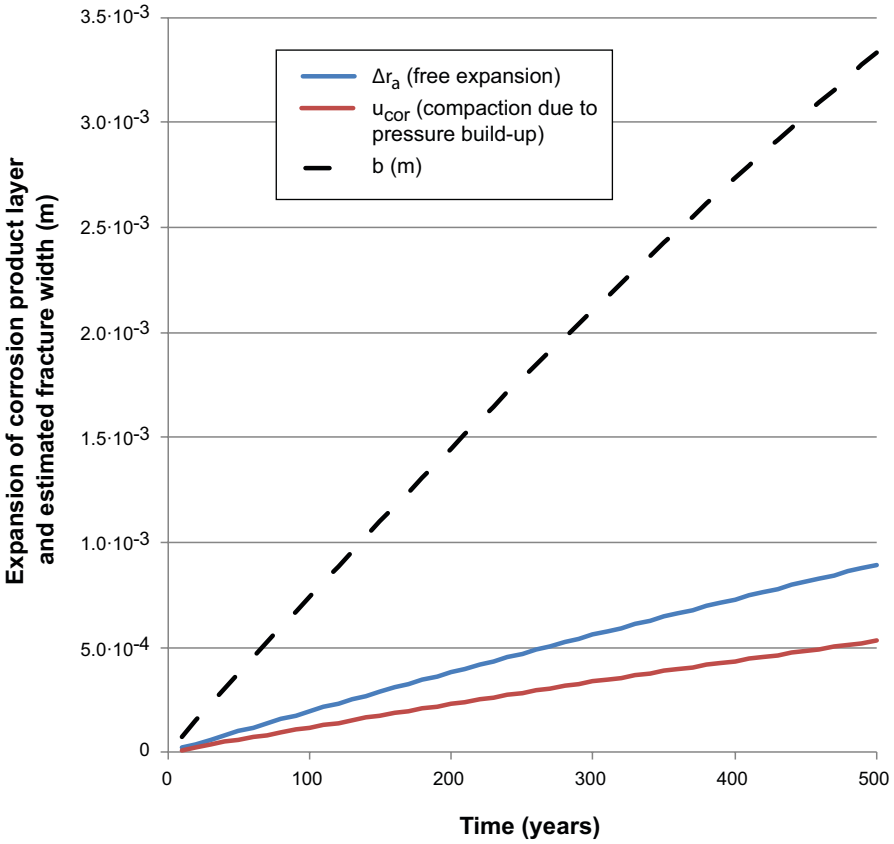

Figure 4-12. *Calculated expansion of the rust layer around reinforcement bars during free expansion and when the expansion is restricted by pressurisation of the rust layer. Estimated fracture aperture widths as a result of the expansion (considering the effect of compaction) are also shown.*

Model for fracture formation in a thick-walled cylinder of concrete

The stress developed in concrete due to corroding reinforcement bars can be modelled as a cylinder with thick walls (Li et al. 2005). An illustration to the approximation of the concrete cover as thick-walled cylinder is presented in Figure 4-13.

This simplified model may also be applicable for estimates of the initiation of fractures around other corroding steel components in concrete, e.g. form rods. The scenario for corroding form rods is somewhat different in that the form rods extend through the thickness of the concrete walls perpendicular to the wall surfaces. As corrosion is initiated, a tensile stress will be induced in the concrete wall, eventually causing fractures that extend along the main axes of the wall, see illustration in Figure 4-14. A reasonable first estimate is that fractures will extend from the form rods to the nearest edge of the wall as indicated in the illustration. Hence, the distance to the nearest edge would be an estimate for the parameter d_c in this case. When several form rods are present in the concrete, fractures extending from different form rods may intersect and form a continuous fracture.

The radius of the concrete cylinder is r_b, and the cover layer has a thickness d_c. It is assumed that the reinforcement bar with diameter d_i is initially surrounded by a thin annular layer of increased porosity (i.e. due to water separation near the steel surface) with thickness d_0, see illustration in Figure 4-15. The outer radius of this layer, r_a, is given by:

$$r_a = \frac{d_i + 2 \cdot d_0}{2}$$ Equation 4-21

$$r_b = r_a + d_c = d_c + \frac{d_i + 2d_0}{2}$$ Equation 4-22

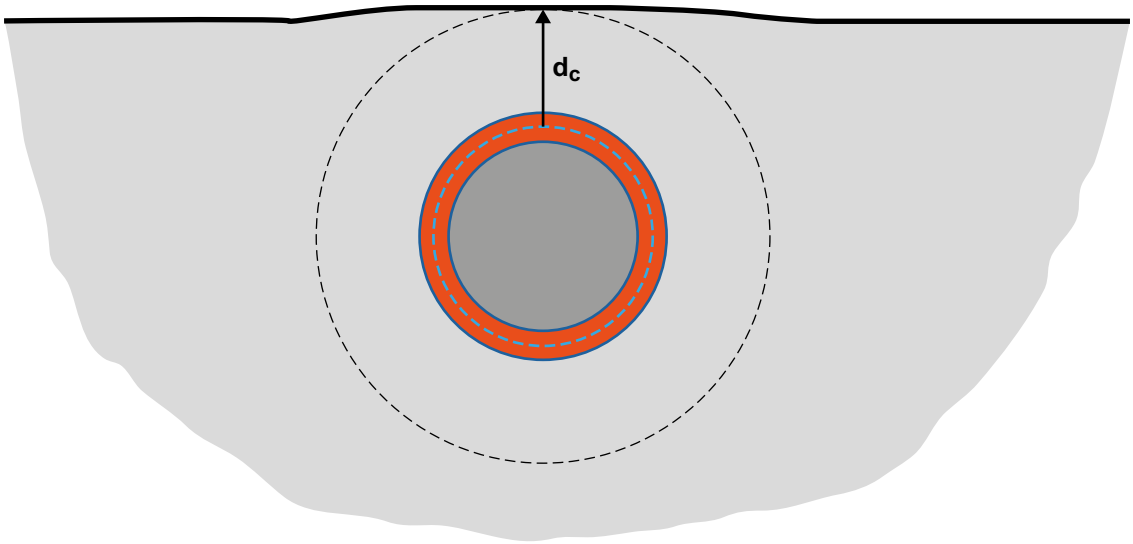

Figure 4-13. *Approximating the geometry of the concrete cover as a cylinder. The cover thickness represents the smallest distance from reinforcement bars to the concrete surface.*

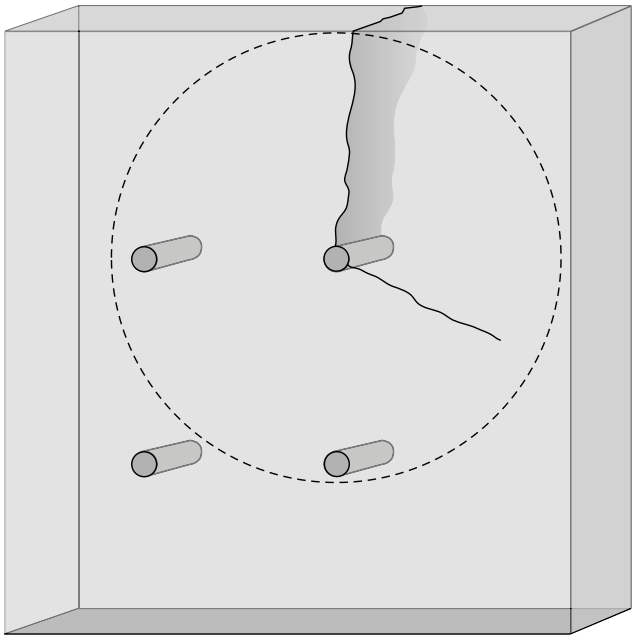

Figure 4-14. *Application of the model for thick-walled cylinder for fracture formation around form rods that penetrate a concrete wall perpendicular to the wall surfaces.*

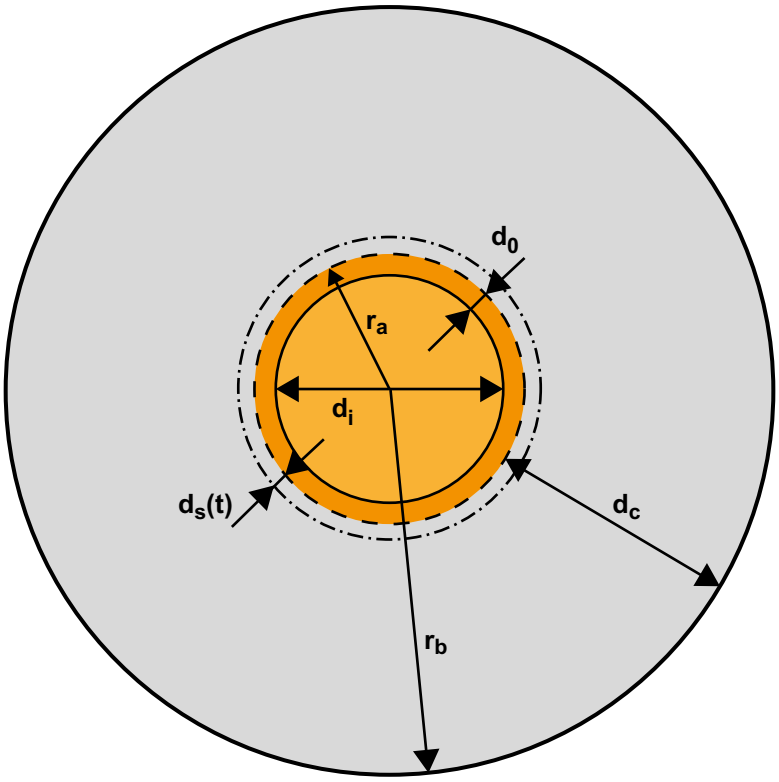

Figure 4-15. *Illustration of corrosion of reinforcement bars causing fracture formation in concrete constructions.*

Once corrosion has been initiated, the corrosion products will first fill the volume of the annular zone of thickness d_0. Thereafter, corrosion products expand into the concrete forming an annular zone of thickness d_s(t), an expression of which is given by (Li et al. 2005):

$$d_s(t) = \frac{w_r(t)}{\pi(d_i+2d_0)\cdot L}\left(\frac{1}{\rho_r} - \frac{\alpha_r}{\rho_{st}}\right) \qquad \text{Equation 4-23}$$

where:

$w_r(t)$= the mass of corrosion products formed at time t (kg)

L = the length of the reinforcement bar (m)

ρ_r = the density of the corrosion products (kg/m^3)

ρ_{st} = the density of the steel (kg/m^3)

α_r = the ratio of the density of the steel and the density of the rust

An expression for the mass of corrosion products formed at time t for a known corrosion current, i_{corr} , is given by (Li et al. 2005):

$$w_r(t) = \sqrt{2\int_0^t 0.105 \cdot \left(\frac{1}{\alpha_r}\right) \cdot \pi \cdot d_i \cdot i_{corr}(t)dt} \qquad \text{Equation 4-24}$$

$$i_{corr}(t) = 0.3586 \cdot \ln(t) + 1.1305 \qquad \text{Equation 4-25}$$

$$w_r(t) = \sqrt{2 \cdot 0.105 \cdot \left(\frac{1}{\alpha_r}\right) \cdot \pi \cdot d_i \cdot (0.3586 \cdot (t \cdot \ln(t) - t) + 1.1305 \cdot t)} \qquad \text{Equation 4-26}$$

This expression is suitable for evaluating corrosion experiments where the corrosion current is measured, but will not be used in this study.

To simplify the estimates, it is assumed that the corrosion rate is constant, r_0, and that the depth of corrosion is negligible in comparison with d_i, this gives:

$$w_r(t) = r_0 \cdot \pi \cdot d_i \cdot L \cdot t \cdot \rho_{st} \cdot \frac{M_{cor}}{M_{Fe}} \cdot \frac{n_{cor}}{n_{Fe}} \qquad \text{Equation 4-27}$$

where:

M_{cor} = molar weight of the corrosion product (kg/kmol)

M_{Fe} = molar weight of iron (kg/kmol)

n_{cor}/n_{Fe} = stoichiometric coefficient of the corrosion reaction

The pressure exerted by the corrosion products causes an outward force on the cylindrical interface between the corrosion products and the concrete. During the expansion, the concrete cylinder passes through three different phases:

1. An initial phase in which the corrosion products precipitate in the annular porous zone and the pressure starts to increase. No fractures form during this phase.
2. A second phase when fractures start to form at the interface between the corrosion products and the concrete. Fractures are only partly penetrating, extending radially from the inner surface. Once initiated, the fractures form a zone that gradually propagates outwards.
3. A third phase when fully penetrating fractures have formed, or a state of equilibrium has been established where the fracture propagation has stopped.

The pressure exerted by the corrosion products is given by the following expressions derived by (Li et al. 2005):

$$P(t) = -\sigma_r(r_a) = \frac{E_{ef} \cdot d_s(t)}{r_a\left(\frac{r_b^2 + r_a^2}{r_b^2 - r_a^2} + \nu_C\right)} = \qquad \text{Equation 4-28}$$

$$= \frac{E_{ef} \cdot \frac{r_0 \cdot \pi \cdot d_i \cdot t \cdot \rho_{st} \cdot \frac{M_{cor}}{M_{Fe}} \cdot \frac{n_{cor}}{n_{Fe}}}{\pi(d_i + 2d_0)} \left(\frac{1}{\rho_r} - \frac{\alpha_r}{\rho_{st}}\right)}{r_a\left(\frac{r_b^2 + r_a^2}{r_b^2 - r_a^2} + \nu_C\right)} \qquad \text{Equation 4-29}$$

where:

σ_r = the radial stress (Pa)

E_{ef} = the effective elastic modulus of concrete (Pa)

ν_c = the Poisson's ratio of concrete

r_a and r_b given by Equations 4-21 and 4-22.

The initial fracture formation occurs at the inner radius of the concrete cylinder, i.e. at $r = a$ at a time t when f_t, the tensile strength of concrete, is exceeded.

An internal pressure of 1.5 MPa (equal to the tensile strength) is reached after a time determined by the corrosion rate. The time required to reach a pressure that leads to formation of fractures in the concrete has been calculated for different corrosion rates (d_i = 12 mm, d_c = 31 mm, ν_c = 0.18, E_{ef} = 30 GPa), see Figure 4-16. This time can be interpreted as the time it takes to create the necessary pressure after corrosion has been initiated (i.e. corrosion may be inhibited initially due to the high pH and low chloride content) and after the first corrosion products have filled out the pore space available in the annular porous zone near the reinforcement bar. Nevertheless, the calculated time is short when the corrosion rate is high. The currently assumed value in the safety assessment is $5 \cdot 10^{-8}$ m/year.

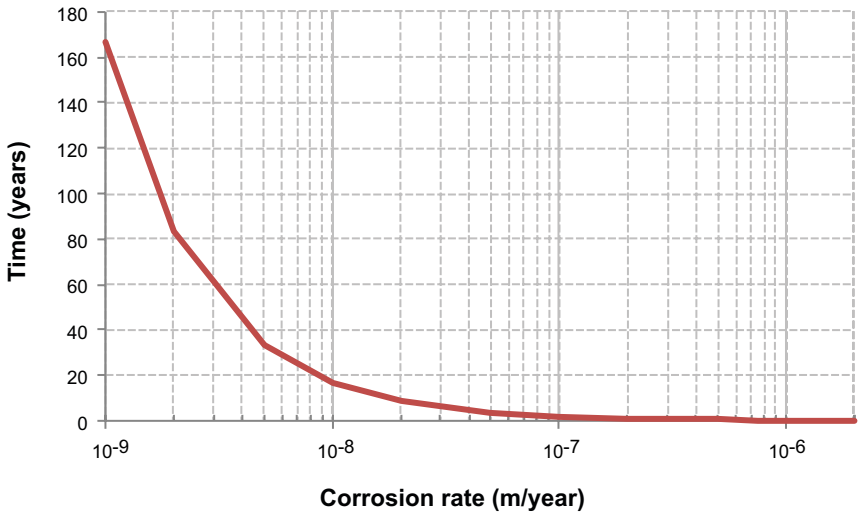

Figure 4-16. *Time calculated to reach the critical stress in the concrete cover for different assumed corrosion rates (r_0) of the reinforcement bars. Initially the steel bars may be passivated; hence the time to initiate corrosion should be added to these estimates.*

The fracture aperture width, b, caused by the corrosion of reinforcement bars can be estimated from (Li et al. 2005):

$$b = \frac{4\cdot\pi\cdot d_s(t)}{(1-\nu_C)\left(\frac{r_a}{r_b}\right)^{\sqrt{\alpha_s}}+(1+\nu_C)\left(\frac{r_a}{r_b}\right)^{\sqrt{\alpha_s}}} - \frac{2\cdot\pi\cdot r_b\cdot f_t}{E_{ef}} \qquad \text{Equation 4-30}$$

where:

$d_s(t)$ = the thickness of the corrosion products (m)

α_s = a stiffness reduction factor

E_{ef} = the effective elastic modulus of concrete (Pa)

ν_C = the Poisson's ratio of concrete

f_t = the tensile strength of concrete (Pa)

Model for internal pressurisation of a thick-walled cylinder

Calculations can also be made for a thick-walled cylinder exposed to an internal pressure denoted P_i, using a more simplified model see Figure 4-17.

The radial and tangential stresses (σ_r and σ_φ respectively) in the concrete in this case are given by (see e.g. Ayob et al. 2009):

$$\sigma_r = \frac{P_i\cdot d_i^2}{d_i^2-d_b^2}\left(1-\frac{d_b^2}{4r^2}\right) \qquad \text{Equation 4-31}$$

$$\sigma_\varphi = \frac{P_i\cdot d_i^2}{d_i^2-d_b^2}\left(1+\frac{d_b^2}{4r^2}\right) \qquad \text{Equation 4-32}$$

The radial expansion u_p, due to the internal pressure P_i, is given by:

$$u_p = \frac{r}{E}\cdot\left(\sigma_\varphi-\nu\cdot\sigma_r\right) = \frac{r}{E}\cdot\left(\frac{P_i\cdot d_i^2}{d_i^2-d_b^2}\left(1+\frac{d_b^2}{4r^2}\right)-\nu\cdot\frac{P_i\cdot d_i^2}{d_i^2-d_b^2}\left(1-\frac{d_b^2}{4r^2}\right)\right) =$$

$$= \frac{r}{E}\cdot\frac{P_i\cdot d_i^2}{d_i^2-d_b^2}\cdot\left(1+\frac{d_b^2}{4r^2}-\nu+\nu\cdot\frac{d_b^2}{4r^2}\right) \qquad \text{Equation 4-33}$$

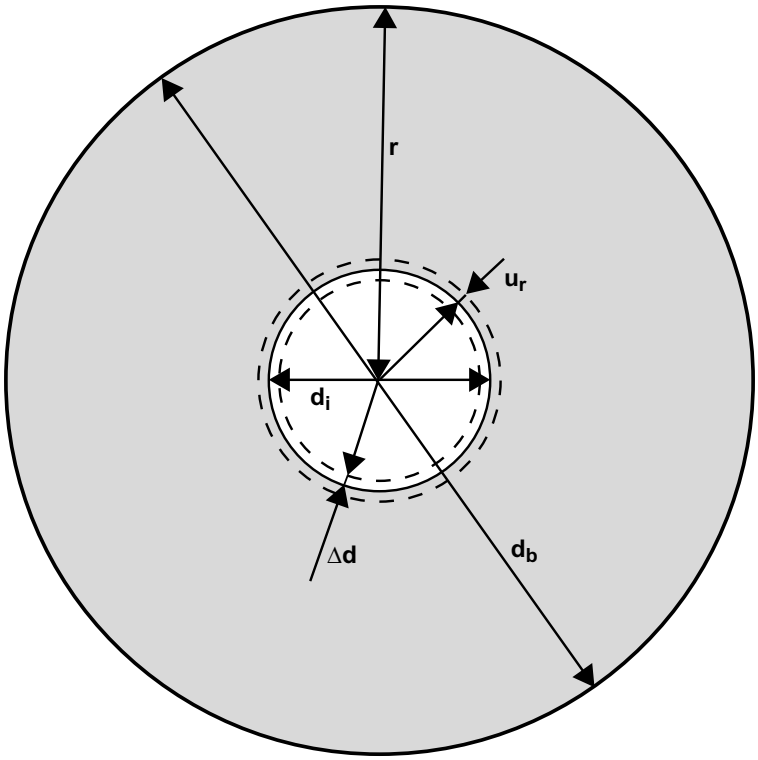

Figure 4-17. *Illustration of corrosion of reinforcement bars causing fracture formation in concrete constructions.*

Fractures will appear first at the inner radius $r = d_i/2$, when the tangential stress equals the tensile strength of the concrete (i.e. $\sigma_\varphi = f_t$), corresponding to a critical internal pressure P_{crit} and a radial expansion $u_{p,crit}$ at $r = d_i/2$:

$$f_t = \sigma_\varphi\Big|_{\left(r=\frac{d_i}{2}\right)} = \frac{P_{crit}\cdot d_i^2}{d_i^2-d_b^2}\left(1+\frac{d_b^2}{d_i^2}\right) \qquad \text{Equation 4-34}$$

$$P_{crit} = f_t \cdot \frac{d_i^2-d_b^2}{d_i^2+d_b^2} \qquad \text{Equation 4-35}$$

$$u_{p,crit} = \frac{d_i}{2E}\cdot f_t \cdot \frac{d_i^2-d_b^2}{d_i^2+d_b^2}\cdot\frac{d_i^2}{d_i^2-d_b^2}\cdot\left(1+\frac{d_b^2}{d_i^2}-\nu+\frac{\nu\cdot d_b^2}{d_i^2}\right) =$$

$$= \frac{f_t}{2E}\cdot\frac{d_i^3}{d_i^2+d_b^2}\cdot\left(1+\frac{d_b^2}{d_i^2}-\nu+\frac{\nu\cdot d_b^2}{d_i^2}\right) \qquad \text{Equation 4-36}$$

The critical internal pressure when the first fracture would appear, P_{crit}, is calculated to be 1.21 MPa and the corresponding radial expansion $u_{p,crit}$ at the inner radius is estimated to be 0.34 µm. This shows that for quite limited corrosion depths, which are related to the radial expansion, fractures may start to form.

A simple linear relationship between the corrosion depth of the reinforcement bars Δd, and the resulting fracture aperture width b, has been proposed by Thoft-Christensen (2005):

$$b = \gamma\Delta d \qquad \text{Equation 4-37}$$

where γ is typically in the range of 1.5–5. An expression for the change of the fracture width is also given by Thoft-Christensen (2005), based on the assumption that the increase in the area of the fracture is equal to the area occupied by the corrosion products formed. This expression can be used to derive an expression for γ based on the following:

$$\frac{1}{2}\left(\frac{\frac{d_i}{2}}{\frac{d_i}{2}+d_c}+1\right)\cdot d_c \cdot b = (\alpha_r - 1)\cdot \pi \cdot d_i \cdot \frac{\Delta d}{2}$$ Equation 4-38

$$b = \frac{(\alpha_r-1)\cdot\pi\cdot d_i\cdot\frac{\Delta d}{2}}{\frac{1}{2}\cdot d_c\cdot\left(\frac{\frac{d_i}{2}}{\frac{d_i}{2}+d_c}+1\right)} = \frac{(\alpha_r-1)\cdot\pi\cdot d_i}{d_c\cdot\left(\frac{\frac{d_i}{2}}{\frac{d_i}{2}+d_c}+1\right)}\cdot\Delta d$$ Equation 4-39

$$\gamma = \frac{b}{\Delta d} = \frac{(\alpha_r-1)\cdot\pi\cdot d_i}{d_c\cdot\left(\frac{\frac{d_i}{2}}{\frac{d_i}{2}+d_c}+1\right)}$$ Equation 4-40

where:

α_r = the ratio of the density of the steel and the density of the rust

d_c = the cover thickness (m)

d_i = diameter of the reinforcement bar (m)

An alternative analytical relationship between the loss of reinforcement bar dimension Δd and the fracture aperture width b, is given by Benin et al. (2010), see Figure 4-18 for the used notation:

$$\Delta d = \frac{b\cdot L}{8\cdot h}$$ Equation 4-41

$$b = \frac{\Delta d\cdot 8\cdot h}{L}$$ Equation 4-42

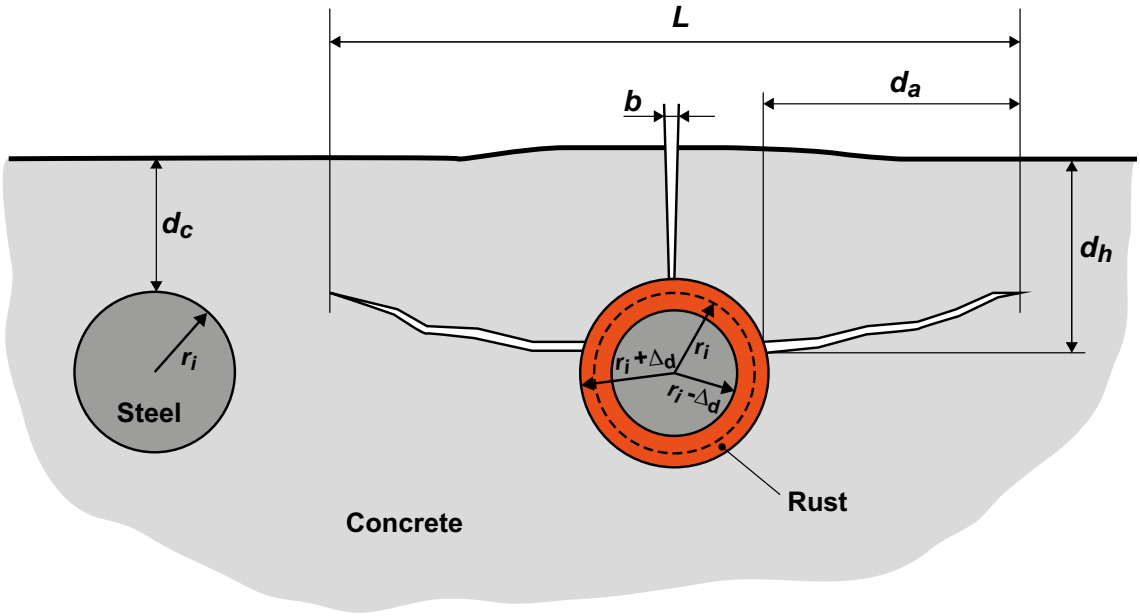

Figure 4-18. *Illustration to formation of horizontal and vertical fractures in concrete constructions due to corrosion of reinforcement bars, modified from Benin et al. (2010).*

Further, an expression is given for the distance d_h of the starting point of horizontal fractures to the concrete surface (Benin et al. 2010):

$$d_h = d_c\left(1 + \frac{1}{\frac{d_c}{r_i}+1}\right) \qquad \text{Equation 4-43}$$

$$b = \frac{\Delta d \cdot 8}{L} \cdot d_c\left(1 + \frac{1}{\frac{d_c}{r_i}+1}\right) \qquad \text{Equation 4-44}$$

The length, L, of the horizontal fractures extending from the reinforcement bars is given by Benin et al. (2010):

$$L = 2r_i \sqrt[3]{\pi(1+\nu)\cdot\left(\frac{d_c}{r_i}+1\right)\cdot\left(\frac{d_c}{r_i}\right)^2\cdot\left(1+\frac{1}{\frac{d_c}{r_i}+1}\right)^2} \qquad \text{Equation 4-45}$$

$$b = \Delta d \cdot \frac{8\cdot d_c\left(1+\frac{1}{\frac{d_c}{r_i}+1}\right)}{2r_i \sqrt[3]{\pi(1+\nu)\cdot\left(\frac{d_c}{r_i}+1\right)\cdot\left(\frac{d_c}{r_i}\right)^2\cdot\left(1+\frac{1}{\frac{d_c}{r_i}+1}\right)^2}} \qquad \text{Equation 4-46}$$

Calculated examples using Equation 4-46 for different corrosion depths Δd are given in Figure 4-19. The lengths of horizontal fractures have been calculated in the range of 0.11–0.17 m for the different variations shown. Obviously, depending on the distance between reinforcement bars in the concrete constructions, the horizontal fractures may combine, leading to spalling of layers of the cover concrete. The calculated fracture widths at different corrosion depths are of the same magnitude as experimental data reported by Tuutti (1982).

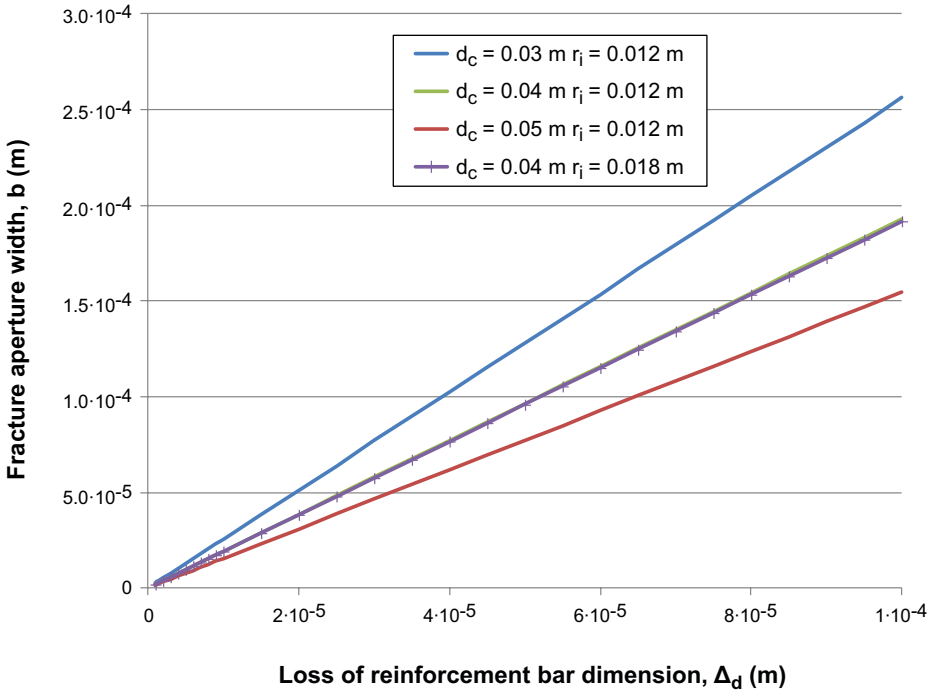

Figure 4-19. *Calculated fracture widths (b) versus corrosion depths (Δ_d) in concrete reinforcement bars. Different dimensions of the concrete cover layer thickness (d_c) and the radius of steel bars (ri) have been assumed.*

A value for γ can be calculated from the above:

$$\gamma = \frac{b}{\Delta d} \qquad \text{Equation 4-47}$$

The calculated values of γ are in the range 1.54–2.56 in the different variations selected, which is well within the range stated by Thoft-Christensen (2005). It should also be noted that it is in reasonable agreement with the simple estimate shown in previous section, see Figure 4-12.

Effects of creep

Creep is the slow, time-dependent deformation of a material under a constant stress state. Concrete is in many aspects a stiff and brittle material. Creep may result in a relaxation of the stress, if the stress does not exceeds a critical value for fracture formation with time. The creep strain is directly proportional to stress up to ~ half the tensile strength. When the stress exceeds ~ 80 % of the tensile strength, failure will occur with time.

In the case of corroding steel components in the concrete barriers, this could be interpreted in the following way. If the corrosion rate is low enough, the strain caused by the formation of corrosion products may be accommodated by creep without leading to fracture formation. For higher corrosion rates, creep could delay the time at which fracture formation occurs.

Numerical studies of creep deformation that eventually leads to fracture formation in concrete exposed to pressurisation by corroding reinforcement bars have been presented by Benin et al. (2010), applying a range of models to describe the material behaviour (elasticity, plasticity etc). The different model assumptions used resulted in a 30% difference in the critical pressures calculated to cause fracture formation.

No attempt is made in the present study to address creep quantitatively since this is beyond the scope of the investigation. It is tentatively concluded that creep may be an important factor when estimating the time when corrosion induced fractures appear in concrete that contain various steel construction components. However, judging from the variations that assume different corrosion rates of reinforcement bars (see Figure 4-16), it is found that, except for very low corrosion rates, the time for corrosion to create a high enough pressure to cause fractures is fairly short. Hence, for the safety assessment, only a fairly short lag time would be possible to account for even if creep is considered, on the order of a few decades.

5 Mathematical derivation of diffusion- and advection-controlled interactions with groundwater

In the first part of this Chapter, the rate of different leaching processes is evaluated over time using simple models. Diffusion-controlled leaching of portlandite and CSH gel is investigated first, followed by advection-controlled leaching. Diffusion-controlled leaching of concrete combined with diffusion into the groundwater that flows past the concrete walls has also been considered. The impact of fractures on diffusion- and advection-controlled leaching is then studied. Finally, as a relevance check, the fracture aperture size required to accommodate all advective flow through the barrier is assessed as a function of fracture spacing.

In the second section of this Chapter, the intrusion of chloride, carbonate, and sulphate into concrete is evaluated using a simple model that includes their reactions with selected cement minerals. This generates an estimation of the penetration depth of these elements into the concrete as a function of time.

5.1 Impact of leaching of concrete

Leaching of calcium may cause the concrete barriers in BMA to gradually deteriorate. Calcium is an important component that contributes significantly to the strength of the hardened concrete. The different calcium minerals in the concrete are alkaline and provide a basis for buffering the chemical conditions at a high pH. During an early stage, sodium and potassium hydroxides may provide additional mineral alkalinity, but due to fairly high solubility and minor amounts of these components the effect on the chemical conditions is relatively short term. For the first set of scoping calculations, the leaching of portlandite, $Ca(OH)_2$, and in selected cases also the combined leaching of the calcium silicate hydrate gel (CSH) is considered. Tentatively the zone depleted in portlandite could be denoted weakly weathered and the zone depleted in CSH-gel denoted severely weathered. It should be stressed that this is an operational definition aimed at scoping calculations rather than a firm scientific basis. The conceptual degradation of concrete and the impact of fractures are illustrated in Figure 5-1.

5.1.1 Leaching of portlandite and CSH gel – diffusion control

In a first step, a simple model for the diffusion controlled leaching of calcium from the concrete is applied. The portlandite leaching process has been represented by a simple shrinking core model for a slab, see e.g. Levenspiel (1972), here given for the progression of a weakly weathered zone where dissolution of portlandite occurs in a sharp front until depleted:

$$h = \sqrt{\frac{2 \cdot D_{e,ww} \cdot c_{sol}^{CH} \cdot t}{q_0^{CH}}} \qquad \text{Equation 5-1}$$

where:

h = thickness of a weakly weathered zone of concrete (m)

$D_{e,ww}$ = effective diffusivity of weakly weathered zone (m^2/a)

c_{sol}^{CH} = solubility of portlandite ($kmol/m^3$)

t = time (a)

q_0^{CH} = initial amount of free portlandite in concrete ($kmol/m^3$)

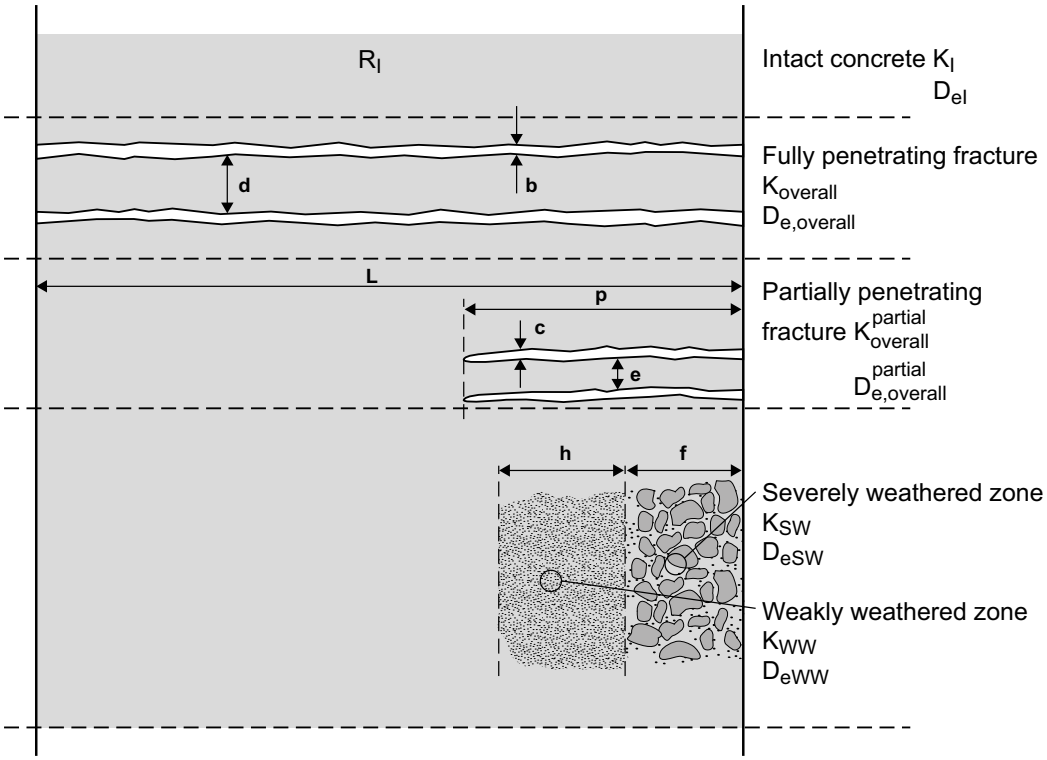

Figure 5-1. *Illustration of different cases of flow and diffusion in fractured and chemically degraded (weathered) concrete.*

The development of a severely weathered zone in response to leaching of CSH-gel can be represented in an equivalent way:

$$f = \sqrt{\frac{2 \cdot D_{e,sw} \cdot c_{sol}^{CSH} \cdot t}{q_0^{CSH}}} \qquad \text{Equation 5-2}$$

where:

f = thickness of a severely weathered zone of concrete (m)

$D_{e,sw}$ = effective diffusivity of severely weathered zone (m^2/a)

c_{sol}^{CSH} = solubility of CSH-gel ($kmol/m^3$)

t = time (a)

q_0^{CSH} = initial amount of CSH-gel in concrete ($kmol/m^3$)

Since the leaching processes of portlandite and CSH-gel involve common chemical compounds, calcium and hydroxide ions, the two leaching processes are coupled and will interact. A small approximate correction may be introduced to the leaching calculations to account for this interaction. This correction is applied in the analytical evaluations in the present section, whereas in subsequent reactive transport calculations using a numerical model (Section 8) the fully coupled chemical system will be considered.

Leaching of portlandite is faster than the leaching of the less soluble CSH-gel. When the leaching of portlandite has reached a certain depth, the corresponding gradient of the porewater concentrations near the surface of the concrete wall will fall below the solubility limit of the CSH-gel, which will start to dissolve. The effect of this is that the leaching of portlandite will slow down to some extent as compared to the case where leaching of portlandite takes place as a pure phase, see illustration in Figure 5-2.

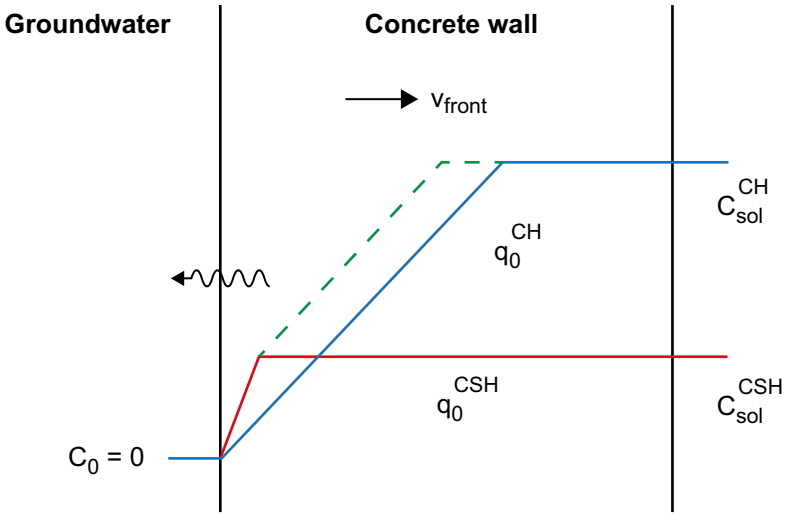

Figure 5-2. *Illustration of diffusion controlled simultaneous leaching of portlandite and CSH-gel in concrete. Blue line corresponds to a concentration gradient for the case of pure phase portlandite, green and red lines correspond to concentration gradients in the presence of both portlandite and CSH phases.*

A corrected estimate of the portlandite leaching can be made using the following expression:

$$h_{corr} = \sqrt{\frac{2 \cdot D_{e,ww} \cdot (c_{sol}^{CH} - c_{sol}^{CSH}) \cdot t}{q_0^{CH}}} \qquad \text{Equation 5-3}$$

where:

h_{corr} = thickness of a weakly weathered zone of concrete corrected for the simultaneous leaching of portlandite and CSH-gel (m)

c_{sol}^{CH} = solubility of portlandite (kmol/m^3)

c_{sol}^{CSH} = solubility of CSH-gel (kmol/m^3)

Example calculations for the 1BMA repository are shown in Figure 5-3. The parameter values assumed in the calculations are presented in Table 5-1.

Table 5-1. Summary of parameter values assumed in the example calculations.

Parameter	Value	Unit	Comment
$D_{e,ww}$	$3.0 \cdot 10^{-11}$	m^2/s	Corresponds to ”Aged concrete” (Thomson et al. 2008)
$D_{e,sw}$	$5.0 \cdot 10^{-11}$	m^2/s	Assumed slightly higher than for ”Aged concrete”
c_{sol}^{CH}	$5.0 \cdot 10^{-3}$	kmol/m^3	Estimated from Portlandite solubility at pH 12.6
c_{sol}^{CSH}	$2.3 \cdot 10^{-3}$	kmol/m^3	Calculated with Medusa (Puigdomènech 2002)
c_0	0	kmol/m^3	Conservative assumption
q_0^{CH}	1.04	kmol/m^3	(Höglund 2001)
q_0^{CSH}	1.23	kmol/m^3	(Höglund 2001)

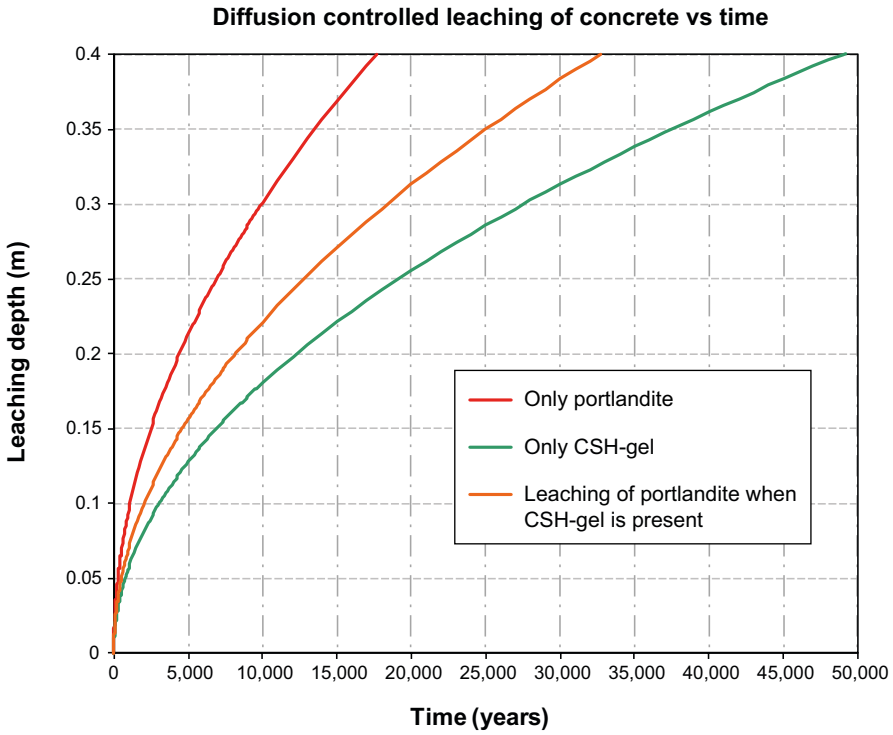

Figure 5-3. *Diffusion controlled leaching of concrete showing the calculated depth of depletion of portlandite or CSH-gel for different cases.*

An extension to the estimation of the leaching depth can be made by taking into account the development of a concentration profile in the groundwater that flows past the concrete structures in the BMA vault, see illustration in Figure 5-4. The concentration c_y at the interface between concrete and the flowing groundwater will reduce the driving force for the leaching and the expression for the leaching depth can be expressed as:

$$h_y = \sqrt{\frac{2 \cdot D_{e,dc} \cdot (c_{sol}^{CH} - C_y) \cdot t}{q_0^{CH}}} \qquad \text{Equation 5-4}$$

where:

h_y = thickness of the leached zone of concrete when the build up of a concentration profile is considered (m)

$D_{e,dc}$ = effective diffusivity of portlandite depleted zone of concrete (m^2/a)

c_{sol}^{CH} = solubility of portlandite ($kmol/m^3$)

c_y = concentration at the interface between concrete and groundwater ($kmol/m^3$)

The concentration profile in the groundwater passing is given by (Bird et al. 1960):

$$c(x,z) = c_y \cdot \mathrm{erfc}\left(\frac{x}{\sqrt{\frac{4 \cdot D_{e,m} \cdot z}{v_0}}}\right) \qquad \text{Equation 5-5}$$

where:

c = concentration in water at a distance x from the concrete surface (mol/m^3)

erfc = the complimentary error function

x = distance from the concrete surface (m)

$D_{e,m}$ = effective diffusivity in the macadam backfill (m^2/s)

z = distance along the concrete surface in the direction of ambient groundwater flow (m)

v_0 = velocity of groundwater (m/s)

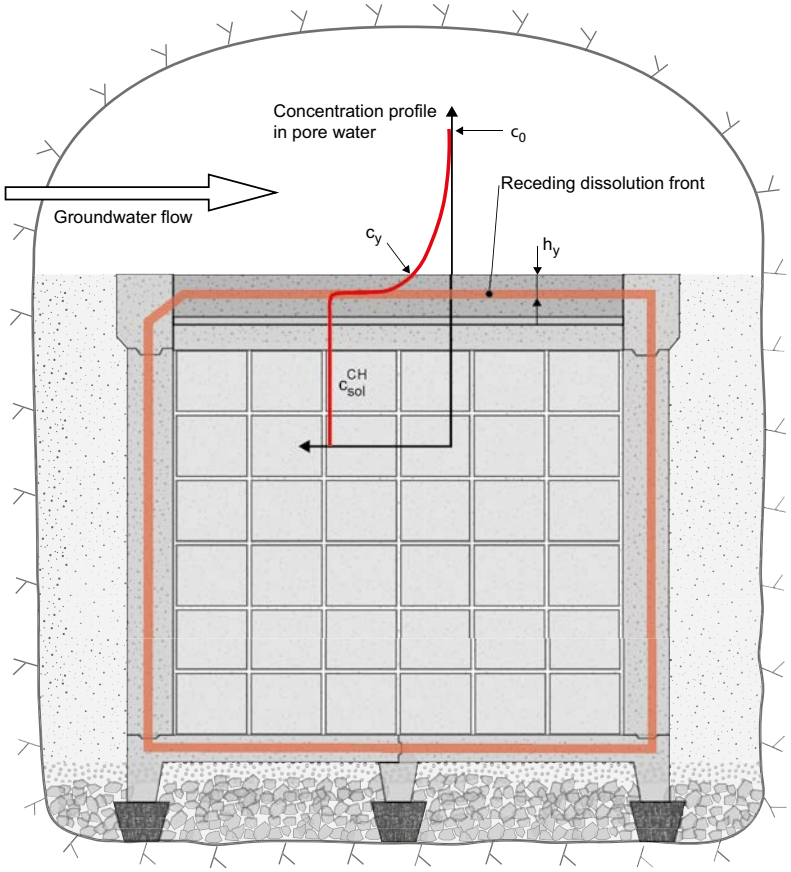

Figure 5-4. *Illustration of leaching of concrete by groundwater passing through the 1BMA vault. Figure is not to scale.*

The flux of dissolved species in the *x*-direction j_x, in the groundwater/macadam near the concrete surface is given by:

$$j_x = -D_{e,m} \cdot \frac{\partial c}{\partial x} = -D_{e,m} \cdot \frac{\partial}{\partial x}\left(c_y \cdot \mathrm{erfc}\left(\frac{x}{\sqrt{\frac{4D_{e,m} \cdot z}{v_0}}} \right) \right) \qquad \text{Equation 5-6}$$

The complimentary error function is defined as:

$$\mathrm{erfc}(\xi) = 1 - \frac{2}{\sqrt{\pi}} \int_0^{\xi} e^{-w^2} dw \qquad \text{Equation 5-7}$$

Using the differentiation rule:

$$\frac{\partial}{\partial x} \int_a^{bx} f(p)\, dp = b \cdot f(x) \qquad \text{Equation 5-8}$$

the molar flux over the concrete – groundwater interface ($x = 0$) is obtained from:

$$j_x|_{x=0} = -D_{e,m} \cdot \left.\frac{\partial c}{\partial x}\right|_{x=0} = D_{e,m} \cdot c_y \cdot \frac{2}{\sqrt{\pi}} \sqrt{\frac{v_0}{4D_{e,m} \cdot z}} = c_y \sqrt{\frac{D_{e,m} \cdot v_0}{\pi \cdot z}} \qquad \text{Equation 5-9}$$

which upon integration over the whole concrete – groundwater interface (with the width B, and length L in the flow direction) yields:

$$J_x = B \cdot \int_0^L j_x|_{x=0}\, dz = B \cdot c_y \sqrt{\frac{D_{e,m} \cdot v_0}{\pi}} \cdot \int_0^L \frac{dz}{\sqrt{z}} =$$

$$= \{A = B \cdot L\} = A \cdot c_y \sqrt{\frac{4 \cdot D_{e,m} \cdot v_0}{\pi \cdot L}} \qquad \text{Equation 5-10}$$

where:

A = the area of the concrete surface (m^2)

B = the width of the concrete surface perpendicular to the flow direction (m)

L = the length of the concrete in the flow direction (m)

Introducing a mass balance over the interface concrete – groundwater:

$$D_{e,dc} \cdot \frac{c_{sol}^{CH} - c_y}{h_y} \cdot A = A \cdot c_y \sqrt{\frac{4 \cdot D_{e,m} \cdot v_0}{\pi \cdot L}} \qquad \text{Equation 5-11}$$

Rearranging and solving for the mean concentration at the interface c_y (see Höglund and Bengtsson 1991 for more detail):

$$c_y = -\frac{\pi \cdot D_{e,dc} \cdot L \cdot q_0^{CH}}{16 \cdot D_{e,m} \cdot v_0 \cdot t} + \sqrt{\left(\frac{\pi \cdot D_{e,dc} \cdot L \cdot q_0^{CH}}{16 \cdot D_{e,m} \cdot v_0 \cdot t}\right)^2 + \frac{\pi \cdot D_{e,dc} \cdot L \cdot q_0^{CH}}{8 \cdot D_{e,m} \cdot v_0 \cdot t} c_{sol}^{CH}} \qquad \text{Equation 5-12}$$

By inserting Equation 5-12 in 5-4, a closed expression for the mean leaching depth over time is obtained:

$$h_y = \sqrt{\frac{2 \cdot D_{e,dc} \cdot t \cdot \left(c_{sol}^{CH} + \frac{\pi \cdot D_{e,dc} \cdot L \cdot q_0^{CH}}{16 \cdot D_{e,m} \cdot v_0 \cdot t} - \sqrt{\left(\frac{\pi \cdot D_{e,dc} \cdot L \cdot q_0^{CH}}{16 \cdot D_{e,m} \cdot v_0 \cdot t}\right)^2 + \frac{\pi \cdot D_{e,dc} \cdot L \cdot q_0^{CH}}{8 \cdot D_{e,m} \cdot v_0 \cdot t} c_{sol}^{CH}} \right)}{q_0^{CH}}} \qquad \text{Equation 5-13}$$

An example calculation using Equation 5-13 is presented in Figure 5-5. The parameter values assumed for the calculations are: an effective diffusivity of $5 \cdot 10^{-12}$ m^2/s in the partly leached zone in the concrete; an effective diffusivity of $1.5 \cdot 10^{-10}$ m^2/s in the macadam backfill; a groundwater velocity of 0.2 m/year; an initial amount of portlandite of 1.04 kmol/m^3 in the concrete and a portlandite solubility of $5 \cdot 10^{-3}$ kmol/m^3.

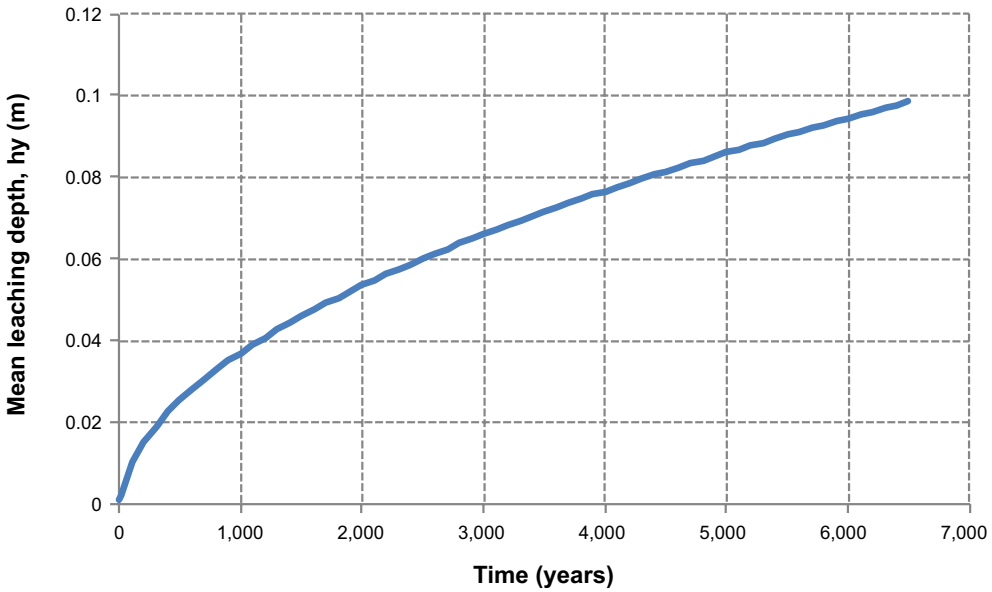

Figure 5-5. *Example calculation of the mean leaching depth in concrete exposed to groundwater flowing past the surface.*

5.1.2 Leaching of portlandite and CSH gel – advection control

The development of leached zones in the concrete may also be estimated for a simple case where the dissolution is assumed to occur due to groundwater flow through the concrete, see Figure 5-6. Hence, it is assumed that advective transport dominates over diffusion, which therefore can be neglected in this case.

Here, the advective flow in the concrete barrier is assumed to resemble a homogeneous porous medium. For an advection-controlled dissolution of the cement minerals, it can be shown:

$$h_a = \frac{c_{sol}^{CH} \cdot q_{gw} \cdot t}{q_0^{CH}} \qquad \text{Equation 5-14}$$

where:

h_a = thickness of a weakly weathered zone of concrete (m)

q_{gw} = groundwater flux ($m^3/m^2/a$)

For a concrete wall of finite thickness L, the degree of leaching X_{CH} can be expressed as:

$$X_{CH} = \frac{h_a}{L} = \frac{c_{sol}^{CH} \cdot q_{gw} \cdot t}{q_0^{CH} \cdot L} \qquad \text{Equation 5-15}$$

An equivalent expression for the development of a leached zone in the CSH-gel:

$$f_a = \frac{c_{sol}^{CSH} \cdot q_{gw} \cdot t}{q_0^{CSH}} \qquad \text{Equation 5-16}$$

where:

f_a = thickness of a weakly weathered zone of concrete (m)

c_{sol}^{CSH} = solubility of CSH-gel ($kmol/m^3$)

q_0^{CSH} = initial amount of CSH-gel in concrete ($kmol/m^3$)

Example calculations for the BMA repository have been made assuming a time dependent ground-water flux through the cavern according to Holmén and Stigsson (2001) as presented in Figure 5-7.

In the calculations it has been assumed that all water flows through the concrete barriers, which would be the most pessimistic case. Other parameter values have been assumed the same as those presented in Table 5-1 where appropriate. The results are shown in Figure 5-8 and Figure 5-9.

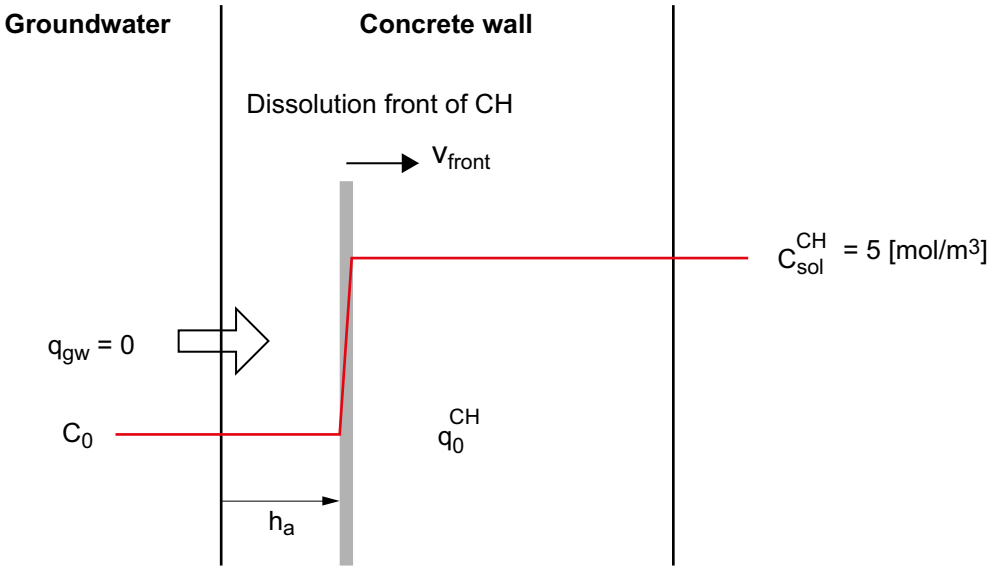

Figure 5-6. *Illustration to advective controlled leaching of portlandite in concrete.*

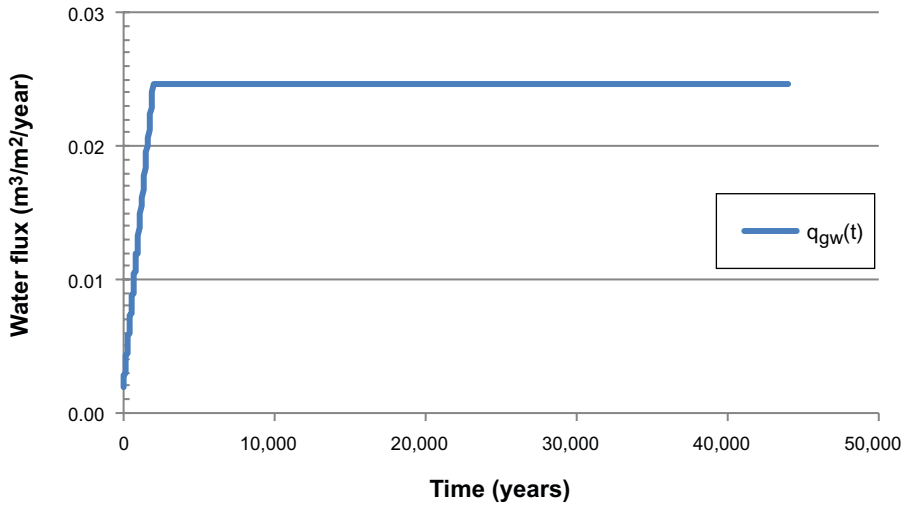

Figure 5-7. *Assumed groundwater flux $q_{gw}(t)$, in the BMA repository for the advection controlled leaching calculations.*

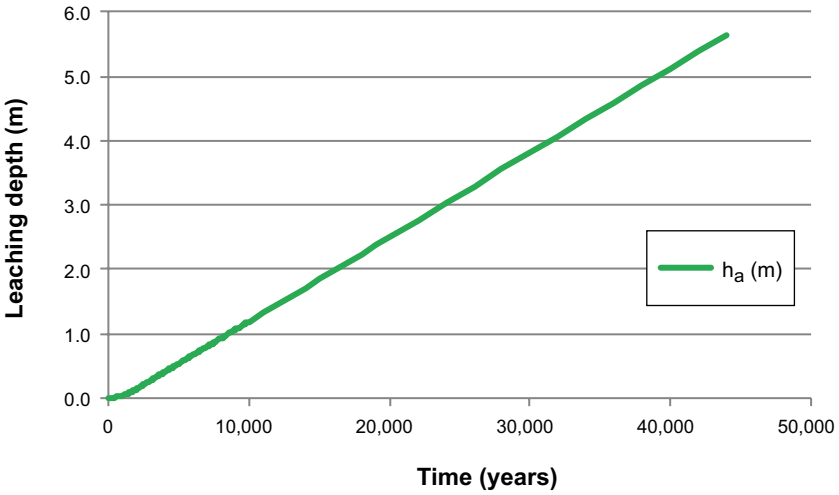

Figure 5-8. *Example calculations showing the leaching depth h_a, versus time for concrete in the BMA repository when assuming advection controlled leaching of portlandite.*

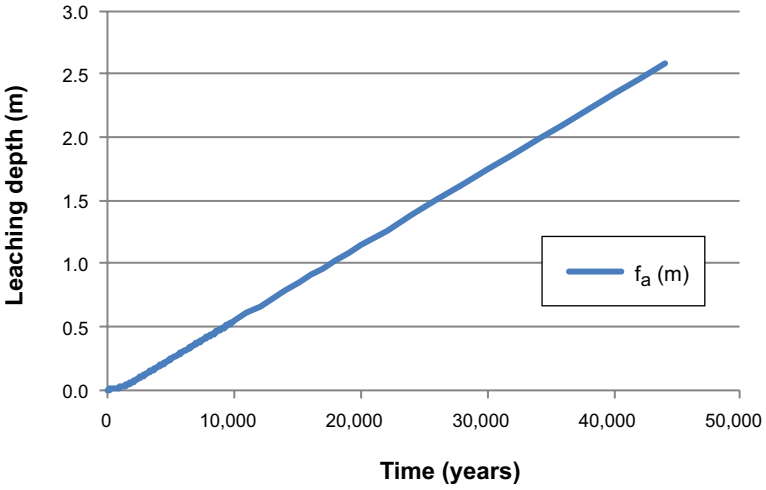

Figure 5-9. *Example calculations showing the leaching depth f_a, versus time for concrete in the BMA repository when assuming advection controlled leaching of CSH-gel.*

5.1.3 Leaching of portlandite – impact of fractures

Here it is assumed that thin fractures have formed through the concrete barrier, or that some other type of heterogeneity is present, e.g. a construction joint. As a pessimistic assumption the advective flow converges to the fractures, but the total advective flow remains the same as in the homogeneous porous media flow case described in Section 5.1:

$$Q_0 = q_{gw} \cdot A_{tot} = q_{\text{fracture}} \cdot A_{\perp\text{fracture}}$$ Equation 5-17

where:

q_{gw} = groundwater flux in homogeneous porous media ($m^3/m^2/a$)

A_{tot} = cross-section of the concrete barrier (= $B \cdot d$) (m^2)

q_{fracture} = advective flux in the fractures ($m^3/m^2/a$)

$A_{\perp\text{fracture}}$ = cross-section of the fracture perpendicular to the flow (= $B \cdot b$) (m^2)

B = width of the concrete barrier (m)

d = fracture spacing (m)

b = fracture width (m)

This means that the flux will increase in proportion to the inverse of the fraction of the surface area that constitutes fractures:

$$q_{\text{fracture}} = \frac{q_{gw} \cdot d}{b}$$ Equation 5-18

The leaching in the fractured concrete may be described by one of the following limiting cases:

a) Congruent dissolution of portlandite over the entire fracture surface (both surfaces).

b) Dissolution of portlandite in a thin surface layer, creating a moving dissolution front along the flow direction in the fracture.

c) Matrix diffusion controlled dissolution in the concrete matrix in the direction perpendicular to the flow direction in the fracture.

Case a) Congruent dissolution over the entire fracture surface

In this case the dissolution takes place over the entire fracture surfaces and creates a dissolution front that moves perpendicular to the direction of the advective flow in the fracture, see Figure 5-10. The total amount of water that flows through the fracture is Q_0. The amount of portlandite dissolved is given by:

$$N_{CH} = Q_0 \cdot c_{sol}^{CH}$$ Equation 5-19

Where:

N_{CH} = rate of portlandite dissolution (mol/a)

Q_0 = groundwater flow in fracture (m^3/a)

c_{sol}^{CH} = solubility of portlandite (mol/m^3)

The volume of concrete depleted of portlandite due to the leaching is:

$$V_Y = \frac{Q_0 \cdot c_{sol}^{CH} \cdot t}{q_0^{CH}}$$ Equation 5-20

where:

V_Y = volume of concrete depleted of portlandite (m^3)

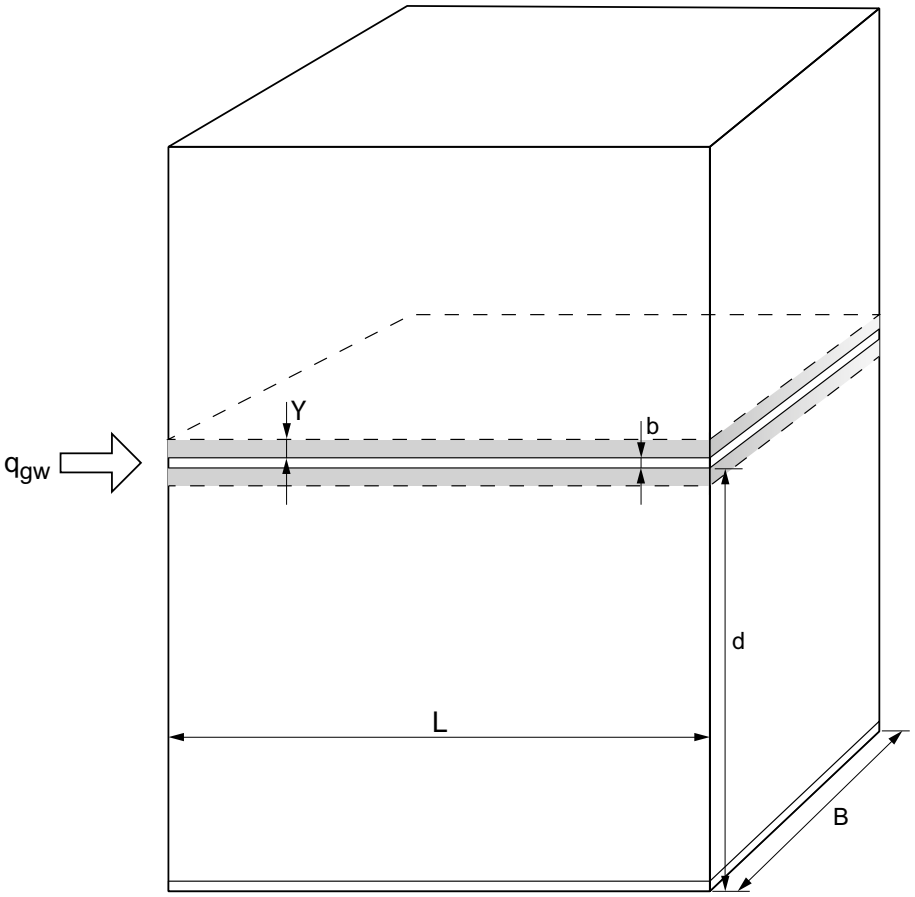

Figure 5-10. *Illustration of uniform dissolution of portlandite in a concrete fracture or construction joint.*

The total fracture surface where the dissolution takes place is:

$$A_{\|\text{fracture}} = 2 \cdot L \cdot B \qquad \text{Equation 5-21}$$

where:
L = thickness of the concrete barrier (m)
B = width of the concrete barrier (m)

The position of the dissolution front (Y) varies with time:

$$Y = \frac{V_Y}{A_{\|\text{fracture}}} = \frac{Q_0 \cdot c_{sol}^{CH} \cdot t}{2 \cdot L \cdot B \cdot q_0^{CH}} = \frac{q_{gw} \cdot d \cdot c_{sol}^{CH} \cdot t}{2 \cdot L \cdot q_0^{CH}} \qquad \text{Equation 5-22}$$

where:

Q_0 = groundwater flow in fracture (m^3/a)

c_{sol}^{CH} = solubility of portlandite (mol/m^3)

q_0^{CH} = initial amount of portlandite in concrete (mol/m^3)

d = fracture spacing (m)

The dissolution front moves a distance Y in each direction from the fracture surface in time t. Hence, if a complete dissolution of all concrete components would occur, the fracture width would increase by $2Y$. Calculated results with parameters from Table 5-1 are presented in Figure 5-11.

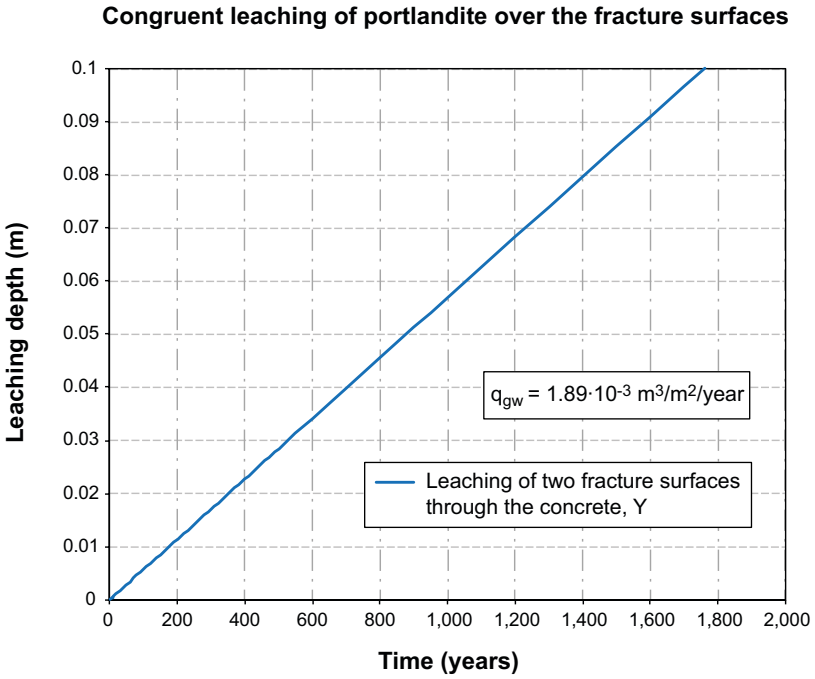

Figure 5-11. *Leaching depth (Y) of concrete in a fracture through the concrete barrier, assuming congruent dissolution of portlandite over the two fracture surfaces.*

Case b) Dissolution of a thin surface layer of portlandite – front moving along the flow in the fracture

The same amount of water Q_0 flows in the fracture as in Case a). Also the amount of dissolved portlandite remains the same. The volume of concrete depleted of portlandite V_δ is then obviously the same as V_Y in Case a):

$$V_\delta = \frac{Q_0 \cdot c_{sol}^{CH} \cdot t}{q_0^{CH}} \qquad \text{Equation 5-23}$$

where:

V_δ = volume of concrete depleted of portlandite (m^3)

Q_0 = groundwater flow in fracture (m^3/a)

c_{sol}^{CH} = solubility of portlandite (mol/m^3)

q_0^{CH} = initial amount of portlandite in concrete (mol/m^3)

In this case, the dissolution is assumed to take place in a thin surface layer with thickness δ over the whole width of the two fracture surfaces, see Figure 5-12. A sharp dissolution front is formed that moves along the direction of the advective flow in the fracture and the distance between the fracture entrance and the leading edge of the front, x_1 varies with time t:

$$x_1 = \frac{V_\delta}{2 \cdot \delta \cdot B} = \frac{Q_0 \cdot c_{sol}^{CH} \cdot t}{2 \cdot \delta \cdot B \cdot q_0^{CH}} = \frac{q_{gw} \cdot d \cdot c_{sol}^{CH} \cdot t}{2 \cdot \delta \cdot q_0^{CH}} \qquad \text{Equation 5-24}$$

where:

V_δ = volume of concrete depleted of portlandite (m^3)

δ = thickness of a surface layer where portlandite dissolves (m)

B = width of the concrete barrier (m)

Q_0 = groundwater flow in fracture (m^3/a)

c_{sol}^{CH} = solubility of portlandite (mol/m^3)

t = time (a)

q_0^{CH} = initial amount of portlandite in concrete (mol/m^3)
q_{gw} = groundwater flux in homogeneous porous media (m^3/m^2/a)
d = fracture spacing (m)

Calculations for this case with parameters from Table 5-1 are presented in Figure 5-13.

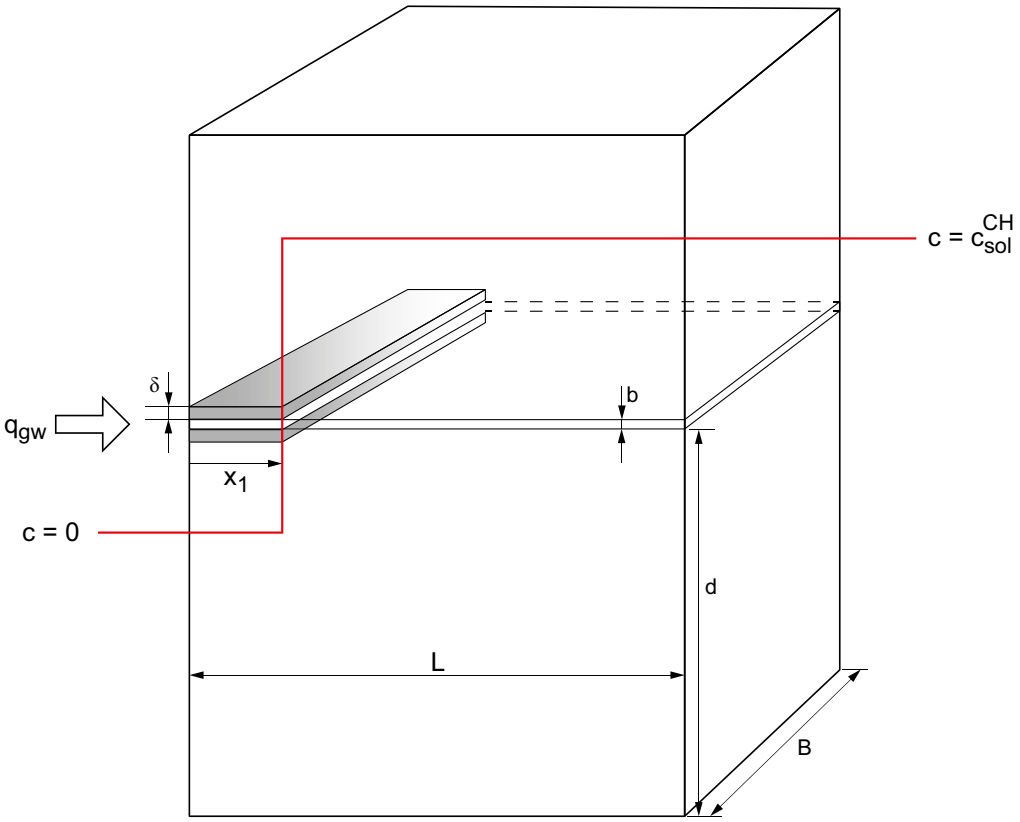

Figure 5-12. *Illustration of dissolution of portlandite in a thin surface layer along a concrete fracture or construction joint.*

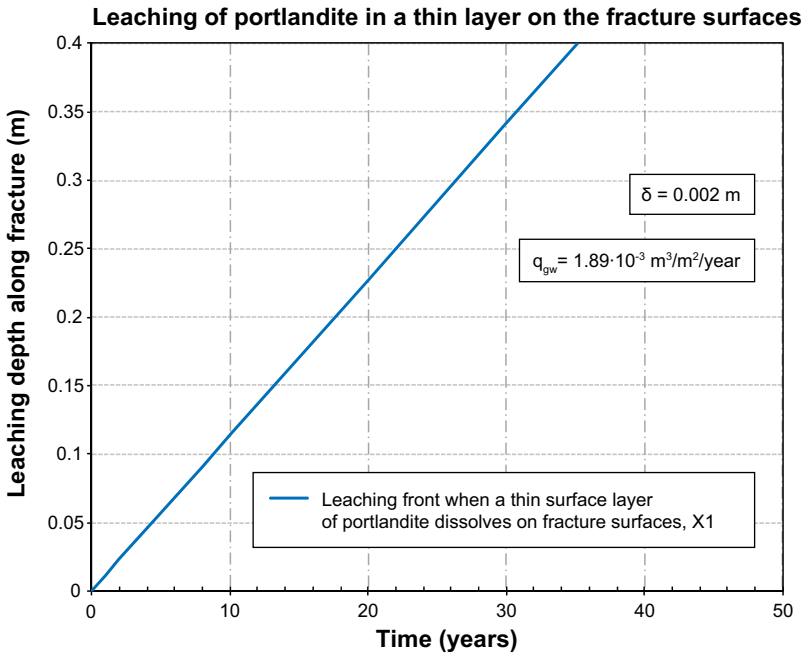

Figure 5-13. *Leaching of concrete in a fracture through the concrete barrier, assuming congruent dissolution of portlandite over the two fracture surfaces.*

Case c) Matrix diffusion controlled dissolution of portlandite in the concrete matrix – front moves along the fracture

In this case, portlandite is assumed to dissolve in a front receding from the fracture surface into the concrete essentially in a direction perpendicular to the water flow in the fracture. Water is assumed to flow only in the fracture, whereas diffusion is the only transport mechanism in the concrete between the fractures. As a zone depleted in portlandite develops, the diffusion resistance increases and dissolution will also start gradually downstream from the fracture entrance. Hence, a wedge shaped dissolution front is formed and propagates through the concrete barrier, see illustration in Figure 5-14. The conceptual description of the dissolution and transport of dissolved portlandite from a fracture in concrete may be regarded more accurate in this case than assumed in cases a) and b). The derivation of the model is not given here but is based on analogy with models describing the movement of a redox front presented in Sidborn (2007), Romero et al. (1992), Neretnieks (1982) and underlying mathematical treatment is given in Cooper and Liberman (1970).

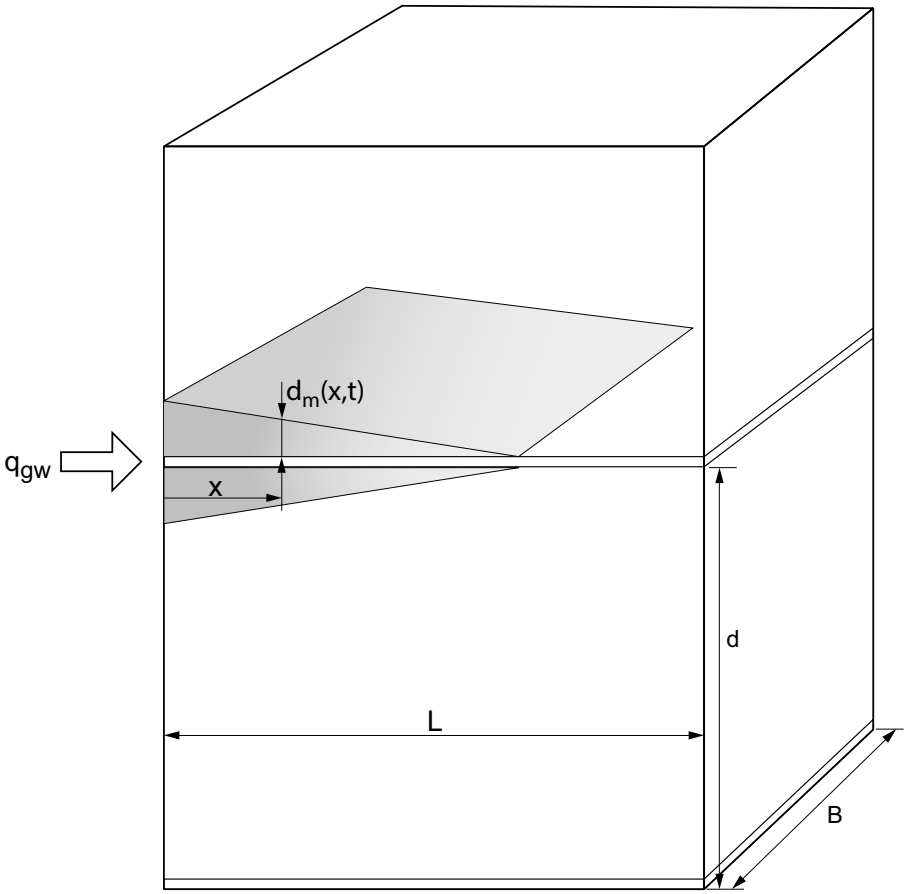

Figure 5-14. *Illustration to matrix diffusion controlled dissolution of portlandite along a concrete fracture or construction joint.*

The movement of the dissolution front of portlandite is described by:

$$d_m(x,t) = \sqrt{\frac{2 \cdot D_{e,ww} \cdot c_{sol}^{CH} \cdot t}{q_0^{CH}}} - \frac{2 \cdot D_{e,ww} \cdot x}{q_{gw} \cdot d} \qquad \text{Equation 5-25}$$

$$d_m(x,t) \geq 0 \qquad \text{Equation 5-26}$$

where:

$d_m(x,t)$ = the position of the portlandite dissolution front (m)

x = the position along the fracture where $d_m(x,t)$ is evaluated (m)

$D_{e,ww}$ = effective diffusivity of weakly weathered zone (m^2/a)

c_{sol}^{CH} = solubility of portlandite (mol/m^3)

q_0^{CH} = initial amount of portlandite in concrete (mol/m^3)

q_{gw} = the groundwater flux outside the concrete structure ($m^3/m^2/a$)

d = fracture spacing (m)

This may be written on a simplified form:

$$d_m = \sqrt{\alpha_a \cdot t} - \beta_a \cdot x \qquad \text{Equation 5-27}$$

where:

$$\alpha_a = \frac{2 \cdot D_{e,ww} \cdot c_{sol}^{CH}}{q_0^{CH}} \qquad \text{Equation 5-28}$$

and

$$\beta_a = \frac{2 \cdot D_{e,ww}}{q_{gw} \cdot d} \qquad \text{Equation 5-29}$$

A water balance gives:

$$q_{gw} \cdot d \cdot B = q_{\text{fracture}} \cdot b \cdot B \qquad \text{Equation 5-30}$$

$$q_{gw} \cdot d = q_{\text{fracture}} \cdot b \qquad \text{Equation 5-31}$$

Hence $q_{gw} \cdot d$ can be exchanged for $q_{\text{fracture}} \cdot b$ in the different equations if found more convenient.

The position x_0 of the leaching front along the fracture is calculated for $d_m = 0$ which gives:

$$x_0 = \sqrt{\frac{\alpha_a \cdot t}{\beta_a^2}} \qquad \text{Equation 5-32}$$

An expression for the rate the front moves is given by:

$$v_{\text{front}} = \frac{dx_0}{dt} = \sqrt{\frac{\alpha_a}{\beta_a^2}} \cdot \frac{d}{dx}\sqrt{t} = \frac{1}{2} \cdot \sqrt{\frac{\alpha_a}{\beta_a^2 \cdot t}} = \frac{1}{2\beta_a} \cdot \sqrt{\frac{\alpha_a}{t}} = \frac{q_{gw} \cdot d}{4 \cdot D_{e,ww}} \cdot \sqrt{\frac{2 D_{e,ww} \cdot c_{sol}^{CH}}{q_0^{CH} \cdot t}} =$$

$$= \frac{q_{gw} \cdot d}{D_{e,ww}} \cdot \sqrt{\frac{D_{e,ww} \cdot c_{sol}^{CH}}{2 \cdot q_0^{CH} \cdot t}} \qquad \text{Equation 5-33}$$

This expression is identical to the expression given by Romero et al. (1992) for the movement of a redox front in a fractured rock.

The extension of the leached zone perpendicular to the direction of the fracture at the fracture entrance is given by:

$$d_m(0,t) = d_0 = \sqrt{\alpha_a \cdot t} \qquad \text{Equation 5-34}$$

The amount of portlandite leached along the fracture is calculated from (valid for short times before the leaching front reaches $x = L$):

$$N_{\text{leached}} = 2 \cdot \frac{d_0 \cdot x_0}{2} \cdot q_0^{CH} = \sqrt{\alpha_a \cdot t} \cdot \frac{\sqrt{\alpha_a \cdot t}}{\beta_a} \cdot q_0^{CH} = \frac{\alpha_a \cdot t}{\beta_a} \cdot q_0^{CH} \qquad \text{Equation 5-35}$$

The amount of dissolved portlandite transported through the fracture is given by:

$$N_{\text{transp}} = q_{gw} \cdot d \cdot c_{sol}^{CH} \cdot t \qquad \text{Equation 5-36}$$

A check of the mass balance is given by:

$$N_{\text{transp}} = N_{\text{leached}} \qquad \text{Equation 5-37}$$

this gives:

$$q_{gw} \cdot d \cdot c_{sol}^{CH} \cdot t = \frac{\alpha_a \cdot t}{\beta_a} \cdot q_0^{CH} \qquad \text{Equation 5-38}$$

$$q_{gw} \cdot d \cdot c_{sol}^{CH} = \frac{\alpha_a}{\beta_a} \cdot q_0^{CH} = \frac{\frac{2 D_{e,ww} \cdot c_{sol}^{CH}}{q_0^{CH}}}{\frac{2 \cdot D_{e,ww}}{q_{gw} \cdot d}} \cdot q_0^{CH} = q_{gw} \cdot d \cdot c_{sol}^{CH} \qquad \text{Equation 5-39}$$

$$q_{gw} \cdot d \cdot c_{sol}^{CH} \equiv q_{gw} \cdot d \cdot c_{sol}^{CH} \qquad \text{Equation 5-40}$$

Hence, the mass balance is fulfilled.

Calculations of the extent of the zone depleted in portlandite at the entrance of the fracture are presented in Figure 5-15. The propagation of the wedge shaped leaching front in the direction of the water flow in the fracture has also been calculated and is shown in Figure 5-16.

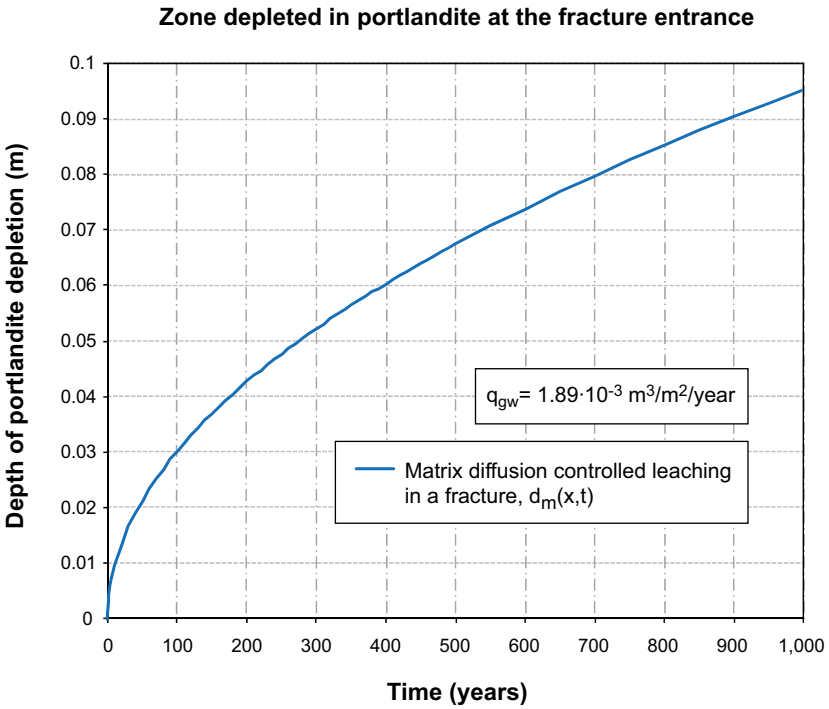

Figure 5-15. *Matrix diffusion controlled leaching of portlandite in a fracture through the concrete barrier. The figure shows the depth of the leaching front from the fracture surface at the entrance of the fracture.*

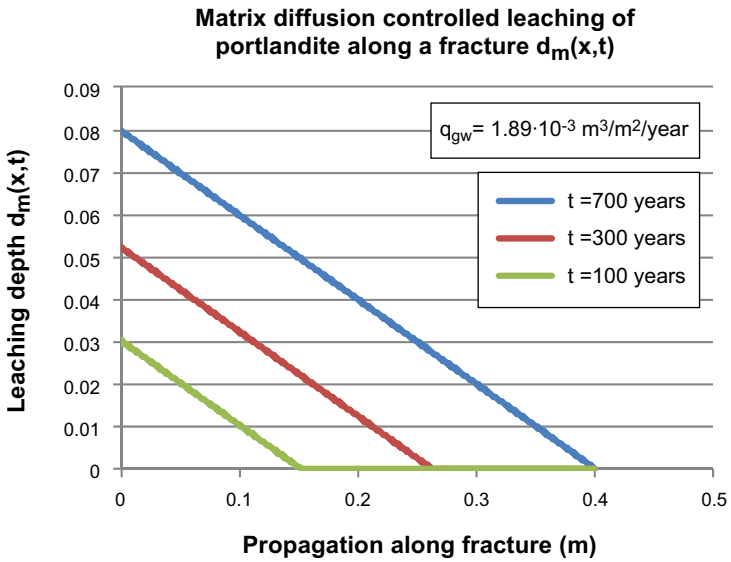

Figure 5-16. *Matrix diffusion controlled leaching of portlandite along a fracture through the concrete barrier. The figure shows the propagation with time of the leaching front along the fracture and the depth of the portlandite depleted zone from the fracture surface.*

The propagation rate of the leaching front is seen to be dependent on the effective diffusivity of the concrete in such a way that for a lower diffusivity the front moves more quickly along the fracture. This means that if the leaching process of portlandite leads to a locally enhanced degradation of the material at the fracture surfaces, this could mean that the dissolution processes leads to widening of the fractures, and that this process is more rapid for high quality concretes with low diffusivity. The effect is illustrated in example calculations presented in Figure 5-17.

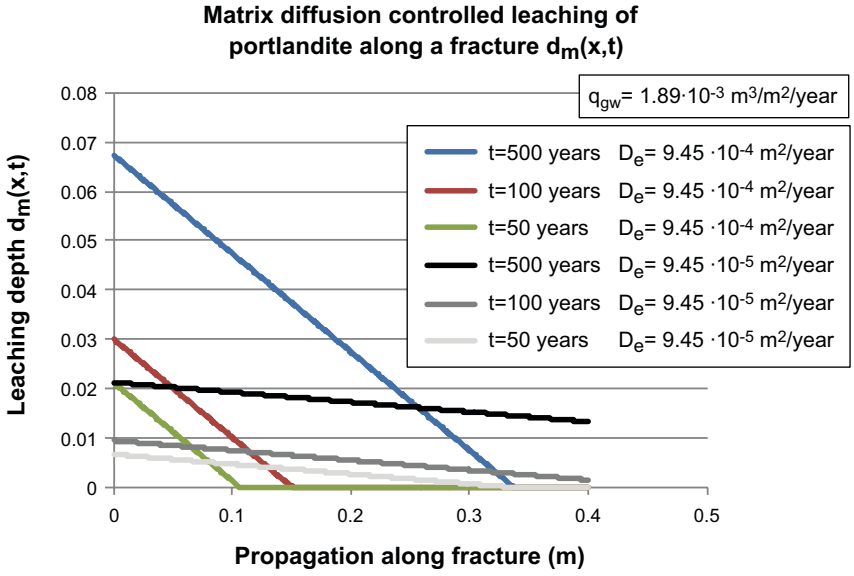

Figure 5-17. *Matrix diffusion controlled leaching of portlandite along a fracture through the concrete barrier. The figure shows the propagation with time of the leaching front along the fracture and the depth of the portlandite depleted zone from the fracture surface.*

An additional check on the validity of the expression for $d_m(x,t)$ can be made by calculating a mass-balance over time. At a given time, the integrated expression for $d_m(x,t)$ over the whole barrier thickness times the initial amount of portlandite must be equal to the amount of water that has passed through the fracture over time multiplied by the portlandite solubility. In mathematical terms:

$$2 \cdot q_0^{CH} \cdot B \cdot \int_0^L d_m(x,t)dx = q_{gw} \cdot B \cdot d \cdot c_{sol}^{CH} \cdot t \qquad \text{Equation 5-41}$$

from which it can be shown:

$$2 \cdot q_0^{CH} \cdot \int_0^L \left(\sqrt{\frac{2 \cdot D_{e,ww} \cdot c_{sol}^{CH} \cdot t}{q_0^{CH}}} - \frac{2 \cdot D_{e,ww} \cdot x}{U_0 \cdot d} \right) dx = q_{gw} \cdot d \cdot c_{sol}^{CH} \cdot t \qquad \text{Equation 5-42}$$

which yields:

$$2 \cdot q_0^{CH} \cdot \left(L \cdot \sqrt{\frac{2 \cdot D_{e,ww} \cdot c_{sol}^{CH} \cdot t}{q_0^{CH}}} - \frac{L^2}{2} \cdot \frac{2 \cdot D_{e,ww}}{q_{gw} \cdot d} \right) = q_{gw} \cdot d \cdot c_{sol}^{CH} \cdot t \qquad \text{Equation 5-43}$$

Introducing the following parameter values:
L = 0.4 (m)
t = 700 (a)
$D_{e,ww}$ = $9.45 \cdot 10^{-4}$ (m^2/a)
c_{sol}^{CH} = 5 (mol/m^3)
q_0^{CH} =1,040 (mol/m^3)
q_{gw} = $1.89 \cdot 10^{-3}$ (m^3/m^2/a)
d = 5 (m)

Here, the left hand expression equals the right hand expression. Hence, the applied models satisfy the requirement to be mass-conservative.

The above formulae are valid as long as the distance between fractures is sufficiently large so that $d_0 < L/2$. If the fracture spacing is small, the leaching fronts can meet and the rate by which the leaching front moves along the fracture is given by (based on Romero et al. 1992):

$$v_{\text{front}} = \frac{q_{gw} \cdot c_{sol}^{CH}}{q_0^{CH}} \qquad \text{Equation 5-44}$$

This formula is identical with the expression for a shrinking-reactive core model for a slab (Levenspiel 1972).

If the leaching fronts of adjacent fractures meet before the leaching front reaches the down-stream end of the fractures (i.e. $d_0 \geq L/2$), see illustration in Figure 5-18, the position $L(t)$ can be calculated from (based on Romero et al. 1992):

$$L(t) = q_{gw} \cdot \left[\frac{c_{sol}^{CH}}{q_0^{CH}} \cdot t + \frac{\left(\frac{d}{2}\right)^2}{2D_{e,ww}} \right] \qquad \text{Equation 5-45}$$

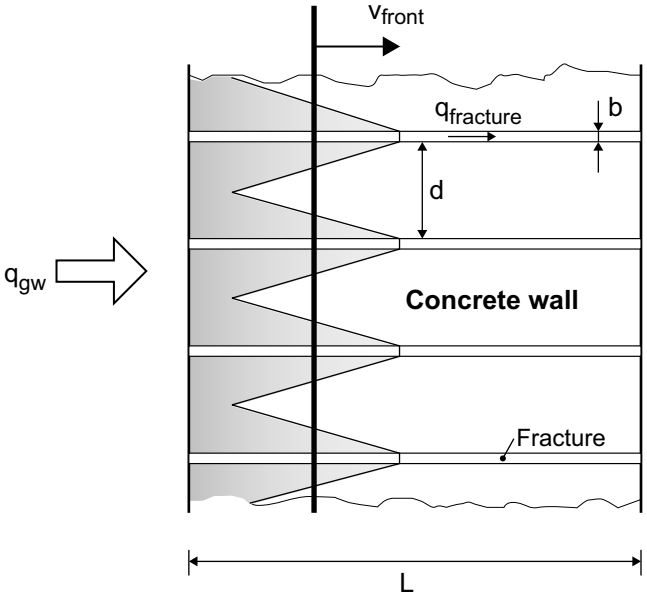

Figure 5-18. *Illustration to leaching in adjacent fractures where the leaching fronts around different fractures meet and forms a moving front that propagates in the flow direction. The water flow only occurs in the fractures.*

5.1.4 Limiting fracture aperture for the assumed flow convergence

If it is assumed that the entire flow is diverted to the fractures, it can be shown that a (theoretical) flow convergence is proportional to $\frac{d}{b}$ where d is the distance between fractures and b is the fracture aperture (width). A condition for the water to be able to pass through the fracture is that the fracture conductivity K_f is high enough. A minimum requirement can be formulated that (see further Section 6.1):

$$K_f \geq \frac{d}{b} \cdot K_I \qquad \text{Equation 5-46}$$

where:
K_I = the conductivity of intact concrete (m/s)

Introducing the expression

$$K_f = \frac{b}{d} \cdot \frac{\rho \cdot g}{\mu} \cdot \frac{b^2}{12} \qquad \text{Equation 5-47}$$

so:

$$\frac{b}{d} \cdot \frac{\rho \cdot g}{\mu} \cdot \frac{b^2}{12} \geq \frac{d}{b} \cdot K_I \qquad \text{Equation 5-48}$$

rearranging:

$$\frac{\rho \cdot g}{\mu} \cdot \frac{b^4}{d^2 \cdot 12} \geq K_I \qquad \text{Equation 5-49}$$

from which follows that:

$$b_{crit} \geq \sqrt[4]{\frac{K_I \cdot d^2 \cdot 12}{\frac{\rho \cdot g}{\mu}}} \qquad \text{Equation 5-50}$$

Introducing the following parameter values:
d = 0–10 (m)
$K_I = 1.10^{-11}$ (m/s)

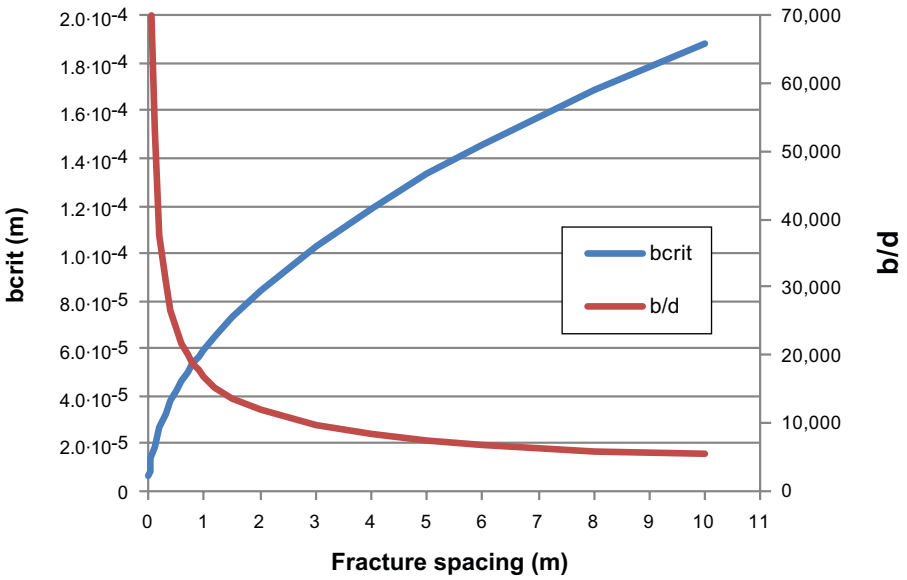

Figure 5-19. *Limiting fracture aperture required to accommodate the assumed flow convergence as a function of the fracture spacing.*

Making a parameter sweep with respect to the assumed fracture spacing, the corresponding value for the critical fracture aperture which would meet the required fracture conductivity to allow the groundwater to flow through the fracture can be calculated and the results are presented in Figure 5-19. The results show that for the assumed groundwater flux in the vault, the entire flow could be accommodated in a few thin fractures, e.g. in one 0.2 mm fracture every 10 m or in one 0.06 mm fracture every metre.

5.2 Intrusion of chloride, carbonate and sulphate

In this section, a simplified approach is taken to estimate the intrusion of chloride, carbonate and sulphate in concrete. The approach assumes that the reaction between the three components are additive when reacted with calcium aluminate minerals in the concrete. In a real system, the different reactants may compete for the same minerals; see further descriptions presented in Chapter 4. However, for the purpose of making first rough and conservative estimates the proposed approach may be appropriate.

The concrete barriers will be exposed to dissolved salts in the groundwater including chloride, carbonate (both in the inflowing groundwater and absorbed from the air) and sulphate. The exposure has started already during the operational phase due to dissolved salts in dripping water from the rock ceiling and due to intrusion of carbon dioxide in the air. The exposure to carbonate may result in lowering of the pH in the concrete and chloride intrusion is known to result in initiation of corrosion of reinforcement bars and other steel components in the concrete constructions which are initially passivated by the high pH.

In Section 4.2.2, the intrusion of chloride in concrete from the groundwater was calculated assuming that no reactions take place between chloride ions and the concrete minerals. In this section calculations taking chemical reactions into consideration are presented. Chloride may react to form different Friedel's salts (different mineral phases with compositions ranging from $C_3A \cdot CaCl_2 \cdot 10H_2O$ to $C_3A \cdot 0.39CaCl_2 \cdot 0.61Ca(OH)_2 \cdot 10H_2O$). The chloride binding capacity of Portland cements have been investigated and different isotherms are presented by Florea and Brouwers (2012). In order to stabilise the formation of Friedel's salt a minimum aqueous concentration of ~ 6 mM chloride was found to be necessary (Balonis 2010).

Carbonate will react to form different carbo aluminate minerals, such as hemicarbo aluminate ($C_2A \cdot 0.5CaCO_3 \cdot 0.5Ca(OH)_2 \cdot 11.5H_2O$) and monocarbo aluminate ($C_3A \cdot CaCO_3 \cdot 11H_2O$). With increasing carbonation calcite will also form.

Sulphate intrusion may lead to formation of expanding ettringite. Sulphate in combination with carbonate may cause formation of thaumasite ($Ca_3Si(OH)_6(SO_4)(CO_3)\cdot 12H_2O$). Both ettringite and thaumasite are considered deleterious reactions in the hardened concrete and may result in complete disintegration and loss of strength.

A common feature of chloride, carbonate and sulphate is that they can all react with calcium aluminates and calcium ferrites (not considered here) in the concrete (e.g. monosulphate, monosulphoferrite, C_3AH_6, and C_3FH_6). This means that they compete for the same reactants in the concrete. This also means that the combined attack may lead to a more rapid depletion of the calcium aluminates/ferrites. However, this does not necessarily imply that the combined action would result in a more severe or rapid deterioration of the concrete, which is a more complex issue and beyond the scope of this simplified estimate. A simplified illustration to the combined attack by chloride, carbonate and sulphate is given in Figure 5-20.

The interaction between dissolved species of chloride, carbonate and sulphate are considered in further detail in the reactive transport modelling presented in Chapter 7, thus there is the opportunity to examine the validity of this simple approach.

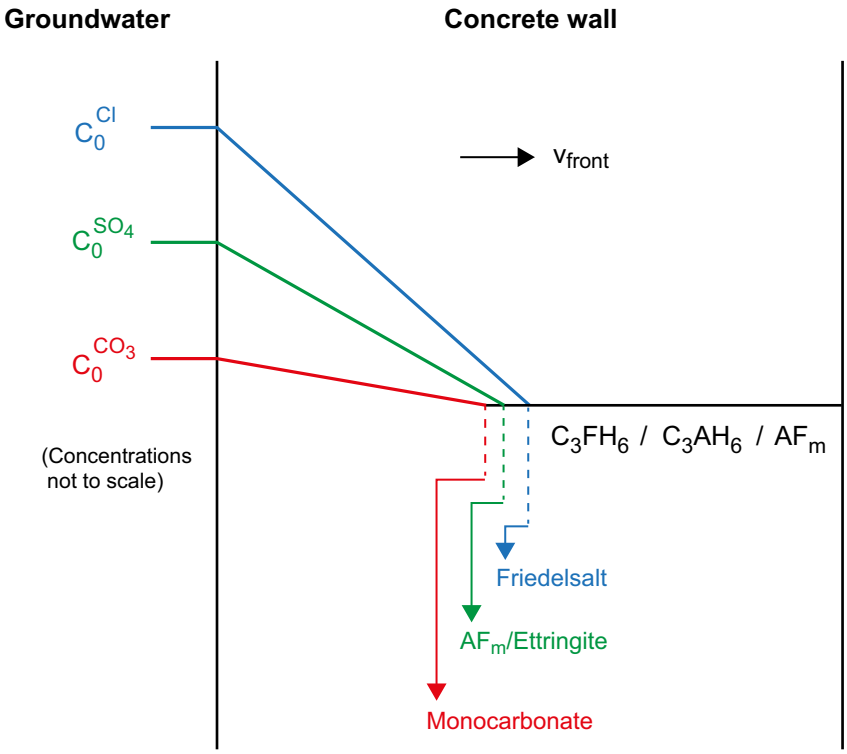

Figure 5-20. *Illustration to the combined attack by chloride, carbonate and sulphate that react with different calcium aluminates/ferrites in the concrete to form Friedel's salt, ettringite and monocarbonate. A_{Fm} denotes monosulphate/monosulphoferrite.*

The reactions with monosulphate (part of AF_m) can be written:

Reactions with monosulphate (corresponding ferrite reactions not considered)

$C_3AC\hat{s}H_{12} + 2\ C\hat{s} + 20\ H \Leftrightarrow C_3A(C\hat{s})_3H_{32}$ Ettringite Equation 5-51

$C_3AC\hat{s}H_{12} + CaCO_3 \Leftrightarrow C_3ACaCO_3H_{11} + C\hat{s} + H$ Monocarboaluminate Equation 5-52

$C_3AC\hat{s}H_{12} + CaCl_2 \Leftrightarrow C_3ACaCl_2H_{10} + C\hat{s} + 2\ H$ Friedel's salt Equation 5-53

varying to

$+ 0.39\ CaCl_2 + 0.61\ CH \Leftrightarrow C_3A{\cdot}0.39CaCl_2{\cdot}0.61CH{\cdot}H_{10} + C\hat{s} + 2\ H$ Equation 5-54

Reactions with hydrogarnet (C_3AH_6)

$C_3AH_6 + C\hat{s} + 6\ H \Leftrightarrow C_3AC\hat{s}H_{12}$ Monosulphate Equation 5-55

$C_3AH_6 + CaCO_3 + 5\ H \Leftrightarrow C_3A\ CaCO_3H_{11}$ Monocarboaluminate Equation 5-56

$C_3AH_6 + CaCl_2 + 4\ H \Leftrightarrow C_3ACaCl_2H_{10}$ Friedel's salt Equation 5-57

varying to

$+ 0.39\ CaCl_2 + 0.61\ CH \Leftrightarrow C_3A{\cdot}0.39CaCl_2{\cdot}0.61CH{\cdot}H_{10}$ Equation 5-58

The monosulphate formed according to Equation 5-55 may react further according to Equation 5-51 to form ettringite.

To simplify the calculations, an operational total concentration of aggressive solutes can be used for Equations 5-55, 5-56 and 5-57 given by:

$$c_{sol}^{Total} = \frac{c_{sol}^{Cl}}{2} + c_{sol}^{SO_4} + c_{sol}^{CO_3} \quad \text{Equation 5-59}$$

and the total amount of solid minerals acting as reactants (Equations 5-51 to 5-53 and 5-55 to 5-57) in the concrete is given by:

$$q_{Total} = q_0^{monosulphate} + q_0^{C3AH6} \quad \text{Equation 5-60}$$

A shrinking-core model can be formulated for the combined attack by chloride, carbonate and sulphate forming monosulphate, monocarboaluminate and Friedel's salt (Equations 5-55, 5-56 and 5-57), see e.g. Levenspiel (1972). The depth of the combined attack is given by:

$$X_{salts} = \sqrt{\frac{2 \cdot D_e \cdot c_{sol}^{Total} \cdot t}{q_{Total}}} \quad \text{Equation 5-61}$$

where:

X_{salts}= depth of attacked zone in the concrete (m)

D_e = effective diffusivity of the concrete (m^2/a)

c_{sol}^{Total} = the operational total concentration of aggressive species in the groundwater ($kmol/m^3$)

t = time (a)

q_{Total} = initial amount of monosulphate and hydrogarnet phases in concrete ($kmol/m^3$)

A corresponding expression for the formation of ettringite from monosulphate can be formulated:

$$X_{ettringite} = \sqrt{\frac{2 \cdot D_e \cdot C_{sol}^{SO4} \cdot t}{2 \cdot q_0^{monosulphate}}} \quad \text{Equation 5-62}$$

Calculated results for the combined attack of chloride, carbonate and sulphate (assuming the concentrations in the groundwater during the saltwater period presented in Chapter 3, the diffusivity for weakly weathered concrete in Table 5-1, and the composition of the construction concrete presented in Appendix H) are presented in Figure 5-21. The results may be interpreted as a first rough estimate of the possible deterioration of the surface layer of the concrete due to formation of expanding minerals, in particular when reactions proceed to form ettringite that may cause cracking and spalling. The intrusion of chloride and carbonate may also affect the passivation of reinforcement bars and thereby induce corrosion that in turn may cause fractures in the concrete.

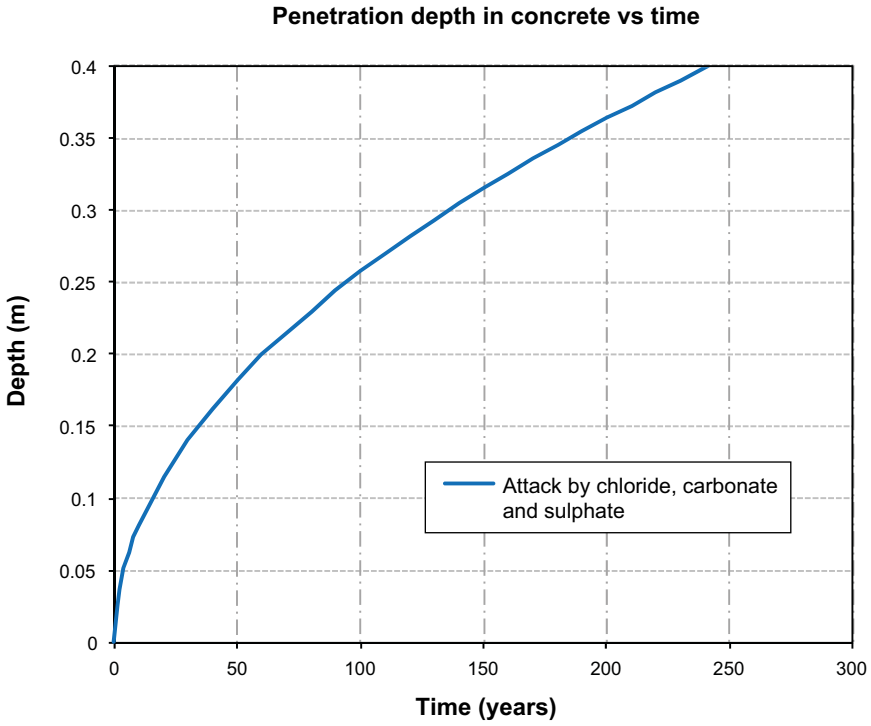

Figure 5-21. *Calculated penetration depth of the combined attack by chloride, carbonate and sulphate on monosulphate and hydrogarnet minerals in concrete versus time. The penetration depth denotes the depth to which the calcium aluminate minerals have been depleted by reaction with the chloride, carbonate and sulphate in the calculation.*

6 Model descriptions for hydraulic conductivities, diffusivities and porosities

In this Chapter, simple models are presented to study the effect of fractures and other discontinuities on the hydraulic conductivity and the effective diffusivity of concrete barriers in the SFR repository. The developed models are then used to estimate the effect of fractures formed by processes such as drying shrinkage during operation of the repository and contraction due to cooling by inflow of groundwater after closure. Furthermore, the models are applied to study the effects of fractures and discontinuities caused by fully or partially corroded steel reinforcement or form rods on the hydraulic conductivity and effective diffusivity of concrete. These data are important for understanding the effect of initial fractures and flow pathways caused by different physical processes, including the disturbances caused by corroded steel on the material properties of the barriers in the early period of repository evolution. The effect of fractures on the porosity is also addressed.

6.1 Hydraulic conductivity of intact concrete

High quality concrete is highly impermeable and will only allow a very restricted flow of water when exposed to a pressure gradient. The flow rate is described by Darcy's law (Darcy 1856):

$$q_{gw} = K_I \cdot i \qquad \text{Equation 6-1}$$

where:

q_{gw} = average water flow rate ($m^3/m^2/s$)

K_I = hydraulic conductivity of intact concrete (m/s)

i = hydraulic gradient (m/m)

Typical values of the hydraulic conductivity in an intact high quality concrete could be of the order of 10^{-11} m/s or less (SKB 2001).

However, if fractures are present the hydraulic conductivity may be significantly higher. Also chemical degradation may affect the hydraulic conductivity of concrete over time.

In the following, the reciprocal entity flow resistance will be used and this is defined by:

$$R_I = \frac{L_I}{K_I} \qquad \text{Equation 6-2}$$

where:

R_I = flow resistance of intact concrete (s)

L_I = flow path length (m)

K_I = hydraulic conductivity of intact concrete (m/s)

The different cases of flow in fractured and chemically degraded concrete considered in this study are illustrated in Figure 5-1.

6.2 Diffusivity of intact concrete

High quality concrete is highly impermeable and will only allow restricted diffusion of dissolved species when exposed to a concentration gradient. In this chapter, diffusion is calculated assuming stationary conditions, i.e. using steady-state diffusion as described by Fick's first law of diffusion (Fick 1855). The ability of Fick's law to describe the diffusion of multi-component ionic species in detail has been disputed in recent literature (e.g. Galíndez and Molinero 2010) in favour of more precise mechanistic descriptions, e.g. ion-ion interactions using the Poisson-Nernst-Planck equations.

However, the level of detail provided by the Fick's law approach is considered appropriate for the present study.

The diffusion rate as described by Fick's first law of diffusion:

$$j = -D_{eI} \cdot \frac{dc}{dx}$$ Equation 6-3

where:

j = molar flux of diffusing species (mol/m^2/s)

D_{eI} = effective diffusivity of the species in intact concrete (m^2/s)

c = molar concentration of the diffusing species (mol/m^3)

x = distance along the concentration gradient (m)

$\frac{dc}{dx}$= concentration gradient along the x-coordinate (mol/m^3/m)

Typical values for the effective diffusivity in intact high quality concrete could be of the order of $3 \cdot 10^{-12}$ m^2/s (SKB 2014b).

The effective diffusivity is a function of the diffusivity in bulk water and the material properties of the porous material (concrete) in which the diffusion takes place:

$$D_{eI} = \phi \cdot \frac{\delta_d}{\tau^2} \cdot D_0$$ Equation 6-4

where:

D_{eI} = effective diffusivity of intact concrete (m^2/s)

ϕ = porosity of the porous material (m^3/m^3)

δ_d = constrictivity factor of the pore system (a measure on the amount of narrow passages along the pores) (–)

τ = tortuosity factor of the pore system (defined as the ratio of the mean length L_p of the path through the porous material to the geometrical length L) (m/m)

D_0 = diffusivity in bulk water (m^2/s)

However, if fractures are present the effective diffusivity may be significantly higher. Also chemical degradation may affect the effective diffusivity of the concrete over time.

In the following, the reciprocal entity effective diffusion resistance will be used and this is defined by:

$$R_{DI} = \frac{L_I}{D_{eI}}$$ Equation 6-5

where:

R_{DI} = diffusion resistance of intact concrete (s/m)

L_I = geometrical diffusion path length (m)

D_{eI} = effective diffusivity of intact concrete (m^2/s)

The different cases of diffusion in fractured and chemically degraded concrete considered in this study are illustrated in Figure 5-1.

6.3 Overall conductivity of concrete with fully penetrating fractures

Assuming a plane fracture with unit porosity, the fracture conductivity can be estimated from (Höglund and Bengtsson 1991, Walton et al. 1990, US DOE 2009):

$$K_{\text{fracture}} = \frac{\rho \cdot g}{\mu} \cdot \frac{b^2}{12}$$ Equation 6-6

where:

$K_{fracture}$ = hydraulic conductivity of a fracture (m/s)

ρ = fluid density (kg/m^3)

g = gravitational constant (m/s^2)

μ = dynamic viscosity of the fluid (kg/m/s)

b = fracture width (aperture) (m)

If it is assumed that the concrete has one fully penetrating fracture with unit porosity of width b every d metres, the hydraulic conductivity of the fraction of the concrete occupied by fractures can be calculated from:

$$K_f = \frac{b}{d} \cdot \frac{\rho \cdot g}{\mu} \cdot \frac{b^2}{12} \qquad \text{Equation 6-7}$$

Finally, the overall hydraulic conductivity of concrete, taking into consideration both the fractures and the intact concrete in between, can be calculated from (Braester and Thunvik 1988, Walton et al. 1990):

$$K_{\text{overall}} = \frac{b}{d} \cdot \frac{\rho \cdot g}{\mu} \cdot \frac{b^2}{12} + \left(1 - \frac{b}{d}\right) \cdot K_I = \frac{b}{d} \cdot K_{\text{fracture}} + \left(1 - \frac{b}{d}\right) \cdot K_I =$$

$$= K_f + (1 - \frac{b}{d}) \cdot K_I \qquad \text{Equation 6-8}$$

where:

$K_{overall}$ = hydraulic conductivity of a fractured concrete (m/s)

K_I = hydraulic conductivity of intact concrete (m/s)

$K_{fracture}$ = hydraulic conductivity of a fracture (m/s)

K_f = hydraulic conductivity of fractures in concrete (m/s)

This assumes that fracture flow takes place as an ideal flow between two parallel plates with smooth surfaces. In real cracks, the surface roughness of the fracture may be important. According to Walton et al. (1990) the flow in real cracks is typically 1/3 to 2/3 of that predicted by the above formula. Furthermore, real cracks typically contain some infill material, e.g. precipitates of ettringite or calcite formed from groundwater-concrete interactions, which to some extent limit the porosity and hence the flow in the fracture. Hence, the equation may give a slight over-estimation of the fracture conductivity. If desired, a factor ξ can be entered to compensate for the surface roughness and other disturbances:

$$K_{\text{overall}} = \frac{b}{d} \cdot \xi \cdot \frac{\rho \cdot g}{\mu} \cdot \frac{b^2}{12} + \left(1 - \frac{b}{d}\right) \cdot K_I = \frac{b}{d} \cdot \xi \cdot K_{\text{fracture}} + \left(1 - \frac{b}{d}\right) \cdot K_I =$$

$$= \xi \cdot K_f + (1 - \frac{b}{d}) \cdot K_I \qquad \text{Equation 6-9}$$

where:

ξ = a factor (< 1) compensating for the surface roughness of fractures (m)

The overall flow resistance for concrete with fully penetrating fractures can be calculated from:

$$R_{\text{overall}} = \frac{L}{K_{\text{overall}}} = \frac{L}{\xi \cdot K_f + \left(1 - \frac{b}{d}\right) \cdot K_I} \qquad \text{Equation 6-10}$$

where:

$R_{overall}$ = flow resistance of a fractured concrete (s)

L= flow length (m)

$K_{overall}$ = hydraulic conductivity of a fractured concrete (m/s)

K_f = hydraulic conductivity of fractures in concrete (m/s)

Some results calculated for concrete with fully penetrating fractures are shown in Figure 6-1. The calculations assume a hydraulic conductivity K_I of $1 \cdot 10^{-11}$ m/s in intact concrete (SKB 2001). The effect of surface roughness is neglected in these calculations, assuming $\xi = 1$. Different cases of the fracture width (aperture) b, and the fracture spacing d, are given in the figure. An important observation is that the overall hydraulic conductivity is much more sensitive to the fracture aperture width than to the fracture spacing. Hence, even for large spacings the presence of wide fractures has a large impact on the overall hydraulic conductivity of the concrete structures.

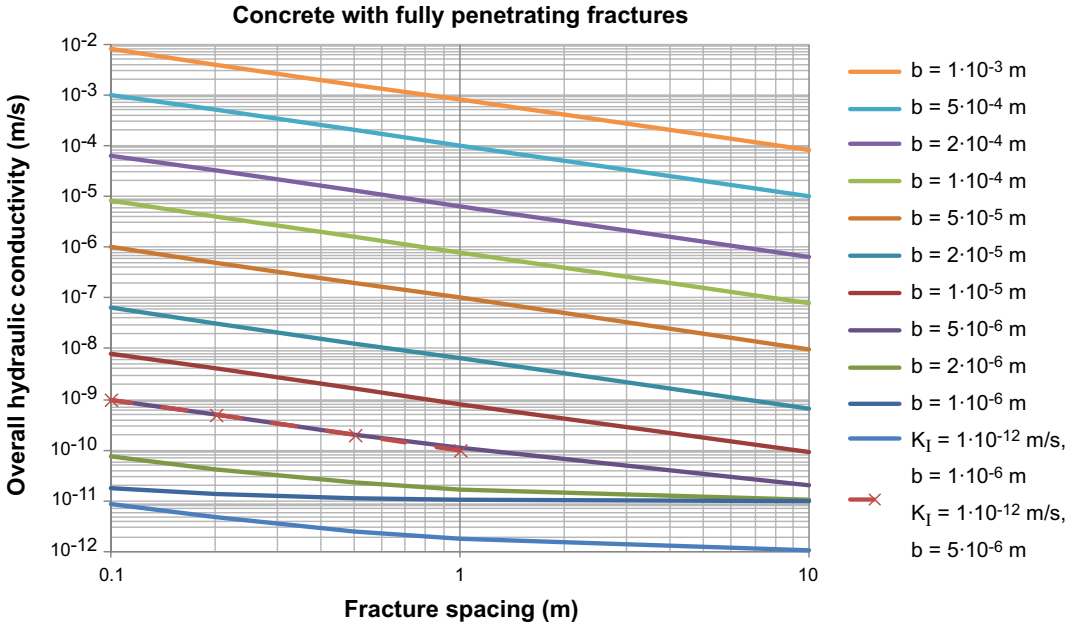

Figure 6-1. *Example calculations for the impact of fully penetrating fractures on the hydraulic conductivity of a concrete barrier.*

6.4 Overall diffusivity of concrete with fully penetrating fractures

The diffusivity in the fracture is assumed to resemble the diffusivity in pure water, i.e. $D_{ef} = D_0$. This assumption is defensible for larger fractures, but may not be applicable for fractures < ~ 20–50 µm, see discussion in SKB (2014b).

If it is assumed that the concrete has one fully penetrating fracture of width b every d metres, the contribution to the overall effective diffusivity of the fractures can be estimated from:

$$D_{ef} = \frac{b}{d} \cdot D_0 \qquad \text{Equation 6-11}$$

where:

D_{ef} = effective diffusivity of fractures in concrete (m^2/s)

D_0 = diffusivity in bulk water (m^2/s)

b = fracture width (aperture) (m)

d = fracture spacing (m)

Finally, the overall effective diffusivity of the concrete, taking into consideration both the fractures and the intact concrete between the fractures can be calculated from:

$$D_{e,\text{overall}} = \frac{b}{d} \cdot D_0 + \left(1 - \frac{b}{d}\right) \cdot D_{eI} = \frac{b}{d} \cdot D_0 + \left(1 - \frac{b}{d}\right) \cdot \phi \cdot \frac{\delta_d}{\tau^2} \cdot D_0 =$$

$$= D_0 \cdot \left(\frac{b}{d} + (1 - \frac{b}{d}) \cdot \phi \cdot \frac{\delta_d}{\tau^2}\right) \qquad \text{Equation 6-12}$$

where:

$D_{e,\text{overall}}$ = effective diffusivity in fractured concrete (m^2/s)

b = fracture width (aperture) (m)

d = fracture spacing (m)

D_0 = diffusivity in bulk water (m^2/s)

D_{eI} = effective diffusivity in intact concrete (m^2/s)

ϕ = porosity of the porous material (m^3/m^3)

δ_d = constrictivity factor of the pore system (–)

τ = tortuosity factor of the pore system (m/m)

Here, it is assumed that diffusion takes place as an ideal process between two parallel plates with smooth surfaces. In real cracks, the surface roughness of the fracture may be important. In analogy with water flow in cracks, it may be inferred that the diffusion may be somewhat hampered by the roughness of the fracture surfaces and any infilling material in the fractures. Hence, the equation may give a slight over-estimation of the diffusivity in fractures. If desired, a factor ξ_D can be entered to compensate for the surface roughness and other disturbances:

$$D_{e,\text{overall}} = \frac{b}{d} \cdot \xi_D \cdot D_0 + \left(1 - \frac{b}{d}\right) \cdot D_{eI} = \frac{b}{d} \cdot \xi_D \cdot D_0 + \left(1 - \frac{b}{d}\right) \cdot \phi \cdot \frac{\delta_d}{\tau^2} \cdot D_0 =$$
$$= D_0 \cdot \left(\frac{b}{d} \cdot \xi_D + (1 - \frac{b}{d}) \cdot \phi \cdot \frac{\delta_d}{\tau^2}\right) \qquad \text{Equation 6-13}$$

where:

ξ_D = a factor (< 1) compensating for the surface roughness and other disturbances such as infilling material in the fractures (–)

The overall diffusion resistance for concrete with fully penetrating fractures can also be calculated:

$$R_{D,\text{overall}} = \frac{L}{D_{e,\text{overall}}} = \frac{L}{\frac{b}{d} \cdot \xi_D \cdot D_0 + \left(1 - \frac{b}{d}\right) \cdot D_{eI}} \qquad \text{Equation 6-14}$$

where:

$R_{D,\text{overall}}$ = diffusion resistance in fractured concrete (s/m)

L = geometrical diffusion path length (m)

$D_{e,\text{overall}}$ = effective diffusivity in a fractured concrete (m^2/s)

b = fracture width (aperture) (m)

d = fracture spacing (m)

ξ_D = a factor (< 1) compensating for the surface roughness and other disturbances in fractures (–)

D_0 = diffusivity in bulk water (m^2/s)

D_{eI} = effective diffusivity in intact concrete (m^2/s)

Some results calculated for concrete with fully penetrating fractures are shown in Figure 6-2. The calculations assume an effective diffusivity D_{eI} of $3 \cdot 10^{-12}$ m^2/s in intact concrete (SKB 2014b) and a 0.4 m thick concrete barrier (L). The effect of surface roughness is neglected in these calculations, assuming $\xi_D = 1$. Different cases of the fracture width (aperture) b, and the fracture spacing d, are given in the figure. The results agree well with the results presented by Gérard and Marchand (2000). When comparing the results with experimental investigations, Gérard and Marchand (2000) found that the model overestimated the effect of cracks induced by freezing and thawing on the diffusivity by a factor of approximately 2.5, which is attributed to an intrinsic tortuosity of the crack network.

Clearly, the results show that the overall effective diffusivity is much less sensitive to the presence of fractures, even large fractures, than the corresponding impact on the overall hydraulic conductivity presented in the previous section. The reason for this is that the ratio D_0/D_{eI} is much smaller than the ratio K_f/K_I.

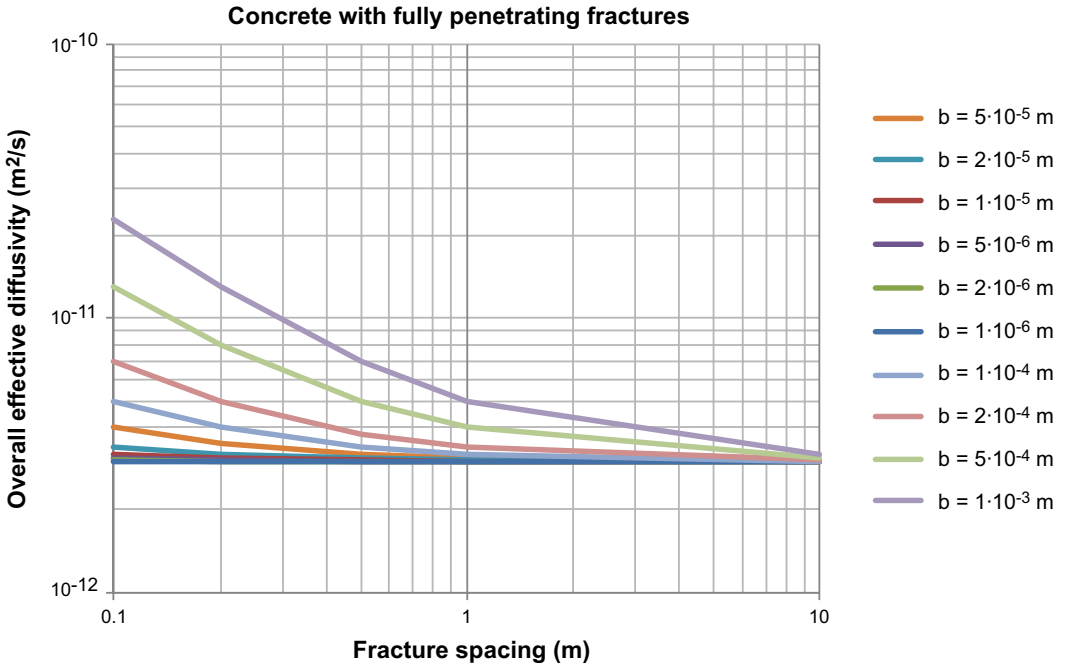

Figure 6-2. *Example calculations for the impact of fully penetrating fractures on the effective diffusivity of a concrete barrier.*

6.5 Overall conductivity of concrete with fully penetrating fractures of distributed fracture width and length

Assuming a finite number of plane fractures that can be grouped into a few classes according to a representative size, i.e. width and length, the fracture conductivity can be calculated. The fraction of the total area occupied by each size-class is calculated from:

$$a_i = \frac{l_i \cdot b_i \cdot n_i}{A_{tot}} = \frac{l_i \cdot b_i \cdot n_i}{B \cdot H} \qquad \text{Equation 6-15}$$

where:

a_i = fraction of the total area occupied by each size-class (m^2/m^2)

l_i = fracture length in size-class i (m)

b_i = fracture width (aperture) in size-class i (m)

n_i = number of fractures in size-class i (m)

A_{tot} = total surface area of the concrete wall (m^2)

B = extension of the concrete wall (m)

H = height of the concrete wall (m)

Recall from Section 6.3, Equation 6-6, the conductivity of a single fracture and compare with Equation 6-15 where the contribution to the overall conductivity by fracture size-class i is given by:

$$K_{f,i} = \frac{l_i \cdot b_i \cdot n_i}{B \cdot H} \cdot \xi \cdot \frac{\rho \cdot g}{\mu} \cdot \frac{b_i^2}{12} \qquad \text{Equation 6-16}$$

where:

$K_{fracture}$ = hydraulic conductivity of a fracture (m/s)

b_i = fracture width (aperture) of size-class i (m)

ξ = a surface roughness factor of fractures (< 1) (m)

Summing up the contribution from all *m* size-classes and adding the contribution from the unfractured parts of the concrete, in analogy with the method presented by Braester and Thunvik (1988) and Walton et al. (1990) an expression for the overall hydraulic conductivity can be obtained:

$$K_{\text{overall}} = \xi \cdot \sum_m \left[\frac{l_i \cdot b_i \cdot n_i}{B \cdot H} \cdot \frac{\rho \cdot g}{\mu} \cdot \frac{b_i^2}{12}\right] + (1 - \sum_m a_i) \cdot K_I \qquad \text{Equation 6-17}$$

where:

K_{overall} = hydraulic conductivity of a fractured concrete (m/s)

The overall flow resistance for concrete with distributed fracture sizes is given by:

$$R_{\text{overall}} = \frac{L}{K_{\text{overall}}} = \frac{L}{\xi \cdot \sum_m \left[\frac{l_i \cdot b_i \cdot n_i}{B \cdot H} \cdot \frac{\rho \cdot g}{\mu} \cdot \frac{b_i^2}{12}\right] + (1 - \sum_m a_i) \cdot K_I} \qquad \text{Equation 6-18}$$

where:

R_{overall} = flow resistance of a fractured concrete (s)

L= flow path length (concrete wall thickness) (m)

6.6 Overall diffusivity of concrete with fully penetrating fractures of distributed fracture width and length

Assuming a finite number of plane fractures that can be grouped into a few classes according to a representative size, i.e. width and length, the fracture conductivity can be calculated. The fraction of the total area occupied by each size-class is calculated from:

$$a_i = \frac{l_i \cdot b_i \cdot n_i}{A_{tot}} = \frac{l_i \cdot b_i \cdot n_i}{B \cdot H} \qquad \text{Equation 6-19}$$

Introducing the contribution to the overall diffusivity by fracture size-class *i* is given by (in analogy with the treatment of hydraulic conductivities in fractures given in Section 6.5):

$$D_{e,f,i} = \frac{l_i \cdot b_i \cdot n_i}{B \cdot H} \cdot \xi_D \cdot D_0 \qquad \text{Equation 6-20}$$

Summing up the contribution from all *m* size-classes and adding the contribution from the unfractured parts of the concrete, an expression for the overall effective diffusivity can be obtained:

$$D_{e,\text{overall}} = \xi_D \cdot \sum_m \left[\frac{l_i \cdot b_i \cdot n_i}{B \cdot H} \cdot D_0\right] + (1 - \sum_m a_i) \cdot D_{eI} \qquad \text{Equation 6-21}$$

where:

$D_{e,\text{overall}}$ = effective diffusivity of a fractured concrete (m^2/s)

D_{eI} = effective diffusivity of intact concrete (m^2/s)

D_0= diffusivity in bulk water in the fracture (m^2/s)

The overall diffusion resistance for concrete with distributed fracture sizes is given by:

$$R_{\text{overall}} = \frac{L}{D_{e,\text{overall}}} = \frac{L}{\xi_D \cdot \sum_m \left[\frac{l_i \cdot b_i \cdot n_i}{B \cdot H} \cdot D_0\right] + (1 - \sum_m a_i) \cdot D_{eI}} \qquad \text{Equation 6-22}$$

where:

R_{overall} = diffusion resistance of a fractured concrete (s)

L= geometrical diffusion path length (wall thickness) (m)

6.7 Overall conductivity of concrete penetrated by circular holes caused by completely corroded form ties

The concrete walls in 1BMA have remnants of form ties that were used as support during construction of the concrete walls on-site in the 1BMA vault. The form ties fully penetrate the concrete walls. Hence when corroded they may constitute passages through the concrete walls. The amount of form ties in the 1BMA concrete walls has been estimated to 12 per m^2.

When the flow takes place through a porous material of uniform permeability k, e.g. corrosion products filling the hole initially occupied by the form tie, the flow through a circular hole is given by Bird et al. (1960):

$$Q = \pi \cdot r^2 \cdot \left(\frac{\Delta P}{L} \cdot \frac{k}{\mu}\right) \cdot \left(1 - 2 \cdot \frac{\sqrt{k}}{r} \cdot \frac{I_1(r/\sqrt{k})}{I_0(r/\sqrt{k})}\right) \quad \text{Equation 6-23}$$

where:

Q = the volumetric flow rate (m^3/s)

r = the radius of the circular hole (m)

ΔP = the pressure drop (Pa)

L = length of flow passage (m)

k = permeability of the porous corrosion products (m^2)

μ = the dynamic viscosity (Pa·s)

$I_1(x)$ and $I_0(x)$ = the modified Bessel functions of first and zero order respectively (Abramowitz and Stegun 1972):

$$I_1(x) = \frac{1}{2} \cdot x \cdot \sum_{k=0}^{\infty} \frac{\left(\frac{1}{4} \cdot x^2\right)^k}{k! \cdot \Gamma(2+k)} \quad \text{Equation 6-24}$$

$$I_0(x) = \sum_{k=0}^{\infty} \frac{\left(\frac{1}{4} \cdot x^2\right)^k}{(k!)^2} \quad \text{Equation 6-25}$$

where:

$\Gamma(n) = (n-1)!$ = the gamma function

For large arguments (i.e. when $r/\sqrt{k}$ approach high value), use is made of:

$$\lim_{(r/\sqrt{k}) \to \infty} \left(\frac{I_1(r/\sqrt{k})}{I_0(r/\sqrt{k})}\right) = 1 \quad \text{Equation 6-26}$$

The flow rate according to the Darcy's law is expressed:

$$Q = A \cdot K \cdot i \quad \text{Equation 6-27}$$

where the hydraulic head gradient is defined as:

$$i = \frac{1}{\rho \cdot g} \cdot \frac{\Delta P}{L} \quad \text{Equation 6-28}$$

Using the two expressions for the flow rate (flow through a circular hole and Darcy's law) above, by identification the hydraulic conductivity of the circular hole is:

$$K_{\text{porous hole}} = \frac{\rho \cdot g}{\mu} \cdot k \cdot \left(1 - 2 \cdot \frac{\sqrt{k}}{r} \cdot \frac{I_1(r/\sqrt{k})}{I_0(r/\sqrt{k})}\right) \quad \text{Equation 6-29}$$

From this it may be calculated that the overall hydraulic conductivity of the concrete wall penetrated by n circular holes with radii r is:

$$K_{\text{overall}}^{\text{porous holes}} = K_I \cdot (A_{tot} - n \cdot \pi \cdot r^2) + K_{\text{porous hole}} \cdot n \cdot \pi \cdot r^2 =$$

$$= K_I \cdot (A_{tot} - n \cdot \pi \cdot r^2) + \frac{\rho \cdot g}{\mu} \cdot k \cdot \left(1 - 2 \cdot \frac{\sqrt{k}}{r} \cdot \frac{I_1(r/\sqrt{k})}{I_0(r/\sqrt{k})}\right) \cdot n \cdot \pi \cdot r^2 \quad \text{Equation 6-30}$$

For low hydraulic conductivities of the porous filling material in the hole the overall conductivity approaches the conductivity calculated from the Darcy's law.

When the flow resistance approaches zero, i.e. the case for an open hole without any porous filling material, the equation simplifies to the Hagen-Poiseuille equation (Bird et al. 1960):

$$Q = \frac{\pi \cdot \Delta P \cdot r^4}{8 \cdot \mu \cdot L} \qquad \text{Equation 6-31}$$

As in previous example, by identification (using the Hagen-Poiseuille equation and Darcy's law) the hydraulic conductivity of the circular hole is:

$$K_{\text{open hole}} = \frac{\rho \cdot g}{\mu} \cdot \frac{r^2}{8} \qquad \text{Equation 6-32}$$

From this it may be calculated that the overall hydraulic conductivity of the concrete wall penetrated by n circular holes with radii r is:

$$K_{\text{overall}}^{\text{open holes}} = K_I \cdot (A_{tot} - n \cdot \pi \cdot r^2) + K_{\text{open hole}} \cdot n \cdot \pi \cdot r^2 =$$

$$= K_I \cdot (A_{tot} - n \cdot \pi \cdot r^2) + \frac{\rho \cdot g}{\mu} \cdot \frac{n \cdot \pi \cdot r^4}{8} \qquad \text{Equation 6-33}$$

A similar expression can be derived using an estimated hydraulic conductivity of the porous fill instead of the expression introduced from Equation 6-33, cf. analogous expression derived for the overall effective diffusivity, Equation 6-37. Hence:

$$K_{\text{overall}}^{\text{porous fill Darcy}} = K_I \cdot (A_{tot} - n \cdot \pi \cdot r^2) + K_{\text{porous fill}} \cdot n \cdot \pi \cdot r^2 \qquad \text{Equation 6-34}$$

The results for a wide range of hydraulic conductivities of the filling material in 12 circular holes, radius 0.01 m, per m^2 in a concrete wall are presented in Figure 6-3. Results are shown for the three different models presented in this section.

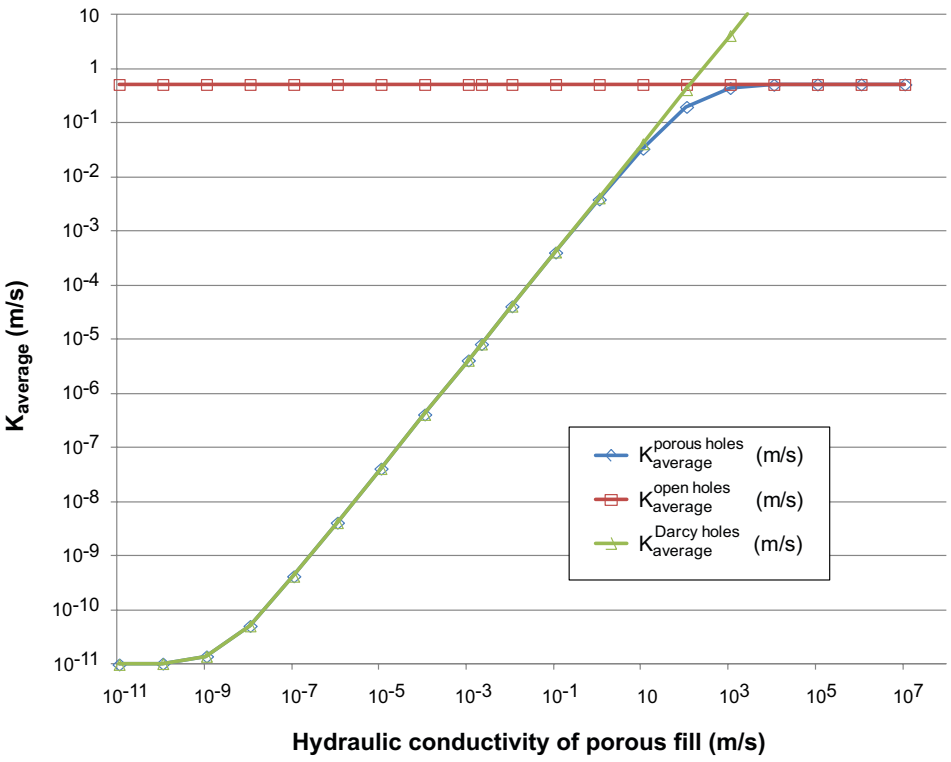

Figure 6-3. *Calculated average hydraulic conductivities for a concrete wall penetrated by 12 circular holes, radius 0.01 m vs. hydraulic conductivity of porous fill in the hole. Three different models are compared: one assuming flow in a porous fill in the hole taking into account also the effect of velocity distribution in the flow cross-section (blue diamond markings, Equation 6-30), one assuming flow in an open hole according to Hagen-Poiseuille law (red square markings, Equation 6-33) and one assuming Darcy flow in a porous fill (green triangular markings, Equation 6-34).*

6.8 Overall diffusivity of concrete penetrated by circular holes caused by completely corroded form ties

The concrete walls in 1BMA have remnants of form ties that were used as support during construction of the concrete walls on-site in the 1BMA vault. The form ties fully penetrate the concrete walls. Hence when corroded they may constitute passages through the concrete walls. The amount of form ties in the 1BMA concrete walls has been estimated to 12 per m^2.

The overall diffusivity can be estimated from the fraction of the total cross-section area occupied by holes:

$$a_h = \frac{n \cdot \pi \cdot r^2}{A_{tot}} \qquad \text{Equation 6-35}$$

where:

a_h = fraction of cross-section area occupied by holes (m^2/m^2)

n = number of holes (–)

r = hole radius (m)

A_{tot} = total crossection area (m^2)

The overall diffusivity is given by:

$$D_{h,\text{overall}} = a_h \cdot D_0 + (1 - a_h) \cdot D_{eI} = n \cdot \pi \cdot r^2 \cdot D_0 + (1 - n \cdot \pi \cdot r^2) \cdot D_{eI} \qquad \text{Equation 6-36}$$

where:

$D_{h,\text{overall}}$ = the overall diffusivity of concrete with holes (m^2/s)

D_0 = diffusivity in bulk water (m^2/s)

D_{eI} = effective diffusivity of intact concrete (m^2/s)

a_h = fraction of crossection area occupied by holes (m^2/m^2)

r = hole radius (m)

Alternatively, by changing the value for diffusivity in bulk water the expression for $D_{h,\text{overall}}$ can be used to estimate the overall diffusivity for cases where the holes are filled with some porous material having another effective diffusivity, $D_{\text{porous fill}}$, than that of concrete, e.g.:

$$D_{h,\text{overall}} = a_h \cdot D_{\text{porous fill}} + (1 - a_h) \cdot D_{eI} = \\ = n \cdot \pi \cdot r^2 \cdot D_{\text{porous fill}} + (1 - n \cdot \pi \cdot r^2) \cdot D_{eI} \qquad \text{Equation 6-37}$$

The results for a wide range of effective diffusivities of the filling material in 12 circular holes per m^2 in a concrete wall are presented in Figure 6-4.

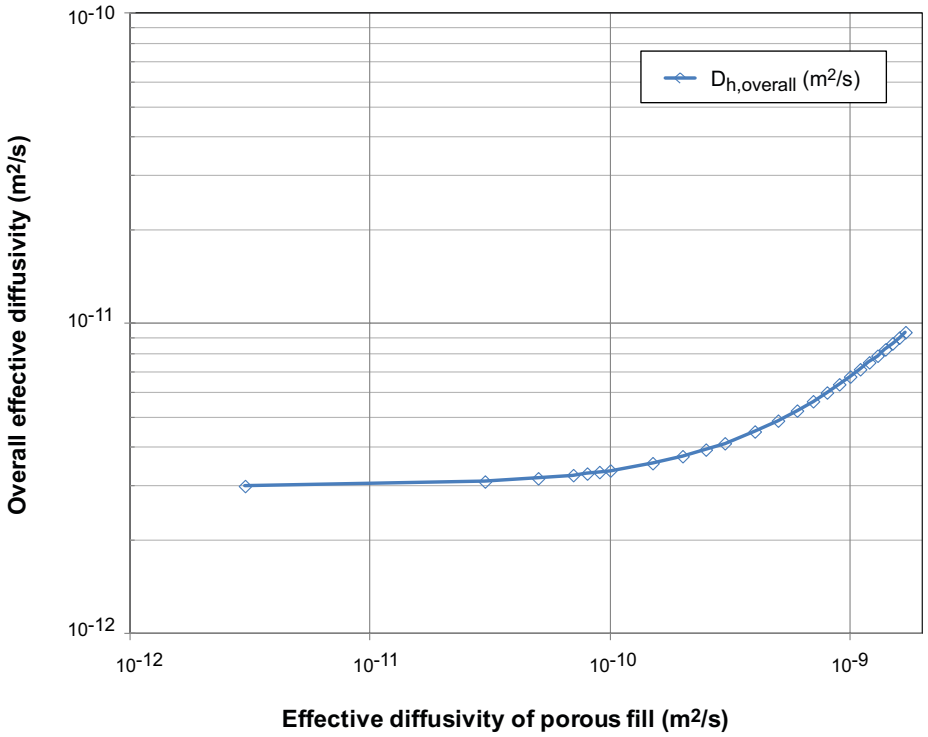

Figure 6-4. *Calculated overall effective diffusivity for a concrete wall penetrated by 12 circular holes, radius 0.01 m versus the effective diffusivity of porous fill in the hole.*

6.9 Overall conductivity of concrete penetrated by an annular shaped space between two coaxial cylinders caused by incompletely corroded form ties

In this case the flow is assumed to occur axially in the annular space between two coaxial cylinders having radii $\kappa \cdot r$ and r respectively, see illustration in Figure 6-5. The volumetric flow rate is given by (Bird et al. 1960):

$$Q = \frac{\pi \cdot \Delta P \cdot r^4}{8 \cdot \mu \cdot L} \cdot \left((1 - \kappa^4) - \frac{(1-\kappa^2)^2}{\ln(1/\kappa)} \right) \qquad \text{Equation 6-38}$$

where:

Q = the volumetric flow rate (m^3/s)

ΔP = the pressure drop (Pa)

r = the radius of the outer coaxial cylinder (m)

κ = ratio of radii of the inner to the outer coaxial cylinders (–)

μ = the dynamic viscosity (Pa·s)

L = length of flow passage (m)

When κ approaches 1 the expression becomes a bit challenging to evaluate in a straightforward manner due to numerical cancellation errors. The calculated results make use of a series expansion:

$$\left((1 - \kappa^4) - \frac{(1-\kappa^2)^2}{\ln(1/\kappa)} \right) = -\frac{4}{3} \cdot (\kappa - 1)^3 - \frac{2}{3} \cdot (\kappa - 1)^4 - \frac{1}{45} \cdot (\kappa - 1)^5 + \frac{1}{90} \cdot (\kappa - 1)^6 -$$

$$\frac{8}{945} \cdot (\kappa - 1)^7 + \frac{1}{140} \cdot (\kappa - 1)^8 - \frac{353}{56700} \cdot (\kappa - 1)^9 + \frac{25}{4536} \cdot (\kappa - 1)^{10} - \frac{2306}{467775} \cdot (\kappa - 1)^{11} +$$

$$\frac{4753}{1069200} \cdot (\kappa - 1)^{12} - \frac{41236667}{10216206000} \cdot (\kappa - 1)^{13} + O((\kappa - 1)^{14})$$

Equation 6-39

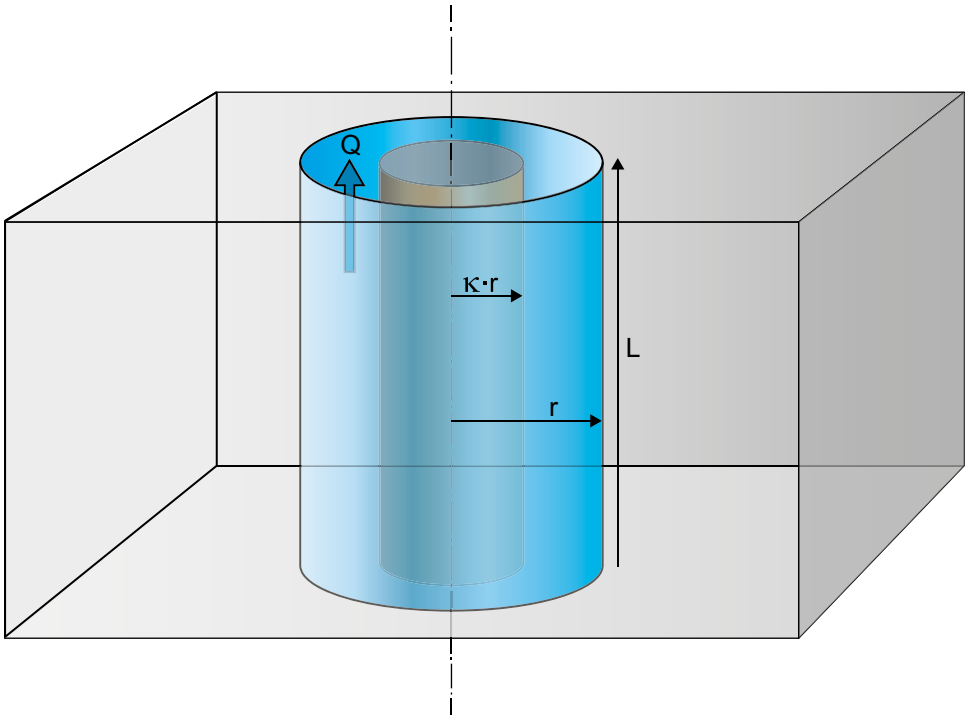

Figure 6-5. *Illustration to flow in an annular shaped hole between two coaxial cylinders.*

Comparing the expression for the flow rate with the Darcy's law:

$$Q = A \cdot K \cdot i \qquad \text{Equation 6-40}$$

and note that:

$$i = \frac{1}{\rho \cdot g} \cdot \frac{\Delta P}{L} \qquad \text{Equation 6-41}$$

By identification, the hydraulic conductivity of the annular space is:

$$K_{\text{annular space}} = \frac{\rho \cdot g}{\mu} \cdot \frac{r^2}{8} \cdot \left((1 - \kappa^4) - \frac{\left(1-\kappa^2\right)^2}{\ln(1/\kappa)} \right) \qquad \text{Equation 6-42}$$

From this it may be calculated that the overall hydraulic conductivity of the concrete wall penetrated by *n* annular spaces is:

$$K_{\text{overall}}^{\text{annular spaces}} = K_I \cdot (A_{tot} - n \cdot \pi \cdot r^2) + K_{\text{annular space}} \cdot n \cdot \pi \cdot r^2 =$$

$$= K_I \cdot (A_{tot} - n \cdot \pi \cdot r^2) + \frac{\rho \cdot g}{\mu} \cdot \frac{r^2}{8} \cdot \left((1 - \kappa^4) - \frac{\left(1-\kappa^2\right)^2}{\ln(1/\kappa)} \right) \cdot n \cdot \pi \cdot r^2 \qquad \text{Equation 6-43}$$

The results of calculated average hydraulic conductivities of a concrete wall penetrated by 12 annular shaped holes per m^2 are presented in Figure 6-6. When κ, i.e. the ratio of outer to inner radii, approaches zero the flow equation simplifies to the Hagen-Poiseuille equation (Bird et al. 1960).

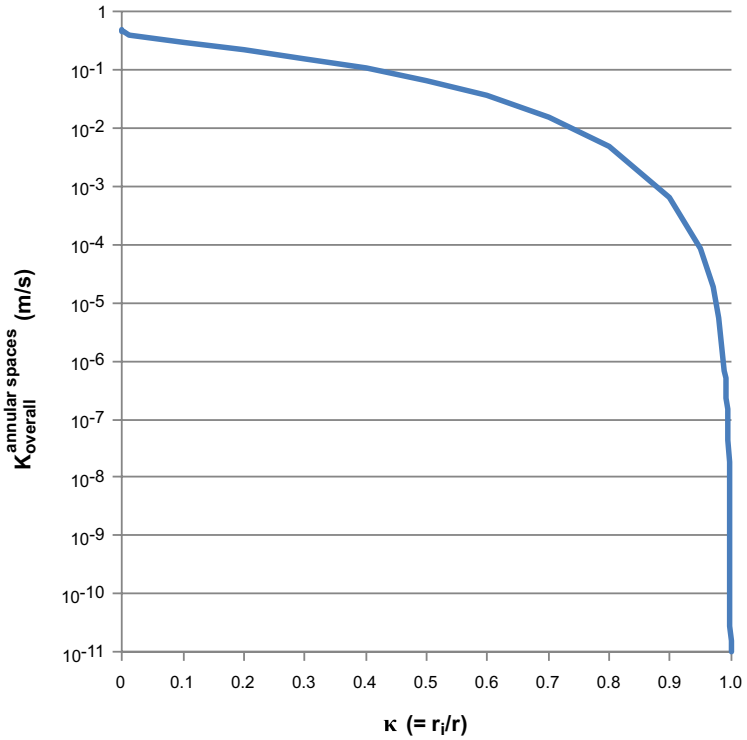

Figure 6-6. *Calculated overall hydraulic conductivities for a concrete wall penetrated by 12 annular shaped holes per m² versus the ratio between outer and inner radii (κ). Outer radius is assumed to be 0.01 m.*

6.10 Overall diffusivity of concrete penetrated by an annular shaped space between two coaxial cylinders caused by incompletely corroded form ties

In this case the diffusion is assumed to occur axially in the annular space between two coaxial cylinders having radii $\kappa \cdot r$ and r respectively, see illustration in Figure 6-5. The concrete walls in 1BMA have remnants of form ties that were used as support during construction of the concrete walls on-site in the 1BMA vault. The form ties fully penetrate the concrete walls. Hence when corroded they may constitute passages through the concrete walls. The amount of form ties in the 1BMA concrete walls has been estimated to 12 per m².

The overall diffusivity can be estimated from the fraction of the total cross-section area occupied by the annular space:

$$a_{ah} = \frac{n \cdot \pi \cdot (r^2 - (\kappa \cdot r)^2)}{A_{tot}} = \frac{n \cdot \pi \cdot r^2 \cdot (1 - \kappa^2)}{A_{tot}} \qquad \text{Equation 6-44}$$

where:

a_{ah} = fraction of crossection area occupied by annular holes (m²/m²)

n = number of holes (–)

r = the radius of the outer coaxial cylinder (m)

κ = ratio of radii of the inner to the outer coaxial cylinders (–)

A_{tot} = total crossection area (m²)

The overall diffusivity is given by:

$$D_{ah,\text{overall}} = a_{ah} \cdot D_0 + (1 - a_{ah}) \cdot D_{eI} =$$

$$= n \cdot \pi \cdot r^2 \cdot (1 - \kappa^2) \cdot D_0 + (1 - n \cdot \pi \cdot r^2 \cdot (1 - \kappa^2)) \cdot D_{eI} \qquad \text{Equation 6-45}$$

where:

$D_{ah,\text{overall}}$ = the overall diffusivity of concrete with annular holes (m^2/s)

D_0 = diffusivity in bulk water (m^2/s)

D_{eI} = effective diffusivity of intact concrete (m^2/s)

a_h = fraction of crossection area occupied by annular holes (m^2/m^2)

r = the radius of the outer coaxial cylinder (m)

κ = ratio of radii of the inner to the outer coaxial cylinders (–)

Alternatively, by changing the value for diffusivity in bulk water the above expression for $D_{h,\text{overall}}$ can be used to estimate the overall diffusivity for cases where the holes are filled with some porous material having another effective diffusivity, $D_{\text{porous fill}}$, than that of concrete, e.g.:

$$D_{ah,\text{overall}} = a_{ah} \cdot D_{\text{porous fill}} + (1 - a_{ah}) \cdot D_{eI} =$$

$$= n \cdot \pi \cdot r^2 \cdot (1 - \kappa^2) \cdot D_{\text{porous fill}} + (1 - n \cdot \pi \cdot r^2 \cdot (1 - \kappa^2)) \cdot D_{eI} \qquad \text{Equation 6-46}$$

6.11 Impact on conductivity by disturbed zones around form ties

During construction of the 1BMA barriers, the form ties are equipped with a conical plastic cap. The cap is removed after casting of the concrete and the form tie is broken at the breakneck. As a result, a conical depression is formed at the surface of the concrete wall for each form tie. The conical depression is mended by concrete, regarded to be of lower quality and higher porosity than the construction concrete of the wall itself. The remaining part of the form ties that penetrate the concrete wall may lead to the formation of a zone around each form tie that have a higher conductivity due to separation of cement paste close to the steel surface that depletes the adjacent concrete, see illustration in Figure 6-7.

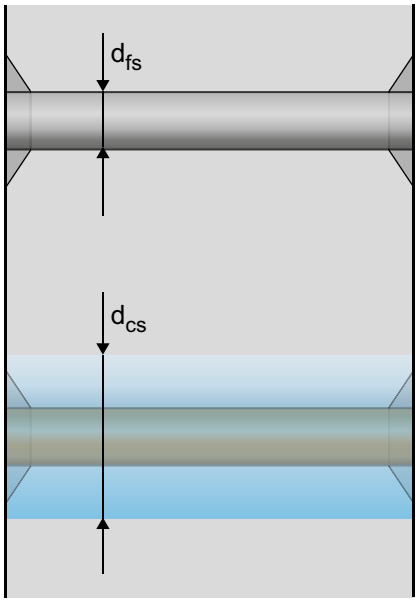

Figure 6-7. *Illustration of remnants of form ties (diameter d_{fs}) in a cross-section of a concrete wall and the possible formation of a zone (of diameter d_{cs}) of higher conductivity around the form ties.*

Assuming that the cement separation effect creates a zone with a diameter d_{cs} and a hydraulic conductivity N_{cs} times higher than the conductivity of the intact concrete, then:

$$d_{cs} = f \cdot d_{fs}$$ Equation 6-47

where:

f = an arbitrary factor ≥1

d_{fs} = the diameter of the form ties (m)

The fraction of the total wall area affected by the cement separation zones can be calculated by:

$$a_{cs} = \frac{\frac{n \cdot \pi}{4} \cdot \left[(f \cdot d_{fs})^2 - {d_{fs}}^2 \right]}{A_{tot}}$$ Equation 6-48

where:

n = number of form ties in the wall

A_{tot} = total surface area of the wall (m^2)

The overall hydraulic conductivity is given by:

$$K_{\text{overall},cs} = K_I \cdot (a_{cs} \cdot N_{cs} + 1 - a_{cs}) =$$
$$= K_I \cdot \left(\frac{\frac{n \cdot \pi}{4} \cdot \left[(f \cdot d_{fs})^2 - {d_{fs}}^2 \right]}{A_{tot}} \cdot N_{cs} + 1 - \frac{\frac{n \cdot \pi}{4} \cdot \left[(f \cdot d_{fs})^2 - {d_{fs}}^2 \right]}{A_{tot}} \right)$$ Equation 6-49

Figure 6-8 presents the overall hydraulic conductivity for different values of the conductivity contrast factor N_{cs}.

In a similar fashion, small cracks may develop around the remnants of form ties in the concrete walls. Such fractures may develop at an early stage during construction and hardening of the concrete, or may develop later, e.g. as a result of corrosion of the form ties.

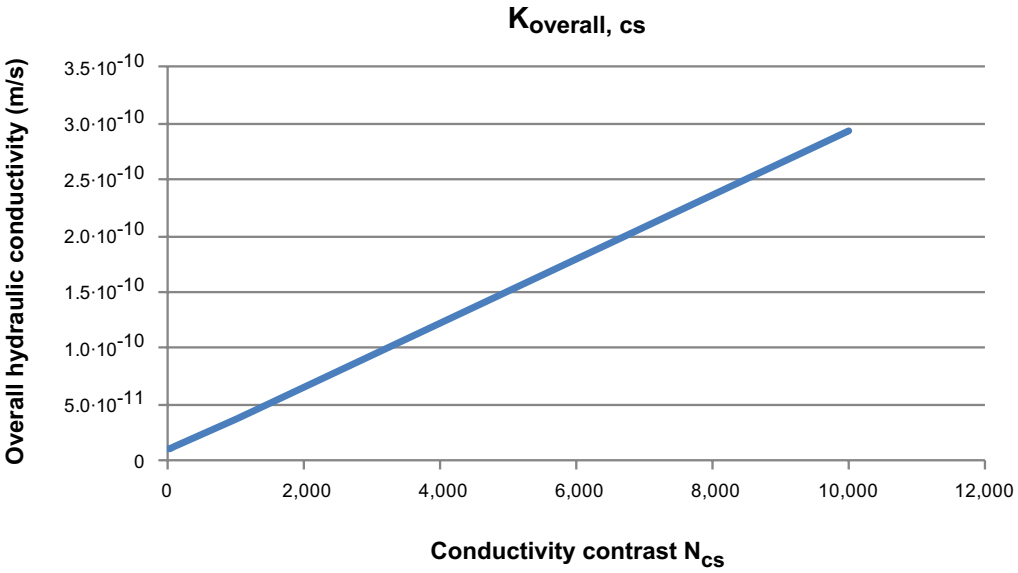

Figure 6-8. *Overall hydraulic conductivity for different conductivity contrasts N_{cs} between intact concrete and disturbed zones around form ties in the walls.*

Assuming that fully penetrating fractures of aperture width b_{ts} and length l_{ts} occur around every m^{th} form tie, the fraction of the total wall area affected by tiny fractures can be calculated as:

$$l_{ts} = u \cdot d_{fs}$$

$$a_{ts} = \frac{\frac{n}{m} \cdot l_{ts} \cdot b_{ts}}{A_{tot}} = \frac{\frac{n}{m} \cdot u \cdot d_{fs} \cdot b_{ts}}{A_{tot}} \qquad \text{Equation 6-50}$$

where:

u = an arbitrary factor ≥0 relating the fracture length to the diameter of the form tie

n = number of form ties in the wall

l_{ts} = length of fracture extending from the form tie (m)

b_{ts} = aperture width of fracture around the form tie (m)

A_{tot} = total surface area of the wall (m^2)

The overall hydraulic conductivity of the concrete wall can be calculated from (cf. Section 6.1):

$$K_{\text{overall},ts} = a_{ts} \cdot \frac{\rho \cdot g}{\mu} \cdot \frac{{b_{ts}}^2}{12} + K_I \cdot (1 - a_{ts}) =$$

$$= \frac{\frac{n}{m} \cdot u \cdot d_{fs} \cdot b_{ts}}{A_{tot}} \cdot \frac{\rho \cdot g}{\mu} \cdot \frac{{b_{ts}}^2}{12} + K_I \cdot \left(1 - \frac{\frac{n}{m} \cdot u \cdot d_{fs} \cdot b_{ts}}{A_{tot}}\right) \qquad \text{Equation 6-51}$$

Figure 6-9 presents the overall hydraulic conductivity versus fracture width of tiny fractures formed around form ties in the walls. Fractures have been assumed to occur around 10% of the form ties.

The combined effect of both cement-depleted zones and tiny fractures around form ties can be calculated from:

$$K_{\text{overall},cs+ts} = K_I \cdot (a_{cs} \cdot N_{cs} + 1 - a_{cs} - a_{ts}) + a_{ts} \cdot \frac{\rho \cdot g}{\mu} \cdot \frac{{b_{ts}}^2}{12} =$$

$$= K_I \cdot \left(\frac{\frac{n \cdot \pi}{4} \cdot \left[(f \cdot d_{fs})^2 - {d_{fs}}^2\right]}{A_{tot}} \cdot N_{cs} + 1 - \frac{\frac{n \cdot \pi}{4} \cdot \left[(f \cdot d_{fs})^2 - {d_{fs}}^2\right]}{A_{tot}} - \frac{\frac{n}{m} \cdot u \cdot d_{fs} \cdot b_{ts}}{A_{tot}}\right)$$

$$+ \frac{\frac{n}{m} \cdot u \cdot d_{fs} \cdot b_{ts}}{A_{tot}} \cdot \frac{\rho \cdot g}{\mu} \cdot \frac{{b_{ts}}^2}{12} \qquad \text{Equation 6-52}$$

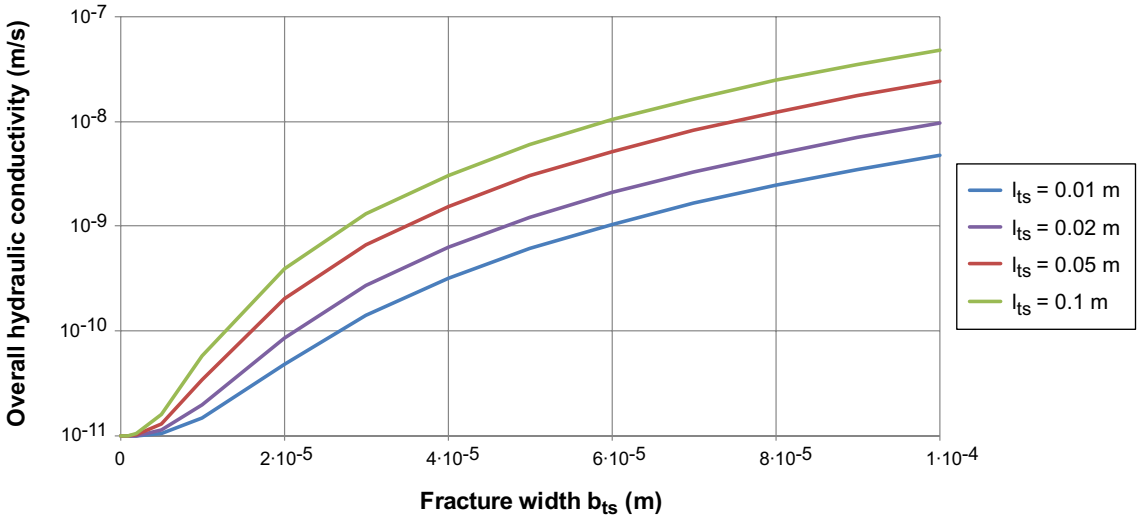

Figure 6-9. *Overall hydraulic conductivity versus fracture width of tiny fractures formed around form ties in the walls. Fractures have been assumed to form around 10% of the form ties in the example.*

6.12 Impact on diffusivity by disturbed zones around form ties

During construction of the 1BMA barriers, the form ties are equipped with a conical plastic cap. The cap is removed after casting of the concrete and the form tie is broken at the breakneck. As a result, a conical depression is formed at the surface of the concrete wall for each form tie. The conical depression is mended by concrete, regarded to be of lower quality and higher porosity than the construction concrete of the wall itself. The remaining part of the form ties that penetrate the concrete wall may lead to the formation of a zone around each form tie that have a higher diffusivity due to separation of cement paste close to the steel surface that depletes the adjacent concrete, see illustration in Figure 6-7.

Assuming that the cement separation effect creates a zone with a diameter d_{cs} and an effective diffusivity N_{cs} times higher than the effective diffusivity of the intact concrete:

$$d_{cs} = f \cdot d_{fs}$$ Equation 6-53

where:

f = an arbitrary factor ≥0

d_{fs} = the diameter of the form ties (m)

The fraction of the total wall area affected by the cement separation zones can be calculated by:

$$a_{cs} = \frac{\frac{n \cdot \pi}{4} \cdot \left[(f \cdot d_{fs})^2 - {d_{fs}}^2 \right]}{A_{tot}}$$ Equation 6-54

where:

n = number of form ties in the wall

A_{tot} = total surface area of the wall (m^2)

The overall effective diffusivity is given by:

$$D_{\text{overall},cs} = D_{eI} \cdot (a_{cs} \cdot N_{cs} + 1 - a_{cs}) = \\ = D_{eI} \cdot \left(\frac{\frac{n \cdot \pi}{4} \cdot \left[(f \cdot d_{fs})^2 - {d_{fs}}^2 \right]}{A_{tot}} \cdot N_{cs} + 1 - \frac{\frac{n \cdot \pi}{4} \cdot \left[(f \cdot d_{fs})^2 - {d_{fs}}^2 \right]}{A_{tot}} \right)$$ Equation 6-55

In a similar fashion, tiny cracks may develop around the remnants of form ties in the concrete walls. Such fractures may develop at an early stage during construction and hardening of the concrete, or may develop later, e.g. as a result of corrosion of the form ties.

Assuming that fully penetrating fractures of aperture width b_{ts} and length l_{ts} form around every m^{th} form tie, the fraction of the total wall area affected by tiny fractures can be calculated as:

$$l_{ts} = u \cdot d_{fs}$$ Equation 6-56

$$a_{ts} = \frac{\frac{n}{m} \cdot l_{ts} \cdot b_{ts}}{A_{tot}} = \frac{\frac{n}{m} \cdot u \cdot d_{fs} \cdot b_{ts}}{A_{tot}}$$ Equation 6-57

where:

u = an arbitrary factor ≥0 relating the fracture length to the diameter of the form tie

n = number of form ties in the wall

l_{ts} = length of fracture extending from the form tie (m)

b_{ts} = width or fracture around the form tie (m)

A_{tot} = total surface area of the wall (m^2)

The overall effective diffusivity of the concrete wall can be calculated from:

$$D_{\text{overall},ts} = a_{ts} \cdot \xi_D \cdot D_0 + D_{eI} \cdot (1 - a_{ts}) = \\ = \frac{\frac{n}{m} \cdot u \cdot d_{fs} \cdot b_{ts}}{A_{tot}} \cdot \xi_D \cdot D_0 + D_{eI} \cdot \left(1 - \frac{\frac{n}{m} \cdot u \cdot d_{fs} \cdot b_{ts}}{A_{tot}} \right)$$ Equation 6-58

The combined effect of both cement-depleted zones and tiny fractures around form ties can be calculated from:

$$D_{\text{overall},cs+ts} = D_{eI} \cdot (a_{cs} \cdot N_{cs} + 1 - a_{cs} - a_{ts}) + a_{ts} \cdot \xi_D \cdot D_0 =$$

$$= D_{eI} \cdot \left(\frac{\frac{n \cdot \pi}{4} \cdot \left[(f \cdot d_{fs})^2 - {d_{fs}}^2 \right]}{A_{tot}} \cdot N_{cs} + 1 - \frac{\frac{n \cdot \pi}{4} \cdot \left[(f \cdot d_{fs})^2 - {d_{fs}}^2 \right]}{A_{tot}} - \frac{\frac{n}{m} \cdot u \cdot d_{fs} \cdot b_{ts}}{A_{tot}} \right) + \frac{\frac{n}{m} \cdot u \cdot d_{fs} \cdot b_{ts}}{A_{tot}} \cdot \xi_D \cdot D_0$$

Equation 6-59

6.13 Overall conductivity of concrete penetrated by cylindrical holes intended for injection of concrete grout

Each compartment in the 1BMA vault has 12 cylindrical holes that will be used to inject concrete grout in the empty voids between waste packages at closure. Assuming the diameter of these holes is 0.1 m, simple estimates on the impact on the overall hydraulic conductivity have been made, assuming the holes are filled with concrete grout. For this case, the model presented in Section 6.7 may be applied directly. Each compartment is about 9.9 m long with a height of 8.4 m (SKB 2001). Varying the hydraulic conductivity of the concrete grout between $8.3 \cdot 10^{-9}$ and $8.3 \cdot 10^{-7}$ m/s gives an overall hydraulic conductivity between $2.9 \cdot 10^{-11}$ and $1.9 \cdot 10^{-9}$ m/s. Hence the impact is not dramatic compared with intact concrete with a hydraulic conductivity of $1 \cdot 10^{-11}$ m/s. If the holes would be left empty the overall hydraulic conductivity would increase to very high numbers (> 30 m/s).

6.14 Overall diffusivity of concrete penetrated by cylindrical holes intended for injection of concrete grout

Each compartment in the 1BMA vault has 12 cylindrical holes that will be used to inject concrete grout in the empty voids between waste packages at closure. Assuming the diameter of these holes is 0.1 m, simple estimates on the impact on the overall effective diffusivity have been made, assuming the holes are filled with concrete grout. For this case, the model presented in Section 6.8 may be applied directly. Each compartment is about 9.9 m long with a height of 8.4 m (SKB 2001). Varying the effective diffusivity of the concrete grout between $1 \cdot 10^{-11}$ and $1 \cdot 10^{-10}$ m^2/s gives an overall effective diffusivity between $3.01 \cdot 10^{-12}$ and $3.1 \cdot 10^{-12}$ m^2/s. Hence the impact is barely noticeable compared with intact concrete with an effective diffusivity of $3 \cdot 10^{-12}$ m^2/s. If the holes would be left empty the overall effective diffusivity would increase to $5.3 \cdot 10^{-12}$ m^2/s.

6.15 Application to the 1BMA vault in SFR

Inspections of fractures and casting joints have been carried out (in 2000 and 2011) of concrete structures in the 1BMA vault (SKBdoc 1430853). The inspection reports show that significant fracturing has occurred, most likely due to temperature movements and shrinkage fracturing following the early hydration process and possibly to a lesser extent shrinking due to partial drying of the concrete to a relative humidity of ~ 80%. The total number of fractures is limited, whereas the sizes of the observed fractures are large (SKBdoc 1430853). The inspection undertaken in 2011, focussed on fractures in floor and the lower parts of the 1BMA vault. Fractures in the upper parts of the 1BMA vault were cursorily inspected, but the observations were not recorded or reported. However, the conclusion was drawn that the number and size of fractures were higher in the lower parts of the concrete constructions in the 1BMA vault (SKBdoc 1430853).

The occurrence of fractures has a significant impact on the hydraulic conductivity of the concrete as was shown earlier in this chapter. The impact of fractures on the porosity (shown next) and the effective diffusivity is on the other hand not necessarily very dramatic. Even a few small fractures, which would only marginally increase the porosity and the effective diffusivity, may have a large impact on the hydraulic conductivity. In case the fracturing has occurred to an extent where the increase in porosity is significant, the hydraulic conductivity can be expected to be very high. The effect on the effective diffusivity is still moderate.

Hydraulic conductivities

An estimate of the overall hydraulic conductivity of the 1BMA concrete structures can be made with the expression presented in Section 6.5, Equation 6-17, and taking into account the actual fractures observed and characterised during the inspection. In Table 6-1 the observed sizes of each individual fracture are summarised. Using these data and applying the model presented in Section 6.5, the overall hydraulic conductivity of the concrete structures in the 1BMA vault is estimated to $5.2 \cdot 10^{-5}$–$1 \cdot 10^{-4}$ m/s for the bottom and western long side wall and $1.1 \cdot 10^{-4}$–$2.2 \cdot 10^{-4}$ m/s for the bottom and eastern long side wall based on the results of the inspection in year 2000 (SKBdoc 1430853). For comparison, the hydraulic conductivity of intact concrete is assumed to be $1 \cdot 10^{-11}$ m/s. A surface roughness factor of 0.5–1 has been assumed in the calculations.

A corresponding calculation based on the reported results of the inspection undertaken in 2011 shows an overall hydraulic conductivity of the concrete walls in 1BMA of $2.6 \cdot 10^{-4}$–$5.3 \cdot 10^{-4}$ m/s. The data assumed for the calculations are shown in Table 6-1.

The results show that very high values for the overall hydraulic conductivity is expected for the concrete structures in the 1BMA vault based on the results of the inspected section. It will remain a priority to verify if these estimates are representative for the parts of the 1BMA vault which have not been inspected.

Effective diffusivities

Making use of the same data shown in Table 6-1 and applying the model presented in Section 6.6 the overall effective diffusivity has been calculated considering the actual fractures observed and characterised during the inspection.

The overall effective diffusivity of the concrete structures in the 1BMA vault is estimated to $3.14 \cdot 10^{-12}$ m^2/s for the bottom and western long side wall and $3.21 \cdot 10^{-12}$ m^2/s for the bottom and eastern long side wall based on the results of the inspection in year 2000 (SKBdoc 1430853). For comparison, the effective diffusivity of intact concrete is assumed to be $3 \cdot 10^{-12}$ m^2/s. A surface roughness factor of 1 has been assumed in the calculations.

A corresponding calculation based on the reported results of the inspection undertaken in 2011 (SKBdoc 1430853) shows an overall effective diffusivity of the concrete walls in 1BMA of $3.5 \cdot 10^{-12}$ m^2/s.

The estimates show that the impact of the observed fractures on the overall effective diffusivity is almost negligible.

Porosities

Effect on porosity by fractures

The overall porosity increase of fractured concrete can be estimated from:

$$\Delta\phi = \frac{b}{d} \qquad \text{Equation 6-60}$$

where:

$\Delta\phi$ = change in porosity due to fractures (m^3/m^3)

b = fracture width (aperture) (m)

d = fracture spacing (m)

Example calculations assuming one fracture every metre of varying width are shown in Figure 6-10 together with calculated overall hydraulic conductivities and overall effective diffusivities. In Figure 6-11, a calculation is shown where the fracture width and the corresponding hydraulic conductivity and effective diffusivity have been calculated assuming a constant porosity increase of $1 \cdot 10^{-5}$ m^3/m^3 for varying fracture spacing.

Using the data from the inspection undertaken in year 2000 and applying the model presented in Section 6.5, the total added fracture width of the inspected 40 m section of the 1BMA vault is 9.7 mm and 12.4 mm, respectively, for the western and eastern sides of the 1BMA vault, which is equivalent to an average shrinkage of 0.24 mm/m and 0.31 mm/m, respectively. The average porosity increase calculated from the fracture aperture widths and fracture lengths (see Table 6-1) amounts to 0.014% and 0.019%, respectively.

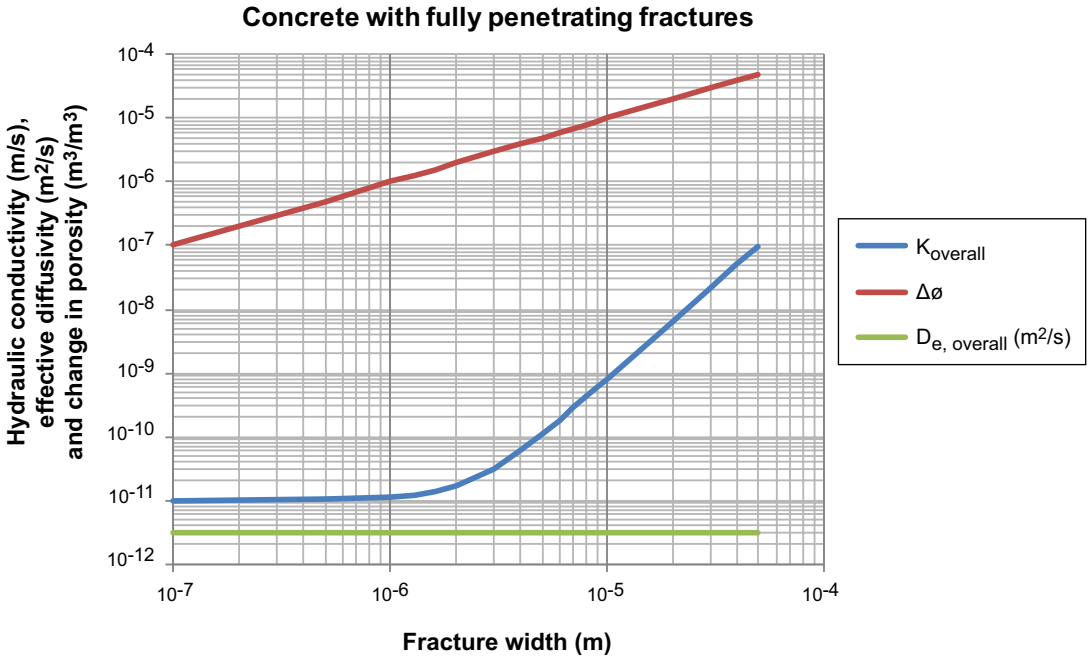

Figure 6-10. *Change of porosity, overall hydraulic conductivity and overall effective diffusivity for different fracture widths assuming one fracture every metre.*

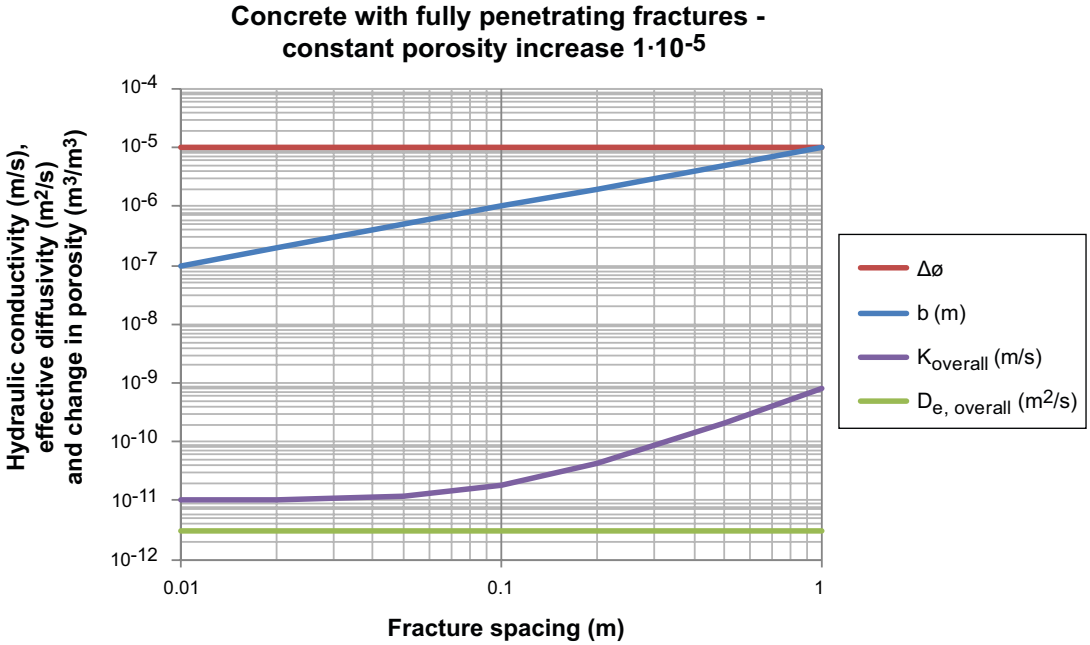

Figure 6-11. *Example calculation showing the change of the overall hydraulic conductivity, overall effective diffusivity and the corresponding fracture aperture widths for a case with constant porosity increase of $1{\cdot}10^{-5}$ m^3/m^3 for varying fracture spacing.*

A corresponding calculation based on the reported results of the inspection undertaken in 2011 shows a total added fracture width of the inspected 40 m section of the 1BMA vault of 12.9 mm, which is equivalent to an average shrinkage of 0.32 mm/m. The corresponding average porosity increase amounts to 0.05%. The data assumed for the calculations are shown in Table 6-1.

The increase of porosity caused by fractures also adds to the connectivity of the pore system and should be regarded as an increase of porosity available for water flow and diffusion.

The value for the initial porosity of 11% that has been assumed for the modelling in this report is slightly higher than the value calculated based on the composition of the concrete (i.e. 9.9%), see Section 2.6, and can be regarded to include the porosity increase by initial fractures.

Table 6-1. Compilation of observed fractures in the 1BMA vault concrete structures (based on SKBdoc 1430853). IpX denotes Inspection point nr X.

Fracture Id/ Inspection point	Fracture length l_i (m)	Fracture aperture width b_i (m)
Inspection 2011 (only fracture aperture widths are given in the report, lengths assumed based on comparison with inspection data from 2000 and photos.)		
Ip1+Ip2	9.8	$1.1 \cdot 10^{-3}$
Ip3	9.8	$4.5 \cdot 10^{-4}$
Ip4	17.1	$1.8 \cdot 10^{-3}$
Ip5	0.5	$3.0 \cdot 10^{-4}$
Ip6	1.2	$1.5 \cdot 10^{-3}$
Ip6	7	$1.6 \cdot 10^{-3}$
Ip7	5.5	$2.5 \cdot 10^{-4}$
Ip9	1	$2.5 \cdot 10^{-4}$
Ip10	1	$2.1 \cdot 10^{-4}$
Ip11	1	$3.0 \cdot 10^{-4}$
Ip12+Ip16	2	$3.0 \cdot 10^{-4}$
Ip13	2	$1.5 \cdot 10^{-4}$
Ip14	2	$3.0 \cdot 10^{-4}$
Ip15	1.5	$3.0 \cdot 10^{-3}$
Ip17	11.8	$1.4 \cdot 10^{-3}$
Inspection 2000 Western long side		
1	2.5	$5.0 \cdot 10^{-4}$
2	4	$1.1 \cdot 10^{-3}$
3	3.5	$5.0 \cdot 10^{-4}$
4	1.5	$2.0 \cdot 10^{-3}$
5	1.2	$2.0 \cdot 10^{-3}$
6	7	$7.9 \cdot 10^{-4}$
7	4	$5.0 \cdot 10^{-4}$
8	1.5	$2.0 \cdot 10^{-3}$
9	3	$3.0 \cdot 10^{-4}$
Inspection 2000 Eastern long side		
10	1.5	$2.0 \cdot 10^{-3}$
11	2.5	$5.0 \cdot 10^{-4}$
12	4	$1.0 \cdot 10^{-3}$
13	4	$3.6 \cdot 10^{-4}$
14	1.5	$3.0 \cdot 10^{-3}$
15	4	$5.0 \cdot 10^{-4}$
16	4	$5.0 \cdot 10^{-4}$
17	4	$5.0 \cdot 10^{-4}$
18	4	$5.0 \cdot 10^{-4}$
19	4	$2.0 \cdot 10^{-3}$
20	7	$5.0 \cdot 10^{-4}$
21	1.2	$1.0 \cdot 10^{-3}$

Effect on porosity by leaching

The leaching of portlandite and CSH-gel will result in increased porosity in concrete. The effect on porosity in the leached zone of concrete is easy to estimate from the loss of solid minerals and the corresponding mineral densities. Thus:

$$\Delta\phi = \sum_i \frac{\Delta q_i \cdot M_i}{\rho_i}$$ Equation 6-61

The total porosity after the change is given by:

$$\phi_t = \phi_0 + \Delta\phi$$ Equation 6-62

where:

$\Delta\phi$ = change in porosity due to changes in the mineral assemblage (m^3/m^3)

ϕ_t = the total porosity after the change (m^3/m^3)

ϕ_0 = the initial porosity at time 0 (m^3/m^3)

Δq_i = change of the amount of a mineral phase *i* due to chemical reactions and leaching ($kmol/m^3$)

ρ_i = density of mineral *i* (kg/m^3)

M_i = molar weight of mineral *i* (kg/kmol)

Using the data in Table 2-7, the porosity increase due to leaching of portlandite can be estimated assuming full depletion (Δq_{CH} = 1.04 $kmol/m^3$, M_{CH} = 74 kg/kmol, ρ_{CH} = 2,230 kg/m^3) to ~ 0.035 m^3/m^3 or an increase by 3.5%. In a similar way the effect of CSH-gel leaching (Δq_{CSH} = 1.23 $kmol/m^3$, M_{CSH} = 193 kg/kmol, ρ_{CSH} = 2,450 kg/m^3) can also be estimated to ~ 0.097 m^3/m^3 or an increase by 9.7%. It must be stressed that a substantial leaching of the CSH-gels would likely cause a disintegration of the concrete; therefore the porosity estimate should be regarded hypothetical.

7 Reactive transport modelling of concrete degradation in BMA

This section presents the reactive transport modelling of the chemical degradation of the concrete barriers in the BMA vaults using the PHAST program, which simulates the reactive transport of multiple chemical components in 1, 2 or 3 dimensions (Parkhurst et al. 2010). The groundwater flow simulator is based on the HST3D program and the geochemical reactions are calculated using the PHREEQC program, which is invoked as a subroutine in PHAST.

The purpose of this section is to look at the evolution of the chemistry of the 1BMA and 2BMA concrete barriers over time as a function of their initial state. A thorough description of the different assumptions and data used in the calculations is given, followed by an extensive discussion of the modelling results over a period of up to 100,000 years. Two geochemical databases were used to assess the sensitivity of the results to the thermodynamic constants used and the mineral assemblage assumed in the calculations. The calculations have been made with the local equilibrium approach, hence the chemical reaction kinetics are assumed to be fast relative to solute transport so that local thermodynamic equilibria are established instantaneously. Ionic strength corrections have been made using the WATEQ extended Debye-Hückel equation (Truesdell and Jones 1974) for aqueous species that have Debye-Hückel parameters defined in the databases MinteqCem-2001 (Höglund 2001, based on the Minteq database (Allison et al. 1991)) and Cemdata07 (Lothenbach et al. 2008, Matschei et al. 2007, Möschner et al. 2008, Lothenbach and Winnefeld 2006, Hummel et al. 2002, Thoenen and Kulik 2003, transformed to PHREEQC format by Jacques 2009, Jacques et al. 2010, Martens et al. 2010) respectively. For other aqueous species the Davies equation is used. For details, see description in the PHREEQC manual (Parkhurst and Appelo 1999, 2013). All calculations have been made at a temperature of 25°C despite the fact that the ambient temperatures are expected to be 10°C or lower in SFR. The reason for this deviation is that not all species and minerals in the database have sufficient data to allow adaptation to other temperatures than 25°C, hence it was considered more ambiguous to change the temperature in the calculations when some entries in the database could not be adjusted to other temperatures.

Alkali metal hydroxides are generally soluble and would be expected to be highly leachable and result in a very high pH in the concrete pore water, above pH 13 for the composition of the cement used in SFR. Studies of the composition of solid concrete phases and porewater show, however, that the alkali hydroxides are associated with the solid phases, most probably the CSH-gels or the ballast. Following the method described in Höglund (2001), the alkali metal concentrations have been coarsely calibrated against measured data for Degerhamn Standard Portland cement (Lagerblad and Trägårdh 1994) assuming an ion exchange process. Berner (1990) addressed this issue by assuming a constant dissolved fraction of 5%. In the modelling the concrete porewater is also equilibrated with portlandite, CSH-gel and the other solid phases specified in Appendix H. The ion exchange reactions have the effect to retard the leaching of the alkali hydroxides and thereby reduce the initial pH of the pore water to ~ 13, but it will also prolong the period during which the pH of the pore water is higher than would be expected from equilibria with portlandite.

In contrast to the 1BMA, the concrete barriers in 2BMA are planned to be constructed without any reinforcement bars, form rods, or other construction elements of steel. Special precautions will be taken to minimise the early formation of fractures due to shrinkage, and thermal expansion and contraction during hydration. Therefore, the 2BMA barriers are expected to be in good condition, and are represented by good quality concrete providing the properties and function of the design criteria at the time of closure.

For 1BMA, calculations were carried out assuming a fractured concrete 1BMA barrier, although not fractured to the extent observed (e.g. SKBdoc 1430853), and following some simple repair measures and using what is thought to be pessimistic assumptions of their longevity. However, the repair measures are not as extensive as those likely to be included in the new Closure Plan for SFR (SKBdoc 1358612). Additionally, as a variation case, the impacts of the material properties remaining constant from 100–10,000 years are investigated. In one additional case, the simplification of the chemistry to a portlandite – pure water system is investigated. This case is useful for assessing the validity of the reactive transport model since it allows comparisons to be made with simplified analytical models presented in previous chapters.

A brief overview of the different cases included and the thermodynamic databases used is given in Table 7-1. The effects of a hydraulic cage created by the crushed rock/macadam have been considered in all cases. In this chapter, the 2BMA and 1BMA models and model cases studied are described, and then the results of each case are presented in detail. Finally, representative differences between the degraded and repaired 1BMA scenarios are compared graphically and discussed to explore the influence of the simple repairs measures investigated directly.

The PHAST program chosen for the calculations can effectively handle groundwater flow and reactive transport, which is a main target of the present study. One short-coming of the PHAST program is that no feed-back is available to couple the changes in the mineral assemblage resulting from the leaching and chemical degradation to changes in the porosity and related changes of the transport properties, e.g. the effective diffusivity and the hydraulic conductivity. Other computer models are available that can take such porosity changes into account in a coupled fashion. Examples of such models are e.g. TOUGHREACT (Xu et al. 2004), CRUNCHFLOW (Steefel 2001) and PFLOTRAN (Hammond et al. 2012). An overview of different models is given in Zhang et al. (2012). The gradual deterioration of the hydraulic properties of the concrete barriers is however expected to be largely governed by physical degradation processes that lead to fracture formation. Various analytical models have been studied in previous chapters in order to estimate possible changes of the hydraulic properties as a result of fracture formation. In the present application, changes of the transport properties are primarily connected to fracture formation during the early period, and at later stages increasingly attributed to chemical degradation. Changes of the material properties have been introduced on a best-estimate basis as step-wise changes of the input data to the program at selected points in time. As far as known, no models are available that can handle the change of material properties due to both physical fracture formation and chemical degradation. The chosen modelling approach would therefore seem appropriate for the purpose of the study.

7.1 Comparison of databases

Benchmark calculations have been made to compare the results when using two different thermodynamic databases for the calculations. This is in line with the recommendation given by Damidot et al. (2011) to conduct sensitivity analyses with respect to the thermodynamic databases used for concrete degradation calculations. The databases selected for the comparison are the database presented by Höglund (2001) which is built on the Minteq database (Allison et al. 1991) and the Cemdata07 database (Lothenbach et al. 2008, Matschei et al. 2007, Möschner et al. 2008, Lothenbach and Winnefeld 2006, Hummel et al. 2002, Thoenen and Kulik 2003, transformed to PHREEQC format by Jacques 2009, Jacques et al. 2010, Martens et al. 2010).

Since the mineral assemblages in the different databases are somewhat different, the input data require some adjustment. The strategy taken has been to adjust the relative amounts of similar minerals while striving to maintain an equal inventory of the chemical components in the different calculations. The mineral assemblies assumed in the calculations for the different databases are specified in Appendix H.

A comparison of the concrete mineral assemblage in the two databases is summarised in Table 7-2. In the model calculations, a feature has been used in the PHREEQC-model that allows the specification of a number of mineral phases that may precipitate and redissolve in response to changes in their thermodynamic stability fields. Hence, the model dynamically calculates the most stable mineral assemblage at each instance. All minerals have been represented as pure solid phases in the calculations; hence no solid solutions have been modelled in the present study.

Table 7-1. Overview of different cases in the modelling of concrete degradation in BMA.

Case	Important features	Thermodynamic database
Large20	2BMA. Full chemistry. This has been selected as the central case for providing data for the safety assessment.	MinteqCem-2001 with addition of thaumasite
Large10	1BMA. Full chemistry.	MinteqCem-2001
Large8	1BMA. Full chemistry.	Cemdata07
Large11	1BMA. Full chemistry. Repair scenario.	MinteqCem-2001
Large12	1BMA. Full chemistry. Repair scenario.	Cemdata07
Large9	1BMA. Full chemistry. Material properties assumed unchanged 100–10,000 years.	MinteqCem-2001
Large7	1BMA.Only portlandite and pure water.	Cemdata07

Table 7-2. Comparison of the concrete mineral assemblage in the two thermodynamic databases used in the modelling.

Mineral	Cemdata07 (Jacques 2009, Jacques et al. 2010, Martens et al. 2010)	MinteqCem-2001 (Höglund 2001)
AFm (aluminoferrite monosulphate)	See Fe-monosulphate /Monosulphoaluminate	Included, however, the calculated constants are for monosulphate specifically
AFt (aluminoferrite trisulphate)	See ettringite	Included, however the calculated constants are for ettringite specifically
$Al(OH)_3am$	Yes	Yes
Anhydrite ($CaSO_4$)	Yes	Yes
Brucite ($Mg(OH)_2$)	Yes	Yes
C_3AH_6(C) Hydrogarnet $(Ca0)_3Al_2O_3{\cdot}3H_2O$	Yes	Yes
C_3FH_6(C) Hydrogarnet-Fe $(Ca0)_3Fe_2O_3{\cdot}3H_2O$	Yes	Yes
C_4AH_{13} $(Ca0)_4Al_2O_3{\cdot}13H_2O$	Yes	No
C_4FH_{13} $(Ca0)_4Fe_2O_3{\cdot}13H_2O$	Yes	No
Calcite ($CaCO_3$)	Yes	Yes
CSH phases $(Ca0)_x{\cdot}SiO_2{\cdot}yH_2O$	CSHjen (C1.67SH2.1); CSHtob1 (C0.83SH1.3) Alt. CSHtob2 (C0.83SH1.3)	CSH_1.8 (C1.8SH1.8); CSH_1.1 (C1.1SH1.1); CSH_0.8 (C0.8SH0.8)
Ettringite $Ca_6Al_2(SO_4)_3(OH)_{12}{\cdot}26H_2O$	Yes	Yes
$Fe(OH)_3mic$	Yes	Yes, ferrihydrite
Fe-ettringite $Ca_6Fe_2(SO_4)_3(OH)_{12}{\cdot}26H_2O$	Yes	See Aft (aluminoferrite trisulphate)
Fe-hemicarbonate $Ca_4Fe_2(CO_3)_{0.5}(OH)_{13}{\cdot}5.5H_2O$	Yes	No
Fe-monocarbonate $Ca_4Fe_2(CO_3)(OH)_{12}{\cdot}5H_2O$	Yes	No
Fe-monosulphate $Ca_4Fe_2(SO_4)(OH)_{12}6H_2O$	Yes	See AFm (aluminoferrite monosulphate)
Fe-stratlingite $Ca_2Fe_2SiO_2(OH)_{10}{\cdot}3H_2O$	Yes	No
Friedel's salt $Ca_4Al_xCl_2(OH)_y$ x=0.86–1.96; y=8.58–11.88	No, but data based on Balonis et al. (2010) has been added in an announced update of the database.	Yes, 7 different phases included
Goethite FeOOH	No	Yes
Gypsum $CaSO_4{\cdot}2H_2O$	Yes	Yes
Hematite Fe_2O_3	Yes	Yes
Hemicarboaluminate $Ca_4Al_2(CO_3)_{0.5}(OH)_{13}{\cdot}5.5H_2O$	Yes	Yes
Hydrotalcite $Mg_4Al_2O_7{\cdot}10H_2O$	Yes (hydrotalciteOH)	Yes
hydrogarnetSi $Ca_3Al_2(SiO_4)_{0.8}(OH)_{8.8}$	Yes	No
hydrotalciteC $Mg_4Al_2(OH)_{12}CO_3{\cdot}3H_2O$	Yes	No
hydrotalciteFe $Mg_4Fe_2(OH)_{14}{\cdot}3H_2O$	Yes	No
Monocarboaluminate $Ca_4Al_2CO_9{\cdot}10.68H_2O$	Yes	Yes
Monosulphoaluminate C_4ASH_{12} $Ca_4Al_2(SO_4)(OH)_{12}{\cdot}6H_2O$	Yes	See AFm (aluminoferrite monosulphate)
Portlandite $Ca(OH)_2$	Yes	Yes
SiO_2am	Yes	Yes
Strätlingite C_2ASH_8 $Ca_2Al_2SiO_2(OH)_{10}{\cdot}3H_2O$	Yes	No
Syngenite $CaK_2(SO_4)_2.H_2O$	Yes	Yes
Thaumasite $(CaSiO_3)_2(CaSO_4)_2(CaCO_3)_2(H_2O)_{30}$	Yes	Added for case Large20
Tricarboaluminate $Ca_6Al_2(CO_3)_3(OH)_{12}{\cdot}26H_2O$	Yes	No

When evaluating the evolution of the porosity caused by changes in the mineral assemblage, the molar volumes according to Table 7-3 and Table 7-4 have been assumed. Molar weights are included for comparison.

Table 7-3. Molar weights and molar volumes of minerals in the MinteqCem 2001 database (Höglund 2001, with the addition of thaumasite (Jacques 2009)).

Mineral notation MinteqCem 2001	Molar weight (kg/kmol)	Molar volume (m^3/kmol)
Al(OH)3(a)	78	0.032233
Talc	379	0.137915
Calcite	100.1	0.03707
Brucite	58	0.0243
Hydrotalcite	443	0.259258
SiO2gel(am	150	0.087813
C0.8SH	122	0.049778
C1.1SH	154	0.062939
C1.8SH	193	0.078961
Portlandite	74	0.033226
Ettringite	1,254	0.724855
AFm	622	0.312563
C3FH6(C)	436	0.173024
C3AH6(C)	378	0.15
Gypsum	172	0.07421
Friedel's salt	489	0.24587
Fried1.96A	486	0.2443
Fried1.42A	444	0.22313
Fried1.34A	438	0.22
Fried1.04A	414	0.20824
Fried0.88A	402	0.20197
Fried0.86A	400	0.20118
CaCl2:6H20	219	0.128115
(CaO)3CaCl	549	0.321317
CaOCaCl2:2	203	0.118769
Syngenite	328	0.12729
Hemicarboaluminate	508	0.297302
Monocarboaluminate	568	0.285657
Thaumasite	622.62	0.33171

Table 7-4. Molar weights and molar volumes of different minerals in the Cemdata07 database (Jacques 2009, Jacques et al. 2010, Martens et al. 2010).

Mineral notation Cemdata07	Molar weight (kg/kmol)	Molar volume (m^3/kmol)
Gypsum	172.17	0.075
Syngenite	328.42	0.126
SiO2am	60.08	0.029
CSHtob1	314.01	0.141
CSHtob2	130.84	0.059
CSHjen	191.34	0.078
Portlandite	74.09	0.033
Ettringite	1,255.11	0.707
Monosulphoaluminate	622.52	0.309
HydrogarnetOH	378.29	0.15
HydrogarnetFe	436.01	0.155
HydrotalciteOH	443.33	0.22
Calcite	100.09	0.037
Brucite	58.32	0.025
Hemicarboaluminate	564.46	0.285
Monocarboaluminate	568.45	0.262
Thaumasite	622.62	0.33171
C2AH8	358.24	0.184
C2FH8	415.97	0.194
C4AH13	560.47	0.274
C4FH13	618.2	0.286
Tricarboaluminate	1,146.94	0.65
Fe-ettringite	1,312.84	0.718
Fe-monosulfate	680.25	0.321
Stratlingite	418.32	0.216
Fe-stratlingite	476.05	0.227
Fe-hemicarbonate	622.19	0.296
Fe-monocarbonate	644.19	0.29
HydrotalciteFe	501.06	0.232
CAH10	338.19	0.194
HydrogarnetSi	397.53	0.143
HydrotalciteC	469.33	0.22
Al(OH)3am	78	0.032
Fe(OH)3mic	106.87	0.034

7.2 Case description – model interpretation of 2BMA

The basic assumptions made for the modelling of chemical degradation processes in concrete barriers in the 2BMA vault are described in this section.

The concrete barriers consist of 14 detached caissons of non-reinforced concrete, see Chapter 2. The floor and walls are cast in one step to minimise joints in the constructions. During filling, a temporary pre-fabricated concrete cover may be used as a radiation shield over the waste, and will be removed when filling is completed. After filling of the caissons with waste packages, a lid is constructed consisting of 0.5 m cast concrete. The concrete constructions are supported from the inside by the waste packages and are backfilled with concrete grout and on the outside by crushed rock/ macadam. The grouting is done in steps to minimise the mechanical stress on the non-reinforced concrete walls. The concrete floor rests on a bed of gravel (grain size 6–20 mm) which also serves the purpose as a part of a hydraulic cage around the caissons.

The concrete walls, floor and lid consists of construction concrete. The composition of the concrete (cement quality, *W*/*C*-ratio, ballast quality and content) is assumed to be the same as in 1BMA. During construction the concrete will experience temperature and moisture variations which cause dimensional changes and may result in mechanical stresses. Such stresses may cause small fractures in the concrete. In the evaluation it is assumed that thin fractures, maximum aperture of 100 μm with an average fracture spacing of 1 m, are present in the concrete at closure.

The purpose of the model is not to mimic the exact geometry of the different concrete constructions in 2BMA, but rather to show the general behaviour of the concrete barriers when exposed to groundwater, as well as the impact of small fractures. The first test calculations made indicated that very long time would be required to perform the calculations, on the order of months for each case. To achieve a reasonable spatial discretisation of a full-scale cross-section of a caisson a large number of nodes would be required. The computational demand is directly dependent of the number of nodes which determines the number of calls to the chemical sub-model PHREEQC. Since time was a critical factor for this study it was necessary to make adjustments to the level of detail in the calculations. In order to reduce the computational demand, the dimensions of the model were reduced which made it possible to reduce the number of nodes in the mesh. The thicknesses of the concrete walls, lid and floor have been kept in the model to ensure that the diffusive transport of dissolved species can be estimated with reasonable accuracy. A schematic illustration of the geometry assumed in the model calculations is given in Figure 7-1.

Case Large20 considers the effect of a hydraulic cage created by the crushed rock/macadam backfill surrounding the concrete structures in the 2BMA vault. The assumed vertical model height of the caisson is 2 m, corresponding from the bottom to the top to a 0.5 m concrete floor, a 1 m high and 0.5 m thick concrete wall intersected by one horizontal fracture with an aperture of 100 μm, and a 0.5 m concrete lid. Inside the concrete walls and below the concrete lid a 0.1 m thick layer of concrete grout is considered. A void volume in the centre part of the caissons marks the position of the waste (which is not a topic of this study). The void is considered an empty space, initially filled with concrete pore water. The void is a part of the mesh but has been assigned transport properties that ensure that there are no practical resistances to flow or diffusion in this volume. The concrete floor and the concrete lid are both penetrated by a 100 μm vertical fracture. Keeping the flow proportions of the true cross-section of the 2BMA vault, the permeable layers below and on top of the caissons have been scaled to 0.1 m and 1.75 m, respectively.

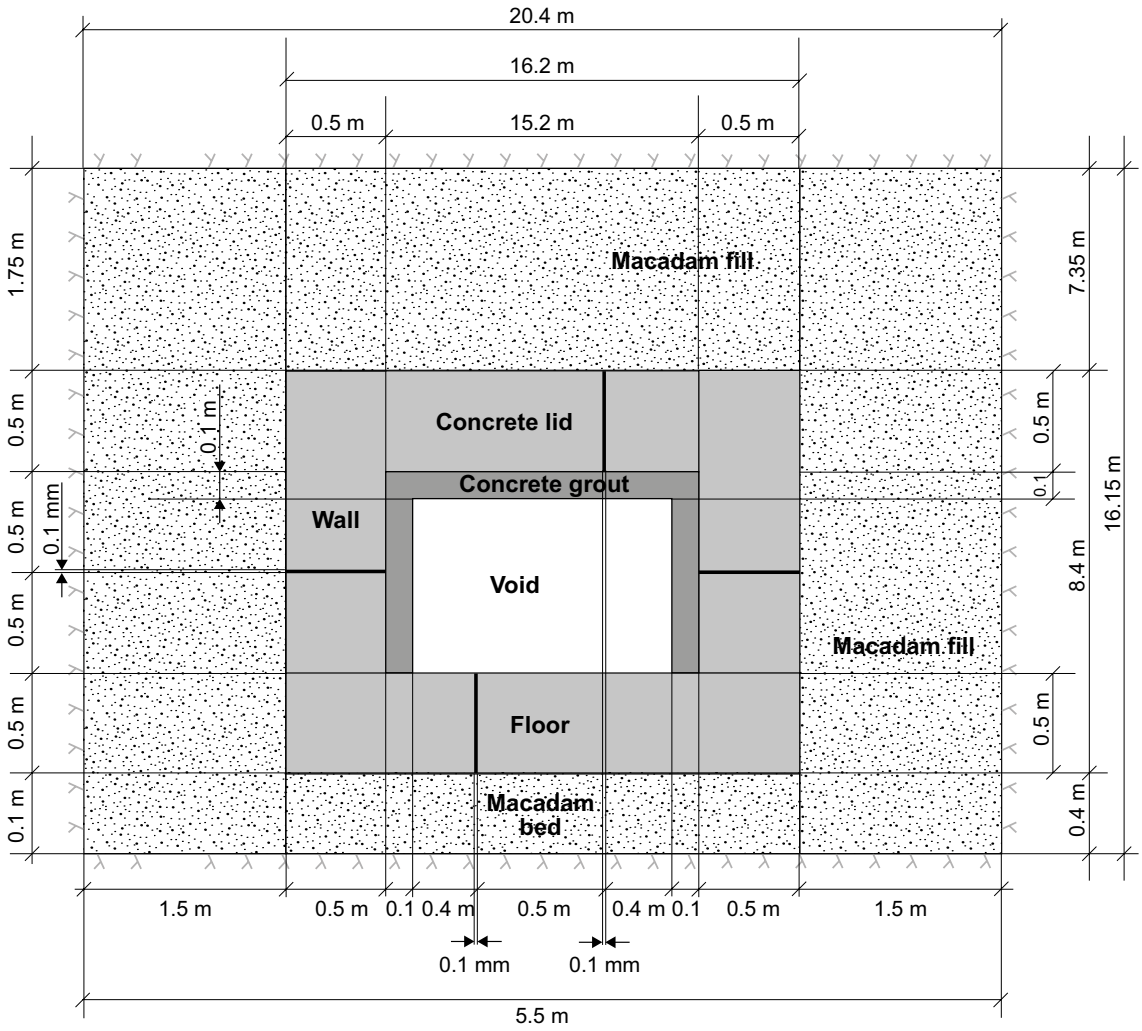

Figure 7-1. *Schematic interpretation of the concrete barriers in the 2BMA vault of SFR. Numbers are given in (m). Numbers on the right-hand side and at the top refer to the real dimensions whereas the numbers on the left-hand side and the bottom refer to the model interpretation.*

If the primary interest was to determine the hydraulic flow around the caisson, the crushed rock/ macadam at the sides should also be scaled in proportion to the real geometry. The scaled values would then be approximately 0.3 m on each side of the concrete walls (up-stream and down-stream sides respectively). However, in the reactive transport modelling, the focus was on studying the different reactions between groundwater and components leached from the concrete that may include precipitation of minerals such as calcite at the concrete surfaces or in the surrounding gravel. For this reason, the geometry of the crushed rock/macadam zones at the side walls (1.5 m thick) has been assumed in the calculations. The crushed rock/macadam is assumed to be an inert material in the calculations, however secondary minerals are allowed to precipitate and re-dissolve as the chemical conditions progress throughout the calculations. The relevance of the geometrical representation of the 2BMA concrete structures are further discussed and quantified in Appendix A.

The calculations use the material property data presented in Table 7-5 and in Figure 7-2; the hydraulic conductivities and the diffusivities of the concrete barriers and estimates of how they change with time are of particular importance. The MinteqCem-2001 thermodynamic database, complemented by data for thaumasite has been used in this case.

The geometry is defined as follows:

- A 1.5 m layer of crushed rock/macadam/gravel is assumed to be present on the left-hand side of the figure between the rock wall and the concrete wall. The groundwater flow is arbitrarily assumed to be horizontal from left to right. This is therefore the inflow side of the model.
- The concrete walls are 0.5 m thick and each of them has one 0.1 mm wide horizontally fully penetrating fracture. By keeping the actual thicknesses of the walls, floor and lid in the model, applying representative groundwater fluxes and hydraulic conductivities of the different structures, and applying relevant diffusivities, both the diffusive and the advective transport of dissolved components can be well described. This enables reasonable estimates to be made of the time for different steps in the leaching sequence.
- To simulate the impact of a hydraulic cage, a 0.1 m bed of gravel has been assumed to lie between the concrete floor and the underlying rock floor.
- The concrete floor is 0.5 m thick and has one 0.1 mm wide vertical fully penetrating fracture/casting crack, assumed to be located at $x = 2.5$ m. This position is somewhat asymmetric relative to the centreline.
- The concrete lid is 0.5 m thick and has one 0.1 mm wide vertical fully penetrating fracture/casting crack, assumed to be located at $x = 3$ m. This position is somewhat asymmetric relative to the centreline and does not fall along the same vertical line as the fracture through the floor.
- A second concrete wall, located on the right-hand side, outflow side of the figure, is 0.5 m thick and with one 0.1 mm wide horizontally fully penetrating fracture.
- The space inside the concrete walls is assumed to be filled with 0.1 m thick cement grout (see Appendix H for a specification of the composition), whereas, no interaction with the waste or waste packaging has been considered in the calculations (this has been the topic of other studies (Cronstrand 2013)). The void has been assumed to be initially filled with concrete pore water and secondary minerals are allowed to precipitate and re-dissolve in response to chemical changes over time.
- A 1.5 m bed of crushed rock/macadam is assumed to be present on the right-hand side, outflow side of the figure between the rock wall and the concrete wall.
- A 1.75 m thick layer of crushed rock/macadam is assumed to cover the concrete construction.
- The outflow of groundwater has been assumed to take place against a hydrostatic boundary on the right-hand side of the model.
- Insulated (impermeable) hydraulic boundaries have been assumed for the rock below and above the vault.
- The boundary conditions for chemical transport are fixed concentrations of different components in the inflowing groundwater (left-hand side of the model). The concentrations change from Salt-water to Fresh-water (see definition of the water composition in Table 3-1 and Table 3-2) after 2,000 years when the flow conditions change from sub-seabed to the inland period.
- The boundary conditions for the chemical transport at the down-stream right-hand side of the model are zero concentration gradients of the different species, which can be interpreted as a pure advective outflow of the dissolved components.

In the PHAST modelling, it is advisable to maintain a constant porosity throughout the calculation in order to maintain the mass balance of dissolved and solid components. When assigning changes to the effective diffusivity over time (which is done by changing the properties given as input to the model at discrete points in time), it was therefore chosen to keep the porosity constant, while assigning the changes to the parameter tortuosity: The tortuosity is only used in the model as a scalar value, together with the porosity and the diffusivity in pure water, to calculate the effective diffusivity.

Two positions in the model were selected for more detailed evaluation of the temporal changes in mineralogy and chemistry, see Figure 7-3. The first position (GH) is at the centreline of the concrete lid and the left-hand side concrete wall, while the second (CH) is at the vertical centreline of the left-hand side concrete wall near the thin horizontal fracture. Two sections have also been evaluated in detail: C-C, which is positioned 1 mm from the thin fracture; and, D-D, which is inside the fracture.

Table 7-5. Assumed material data and their variation over time for different model components in concrete barriers in 2BMA.

Model components		0–100 years	100–10,000 years	10,000–20,000 years	20,000–100,000 years
2BMA					
Concrete wall/floor/lid	Porosity	0.11	0.11	0.11	0.11
	Tortuosity[1]	0.032	0.045	0.091	1.818
	D_e (m^2/s)	$3.5 \cdot 10^{-12}$	$5.0 \cdot 10^{-12}$	$1.0 \cdot 10^{-11}$	$1.0 \cdot 10^{-10}$
	K (m/s)	$8.3 \cdot 10^{-10}$ [2]	$8.0 \cdot 10^{-8}$ [3]	$1.0 \cdot 10^{-6}$ [4]	$1.0 \cdot 10^{-5}$ [5]
Fractures in concrete walls/floor/lid	Aperture (mm)	0.1	0.1	0.1	0.1
	Porosity	1	1	1	1
	Tortuosity	1	1	1	1
	D_e (m^2/s)	$1 \cdot 10^{-9}$	$1 \cdot 10^{-9}$	$1 \cdot 10^{-9}$	$1 \cdot 10^{-9}$
	K (m/s)	0.008	0.008	0.008	0.008
Concrete grout	Porosity	0.3	0.3	0.3	0.3
	Tortuosity[1]	0.167	0.267	0.33	0.5
	D_e (m^2/s)	$5.0 \cdot 10^{-11}$	$8.0 \cdot 10^{-11}$	$1.0 \cdot 10^{-10}$	$1.5 \cdot 10^{-10}$
	K (m/s)	$8.3 \cdot 10^{-9}$	$8.0 \cdot 10^{-7}$	$3.0 \cdot 10^{-5}$	$8.0 \cdot 10^{-5}$
Crushed rock/macadam at the side walls and above the caissons	Porosity	0.3	0.3	0.3	0.3
	Tortuosity	0.5	0.5	0.5	0.5
	D_e (m^2/s)	$1.5 \cdot 10^{-10}$	$1.5 \cdot 10^{-10}$	$1.5 \cdot 10^{-10}$	$1.5 \cdot 10^{-10}$
	K (m/s)	$1.0 \cdot 10^{-3}$	$1.0 \cdot 10^{-3}$	$1.0 \cdot 10^{-3}$	$1.0 \cdot 10^{-3}$
Crushed rock/macadam (6–20 mm) below the concrete floor	Porosity	0.3	0.3	0.3	0.3
	Tortuosity[1]	0.5	0.33	0.33	0.33
	D_e (m^2/s)	$1.5 \cdot 10^{-10}$	$1.0 \cdot 10^{-10}$ [6]	$1.0 \cdot 10^{-10}$	$1.0 \cdot 10^{-10}$
	K (m/s)	$1.0 \cdot 10^{-3}$	$1.0 \cdot 10^{-4}$ [7]	$1.0 \cdot 10^{-4}$	$1.0 \cdot 10^{-4}$
Void space	Porosity	1	1	1	1
	Tortuosity[1]	1	1	1	1
	D_e (m^2/s)	$1.0 \cdot 10^{-9}$	$1.0 \cdot 10^{-9}$	$1.0 \cdot 10^{-9}$	$1.0 \cdot 10^{-9}$
	K (m/s)	0.1	0.1	0.1	0.1

[1] In order to maintain a constant porosity in the numerical modelling, all assumed changes in the pore structure have been assigned to changes in the tortuosity for a given domain in time. This ensures that the mass balance is maintained in the PHAST calculations.

[2] This corresponds to an intact concrete with a conductivity of $1 \cdot 10^{-11}$ m/s intersected by 1 fracture per m with an aperture of ~ 10 µm.

[3] This corresponds e.g. to concrete intersected by 1 fracture per m with an aperture of ~ 45 µm, or 10 fractures per m with an aperture of ~ 20 µm.

[4] This corresponds e.g. to concrete intersected by 1 fracture per m with an aperture of ~ 100 µm, or 10 fractures per m with an aperture of ~ 50 µm.

[5] This corresponds e.g. to concrete intersected by 10 fractures per m with an aperture of ~ 100 µm.

[6] A decrease in the effective diffusivity of the macadam has been assumed after 100 years as a result of segregation of fine particles that accumulate in the lower parts of the vault.

[7] Ditto for the hydraulic conductivity, c.f. footnote 6.

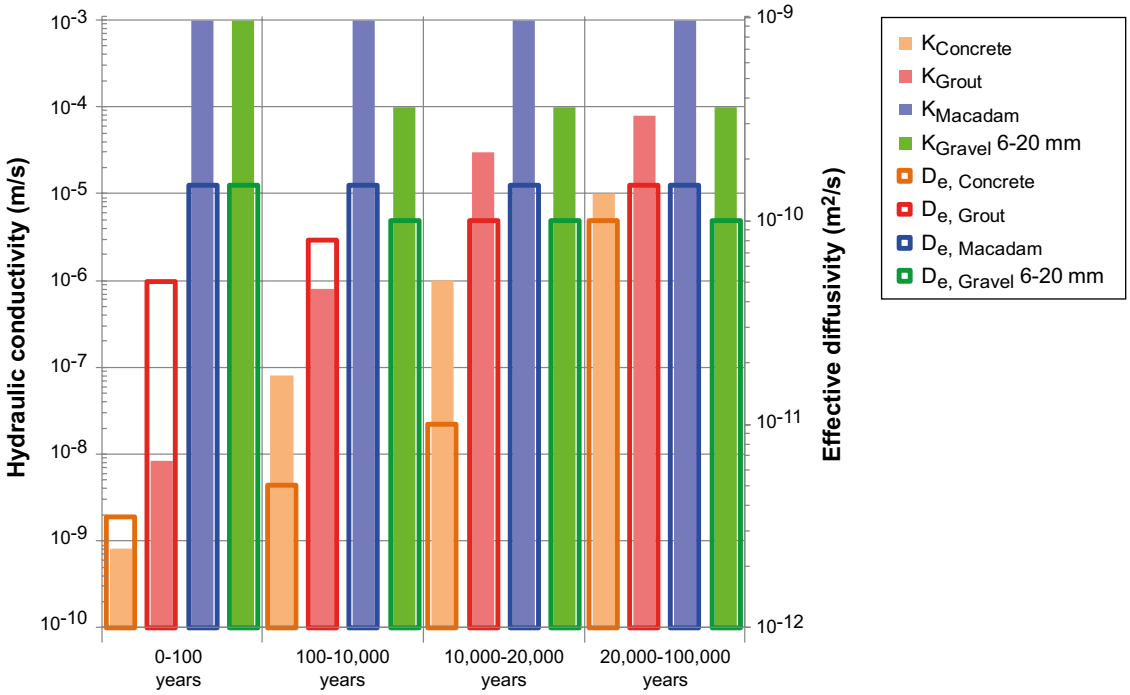

Figure 7-2. *Graphic presentation of the selected data for the hydraulic conductivity (K) and effective diffusivity (D_e) in various materials assumed in the calculations for the 2BMA vault.*

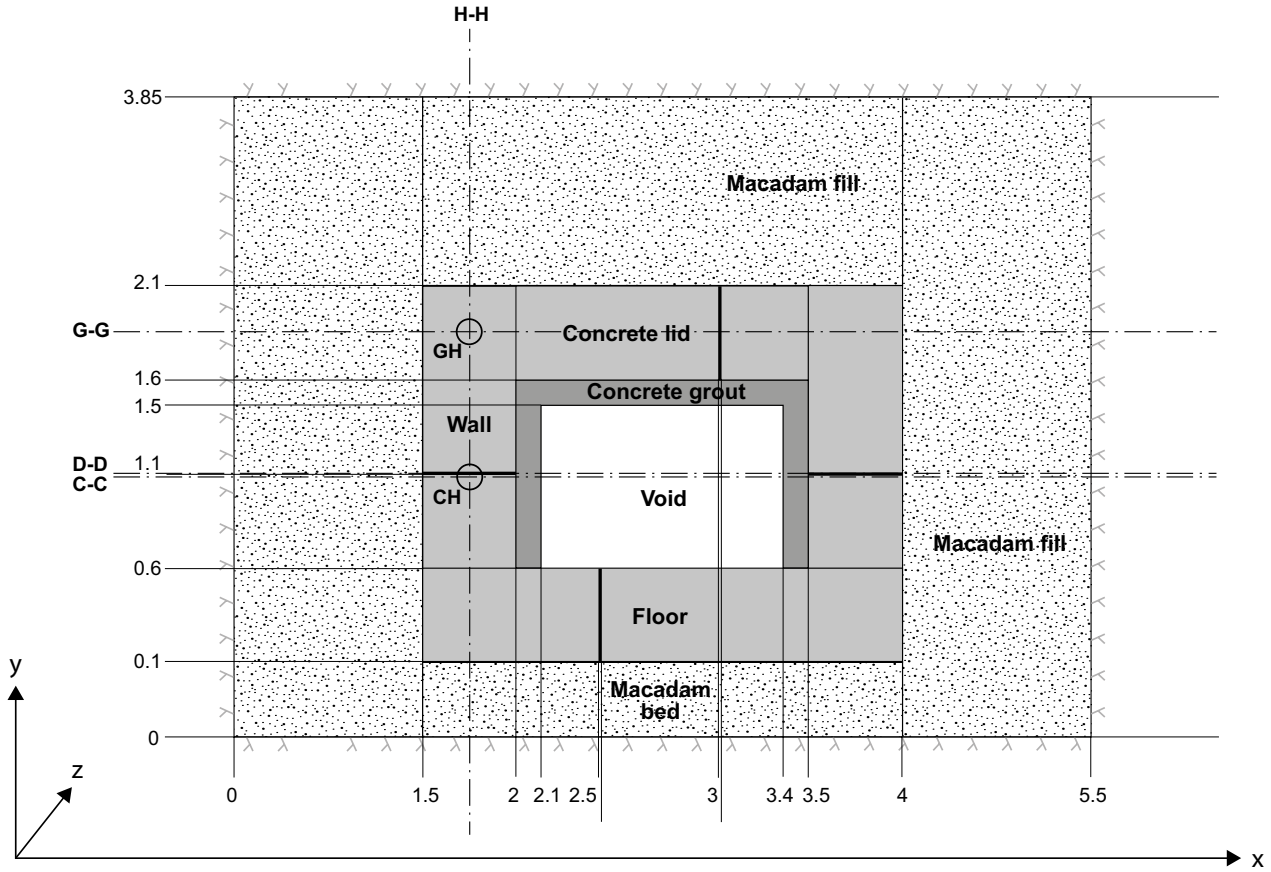

Figure 7-3. *Definition of vertical and horizontal sections and intersection points used for evaluation of the PHAST modelling results of case Large20 for the 2BMA vault. Numbers refer to distances in meters relative to the origin located in the lower left corner of the drawing.*

7.2.1 Model discretisation – 2BMA

The spatial discretisation of the geometry shown in Figure 7-1 has been implemented as a cell grid, see Figure 7-4. The PHAST model consists of 4,752 cells with 9,782 nodes. The smallest and largest cell sizes are $2 \cdot 10^{-5}$ and 0.6 m respectively.

A constant time step of 1 year has been used for the presented calculations. In order to check the quality of the performed calculations, an additional set of calculations were run for the period 0–20,000 years with a time step of 0.1 years and the results were compared with the calculations using a 1 year time step. The results of the comparisons are presented in Appendix A.

7.2.2 Groundwater flow – 2BMA

The groundwater flux assumed as a boundary condition for the 2BMA vault has been calculated from the total inflow of groundwater in the cavern presented in Abarca et al. (2013) and the cross-section area of the 2BMA vault (275 m × 16.8 m = 4,620 m^2). Hence, in the modelling here, the same average groundwater fluxes have been assumed as predicted in the hydrogeological calculations for the 2BMA vault. Stepwise changes in the flux have been assumed after 1,000 years (3000 AD) and 3,000 years (5000 AD) respectively, reflecting the transition from the saltwater period to the freshwater period, see Table 7-6. This transition is caused by the land rise in the Forsmark area which moves the shoreline over and beyond the SFR repository.

The head distribution and the direction of the groundwater flux are presented in Figure 7-5 for the first 100 years with stationary boundary conditions.

Table 7-6. Assumed groundwater composition and flow into the 2BMA vault at different times and the corresponding fluxes assumed as boundary conditions for the reactive transport calculations.

Period	Groundwater composition	Total inflow in 2BMA vault (m^3/year)	Average flux of groundwater inflow in 2BMA vault (m^3/m^2/year)
0–1,000 years (2000–3000 AD)	Salt-water (see Table 3-1)	0.3	$6.5 \cdot 10^{-5}$
1,000–2,000 years (3000–4000 AD)		24.4	$5.3 \cdot 10^{-3}$
2,000–3,000 years (4000–5000 AD)	Fresh water (see Table 3-2)		
3,000– years (5000 AD –)		31.1	$6.7 \cdot 10^{-3}$

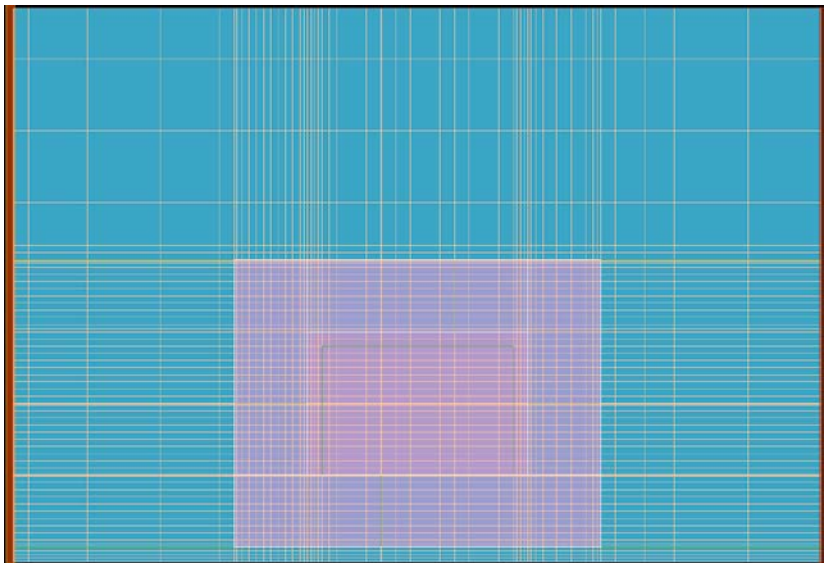

Figure 7-4. *Geometrical representation of the model geometry for 2BMA in PHAST. The caisson is represented by the light purple colour.*

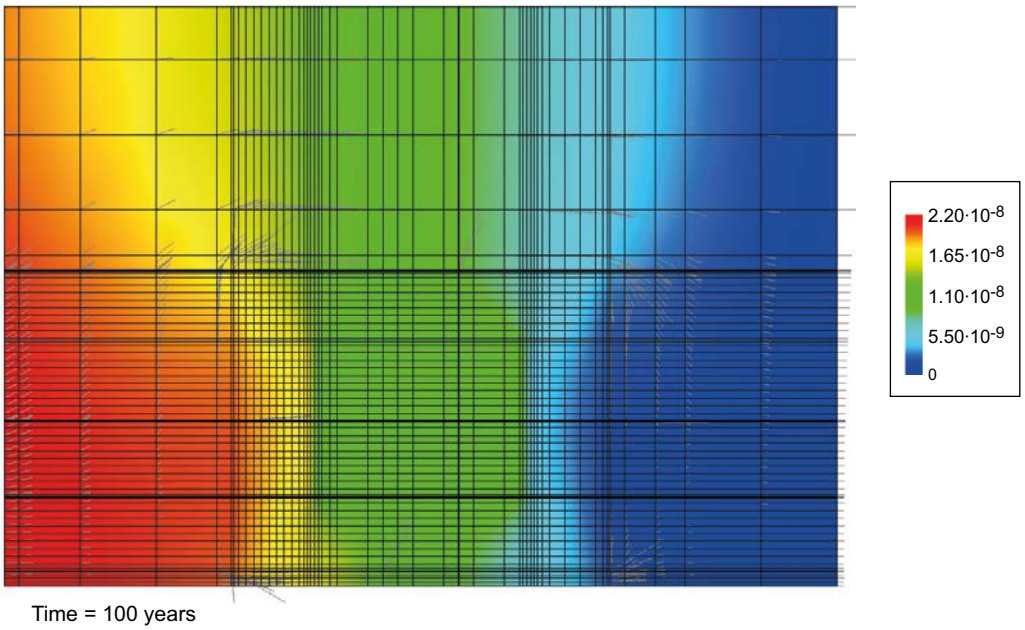

Figure 7-5. *Calculated hydraulic head (m) and flux arrows (m/s) (logarithmic scale) in 2BMA vault after 100 years. The caisson is in the central lower half of the plot. The hydraulic cage effect is clearly visible from the direction of the thin flux arrows. Locally enhanced fluxes can also be seen in the thin fractures.*

7.3 Case description – model interpretation of 1BMA

The basic assumptions made for the calculations are similar in the different cases. This section describes the common features of the different cases. The first aim was to study the leaching and degradation of concrete barriers in the 1BMA vault in a degraded state. Fractures in the concrete floor and walls have been reported following visual inspections of about 25% of the concrete structures in the vault, and Section 6.15 showed that this limits its barrier function. Therefore, here, it was decided that major fractures will need to be filled prior to closure thus the base case assumes a less degraded state than that observed. The second scenario modelled included simple repair measures, to assess their influence on the barrier degradation.

The purpose of the model is not to mimic the exact geometry of the different concrete constructions, but rather to show the general behaviour of the fractured concrete barriers when exposed to groundwater. The calculations for 1BMA were actually made before starting the calculations for 2BMA. First attempts made showed that the computational time was very long, on the order of several months for one case. The calculations also demonstrated that the computational efforts were strongly related to the size of the cell grid of the model. In order to restrict the size of the computational grid, it was therefore decided that only the lower part of the concrete constructions would be included in the model, introducing a closed internal boundary acting as a reflexion boundary (the inactive volume). Hence, the geometrical conceptualisation is a compromise between the geometrical representation and the computational demand. A schematic illustration of the geometry assumed in the model calculations is given in Figure 7-6.

The 1BMA model includes the possible effect of a hydraulic cage created by the crushed rock/macadam backfill surrounding the concrete structures in the 1BMA vault. The impact on the function of the hydraulic cage of the set of concrete beams beneath the concrete floor in 1BMA has been studied in more detail in Abarca et al. (2013). The crushed rock/macadam is assumed to be an inert material in the calculations, however secondary minerals are allowed to precipitate and re-dissolve as the chemical conditions progress throughout the calculations. The calculations use the material property data presented in Table 7-7. The hydraulic conductivity and the diffusivity of the concrete barriers, the groundwater flow, and estimates of how they change with time are of particular importance; therefore these are also shown in Figure 7-7. For comparison, the values for both 1BMA and 2BMA are shown in Figure 7 7.

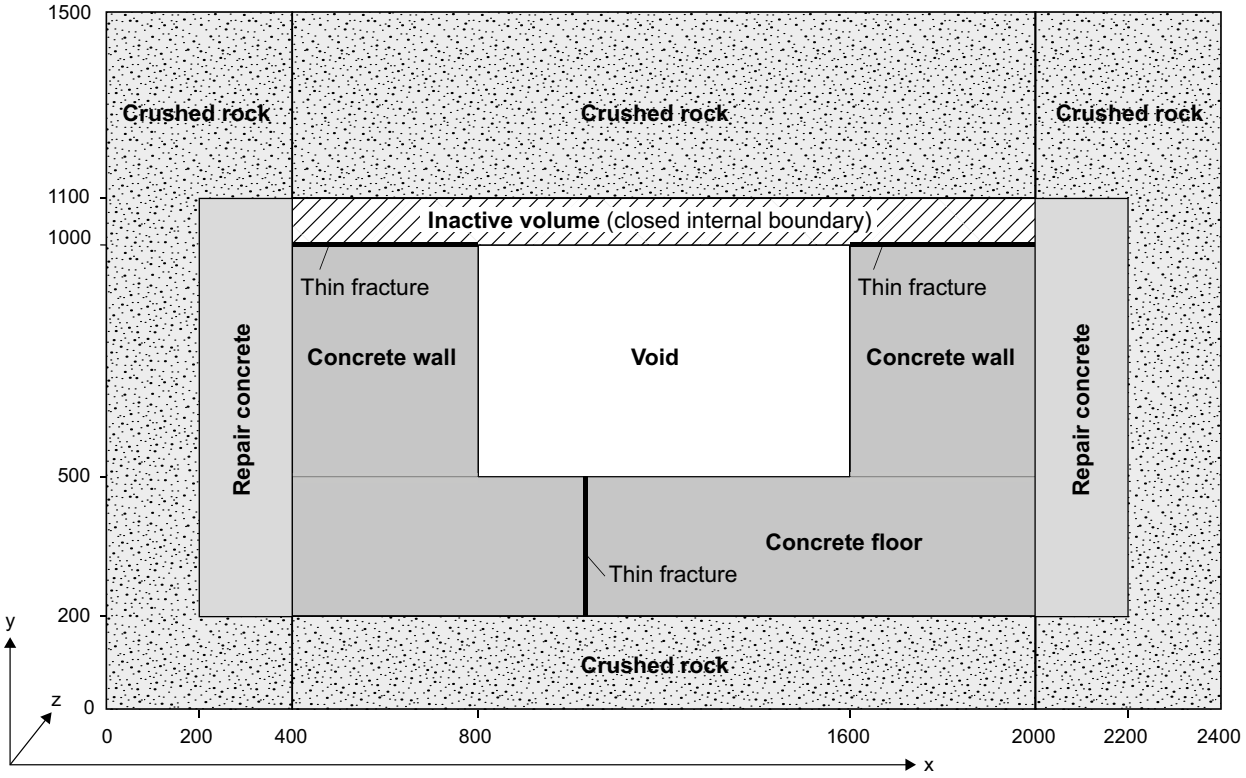

Figure 7-6. *Schematic interpretation of the concrete barriers in the 1BMA vault of SFR. Dimensions are given in mm. The repair concrete is only considered in certain scenarios.*

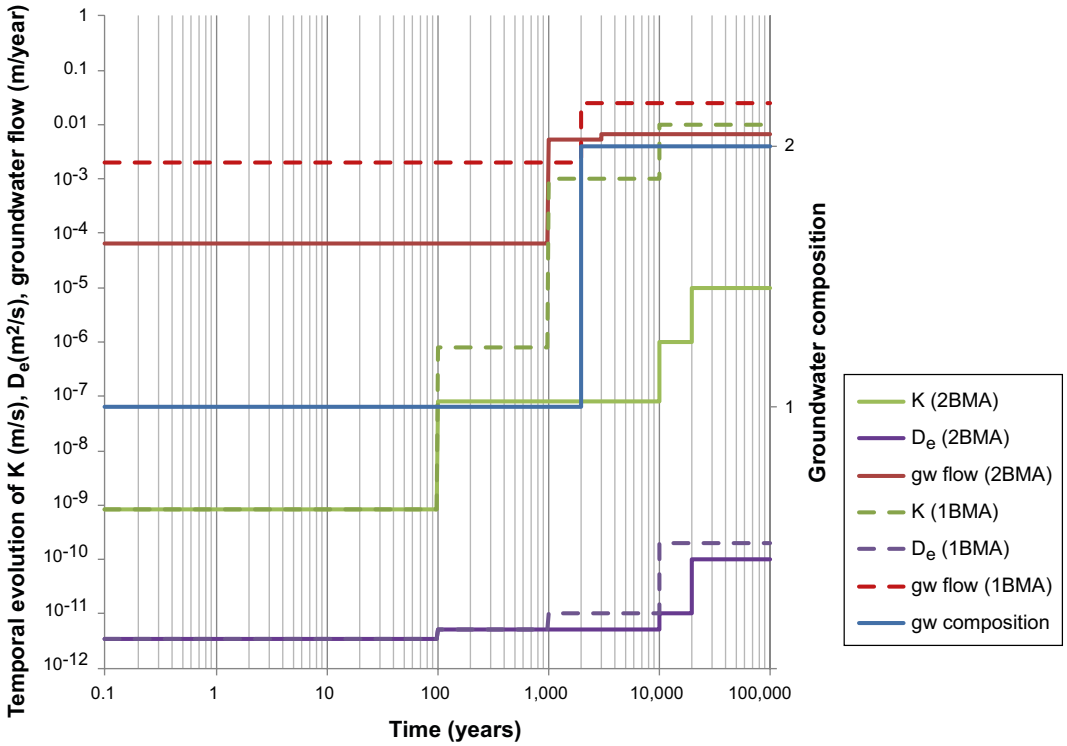

Figure 7-7. *Illustration to the temporal evolution of transport properties, groundwater flow and groundwater composition assumed in the reactive transport modelling. The figure shows the values for both 1BMA and 2BMA for comparison.*

The geometry is defined as follows:

- A 0.4 m layer of crushed rock/macadam is assumed to be present on the left-hand side of the figure between the rock wall and the concrete wall. The groundwater flow is arbitrarily assumed to be horizontal from left to right. This is therefore the inflow side of the model.
- The concrete wall is 0.4 m thick and has one 1 mm wide horizontally penetrating fracture (due to symmetry reasons only half of the fracture is modelled). It was decided to keep the actual thickness of the concrete wall in the model, applying representative groundwater fluxes and hydraulic conductivities of the different structures, and applying relevant diffusivities, in order to obtain a fair representation of both the diffusive and the advective transport of dissolved components. This enables reasonable estimates to be made of the time for different steps in the leaching sequence.
- To simulate the impact of a possible hydraulic cage, a 0.2 m bed of gravel has been assumed to lie between the concrete floor and the underlying rock floor.
- The concrete floor is 0.3 m thick and has one 1 mm wide vertical penetrating fracture/casting crack, assumed to be located at x = 1,000 mm. This position is somewhat asymmetric relative to the centreline.
- A second concrete wall, located on the right-hand, outflow side of the figure, is 0.4 m thick and with one 1 mm wide horizontally penetrating fracture (due to symmetry reasons only half of the fracture is modelled).
- The space inside the concrete walls is assumed to be a water-filled void. Hence, no interaction with the waste or waste packaging has been considered in the calculations since this have been the topics of other studies. The void is part of the mesh and is solved in the calculations. The void acts as a shortcut for transport of dissolved components inside the concrete walls. The void is assumed to initially be filled with concrete pore water.
- A 0.4 m bed of crushed rock/macadam is assumed to be present on the right-hand, outflow side of the figure between the rock wall and the concrete wall.
- A 0.4 m layer of crushed rock/macadam is assumed to cover the concrete construction.
- The outflow of groundwater has been assumed to take place against a hydrostatic boundary on the right-hand side of the model.
- Insulated (impermeable) hydraulic boundaries have been assumed for the rock below and above the vault.
- A special feature of the model is an inactive volume, which has the effect of an internal symmetry boundary. Hence, the modelling of only half of each horizontal fracture. The rationale for introducing this symmetry boundary has been to reduce the computational efforts.
- The impact of the hydraulic cage is addressed by flow through the upper and lower zones of crushed rock/macadam. To some extent, the dilution effect may be slightly exaggerated due to the absence of contact between concrete surfaces and the groundwater flowing in the upper crushed rock layer.
- In scenario calculations, the impact of the installation of a 0.2 m thick concrete wall outside the fractured concrete walls in the 1BMA vault is considered (Repair scenario, see further detail below on a possible repair method).

Two positions in the model were selected for more detailed evaluation of the temporal changes in mineralogy and chemistry, see Figure 7-8. The first position (AE) is at the centreline of the concrete floor and the left-hand side concrete wall, while the second (DE) is at the vertical centreline of the left-hand side concrete wall near the thin horizontal fracture.

Table 7-7. Assumed material data and their variation over time for different model components in fractured concrete barriers in 1BMA including repair measures (repair scenario cases only).

Model components		0–100 years	100–1,000 years	1,000–10,000 years	10,000–100,000 years
Concrete wall/floor (fractured scenario)	Porosity	0.11	0.11	0.11	0.11
	Tortuosity [1]	0.032	0.045	0.091	1.818
	D_e (m^2/s) [2]	$3.5 \cdot 10^{-12}$	$5.0 \cdot 10^{-12}$	$1.0 \cdot 10^{-11}$	$2.0 \cdot 10^{-10}$
	K (m/s)	$8.3 \cdot 10^{-10}$ [3]	$8.0 \cdot 10^{-7}$ [4]	$1.0 \cdot 10^{-3}$ [5]	$1.0 \cdot 10^{-2}$ [6]
Fractures in old concrete walls and floor (fractured scenario)	Aperture (mm)	1	1	1	1
	Porosity	1	1	1	1
	Tortuosity [1]	1	1	1	1
	D_e (m^2/s) [2]	$1 \cdot 10^{-9}$	$1 \cdot 10^{-9}$	$1 \cdot 10^{-9}$	$1 \cdot 10^{-9}$
	K (m/s)	0.01	0.01	0.01	0.01
Repair concrete (only walls) (repair scenario – briefly fractured scenario data)	Porosity	0.1	0.1	0.1	0.1
	Tortuosity [1]	0.030	0.040	0.100	2.000
	D_e (m^2/s) [2]	$3.0 \cdot 10^{-12}$	$4.0 \cdot 10^{-12}$	$1.0 \cdot 10^{-11}$	$2.0 \cdot 10^{-10}$
	K (m/s)	$8.3 \cdot 10^{-10}$	$8.0 \cdot 10^{-7}$	$1.0 \cdot 10^{-3}$	$1.0 \cdot 10^{-2}$
Fractures in old concrete walls (repair scenario)	Aperture (mm)	0.1	0.1	0.1	0.1
	Porosity	1	1	1	1
	Tortuosity [1]	1	1	1	1
	D_e (m^2/s) [2]	$1 \cdot 10^{-9}$	$1 \cdot 10^{-9}$	$1 \cdot 10^{-9}$	$1 \cdot 10^{-9}$
	K (m/s)	0.01	0.01	0.01	0.01
Fractures in old concrete floor (repair scenario)	Aperture (mm)	1	1	1	1
	Porosity	1	1	1	1
	Tortuosity [1]	1	1	1	1
	D_e (m^2/s) [2]	$1 \cdot 10^{-9}$	$1 \cdot 10^{-9}$	$1 \cdot 10^{-9}$	$1 \cdot 10^{-9}$
	K (m/s)	0.01	0.01	0.01	0.01
Crushed rock/macadam	Porosity	0.3	0.3	0.3	0.3
	Tortuosity [1]	0.5	0.5	0.5	0.5
	D_e (m^2/s) [2]	$1.5 \cdot 10^{-10}$	$1.5 \cdot 10^{-10}$	$1.5 \cdot 10^{-10}$	$1.5 \cdot 10^{-10}$
	K (m/s)	$1.0 \cdot 10^{-3}$	$1.0 \cdot 10^{-3}$	$1.0 \cdot 10^{-3}$	$1.0 \cdot 10^{-3}$
Void space	Porosity	1	1	1	1
	Tortuosity [1]	1	1	1	1
	D_e (m^2/s) [2]	$1.0 \cdot 10^{-9}$	1.0^{-9}	$1.0 \cdot 10^{-9}$	$1.0 \cdot 10^{-9}$
	K (m/s)	0.1	0.1	0.1	0.1
Inactive volume	Porosity	0	0	0	0
	Tortuosity	0	0	0	0
	D_e (m^2/s)	0	0	0	0
	K (m/s)	0	0	0	0

[1] In order to maintain a constant porosity in the numerical modelling, all changes in the pore structure have been assigned to changes in the tortuosity for a given domain in time. This ensures that the mass balance is maintained in the PHAST calculations.

[2] A constant value of $1 \cdot 10^{-11}$ m has been assumed for the dispersivity (longitudinal, horizontal and vertical) for all model components in the modelling. For discussion on numerical dispersion, see Appendix A.

[3] This corresponds to an intact concrete with a conductivity of 1.10^{-11} m/s intersected by 1 fracture per m with an aperture of ~10 µm.

[4] This corresponds e.g. to concrete intersected by 1 fracture per m with an aperture of ~ 100 µm, or 10 fractures per m with an aperture of ~45 µm.

[5] This corresponds e.g. to concrete intersected by 1 fracture per m with an aperture of ~ 1,000 µm, or 10 fractures per m with an aperture of ~500 µm.

[6] This corresponds e.g. to concrete intersected by 10 fractures per m with an aperture of ~1,000 µm.

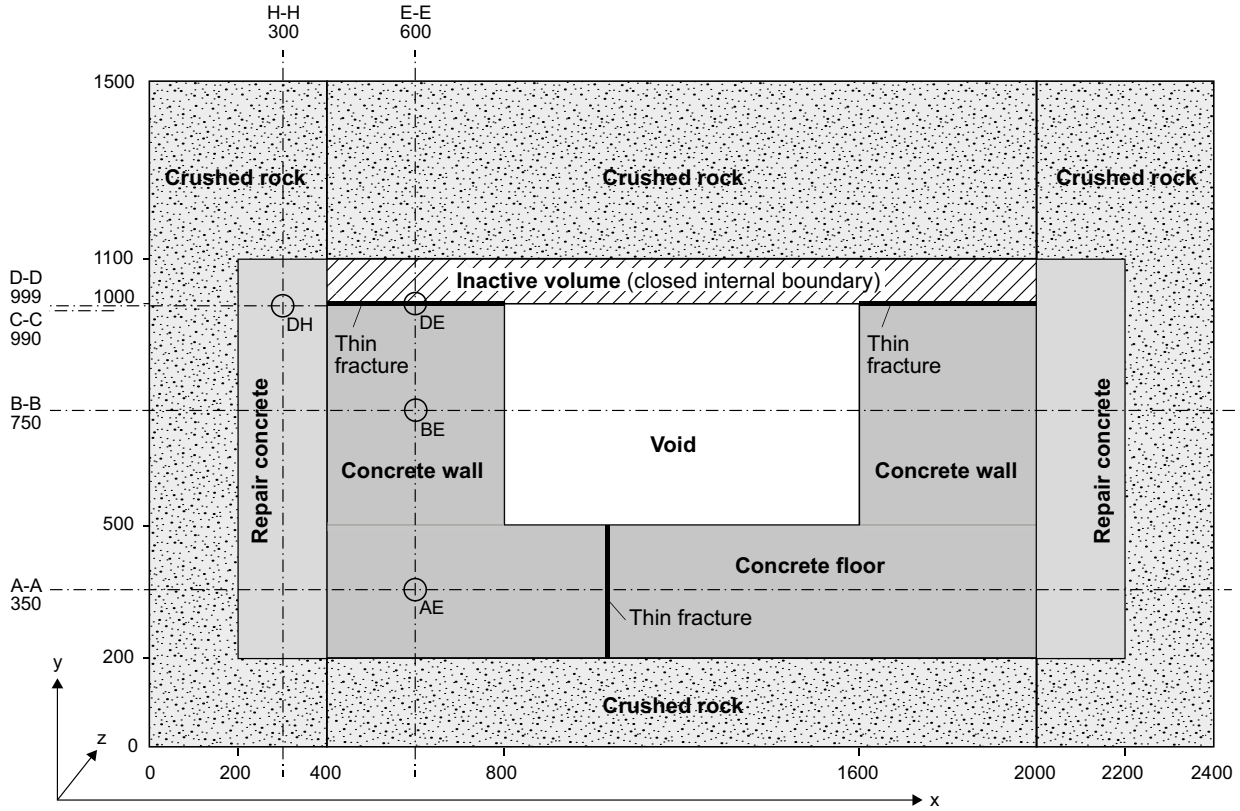

Figure 7-8. *Definition of vertical and horizontal sections and intersection points used for evaluation of the PHAST modelling results. Numbers refer to distances in mm relative to the origin located in the lower left corner of the drawing.*

7.3.1 Description of a possible repair method – 1BMA walls

An investigation of the 1BMA concrete structure has been carried out, which showed that extensive repair and reinforcement measures need to be adopted to achieve the desired properties at closure. The Closure Plan for SFR (SKBdoc 1358612) describes the planned measures for closure of 1BMA and it is assumed in the SR-PSU safety assessment that the 1BMA concrete barriers will be in good condition at closure.

A possible method for such repair, which has been assumed for the simplistic repair scenarios considered in this report (Large11 and Large12), may comprise (see illustration in Figure 7-9):

- Damaged concrete as a result of corrosion of reinforcement bars is removed by e.g. hydrodemolition /water-jet technique on both the inside and the outside of the concrete walls. The floor can however, only be accessed from above.
- Reinforcement bars affected by corrosion are cleaned of rust, or, if more severe damage is found, replaced by new reinforcement bars.
- New concrete is cast to restore the initial dimensions of the concrete walls and floor (walls 0.4 m, floor 0.25 m). Equivalent concrete quality based on Degerhamn cement as was used for the construction concrete is assumed for the repair.
- Observed fractures are injected with grout, which is judged practical down to a fracture aperture size of 100 μm.
- A complementary layer of 0.2 m concrete is cast on the outside of the present walls. This concrete layer is assumed to be reinforced with steel that would be able to restrict fracture widths caused by e.g. drying-shrinkage and thermal movements. The quality of this concrete layer is assumed to resemble that of construction concrete based on Degerhamn cement.

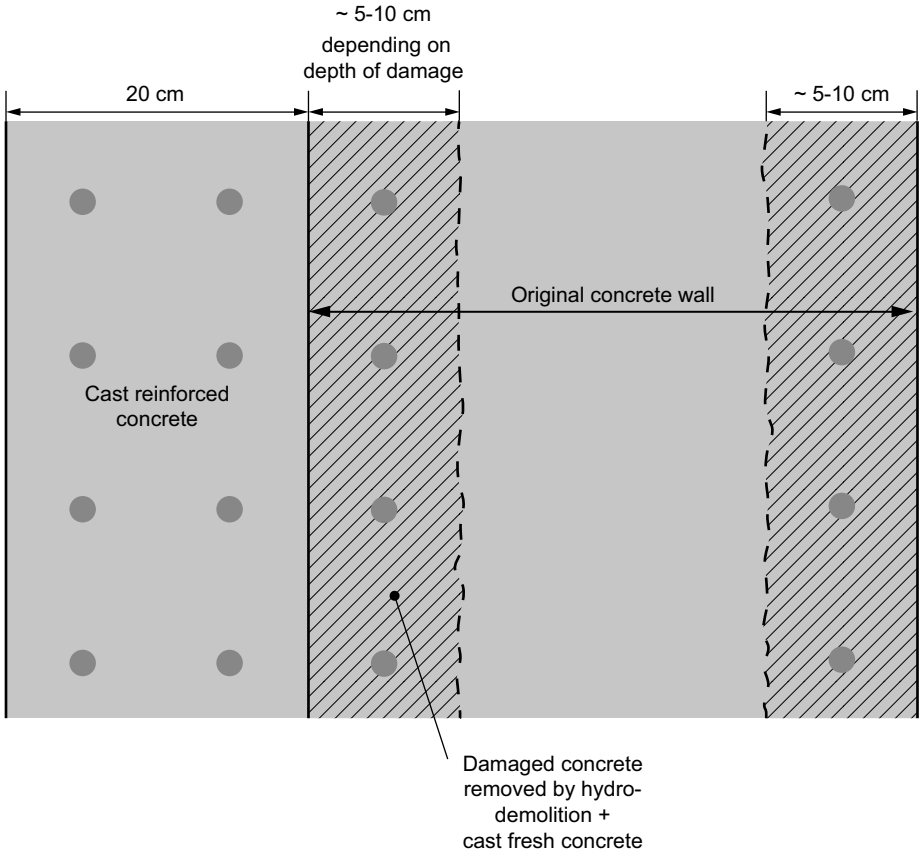

Figure 7-9. *Illustration of a possible method to repair the concrete walls in 1BMA.*

7.3.2 Model discretisation – 1BMA

The spatial discretisation of the geometry shown in Figure 7-6 has been implemented as a cell grid, see Figure 7-10. The PHAST model consists of 1,152 cells with 2,442 nodes (1,184 cells with 2,508 nodes in the repair scenarios). The smallest and largest cell sizes are $5 \cdot 10^{-4}$ and 0.2 m respectively.

Model calculations have been performed with different time step lengths, as well as different spatial discretisations in the major groundwater flow direction, to test that a correct numerical solution of the transport equation is obtained. The results of the numerical tests are presented in Appendix A. Slightly different time steps have been used for different periods of time. The most detailed calculations have been performed using a time step which is 0.01 years or less. Since some of the model cases cover more than 60,000 years, a total of ~ 6,000,000 time steps are required in the PHAST modelling. For each time-step and for each node, PHAST first calculates the water flow and resulting changes in the bulk composition of the pore water, thereafter PHREEQC is called and the chemical calculations involving aqueous speciation, mineral dissolution/precipitation and ion exchange reactions are carried out. The resulting changes of the bulk composition of dissolved components and the mineral assemblage are then returned to PHAST and the next time step is initiated. Typically, the calculations of each case require several weeks execution time on an eight-processor parallel computer. The parallelisation efficiency of the PHAST program in the present application is 90% or better.

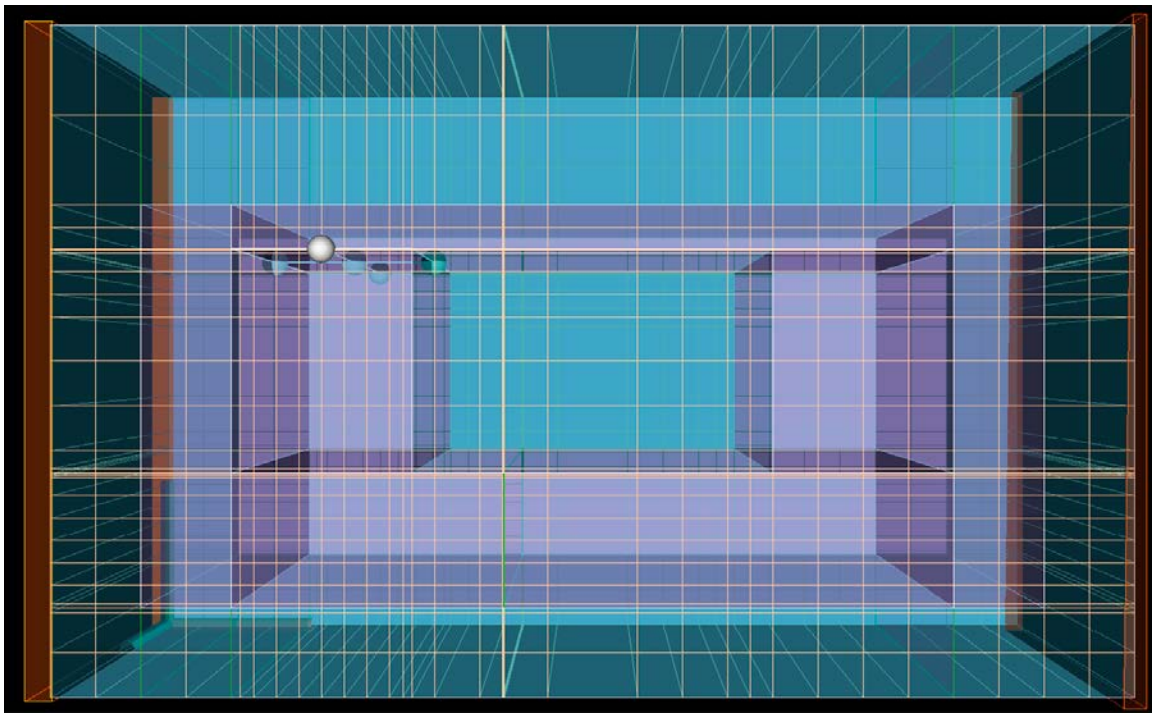

Figure 7-10. *Geometrical representation of the model geometry in PHAST. The presence of the thin horizontal fracture in the upper part of the left-hand side concrete wall is marked in the figure by ball symbols.*

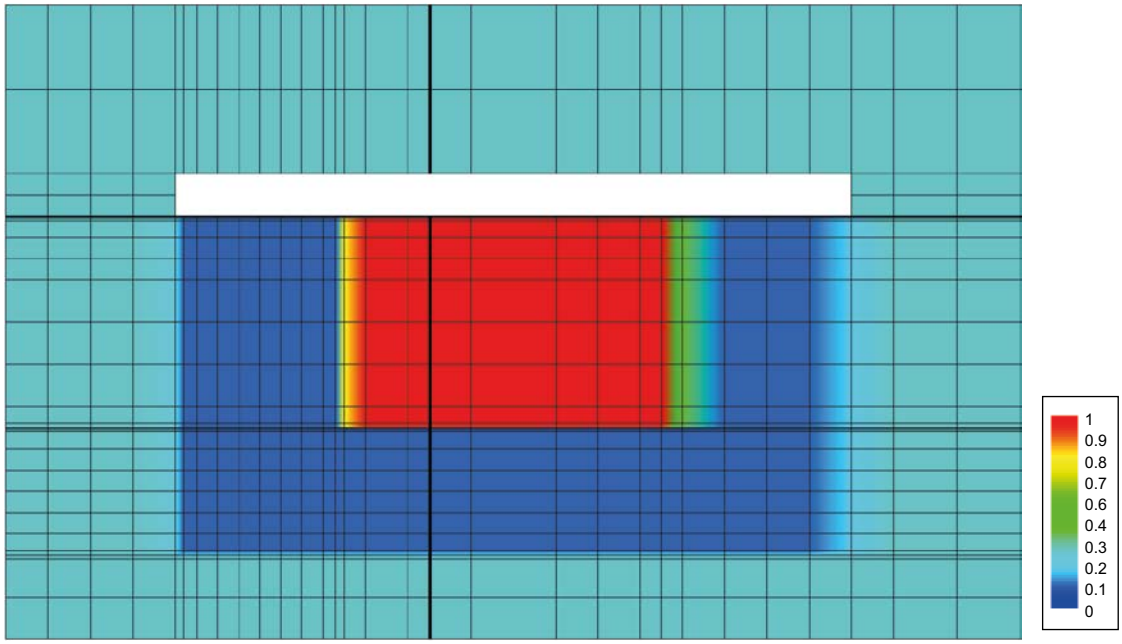

Figure 7-11. *2-D view of grid used in case Large8 for the 1BMA vault. The view shows the porosity in different model components. The smeared-out colouring of the porosity when passing from left to right through the mesh is due to the coarse discretisation causing interpolation effects in the plotting routine (blue = concrete wall, red = void volume, turquoise = macadam, yellow = green = interpolation effects, white = inactive volume).*

7.3.3 Groundwater flow – 1BMA

Groundwater is assumed to flow into the 1BMA vault with a flux corresponding to the results presented by Holmén and Stigsson (2001). A step change in the flux has been assumed after 2,000 years, reflecting the transition from the saltwater period to the freshwater period, see Figure 7-12. This transition is caused by the land rise in the Forsmark area. The calculations for 1BMA were initiated prior to the results of the hydrogeological modelling (Abarca et al. 2013) became available. The assumed groundwater fluxes are therefore different from those used in the calculations for 2BMA, cf. Section 7.2.2. The groundwater flux assumed for 2BMA is factor ~30 lower than assumed for 1BMA during the first 1,000 years, a factor ~2.7 higher between 1,000 and 2,000 years, a factor 4.7 lower between 2,000 and 3,000 years, and a factor ~3.7 lower after 3,000 years.

The groundwater flow in the vault is calculated by PHAST using the assumed hydraulic data of the different materials (Table 7-7). The head distribution and the direction of the flux are presented in Figure 7-13 for the first 2,000 years with stationary boundary conditions. The flux into the vault has been assumed to vary according to the data in Figure 7-12. The white rectangle is an inactive volume acting as an internal boundary in the model.

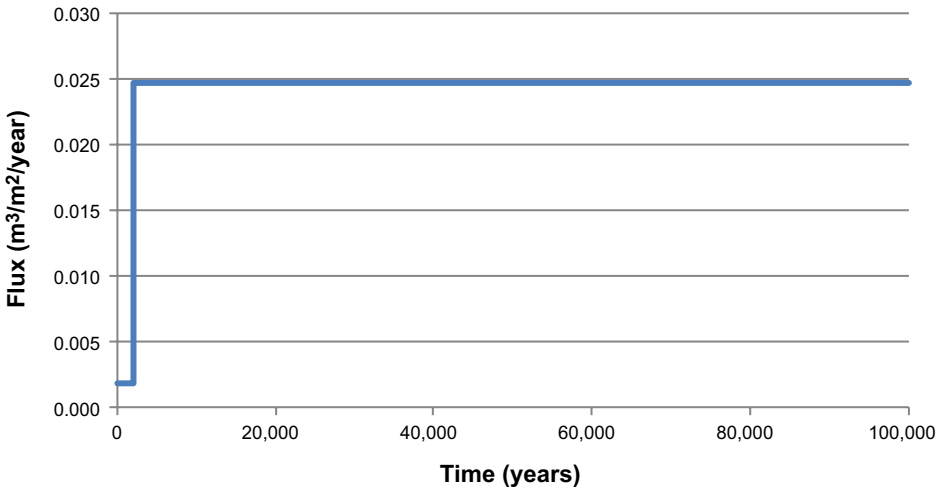

Figure 7-12. *Assumed groundwater flux (m^3/m^2/year) versus time (years) in the 1BMA vault that have been used in the PHAST calculations. Flux estimates are based on results by Holmén and Stigsson (2001).*

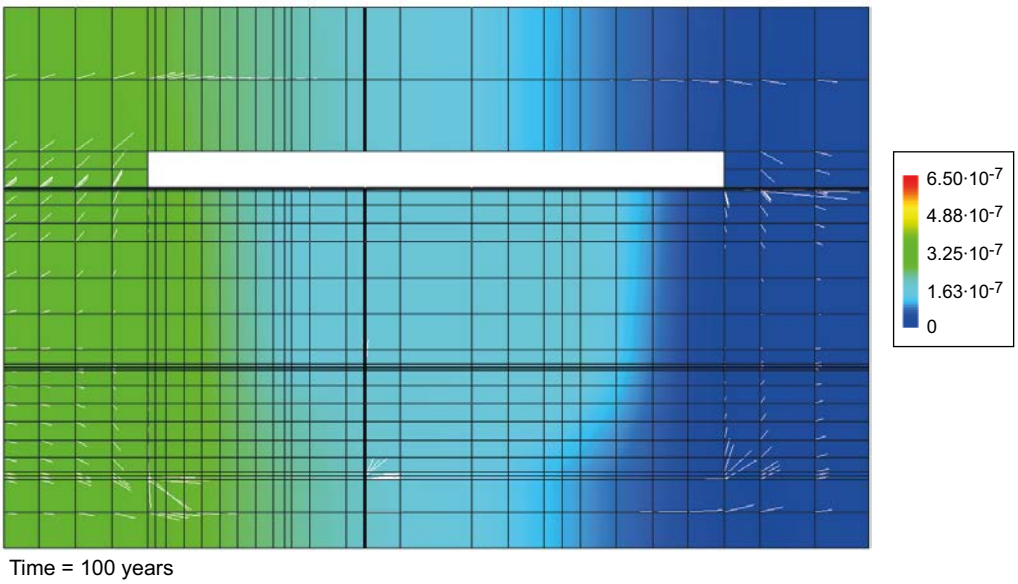

Figure 7-13. *Hydraulic head (m) during the first 2,000 years (here arbitrarily presented at 100 years) where the direction of the groundwater flow is indicated by thin white arrows.*

7.4 Case Large20 (2BMA)

Case Large20 addresses concrete degradation in the 2BMA vault. The parameters applied and assumptions made in the calculations are presented in Section 7.2. In this section, the evolution of the porewater chemistry at the evaluation point GH is first examined and then the mineralogical changes at both GH and CH are compared. Changes along the 1-D pathways C-C and D-D are then examined before looking at the chemical and mineralogical changes in the entire 2-D system.

7.4.1 Evolution of chemistry and mineralogy at evaluation points

Evaluation point GH – at the centreline of the concrete lid and the left-hand side concrete wall

The gradual evolution of the concentrations of dissolved components in the concrete pore water at evaluation point GH is presented in Figure 7-14. Calcium is one of the most important chemical components in concrete, contributing to both pH buffering and mechanical strength. Initially, the concentration of dissolved calcium is suppressed by the low solubility of portlandite ($Ca(OH)_2$) in the presence of potassium and sodium hydroxides in the fresh concrete. The profile shows that the dissolved calcium concentration increases after ~1,000 years, as the sodium concentration decreases. The pH also decreases as the highly alkaline potassium and sodium hydroxides are leached, reaching portlandite-buffered conditions (pH 12.5) after ~1,500 years. Silica leaching increases after 15,000 years, when portlandite no longer controls the conditions.

The results from the ion exchange model of the alkali hydroxides are presented in Figure 7-15. Using this model, approximately 0.6% of the total calcium content at 4,000 years and ~ 0.7% at the peak at 14,000 years will be bound as exchangeable ions, see Figure 7-16. If these ions are assumed to bind primarily to the CSH-gel, the extra calcium would correspond to ~ 1.8% of the calcium content in the CSH-gel.

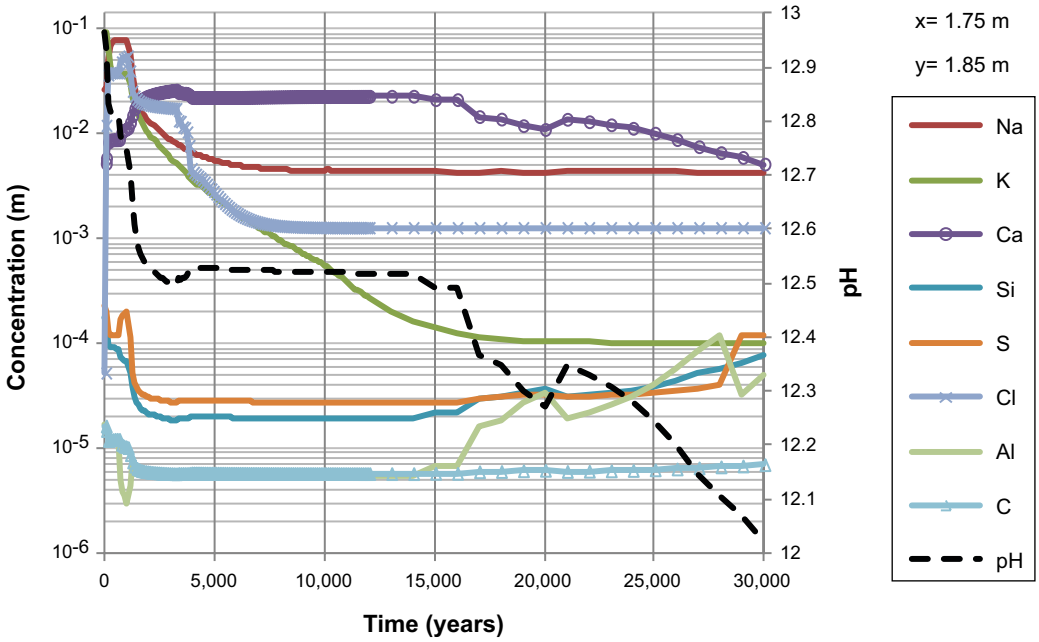

Figure 7-14. *Evolution of dissolved components (logarithmic concentration scale) in concrete pore water during the first 30,000 years (linear scale) at position GH, (MinteqCem-2001 database, Case Large20). The evolution of pH is also indicated.*

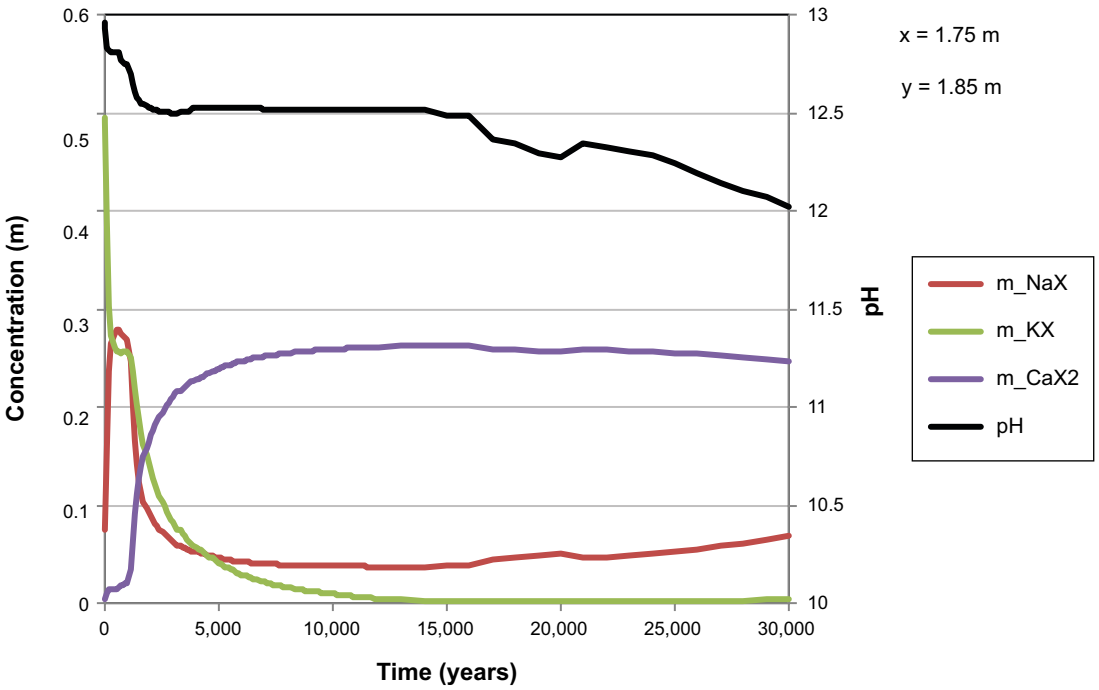

Figure 7-15. *Evolution of ion exchange species (linear scale) in concrete during the first 30,000 years (linear scale) at position GH, (MinteqCem-2001 database, Case Large20). The concentrations of ion exchange species are presented in the unit (kmol/m³ pore water).*

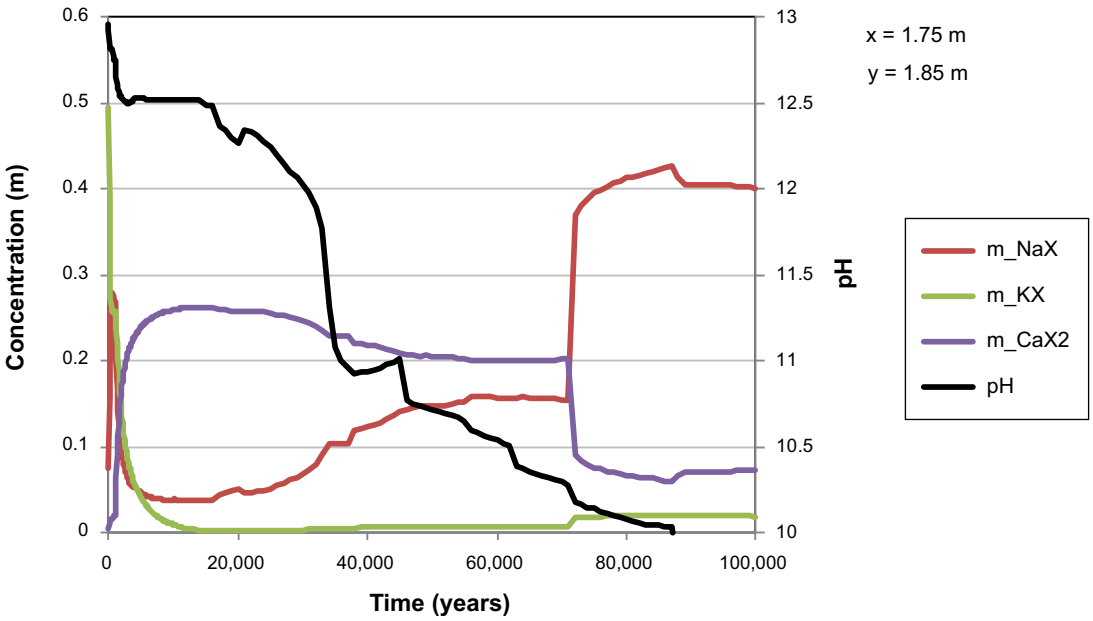

Figure 7-16. *Evolution of ion exchange species (linear scale) in concrete over 100,000 years (linear scale) at position GH, (MinteqCem-2001 database, Case Large20). The concentrations of ion exchange species are presented in the unit (kmol/m³ pore water).*

The gradual change of the chemical conditions causes dissolution/precipitation of different minerals (Figure 7-17). Since the minerals have different densities, these changes modify the total volume of the solid phases within the mineral assemblage. The change in the solid volume causes gradual changes in the porosity, which affects the pore structure of the concrete, and hence the hydraulic conductivity and the effective diffusivity. It is not possible to account for the changing porosity, or its influence on the effective diffusivity and the hydraulic conductivity, explicitly in the PHAST model. Therefore, the gradual evolution of the mineral assemblage has been evaluated and the volume of the different mineral phases calculated in the post-processing of the model results, using Equations 6-61 and 6-62, and the molar volumes specified in Table 7-3. The resultant changes in porosity are shown in Figure 7-17 and suggest that an initial concrete porosity of 11% would increase marginally to ~ 11.5% after 10,000 years. A minor decrease in porosity occurs in response to an early reaction between chloride in the groundwater and monocarboaluminate which causes the precipitation of Friedel's salt, a process essentially starting at 300 years and completed by 700 years. The reaction also consumes some portlandite, cf. Equation 5-58. From 2,300 to 3,300 years Friedel's salt decomposes and monocarboaluminate and portlandite are regained. At observation point GH, there is no significant change in the amount of ettringite during the first 10,000 years, hence the risk for fracture formation due to ettringite formation is apparently low, see Figure 7-18 where the change of individual minerals may be easier to observe.

After 10,000 years the onset of a significant reduction in the amount of portlandite causes a steady rise in the porosity to ~ 14% by 15,000 years, when portlandite is depleted, see Figure 7-17. Silica is a major component of CSH-gel, and is present in the groundwater flowing into the vault. Silica leaching is intimately coupled to the leaching of portlandite, since Ca is present in both portlandite and CSH gels. As long as portlandite remains in the system, it will buffer the chemical conditions and suppress the solubility of silica in the CSH-gels. When portlandite becomes depleted, the solubility changes in the altered chemical environment and the CSH-gel phases starts to dissolve. The dissolution process involves a gradual transformation from calcium-rich to more silica-rich gel-phases. During this time the silica remains in the system essentially as conservative component.

The porosity continues to increase to 17% by 19,000 years as a result of incongruent leaching of CSH_1.8, which is transformed to CSH_1.1. Between 19,000 years and 29,000 years, the transformation of monocarboaluminate to ettringite reduces the porosity to ~ 16% , and causes a slight precipitation of calcite. After 31,000 years, ettringite and CSH_1.1 are destabilised and transform to thaumasite and CSH_0.8, respectively. Ettringite is depleted after 38,000 years and CSH_0.8 disappears after 56,000 years. The porosity increases during this period to ~ 21%, reaching a peak value of ~ 26% after 72,000 years, thereafter slowly decreasing to ~ 25% at 100,000 years. Thaumasite grows steadily from 31,000 years to 56,000 years (which consumes the calcite after ~34,000 years), and is depleted after 72,000 years. The iron-substituted hydrogarnet phase C_3FH_6 remains passive until 38,000 years, when a small precipitation starts. This reaches a maximum at 46,000 years which is followed by dissolution and depletion after 63,000 years. Brucite precipitation increases from 32,000 years resulting in a peak at 70,000 years. After this, dissolution eventually leads to depletion of brucite after 88,000 years. After 48,000 years, calcite starts to precipitate in response to dissolution of first monocarboaluminate and then thaumasite, a process which is still in progress at 100,000 years. A slight formation of SiO_2gel(am) is noted from 91,000 years and onwards.

The significant changes in the amount of ettringite and thaumasite show that there is a risk of fracture formation at position GH. Since this occurs between 20,000 to 70,000 years, it is considered to be a long term effect.

An alternative presentation of the results is given in Figure 7-18 where the volumes of the individual minerals are shown as separate curves (not the accumulated volumes).

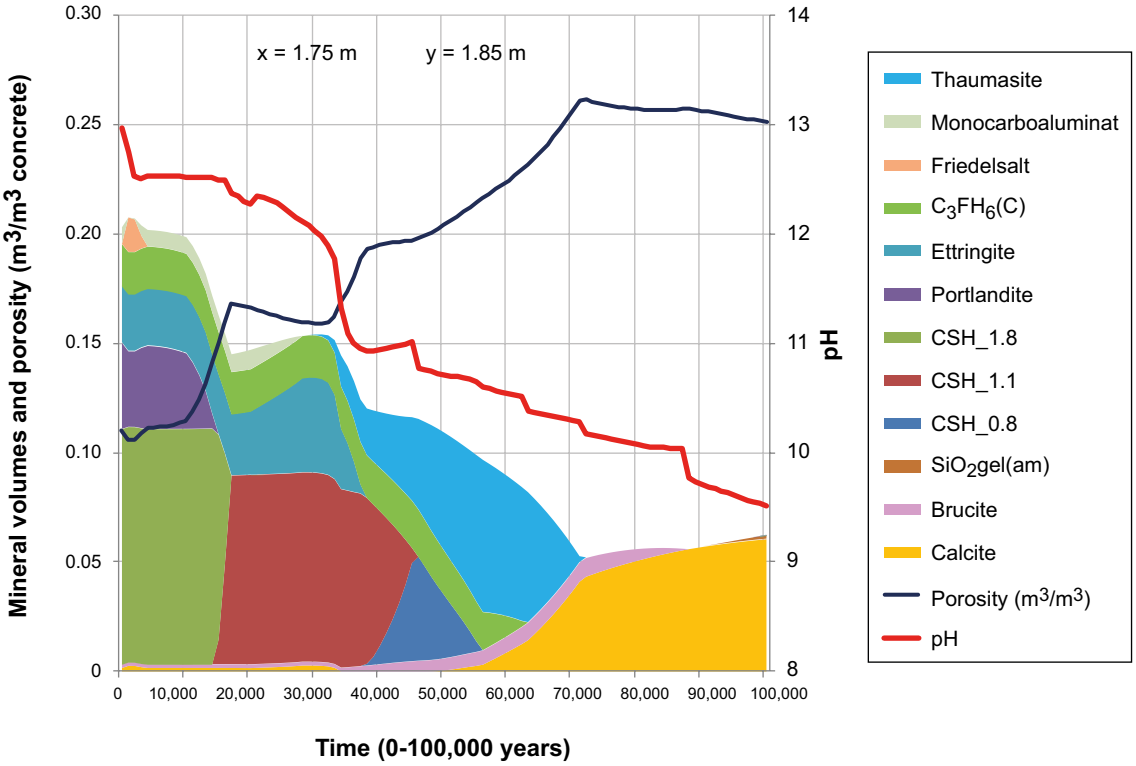

Figure 7-17. *Evolution of mineral volumes and porosity in concrete over the full 100,000 years period (linear scale) at position GH, (MinteqCem-2001 database, Case Large20). The evolution of pH is also indicated.*

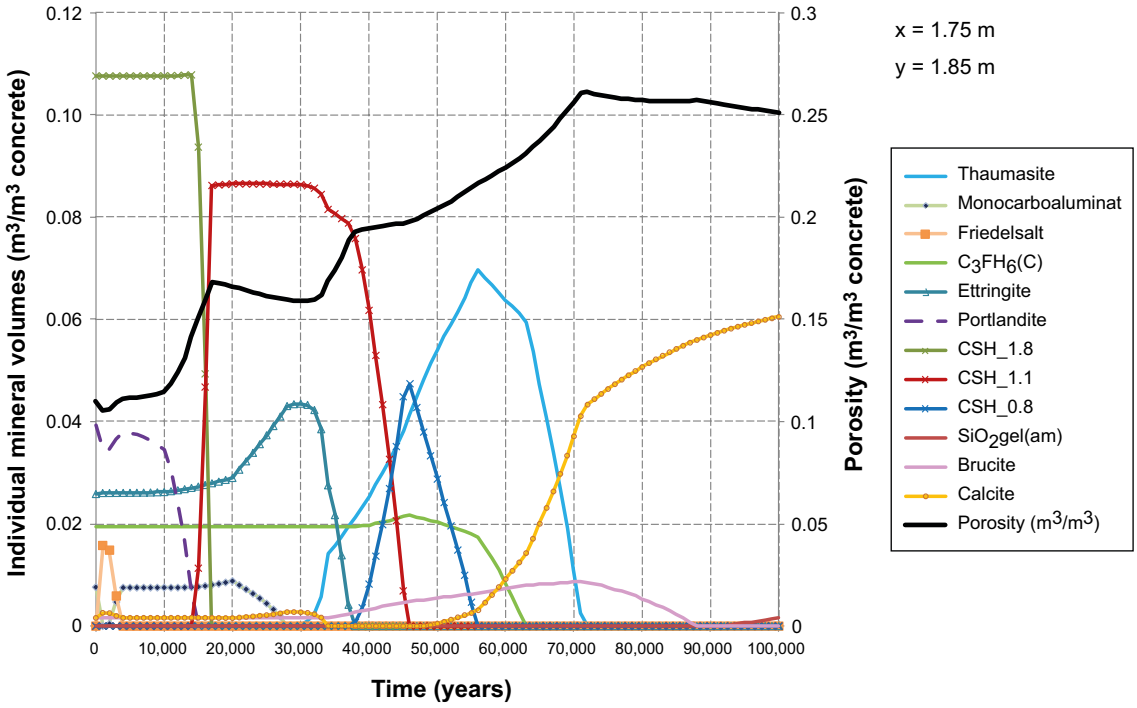

Figure 7-18. *Evolution of the individual mineral volumes and porosity in concrete over the full 100,000 years period (linear scale) at position GH, (MinteqCem-2001 database, Case Large20).*

Evaluation point CH- at the vertical centreline of the left-hand side concrete wall near the thin horizontal fracture

The gradual evolution of the mineral assemblage at point CH is shown in Figure 7-19 together with the calculated changes of the porosity over the first 10,000 years. The general progression of the mineralogical changes is similar to that seen at point GH; however the rate of change is somewhat slower. This also holds true for the full 100,000 year period shown in Figure 7-20 and shows that despite the presence of the fracture, the upper part of the concrete caisson is more exposed to groundwater than the mid-height wall, where the fracture is located. Based on this it can be tentatively concluded that the presence of thin fractures in the concrete wall has minor impact on the chemical degradation processes in this case.

The porosity is presented over the range of 0–25% in Figure 7 19 and 0–30% in Figure 7-20; the maximum porosity corresponding to fully depleted cement minerals would be ~ 30%, the remaining volume constitutes the ballast material which is assumed to be inert.

An alternative presentation of the results is given in Figure 7-21 where the volumes of the individual minerals are shown as separate curves (not the accumulated volumes).

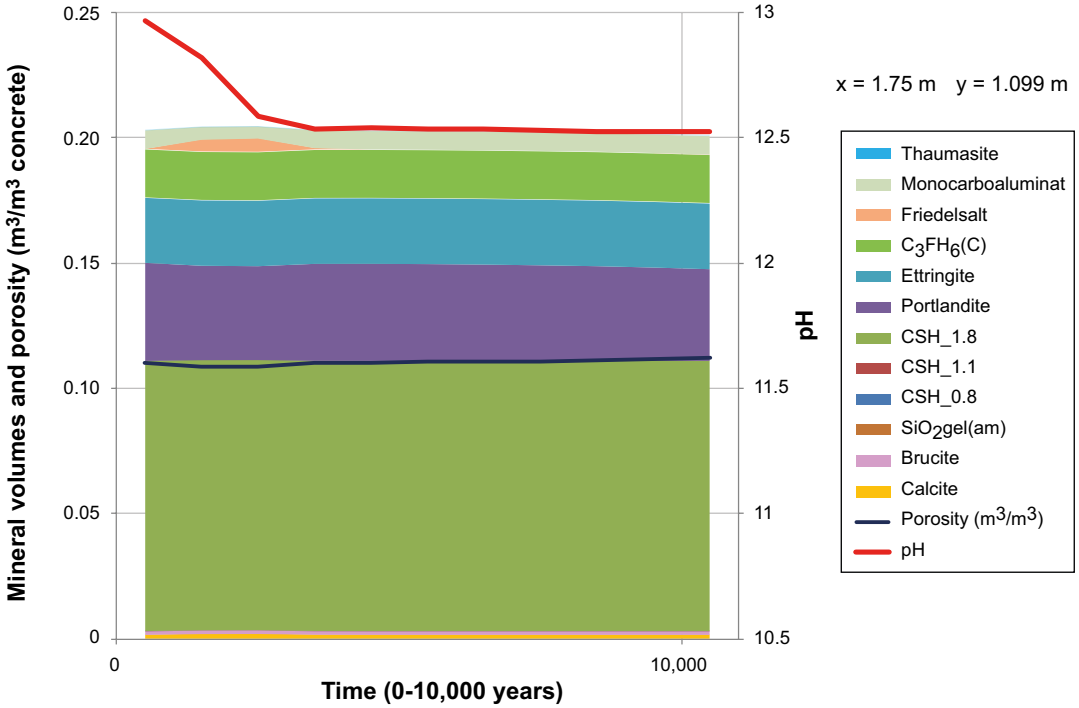

Figure 7-19. *Evolution of mineral volumes and porosity in concrete during the first 10,000 years at position CH, (MinteqCem-2001 database, Case Large20). The evolution of pH is also indicated.*

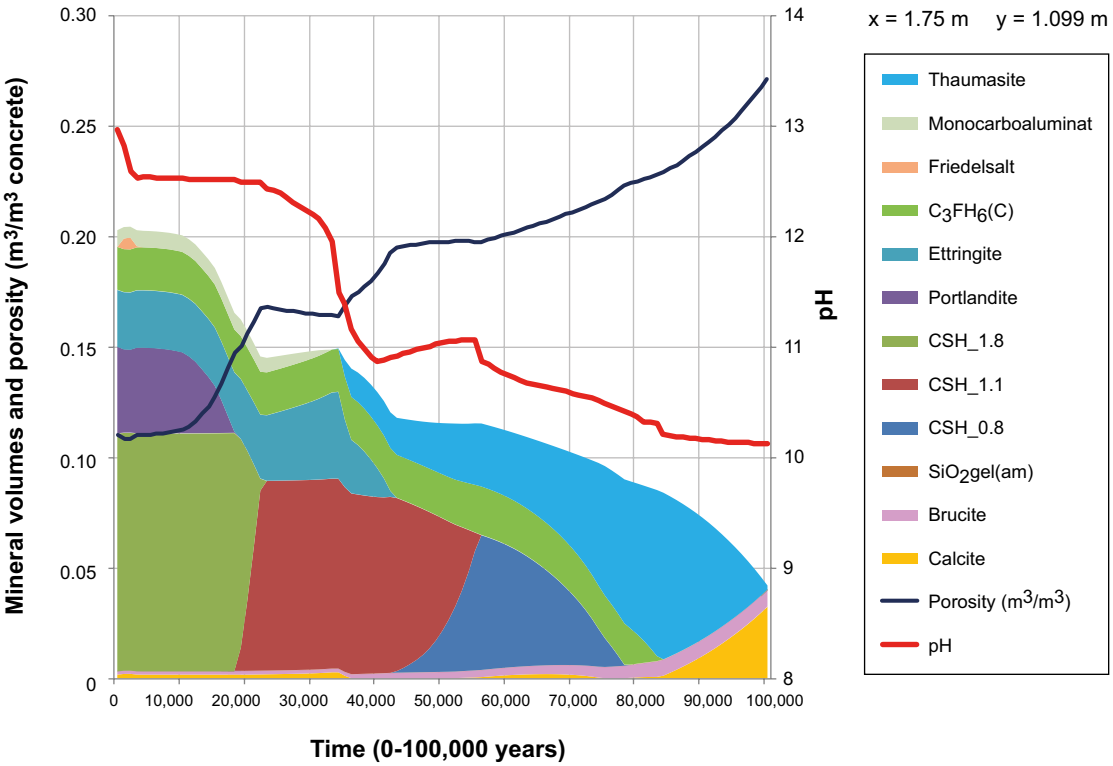

Figure 7-20. *The amount of minerals in concrete over the full 100,000 years period at position CH (1 mm from an open fracture), (MinteqCem-2001 database, Case Large20). The evolution of pH with time is also indicated.*

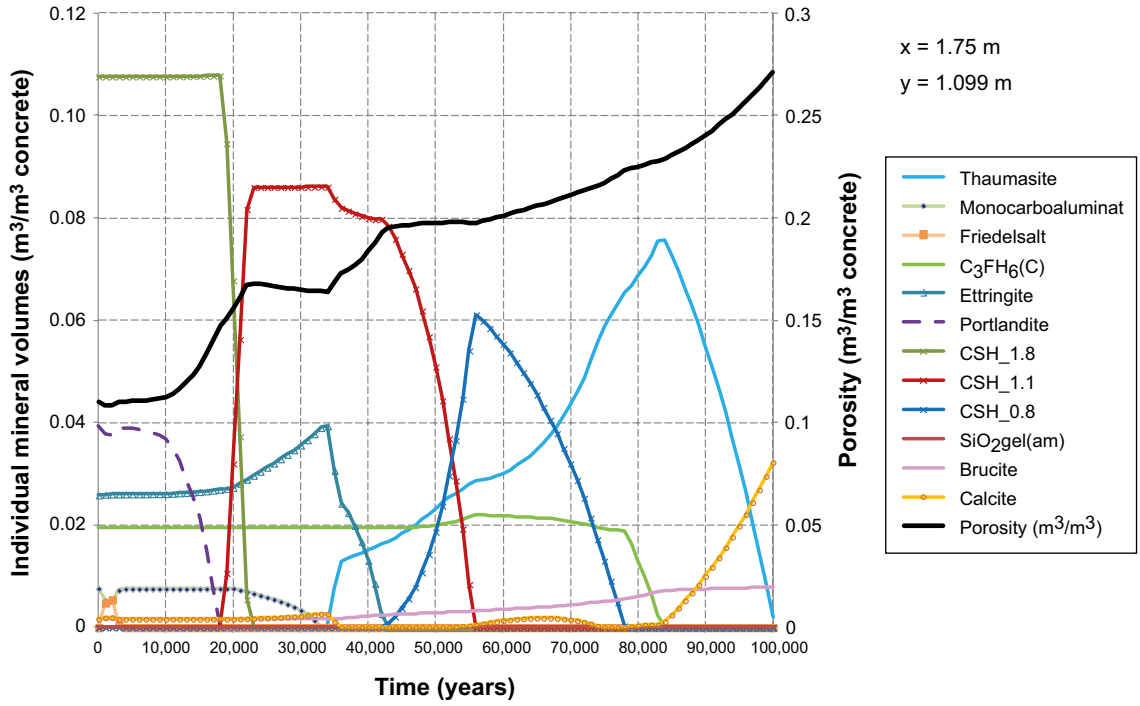

Figure 7-21. *Evolution of the individual mineral volumes and porosity in concrete over the full 100,000 years period (linear scale) at position CH (1 mm from an open fracture), (MinteqCem-2001 database, Case Large20).*

Evolution of porosity in and near the thin fracture (sections C-C and D-D)

The gradual evolution of the mineral assemblage and calculated porosity in the concrete along two sections (in and 1 mm from the fracture) through the concrete wall are summarised in Figure 7-22. The results suggest a minor reduction of porosity in the fracture caused by ettringite precipitation; however this was not sufficient for any significant clogging to occur. Clogging of pores has been observed in previous modelling studies, e.g. Steefel and Lichtner (1994), as well as in field observations at Maqarin in Jordan (Pitty and Alexander 2011).

A slight reduction of the porosity is observed in the concrete at a depth of 1 mm from the fracture. This is caused by the precipitation of Friedel's salt in a zone propagating to ~ 0.05 m from the fracture entrance at 100 years and ~ 0.15 m at 1,000 years. After 10,000 years a significant increase of the porosity is observed to a depth of ~ 0.1–0.15 m from the fracture entrance, reflecting the dissolution of CSH_1.8 followed by precipitation of CSH_1.1, which is accompanied by a slight dissolution of ettringite. It may be hypothesised that the increased water flow rate in the fracture may counteract precipitation by effectively removing the dissolved concrete components that enter the fracture. The causes of this phenomenon need to be further scrutinised.

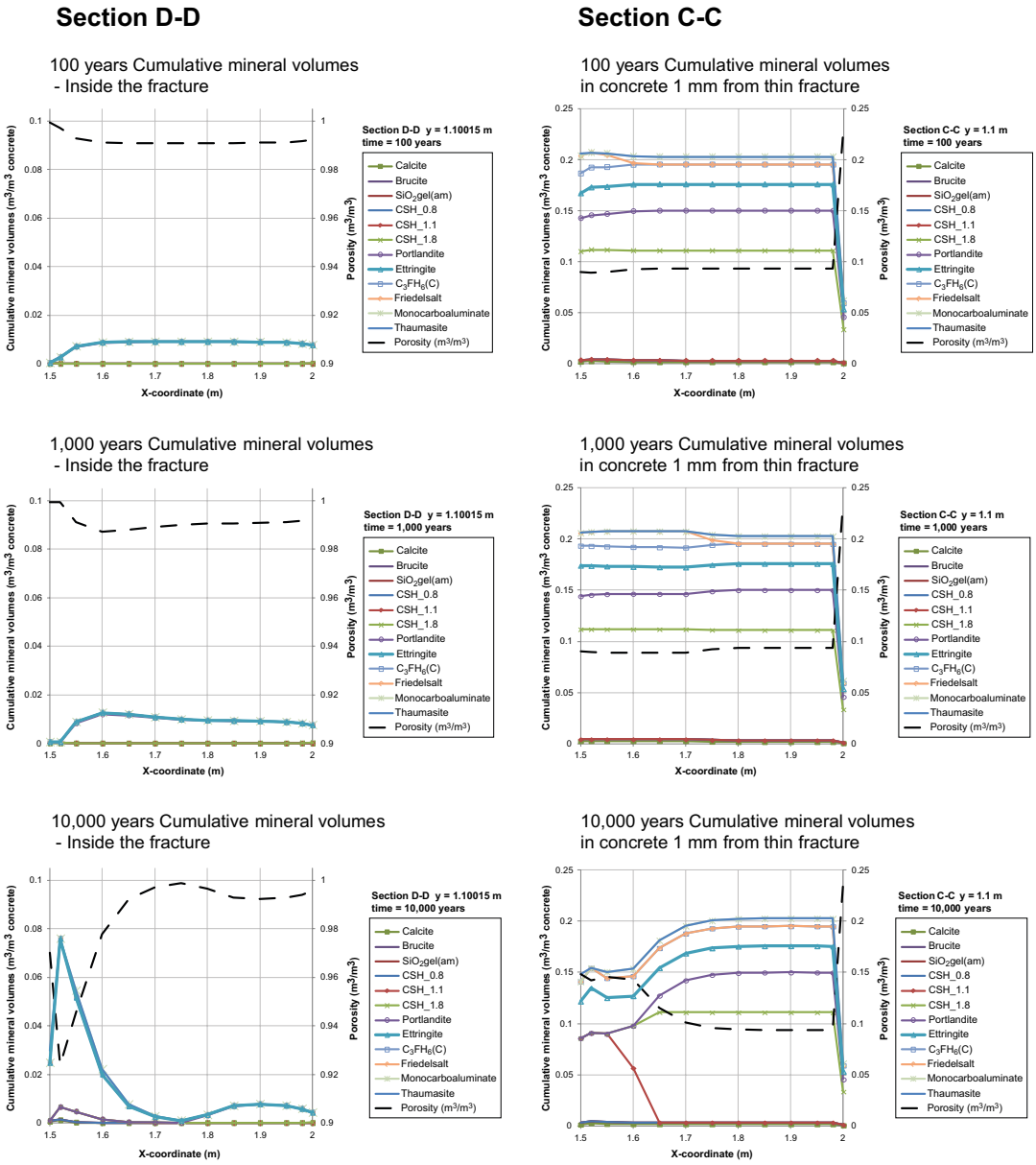

Figure 7-22. *Calculated porosity in the concrete wall at the left-hand upstream side of the model at different times. The results are show along a section through the horizontal fracture (left column) and along a section through the concrete parallel to the fracture at a distance of 1 mm (right column).*

7.4.2 Evolution of the chemistry and mineralogy of the 2-D system

The 2-D presentation of the results encompasses the results presented above and gives a spatial overview of the changes occurring in case Large20.

pH evolution, calcium and silica depletion

The initial pH in the concrete pore water is around 13 governed by alkali hydroxide ions. Due to the low groundwater flow rate during the early period, diffusion of soluble alkali hydroxides from the concrete will establish a high pH in the vault. Continuous leaching of alkaline components from the concrete barriers will maintain a pH > 12.5 in the 2BMA vault throughout the first 1,000 years post closure. At 2,000 years the pH in the macadam fill at the left-hand upstream side has decreased to between 10 and 12 as a result of the increased groundwater inflow, see Figure 7-23. The pH slowly progresses and after 10,000 years the pH inside the caissons still remains at 12.5, whereas the pH in the macadam fill is in the range 8–10 at the left-hand side and above the caissons, and in the range 11–12.5 in the macadam fill at the right-hand downstream side and in the macadam bed below the caisson floor. This situation remains essentially the same up to 20,000 years when a change of material properties (see Table 7-7) leads to enhanced leaching of the concrete and the pH in the surrounding macadam fill again increases. Inside the caissons the pH remains at 12.5 after 20,000 years. At 35,000 years (not shown) the pH in the entire vault is 11.5 or lower, and after 40,000 years the pH is below 11 throughout the vault. A marginal increase in pH occurs after 44,000 years to slightly above 11. The pH then remains almost constant until ~ 80,000 years when the pH drops to 10.3. Thereafter the pH remains fairly constant until 100,000 years when the calculations were terminated.

The calcium concentration in the pore water increases during the period 0–3,000 years as the alkali hydroxides are leached out by the groundwater. The following period is almost entirely determined by the solubility of portlandite with a calcium concentration of ~ 25 mM – a period which stretches up to almost 20,000 years.

At 1,000 and 2,000 years, significant increases in the groundwater flow rate are assumed due to the change in position of the shoreline (caused by the land rise in the Forsmark area) resulting in a transition from initially saline groundwater to freshwater. There also means a significant change in the chemical composition of the groundwater during this period. As can be seen in Figure 7-23, a gradual depletion of calcium starts to show at 5,000 years and propagates over time. By 25,000–30,000 years, only small parts at the right-hand down-stream side of the concrete constructions contribute any significant concentrations of calcium to the pore water. At 30,000 years the calcium concentrations have been significantly reduced almost throughout the vault and further drop after 37,000 years (note the change of scale in the figure). Calcium concentrations drops to fairly low levels during the period 60,000–70,000 years, then again increases somewhat from 80,000 years and remains fairly constant until 100,000 years.

The dependence of pH on the gradual depletion and transformation of portlandite and the minerals representing the CSH-gel in the model (CSH_1.8, CSH_1.1, and CSH_0.8, which have the stated Ca/Si ratios) is shown in Figure 7-23. During the initial phase, the pH is determined by the solubility of portlandite and the CSH-gel (CSH_1.8) remains inactive. When portlandite is depleted, the CSH-gel starts to respond to the changed chemical conditions. Following depletion of calcium, CSH_1.8 (Ca/Si = 1.8) is predicted to gradually dissolve, which initiates precipitation of the less alkaline CSH_1.1 (Ca/Si = 1.1) this starts to appear after ~ 3,000 years). After 25,000–30,000 years a substantial replacement of CSH_1.8 by CSH_1.1 has occurred in the concrete walls and the concrete floor. No visible effect can be seen near the fractures through the wall or through the floor, indicating although not proving that the effects of fractures may diminish when fracture apertures are small. After 25,000–30,000 years portlandite is almost entirely depleted and the transformation of CSH_1.8 to CSH_1.1 progresses. After ~ 37,000 years (not shown) a further transformation of CSH_1.1 to the least alkaline gel-phase CSH_0.8 starts. After ~ 80,000 years the only remaining CSH-component is CSH_0.8, which is still prominent after 100,000 years. A small amount of amorphous silica (SiO_2am) is formed at the upper rim of the concrete caisson after ~ 85,000 years (not shown in figure). At this point, any resemblance of the remaining material to the initial concrete is difficult to envisage since very little remains of the binding CSH-gels and portlandite is since long depleted.

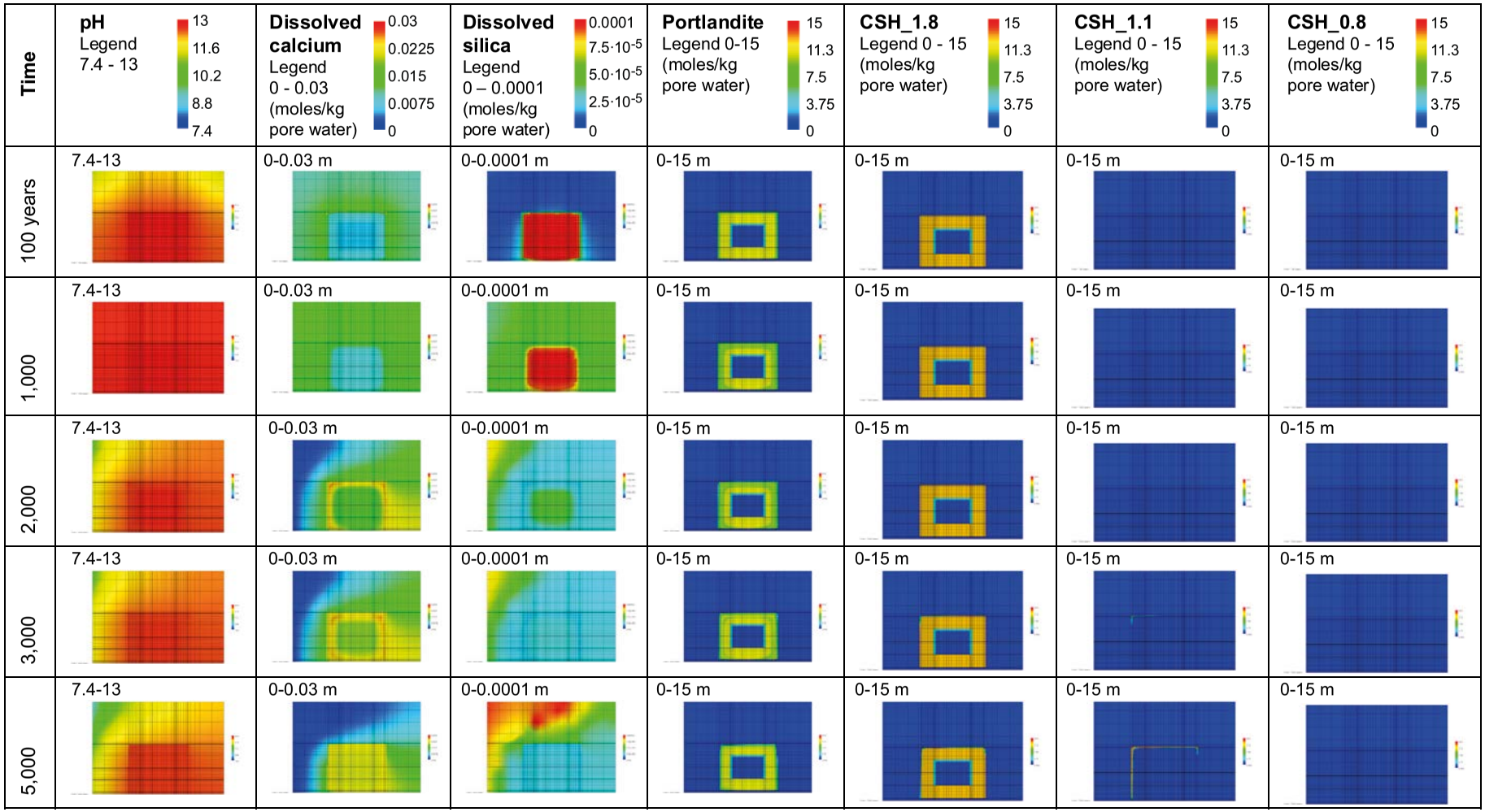

Figure 7-23. *Illustration of the gradual evolution of pH, dissolved calcium and silica as a result of depletion and transformation of mineral phases containing calcium over time (MinteqCem-2001 database, Case Large20). Red colour corresponds to the high-end value of the interval given in each legend, green colour corresponds to the mid-range value and blue corresponds to the low-end value of the range. Note the change of scale for dissolved silica after 40,000 years.*

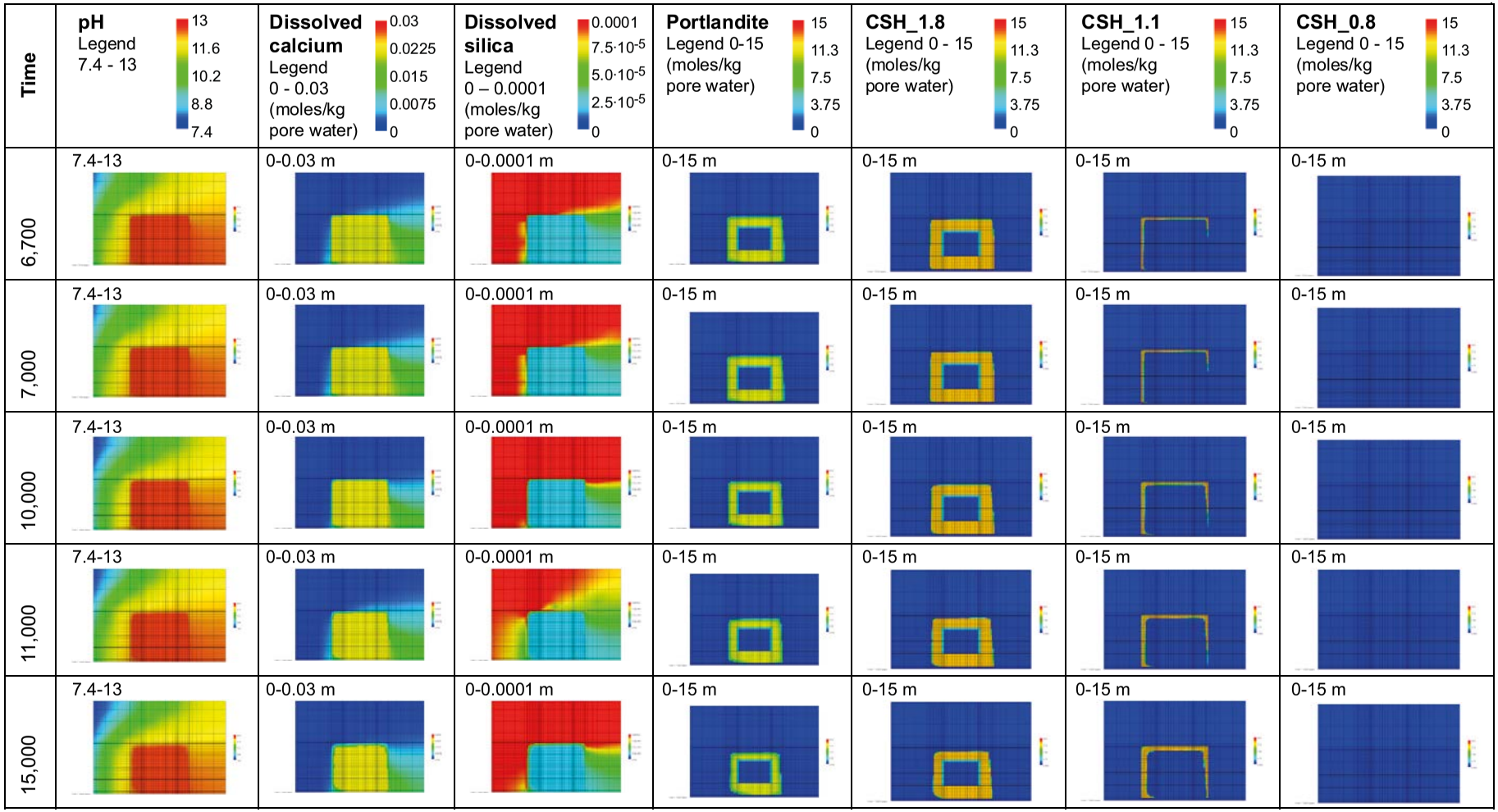

Figure 7-23. *Continued.*

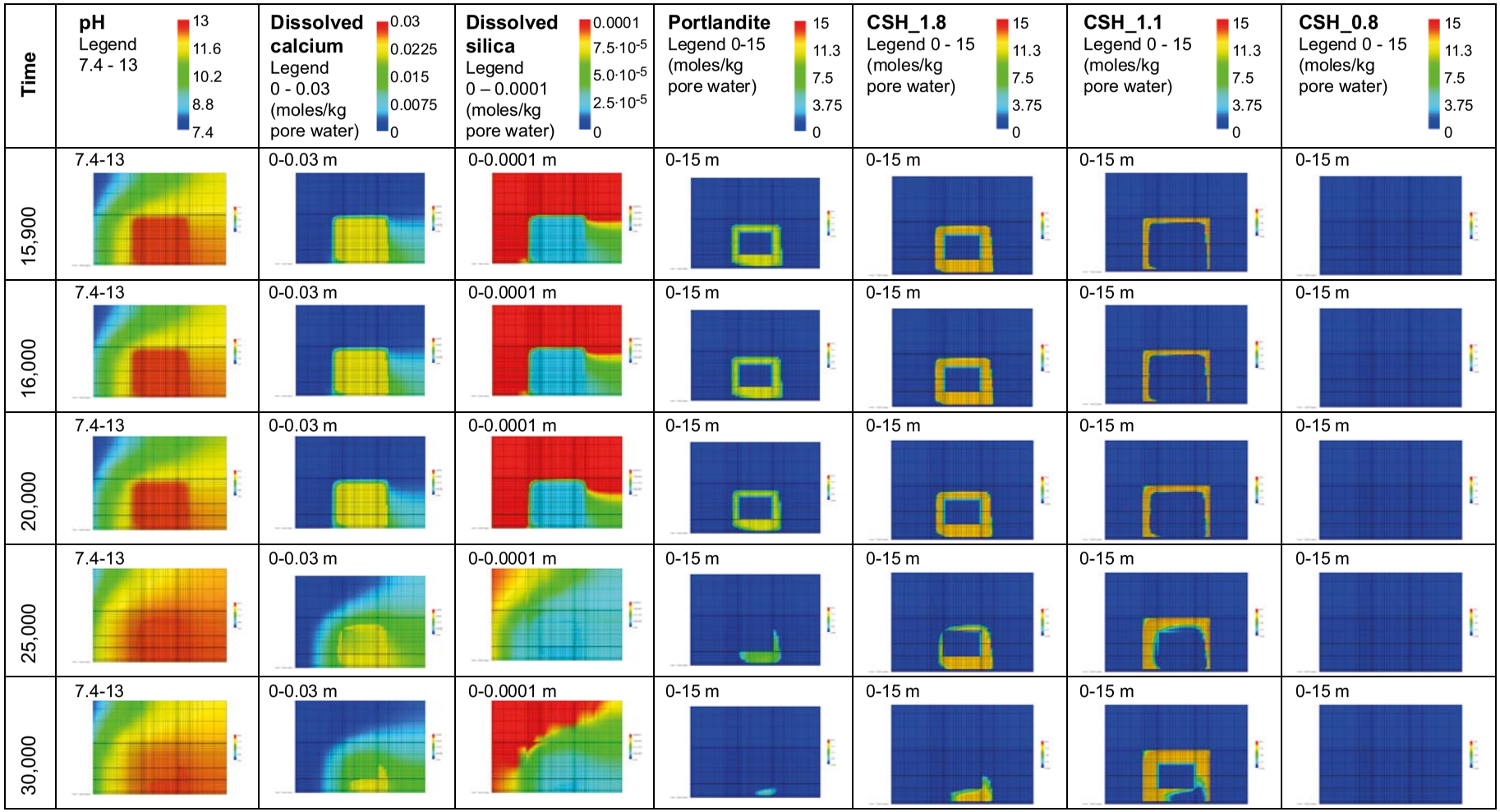

Figure 7-23. *Continued.*

Time	**pH** Legend 7.4 - 13 13 11.6 10.2 8.8 7.4	**Dissolved calcium** Legend 0 - 0.001 (moles/kg pore water) 0.001 0.00075 0.0005 0.00025 0	**Dissolved silica** Legend 0 – 0.003 (moles/kg pore water) 0.003 0.00225 0.0015 0.00075 0	**Portlandite** Legend 0-15 (moles/kg pore water) 15 11.3 7.5 3.75 0	**CSH_1.8** Legend 0 - 15 (moles/kg pore water) 15 11.3 7.5 3.75 0	**CSH_1.1** Legend 0 - 15 (moles/kg pore water) 15 11.3 7.5 3.75 0	**CSH_0.8** Legend 0 - 15 (moles/kg pore water) 15 11.3 7.5 3.75 0
40,000	7.4-13 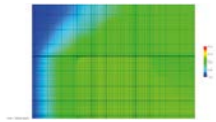	0-0.001 m 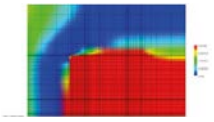	0-0.003 m 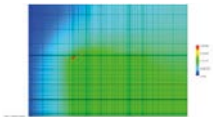	-	-	0-15 m 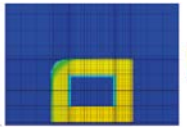	0-15 m 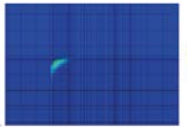
50,000	7.4-13 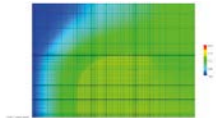	0-0.001 m 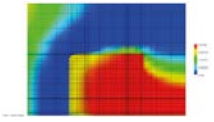	0-0.003 m 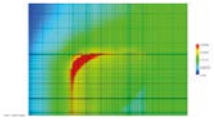	-	-	0-15 m 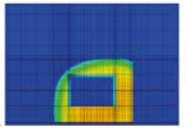	0-15 m 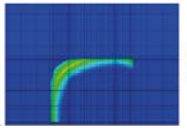
60,000	7.4-13 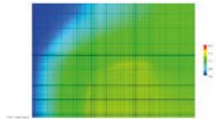	0-0.001 m 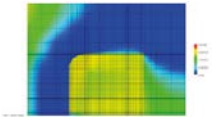	0-0.003 m 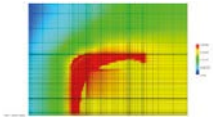	-	-	0-15 m 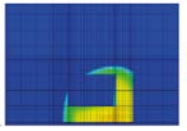	0-15 m 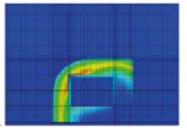
80,000	7.4-13 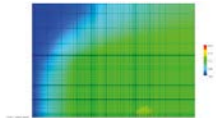	0-0.001 m 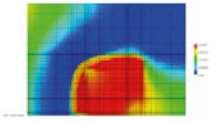	0-0.003 m 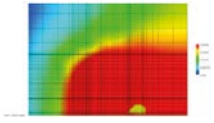	-	-	0-15 m 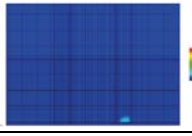	0-15 m 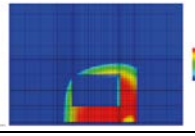
90,000	7.4-13 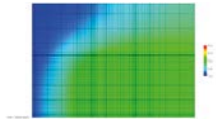	0-0.001 m 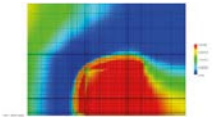	0-0.003 m 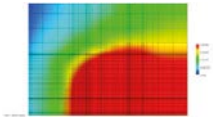	-	-	0-15 m -	0-15 m 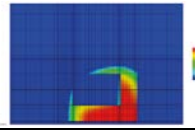
100,000	7.4-13 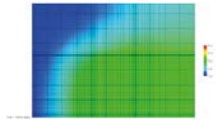	0-0.001 m 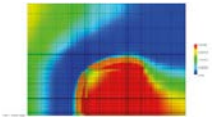	0-0.003 m 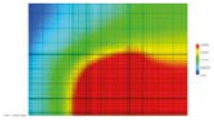	-	-	0-15 m -	0-15 m 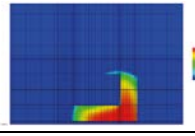

Figure 7-23. *Continued.*

Carbonate, sulphate, chloride, calcite, ettringite, monocarboaluminate, Friedel's salt and thaumasite

The carbonate concentration increases as the groundwater changes from salt- to freshwater, (assumed in the calculations to take place in a stepwise manner) at 2,000 years. Chloride concentrations are assumed to be low in the fresh concrete, whereas the chloride content of the groundwater is high during the saltwater period. The sulphate and chloride concentrations in the groundwater (assumed to fill the porosity of the macadam fill when calculations start) are comparatively high, but they quickly decrease due to interactions with soluble components leached from the concrete, which causes a precipitation of minor amounts of ettringite and Friedel's salt. Initially, the carbonate in the concrete is in the form of monocarboaluminate and calcite. During the period 500–5,000 years, calcite continues to precipitate primarily in the macadam fill at the left-hand upstream side close to the rock wall that limits the increase of dissolved carbonate. The maximum impact on the porosity due to precipitation of calcite during the first 5,000 years is a reduction of the porosity in the macadam from 30% to ~ 27.3%. During the remaining simulation period (10,000–100,000 years) calcite precipitation takes place in the macadam fill (reaching a lowest porosity of ~19% at 100,000 years) and on the outside of the concrete wall at the left side, as well as above the concrete lid, where the carbonate in groundwater meets calcium leached from the concrete constructions (see Figure 7-24). The porosity has been estimated to change from 11% to 4.7% after 100,000 years as a result of calcite precipitation in the most exposed parts of the concrete constructions. Hence, the precipitation of calcite is not expected to result in extensive blocking of the porosity. In the concrete structures, calcite replaces monocarboaluminate which decomposes with simultaneous formation of Friedel's salt. The formation of Friedel's salt requires the supply of chloride ions from the salt groundwater. A minor formation of thaumasite is indicated in a thin rim at the side walls and the lid during the early period, however disappearing at 2,000 years. There is also a very small precipitation of thaumasite in the macadam during the first 1,000 years (on the order of ~ 10^{-4} moles/kg w, not visible in the plots), which contribute to explain the reduced concentrations of dissolved silica during the first 1,000 years (cf. Figure 7-23). After 2,000 years the composition of the groundwater changes and in response to this the Friedel's salt gradually decomposes (depleted after 4,600 years), accompanied by neoformation of monocarboaluminate. From 5,000–37,000 years dissolution of monocarboaluminate is accompanied by an increased precipitation of ettringite. After 5,000 years thaumasite reappears in minor quantity. After 20,000 years the thaumasite formation is activated and gradually replaces ettringite. During the period 37,000–50,000 years ettringite is dissolved and disappears completely. The occurrence of a moving front of precipitating and redissolving ettringite observed in other calculations is less pronounced in case Large20, which may indicate that the concrete barriers may be less vulnerable to this deleterious process. However, the formation of thaumasite is pronounced from ~ 35,000 years and continuing as a moving front still progressing at 100,000 years when the calculations were terminated. This demonstrates that including thaumasite in the database has an impact on the predicted results.

The changes in the porosity in the macadam caused by precipitation of secondary minerals (predominantly calcite) are not very dramatic. As discussed above, the macadam will still have a fairly high porosity and most parts of the macadam are affected only marginally. In line with this, the impact on the transport properties of the macadam would be expected to be limited and the hydraulic cage function should remain. Therefore, the model assumption/limitation that the hydraulic function of the macadam (except below the concrete floor) did not change over time was reasonable. Further, the calculations show that the porosity of the concrete was only blocked locally and to a limited extent. Therefore, the fact that PHAST does not account for porosity changes automatically does not have an adverse effect on the results presented here.

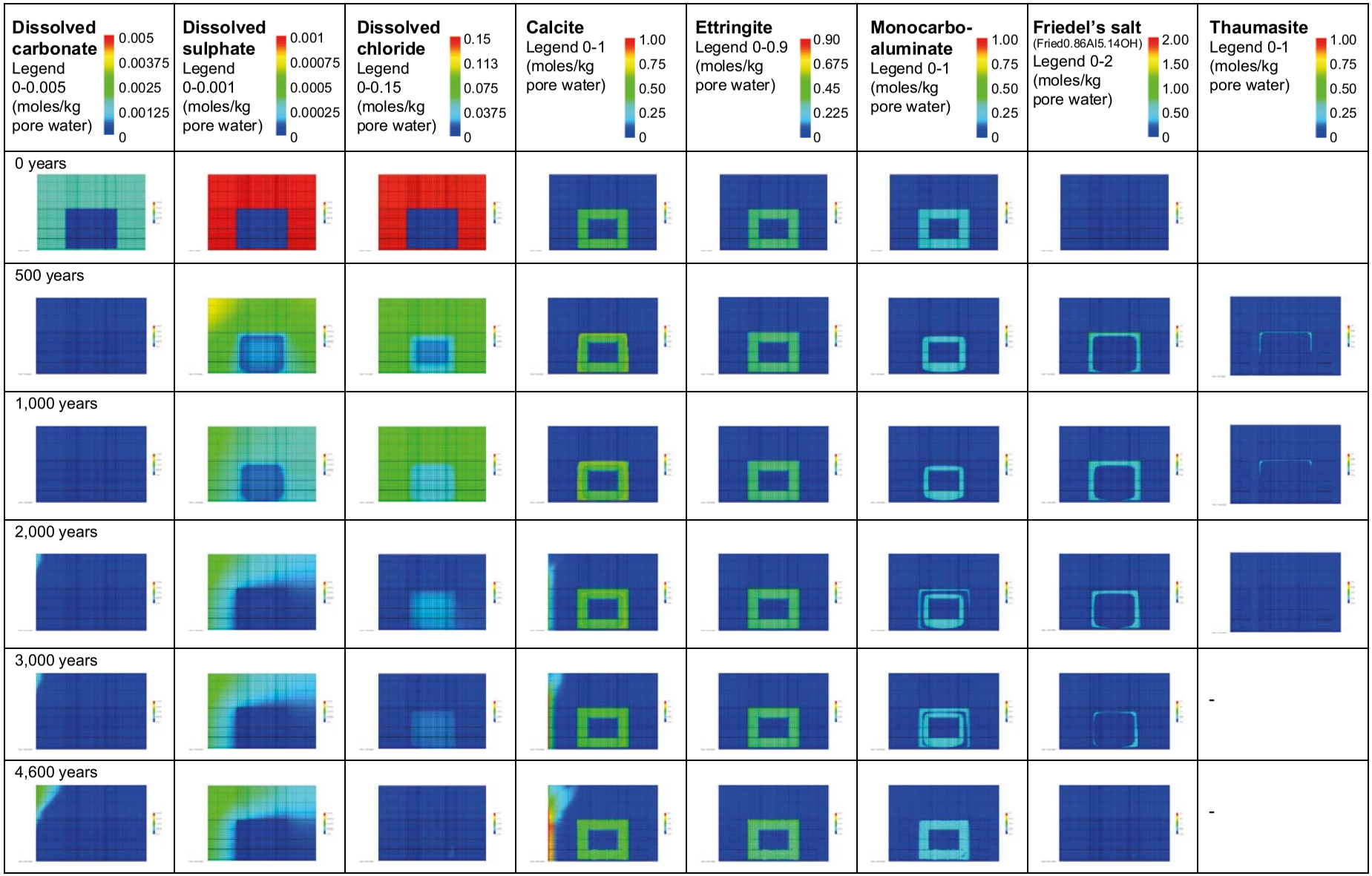

Figure 7-24. *Illustration of the change of dissolved carbonate, sulphate and chloride, and of the gradual transformations between concrete mineral phases containing carbonate, sulphate, chloride and/or aluminium over time. (MinteqCem-2001 database, Case Large20).*

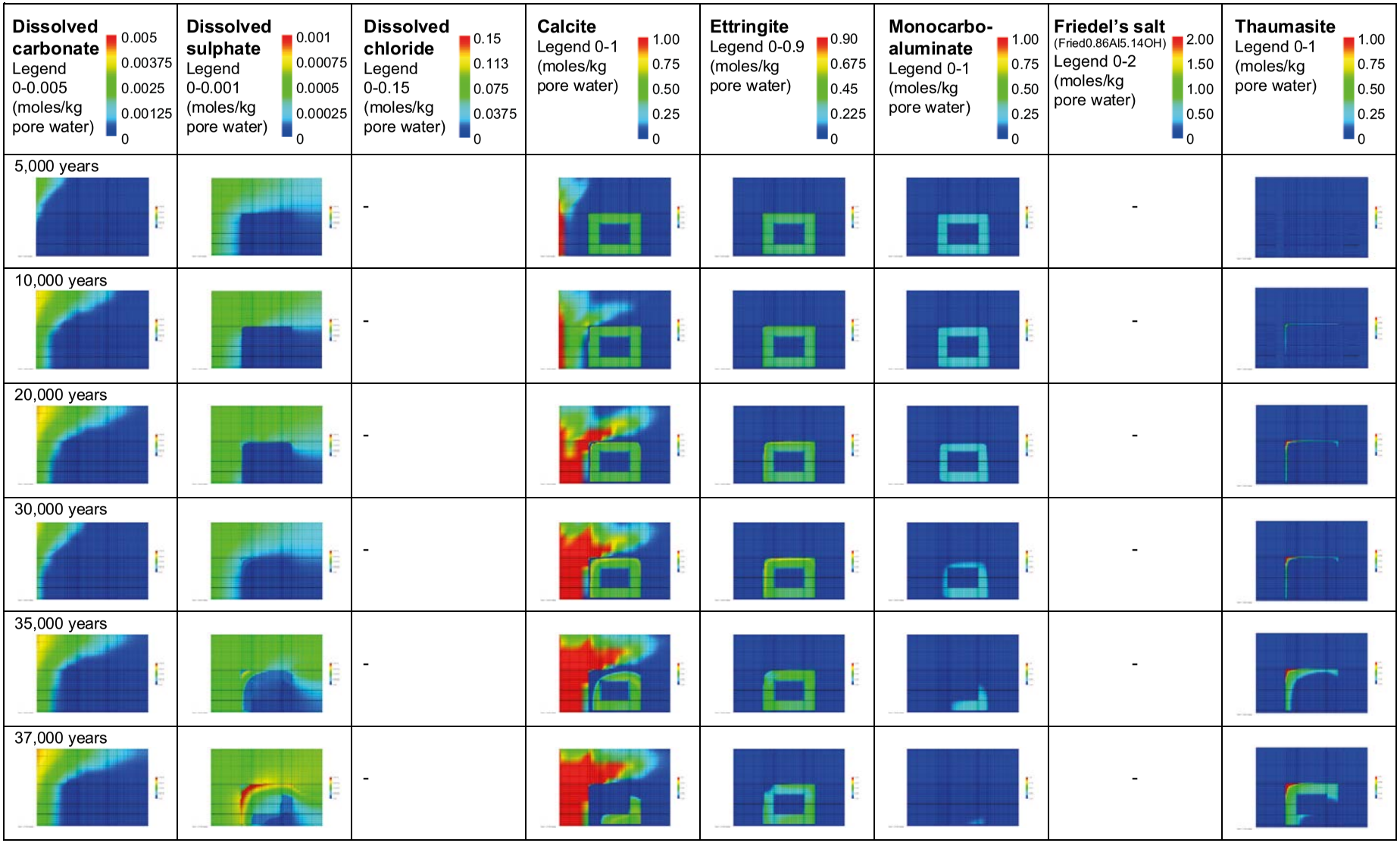

Figure 7-24. *Continued.*

Dissolved carbonate Legend 0-0.005 (moles/kg pore water) 0.005 0.00375 0.0025 0.00125 0	**Dissolved sulphate** Legend 0-0.001 (moles/kg pore water) 0.001 0.00075 0.0005 0.00025 0	**Dissolved chloride** Legend 0-0.15 (moles/kg pore water) 0.15 0.113 0.075 0.0375 0	**Calcite** Legend 0-1 (moles/kg pore water) 1.00 0.75 0.50 0.25 0	**Ettringite** Legend 0-0.9 (moles/kg pore water) 0.90 0.675 0.45 0.225 0	**Monocarbo-aluminate** Legend 0-1 (moles/kg pore water) 1.00 0.75 0.50 0.25 0	**Friedel's salt** (Fried0.86Al5.14OH) Legend 0-2 (moles/kg pore water) 2.00 1.50 1.00 0.50 0	**Thaumasite** Legend 0-1 (moles/kg pore water) 1.00 0.75 0.50 0.25 0
40,000 years		-			-	-	
50,000 years		-			-	-	
60,000 years		-		-	-	-	
80,000 years		-		-	-	-	
90,000 years		-		-	-	-	
100,000 years		-		-	-	-	

Figure 7-24. *Continued.*

Magnesium, iron and mineral reactions involving magnesium and iron

Dissolved magnesium is present in fairly high concentrations in the saline groundwater, whereas the concentration drops significantly as the groundwater changes to freshwater after 2,000 years. However, in the vault, dissolved magnesium will only be present in low concentrations due to the low solubility of brucite in the alkaline environment created by concrete. This means that the solubility limit of hydrotalcite is not exceeded and does not precipitate in this case.

As the pH in the vault drops after 3,000 years, the dissolved magnesium concentration gradually increases in the macadam fill around the concrete constructions. From 5,000–30,000 years, a fine front of precipitating brucite is visible on the left-hand, up-stream side of the left concrete wall, see Figure 7-25.

After ~ 40,000 years, in response to decreasing pH, the brucite starts to dissolve in the macadam fill on the upstream side which boosts the dissolved magnesium, while precipitation continues on the downstream side of the front. After 40,000 years the magnesium concentration is determined by the inflowing groundwater. Brucite is still present in significant amounts in the concrete after 100,000 years.

Following the gradual depletion of alkaline components in concrete, the magnesium concentrations in the concrete pore water slowly increase towards the end of the simulation (50,000–100,000 years) in Figure 7-25.

Iron is present at low concentrations in groundwater, unless very reducing conditions occur. Iron is a constituent of concrete and may appear in various minerals including iron hydroxides, iron-substituted ettringite and hydrotalcite, etc. In the MinteqCem-2001 database, iron appears as an iron-substituted hydrogarnet C_3FH_6, whereas other minerals containing iron have been neglected. The dissolved iron concentrations start to increase from the left-hand upstream side of the left concrete wall after ~ 40,000 years in response to decreasing pH and increased leaching of calcium, cf. Figure 7-23. The dissolution of C_3FH_6 slowly progresses as a front from left to right but a significant proportion is still present after 100,000 years.

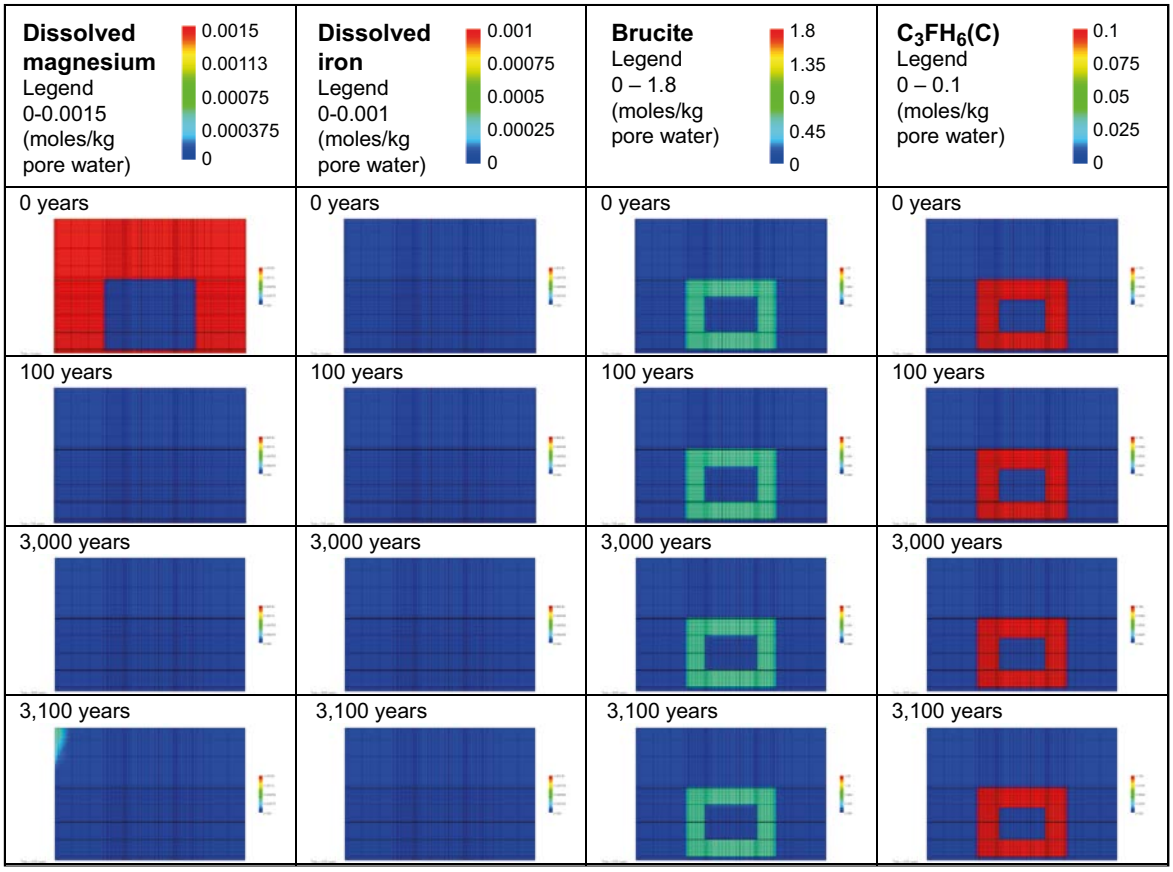

Figure 7-25. *Illustration of the change of dissolved magnesium and iron and the gradual transformations between concrete mineral phases containing magnesium and iron over time. (MinteqCem-2001 database, Case Large20).*

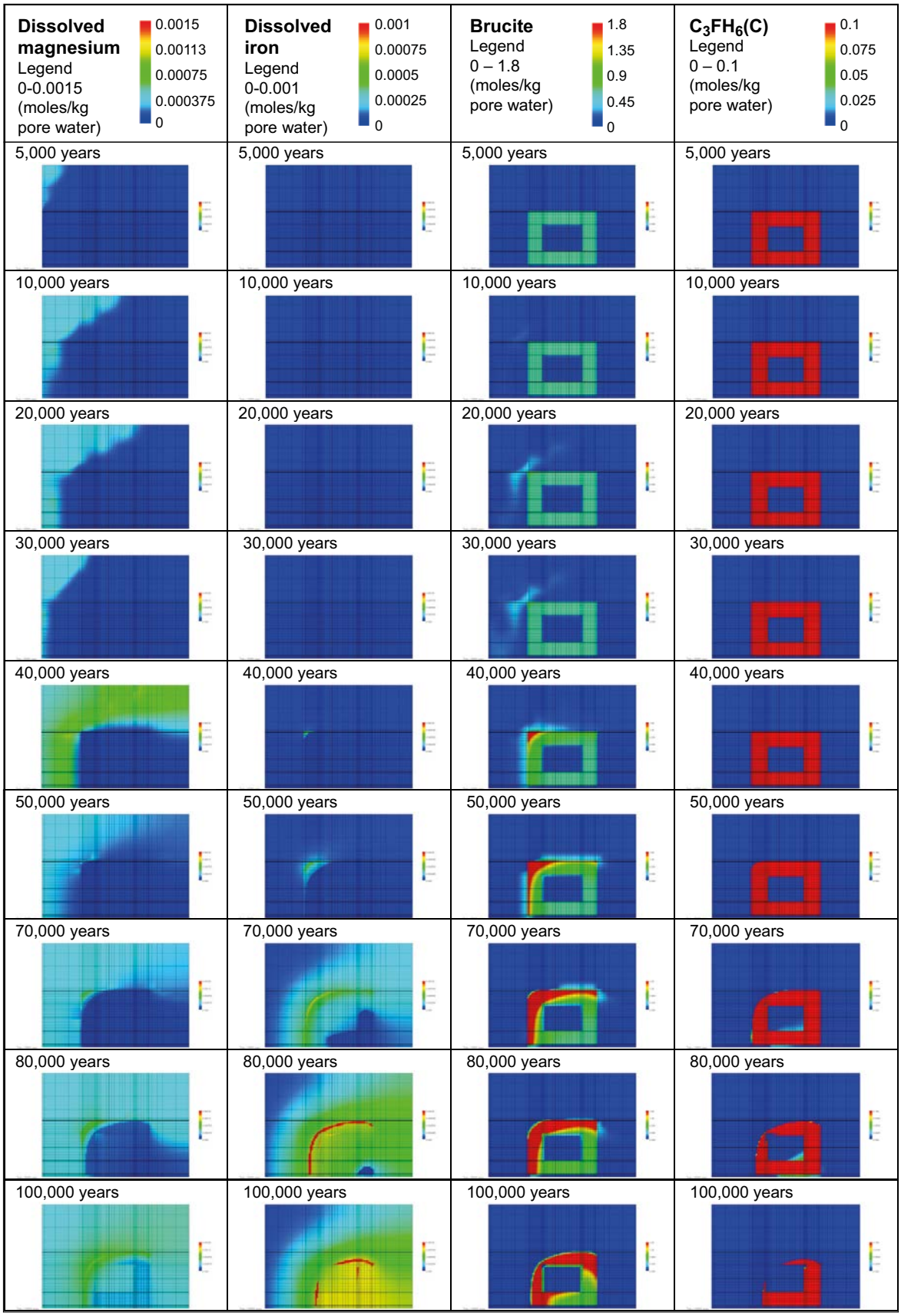

Figure 7-25. *Continued.*

7.5 Case Large10 (1BMA)

This section describes the results from the modelling of case Large10.

The basic assumptions regarding geometries and physical/hydraulic/transport parameters are given in Section 7.3. The same thermodynamic database was used as in case Large20 for 2BMA (MinteqCem-2001). A detailed specification of the amounts of different minerals given as input data is presented in Appendix H.

The presentation of the results first gives a brief overview of the evolution of the pore water chemistry and the mineral assemblage in one point in the cell grid at position AE, see Figure 7-8. Following this, the changes in the mineralogy at point DE, near the fracture, are presented. Finally, the evolution in the full 2-D-grid is presented and more detailed comments are given. For additional information on the results, see graphical representations shown in Appendix D.

7.5.1 Evolution of chemistry and mineralogy at evaluation points

Evaluation point AE – at the intersection of the centrelines of the concrete floor and the left-hand side concrete wall

The evolution of the porewater at evaluation point AE is presented in Figure 7-26. The initial pore water composition is determined by the composition of the cement minerals. During the early stage, equilibration with the inflowing ground water takes place, which also causes changes due to ion exchange processes in the CSH-gel (not shown here but is similar to the results presented and discussed for cases Large20 and Large8). The pH is initially high, but levels off at ~ 12.5 until a sharp drop at ~2,800 years, followed by a second sharp decrease at ~3,200 years and a third drop at ~5,400 years, where a new plateau is established at slightly above pH 10. This plateau stretches to ~ 8,800 years where the pH drops to slightly below 10.

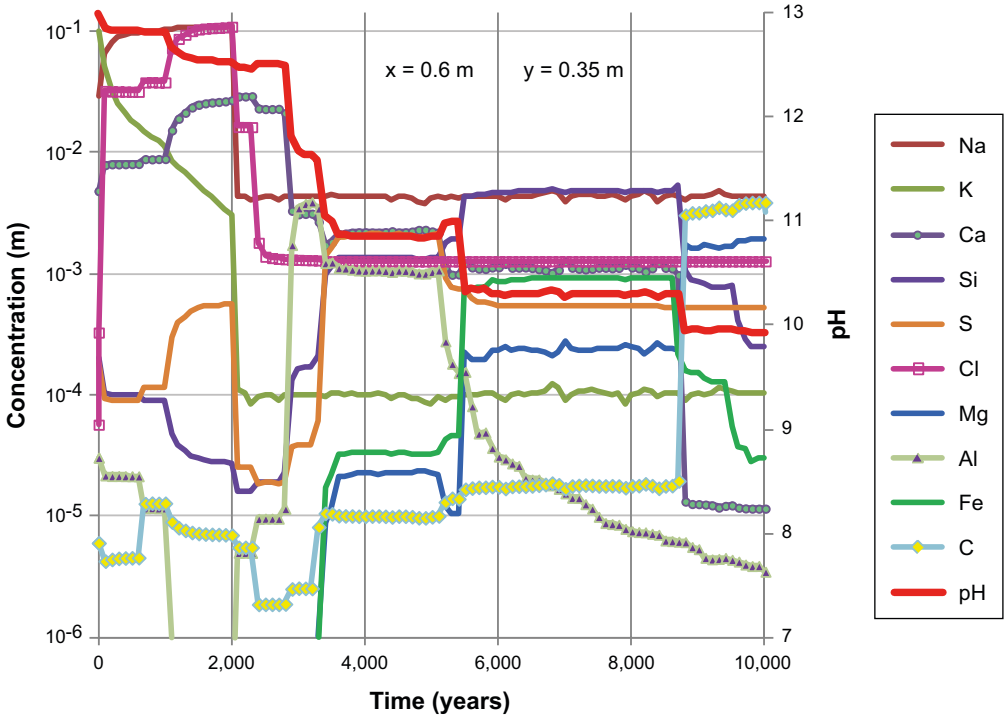

Figure 7-26. *The evolution of the pore water chemistry (during the first 10,000 years) at position AE (a point located at the intersection of a vertical centreline through the left-hand side concrete wall and a horizontal centreline through the concrete floor), case Large10.*

After the initial drop in pH due to leaching of alkali hydroxides, portlandite determines the pH during the first 2,800 years. An interesting interplay between portlandite, monocarboaluminate and Friedel's salt is shown in response to the ingress of chloride during the first 2,000 year, cf. Figure 7-26, Figure 7-27 and Figure 7-29. As the Friedel's salt is destabilised by the changed ground water composition at 2,200 years (cf. Figure 7-26), the chloride concentration stabilises at ~1.3 mM which is the concentration assumed in the ground water during the freshwater period, and the released aluminium is precipitated as monocarboaluminate and C_3AH_6. The CSH-gel is not affected by leaching until depletion of portlandite. The transition from the CSH_1.8 (Ca/Si = 1.8) to the less alkaline CSH_1.1 (Ca/Si = 1.1) takes place between ~2,700 and 2,900 years, accompanied by a distinct drop in pH. C_3AH_6 also forms just after this, which then reacts with sulphate to form ettringite. The peak amount of ettringite appears after ~3,500 years. Slow transformation of CSH_1.1 to CSH_0.8 (Ca/Si = 0.8) and slow ettringite dissolution initiate after ~3,500 years, when the pH has dropped to ~ 10.85 and with a slight reduction in the dissolved calcium concentration. The CSH_1.1 transformation and ettringite dissolution then occur more rapidly, so that they are completed depleted by 5,500 and ~5,200 years, respectively. A gradual enrichment of C_3FH_6 is observed from ~4,500 years caused by upstream dissolution and precipitation in more alkaline downstream environment. This is at its maximum from ~5,500–~6,000 years. After ~5,500 years the only remaining CSH mineral is CSH_0.8, the pH is ~10.3, accompanied by a fairly low concentration of dissolved calcium (~1 mM) and an increased concentration of dissolved silica (~3 mM), see Figure 7-26. Hereafter dissolution of CSH_0.8 progresses and is accompanied by dissolution of C_3FH_6 which is destabilised by the lower pH. Depletion of CSH_0.8 occurs at ~8,800 years and is accompanied by a pH drop to ~10. Gradually, the precipitation of calcite and brucite (which peaks at ~8,800 years) becomes more pronounced. At ~12,000 years brucite is totally depleted, whereas calcite continuously precipitates until reaching a final pH of ~7.5 after ~30,000 years, see Figure 7-28. The results are shown up to 43,000 years.

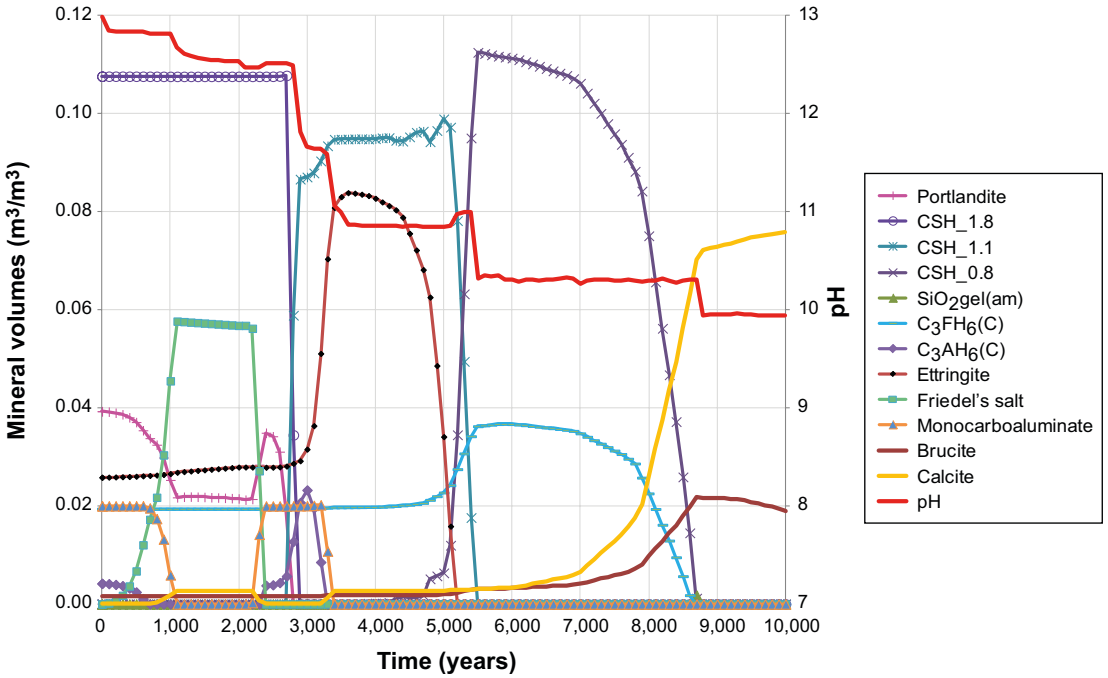

Figure 7-27. *The evolution of the mineral assemblage (during the first 10,000 years) at position AE (a point located at the intersection of a vertical centreline through the left-hand side concrete wall and a horizontal centreline through the concrete floor), case Large10.*

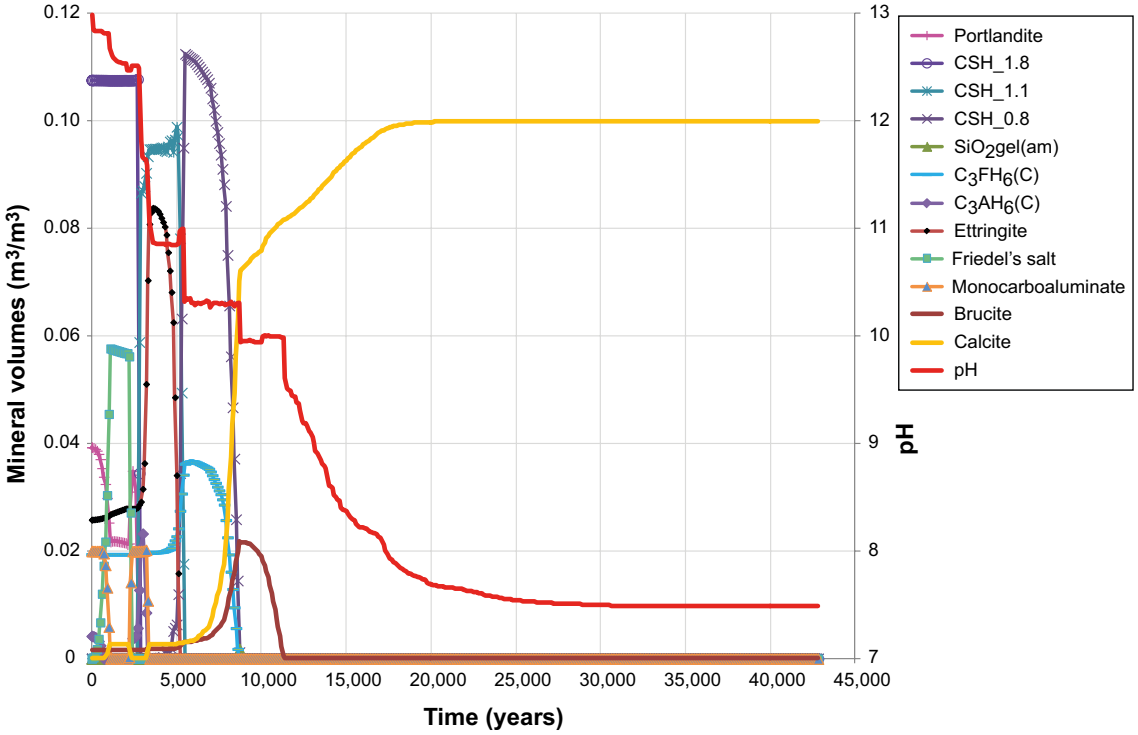

Figure 7-28. *The evolution of the mineral assemblage (during 43,000 years) at position AE (a point located at the intersection of a vertical centreline through the left-hand side concrete wall and a horizontal centreline through the concrete floor), case Large10.*

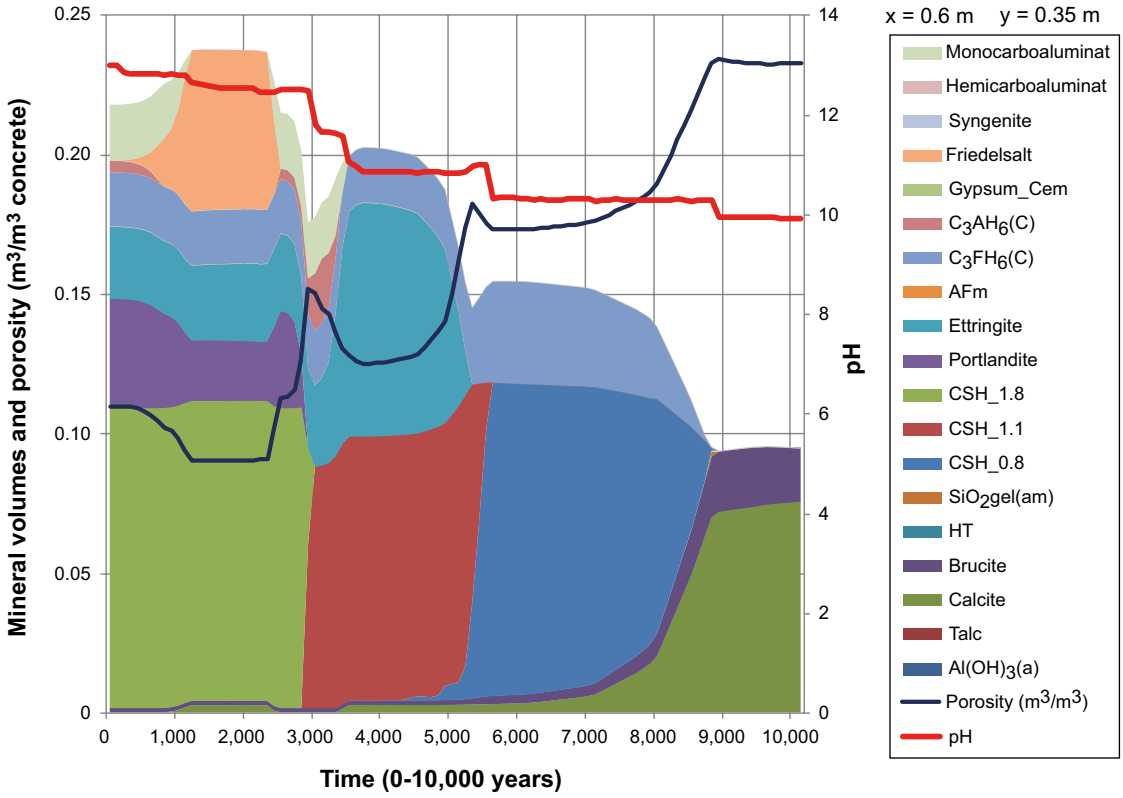

Figure 7-29. *The change of mineral volumes and porosity in concrete during 10,000 years at position AE (a point located at the intersection of a vertical centreline through the left-hand side concrete wall and a horizontal centreline through the concrete floor), (MinteqCem-2001 database, Case Large10). The evolution of pH is also indicated.*

The mineral assemblage changes in response to the gradual leaching by the groundwater. The porosity increased from 11% to ~ 23% after 9,000 years. The porosity is presented over the range of 0–25% in Figure 7-29; the maximum porosity corresponding to fully depleted cement minerals would be ~ 30 %, the remaining volume constitutes the ballast material which is assumed to be inert. This is a much greater change than seen at position GH in case Large20 (2BMA), where the porosity had only increased to 11.5% by 10,000 years (Section 7.4.1). The depletion of Friedel's salt after 2,200–2,500 years, followed by dissolution of portlandite after ~ 2,500–2,900 years causes the porosity to first increase, followed by a transformation of CSH_1.8 to CSH_1.1 and a growth of ettringite which causes a reduction of the porosity during the period 3,000–3,800 years. Following subsequent dissolution of ettringite and the transformation of CSH_1.1 to CSH_0.8 the porosity again rises after ~ 4,500 years, reaching a peak at 5,300 years and a small reduction to 5,600 years. Starting at ~ 6,000 years the porosity increases gradually as a result of dissolution of the iron-substituted hydrogarnet C_3FH_6, accompanied by precipitation of calcite and brucite.

The change of the porosity during the 2,000–5,500 years period is a matter of concern for the integrity of the concrete. In particular, periods during which ettringite precipitation may cause cracking of concrete due to the expansive nature of this mineral, see discussion on the theoretical background to this in Chapter 4 of the report.

Evaluation point DE – at the vertical centreline of the left-hand side concrete wall near the thin horizontal fracture

The progression of the dissolved components and the pH follows the general pattern as shown for evaluation point AE discussed above, although the observed changes occur more rapidly near the fracture, compare Figure 7-30 and Figure 7-29.

The gradual evolution of the mineral assemblage with time is shown together with the calculated changes of porosity during the first 10,000 years. The results show that a porosity increase from 11% to ~ 24% at 6,300 years would be expected. The porosity is presented over the range of 0–30% in Figure 7-30; the maximum porosity corresponding to fully depleted cement minerals would be ~ 30%, the remaining volume constitutes the ballast material which is assumed to be inert.

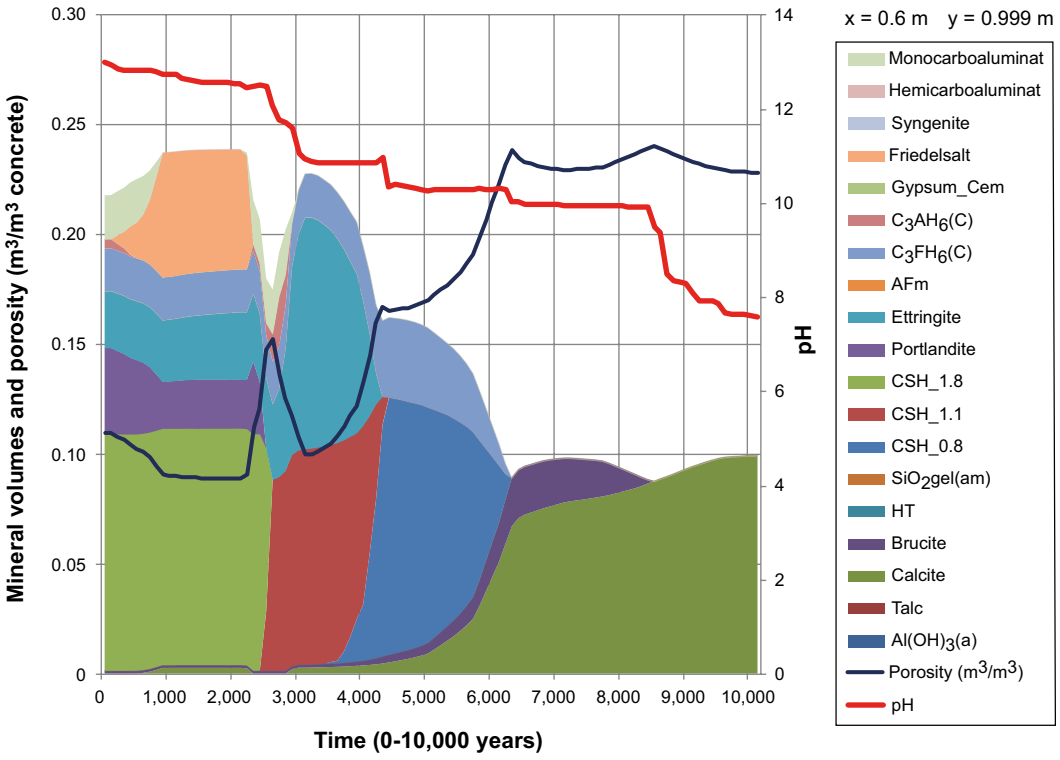

Figure 7-30. *The change of mineral volumes and porosity in concrete during 10,000 years at position DE (a point located at the vertical centreline through the left-hand side concrete wall, 1 mm from an open fracture), (MinteqCem-2001 database, Case Large10). The evolution of pH with time is also indicated.*

7.5.2 Evolution of the chemistry and mineralogy of the 2-D system

pH evolution, calcium and silica depletion

The evolution of pH over time in full 2-D-section of the model is summarised in Figure 7-31. Initially, the pH is high in the concrete due to the presence of alkali hydroxides. Calcium is one of the most important chemical components responsible for pH buffering and the mechanical strength of the concrete system. During the early period the concentration of dissolved calcium is low due to the suppression of the solubility of portlandite at the high pH created by the alkali hydroxides. Following the gradual exchange of soluble components with the groundwater, the alkali hydroxides are washed out and the calcium concentration increases as the solubility of portlandite becomes the major pH-regulating component in the system. The model results show that a high pH (> 12.5) is maintained inside the concrete constructions over the first 2,000 years. After ~ 500 years, the conditions are determined by the solubility of portlandite – a period which stretches up to ~ 2,000 years. At this point, a significant increase in the groundwater flow rate is assumed due to the transition from the saltwater period to the freshwater period (caused by the land rise in the Forsmark area). There is also a significant change in the chemical composition of the groundwater at this time. Thereafter the pH gradually drops, starting at the left-hand inflow side, where the pH approaches about 11 in the outer layers of the concrete wall. This effect is accentuated adjacent to the horizontal fracture after about 3,000 years. As can be seen in Figure 7-31, a gradual depletion of calcium starts after 3,000 years and propagates over time. During the period 5,000 through 6,700 years, the pH of the concrete wall on the left-hand inflow side of the model drops to about 10, while the pH inside the open void (representing the vaults where the waste is stored) remains at about pH 11. By 5,800 years, only small parts of the right-hand down-stream side of the concrete constructions contribute any significant amounts of calcium to the pore water (note the change of scale in the figure at 5,900 years). After 10,000 years, almost the entire vault has reached a pH of ~ 10 or lower, after 20,000 years the pH approaches ~ pH 9 and after 30,000 years, the natural pH of the groundwater – bedrock system has been re-established.

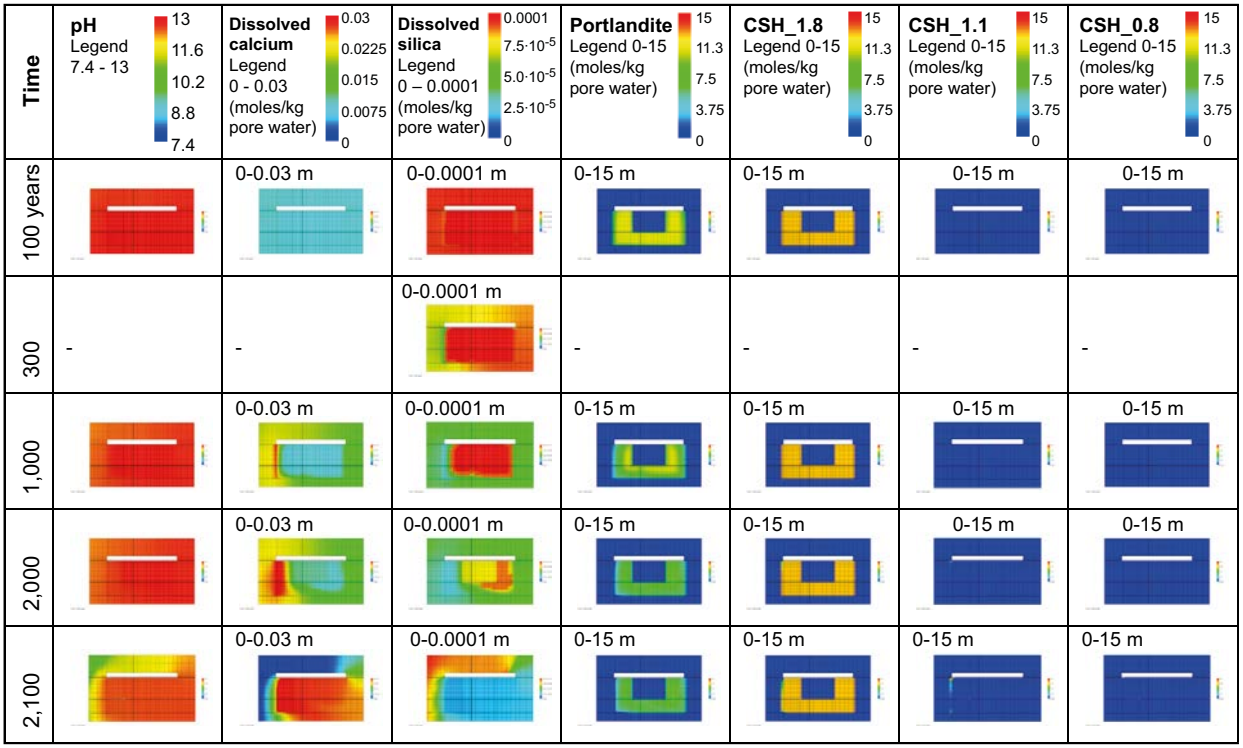

Figure 7-31. *Illustration of the gradual evolution of pH and concentration of dissolved calcium as a result of depletion and transformation of mineral phases containing calcium. (MinteqCem-2001 database, Case Large10).*

Time	pH Legend 7.4 - 13 13 11.6 10.2 8.8 7.4	Dissolved calcium Legend 0 - 0.03 (moles/kg pore water) 0.03 0.0225 0.015 0.0075 0	Dissolved silica Legend 0 – 0.0001 (moles/kg pore water) 0.0001 $7.5\cdot10^{-5}$ $5.0\cdot10^{-5}$ $2.5\cdot10^{-5}$ 0	Portlandite Legend 0-15 (moles/kg pore water) 15 11.3 7.5 3.75 0	CSH_1.8 Legend 0-15 (moles/kg pore water) 15 11.3 7.5 3.75 0	CSH_1.1 Legend 0-15 (moles/kg pore water) 15 11.3 7.5 3.75 0	CSH_0.8 Legend 0-15 (moles/kg pore water) 15 11.3 7.5 3.75 0
3,000	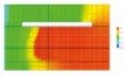	0-0.03 m 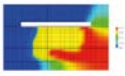	0-0.0001 m  0-0.006 m 	0-15 m 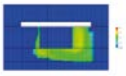	0-15 m 	0-15 m 	0-15 m 
5,000	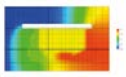	0-0.03 m 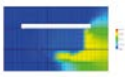	0 – 0.006 m 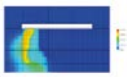	0-15 m 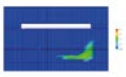	0-15 m 	0-15 m 	0-15 m 
5,800	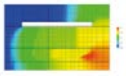	0-0.03 m 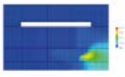	0 – 0.006 m 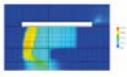	0-15 m 	0-15 m 	0-15 m 	0-15 m 
5,900	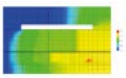	0-0.001 m 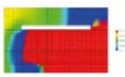	0 – 0.006 m 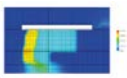	0-15 m 	0-15 m 	0-15 m 	0-15 m 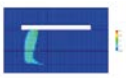
6,700	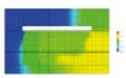	0-0.001 m 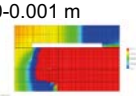	0 – 0.006 m 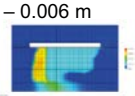	0-15 m 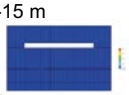	0-15 m 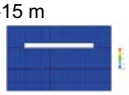	0-15 m 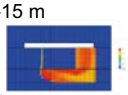	0-15 m 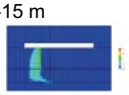
10,000	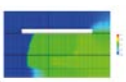	0-0.001 m 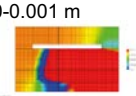	0 – 0.006 m 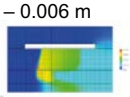	0-15 m 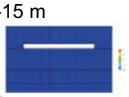	0-15 m 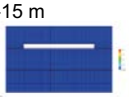	0-15 m 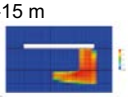	0-15 m 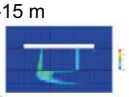
13,400	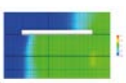	0-0.001 m 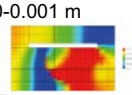	0 – 0.006 m 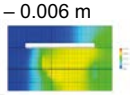	-	-	0-15 m 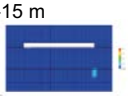	0-15 m 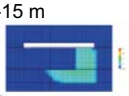
15,000	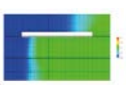	0-0.001 m 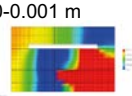	0 – 0.006 m 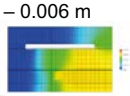	-	-	0-15 m 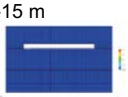	0-15 m 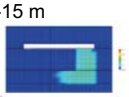
21,600	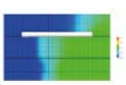	0-0.001 m 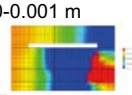	0 – 0.006 m 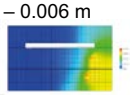	-	-	-	0-15 m 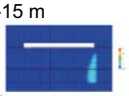
23,800	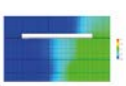	0-0.001 m 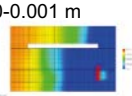	0 – 0.006 m 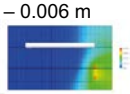	-	-	-	0-15 m 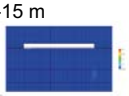
30,500		0-0.001 m 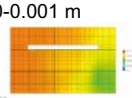	0 – 0.006 m 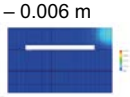	-	-	-	
31,000		0-0.001 m 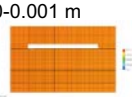	-	-	-	-	

Figure 7-31. *Continued.*

Silica is another major binding component of concrete and constitutes an important part of the CSH-gel. As shown in Figure 7-31 silica leaching produces a complex interaction between different CSH-gel phases, in which calcium also plays a dominant role. Silica leaching is intimately coupled to the leaching of portlandite due to the common chemical element calcium in both the portlandite and the CSH-gels. As long as the portlandite remains in the system it will buffer the chemical conditions and suppress the solubility of silica in the CSH-gels. When portlandite becomes depleted, the solubility of the more calcium-rich CSH-gel phases increase and the gel starts to dissolve. Three different CSH phases are included in the MinteqCem-2001 database. The dissolution process involves a gradual transformation from calcium-rich CSH_1.8 (Ca/Si = 1.8) to the more silica-rich gel-phases CSH_1.1 (Ca/Si = 1.1) and CSH_0.8 (Ca/Si = 0.8). However, the patterns and timescales of the dissolution of the CSH gel phases seen after the depletion of portlandite are similar to those in case Large8. The CSH-gels dissolve and finally disappear after ~ 23,800 years, see Figure 7-31.

Carbonate, calcite, ettringite, monocarboaluminate and Friedel's salt

As in Large20, the carbonate in the concrete is initially in the form of monocarboaluminate, see Figure 7-32. During the first 2,000 years, calcite continuously precipitates primarily on the left-hand upstream side of the vault. Increasingly the precipitation progresses from ~ 1,000 years and onwards also on the outside of the concrete wall at the right side, as well as on the underside of the concrete floor, where the carbonate in groundwater meets calcium leached from the concrete constructions. In the concrete structures, the calcite replaces the monocarboaluminate which decomposes with simultaneous formation of Friedel's salt. The formation of Friedel's salt requires the supply of chloride ions from the salt groundwater. After 2,000 years the composition of the groundwater changes and in response to this the Friedel's salt is decomposed, accompanied by transformation of calcite to monocarboaluminate and an increased precipitation of ettringite. From ~ 3,000 years and onward precipitation of calcite takes place at the left-hand upstream side where groundwater enters the vault. Continuing over the period 2,000–7,000 years, enhanced precipitation of ettringite replacing monocarboaluminate propagates as a front from left to right through the concrete structures. Following this, ettringite is dissolved as pH drops and disappears completely after ~ 11,000–12,000 years. Calcite continues to precipitate at a slow rate. After 60,000 years the natural conditions of the groundwater – bedrock system has been re-established and is governed mainly by carbonate-calcite equilibria.

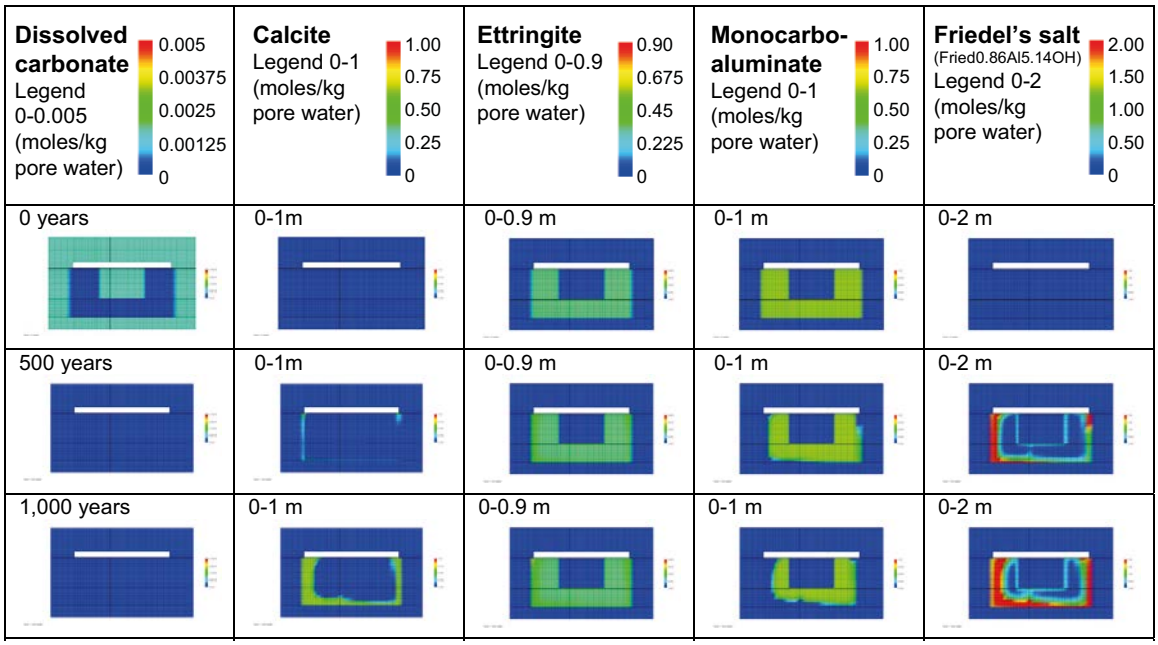

Figure 7-32. *Illustration of the change of dissolved carbonate and of the gradual transformations between concrete mineral phases containing carbonate and/or aluminium over time. (MinteqCem-2001 database, Case Large10).*

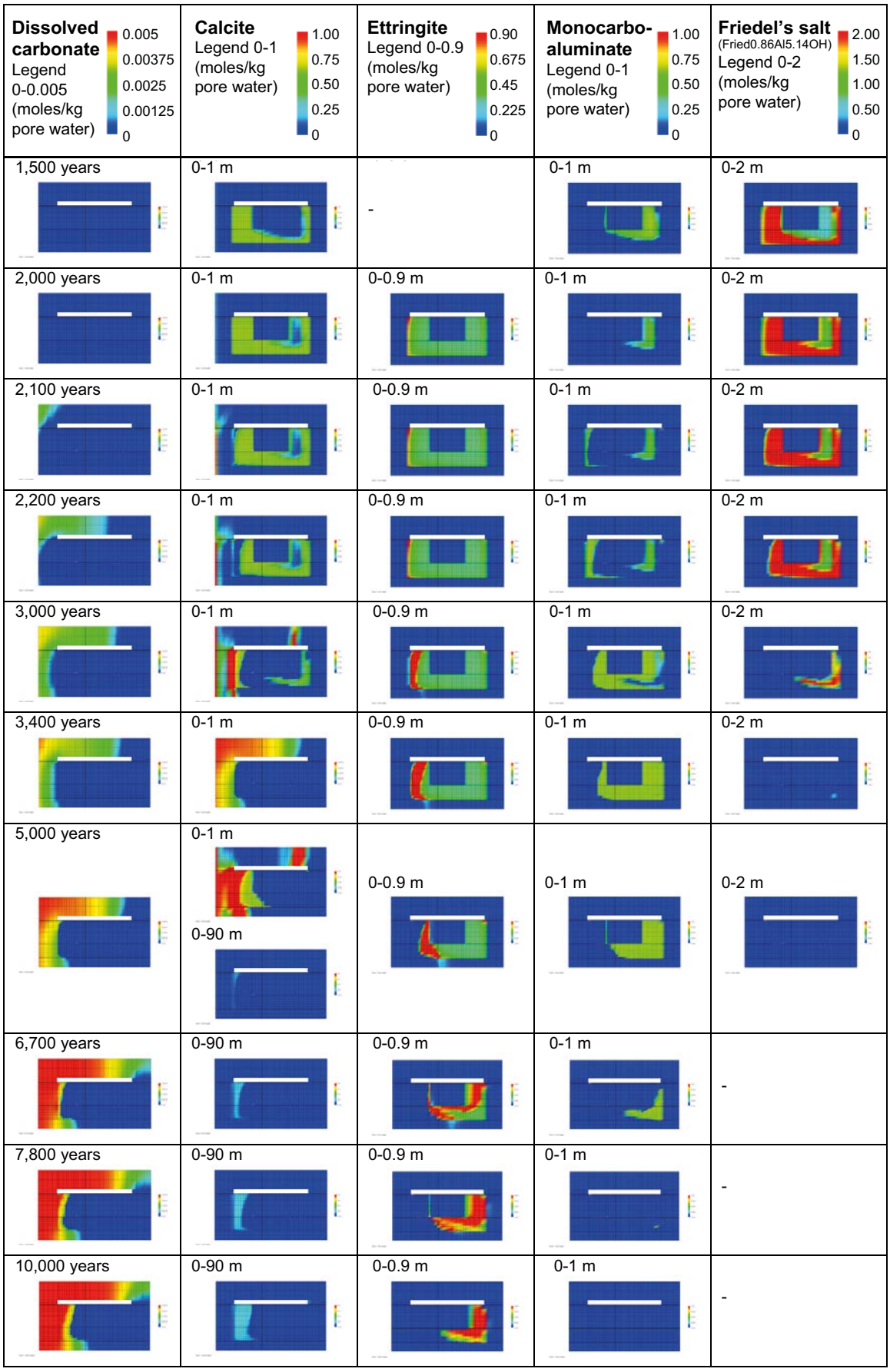

Figure 7-32. *Continued.*

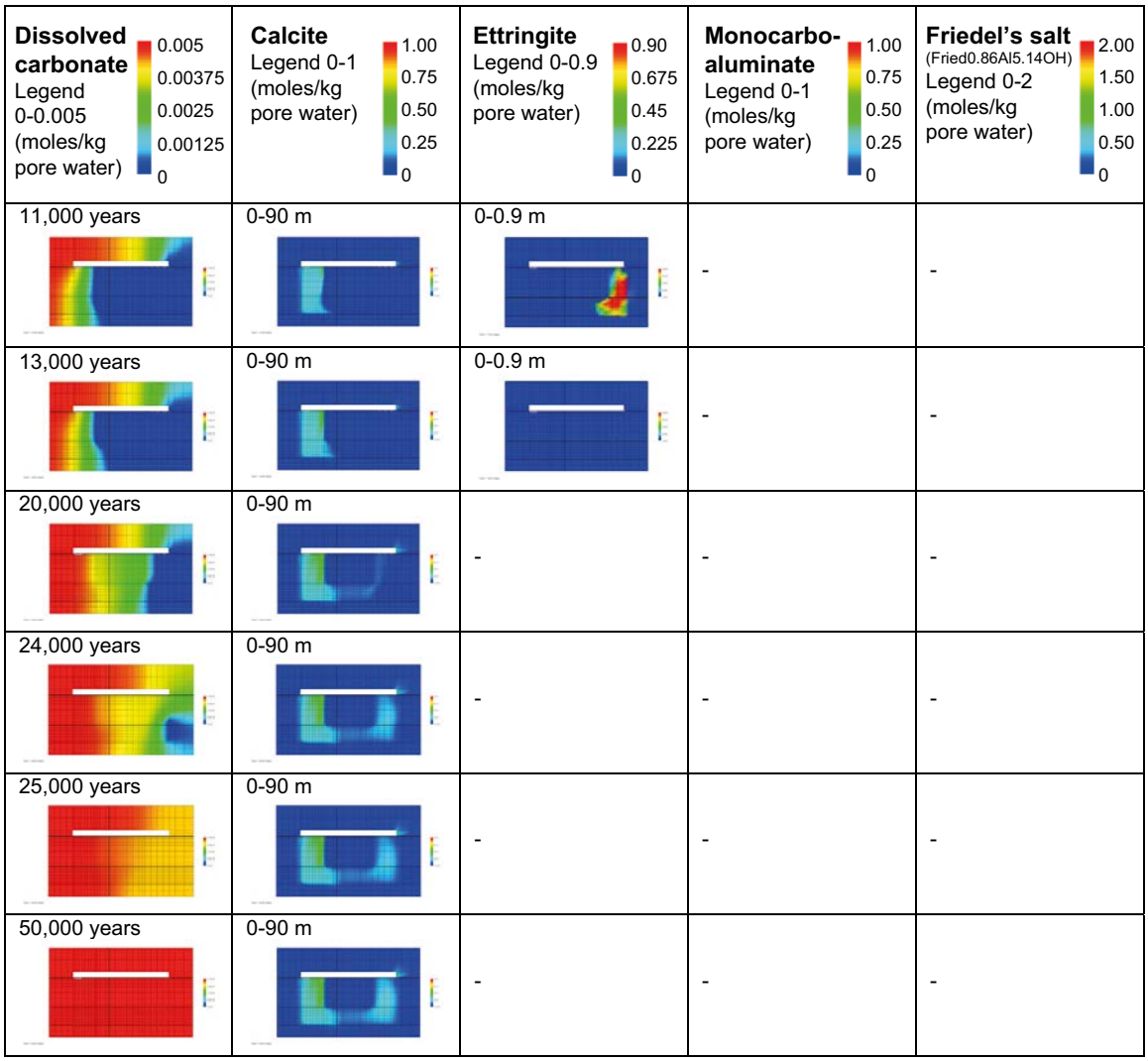

Figure 7-32. *Continued.*

Sulphate, chloride, hydrogarnet, ettringite, monocarboaluminate and Friedel's salt

Initially the dissolved sulphate and chloride concentrations are comparatively high, but they quickly decrease due to interactions with soluble components leached from the concrete, which causes a slight precipitation of ettringite and Friedel's salt. Hydrogarnet (C_3AH_6) and monocarboaluminate are consumed in the reaction with chloride ions to form Friedel's salt. The hydrogarnet phase disappears after 1,000–1,500 years and the monocarboaluminate almost disappears after ~ 2,000 years, see Figure 7-33. After 2,000 years, the composition of the groundwater changes and in response to this the Friedel's salt decomposes and disappears completely after ~ 3,400 years. Decomposition of the Friedel's salt leads to neoformation of monocarboaluminate. The monocarboaluminate in turn is replaced by an increased precipitation of ettringite, which is also accompanied by the reappearance of hydrogarnet (C_3AH_6). Both of these processes propagate as a front from left to right through the concrete structures during the period 2,200–7,000 years. Following this, ettringite dissolves and disappears completely by ~ 11,000–12,000 years. The reappearance of the hydrogarnet (C_3AH_6) is seemingly contradictory to the findings of Matschei and Glasser (2010) that the hydrogarnet would be destabilised in the presence of carbonate at temperatures < 40°C. However, these investigations assumed the presence of portlandite for all conditions, whereas the reappearance of hydrogarnet in the present study occurs in a section of the concrete wall where portlandite has been depleted.

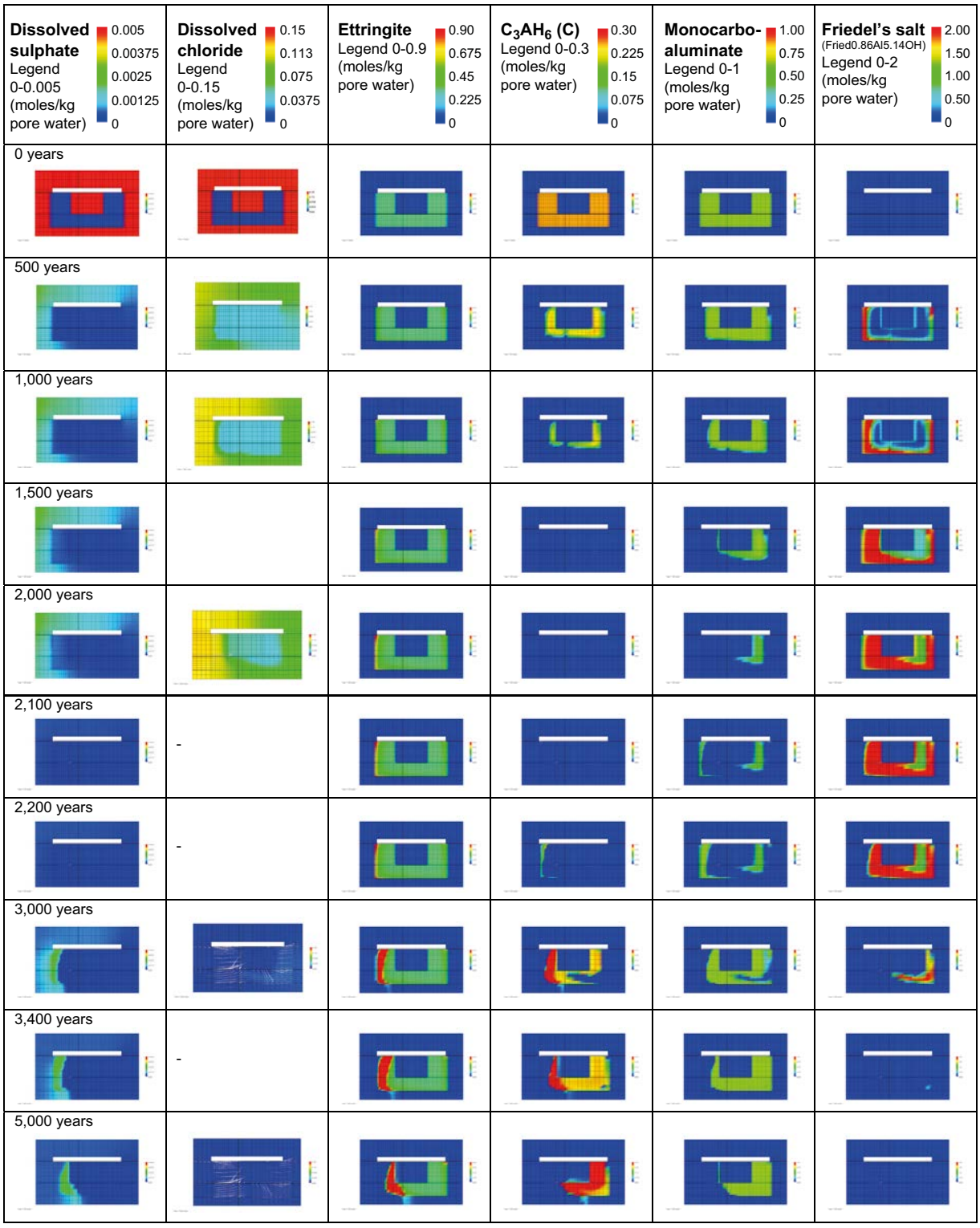

Figure 7-33. *Illustration of the gradual transformations between concrete mineral phases containing sulphate, chloride and/or aluminium over time. (MinteqCem-2001 database, Case Large10).*

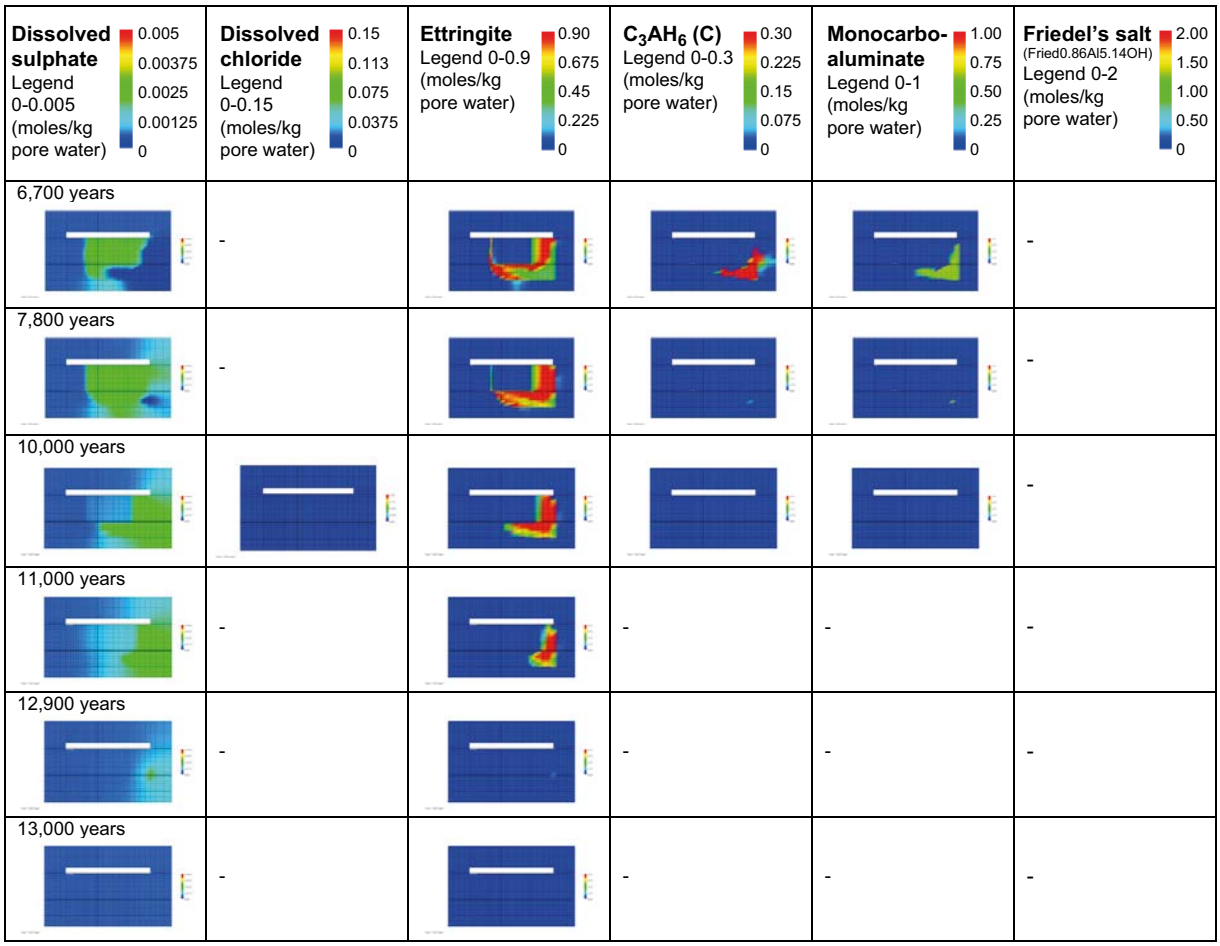

Figure 7-33. *Continued.*

The chloride intrusion is of importance also for the initiation of corrosion of steel components in the concrete. Applying criterion 1 (see Section 4.2.2), the threshold concentration of chloride is in the range of 0.023–0.04 M. The modelling results show that, due to ingress of chloride in the SFR groundwater, the lower-end of this threshold-range of chloride concentrations is exceeded within the first 100 years after closure of the repository, whereas the upper-end of the threshold-range is reached after ~ 500 years throughout the depth of the up-stream concrete wall. Consequently, chloride induced depassivation of steel in the concrete can be expected to initiate corrosion of steel components at an early time in the 1BMA vault. It should be noted that in this case (Large10) the thermodynamic database includes Friedel's salts. This means that the behaviour of the chloride ions includes chemical retention, which means that the chloride ingress is much slower compared with the case where Friedel's salts are neglected, cf. calculations for case Large8. The results expressed as the concentration profile of Friedel's salt through the concrete wall are presented at selected times in Figure 7-34.The numerical results of the chloride intrusion (considering the formation of Friedel's salts) also compare reasonably well with the results using a simplified analytical expression for a shrinking-core model in Section 5.2, Equation 5-61, see Figure 7-35.

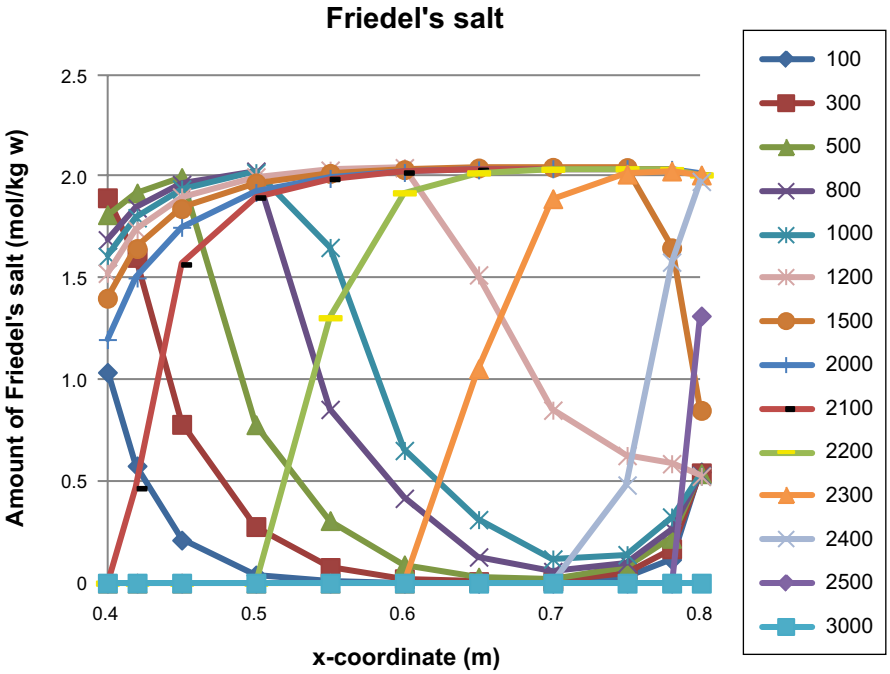

Figure 7-34. *Evolution of concentration profiles for Friedel's salt in a horizontal section through the up-stream side concrete wall. Legend shows the concentration profiles at different times (years).*

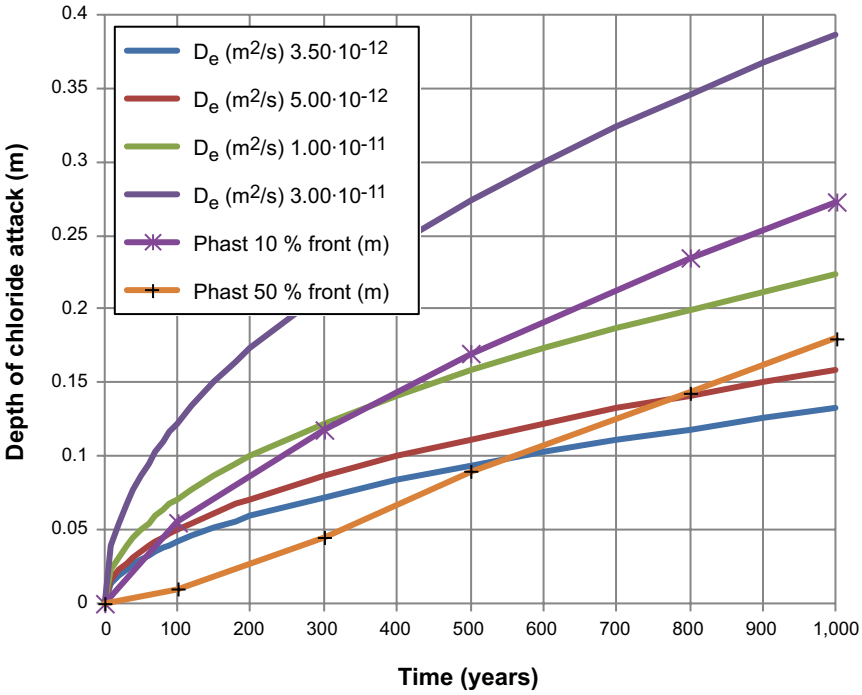

Figure 7-35. *Comparison of the chloride intrusion calculated by PHAST for case Large 10 (represented by the approximate front movement where 10% and 50% respectively of the maximum amount of Friedel's salt has formed) with a simple analytical shrinking-core model (assuming different effective diffusivities for illustration). During the first 1,000 years the diffusivity in the PHAST calculations changes in a stepwise manner from $3.5 \cdot 10^{-12}$ m^2/s (1–100 years) to $5 \cdot 10^{-12}$ m^2/s (100–1,000 years).*

Magnesium, iron and mineral reactions involving magnesium and iron

As in case Large20, the results show that the solubility limit of hydrotalcite is not exceeded and magnesium precipitates as brucite.

As the pH in the vault drops between 2,000–3,000 years, the dissolved magnesium concentration gradually increases in the sand/crushed rock bed around the concrete constructions. From 3,000 years, a sharp front of precipitating brucite on the left-hand, up-stream side of the left concrete wall is seen (Figure 7-36).

After ~ 10,000 years, in response to decreasing pH, the brucite starts to dissolve on the upstream side, while precipitation continues on the downstream side of the front.

Following the gradual depletion of alkaline components in the concrete, the magnesium concentrations in the concrete pore water increase, as seen from (~ 10,000 to ~ 30,000 years) in Figure 7-36 and ultimately levels off at the concentration determined by the inflowing groundwater after ~ 40,000 years as brucite becomes totally depleted, cf. case Large20 where brucite still is predicted to be present after 100,000 years.

The dissolved iron concentrations start to increase from the left-hand upstream side of the left concrete wall after ~ 3,000 years in response to decreasing pH and increased leaching of calcium, cf. Figure 7-36. The dissolution of C_3FH_6 slowly progresses as a front from left to right and results in a total depletion after ~ 24,000 years, cf. case Large20 where only a partial dissolution of C_3FH_6 is predicted to occur.

7.6 Case Large8 (1BMA)

This section describes the results from the modelling of case Large8. Supporting figures and diagrams are also presented in Appendix C. The basic assumptions regarding geometries and physical/hydraulic/transport parameters are the same as for case Large10 and the reader is referred to Section 7.3 for details. The major difference between the two cases is the thermodynamic database used, which is the Cemdata-07 database here rather than the MinteqCem-2001 database (Höglund 2001) for case Large10. A comparison of the mineral assemblages included in the different databases is presented in Section 7.1.

The presentation of the results first gives a brief overview of the evolution of the pore water chemistry and the mineral assemblage in one point in the cell grid at position AE, see Figure 7-8. Following this, the changes in the mineralogy at point DE, near the fracture, are presented. Finally, the evolution in the full 2-D-grid is presented and more detailed comments are given.

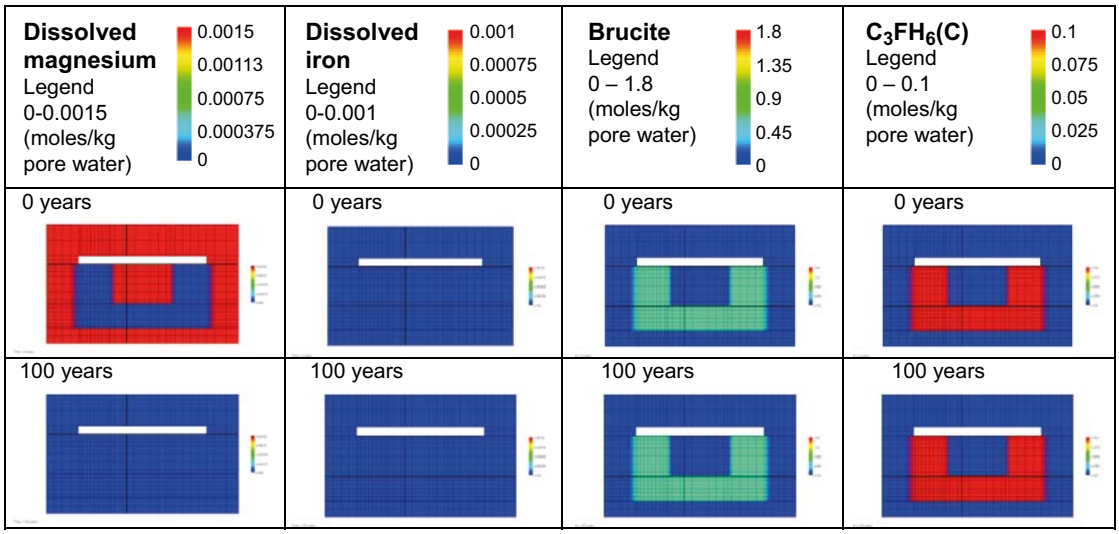

Figure 7-36. *Illustration of the change of dissolved magnesium and iron and the gradual transformations between concrete mineral phases containing magnesium and iron over time. (MinteqCem-2001 database, Case Large10).*

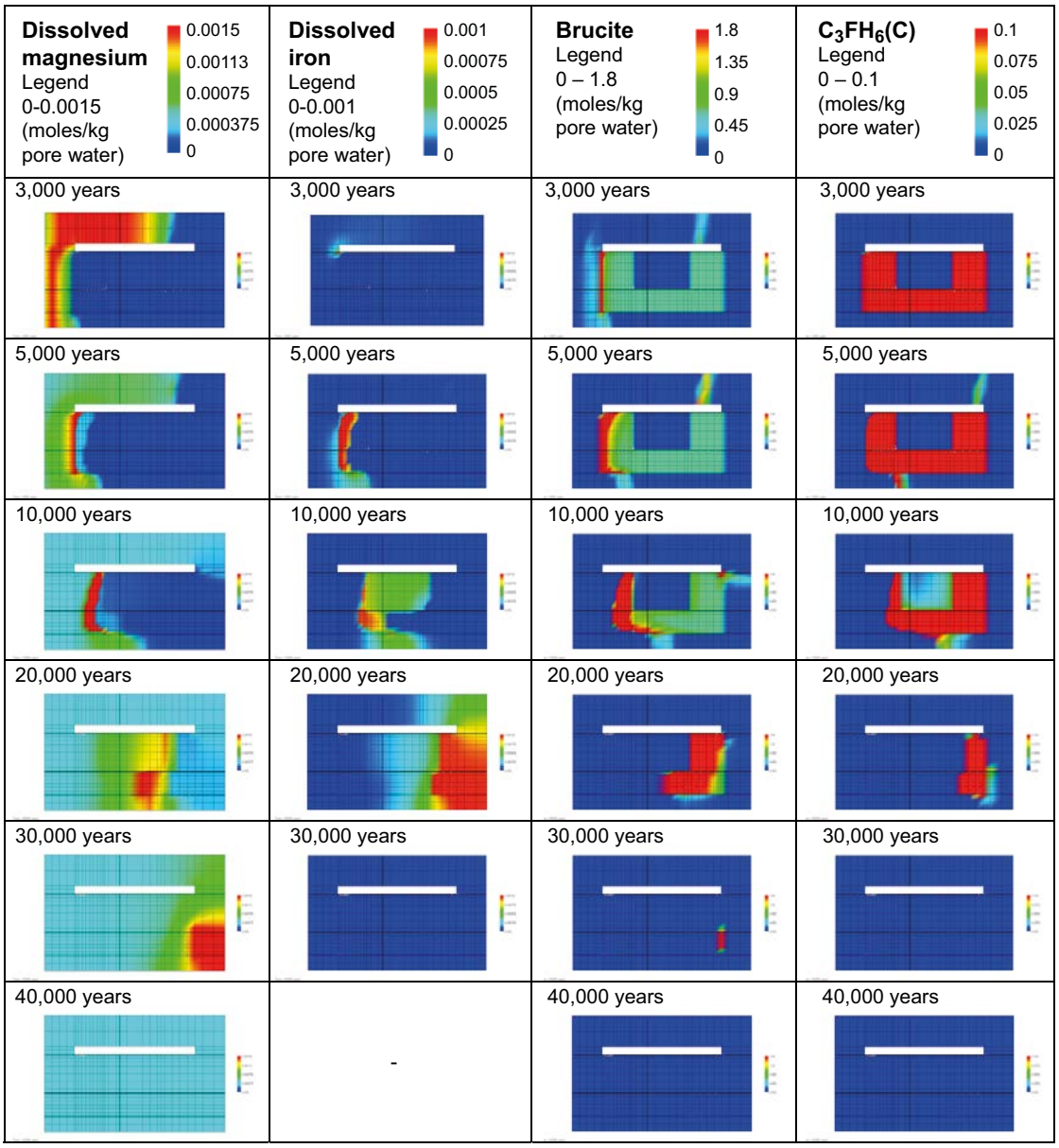

Figure 7-36. *Continued.*

7.6.1 Evolution of chemistry and mineralogy at evaluation points

Evaluation point AE – at the intersection of the centrelines of the concrete floor and the left-hand side concrete wall

The ingress of chloride and gradual exchange of potassium for sodium in the CSH-gel is evident during the first 2,000 years, which is followed by a significant drop in the chloride concentration after 2,000 years, see Figure 7-37. The pH is initially high, but decreases as different buffers are leached out of the system. The evolution of pH and dissolved components over longer times is shown in Figure 7-38. After ~ 30,000 years, the pH approaches a final value of ~ 7.5, corresponding to the natural groundwater.

The changes in mineralogy and porosity over the first 43,000 years are shown in Figure 7-39 (volume of individual minerals) and in Figure 7-40 (accumulated mineral volumes) over the first 10,000 years. The results suggest that an initial concrete porosity of 11% at position AE would increase to ~ 22% by 8,000 years, which is broadly similar to the porosity of 23% after 9,000 years calculated in Large10. However, since different databases were used, there are distinct differences in the mineral assemblages calculated over time, as well as in the detailed porosity changes over time. The porosity is presented over the range of 0–30% in Figure 7-39 and Figure 7-40; the maximum porosity corresponding to fully depleted cement minerals would be ~ 30%, the remaining volume constitutes the ballast material which is assumed to be inert.

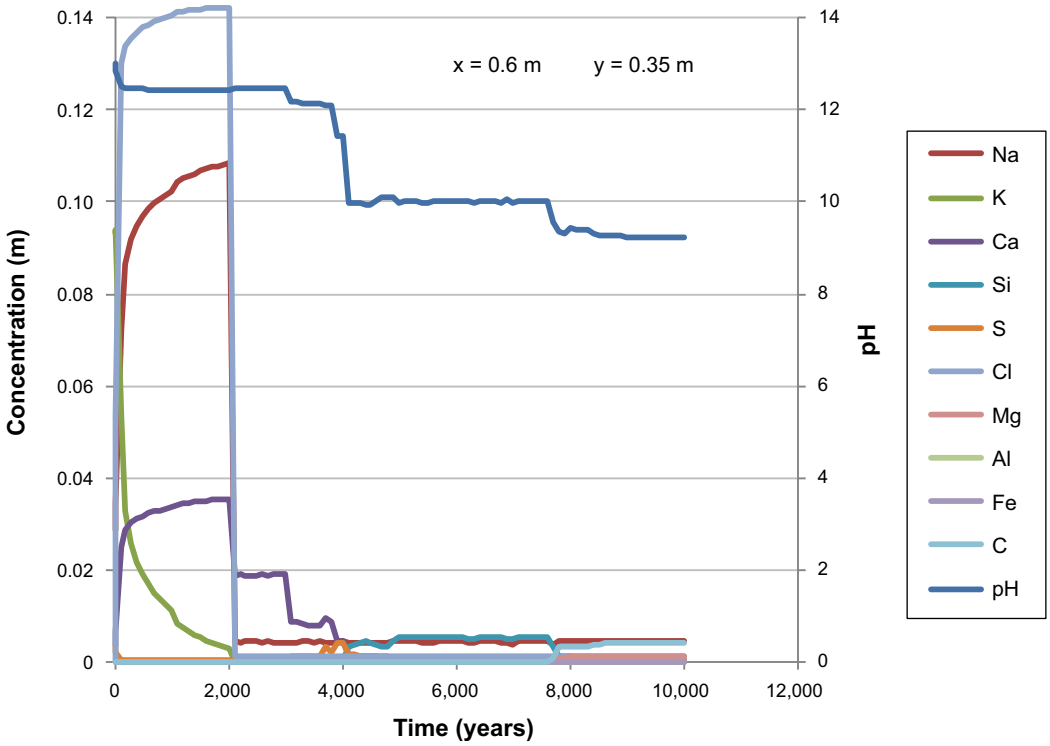

Figure 7-37. *The development of the concentration of dissolved components in concrete pore water over time (during the first 10,000 years) at position AE (a point located at the intersection of a vertical centreline through the left-hand side concrete wall and a horizontal centreline through the concrete floor), case Large8.*

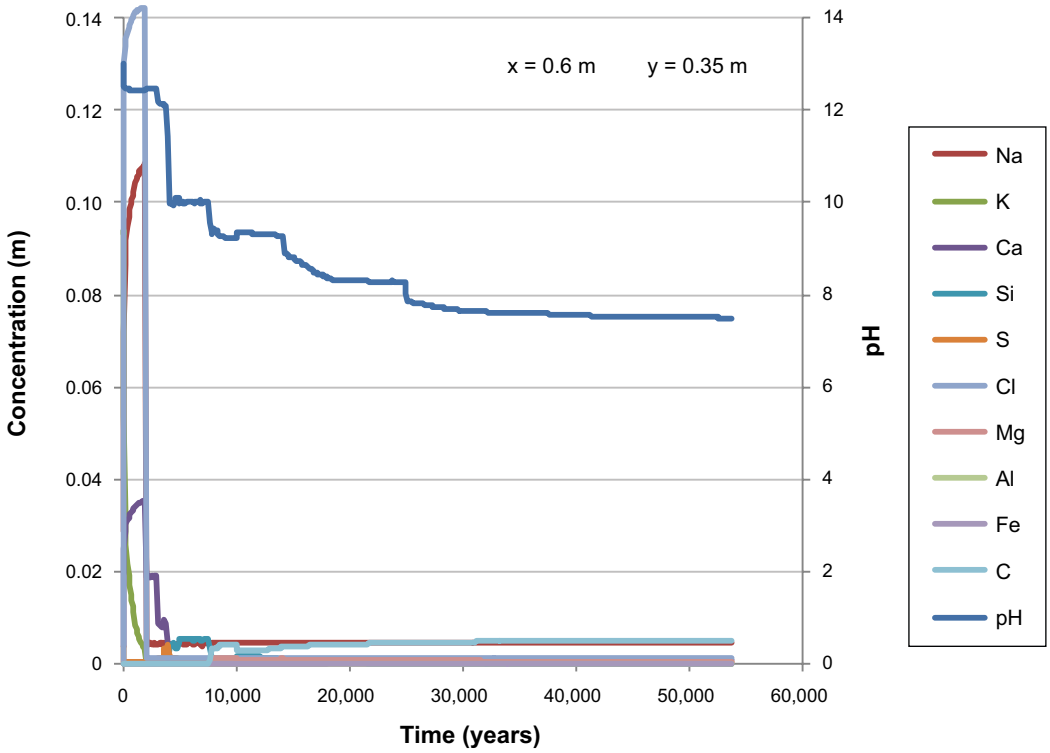

Figure 7-38. *The development of the concentration of dissolved components in concrete pore water over time (during the first 53,800 years) at position AE (a point located at the intersection of a vertical centreline through the left-hand side concrete wall and a horizontal centreline through the concrete floor), case Large8.*

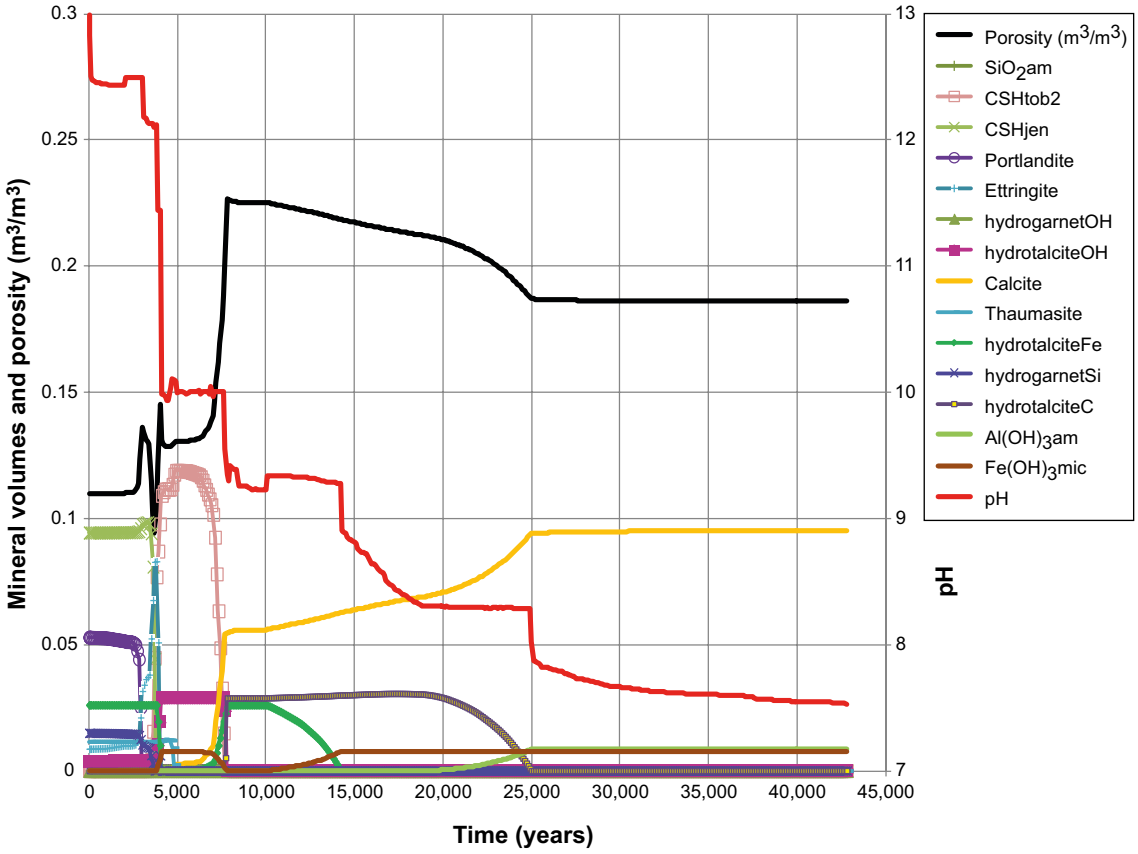

Figure 7-39. *Evolution of the mineral assemblage (during the first 43,000 years) at position AE (a point located at the intersection of a vertical centreline through the left-hand side concrete wall and a horizontal centreline through the concrete floor), case Large8.*

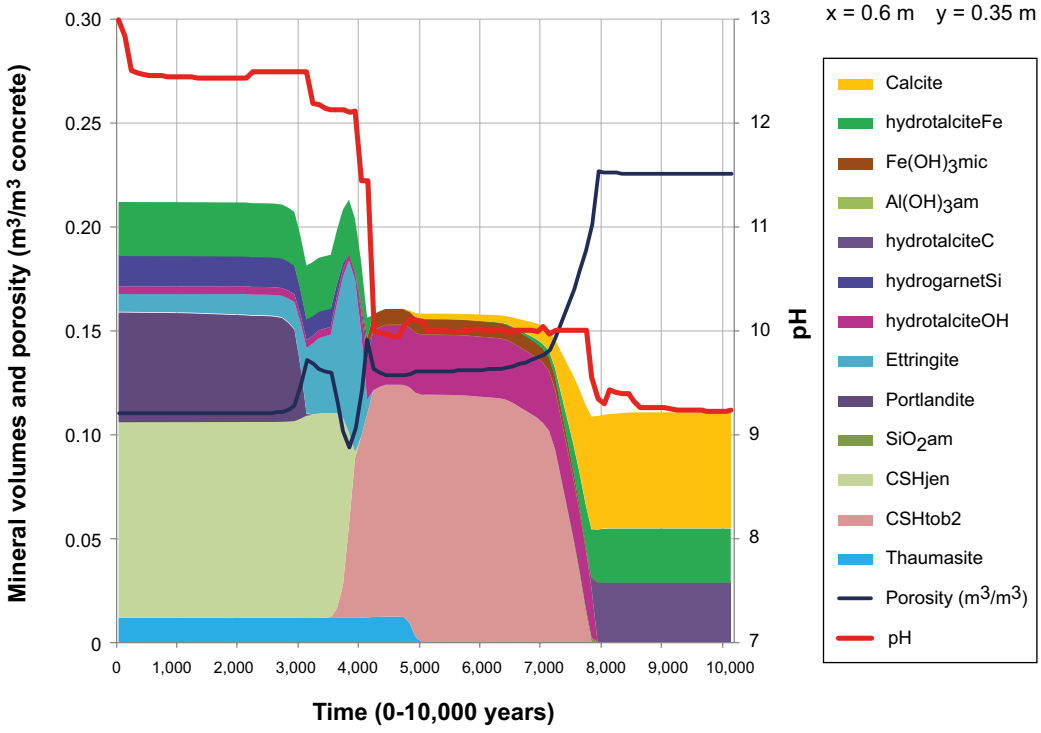

Figure 7-40. *The change of mineral volumes and porosity in concrete during 10,000 years at position AE (a point located at the intersection of a vertical centreline through the left-hand side concrete wall and a horizontal centreline through the concrete floor), case Large8. The evolution of pH with time is also indicated.*

In terms of the mineralogical changes, an enhanced rate of portlandite dissolution after 2,000 years causes the porosity to increase, while the precipitation of ettringite then causes a reduction of the porosity between 3,000–4,000 years. Following the subsequent dissolution of ettringite, the porosity again rises distinctly after ~4,000 years. The next significant events are the transformation of CSHjen to CSHtob2, dissolution of hydrotalciteFe and the precipitation of hydrotalciteOH and $Fe(OH)_3$mic, which is accompanied by a decrease in porosity after ~ 4,200 years. From ~ 4,500 years, thaumasite is dissolved and leads to precipitation of CSHtob2 and small amounts of calcite, thereafter the porosity increases gradually as a result of dissolution of CSHtob2 and hydrotalciteOH, accompanied by further precipitation of calcite. The evolution of pH, dissolved calcium and silica follow the evolution of portlandite and the CSH-gels and relates well with the observations in nature, e.g. Miller et al. (2000). After ~7,000 years $Fe(OH)_3$mic dissolves and hydrotalciteFe reappears. Increased calcite precipitation occurs after ~6,500 years, accompanied by dissolution of CSHtob2, and as CSHtob2 is depleted after ~7,700 years a transformation occurs of hydrotalciteOH to hydrotalciteC.

Similar to Large10, the changes in the porosity between 2,000–5,000 years are a matter of some concern for the integrity of the concrete. In particular, ettringite and thaumasite precipitation may cause detrimental fracturing of the concrete due to the expanding character of these minerals, see discussions on the theoretical background to this in Chapter 4 of the report.

Evaluation point DE – at the vertical centreline of the left-hand side concrete wall near the thin horizontal fracture

The progression of the dissolved components and the pH follows the same general pattern as at evaluation point AE discussed above, although the observed changes occur more rapidly near the fracture, compare Figure 7-37 and Figure 7-38 with Figure 7-41 and Figure 7-42.

The gradual evolution of the mineral assemblage is shown in Figure 7-43 together with the calculated changes of the porosity during the first 10,000 years. The results show that the porosity would be expected to increase from the initial value of 11% to ~ 22% after 6,000 years. The porosity is presented over the range of 0–25% in Figure 7-43; the maximum porosity corresponding to fully depleted cement minerals would be ~ 30%, the remaining volume constitutes the ballast material which is assumed to be inert.

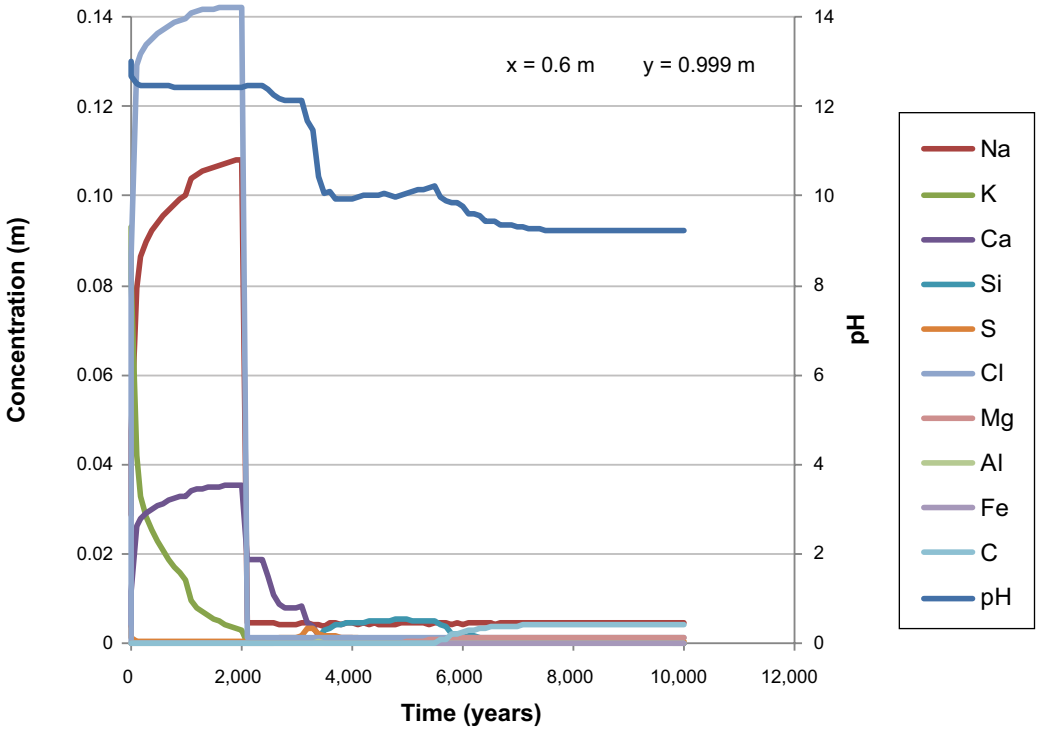

Figure 7-41. *The development of the concentration of dissolved components in concrete pore water over time (during the first 10,000 years) at position DE (1 mm from the centreline of an open fracture), case Large8.*

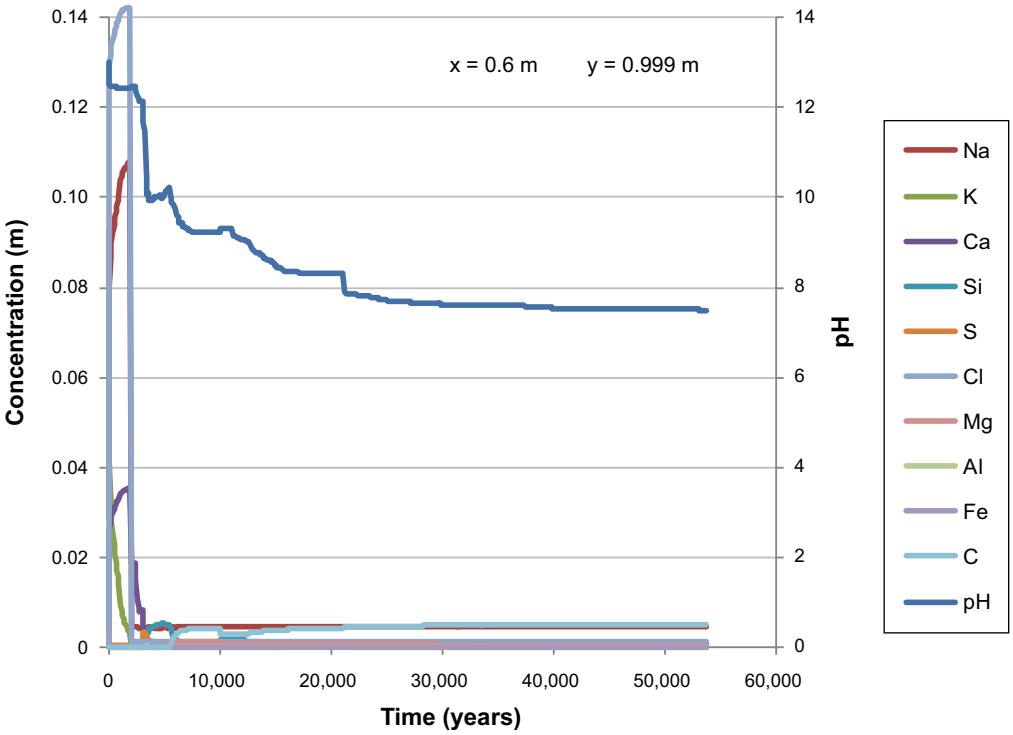

Figure 7-42. *The development of the concentration of dissolved components in concrete pore water over time (during the first 53,800 years) at position DE (1 mm from the centreline of an open fracture), case Large8.*

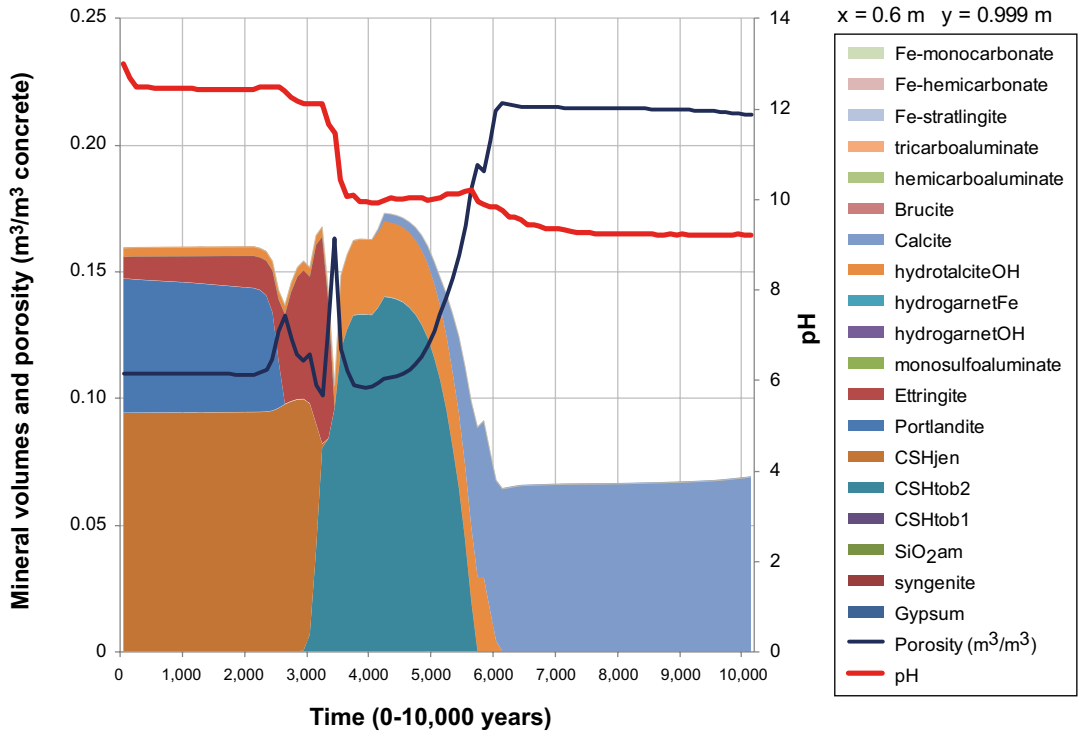

Figure 7-43. *The change of mineral volumes and porosity in concrete during 10,000 years at position DE (1 mm from the centreline of an open fracture), case Large8. The evolution of pH with time is also indicated.*

7.6.2 Evolution of the chemistry and mineralogy of the 2-D system

Ion exchange reactions of alkali metals and calcium

Initially, the high pH in the concrete is due primarily to the presence of potassium hydroxide, whereas the content of sodium is somewhat lower. The concentration of calcium is also low due to the suppression of the solubility of portlandite at the high pH created by the potassium hydroxide. Following the gradual exchange of soluble components with the groundwater, which is rich in sodium, the potassium is washed out and the calcium concentration increases as the solubility of portlandite becomes the major pH-regulating component in the system, see Figure 7-44.

pH evolution, calcium and silica depletion

The evolution of the pH, along with calcium and silica leaching is summarised in Figure 7-45. As in case Large10, the leaching processes are seen to occur much more rapidly than calculated for intact concrete (Large20, 2BMA). Portlandite is first dissolved at the surface of the inflow side of the upstream-side concrete wall after ~2,000–3,000 years. Consistent with this, the model results show that a high pH (> 12.5) is only maintained throughout the concrete constructions over the first 2,000 years. After this point, a significant increase in the groundwater flow rate is assumed due to the transition from the saltwater period to the freshwater period (caused by the land rise that moves the shore-line in the Forsmark area), with an associated change in the chemical composition of the groundwater. As can be seen in Figure 7-45, the pH gradually drops, starting at the left-hand inflow side, where the pH approaches ~ 11 in the outer layers of the concrete wall and accentuated adjacent to the horizontal fracture after ~ 3,000 years. A gradual depletion of calcium also starts to show at 3,000 years and propagates over time. During the period 5,000 through 6,700 years, the pH of the concrete wall on the left-hand inflow side of the model drops to ~ 10, while the pH inside the open void (representing the vaults where the waste is stored) remains at ~ pH 11. By 10,000 years, only small parts at the right-hand down-stream side of the concrete constructions contribute any significant concentrations of calcium to the pore water (note the change of scale in the figure). After 10,000 years, almost the entire vault has reached a pH of ~ 10 or lower, after 20,000 years the pH approaches ~ pH 9 and after 60,000 years, the natural pH of the groundwater – bedrock system has been re-established.

The dependence of pH on the gradual depletion and transformation of the minerals representing the CSH-gel (CSHjen and CSHtob2 respectively) are presented in Figure 7-45. During the portlandite-controlled phase, the CSH-gel (CSHjen) remains inactive. When portlandite is depleted, the CSH-gel starts to respond to the changed chemical conditions. The amount of CSHjen (Ca/Si = 1.67) is gradually transformed into the less alkaline CSHtob2 (Ca/Si = 0.83) (which starts to appear after ~ 3,000 years). After 5,000 years a substantial replacement of CSHjen by CSHtob2 has occurred in the concrete wall and the concrete floor at the left-hand side (near the inflow). A pronounced effect is also visible near the horizontal fracture through the wall, where the transformation is more rapid. After 6,700 years portlandite is almost entirely depleted and the transformation of CSHjen to CSHtob2 progresses. After 10,000 years the only remaining CSH-component is CSHtob2, which in turn becomes depleted after ~ 15,000 years. At this point, any resemblance of the remaining material to the initial concrete is difficult to envisage. Towards the final stages of CSH-gel degradation, pure silica (SiO_2am) forms near the receding rim of the dissolving CSHtob2 (not shown here). The silica thereafter dissolves and finally disappears after ~ 22,000 years, see Appendix C for additional details. Although the CSH phases included in the Cemdata-07database are slightly different to those in MinteqCem-2001, the patterns and timescales of the dissolution of the CSH gel phases seen after the depletion of portlandite are similar to those in case Large10.

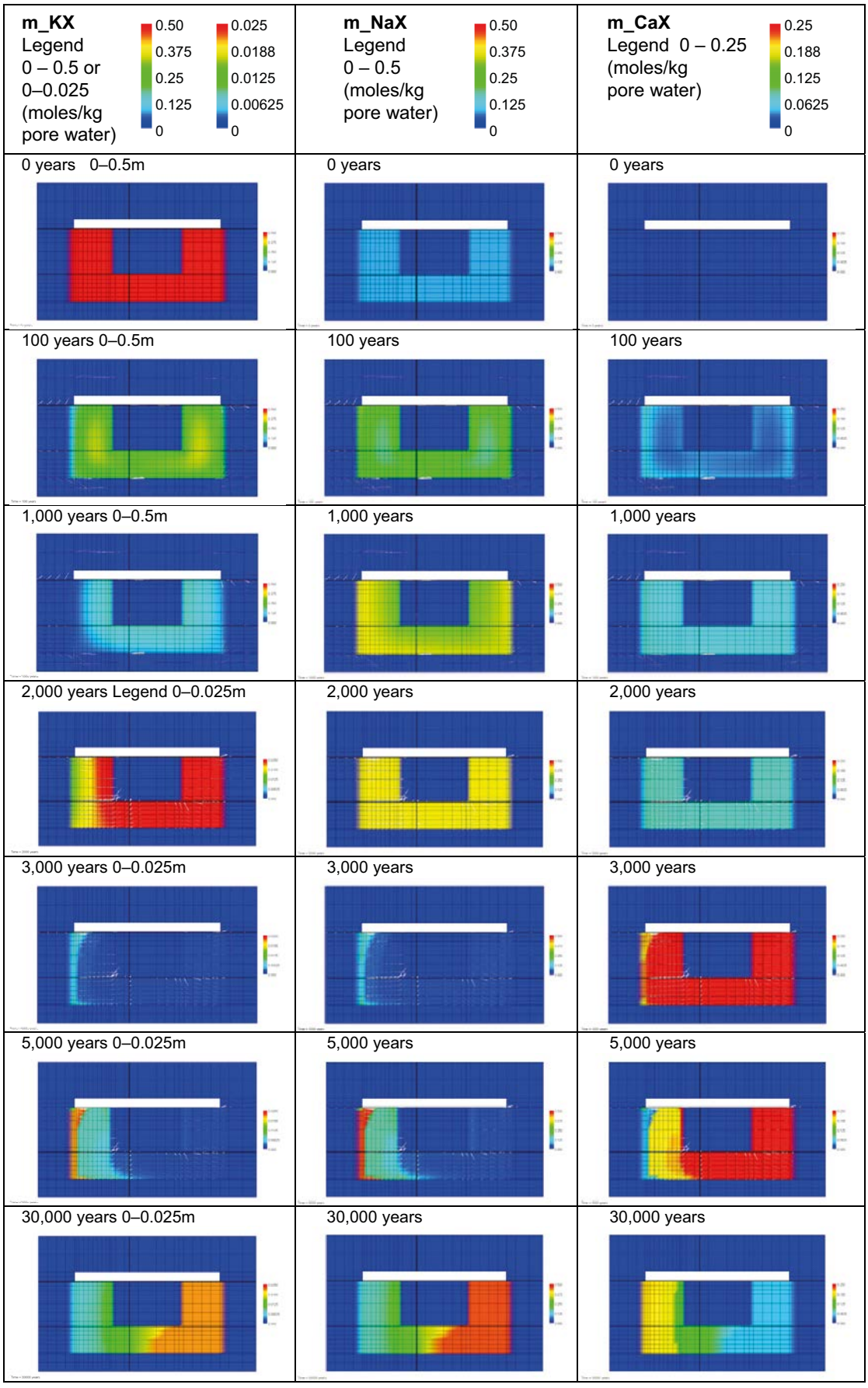

Figure 7-44. *Illustration of the gradual ion exchange processes of potassium, sodium and calcium ions during the first 30,000 years. (Cemdata07 database, Case Large8). Observe the change of scale in the legend for potassium exchange species after 2,000 years.*

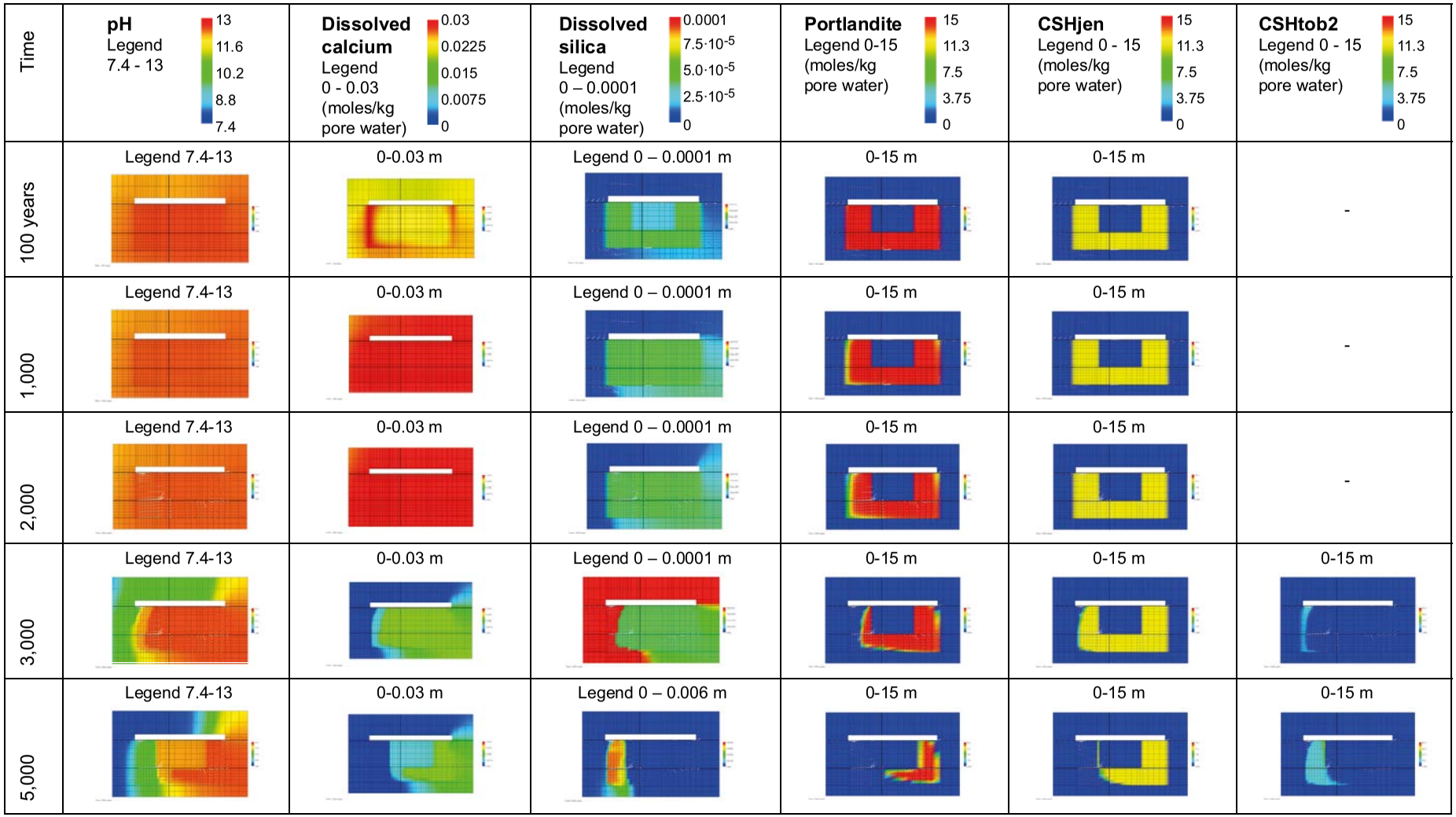

Figure 7-45. *Illustration of the gradual evolution of pH and concentration of dissolved calcium and silica as a result of depletion and transformation of portlandite and CSH-gel phases. (Cemdata07 database, Case Large8).*

Time	**pH** Legend 7.4 - 13 (13, 11.6, 10.2, 8.8, 7.4)	**Dissolved calcium** Legend 0 - 0.03 (moles/kg pore water) (0.03, 0.0225, 0.015, 0.0075, 0)	**Dissolved silica** Legend 0 – 0.0001 (moles/kg pore water) (0.0001, $7.5{\cdot}10^{-5}$, $5.0{\cdot}10^{-5}$, $2.5{\cdot}10^{-5}$, 0)	**Portlandite** Legend 0-15 (moles/kg pore water) (15, 11.3, 7.5, 3.75, 0)	**CSHjen** Legend 0 - 15 (moles/kg pore water) (15, 11.3, 7.5, 3.75, 0)	**CSHtob2** Legend 0 - 15 (moles/kg pore water) (15, 11.3, 7.5, 3.75, 0)
6,700	Legend 7.4-13 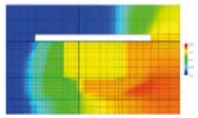	0-0.03 m 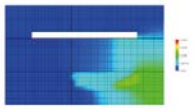 0-0.001 m 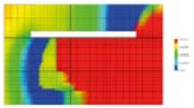	Legend 0 – 0.006 m 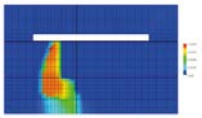	0-15 m 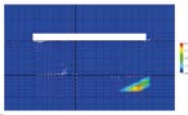	0-15 m 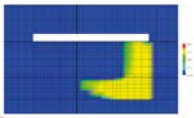	0-15 m 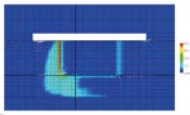
10,000	Legend 7.4-13 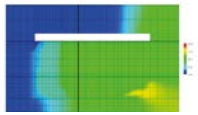	0-0.001 m 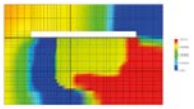	Legend 0 – 0.006 m 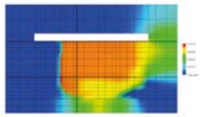	-	0-15 m 	0-15 m 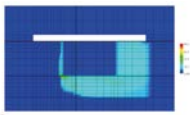
15,000	Legend 7.4-13 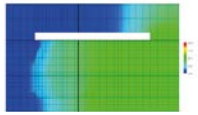	0-0.001 m 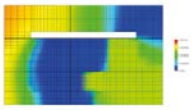	Legend 0 – 0.006 m 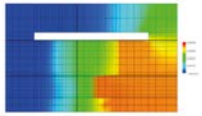	-	-	0-15 m 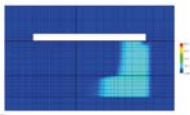
20,000	Legend 7.4-13 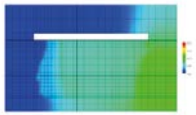	0-0.001 m 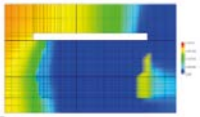	-	-	-	-
60,000	Legend 7.4-13 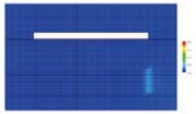	0-0.001 m 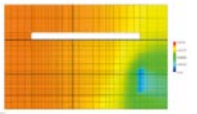	-	-	-	-

Figure 7-45. *Continued.*

Carbonate, calcite, thaumasite, monocarboaluminate and hydrotalciteC

The model results show that calcite precipitation occurs at an early stage near the groundwater inflow at the left-hand side of the model. This involves the reaction of the dissolved calcium released from the concrete with carbonate in the groundwater that enters the vault. The carbonate content of the groundwater is fairly low during the saltwater period and will be further reduced by this reaction. Figure 7-46 shows the calcite precipitated at 100 years.

The carbonate concentration increases as the groundwater changes from salt- to freshwater after 2,000 years, see Figure 7-47. During the period 2,000–5,000 years, calcite continues to precipitate primarily on the left-hand upstream side of the vault (see Figure 7-47), where the carbonate in groundwater meets calcium leached from the concrete constructions. Following the gradual depletion of minerals containing calcium, hydrotalciteC replaces the dissolving CSHtob2, followed by a complete replacement of hydrotalciteC by calcite at later stages, see Figure 7-47. The precipitation of thaumasite (a mineral containing sulphate, carbonate and silica) is activated by the approaching major front of calcite precipitation that occurs after approximately 3,000 years. However, an increased in thaumasite precipitation only takes place in a thin zone, behind which the thaumasite dissolves. Nevertheless, the occurrence of a moving front of precipitating and redissolving thaumasite may be detrimental for the integrity of the concrete. Monocarboaluminate remains passive and is of subordinate importance in this case. After 60,000 years the natural conditions of the groundwater – bedrock system has been re-established and is governed mainly by carbonate-calcite equilibria.

Figure 7-46. *Calcite precipitation due to the reaction between calcium leached from the concrete and carbonate in the inflowing groundwater. Units are kmol/m³ of pore water. Blue colour denotes that no calcite is present, red colour denotes the maximum precipitation of 0.01 kmol/m³ of pore water.*

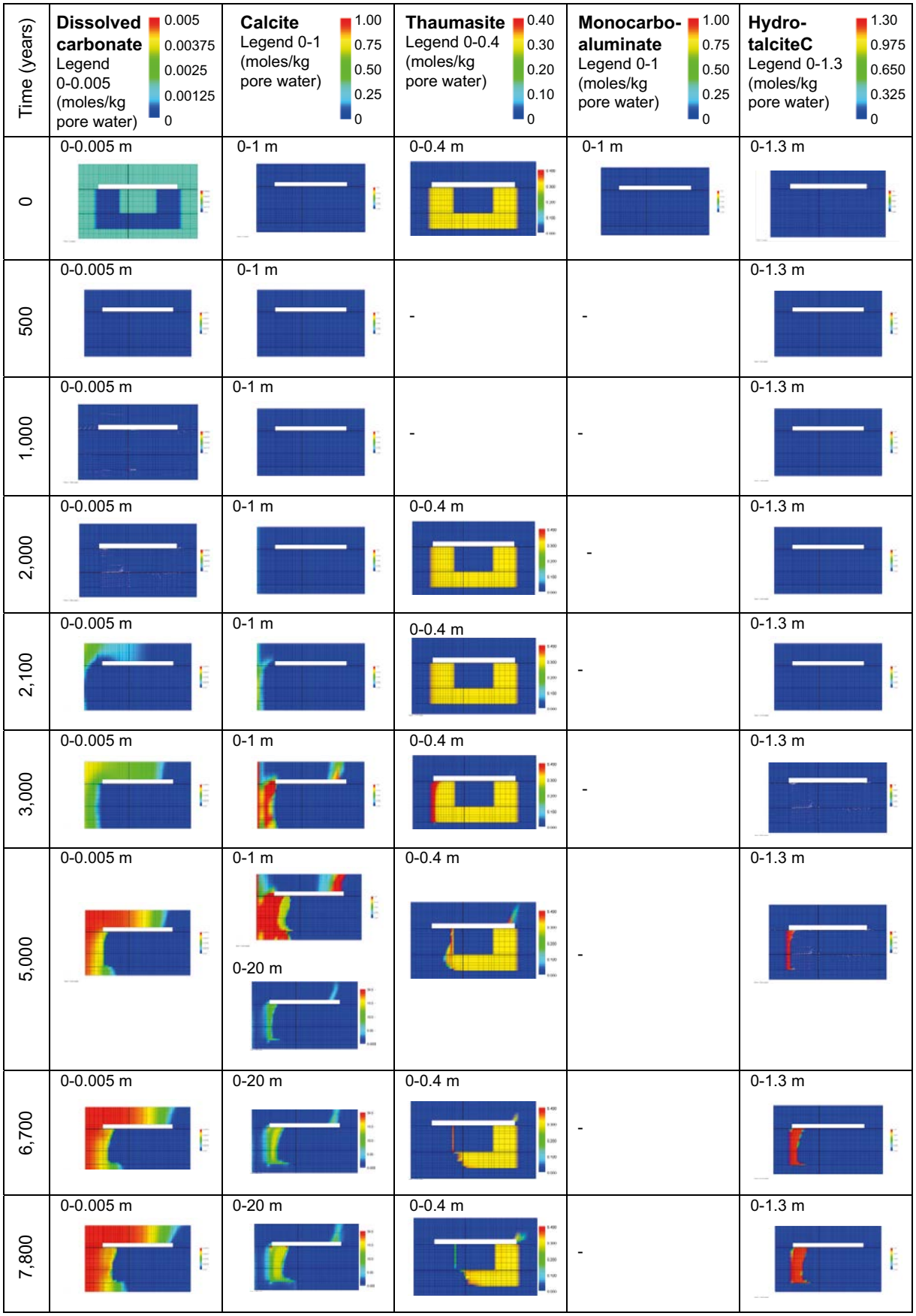

Figure 7-47. *Illustration of the change of dissolved carbonate and of the gradual transformations between concrete mineral phases containing carbonate and/or aluminium over time. (Cemdata07 database, Case Large8). Observe the changes of scale in the legend for calcite after 5,000 years and 20,000 years.*

Time (years)	**Dissolved carbonate** Legend 0-0.005 (moles/kg pore water) 0.005 0.00375 0.0025 0.00125 0	**Calcite** Legend 0-1 (moles/kg pore water) 1.00 0.75 0.50 0.25 0	**Thaumasite** Legend 0-0.4 (moles/kg pore water) 0.40 0.30 0.20 0.10 0	**Monocarbo-aluminate** Legend 0-1 (moles/kg pore water) 1.00 0.75 0.50 0.25 0	**Hydro-talciteC** Legend 0-1.3 (moles/kg pore water) 1.30 0.975 0.650 0.325 0
10,000	0-0.005 m 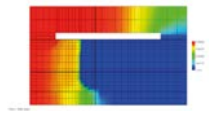	0-20 m 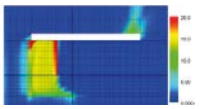	0-0.4 m 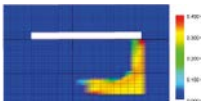	-	0-1.3 m 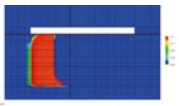
11,000	0-0.005 m 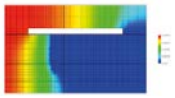	0-20 m 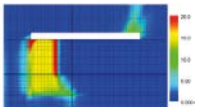	0-0.4 m 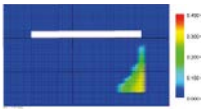	-	0-1.3 m 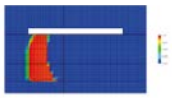
13,000	0-0.005 m 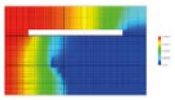	0-20 m 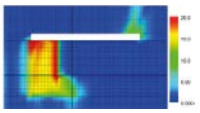	-	-	0-1.3 m 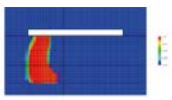
16,000	0-0.005 m 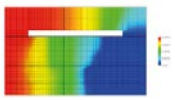	0-20 m 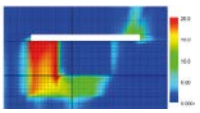	-	-	0-1.3 m 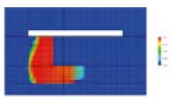
20,000	0-0.005 m 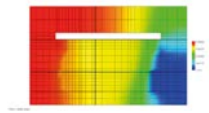	0-40 m 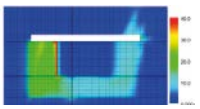	-	-	0-1.3 m 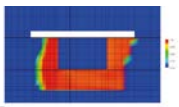
25,000	0-0.005 m 	0-40 m 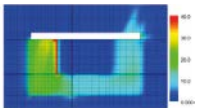	-	-	0-1.3 m 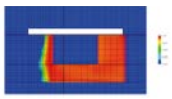
30,000	0-0.005 m 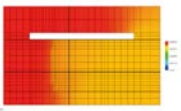	0-40 m 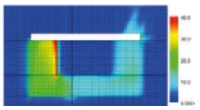	-	-	0-1.3 m 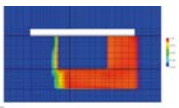
40,000	0-0.005 m 	0-40 m 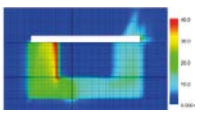	-	-	0-1.3 m 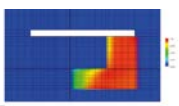
50,000	0-0.005 m 	0-40 m 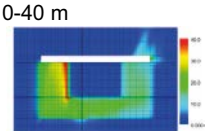	-	-	0-1.3 m 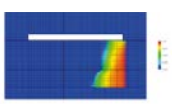
60,000	0-0.005 m 	0-40 m 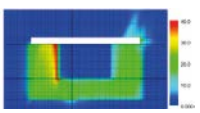	-	-	0-1.3 m 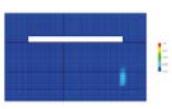

Figure 7-47. *Continued.*

Chloride

Chloride concentrations are assumed to be low in the fresh concrete, whereas the chloride content of the groundwater is high during the saltwater period. Chloride will act as a tracer in the calculations for case Large8 since there are no minerals containing chloride in the database Cemdata07 that have low enough solubility to precipitate. Hence, a rapid ingress of chloride in the concrete pores is shown by the results in Figure 7-48. After 2,000 years the groundwater changes character and the chloride is rapidly washed out.

The results show that after only a few decades, the pH in the concrete drops to ~ 12.75–12.5, corresponding to a hydroxide ion concentration in the range of 0.038–0.067 M (cf. Figure 7-45). The chloride intrusion is of importance also for the initiation of corrosion of steel components in the concrete. Applying criterion 1 (see Section 4.2.2), the threshold concentration of chloride is in the range of 0.023–0.04 M. The modelling results show that the threshold chloride concentrations are exceeded shortly after closure of the repository, due to ingress of chloride in the SFR groundwater. Consequently, chloride induced depassivation of steel in concrete can be expected to initiate corrosion of steel components at an early time in the 1BMA vault. It should be noted that in case Large8 the thermodynamic database used does not include Friedel's salts. This means that in this case the chloride ions behave as conservative species without chemical retention and the chloride ingress is very rapid, cf. calculations for case Large10 which considers the effects of formation of Friedel's salts. After 3,000 years the changes of the chloride concentrations are negligible and have therefore been omitted from the figure.

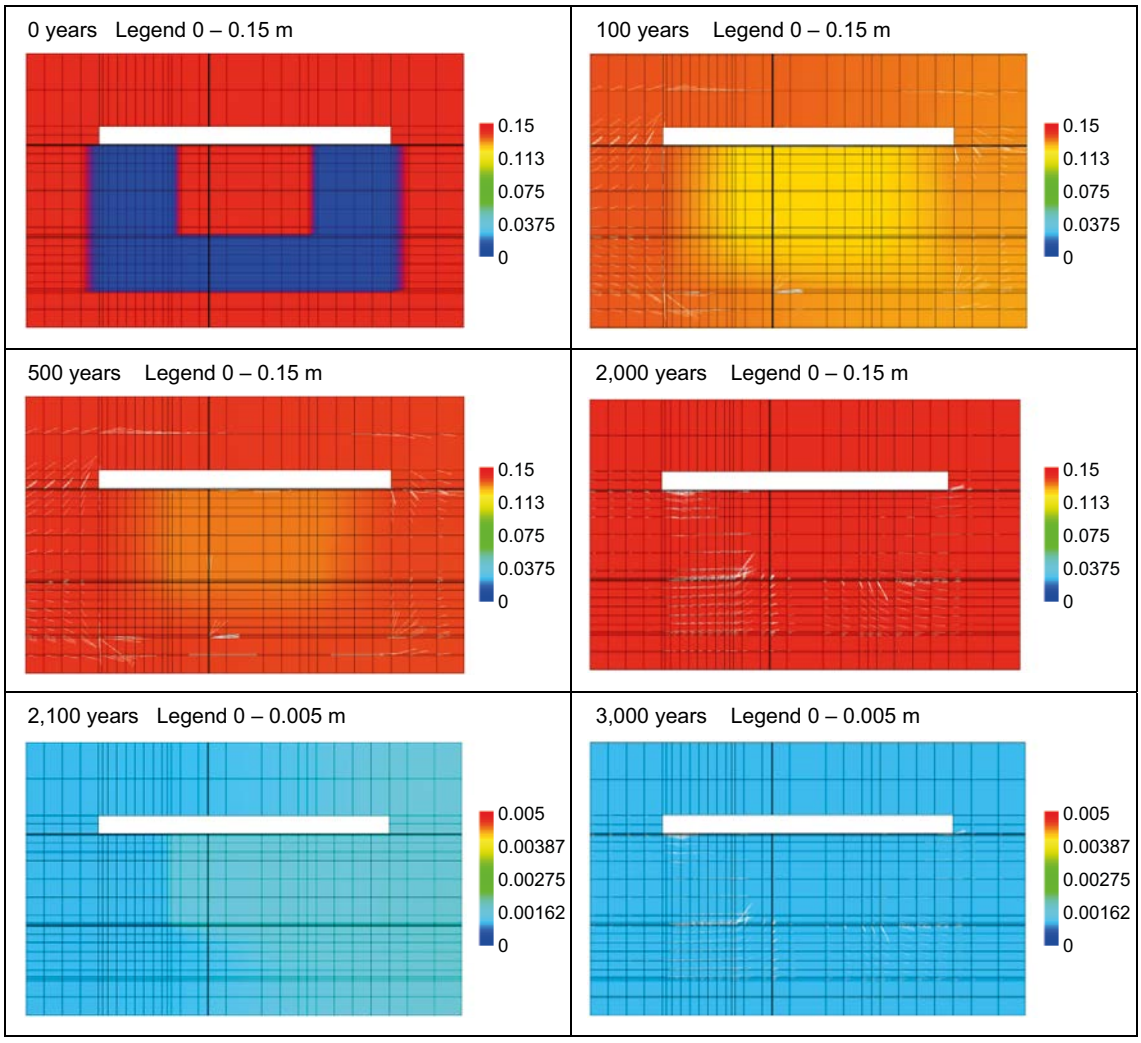

Figure 7-48. *Snap-shots of the dissolved chloride concentrations after 0, 100, 500, 2,000, 2,100 and 3,000 years. Observe the change of scale after 2,100 years. (Cemdata07 database, Case Large8). Units in (moles/kg pore water).*

Sulphate, hydrogarnet, ettringite, thaumasite and aluminium

Initially the dissolved sulphate concentration is comparatively high, but it is rapidly reduced through interactions with soluble components leached from hydrogarnetSi (which acts as a source of aluminium) and causes a slight precipitation of ettringite. This system then remains fairly constant up to 2,000 years. After this, the available aluminium increases as a result of dissolution of hydrogarnetSi and the precipitation of ettringite becomes more pronounced from 3,000 to 10,000 years, see Figure 7-49. From 3,000 years, thaumasite (a mineral containing sulphate, carbonate and silica) also becomes active and forms an enriched rim that precipitates in the same area as ettringite. However, this subsequently dissolves in a moving front and is eventually depleted after 11,500 years. Both the ettringite and thaumasite formation should be regarded as deleterious processes that may cause the concrete to lose strength and integrity, potentially peeling off parts of the concrete along the moving fronts. Starting at 10,000 years, the precipitation of $Al(OH)_3am$ progresses as a front in the direction of the groundwater flow where it replaces dissolving hydrotalciteC (c.f. Figure 7-47).

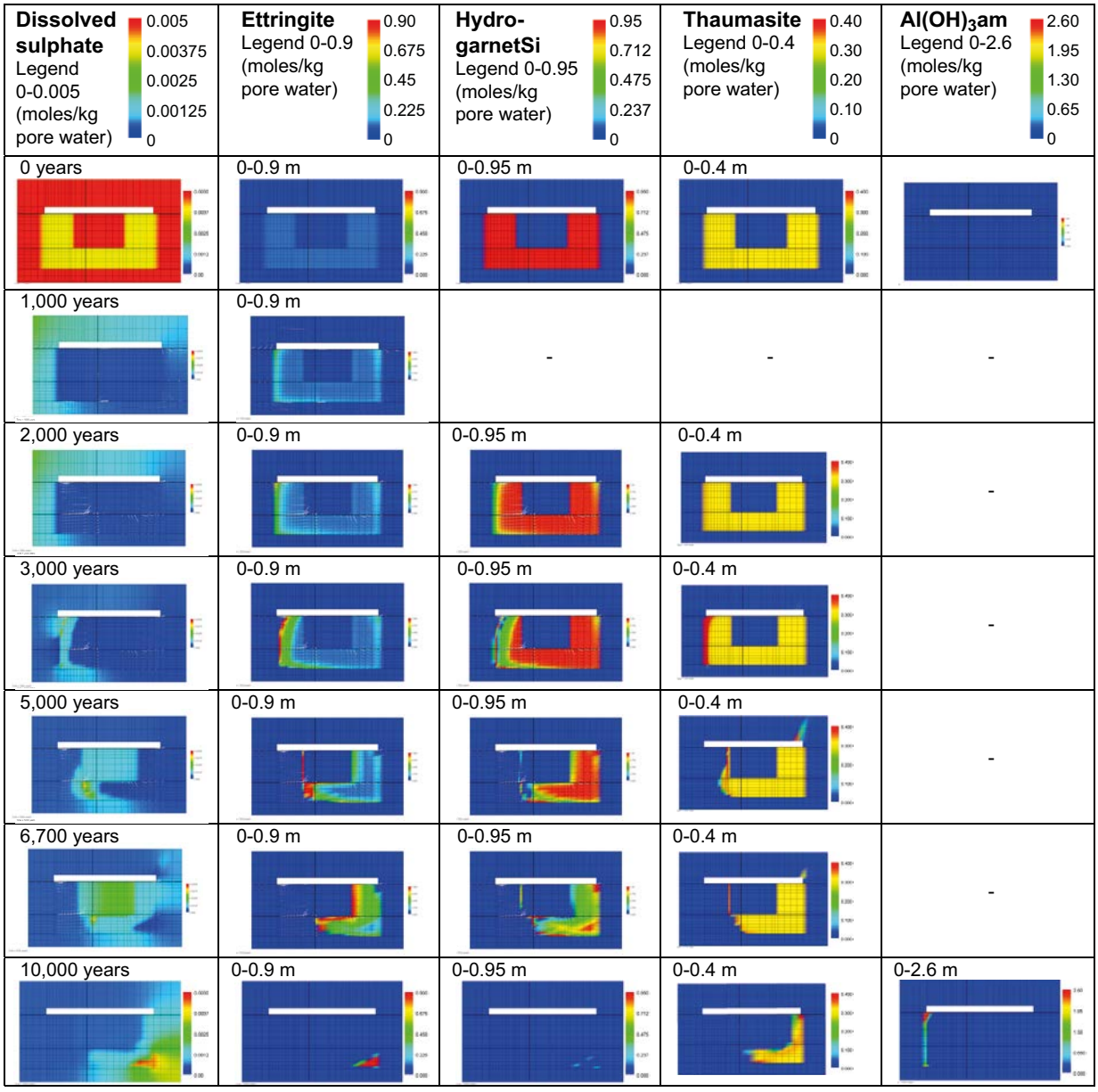

Figure 7-49. *Illustration of the gradual transformations between concrete mineral phases containing sulphate and/or aluminium over time. (Cemdata07 database, Case Large8).*

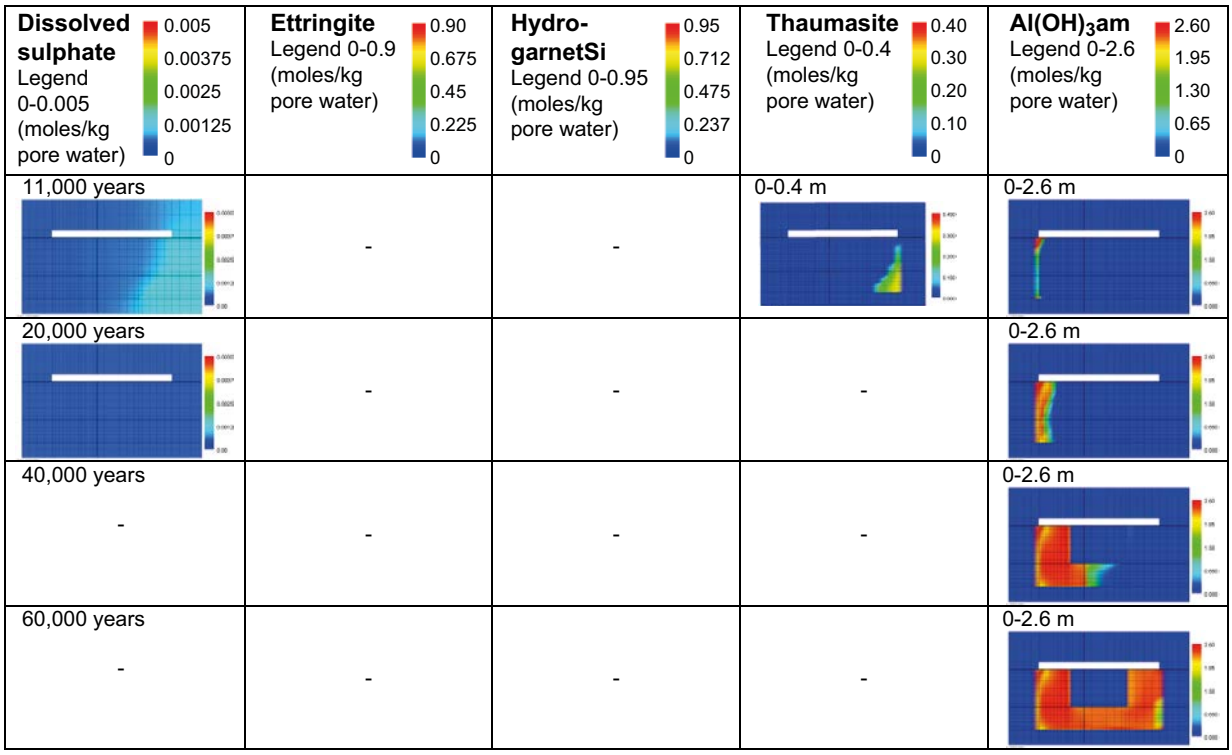

Figure 7-49. *Continued.*

Magnesium, iron and mineral reactions involving magnesium and iron

Using the Cemdata-07 database changes the relative stability of brucite and hydrotalcite minerals (cf. MinteqCem-2001), and hydrotalcite minerals are calculated to form. Dissolved magnesium in the saline groundwater therefore precipitates in the alkaline environment created by the concrete. Different forms of hydrotalcite precipitate, which incorporates carbonate or iron as well as magnesium and aluminium. As the pH in the vault drops after the first 2,000–3,000 years, the dissolved magnesium concentration will gradually increase in the sand/crushed rock bed around the concrete constructions. Following the gradual depletion of alkaline minerals containing calcium, the magnesium concentrations in the concrete increase, as seen from 10,000–40,000 years in Figure 7-50.

The different magnesium containing minerals display an intricate interaction from 3,000 years onwards as shown in Figure 7-50. HydrotalciteFe starts to dissolve at the left-hand, up-stream side and hydrotalciteOH precipitates in a zone that gradually moves through the concrete structure towards the right (in the direction of the groundwater flow). However by 5,000 years, hydrotalciteFe once again has precipitated together with hydrotalciteC behind the moving zone of hydrotalciteOH. This process goes on until hydrotalciteOH becomes depleted after 21,000 years. During the period 20,000–40,000 years, hydrotalciteFe is gradually replaced by hydrotalciteC.

Iron is present in low concentrations in groundwater, unless the conditions are very reducing. Iron is a constituent of concrete and may appear in various minerals including iron hydroxides, hydrotalciteFe, iron-substituted ettringite etc. Iron also appears in large amounts in the waste and waste packaging, as well as in reinforcement and other steel construction details. Iron in the form of metal that may undergo corrosion and form dissolved or solid reactions products have not been considered in the present modelling but could be addressed in future studies. In the Cemdata-07 database, iron appears in two major forms plausible for the concrete environment, $Fe(OH)_3am$ and hydrotalciteFe. Similar to the magnesium-containing minerals, the iron-containing minerals display a complex interaction. By 10,000 years, a zone of hydrotalciteFe has replaced $Fe(OH)_3am$ in the left-hand concrete wall, (also shown in Figure 7-39). This zone moves towards the right, but is again replaced by $Fe(OH)_3am$ on the up-stream side of the moving zone. By 30,000 years, the zone of hydrotalciteFe has reached the right-hand side of the concrete constructions and has started to be depleted and, after 40,000 years, the hydrotalciteFe has been almost completely replaced by $Fe(OH)_3am$. After ~ 40,000 years only minor changes of the conditions occur and have therefore been omitted from the figure.

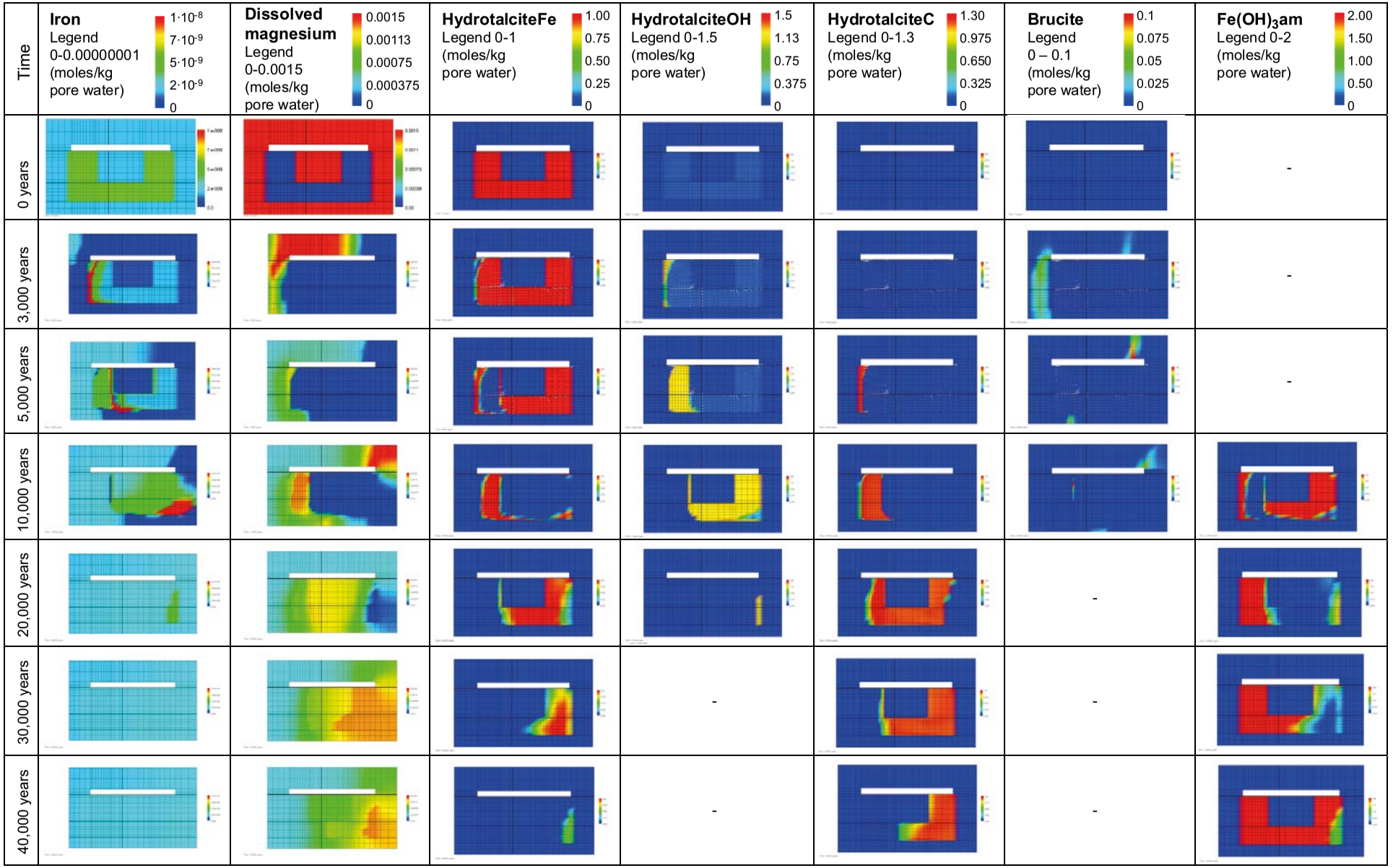

Figure 7-50. *Illustration of the change of dissolved magnesium and iron and the gradual transformations between concrete mineral phases containing magnesium and iron over time. (Cemdata07 database, Case Large8).*

7.7 Case Large11 (1BMA)

Case Large11 is a variation case of Large10, examining the impact of repair measures for the side walls. It has been assumed that new concrete walls, 0.2 m thick, are built outside the present concrete walls, see illustrations in Figure 7-6 and Figure 7-9. The basic assumptions regarding geometries and physical/hydraulic/transport parameters for the old concrete structures are the same as for case Large10. The same thermodynamic database, MinteqCem-2001 (Höglund 2001) is used as in case Large10.

The boundary conditions for the groundwater flow are the same as for case Large10, whereas additional hydraulic data are introduced for the new repair concrete barriers, see Table 7-7.

The presentation of the results first gives a brief overview of the evolution of the pore water chemistry and the mineral assemblage in one point in the cell grid at position AE, see Figure 7-8. Following this, the changes in the mineralogy at point DE, near the fracture, are presented. Finally, the evolution in the full 2-D-grid is presented and more detailed comments are given. For additional information on the results, see graphical representations shown in Appendix E. Representative data from Large10 and Large11 are compared directly in Section 7.11.

7.7.1 Evolution of chemistry and mineralogy at evaluation points

Evaluation point AE – at the intersection of the centrelines of the concrete floor and the left-hand side concrete wall

The ingress of chloride during the first 2,000 year affects the mineralogy in a similar way to that seen in case Large10, cf. Figure 7-51 and Figure 7-52. As the Friedel's salt is destabilised by the changed ground water composition at 2,000 years (cf. Figure 7-51), the chloride concentration stabilises at ~1.3 mM after ~2,600 years which is the concentration assumed in the ground water during the freshwater period, and the released aluminium is precipitated as monocarboaluminate and C_3AH_6, see Figure 7-52. The transition from the CSH_1.8 (Ca/Si = 1.8) to the less alkaline CSH_1.1 (Ca/Si = 1.1) takes place between ~3,200 and 3,500 years, accompanied by a distinct drop in pH. The formed C_3AH_6 reacts with sulphate to form ettringite, which peaks after ~4,500 years. As the gradual transformation of CSH_1.1 to CSH_0.8 (Ca/Si = 0.8) is initiated the pH has dropped to ~ 10.85 and ettringite is destabilised and slowly starts to dissolve after ~4,600 years. A gradual enrichment is observed for C_3FH_6 during the period ~6,000–7,400 years caused by upstream dissolution and subsequent precipitation in the more alkaline downstream environment. After ~7,400 years the only remaining CSH mineral is CSH_0.8, the pH is ~10.3, accompanied by a fairly low concentration of dissolved calcium and an increased concentration of dissolved silica, see Figure 7-51. Hereafter dissolution of CSH_0.8 progresses and is accompanied by dissolution of C_3FH_6 which is destabilised by the lower pH. Depletion of CSH_0.8 occurs at ~12,000 years and is accompanied by a pH drop to ~10. These processes are delayed to an extent compared to case Large10, but still occur much more rapidly than the equivalent processes in Large20 (2BMA).

Gradually, the precipitation of calcite and brucite (which peaks at ~12,000 years) becomes more pronounced, see Figure 7-53. At 15,000 years brucite is totally depleted, whereas calcite continuously precipitates until the reaching a final pH of ~7.5 after ~30,000 years. The results are shown up to 43,000 years.

Figure 7-54 shows that the porosity is expected to increase from 11% to ~ 18% after 10,000 years, which is slightly less than the porosity change in case Large10. The most damaging changes in the porosity (e.g. due to ettringite formation) are calculated to occur between 3,800–5,000 years in this case, suggesting that the repair measures modelled with the pessimistic assumptions made, would not prevent fracturing at a relatively early period in the repository evolution. The porosity is presented over the range of 0–25% in Figure 7-54; the maximum porosity corresponding to fully depleted cement minerals would be ~ 30%, the remaining volume constitutes the ballast material which is assumed to be inert.

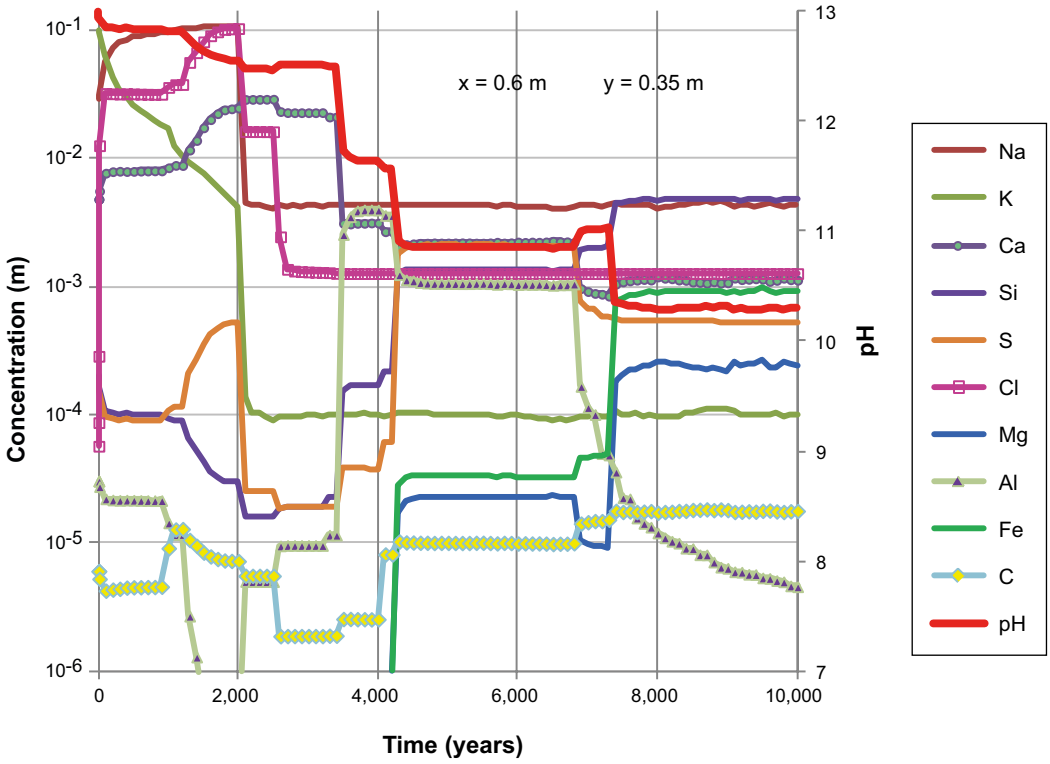

Figure 7-51. *The evolution of the pore water chemistry (during the first 10,000 years) at position AE (a point located at the intersection of a vertical centreline through the left-hand side concrete wall and a horizontal centreline through the concrete floor), case Large11.*

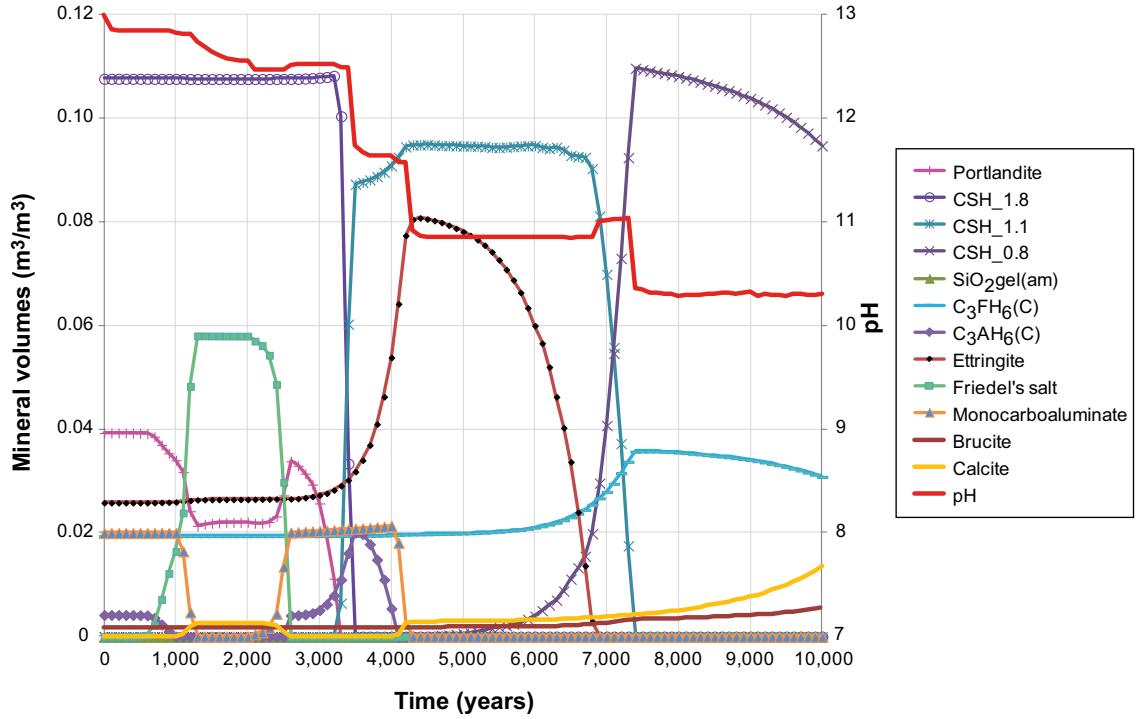

Figure 7-52. *The evolution of the mineral assemblage (during the first 10,000 years) at position AE (a point located at the intersection of a vertical centreline through the left-hand side concrete wall and a horizontal centreline through the concrete floor), case Large11.*

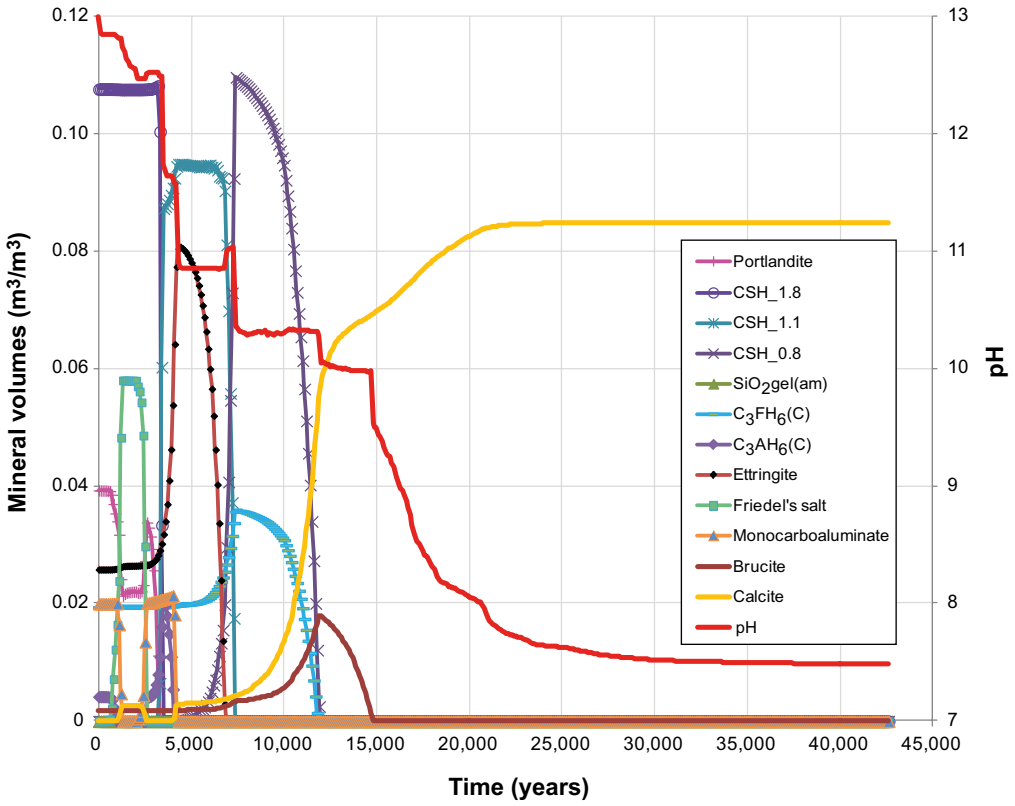

Figure 7-53. *The evolution of the mineral assemblage (during 43,000 years) at position AE (a point located at the intersection of a vertical centreline through the left-hand side concrete wall and a horizontal centreline through the concrete floor), case Large11.*

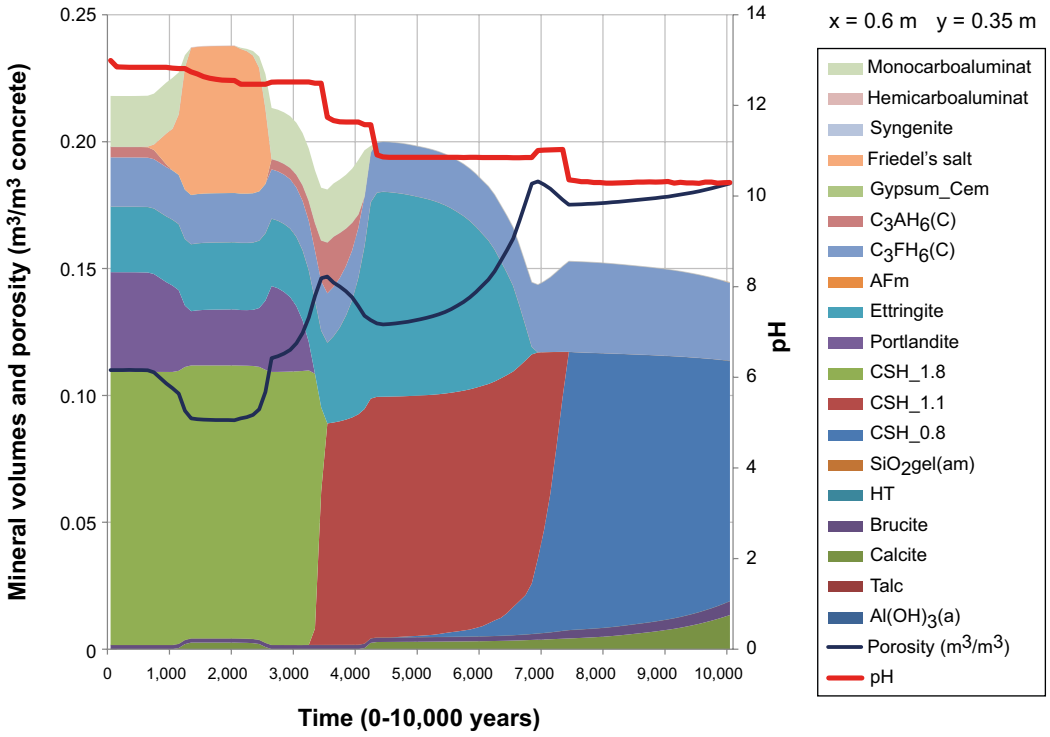

Figure 7-54. *The change of mineral volumes and porosity in concrete during 10,000 years at position AE (a point located at the intersection of a vertical centreline through the left-hand side concrete wall and a horizontal centreline through the concrete floor), (MinteqCem-2001 database, Case Large11). The evolution of pH is also indicated.*

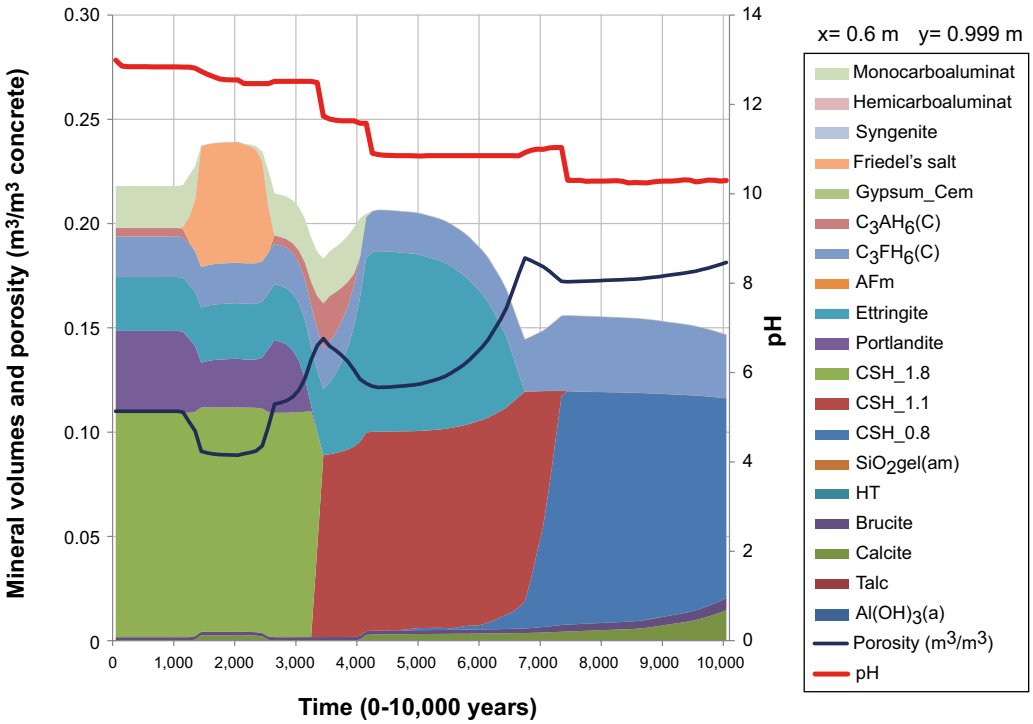

Figure 7-55. *The amount of minerals in concrete during 10,000 years at position DE (a point located at the vertical centreline through the left-hand side concrete wall, 1 mm from an open fracture), (MinteqCem-2001 database, Case Large11). The evolution of pH with time is also indicated.*

Evaluation point DE – at the vertical centreline of the left-hand side concrete wall near the thin horizontal fracture

The progression of the dissolved components and the pH follows the general pattern as shown for evaluation point AE discussed above. The observed changes occur at an almost equivalent rate despite the vicinity of the fracture, which demonstrates that the fracture is less important in this repair scenario, compare Figure 7-55 and Figure 7-54.

The gradual evolution of the mineral assemblage with time is shown together with the calculated changes of the porosity during the first 10,000 years. The results show that a porosity increase from 11% initially to ~ 18% at 7,000 years would be expected. The porosity is presented over the range of 0–30% in Figure 7-55; the maximum porosity corresponding to fully depleted cement minerals would be ~ 30%, the remaining volume constitutes the ballast material which is assumed to be inert.

7.7.2 Evolution of the chemistry and mineralogy of the 2-D system

pH evolution, calcium and silica depletion

The evolution of pH over time in full 2-D-section of the model is summarised in Figure 7-56. The model results show that a high pH (> 12.5) is maintained inside the concrete constructions over the first 2,000–2,500 years. The evolution of the pH is similar to cases Large8 and Large10 but, as seen at the evaluation points, slightly delayed. The same is true of the calcium leaching patterns, so that only small parts at the right-hand down-stream side of the concrete constructions contribute any significant concentrations of calcium to the pore water after 10,000 years (note the change of scale in the figure), rather than 5,800 years (Case Large10).

The gradual depletion and transformation of portlandite and the minerals representing the CSH-gel (CSH_1.8, CSH_1.1 and CSH_0.8 respectively) are presented in Figure 7-56. The evolution of dissolved silica concentrations are presented together with the CSH-gel minerals in Figure 7-57. The patterns are similar to those in case Large8, although again delayed to an extent. After ~ 15,000 years the only remaining CSH-component is CSH_0.8, which in turn becomes depleted after ~ 27,000 years. After ~ 15,000 years, all CSH-gels have become depleted in the concrete barriers at the upstream side of the vault. At this point, any resemblance of the remaining material to the initial concrete is difficult to envisage.

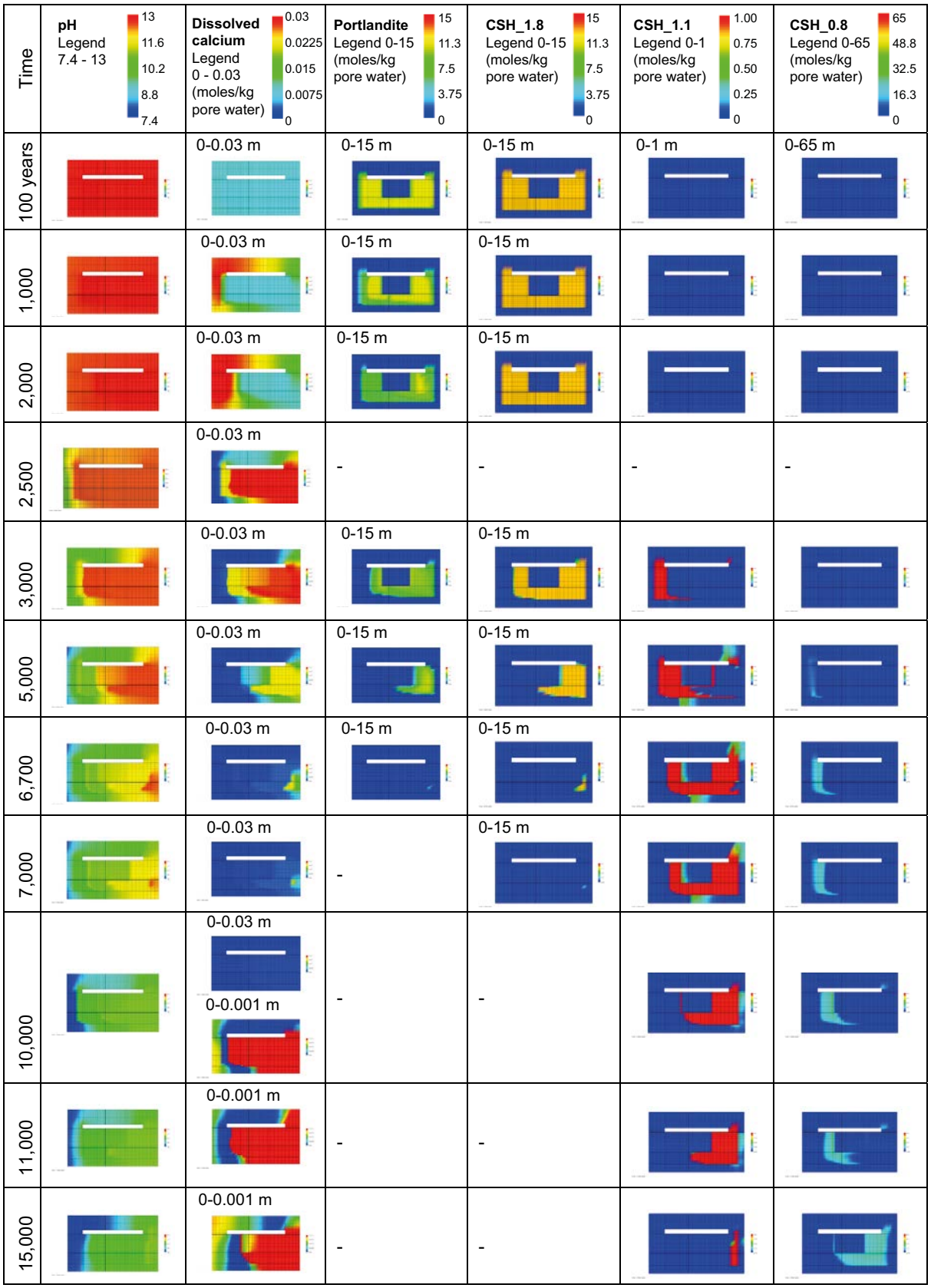

Figure 7-56. *Illustration of the gradual evolution of pH as a result of depletion and transformation of mineral phases containing calcium. (MinteqCem-2001 database, Case Large11). Observe the change of scale in the label for dissolved calcium after 10,000 years.*

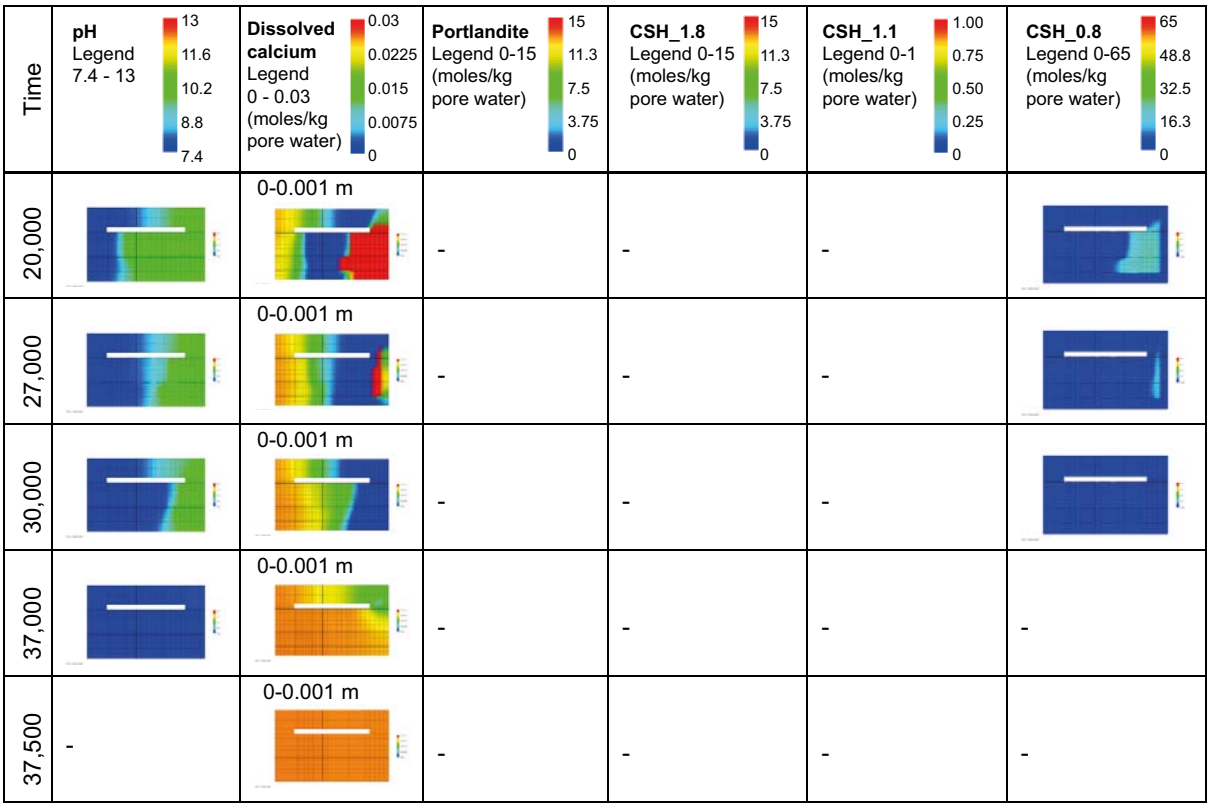

Figure 7-56. *Continued.*

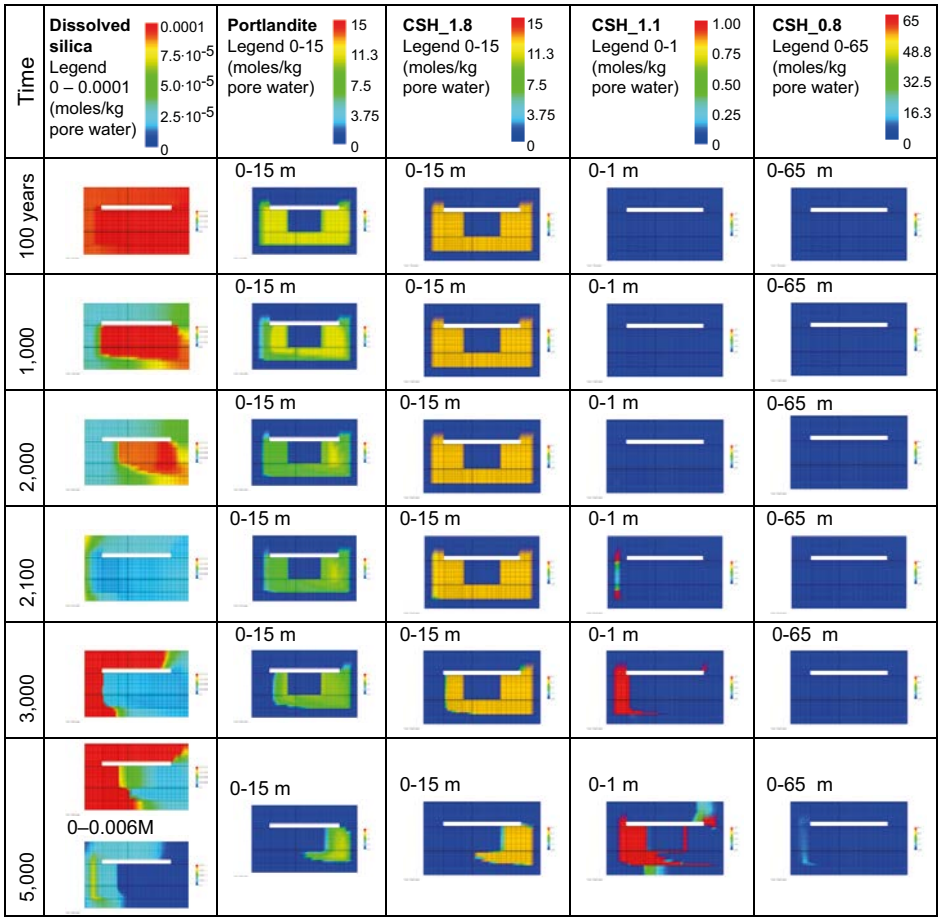

Figure 7-57. *Illustration of the gradual change in the concentration of dissolved silica in response to depletion and transformation of CSH-gel phases and portlandite. (MinteqCem-2001 database, Case Large11). Observe the change of scale in the legend for dissolved silica after 5,000 years.*

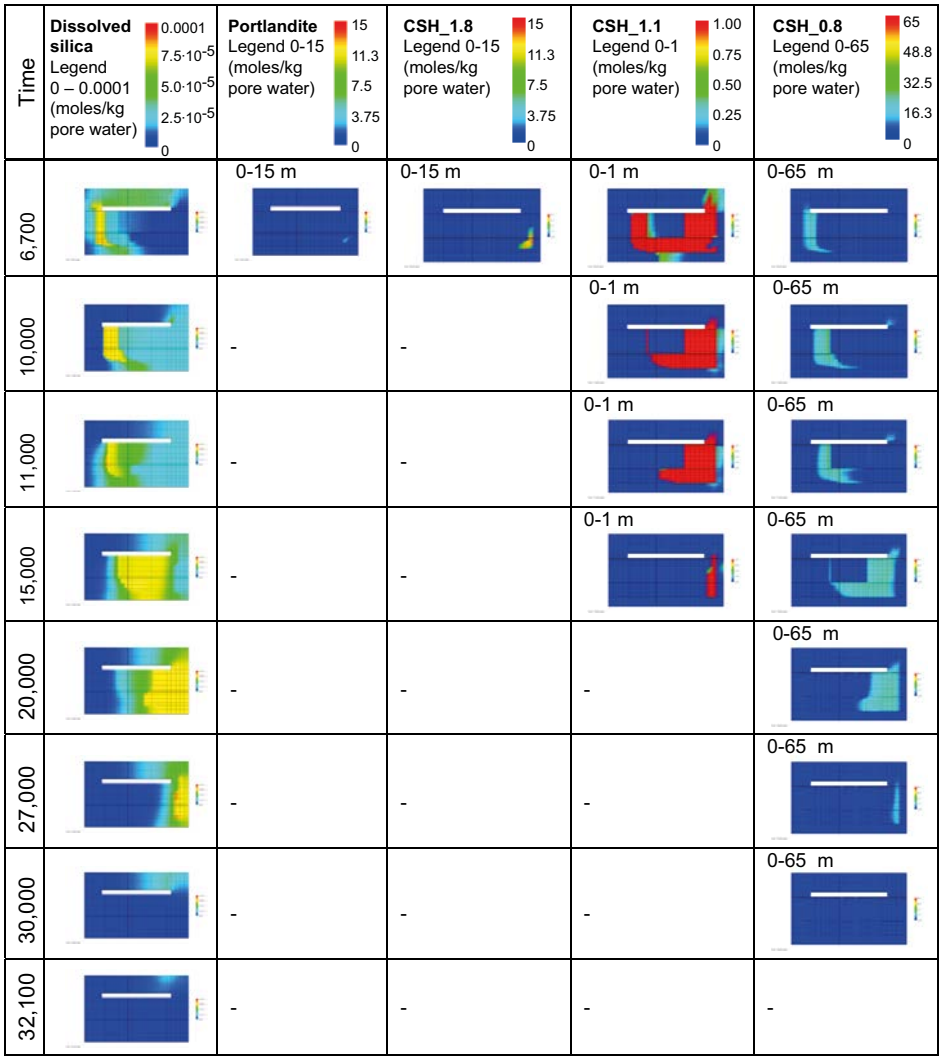

Figure 7-57. *Continued.*

Carbonate, calcite, ettringite, monocarboaluminate and Friedel's salt

The evolution of dissolved carbonate, calcite, ettringite, monocarboaluminate and Friedel's salt follow a similar pattern to that calculated for Large10, see Figure 7-58. Processes that are controlled by the groundwater composition, such as calcite precipitation and the formation and dissolution of Friedel's salt, also occur at a very similar rate. However, other processes are delayed by the presence of the simple repair measures. For example, an enhanced precipitation of ettringite replacing mono-carboaluminate propagates as a front from left to right through the concrete structures in a period that lasts up to 9,000 years, as opposed to 7,000 years in case Large10. Ettringite is also completely depleted in the system after 15,000 years, as opposed to ~11,000 years. Calcite continues to precipitate at a slow rate in both cases. Here, only small changes occur after ~ 37,000 years.

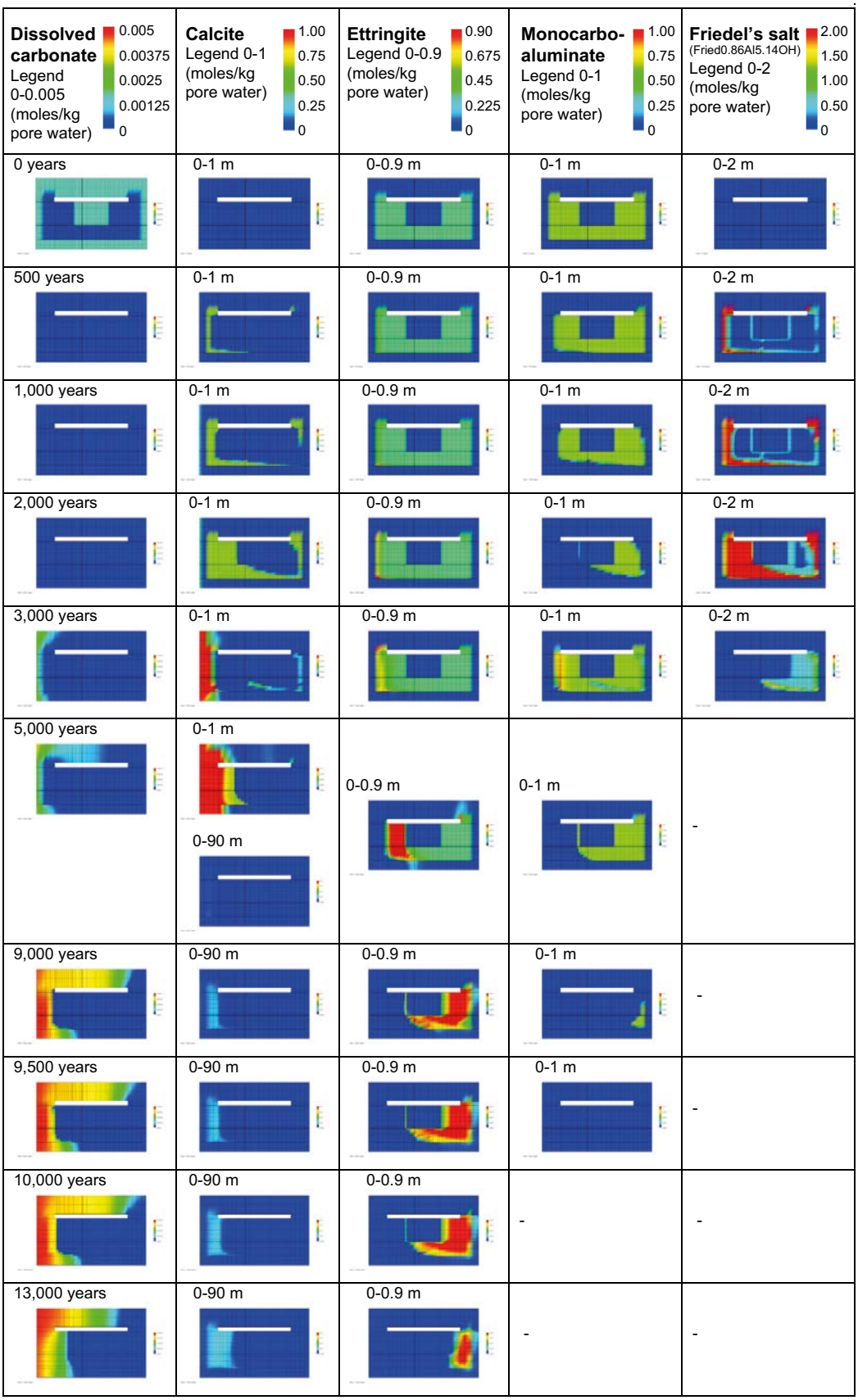

Figure 7-58. *Illustration of the change of dissolved carbonate and of the gradual transformations between concrete mineral phases containing carbonate and/or aluminium over time. (MinteqCem-2001 database, Case Large11). Observe the change of scale in the legend for calcite after 5,000 years.*

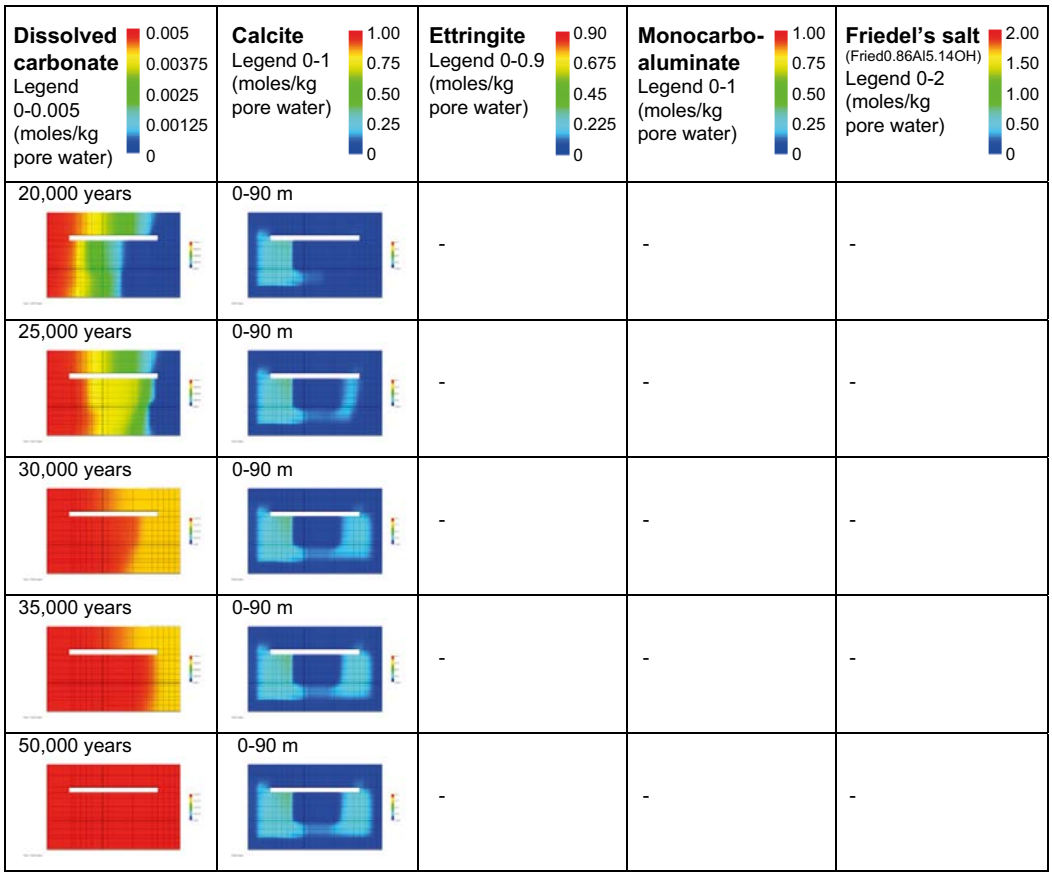

Figure 7-58. *Continued.*

Sulphate, chloride, hydrogarnet, ettringite, monocarboaluminate and Friedel's salt

Initially the dissolved sulphate and chloride concentrations are comparatively high, but they quickly decrease due to interactions with soluble components leached from the concrete, which causes a slight precipitation of ettringite and Friedel's salt. Hydrogarnet (C_3AH_6) and monocarboaluminate are consumed in the reaction with chloride ions to form Friedel's salt. The hydrogarnet phase disappears after 2,200 years and the monocarboaluminate almost disappears after ~ 9,000 years, see Figure 7-59. After 2,000 years, the composition of the groundwater changes and in response to this the Friedel's salt decomposes and disappears completely after ~ 3,300 years. Decomposition of the Friedel's salt leads to neoformation of monocarboaluminate. The monocarboaluminate in turn is replaced by an increased precipitation of ettringite, which is also accompanied by the reappearance of hydrogarnet (C_3AH_6).

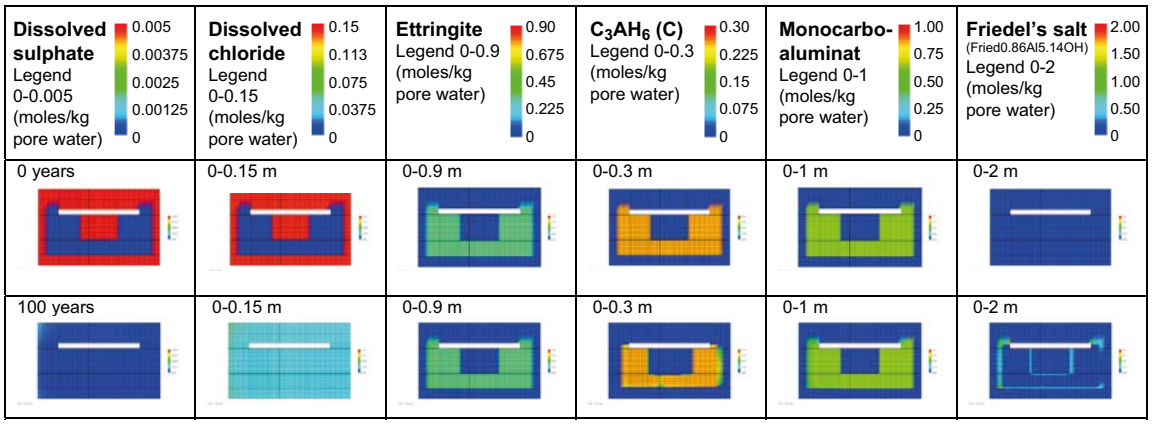

Figure 7-59. *Illustration of the gradual transformations between concrete mineral phases containing sulphate, chloride and/or aluminium over time. (MinteqCem-2001 database, Case Large11). Observe the change of scale in the label for dissolved chloride after 2,100 years.*

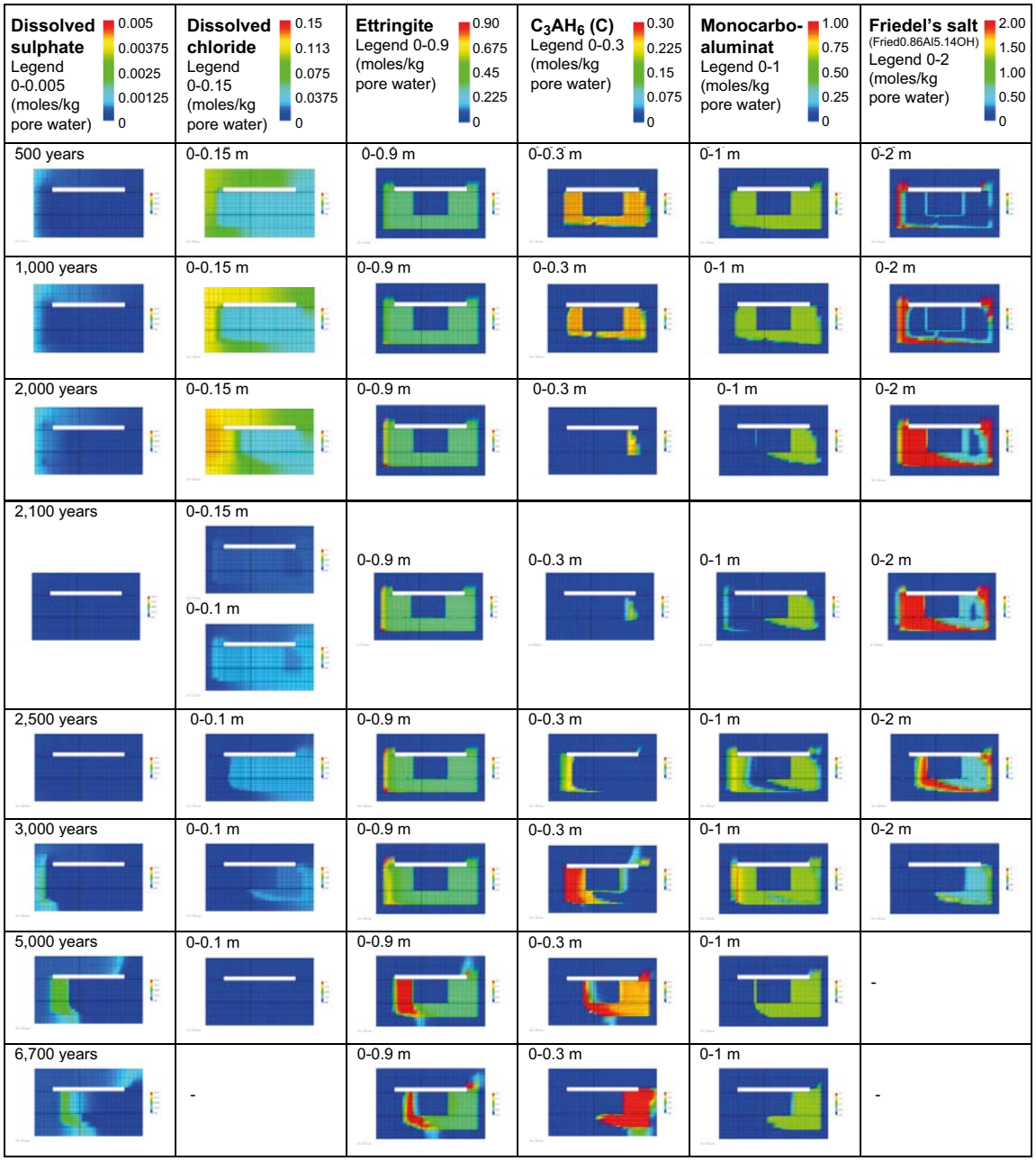

Figure 7-59. *Continued.*

Magnesium, iron and mineral reactions involving magnesium and iron

As the pH in the vault drops between 2,000–3,000 years, the dissolved magnesium concentration gradually increases in the sand/crushed rock bed around the concrete constructions. From 3,000 years, a sharp front of precipitating brucite on the left-hand, up-stream side of the left concrete wall is seen (Figure 7-60).

After ~ 10,000 years, in response to decreasing pH, the brucite starts to dissolve on the upstream side, while precipitation continues on the downstream side of the front.

Following the gradual depletion of alkaline components in the concrete, the magnesium concentrations in the concrete pore water increase, as seen from (10,000 – ~ 30,000 years) in Figure 7-60 and ultimately levels off at the concentration determined by the inflowing groundwater after ~ 37,000 years.

The dissolved iron concentrations start to increase from the left-hand upstream side of the left concrete wall after ~ 3,000–5,000 years in response to decreasing pH and increased leaching of calcium, cf. Figure 7-56. The dissolved iron precipitates again further downstream and forms an enriched zone of C_3FH_6.The dissolution/precipitation of C_3FH_6 slowly progresses as a dual front moving from left to right and disappears after ~ 28,000 years.

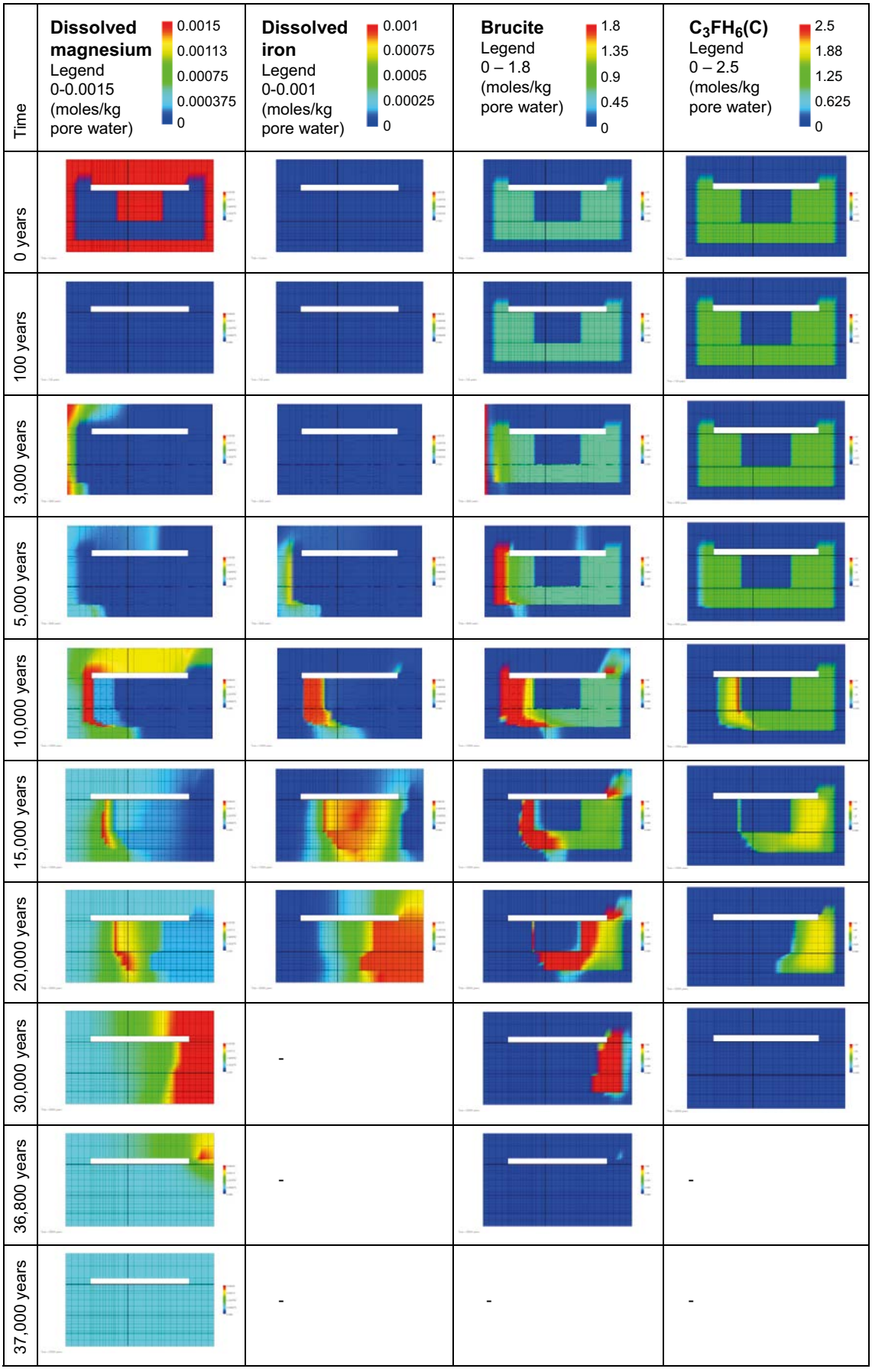

Figure 7-60. *Illustration of the change of dissolved magnesium and iron and the gradual transformations between concrete mineral phases containing magnesium and iron over time. (MinteqCem-2001 database, Case Large11).*

7.8 Case Large12 (1BMA)

Case Large12 is a variation case of Large8, examining the impact of repair measures for the side walls. It has been assumed that new concrete walls, 0.2 m thick, are built outside the present concrete walls, see illustration in Figure 7-6 and Figure 7-9. The basic assumptions regarding geometries and physical/hydraulic/transport parameters for the old concrete structures are the same as for case Large8. The same thermodynamic database, Cemdata07 is used as in case Large8. Supporting figures and diagrams are also presented in Appendix F.

The presentation of the results first gives a brief overview of the evolution of the pore water chemistry and the mineral assemblage in one point in the cell grid at position AE, see Figure 7-8. Following this, the changes in the mineralogy at point DE, near the fracture, are presented. Finally, the evolution in the full 2-D-grid is presented and more detailed comments are given.

The boundary conditions for the groundwater flow are the same as for case Large8, whereas additional hydraulic data are introduced for the new repair concrete barriers, see Table 7-7.

7.8.1 Evolution of chemistry and mineralogy at evaluation points

Evaluation point AE – at the intersection of the centrelines of the concrete floor and the left-hand side concrete wall

Figure 7-61 shows that the pH is initially high, but levels off at ~ 12.5 until a decline starts at ~ 3,700 years, followed by a decrease at ~ 5,000 years where a new plateau is established at pH 10. This plateau continues to ~ 12,900 years, when the pH drops to ~ 9.3. The evolution of pH and dissolved components over time is shown in Figure 7-61. After ~ 21,800 years, the pH drops below 9, reaching a value of ~ 8.3 after 27,000 years and approaches a final value of ~ 7.5, corresponding to the natural groundwater during the period 40,000–50,000 years.

The gradual evolution of the mineral assemblage and the calculated changes of the porosity during the first 10,000 years are shown in Figure 7-62. The results suggest that an initial concrete porosity of 11% would increase to ~ 16% by 5,400 years, then decrease to ~ 12.6% at 6,000 years, followed by a steady increase to ~ 15% at 10,000 years. A peak porosity of 23% is obtained at 13,300 years, thereafter steadily decreasing in response to slowly progressing calcite precipitation. The porosity stabilises at ~ 19% after 37,000 years showing little change hereafter. The porosity is presented over the range of 0–20% in Figure 7-62; the maximum porosity corresponding to fully depleted cement minerals would be ~ 30%, the remaining volume constitutes the ballast material which is assumed to be inert.

During the period 2,000–5,800 years complex changes in the mineral assemblage causes significant changes in the porosity, see Figure 7-62 and Figure 7-63. The dissolution of portlandite starting after ~ 2,000 years causes the porosity to increase, but the growth of ettringite starting after ~3,000 years slows down the porosity increase. The porosity peaks at 5,400 years, then decreases from 16% to 12.6% during the period 5,400–6,000 years when first ettringite replaces hydrogarnetSi, followed by a replacement of ettringite and hydrotalciteFe by thaumasite and hydrotalciteOH. A significant event is also the transformation of CSHjen to CSHtob2 during the period 4,500–5,400 years. The precipitation of CSHtob2 and hydrotalciteOH is accompanied by a decrease in porosity after ~ 5,200 years. From ~ 8,000–14,000 years, the porosity increases gradually as a result of dissolution of CSHtob2 and hydrotalciteOH, accompanied by precipitation of calcite.

The changes in the porosity between 3,000–5,400 years are a matter of some concern for the integrity of the concrete. In particular, ettringite and thaumasite precipitation may cause detrimental fracturing of the concrete due to the expanding character of these minerals, see discussions on the theoretical background to this in Chapter 4.

The long-term evolution of the minerals and the porosity show a slow but steady precipitation of calcite up to ~38,000 years, thereafter only minor changes, see Figure 7-64.

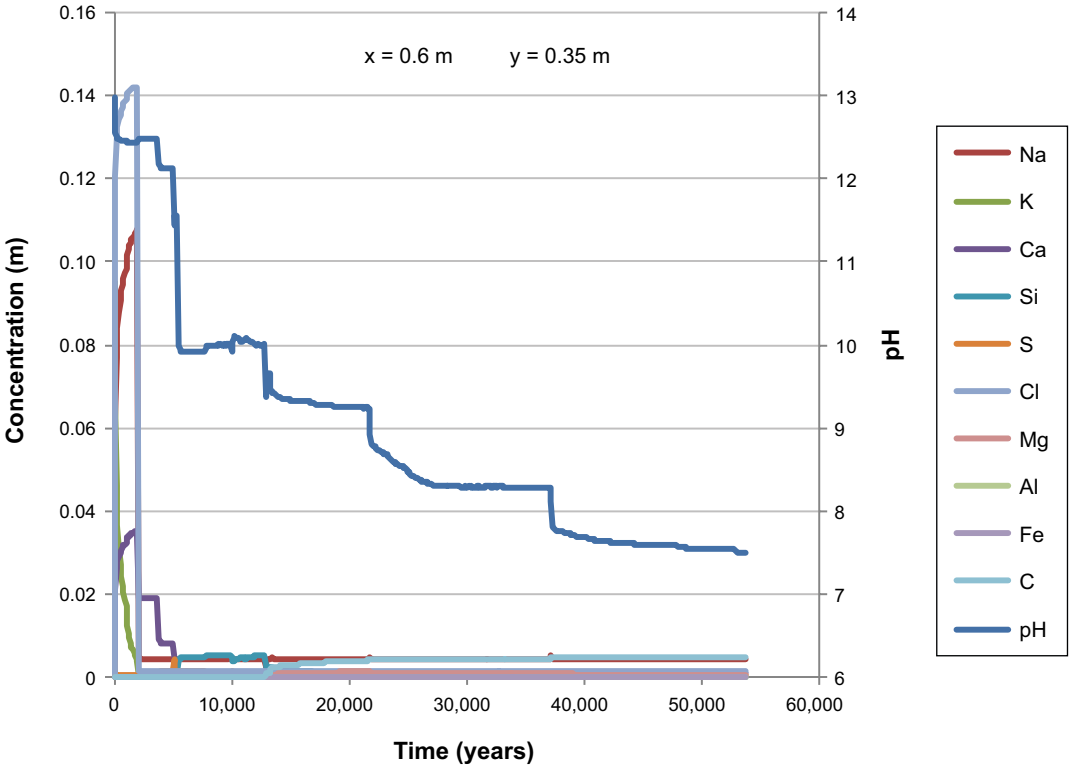

Figure 7-61. *The development of the concentration of dissolved components in concrete pore water over time (during the first 54,000 years) at position AE (a point located at the intersection of a vertical centreline through the left-hand side concrete wall and a horizontal centreline through the concrete floor), case Large12.*

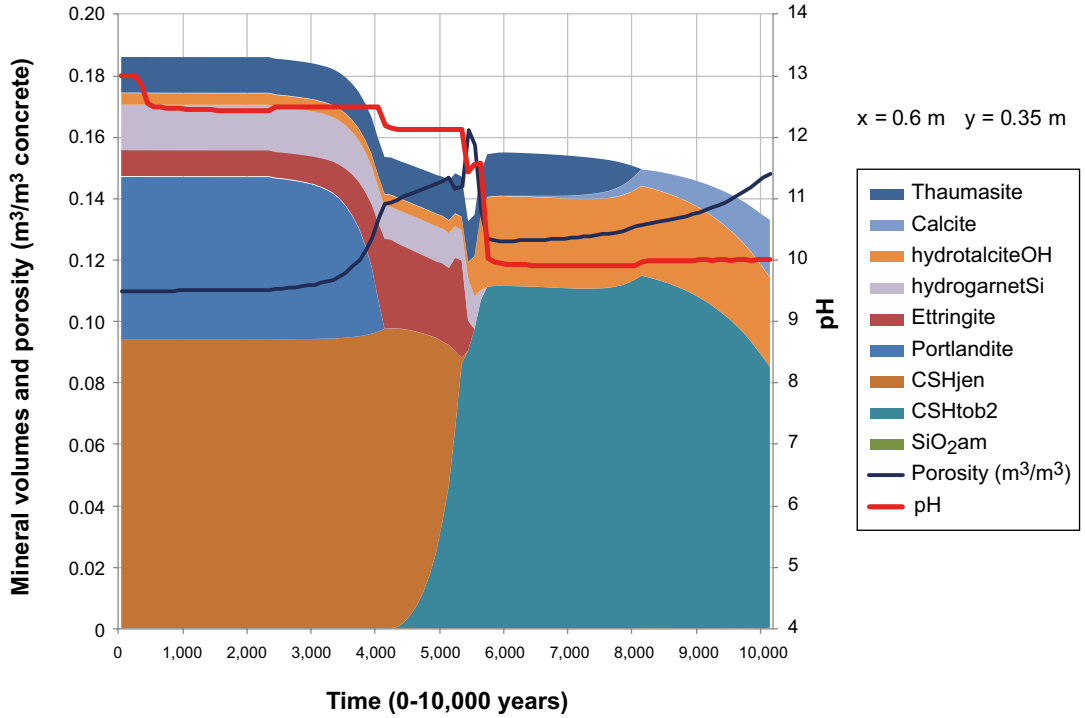

Figure 7-62. *The change of mineral volumes and porosity in concrete during the first 10,000 years at position AE (a point located at the intersection of a vertical centreline through the left-hand side concrete wall and a horizontal centreline through the concrete floor), case Large12. The evolution of pH with time is also indicated.*

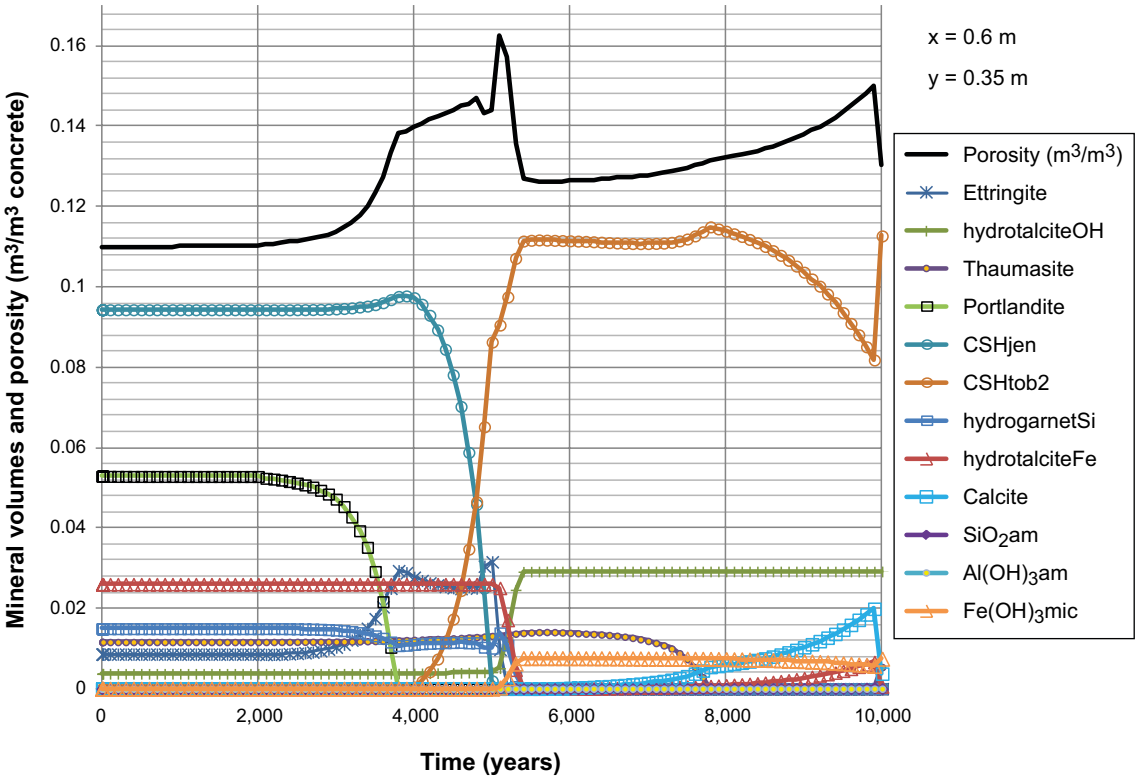

Figure 7-63. *Development of selected mineral volumes and porosity over time (during the first 10,000 years) at position AE (a point located at the intersection of a vertical centreline through the left-hand side concrete wall and a horizontal centreline through the concrete floor), case Large12.*

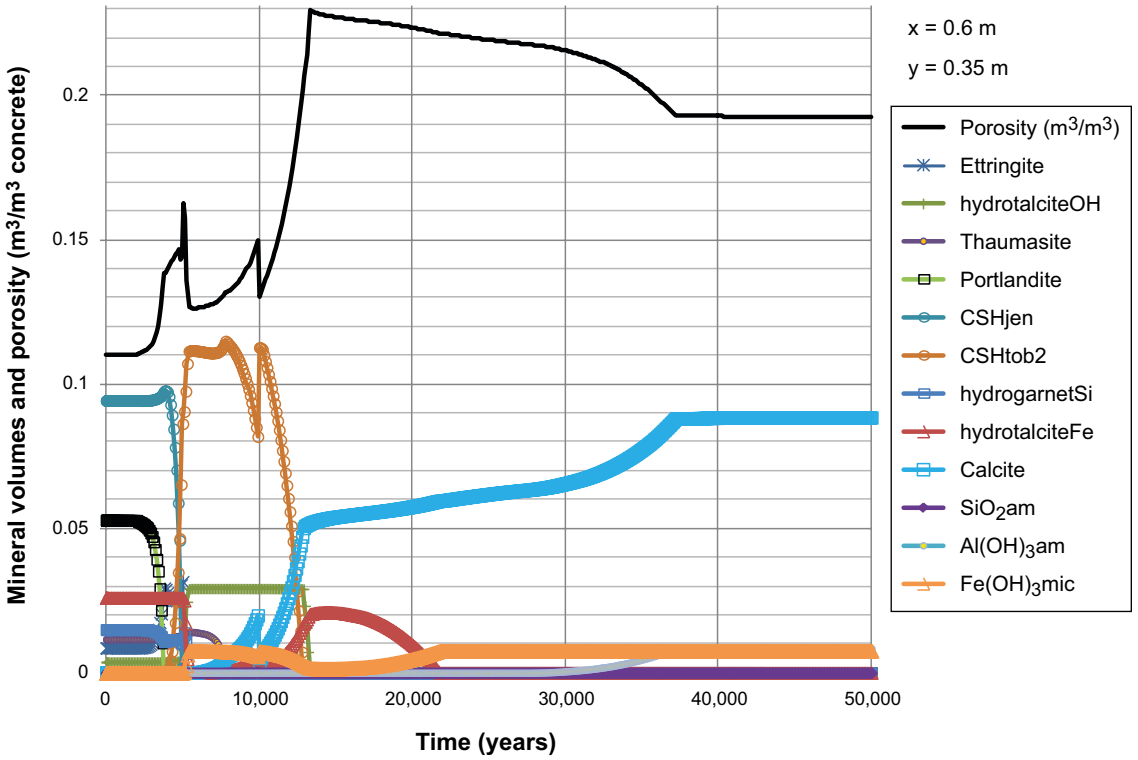

Figure 7-64. *Development of selected mineral volumes and porosity over time (during 50,000 years) at position AE (a point located at the intersection of a vertical centreline through the left-hand side concrete wall and a horizontal centreline through the concrete floor), case Large12.*

Evaluation point DE – at the vertical centreline of the left-hand side concrete wall near the thin horizontal fracture

The progression of the dissolved components and the pH follows the same general pattern as at evaluation point AE discussed above, although the observed changes occur slightly faster near the fracture, compare Figure 7-62 with Figure 7-65.

The gradual evolution of the mineral assemblage over time is shown in Figure 7-65 together with the calculated changes of the porosity during the first 10,000 years. The results show that the porosity would be expected to increase from the initial value of 11% to ~ 17% after 5,400 years, followed by a decrease to ~ 12.7% and then slowly increasing. The evolution of individual mineral volumes are shown in Figure 7-66 (during the first 10,000 years) and in Figure 7-67 (during 50,000 years). The porosity is presented over the range of 0–20% in Figure 7-65 and 0–23% in Figure 7-67; the maximum porosity corresponding to fully depleted cement minerals would be ~ 30%, the remaining volume constitutes the ballast material which is assumed to be inert.

For additional information on the results, see graphical representations shown in Appendix F.

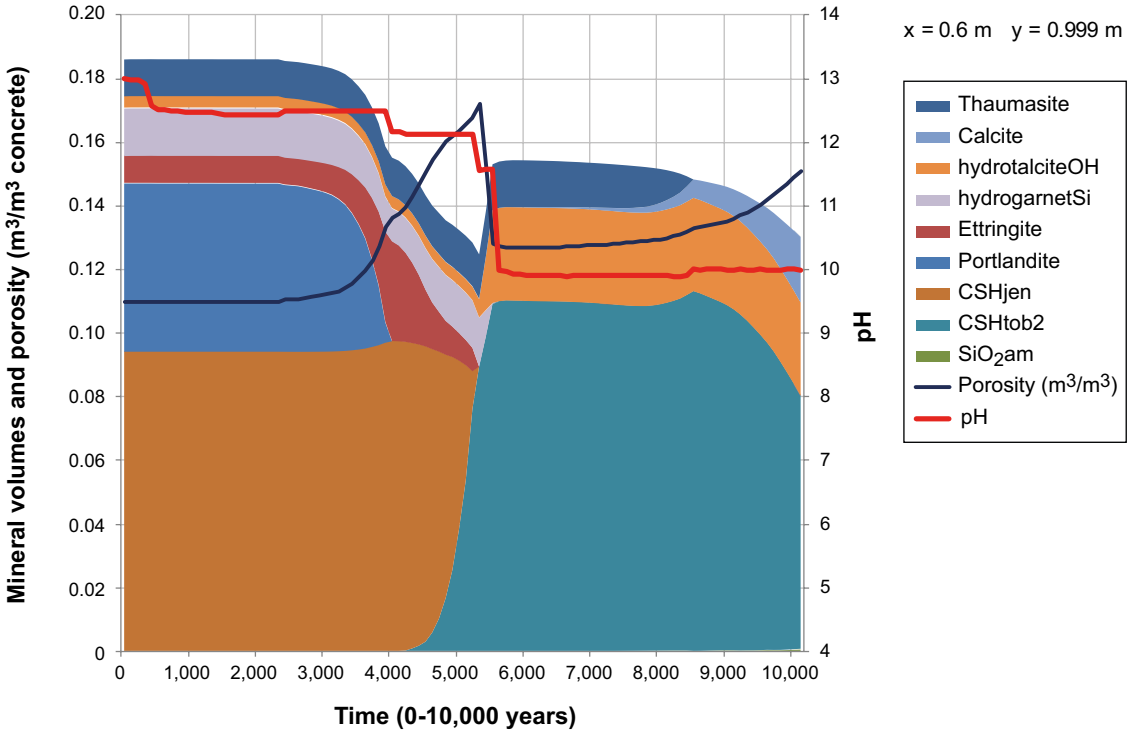

Figure 7-65. *The change of mineral volumes and porosity in concrete during the first 10,000 years at position DE (a point located at the vertical centreline through the left-hand side concrete wall, 1 mm from an open horizontal fracture), case Large12. The evolution of pH with time is also indicated.*

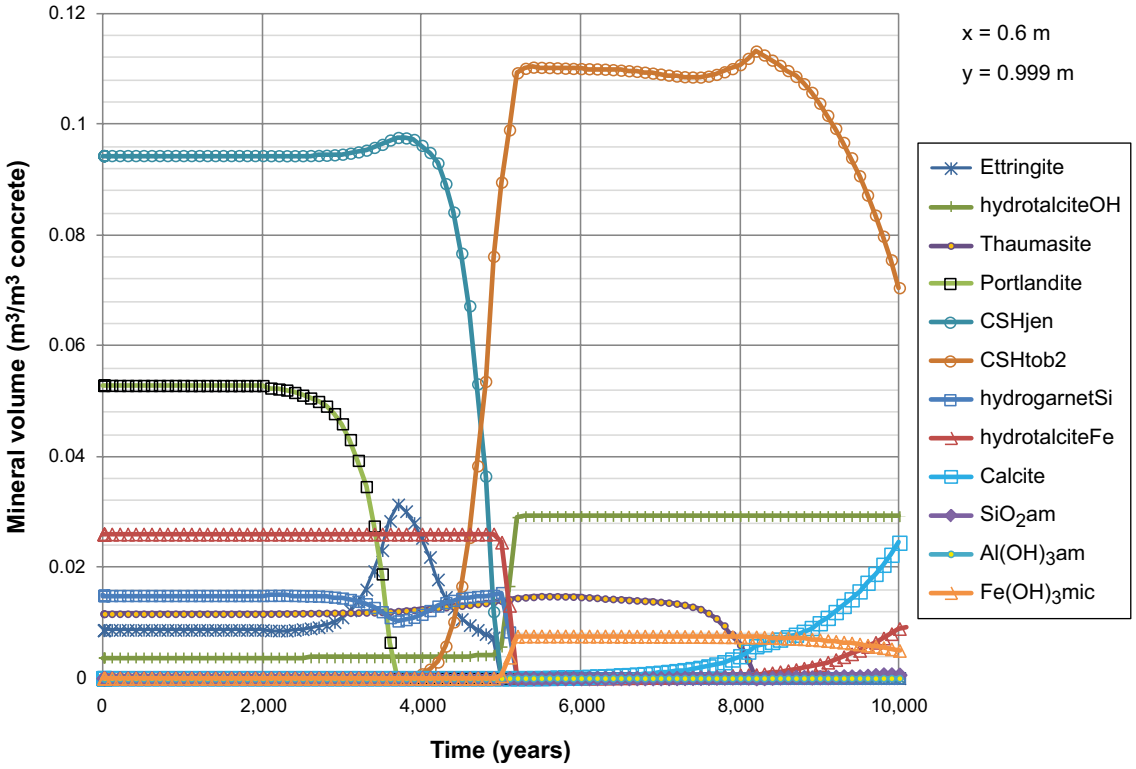

Figure 7-66. *Development of selected mineral volumes over time (during the first 10,000 years) at position DE (a point located at the vertical centreline through the left-hand side concrete wall, 1 mm from an open horizontal fracture), case Large12.*

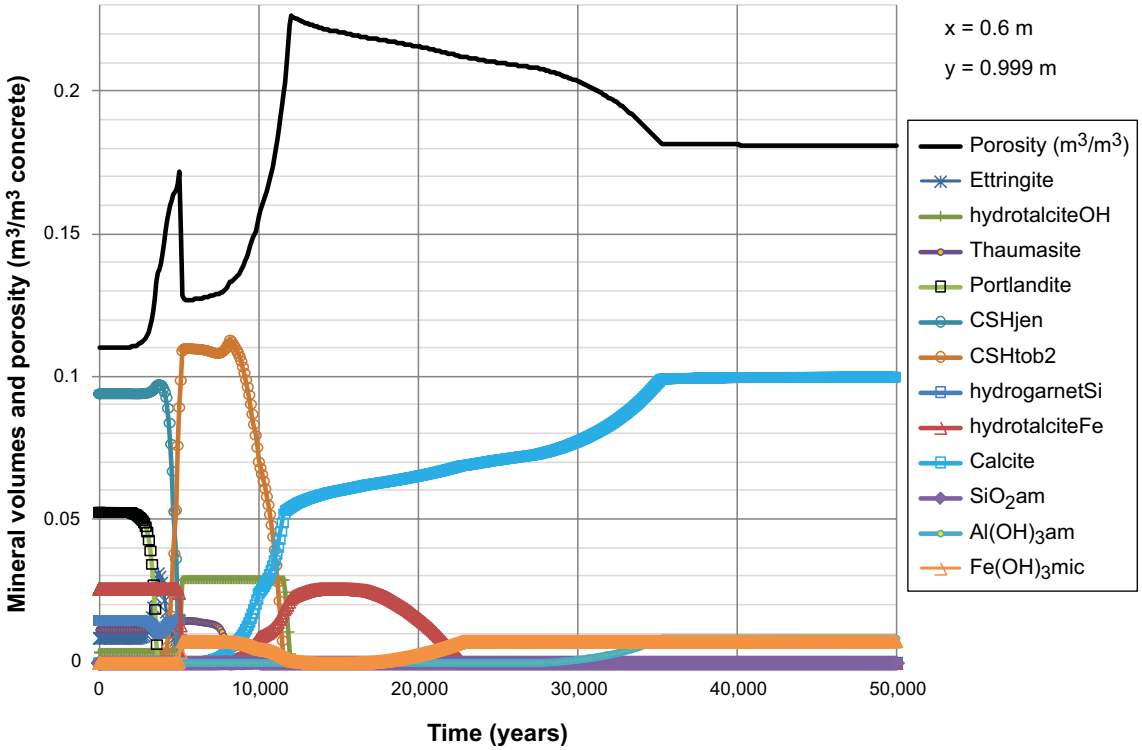

Figure 7-67. *Development of selected mineral volumes and porosity over time (during 50,000 years) at position DE (a point located at the vertical centreline through the left-hand side concrete wall, 1 mm from an open horizontal fracture), case Large12.*

7.8.2 Evolution of the chemistry and mineralogy of the 2-D system

pH evolution, calcium and silica depletion

The evolution of pH is summarised in Figure 7-68 and a high pH (~ 12.5) is maintained inside the concrete constructions over the first 3,000 years. Thereafter the pH gradually drops, starting at the left-hand inflow side, where the pH approaches ~ 11 in the outer layers of the concrete wall. No distinctive effect is observed adjacent to the horizontal fracture through the old concrete wall, which demonstrates a beneficial impact by repair measures. During the period 5,000 through 6,700 years, the pH of the concrete wall on the left-hand inflow side of the model drops to ~ 10, while the pH inside the open void (representing the vaults where the waste is stored) remains at ~ pH 11. After 15,000 years, almost the entire vault has reached a pH of ~ 10 or lower, after 26,000 years the pH approaches ~ pH 9.2 and after almost 60,000 years a pH of 8.5 is reached, thereafter very slowly approaching the natural pH of the groundwater – bedrock system of ~ 7.4 (calculations were terminated at 69,500 years at which time a small part of the downstream side of the vault still maintained a pH of ~ 8.3).

After ~ 500 years, the conditions are almost entirely determined by the solubility of portlandite – a period which stretches up to ~ 2,000 years. At this point, a significant increase in the groundwater flow rate is assumed due to the transition from the saltwater period to the freshwater period (caused by the land rise in the Forsmark area). There is also a significant change in the chemical composition of the groundwater at this time. As can be seen in Figure 7-68, a gradual depletion of calcium starts to show at 3,000 years and propagates over time. By 15,000 years, only small parts at the right-hand down-stream side of the concrete constructions contribute any significant concentrations of calcium to the pore water (note the change of scale of the dissolved calcium concentrations at 6,700 years in the figure).

The dependence of pH on the gradual depletion and transformation of portlandite and the minerals representing the CSH-gel (CSHjen and CSHtob2 respectively) are presented in Figure 7-68. During the initial phase, the pH is determined by the solubility of the portlandite and the CSH-gel (CSHjen) remains inactive. When portlandite also becomes depleted, the CSH-gel starts to respond to the changed chemical conditions. CSHjen is gradually transformed into the less alkaline CSHtob2 (which starts to appear after ~ 3,000 years). After 5,000 years a substantial replacement of CSHjen by CSHtob2 has occurred in the concrete wall and the concrete floor at the left-hand side (near the inflow). No effect of the presence of a horizontal fracture through the old concrete wall is seen in this case, which demonstrates the impact of the repair measures. After 10,000 years portlandite is almost entirely depleted and the transformation of CSHjen to CSHtob2 progresses. After 12,700 years (not shown) the only remaining CSH-component is CSHtob2, which in turn becomes depleted after ~ 26,000 years. At this point, any resemblance of the remaining material to the initial concrete is difficult to envisage.

As shown in Figure 7-69, silica leaching produces a complex interaction between different CSH-gel phases, in which calcium also plays a dominant role. Silica leaching is intimately coupled to the leaching of portlandite, due to the common chemical element calcium in both the portlandite and the CSH-gels. As long as the portlandite remains in the system it will buffer the chemical conditions and suppress the solubility of silica in the CSH-gels. When portlandite becomes depleted, the solubility of the more calcium-rich CSH-gel phases increase and the gel starts to dissolve. The dissolution process also involves a gradual transformation from calcium-rich to more silica-rich gel-phases. During this time the silica remains in the system essentially as a conservative component. Towards the final stages of CSH-gel degradation, pure silica (SiO_2am) forms near the receding rim of the dissolving CSHtob2. The silica thereafter dissolves and finally disappears after ~ 29,000 years. The interaction with the silicate mineral thaumasite is discussed in next section.

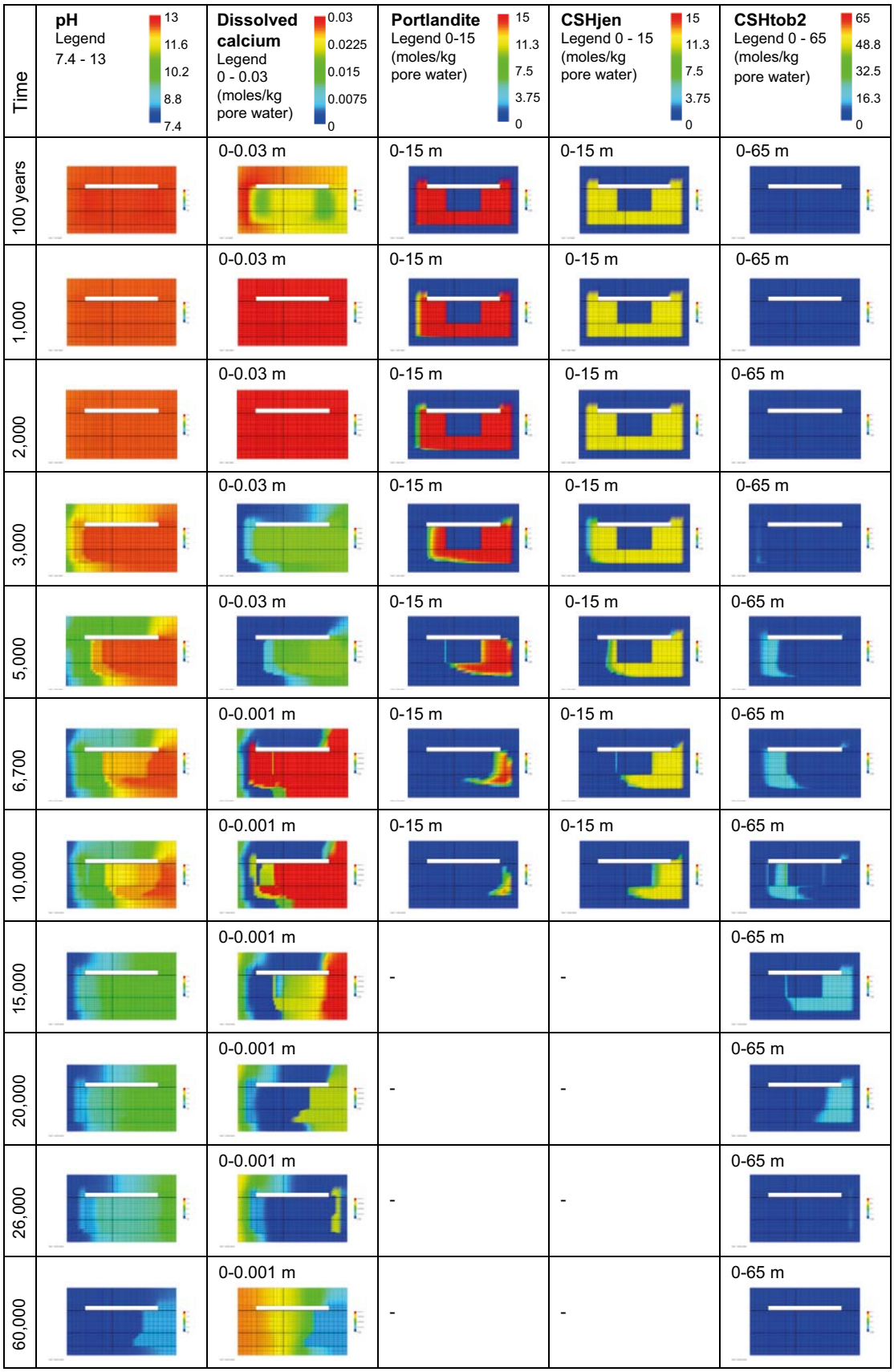

Figure 7-68. *Illustration of the gradual evolution of pH and concentration of dissolved calcium as a result of depletion and transformation of mineral phases containing calcium at different times (Cemdata07 database, Case Large12). Observe the change of scale in the legend for dissolved calcium after 6,700 years.*

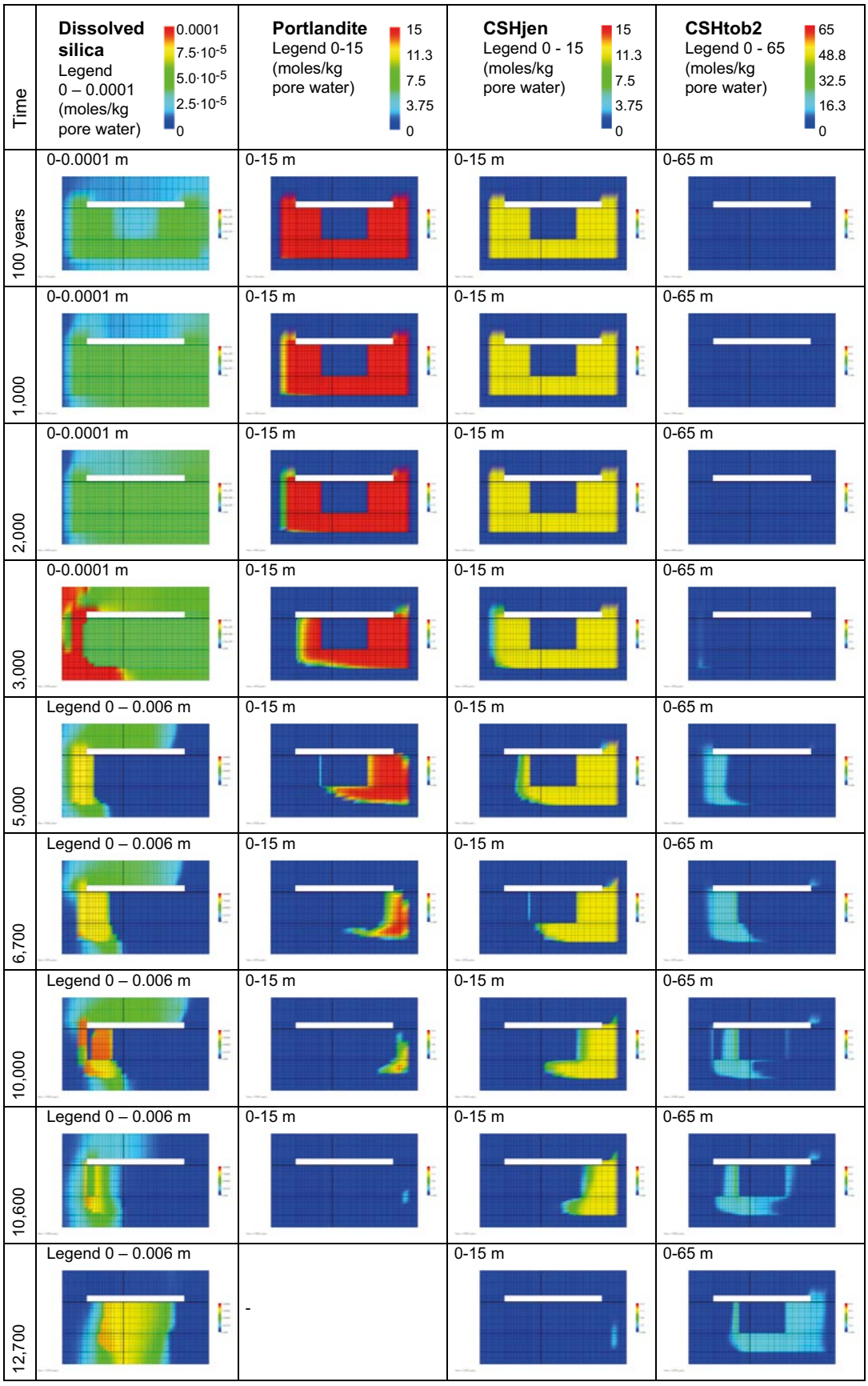

Figure 7-69. *Illustration of the gradual change in the concentration of dissolved silica in response to depletion and transformation of CSH-gel phases and portlandite at different times (Cemdata07 database, Case Large12). Observe the change of scale in the legend for dissolved silica after 5,000 years.*

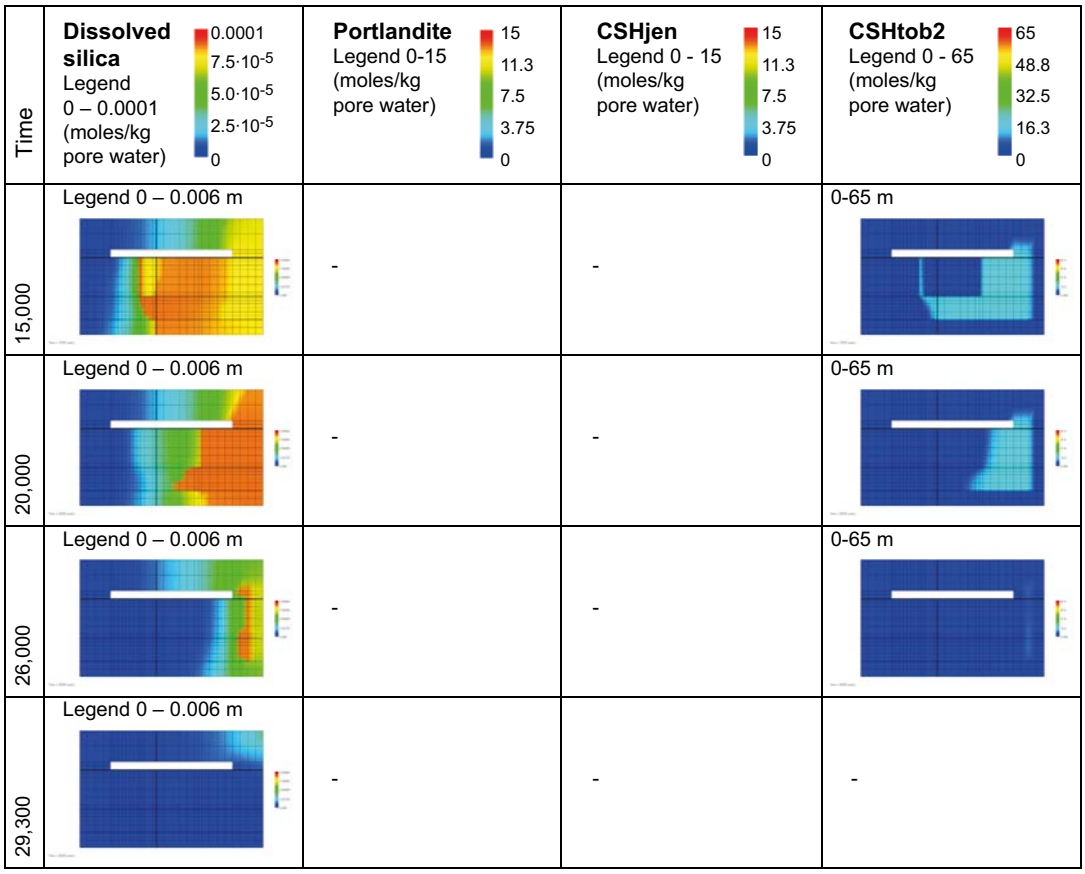

Figure 7-69. *Continued.*

Carbonate, calcite, thaumasite, monocarboaluminate and hydrotalciteC

The carbonate concentration increases as the groundwater changes from salt- to freshwater after 2,000 years, barely visible in the plots until ~ 3,000 years due to calcite precipitation, see Figure 7-70. During the period 2,000–5,000 years, calcite continuously precipitates primarily on the left-hand upstream side of the vault (see Figure 7-70), where the carbonate in groundwater meets calcium leached from the concrete constructions. Following the gradual depletion of minerals containing calcium, hydrotalciteC replaces the dissolving CSHtob2, followed by a complete replacement of hydrotalciteC by calcite at later stages, see Figure 7-70. The precipitation of thaumasite (a mineral containing sulphate, carbonate and silica) is activated by the approaching major front of calcite precipitation and the increased concentration of dissolved silica (see Figure 7-69) that occurs after approximately 3,000 years. However, an increased thaumasite precipitation only takes place in a thin zone, behind which the thaumasite disintegrates. Nevertheless, the occurrence of a moving front of precipitating and redissolving thaumasite may be detrimental for the integrity of the concrete. Monocarboaluminate is of subordinate importance in this case. At the end of the simulation, after 69,500 years the natural conditions of the groundwater – bedrock system has been essentially re-established and is governed mainly by carbonate-calcite equilibria.

Figure 7-70. *Illustration of the change of dissolved carbonate and of the gradual transformations between concrete mineral phases containing carbonate and/or aluminium over time. (Cemdata07 database, Case Large12). Observe the change of scale in the legend for calcite after 5,000 years.*

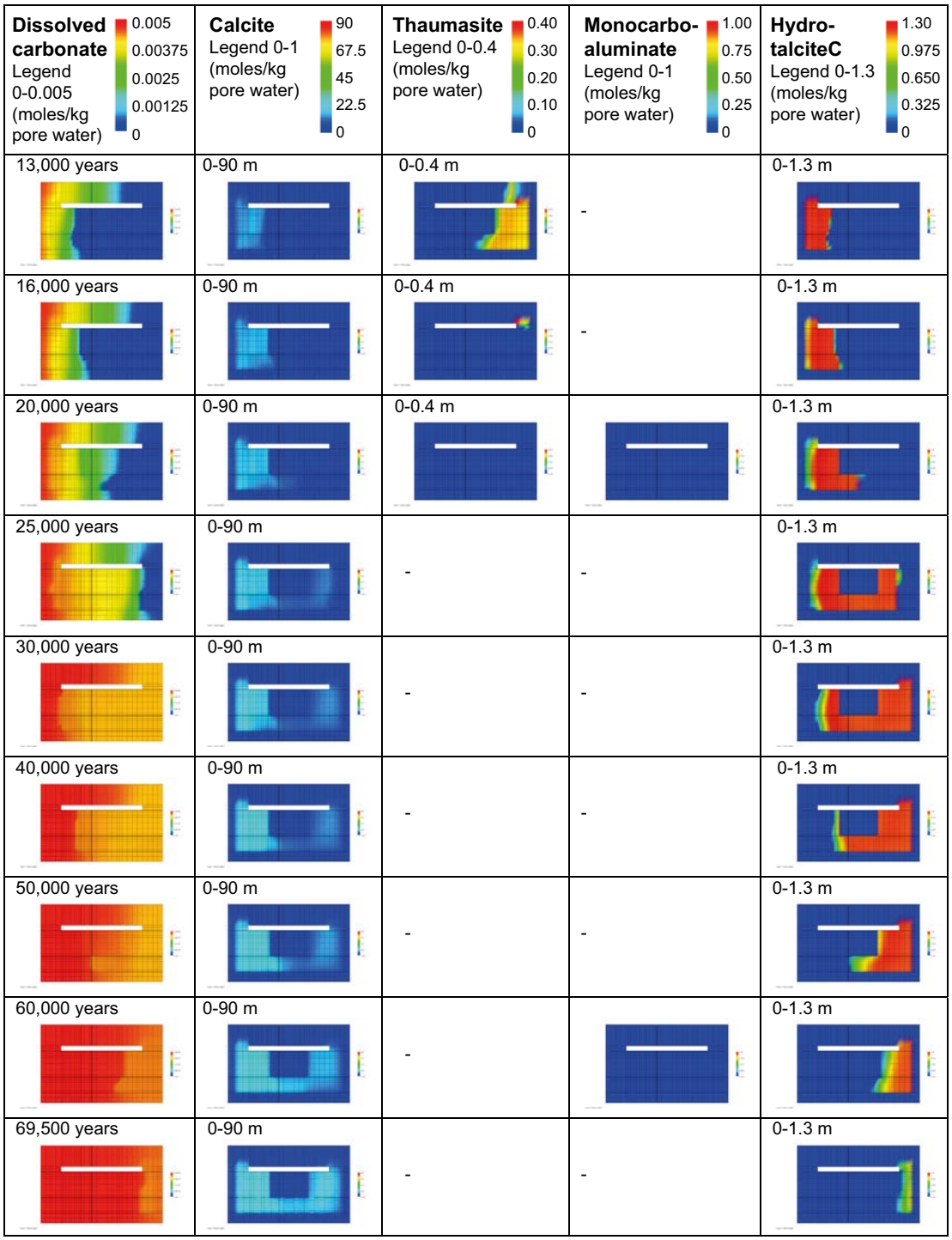

Figure 7-70. *Continued.*

Chloride

Chloride concentrations are assumed to be low in the fresh concrete, whereas the chloride content of the groundwater is high during the saltwater period. Chloride will act as a tracer in the calculations for case Large12 since there are no minerals containing chloride in the database Cemdata07 that have low enough solubility to precipitate. Hence, a fairly rapid ingress of chloride in the concrete pores is shown by the results in Figure 7-71. After 2,000 years the groundwater changes character and the chloride is washed out after short time.

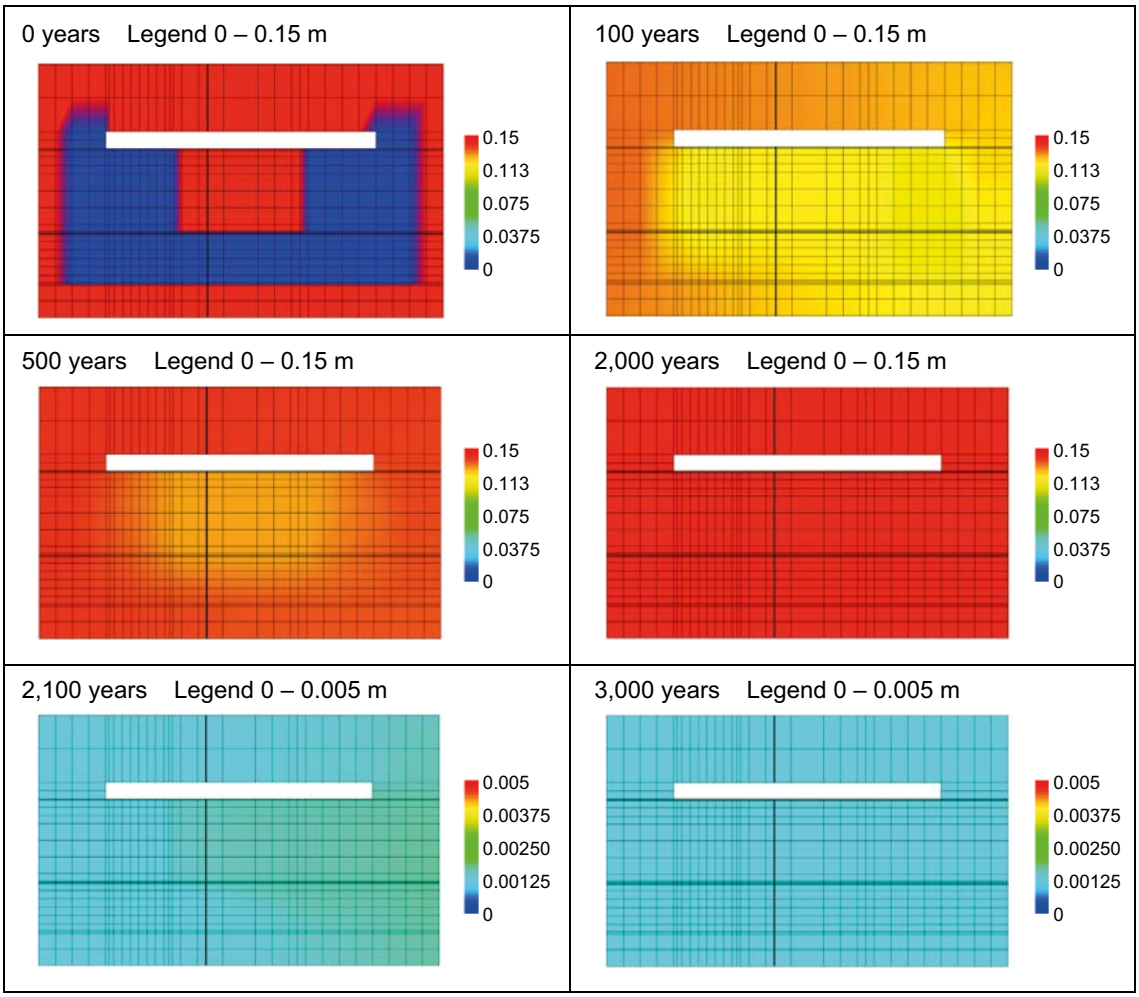

Figure 7-71. *Snap-shots of the dissolved chloride concentrations after 0, 100, 500, 2,000, 2,100 and 3,000 years. Observe the change of scale after 2,100 years. (Cemdata07 database, Case Large12).*

Sulphate, hydrogarnet, ettringite, thaumasite and aluminium

Initially the dissolved sulphate concentration is comparatively high, but it is reduced through interactions with soluble components leached from hydrogarnetSi (acting as a source of aluminium), which causes a slight precipitation of ettringite. This system then remains fairly constant up to 2,000 years. After this, the available aluminium increases as a result of dissolution of hydrogarnetSi and the precipitation of ettringite becomes more pronounced, particularly from 3,000 to 11,000 years, see Figure 7-72. From ~ 3,000 years, thaumasite (a mineral containing sulphate, carbonate and silica) also becomes active and forms an enriched rim that precipitates near ettringite and over time essentially replaces both ettringite and hydrogarnetSi. Ettringite and hydrogarnetSi are both depleted after ~ 13,700 years. Thaumasite subsequently dissolves in a moving front and is eventually depleted after a little more than 15,000 years. Both the ettringite and thaumasite formation should be regarded as deleterious processes that may cause the concrete to lose strength and integrity by peeling off parts of the concrete along the moving fronts. Starting at 15,000 years, the precipitation of $Al(OH)_3am$ progresses as a front in the direction of the groundwater flow where it replaces dissolving hydrotalciteC, cf. Figure 7-70.

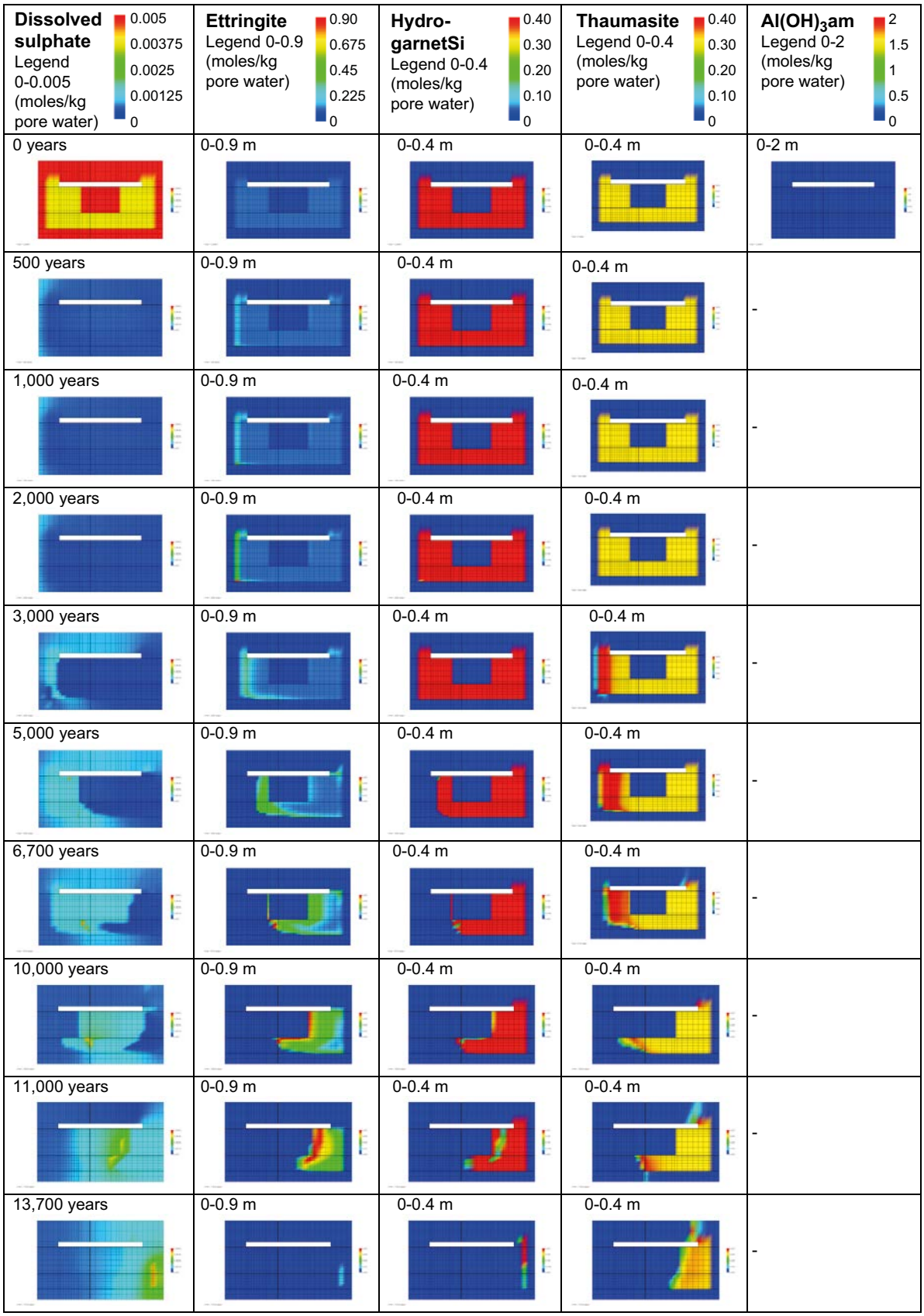

Figure 7-72. *Illustration of the gradual transformations between concrete mineral phases containing sulphate and/or aluminium over time. (Cemdata07 database, Case Large12).*

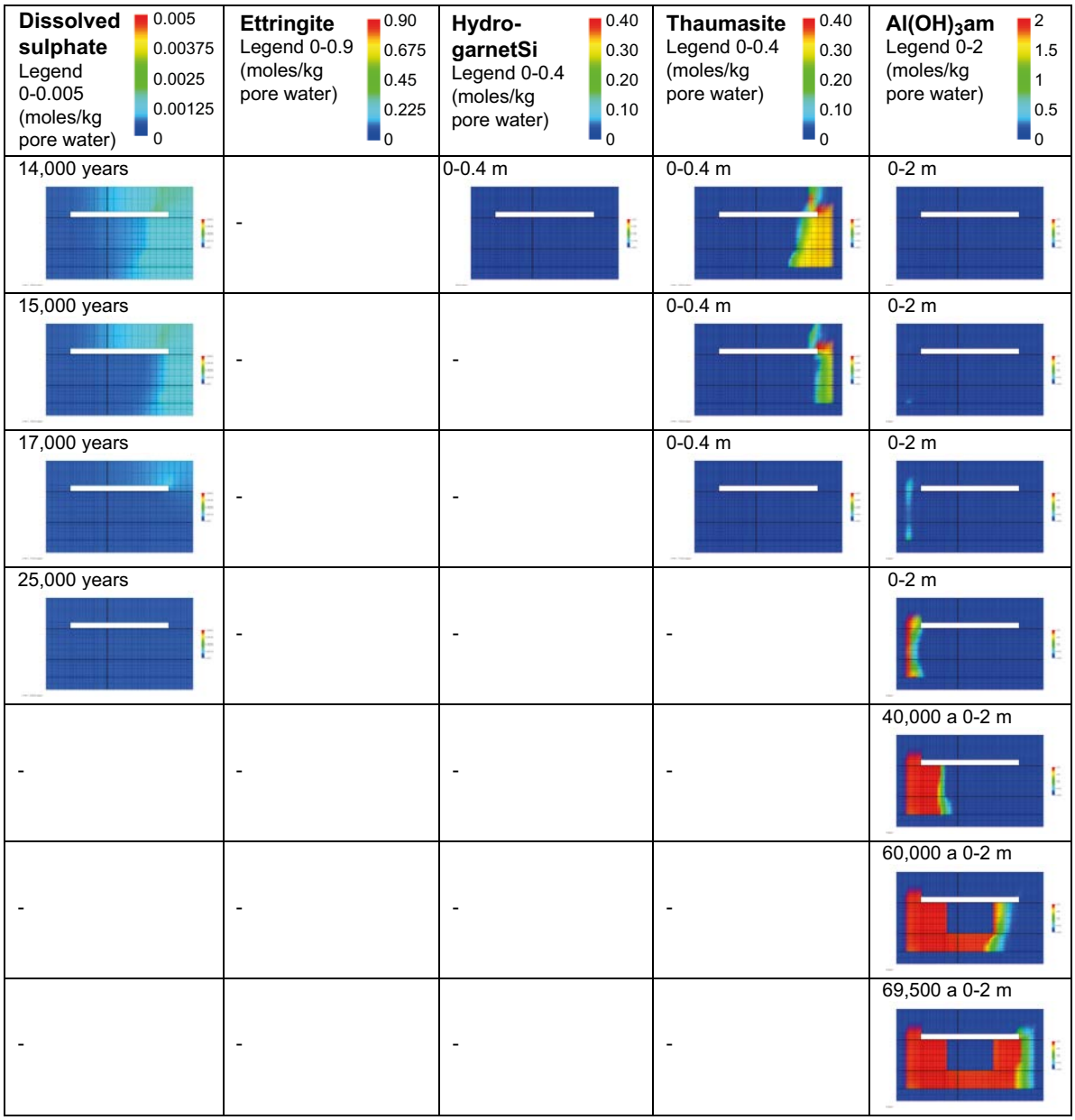

Figure 7-72. *Continued.*

Magnesium, iron and mineral reactions involving magnesium and iron

As the pH in the vault drops after the first 2,000–3,000 years, and then following the gradual depletion of calcium-containing minerals (10,000–40,000), the dissolved magnesium concentration gradually increases in the sand/crushed rock bed around the concrete constructions and then in the concrete itself, see Figure 7-73.

The different magnesium and iron containing minerals display an intricate interaction from 3,000 years onwards. HydrotalciteFe starts to dissolve at the left-hand, up-stream side and hydrotalciteOH precipitates in a zone that gradually moves through the concrete structure towards the right (in the direction of the groundwater flow), see Figure 7-73. $Fe(OH)_3$mic and hydrotalciteOH replace hydrotalciteFe in a thin zone moving from left to right during the period 5,000 up to almost 30,000 years. As the zone moves to the right, $Fe(OH)_3$mic and hydrotalciteOH are again replaced by hydrotalciteFe and hydrotalciteC starting after ~10,000 years at the left-hand upstream side and moving to the right. Starting during the period 10,000–20,000 years, $Fe(OH)_3$mic once again precipitates in a zone moving from the left to the right, replacing hydrotalciteFe and partly coexisting with hydrotalciteC. Eventually, hydrotalciteC is depleted while $Fe(OH)_3$mic remains stable towards the end of the simulation.

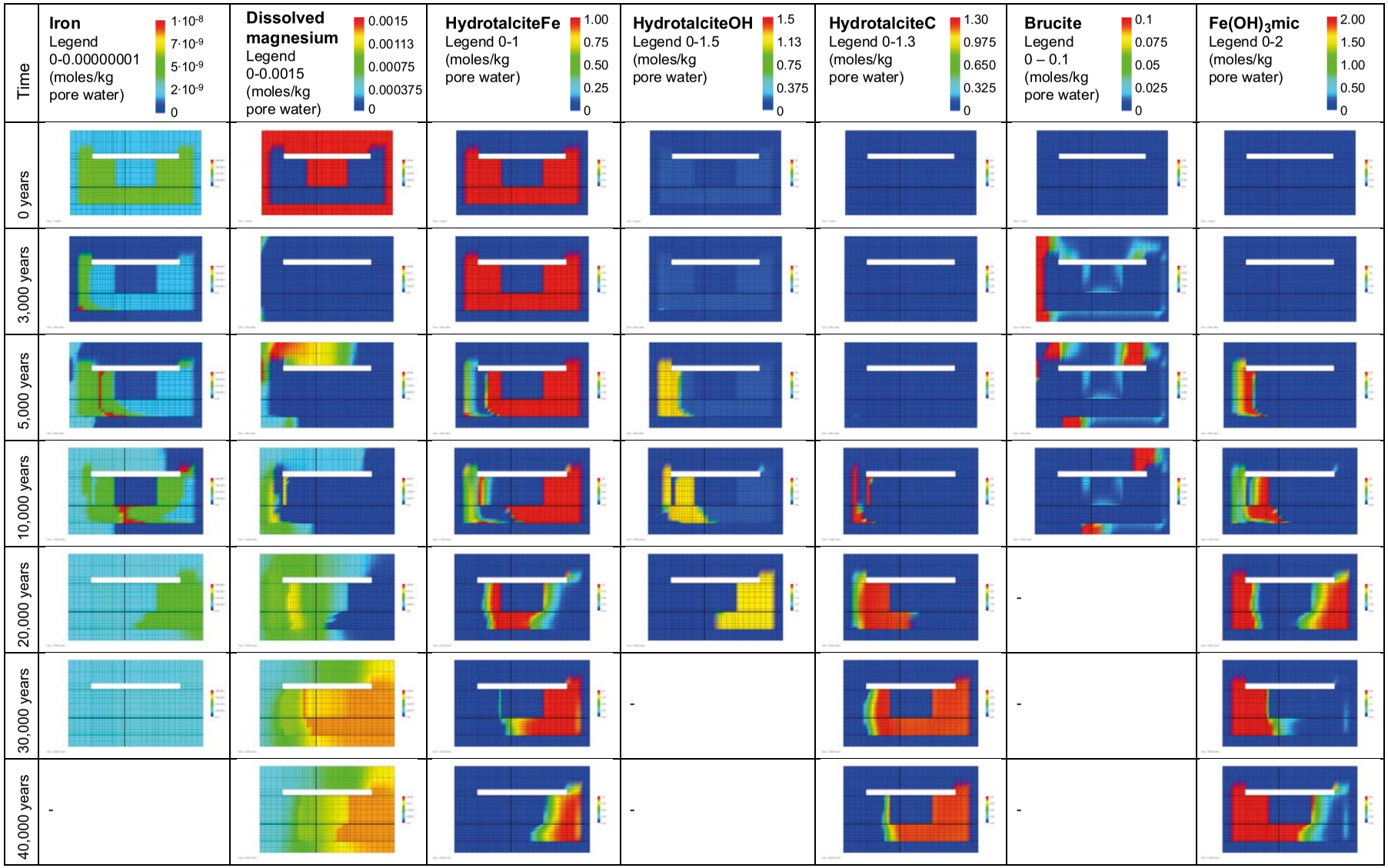

Figure 7-73. *Illustration of the change of dissolved magnesium and iron and the gradual transformations between concrete mineral phases containing magnesium and iron over time. (Cemdata07 database, Case Large12).*

7.9 Case Large9 (1BMA)

Case Large9 is a variation of case Large10. Like in case Large10 there is a slight change in the material properties at 100 years, but case Large 9 thereafter examines the effect of assuming that the material properties of the concrete barriers are constant during the period 100–10,000 years. This means that the barrier properties are assumed to maintain a better integrity than has been assumed for case Large10.

The presentation of the results first gives a brief overview of the evolution of the pore water chemistry and the mineral assemblage in one point in the cell grid at position AE, see Figure 7-8. Following this, the changes in the mineralogy at point DE, near the fracture, are presented. Finally, the evolution in the full 2-D-grid is presented and more detailed comments are given.

For additional information of the results, see graphical representations shown in Appendix G.

7.9.1 Evolution of chemistry and mineralogy at evaluation points

Evaluation point AE – at the intersection of the centrelines of the concrete floor and the left-hand side concrete wall

The gradual evolution of the mineral assemblage and the calculated changes of the porosity during the first 10,000 years are shown in Figure 7-74 . The results suggest that an initial concrete porosity of 11% would increase to ~ 17% by 8,700 years. The porosity is presented over the range of 0–30% in Figure 7-74; the maximum porosity corresponding to fully depleted cement minerals would be ~ 30%, the remaining volume constitutes the ballast material which is assumed to be inert.

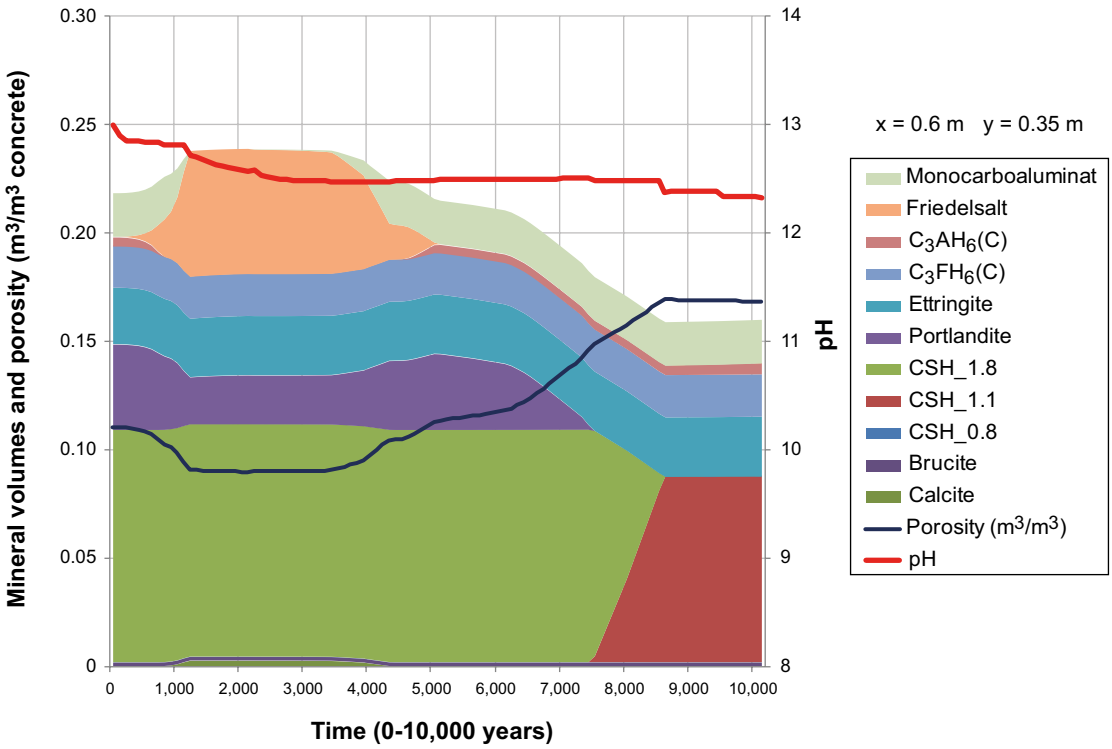

Figure 7-74. *The change of mineral volumes and porosity in concrete during the first 10,000 years at position AE (a point located at the intersection of a vertical centreline through the left-hand side concrete wall and a horizontal centreline through the concrete floor), (MinteqCem-2001 database, Case Large9). The evolution of pH is also indicated.*

During the first 10,000 years, the changes in the mineral assemblage affect the porosity. An early reaction between chloride in the groundwater and monocarboaluminate and hydrogarnet (C_3AH_6) causes the precipitation of Friedel's salt, a process essentially completed after 1,200 years. The reaction also consumes some portlandite in the concrete. From 3,400–4,400 years Friedel's salt partly decomposes and monocarboaluminate, portlandite are regained, from 4,400–5,000 years a small amount of hydrogarnet reappears, leading to depletion of Friedel's salt after ~5,100 years. At 7,500–8,600 years CSH_1.8 is transformed to CSH_1.1. There is no significant change in the amount of ettringite (at observation point AE) during the first 10,000 years, hence the risk for fracture formation due to ettringite formation identified in case Large10 is not identified in this simplified case.

Evaluation point DE – at the vertical centreline of the left-hand side concrete wall near the thin horizontal fracture

The gradual evolution of the mineral assemblage over time is shown in Figure 7-75 together with the calculated changes of the porosity during the first 10,000 years. The results show that the porosity would be expected to increase from the initial value of 11% to ~ 16% after 3,300 years. Interestingly, the porosity thereafter consistently drops during the period 3,300–8,000 years when the calculated porosity approaches zero, i.e. a complete blocking of the pore space by precipitating minerals. Ettringite formation is the main responsible process for the observed effect. It can be argued that when porosity blocked the transport of reactants would stop and no further reactions would be possible. Since the PHAST model does not account for the changed porosity, the calculations carry on despite the physical ambiguities. However, since ettringite is known to cause fractures while exerting high expansion pressures during precipitation, the results may still not be entirely unrealistic. As ettringite precipitates in the form of thin needles, new fractures may form as these needles overbridge the pores and thin fractures causing mechanical tension in the concrete. This may form new transport routes for the supply of reactants and the degradation can continue. Comparison of this with the results from case Large10 again shows that the variation of the assumed material properties has a marked impact on the results in the vicinity of the thin fracture.

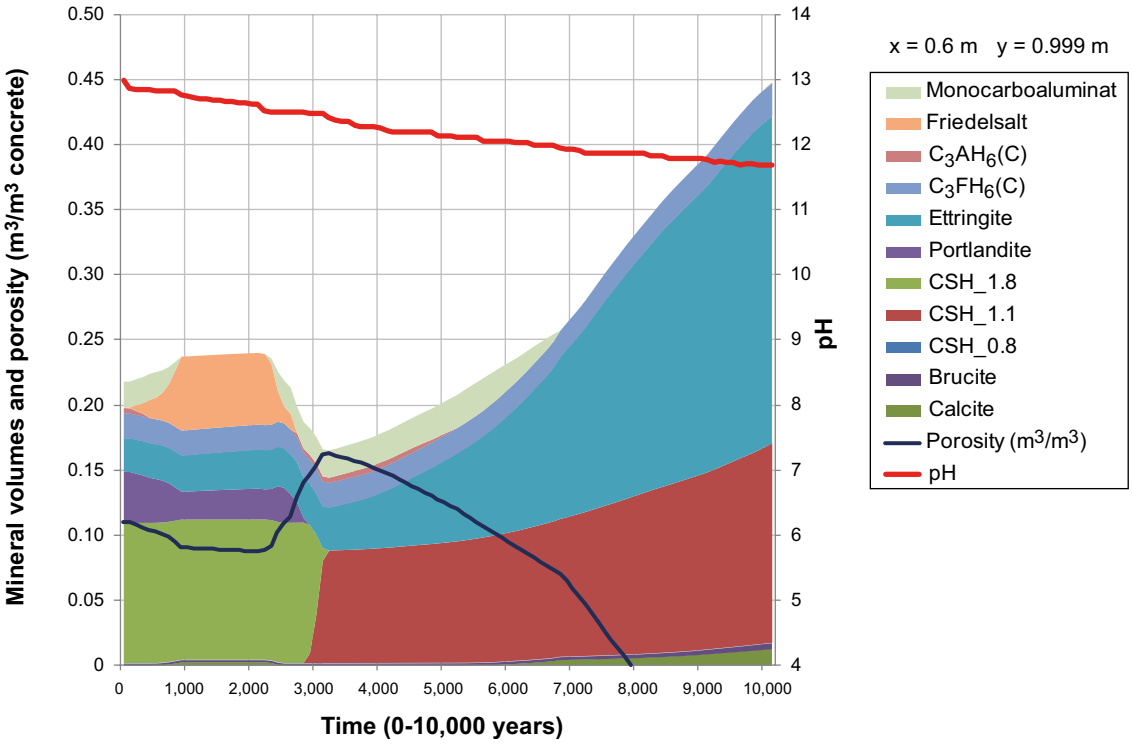

Figure 7-75. *The amount of minerals and porosity in concrete during the first 10,000 years at position DE (a point located at the vertical centreline through the left-hand side concrete wall, 1 mm from an open fracture), (MinteqCem-2001 database, Case Large9). The evolution of pH with time is also indicated.*

7.9.2 Evolution of the chemistry and mineralogy of the 2-D system

pH evolution, calcium and silica depletion

The evolution of pH is summarised in Figure 7-76. The model results show that a high pH (> 12.5) is maintained inside the concrete constructions over the first 2,000 years. Thereafter the pH gradually drops, starting at the left-hand inflow side, where the pH approaches ~ 12 in the outer layers of the concrete wall. This effect is accentuated adjacent to the horizontal fracture after ~ 3,000 years. Up to 10,000 years, the pH of the concrete wall on the left-hand inflow side of the model drops to ~ 11.5, while the pH inside the open void (representing the vaults where the waste is stored) remains at ~ pH 12.5. After 11,000 years, the left-hand upstream side of the vault has reached a pH of ~ 11.5, at 12,000 years the entire vault has a pH of 11.6 or lower, at 12,800 years a pH of 11 or lower and after 20,000 years the pH is lower than pH 10.5 in the entire vault. At 30,000 years, the pH drops below 10 throughout the vault. At 32,000 years the entire vault, with exception for the right-hand downstream side of the vault, has a pH of ~ 8. At ~ 36,000 years the entire vault has a pH below 8.

After ~ 500 years, the conditions are almost entirely determined by the solubility of portlandite – a period which stretches up to ~ 3,000 years. As can be seen in Figure 7-76, a gradual depletion of calcium starts to show at 3,000 years and propagates over time. At 5,000 years, a distinct effect of the fractures is shown by zones depleted in portlandite. By 11,000 years, only small parts at the right-hand down-stream side of the concrete constructions contribute any significant concentrations of calcium to the pore water (note the change of scale in the figure).

The slow evolution of the pH (in comparison with Large10) results from the better concrete integrity assumed in this case, which leads to slower leaching and transformation of portlandite and CSH phases. Portlandite is almost entirely depleted after 10,000–11,000 years, while the transformation of CSH_1.1 to the least alkaline gel-phase CSH_0.8 starts after 15,000 years. After ~ 19,000 years the only remaining CSH-component is CSH_0.8, which in turn becomes depleted after ~ 28,000 years.

Carbonate, calcite, ettringite, monocarboaluminate and Friedel's salt

The delay in the chemical processes introduced by the simplification applied here is also apparent in Figure 7-78. During the period 500–2,000 years, calcite continues to precipitate primarily on the outside of the concrete wall at the left side as well as on the underside of the concrete floor, where the carbonate in groundwater meets calcium leached from the concrete constructions (see Figure 7-78), but increasingly from ~ 2,000 years and onwards also on the left-hand upstream side of the vault. After 2,000 years the composition of the groundwater changes and in response to this the Friedel's salt is decomposed, accompanied by transformation of calcite to monocarboaluminate and an increased precipitation of ettringite. From ~ 3,000 years and onward an intense precipitation of calcite takes place at the left-hand upstream side where groundwater enters the vault. Continuing over the period 2,000–9,000 years Friedel's salt is depleted. Enhanced precipitation of ettringite replacing monocarboaluminate propagates as a front from left to right through the concrete structures during the period 5,000–13,000 years, at which point ettringite is dissolved and disappears completely. The occurrence of a moving front of precipitating and redissolving ettringite may be detrimental for the integrity of the concrete. Calcite continues to precipitate (note the change of scale at 6,700 years). After ~ 30,000 years calcite has replaced essentially all other minerals in the vault. Calcite precipitation continues very slowly hereafter.

Sulphate, chloride, hydrogarnet, ettringite, monocarboaluminate and Friedel's salt

Chloride concentrations are assumed to be low in the fresh concrete, whereas the chloride content of the groundwater is high during the saltwater period. Initially the dissolved sulphate and chloride concentrations are comparatively high, but they quickly decrease due to interactions with soluble components leached from the concrete, which causes a slight precipitation of ettringite and Friedel's salt. Hydrogarnet (C_3AH_6) and monocarboaluminate are consumed in the reaction with chloride ions to form Friedel's salt. The hydrogarnet phase disappears after ~1,500 years and the monocarboaluminate almost disappears after ~ 2,000 years, see Figure 7-79. After 2,000 years, the composition of the groundwater changes and in response to this the Friedel's salt gradually decomposes and disappears completely after ~ 8,000 years. Decomposition of the Friedel's salt leads to neoformation of monocarboaluminate. The monocarboaluminate in turn is replaced by an increased precipitation of ettringite, which is also accompanied by the reappearance of hydrogarnet (C_3AH_6). Both of these processes propagate as a front from left to right through the concrete structures during the period 2,000–12,300 years when hydrogarnet again disappears. Following this, ettringite dissolves and disappears completely by ~ 17,000 years.

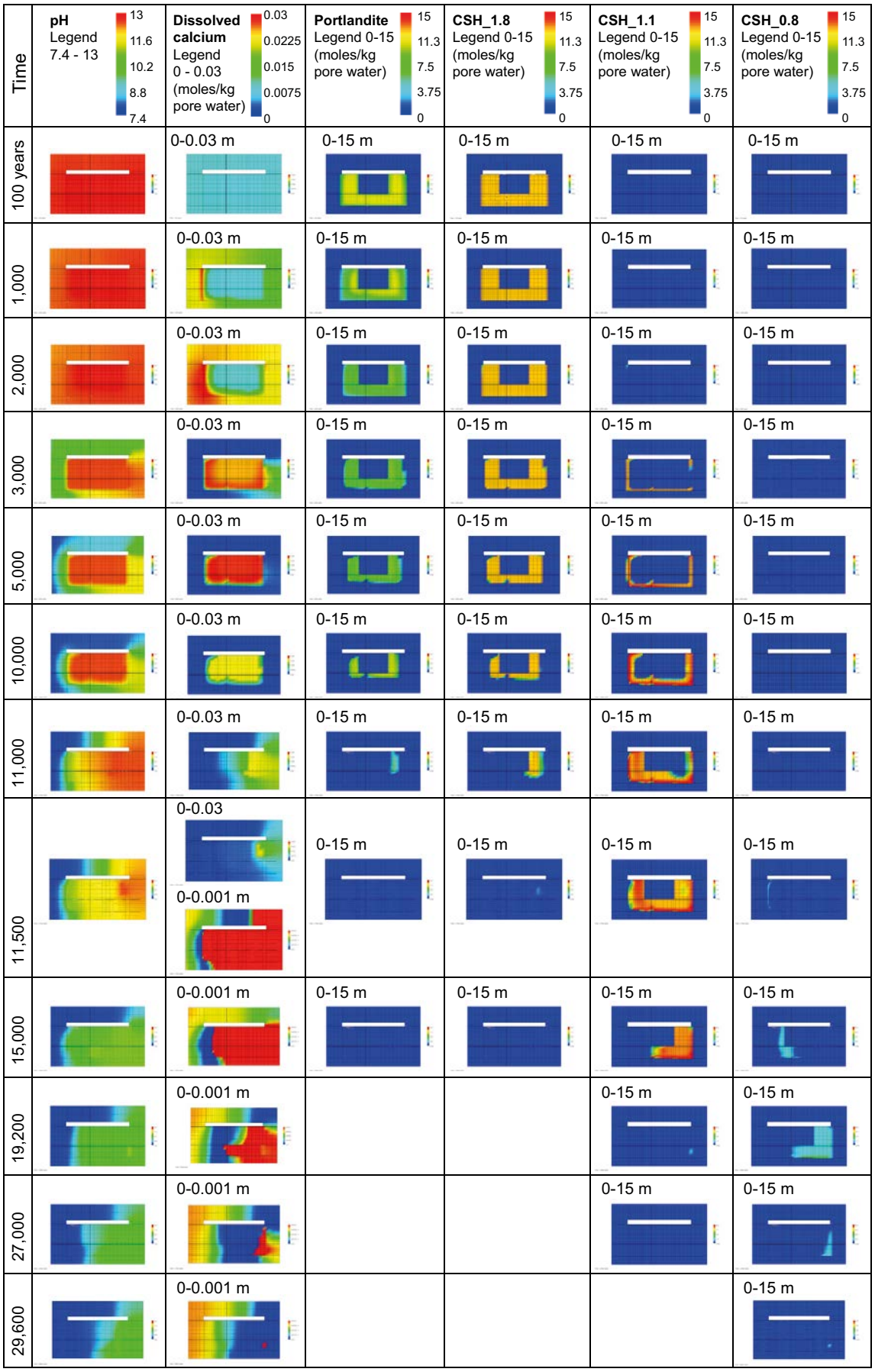

Figure 7-76. *Illustration of the gradual evolution of pH as a result of depletion and transformation of mineral phases containing calcium over time. (MinteqCem-2001 database, Case Large9). Observe the change of scale in the legend for dissolved calcium after 11,500 years.*

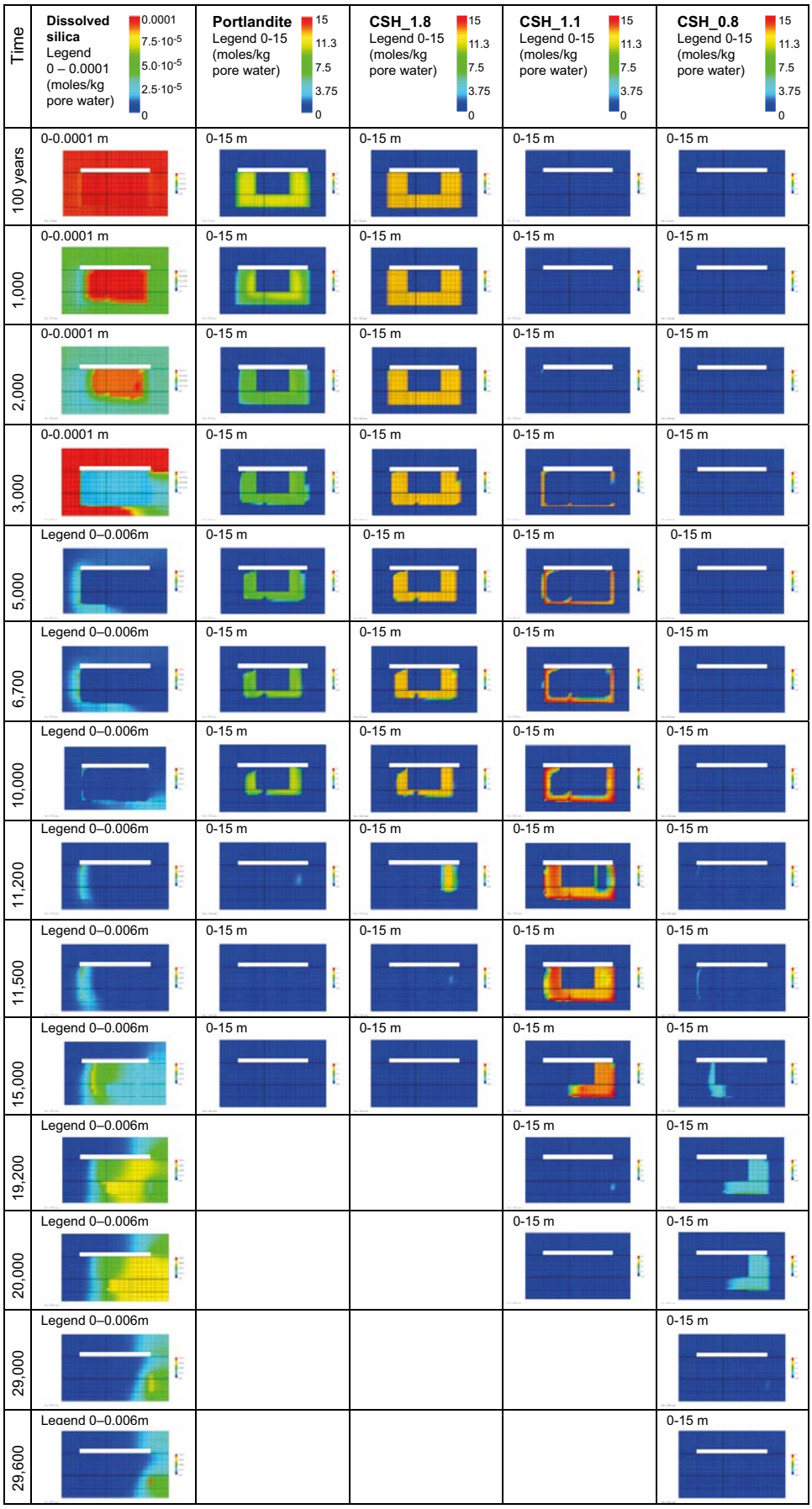

Figure 7-77. *Illustration of the gradual change in the concentration of dissolved silica in response to depletion and transformation of CSH-gel phases and portlandite over time (MinteqCem-2001 database, Case Large9). Observe the change of scale in the legend for dissolved silica after 5,000 years.*

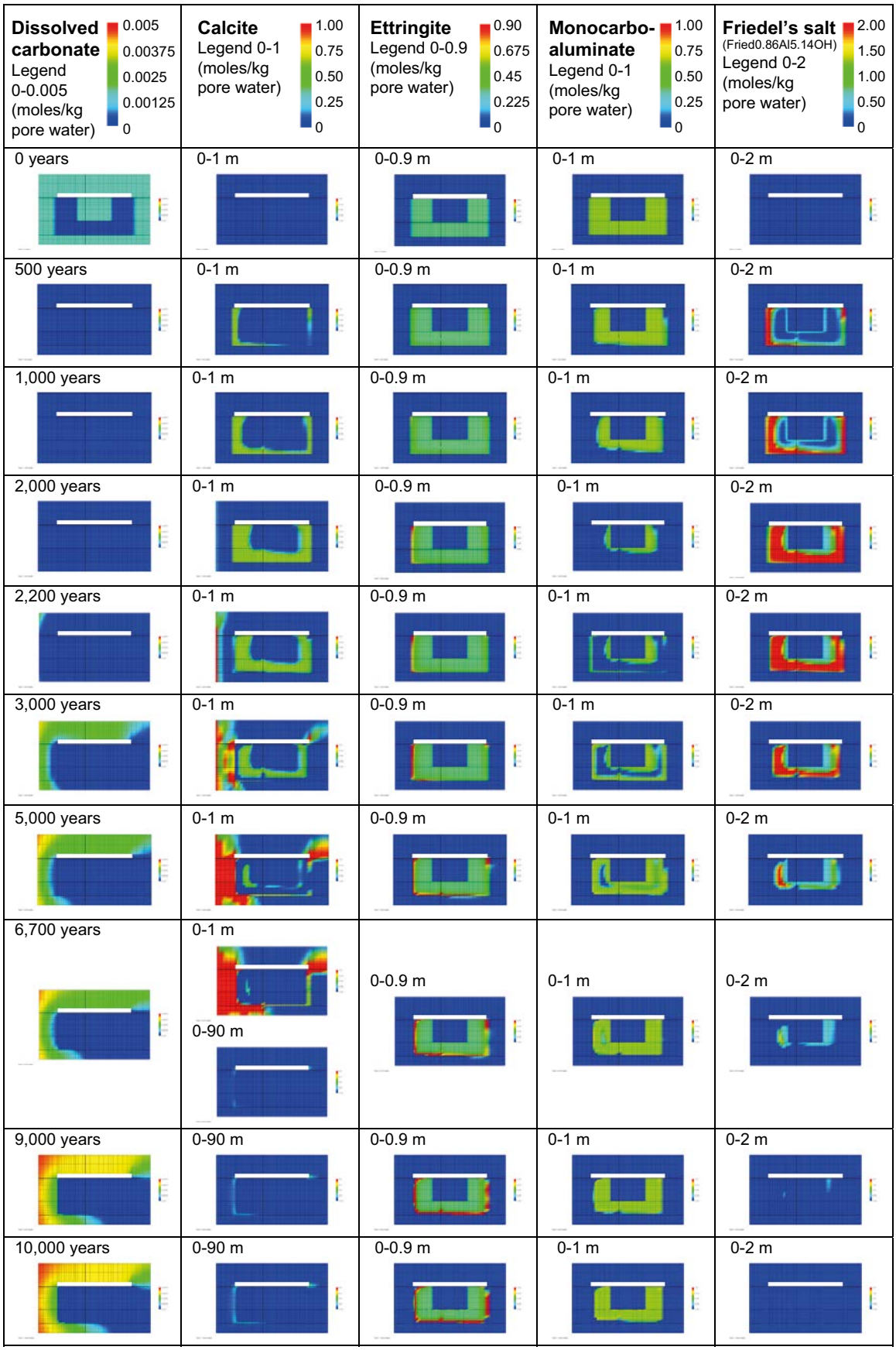

Figure 7-78. *Illustration of the change of dissolved carbonate and of the gradual transformations between concrete mineral phases containing carbonate and/or aluminium over time. (MinteqCem-2001 database, Case Large9). Observe the change of scale in the legend of calcite after 6,700 years.*

Dissolved carbonate Legend 0-0.005 (moles/kg pore water) 0.005 0.00375 0.0025 0.00125 0	**Calcite** Legend 0-1 (moles/kg pore water) 1.00 0.75 0.50 0.25 0	**Ettringite** Legend 0-0.9 (moles/kg pore water) 0.90 0.675 0.45 0.225 0	**Monocarbo-aluminate** Legend 0-1 (moles/kg pore water) 1.00 0.75 0.50 0.25 0	**Friedel's salt** (Fried0.86Al5.14OH) Legend 0-2 (moles/kg pore water) 2.00 1.50 1.00 0.50 0
11,000 years 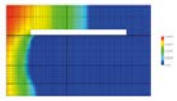	0-90 m 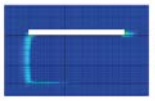	0-0.9 m 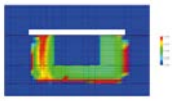	0-1 m 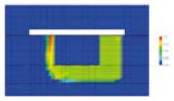	-
12,300 years 	0-90 m 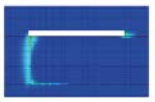	0-0.9 m 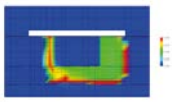	0-1 m 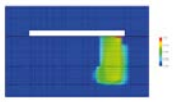	-
13,000 years 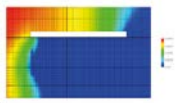	0-90 m 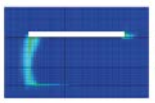	0-0.9 m 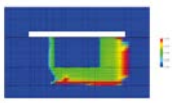	-	-
17,700 years 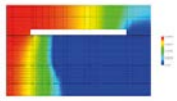	0-90 m 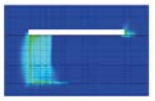	0-0.9 m 	-	-
20,000 years 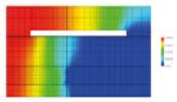	0-90 m 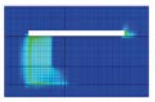	-	-	-
25,000 years 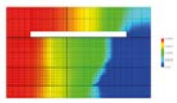	0-90 m 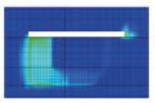	-	-	-
30,000 years 	0-90 m 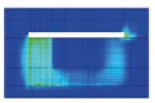	-	-	-
50,000 years 	0-90 m 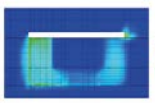	-	-	-

Figure 7-78. *Continued.*

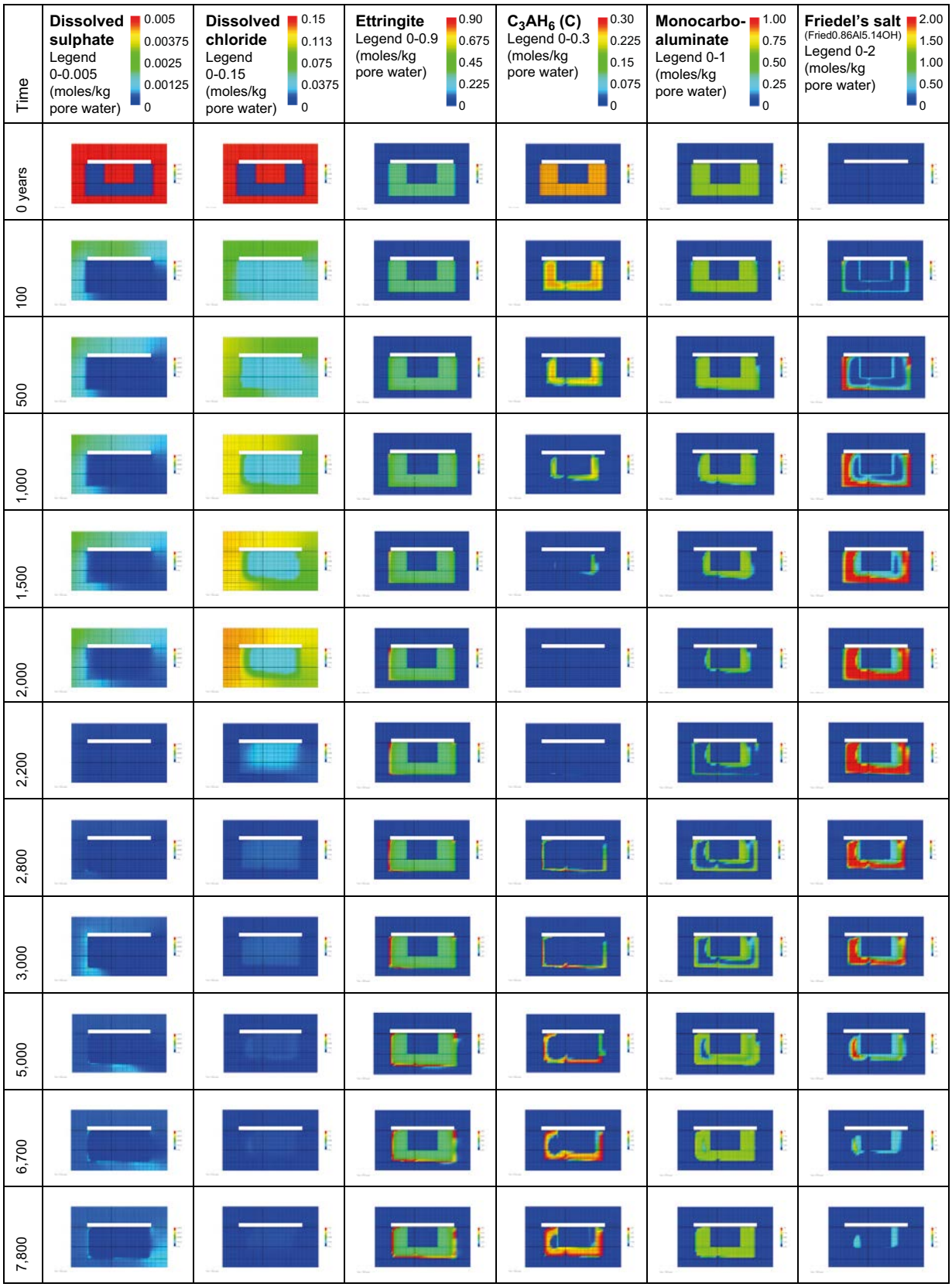

Figure 7-79. *Illustration of the gradual transformations between concrete mineral phases containing sulphate, chloride and/or aluminium over time. (MinteqCem-2001 database, Case Large9).*

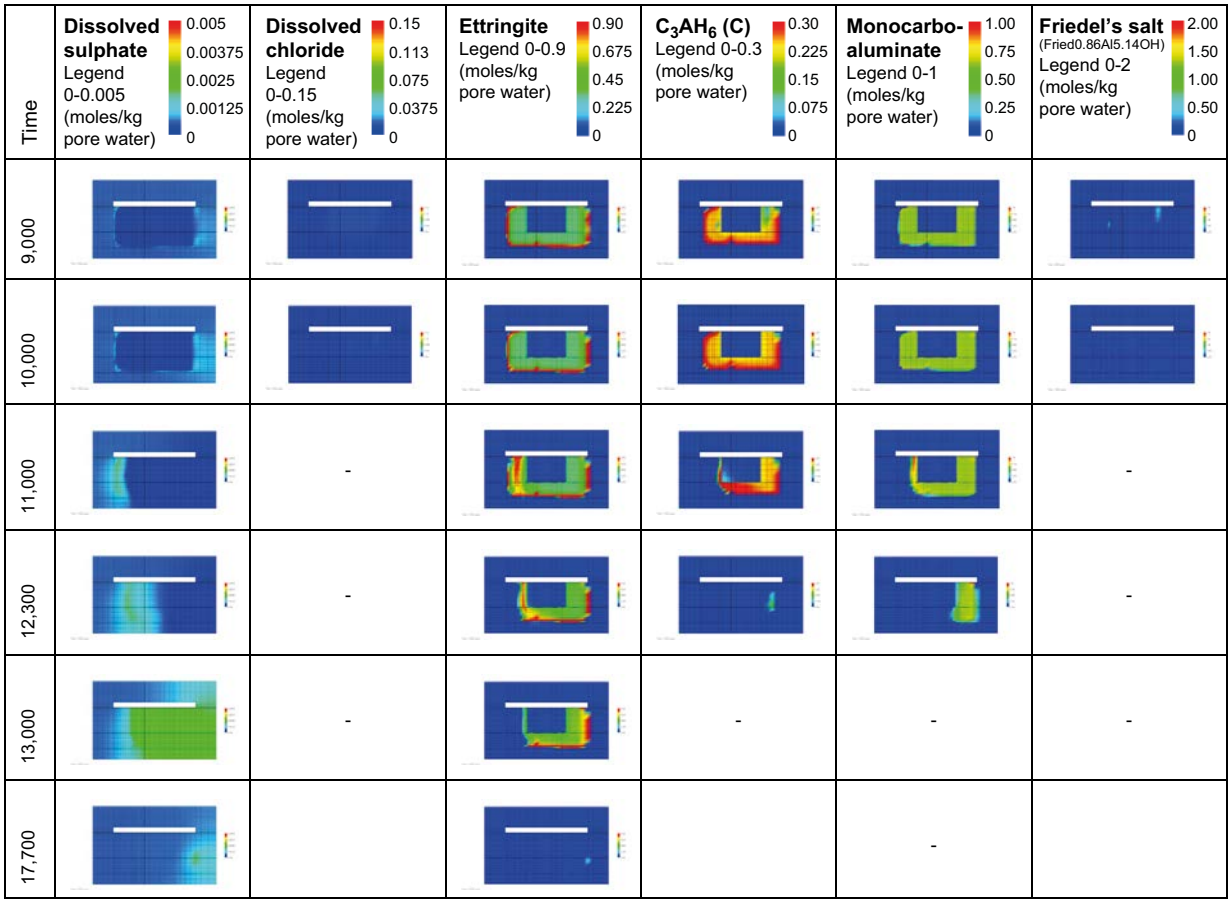

Figure 7-79. *Continued.*

Magnesium, iron and mineral reactions involving magnesium and iron

Dissolved magnesium is present in fairly high concentrations in the saline groundwater, whereas the concentration drops significantly as the groundwater changes to freshwater after 2,000 years. However, in the vault, dissolved magnesium will only be present in low concentrations due to the low solubility of brucite that precipitates in the alkaline environment created by the concrete.

As the pH in the vault drops between 2,000–3,000 years, the dissolved magnesium concentration gradually increases in the sand/crushed rock bed around the concrete constructions. From ~ 5,000 years, a sharp front of precipitating brucite on the left-hand, up-stream side of the left concrete wall is seen (Figure 7-80).

After ~ 10,000 years, in response to decreasing pH, the brucite starts to dissolve on the upstream side, while precipitation continues on the downstream side of the front.

Following the gradual depletion of alkaline components in the concrete, the magnesium concentrations in the concrete pore water increase, as seen from (10,000 – ~ 30,000 years) in Figure 7-80 and ultimately levels off at the concentration determined by the inflowing groundwater after ~ 30,000–40,000 years.

Iron occurs in low concentration in groundwater, unless very reducing conditions. Iron is a constituent of concrete and may appear in various minerals including iron hydroxides, iron-substituted ettringite and hydrotalcite etc. In case Large9, iron appears as an iron substituted hydrogarnet C_3FH_6, whereas other minerals containing iron have been neglected. The dissolved iron concentrations start to increase from the left-hand upstream side of the left concrete wall after ~ 10,000–15,000 years in response to decreasing pH and increased leaching of calcium, see Figure 7-80. The dissolution of C_3FH_6 slowly progresses as a front from left to right in the figures and disappears after ~ 29,000 years.

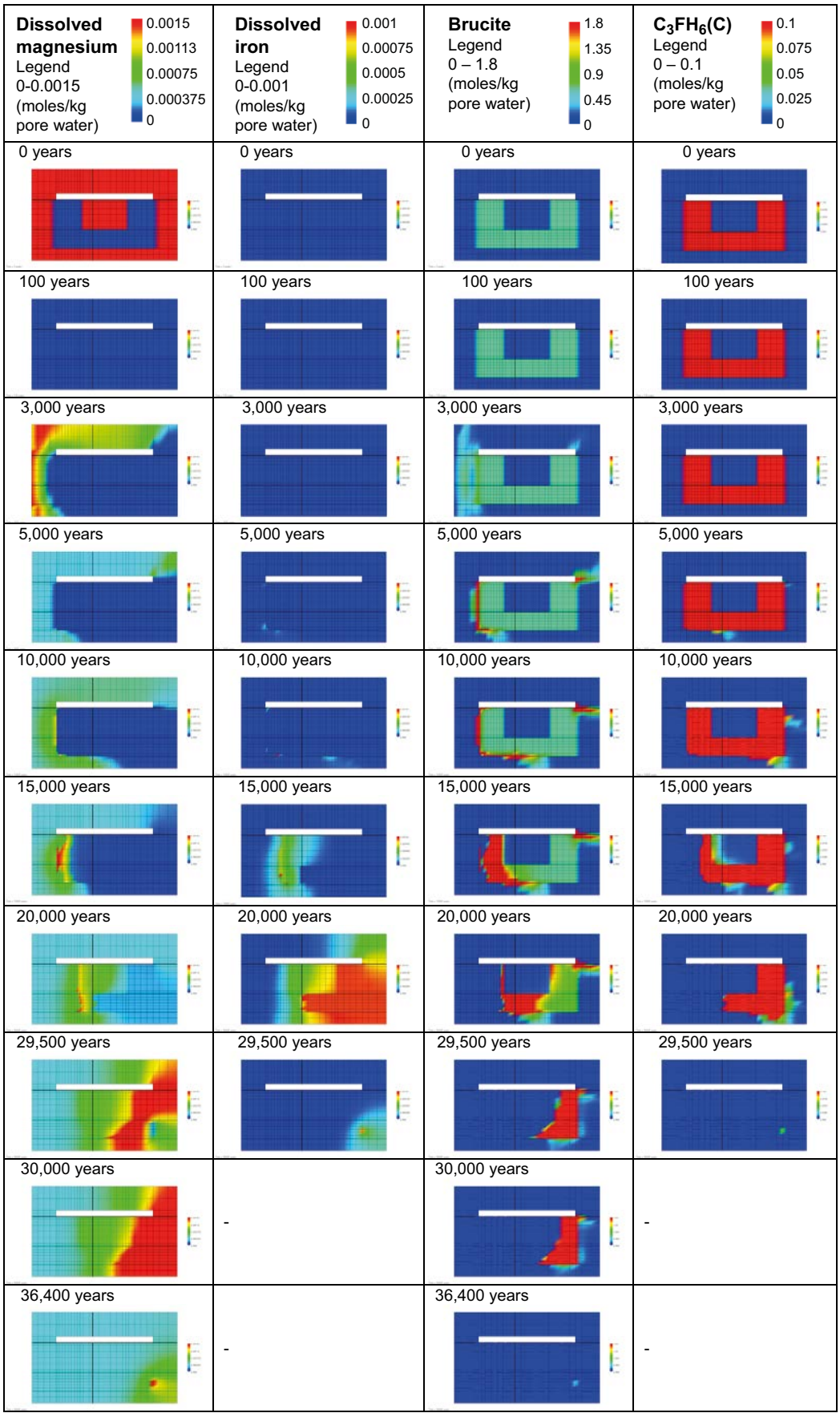

Figure 7-80. *Illustration of the change of dissolved magnesium and iron and the gradual changes of concrete mineral phases containing magnesium and iron over time. (MinteqCem-2001 database, Case Large9).*

7.10 Case Large7 (1BMA)

Case Large7 is a variation of case Large8 with highly simplified chemistry where the only solid phase considered is portlandite. One further simplification is that the aqueous phase is assumed to be pure water instead of groundwater. Hence, this represents a conservative case where the leaching of calcium is very fast since no chemical interactions with other alkaline minerals are taken into account. The rationale for this calculation is to serve as a benchmark for comparison with simple analytical calculations where more complex chemistry is not possible to address. The thermodynamic database Cemdata07 is used.

The evolution of pH, dissolved calcium concentrations and the amount of portlandite are presented in Figure 7-81. The results show that calcium is spread throughout the vault in short time, giving a pH of ~12.5 in the concrete porewater, and reaching a pH in the range 12.3–12.5 in the macadam porewater, within 100 years. As the groundwater flow changes at 2,000 years a flushing of the leachate from left to right in the figures become apparent, demonstrating the transition to an advection dominated regime. The calcium concentration in the concrete pore water is governed by the dissolution of portlandite at a constant level of ~0.02 m.

pH evolution, calcium and portlandite

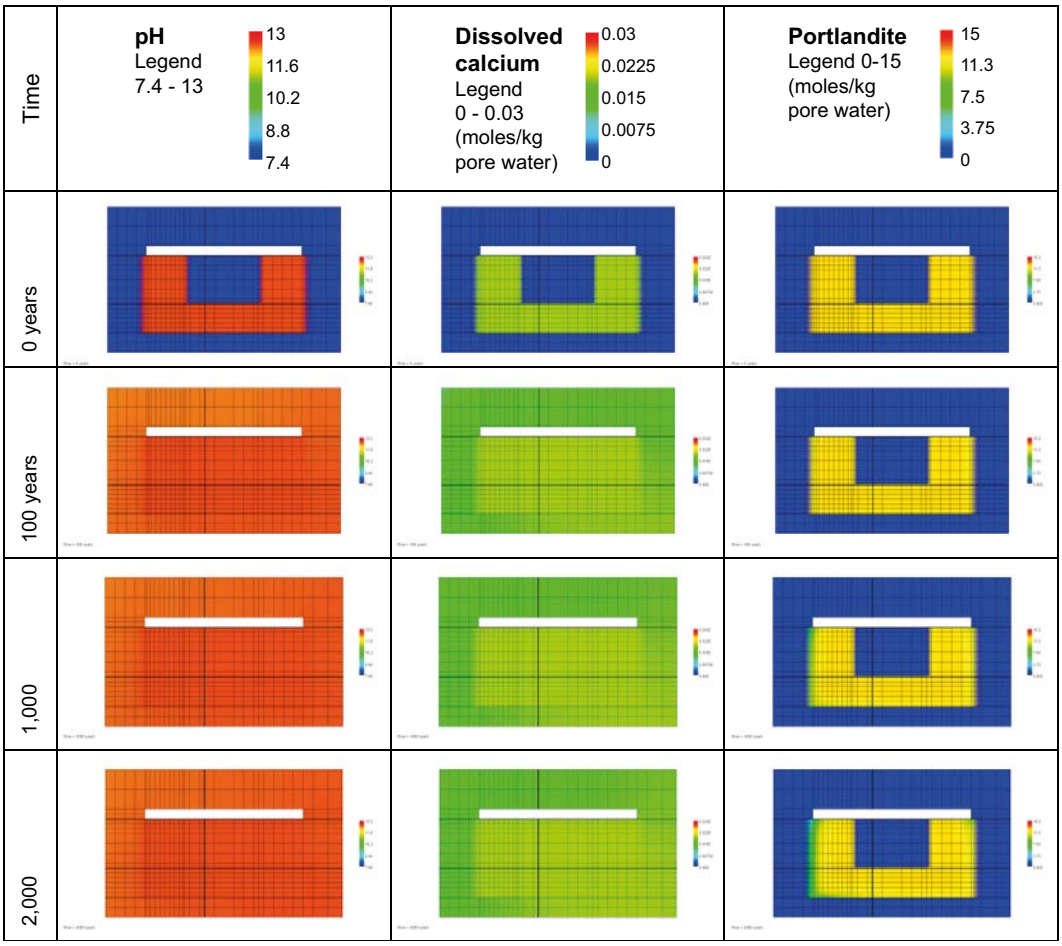

Figure 7-81. *Illustration of the gradual evolution of pH and concentration of dissolved calcium as a result of depletion and transformation of mineral phases containing calcium over time. (Cemdata07 database, Case Large7).*

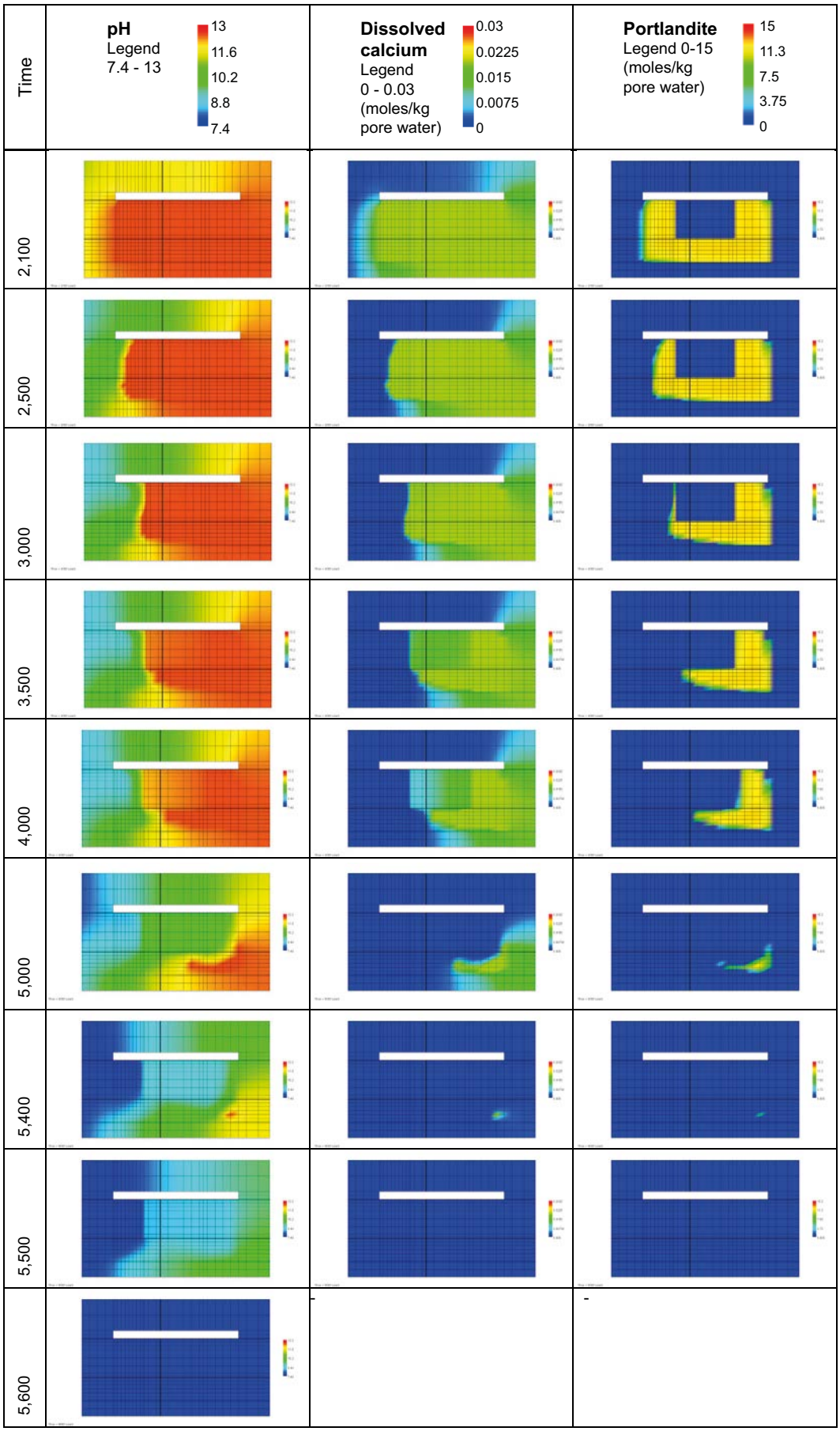

Figure 7-81. *Continued.*

7.10.1 Comparison of results from PHAST modelling and analytical shrinking-core models

The numerical results for case Large7 have been compared with simple analytical shrinking-core models that may be applicable to different conditions: one model assuming leaching by pure diffusion and one model assuming leaching by pure advective flow; see Section 5.1 for details.

The following basic data and variables have been used in the evaluation:

$D_{e,ww}$ = effective diffusivity of weakly weathered zone (see Figure 7-82)(m^2/a)

c_{sol}^{CH} = solubility of portlandite = $1.95 \cdot 10^{-2}$($kmol/m^3$)

t = time (a)

q_0^{CH} = initial amount of free portlandite in concrete = 1.3345($kmol/m^3$)

q_{gw} = groundwater flux (see Figure 7-87)($m^3/m^2/a$)

Leaching due to pure diffusion in concrete walls

The effective diffusivity has been assumed to follow the evolution over time according to the assumptions made for case Large7, see Table 7-7. To allow a direct comparison, the same data as described above were assumed.

The calculated leaching depths caused by diffusion are presented in Figure 7-82. Comparing the analytical calculations with the results of the numerical model using PHAST, cf. Figure 7-97, significantly smaller leaching depths are observed at longer times for the shrinking-core model than for the numerical model. The obvious reason being the transition from a diffusion-dominated to an advection-dominated regime after 1,000 years assumed in the numerical modelling, cf. Figure 7-88. However, the leaching depth due to diffusion is still greater up to 2,000 years, compare Figure 7-82 and Figure 7-89.

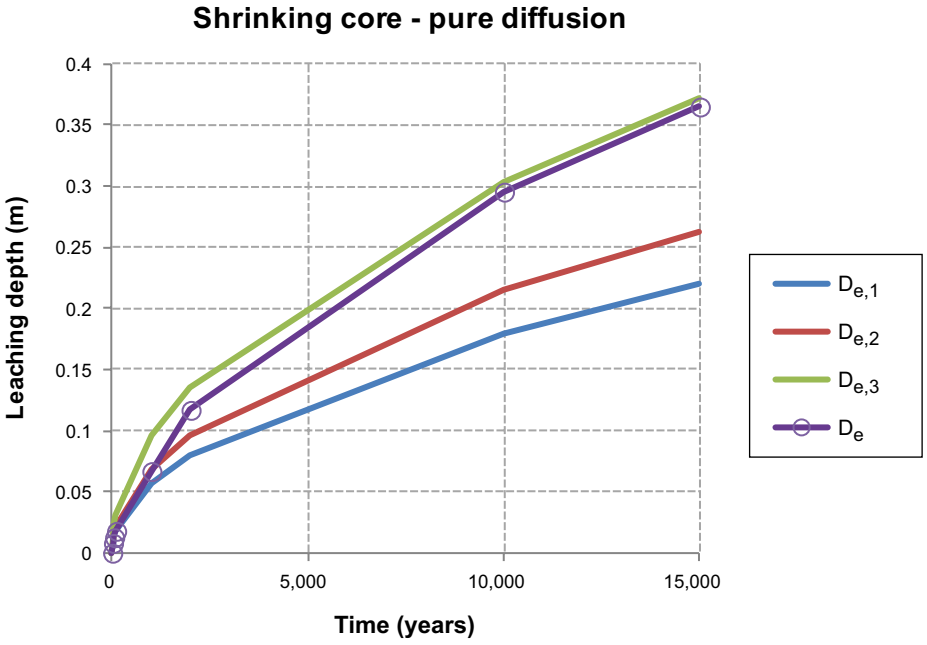

Figure 7-82. *Calculated leaching depths during the first 15,000 years with a shrinking-core model assuming pure diffusion. The different curves represent different values of the effective diffusivity ($D_{e,1}$= $3.5 \cdot 10^{-12}$ m^2/s, $D_{e,2}$= $5 \cdot 10^{-12}$ m^2/s, $D_{e,3}$= $1 \cdot 10^{-11}$ m^2/s, whereas the curve denoted D_e takes into consideration the changes of the effective diffusivity with time: $D_{e,1}$ (0–100 years), $D_{e,2}$ (100–1,000 years) and $D_{e,3}$ (1,000–10,000 years).*

Leaching due to advective groundwater flow in concrete walls

For the advection calculations, the flux in the upstream-side concrete wall has been collected from the PHAST modelling. Details of the horizontal flux distribution along a vertical section (E-E) through the concrete wall at $x = 0.6$ m are presented for different times in Figure 7-83, Figure 7-84, Figure 7-85 and Figure 7-86. As a representative flux, the water velocity at the evaluation point BE at $x = 0.6$ m and $y = 0.75$ m was selected and multiplied with the porosity (0.11 m^3/m^3). The resulting fluxes $q_{ha,1}$ to $q_{ha,4}$ (corresponding to different degradation steps $h_{a,1}$ to $h_{a,4}$) at different times are presented in Figure 7-87. Other data assumed in the calculations were described above.

The calculated leaching depths caused by advective flow through the concrete wall are presented in Figure 7-89. The calculations are presented for one case taking into consideration a transient flux q_{ha} due to gradual degradation of the concrete wall. As a comparison, Figure 7-89 also presents results for different cases assuming constant water fluxes ($q_{ha,1}$, $q_{ha,2}$, $q_{ha,3}$ and $q_{ha,4}$) according to the different degradation steps and hydraulic regimes (as show in Figure 7-87).

The leaching depths calculated with the shrinking core model for advective flow compare reasonably well with the numerical modelling results using PHAST, see next section. The calculations using the shrinking core model suggest a time to dissolve the portlandite content of the upstream left-hand side concrete wall (0.4 m) at the section B-B (y-coordinate 0.75 m) of ~ 2,700–2,800 years, see Figure 7-89. The corresponding calculations using PHAST show depletion of portlandite after ~3,000 years, cf. Figure 7-98.

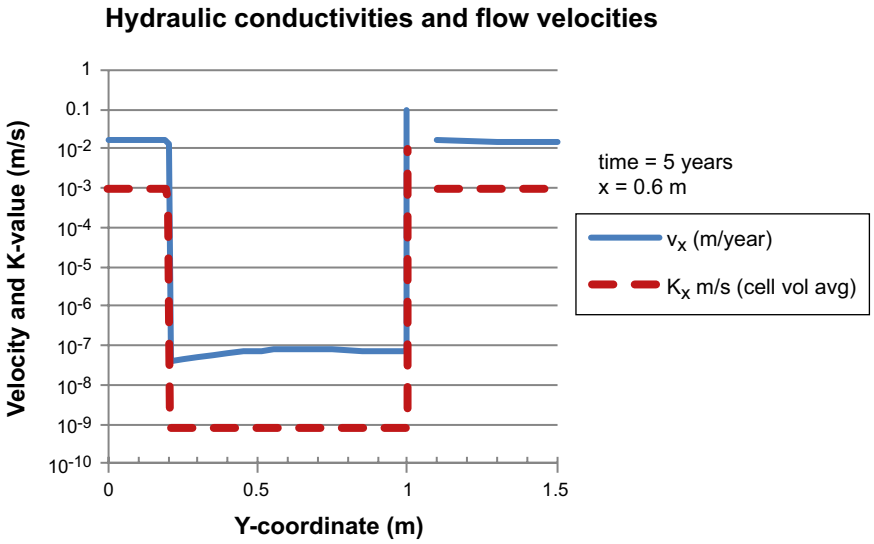

Figure 7-83. *Calculated horizontal velocities (v_x in m/year) and the corresponding hydraulic conductivities K_x (in m/s) in a vertical section (E-E) through the model at x=0.6 m and time = 5 years, representing the flow conditions during the period 0–100 years.*

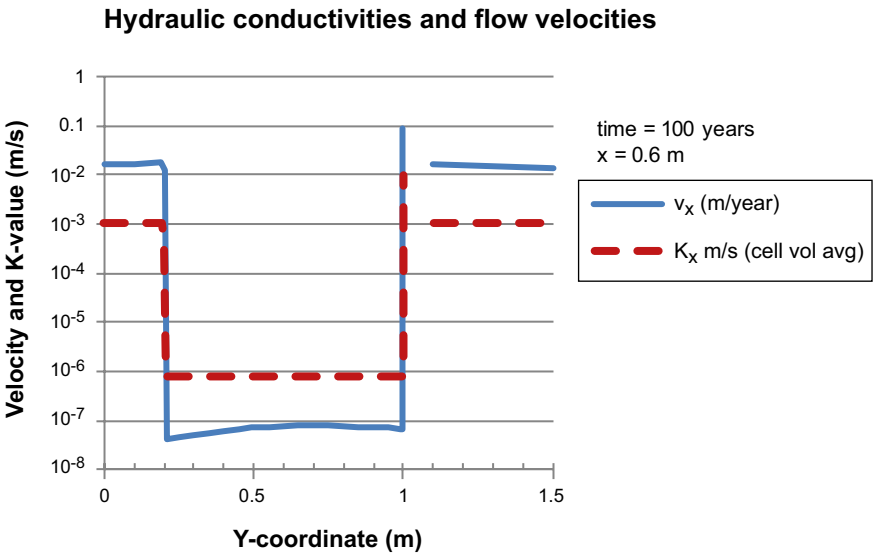

Figure 7-84. *Calculated horizontal velocities (v_x in m/year) and the corresponding hydraulic conductivities K_x (in m/s) in a vertical section (E-E) through the model at x=0.6 m and time = 100 years, representing the flow conditions during the period 100–1,000 years.*

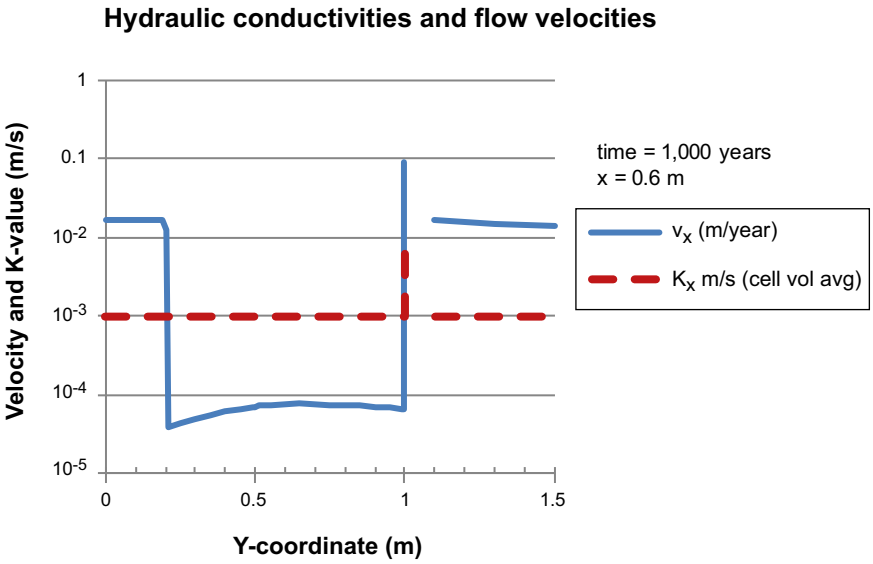

Figure 7-85. *Calculated horizontal velocities (v_x in m/year) and the corresponding hydraulic conductivities K_x (in m/s) in a vertical section (E-E) through the model at x=0.6 m and time = 1,000 years, representing the flow conditions during the period 1,000–2,000 years.*

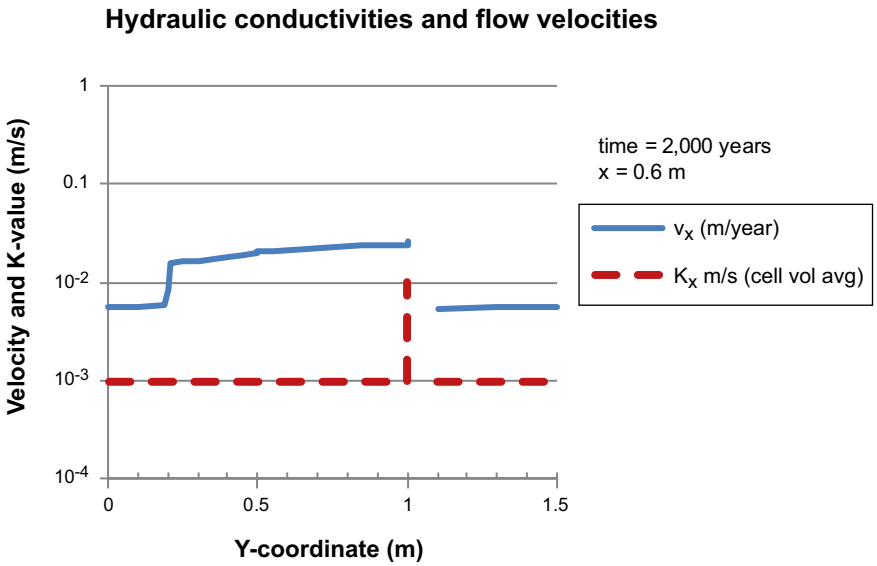

Figure 7-86. *Calculated horizontal velocities (v_x in m/year) and the corresponding hydraulic conductivities K_x (in m/s) in a vertical section (E-E) through the model at x=0.6 m and time = 2,000 years, representing the flow conditions during the period 2,000–10,000 years.*

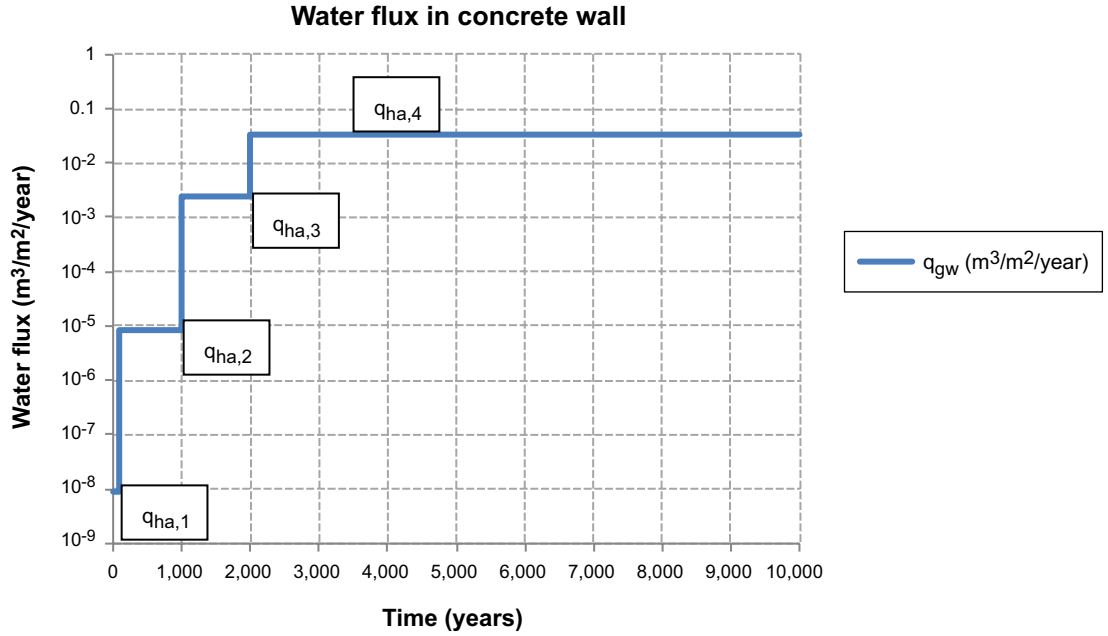

Figure 7-87. *Calculated water fluxes in the upstream side concrete wall during the first 10,000 years at the evaluation point BE located at x=0.6 m, y=0.75 m based on the horizontal velocities (v_x) calculated by PHAST and a porosity of 0.11 m^3/m^3. Fluxes change in different steps $q_{ha,1}$–$q_{ha,4}$.*

A comparison of the dominant mechanism for leaching at different times can be made by calculating the Peclet number:

$$Pe = \frac{q_{gw} \cdot L}{D_e}$$ Equation 7-1

where:

q_{gw} = water flux in the horizontal direction($m^3/m^2/s$)

L = thickness of the concrete wall in the transport direction(m)

D_e = effective diffusivity of the concrete wall(m^2/s)

Using the values of the water flux according to Figure 7-87 and the effective diffusivities at different times according to Table 7-7 the resulting Peclet numbers are shown in Figure 7-88. In this case, the leaching of portlandite shifts from a diffusion dominated regime to an advection dominated regime at 1,000 years. This can be demonstrated by comparing the calculations for pure diffusion (Figure 7-82) and pure advection (Figure 7-89). The leaching depth during the first 1,000 years is ~ 0.07 m for pure diffusion, but only ~ 0.0001 m for pure advection. However, after ~ 2,700–2,800 years advection has depleted the portlandite in the concrete wall to the full depth of 0.4 m, whereas this would require more than 15,000 years by pure diffusion.

Results of PHAST modelling

Some additional results of the PHAST modelling in case Large7 are presented here. The results are presented as profiles of the portlandite content along a vertical section (E-E) through the upstream-side concrete wall at x = 0.6 m (i.e. at a depth of 0.2 m in the wall) at different times, see Figure 7-90, Figure 7-91, Figure 7-92, Figure 7-93, Figure 7-94, Figure 7-95 and Figure 7-96. The amount of portlandite is expressed as kmol/m^3 pore water in the different plots which is a convenient unit for calculations with PHAST and PHREEQC. A more practical unit is obtained by multiplying with the porosity to obtain the amount of portlandite as kmol/m^3 concrete. However, for the purpose of illustrating the gradual leaching and eventual depletion of portlandite, the unit can be selected arbitrarily.

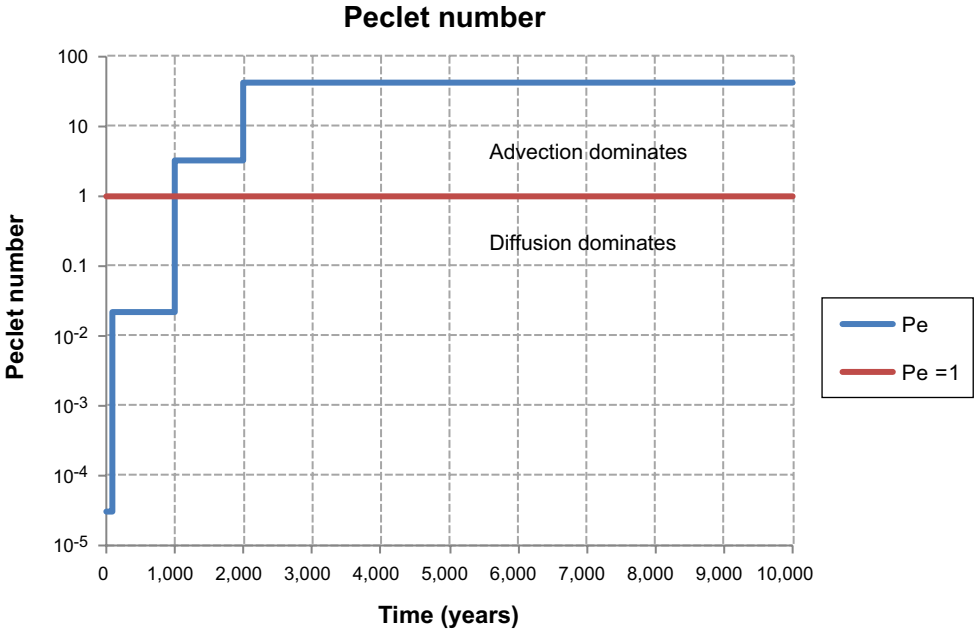

Figure 7-88. *Calculated Peclet numbers in the concrete wall at different times. For Pe < 1 diffusion dominates the transport and for Pe > 1 advection dominates.*

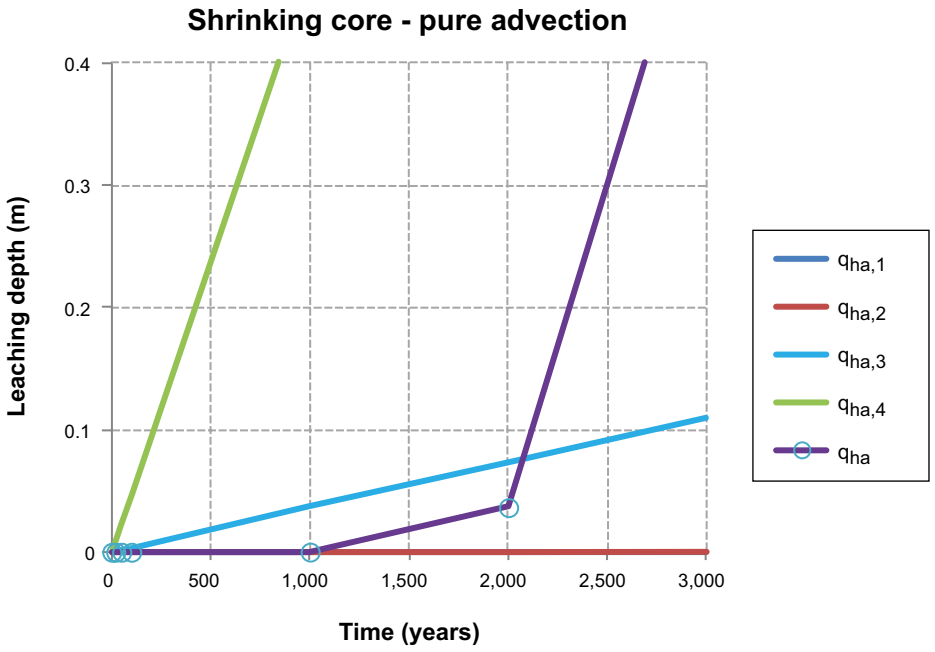

Figure 7-89. *Calculated leaching depths during the first 3,000 years with a shrinking-core model assuming pure advection. The different curves represent different constant values of the water flux through the concrete wall ($q_{ha,1} = 9 \cdot 10^{-9}$ m³/m²/year, $q_{ha,2} = 8 \cdot 10^{-6}$ m³/m²/year, $q_{ha,3} = 2.5 \cdot 10^{-3}$ m³/m²/year, $q_{ha,4} = 3.25 \cdot 10^{-2}$ m³/m²/year), whereas the curve denoted by q_{ha} takes into consideration the stepwise changes of the water flux: $q_{ha,1}$ (0–100 years), $q_{ha,2}$ (100–1,000 years), $q_{ha,3}$ (1,000–2,000 years) and $q_{ha,4}$ (2,000–10,000 years).*

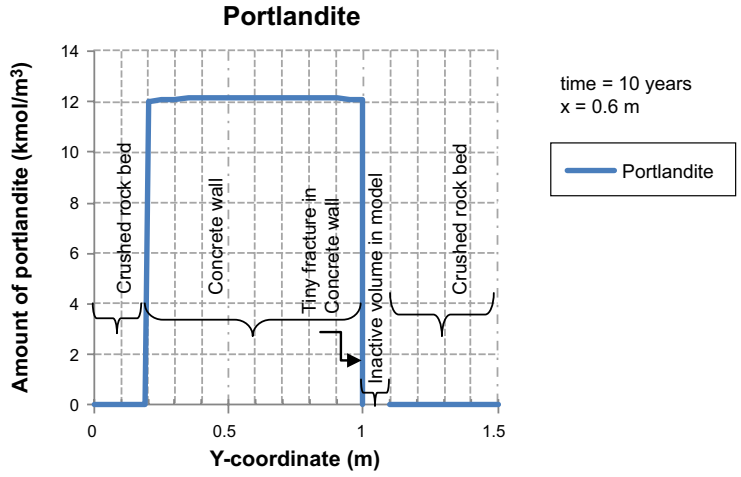

Figure 7-90. *Amount of portlandite (expressed as a fictive concentration in the pore water) in a vertical section (E-E) through the model at x=0.6 m and time = 0 years.*

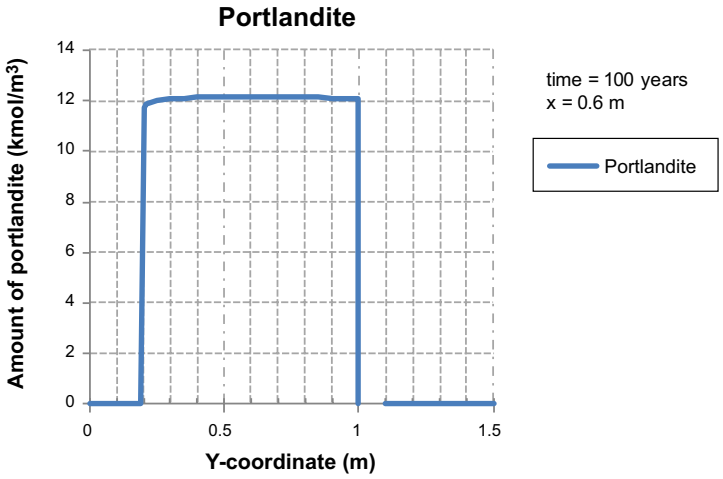

Figure 7-91. *Amount of portlandite (expressed as a fictive concentration in the pore water) in a vertical section (E-E) through the model at x=0.6 m and time = 100 years.*

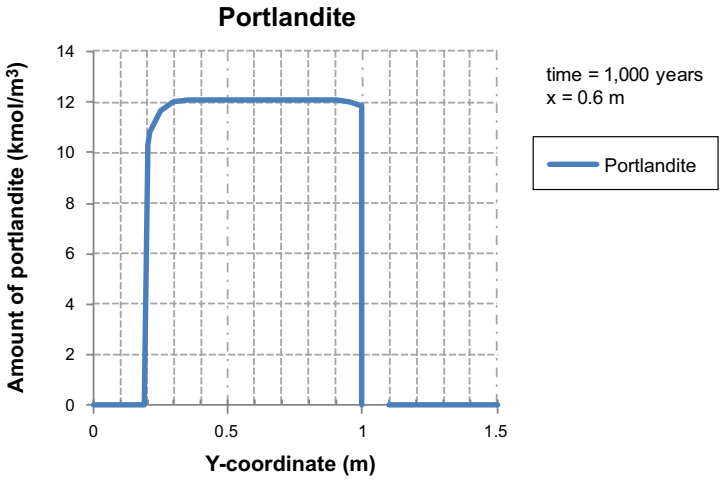

Figure 7-92. *Amount of portlandite (expressed as a fictive concentration in the pore water) in a vertical section (E-E) through the model at x=0.6 m and time = 1,000 years.*

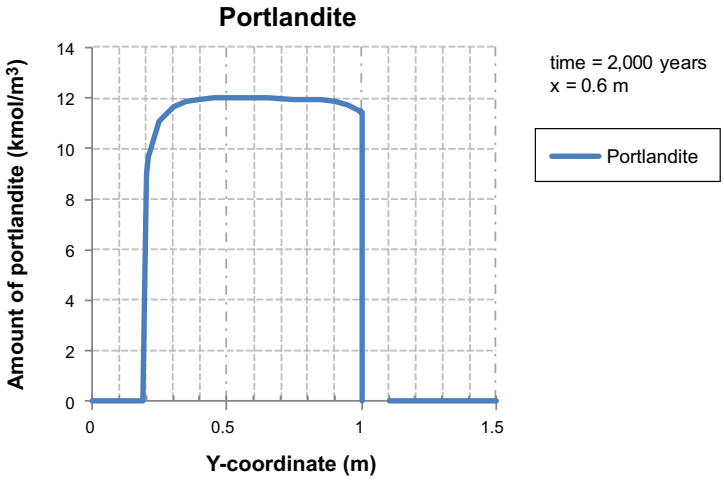

Figure 7-93. *Amount of portlandite (expressed as a fictive concentration in the pore water) in a vertical section (E-E) through the model at x=0.6 m and time = 2,000 years.*

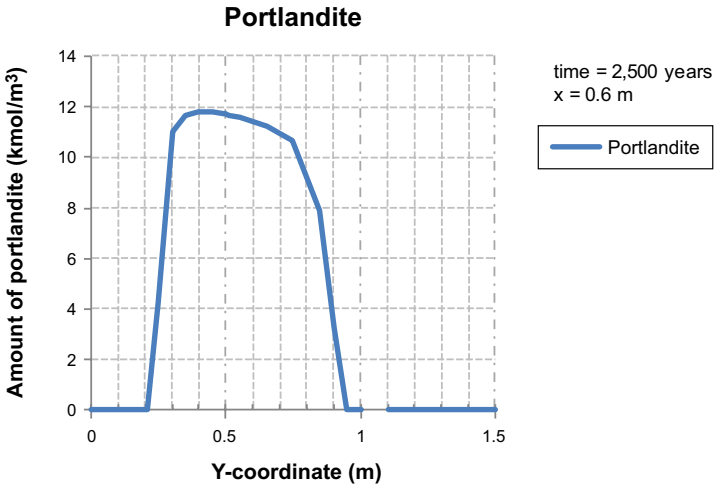

Figure 7-94. *Amount of portlandite (expressed as a fictive concentration in the pore water) in a vertical section (E-E) through the model at x=0.6 m and time = 2,500 years.*

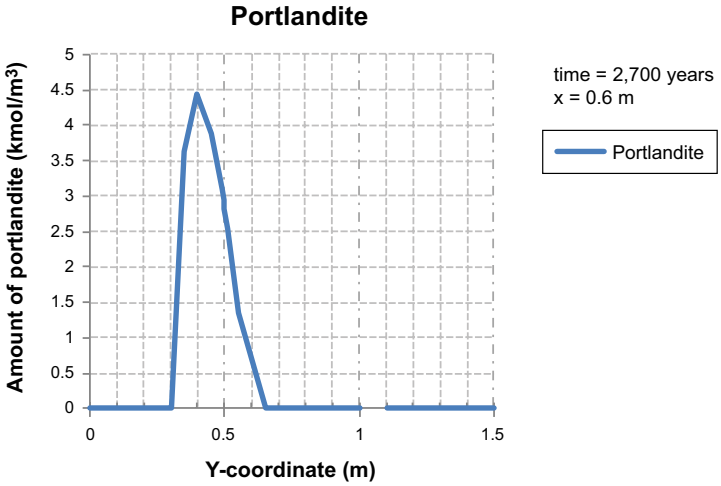

Figure 7-95. *Amount of portlandite (expressed as a fictive concentration in the pore water) in a vertical section (E-E) through the model at x=0.6 m and time = 2,700 years.*

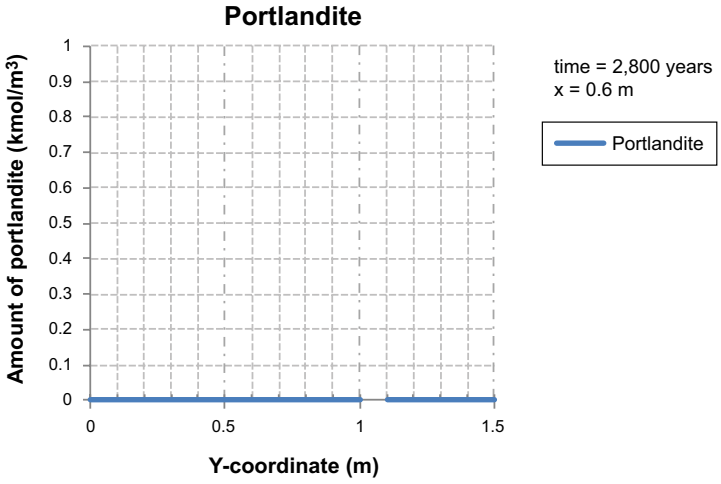

Figure 7-96. *Amount of portlandite (expressed as a fictive concentration in the pore water) in a vertical section (E-E) through the model at x=0.6 m and time = 2,800 years.*

After 1,000 years, the leaching of portlandite starts to become apparent near the bottom of the concrete wall (y-coordinate 0.2–0.3 m) and adjacent to the tiny fracture at the top (x-coordinate 0.95–1.0), see Figure 7-92, which progresses at 2,000 years, see Figure 7-93.

At 2,500 years, portlandite is depleted (to a depth of more than 0.2 m) near the (initial) tiny fracture in a zone which is ~ 5 cm wide or more (see Figure 7-94). The lower part of the concrete wall (y-coordinate 0.2–0.5 m) is connected to the concrete floor; hence the flow resistance of water is higher than in the upper part of the concrete wall (y-coordinate 0.5–1.0 m) and the water flux varies accordingly, cf. Figure 7-83 to Figure 7-86. The leaching of portlandite would therefore be expected to be more pronounced for y-coordinates larger than 0.5 m. This is also shown in Figure 7-94; although the effect of leaching along the bottom (y-coordinates 0.2–0.3 m) and the leaching near the (initial) thin fracture (near y-coordinate 1.0 m) need separate consideration.

At 2,700 years, an almost complete degradation of portlandite has occurred in the concrete wall (to a depth of more than 0.2 m), except in the lower part connected to the concrete floor where the water flux is lower due to higher resistance to water flow, see Figure 7-95. After 2,800 year also the lower part of the concrete wall is depleted in portlandite at x-coordinate 0.6 m, see Figure 7-96. Due to the remaining portlandite near the concrete floor, the leaching of the portlandite in the upper parts of the concrete wall will be influenced, which may slow down the depletion to some extent.

Some additional results are presented in Figure 7-97 to Figure 7-103 which show the amount of portlandite at different times in section A-A (through the concrete floor), section B-B (through the concrete wall 0.25 m above the concrete floor), section C-C (through the concrete wall 0.01 m below the initial tiny horizontal fracture), section C'-C' (through the concrete wall 0.005 m below the initial tiny horizontal fracture) and section D-D (through the concrete wall 0.0005 m below the initial tiny horizontal fracture).

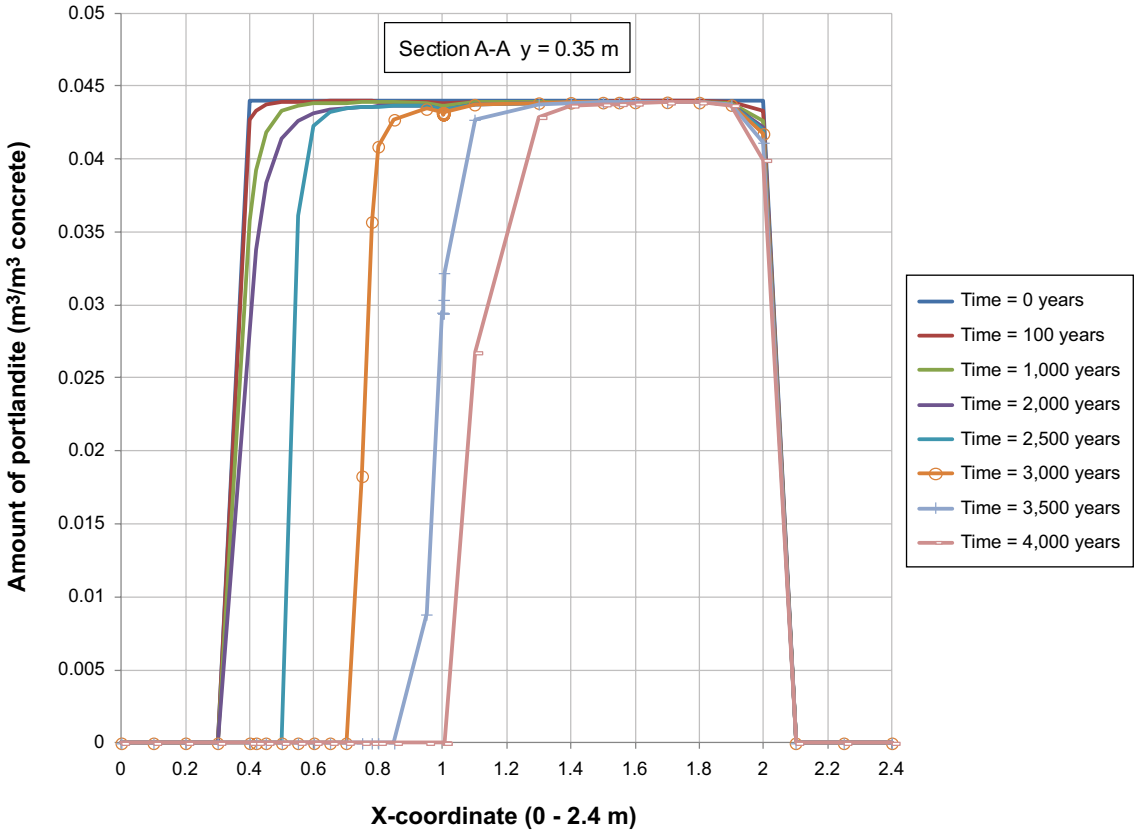

Figure 7-97. *Amount of portlandite (expressed as m^3 of portlandite/m^3 of concrete) in a horizontal section (A-A) through the model at y=0.35 m during the first 4,000 years. This section passes through the concrete floor (x-coordinate 0.4–2.0 m).*

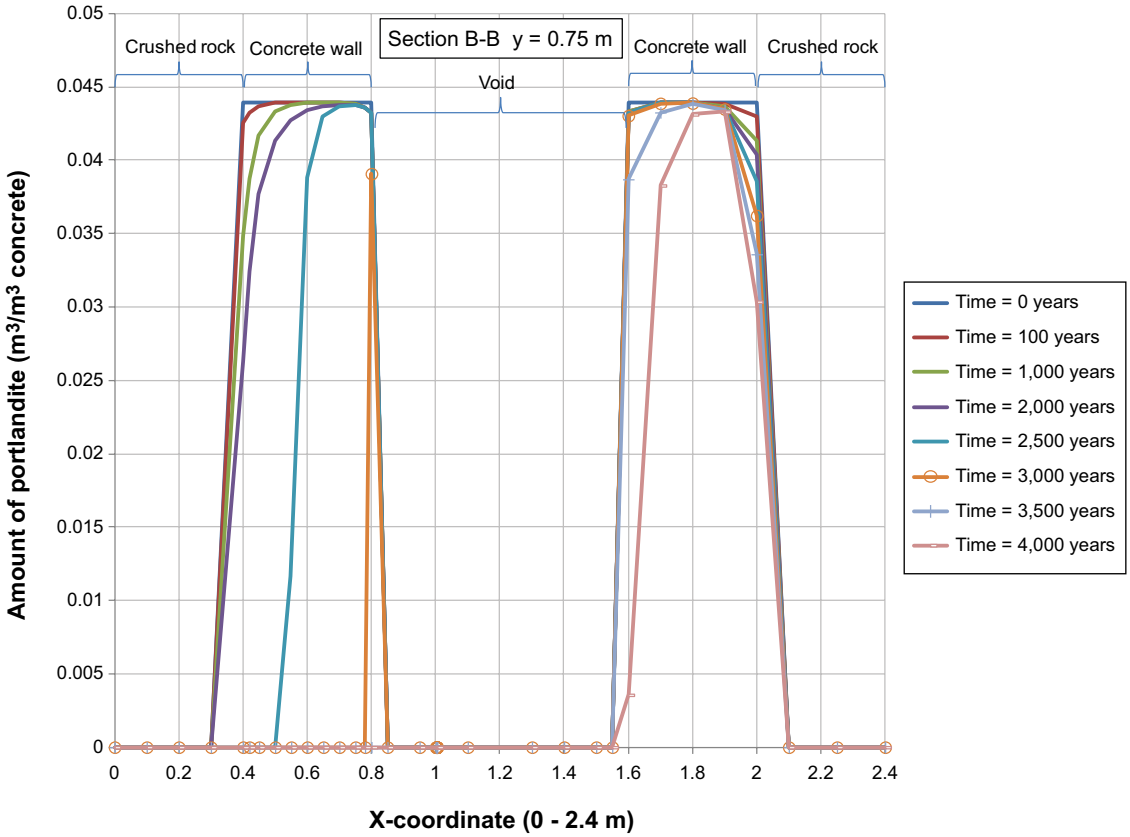

Figure 7-98. *Amount of portlandite (expressed as m^3 of portlandite/m^3 of concrete) in a horizontal section (B-B) through the model at y=0.75 m during the first 4,000 years. The left-side peak represents the up-stream side concrete wall and the right-hand peak the down-stream concrete wall.*

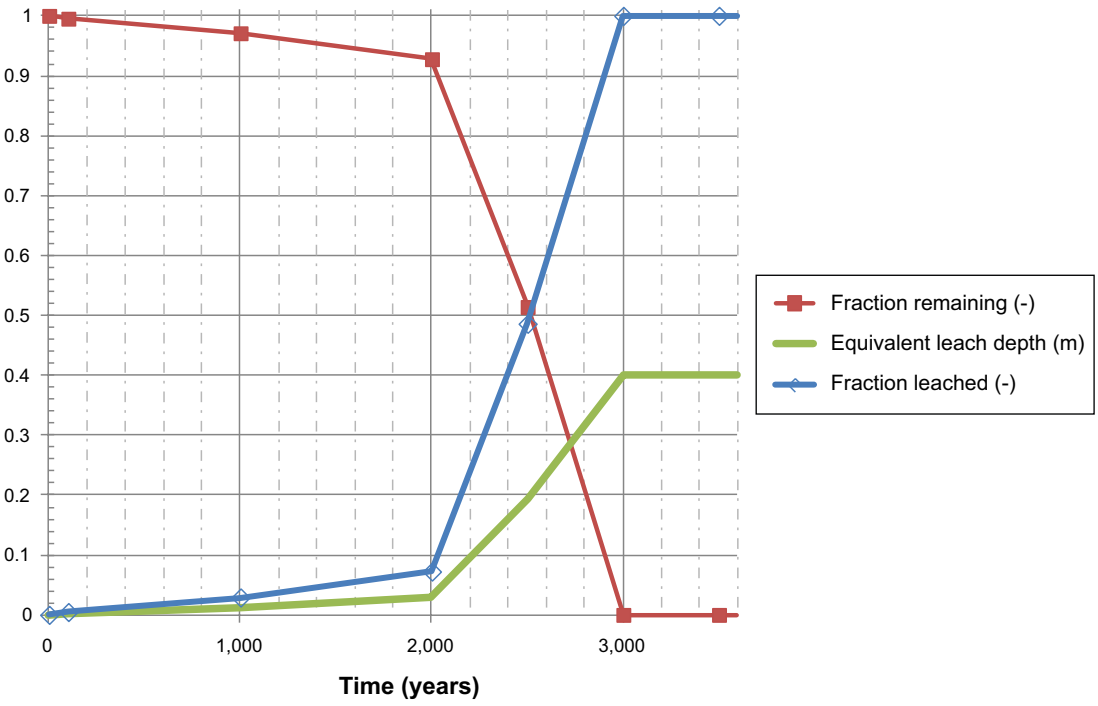

Figure 7-99. *Calculated fraction of portlandite remaining and the corresponding fraction leached in the concrete versus time and the equivalent leaching depth in the upstream-side concrete wall for case Large 7 using the PHAST model.*

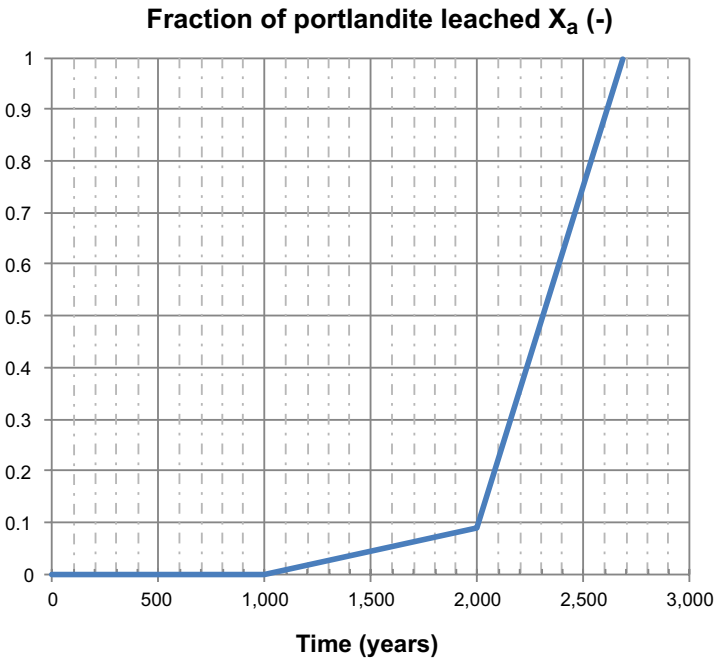

Figure 7-100. *Calculated fraction of portlandite leached from concrete by advection-controlled leaching using a shrinking-core model.*

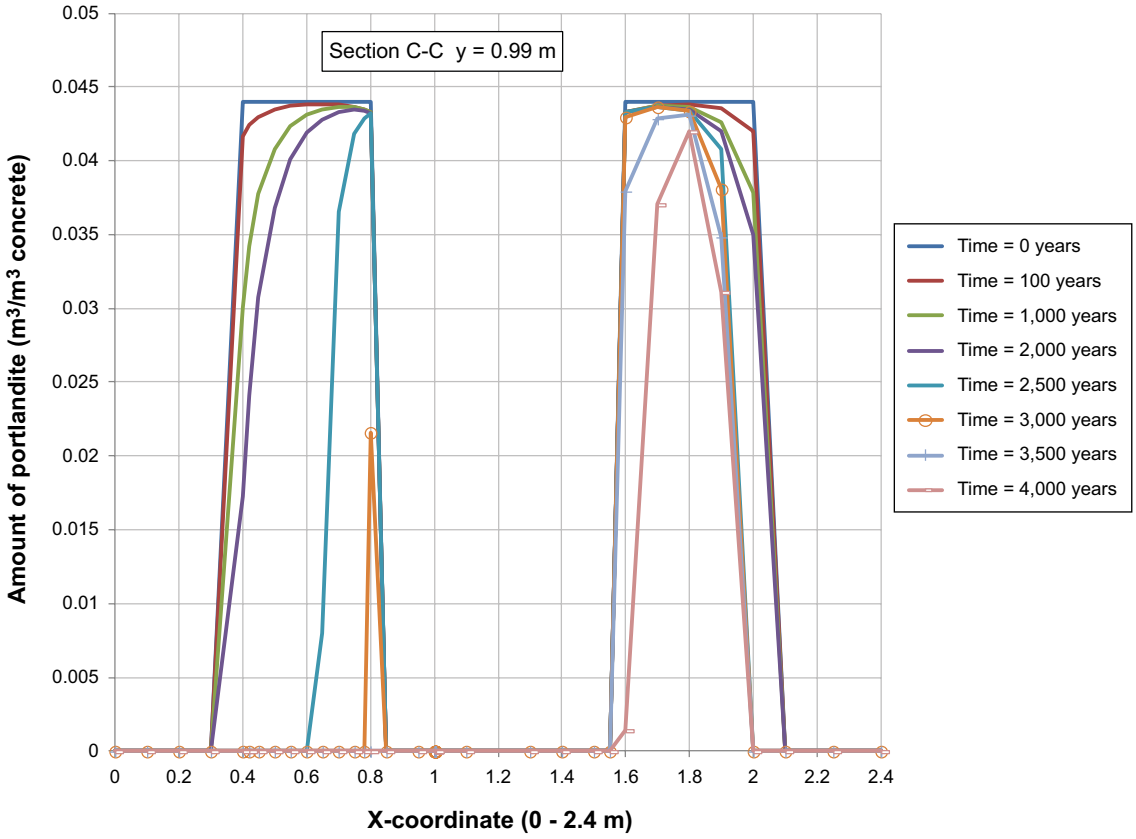

Figure 7-101. *Amount of portlandite (expressed as m^3 of portlandite/m^3 of concrete) in a horizontal section (C-C) through the model at y=0.99 m during the first 4,000 years. The left-side peak represents the up-stream side concrete wall and the right-hand peak the down-stream concrete wall.*

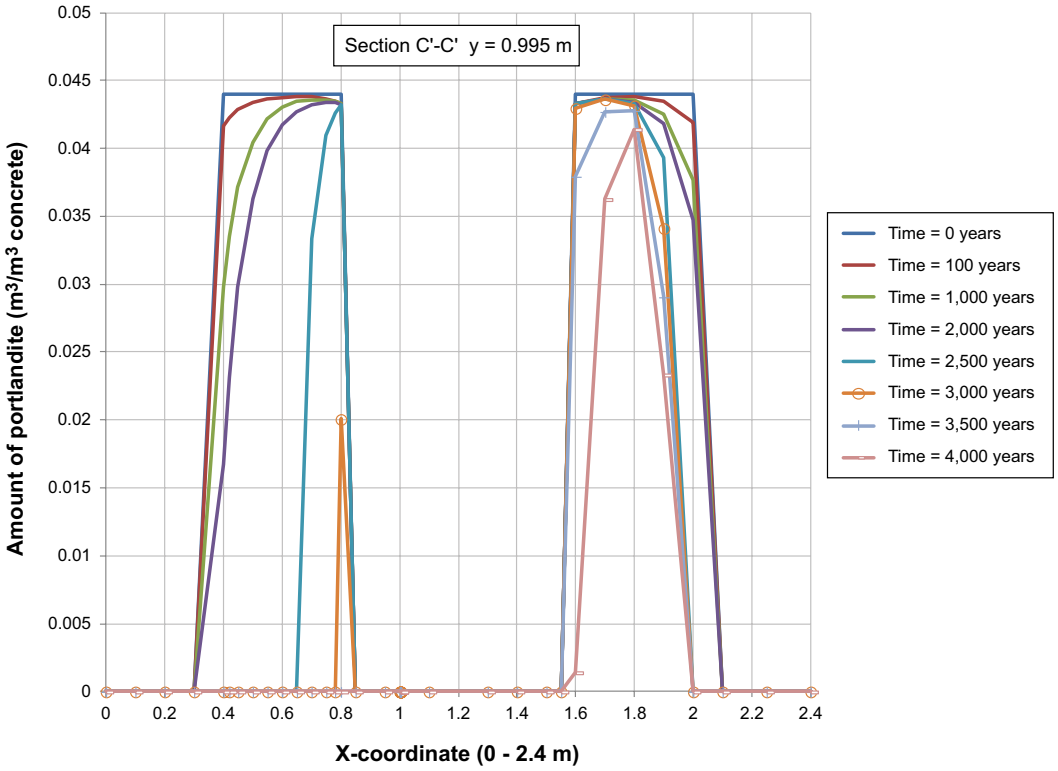

Figure 7-102. *Amount of portlandite (expressed as m^3 of portlandite/m^3 of concrete) in a horizontal section (C'-C') through the model at y=0.995 m during the first 4,000 years. The left-side peak represents the up-stream side concrete wall and the right-hand peak the down-stream concrete wall.*

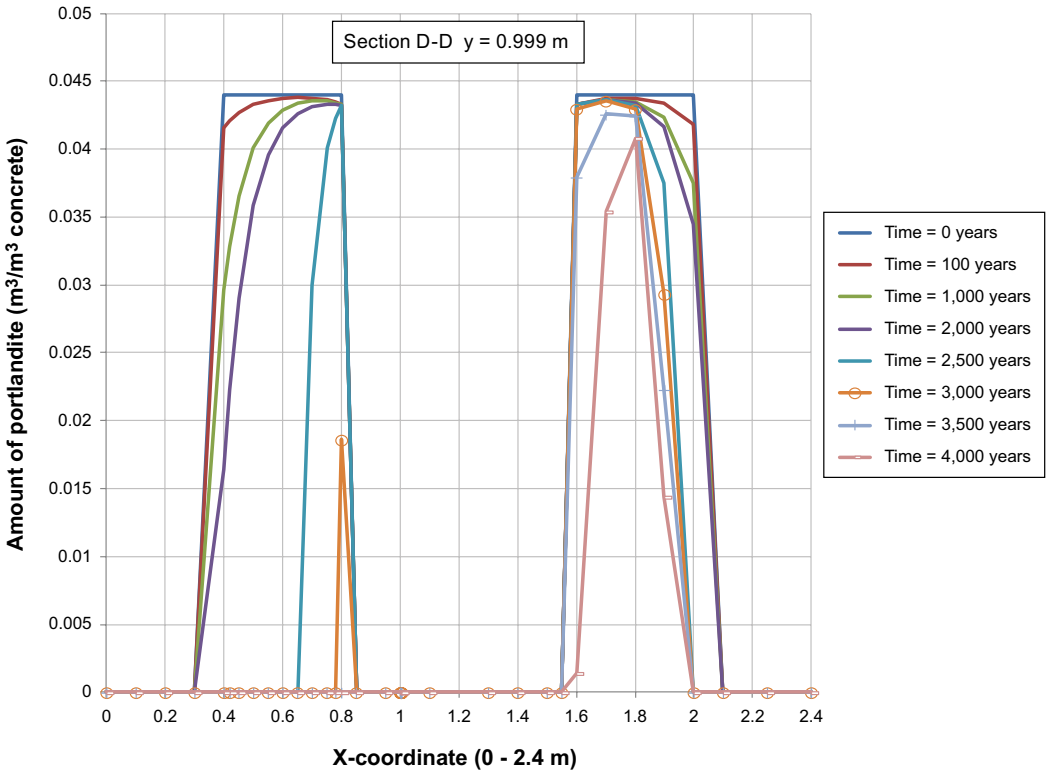

Figure 7-103. *Amount of portlandite (expressed as m^3 of portlandite/m^3 of concrete) in a horizontal section (D-D) through the model at y=0.999 m during the first 4,000 years. The left-side peak represents the up-stream side concrete wall and the right-hand peak the down-stream concrete wall.*

The PHAST results for section B-B are considered reasonable for comparison with the shrinking-core models for diffusion and advection. After ~ 3,000 years the PHAST results show a depletion of portlandite in the upstream-side concrete wall. To facilitate comparison, the leaching has been calculated as the leached fraction and is shown in Figure 7-99. An equivalent calculation using a shrinking-core model for advection-controlled leaching (see Section 5.1 for details) is presented in Figure 7-100. The results show that the shrinking-core model and the PHAST numerical model yield reasonably comparable results. There is a slight difference in the time required to reach complete depletion of the portlandite. The shrinking-core model predicts a complete leaching after ~ 2,700 years, compared with the 3,000 years calculated by PHAST. The difference can be attributed to the impact of a larger concrete structure in the PHAST model where a certain influence is expected on the leaching of the vertical concrete wall by dissolved portlandite leached from the adjacent horizontal concrete floor.

Conclusions

The conclusions of the comparison between simple analytical models and the numerical model are that:

- The results of the shrinking-core model for the diffusion case compare well with the numerical model results during the first 2,000–3,000 years. This is reasonable since the transport in the numerical model is diffusion dominated during the first 1,000 years and in steps transform to advection dominated transport after 3,000 years.
- The shrinking-core model for diffusion underestimates the leaching depth at times > 3,000 years, as expected.
- The shrinking-core model for advection underestimates the leaching depth compared with the numerical model for the first ~ 2,500 years, but show reasonable agreement after ~ 3,000 years.
- The results of the comparison suggest that the analytical and numerical models compare well when applied to comparable flow regimes. Thus, the results of the analytical shrinking-core models support the numerical results.

The more detailed analysis of the effects of the tiny fracture included in the numerical model shows a minor impact during the first ~ 1,000 years when diffusion dominates. After 2,000 years the impact of the fracture is shown as a small dip in the portlandite concentration extending ~ 0.1 m from the fracture in the centre of the concrete wall. After ~ 2,500 years the impact of the fracture is significant and has resulted in depletion of portlandite in a 0.05 m zone along the fracture, to the half depth of the upstream-side concrete wall. After 2,700 years the portlandite is depleted in a zone ~ 0.35 m wide along the fracture. The results show that when advection dominates the impact of fractures may be significant and lead to locally enhanced leaching of concrete along the fractures. This may potentially result in enhance deterioration of the barrier properties. However, it must be stressed that this analysis is based on a simplified chemical system where possible interactions with the groundwater, such as calcite precipitation, have been neglected.

7.11 Comparison of results from different cases

In this section some direct comparisons are made of the results from different cases. The results are presented as the evolution of pH and different minerals. The evaluation point AE at the intersection of the centrelines of the concrete floor and the left-hand side concrete wall has been selected for the presented examples.

Comparison of cases Large10 and Large8 – showing the impact of the thermodynamic database

The comparison is presented in Figure 7-104 (0–5,000 years) and Figure 7-105 (0–20,000 years) and displays the evolution of pH and the amounts of portlandite, CSH_1.8, CSH_1.1 and CSH_0.8. The comparison shows that the pH passes through similar major stages but results in an earlier reduction of pH for case Large8, e.g. a drop to pH ~12.5 occurs during the first 200 years. This seems to be connected to the formation of Friedel's salt, cf. Figure 7-106, a mineral which is not formed in case Large8, and the depletion of monocarboaluminate. During the period 2,000–2,800 years the pH is determined by portlandite dissolution and is equivalent in the two cases. In case Large10, a pH drop to an intermediate pH ~11.6 occurs between 2,800–3,300 years, and during ~3,300–3,600 years another pH drop to ~10.8 in response to the transition of CSH_1.8 to CSH_1.1, and CSH_1.1 to CSH_0.8 respectively. In case Large8, only a slight reduction of pH to 12.2 occurs after 3,100 years when after depletion of portlandite CSHjen becomes the phase determining the pH. However, during the period ~3,800–4,200 years, as CSHjen transforms to CSHtob2, and hydrotalciteFe dissolves while hydrotalciteOH precipitates, a major pH drop to ~10 occurs in case Large8.

For the other minerals, see Figure 7-106 and Figure 7-107, the two cases display quite different sequences of appearance, owing to the differences in the assemblages. An interesting notation is however, that despite the observed differences there are also large similarities in the results in the sense that the leaching proceeds in sequential steps, basically following a general path with gradually decreasing calcium content, a gradual drop of pH and conservation of the less soluble compounds, e.g. silica, aluminium, magnesium and to some extent sulphate, via the transformation between different solid phases as the leaching progresses. This indicates a robustness of the chemical system in concrete, albeit the details may vary between different conceptual realisations of the mineral assemblies.

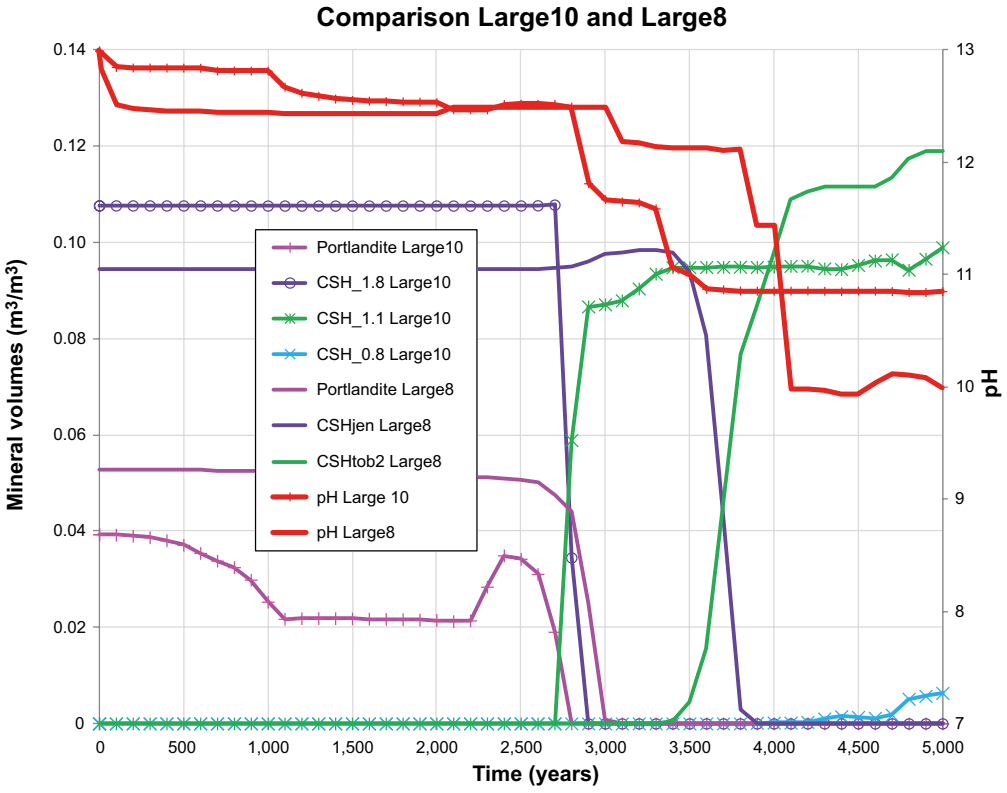

Figure 7-104. *Comparison of cases Large10 and Large8 with respect to evolution of pH and the amounts of portlandite and different CSH minerals during the first 5,000 years.*

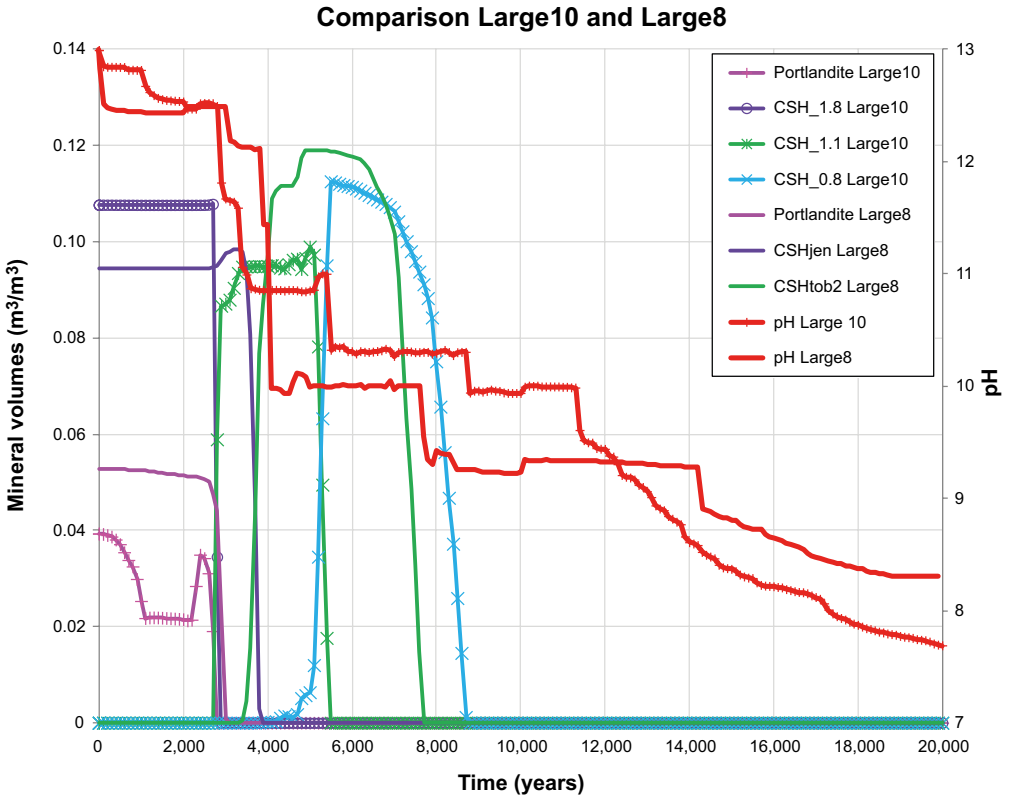

Figure 7-105. *Comparison of cases Large10 and Large8 with respect to evolution of pH and the amounts of portlandite and different CSH minerals during the first 20,000 years.*

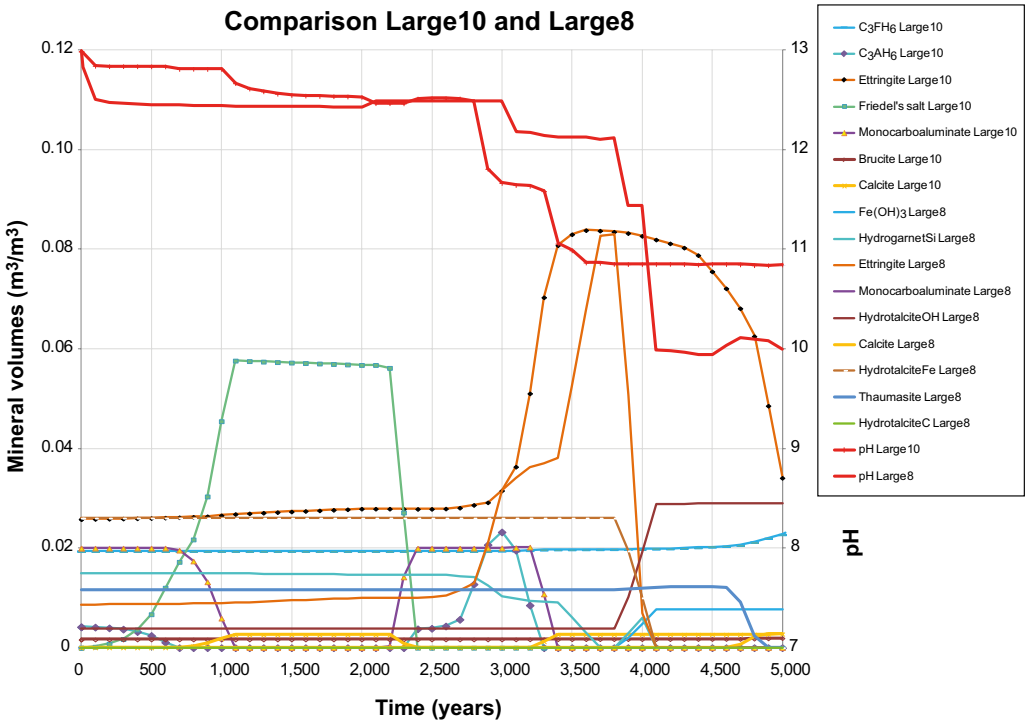

Figure 7-106. *Comparison of cases Large10 and Large8 with respect to evolution of pH and the amounts of different minerals containing aluminium, iron and magnesium (hydrogarnets, hydrotalcites, ettringite, thaumasite, monocarboaluminate, Friedel's salt, brucite and calcite) during the first 5,000 years.*

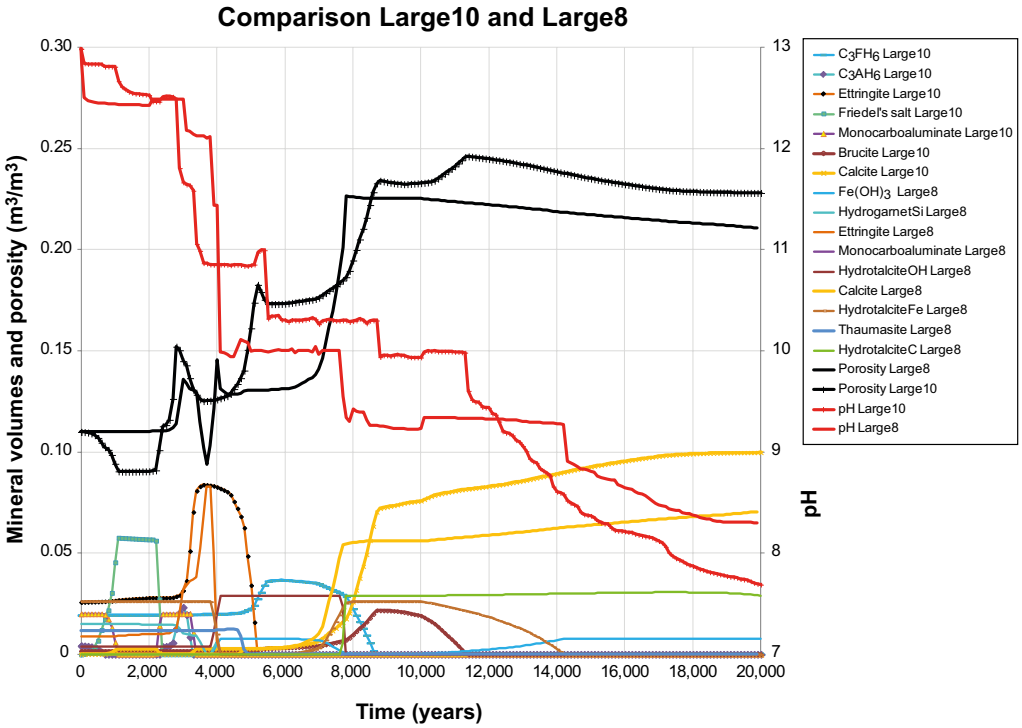

Figure 7-107. *Comparison of cases Large10 and Large8 with respect to evolution of pH and the amounts of different minerals (hydrogarnets, hydrotalcites, ettringite, thaumasite, monocarboaluminate, Friedel's salt, brucite and calcite) and porosity during the first 20,000 years.*

Comparison of cases Large10 and Large11 – showing the impact of the Repair scenario

The comparison is presented in Figure 7-108 (0–5,000 years) and Figure 7-109 (0–20,000 years) and displays the evolution of pH and the amounts of portlandite, CSH_1.8, CSH_1.1 and CSH_0.8. The comparison shows that the pH passes through the same stages but is delayed for case Large11, e.g. a drop to pH below 12 occurs ~600 years later and pH 10 is reached ~3,000 years later in the repair scenario. Similar delays are shown for the associated changes of the mineral assemblage.

Also for the other minerals in the assemblage, see Figure 7-110 and Figure 7-111, the two cases display very similar sequences of appearance, however, delayed in the repair scenario (Large11).

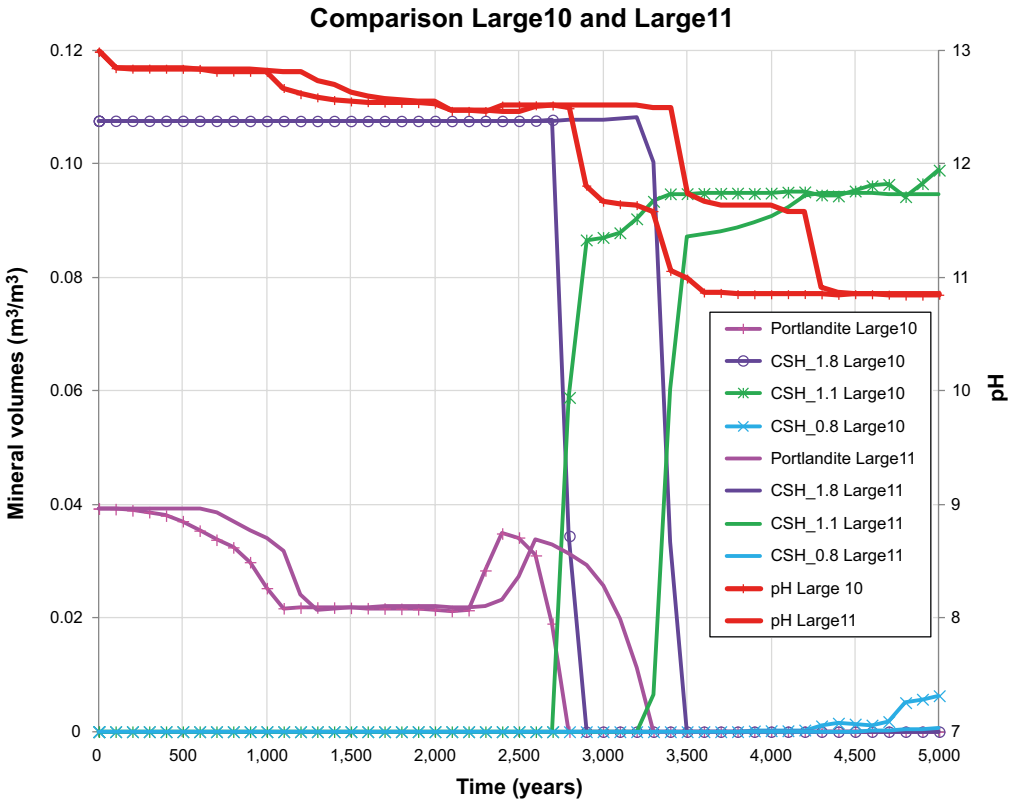

Figure 7-108. *Comparison of cases Large10 and Large11 (repair scenario) with respect to evolution of pH and the amounts of portlandite and different CSH minerals during the first 5,000 years.*

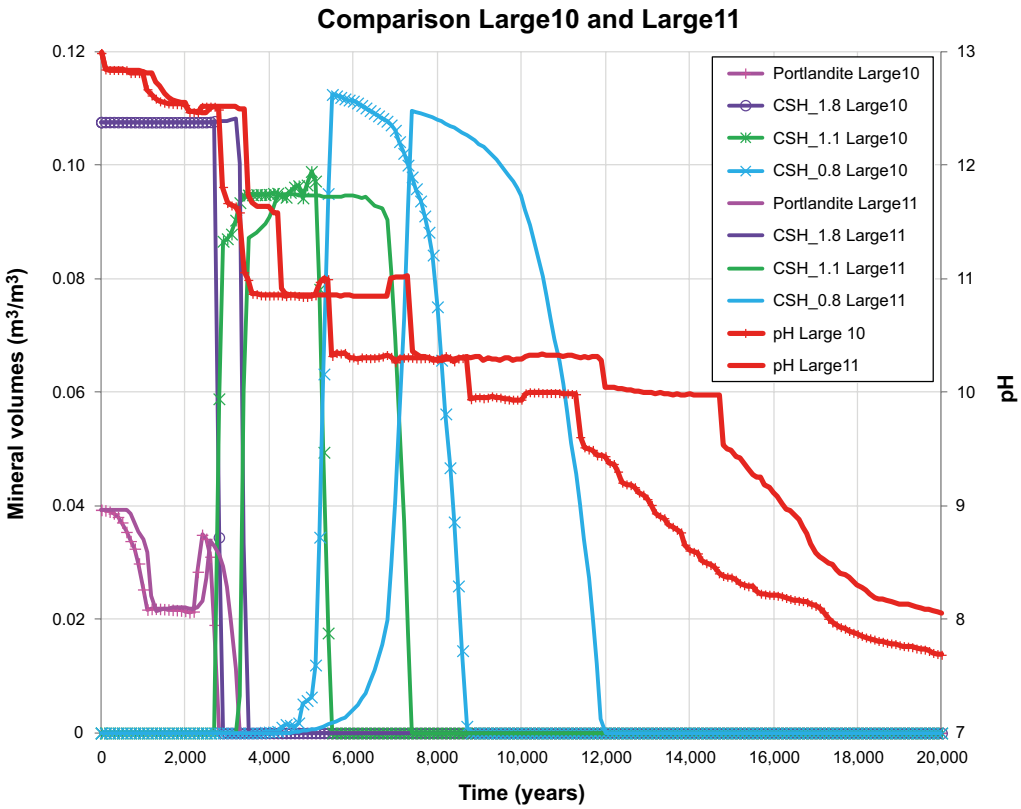

Figure 7-109. *Comparison of cases Large10 and Large11 (repair scenario) with respect to evolution of pH and the amounts of portlandite and different CSH minerals during the first 20,000 years.*

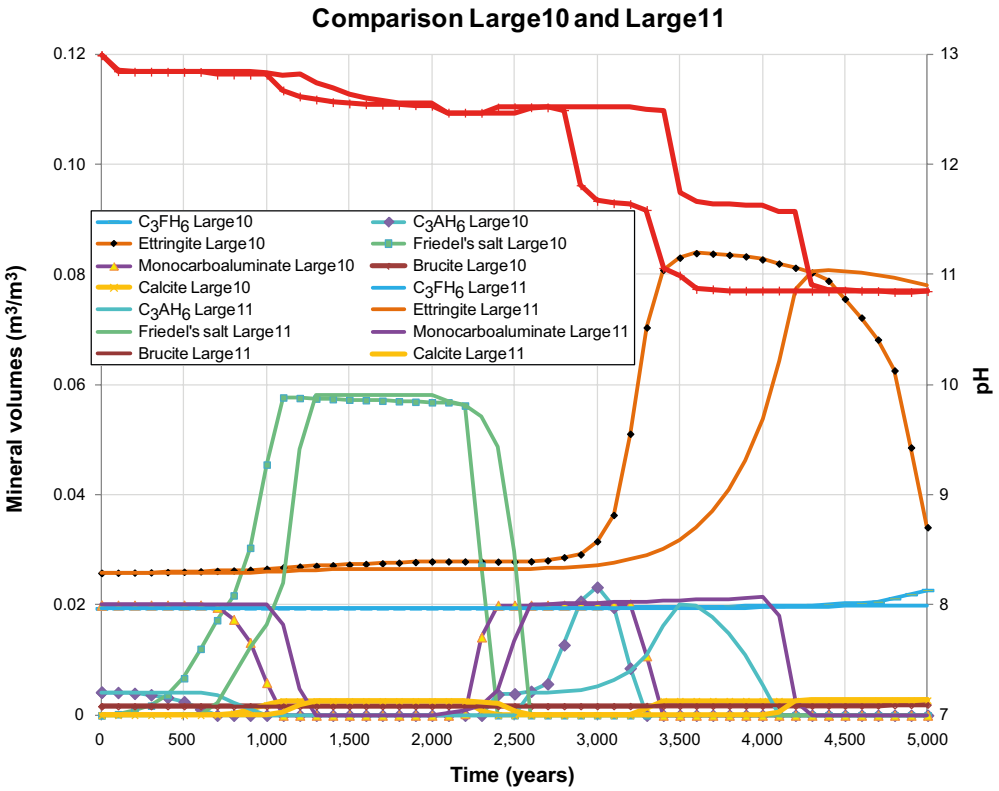

Figure 7-110. *Comparison of cases Large10 and Large11 (repair scenario) with respect to evolution of pH and the amounts of different minerals (C_3FH_6, C_3AH_6, ettringite, monocarboaluminate, Friedel's salt, brucite and calcite) during the first 5,000 years.*

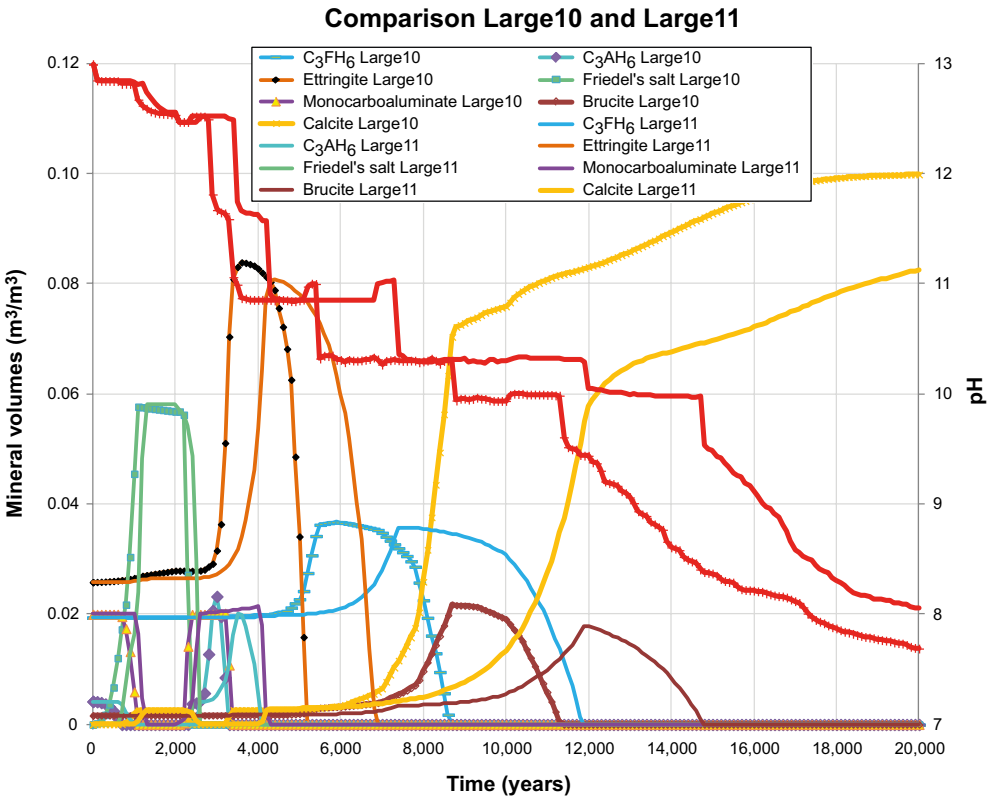

Figure 7-111. *Comparison of cases Large10 and Large11 (repair scenario) with respect to evolution of pH and the amounts of different minerals (C_3FH_6, C_3AH_6, ettringite, monocarboaluminate, Friedel's salt, brucite and calcite) during the first 20,000 years.*

8 Impact of chemical degradation on the function of concrete barriers in SFR

The aim of this chapter is to assess the effects of chemical degradation on the function of the concrete barriers in SFR, using the results from the reactive transport modelling (Chapter 7).The results presented in Chapters 5–7 show that significant chemical degradation of the concrete barriers is possible over long time scales. The results also indicate that thin fractures constitute weak zones where increased groundwater flow can be expected, causing locally enhanced leaching of alkaline components from the concrete. Portlandite is fairly soluble and also constitutes one of the components that contribute to the strength and alkaline buffering of the concrete. Therefore leaching leads to a gradual loss of mechanical strength, loss of alkaline buffering of the chemical conditions in the vault, and may over time also increase the porosity. The changes in porosity may cause changes in the very complex pore structure of concrete, which may result in increased hydraulic conductivity and increased effective diffusivity. Hence, leaching can affect the ability of the barriers to maintain a high pH and the ability to restrict the groundwater flow, both of which are regarded important safety functions of the barriers in the BMA vaults.

This chapter describes the approaches followed to estimate the impact of changes in concrete porosity on the barrier's material properties. First, a generic relationship between porosity and effective diffusivity is explored (this section), and then a detailed analysis of the changes in the properties of the 2BMA walls is presented over time, based on the chemical degradation calculated in case Large20 (Section 7.4). This includes a 1-D analysis of the changes in porosity and effective diffusivity through the concrete wall and through a fully penetrating fracture, and the changes in the hydraulic conductivity through the concrete wall. Additionally, a 2-D analysis has been carried out of the changes in porosity, effective diffusivity and hydraulic conductivity of the system used to represent 2BMA in the reactive transport modelling (cf. Figure 7-1). Given the currently heterogeneous state of the 1BMA walls, with fractured concrete and corroding steel reinforcement and form ties, locations in the modelled system (cf. Figure 7-8) were selected and the changes in their porosity, effective diffusivity, and hydraulic conductivity were calculated over time. The impact of chemical degradation on the ability to maintain a high pH has been discussed in some detail in Chapter 7 and is not treated further here.

8.1 Evolution of effective diffusivity and hydraulic conductivity with a changing porosity due to chemical degradation

A generic relationship for effective diffusivity is given by (Skagius 1986):

$$D_{eI} = \phi \cdot \frac{\delta_d}{\tau^2} \cdot D_0 \qquad \text{Equation 8-1}$$

where:

D_{eI} = effective diffusivity of concrete (m^2/s)

ϕ = porosity of the porous material (m^3/m^3)

δ_d = constrictivity factor of the pore system (a measure on the amount of narrow passages along the pores) (–)

τ = tortuosity factor of the pore system (defined as the ratio of the mean length L_p of the path through the porous material to the geometrical length L) (m/m)

D_0= diffusivity in bulk water (m^2/s)

The change in porosity resulting from the gradual chemical degradation of concrete can be estimated using the method presented in Section 6.15 (Equation 6-61), and the results have been shown in Chapter 7. Different studies have addressed the impact of cracking (e.g. Gérard and Marchand 2000), the issue of up-scaling from micro structure to macro properties of concrete (e.g. Bejaoui and Bary 2007, Stora et al. 2008), and transport in pore networks (e.g. Raoof et al. 2012). However, generally accepted and well tested tools are presently scarce, to estimate the impact on the internal pore structure, represented by the tortuosity and the constrictivity in the equation above. Different expressions/ models have been suggested to relate changes in these parameters to changes in porosity. Typically the relationship would have the form:

$$D_e = f(\phi) \cdot D_{e,0}$$ Equation 8-2

Where $f(\phi)$ can be in the form of a power law, e.g.:

$$f(\phi) = \left(\frac{\phi}{\phi_0}\right)^n$$ Equation 8-3

n = some exponent in the range of 1–5, most commonly in the range 1.5–3 for sand, sandstone and sediments. Other studies that present models to relate the effective diffusivity to the porosity include the work of e.g. Tognazzi (1998) and Nguyen (2005). One common example of this type of expression is the famous Archie's law, which was derived as an empirical relationship between porosity, electrical conductivity and brine saturation of rocks.

A relationship derived specifically for concrete has been presented by Bentz and Garboczi (1992) in which a value for the percolation threshold ϕ_{th} is introduced:

$$D_c = D_0 \cdot (0.001 + 0.07 \cdot \phi^2 + 1.8 \cdot H(\phi - \phi_{th}) \cdot (\phi - \phi_{th})^2)$$ Equation 8-4

$$H(x) = 0 \text{ if } x < 0$$ Equation 8-5

$$H(x) = 1 \text{ if } x < 1$$ Equation 8-6

where:

D_c = Diffusivity of the leached concrete (m^2/s)

D_0 = Diffusivity of the intact concrete (m^2/s)

ϕ = the porosity of the leached concrete (m^3/m^3)

ϕ_{th} = threshold porosity for percolation to start (m^3/m^3)

$H(x)$ = the Heaviside function

The relationship derived by Tognazzi (1998):

$$D_e = D' \cdot e^{(9.95 \cdot \phi - 29.1)}$$ Equation 8-7

The relationship derived by Nguyen (2005):

$$D_e = D'' \cdot e^{(\omega \cdot \phi)}$$ Equation 8-8

where ω is an empirical parameter.

However, in concrete, the tortuosity and constrictivity contribute significantly to the diffusion resistance. Hence, changes in porosity may have a stronger impact on the diffusivity in concrete than would be expected from porosity changes in other materials, such as sediments. Tentative estimates of the effective diffusivity for different exponents and other suggested relationships presented above (Equations 8-2 to 8-8) are shown in Figure 8-1.

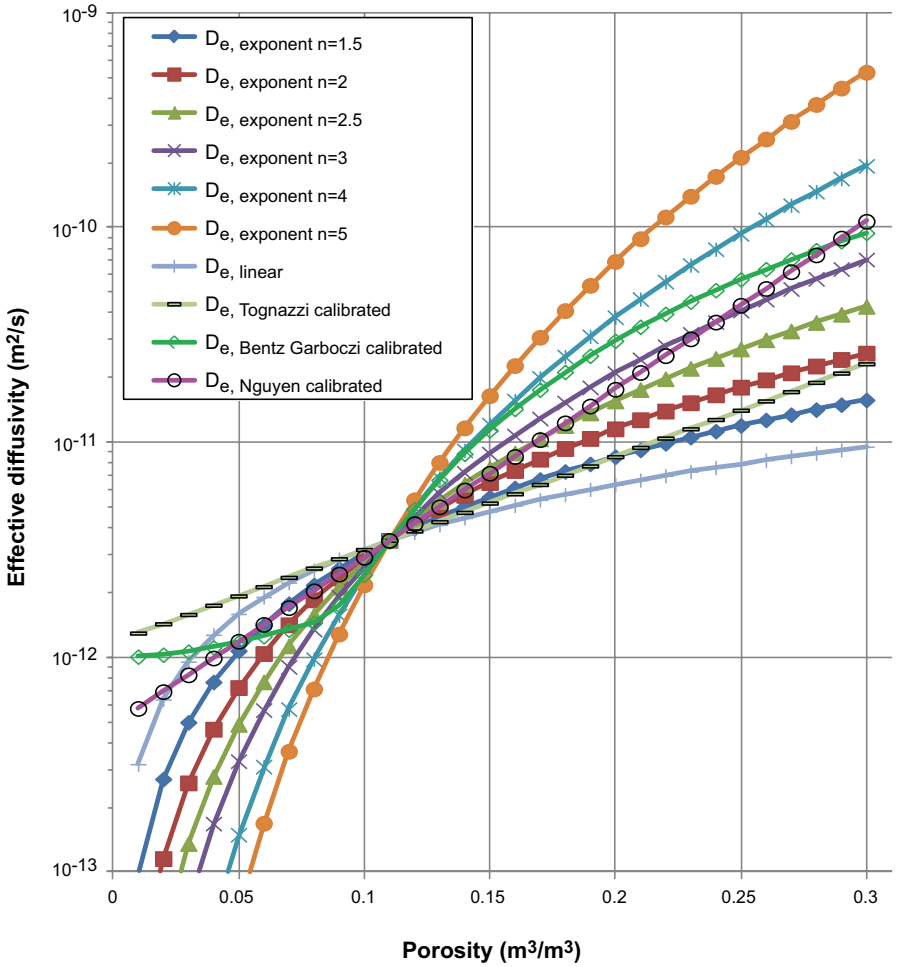

Figure 8-1. *Tentative models for the evolution of effective diffusivity with change in porosity due to chemical degradation.*

Power law dependence between effective diffusivity and porosity

The effective diffusivity has been calculated for each cell in the concrete barriers using the power law relationship presented in Equation 8-2 and 8-3. The overall effective diffusivity has been calculated by averaging over the *x*- and *y*-directions using an analogy with hydraulic conductance in composite media (see e.g. Freeze and Cherry 1979):

$$D_{e,\text{overall}} = \frac{\Sigma_j \left(y_j \cdot \left(\frac{\Sigma_i x_{i,j}}{\Sigma_i \left(\frac{x_{i,j}}{D_{e,i,j}} \right)} \right) \right)}{\Sigma_j y_j} \qquad \text{Equation 8-9}$$

where:

y_j = cell size in the *y*-direction (m)

$x_{i,j}$ = cell size in the *x*-direction (m)

$D_{e,i,j}$ = local effective diffusivity in one cell (m)

and

$$D_{e,i,j} = f(\phi_{i,j}) \cdot D_{e,0} \qquad \text{Equation 8-10}$$

$$f(\phi_{i,j}) = \left(\frac{\phi_{i,j}}{\phi_0} \right)^n \qquad \text{Equation 8-11}$$

n = 3, 4 or 5

The overall effective diffusivity data calculated for the upstream side of the concrete wall are shown in Figure 8-2. The results indicate that chemical degradation during the first 10,000 years would only be expected to result in small changes in the overall effective diffusivity. The results suggest there may be a small reduction in the overall effective diffusivity during the first 1,000 years. Thereafter, the diffusivity will increase slowly but steadily. After ~ 10,000–20,000 years, a more rapid increase in the diffusivity may occur as a result of chemical degradation.

A similar calculation of the changes in the overall hydraulic conductivity of the concrete wall has been made by averaging over the *x*- and *y*-directions of the hydraulic conductance in composite media (see e.g. Freeze and Cherry 1979):

$$K_{\text{overall}} = \frac{\sum_j \left(y_j \cdot \left(\frac{\sum_i x_{i,j}}{\sum_i \left(\frac{x_{i,j}}{K_{i,j}} \right)} \right) \right)}{\sum_j y_j} \qquad \text{Equation 8-12}$$

where:

y_j = cell size in the *y*-direction (m)

$x_{i,j}$ = cell size in the *x*-direction (m)

$K_{i,j}$ = local hydraulic conductivity in one cell (m)

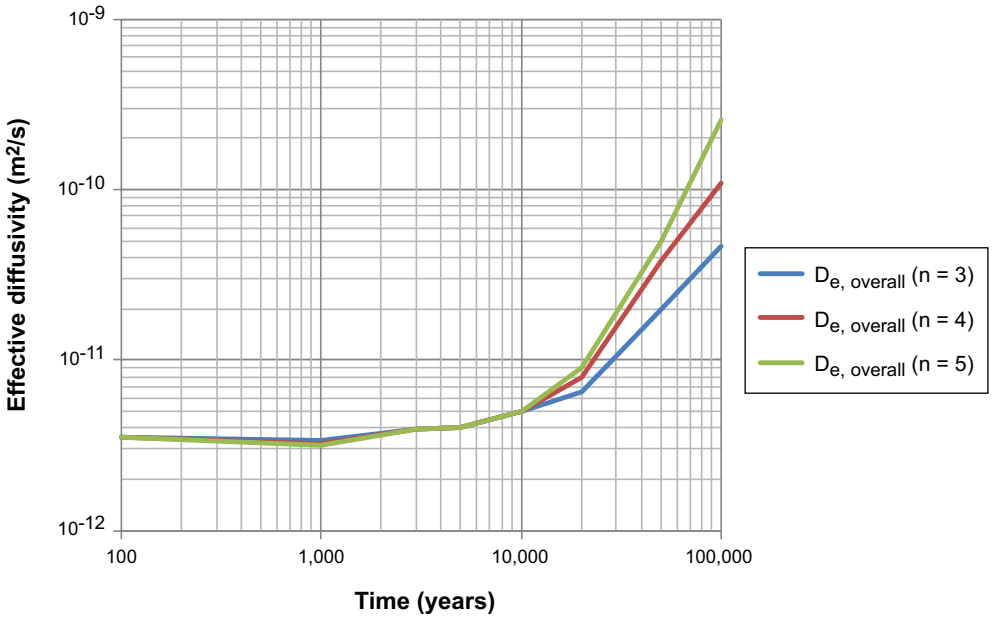

Figure 8-2. *Calculated overall effective diffusivities in the upstream side concrete wall in 2BMA. Calculations have been made for three different power law models (Equations 8-8 and 8-9; n = 3, 4, and 5) and are shown at selected time-steps (100, 1,000, 3,000, 5,000, 10,000, 20,000, 50,000 and 100,000 years.) Scales are logarithmic for both the time and the overall effective diffusivity.*

Kozeny-Carman relation for the hydraulic conductivity

Based on the porosity change calculated, the change in the hydraulic conductivity has been calculated based on the well-known Kozeny-Carman relation as proposed by Benbow et al. (2005).

$$K(\phi) = K(\phi_0) \cdot G(\phi)$$ Equation 8-13

$$G(\phi) = \frac{(1-\phi_0)^2}{\phi_0^3} \cdot \frac{\phi^3}{(1-\phi)^2}$$ Equation 8-14

where:

$K(\phi)$ = the hydraulic conductivity for the calculated porosity (m/s)

$K(\phi_0)$ = the hydraulic conductivity for the initial porosity (m/s)

$G(\phi)$ = a scaling function based on the change of porosity (–)

ϕ = calculated porosity (m^3/m^3)

ϕ_0 = initial porosity (m^3/m^3)

Modified Kozeny-Carman relation for hydraulic conductivity

A modified expression has also been proposed by Benbow et al. (2005), suitable for composite media. The starting assumption is that it would be reasonable for the hydraulic conductivity to be scalable between the initial conductivity of the intact concrete and a final state where all cement minerals have been depleted; leaving a skeleton of the initial ballast material that controls the conductivity. The original Kozeny-Carman relation cannot be extrapolated to totally leached concrete, thus the modified version includes a logarithmic scaling procedure to achieve this.

The porosity, ϕ, is related to the volume fraction of ballast material, v_b, in concrete and the volume fraction of cement minerals, v_c, according to:

$$\phi = 1 - (v_b + v_c)$$ Equation 8-15

The hydraulic conductivity is expressed as:

$$K_m = C_m(v_c) \cdot \frac{\phi^3}{(1-\phi)^2}$$ Equation 8-16

where:

C_m = property function in the Kozeny-Carman relation for material m

m = concrete and pure ballast, respectively

$$C_{\text{pure ballast}} = K(\phi_{ref}) \cdot \frac{(1-\phi_{ref})^2}{\phi_{ref}^3}$$ Equation 8-17

$$C_{\text{concrete}} = K(\phi_0) \cdot \frac{(1-\phi_0)^2}{\phi_0^3}$$ Equation 8-18

where:

ϕ_{ref} = porosity of pure ballast (m^3/m^3)

A log-linear interpolation is introduced using the expression:

$$\log C(v_c) = \left(1 - \frac{v_c}{v_{c,0}}\right) \cdot \log C_{\text{pure ballast}} + \frac{v_c}{v_{c,0}} \cdot \log C_{\text{concrete}}$$ Equation 8-19

where $v_{c,0}$ and v_c are the volume fractions of cement minerals in intact concrete and in concrete partly leached from its cement content, respectively.

From this, the hydraulic conductivity is calculated as:

$$K = C(v_c) \cdot \frac{\phi^3}{(1-\phi)^2}$$ Equation 8-20

Figure 8-3 compares the results from the Kozeny-Carman and the modified Kozeny-Carman relations over the porosity interval 0.1–0.31 m^3/m^3, which encompasses the evolution from intact to fully leached 2BMA construction concrete. Figure 8-4 shows the changing hydraulic conductivity in the upstream side concrete wall in 2BMA, calculated using the modified Kozeny-Carman relation (Equation 8-18).

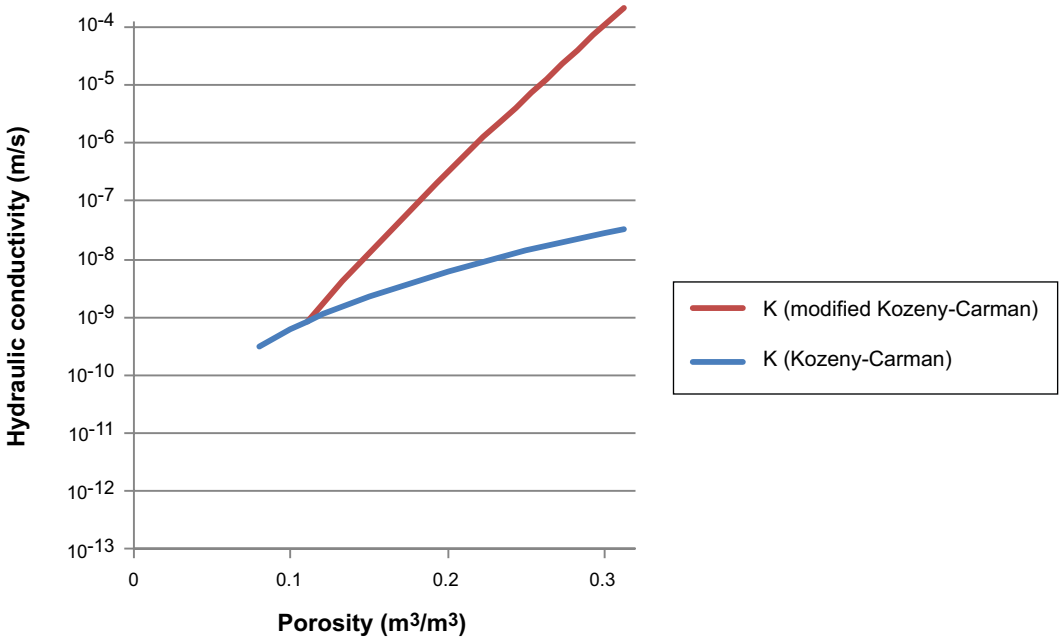

Figure 8-3. *Hydraulic conductivity, K, calculated by the Kozeny-Carman (Equation 8-13) and the modified Kozeny-Carman (Equation 8-20) relations. The conductivity of intact concrete, $K(\phi_0)$, has been assumed to be $8.3 \cdot 10^{-10}$ m/s and the conductivity of fully degraded concrete consisting only of pure ballast material, $K(\phi_{ref})$, has been assumed to be $1 \cdot 10^{-4}$ m/s.*

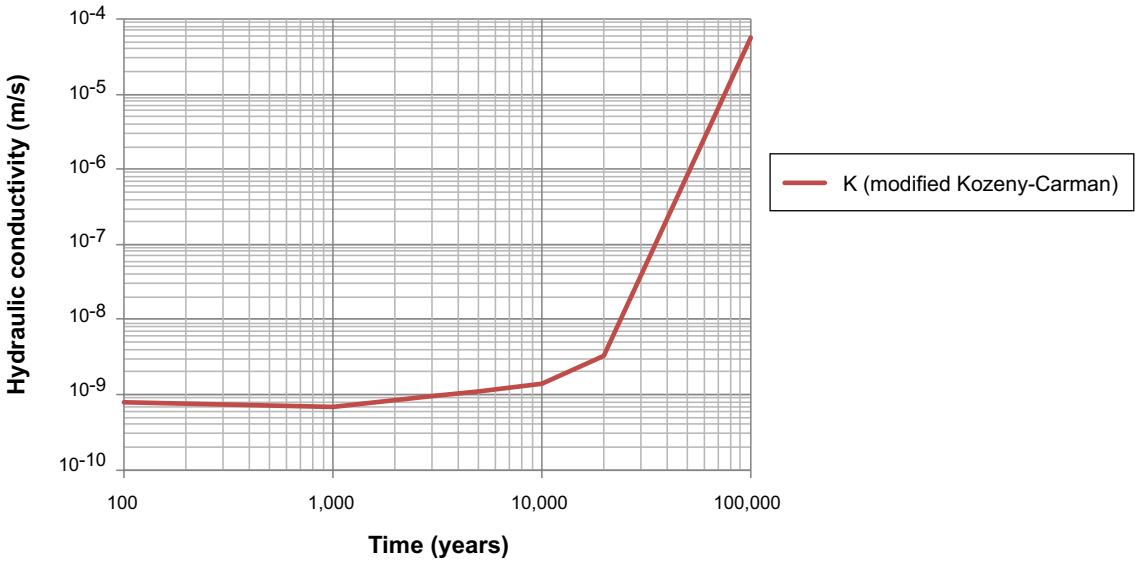

Figure 8-4. *Calculated overall hydraulic conductivities using the modified Kozeny-Carman relation (Equation 8-20) in the upstream side concrete wall in 2BMA. Calculations have been made for selected time-steps in the PHAST modelling (100, 1,000, 3,000, 5,000, 10,000, 20,000, 50,000 and 100,000 years).*

Modified Archie's law relation for the effective diffusivity

An analogous method for log-linear interpolation of the effective diffusivity has been presented by Benbow et al. (2005), starting from Archie's law:

$$D_e = \phi^{m-1} \cdot D_p \qquad \text{Equation 8-21}$$

Where:

m = 1.3–2.5, here a value of 2 is assumed, and D_p is the pore diffusivity.

Rewriting the above expression:

$$D_e(\phi, \nu_c) = \phi^{m-1} \cdot D_p(\nu_c) \qquad \text{Equation 8-22}$$

Introducing:

$$\log D_p(\nu_c) = \left(1 - \frac{\nu_c}{\nu_{c,0}}\right) \cdot \log D_{p,\text{pure ballast}} + \frac{\nu_c}{\nu_{c,0}} \cdot \log D_{p,\text{concrete}} \qquad \text{Equation 8-23}$$

Applying the conditions:

$$D_e(\phi, 0) = D_{e,\text{pure ballast}}(\phi) \qquad \text{Equation 8-24}$$

$$D_e\left(\phi, \nu_{c,0}\right) = D_{e,\text{concrete}}(\phi) \qquad \text{Equation 8-25}$$

Effective diffusivity (Equation 8-22, considering Equations 8-23–8-25) values calculated for the porosity range of relevance during the leaching of 2BMA construction concrete are presented in Figure 8-5.

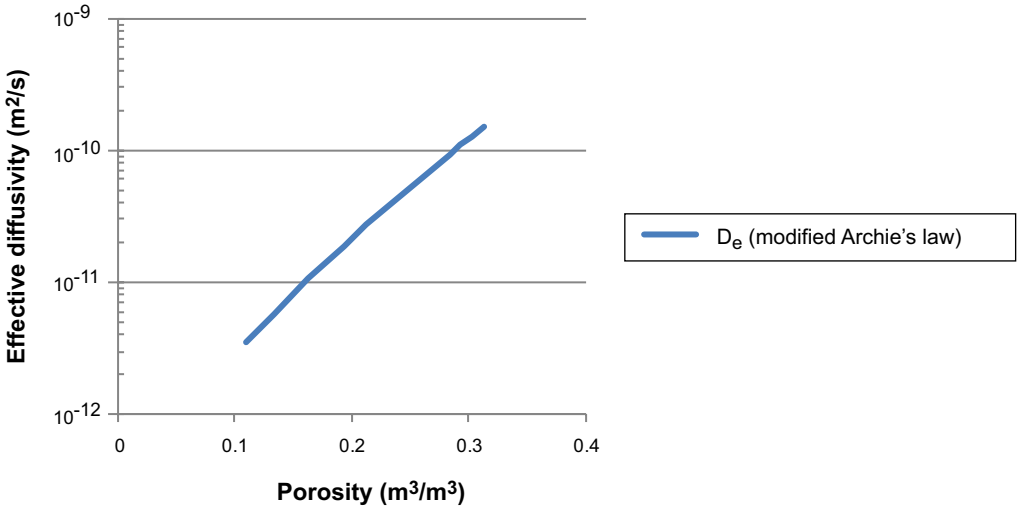

Figure 8-5. *Effective diffusivity calculated by the modified Archie's law (Equation 8-22) relation. The effective diffusivity of intact concrete, $D_e(\phi,\nu_{c,0})$, has been assumed to be $3.5 \cdot 10^{-12}$ m^2/s and the effective diffusivity of fully degraded concrete consisting only of pure ballast material, $D_e(\phi,\nu_c = 0)$, has been assumed to be $1.5 \cdot 10^{-10}$ m^2/s. The figure shows the effective diffusivity versus porosity.*

8.2 Calculations for 2BMA

The evaluation of the effect of porosity changes for 2BMA concrete barriers was based on the numerical models described below. The reactive transport modelling output from the Large20 case was used to determine the porosity changes of the barrier over a 2 dimensional area using the method presented in Section 6.15 (Equation 6-61), which in turn allowed estimation of the spatial changes in effective diffusivity. This grid has been used to assess the distribution of the effective diffusivities in different sections of the concrete walls at selected times. Calculations have also been carried out to estimate changes in the hydraulic conductivity of a section through the barrier over time. The results have also been utilised to calculate the overall effective diffusivity and hydraulic conductivity of the concrete barriers at selected times.

Results at the different time points

The methodology described above has been applied to the 2BMA barriers, using the results from the PHAST model numerical simulations. The results are presented as time-series of figures, showing the calculated spatial changes in porosity, effective diffusivity and hydraulic conductivity. The results are shown for individual 1-D pathways through the upstream-side of the concrete wall, average values integrated over the upstream-side concrete wall, and a 2-D-cross section of the 2BMA vault (see Figure 7-1). The 1-D pathways selected are through initially intact concrete and through a fully penetrating fracture along the *x*-axis.

For the first plotted time step (100 years), four different results of the effective diffusivity are presented, calculated using the power-law model with three different exponents and the modified Archie's law relationship. Since the results obtained for the different models were reasonably coherent, the data from the exponential model with an exponent 4 are presented for the other times. In a similar manner, the results for the hydraulic conductivity using both the Kozeny-Carman and the modified Kozeny-Carman relationships are presented for the first time step (100 years), whereas only the modified Kozeny-Carman relationship for the hydraulic conductivity is presented for the following time steps.

100 years

The porosity and the changes in porosity have been evaluated through two sections of the concrete wall and are presented in Figure 8-6 and Figure 8-7. In the intact concrete, the porosity was constant across the majority of the section and had the initial value applied of 0.11 m^3/m^3. The exception to this was within ~2 cm of the surfaces of the concrete wall, where the concrete was calculated to have a maximum porosity of 0.25 m^3/m^3 (in-flow surface). This resulted in steep gradients in porosity of the wall. The porosity changes shown for 100 years are low, which indicates that the enhanced surface porosity was largely present at time zero. This may be an artefact relating to the discretisation in the model, which is not very detailed; the model interpolates between the properties of adjacent materials at interfaces, thus, here between the concrete and the surrounding macadam.

A fracture is initially free space, i.e. has a porosity of 1.0 m^3/m^3. However, at 100 years, the porosity of the fracture was below 1.0 near the surfaces of the wall (~2 cm), and the porosity change data indicate this was also the case at time zero. This therefore reflects the interpolation of the properties of the macadam and fracture.

The effective diffusivities have been calculated using power law model (cf. Equations 8-10, 8-11) with three different exponents, see Figure 8-8 and the modified Archie's law relation (Equation 8-22), see Figure 8-9. The different models show reasonable agreement.

The hydraulic conductivities have been calculated using the Kozeny-Carman and the modified Kozeny-Carman relations and the results are presented in Figure 8-10.

2-D plots at 100 years show the calculated changes in porosity (cf. Equation 6-61) (Figure 8-11), the effective diffusivity using a power law model (cf. Equations 8-10, 8-11) with exponent 3 (Figure 8-12), with exponent 4 (Figure 8-13), and with exponent 5 (Figure 8-14). Figure 8-15 presents an assemblage of the 2-D-plots at 5,000 years together with the calculated porosity distribution and resulting effective diffusivity distributions using a power law model for three different exponents.

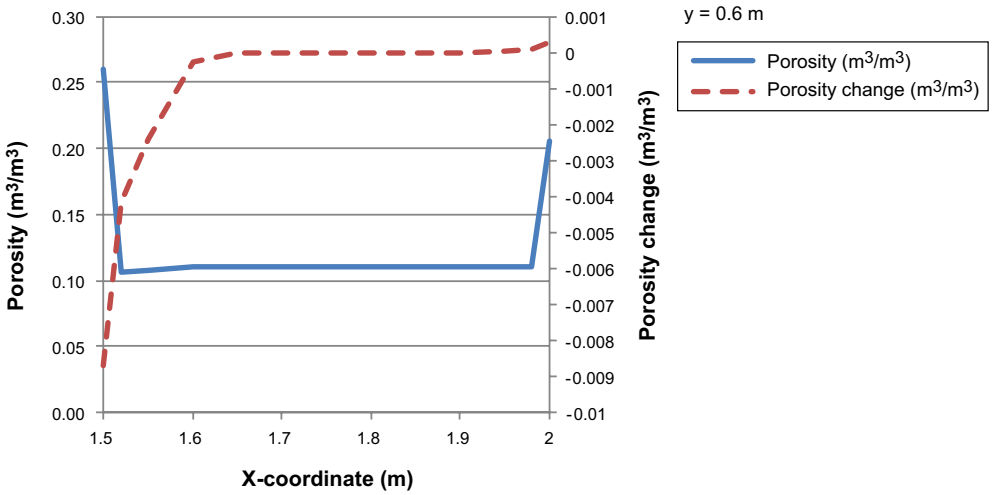

Figure 8-6. *Calculated porosity and porosity change (cf. Equation 6-61) along a horizontal section through the upstream side concrete wall (at y = 0.6 m, see Figure 7-3) in 2BMA at 100 years.*

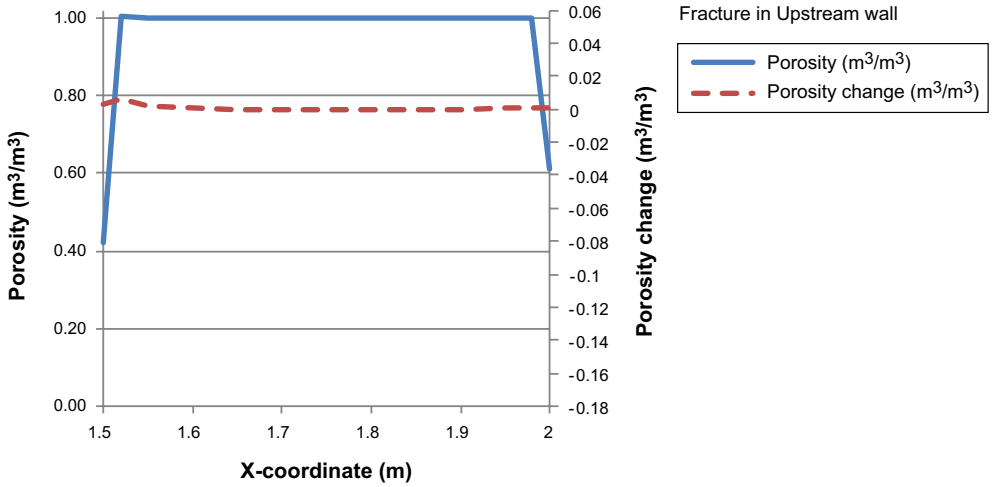

Figure 8-7. *Calculated porosity and porosity change (cf. Equation 6-61) along a section through the upstream side concrete wall near the thin fracture in 2BMA at 100 years.*

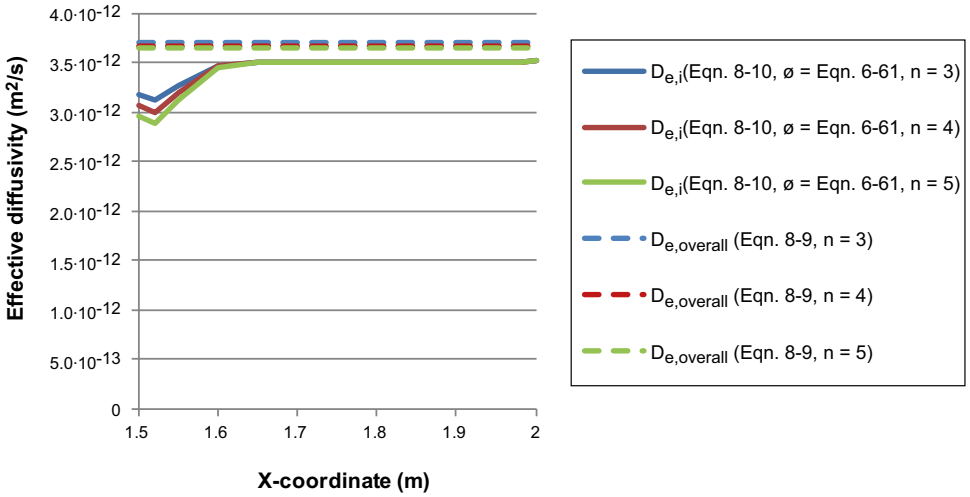

Figure 8-8. *Calculated effective diffusivities along a section through the upstream side concrete wall in 2BMA. Calculations have been made for three different power law models (cf. Equation 8-10 and 8-11) and are shown at 100 years. The figure also shows the calculated overall effective diffusivities calculated over the whole cross-section for the three models.*

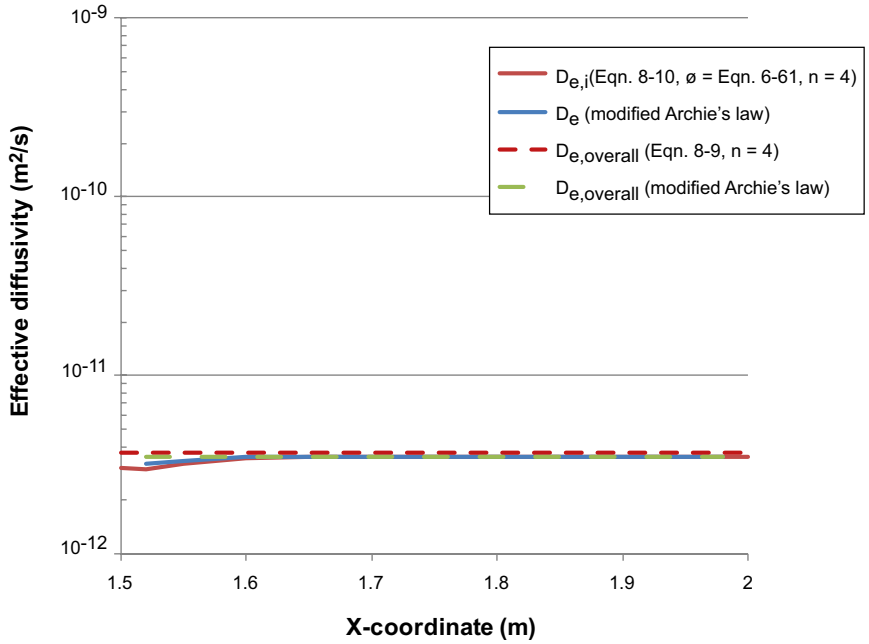

Figure 8-9. *Calculated effective diffusivities along a section through the upstream side concrete wall in 2BMA. Calculations have been made with the modified Archie's law relation (cf. Equation 8-22), and are shown at 100 years. For comparison, the results of the power law model (cf. Equation 8-10 and 8-11) with an exponent 4 are also shown. The figure also shows the calculated overall effective diffusivities (Equation 8-9) calculated over the whole cross-section for the two models.*

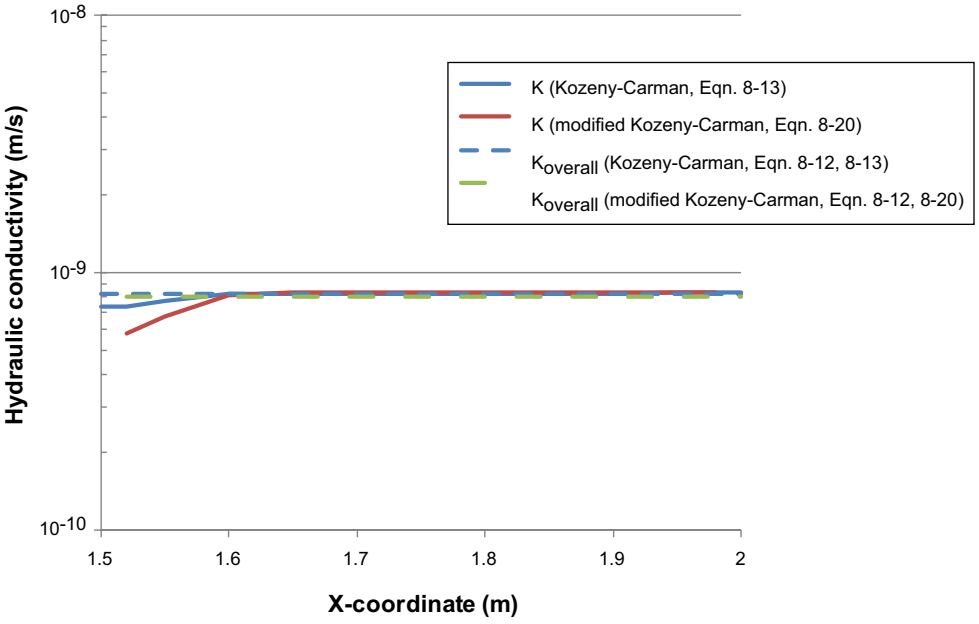

Figure 8-10. *Calculated hydraulic conductivities along a section through the upstream side concrete wall in 2BMA. Calculations have been made with the Kozeny-Carman (Equation 8-13) and the modified Kozeny-Carman (Equation 8-20) relations as a function of the x-coordinate and are shown at 100 years. The figure also shows the calculated overall hydraulic conductivities (Equation 8-12) calculated over the whole cross-section for the two models.*

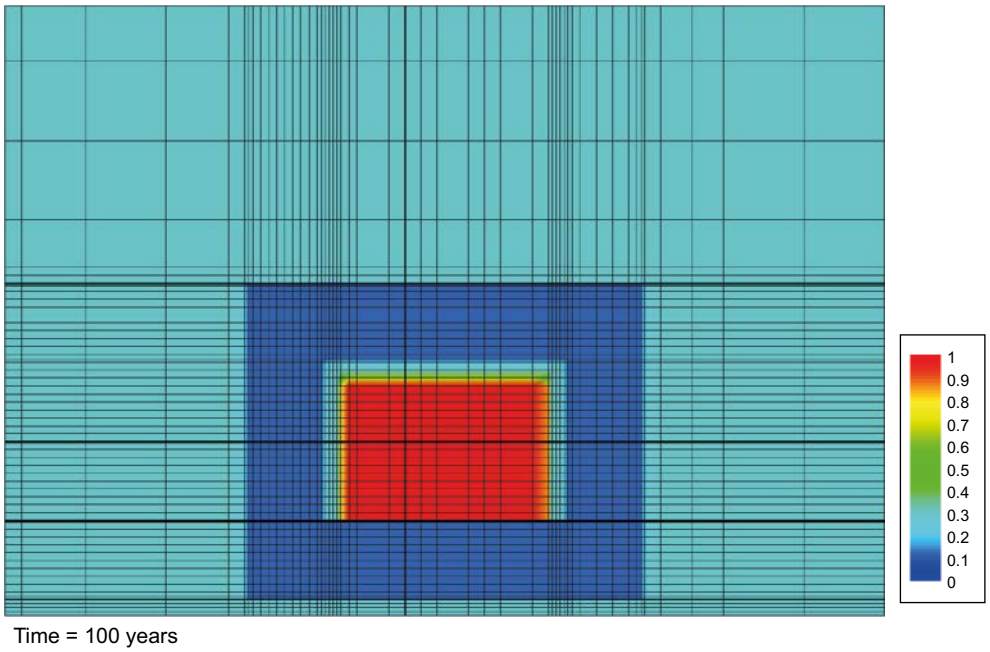

Figure 8-11. *Calculated porosity (Equation 6-62) in the full 2-D-section including the concrete walls, floor and lid, the concrete grout, and the macadam fill in 2BMA. Results are shown at 100 years. The colour scale is linear with blue representing 0.0 m^3/m^3 and red 1.0 m^3/m^3.*

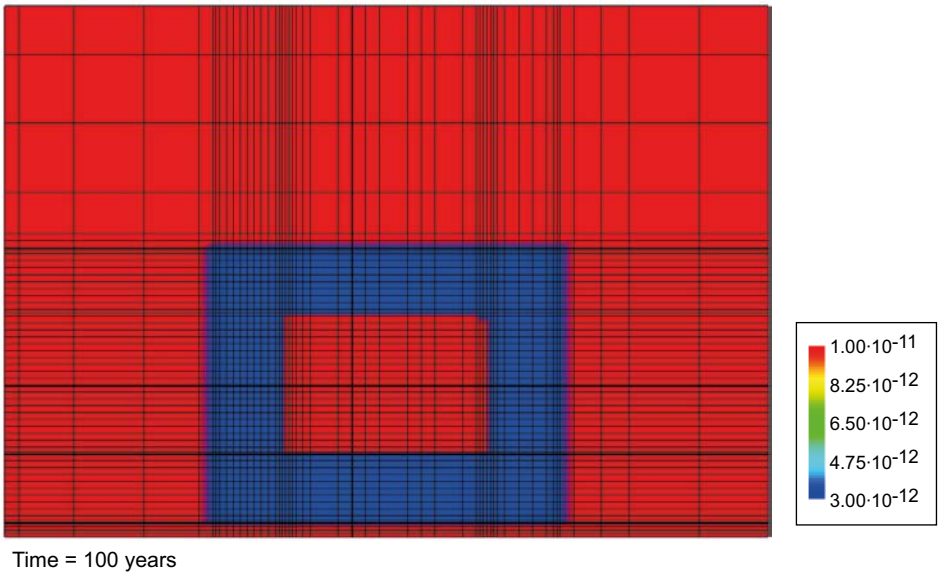

Figure 8-12. *Calculated effective diffusivities in the full 2-D-section including the concrete walls, floor and lid, the concrete grout, and the macadam fill in 2BMA. Results shown in the figure represent the power law model (cf. Equations 8-10, 8-11) with an exponent 3 and are shown at 100 years. The colour scale is logarithmic with blue representing $3 \cdot 10^{-12}$ m^2/s and red $\geq 1 \cdot 10^{-11}$ m^2/s.*

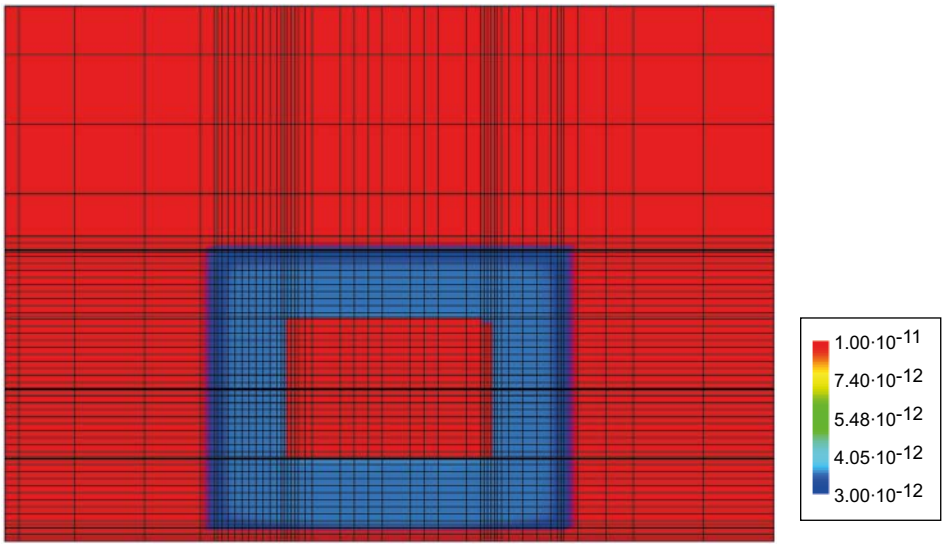

Figure 8-13. *Calculated effective diffusivities in the full 2-D-section including the concrete walls, floor and lid, the concrete grout, and the macadam fill in 2BMA. Results shown in the figure represent the power law model (cf. Equations 8-10, 8-11) with an exponent 4 and are shown at 100 years. The colour scale is logarithmic with blue representing $3 \cdot 10^{-12}$ m^2/s and red $\geq 1 \cdot 10^{-11}$ m^2/s.*

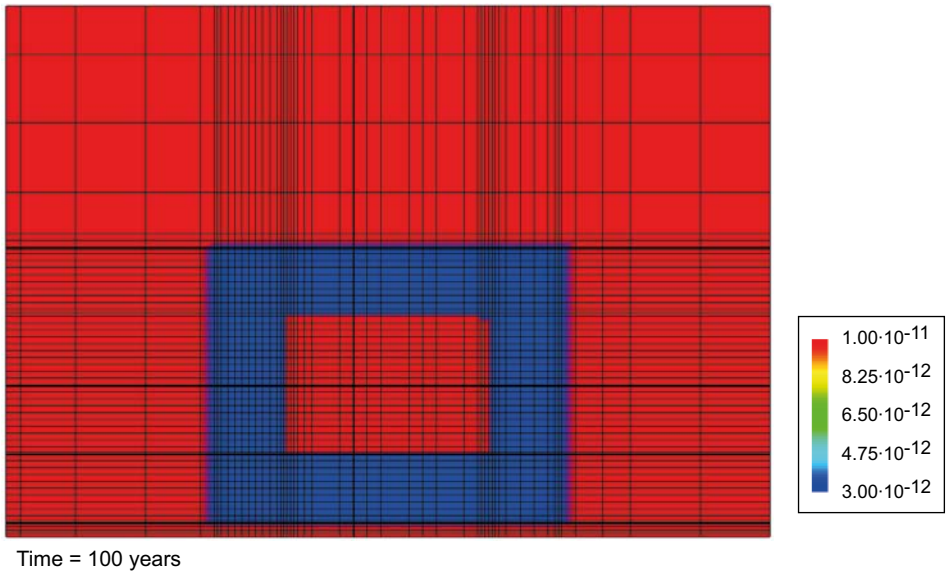

Figure 8-14. *Calculated effective diffusivities in the full 2-D-section including the concrete walls, floor and lid, the concrete grout, and the macadam fill in 2BMA. Results shown in the figure represent the power law model (cf. Equations 8-10, 8-11) with an exponent 5 and are shown at 100 years. The colour scale is logarithmic with blue representing $3 \cdot 10^{-12}$ m^2/s and red $\geq 1 \cdot 10^{-11}$ m^2/s.*

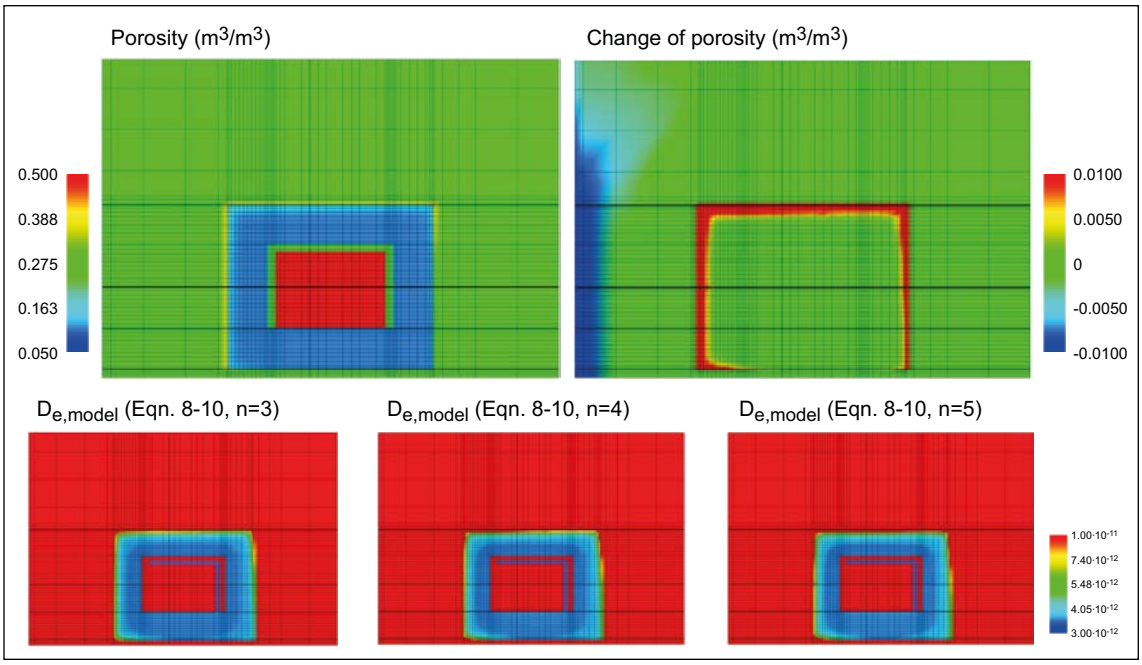

Figure 8-15. *Calculated porosity (Equation 6-62), change of porosity (Equation 6-61) and effective diffusivity using three different power law models (cf. Equations 8-10, 8-11) in the full 2-D-section including the concrete walls, floor and lid, the concrete grout, and the macadam fill in 2BMA. Results are show at 5,000 years. The colour scale of the porosity is linear with blue representing ≤ 0.05 m^3/m^3 and red ≥ 0.5 m^3/m^3. The colour scale of the porosity change is linear with blue representing ≤ –0.01 m^3/m^3 and red ≥ 0.01 m^3/m^3. The colour scale of the effective diffusivity is logarithmic with blue representing $3 \cdot 10^{-12}$ m^2/s and red $1 \cdot 10^{-11}$ m^2/s.*

Time series data: Porosity

The porosity and the change in porosity were calculated using Equation 6-61 for the 1-D sections through intact concrete and the fully penetrating fracture. The results are presented in Figure 8-16.

Intact concrete: The porosity of the wall ~ 2–15 cm from the inflow surface has changed notably between 3,000–10,000 years, from ~ 0.11–0.12 m^3/m^3 to ~ 0.12–0.17 m^3/m^3. This progression is seen to continue in the period up to 20,000 years, with the porosity of the wall increasing 10–20 cm along the section. However, there was also a decrease in the porosity of the wall ~ 2–6 cm from the inflow surface in this time, showing that precipitation has occurred. By 50,000 years, the porosity along the section through the wall had increased to ~ 0.20 m^3/m^3, except within a few centimetres of the outer surface. A similar trend was seen after 100,000 years, although the porosity in the section was higher again (~ 0.24–0.28 m^3/m^3). The overall trend in intact concrete is therefore an increased porosity over time with fairly uniform distribution along the flow direction. The porosity changes indicated at the inflow surface is an artefact due to interpolation between the concrete and the macadam at the interface of the two materials and should be disregarded.

Along a fully penetrating fracture: The porosity changes between 100–3,000 years were limited. However, by 10,000 years, the porosity had decreased ~ 2–10 cm from the inflow surface, to ~ 0.94–0.99 m^3/m^3. Relative to time zero, the largest change in porosity at 10,000 years was located ~ 2 cm from the inflow surface, reflecting lower change at the surface itself than further along the fracture. This feature was more marked by 20,000 years, when the actual porosity had decreased to 20 cm along the path of the fracture.

The porosity profile along the fracture changed markedly by 50,000 years, and the porosity was below 1.0 along the entire section. Although the general trend was of decreased porosity, the porosity had increased ~ 2–8 cm from the inflow surface. By 100,000 years, the porosity had decreased further throughout the profile. Therefore, the sequence shows the general trend of reduced porosity in the fractures over time. Precipitation reactions occur first at the inflow side of the fracture and then progressively along the fracture, as the reactivity of the surface zone is reduced (Chapter 7).

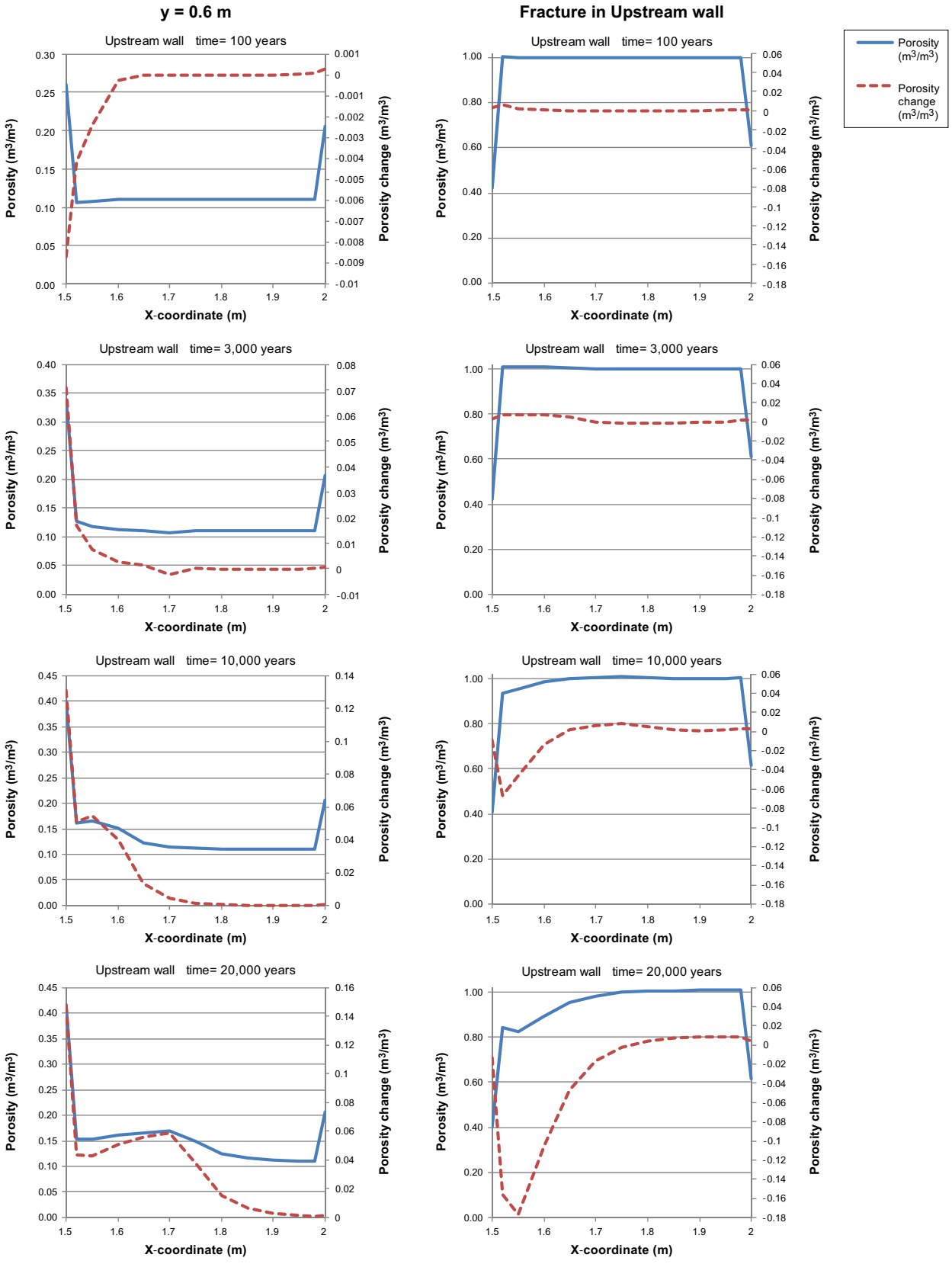

Figure 8-16. *Calculated porosity (Equation 6-62), and porosity change (Equation 6-61) along a section of initially intact concrete (left hand side) and a fully penetrating fracture (right hand side) through the upstream side of the concrete wall in 2BMA after 100, 3,000, 10,000, 20,000, 50,000 and 100,000 years.*

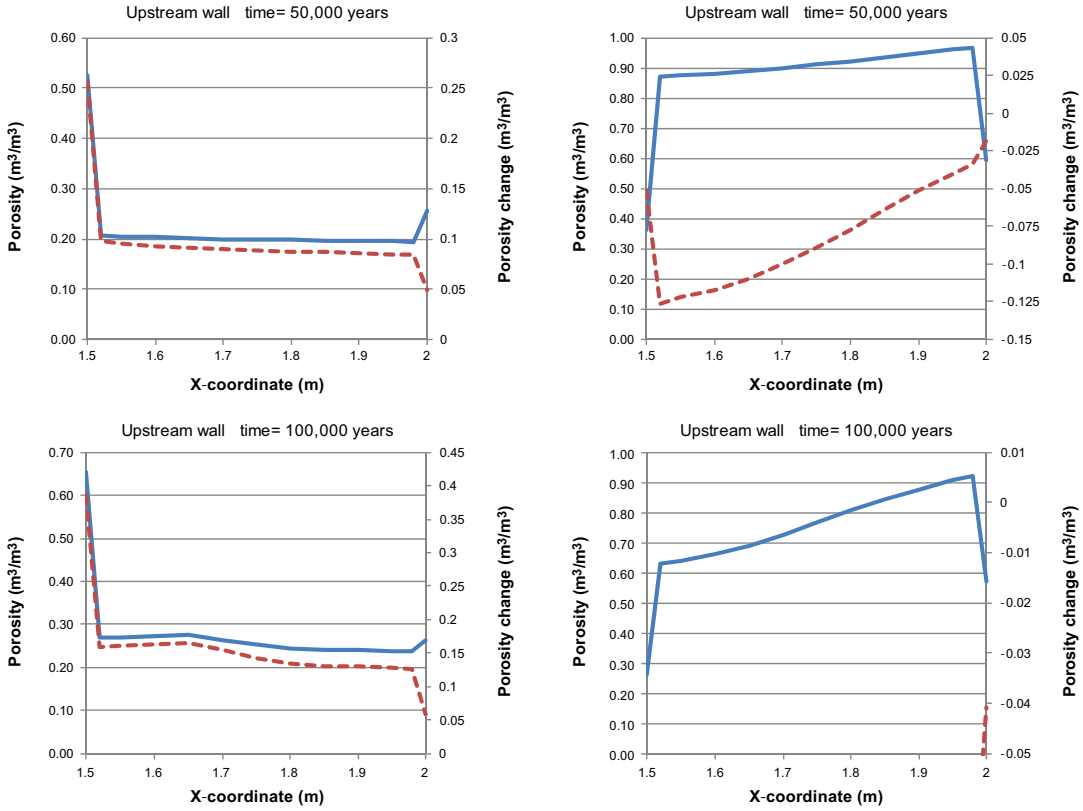

Figure 8-16. *Continued.*

Time series data: Effective diffusivity

The time series of effective diffusivity data, calculated for intact concrete using the power law model with an exponent of 4, is presented in Figure 8-17 (left hand side). Consistent with the changes in porosity, the changes in effective diffusivity appear first near the inflow surface of the wall. By 3,000 years, the surface diffusivity had increased from $3.5 \cdot 10^{-12}$ to ~ $9 \cdot 10^{-12}$ m^2/s. By 10,000 years, the effective diffusivity of both the surface concrete and along the section to ~ 15 cm had increased markedly, and by 20,000 years, approximately half of the section had an effective diffusivity above 10^{-11} m^2/s. After 50,000 years, the effective diffusivity had become quite even along the section, at ~ $3 \cdot 10^{-11}$–$5 \cdot 10^{-11}$ m^2/s, except very close to the outer surface. A similar trend was calculated for 100,000 years, but with higher values and wider range of effective diffusivities (approximately $7 \cdot 10^{-11}$–$1.2 \cdot 10^{-10}$ m^2/s). The effective diffusivity is controlled directly by the porosity, and their close relationship is apparent when comparing Figure 8-16, Figure 8-17 and Figure 8-18.

Time series data: Hydraulic conductivity

The hydraulic conductivities calculated using the modified Kozeny-Carman model are presented in Figure 8-17 (right hand side). The hydraulic conductivity was found to be lower at the inflow surface of the wall after 100 years, but this trend had reversed by 3,000 years. The trends over time then followed the same general patterns seen for the effective diffusivity, although the extent of change was more marked. The hydraulic conductivity changed by 5 orders of magnitude over the 100,000 year period investigated. Changes in porosity clearly affect the hydraulic conductivity to a large degree.

However, hydraulic conductivity is also affected by a number of factors that were not included in these calculations. As shown in Chapters 4.2 and 6, as well as discussed below in Section 9.1, the hydraulic conductivity is very sensitive to presence of fractures and the size of these fractures. Chemical degradation may cause three major effects related to fractures:

- The possible formation of expanding minerals such as ettringite and thaumasite in the hardened concrete that may result in formation of new cracks and widening of existing fractures.
- A locally enhanced leaching of soluble minerals adjacent to small fractures in the concrete constructions, potentially leading to increased fractures apertures.
- Clogging of fractures due to mineral precipitation.

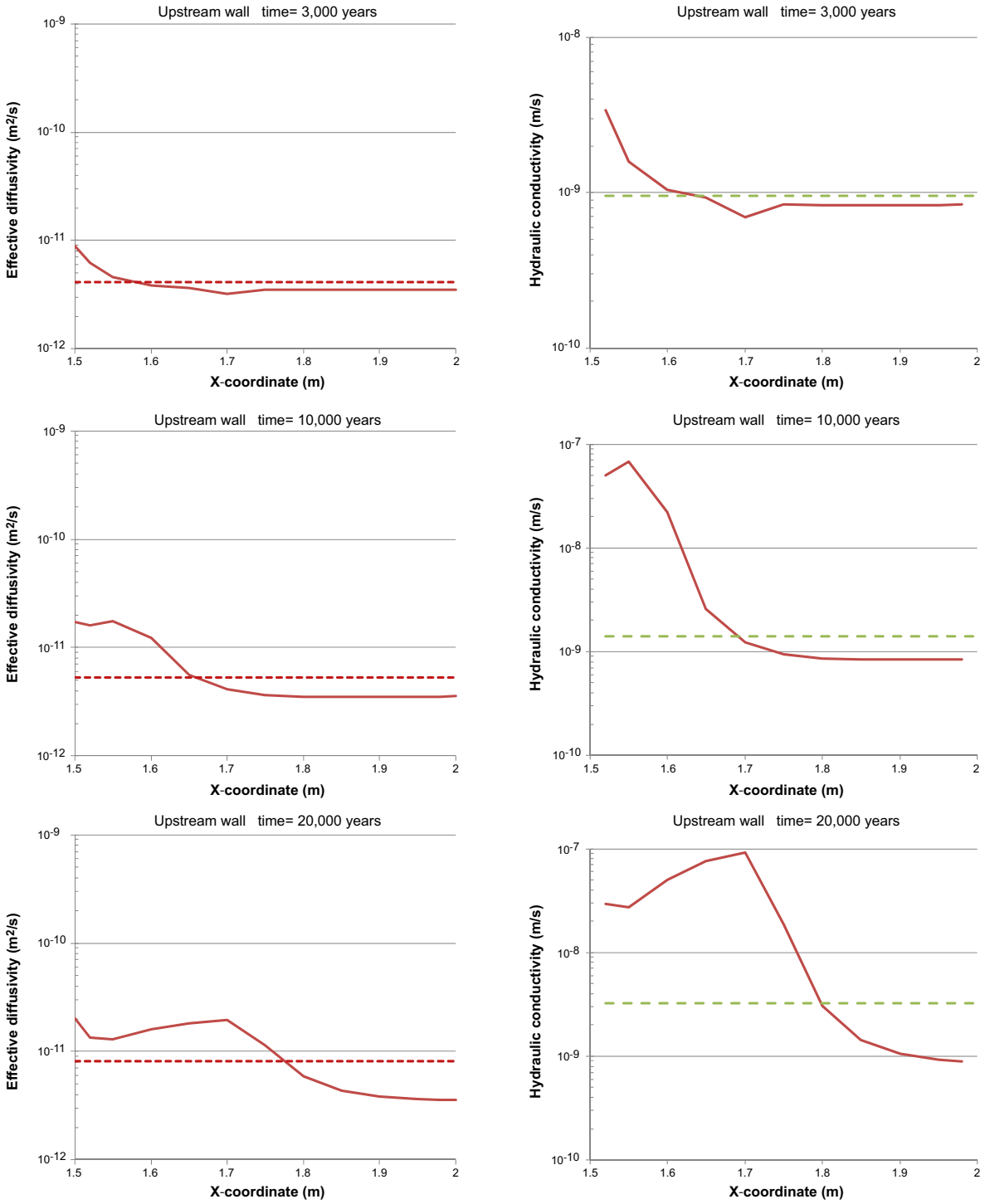

Figure 8-17. *Calculated effective diffusivities (left hand side; power law model (cf. Equations 8-10, 8-11) with exponent 4) and hydraulic conductivities (right hand side; modified Kozeny-Carman relation Equation 8-20) from 3,000–100,000 years along a section of intact concrete through the upstream side of the concrete wall in 2BMA. The figure also shows the calculated overall effective diffusivities (Equation 8-9) and overall hydraulic conductivities (Equation 8-12) calculated over the whole cross-section (dotted lines).*

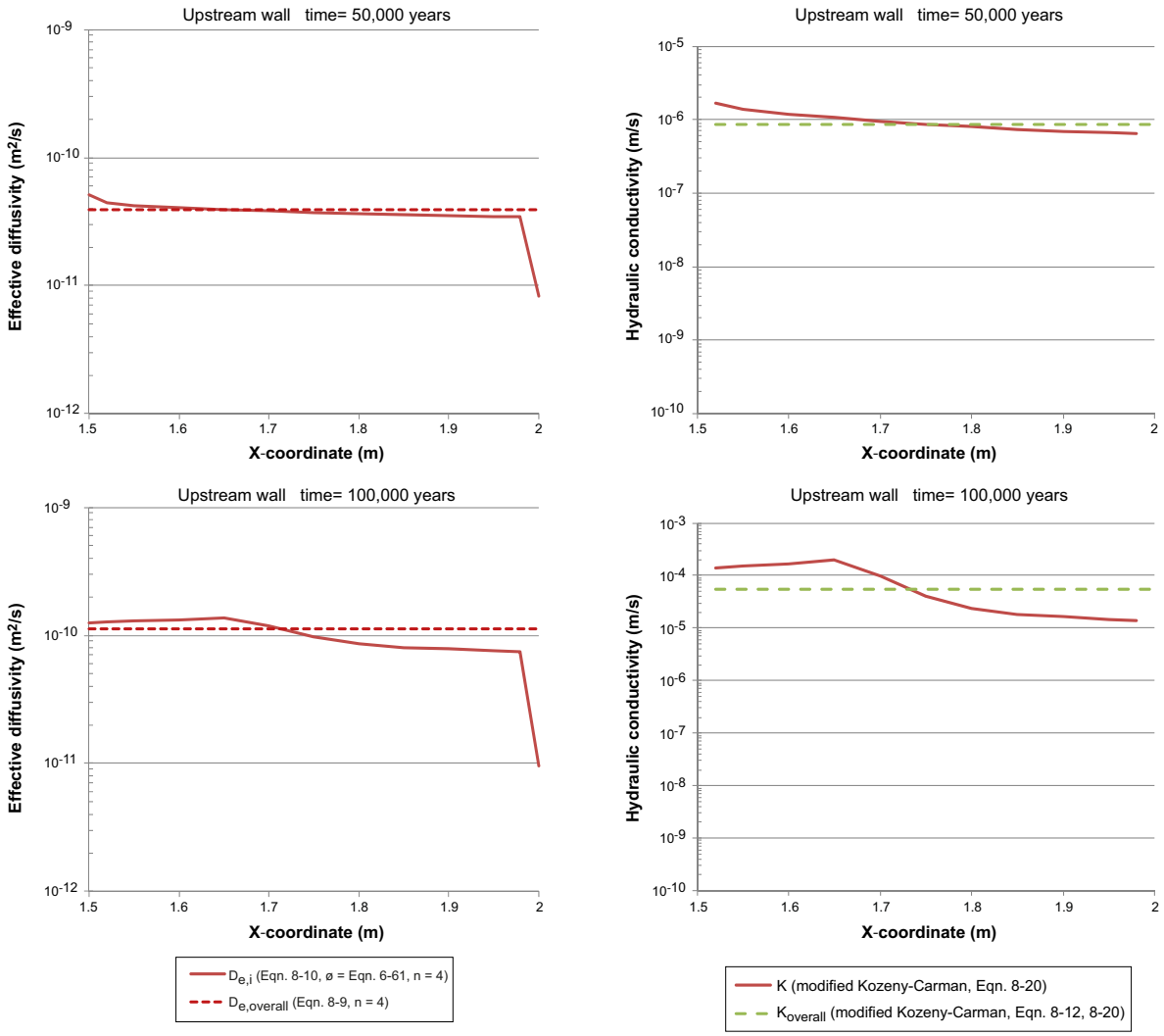

Figure 8-17. *Continued.*

Neither of these processes can be ruled out based on the results of the reactive transport modelling. The possible effect of new cracks formed as a result of the precipitation of expanding minerals or a gradual widening of existing fractures due to leaching must therefore be accounted for when selecting material data for the barriers in both 1BMA and 2BMA.

Time series data: 2-D plots of porosity and effective diffusivity

The 2-D plots of the calculated porosities and effective diffusivities using the power law model with exponent 4 are presented in Figure 8-18.

The 2-D figures show the overall changes in the porosity of the system modelled (i.e. case Large20). Since the 2BMA barrier has been designed to avoid large fractures, the fractures present in the system are narrow and their influence is not visible in the 2-D plots of porosity over time. The results from the analysis of the changes along one of the fractures showed that the porosity of the fracture would decrease over time and so the influence on the overall porosity would also decrease.

The 2-D plots show the importance of position relative to the surface and flow direction. By 20,000 years, the majority of the concrete has an increased porosity relative to the original value, and none of the concrete has the original porosity after 50,000 years.

The changes in diffusivity show a similar pattern; although the increases in diffusivity are observed slightly earlier than the increases in porosity. The reason for this is the assumed power law dependency of the effective diffusivity on the porosity.

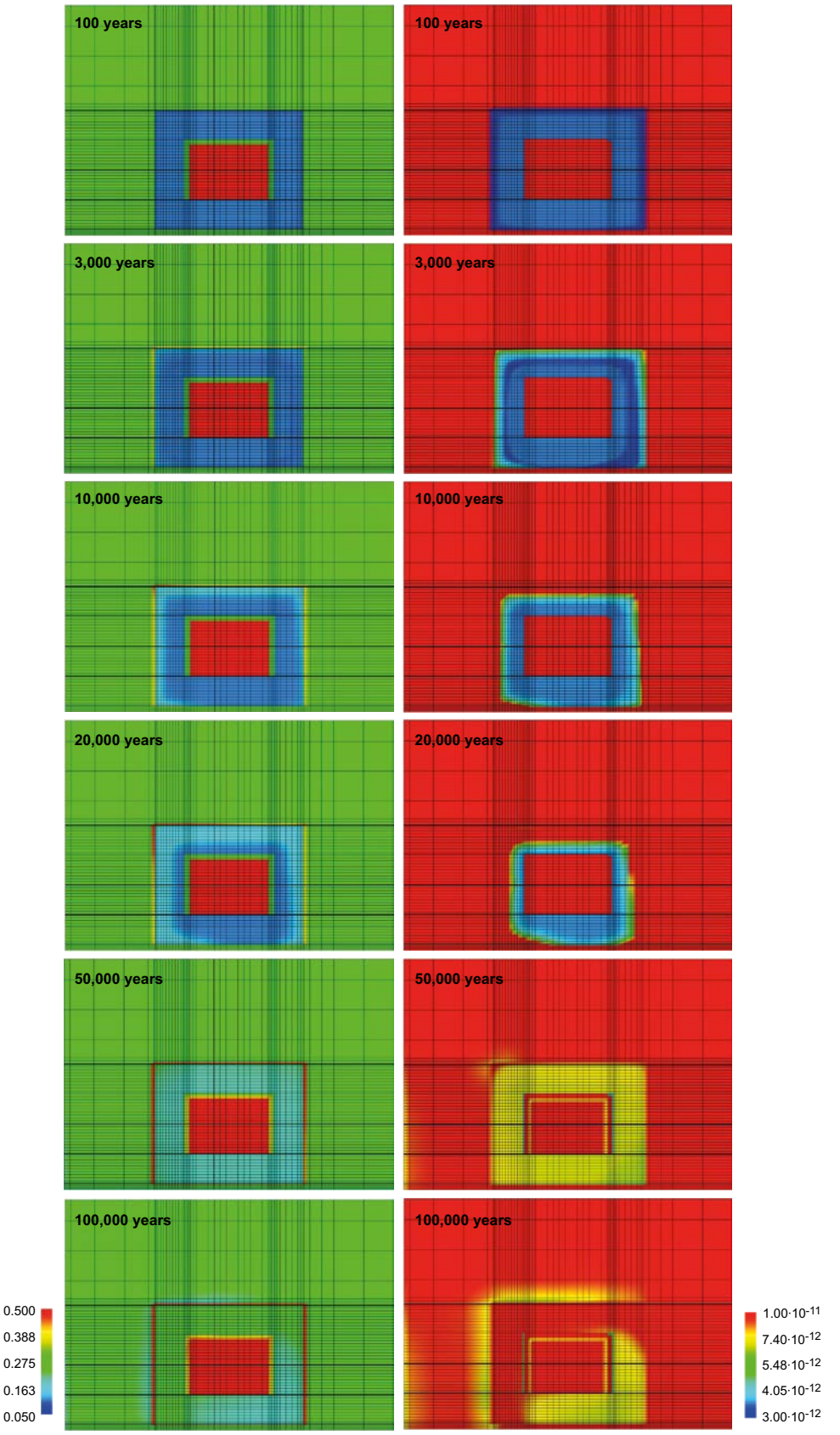

Figure 8-18. *Calculated porosity (Equation 6-62) (left hand side) and effective diffusivity (Equations 8-10, 8-11) (right hand side) over time in the full 2-D-section including the concrete walls, floor and lid, the concrete grout, and the macadam fill in 2BMA. The colour scale of the porosity at the left-hand side is linear with blue colour representing 0.05 m^3/m^3 and red colour ≥ 0.5 m^3/m^3. The colour scale of the effective diffusivity at the right-hand side is linear with blue colour representing $3 \cdot 10^{-12}$ m^2/s and red colour $1 \cdot 10^{-11}$ m^2/s.*

8.3 Calculations for 1BMA

The integrated approach applied to 2BMA was not considered meaningful for 1BMA, due to the highly heterogeneous nature of the concrete walls in their current state, with fractured concrete and corroding steel reinforcement and form ties. Therefore, the evaluations and analyses were restricted to selected locations in the concrete walls where the changes in the concrete porosity were calculated, using the data from the modelling cases presented in Chapter 7.

The changes in the porosity of 1BMA are shown for location A-E (at the intersection of the centreline through the floor and the left-hand side concrete wall) and location DE (near the thin fracture at the centreline through the left-hand side concrete wall) in Figure 8-19 and Figure 8-20, respectively. Two equivalent cases were investigated using two different thermodynamic databases: Large8 (Cemdata07) and Large10 (MinteqCem-2001) show 1BMA in a fractured state and Large 11 (MinteqCem-2001) and Large12 (Cemdata07) show the simple 1BMA repair scenario. In case Large9, the material properties have been assumed to remain unchanged over an extended period (100–10,000 years) (MinteqCem-2001).

At location AE, all of the model systems except Large12 suggest that precipitation dominates the early period. The porosity then increases up to ~ 7,000–15,000 years, and then reaches a plateau. The different modelling assumptions lead to differences in the rate of porosity increase and the long term porosity calculated. The Cemdata07 thermodynamic data predicted a lower porosity than MinteqCem-2001 for both cases.

In the fracture (inspection point DE), there is greater variation between the different model cases both in terms of the trends in the first 15,000 years and the final porosities. The assumption that material properties remain unchanged in the first 10,000 years (Large9) has a particularly notable influence on the results, with extensive precipitation of ettringite leading to blocking of the pores. The results for the current state of 1BMA were not particularly sensitive to the thermodynamic database applied but, for the repair scenario, the two databases resulted in significant porosity differences throughout most of the time period considered. However, with the exception of case Large9, there is an earlier increase in porosity at DE than AE in all cases considered, and all results reach a plateau in porosity. This result may be indicative of the impact of small fractures on the leaching and degradation of concrete barriers, even post repair.

The effective diffusivity at point AE was calculated over time, assuming that the exponent in Equation 8-11 has a value of 3 or 5 (Figure 8-21 and Figure 8-22, respectively). The results show that the exponent applied has a significant influence on the magnitude of the results. Thus both figures show the same trends as Figure 8-19, but with a greater relative spread in the data, particularly when the higher exponent was applied. The effective diffusivities calculated using an exponent of 5 were an order of magnitude higher than from with an exponent of 3.This was also apparent in the evolution of the effective diffusivity at point DE, which reflected the porosity data (Figure 8-23 and Figure 8-24) but with increased divergence that depended on the exponent used.

The results for 1BMA, both in its current state and after repair, are a reminder that the data are highly dependent on the modelling assumptions and thermodynamic databases used. However, all cases show that the increase in porosity of the barrier is effectively complete after the first 10,000–15,000 years, and that this results in a significant increase in the effective diffusivity. According to this analysis, the assumption that the material properties remain unchanged from 100–10,000 years (case Large9) is not valid.

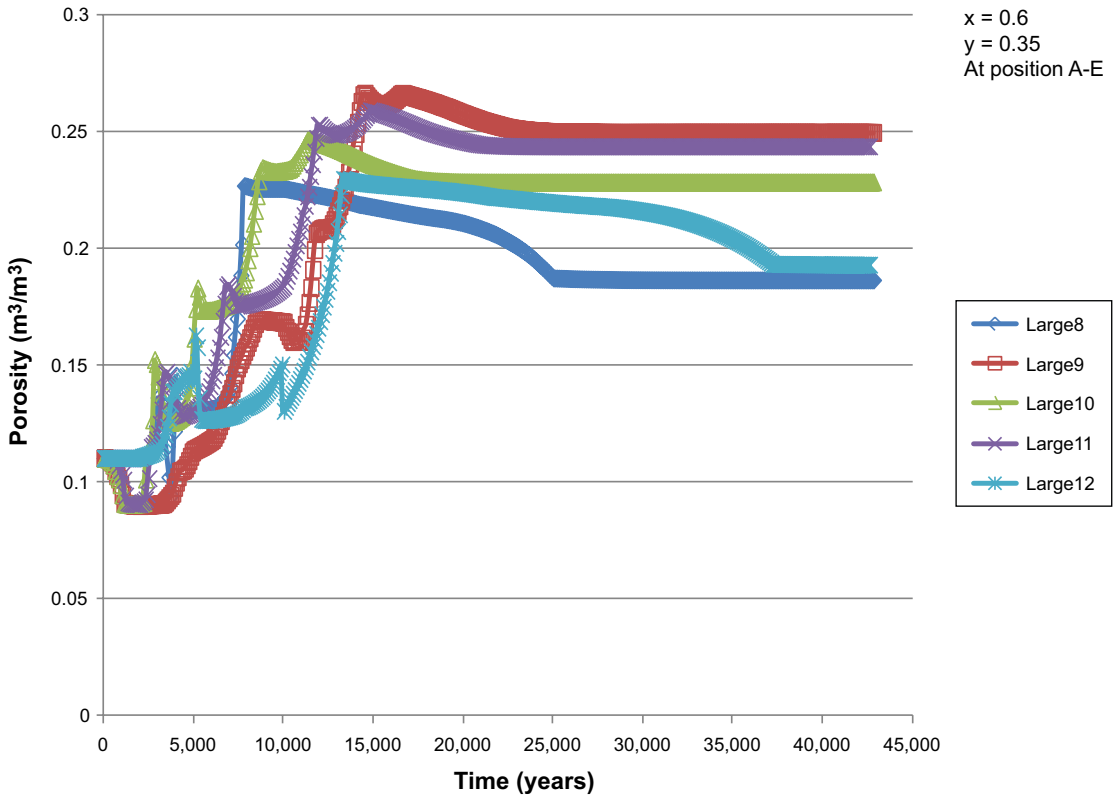

Figure 8-19. *Calculated changes in the porosity (Equation 6-61) at location AE (at the intersection of the centreline through the floor and the left-hand side concrete wall) for different cases.*

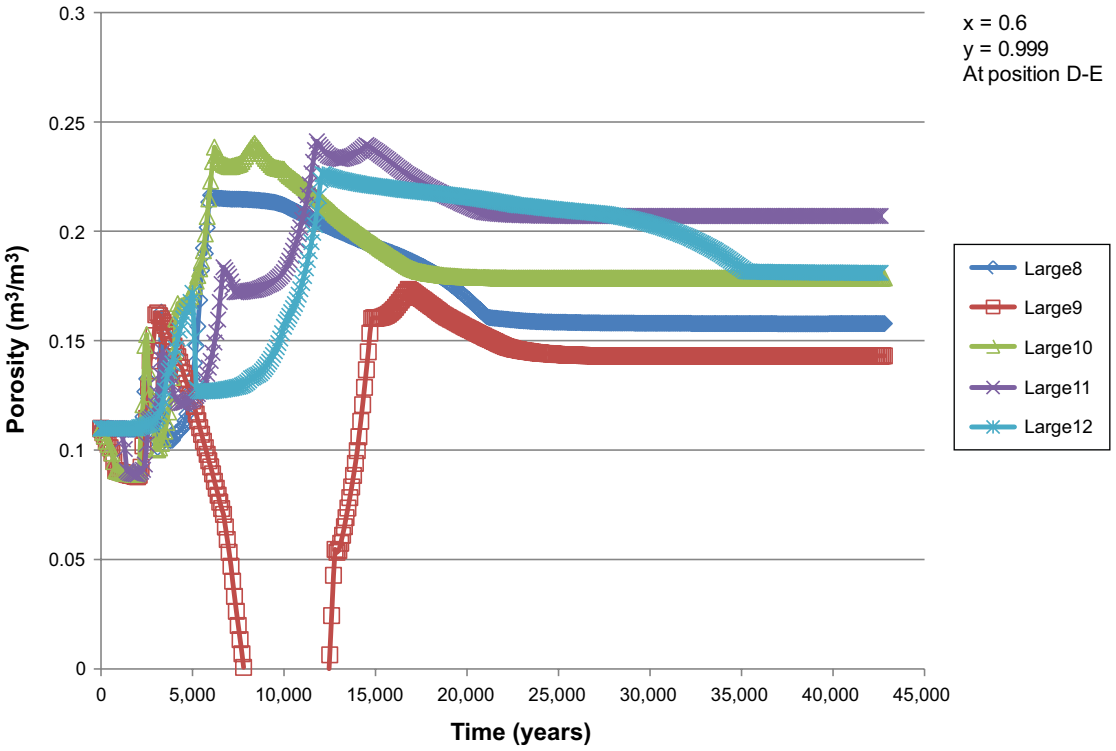

Figure 8-20. *Calculated changes in the porosity (Equation 6-61) at location DE (near the thin fracture at the centreline through the left-hand side concrete wall) for different cases.*

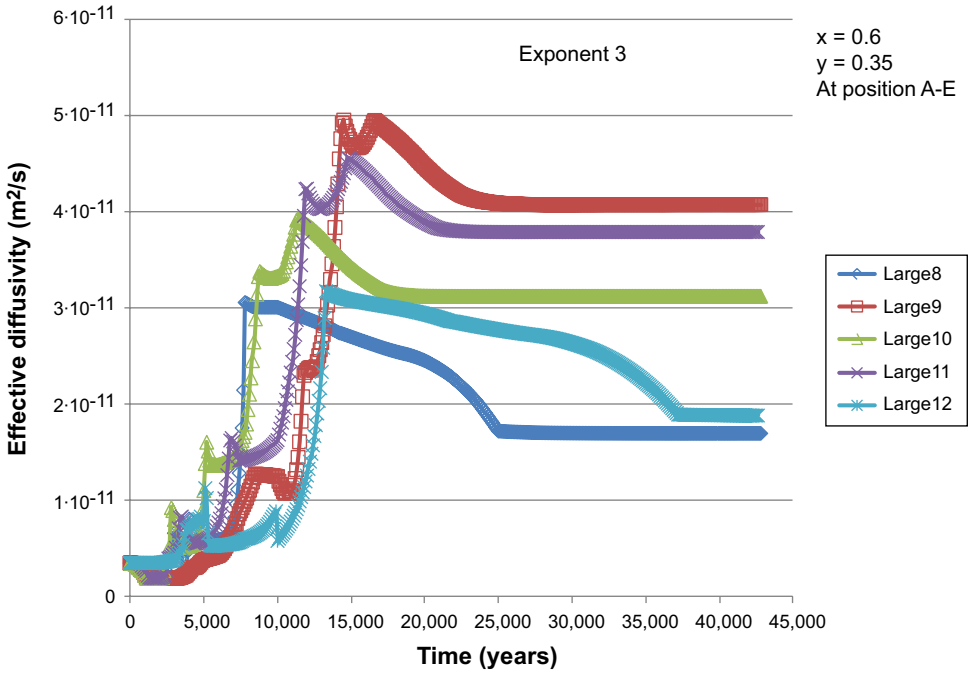

Figure 8-21. *Calculated evolution of the effective diffusivity in response to changes in the porosity at location AE (at the intersection of the centreline through the floor and the left-hand side concrete wall) for different cases. Cf. Equation 8-10 and 8-11. Assumed exponent = 3.*

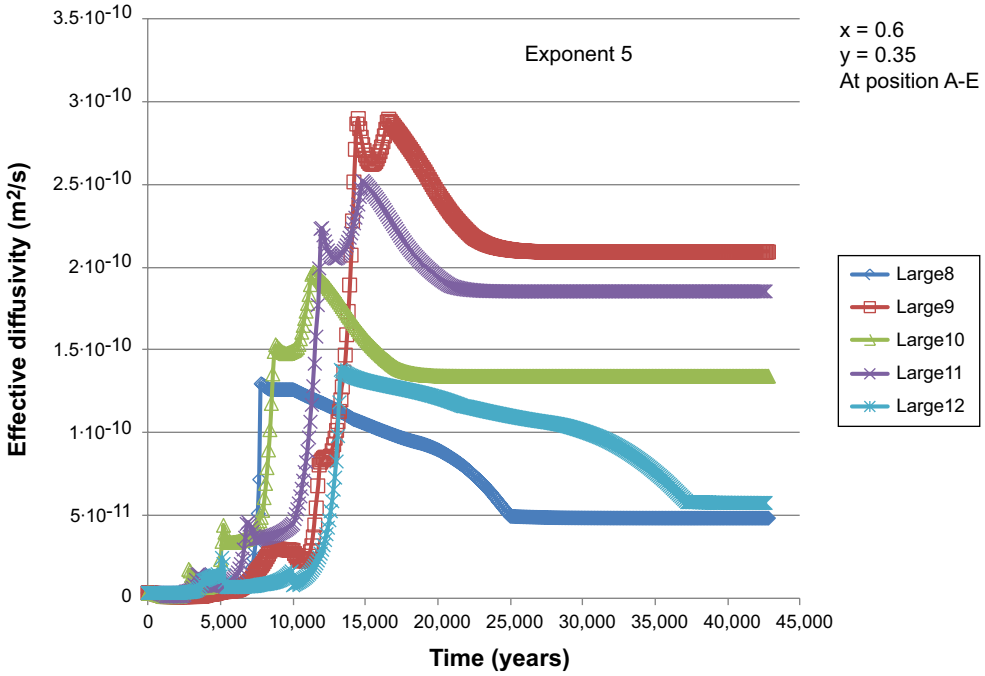

Figure 8-22. *Calculated evolution of the effective diffusivity in response to changes in the porosity at location AE (at the intersection of the centreline through the floor and the left-hand side concrete wall) for different cases. Cf. Equation 8-10 and 8-11. Assumed exponent = 5.*

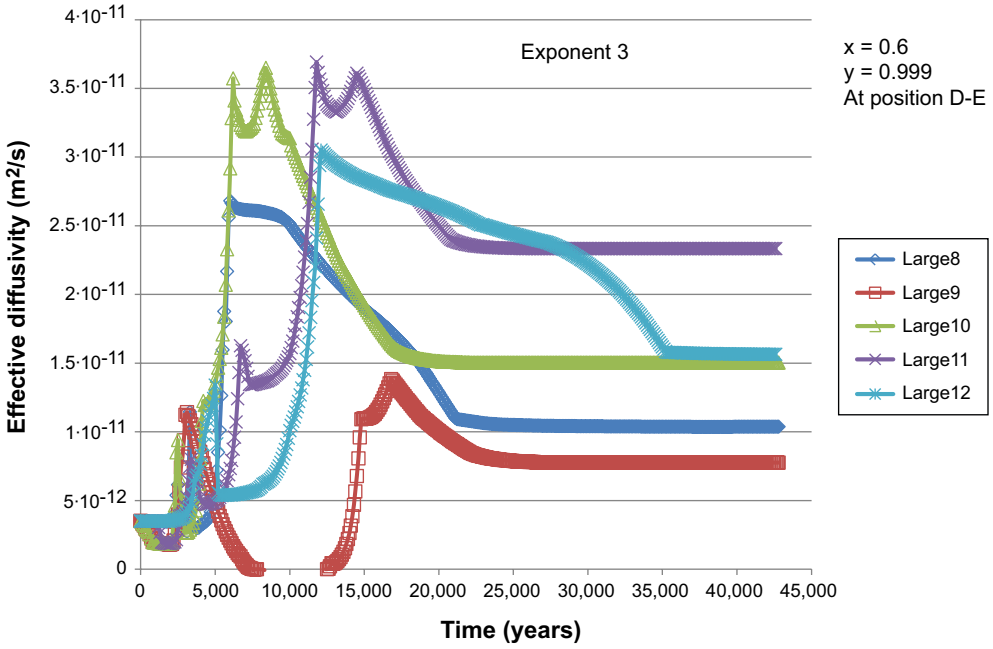

Figure 8-23. *Calculated evolution of the effective diffusivity in response to changes in the porosity at location DE (near the thin fracture at the centreline through the left-hand side concrete wall) for different cases. Cf. Equation 8-10 and 8-11. Assumed exponent = 3.*

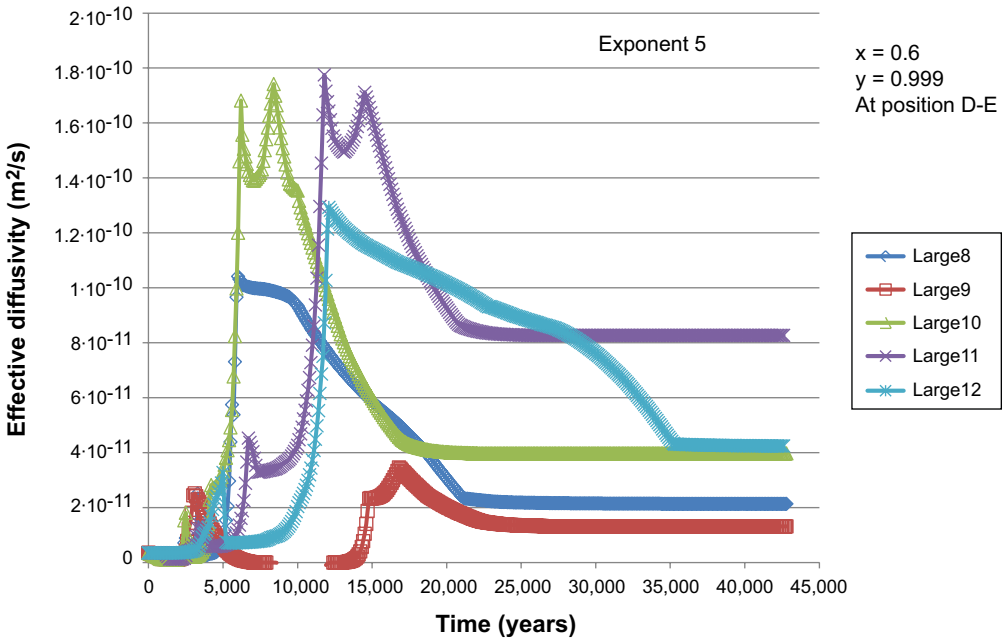

Figure 8-24. *Calculated evolution of the effective diffusivity in response to changes in the porosity at location DE (near the thin fracture at the centreline through the left-hand side concrete wall) for different cases. Cf. Equation 8-10 and 8-11. Assumed exponent = 5.*

9 Conclusions and selection of data for the Safety Assessment PSU

The purpose of this chapter is to summarise and compare the results of the models presented in Chapters 4–8, identify the main uncertainties, select data for use in the Safety Assessment PSU, and justify the values selected. A succession of models was applied to investigate the influence of chemical leaching and of fractures and fracturing on the performance of concrete barriers. Each model contributed to the understanding of physical or chemical degradation processes in the barrier, or the impact of the disturbance on barrier performance. The work was commissioned in response to questions raised by Strålsäkerhetsmyndigheten (SSM) and as a result of the fractures observed in the 1BMA barriers. Although the data ultimately suggested for the 1BMA barriers in SR-PSU assume that they will be repaired to a state where their barrier function is equivalent to the planned 2BMA barriers, understanding the impact of fractures is very relevant for responding to SSM, improving the design of new barriers and, in the future, for evaluating the 1BMA repair strategy.

9.1 Physical degradation processes

9.1.1 Degradation in the operational period

In Chapter 4, a comprehensive overview was given of processes known to result in fracturing, and the most relevant of these have been evaluated in this report. The theoretical analysis showed that drying shrinkage and temperature movements during early hydration in the construction phase, and steel corrosion are major factors behind the formation of fully penetrating fractures (Section 4.2.2). This illustrates an important challenge associated with constructing good quality concrete: adequate reinforcement reduces the total fracturing due to drying shrinkage and temperature changes, and results in a more even distribution of fractures, but also causes fracturing as the steel corrodes. In the case of 1BMA, the amount of reinforcement does not meet modern standards for construction concrete and so the extensive, fully penetrating fractures observed (SKBdoc 1430853) are likely to reflect the occurrence of drying shrinkage. However, deterioration due to steel corrosion has also been observed in 1BMA; layers of concrete have spalled near the reinforcement bars in areas where the concrete has been exposed to salty groundwater dripping from the roof of the vault.

The fractures arising from steel corrosion in 1BMA are expected to be significant in both number, due to amount of reinforcement and form ties present in 1BMA, and width. Therefore both the observations and the theory support the idea that steel corrosion in concrete will lead to significant deterioration of the barrier. SFR contains other steel components embedded in concrete, such as grouted waste drums and steel in concrete-conditioned waste, which is outside the scope of this report. The corrosion of these may also affect the performance of SFR and may need to be considered in future studies. Section 4.2.2 suggested that the drying and shrinkage of BMA concrete barriers during the operational phase of SFR would cause the formation of thin fractures (tens of μm wide), and post-closure temperature variations due to inflow of cold groundwater could enhance this fracturing further. Although these fractures are not as large as those induced by shrinkage and temperature movements during the construction phase, or by steel corrosion, their impact on the hydraulic conductivity and effective diffusivity of the concrete were shown to reduce the barrier function significantly. Fracture width was found to be more important than the frequency in terms of degraded barrier characteristics.

9.1.2 Post closure corrosion-induced concrete degradation

Once 1BMA has resaturated, the corrosion processes may initially be very slow due to alkaline passivation of the non-corroded steel surfaces. However, depassivation may be induced over time by chloride intrusion, carbonation, and loss of alkaline buffering due to leaching (cf. analytical calculations in Sections 4.2.2 and 5.2, and numerical results of the reactive transport modelling in Section 7.6.2 (without Friedel's salt) and Section 7.5.2 (including Friedel's salt). The simplest

approach considered non-reactive Cl^- ingression (4.2.2), and estimated that the threshold Cl^- concentration that would initiate more rapid steel corrosion would be reached at depth (0.4 m) in the concrete after 100–200 years. Including the chemical reactions of Cl^-, SO_4^{2+} and CO_3^{2-} as additive processes in a simplified analytical shrinking-core expression (5.2), slowed the calculated intrusion of Cl^-, so that it took more than 200 years to penetrate to a depth of 0.4 m. Although the formation of Friedel's salt significantly delays the intrusion of Cl^- in the concrete walls, it does not prevent chloride from eventually exceeding the threshold concentration (that has been estimated in the range of 0.023–0.04 M Cl^-) (cf. Section 4.2.2 Criterion 1). The reactive transport approach for 1BMA also showed the effect of delayed Cl^- transport due to Friedel's salt formation. Chloride concentrations approached their maximum at depth in the inflow wall after 500 years when Friedel's salt was not included (Large8, Section 7.6 and Appendix C), and ~ 1,300 years when Friedel's salt was considered (Large10, Section 7.5 and Appendix D). The 2BMA barrier (Large 20: Section 7.4) represents good quality concrete, and the results indicated that the intrusion of Cl^- and precipitation of Friedel's salt will peak between 500–1,000 years. Therefore, although inclusion of the simplified chemical reactions (5.2) gives a better estimate than excluding these reactions (4.2.2), it still gives a somewhat conservative estimate of Cl^- intrusion into good quality concrete. Corrosion is therefore expected to initiate at gradually increasing depths in the concrete barriers over time, likely within one hundred to several hundred years in the most protected positions in the centre of the concrete walls.

Once corrosion has been initiated, the accumulation of corrosion products (rust), which have larger volume than the non-corroded steel, will lead to a build up of mechanical pressure resulting in a tensile stress in the surrounding concrete. Following this, even low corrosion rates of the order 0.05 μm/year were calculated to cause fractures in the concrete after a few decades.

The concrete covering reinforcement bars close to the concrete surface will develop longitudinal fractures alongside the steel bars. Fractures may start at the interface between the rust layer and the concrete, gradually propagating outwards to the concrete surface. Also, corrosion will continue, gradually forming an increasing layer of rust that will force the initial fracture to gradually become wider.

The character of these fractures will depend on the spacing of the reinforcement bars (Chapter 6). When there are large distances between the steel bars, the concrete cover may crack with a single fracture along each steel bar, or by forming a wedge-formed double-fracture that may lead to spalling of pieces of concrete along the steel bar. However, fractures may also extend parallel to the concrete surface and, if the reinforcement is dense, these fractures may form a continuous network leading to spalling of the surface concrete layer. The result of this type of process is that the thickness of the intact concrete decreases and the reinforcement bars become fully exposed to the groundwater. Following the depassivation of the steel, corrosion will result in expansion of the rust layer causing a tensile stress that is high enough to fracture the concrete within a few decades.

The corrosion of form ties will induce a tensile stress perpendicular to the direction of the ties. This means that radial or tangential fractures will form around the form ties. Depending on the rate of corrosion, the tensile stress in the concrete walls may eventually lead to the formation of fractures that penetrate the entire wall. Continued corrosion will gradually increase the width of the fractures, and the length of the cracks formed may extend to the edges of the wall. During the early fracture process, radial areas around the form ties may form where small fractures give rise to zones of increased hydraulic conductivity. The models developed to describe the effects of this phenomenon indicate an increase in the overall hydraulic conductivity of 4 orders of magnitude if 10% of the form ties cause fractures with a fracture width of $1 \cdot 10^{-4}$ m (Section 6.11). This process is estimated to occur within a few hundred years of the closure of the repository.

9.2 Effect of fractures on chemical degradation processes

Both simple analytical expressions and reactive transport modelling have been used to investigate the effect of fractures on the leaching of calcium and other important chemical components from the concrete. In this section, the results from the analytical solutions are compared with the results from the reactive transport modelling to examine the processes and the associated uncertainties, as well as evaluate the extent to which simplifications can be applied when making conservative estimates of processes.

9.2.1 Comparison of different modelling approaches for estimating the Ca leaching depth

As discussed in detail in Section 7.10.1, the models of Ca leaching from portlandite and CSH gel (5.1.1 and 5.1.2) and a shrinking core model (defined in 5.1.3, applied in 7.10.1) were in reasonable agreement with the simplified version of the reactive transport modelling of the 1BMA barrier (Case Large7). The mean leaching depth of concrete via diffusion or advection reached 0.4 m within 3,000–4,000 years (5.1.1/5.1.2), the shrinking-core model predicted a complete leaching of the inflow wall after ~ 2,700 years, and PHAST calculated that this would take 3,000 years. Case Large8, which includes the full chemistry using the same database as Large7 (Cemdata-07) showed complete portlandite depletion in the inflow wall between 3,000 and 5,000 years. Therefore, the simplified versions gave reasonable, although conservative, estimates. The relatively close resemblance of the results of the simplified case (Large7) and the case considering the more complex chemical situation (Large8) is reasonable taking into account that the portlandite is more soluble than the other solid compounds in the concrete. This means that portlandite will be the major buffering component in the concrete when groundwater flows through the vaults. Since the solubility of the portlandite is significantly higher than other components, e.g. the CSH-gel, these will remain fairly passive as long as portlandite is present. This means that in both the simplified case and the more complex cases the portlandite will be the main component that dissolves from the concrete. Therefore, the difference in the portlandite leaching time would be expected to be small.

9.2.2 Comparison of the different reactive transport modelling cases

The leaching of Ca and the formation of the expansive minerals ettringite (included in both MinteqCem-2001 and Cemdata-07) and thaumasite (in Cemdata-07) are good indicators of concrete degradation processes, thus this section focuses on these processes in the inflow wall to compare the rate of concrete degradation for the cases presented in Chapter 7.

The reactive transport modelling showed that fractures (Large 10 (1BMA – current state) vs. Large 20 (2BMA)) have a very significant effect on the rate at which the barriers are leached. Using the MinteqCem-2001 database, calcium leaching is represented by the dissolution of portlandite and successive formation of CSH_1.8, CSH_1.1 and CSH_0.8. In Large20, CSH_0.8 appeared and portlandite and CSH_1.8 disappeared completely from the inflow wall after 37,000 years. However, the first CSH_0.8 appeared at the inflow wall after just 3,000 years, and the portlandite and CSH_1.8 were completely leached from this wall by 6,700 years.

The repair scenario for 1BMA using the MinteqCem-2001 database (Large11; for comparison with Large10 and Large20), showed that the addition of intact, 0.2 m thick concrete walls that contain no reinforcement or form ties only slightly improved the performance of the fractured barrier. It should be stressed that fairly pessimistic assumptions were made in the repair scenario for the gradual deterioration of the hydraulic conductivity and the effective diffusivity over time. In this case, portlandite and CSH_1.8 were predicted to be completely leached from the inflow wall (0.2 + 0.4 m thick) after ~ 7,000 years and CSH_0.8 appeared after 5,000 years.

In terms of expansive mineral formation, ettringite precipitated much earlier in the fractured 1BMA barrier (Large10) than the 2BMA barrier (Large20), at significantly higher amounts, and the maximum amounts were present throughout a greater part of the inflow wall. Maximum ettringite was predicted after ~ 30,000 years in Large20, and 3,000–5,000 years in Large10. Therefore, the presence of the initial fractures causes much earlier and tentatively more damaging formation of ettringite. The repair scenario (Large11) changed the profile of the moving front of precipitating/dissolving ettringite, but did not reduce the maximum concentrations of ettringite or its spatial abundance significantly. The data therefore suggest that both leaching of Ca and formation of ettringite are more rapid and pronounced in the fractured barriers, even after the addition of the repair wall. A conclusion from this is that a high quality of the concrete barriers would significantly extend the barrier performance in time.

Two different databases were applied to model the fractured 1BMA barrier (Large8 and 10) and the repair scenario (Large11 and 12). With Cemdata-07 (Large8), portlandite and CSHjen were completely leached from the fractured 1BMA inflow wall by ~ 5,000 years and CSHtob2 appeared after 3,000 years. This is broadly consistent with the leaching patterns seen in Large10, which used

MinteqCem-2001. The ettringite front also peaked between 3,000–5,000 years using both databases, although it was also seen to be accompanied by precipitation/dissolution fronts of the sulphate-containing silicate mineral thaumasite, contained in the Cemdata-07 database.

The repair scenario using Cemdata-07 (Large12) suggested that portlandite and CSHjen would be completely leached in the inflow wall after ~ 6,700 years, and CSHtob2 would first appear after 3,000 years. This is therefore also in reasonable agreement with the MinteqCem-2001 data (Large11). Thaumasite was predicted to precipitate at significantly higher amounts than ettringite in this case, and this occurred between 3,000–6,700 years. Therefore, the repair scenario favours the precipitation of thaumasite, compared to the fractured 1BMA barrier. However, since both thaumasite and ettringite are potentially deleterious minerals, the barrier performance is likely deteriorated in both cases. Despite the reasonable agreement between these aspects of the concrete degradation, the overall mineralogical changes over time and their impact on the porosity and effective diffusivity of 1BMA were found to be sensitive to the database applied (Section 8.3).

Assuming the material properties remain unchanged between 100–10,000 years was found to affect the results significantly (Large9), with a long delay in the predicted degradation processes. In this case, portlandite and CSH 1.8 were completely removed from the inflow wall after 10,000 years, and the ettringite front moved across this wall between 5,000–13,000 years. The inclusion of only portlandite and pure water in the model (Large7) clearly reduces the information that the model supplies. However, portlandite was calculated to leach completely from the inflow wall within 3,500 years and, as discussed above, this is in good agreement with simpler models (5.1.1, 5.1.2, 7.10.1) and case Large8, which applied the full chemistry using the same database.

As for the data from Chapter 7, the data from Chapter 8 for the 1BMA (Section 8.3) allow the repair strategy to be evaluated and the sensitivity of the results to the database and certain simplifications in the reactive transport modelling to be assessed. As discussed in Section 8.3, the database and assumptions applied affect the porosity and effective diffusivity calculated. This was not apparent in the broad comparison of Ca leaching and the formation of expansive minerals above, but reflects the overall changes in the mineralogy presented in Chapter 7. Despite these differences, all cases showed that the increase in porosity of the barrier is effectively complete after the first 10,000–15,000 years, and that this results in a significant increase in the effective diffusivity.

9.3 Overall conclusions

The results of the different analyses demonstrate the importance of minimising fracture formation in the concrete barriers during the operational and early post-closure phases. The most effective way of reducing fracture formation by design has been shown to be by careful control of the initial hydration process during the construction to minimise shrinkage and temperature movements, and when possible avoiding metal reinforcement and injection holes in the concrete barriers. If this is accomplished, the main cause of early fractures will be the concrete drying in the operational phase and cooling during the resaturation, and these are expected to be relatively thin/of low frequency. This approach has therefore been adopted for the planned 2BMA. Constructing large concrete structures without reinforcement or form ties introduces challenges of its own, but the modelling results suggest that it will slow down concrete degradation processes by a factor of ~10. It can also be suggested that using a concrete of lower porosity, e.g. but using an optimised lower W/C ratio, and possibly filler admixtures in the concrete, could also improve performance.

The proposed design of the 2BMA concrete barriers suggests that, provided that great care is taken during construction to avoid the early formation of fractures, significantly better properties in the long term can be expected than the 1BMA concrete barriers. The major factor for this is the absence of reinforcement bars and form ties, which means that corrosion processes will not induce fracture formation. High demands will be put on the construction and quality control during both the construction phase and operational phase to be able to achieve the desired barrier properties at the time of closure. In line with this, the barriers may be assigned improved long-term properties with reasonable confidence. Corrosion of other steel components in the vault, such as waste steel drums and steel components in the waste may need separate consideration. The results of the simulations tentatively suggest that the thin fractures assumed to exist in the concrete may have limited impact

on the chemical degradation of the concrete barriers. Larger fractures, which may occur during the operational phase due to drying, are assumed to have been observed and repaired prior to closure. The analysis shows that the width of fractures is more critical than the frequency, and it is easier to repair wide fractures.

The situation for 1BMA is less clear. Section 6.15 suggested that the observed fracturing in the current, unrepaired BMA barrier (SKBdoc 1430853) increases the initial hydraulic conductivity of the concrete barriers from $1 \cdot 10^{-11}$ m/s, assumed for intact concrete, to between $2.6 \cdot 10^{-4}$–$5.3 \cdot 10^{-4}$ m/s. The reactive transport model of the fractured 1BMA barrier used parameters related to a lesser degree of fracturing (initial hydraulic conductivity of $8.3 \cdot 10^{-10}$ m/s) and even this was seen to drastically reduce the lifetime of the barrier in the reactive transport modelling. Moreover, the repair measure modelled in this report (Large11 and Large12), of constructing an additional wall around the fractured barrier, was found to be largely ineffective (based on fairly pessimistic assumptions regarding the transport properties). This demonstrates that the advanced repair plan (SKBdoc 1358612) will need to be modelled and critically evaluated before the repaired barrier can be considered to have the characteristics assigned in Section 9.4, and function as well as the proposed metal- and injection hole-free 2BMA barrier.

The poor performance of the reinforced concrete structures also raises questions about the effect of metal corrosion and fractures in the monolithic concrete structures created by grouting the empty space between the waste packages and the barriers. When corrosion of e.g. a steel drum creates a growing layer of rust, the mechanical pressure exerted by the rust will cause a tensile stress that may propagate via the concrete grout to the concrete barriers. So, corrosion of steel in the waste and waste packages may affect the integrity of the concrete barriers.

It is clear that the uncertainties are large at a conceptual level, in the model applications, and in the interpretation of the model results. This calls for careful selection of the set of parameters that will be used as a basis for the safety assessments.

9.4 Proposed data for the Data report – BMA vaults

The investigation of the 1BMA concrete structure showed that extensive repair and reinforcement measures need to be adopted to achieve the desired barrier properties at closure. The Closure Plan for SFR (SKBdoc 1358612) describes the planned measures for closure of 1BMA. Although these have not been evaluated in detail here, it is assumed for the proposed data for the Data report for the PSU safety assessment that the 1BMA concrete barriers will be in good condition at closure.

A modified barrier system has been designed for the new 2BMA vault to minimise the groundwater flow through the waste and to overcome the issues associated with the corrosion of reinforcement. The concrete barriers consist of 14 detached caissons of non-reinforced concrete.

For the BMA vaults, data have been selected based on the new design of the 2BMA concrete caissons. As in previous assessment (SAR-08), the hydraulic conductivity of intact concrete has been assumed to $1 \cdot 10^{-11}$ m/s, further it was assumed to contain 1 fracture per metre with an aperture of 10 µm. This equals an overall hydraulic conductivity of the intact but slightly fractured concrete of $8.3 \cdot 10^{-10}$ m/s. This is suggested as an initial value for the concrete barriers of the BMA vaults for the SR-PSU safety assessment.

The grout is not considered to be a barrier that restricts the flow of groundwater through the vault and should therefore have a hydraulic conductivity that is larger than the construction concrete. However, if a too high value is assumed this could have the effect to divert the flow around the waste packages. Therefore it is expected to be pessimistic to assume a value for the hydraulic conductivity that is slightly higher than in the construction concrete. Hence, for the safety assessment an initial hydraulic conductivity of $8.3 \cdot 10^{-9}$ m/s is suggested for the grout. Over time, a hydraulic conductivity 10 times higher than for the construction concrete is suggested.

As discussed in previous sections, the selection of representative data for different concrete barriers in varying stages of degradation is not an easy task. The strategy used here is to define different stages in the degradation and deduct reasonable parameter values for each of these stages. Due

to the difficulties in defining the evolution of degradation over time, due to the complex interplay between the physical and chemical processes involved, the uncertainties associated with the temporal change of the material properties are significant. The time-scales are therefore only indicative of the different degradation stages represented by the proposed material data (i.e. porosities, hydraulic conductivities and effective diffusivities).

The proposed data for the change in the hydraulic conductivity during the first 10,000 years is primarily based on consideration of the physical degradation processes that appear to be difficult to avoid, such as drying shrinkage and temperature changes. Further uncertaincies not accounted for concern the impact of corrosion of reinforcement bars and other steel components if present in the concrete (not planned for the concrete caissons in the 2BMA vault) and in the waste and waste packaging. The physical processes are likely to occur at a fairly early time, although it is difficult to assess with precision when the fractures will occur. The proposed change in the hydraulic conductivity of the construction concrete in 2BMA is shown in Figure 9-1 where the calculated progression of the hydraulic conductivity in response to porosity changes (modified Kozeny-Carman expression) is shown for comparison. Clearly, the effect on the hydraulic conductivity of porosity changes due to the chemical degradation will become prominent only after ~ 10,000 years. Hence, the proposed values have been based on expected physical degradation processes during the first ~ 10,000 years, thereafter the increase of the hydraulic conductivity has been assumed to gradually approach the hydraulic conductivity calculated by the modified Kozeny-Carman expression. Since the porosity changes are limited during the first ~ 10,000 years, the expected changes of the hydraulic conductivity due to the chemical degradation are small. Hence, the possible short-comings of the PHAST model to account for the porosity changes in a fully coupled fashion is by far overshadowed by the impact by the physical processes leading to fracture formation. This can be viewed in Figure 9-1 as the difference between the calculated effect of porosity changes (red line) and the assumed input data used to model the chemical degradation where the expected impact of physical fracturing processes is accounted for (orange line). It is therefore judged unlikely that the assessment of the evolution of the hydraulic properties would significantly change by implementation of the impact of porosity changes in a coupled fashion in the model.

The changes in the effective diffusivities are expected to be both slower and smaller, and to a higher degree governed by the chemical degradation processes that lead to porosity changes. The proposed values for the effective diffusivities for the construction concrete are presented in Figure 9-2 where the calculated change of the effective diffusivity in response to porosity changes (power-law expressions based on modified Archie's law assuming three different exponents) is shown for comparison. The figure also shows the assumed effective diffusivities used in the modelling of chemical degradation.

The effective diffusivity data for the concrete grout would be expected to be high due to the high porosity. For the effective diffusivity it is pessimistic to assume a high value since this will constitute a low resistance to diffusive transport of dissolved components inside the concrete constructions. Hence, for the safety assessment an initial effective diffusivity of $3.5 \cdot 10^{-10}$ m^2/s is suggested for the grout. Since this initial value is high, only a slow increase over time has been suggested for the effective diffusivity of the concrete grout.

The assumptions adopted in the modelling studies in this report are not dissimilar from the values proposed for the safety assessment. To some extent, this reflects the fact that they were used in the models in the first place. However, physical/mechanical concrete fracturing processes have been assessed for the first time here, and are shown to have very significant consequences for barrier function. Calculations have been made assuming a higher quality of the new 2BMA barriers design, which does not include steel reinforcement or form rods. These new barriers were designed in response to the results of inspections of the 1BMA barrier status and the initial results of this study. For the safety assessment, the values for 1BMA are based on the assurance that it will be repaired to the same functional level as 2BMA.

The different stages of degradation for the BMA concrete barriers are described in Table 9-1 together with the proposed parameter values.

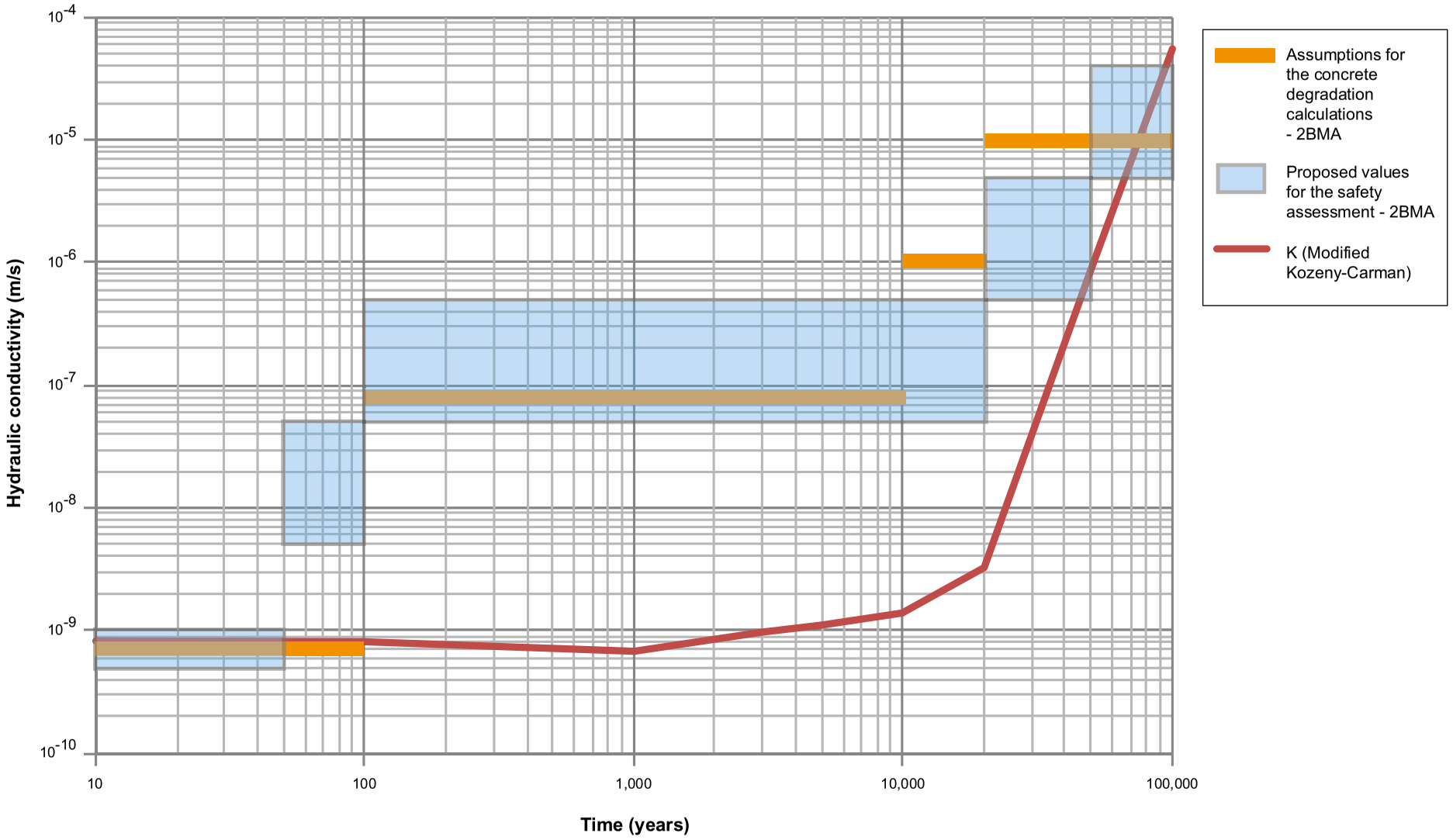

Figure 9-1. *Proposed range of values for the hydraulic conductivity (blue shading) in construction concrete in 2BMA. The hydraulic conductivities calculated based on the modified Kozeny-Carman model (cf. Equation 8-20) using porosity changes extracted from the PHAST modelling (cf. Equation 6-61) is show as comparison (red line). The initial estimates of the gradual change of the hydraulic conductivity assumed in the PHAST modelling are also show in the figure (orange lines).*

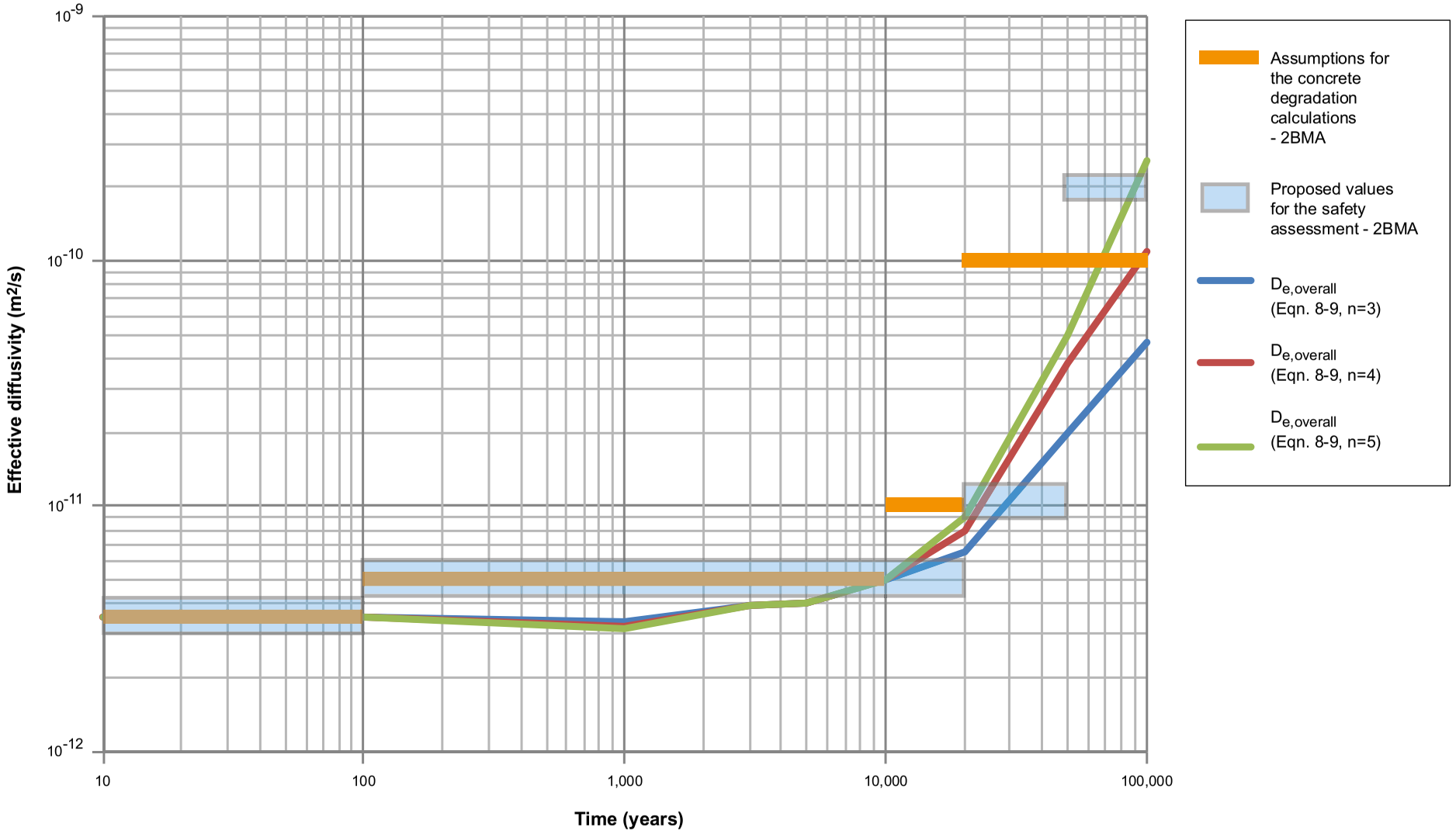

Figure 9-2. *Proposed values for the effective diffusivity (light blue shading) in construction concrete in 2BMA. The effective diffusivities calculated based on three different power law models (blue, red and green lines) (cf. Equations 8-10 and 8-11) using porosity changes extracted from the PHAST modelling (cf. Equation 6-61) is show as comparison. The initial estimates of the gradual change of the effective diffusivities assumed in the PHAST modelling are also show in the figure (orange lines).*

Table 9-1. Description of different stages of concrete degradation in the BMA vaults and proposed values of the hydraulic conductivity, effective diffusivity and porosity. The time scale is indicative.

Condition of concrete barriers in BMA	General description	pH	Hydraulic conductivity (m/s)	Effective diffusivity [1] (m^2/s)	Porosity [1] (m^3/m^3)	Indicative time scale [2]
Initial state	Fresh, fully hydrated concrete, essentially unaffected by degradation processes. Some carbonation during operational phase. No significant leaching by groundwater. No significant impact by components in groundwater or waste. Drying shrinkage may have caused or dilated fractures, but any major fractures can be observed and be repaired before closure.	12.5–13 determined by alkali hydroxides	$8.3 \cdot 10^{-10}$ (construction) $8.3 \cdot 10^{-10}$ (moulds) $8.3 \cdot 10^{-9}$ (grout)	$3.5 \cdot 10^{-12}$ (c) $3.5 \cdot 10^{-12}$ (m) $3.5 \cdot 10^{-10}$ (g)	0.11 (c) 0.1 (m) 0.3 (g)	0 years
Change of temperature due to groundwater inflow	Contraction of the concrete barriers due to decreased temperature, but saturation with water may partly counteract this process. No significant leaching of any major components at this stage. No significant interaction with components in groundwater or waste.	12.5–13 determined by alkali hydroxides	$5 \cdot 10^{-9}$–$5 \cdot 10^{-8}$ (construction) $5 \cdot 10^{-9}$–$5 \cdot 10^{-8}$ (moulds) $5 \cdot 10^{-8}$–$5 \cdot 10^{-7}$ (grout)	$3.5 \cdot 10^{-12}$ (c) $3.5 \cdot 10^{-12}$ (m) $3.5 \cdot 10^{-10}$ (g)	0.11 (c) 0.1 (m) 0.3 (g)	Before 100 years
Leaching of portlandite	Leaching of portlandite has progressed at the up-stream side of the vault. The porosity has increased accordingly. However, the ingrowth of Friedel's salt and its interaction with monocarboaluminate may counteract porosity changes, but it remains uncertain if this has other effects that may be negative for the concrete properties.	12.5 determined by portlandite	$5 \cdot 10^{-8}$–$5 \cdot 10^{-7}$ (construction) $5 \cdot 10^{-8}$–$5 \cdot 10^{-7}$ (moulds) $5 \cdot 10^{-7}$–$5 \cdot 10^{-6}$ (grout)	$5 \cdot 10^{-12}$ (c) $2 \cdot 10^{-11}$–$5 \cdot 10^{-11}$ (m) $4 \cdot 10^{-10}$ (g)	0.11–0.16 (c) 0.11–0.16 (m) 0.4 (g)	100–10,000 / 20,000 years
Leaching of CSH-gels, ingrowth of ettringite and thaumasite	Portlandite has been depleted. A gradual transformation of the concrete from calcium-rich to calcium-depleted minerals proceeds. The ingrowth of ettringite and thaumasite may potentially cause fractures and may degrade the mechanical strength.	12.5–10.8 determined by CSH-gels of varying composition	$5 \cdot 10^{-7}$–$5 \cdot 10^{-6}$ (construction) $5 \cdot 10^{-7}$–$5 \cdot 10^{-6}$ (moulds) $5 \cdot 10^{-6}$–$5 \cdot 10^{-5}$ (grout)	$1 \cdot 10^{-11}$ (c) $1 \cdot 10^{-10}$ (m) $5 \cdot 10^{-10}$ (g)	0.16–0.2 (c) 0.16–0.2 (m) 0.5 (g)	20,000–50,000 years
Severely leached and altered concrete	The concrete is essentially depleted of its cement hydrates. Different reaction fronts have passed through the structure, including ettringite, thaumasite, monocarboaluminate and brucite. Significant precipitation of calcite. The ballast material is assumed to remain largely intact after leaching of the cement phases.	11.5–10.3	$5 \cdot 10^{-6}$–$5 \cdot 10^{-5}$ (construction) $5 \cdot 10^{-6}$–$5 \cdot 10^{-5}$ (moulds) $5 \cdot 10^{-5}$–$5 \cdot 10^{-4}$ (grout)	$2 \cdot 10^{-10}$ (c) $5 \cdot 10^{-10}$ (m) $1 \cdot 10^{-9}$ (g)	0.3 (c) 0.3 (m) 0.5 (g)	50,000–100,000 years

[1] (c) = construction concrete , (m) = concrete moulds, (g) = concrete grout

[2] The time scale is deliberately fairly coarse in order to fit the needs of the safety assessment. The suggested data supply a basis for further judgment and simplification by the SKB PSU safety assessment team.

References

SKB's (Svensk Kärnbränslehantering AB) publications can be found at www.skb.se/publications. References to SKB's unpublished documents are listed separately at the end of the reference list. Unpublished documents will be submitted upon request to document@skb.se.

Abarca E, Idiart A, de Vries L M, Silva O, Molinero J, von Schenck H, 2013. Flow modelling on the repository scale for the safety assessment SR-PSU. SKB TR-13-08, Svensk Kärnbränslehantering AB.

Abramowitz M, Stegun I A (eds), 1972. Handbook of mathematical functions: with formulas, graphs, and mathematical tables. New York: Dover.

Allard B, Dario M, Borén H, Torstenfelt B, Puigdomenech I, Johansson C, 2002. Karboxylatjonbytarmassans egenskaper. SKB R-02-40, Svensk Kärnbränslehantering AB. (In Swedish.)

Allen A J, Thomas J J, Jennings H M, 2007. Composition and density of nanoscale calcium-silicate-hydrate in cement. Nature Materials 6, 311–316.

Allison J D, Brown D S, Novo-Gradac K J, 1991. MINTEQA2/PRODEFA2, a geochemical assessment model for environmental systems. EPA/600/3-91/021, U.S. Environmental Protection Agency.

Álvarez J I, Navarro I, Martín A, García Casado P J, 2000. A study of the ancient mortars in the north tower of Pamplona's San Cernin church. Cement and Concrete Research 30, 1413–1419.

Andrade C, Tavares F, Toro L, Fullea J, 2011. Observation on the morphology of oxide formation due to reinforcement corrosion. In Andrade C, Mancini G (eds). Modelling of corroding concrete structures: proceedings of the Joint fib-RILEM Workshop, Madrid, Spain, 22–23 November 2010. Dordrecht: Springer, 179–194.

Auqué L F, Gimeno M, Acero P, Gómez J, 2013. Compositions of groundwater for SFR and its extension, during different climatic cases, SR-PSU. SKB R-13-16, Svensk Kärnbränslehantering AB.

Ayob A B, Tamin M N, Kabashi Elbasheer M, 2009. Pressure limits of thick-walled cylinders. In Proceedings of the International MultiConference of Engineers and Computer Scientists, Hong Kong, 18–20 March 2009. Vol 2, 1649.

Balafas I, Burgoyne C J, 2010. Environmental effects on cover cracking due to corrosion. Cement and Concrete Research 40, 1429–1440.

Balonis M, 2010. The influence of inorganic chemical accelerators and corrosion inhibitors on the mineralogy of hydrated Portland cement systems. PhD thesis. Department of Chemistry, University of Aberdeen, United Kingdom.

Balonis M, Lothenbach B, Le Saout G, Glasser F P, 2010. Impact of chloride on the mineralogy of hydrated Portland cement systems. Cement and Concrete Research 40, 1009–1022.

Barbarulo R, Marchand J, Snyder K A, Prené S, 2000. Dimensional analysis of ionic transport problems in hydrated cement systems Part 1. Theoretical considerations. Cement and Concrete Research 30, 1955–1960.

Barbarulo R, Peycelon H, Leclercq S, 2007. Chemical equilibria between C-S-H and ettringite, at 20 and 85°C. Cement and Concrete Research 37, 1176–1181.

Baur I, Keller P, Mavrocordatos D, Wehrli B, Johnson A, 2004. Dissolution-precipitation behaviour of ettringite, monosulfate, and calcium silicate hydrate. Cement and Concrete Research 34, 341–348.

Bejaoui S, Bary B, 2007. Modeling the link between microstructure and effective diffusivity of cement pastes using a simplified composite model. Cement and Concrete Research 37, 469–480.

Bellmann F, 2004. On the formation of thaumasite $CaSiO_3 \cdot CaSO_4 \cdot CaCO_3 \cdot 15H_2O$: Part I. Advances in Cement Research 16, 55–60.

Benbow S, Watson C, Savage D, 2005. Investigating conceptual models for physical property couplings in solid solution models of cement. SKI Report 2005:64, Statens kärnkraftinspektion (Swedish Nuclear Power Inspectorate).

Benbow S, Walker C, Savage D, 2007. Intercomparison of cement solid-solution models. Issues affecting the geochemical evolution of repositories for radioactive waste. SKI Report 2007:29, Statens kärnkraftinspektion (Swedish Nuclear Power Inspectorate).

Benin A V, Semenov A S, Semenov S G, 2010. Modelling of fracture process in concrete reinforced structures under steel corrosion. Journal of Achievements in Materials and Manufacturing Engineering 39, 168–175.

Bentz D P, 1999. Modelling cement microstructure: pixels, particles, and property prediction. Materials and Structures 32, 187–195.

Bentz D P, 2010. Critical observations for the evaluation of cement hydration models. International Journal of Advances in Engineering Sciences and Applied Mathematics 2, 75–82.

Bentz D P, Garboczi E J, 1992. Modelling the leaching of calcium hydroxide from cement paste: effects on pore space percolation and diffusivity. Materials and Structures 25, 523–533.

Bentz D P, Garboczi E J, Haecker C J, Jensen O M, 1999. Effects of cement particle size distribution on performance properties of Portland cement-based materials. Cement and Concrete Research 29, 1663–1671.

Berner U, 1990. A thermodynamic description of the evolution of pore water chemistry and uranium speciation during the degradation of cement. Nagra Technical Report NTB 90-12, Nagra, Switzerland.

Bertills U, 1995. Grundvattnets kemi i Sverige. Rapport 4415, Naturvårdsverket. (In Swedish.)

Betongföreningen, 2007. Vägledning för livslängdsdimensionering av betongkonstruktioner. Stockholm: Svenska betongföreningen. (Betongrapport 12) (In Swedish.)

Bird R B, Stewart W E, Lightfoot E N, 1960. Transport phenomena. New York: Wiley.

Birnin-Yauri U A, Glasser F P, 1998. Friedel's salt, $Ca_2Al(OH)_6(Cl,OH)\cdot 2H_2O$: its solid solutions and their role in chloride binding, Cement and Concrete Research 28, 1713–1723.

Boverket, 2004. Boverkets handbok om betongkonstruktioner: BBK 04. 3rd ed. Karlskrona: Boverket. (In Swedish.)

Braester C, Thunvik R, 1988. Gas migration from low-level radioactive waste repositories in hard rocks. Nuclear Technology 82, 60–70.

Börjesson K S, Emrén A T, Ekberg C, 1997. A thermodynamic model for the calcium silicate hydrate gel, modelled as a non-ideal binary solid solution. Cement and Concrete Research 27, 1649–1657.

Carde C, François R, Torrenti J-M, 1996. Leaching of both calcium hydroxide and C-S-H from cement paste: modelling the mechanical behaviour. Cement and Concrete Research 26, 1257–1268.

Catinaud S, Beaudoin J J, Marchand J, 2000. Influence of limestone addition on calcium leaching mechanisms in cement-based materials. Cement and Concrete Research 30, 1961–1968.

Chen J J, Thomas J J, Taylor H F W, Jennings H M, 2004. Solubility and structure of calcium silicate hydrate. Cement and Concrete Research 34, 1499–1519.

Cooper R S, Liberman D A, 1970. Fixed-bed adsorption kinetics with pore diffusion control. Industrial & Engineering Chemistry Fundamentals 9, 620–623.

Cronstrand P, 2007. Modelling the long-time stability of the engineered barriers of SFR with respect to climate changes. SKB R-07-51, Svensk Kärnbränslehantering AB.

Cronstrand P, 2013. Evolution of pH in SFR 1. SKB R-14-01. Svensk Kärnbränslehantering AB.

Damidot D, Glasser F P, 1993. Thermodynamic investigation of the $CaO\text{-}Al_2O_3\text{-}CaSO_4\text{-}H_2O$ system at 25°C and the influence of Na_2O. Cement and Concrete Research 23, 221–238.

Damidot D, Glasser F P, 1995. Thermodynamic investigation of the $CaO-Al_2O_3-CaSO_4-CaCO_3-H_2O$ closed system at 25°C and the influence of Na_2O. Advances in Cement Research 7, 129–134.

Damidot D, Atkins M, Kindness A, Glasser F P, 1992. Sulphate attack on concrete: limits of the AF_t stability domain. Cement and Concrete Research 22, 229–234.

Damidot D, Birnin-Yauri U A, Glasser F P 1994a. Thermodynamic investigation of the $CaO-Al_2O_3-CaCl_2-H_2O$ system at 25°C and the influence of Na_2O. Cemento 91, 243.

Damidot D, Stronach S, Kindness A, Atkins M, Glasser F P, 1994b. Thermodynamic investigation of the $CaO-Al_2O_3-CaCO_3-H_2O$ closed system at 25°C and the influence of Na_2O. Cement and Concrete Research 24, 563–572.

Damidot D, Barnett S, Glasser F, Macphee D, 2004. Investigation of the $CaO-Al_2O_3-SiO_2-CaSO_4-CaCO_3-H_2O$ system at 25°C by thermodynamic calculation. Advances in Cement Research 16, 69–76.

Damidot D, Lothenbach B, Herfort D, Glasser F P, 2011. Thermodynamics and cement science. Cement and Concrete Research 41, 679–695.

Darcy H, 1856. Les fontaines publiques de la ville de Dijon. Paris: Dalmont.

de Silva P S, Glasser F P, 1993. Phase relations in the system $CaO-Al_2O_3-SiO_2-H_2O$ relevant to metakaolin – Calcium hydroxide hydration. Cement and Concrete Research 23, 627–639.

Edvardsen C, Engelund S, Mohr L, 2000. General guidelines for durability design and redesign: DuraCrete, probabilistic performance based durability design of concrete structures. Gouda: Civieltechnisch Centrum Uitvoering Research en Regelgeving.

Ekström T, 2003. Leaching of concrete: the leaching process and its effects. PhD thesis. Lund Institute of Technology, Sweden.

Faucon P, Adenot F, Jacquinot J F, Petit J C, Cabrillac R, Jorda M, 1998. Long-term behaviour of cement pastes used for nuclear waste disposal: review of physico-chemical mechanisms of water degradation. Cement and Concrete Research, 847–857.

Fick A, 1855. Über Diffusion. Annalen der Physik 170, 59–86.

Florea M V A, Brouwers H J H, 2012. Chloride binding related to hydration products: Part I: ordinary Portland cement. Cement and Concrete Research 42, 282–290.

Freeze R A, Cherry J A, 1979. Groundwater. Englewood Cliffs: Prentice Hall.

Galíndez J M, Molinero J, 2010. On the relevance of electrochemical diffusion for the modelling of degradation of cementitious materials. Cement and Concrete Composites 32, 351–359.

Gaucher E, Tournassat C, Nowak C, 2005. Modelling the geochemical evolution of the multi-barrier system of the Silo of the SFR repository. Final report. SKB R-05-80, Svensk Kärnbränslehantering AB.

Gérard B, Marchand J, 2000. Influence of cracking on the diffusion properties of cement-based materials. Part I: Influence of continuous cracks on the steady-state regime. Cement and Concrete Research 30, 37–43.

Glasser F P, 1996. The role of sulphate mineralogy and cure temperature in delayed ettringite formation. Cement and Concrete Research 18, 187–193.

Glasser F P, Matschei T, 2007. Interactions between Portland cement and carbon dioxide. In Proceedings of the 12th International Congress on the Chemistry of Cement, Montreal, Canada, 8–13 July 2007.

Glasser F P, Angus M J, McCulloch C E, Macphee D, Rahman A A, 1985. The chemical environments in cements. In Jantzen C M (ed). Scientific basis for nuclear waste management VIII: symposium held in Boston, Massachusetts, USA, 26–29 November 1984. Pittsburgh, PA: Materials Research Society. (Materials Research Society Symposium Proceedings 44), 849–858.

Glasser F P, Kindness A, Stronach S A, 1999. Stability and solubility in AF_m phases: Part I. Chloride, sulfate and hydroxide. Cement and Concrete Research 29, 861–866.

Grandia F, Galíndez J-M, Arcos D, Molinero J, 2010. Quantitative modelling of the degradation processes of cement grout. Project CEMMOD. SKB TR-10-25, Svensk Kärnbränslehantering AB.

Guerrero A, Goñi S, Allegro V R, 2009. Effect of temperature on the durability of class C fly ash belite cement in simulated radioactive liquid waste: synergy of chloride and sulphate ions. Journal of Hazardous Materials 165, 903–908.

Haga K, Shibata M, Hironaga M, Tanaka S, Nagasaki S, 2002. Silicate anion structural change in calcium silicate hydrate gel on dissolution of hydrated cement. Journal of Nuclear Science and Technology 39, 540–547.

Hakanen M, Ervanne H, 2006. The influence of organic cement additives on radionuclide mobility: a literature survey. Posiva Working Report 2006-06, Posiva Oy, Finland.

Hammond G E, Lichtner P C, Lu C, Mills R T, 2012. PFLOTRAN: Reactive flow & transport code for use on laptops to leadership-class supercomputers. Groundwater Reactive Transport Models 1, 141–159.

Heidelberg Cement, 2013. Anläggningscement Deg: CEM I 42.5 N – SR 3 MH/LA (Technical data sheet). Available at: http://www.heidelbergcement.com/NR/rdonlyres/9B336CE3-1A63-43BC-801B-6439A7D86E0E/0/AnläggningscementDEGERHAMN_Produktblad_2013_ENG_NY.pdf

Hidalgo A, Petit S, Domingo C, Alonso C, Andrade C, 2007. Microstructural characterization of leaching effects in cement pastes due to neutralisation of their alkaline nature: Part I: Portland cement pastes. Cement and Concrete Research 37, 63–70.

Holmén J G, Stigsson M, 2001. Modelling of future hydrogeological conditions at SFR. SKB R-01-02, Svensk Kärnbränslehantering AB.

Hummel W, Berner U, Curti E, Pearson F J, Thoenen T, 2002. Nagra/PSI Chemical thermodynamic data base 01/01. Nagra NTB 02-16, Nagra, Switzerland.

Höglund L O, 1992. Some notes on ettringite formation in cementitious materials; Influence of hydration and thermodynamic constraints for durability. Cement and Concrete Research 22, 217–228.

Höglund L O, 2001. Project SAFE. Modelling of long-term concrete degradation processes in the Swedish SFR repository. SKB R-01-08, Svensk Kärnbränslehantering AB.

Höglund L O, Bengtsson A, 1991. Some chemical and physical processes related to the long-term performance of the SFR repository. SKB SFR 91-06, Svensk Kärnbränslehantering AB.

Höglund L O, Karlsson F, Allard B, 1997. Geokemiska förhållanden i svensk berggrund. Rapport 4773, Naturvårdsverket.

Jacobsen S, Gjörv O, 1987. Hydraulisk konduktivitet i SFR silobetong. SKB Teknisk PM 45, Svensk Kärnbränslehantering AB.

Jacques D, 2009. Benchmarking of the cement model and detrimental chemical reactions including temperature dependent parameters. Project near surface disposal of category A waste at Dessel. NIRAS-MP5-03 DATA-LT(NF) Version 1. NIROND-TR 2008–30 E, ONDRAF/NIRAS, Belgium.

Jacques D, Wang L, Martens E, Mallants D, 2010. Modelling chemical degradation of concrete during leaching with rain and soil water types. Cement and Concrete Research 40, 1306–1313.

Justnes H, 2003. Thaumasite formed by sulfate attack on mortar with limestone filler. Cement & Concrete Composites 25, 955–959.

Kulik D A, Kersten M, 2002. Aqueous solubility diagrams for cementitious waste stabilization systems. 4. A carbonation model for Zn-doped calcium silicate hydrate by Gibbs energy minimization. Environmental Science & Technology 36, 2926–2931.

Kunther W, Lothenbach B, Scrivener K L, 2013. On the relevance of volume increase for the length changes of mortar bars in sulfate solutions. Cement and Concrete Research 46, 23–29.

Lagerblad B, 2001. Leaching performance of concrete based on studies of samples from old concrete constructions. SKB TR-01-27, Svensk Kärnbränslehantering AB.

Lagerblad B, Trägårdh J, 1994. Conceptual model for concrete long time degradation in a deep nuclear waste repository. SKB TR 95-21, Svensk Kärnbränslehantering AB.

Leeman A, Loser R, 2011. Analysis of concrete in a vertical ventilation shaft exposed to sulfate-containing groundwater for 45 years. Cement and Concrete Composites 33, 74–83.

Levenspiel O, 1972. Chemical reaction engineering. 2nd ed. New York: Wiley.

Li C Q, Lawanwisut W, Zheng J J, Kijawatworawet W, 2005. Crack width due to corroded bar in reinforced concrete structures. International Journal of Materials & Structural Reliability 3, 87–94.

Lothenbach B, Winnefeld F, 2006. Thermodynamic modelling of the hydration of Portland cement. Cement and Concrete Research 36, 209–226.

Lothenbach B, Matschei T, Möschner G, Glasser F, 2008. Thermodynamic modelling of the effect of temperature on the hydration and porosity of Portland cement. Cement and Concrete Research 38, 1–18.

Maltais Y, Samson E, Marchand J, 2004. Predicting the durability of Portland cement systems in aggressive environments – laboratory validation. Cement and Concrete Research 34, 1579–1589.

Marchand J, Bentz D P, Samson E, Maltais Y, 2001. Influence of calcium hydroxide dissolution on the transport properties of hydrated cement systems. In Materials Science of Concrete; proceedings of the Workshop on the Role of Calcium Hydroxide in Concrete, Holmes Beach, Anna Maria Island, Florida, 2001. Westerville, OH: American Ceramic Society, 113–129.

Marchand J, Samson E, Maltais Y, Beaudoin J J, 2002. Theoretical analysis of the effect of weak sodium sulfate solutions on the durability of concrete. Cement and Concrete Composites 24, 317–329.

Martens E, Jacques D, Van Gerven T, Wang L, Mallants D, 2010. Geochemical modeling of leaching of Ca, Mg, Al, and Pb from cementitious waste forms. Cement and Concrete Research 40, 1298–1305.

Matschei T, Glasser F P, 2010. Temperature dependence, 0 to 40°C, of the mineralogy of Portland cement paste in the presence of calcium carbonate. Cement and Concrete Research 40, 763–777.

Matschei T, Lothenbach B, Glasser F, 2007. Thermodynamic properties of Portland cement hydrates in the system CaO-Al_2O_3-SiO_2-$CaSO_4$-$CaCO_3$-H_2O. Cement and Concrete Research 37, 1379–1410.

Miller W, Alexander W, Chapman N, McKinley I, Smellie J, 2000. Geological disposal of radioactive wastes and natural analogues: lessons from nature and archaeology. Amsterdam: Pergamon. (Waste management series 2)

Milodowski A E, Nancarrow P H A, Spiro B, 1989. A mineralogical and stable isotope study of natural analogues of ordinary Portland cement (OPC) and CaO-SiO_2-H_2O (CSH) compounds. UK Nirex Safety Studies Report, NSS/R240, NDA-RWMD, UK Nirex Ltd.

Milodowski A E, Pearce J M, Hyslop E K, Hughes C R, Inglethorpe S D J, Strong G E, Wheal N, McKenzie A B, Karnland O, Khoury H N, 1998. Mineralogy and petrology. In Linklater C M (ed). A natural analogue study of cement-buffered, hyperalkaline groundwaters and their interaction with a repository host rock. Phase II. Nirex Science Studies Report S/98/003, UK Nirex Ltd., Chapter 6.

Milodowski A E, Lacinska A, Wagner D, 2009. A natural analogue study of CO_2-cement interaction: carbonate alteration of calcium silicate hydrate-bearing rocks from Northern Ireland. British Geological Survey Commissioned Report, CR/09/096.

Moranville M, Kamali S, Guillon E, 2004. Physicochemical equilibria of cement-based materials in aggressive environments – experiment and modelling. Cement and Concrete Research 34, 1569–1578.

Möller G, Petersons N, Samuelsson P (eds), 1980. Betonghandbok. Material. 2nd ed. Stockholm: Svensk byggtjänst. (In Swedish.)

Möschner G, 2007. A thermodynamic approach to cement hydration: the role of retarding admixtures and Fe-minerals during the hydration of cements. PhD thesis. ETH Zürich.

Möschner G, Lothenbach B, Rose J, Ulrich A, Figi R, Kretzschmar R, 2008. Solubility of Fe-ettringite ($Ca_6[Fe(OH)_6]_2(SO_4)_3 \cdot 26H_2O$). Geochimica et Cosmochimica Acta 72, 1–18.

Neretnieks I, 1982. The movement of a redox front downstream from a repository for nuclear waste. SKBF/KBS TR 82-16, Svensk Kärnbränsleförsörjning AB.

Nguyen V-H, 2005. Couplage degradation chimique – Comportement en compression du beton. PhD thesis. L'Ecole Nationale des Ponts et Chaussées, Paris.

Parkhurst D L, Appelo C A J, 1999. User's guide to PHREEQC (version 2): a computer program for speciation, batch-reaction, one-dimensional transport, and inverse geochemical calculations. Water-Resources Investigations Report 99-4259, U.S. Geological Survey, Denver, Colorado. Available at: ftp://brrftp.cr.usgs.gov/pub/charlton/phreeqc/Phreeqc_2_1999_manual.pdf

Parkhurst D L, Kipp K L, Charlton S R, 2010. PHAST version 2: a program for simulating ground-water flow, solute transport, and multicomponent geochemical reactions. Techniques and Methods 6–A35, U.S. Geological Survey, Denver, Colorado.

Parkhurst, D L, and Appelo, C A J, 2013. Description of input and examples for PHREEQC version 3 – A computer program for speciation, batch-reaction, one-dimensional transport, and inverse geochemical calculations. Techniques and Methods 6–A43, U.S. Geological Survey, Denver, Colorado. Available at: http://pubs.usgs.gov/tm/06/a43/pdf/tm6-A43.pdf?bcsi_scan_24808174482c3926=0&bcsi_scan_filename=tm6-A43.pdf

Parsons I, 2010. Nice day out for a material scientist. Elements 6, 271.

Perkins R B, Palmer C D, 1999. Solubility of ettringite ($Ca_6(Al(OH)_6)_2(SO_4)_3 \cdot 26H_2O$ at 5–75°C. Geochimica et Cosmochimica Acta 63, 1969–1980.

Pfingsten W, 2001. Indications for self-sealing of a cementitious L&ILW repository. PSI Bericht 01-09, Paul Scherrer Institute, Switzerland, Nagra Technical Report NTB 01-05, Nagra, Switzerland.

Pitty A F, Alexander W R (eds), 2011. A natural analogue study of cement buffered, hyperalkaline groundwaters and their interaction with a repository host rock IV: an examination of the Khushaym Matruk (central Jordan) and Maqarin (northern Jordan) sites. Bedrock Geosciences Technical Report 11-02, NDA-RWMD, Harwell, UK.

Puigdomenech I, 2002. MEDUSA Make Equilibrium Diagrams Using Sophisticated Algorithms, Windows interface to MS-DOS versions of INPUT, SED, and PREDOM: Computer programs drawing equilibrium diagrams. Inorganic Chemistry, Royal Institute of Technology, Stockholm.

Ramezanianpour A M, Hooton R D, 2013. Thaumasite sulfate attack in Portland and Portland-limestone cement mortars exposed to sulfate solution. Construction and Building Materials 40, 162–173.

Raoof A, Nick H M, Wolterbeek T K T, Spiers C J, 2012. Pore-scale modeling of reactive transport in wellbore cement under CO_2 storage conditions. International Journal of Greenhouse Gas Control 11, S67–S77.

Richardson I G, 2004. Tobermorite/jennite- and tobermorite/calcium hydroxide-based models for the structure of C-S-H: applicability to hardened pastes of tricalcium silicate, β-dicalcium silicate, Portland cement, and blends of Portland cement with blast-furnace slag, metakaolin, or silica fume. Cement and Concrete Research 34, 1733–1777.

Romero L, Neretnieks I, Moreno L, 1992. Movement of the redox front at the Osamu Utsumi uranium mine, Poços de Caldas, Brazil. Journal of Geochemical Exploration 45, 471–502.

Sahmaran M, Kasap O, Duru K, Yaman I O, 2007. Effects of mix composition and water-cement ratio on the sulfate resistance of blended cements. Cement and Concrete Composites 29, 159–167.

Saito H, Deguchi A, 2000. Leaching tests on different mortars using accelerated electrochemical method. Cement and Concrete Research 30, 1815–1825.

Santhanam M, Cohen M D, Olek J, 2001. Sulfate attack research – whither now? Cement and Concrete Research 31, 845–851.

Savage D, Soler J M, Yamaguchi K, Walker C, Honda A, Inagaki M, Watson C, Wilson J, Benbow S, Gaus I, Rüedi J, 2011. A comparative study of the modelling of cement hydration and cement-rock laboratory experiments. Applied Geochemistry 26, 1138–1152.

Schmidt T, Lothenbach B, Romer M, Neuenschwander J, Scrivener K, 2009. Physical and microstructural aspects of sulfate attack on ordinary and limestone blended Portland cements. Cement and Concrete Research 39, 1111–1121.

Sidborn M, 2007. Modelling long-term redox processes and oxygen scavenging in fractured crystalline rocks. PhD thesis. KTH School of Chemical Science and Engineering, Stockholm.

Skagius K, 1986. Diffusion of dissolved species in the matrix of some Swedish crystalline rocks. PhD thesis. Royal Institute of Technology, Stockholm.

SKB, 2001. Project SAFE. Compilation of data for radionuclide transport analysis. SKB R-01-14, Svensk Kärnbränslehantering AB.

SKB, 2006. Climate and climate-related issues for the safety assessment SR-Can. SKB TR-06-23, Svensk Kärnbränslehantering AB.

SKB, 2008. Safety analysis SFR 1. Long-term safety. SKB R-08-130, Svensk Kärnbränslehantering AB.

SKB, 2010. RD&D Programme 2010. Programme for research, development and demonstration of methods for the management and disposal of nuclear waste. SKB TR-10-63, Svensk Kärnbränslehantering AB.

SKB, 2014a. Engineered barrier process report for the safety assessment SR-PSU. SKB TR-14-04, Svensk Kärnbränslehantering AB.

SKB, 2014b. Data report for the safety assessment SR-PSU. SKB TR 14-10, Svensk Kärnbränslehantering AB.

SKB, 2014c. Initial state report for the safety assessment SR-PSU. SKB TR-14-02, Svensk Kärnbränslehantering AB.

SKB, 2014d. Waste form and packaging process report for the safety assessment SR-PSU. SKB TR-14-03, Svensk Kärnbränslehantering AB.

Smellie J A T (ed), 1998. MAQARIN natural analogue study: Phase III. SKB TR 98-04, Vols I and II, Svensk Kärnbränslehantering AB.

Soler J M, 2007. Thermodynamic description of the solubility of C-S-H gels in hydrated Portland cement – literature review. Posiva Working Report 2007-88, Posiva Oy, Finland.

Steefel C I, 2001. GIMRT, Version 1.2: Software for modeling multicomponent, multidimensional reactive transport, User's guide. Report UCRL-MA-143182, Lawrence Livermore National Laboratory, Livermore, California.

Steefel C I, Lichtner P C, 1994. Diffusion and reaction in rock matrix bordering a hyperalkaline fluid-filled fracture. Geochimica et Cosmochimica Acta 58, 3595–3612.

Stora E, Bary B, He Q-C, 2008. On estimating the effective diffusive properties of hardened cement pastes. Transport in Porous Media 73, 279–295.

Stronach S A, Glasser F P, 1997. Modelling the impact of abundant geochemical components on phase stability and solubility of the $CaO\text{-}SiO_2\text{-}H_2O$ system at 25°C: Na^+, K^+, SO_4^{2-}, Cl^- and CO_3^{2-}. Advances in Cement Research 9, 167–181.

Stumm W, 1992. Chemistry of the solid-water interface: processes at the mineral-water and particle-water interface in natural systems New York: Wiley.

Sugiyama D, Fujita T, 2005. A thermodynamic model of dissolution and precipitation of calcium silicate hydrates. Cement and Concrete Research 36, 227–237.

Sun C, Chen J, Zhu J, Zhang M, Ye J, 2013. A new diffusion model of sulphate ions in concrete. Construction and Building Materials 39, 39–45.

Swanton S, Alexander W R, Berry J A (2010). Review of the behaviour of colloids in the near field of a cementitious repository. Report to NDA-RWMD, Serco/TAS/000475/01. NR3213/008, Nuclear Decommissioning Authority, UK.

Thoenen T, Kulik D, 2003. Nagra/PSI chemical thermodynamic database 01/01 for the GEM-Selektor (V.2-PSI) geochemical modeling code. Paul Sherrer Institute, Switzerland. Available at: http://gems.web.psi.ch/TDB/doc/pdf/TM-44-03-04-web.pdf

Thomson G, Miller A, Smith G, Jackson D, 2008. Radionuclide release calculations for SAR-08. SKB R-08-14, Svensk Kärnbränslehantering AB.

Thoft-Christensen P, 2005. Safety and corrosion cracking of concrete structures. In Proceedings of 4th international workshop on life-cycle cost analysis and design of civil infrastructure systems, Cocoa Beach, Florida, 8–11 May 2005, 135–142.

Tian B, Cohen M D, 2000. Does gypsum formation during sulfate attack lead to expansion? Cement and Concrete Research 30, 117–123.

Tognazzi C, 1998. Couplage fissuration-dégradation chimique dans des matériaux cimentaires: caractérisation et modélisation. Thèse: INSA – Institut National des Sciences Appliquées, Toulouse.

Torres S M, Kirk C A, Lynsdale C J, Swamy R N, Sharp J H, 2004. Thaumasite-ettringite solid solutions in degraded mortars. Cement and Concrete Research 34, 1297–1305.

Trafikverket, 2012. TRVMB 114: Bearbetning av deflektionsmätdata, erhållna vid provbelastning av väg med FWD-apparat. TRV 2012:051, Trafikverket. (In Swedish.)

Truesdell A H, Jones B F, 1974. WATEQ, a computer program for calculating chemical equilibria of natural waters. Journal of Research, U.S. Geological Survey 2, 233–274.

Tuutti K, 1982. Corrosion of steel in concrete, fo 4-82, Swedish Cement and Concrete Research Institute CBI.

US DOE, 2009. Review of mechanistic understanding and modeling and uncertainty analysis methods for predicting cementitious barrier performance. Cementitious Barriers Partnership. CBP-TR-2009-002, Rev.0, U.S. Department of Energy.

Walker C S, 2003. Characterisation and solubility behaviour of synthetic calcium silicate hydrates. PhD thesis. Earth Sciences, University of Bristol, UK.

Walton J C, Plansky L E, Smith R W, 1990. Models for estimation of service life of concrete barriers in low-level radioactive waste disposal. NUREG/CR-5542, EGG-2597 RW, CC, Idaho National Engineering Laboratory, EG&G Idaho, Inc.

Wikberg P, 1999. Grundvattenkemi i SFR under 1998. Årsrapport SFR. Svensk Kärnbränslehantering AB. (In Swedish.)

Xu T, Sonnenthal E L, Spycher N, Pruess K, 2004. TOUGHREACT user's guide: a simulation program for non-isothermal multiphase reactive geochemical transport in variably saturated geologic media. Report LBNL-55460, Lawrence Berkeley National Laboratory, Berkeley, California.

Yokozeki K, Watanabe K, Sakata N, Otsuki N, 2004. Modelling of leaching from cementitious materials used in underground environment. Applied Clay Science 26, 293–308.

Zhang F, Yeh G-T, Parker J C (eds), 2012. Ground water reactive transport models. Sharjah: Behtham Science Publishers.

Zhang M, Chen J, Lv Y, Wang D, Ye J, 2013. Study on the expansion of concrete under attack of sulfate and sulfate-chloride ions. Construction and Building Materials 39, 26–32.

Unpublished documents

SKBdoc id, version	Title	Issuer, year
1032170 ver 4.0	Salters påverkan på betong i SFR	SwedPower AB, 2004
1358612 ver 1.0	SFR förslutningsplan	SKB, 2014
1417785 ver 1.0	Översiktlig bedömning av konsekvenser för omgivande barriärer i BMA (SFR) till följd av ny behandling och förpackning av indunstar-koncentrat i Forsmark	Kemakta Konsult AB, 2000
1430853 ver 1.0	Sprickor i BMA:s betongbarriär – Inspektion och orsak.	Vattenfall, 2012.
1432256 ver 1.0	Mineralogisk analys av betong från BMA. (In Swedish.)	Vattenfall Research & Development AB, 2013

Appendix A

Test of numerical accuracy

Hydrodynamic dispersion

In the calculations a low hydrodynamic dispersivity of $1 \cdot 10^{-11}$ m has been assumed. The hydrodynamic dispersion coefficient is given by multiplication with the flow velocity. As an example, the velocity calculated by PHAST at observation point A–E (see the main report for orientation) during the period 0–100 years in case Large11 was $4.6 \cdot 10^{-8}$ m/year, which gives the hydrodynamic dispersion coefficient $1.4 \cdot 10^{-26}$ m^2/s. This number can be compared with the value for the effective diffusivity of $3.5 \cdot 10^{-12}$ m^2/s. Hence, we can conclude that the assumed hydrodynamic dispersion coefficient is negligible in comparison with the effective diffusivity in the example.

Numerical dispersion

Different judgments have been made regarding the possible effects of numerical dispersion in the reactive transport modelling. The PHAST manual (Parkhurst et al. 2010) gives a fairly detailed description of different types of numerical dispersion, some of which are exemplified in the following.

In general, the numerical dispersivity a_n (m) is given by:

$$\alpha_n = \alpha_{ns} + \alpha_{nt} \qquad \text{Equation A-1}$$

where:

α_{ns} = numerical dispersivity caused by spatial discretisation (m)

α_{nt} = numerical dispersivity caused by time discretisation (time step length) (m)

A measure of numerical dispersivity due to spatial discretisation is:

$$\alpha_{ns} = \frac{\Delta x}{2} \qquad \text{Equation A-2}$$

where:

Δx = the spatial discretisation (cell length in the model) (m)

A typical value for Δx used in the model is about 0.05 m, which gives a_{ns} = 0.025 m. The numerical dispersion coefficient D_{ns} (m^2/s) is given by:

$$D_{ns} = \frac{v_x \cdot \Delta x}{2} \qquad \text{Equation A-3}$$

where:

v_x = the flow velocity along the x-coordinate (m/s)

As an example, the velocity calculated by PHAST at observation point A–E (see the main report for orientation) during the period 0–100 years in case Large11 was $4.6 \cdot 10^{-8}$ m/year. From this we can estimate the numerical dispersion coefficient due to the spatial discretisation (Δx = 0.05 m) to $1.2 \cdot 10^{-9}$ m^2/year, equivalent to $3.7 \cdot 10^{-17}$ m^2/s. This number can be compared with the value for the effective diffusivity of $3.5 \cdot 10^{-12}$ m^2/s. Hence, we can conclude that the numerical dispersion coefficient representing the spatial discretisation is much smaller than the effective diffusivity in the example. Calculations have been carried out for different periods of time since the flow velocities and the diffusivity coefficients are assumed to change over time. It was found that the highest risk for an impact of the numerical dispersion due to spatial discretisation can be expected during the period 2,000–10,000 years when the numerical dispersion coefficient is somewhat higher than the effective diffusivity.

The numerical dispersivity a_{nt} and numerical dispersion coefficient D_{nt} due to time discretisation are given by:

$$\alpha_{nt} = \frac{v_x \cdot \Delta t}{2}$$ Equation A-4

$$D_{nt} = \frac{v_x^2 \cdot \Delta t}{2}$$ Equation A-5

where:

Δt = the time step (years)

The value of D_{nt} has been calculated for different periods of time. For the early period, 0–100 years, a very low value of $3.4 \cdot 10^{-25}$ m^2/s was calculated for a time step $\Delta t = 0.01$ years. This can be compared with the effective diffusivity of $3.5 \cdot 10^{-12}$ m^2/s. It was found that numerical dispersion due to time discretisation can be expected to have a minor impact during the period 2,000–10,000 years, since the numerical dispersion coefficient approaches, but still is smaller than, the effective diffusivity.

Calculations of the Peclet number have been made to determine whether the mass transport is dominated by diffusion or advection:

$$Pe = \frac{v_x \cdot \Delta x}{D_e}$$ Equation A-6

where:

D_e = the effective diffusivity (m^2/s)

Diffusion processes dominate if Pe < 1 and advection dominates when Pe > 1. It was found that the mass transport is dominated by diffusion during the early period up to 1,000 years. At this time the hydraulic conductivity of the concrete has been assumed to increase and the water flow rate increases in response. Hereafter the mass transport is dominated by advection. Advection is particularly predominant during the period 2,000–10,000 years. Thereafter the effective diffusivity has also been assumed to increase and diffusion processes again contribute to a certain extent to the mass transport. It can be noted that during the advection dominated periods, the impact of the numerical dispersion on the mass transport is less important.

The Courant number relates the time for a water package to pass through a cell in the model to the time step, and gives an indication of a suitable time step length:

$$C_r = \frac{v_x \cdot \Delta t}{\Delta x}$$ Equation A-7

Considering only the mass transport, thus neglecting any reactions, a criterion for the numerical accuracy, when upstream-in-time and backward-in time differencing is used (which is the method applied through-out this study), is given by:

$$Pe \cdot (1 + C_r) \ll 2$$ Equation A-8

Calculations for the example used show that the criterion is well fulfilled during the first 1,000 years, not quite fulfilled from 1,000–2,000 years, not fulfilled from 2,000–10,000 years and reasonably well fulfilled after 10,000 years.

In response to this, the numerical accuracies of different variations of selected cases have been investigated using the PHAST program to study the possible impact of the spatial and time discretisation. The results are presented in the following subsections.

Tests of the numerical accuracy using PHAST

The quality of the numerical solution in the PHAST modelling has been tested by varying the time step length and the spatial discretisation in the direction of the major groundwater flow. The tests have been performed for two different cases:

- Large11 (test of time step length) and
- Large10 (test of time step length and spatial discretisation).

Case Large11

A comparison of the time step length variations for case Large11 is shown in Table A-1.

The calculated porosity changes over time for the two variations are presented in Figure A-1. The comparison shows that there are some minor deviations caused by the time discretisation. In particular, longer time steps result in a smoothened porosity evolution. The examples are shown for evaluation point A–E.

The corresponding evolution of the mineral assemblies for the two variations is shown in Figure A-2 and Figure A-3. The two variations show essentially the same results, however, the case with longer time steps has a slight tendency to smear out the changes of the different regimes of the different minerals.

Table A-1. Comparison of time step lengths in two variations of case Large11.

	Time step (years)	
Period (years)	**Large11**	**Large11_0.01 yr**
0–0.5	0.005	0.005
0.5–1	0.01	0.001
1–10	0.02	0.002
10–2,000	0.05	0.005
2,000–10,000	0.2	0.01
10,000–100,000	0.2	0.01

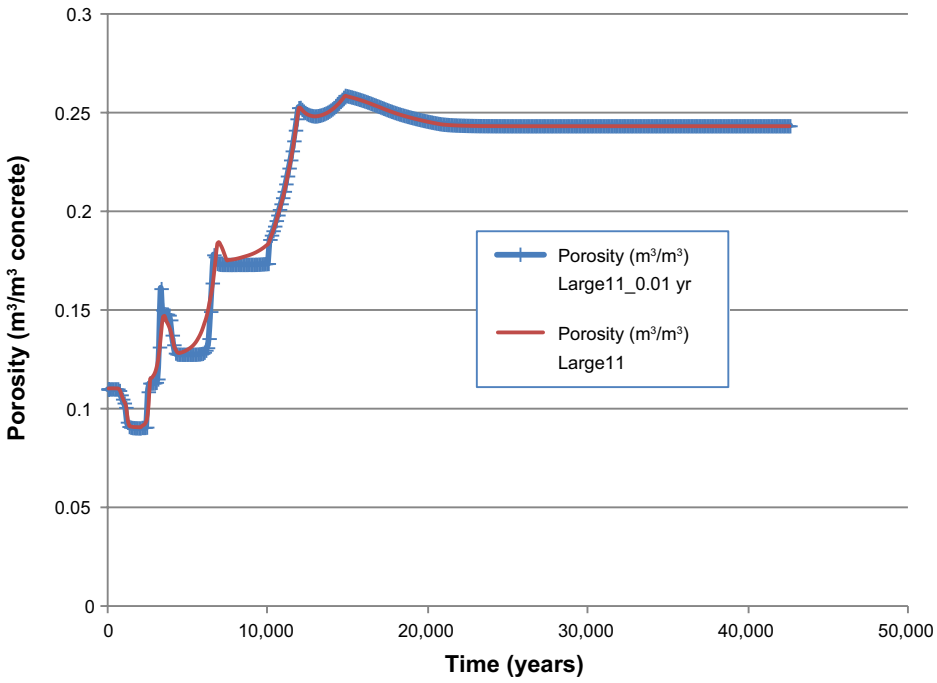

Figure A-1. *Comparison of calculated porosity changes over time when using different time step lengths in the PHAST calculations for Case Large11.*

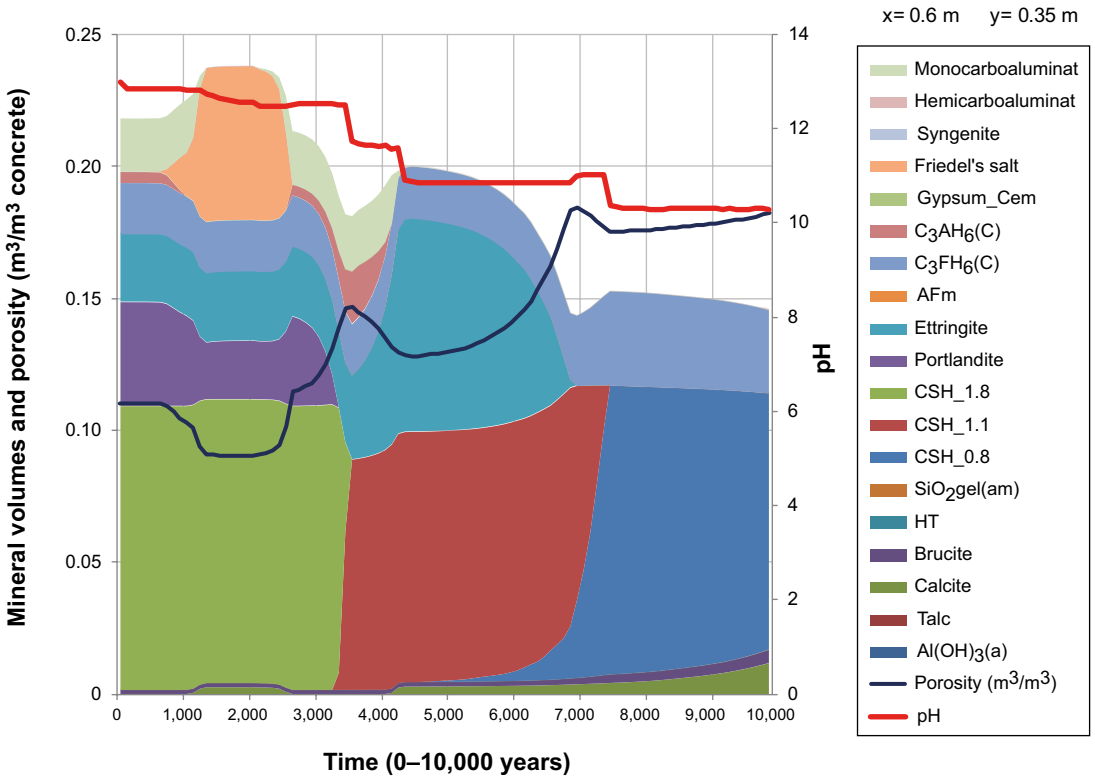

Figure A-2. *Evolution of mineral volumes over time in case Large11.*

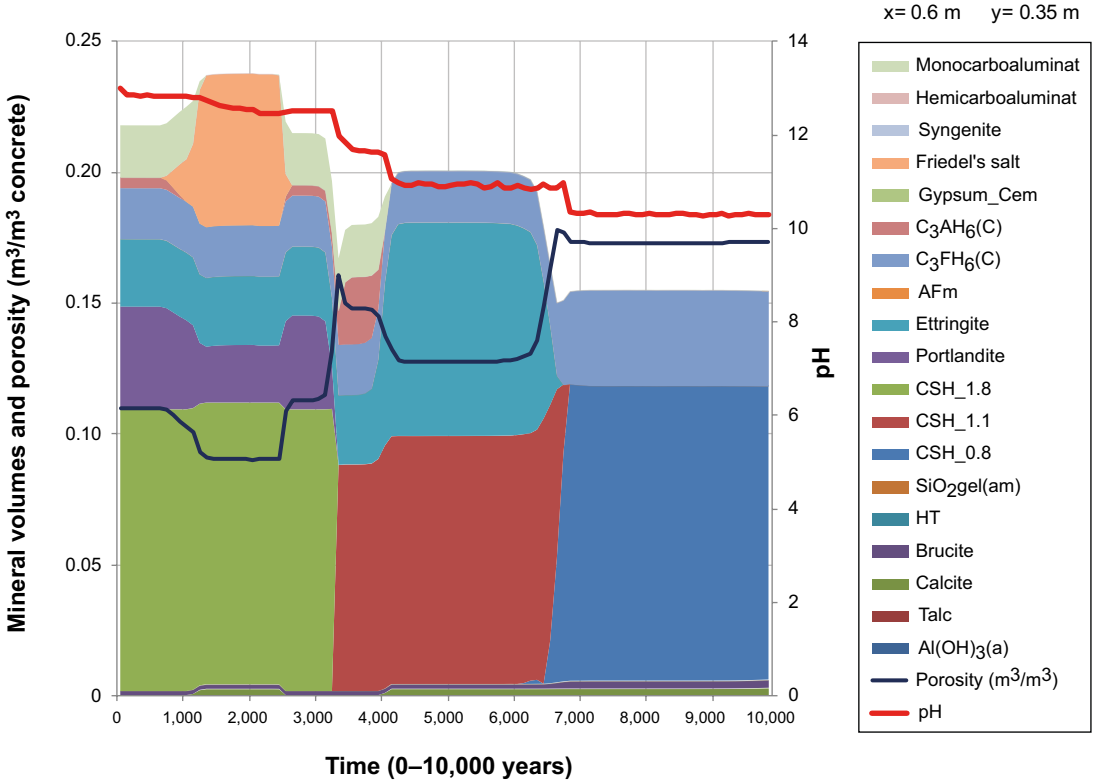

Figure A-3. *Evolution of mineral volumes over time in case Large11_0.01 yr.*

Case Large10

A comparison of the time step length variations for case Large10 is shown in Table A-2.

The calculated porosity changes over time for the two variations are presented in Figure A-4. The comparison shows that there are some minor deviations caused by the time discretisation. In particular, longer time steps give a somewhat smoothened porosity evolution. However, after about 11,000 years the two calculations start to deviate to some degree, levelling off at an absolute porosity difference of 0.009, equivalent to 4% in relative numbers. The examples are shown for evaluation point A–E.

The corresponding evolution of the mineral volume assemblies for the two variations is shown in Figure A-5 and Figure A-6.

A comparison of the impact of different spatial discretisations for three variations of case Large10 is given in Figure A-10. The results show that the spatial discretisation used in the calculations (the normal case) is satisfactory for the purpose of the present study. The discretisations used in the three variations are given in Figure A-7, Figure A-8 and Figure A-9.

The corresponding evolution of the mineral volume assemblies are presented in Figure A-11, Figure A-12 and Figure A-13. The three variations show in essence the same results, however, the coarse discretisation has a slight tendency to smear out the changes of the different regimes of the different minerals.

Table A-2. Comparison of time step lengths in two variations of case Large10.

Period (years)	Time step (years)	
	Large10	Large10_0.01 yr
0–1	1	0.001
1–10	1	0.002
10–2,000	1	0.005
2,000–10,000	0.025	0.01
10,000–100,000	0.05	0.01

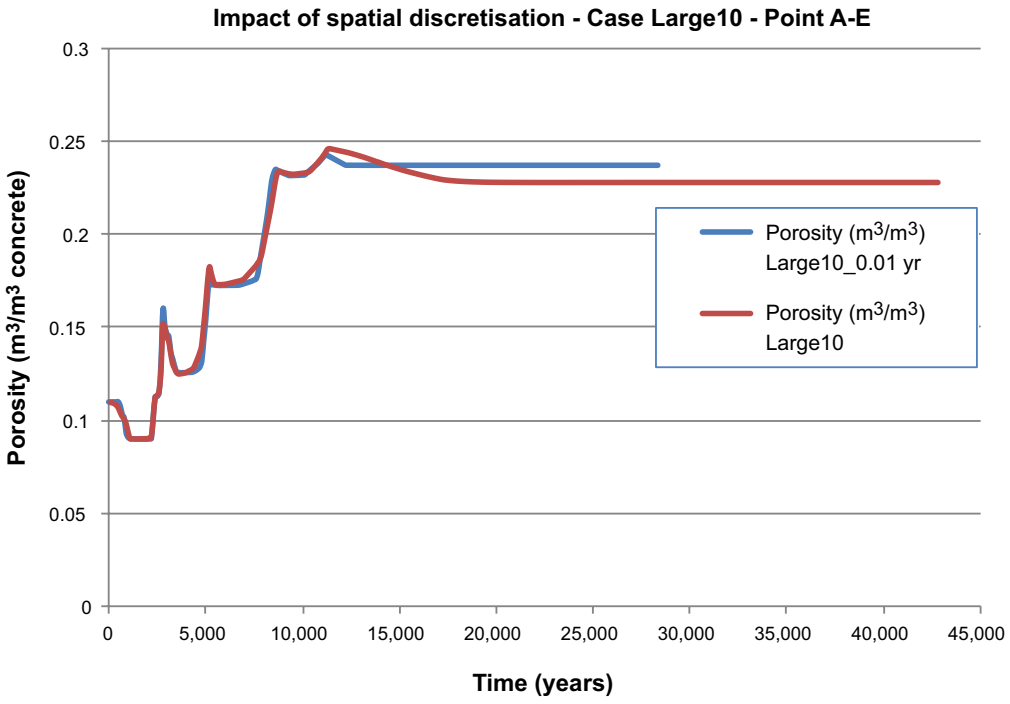

Figure A-4. *Comparison of calculated porosity changes over time when using different time step lengths in the PHAST calculations for Case Large10.*

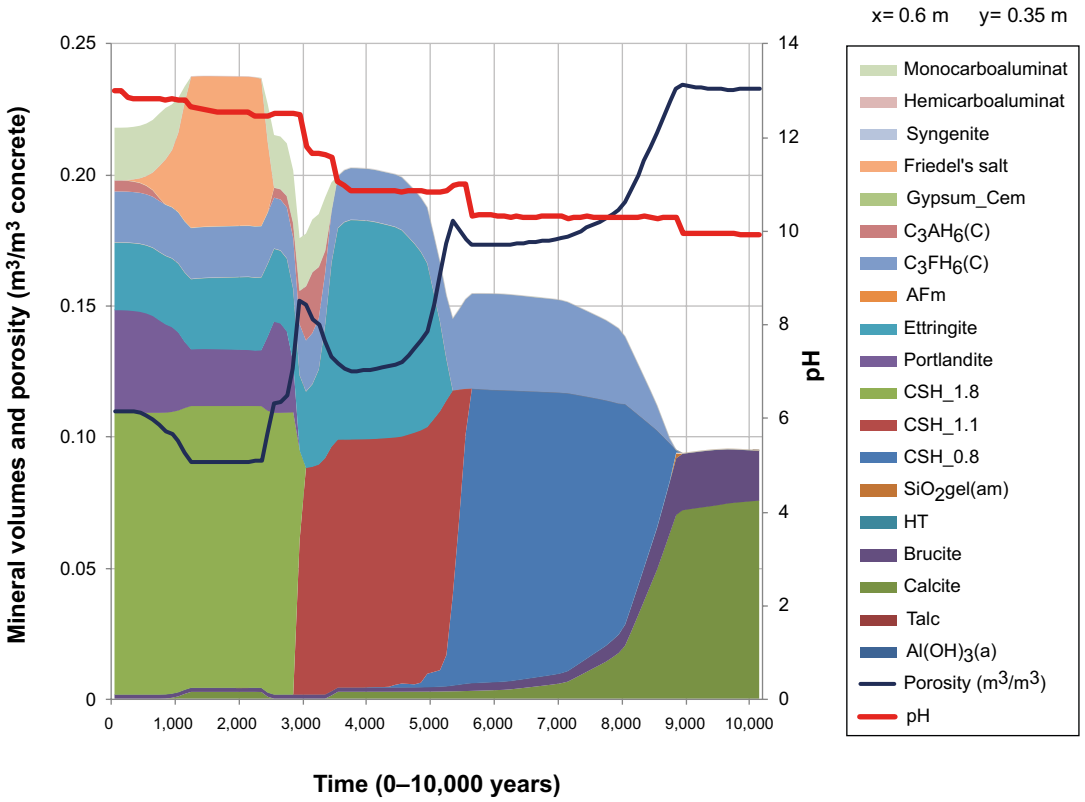

Figure A-5. *Evolution of mineral volumes over time in case Large10.*

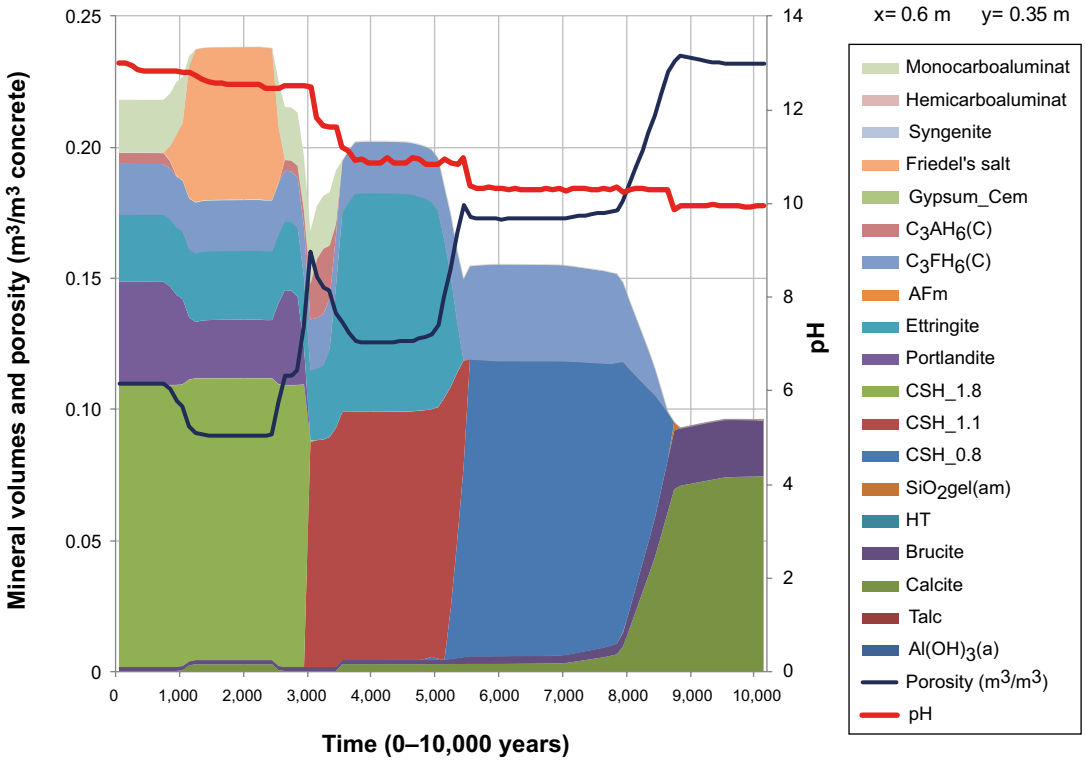

Figure A-6. *Evolution of mineral volumes over time in case Large10_0.01 yr.*

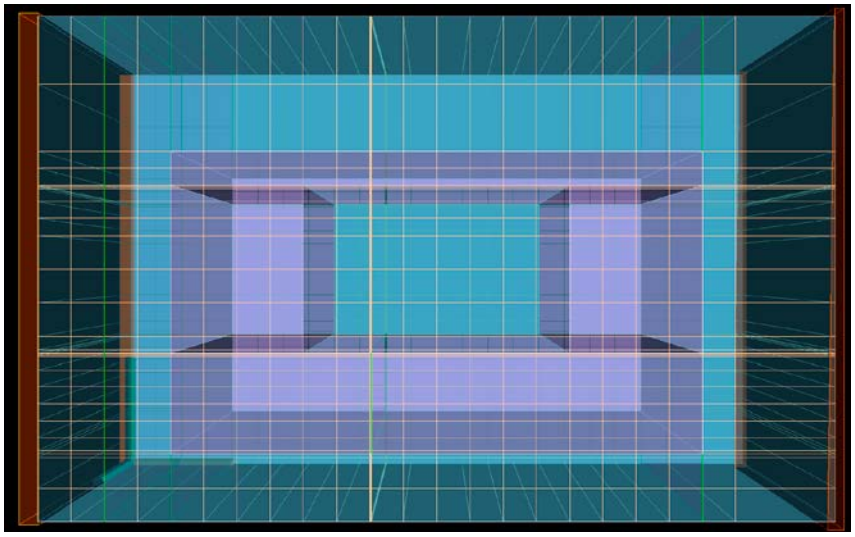

Figure A-7. *Discretisation used in case Large10_coarse.*

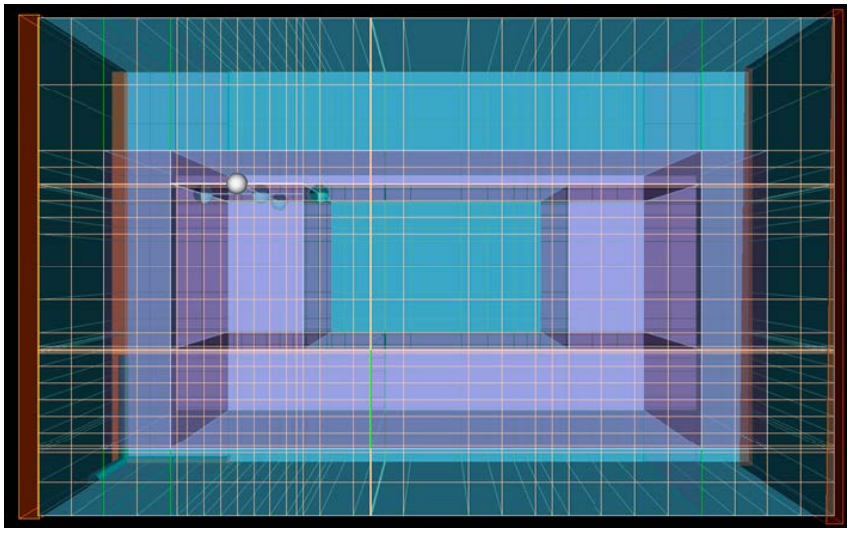

Figure A-8. *Discretisation used in case Large10_normal.*

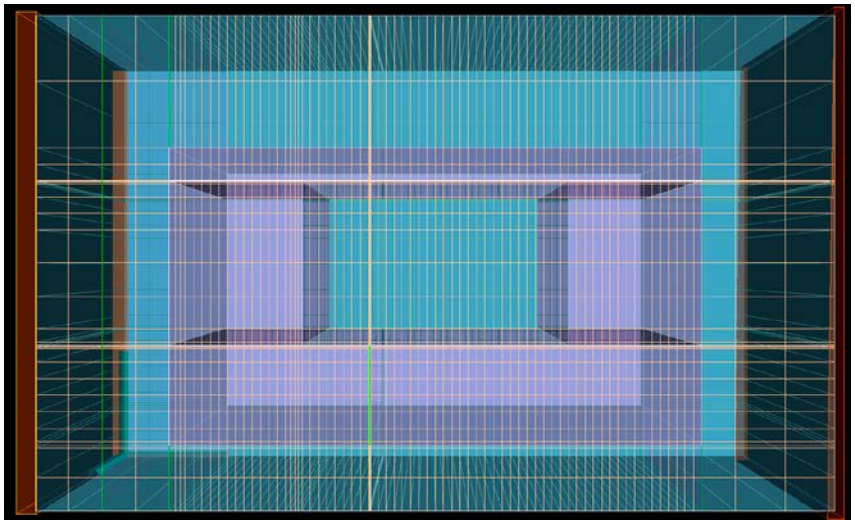

Figure A-9. *Discretisation used in case Large10_fine.*

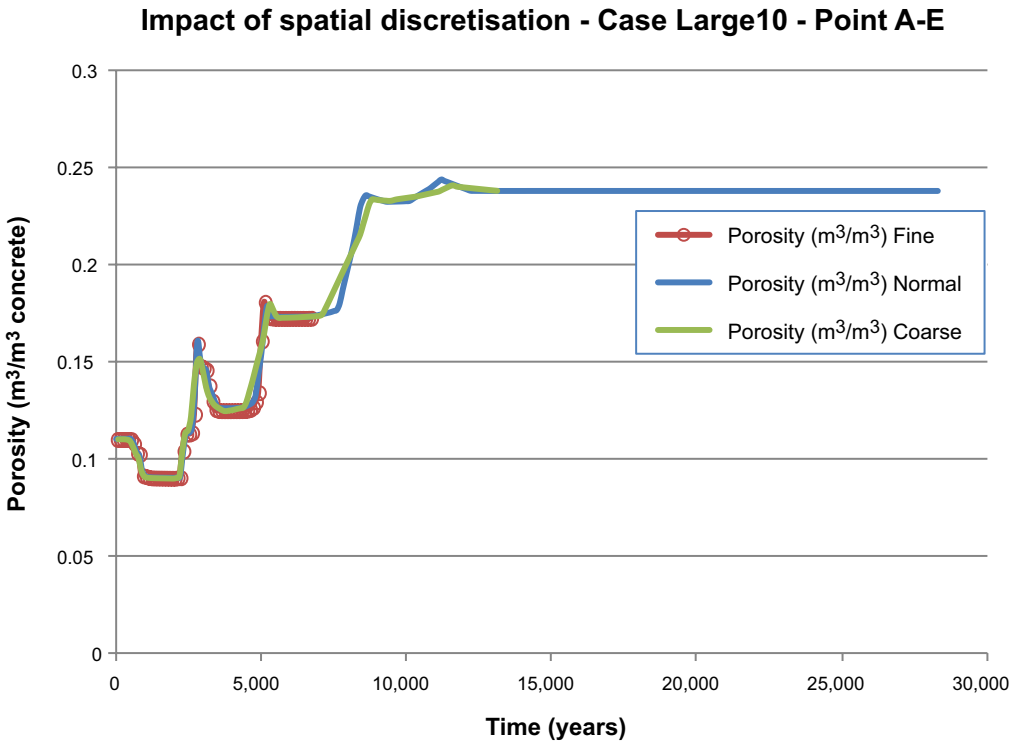

Figure A-10. Comparison of calculated porosity changes over time when using three different spatial discretisations in the PHAST calculations for Case Large10.

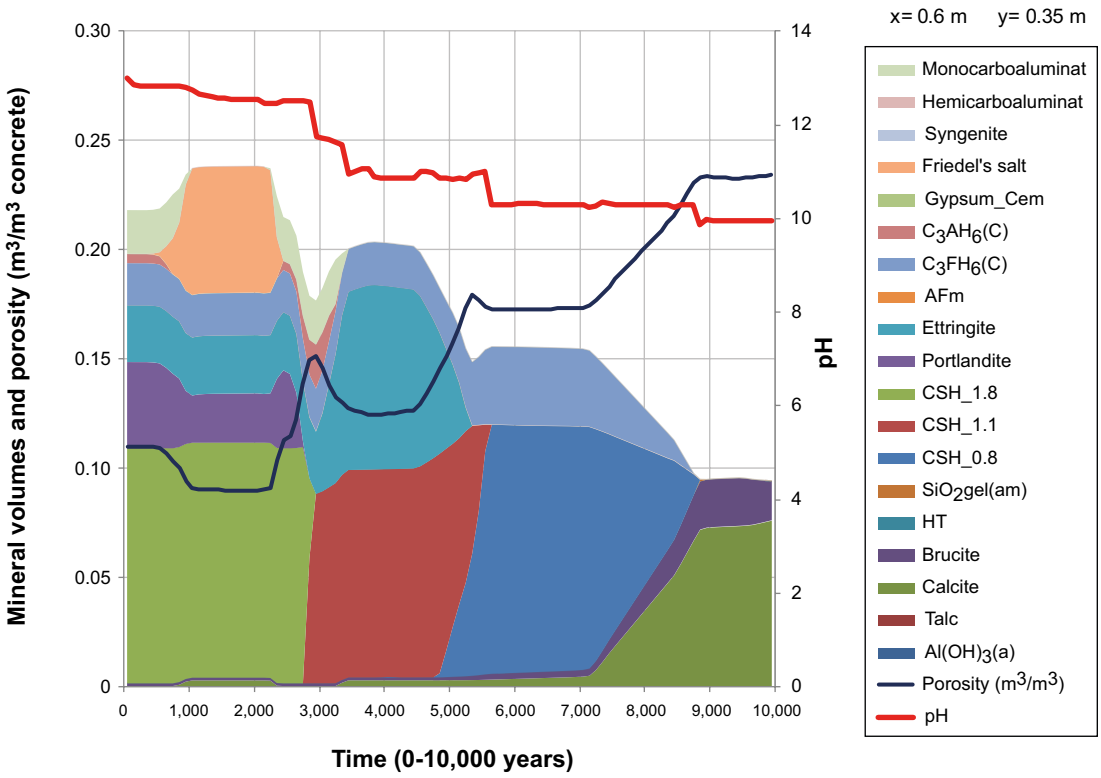

Figure A-11. Evolution of mineral volumes over time in case Large10_0.01 yr using a coarse spatial discretisation.

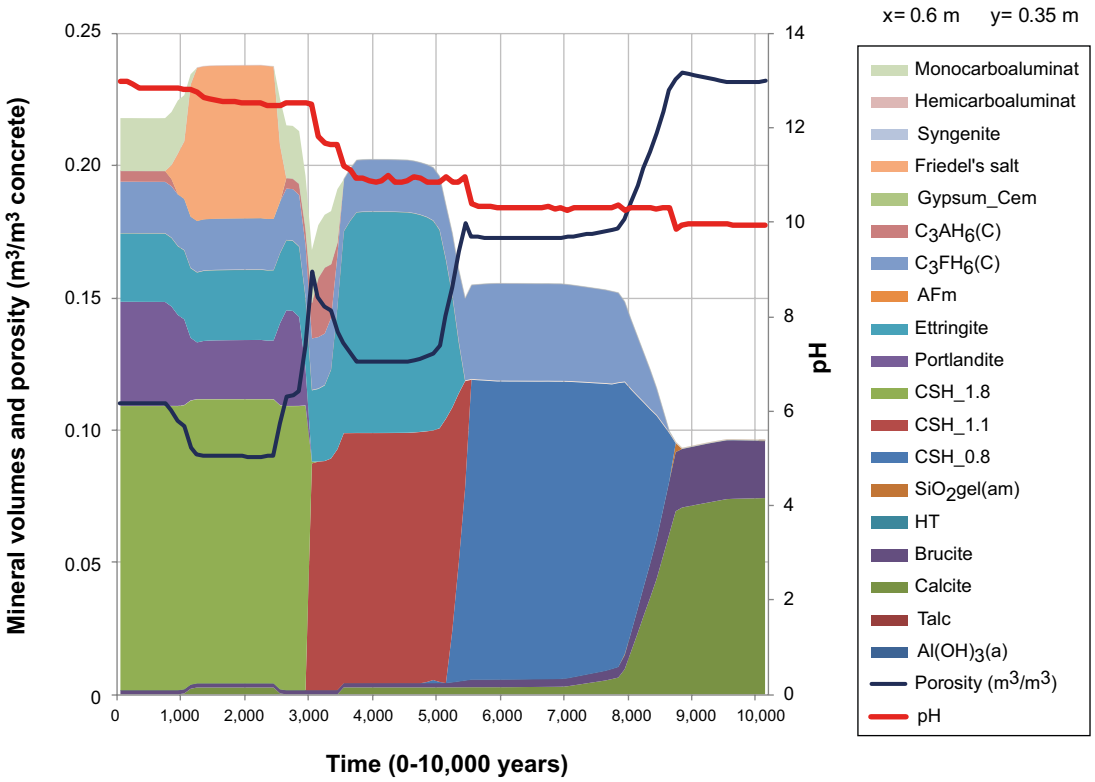

Figure A-12. *Evolution of mineral volumes over time in case Large10_0.01 yr using an intermediate (normal) spatial discretisation.*

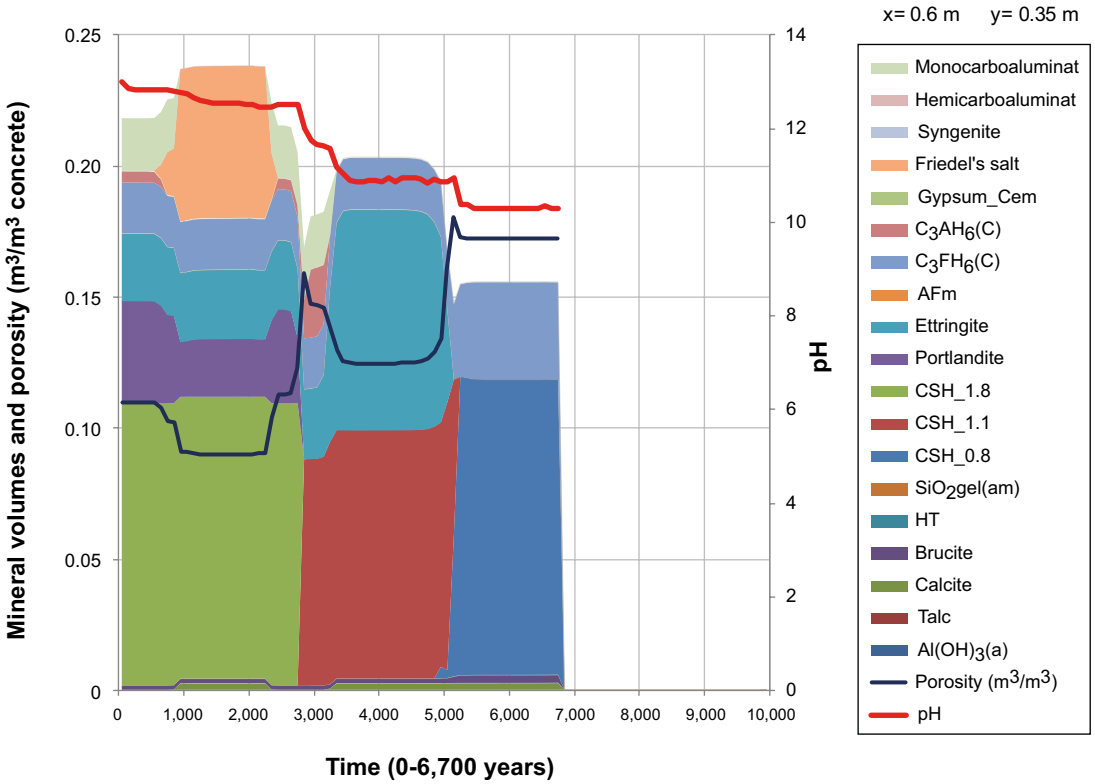

Figure A-13. *Evolution of mineral volumes over time in case Large10_0.01 yr using a fine spatial discretisation (calculations terminated by operator at 6,700 years).*

Case Large20

A comparison of the time step length variations for case Large20 (i.e. the calculations for the 2BMA vault) is shown in Table A-3.

The calculated concentrations of different dissolved components at inspection point GH is shown in Figure A-14. There are only negligible differences between the two time discretisations at inspection point GH.

The calculated concentrations of different dissolved components at inspection point DD, which is located in the thin horizontal fracture in the concrete wall, is shown in Figure A-15. There are only negligible differences between the two different time discretisations at inspection point DD.

The calculated concentrations of different dissolved components at an inspection point located at the downstream side of the concrete barriers in the macadam fill in the 2BMA vault are shown in Figure A-16. There are minor differences between the two different time discretisations at inspection point in the macadam downstream the concrete barriers in 2BMA.

Table A-3. Comparison of time step lengths in two variations of case Large20.

Period (years)	Time step (years)	
	Large20_1_a	Large20_0.1 yr
0–100	1	0.1
100–10,000	1	0.1
10,000–20,000	1	0.1
20,000–100,000	1	0.1

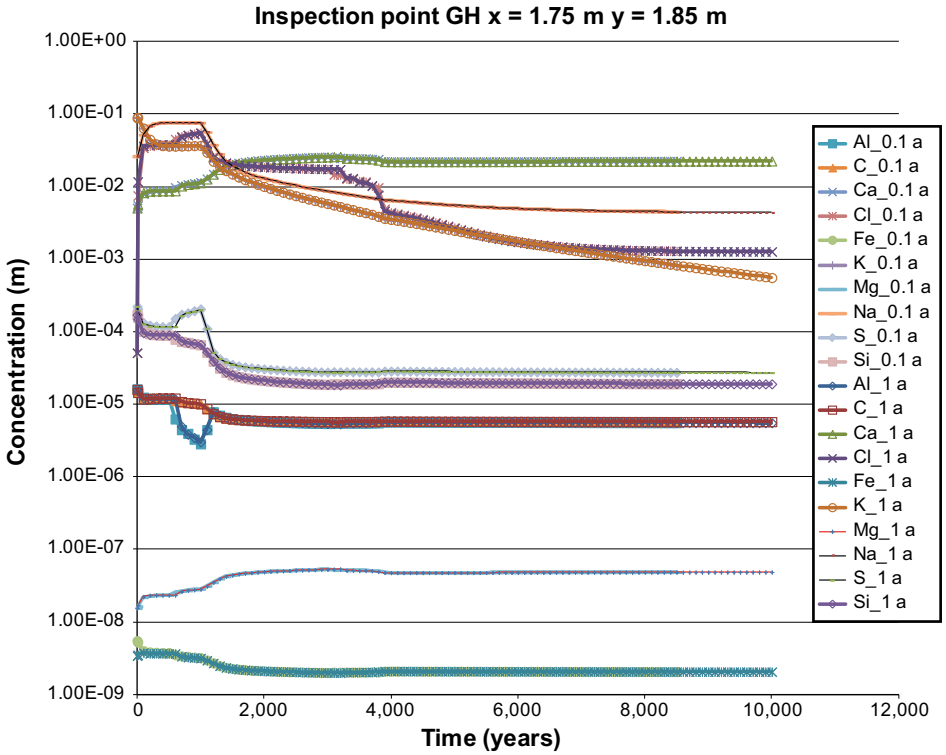

Figure A-14. *Comparison of calculated solute concentrations over time at inspection point GH when using different time step lengths in the PHAST calculations for Case Large20 (2BMA).*

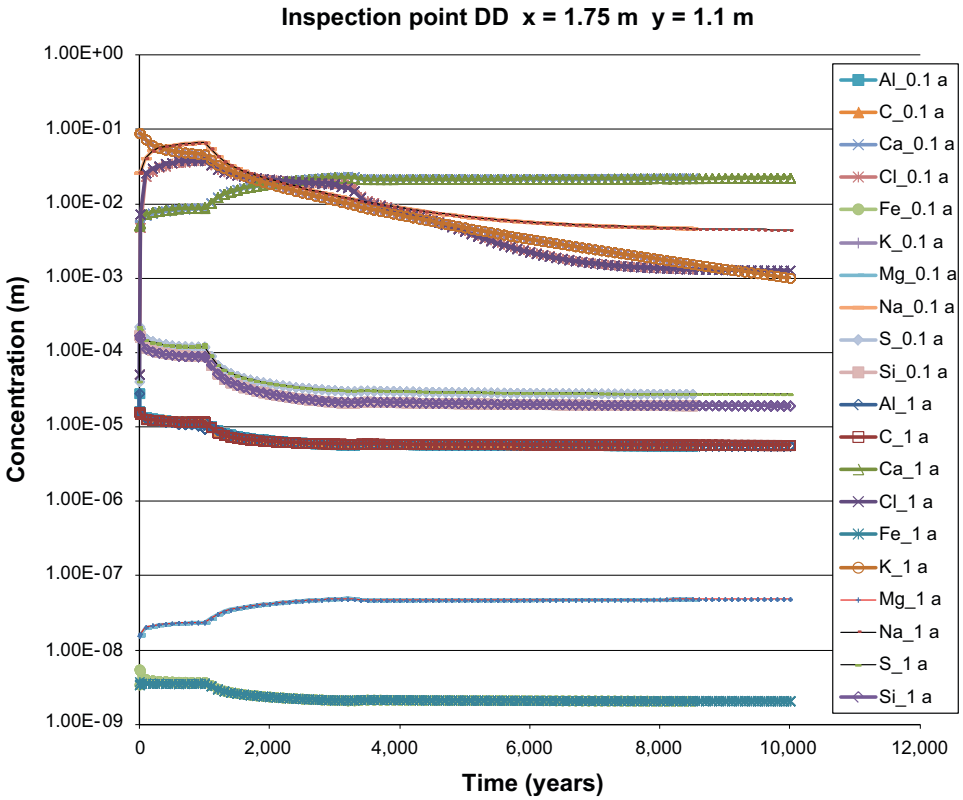

Figure A-15. *Comparison of calculated solute concentrations over time at inspection point DD located in the thin horizontal fracture in the concrete wall when using different time step lengths in the PHAST calculations for Case Large20 (2BMA).*

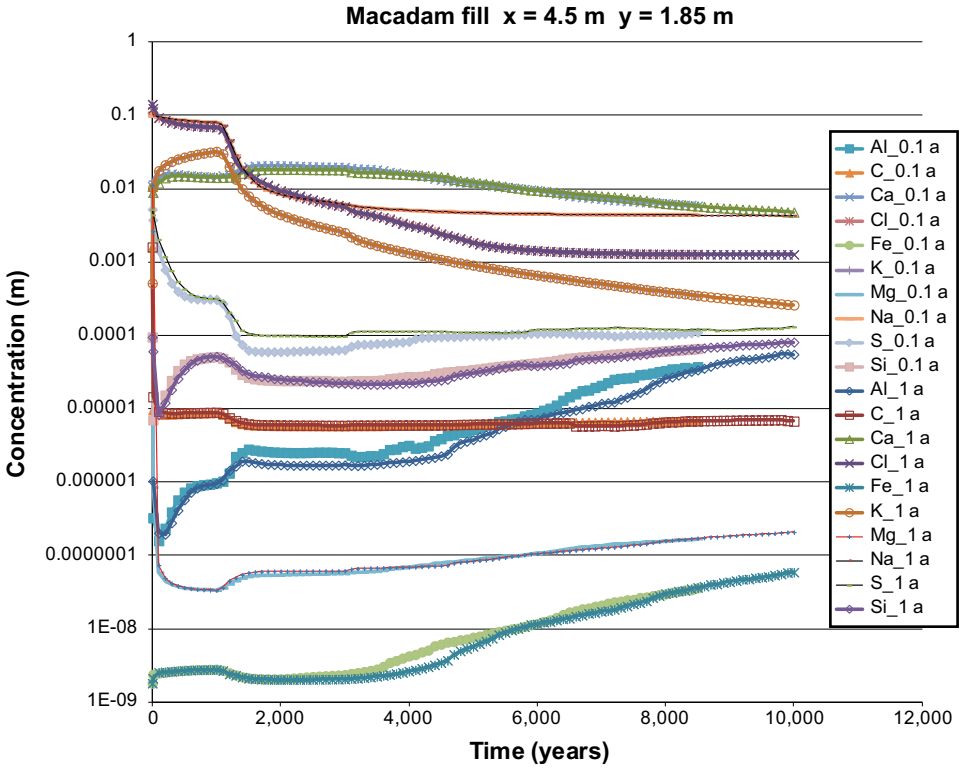

Figure A-16. *Comparison of calculated solute concentrations over time at an observation point in the macadam fill at the downstream side of the 2BMA vault concrete barriers when using different time step lengths in the PHAST calculations for Case Large20 (2BMA).*

The calculated porosity changes over time for the two variations are presented in Figure A-17. The comparison shows that there are some minor deviations caused by the time discretisation. In particular, longer time steps give a somewhat smoothened porosity evolution. The examples are shown for evaluation point G–H.

The corresponding evolution of the mineral volume assemblies for the two variations is shown in Figure A-18 and Figure A-19. Only minor differences between the two variations can be noticed, basically the depletion of the different minerals occur more distinctly in the case with the smaller time steps and is a bit more stretched out in time for the case with larger time steps.

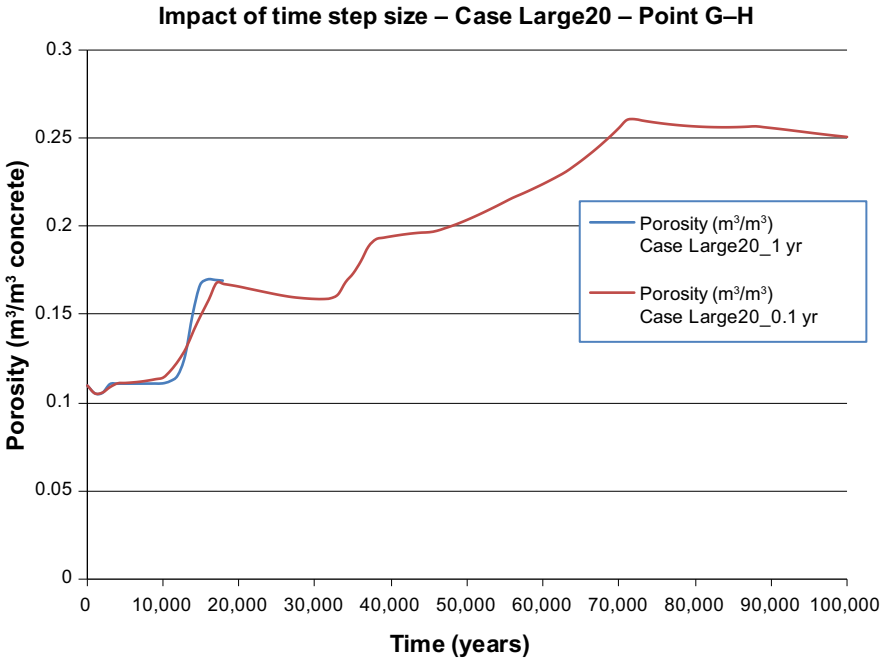

Figure A-17. *Comparison of calculated porosity changes over time when using different time step lengths in the PHAST calculations for Case Large20.*

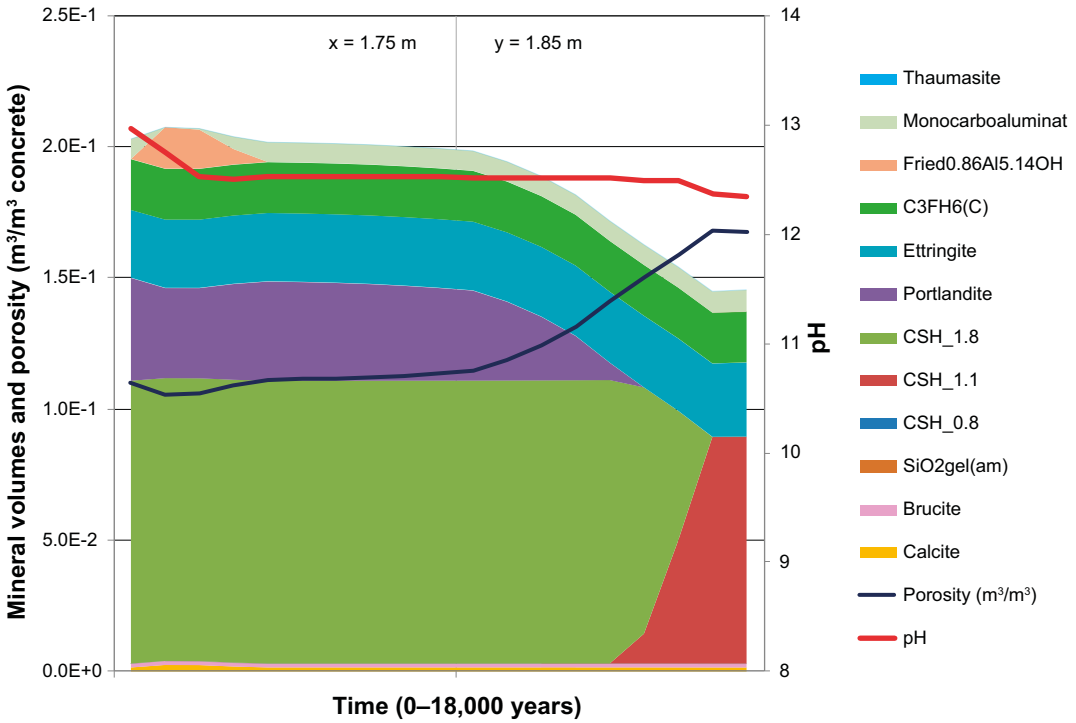

Figure A-18. *Evolution of mineral volumes over time (0–18,000 years) in case Large20_1 yr.*

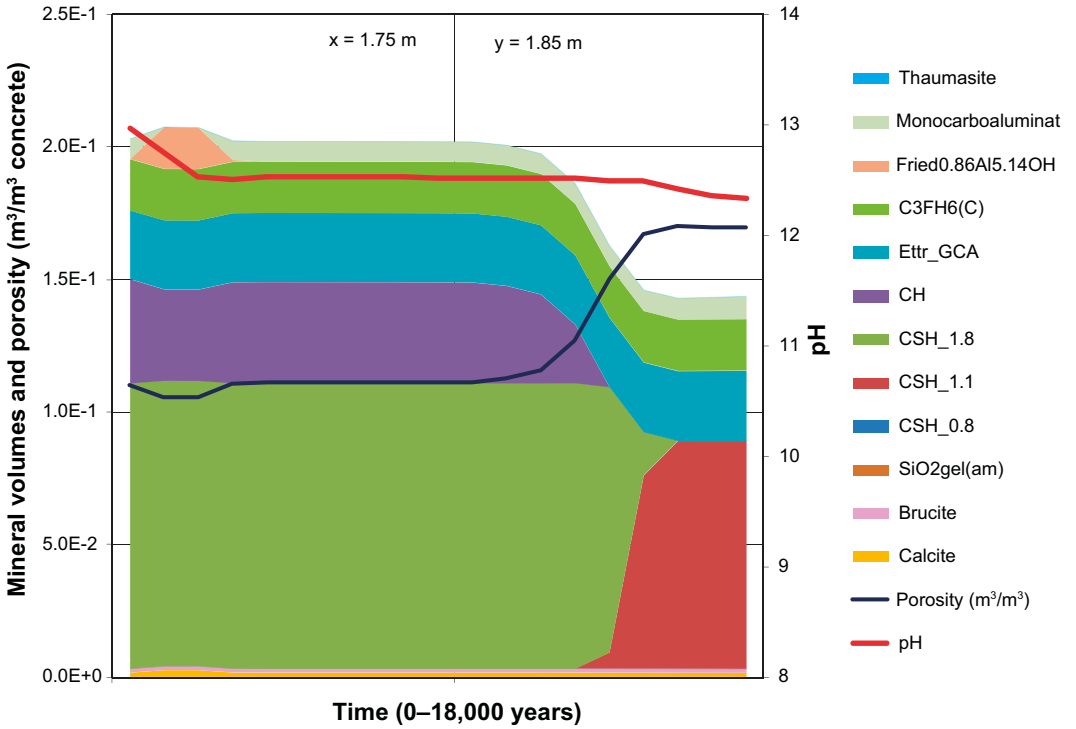

Figure A-19. *Evolution of mineral volumes over time (0–18,000 years) in case Large20_0.1 yr.*

Test of model representation for 2BMA

The simplifications in representation of the flow geometry made in the PHAST modelling of the 2BMA (case Large20) has been investigated. In case Large20 the concrete caissons are represented at a reduced scale. To test the assumption, a full scale model using the actual dimensions of the vault cross-section and a 3-dimensional model of a vault has been set up in PHAST. The model geometry consists of 106,596 cells and is shown in Figure A-20. The results of a steady-state calculation are presented in Figure A-21–Figure A-25. An illustration of the inspection zones and boundary conditions (BC) for which the flow has been evaluated is presented in Figure A-26. A compilation of the distribution of the flow between different zones in the model is presented in Figure A-27.

The calculated flow distribution in case Large20 compare well with the more detailed hydrological simulation using the 3D-model presented above, see a direct comparison of the results from the two models in Figure A-28. Hence, the calculations show that the flow conditions in 2BMA is well represented by the assumptions and geometrical simplifications made for case Large20 used in the numerical modelling of concrete degradation in 2BMA.

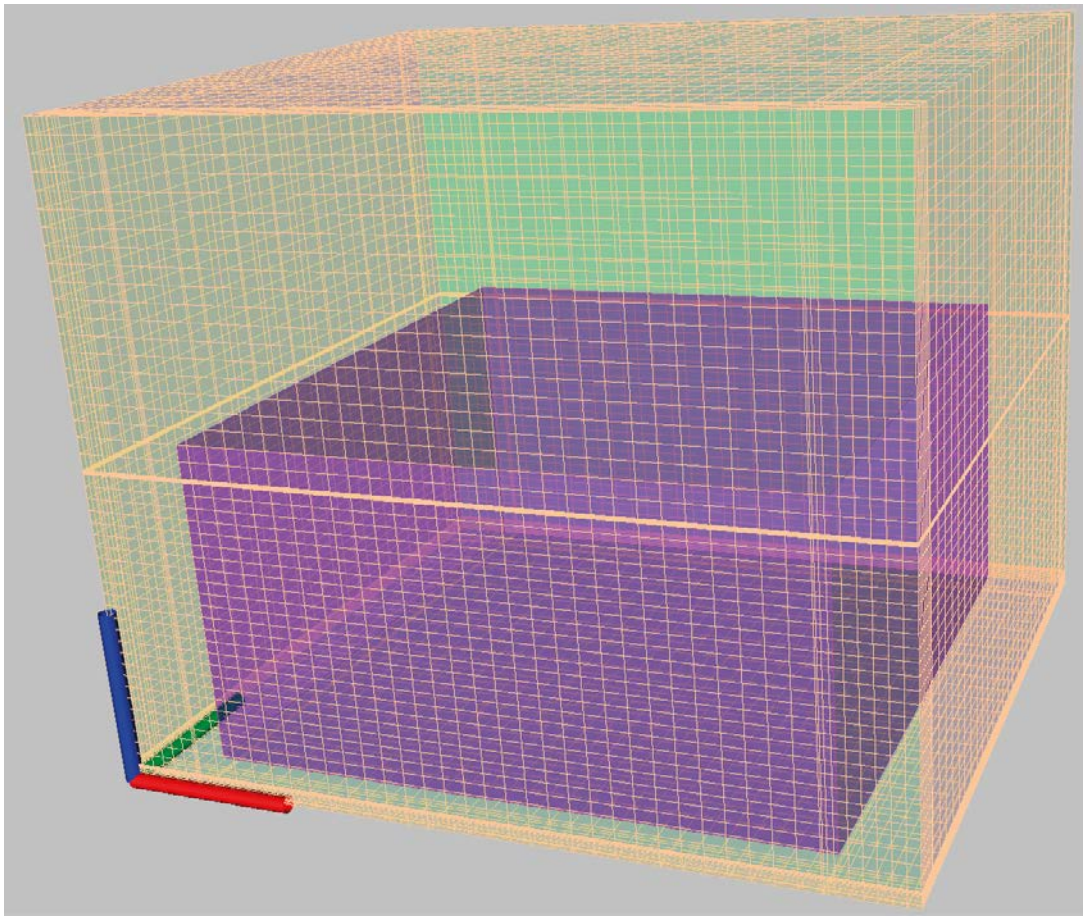

Figure A-20. *Perspective view of the 3D-model of the 2BMA vault used for the evaluation of the flow distribution. The concrete caisson is shown in purple colour.*

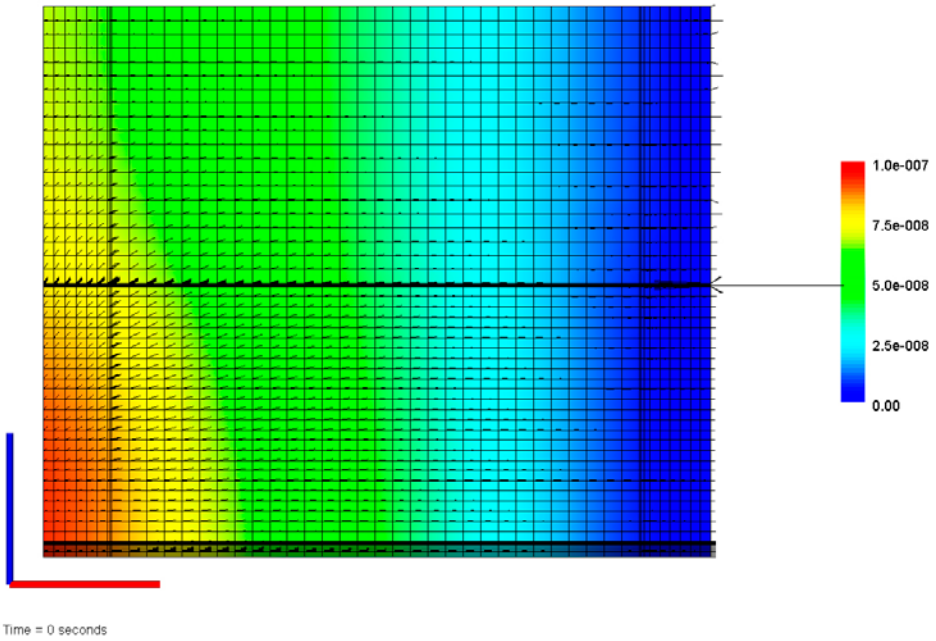

Figure A-21. *2BMA-fine grid – Vertical section perpendicular to the main axis of the 2BMA vault in macadam fill at the side of the concrete caisson. Flux vectors are shown in black. Red axis=horizontal direction perpendicular to the main axis of the 2BMA vault. Blue axis= vertical direction. The legend shows the hydraulic head (m).*

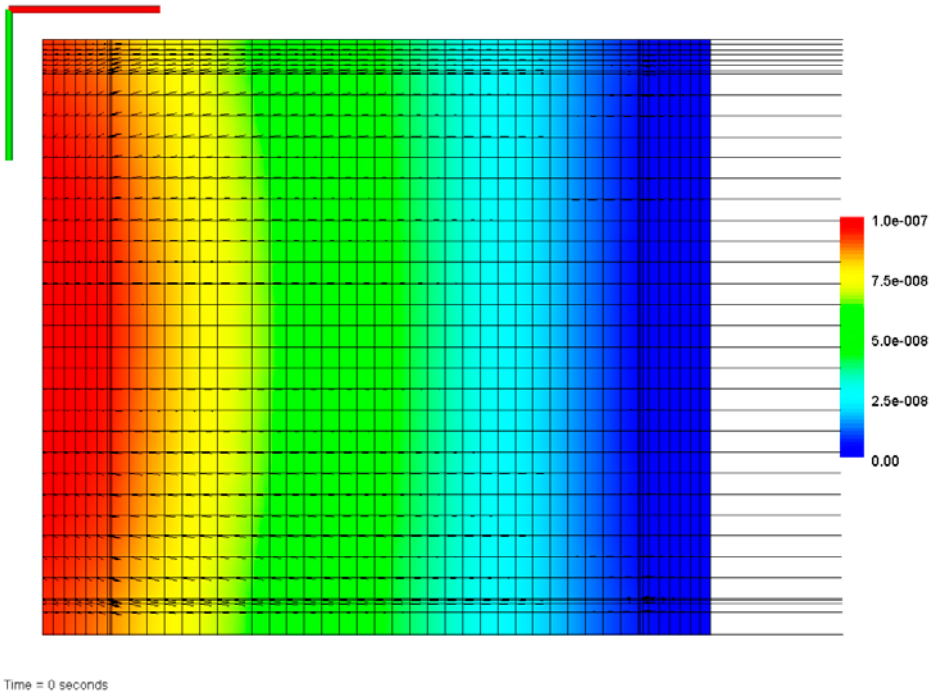

Figure A-22. *2BMA-fine grid – Horizontal section in the macadam at the bottom of the vault. Flux vectors are shown in black. Red axis=horizontal direction perpendicular to the main axis of the 2BMA vault. Green axis= horizontal direction along to the main axis of the 2BMA vault. The legend shows the hydraulic head (m).*

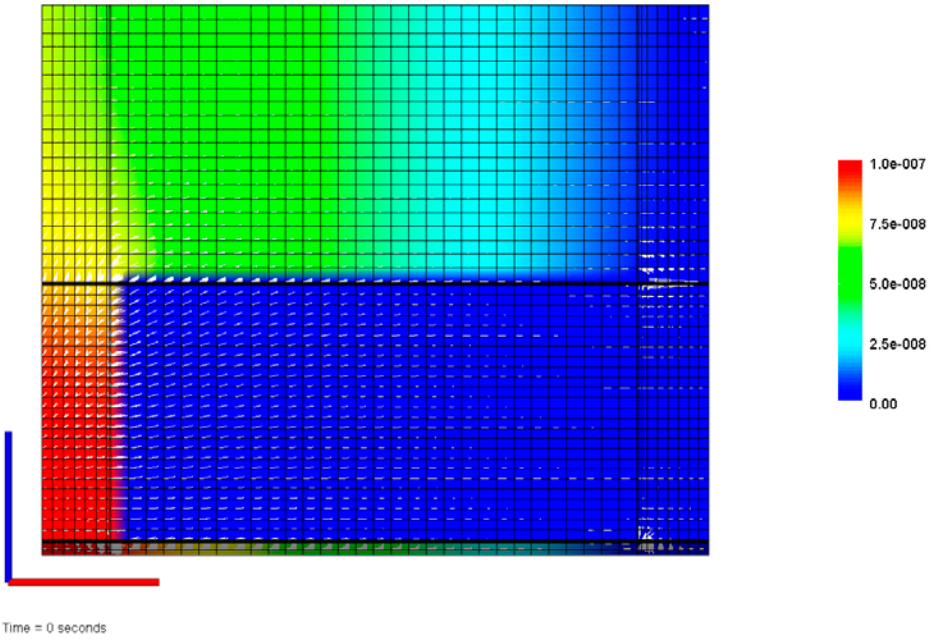

Figure A-23. *Vertical section through the centre of the caisson perpendicular to the main axis of the 2BMA vault. The inflow of groundwater is assumed at the left-hand side and the outflow at the right-hand side. Flux vectors are shown in white. Red axis=horizontal direction perpendicular to the main axis of the 2BMA vault. Blue axis= vertical direction. The legend shows the hydraulic head (m).*

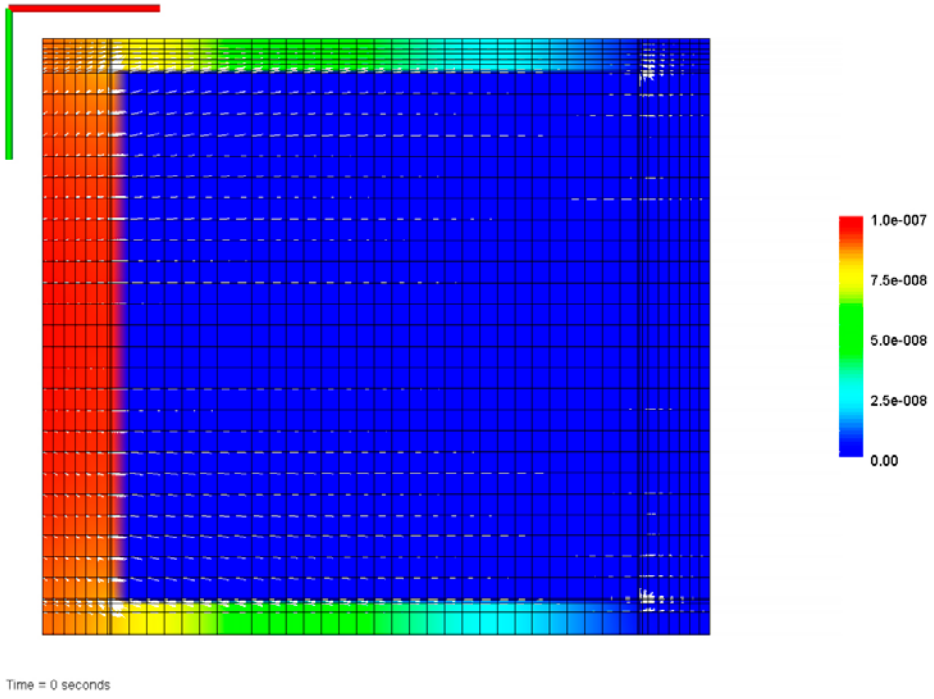

Figure A-24. *Horizontal section through the centre of the caisson. The inflow of groundwater is assumed at the left-hand side and the outflow at the right-hand side. Flux vectors are shown in white. Red axis=horizontal direction perpendicular to the main axis of the 2BMA vault. Green axis=horizontal direction along to the main axis of the 2BMA vault. The legend shows the hydraulic head (m).*

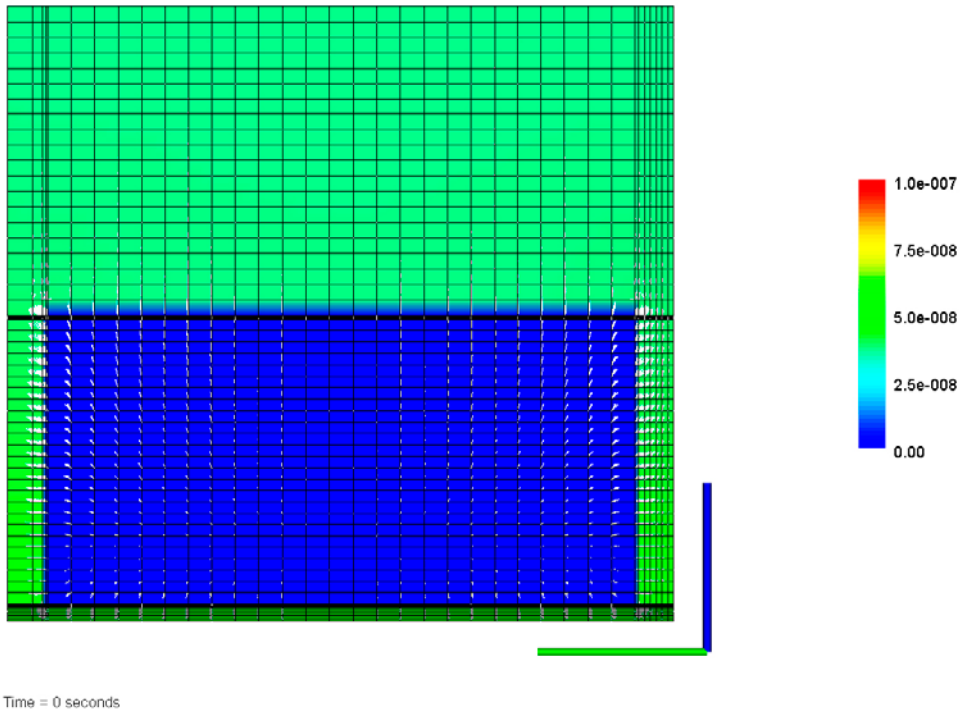

Figure A-25. *Vertical section through the centre of the caisson along the main axis of the 2BMA vault. The macadam fill between the caissons are shown at the left- and right-hand sides in the picture. Flux vectors are shown in white. Green axis=horizontal direction along to the main axis of the 2BMA vault. Blue axis= vertical direction. The legend shows the hydraulic head (m).*

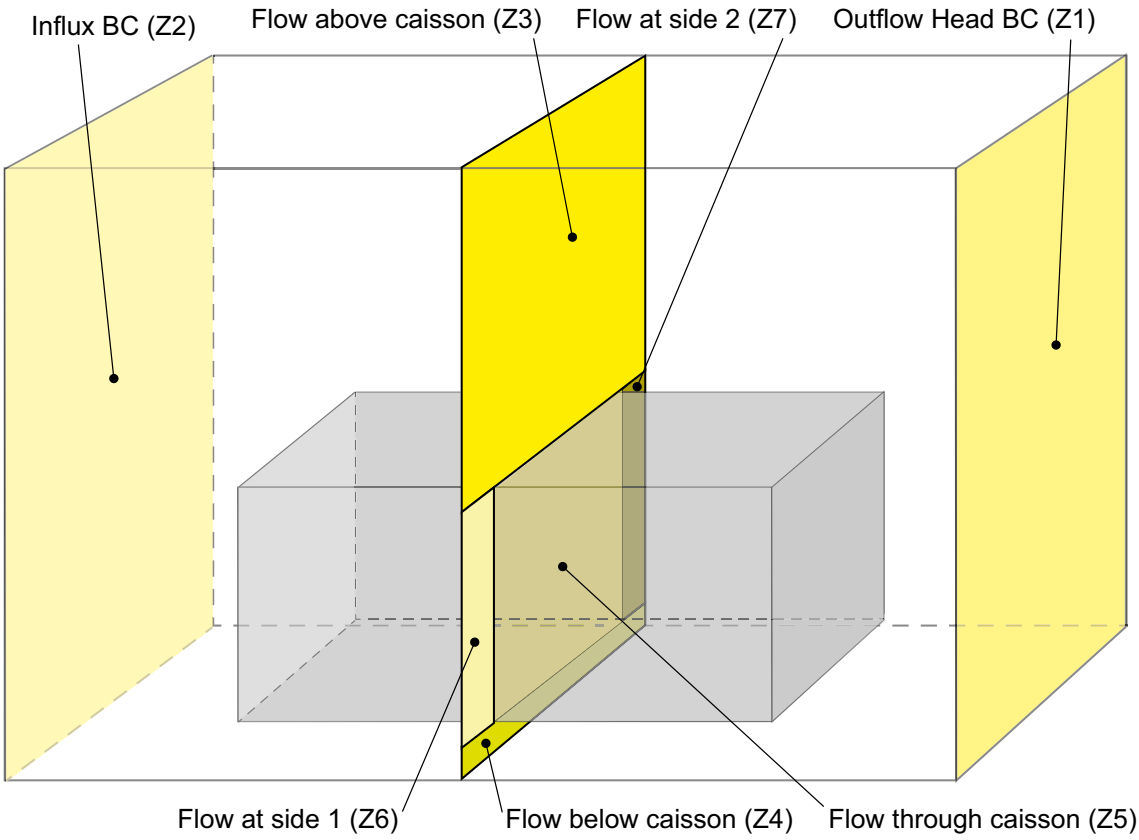

Figure A-26. *Illustration of the inspection zones assumed for evaluation of the flow distribution in the 3D-model of the 2BMA vault.*

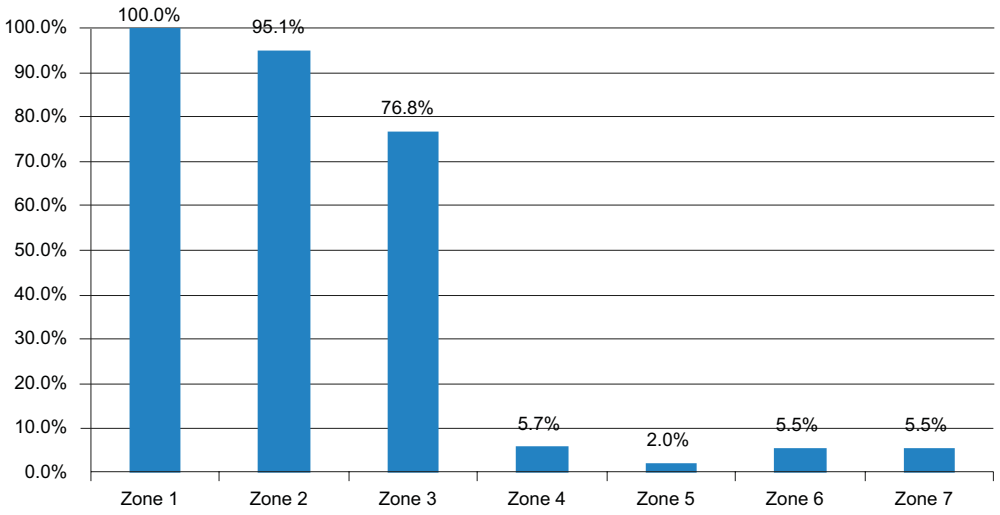

Figure A-27. *Flow distribution between zones in the model for 2BMA. Zone 5 is the flow through the caisson. Zone 3 and 4 are the flow above and below the caisson in the macadam fill. Zone 6 and 7 are the flow in the macadam at the sides, i.e. between different caissons.*

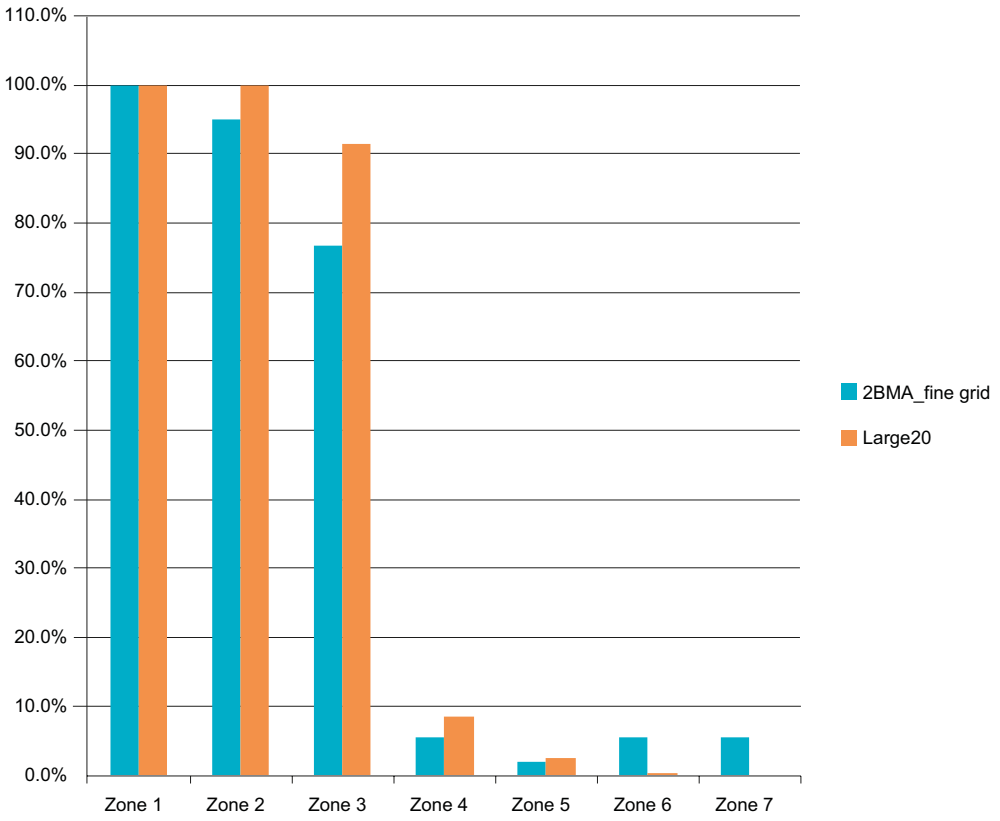

Figure A-28. *Comparison of flow distribution calculated for 2BMA with different models. The flow distribution calculated with the cell grid geometry used for the reactive transport modelling of 2BMA is denoted Large20. Zone 5 is the flow through the caisson. Zone 3 and 4 are the flow above and below the caisson in the macadam fill. Zone 6 and 7 are the flow in the macadam at the sides, i.e. between different caissons.*

Appendix B

Considerations for the Silo

B1 Assessment of physical fracturing processes in the Silo

The impact of fractures needs to be considered for the reinforced concrete barriers of the Silo. However, since the concrete is surrounded by bentonite, the impact of fractures on the groundwater flow may be less pronounced than in other parts of SFR. Nonetheless, fractures in the wall or bottom of the Silo may affect the hydraulic properties of the bentonite. Bentonite may tend to fill the fractures in the concrete, a process that may lead to a locally decreased bentonite concentration outside the concrete wall. Tests have shown that intrusion of bentonite into fractures is restricted to a depth of about 10 times the fracture aperture, which is judged negligible when fractures are small. Although the possible impact on the local hydraulic properties of bentonite in response to such fractures may need to be addressed in further studies, it has been judged to be beyond the scope of the present investigation.

For the Silo, the intrusion of chloride ions from the groundwater may be a limiting factor for the initiation of corrosion of reinforcement bars in the concrete walls and bottom. The latent period before corrosion is initiated depends on the thickness of concrete cover over the reinforcement bars at the outer part of the Silo wall. Since chloride intrusion has not been calculated for the Silo wall in this report, some rough estimates have been made based on earlier work. Gaucher et al. (2005) studied degradation processes in the Silo, but used an initial concentration of chloride in the concrete that is above the threshold chloride concentrations for depassivation of steel embedded in concrete. Comparing the calculations by Gaucher et al. (2005) with those presented in this report for chloride intrusion into the 2BMA barriers, suggests that an indicative latent period of about a hundred or a few hundred years could be relevant for the initiation of corrosion in the Silo wall. Reinforcement bars near the concrete surface will result in fractures in the overlying concrete, possibly leading to spalling of the surface layer. Corrosion of radial reinforcement bars may take longer, but is expected to eventually cause penetrating fractures in the Silo wall and bottom. Estimates of the progression of corrosion after initiation, using two different models (see description of models in the main report, Section 4.2), show that even low corrosion rates, of the order 0.05 µm/year would cause fractures in concrete after a few tens of years, see marking in Figure B-1 and Figure B-2.

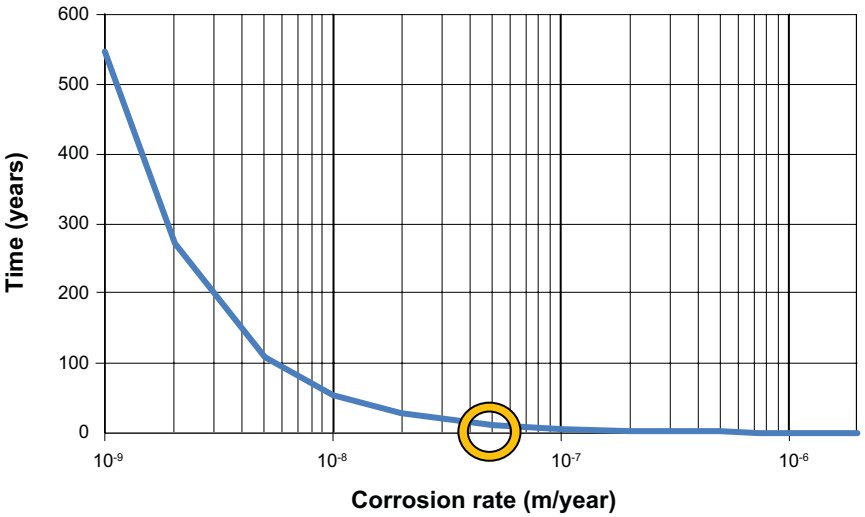

Figure B-1. *Calculated time to reach the critical stress that may initiate fracturing in the concrete cover due to corrosion of reinforcement bars. Solid, non-porous magnetite is assumed to form in this case. Initially the steel bars may be passivated; hence the time to initiate corrosion should be added to these estimates. The ring marks a corrosion rate of 0.05 µm/yr.*

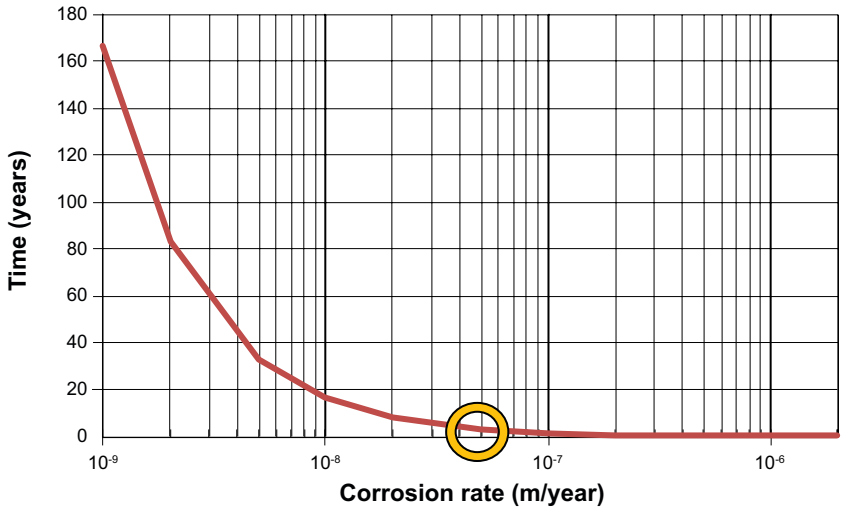

Figure B-2. *Calculated time to reach the critical stress in the concrete cover for different assumed corrosion rates of the reinforcement bars. Initially the steel bars may be passivated; hence the time to initiate corrosion should be added to these estimates. Model according to Li et al. (2005). The ring marks a corrosion rate of 0.05 µm/yr.*

Comparing the results of the chemical degradation modelling for 2BMA (this report) with earlier model studies for the Silo (Gaucher et al. 2005) suggests that leaching and other effects of chemical degradation would have a lower impact on the porosity, the effective diffusivity and the hydraulic conductivity of the Silo walls and bottom. The impact of physical degradation processes, in particular processes leading to formation of fractures (corrosion of reinforcement bars, dry-shrinkage, thermal contraction etc) has been found to be the dominating influence that reduces the barrier function of the Silo concrete barriers.

The propagation of the fracture width during corrosion is estimated to be fairly rapid, see Figure B-3.

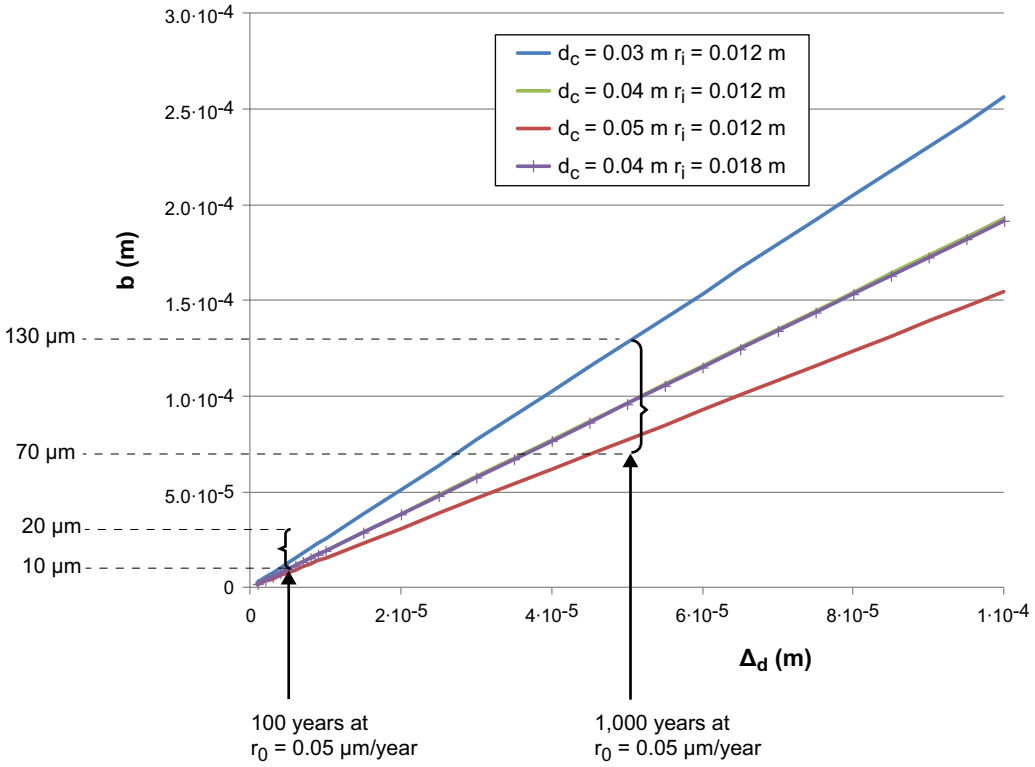

Figure B-3. *Calculated fracture widths b (m) versus corrosion depths (Δ_d) in concrete reinforcement bars. Different dimensions of the concrete cover layer (d_c) and the steel bars (r_i) have been assumed.*

The hydraulic conductivity of the Silo wall and bottom has been estimated, assuming that one fracture forms for every reinforcement bar. The results are presented in Figure B-4, and the two vertical lines show the limits of the likely distance between reinforcement bars, and therefore fractures (0.1–0.2 m). The green and red rings in Figure B-4 show the boundary hydraulic conductivities relating to the expected range of fracture widths after 100 and 1,000 years, respectively. The corresponding hydraulic conductivity intervals are $K = 4 \cdot 10^{-9}$–$7 \cdot 10^{-8}$ m/s (100 years) and $K = 1 \cdot 10^{-6}$–$2 \cdot 10^{-5}$ m/s (1,000 years).

As for the 2BMA vault, other parts of the SFR repository may be subjected to mechanical stresses caused by drying during operation and cooling due to resaturation with groundwater post-closure.

Since the Silo is reinforced, the total fracture width will be distributed over a larger number of fractures, hence the change in the width of each fracture will be reduced. The Silo is cylindrical, meaning that, as a pessimistic assumption, the dry-shrinkage/temperature contraction will cause a radial, longitudinal and tangential contraction of the construction. Due to the cylindrical form of the Silo, the tensile stresses may be lower than for the concrete barriers in other parts of the SFR repository. However, for the scoping calculations of this report it has been assumed that fractures may form, or that small fractures already present become dilated. The temperature in the silo constructions at the time of closure is assumed to be 12°C (based on measurements during operation in SFR) and the temperature in the groundwater has been assumed to 5–7°C (SKB 2014c). This gives a maximum temperature change of 7°C. Scoping calculations estimate that the dimensional change due to this is $-70 \cdot 10^{-6}$ m/m. This is within the range of threshold strains for concrete, i.e. 0.1–0.2‰. The total contraction would equal 3.7 mm over the full height of the Silo (52 m) and 6.1 mm over the periphery of the wall. Since the Silo has a significant diameter, a gradual cooling in contact with groundwater may create a radial temperature gradient in the construction, which means that there could be a tendency for increased tensile stresses in the longitudinal and tangential directions, which may promote fracturing or dilation of small fractures. This effect depends on whether the transport of heat is sufficiently rapid for temperature equilibrium to be established throughout the silo structure during the cooling, but this has not been quantified here.

The estimated impact on the overall hydraulic conductivity of the Silo concrete wall due to post-closure temperature contraction is presented in Figure B-5.

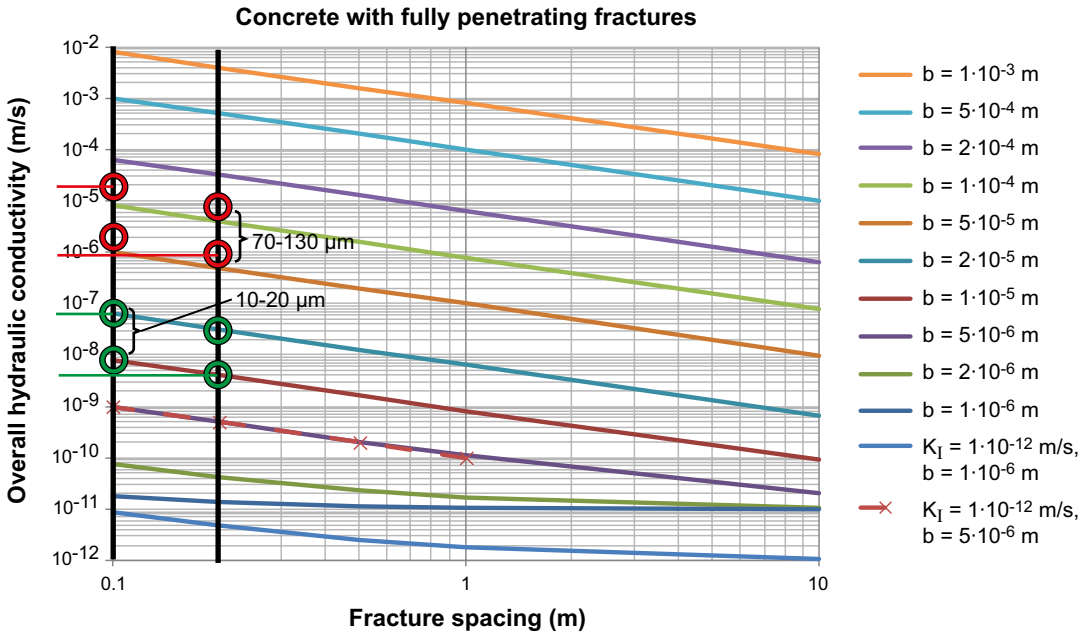

Figure B-4. *Hydraulic conductivities of the Silo concrete as a result of fractures formed by corrosion of reinforcement bars.*

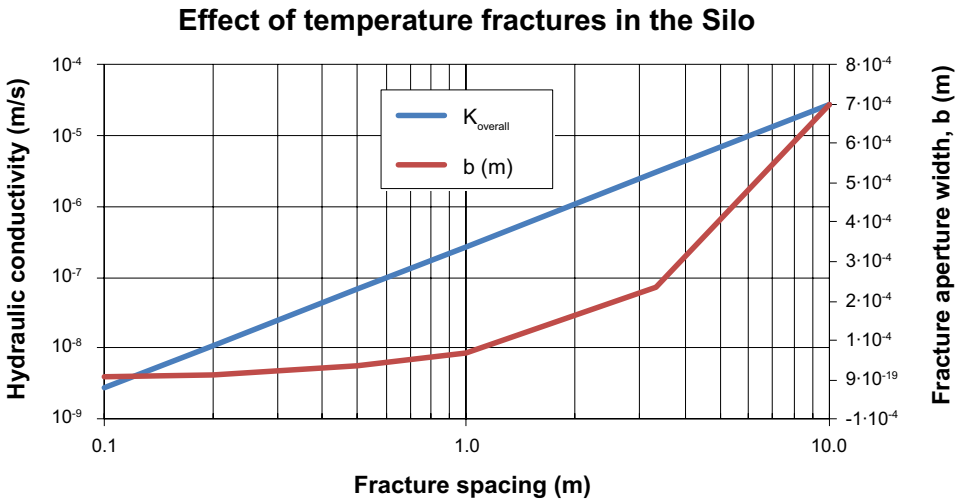

Figure B-5. *Estimated impact on the overall hydraulic conductivity of concrete barriers in the Silo caused by temperature contraction when groundwater resaturates the repository after closure. The figure also shows the predicted fracture aperture (b) as a function of the fracture spacing. A temperature change of 7°C has been assumed.*

B1.1 Chemical degradation of the Silo

No modelling has been conducted for the Silo concrete in this report. However, the general sequence of chemical leaching and interaction with different components in the groundwater calculated in this report for 2BMA shows similarities with the results of Gaucher et al. (2005) for the Silo. The differences in the timescales calculated reflect the reduced water transport in the Silo, due to the bentonite barrier, and some different basic assumptions of the studies such as the used databases and assumed initial conditions also affect the results. In brief, portlandite was found to be depleted to about 50% in the Silo wall after 10,000 years (Gaucher et al. 2005), whereas for 2BMA the portlandite is depleted after about 25,000 years (this report). The in-growth of ettringite in the Silo wall takes place during the period 500–10,000 years (Gaucher et al. 2005), compared with in-growth of ettringite in 2BMA from 10,000–40,000 years and of thaumasite from 20,000–100,000 years (this report). Leaching of the CSH-gel shows a minor transformation from CSH_1.8 to CSH_1.1 during a 100,000 year period for the Silo (Gaucher et al. 2005), whereas in 2BMA a significant transformation takes place of CSH_1.8 to CSH_1.1 during the period 3,000–30,000 years and further to CSH_0.8 during 35,000–70,000 years, followed by a partial depletion of the CSH_0.8 up to 100,000 years (this report). For the Silo, no final state of severely chemically degraded concrete is reached during 100,000 years (Gaucher et al. 2005).

B1.2 Proposed data for the Data report – the Silo

Parameter values for the Silo have been proposed following the same general strategy as for BMA (see previous section). It can be noted that the Silo concrete has a considerable number of reinforcement bars; hence the impact of fractures caused by corrosion has been considered (see main report Section 4.2). The proposed ranges of values for the hydraulic conductivity of the concrete walls of the Silo are presented in Figure B-6 and the corresponding values for the effective diffusivity are presented in Figure B-7. In both figures the proposed values for 2BMA as well as the values used in the concrete degradation modelling of 2BMA are shown for comparison.

The different stages of degradation for the concrete barriers in the Silo are described in Table B-1.

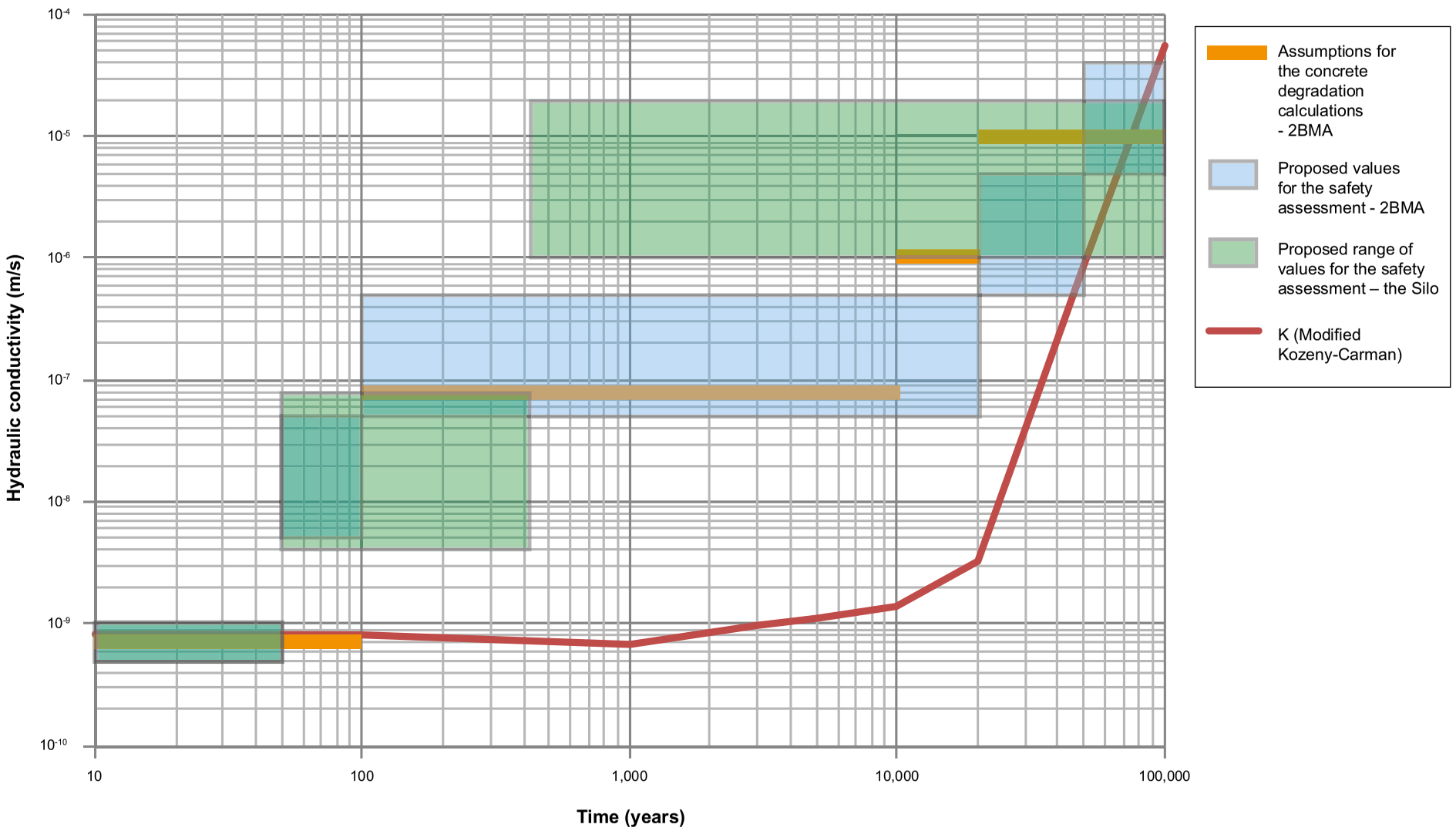

Figure B-6. *Proposed range of values for the hydraulic conductivity in construction concrete in the Silo. The hydraulic conductivities calculated for 2BMA as well as the initial estimates of the gradual change of the hydraulic conductivity assumed in the PHAST modelling for 2BMA are shown as comparison.*

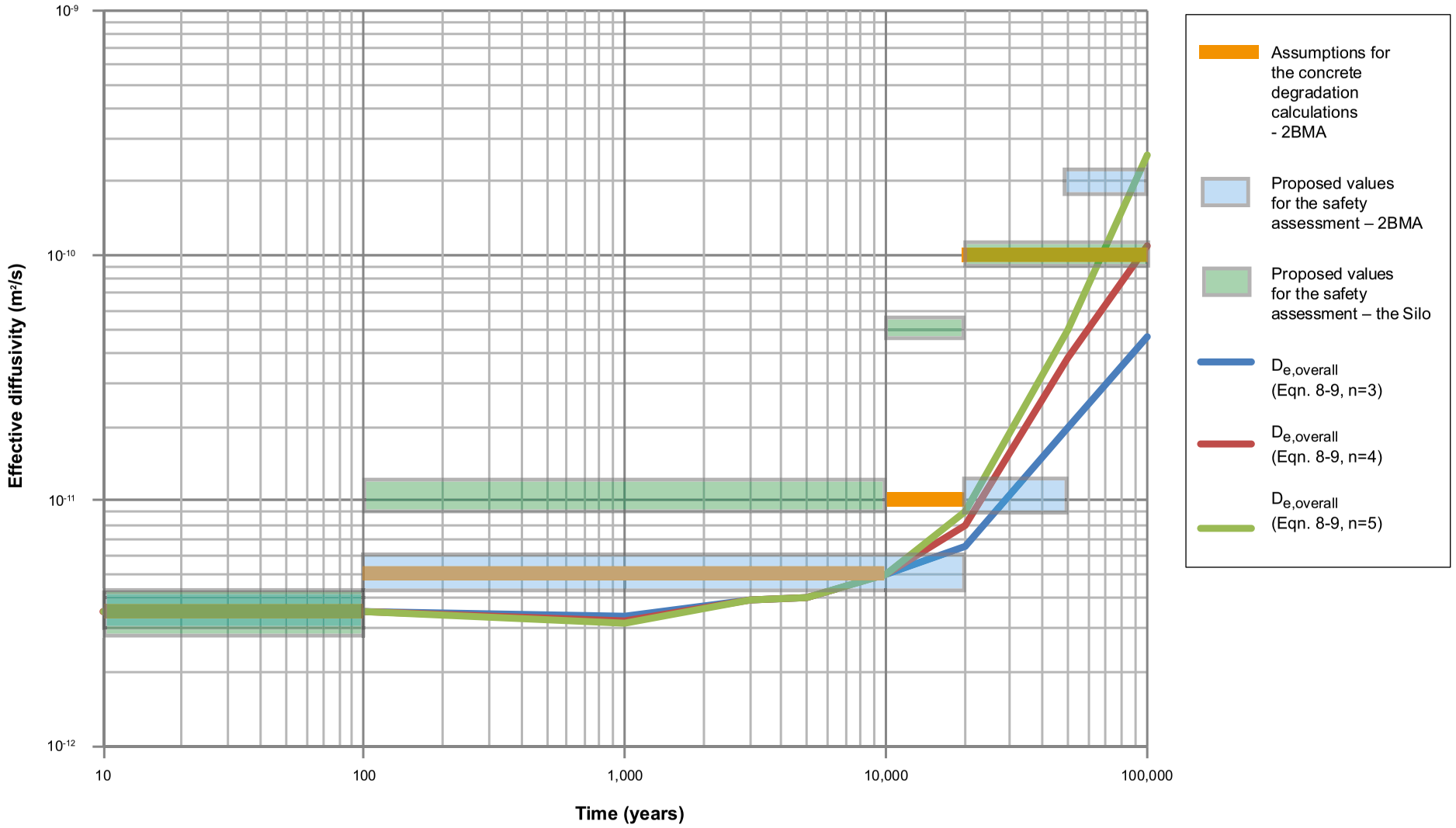

Figure B-7. *Proposed values for the effective diffusivity in construction concrete in the Silo. The effective diffusivities calculated for 2BMA as well as the initial estimates of the gradual change of the effective diffusivity assumed in the PHAST modelling for 2BMA are shown as comparison.*

Table B-1. Description of different stages of concrete degradation in the Silo and proposed values of the hydraulic conductivity, effective diffusivity and porosity. The time scale is indicative.

Condition of concrete barriers in the silo	General description	Typical pH	K-value (m/s)	Effective diffusivity [1] (m^2/s)	Porosity [1] (m^3/m^3)	Indicative time scale (preliminary)
Initial state	Fresh, fully hydrated concrete, essentially unaffected by degradation processes. Some carbonatisation during operational phase. Some minor interaction with soluble components in the bentonite may be initiated. No significant leaching by groundwater. No significant impact by components in groundwater or waste. Dry shrinkage may have caused or dilated fractures but is restricted by the presence of reinforcement.	12.5–13 determined by alkali hydroxides	$8.3\cdot10^{-10}$ (construction) $8.3\cdot10^{-10}$ (moulds) $8.3\cdot10^{-9}$ (grout)	$3.5\cdot10^{-12}$ (c) $3.5\cdot10^{-12}$ (m) $3.5\cdot10^{-10}$ (g)	0.11 (c) 0.11 (m) 0.3 (g)	0 yr
Change of temperature due to groundwater inflow	Contraction of the concrete barriers due to decreased temperature but the effect on formation or dilation of fractures is restricted by the presence of reinforcement. Effects of radial temperature gradients need consideration. No significant leaching of any major components at this stage. No significant interaction with components in groundwater or waste.	12.5–13 determined by alkali hydroxides	$4\cdot10^{-9}$–$1\cdot10^{-7}$ (construction) $2\cdot10^{-7}$ (moulds) $4\cdot10^{-7}$ (grout)	$3.5\cdot10^{-12}$ (c) $3.5\cdot10^{-12}$ (m) $3.5\cdot10^{-10}$ (g)	0.11 (c) 0.11 (m) 0.3 (g)	before 100 yr
Corrosion of reinforcement bars	Chloride initiation may take time. However, Gaucher et al. (2005) has assumed an initial chloride concentration which is above the threshold concentration where corrosion can be assumed to be initiated. Assuming a low initial chloride concentration in the concrete and the bentonite, estimates for 2BMA (this report) combined with rough estimates from Gaucher et al. (2005) give that the time lag for reaching chloride concentrations above the threshold concentration may be of the order of one hundred – a few hundreds of years. The estimates are dependent on the thickness of the concrete cover of the reinforcement bars. Reinforcement in the outer part of the wall will start corrode first. Bars in the longitudinal and tangential direction of the silo wall will cause fractures near the surface and may eventually cause peeling of the cover layer. Radial reinforcement bars (assuming such bars are present) will cause penetrating fractures in the wall. Slow general corrosion estimated for 1BMA show that fractures may appear in the concrete after a few decades, at most 100 years after initiation (this report, Figure B-1 and Figure B-2). Propagation of fracture dilatation due to corroding reinforcement is fairly rapid. Possible presence of radial reinforcement bars will cause penetrating fractures through the silo wall. Estimated fracture width after 100 years may be in the range of 10–20 µm (see Figure B-3, this report), one fracture formed for each reinforcement bar. After 1,000 years the fracture width is estimated to 70–130 µm, one fracture formed for each reinforcement bar. Assuming a spacing between reinforcement bars of 0.1–0.2 m give (Figure B-4 this report) Koverall = $4\cdot10^{-9}$–$7\cdot10^{-8}$ m/s (at 100 years) and at 1,000 years Koverall = $1\cdot10^{-6}$–$2\cdot10^{-5}$ m/s.	12.5 determined by portlandite	$4\cdot10^{-9}$–$7\cdot10^{-7}$ (construction) $2\cdot10^{-7}$ (moulds) $4\cdot10^{-7}$ (grout)		0.11 (c) 0.11 (m) 0.3 (g)	50–500 yr
				$1\cdot10^{-11}$ (c) $2\cdot10^{-11}$ (m) $3.5\cdot10^{-10}$ (g)		100– 10,000 yr

Condition of concrete barriers in the silo	General description	Typical pH	K-value (m/s)	Effective diffusivity [1] (m^2/s)	Porosity [1] (m^3/m^3)	Indicative time scale (preliminary)
Corrosion of reinforcement bars	It must be considered likely that the surrounding bentonite may relocate and partly fill up the fractures close to the fracture entrance. However, tests with bentonite suggest that fractures may be filled by bentonite to a maximum depth of 10 times the fracture aperture. For the fracture apertures calculated for the silo wall the effect on the overall hydraulic conductivity by infilling bentonite is therefore judged negligible.					
Leaching of portlandite	Leaching of one of the most prominent cement components, the portlandite, has progressed at the interface with the bentonite. The porosity has locally increased as a result of the leaching. However, the ingrowths of minerals like ettringite and possibly also Friedel's salts and its interaction with monocarboaluminate may counteract porosity changes, but it remains uncertain if this has other effects that may be negative for the concrete properties. The calculations for the silo presented by Gaucher et al. (2005) and the calculations for 2BMA presented in this report are reasonably coherent.	12.5 determined by portlandite	$1 \cdot 10^{-6}$–$2 \cdot 10^{-5}$ (construction) $2 \cdot 10^{-5}$ (moulds) $4 \cdot 10^{-5}$ (grout) The impact by leaching on the hydraulic conductivity is negligible in comparison with the impact of fractures		0.15–0.17(c) 0.11 (m) 0.3 (g)	500–20,000 yr
				$5 \cdot 10^{-11}$ (c) $1 \cdot 10^{-10}$ (m) $5 \cdot 10^{-10}$ (g)		10,000–20,000 yr
Leaching of CSH-gels, ingrowths of ettringite and thaumasite	Portlandite has been depleted. A gradual transformation of the concrete from calcium-rich to calcium-depleted minerals proceeds. The ingrowths of ettringite and thaumasite may potentially cause fractures and may restrict the mechanical strength. Calculations by Gaucher et al. (2005) show a limited transformation of CSH-gels to less calcium-rich phases during 100,000 years. A certain ingrowth of ettringite takes place during 500–>10,000 years in reasonable agreement with calculations for 2BMA (this report). Gaucher et al. (2005) do not consider thaumasite.	12.5–10.8 determined by CSH-gels of varying composition	$1 \cdot 10^{-6}$–$2 \cdot 10^{-5}$ (construction) $2 \cdot 10^{-5}$ (moulds) $4 \cdot 10^{-5}$ (grout) The impact by leaching on the hydraulic conductivity is negligible in comparison with the impact of fractures	$1 \cdot 10^{-10}$ (c) $1 \cdot 10^{-10}$ (m) $1 \cdot 10^{-9}$ (g)	0.17–0.25 (c) 0.11 (m) 0.3 (g)	20,000–100,000 yr
Severely leached and altered concrete	The concrete is essentially depleted of its cement mineral. Different reaction fronts have passed through the structure, including ettringite, thaumasite, monocarboaluminate and brucite. Significant precipitation of calcite. This state is not expected to be reached during the first 100,000 years according to the calculations by Gaucher et al. (2005).	–	–	–	–	> 100,000 yr

[1] (c) = construction concrete.
(m) = concrete moulds.
(g) = concrete grout.

Appendix C

Results for Case Large8

In this appendix provides supplemental graphical presentation of the model results for case Large8. The reader i referred to the corresponding chapter in the main report for comments on the identified interactions between the different chemical components, as well as for orientation about the position of the different evaluation points and sections through the model used in some of the graphs.

pH evolution during the first 100 years

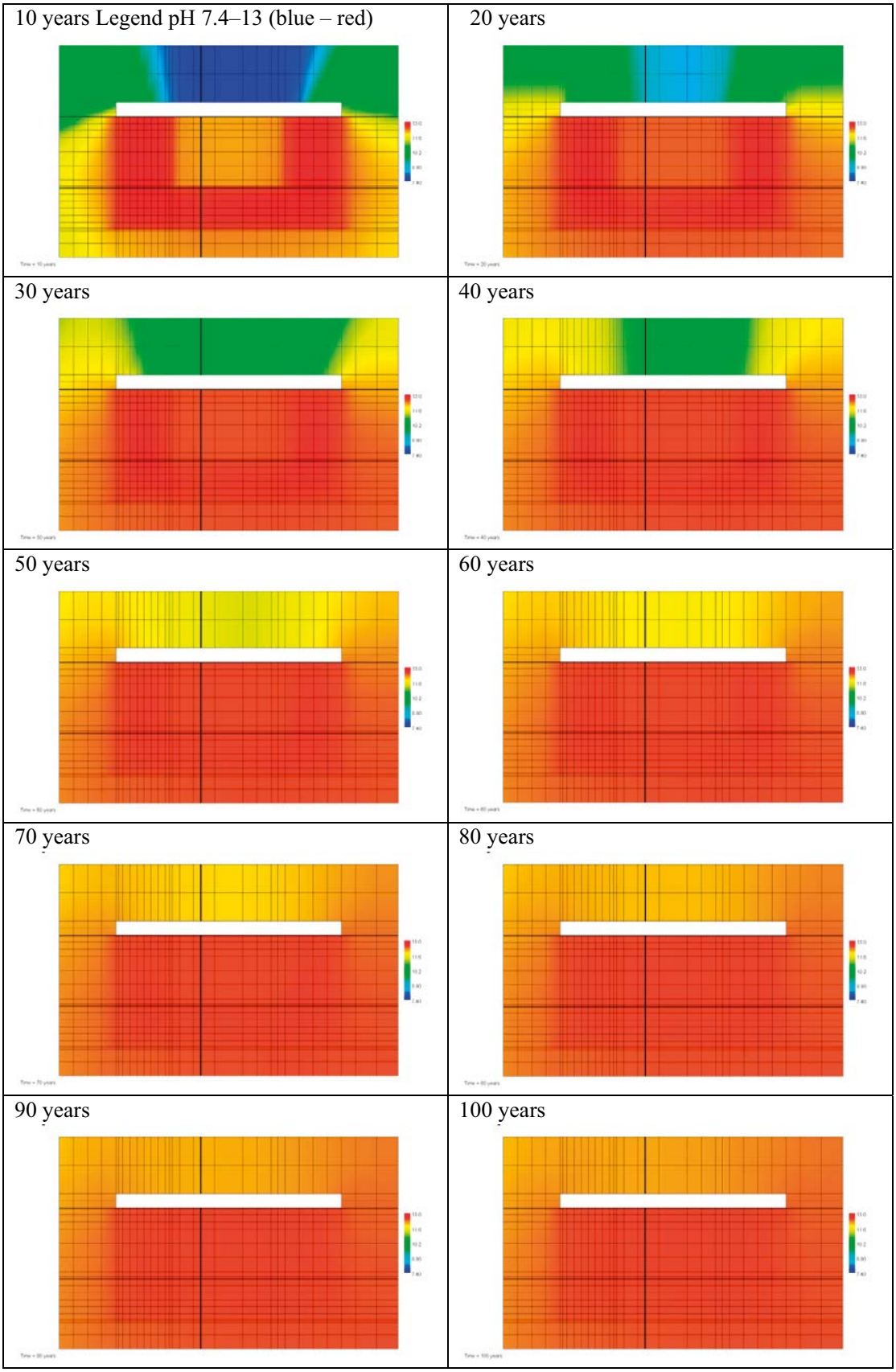

Figure C-1. *Details of the pH evolution during the first 100 years in 10 year steps. (Cemdata07 database, Case Large8.) The legend shows the pH span 7.4 (blue)–13 (red).*

pH evolution over longer time

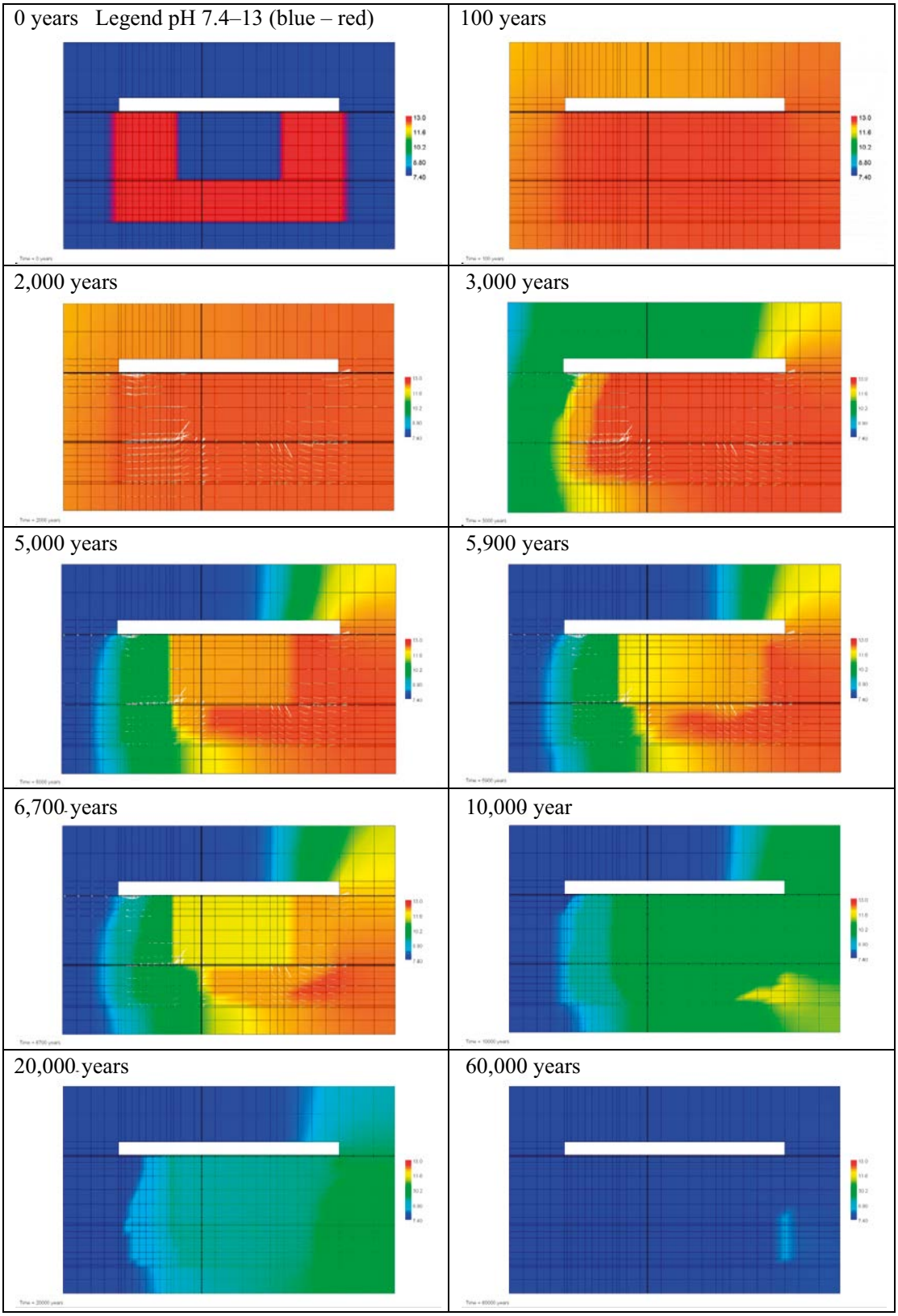

Figure C-2. *Snap-shots of the pH distribution at 0, 100, 2,000, 3,000, 5,000, 5,900, 6,700, 10,000, 20,000 and 60,000 years. (Cemdata07 database, Case Large8.) The legend shows the span pH 7.4 (blue)–13 (red).*

Depletion of calcium (mol/kg pore water)

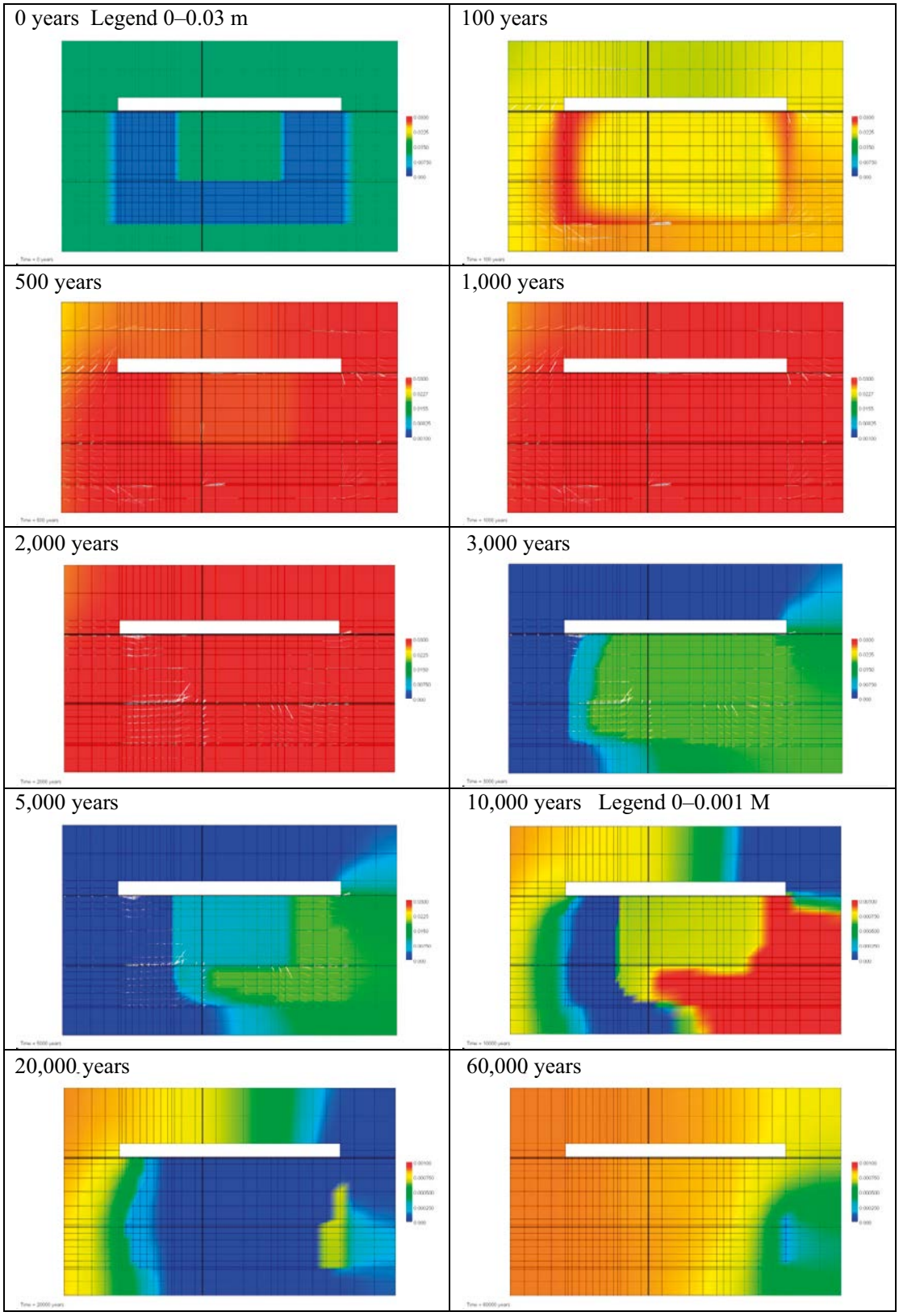

Figure C-3. *Snap-shots of the dissolved calcium concentrations at 0, 100, 500, 1,000, 2,000, 3,000, 5,000, 10,000, 20,000 and 60,000 years. Observe the change of scale after 10,000 years (Legend shows 0–0.03 m during the first 5,000 years and 0–0.001 m after 10,000 years). (Cemdata07 database, Case Large8.) Units (mol/kg pore water).*

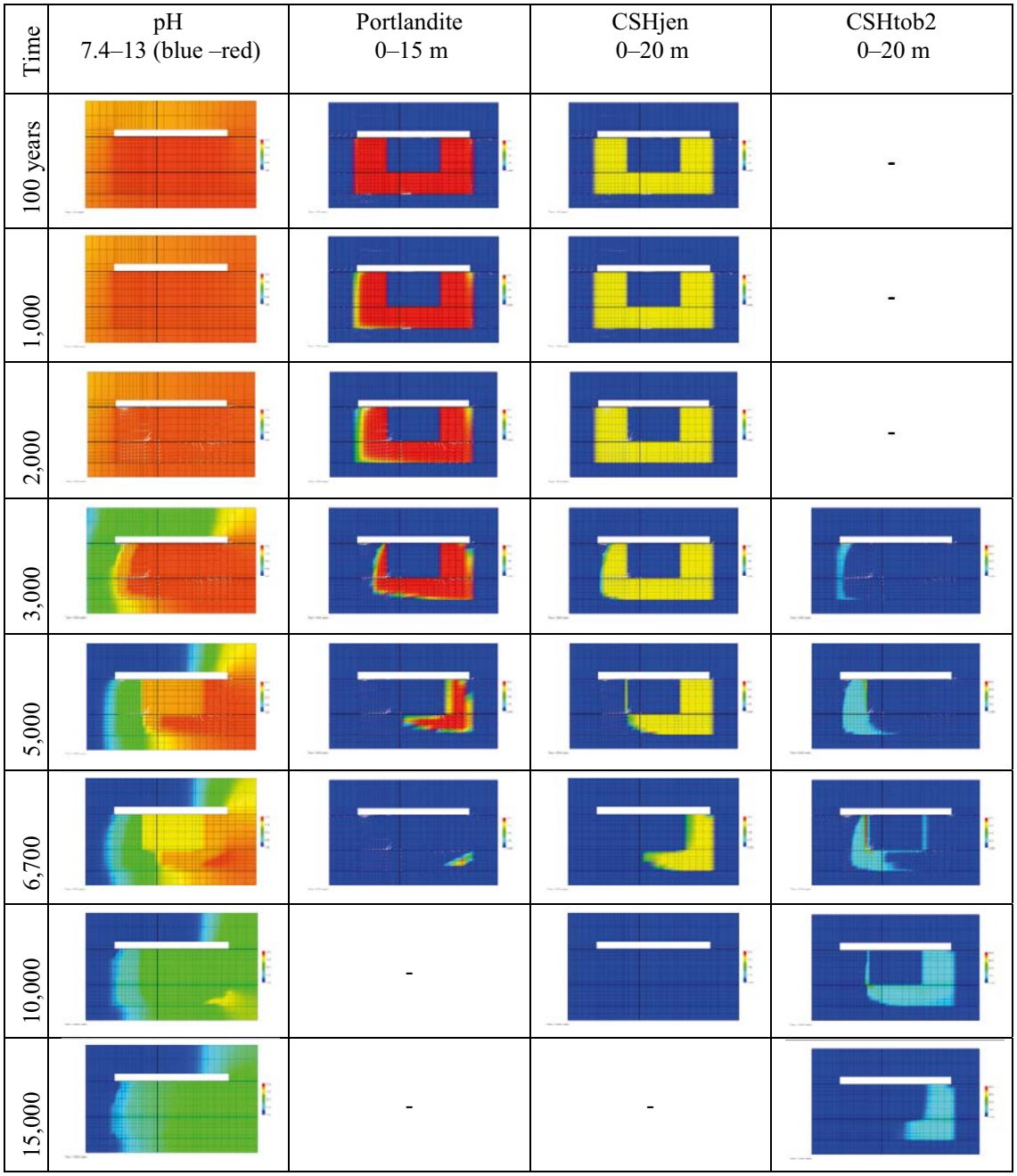

Figure C-4. *Illustration of the gradual evolution of pH as a result of depletion and transformation of mineral phases containing calcium after 100, 1,000, 2,000, 3,000, 5,000, 6,700, 10,000 and 15,000 years. (Cemdata07 database, Case Large8.) Units (mol/kg pore water).*

Silica depletion

Time	Dissolved silica Legend 0 – 0.0001 m	Portlandite Legend 0 – 15 m	CSHjen Legend 0 – 20 m	CSHtob2 Legend 0 – 20 m
100 years	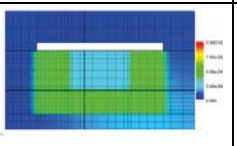	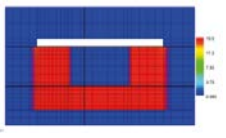	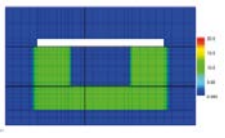	-
1,000	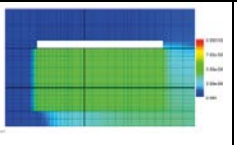		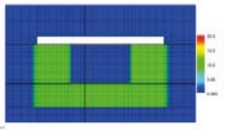	-
2,000	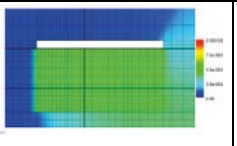		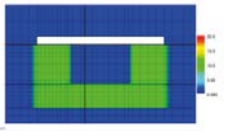	-
3,000	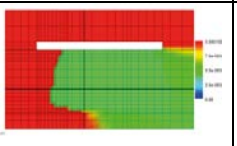	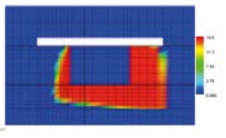	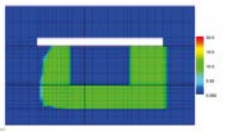	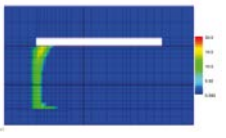
5,000	Legend 0 – 0.006 M 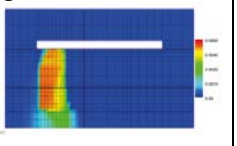	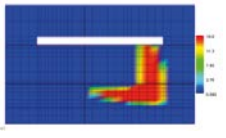	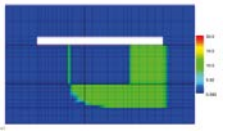	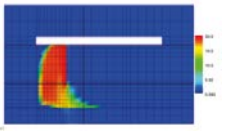
6,700	Legend 0 – 0.006 M 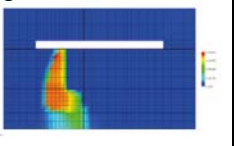	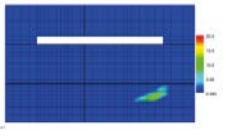	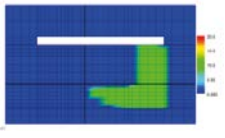	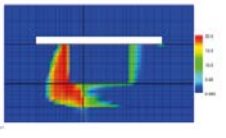
10,000	Legend 0 – 0.006 M 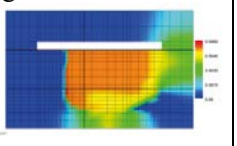	-		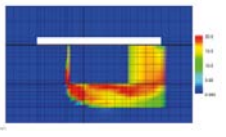
15,000	Legend 0 – 0.006 M 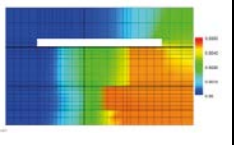	-	-	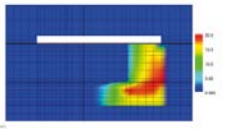
20,000	Legend 0 – 0.006 M 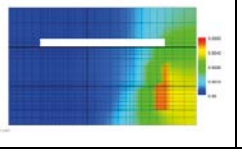	-	-	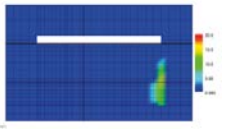

Figure C-5. *Illustration of the gradual change in the concentration of dissolved silica in response to depletion and transformation of CSH-gel phases and portlandite after 100, 1,000, 2,000, 3,000, 5,000, 6,700, 10,000, 15,000 and 20,000 years. (Cemdata07 database, Case Large8). Units (mol/kg pore water).*

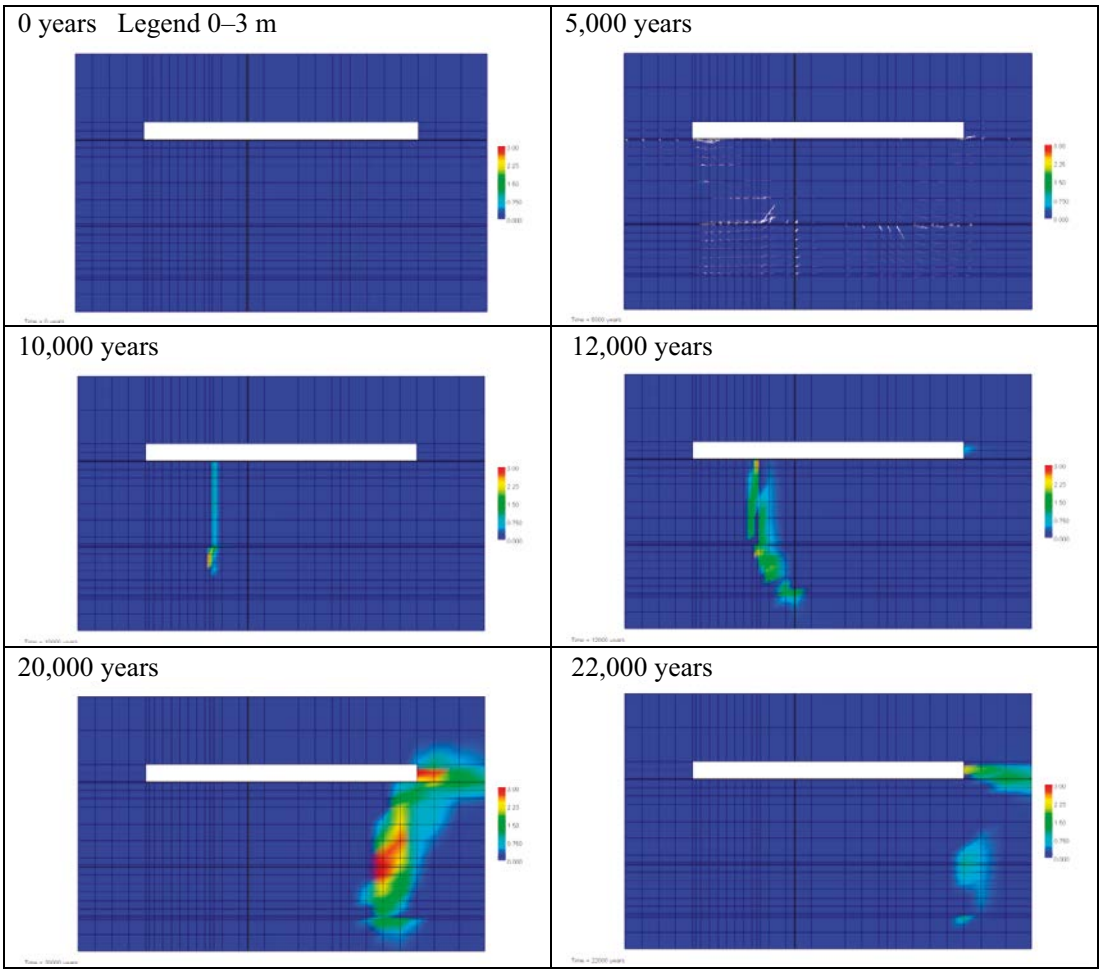

Figure C-6. *Snap-shots of SiO_2am at 0, 5,000, 10,000, 12,000, 20,000 and 22,000 years. (Cemdata07 database, Case Large8.) Units (mol/kg pore water).*

Carbonate and minerals containing carbonate

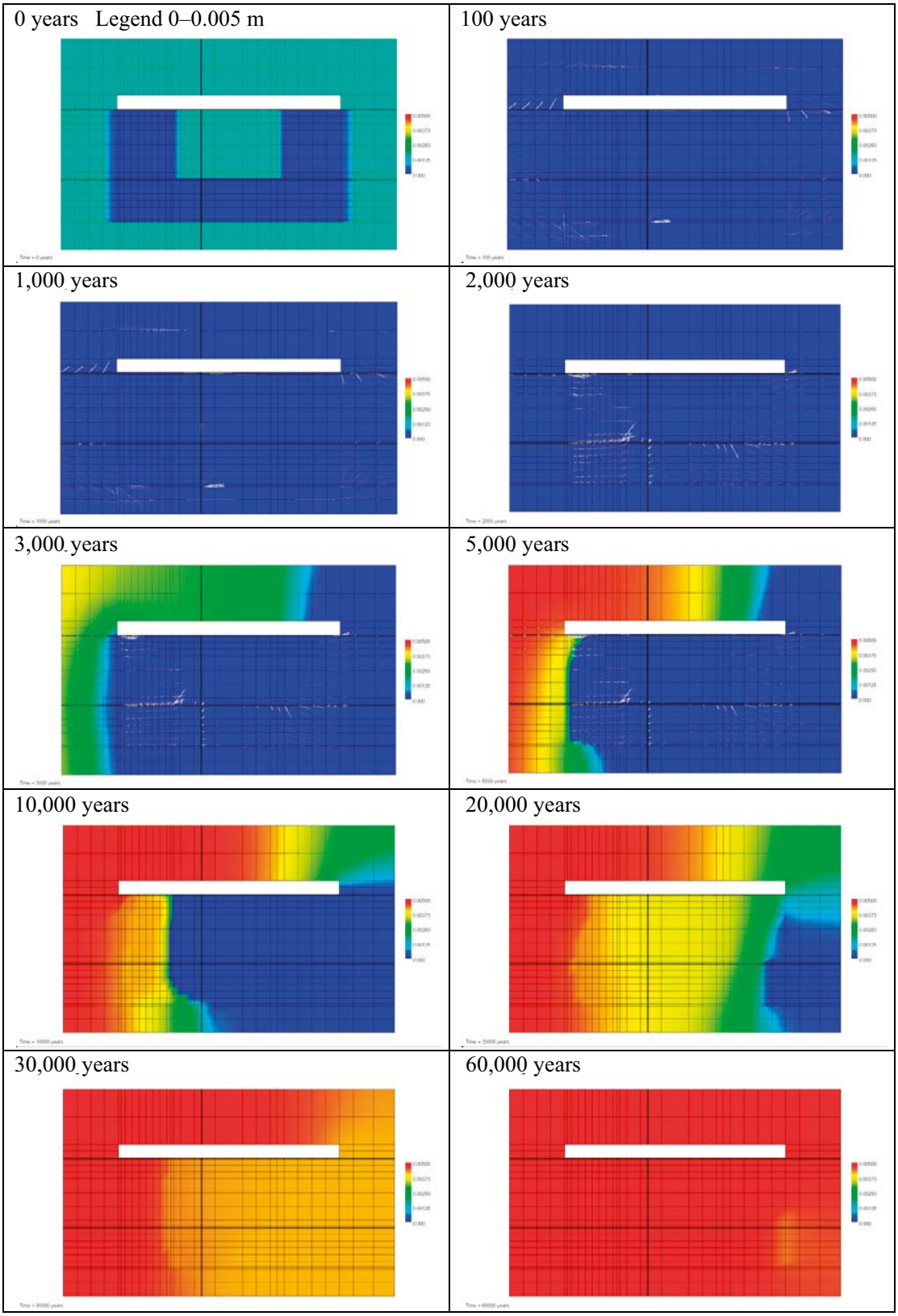

Figure C-7. *Snap-shots of the dissolved carbonate concentrations after 0, 100, 1,000, 2,000, 3,000, 5,000, 10,000, 20,000, 30,000 and 60,000 years. (Cemdata07 database, Case Large8.) Units (mol/kg pore water).*

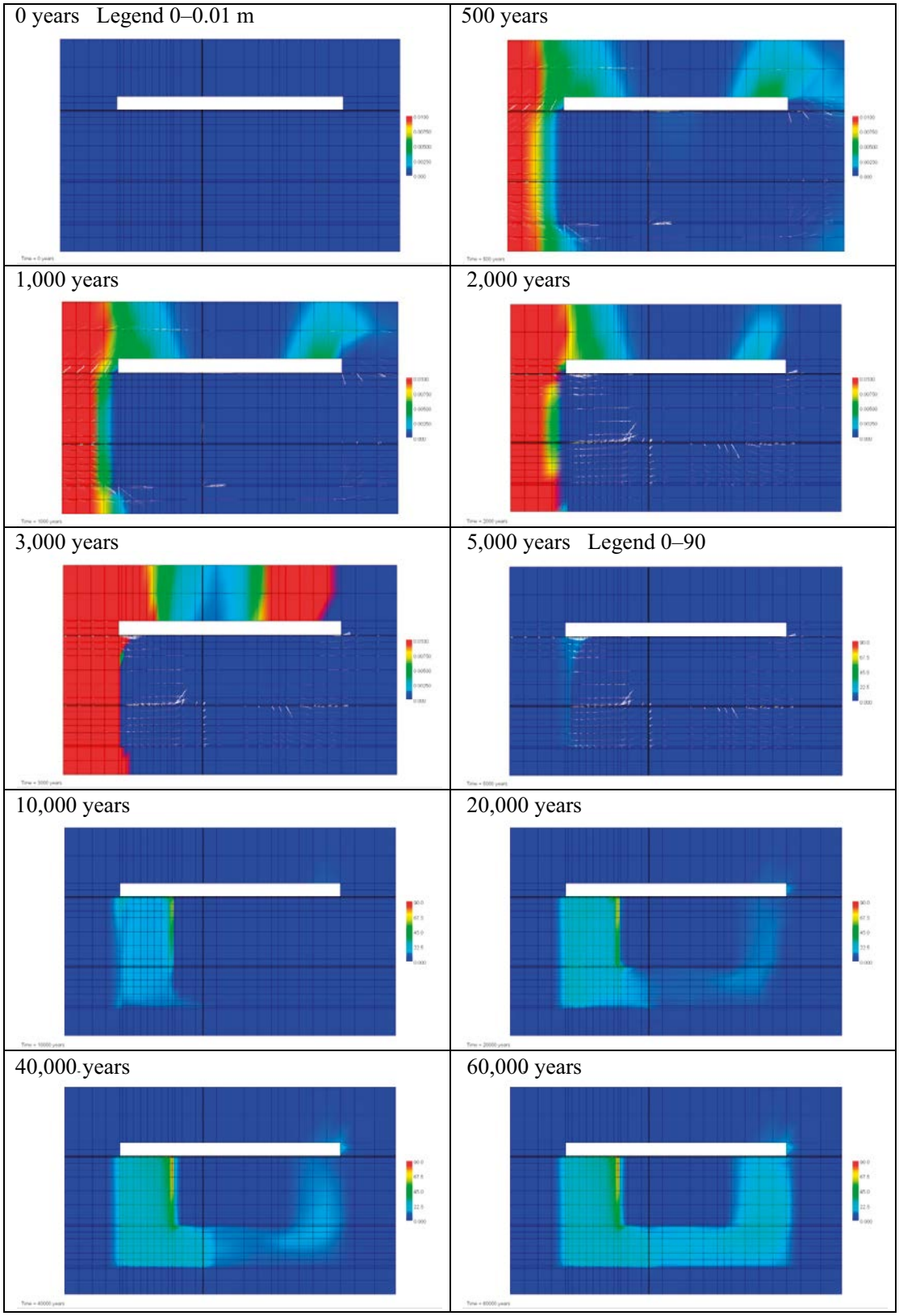

Figure C-8. *Snap-shots of calcite after 0, 500, 1,000, 2,000, 3,000, 5,000, 10,000, 20,000, 40,000 and 60,000 years. Observe the change of scale after 5,000 years. (Cemdata07 database, Case Large8.) Units (mol/kg pore water).*

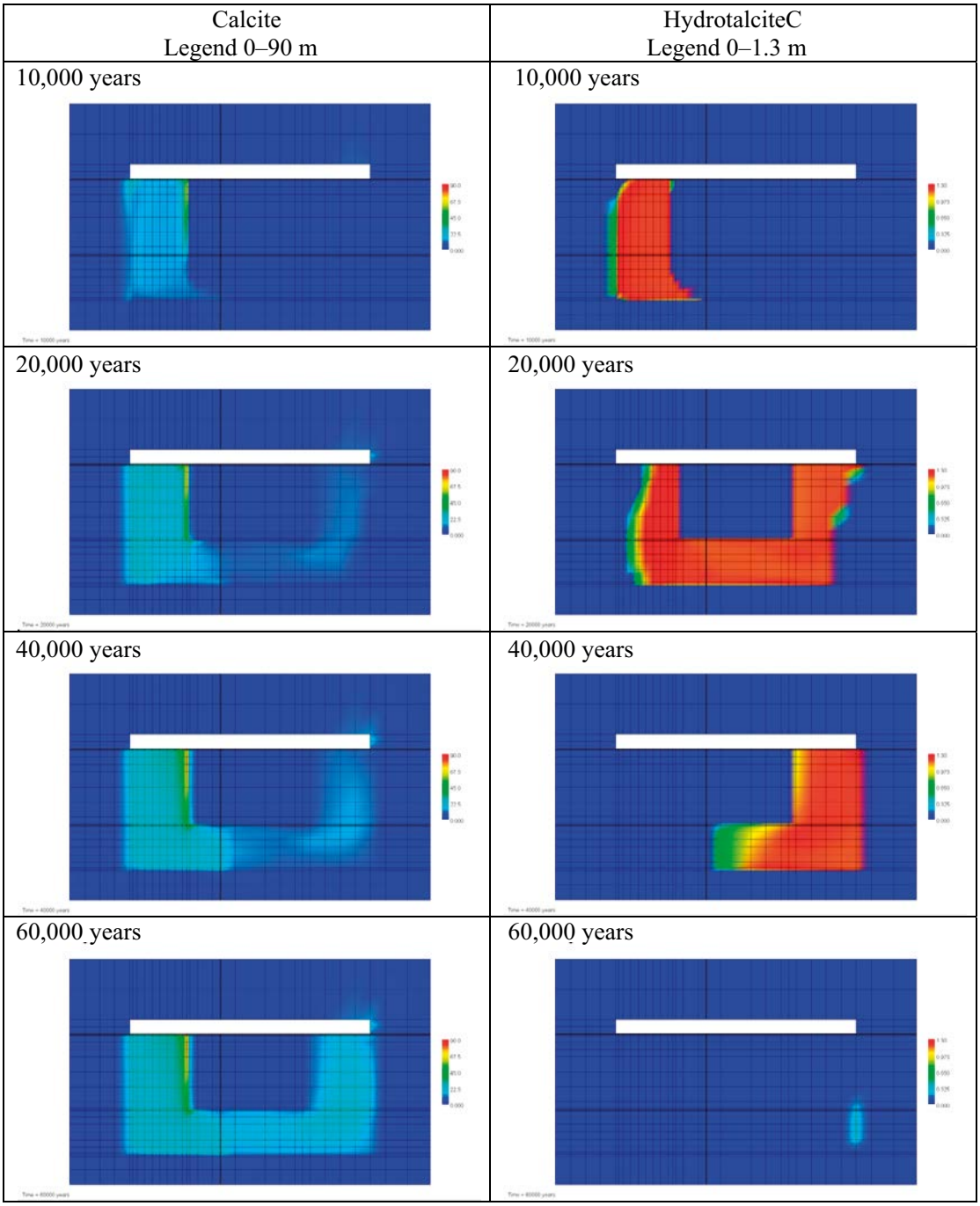

Figure C-9. *Illustration of the gradual transformations between concrete mineral phases containing carbonate over time. (Cemdata07 database, Case Large8.) Units (mol/kg pore water).*

Magnesium and minerals containing magnesium

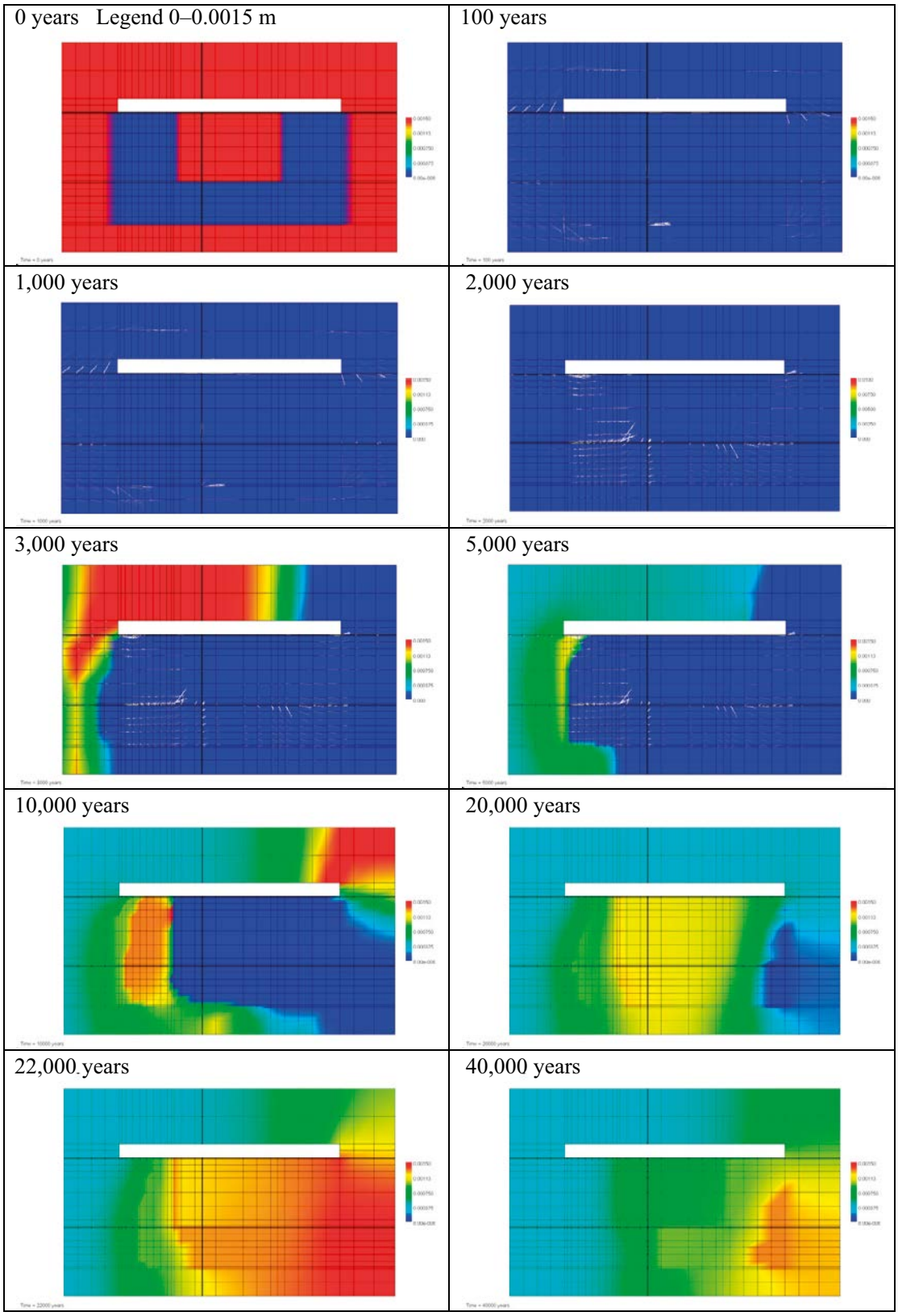

Figure C-10. *Snap-shots of the dissolved magnesium concentrations after 0, 100, 1,000, 2,000, 3,000, 5,000, 10,000, 20,000, 22,000 and 40,000 years. (Cemdata07 database, Case Large8.) Units (mol/kg pore water).*

HydrotalciteFe Legend 0–1 m	HydrotalciteOH Legend 0–1.5 m	HydrotalciteC Legend 0–1.3 m	Brucite Legend 0–0.1 m
0 years 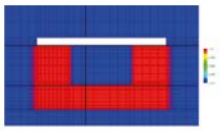	0 years 	0 years 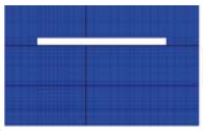	0 years 
3,000 years 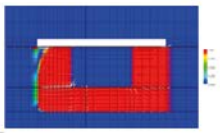	3,000 years 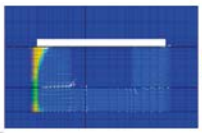	3,000 years 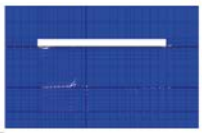	3,000 years 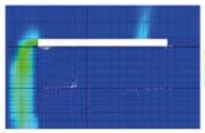
5,000 years 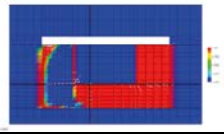	5,000 years 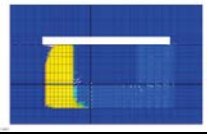	5,000 years 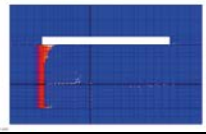	5,000 years 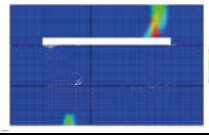
10,000 years 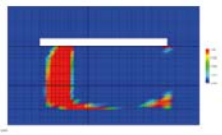	10,000 years 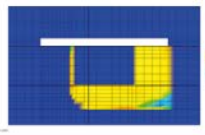	10,000 years 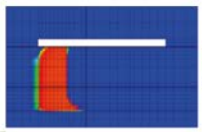	10,000 years 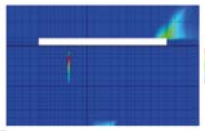
20,000 years 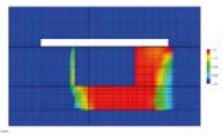	21,000 years 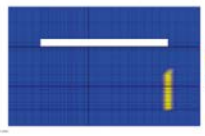	20,000 years 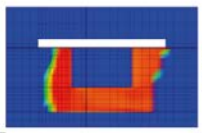	-
30,000 years 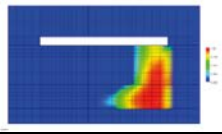	-	30,000 years 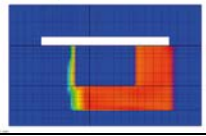	-
40,000 years 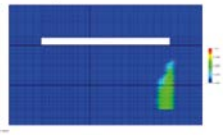	-	40,000 years 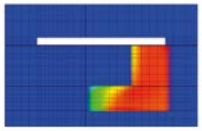	-

Figure C-11. *Illustration of the gradual transformations between concrete mineral phases containing magnesium over time. (Cemdata07 database, Case Large8.) Units (mol/kg pore water).*

Iron and minerals containing iron

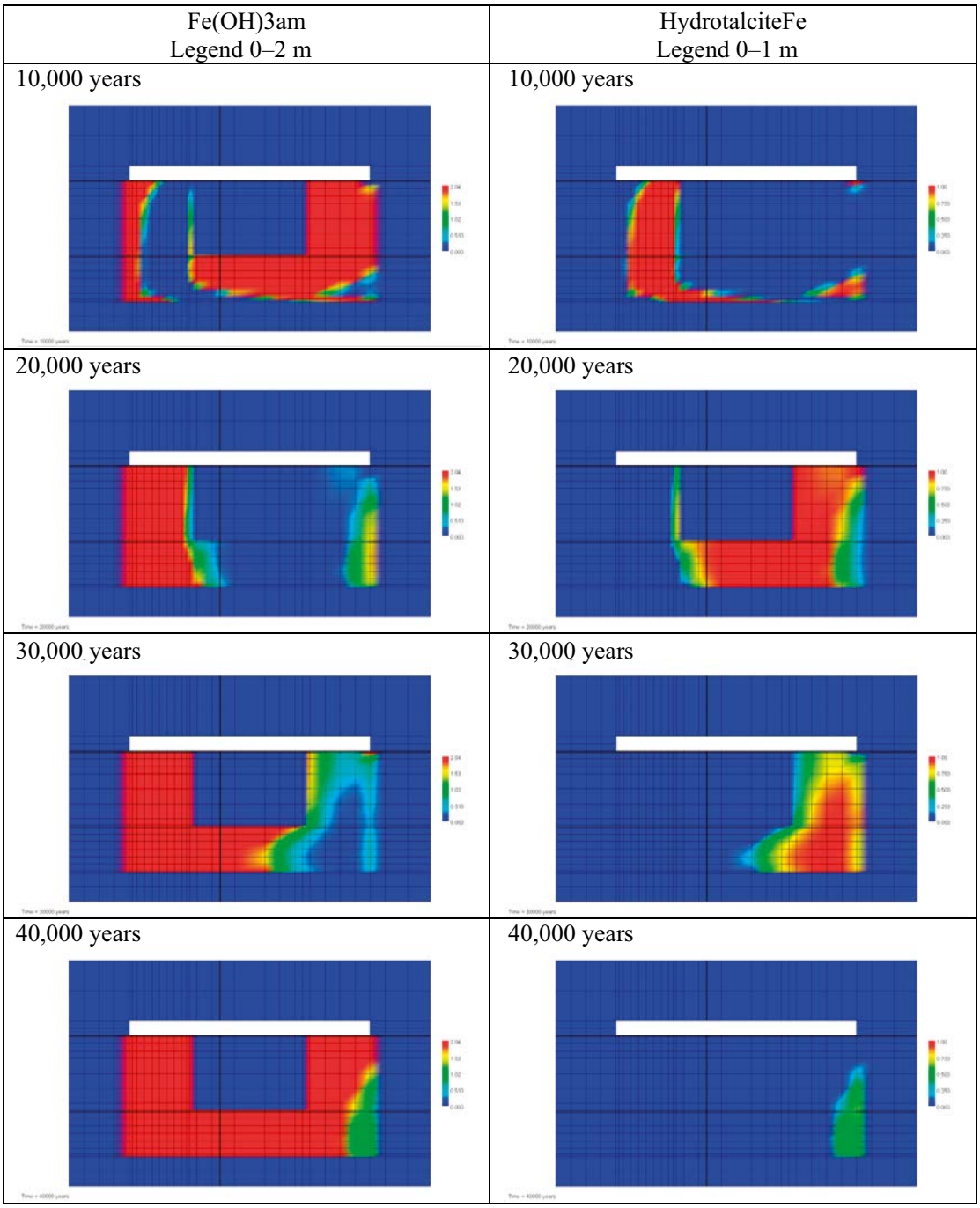

Figure C-12. *Illustration of the gradual transformations between concrete mineral phases containing iron over time. (Cemdata07 database, Case Large8.) Units (mol/kg pore water).*

Dissolved species – inspection point AE

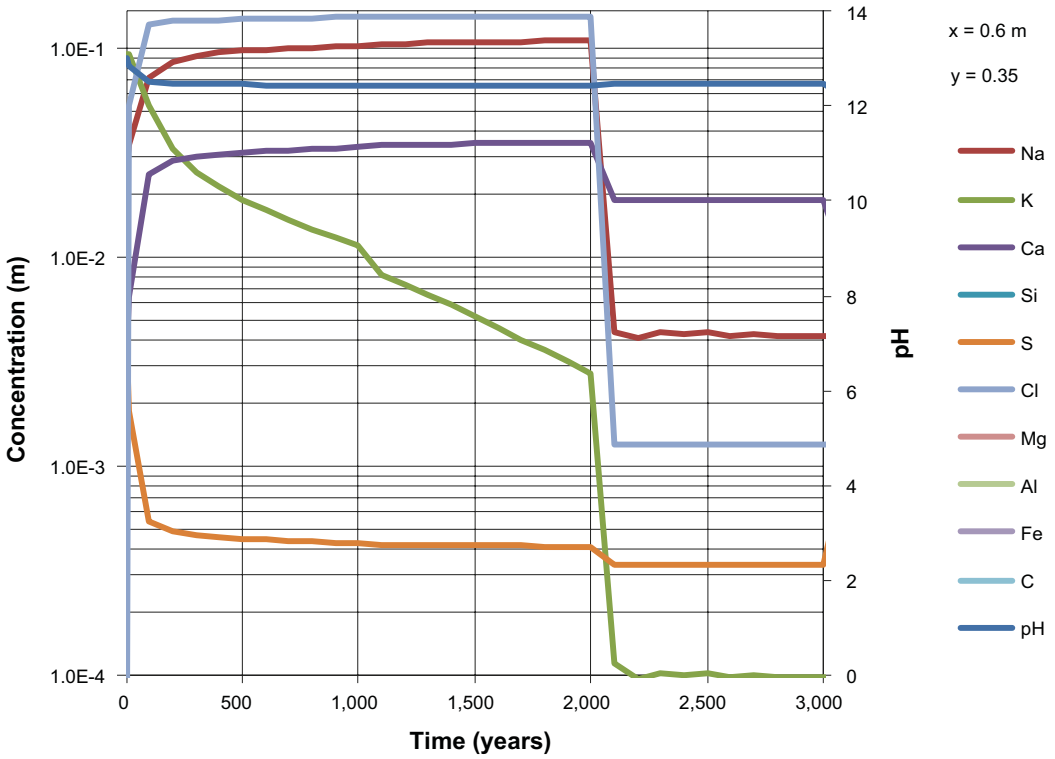

Figure C-13. *The development of the concentration of dissolved components in concrete pore water over time (during the first 3,000 years) at position AE, case Large8. Observe the logarithmic concentration scale. Units (mol/kg pore water).*

Ion exchange species – inspection point AE

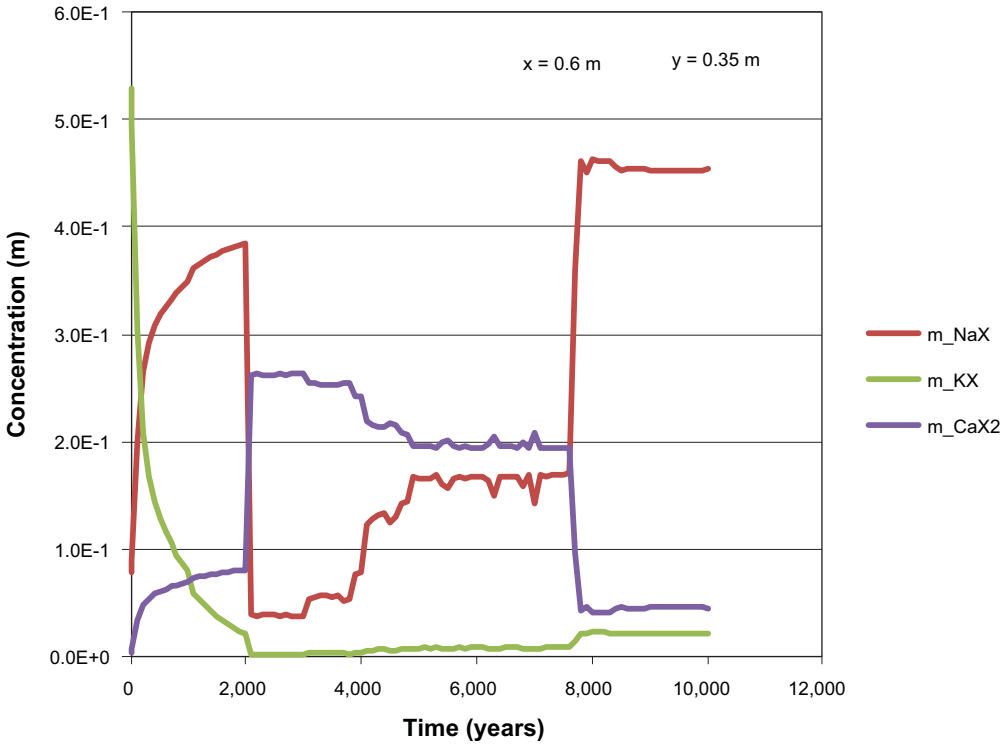

Figure C-14. *The development of the concentration of ion exchange species in concrete over time (during the first 10,000 years) at position AE, case Large8. Units (mol/kg pore water).*

Ion exchange species – inspection point DE

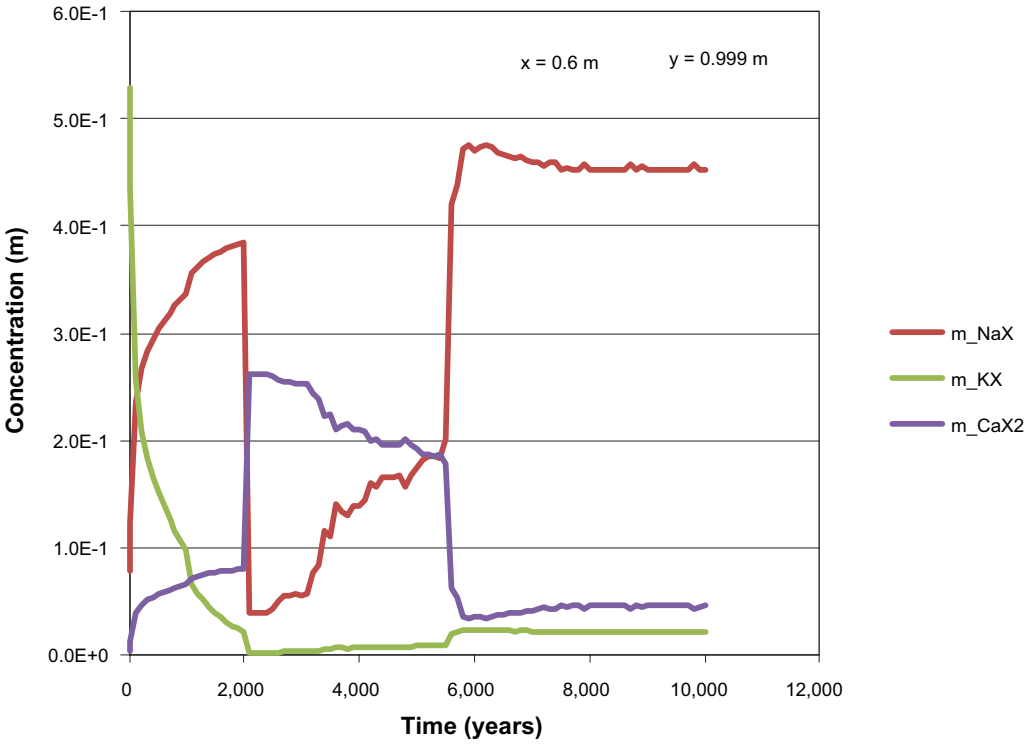

Figure C-15. *The development of the concentration of ion exchange species in concrete over time (during the first 10,000 years) at position DE (1 mm from the centreline of an open fracture), case Large8. Units (mol/kg pore water).*

Profiles along section E-E at selected times

The initial cumulative distribution of different minerals along a profile through the centreline (section E-E) is shown in Figure C-16. The initial assembly consists of CSHjen, portlandite, ettringite and hydrotalciteOH. The picture shows the initial porosity of the sand/crushed rock of 0.3 m^3/m^3, the concrete 0.11 m^3/m^3 and the thin fracture 1 m^3/m^3.

After 100 years the conditions remain essentially the same. After 1,000 years a slight reduction of portlandite is visible for y-coordinates 0.2–0.35 indicating leaching at the bottom of the concrete floor. A small reduction of portlandite due to leaching is also indicated near the thin fracture for y-coordinates between 0.9–1.0. These effects proceed up to 2,000 years with continued leaching of portlandite and a slight increase of ettringite. At 3,000 years, a significant leaching of portlandite has occurred and ettringite has formed in significant amount. At 5,000 years a reduction of the porosity in the thin fracture is noted, whereas the porosity in the concrete wall in general has increased from 11% to about 13%. At 10,000 years the concrete structures are in a stage of severe degradation and the cement minerals have been replaced by calcite to a high degree. After 5,000 years a slight reduction of the porosity in the sand/crushed rock bed around the concrete constructions due to precipitation of calcite is visible (y-coordinates 0–0.2 m). The calcite precipitation continues up to about 20,000 years.

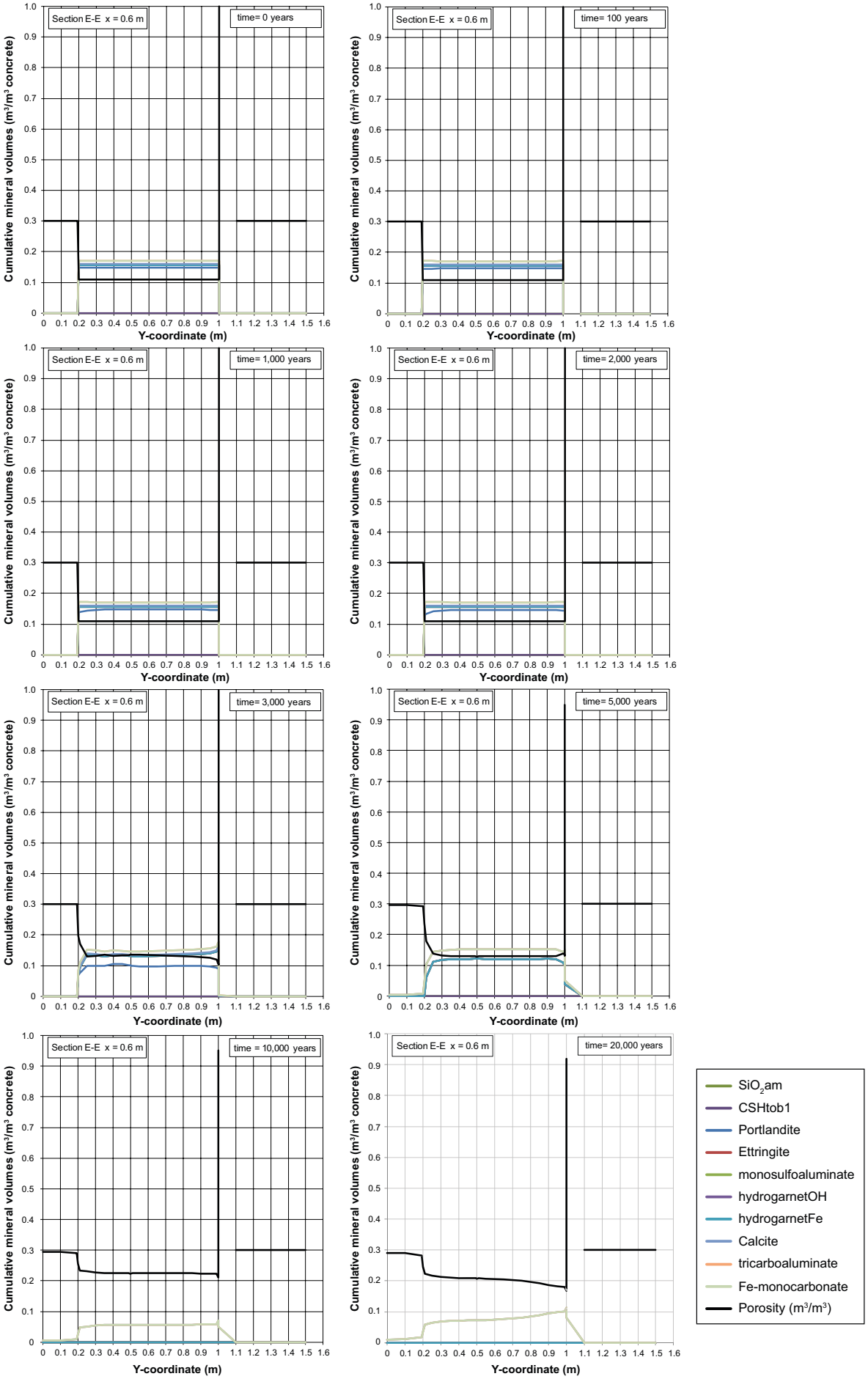

Figure C-16. *Cumulative representation of the mineral composition in concrete and calculated porosity (left axis) along the vertical Section E-E at time 100 years, case Large8. Units (m^3/m^3).*

Appendix D

Results for Case Large10

In this appendix provides supplemental graphical presentation of the model results for case Large10. The reader i referred to the corresponding chapter in the main report for comments on the identified interactions between the different chemical components, as well as for orientation about the position of the different evaluation points and sections through the model used in some of the graphs.

pH evolution over time

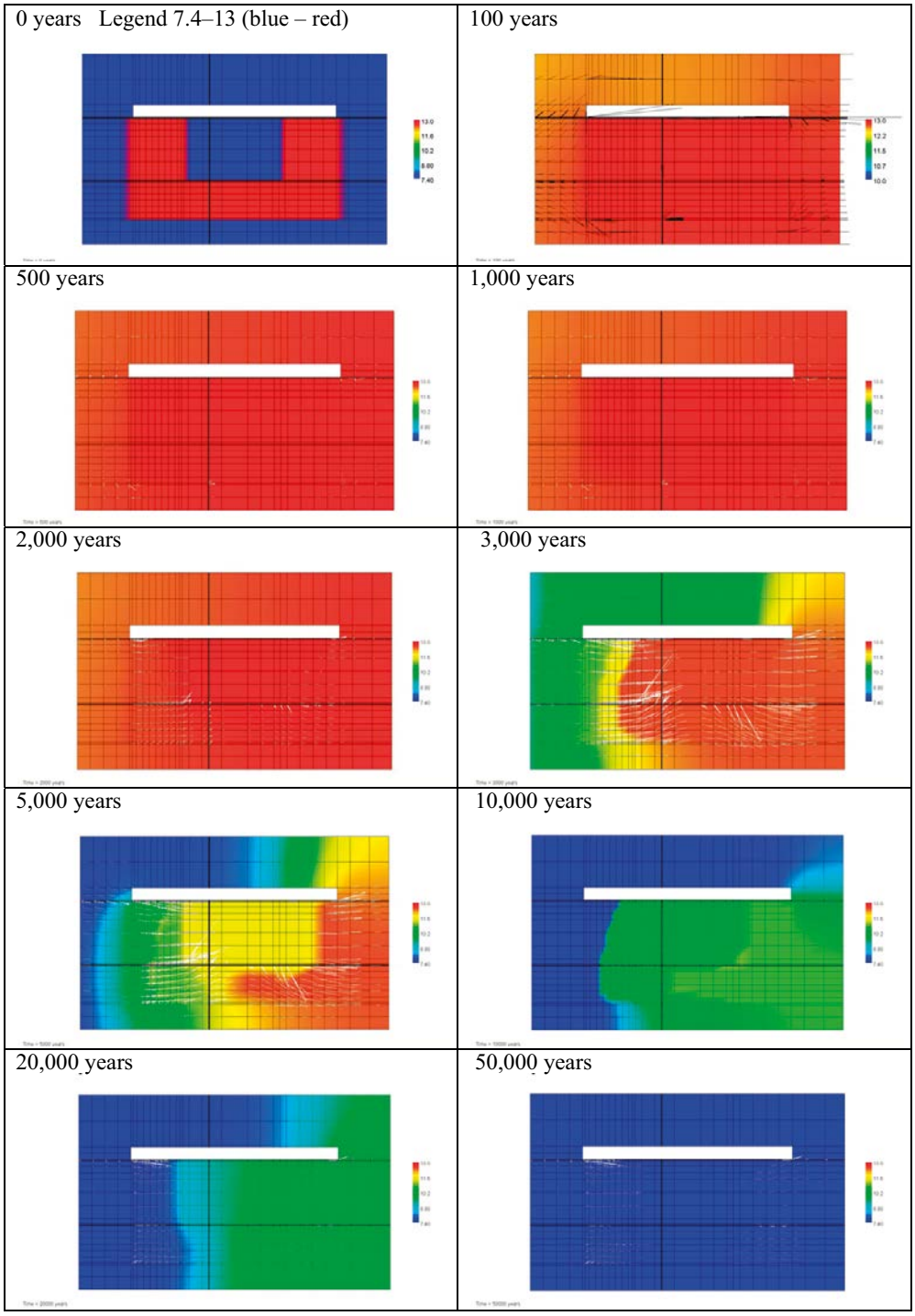

Figure D-1. *Snap-shots of the pH distribution at selected times up to 50,000 years. (MinteqCem-2001 database, Case Large10.) The legend shows the span pH 7.4–13.*

Dissolved sodium concentrations at different times

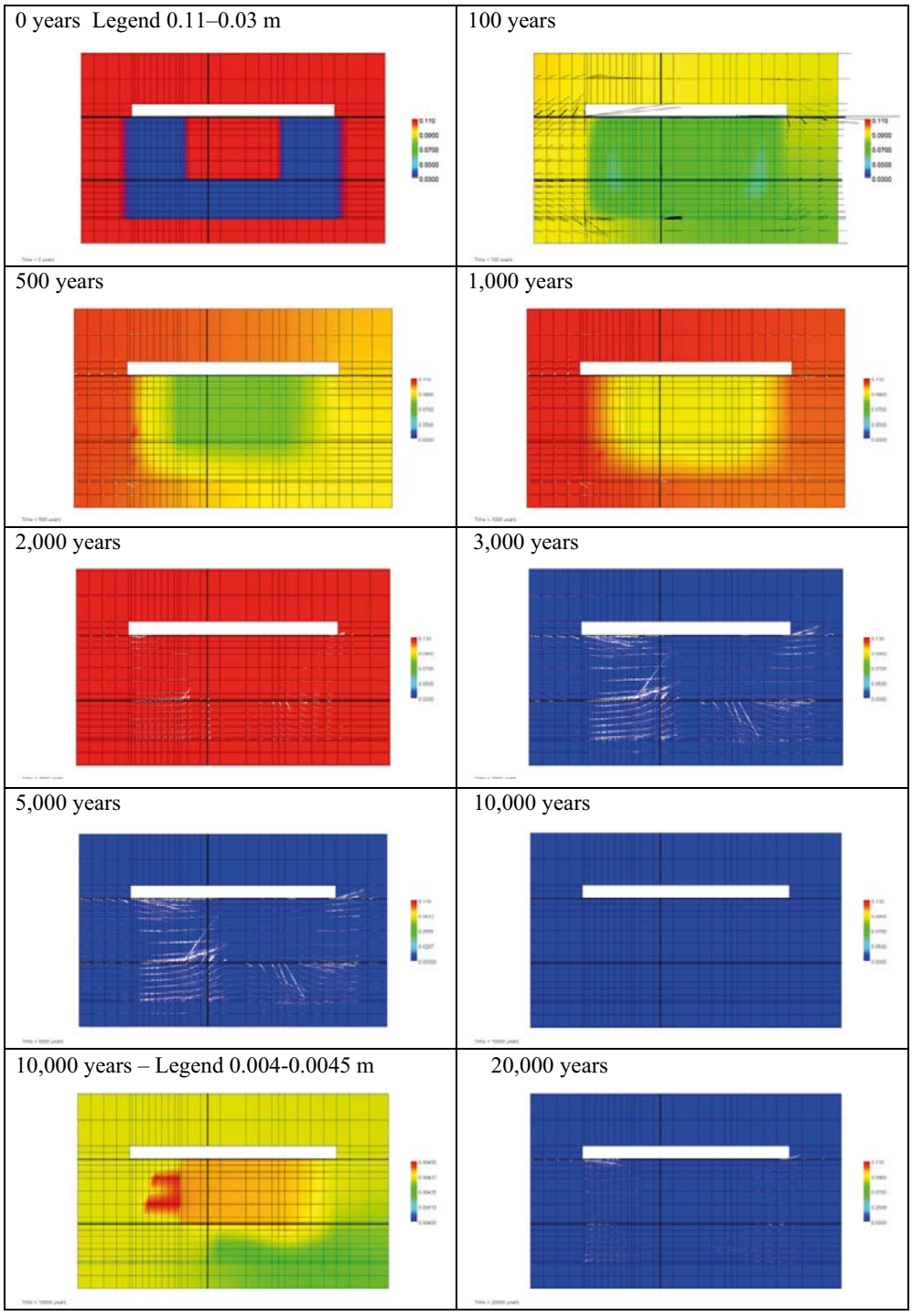

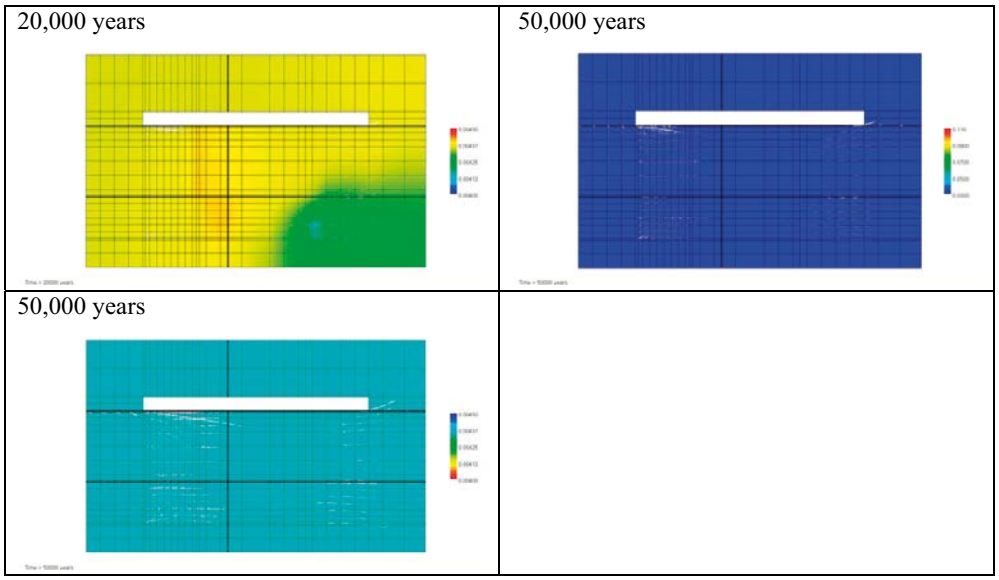

Figure D-2. *Snap-shots of the dissolved sodium concentrations at selected times up to 50,000 years. Observe the change of scale after 10,000 years. (MinteqCem-2001 database, Case Large10.) Units (mol/kg pore water).*

Dissolved potassium concentrations at different times

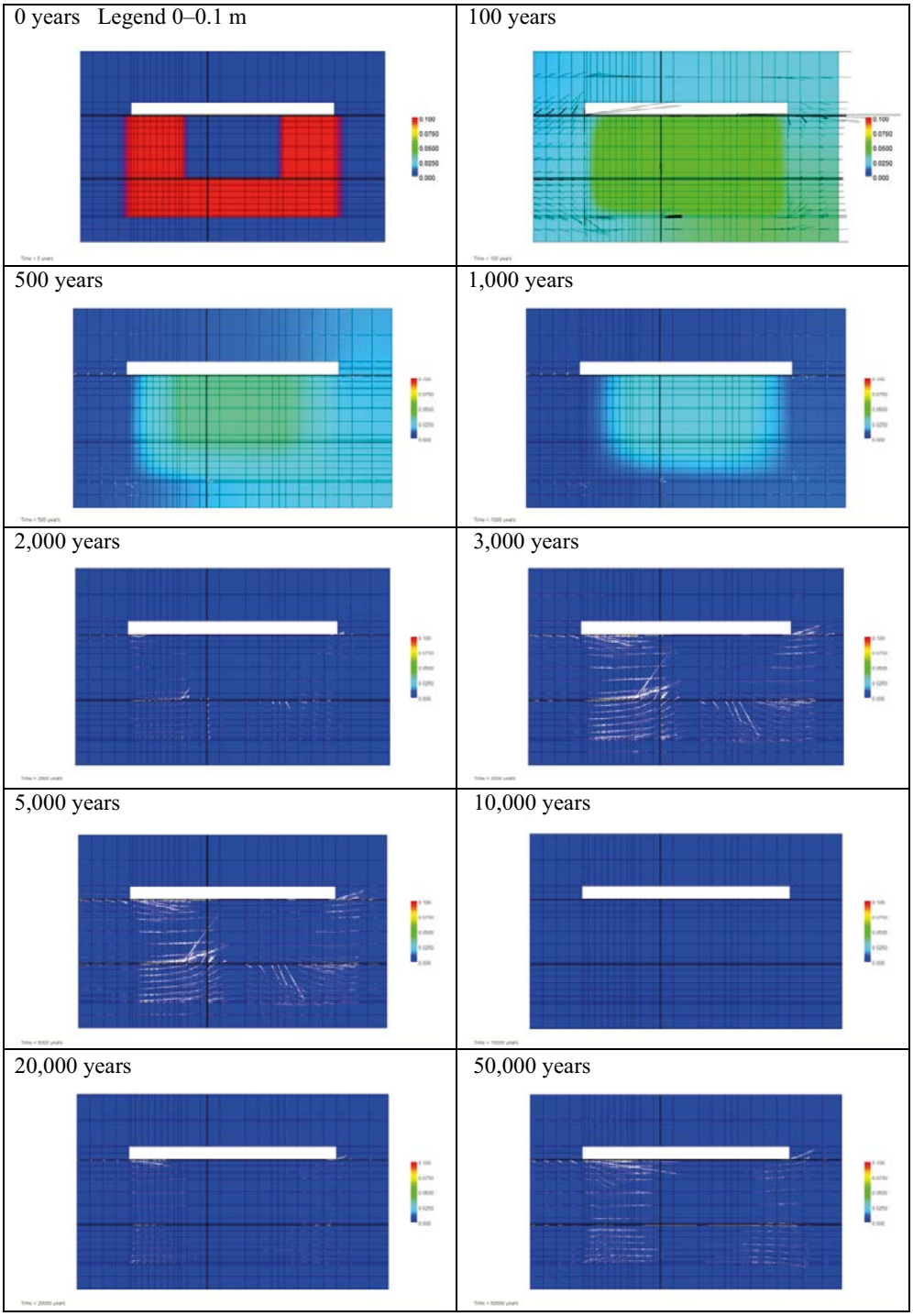

Figure D-3. *Snap-shots of the dissolved potassium concentrations at selected times up to 50,000 years. (MinteqCem-2001 database, Case Large10.) Units (mol/kg pore water).*

Dissolved calcium concentrations at different times

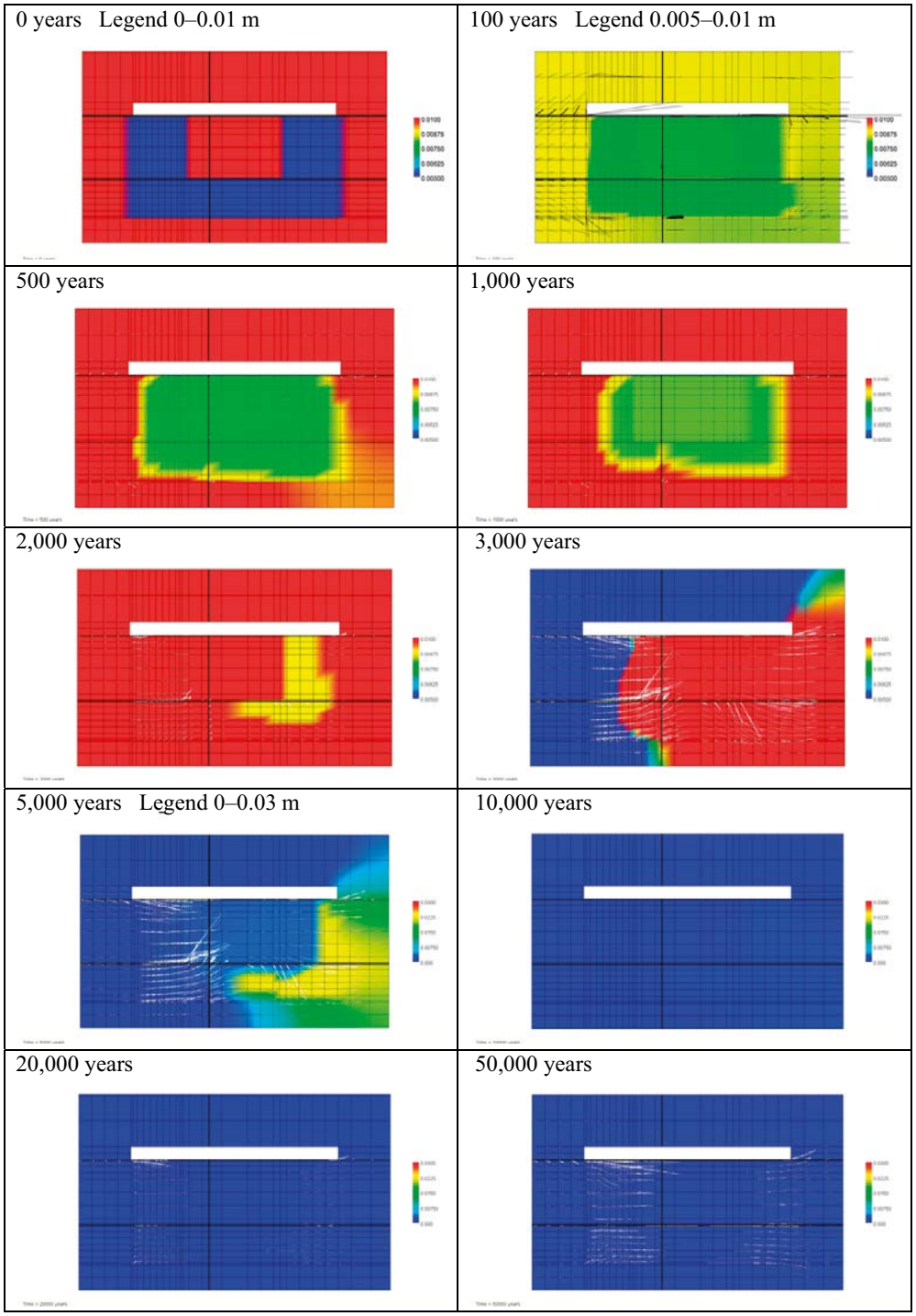

Figure D-4. *Snap-shots of the dissolved calcium concentrations at selected times up to 50,000 years. Observe the change of scale after 100 years and after 5,000 years. (MinteqCem-2001 database, Case Large10.) Units (mol/kg pore water).*

Dissolved silica concentrations at different times

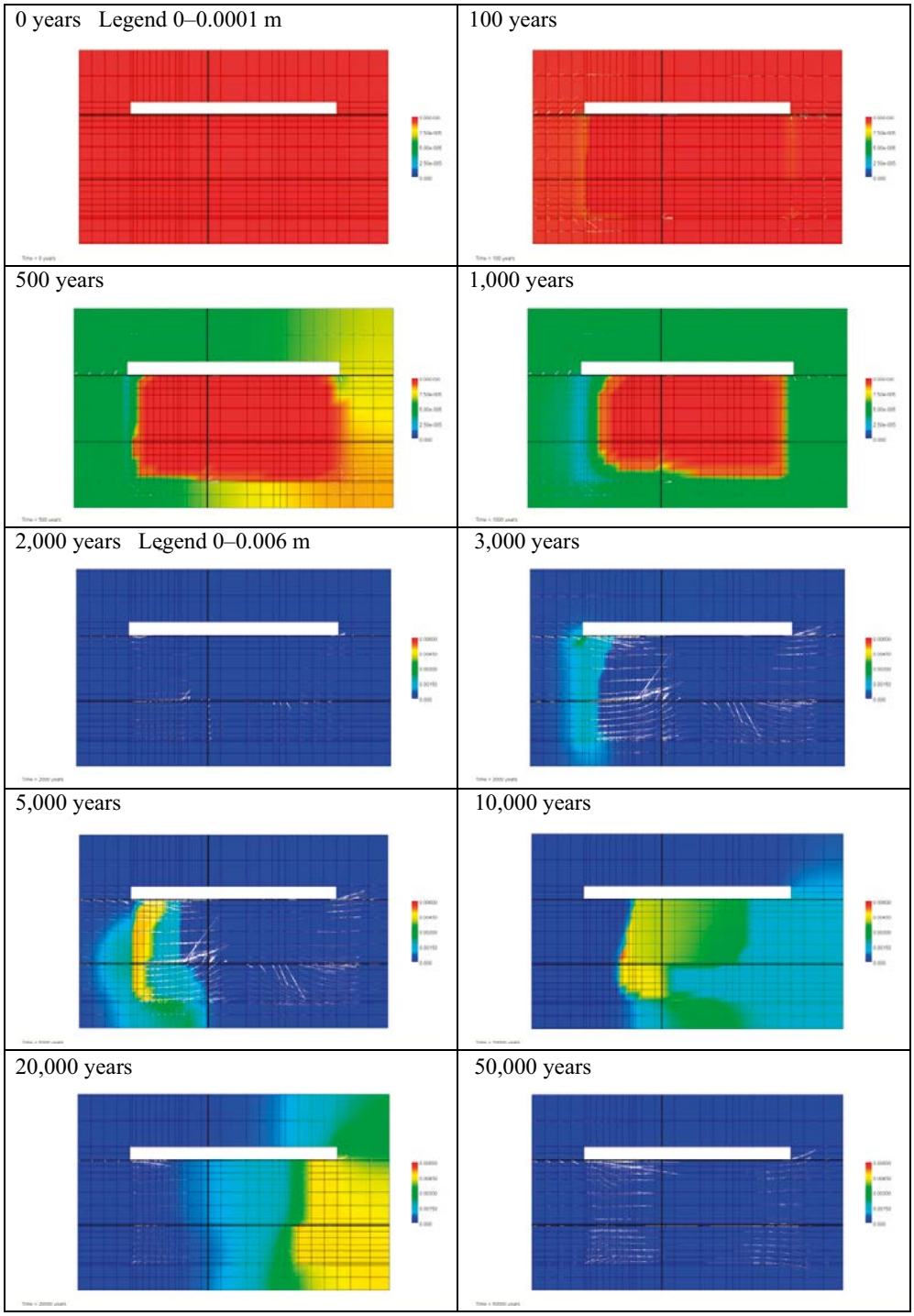

Figure D-5. *Snap-shots of the dissolved silica concentrations at selected times up to 50,000 years. Observe the change of scale after 2,000 years. (MinteqCem-2001 database, Case Large10.) Units (mol/kg pore water).*

Dissolved sulphate concentrations at different times

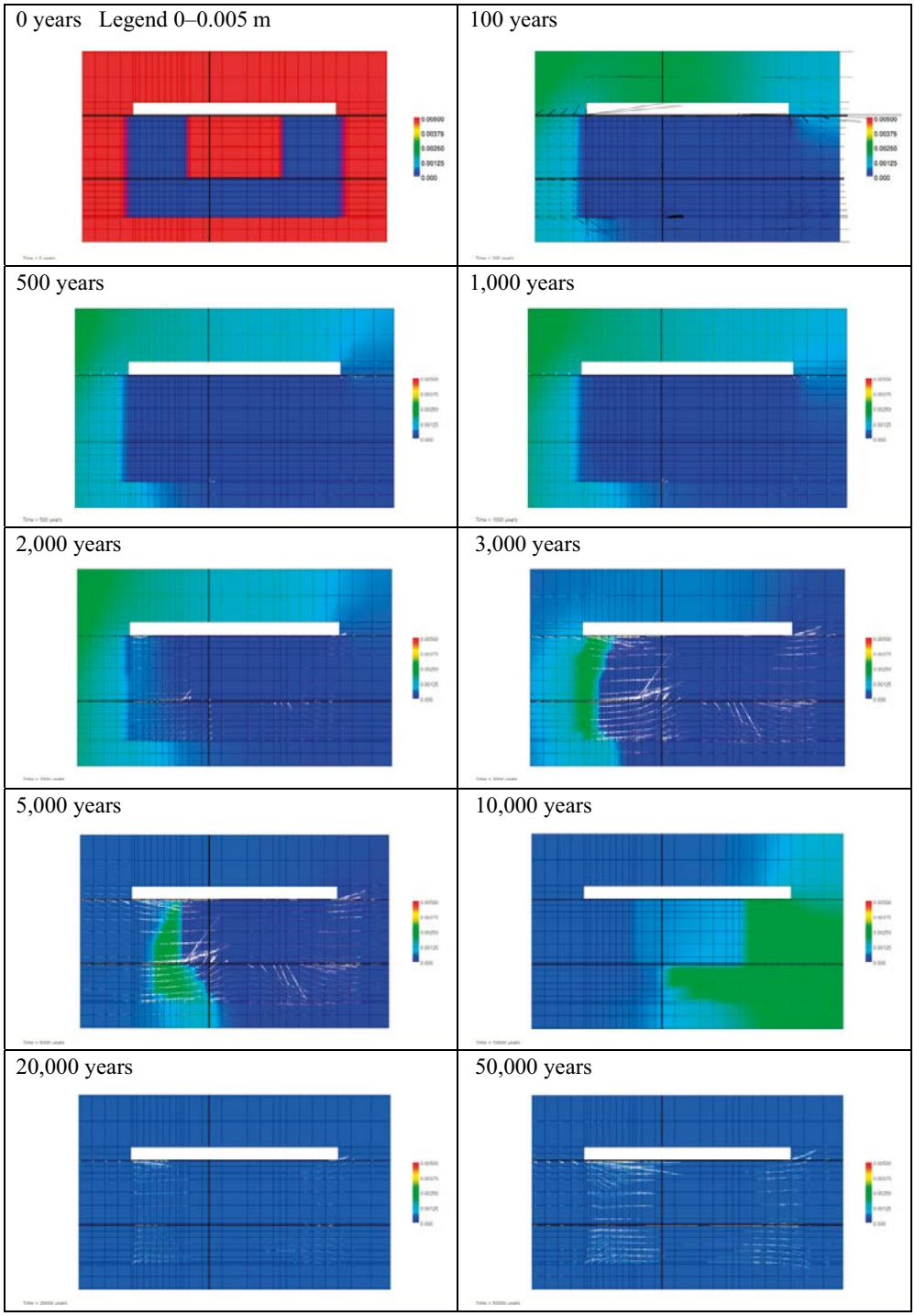

Figure D-6. *Snap-shots of the dissolved sulphur (i.e. sulphate) concentrations at selected times up to 50,000 years. (MinteqCem-2001 database, Case Large10.) Units (mol/kg pore water).*

Dissolved chloride concentrations at different times

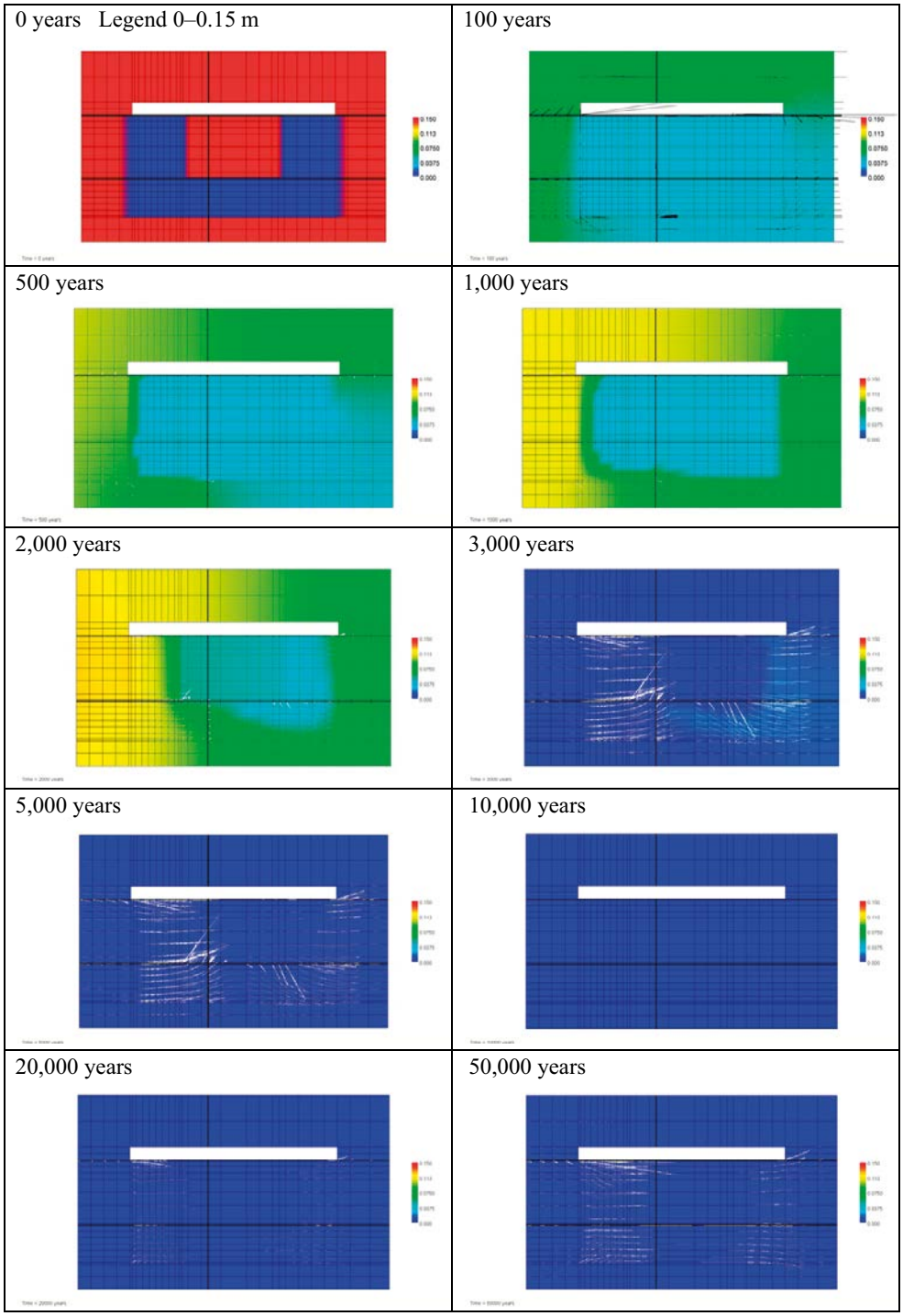

Figure D-7. *Snap-shots of the dissolved chloride concentrations at selected times up to 50,000 years. (MinteqCem-2001 database, Case Large10.) Units (mol/kg pore water).*

Dissolved magnesium concentrations at different times

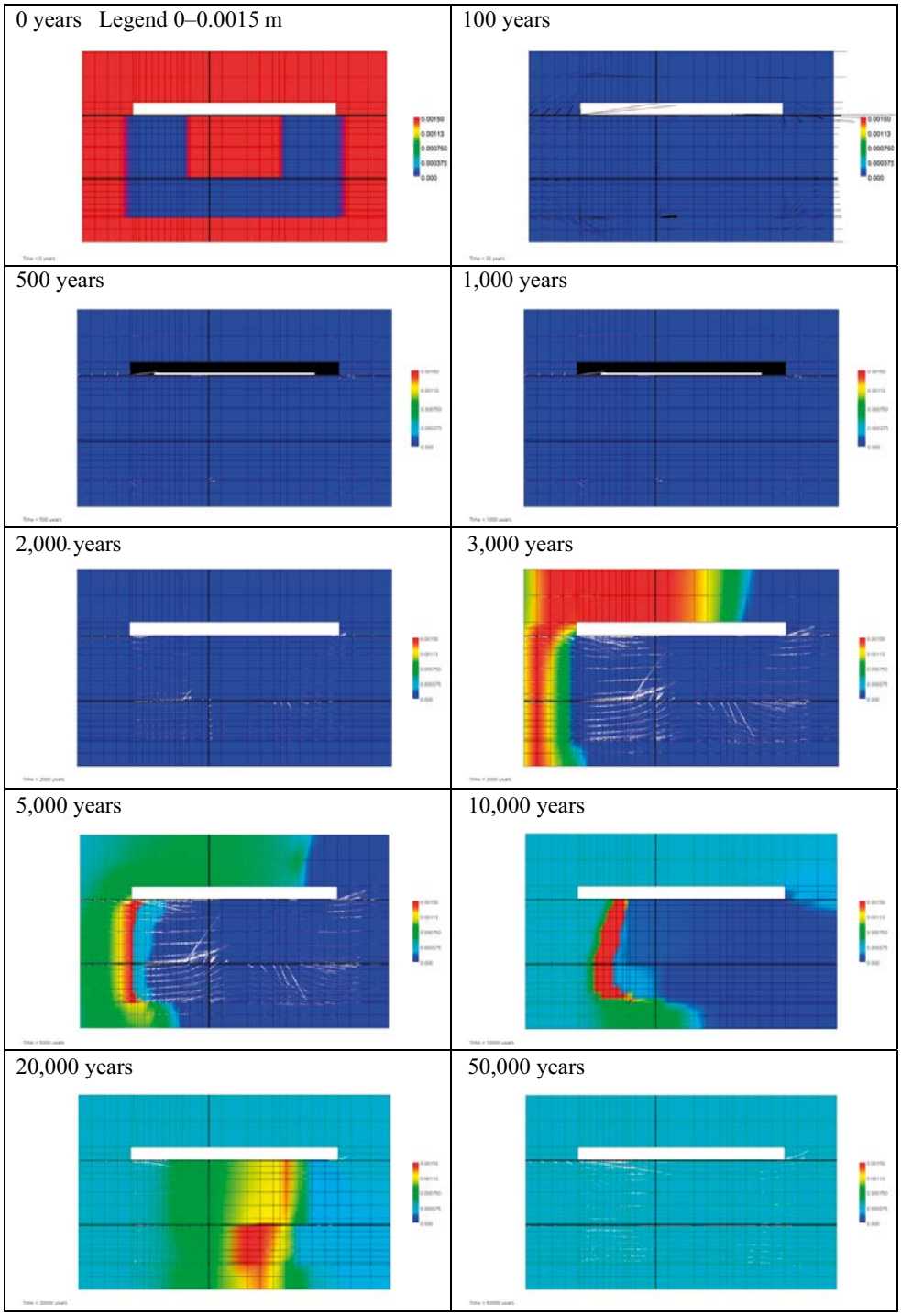

Figure D-8. *Snap-shots of the dissolved magnesium concentrations at selected times up to 50,000 years. Observe the change of scale after 10,000 years. (MinteqCem-2001 database, Case Large10.) Units (mol/kg pore water).*

Dissolved aluminium concentrations at different times

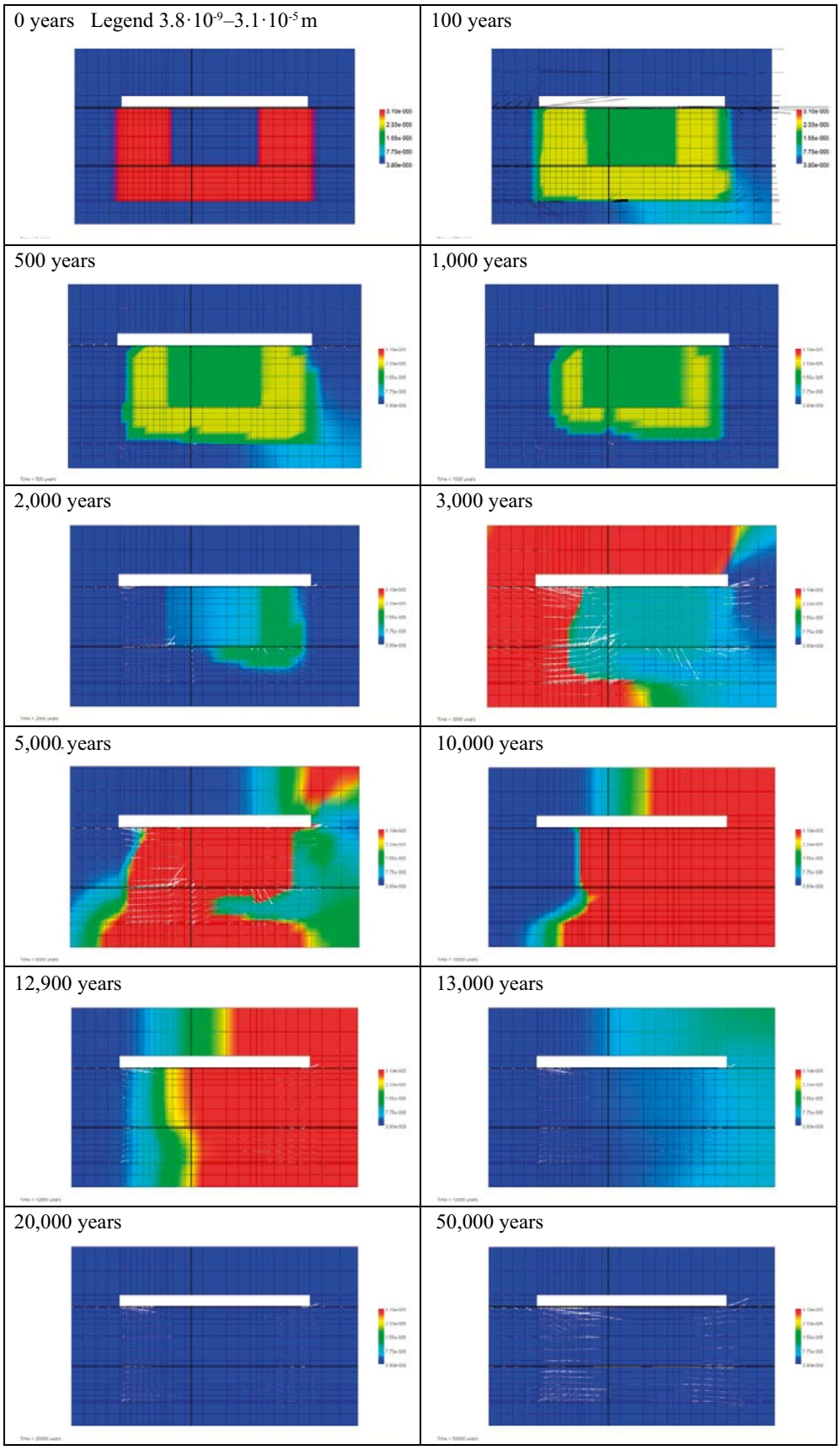

Figure D-9. *Snap-shots of the dissolved aluminium concentrations at selected times up to 50,000 years. (MinteqCem-2001 database, Case Large10.) Units (mol/kg pore water).*

Dissolved iron concentrations at different times

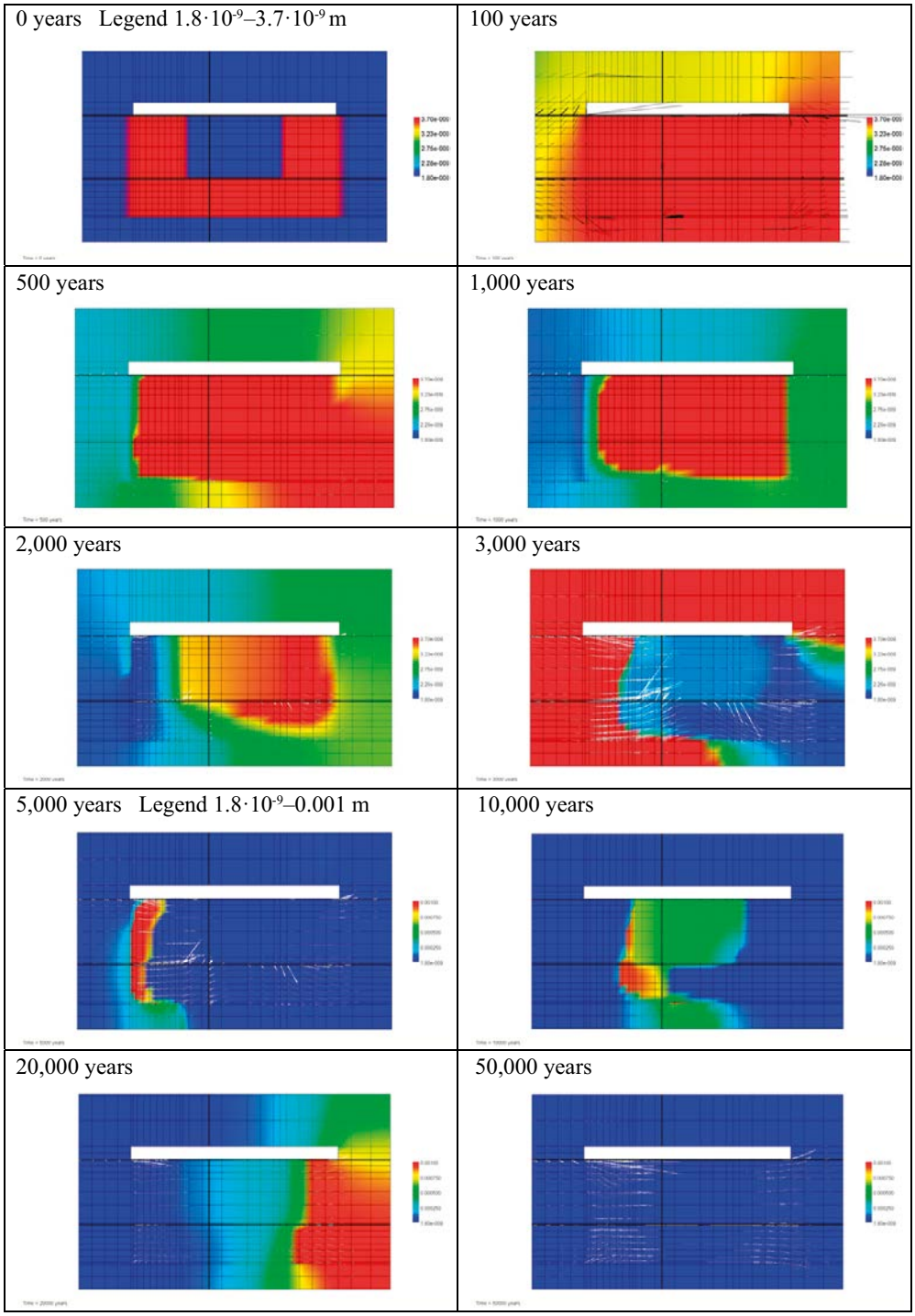

Figure D-10. *Snap-shots of the dissolved iron concentrations at selected times up to 50,000 years. Observe the change of scale after 5,000 years. (MinteqCem-2001 database, Case Large10.) Units (mol/kg pore water).*

Dissolved carbonate concentrations at different times

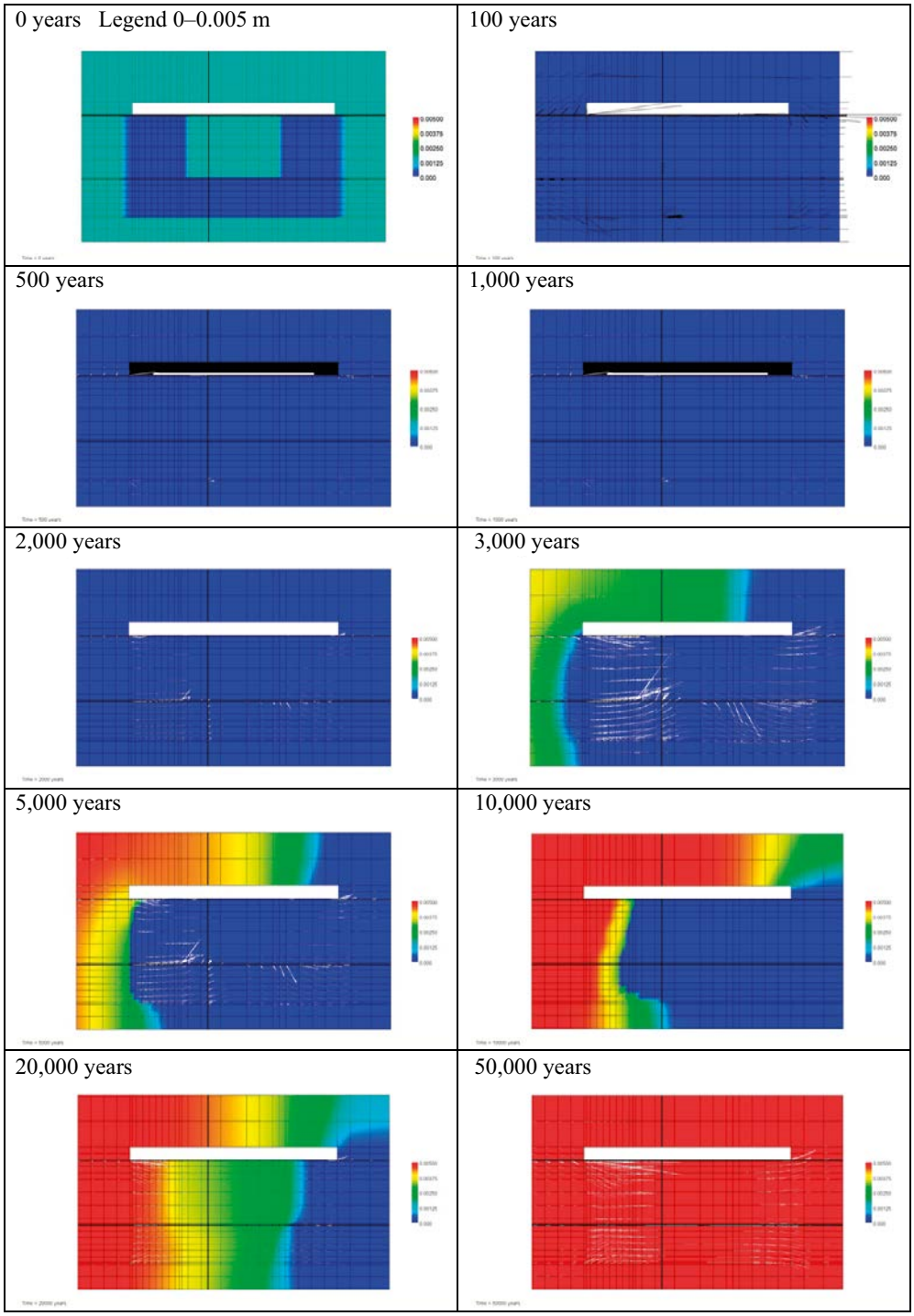

Figure D-11. *Snap-shots of the dissolved carbonate concentrations at selected times up to 50,000 years. (MinteqCem-2001 database, Case Large10.) Units (mol/kg pore water).*

Ion exchange species at different times

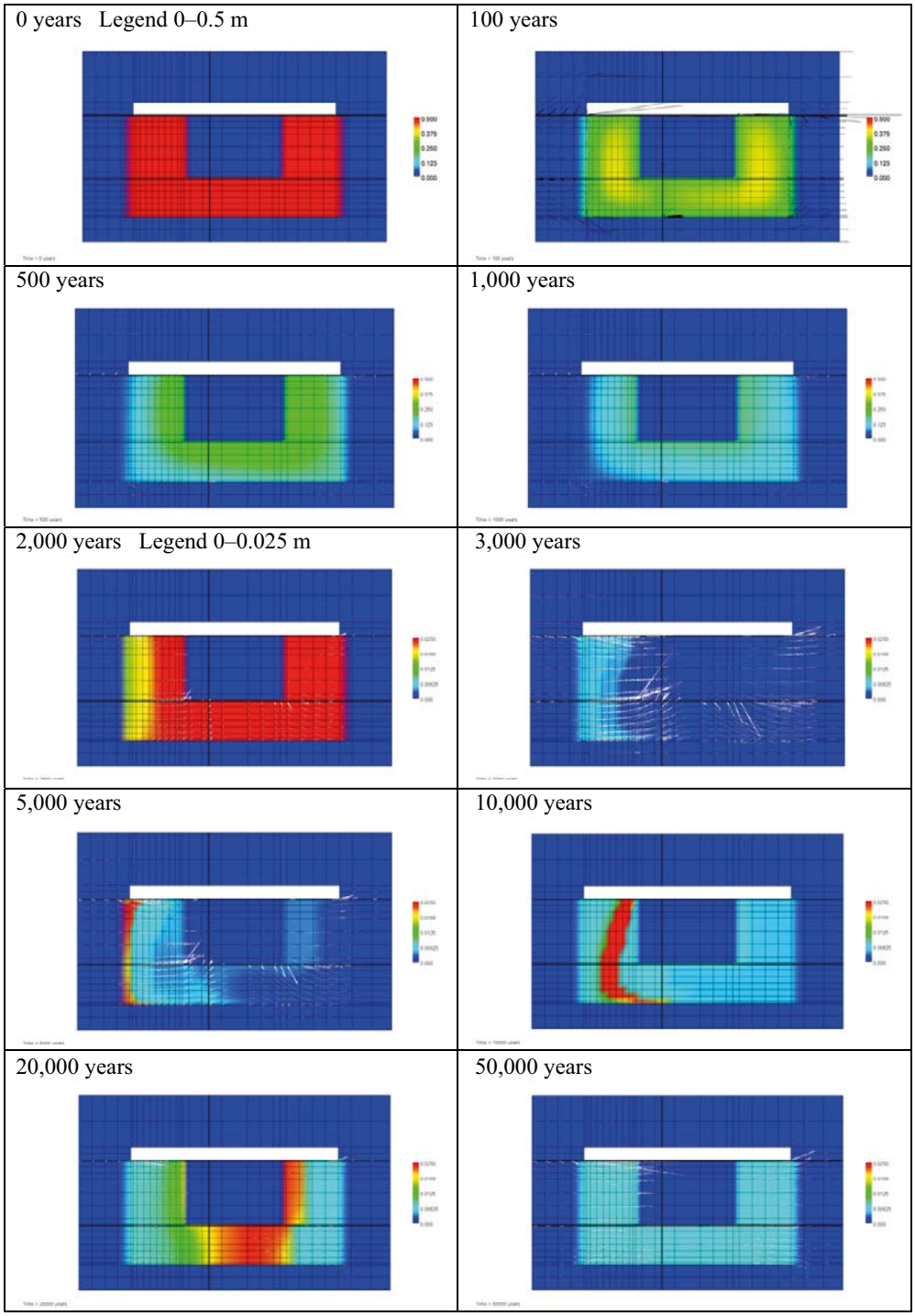

Figure D-12. *Snap-shots of the concentrations of ion exchange species of potassium (m_KX) at selected times up to 50,000 years. (MinteqCem-2001 database, Case Large10.) Units (mol/kg pore water).*

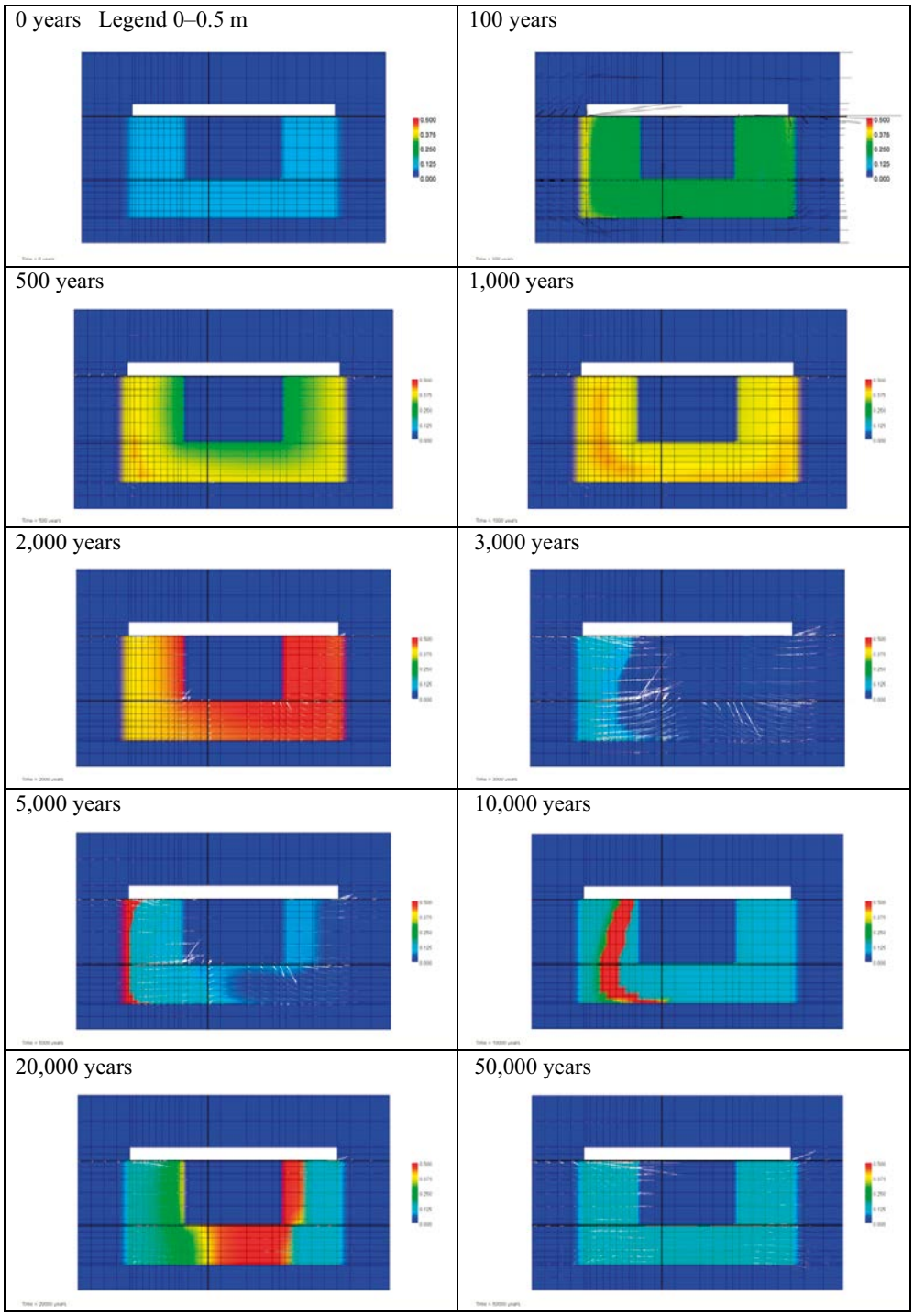

Figure D-13. *Snap-shots of the concentrations of ion exchange species of sodium (m_NaX) at selected times up to 50,000 years. (MinteqCem-2001 database, Case Large10.) Units (mol/kg pore water).*

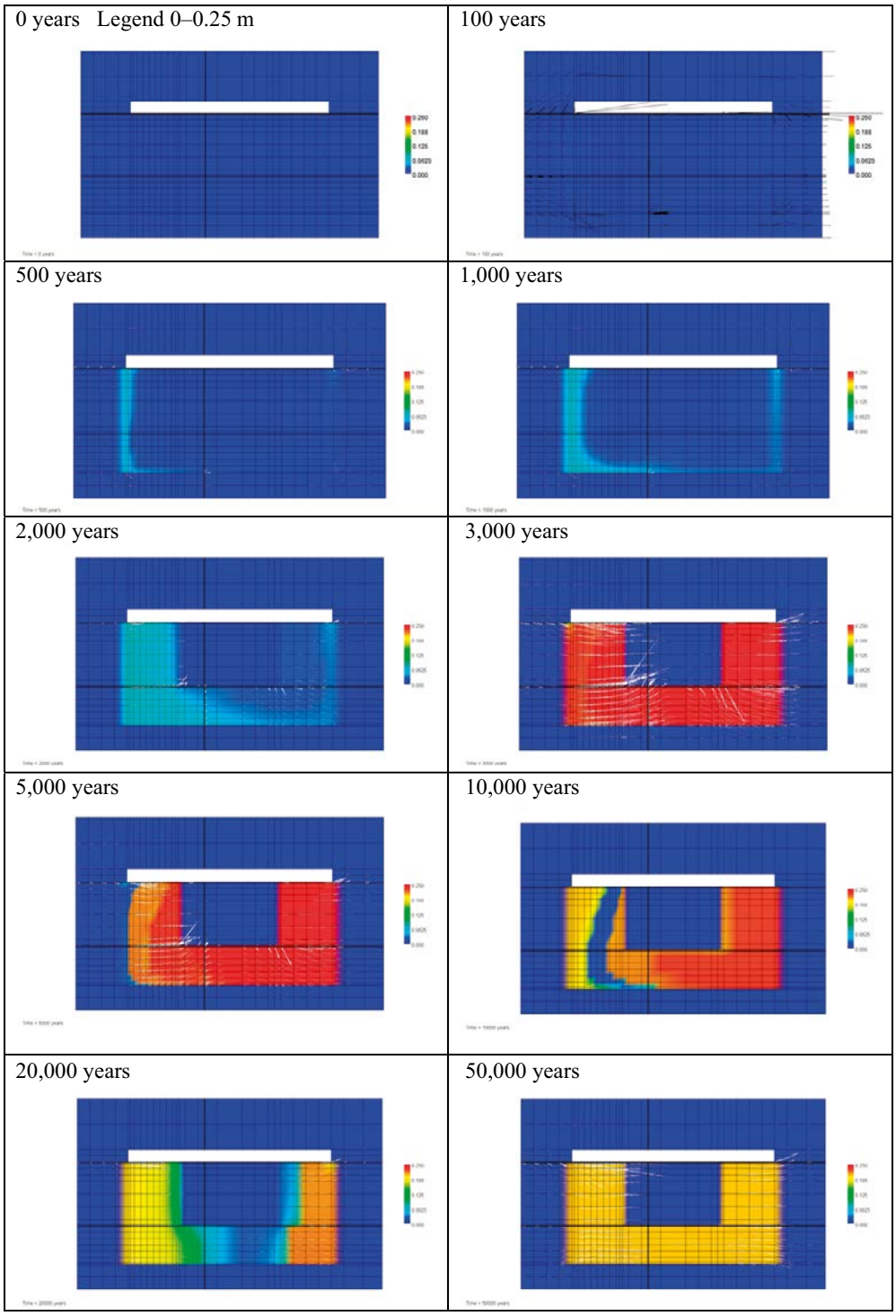

Figure D-14. *Snap-shots of the concentrations of ion exchange species of calcium (m_CaX2) at selected times up to 50,000 years. (MinteqCem-2001 database, Case Large10.) Units (mol/kg pore water).*

Calcite concentrations at different times

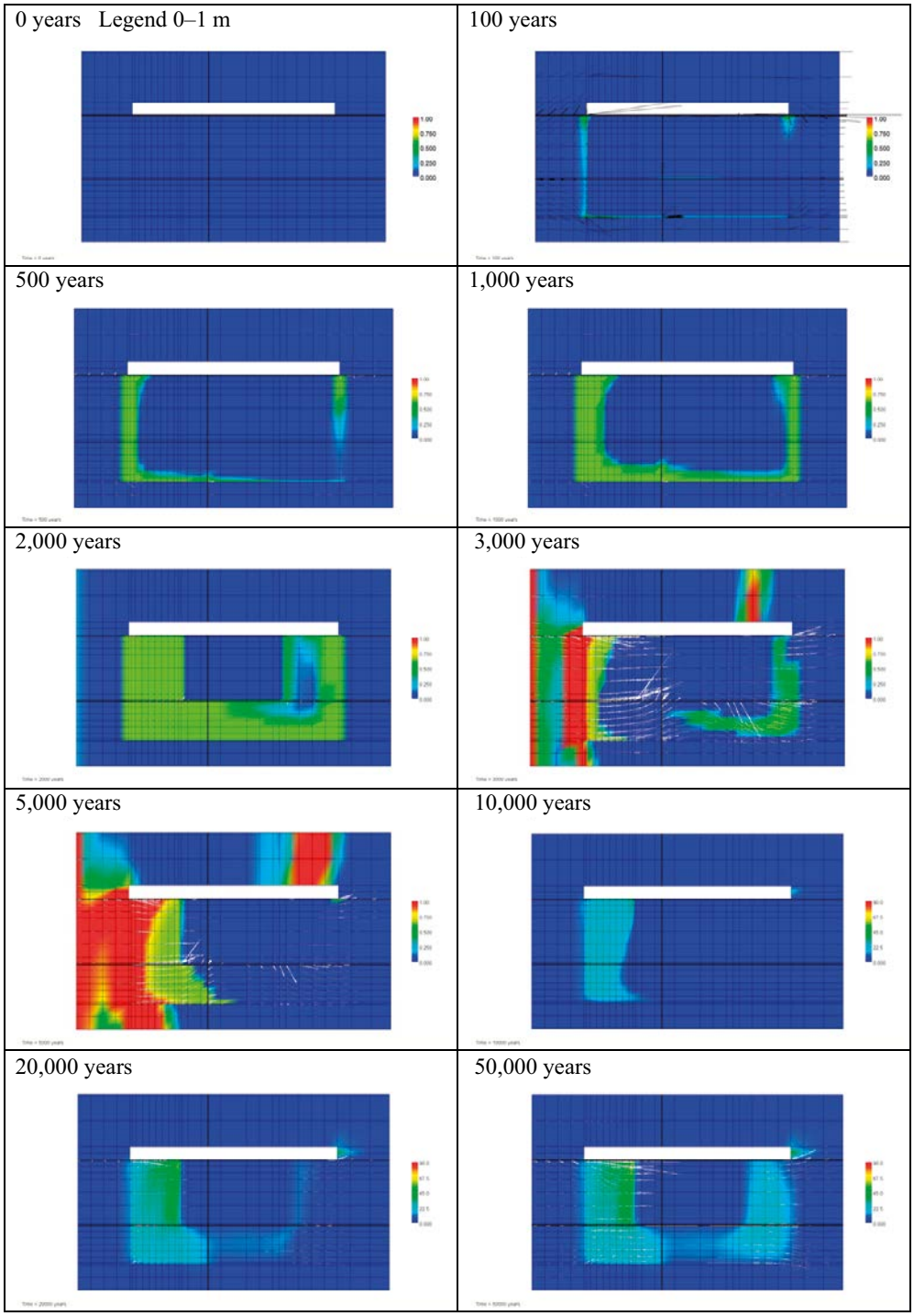

Figure D-15. *Snap-shots of the amount of calcite at selected times up to 50,000 years. Legend is presented in units of (kmoles per m^3 of porewater) (MinteqCem-2001 database, Case Large10.)*

Brucite concentrations at different times

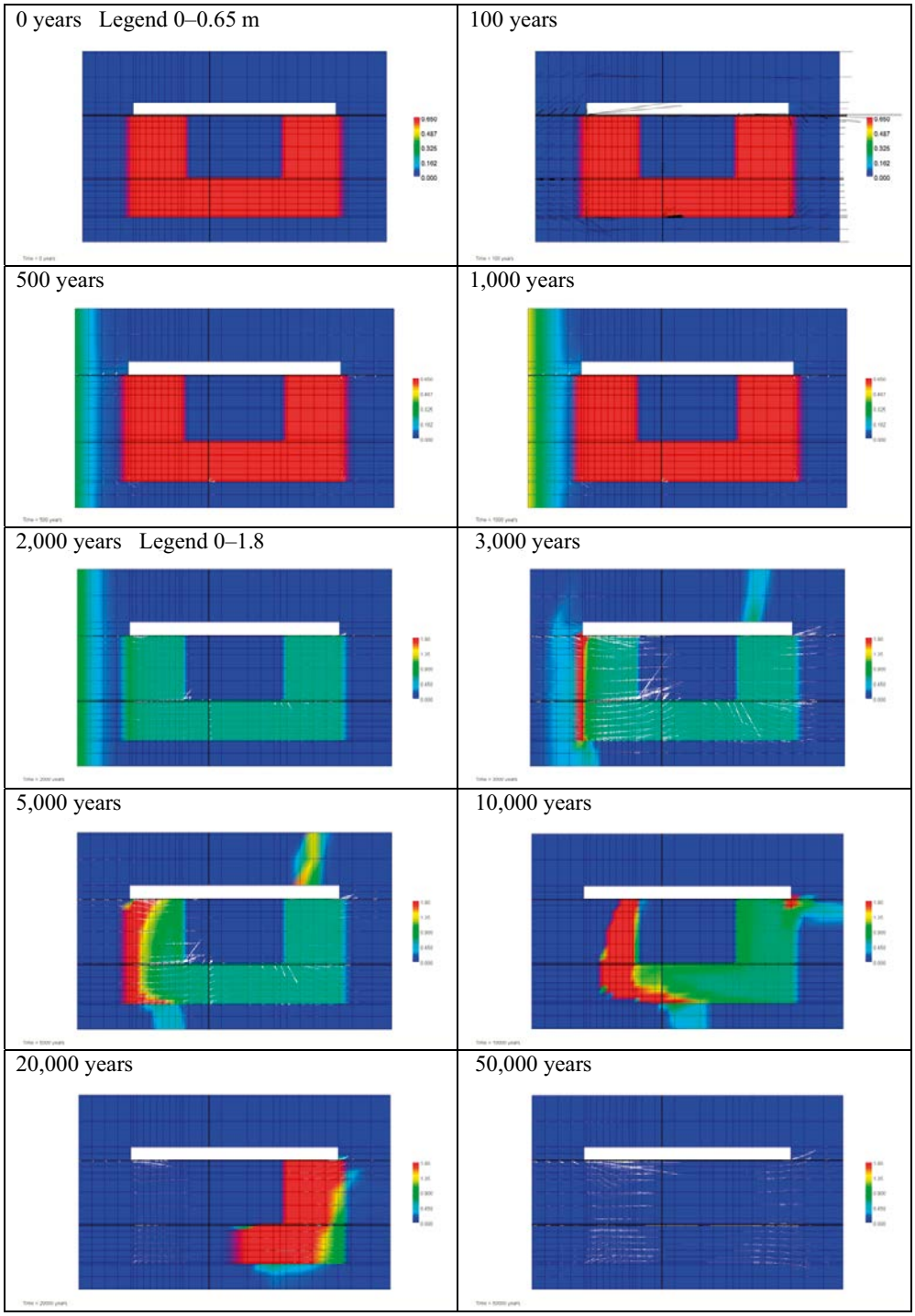

Figure D-16. *Snap-shots of the amount of brucite at selected times up to 50,000 years. Legend is presented in units of (kmoles per m^3 of porewater). Observe the change of scale after 2,000 years. (MinteqCem-2001 database, Case Large10.)*

Portlandite concentrations at different times

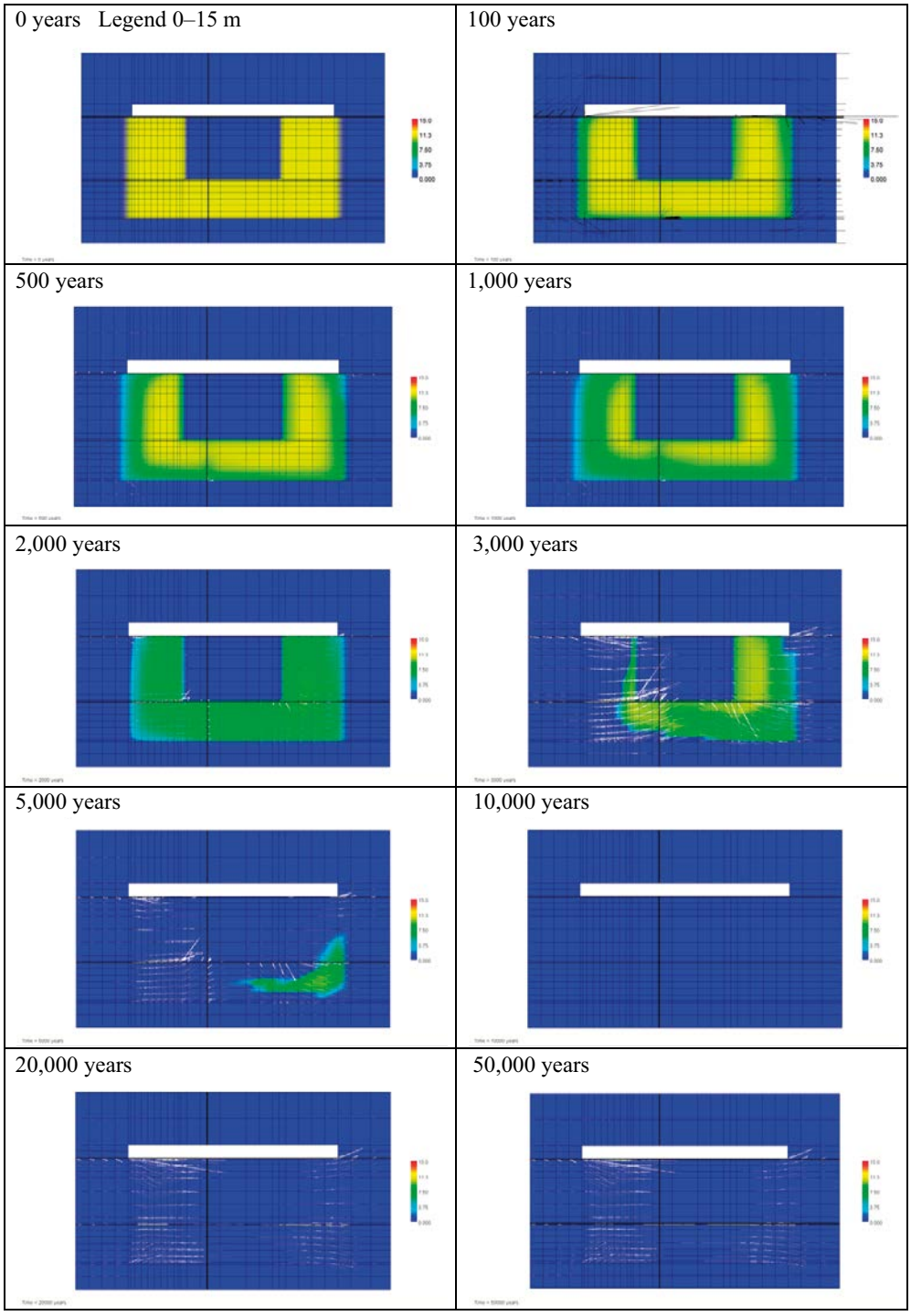

Figure D-17. *Snap-shots of the amount of CH (Portlandite) at selected times up to 50,000 years. Legend is presented in units of (kmoles per m^3 of porewater). (MinteqCem-2001 database, Case Large10.)*

CSH_1.8-concentrations at different times

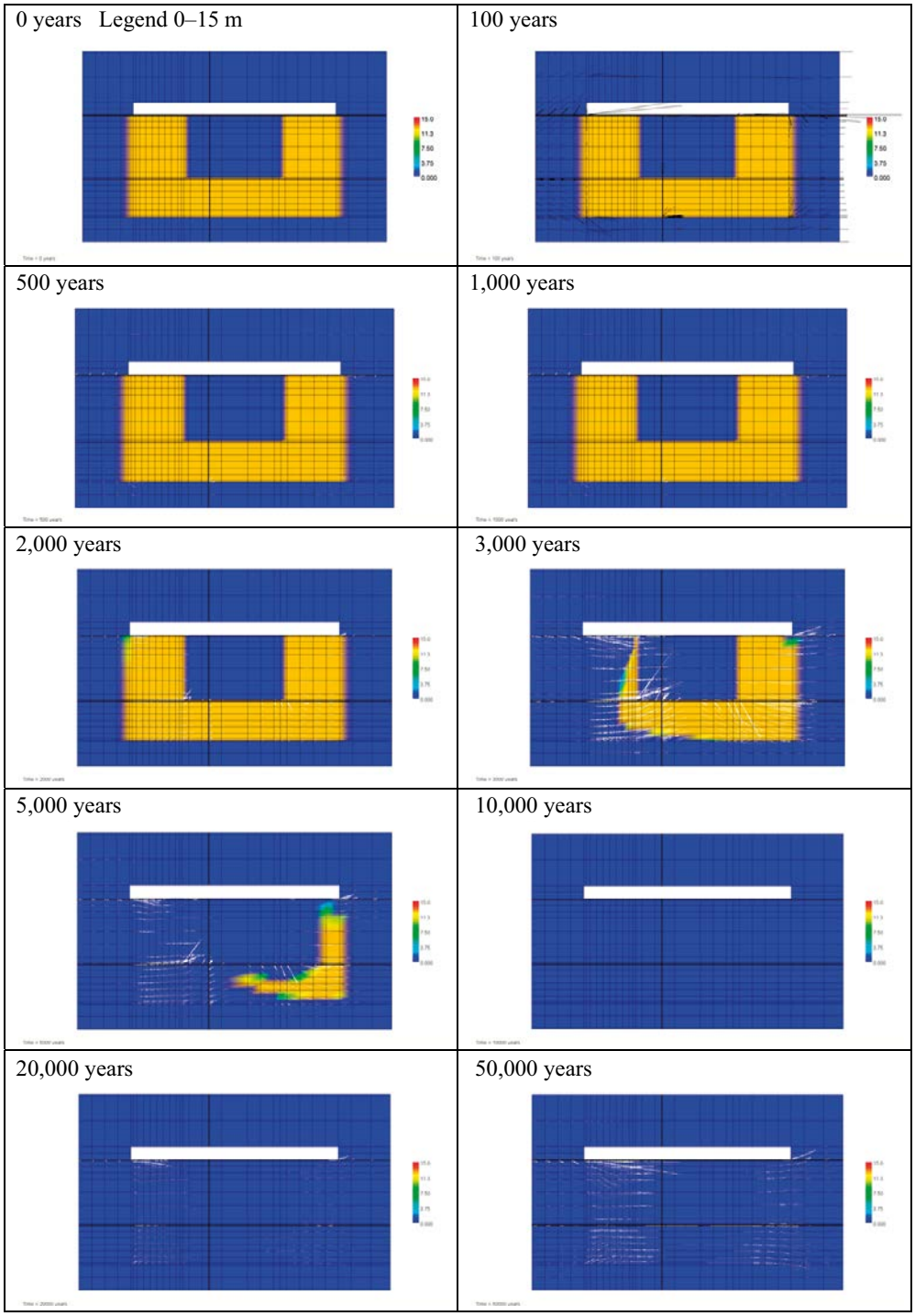

Figure D-18. *Snap-shots of the amount of CSH_1.8 at selected times up to 50,000 years. Legend is presented in units of (kmoles per m^3 of porewater). (MinteqCem-2001 database, Case Large10.)*

CSH_1.1-concentrations at different times

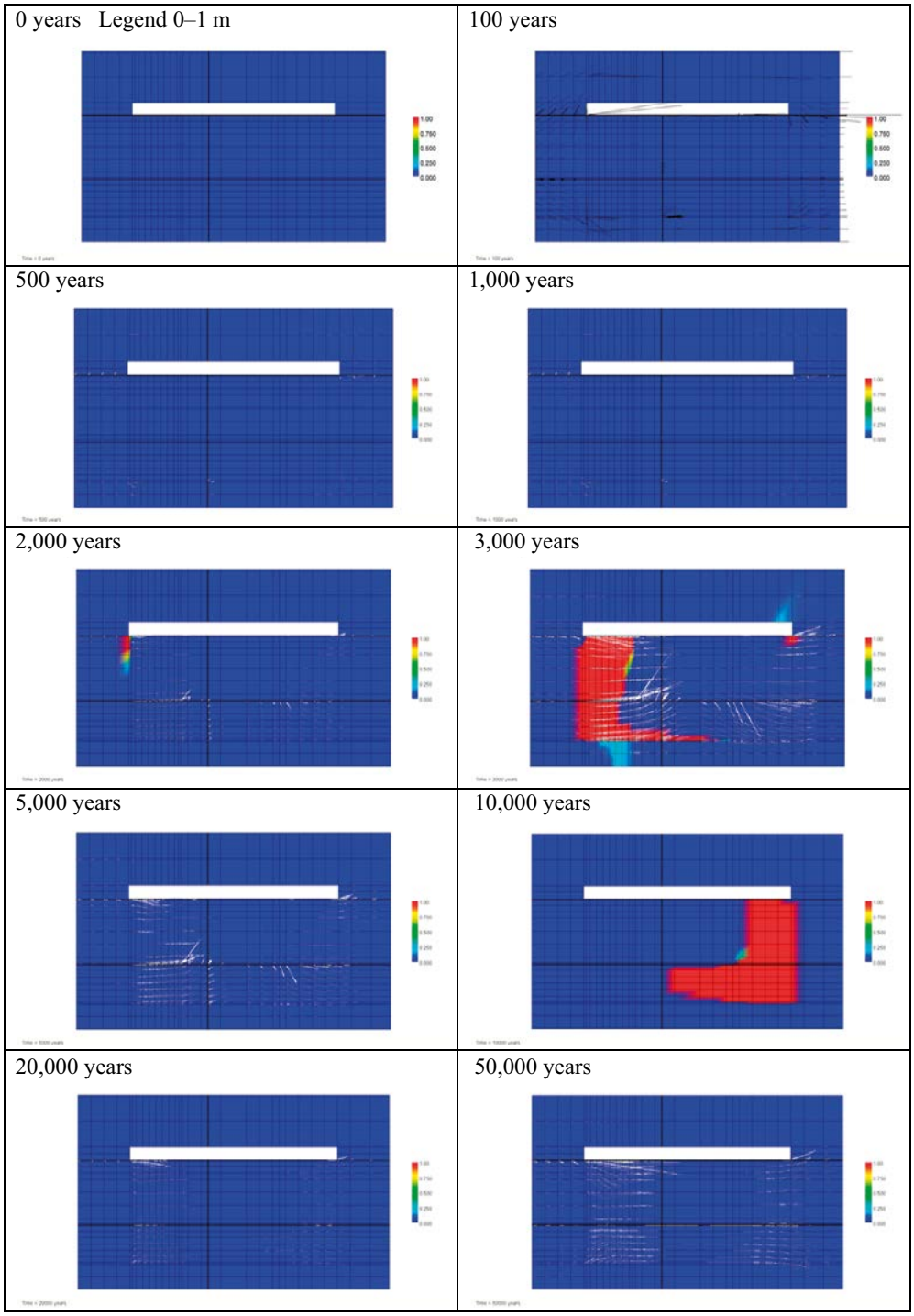

Figure D-19. *Snap-shots of the amount of CSH_1.1 at selected times up to 50,000 years. Legend is presented in units of (kmoles per m^3 of porewater). (MinteqCem-2001 database, Case Large10.)*

CSH_0.8-concentrations at different times

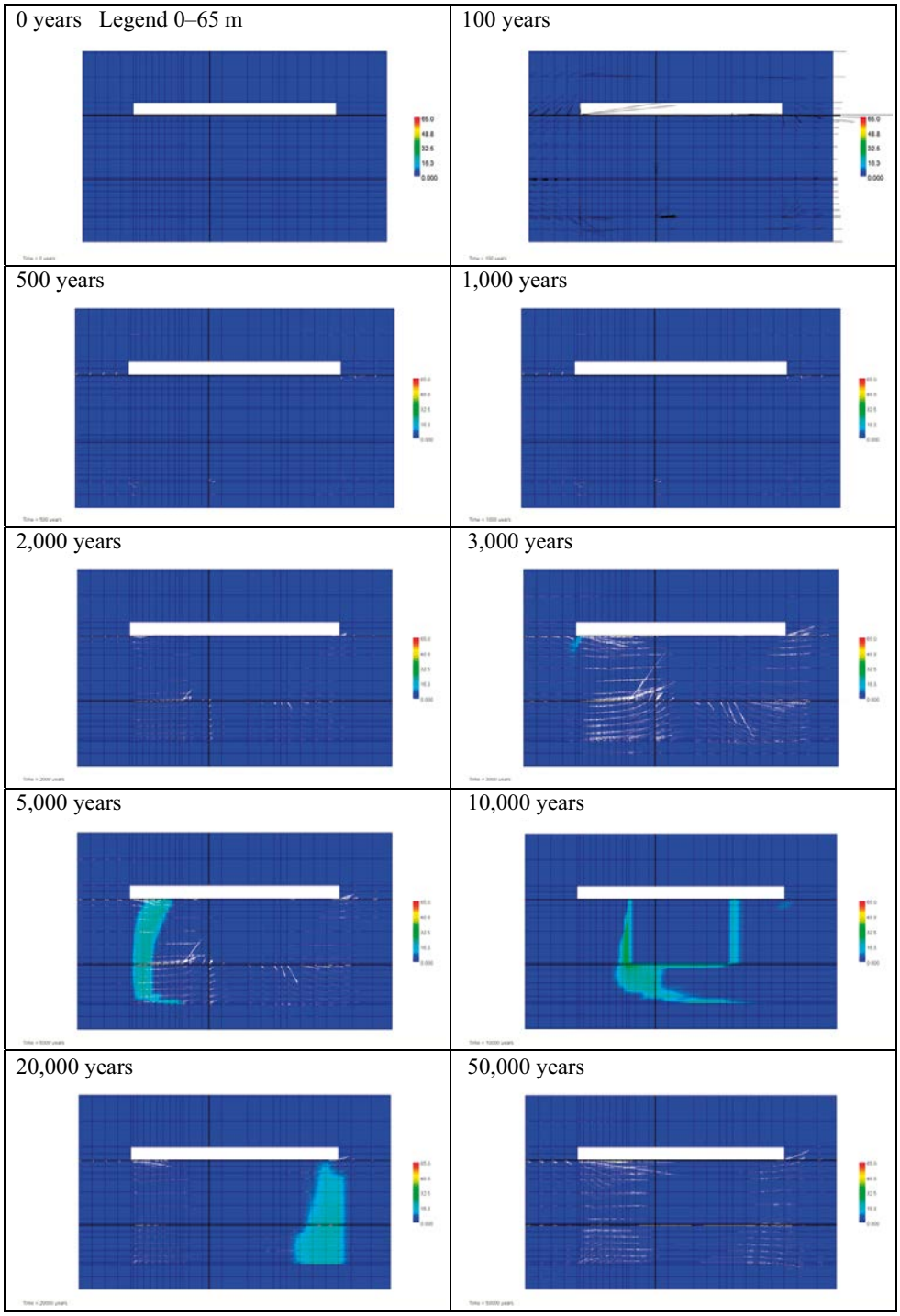

Figure D-20. *Snap-shots of the amount of CSH_0.8 at selected times up to 50,000 years. Legend is presented in units of (kmoles per m^3 of porewater). (MinteqCem-2001 database, Case Large10.)*

Ettringite concentrations at different times

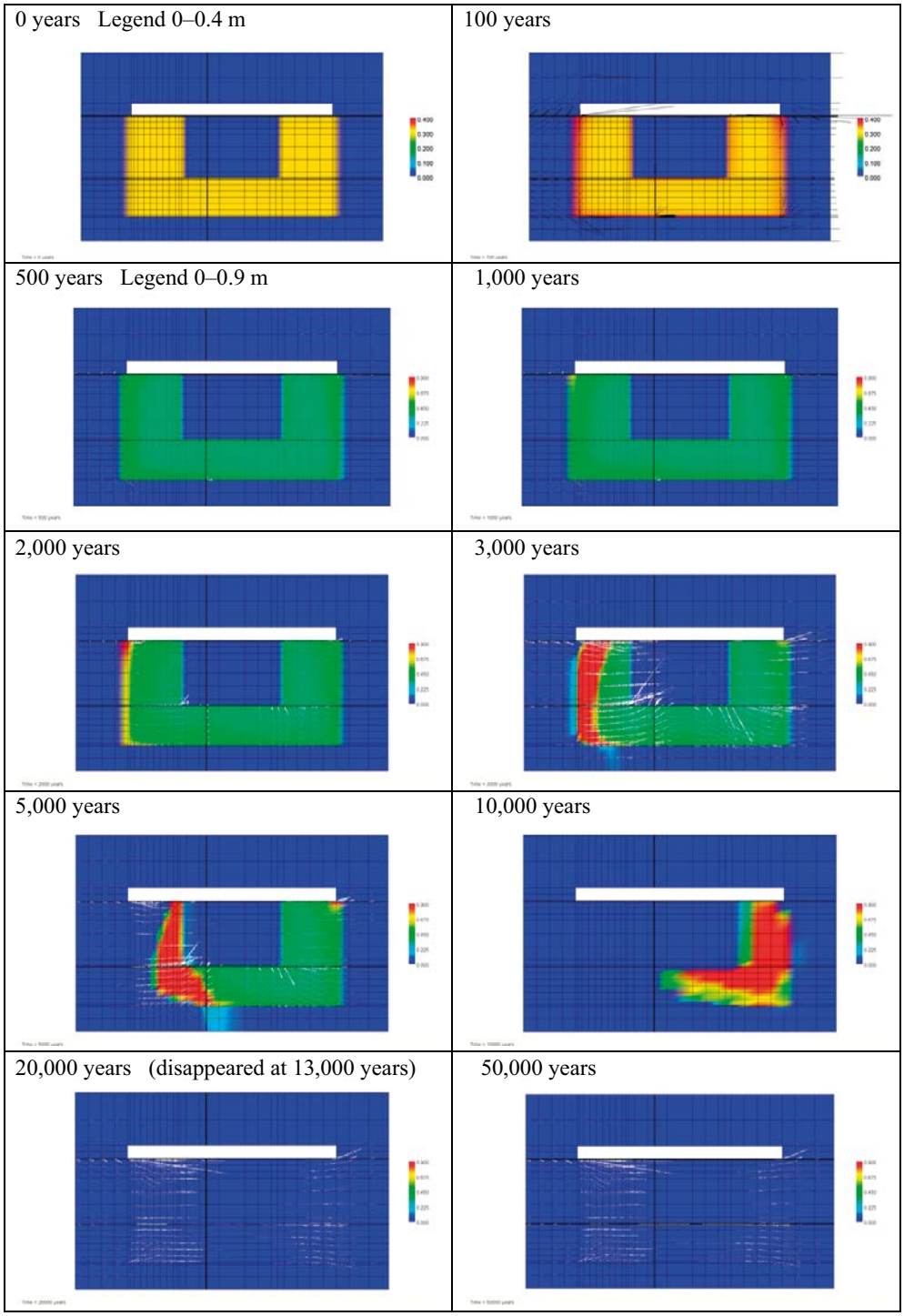

Figure D-21. *Snap-shots of the amount of Ettringite at selected times up to 50,000 years. Legend is presented in units of (kmoles per m³ of porewater). Observe the change of scale after 500 years. (MinteqCem-2001 database, Case Large10.)*

C3FH6-concentrations at different times

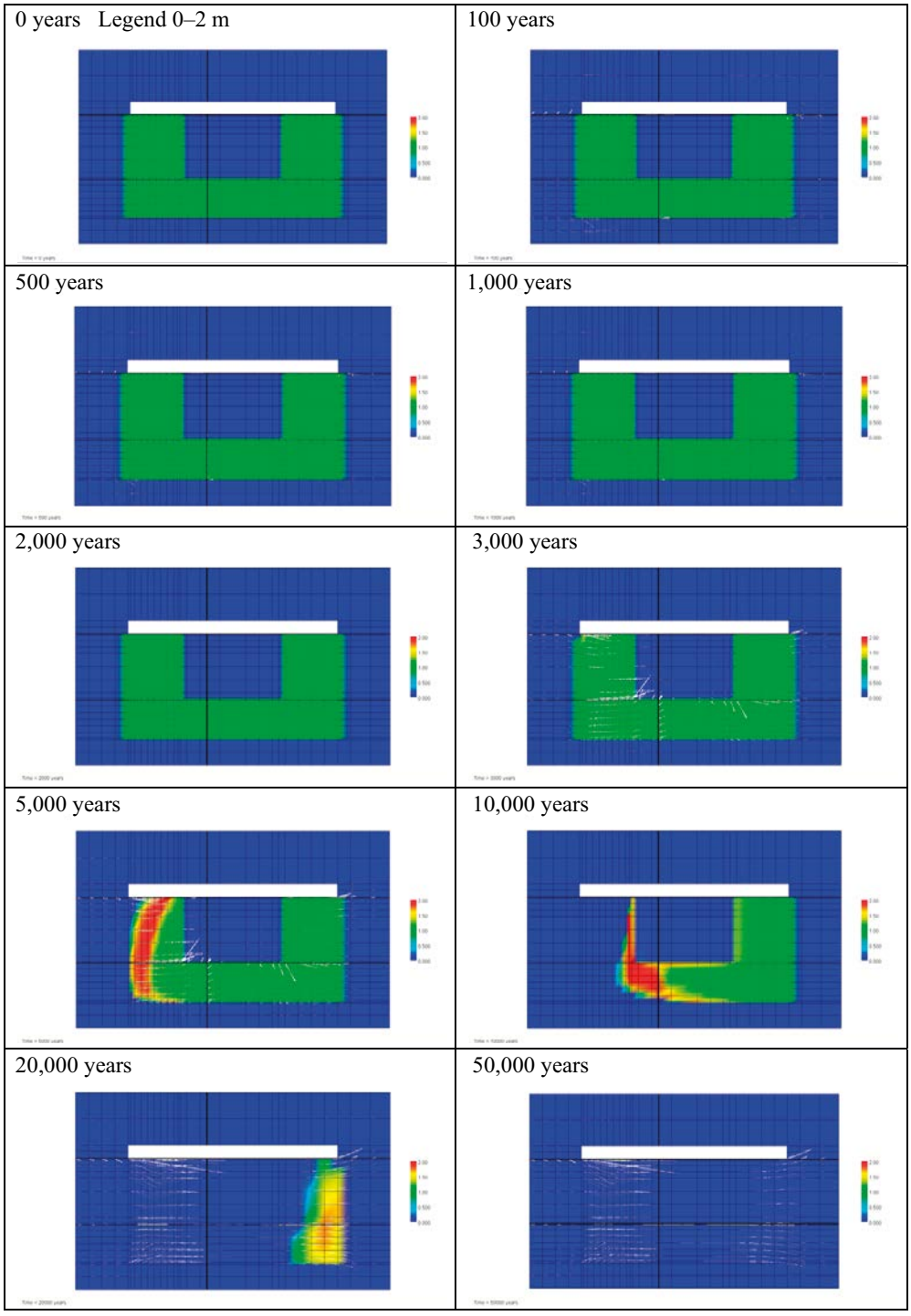

Figure D-22. *Snap-shots of the amount of C3FH6 at selected times up to 50,000 years. Legend is presented in units of (kmoles per m^3 of porewater). (MinteqCem-2001 database, Case Large10.)*

Friedel's salt-concentrations at different times

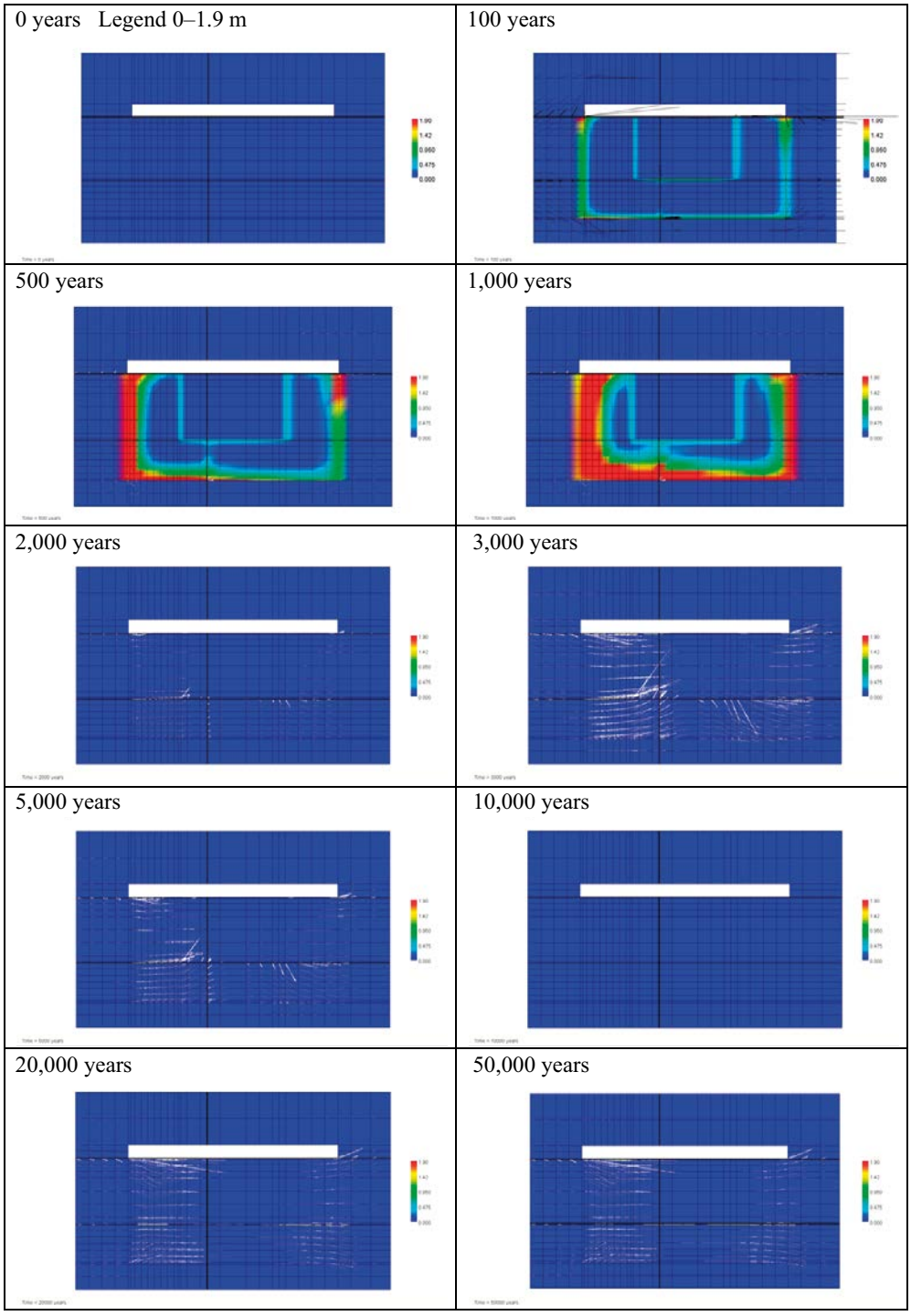

Figure D-23. *Snap-shots of the amount of Friedelsalt at selected times up to 50,000 years. Legend is presented in units of (kmoles per m^3 of porewater). (MinteqCem-2001 database, Case Large10.)*

Monocarboaluminate-concentrations at different times

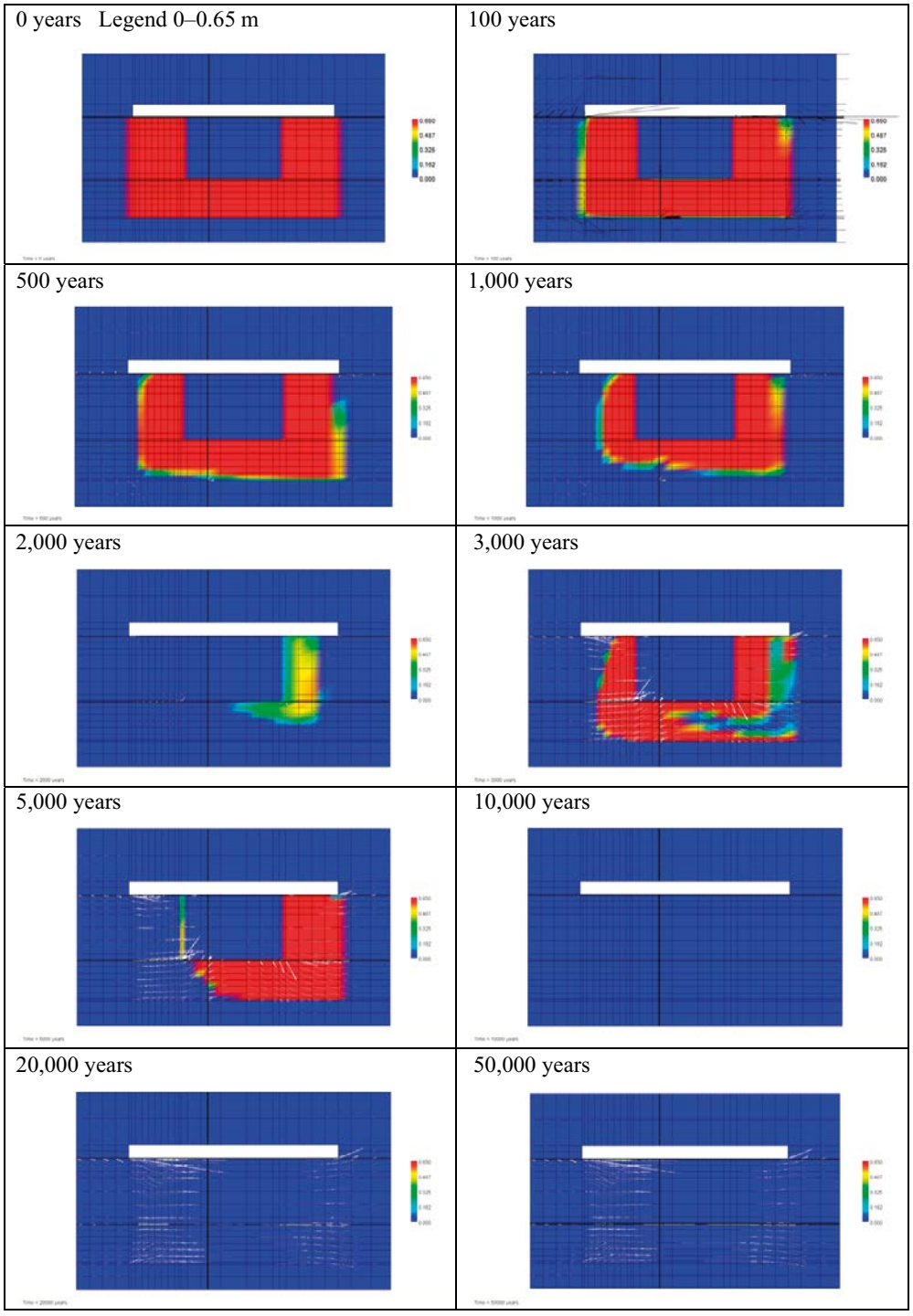

Figure D-24. *Snap-shots of the amount of Monocarboaluminate at selected times up to 50,000 years. Legend is presented in units of (kmoles per m^3 of porewater). (MinteqCem-2001 database, Case Large10.)*

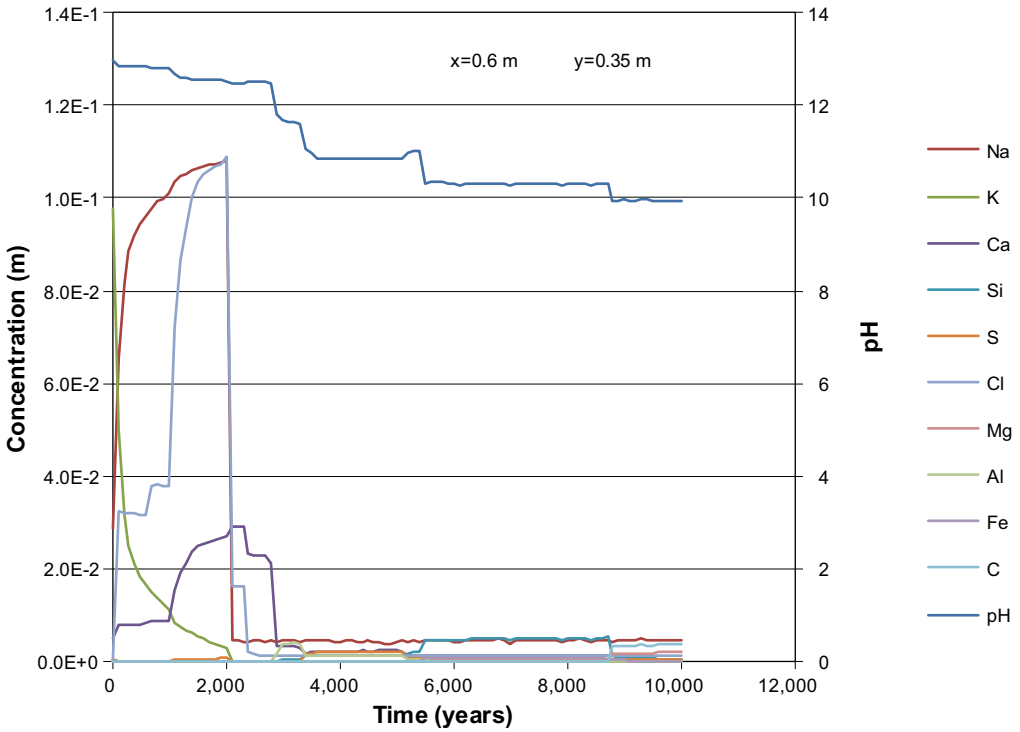

Figure D-25. *The development of the concentration of dissolved components in concrete pore water over time (during the first 10,000 years) at position AE, case Large10. Units (mol/kg pore water).*

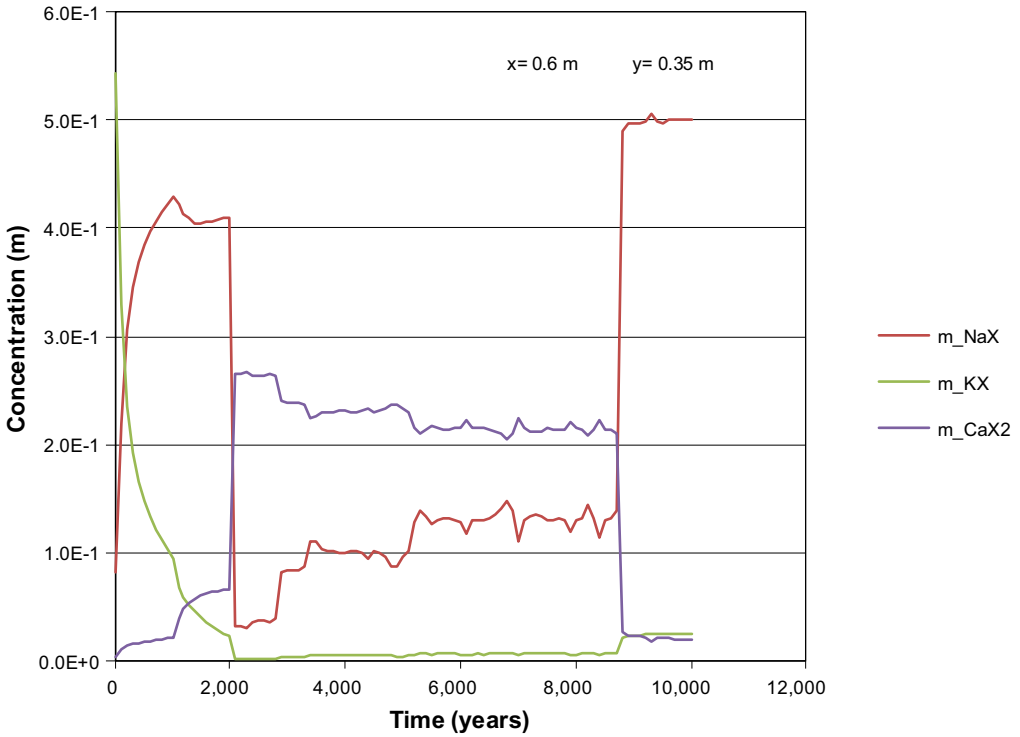

Figure D-26. *The development of the concentration of ion exchange species in concrete over time (during the first 10,000 years) at position AE, case Large10. Units (mol/kg pore water).*

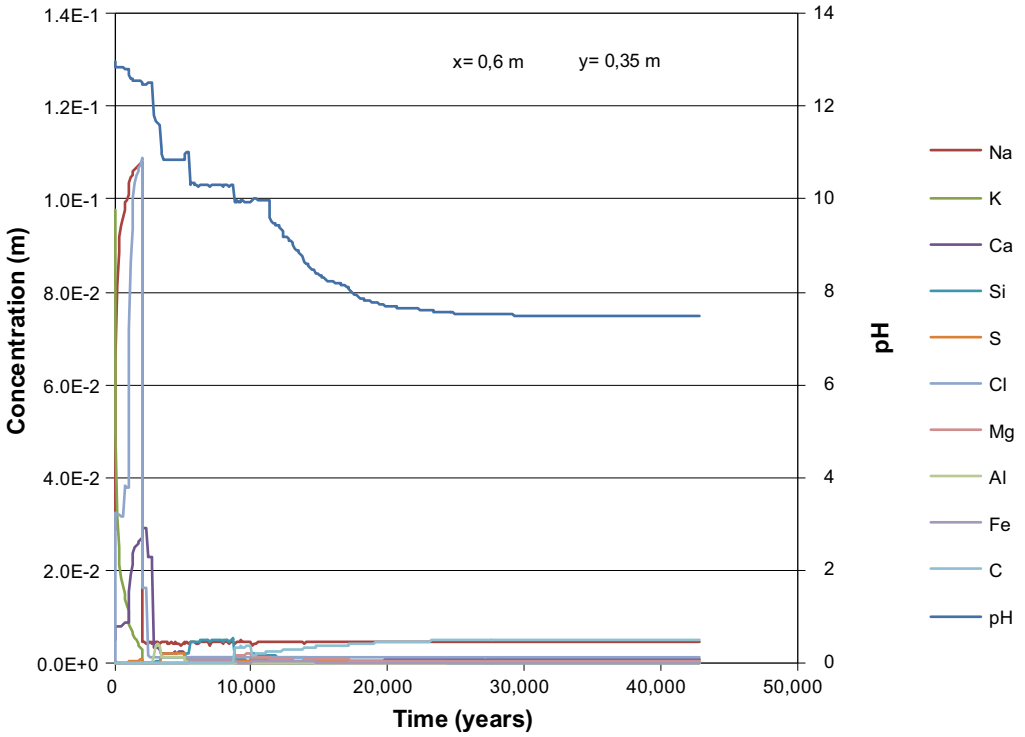

Figure D-27. *The development of the concentration of dissolved components in concrete pore water over time (during the first 42,800 years) at position AE, case Large10. Units (mol/kg pore water).*

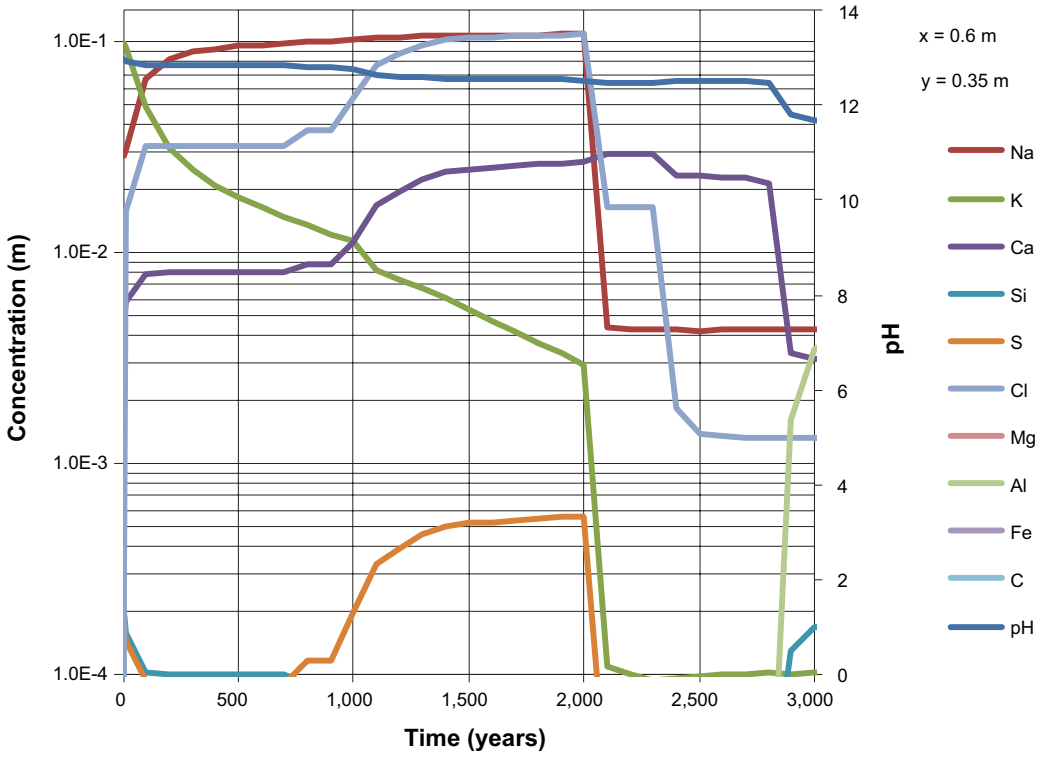

Figure D-28. *The development of the concentration of dissolved components in concrete pore water over time (during the first 3,000 years) at position AE, case Large10. Observe the logarithmic concentration scale. Units (mol/kg pore water).*

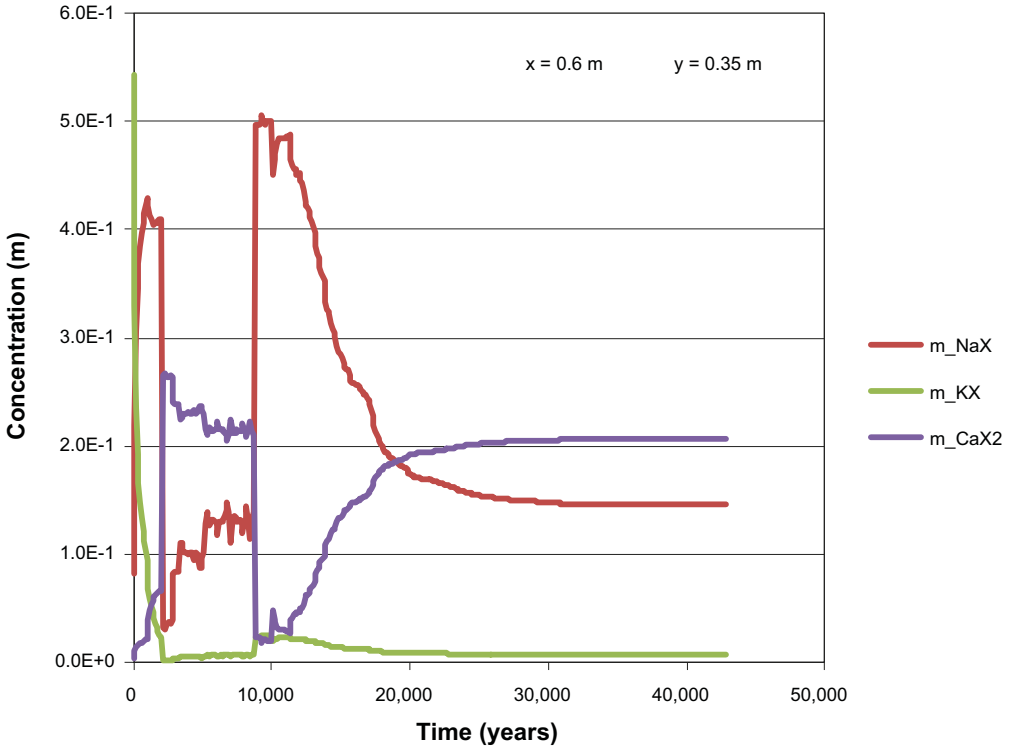

Figure D-29. *The development of the concentration of ion exchange species in concrete over time (during the first 42,800 years) at position AE, case Large10. Units (mol/kg pore water).*

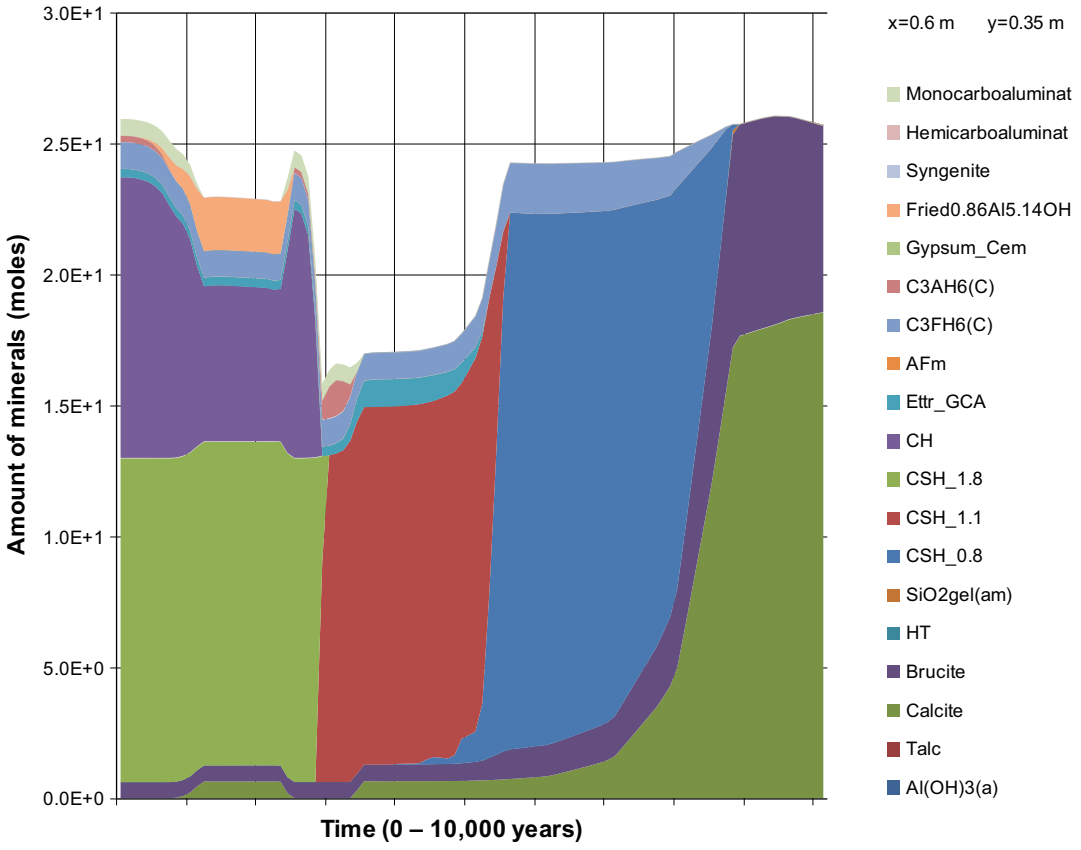

Figure D-30. *The amount of minerals in concrete over time at position AE, case Large10. Units (mol/kg pore water).*

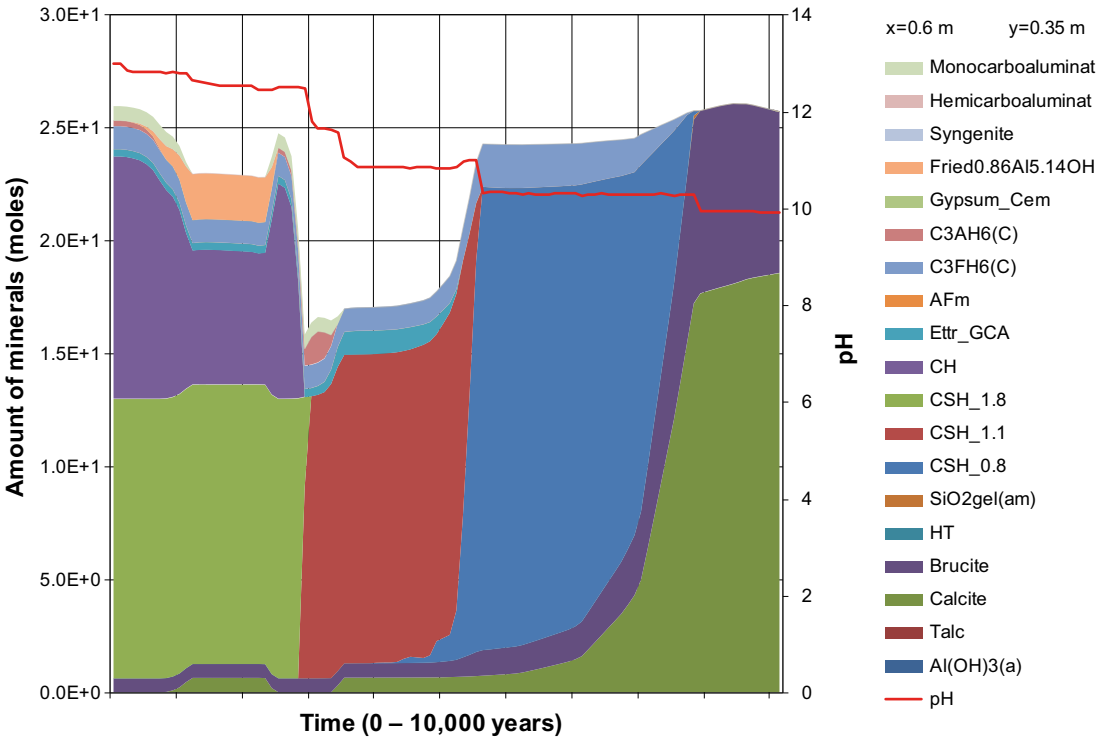

Figure D-31. *The amount of minerals in concrete over time at position AE, case Large10. The evolution of pH with time is also indicated. Units (mol/kg pore water).*

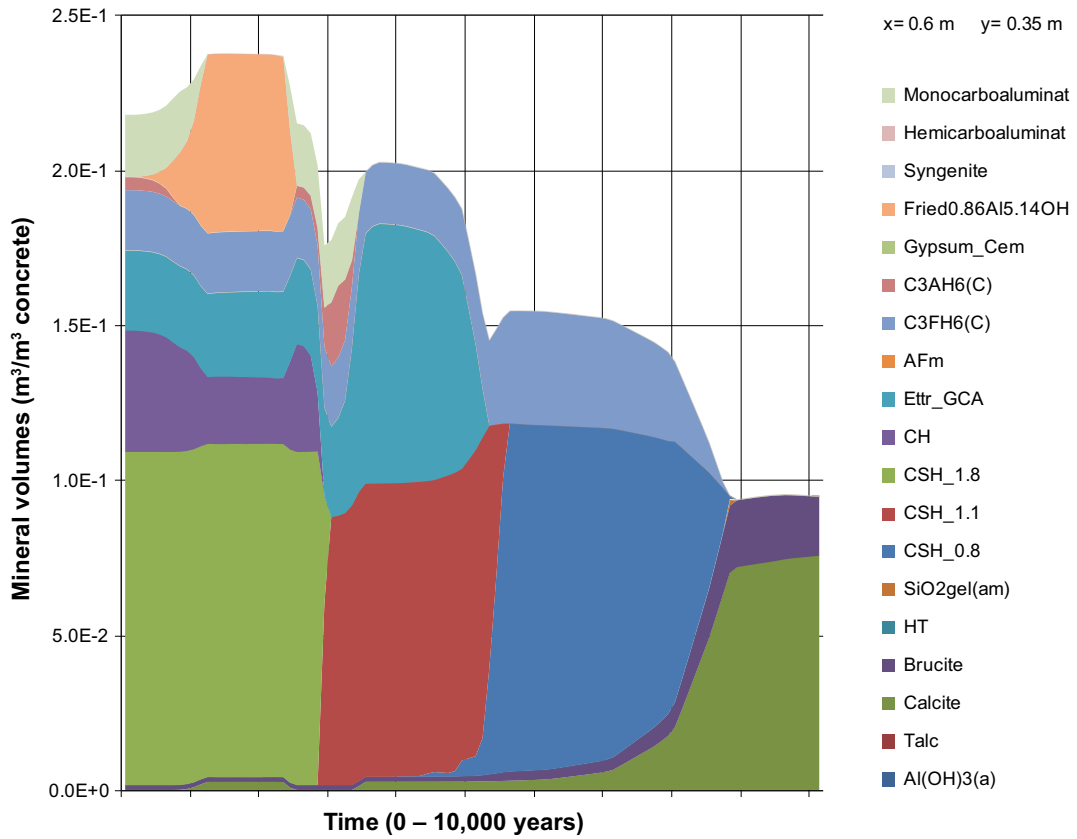

Figure D-32. *The change of mineral volumes in concrete over time at position AE, case Large10.*

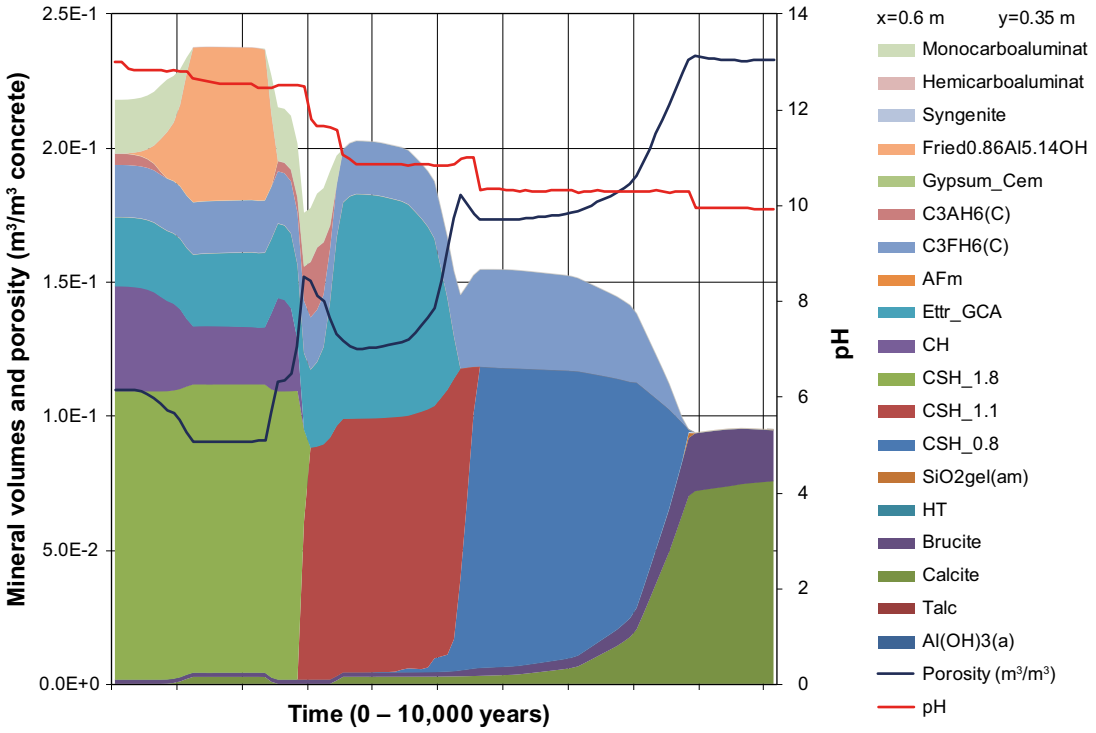

Figure D-33. *The change of mineral volumes and porosity in concrete over time at position AE, case Large10. The evolution of pH with time is also indicated.*

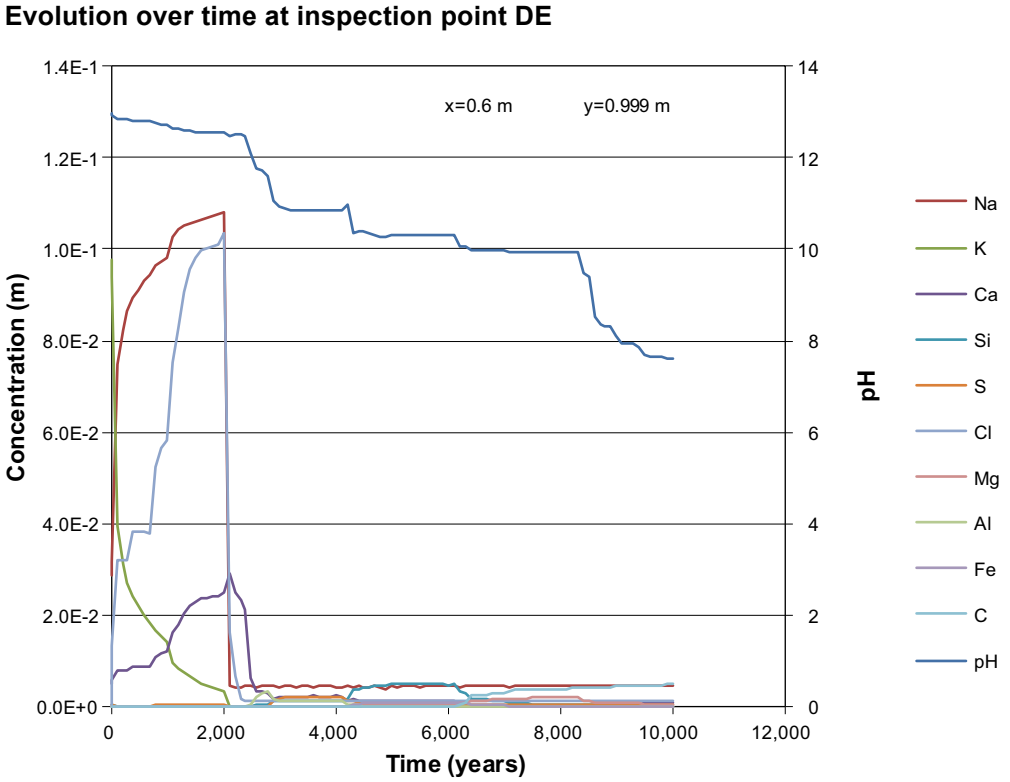

Figure D-34. *The development of the concentration of dissolved components in concrete pore water over time (during the first 10,000 years) at position DE (1 mm from an open fracture), case Large10. Units (mol/kg pore water).*

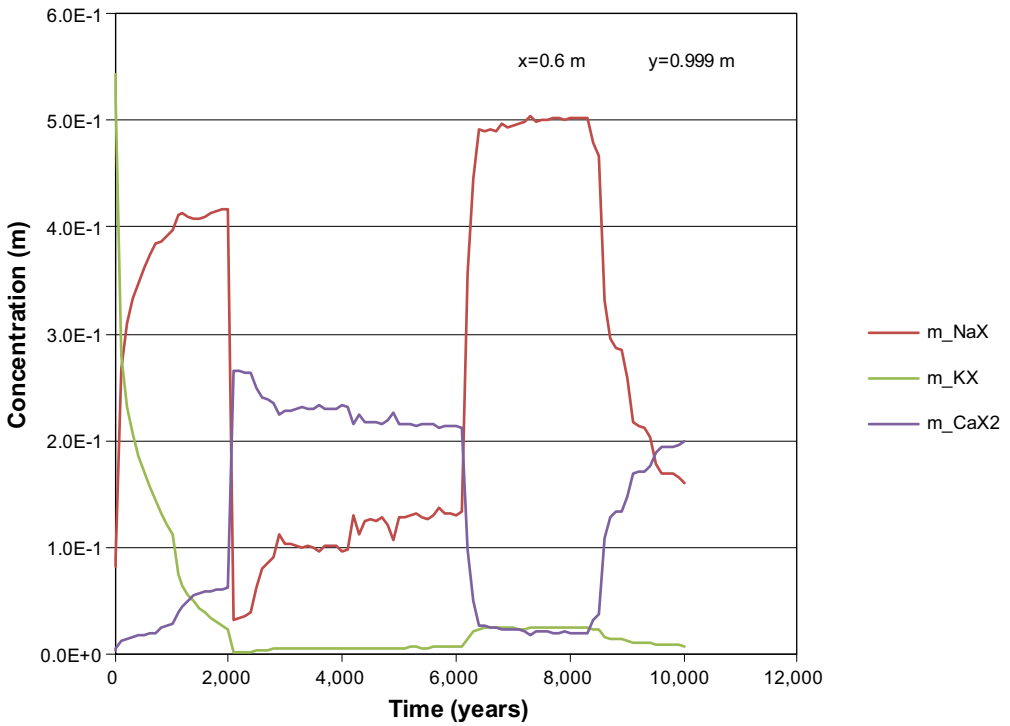

Figure D-35. *The development of the concentration of ion exchange species in concrete over time (during the first 10,000 years) at position DE (1 mm from an open fracture), case Large10. Units (mol/kg pore water).*

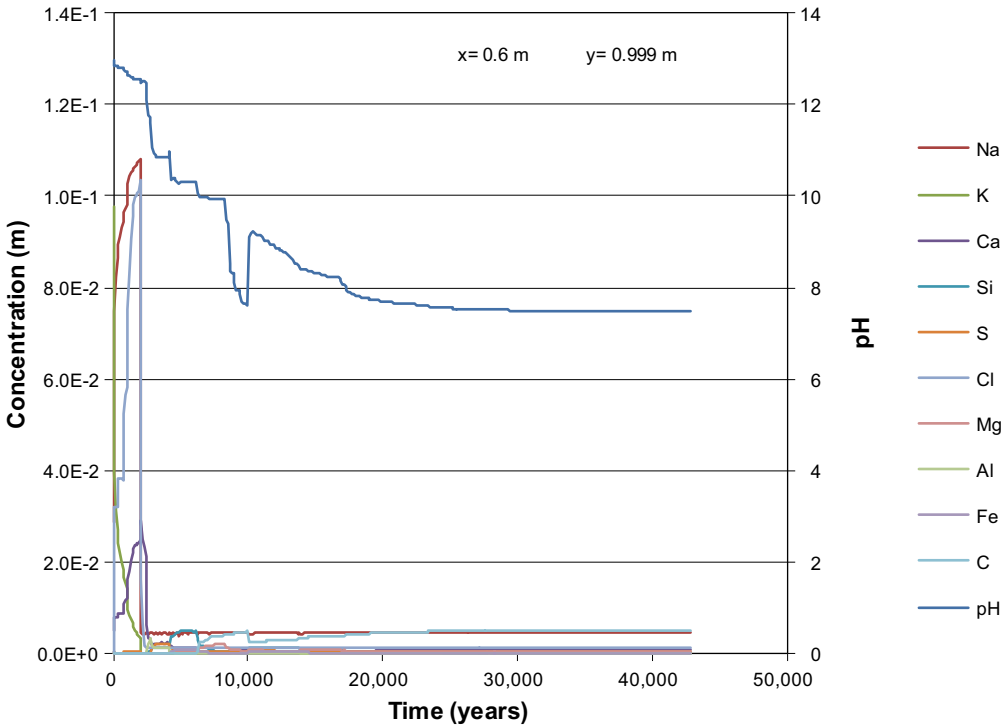

Figure D-36. *The development of the concentration of dissolved components in concrete pore water over time (during the first 42,800 years) at position DE (1 mm from an open fracture), case Large10. Units (mol/kg pore water).*

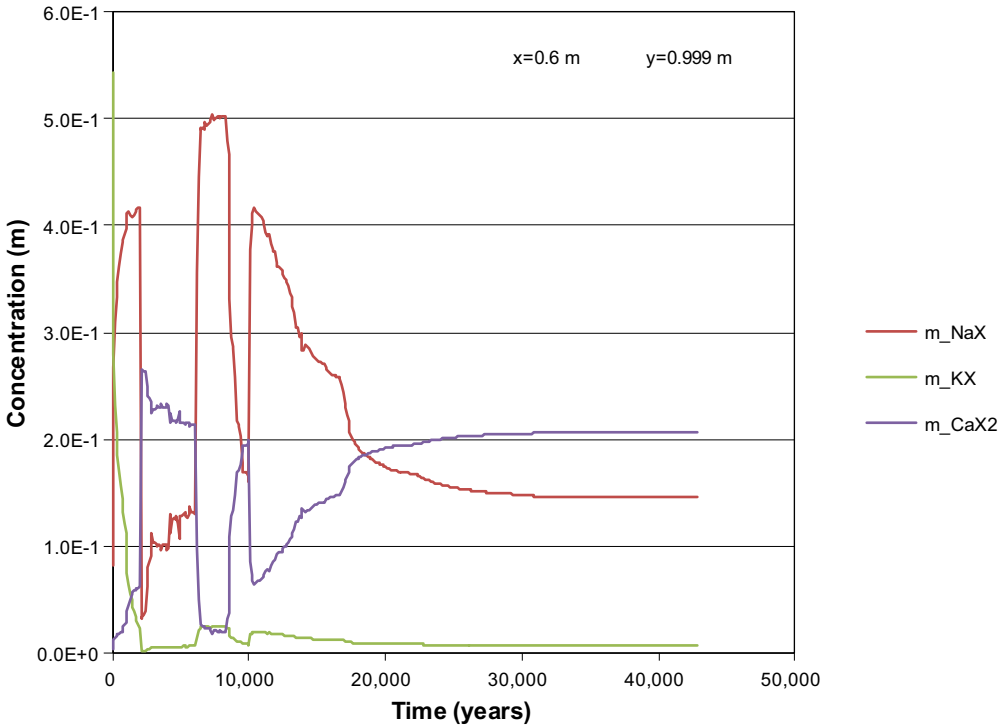

Figure D-37. *The development of the concentration of ion exchange species in concrete over time (during the first 42,800 years) at position DE (1 mm from an open fracture), case Large10. Units (mol/kg pore water).*

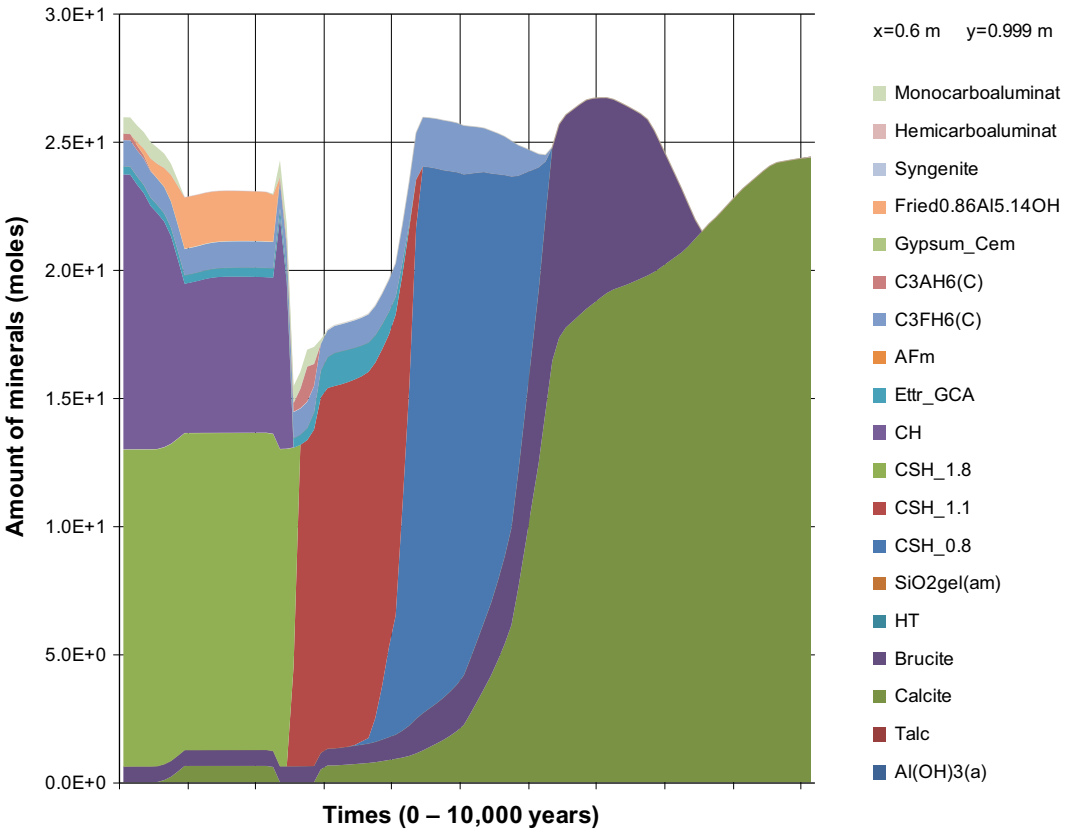

Figure D-38. *The amount of minerals in concrete over time at position DE (1 mm from an open fracture), case Large10. Units (mol/kg pore water).*

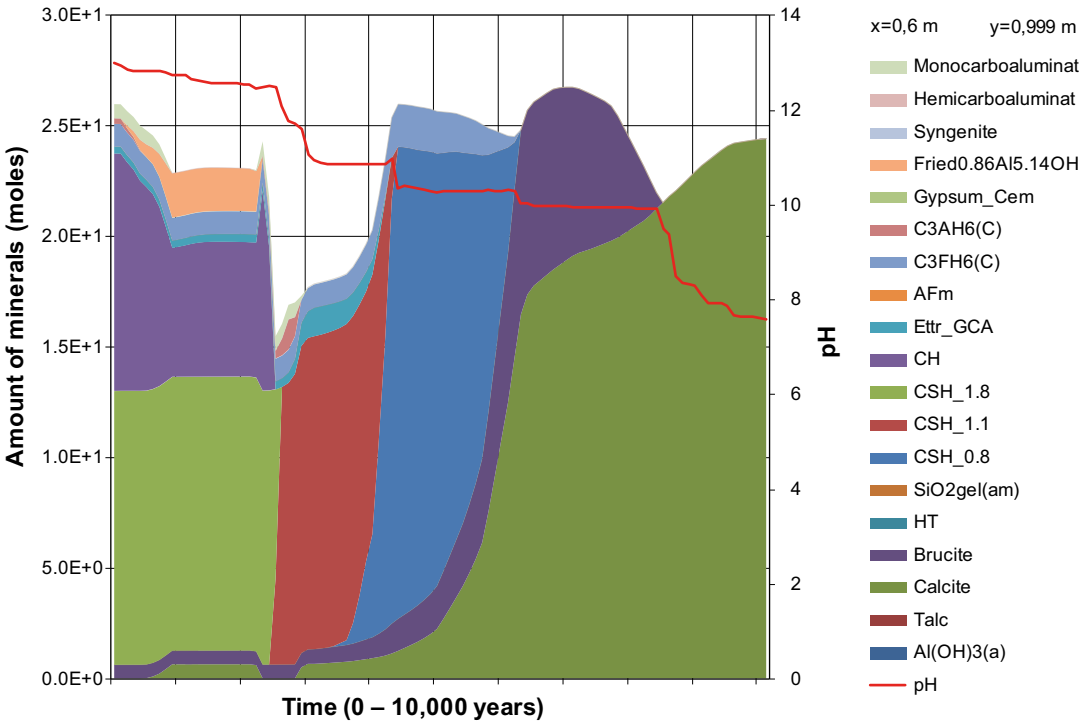

Figure D-39. *The amount of minerals in concrete over time at position DE (1 mm from an open fracture), case Large10. The evolution of pH with time is also indicated. Units (mol/kg pore water).*

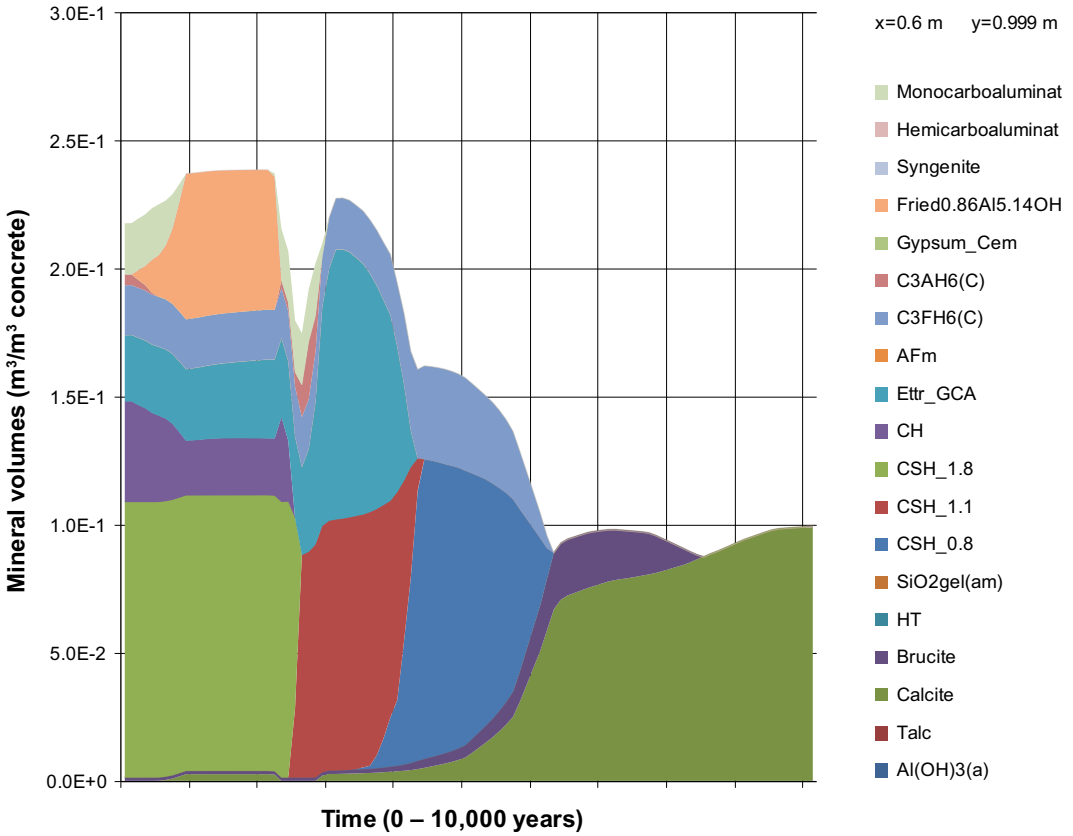

Figure D-40. *The change of mineral volumes in concrete over time at position DE (1 mm from an open fracture), case Large10.*

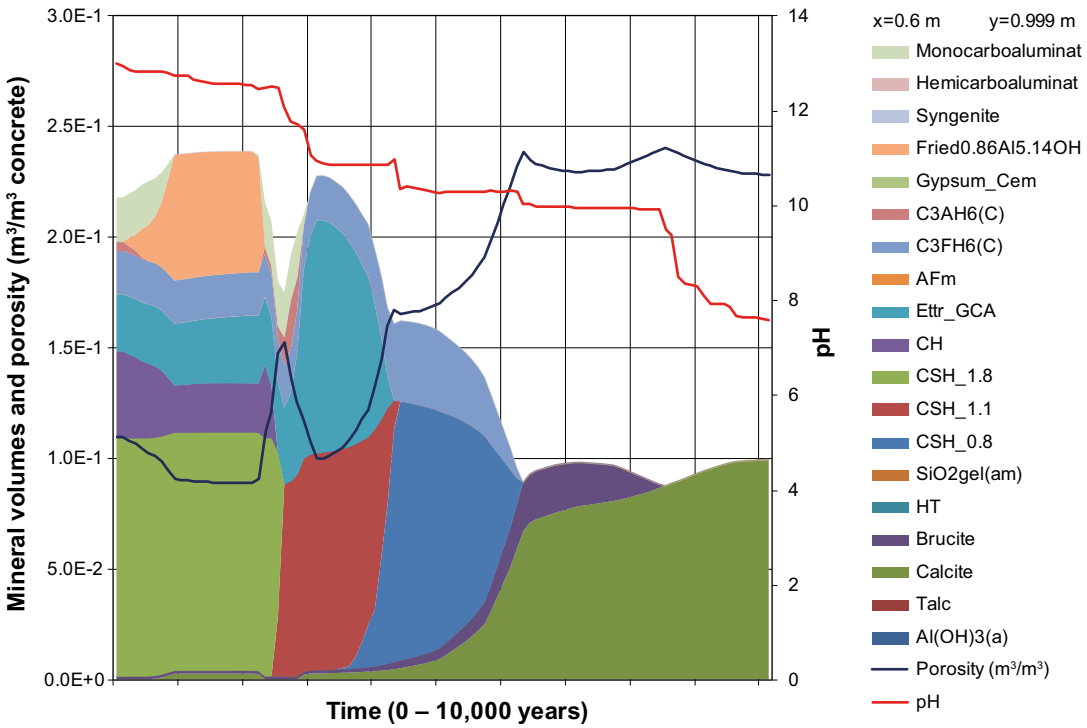

Figure D-41. *The change of mineral volumes and porosity in concrete over time at position DE (1 mm from an open fracture), case Large10. The evolution of pH with time is also indicated.*

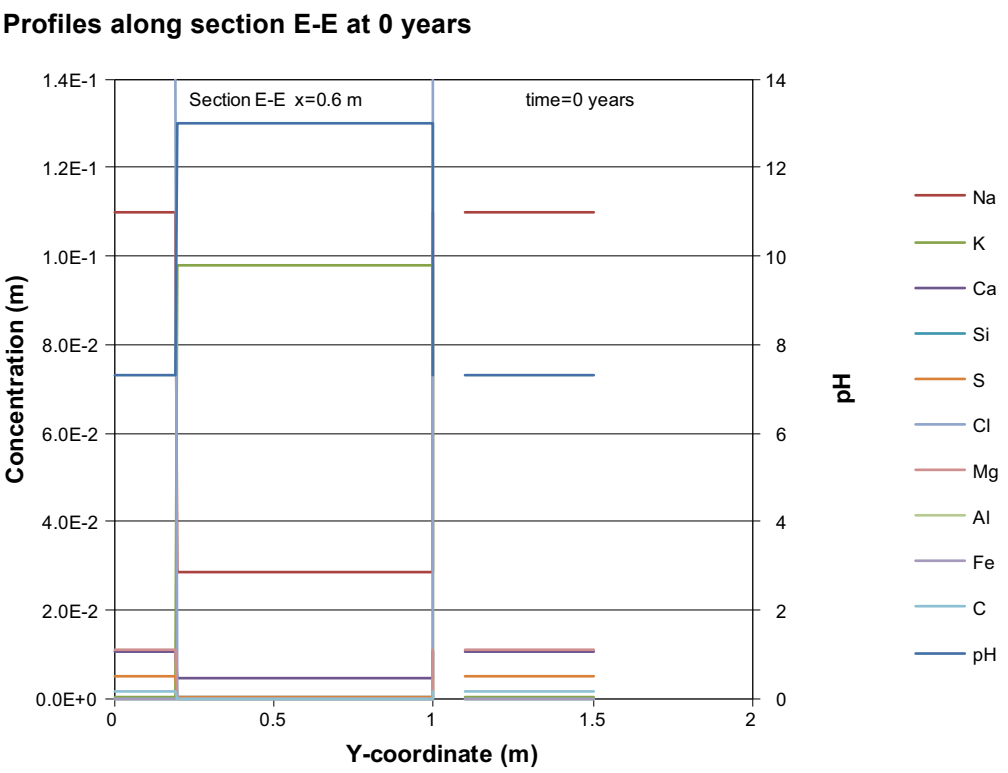

Figure D-42. *Concentration profiles of dissolved components in concrete pore water along the vertical Section E-E at time 0 years, case Large10. Units (mol/kg pore water).*

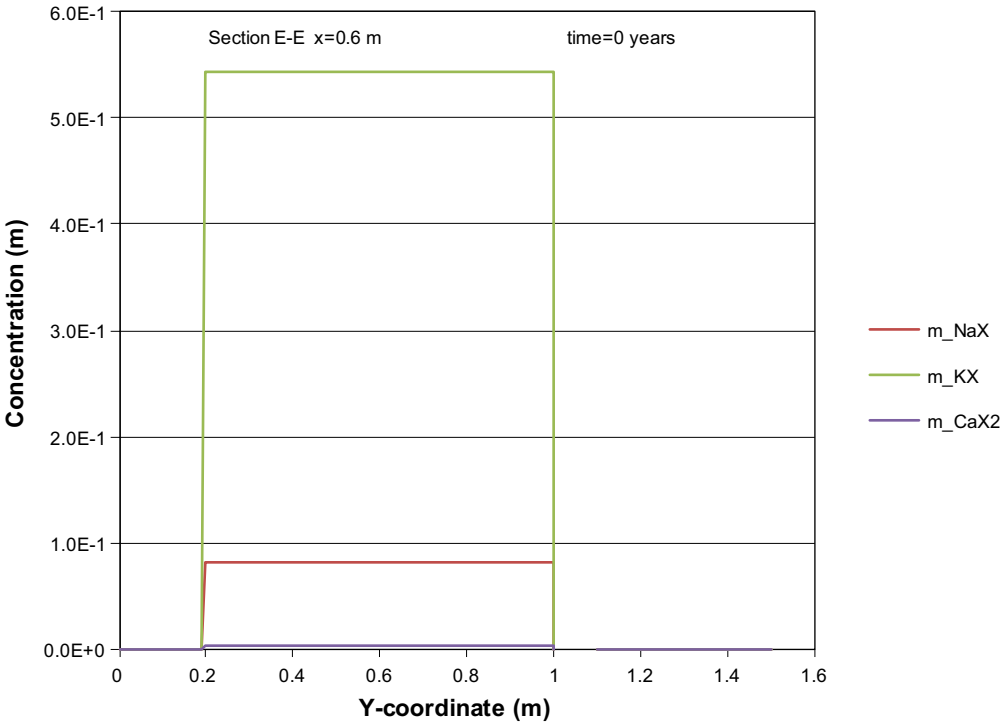

Figure D-43. *The assembly of ion exchange species in concrete along the vertical Section E-E at time 0 years, case Large10. Units (mol/kg pore water).*

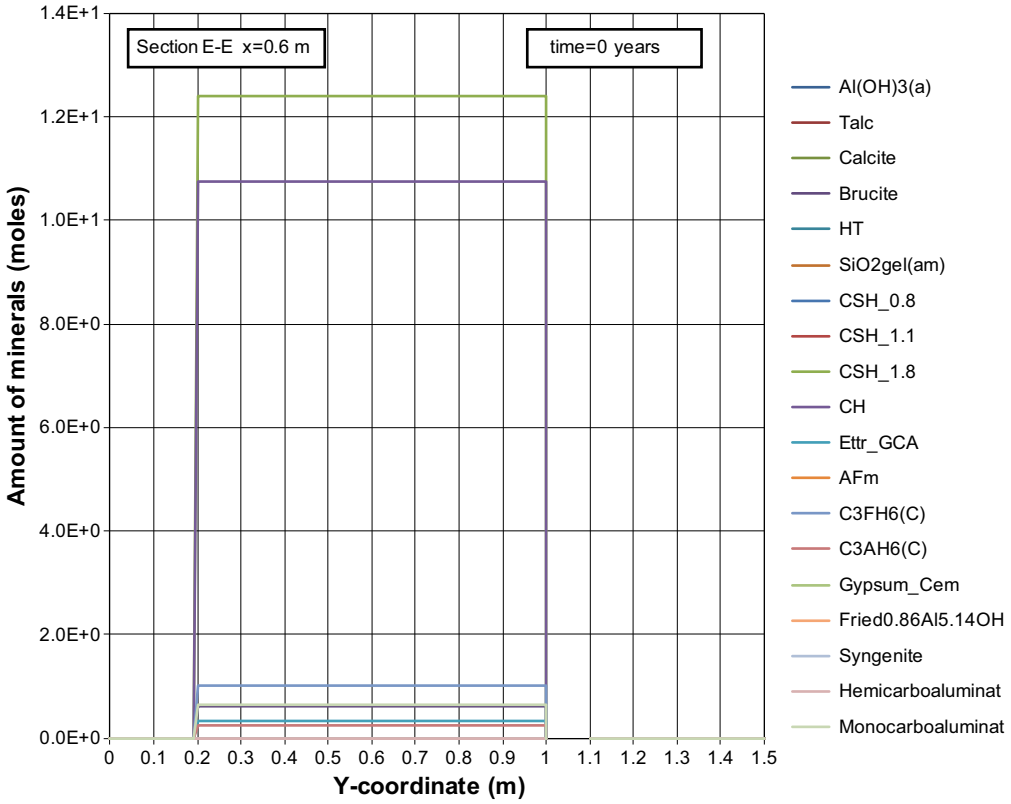

Figure D-44. *The mineral composition in concrete along the vertical Section E-E at time 0 years, case Large10. Units (mol/kg pore water).*

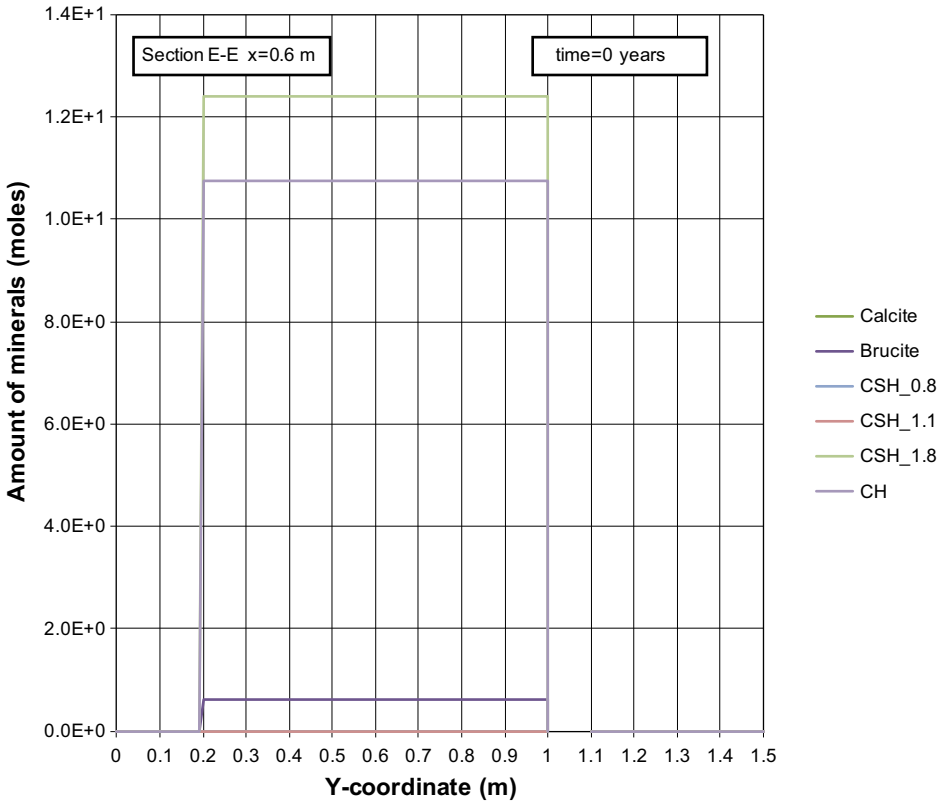

Figure D-45. *The mineral composition in concrete along the vertical Section E-E at time 0 years, case Large10. Units (mol/kg pore water).*

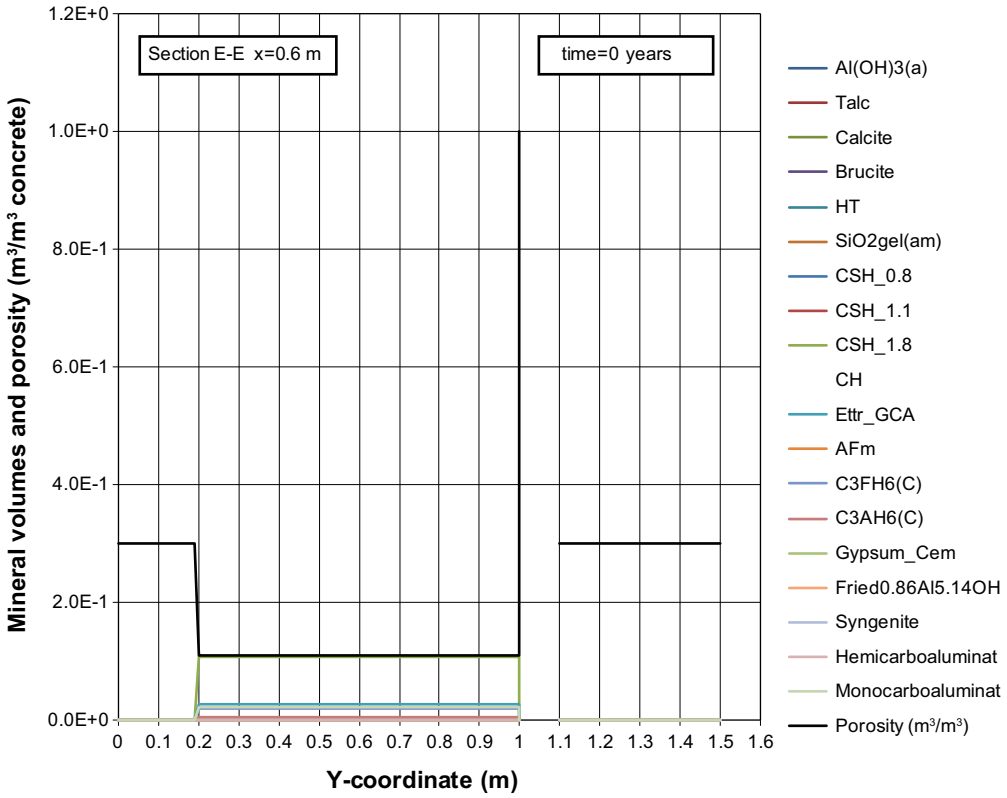

Figure D-46. *Mineral composition in concrete and calculated porosity along the vertical Section E-E at time 0 years, case Large10.*

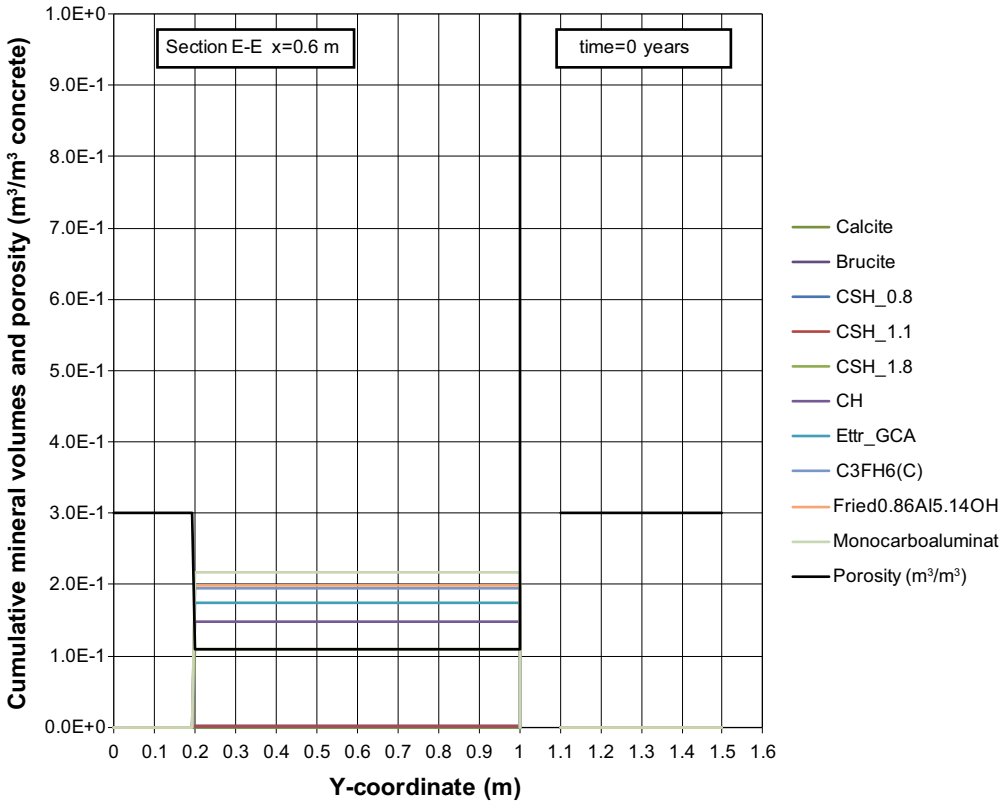

Figure D-47. *Cumulative representation of the mineral composition in concrete and calculated porosity along the vertical Section E-E at time 0 years, case Large10.*

Profiles along section E-E at 100 years

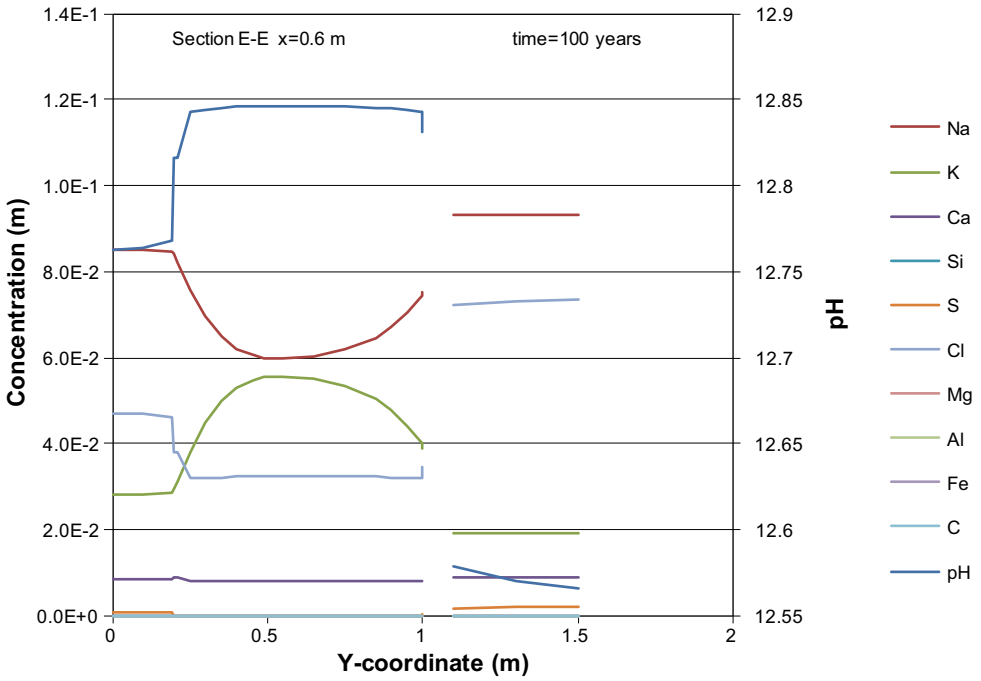

Figure D-48. *Concentration profiles of dissolved components in concrete pore water along the vertical Section E-E at time 100 years, case Large10. Units (mol/kg pore water).*

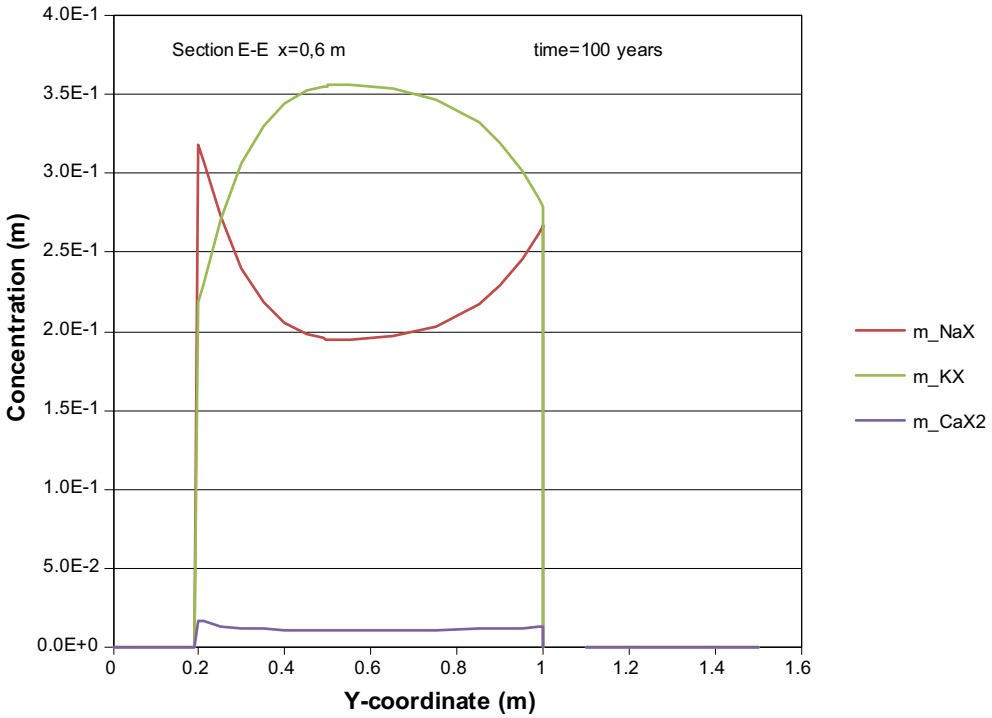

Figure D-49. *The assembly of ion exchange species in concrete along the vertical Section E-E at time 100 years, case Large10. Units (mol/kg pore water).*

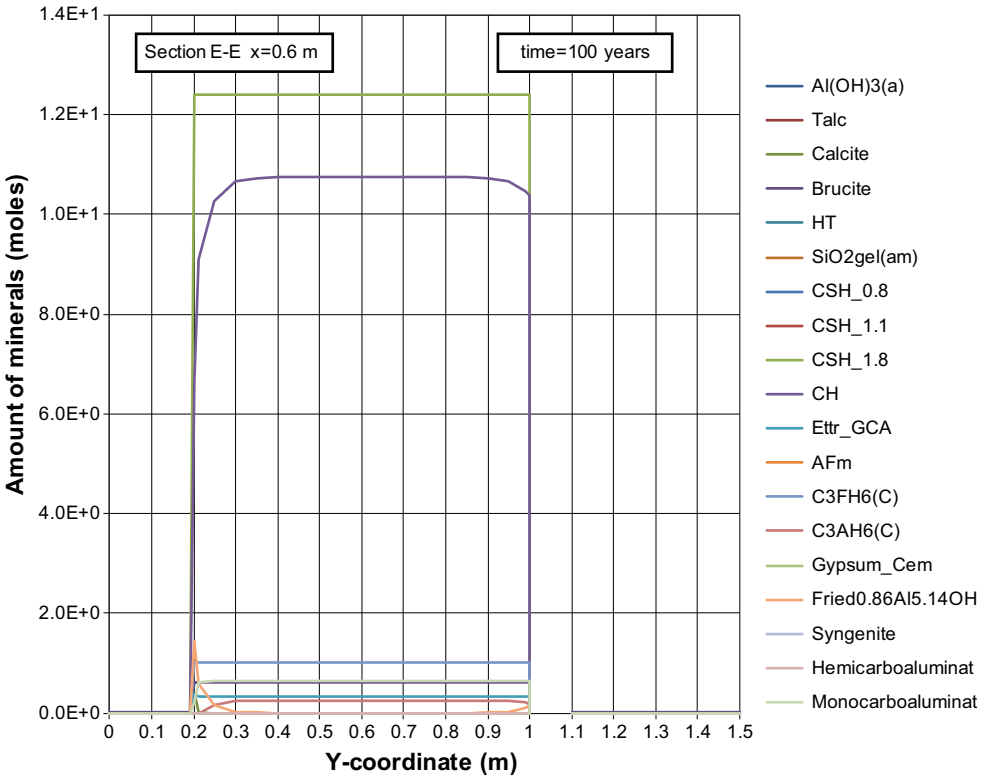

Figure D-50. *The mineral composition in concrete along the vertical Section E-E at time 100 years, case Large10. Units (mol/kg pore water).*

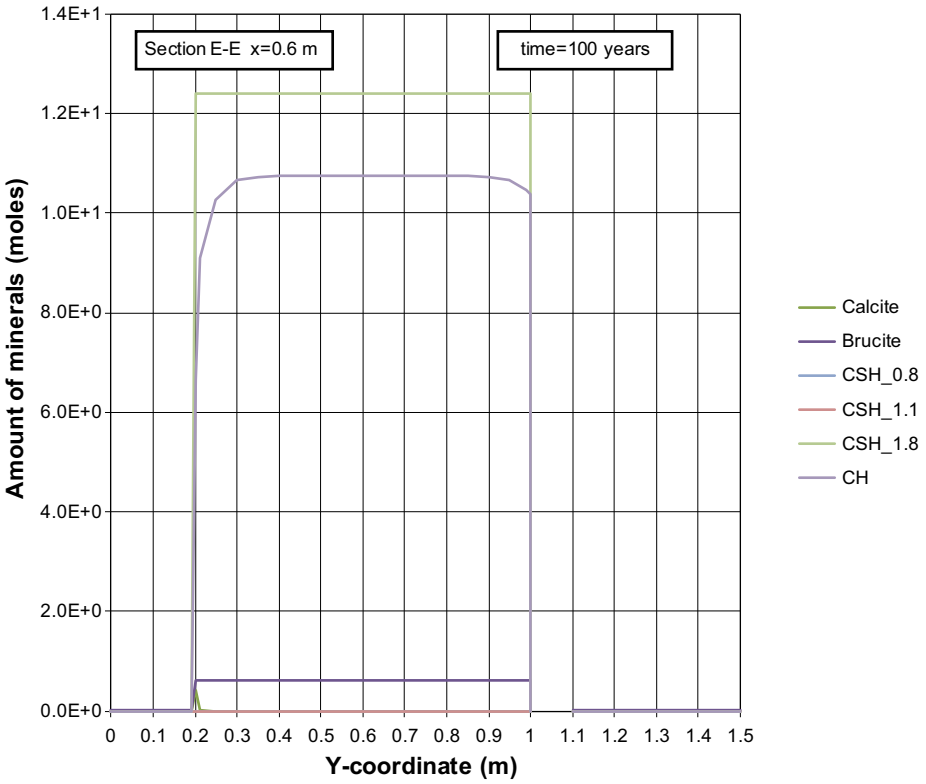

Figure D-51. *The mineral composition in concrete along the vertical Section E-E at time 100 years, case Large10. Units (mol/kg pore water).*

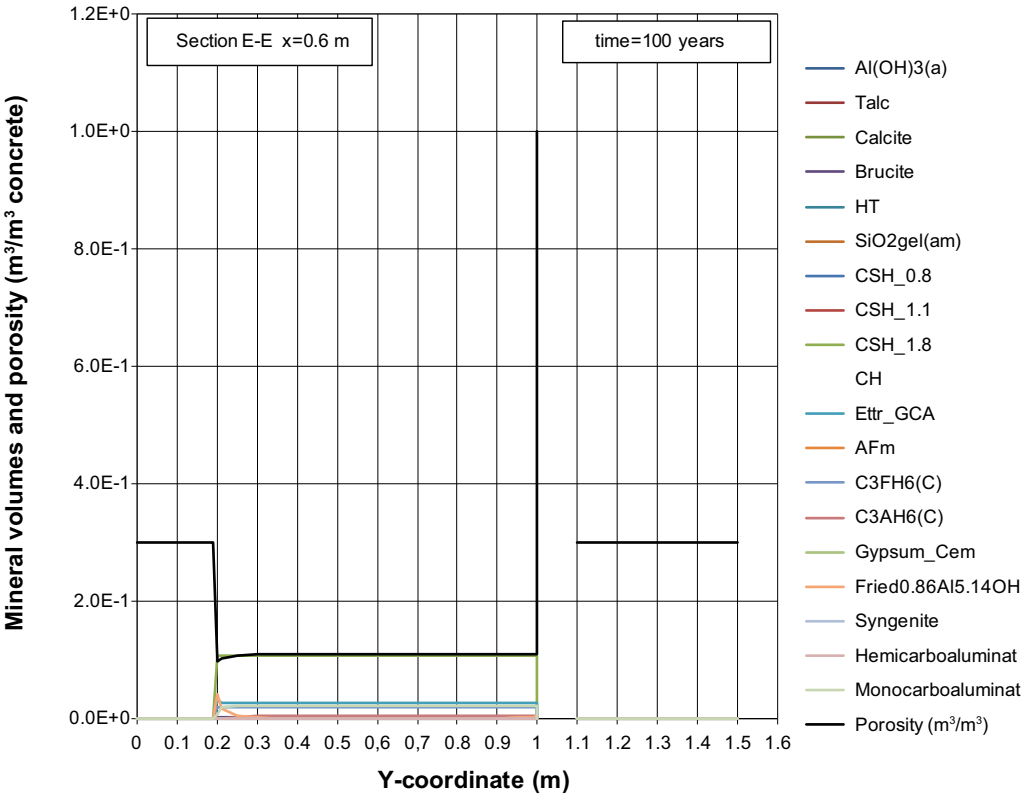

Figure D-52. *Mineral composition in concrete and calculated porosity along the vertical Section E-E at time 100 years, case Large10.*

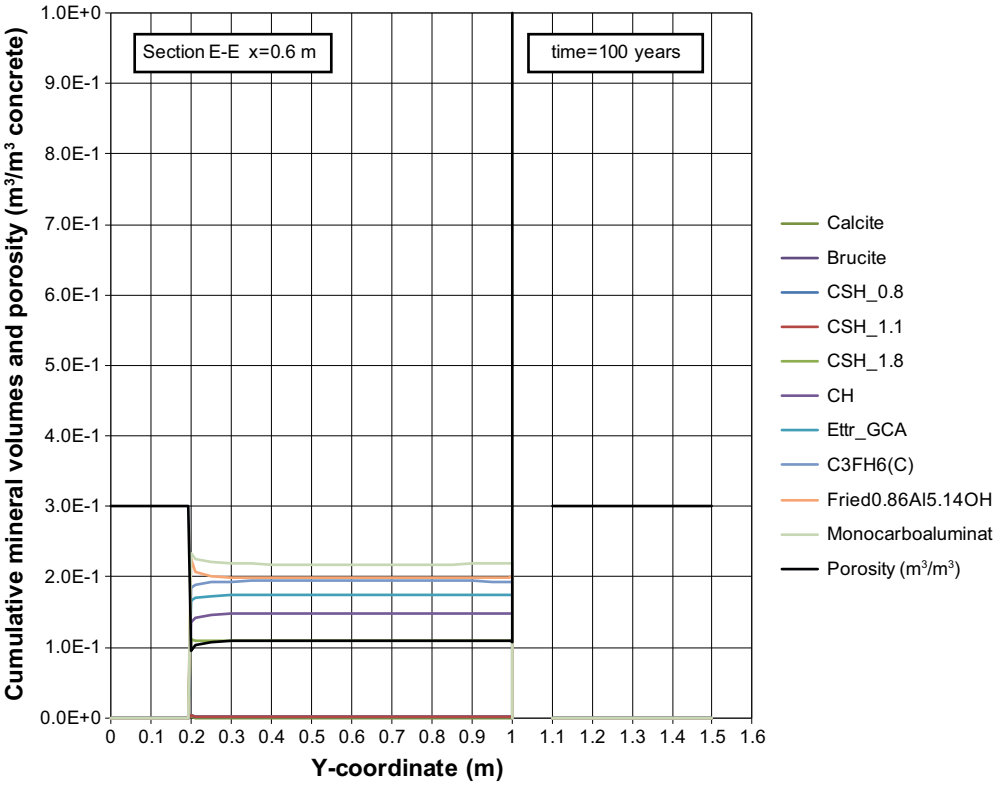

Figure D-53. *Cumulative representation of the mineral composition in concrete and calculated porosity along the vertical Section E-E at time 100 years, case Large10.*

Profiles along section E-E at 1,000 years

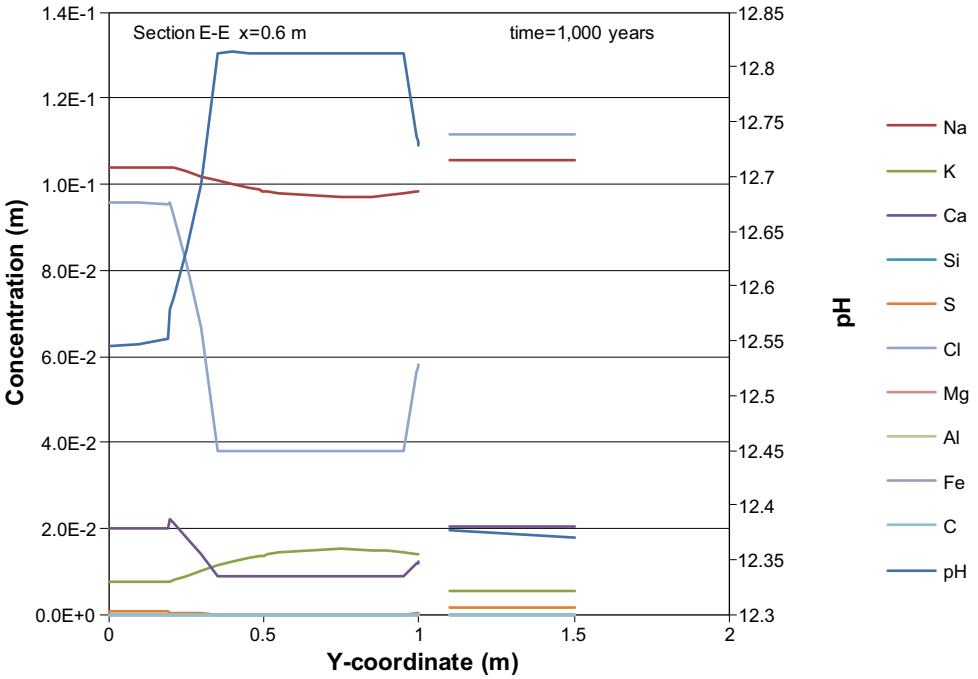

Figure D-54. *Concentration profiles of dissolved components in concrete pore water along the vertical Section E-E at time 1,000 years, case Large10. Units (mol/kg pore water).*

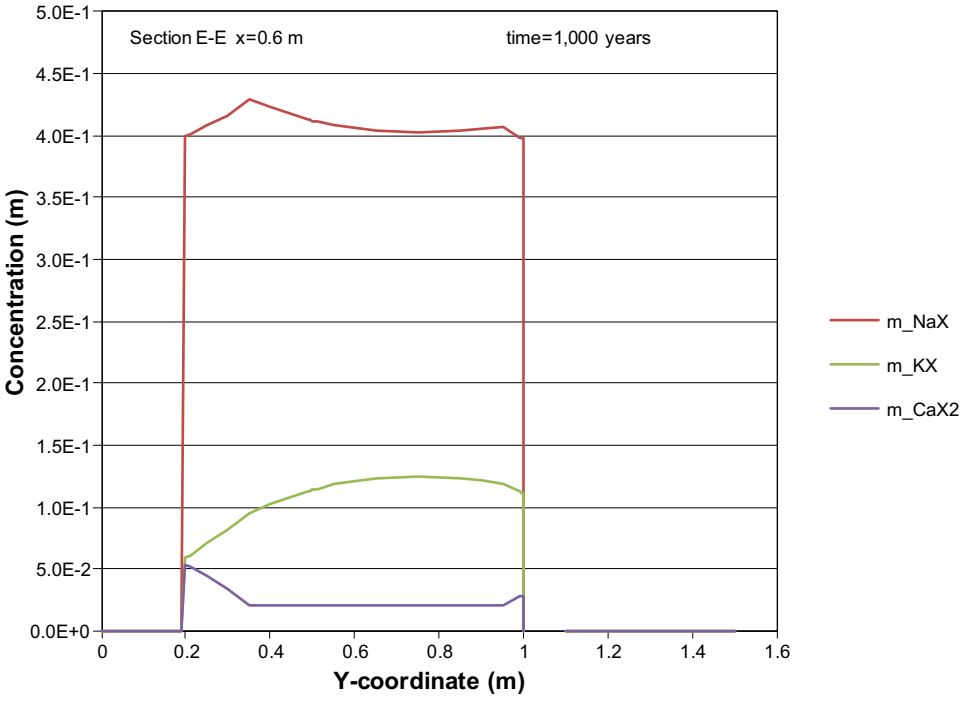

Figure D-55. *The assembly of ion exchange species in concrete along the vertical Section E-E at time 1,000 years, case Large10. Units (mol/kg pore water).*

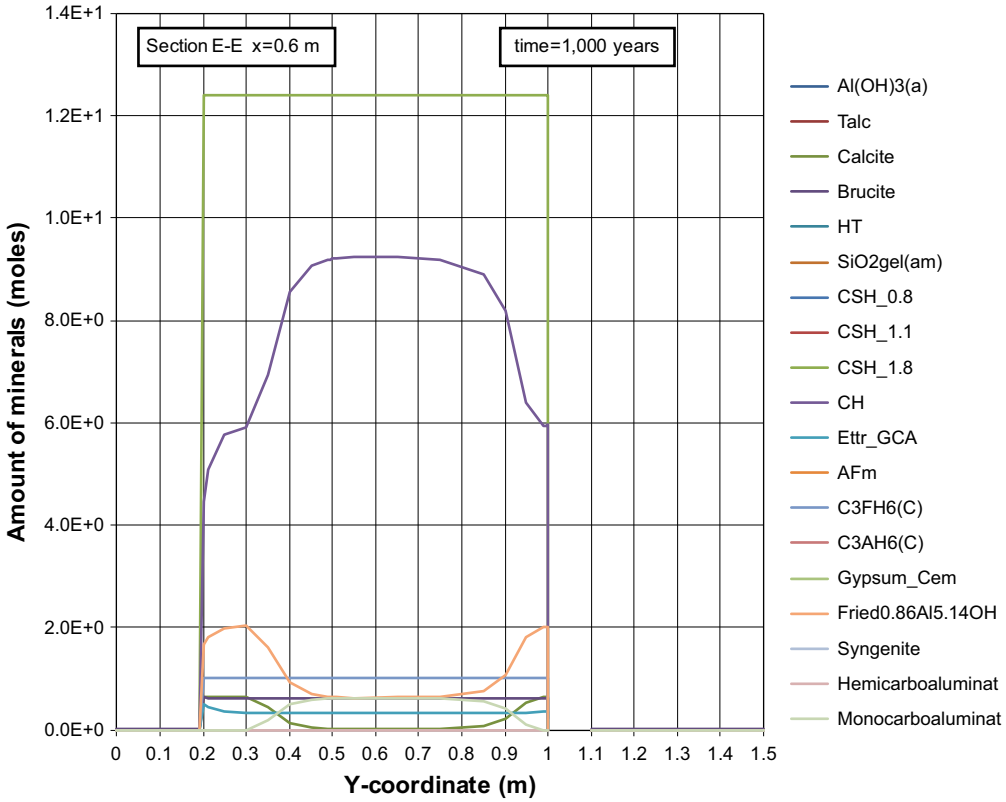

Figure D-56. *The mineral composition in concrete along the vertical Section E-E at time 1,000 years, case Large10. Units (mol/kg pore water).*

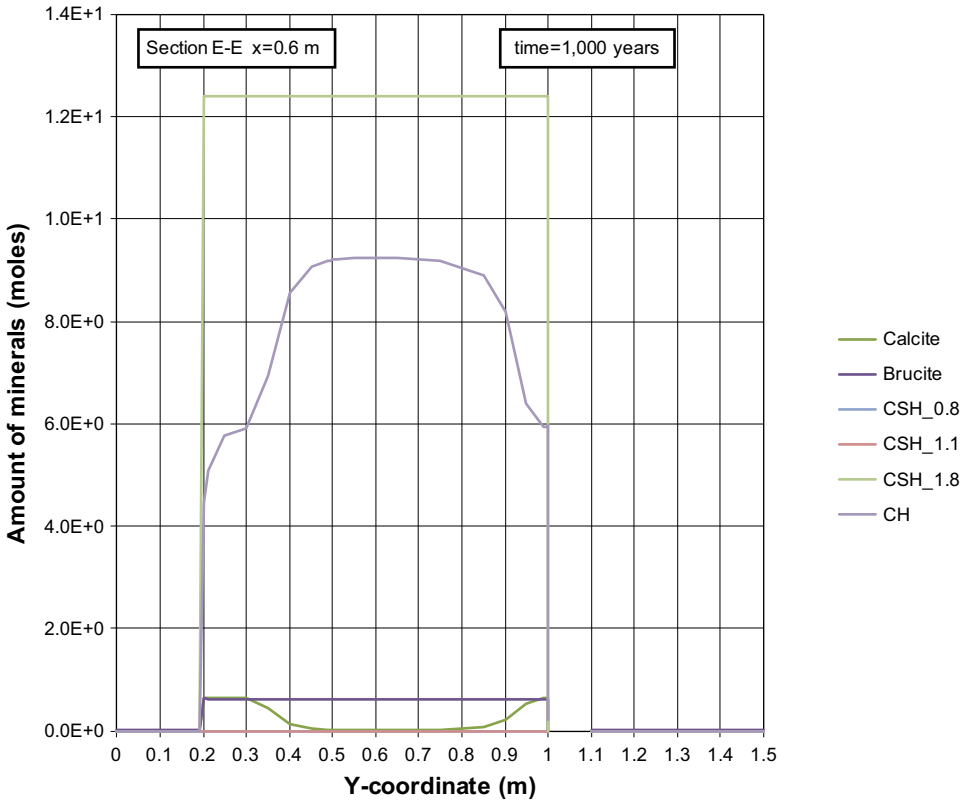

Figure D-57. *The mineral composition in concrete along the vertical Section E-E at time 1,000 years, case Large10. Units (mol/kg pore water).*

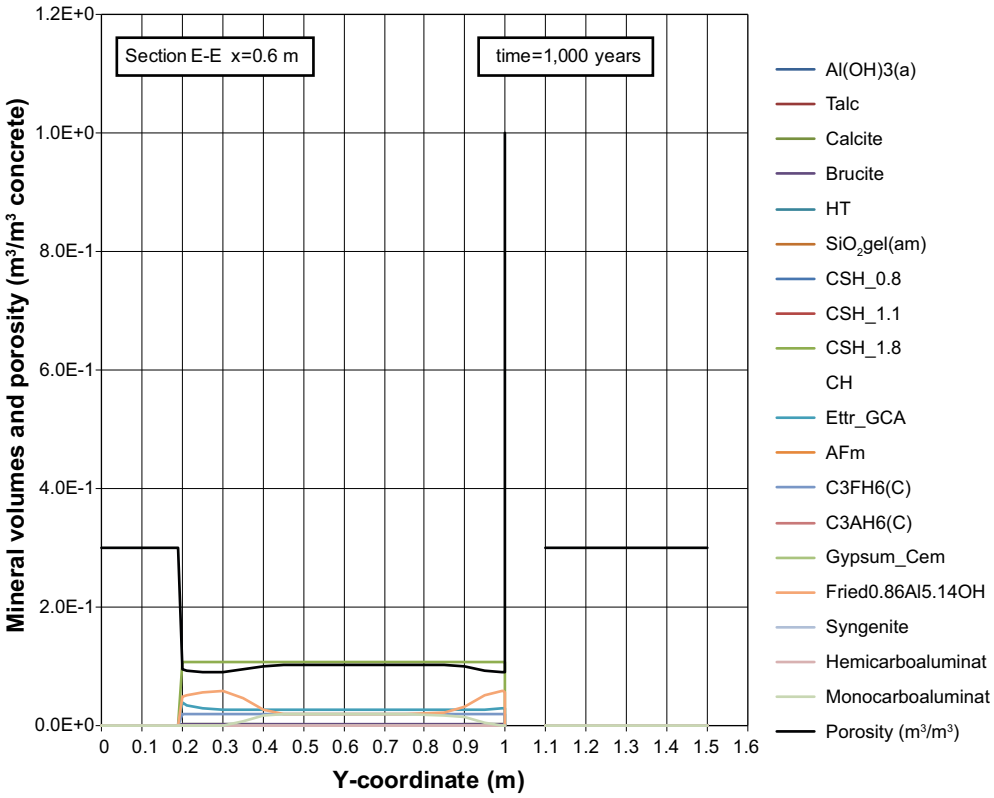

Figure D-58. *Mineral composition in concrete and calculated porosity along the vertical Section E-E at time 1,000 years, case Large10.*

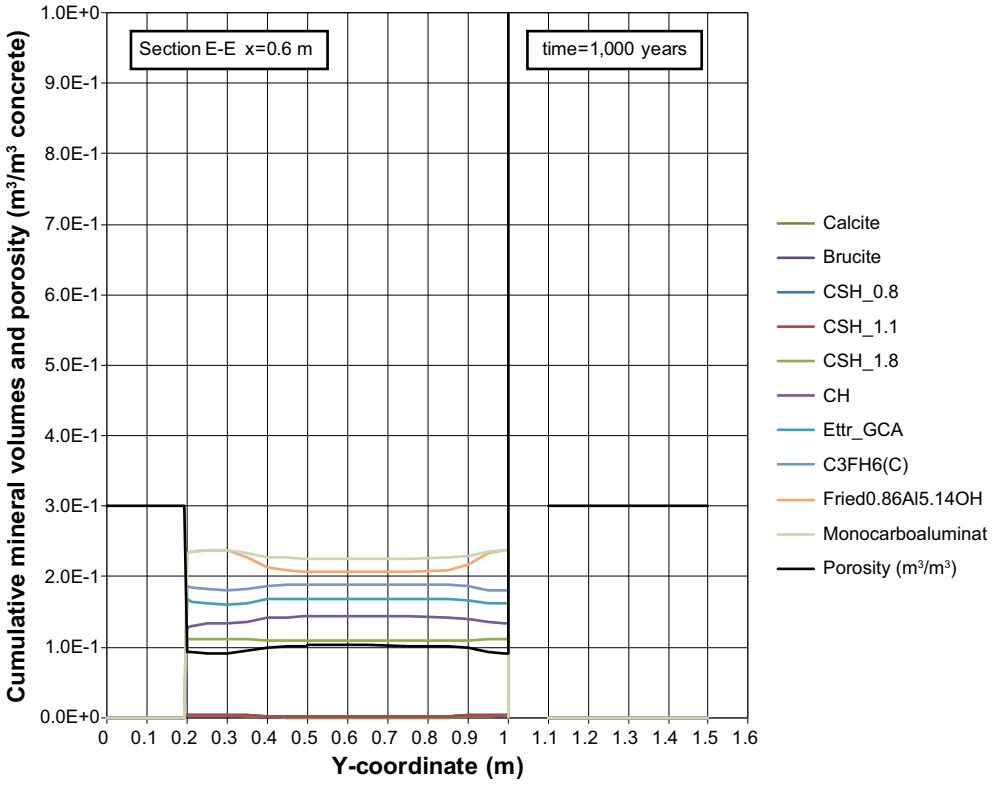

Figure D-59. *Cumulative representation of the mineral composition in concrete and calculated porosity along the vertical Section E-E at time 1,000 years, case Large10.*

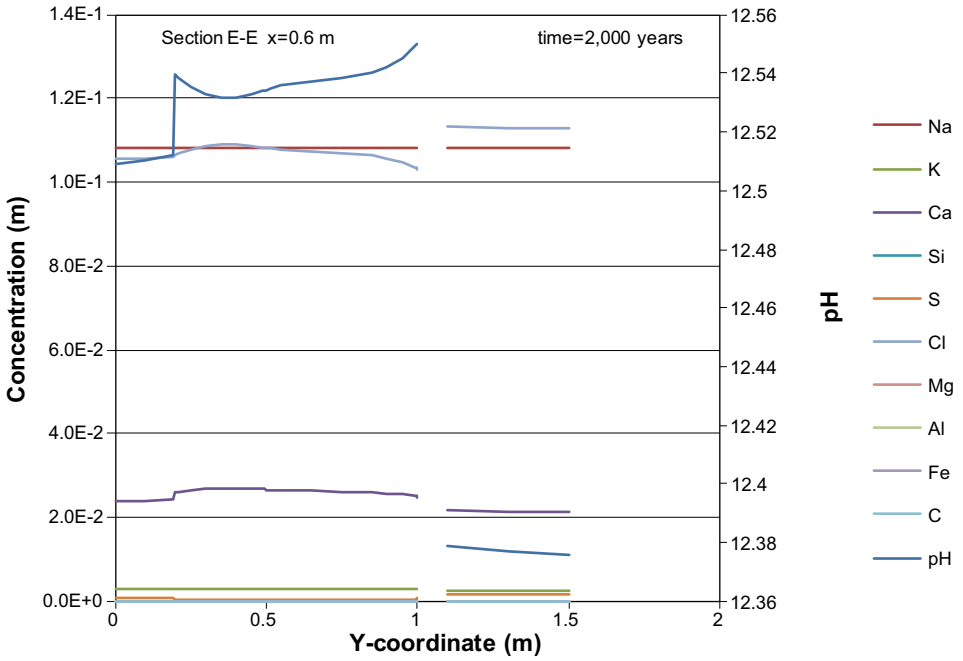

Figure D-60. *Concentration profiles of dissolved components in concrete pore water along the vertical Section E-E at time 2,000 years, case Large10. Units (mol/kg pore water).*

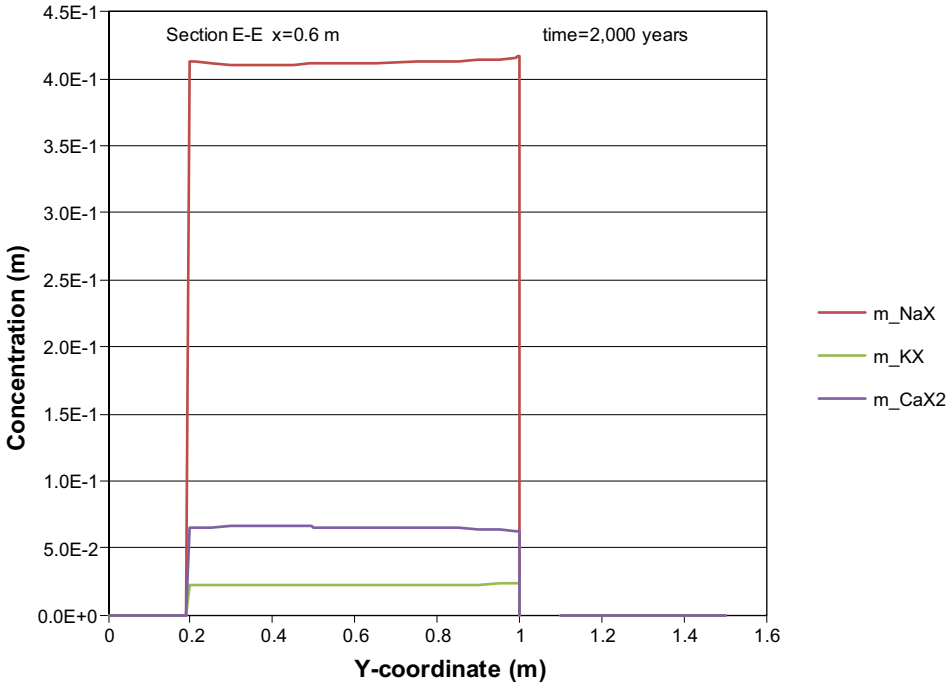

Figure D-61. *The assembly of ion exchange species in concrete along the vertical Section E-E at time 2,000 years, case Large10. Units (mol/kg pore water).*

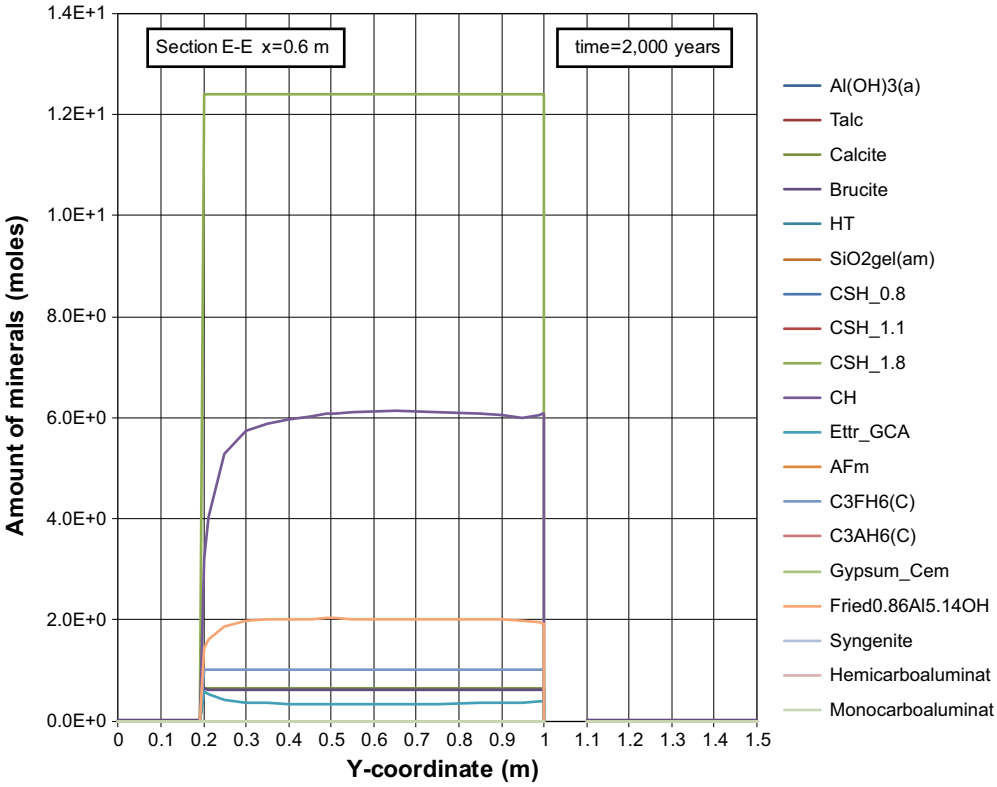

Figure D-62. *The mineral composition in concrete along the vertical Section E-E at time 2,000 years, case Large10. Units (mol/kg pore water).*

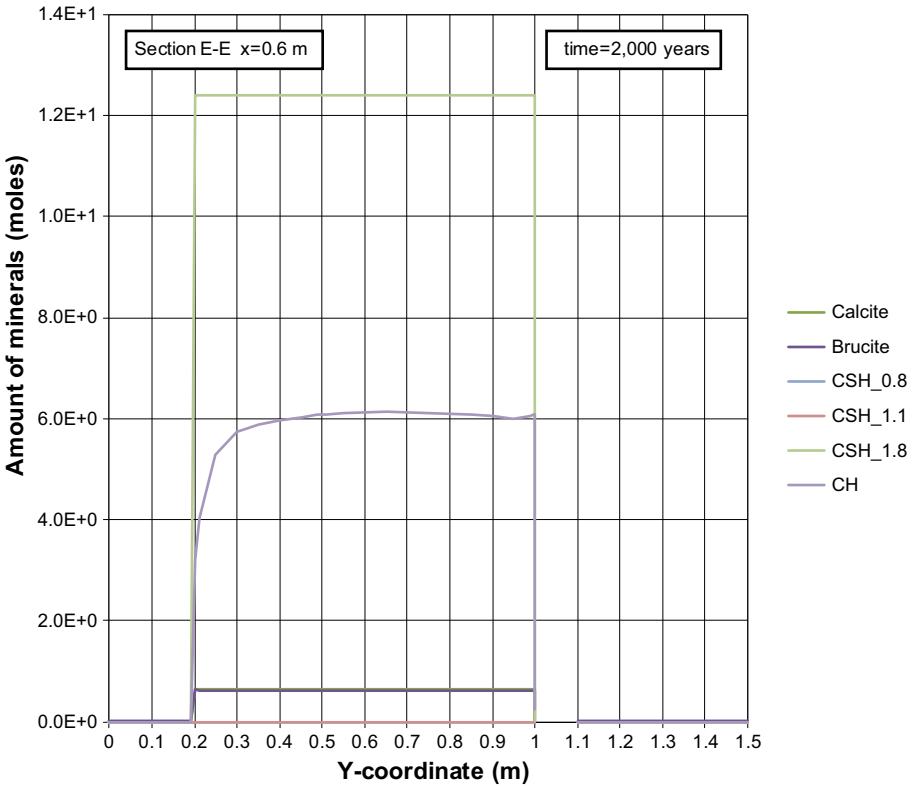

Figure D-63. *The mineral composition in concrete along the vertical Section E-E at time 2,000 years, case Large10. Units (mol/kg pore water).*

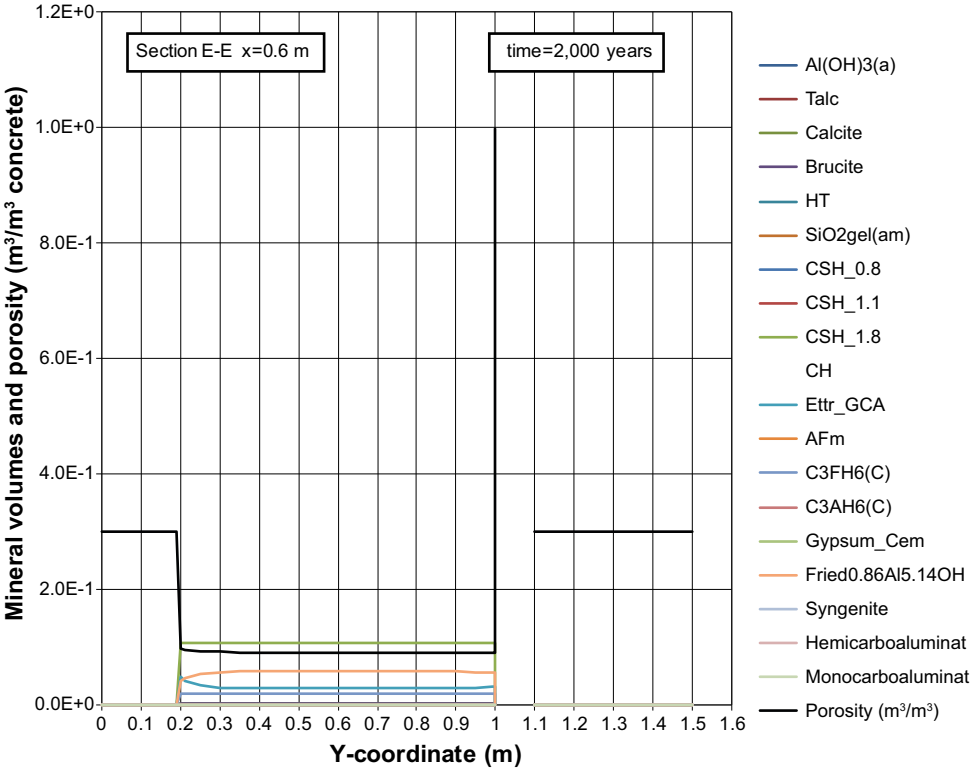

Figure D-64. *Mineral composition in concrete and calculated porosity along the vertical Section E-E at time 2,000 years, case Large10.*

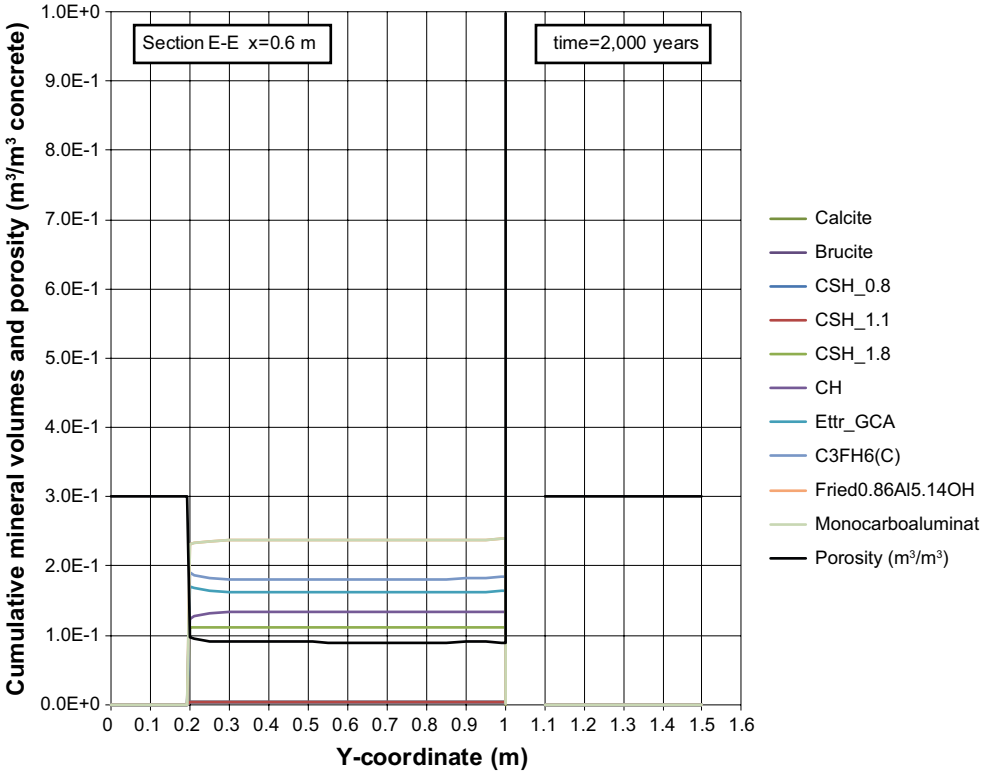

Figure D-65. *Cumulative representation of the mineral composition in concrete and calculated porosity along the vertical Section E-E at time 2,000 years, case Large10.*

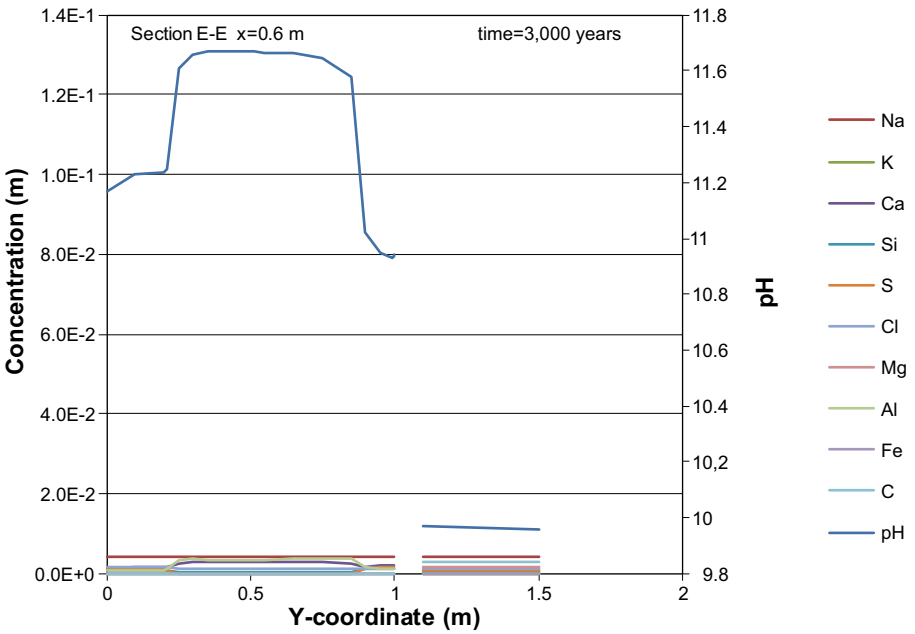

Figure D-66. *Concentration profiles of dissolved components in concrete pore water along the vertical Section E-E at time 3,000 years, case Large10. Units (mol/kg pore water).*

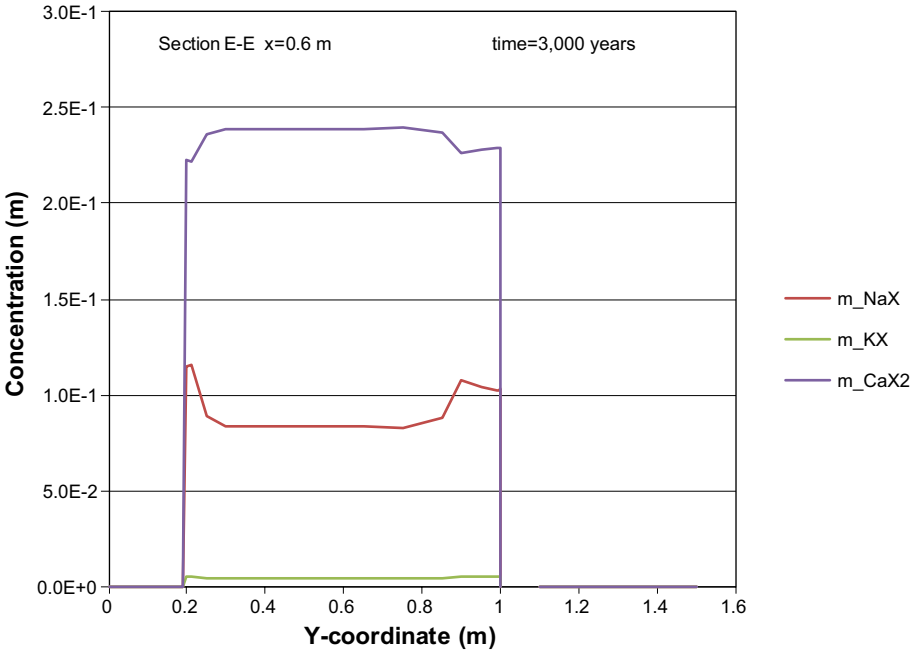

Figure D-67. *The assembly of ion exchange species in concrete along the vertical Section E-E at time 3,000 years, case Large10. Units (mol/kg pore water).*

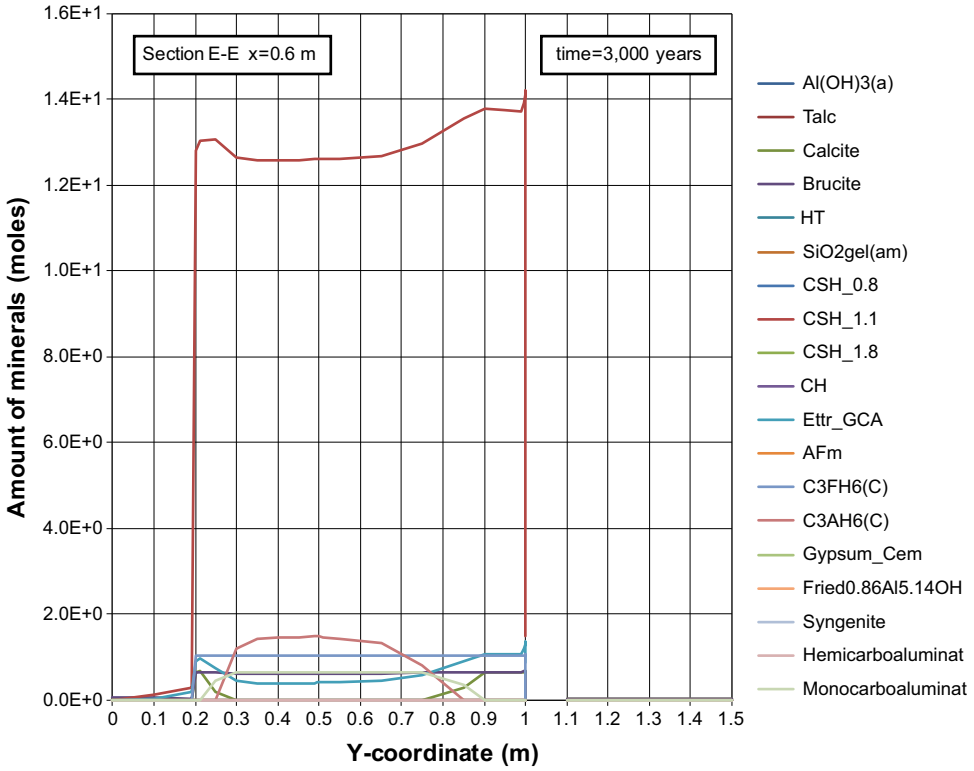

Figure D-68. *The mineral composition in concrete along the vertical Section E-E at time 3,000 years, case Large10. Units (mol/kg pore water).*

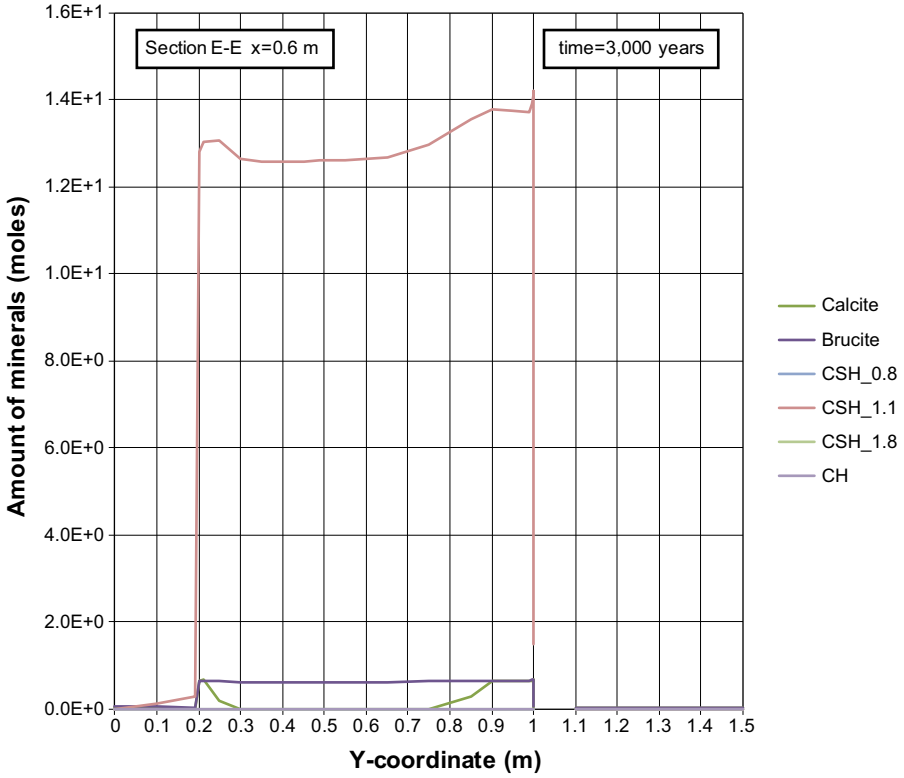

Figure D-69. *The mineral composition in concrete along the vertical Section E-E at time 3,000 years, case Large10. Units (mol/kg pore water).*

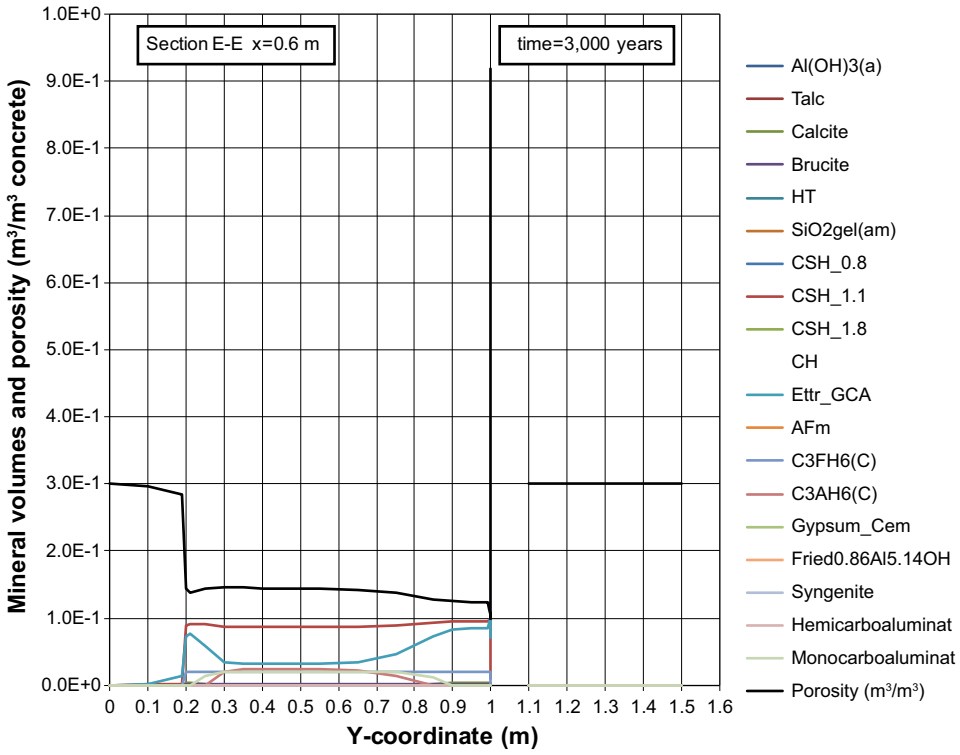

Figure D-70. *Mineral composition in concrete and calculated porosity along the vertical Section E-E at time 3,000 years, case Large10.*

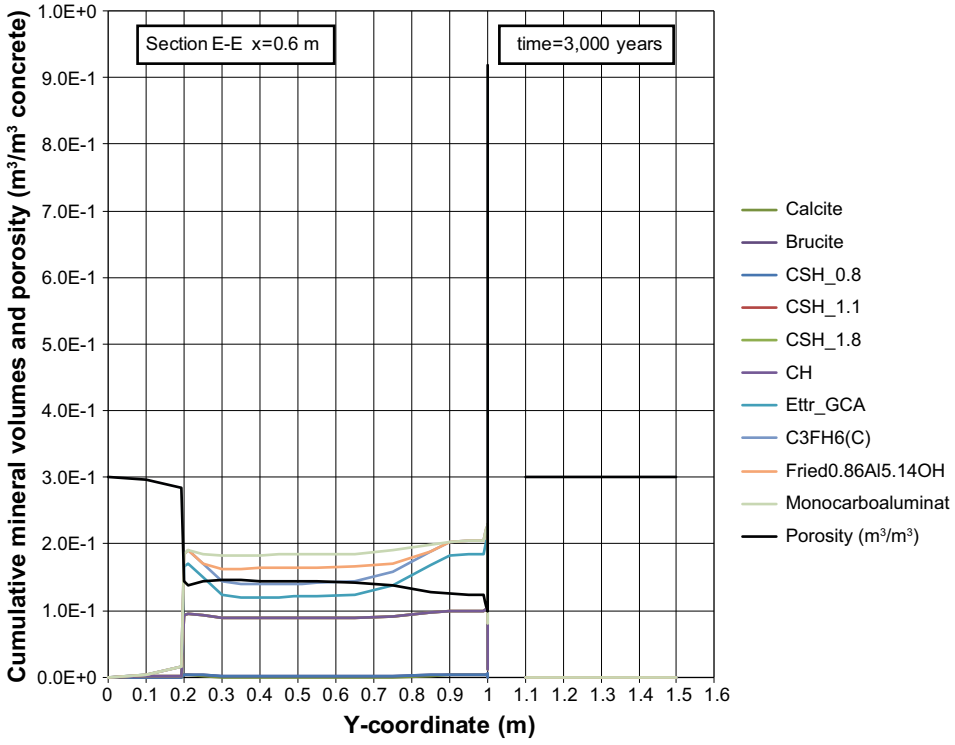

Figure D-71. *Cumulative representation of the mineral composition in concrete and calculated porosity along the vertical Section E-E at time 3,000 years, case Large10.*

Profiles along section E-E at 5,000 years

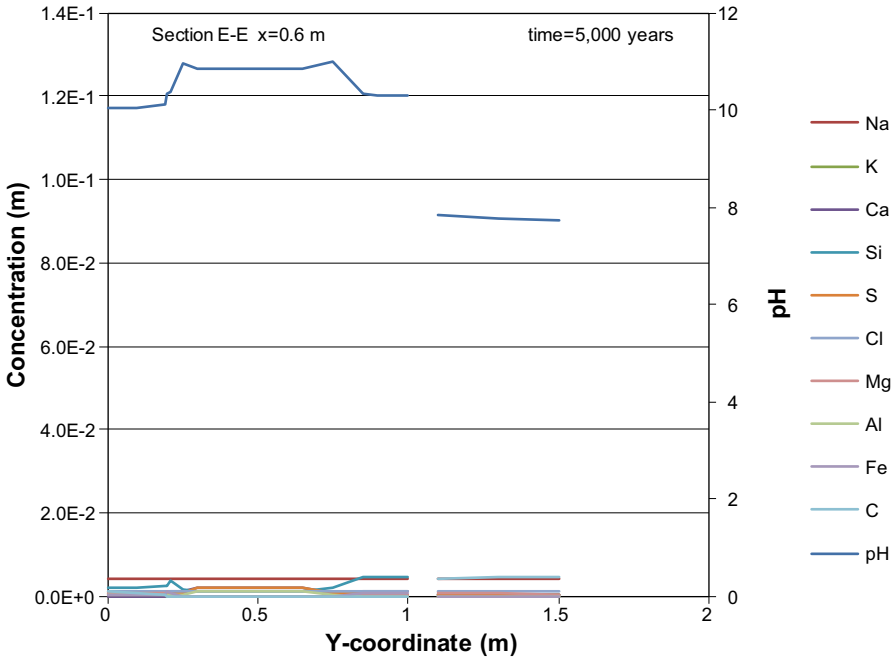

Figure D-72. *Concentration profiles of dissolved components in concrete pore water along the vertical Section E-E at time 5,000 years, case Large10. Units (mol/kg pore water).*

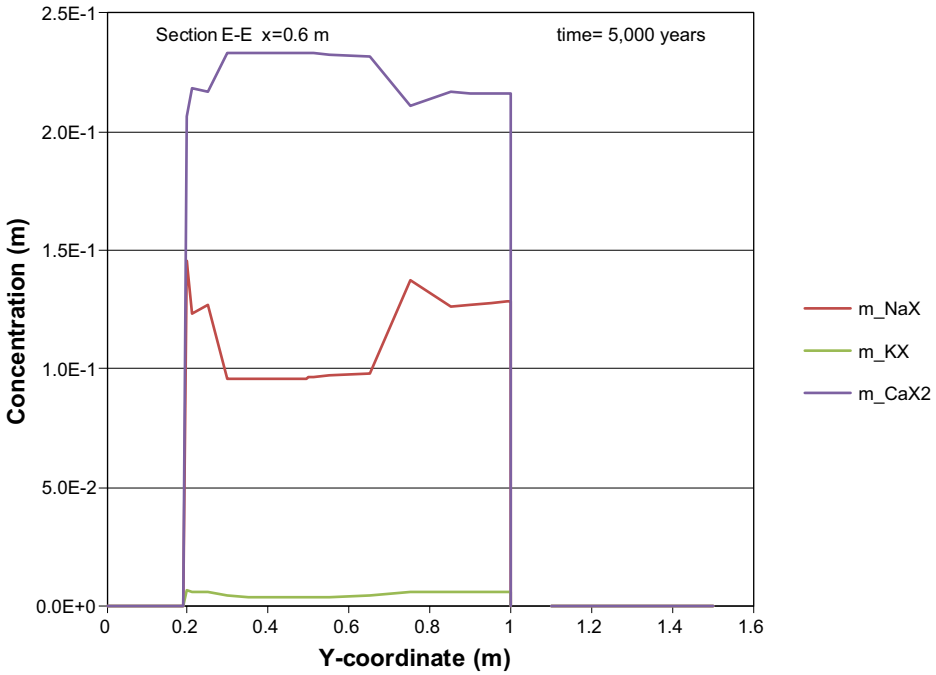

Figure D-73. *The assembly of ion exchange species in concrete along the vertical Section E-E at time 5,000 years, case Large10. Units (mol/kg pore water).*

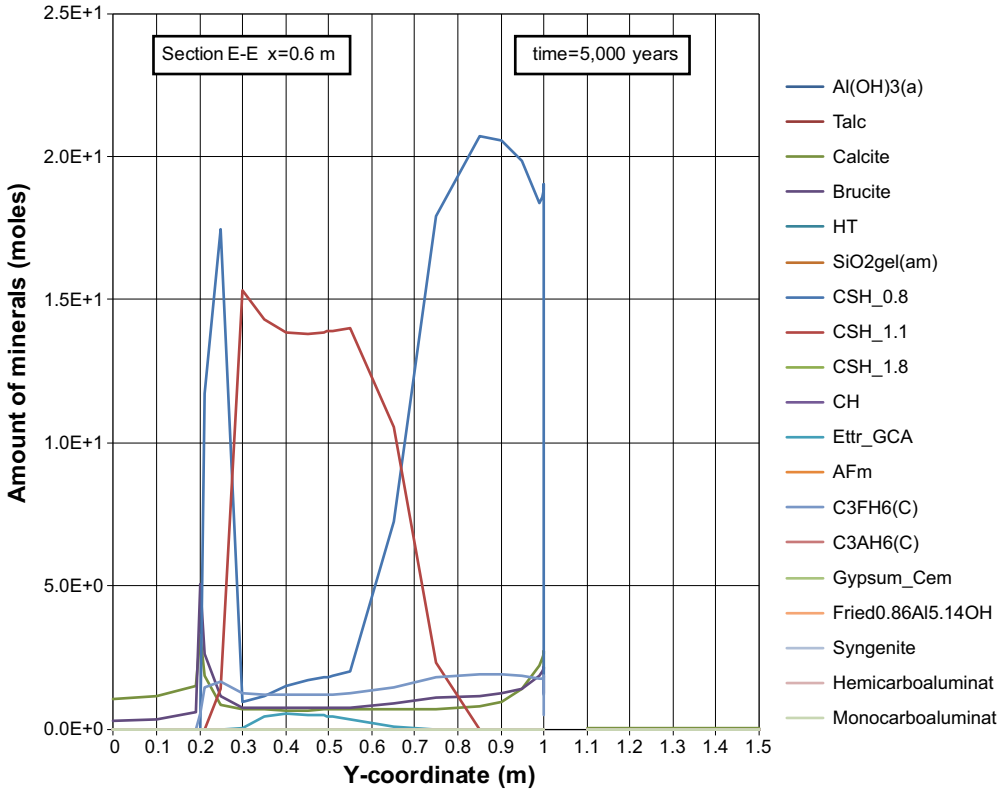

Figure D-74. *The mineral composition in concrete along the vertical Section E-E at time 5,000 years, case Large10. Units (mol/kg pore water).*

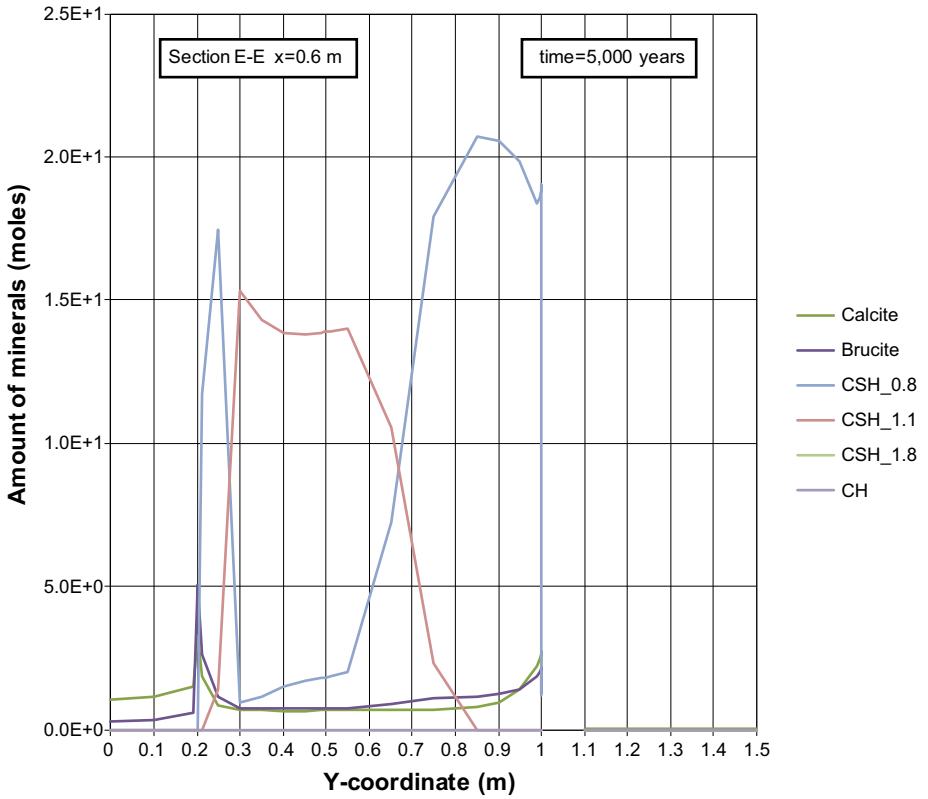

Figure D-75. *The mineral composition in concrete along the vertical Section E-E at time 5,000 years, case Large10. Units (mol/kg pore water).*

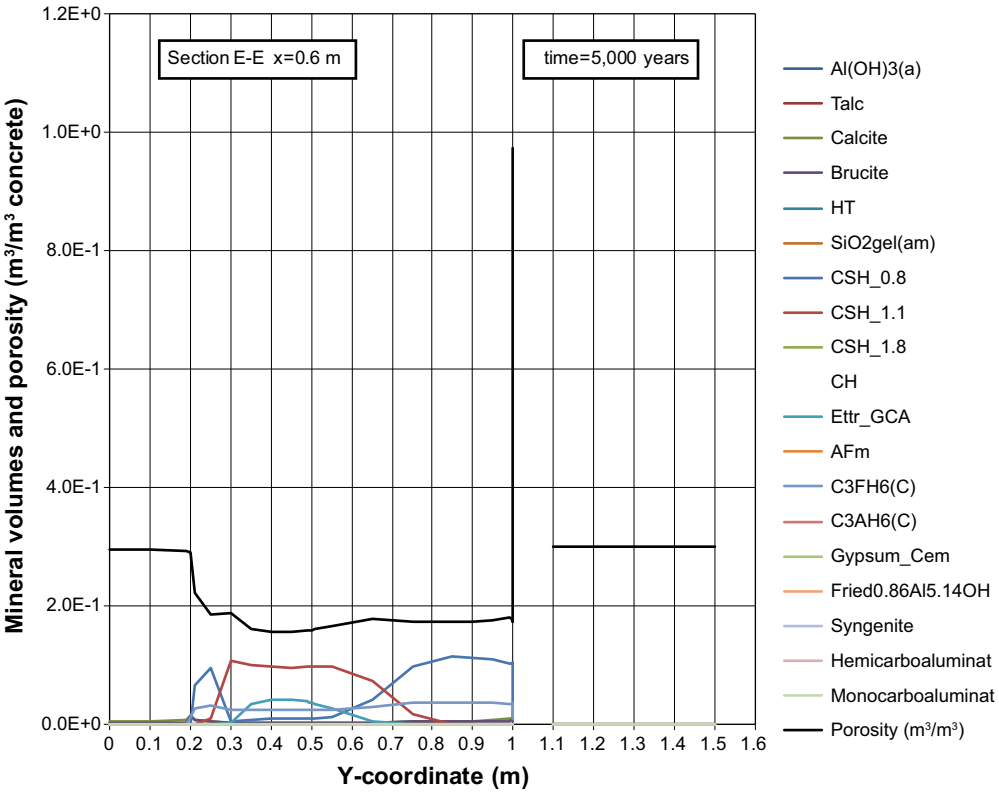

Figure D-76. *Mineral composition in concrete and calculated porosity along the vertical Section E-E at time 5,000 years, case Large10.*

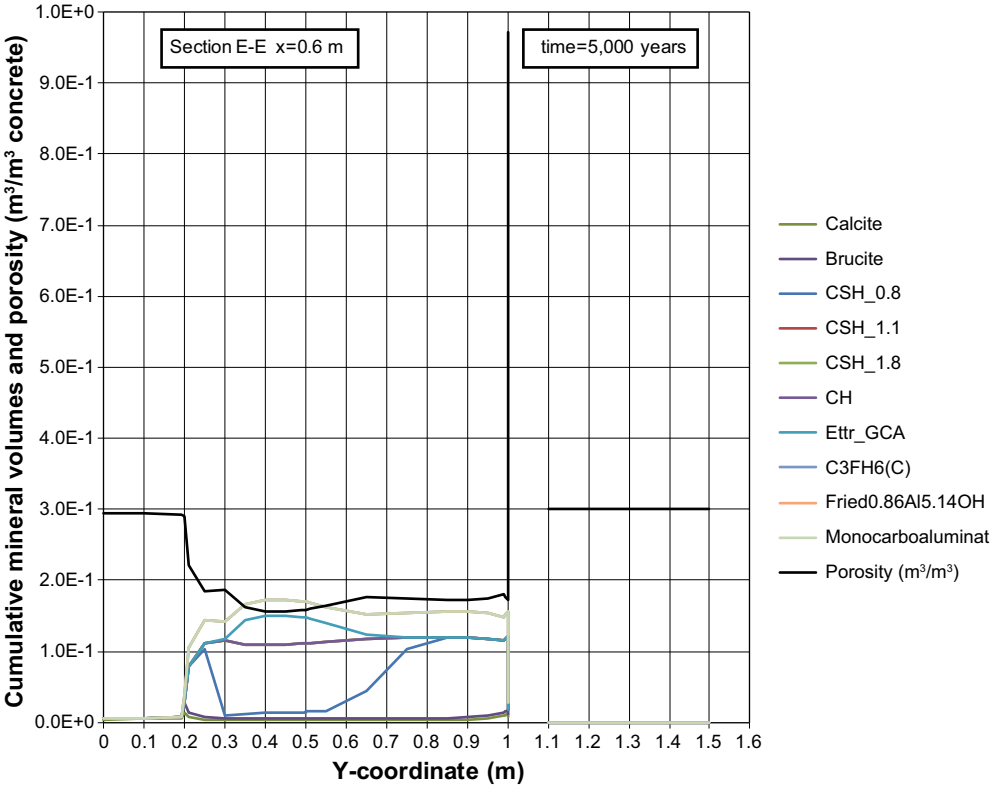

Figure D-77. *Cumulative representation of the mineral composition in concrete and calculated porosity along the vertical Section E-E at time 5,000 years, case Large10.*

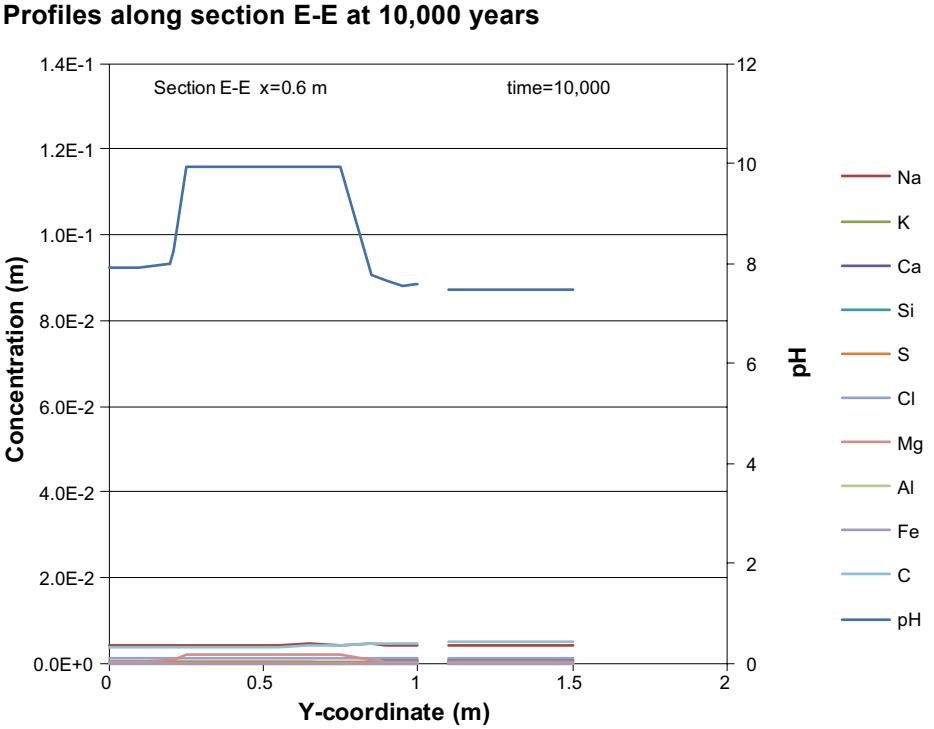

Figure D-78. *Concentration profiles of dissolved components in concrete pore water along the vertical Section E-E at time 10,000 years, case Large10. Units (mol/kg pore water).*

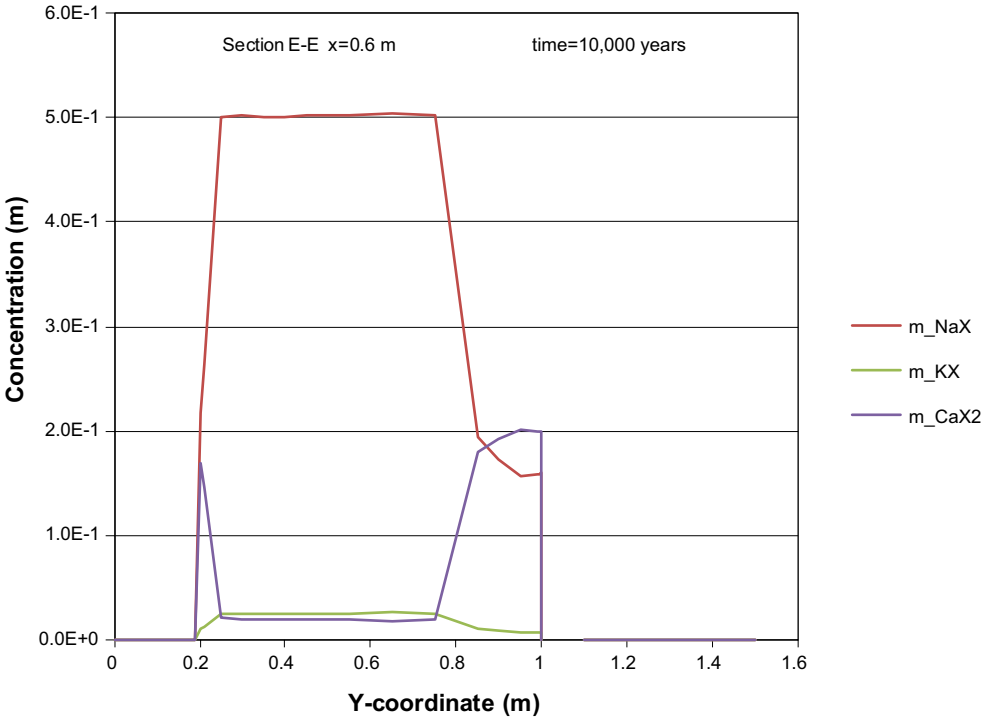

Figure D-79. *The assembly of ion exchange species in concrete along the vertical Section E-E at time 10,000 years, case Large10. Units (mol/kg pore water).*

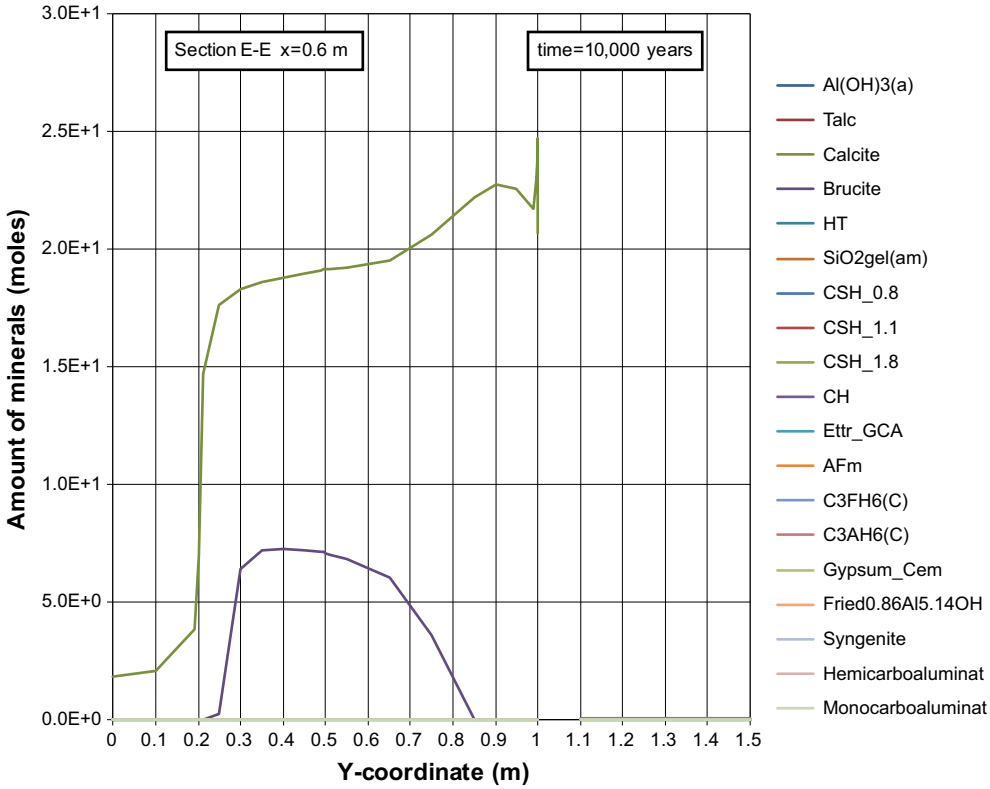

Figure D-80. *The mineral composition in concrete along the vertical Section E-E at time 10,000 years, case Large10. Units (mol/kg pore water).*

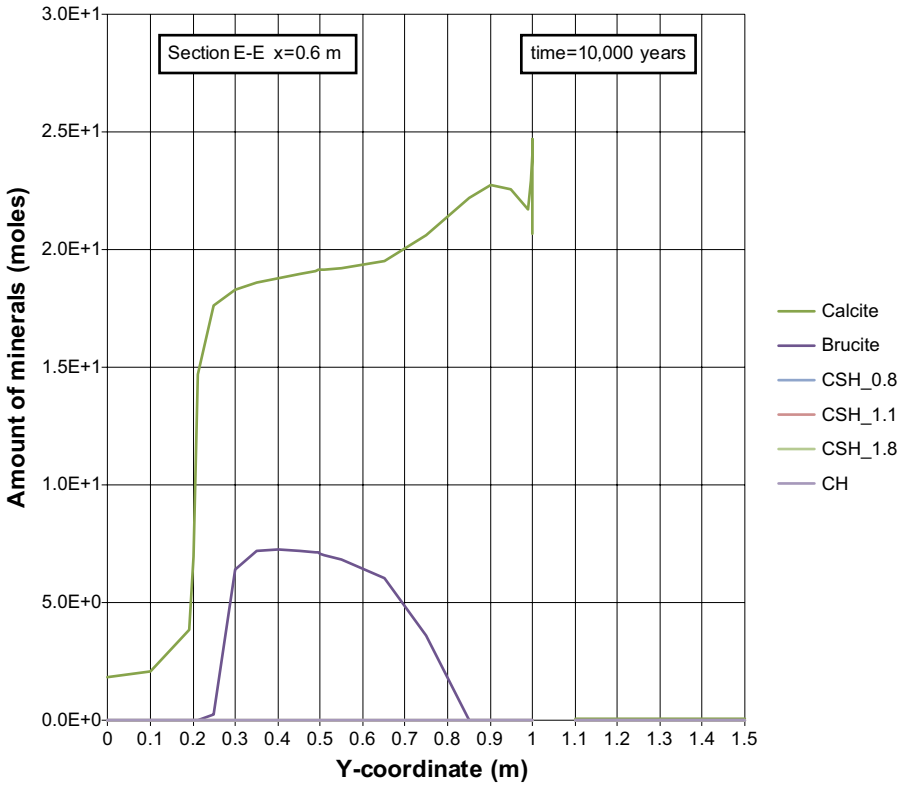

Figure D-81. *The mineral composition in concrete along the vertical Section E-E at time 10,000 years, case Large10. Units (mol/kg pore water).*

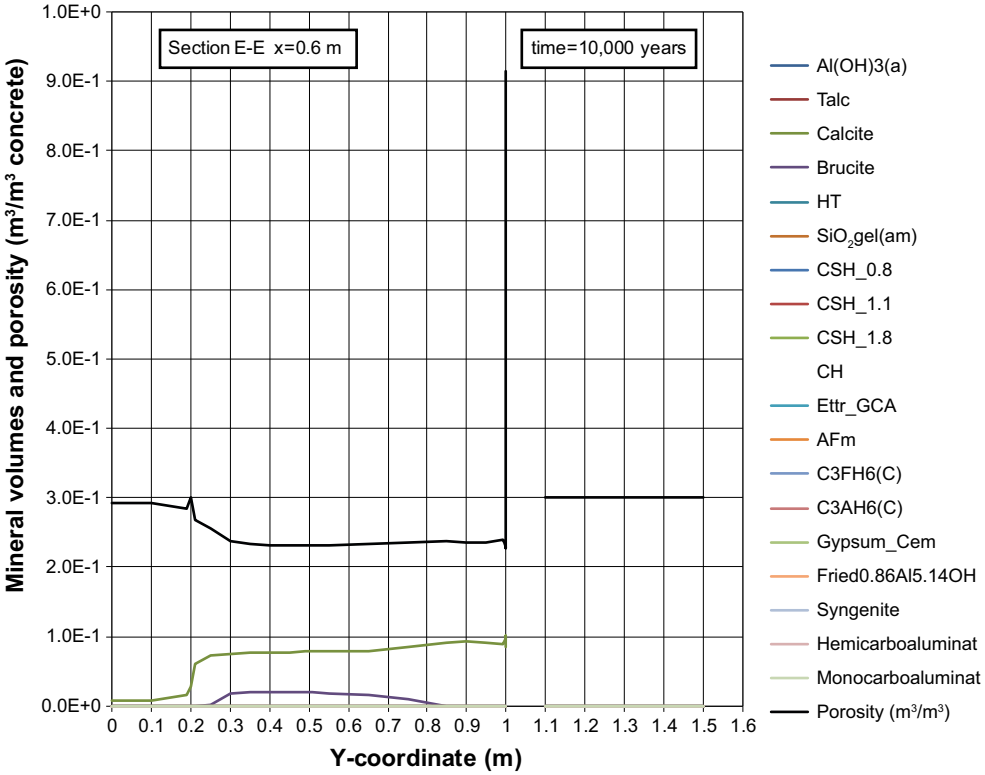

Figure D-82. *Mineral composition in concrete and calculated porosity along the vertical Section E-E at time 10,000 years, case Large10.*

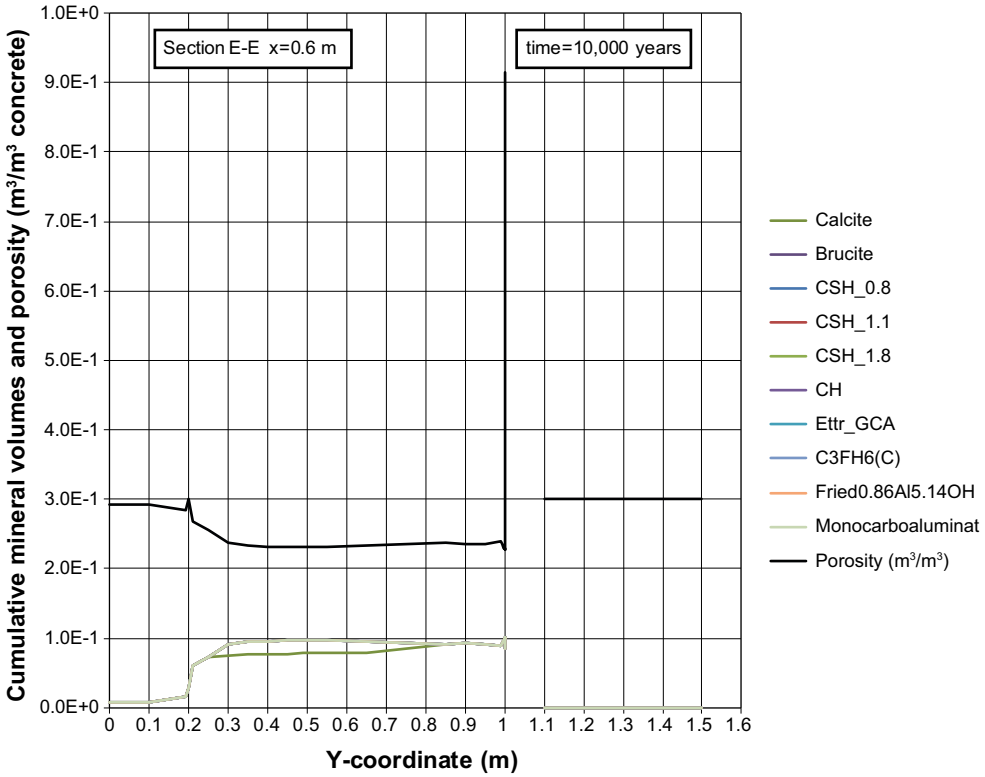

Figure D-83. *Cumulative representation of the mineral composition in concrete and calculated porosity along the vertical Section E-E at time 10,000 years, case Large10.*

Profiles along section E-E at 20,000 years

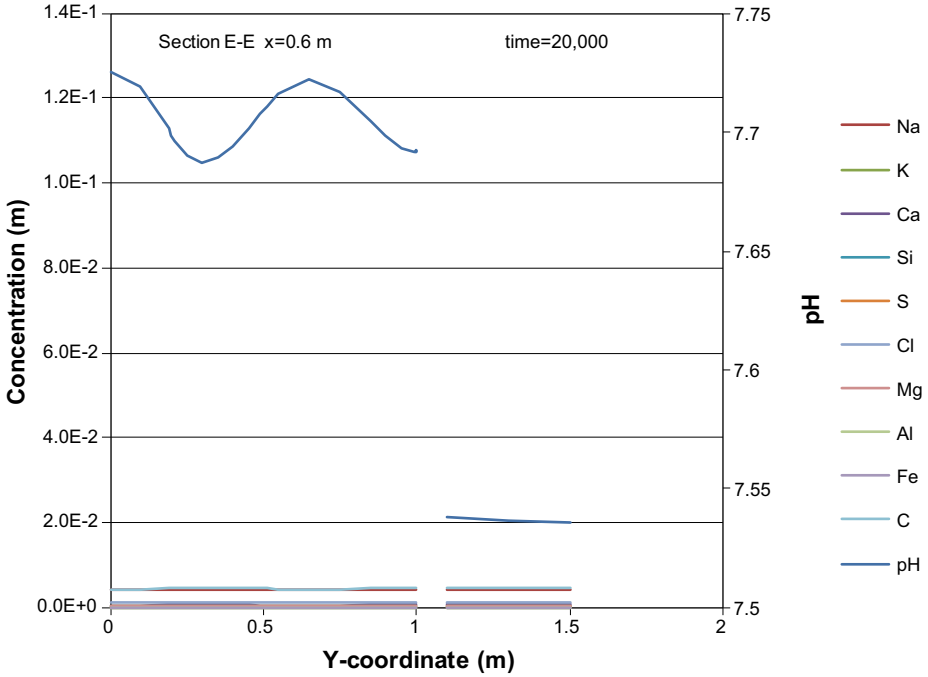

Figure D-84. *Concentration profiles of dissolved components in concrete pore water along the vertical Section E-E at time 20,000 years, case Large10. Units (mol/kg pore water).*

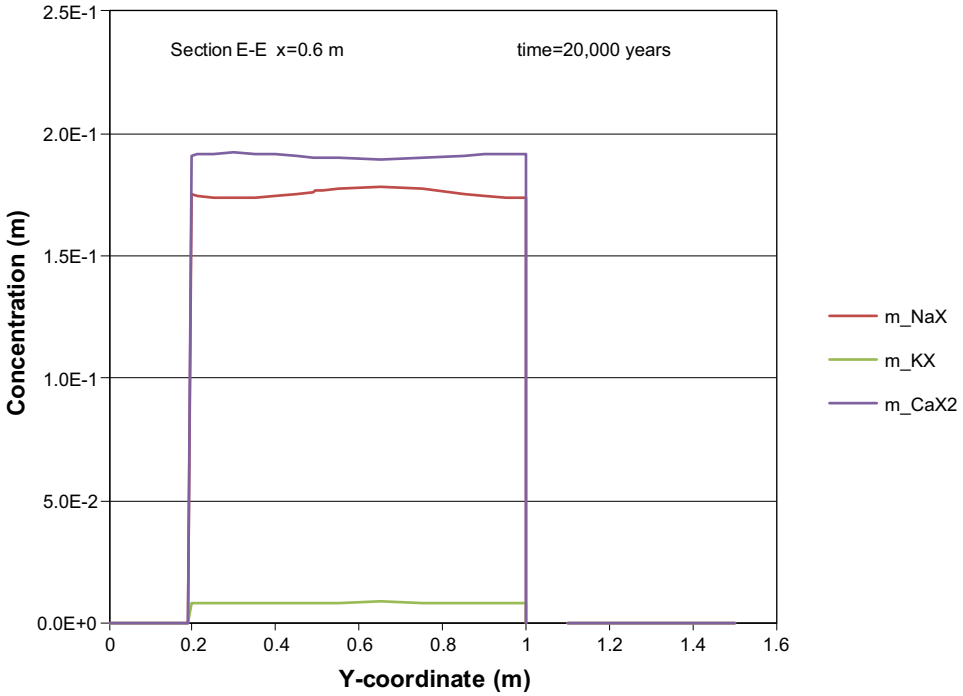

Figure D-85. *The assembly of ion exchange species in concrete along the vertical Section E-E at time 20,000 years, case Large10. Units (mol/kg pore water).*

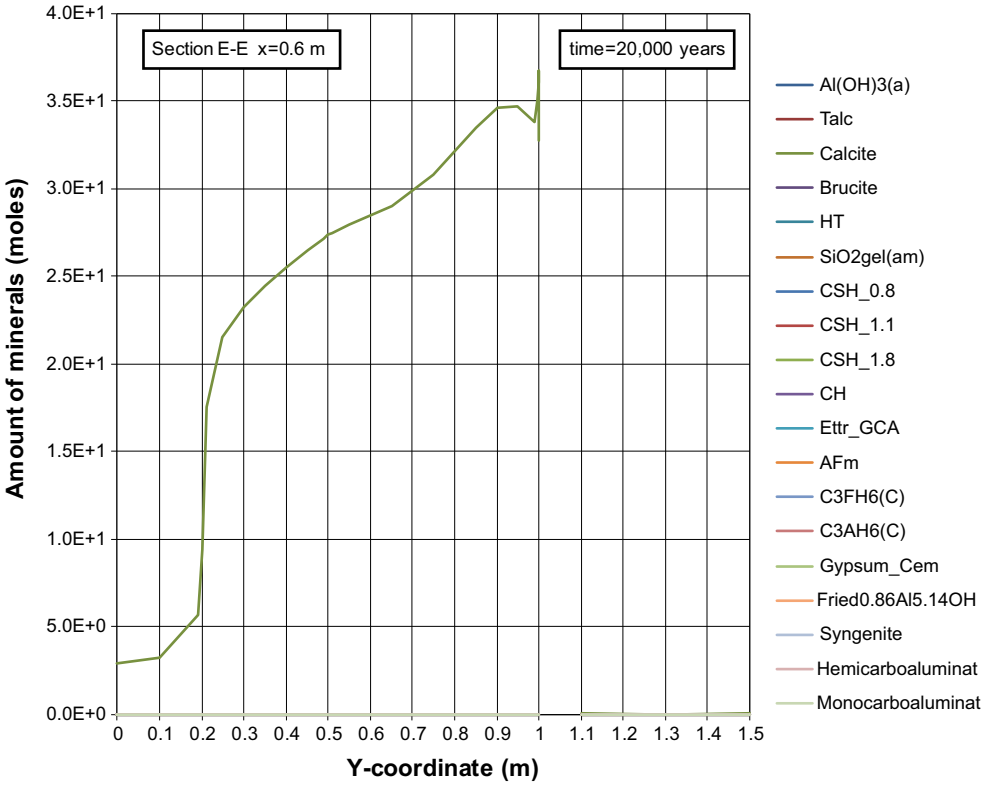

Figure D-86. *The mineral composition in concrete along the vertical Section E-E at time 20,000 years, case Large10. Units (mol/kg pore water).*

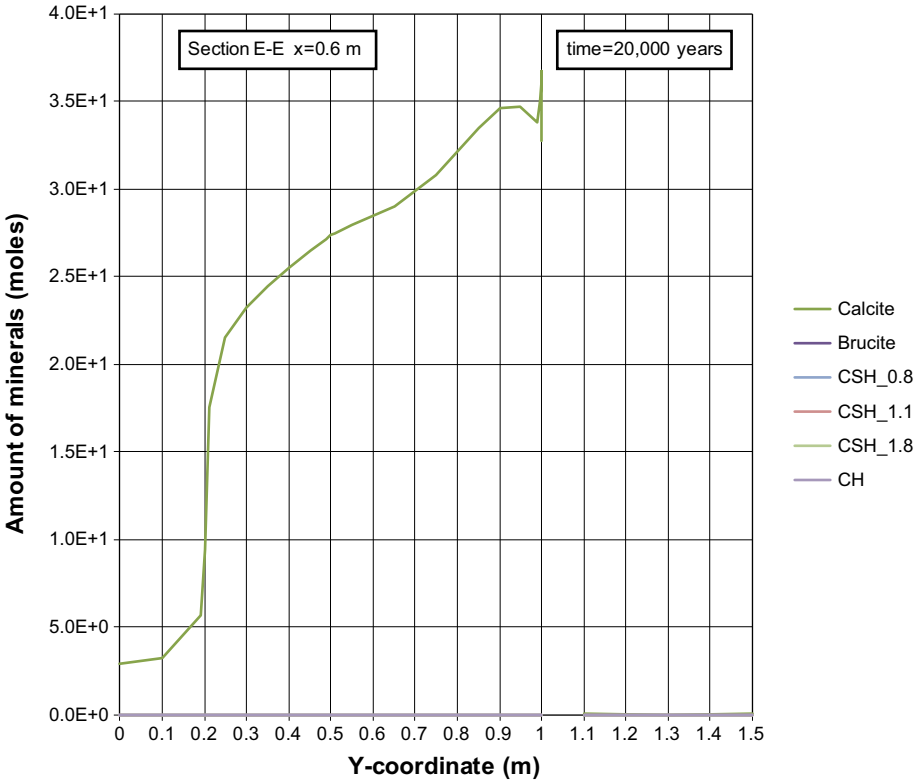

Figure D-87. *The mineral composition in concrete along the vertical Section E-E at time 20,000 years, case Large10. Units (mol/kg pore water).*

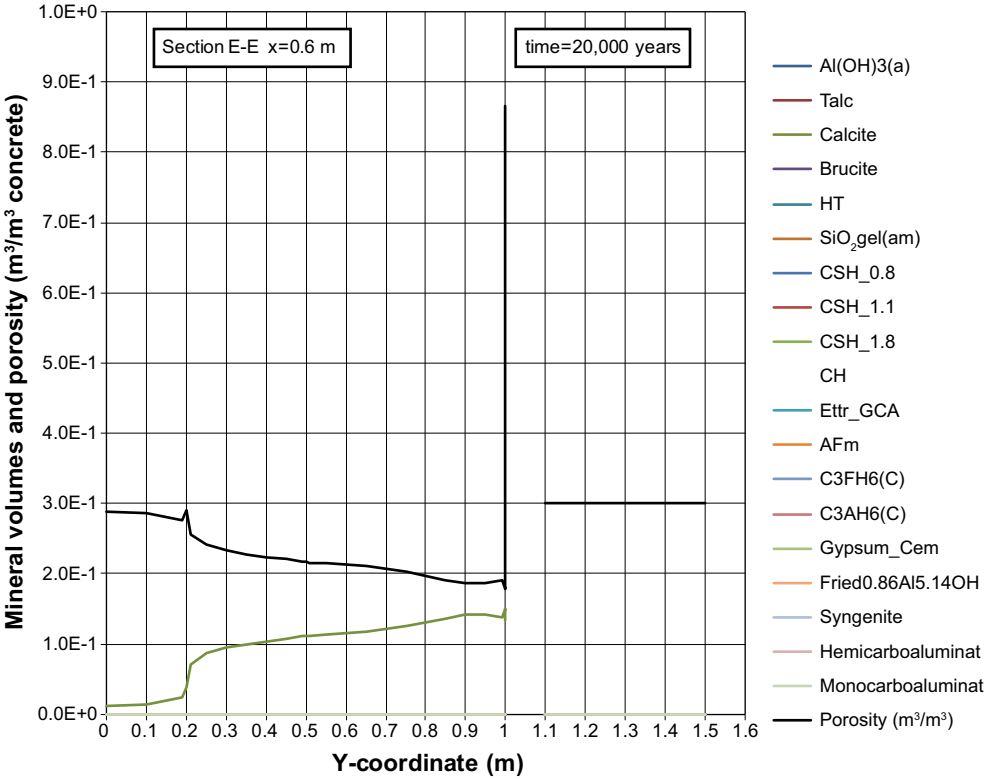

Figure D-88. *Mineral composition in concrete and calculated porosity along the vertical Section E-E at time 20,000 years, case Large10.*

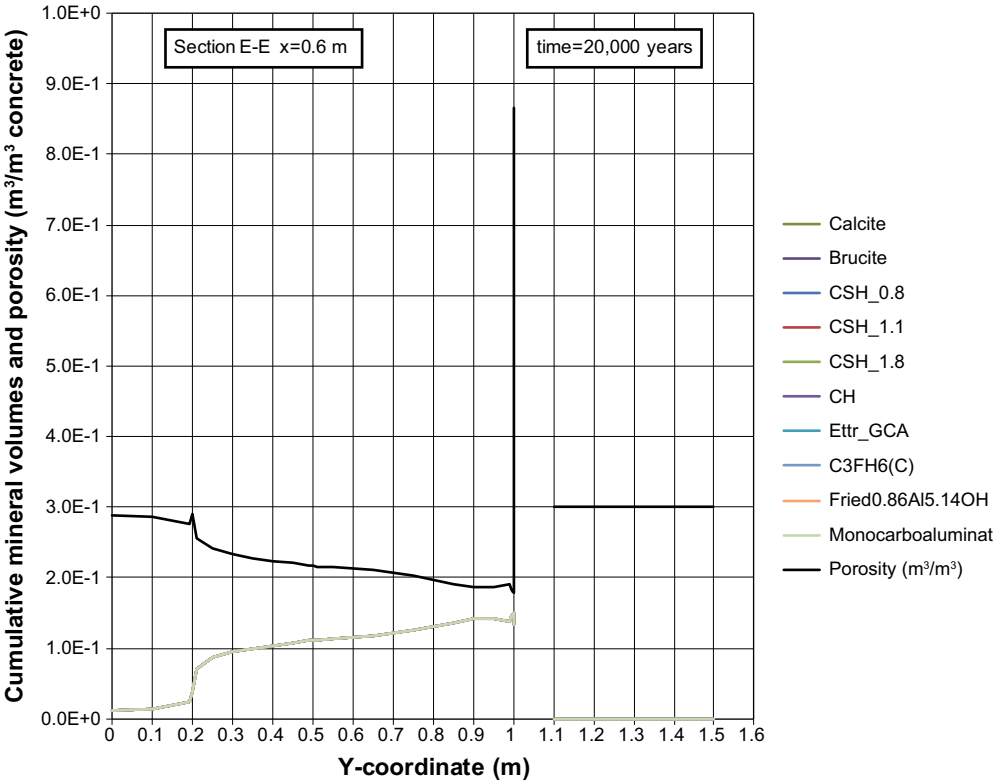

Figure D-89. *Cumulative representation of the mineral composition in concrete and calculated porosity along the vertical Section E-E at time 20,000 years, case Large10.*

Appendix E

Results for Case Large11

Concrete wall at position AE

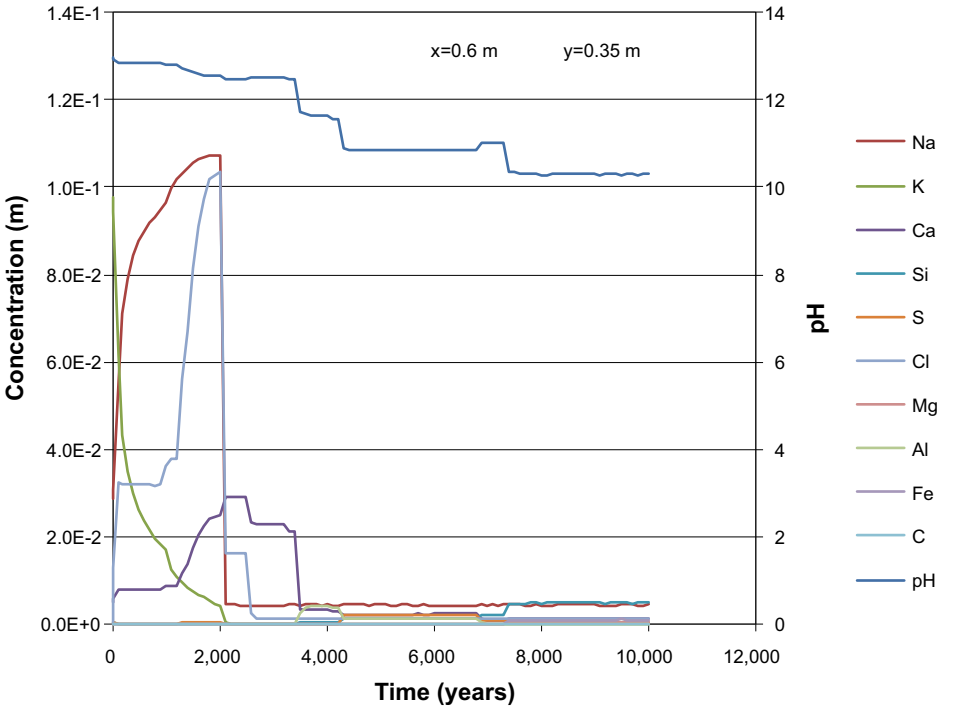

Figure E-1. *The development of the concentration of dissolved components in concrete pore water over time (during the first 10,000 years) at position AE, case Large11. Units (mol/kg pore water).*

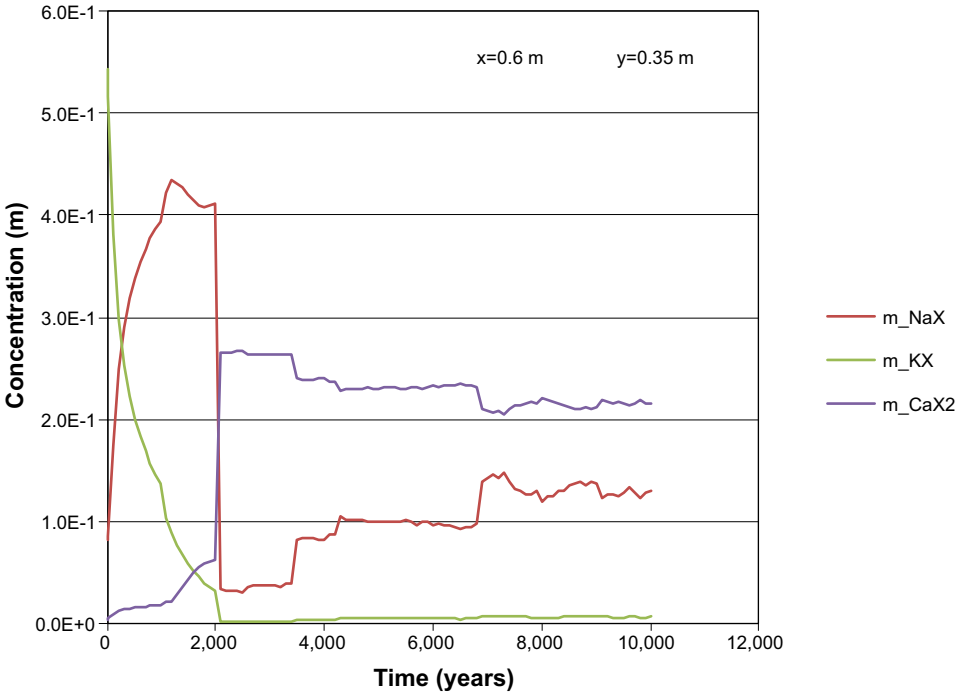

Figure E-2. *The development of the concentration of ion exchange species in concrete over time (during the first 10,000 years) at position AE, case Large11. Units (mol/kg pore water).*

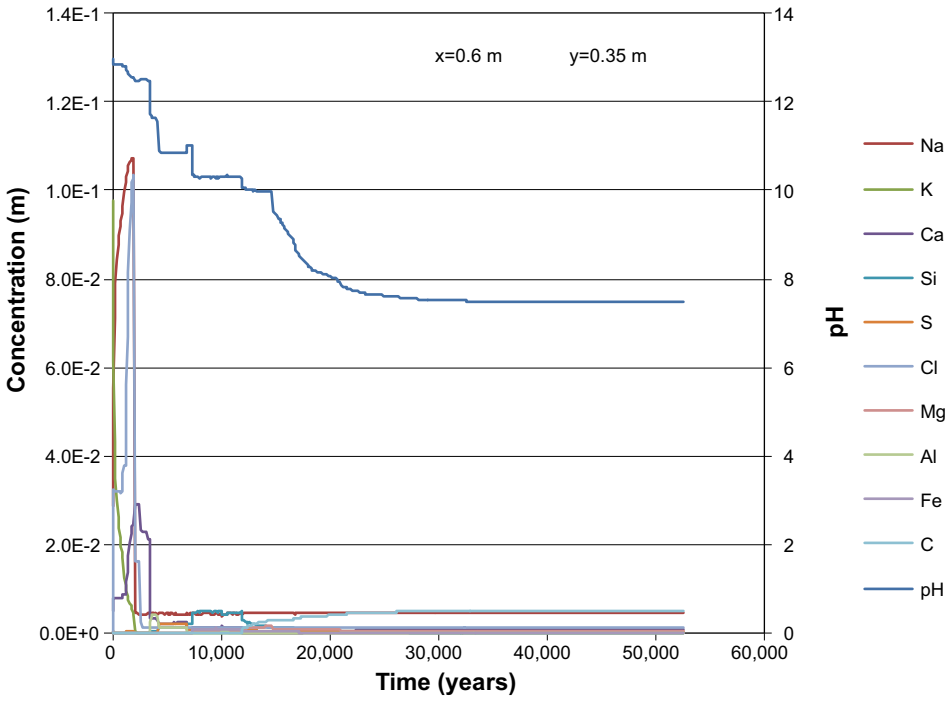

Figure E-3. *The development of the concentration of dissolved components in concrete pore water over time (during the first 52,600 years) at position AE, case Large11. Units (mol/kg pore water).*

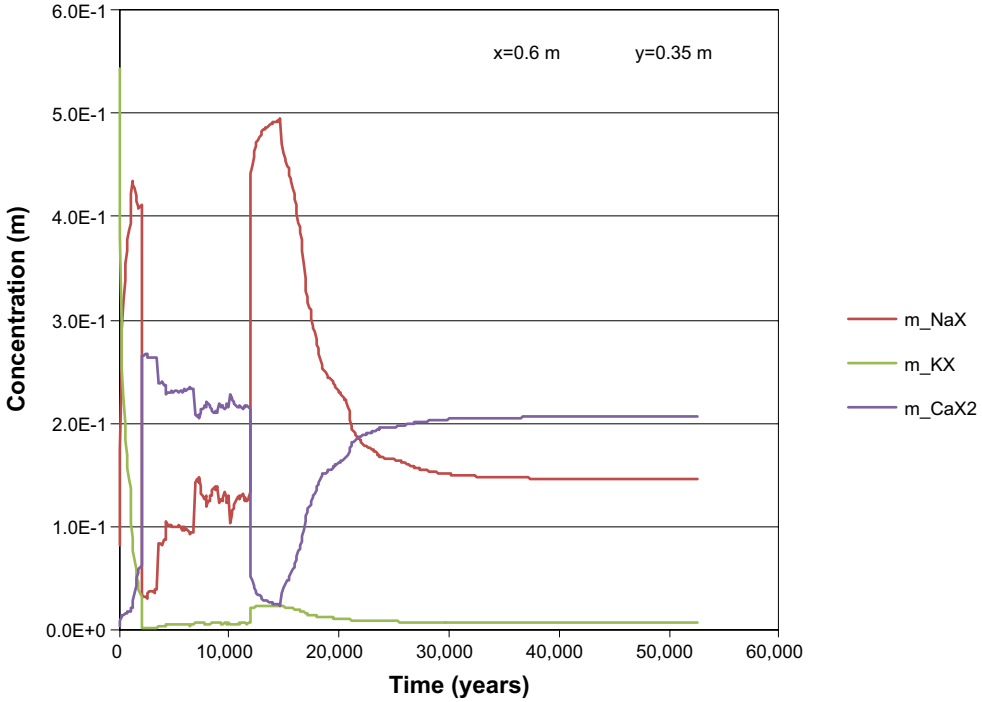

Figure E-4. *The development of the concentration of ion exchange species in concrete over time (during the first 52,600 years) at position AE, case Large11. Units (mol/kg pore water).*

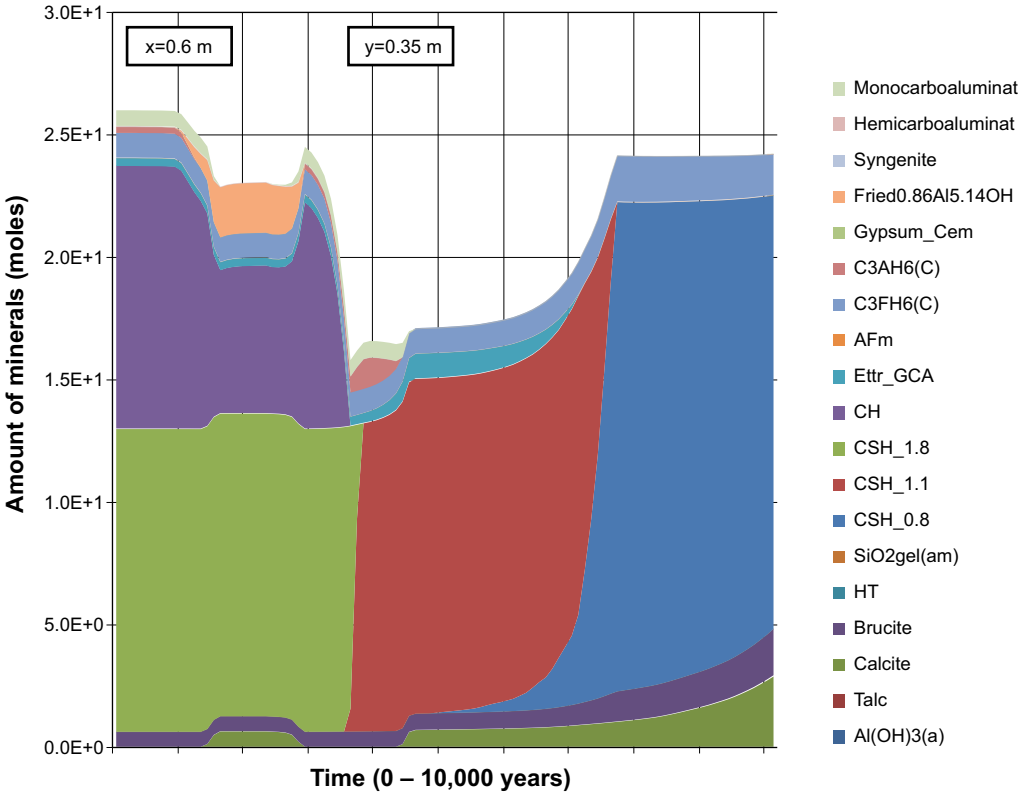

Figure E-5. *The amount of minerals in concrete over time at position AE, case Large11. Units (mol/kg pore water).*

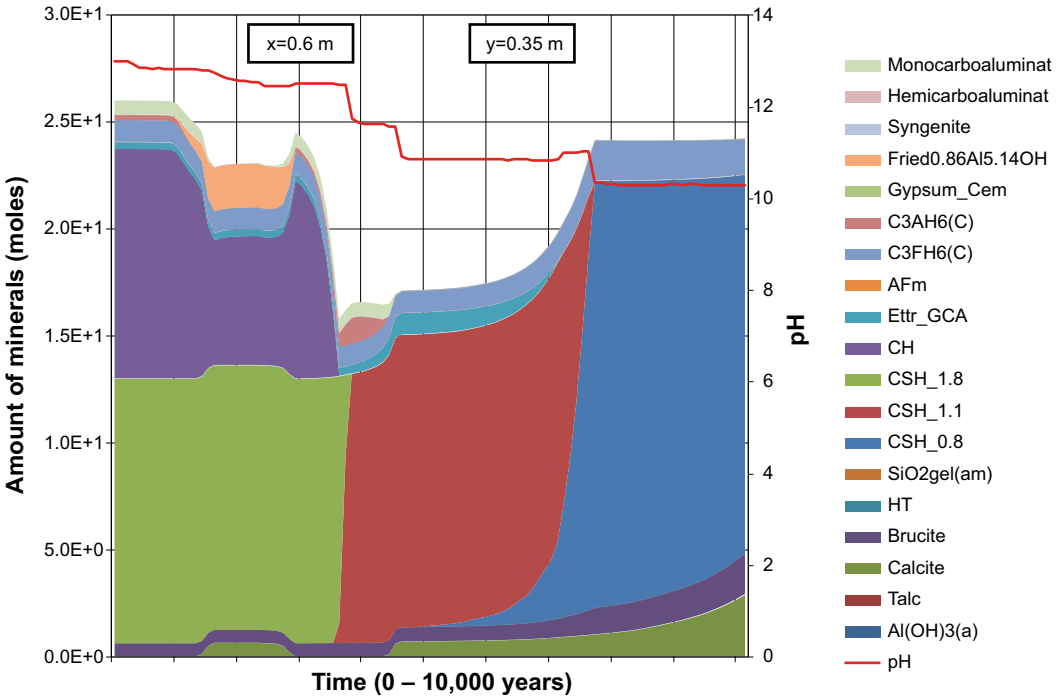

Figure E-6. *The amount of minerals in concrete over time at position AE, case Large11. The evolution of pH with time is also indicated. Units (mol/kg pore water).*

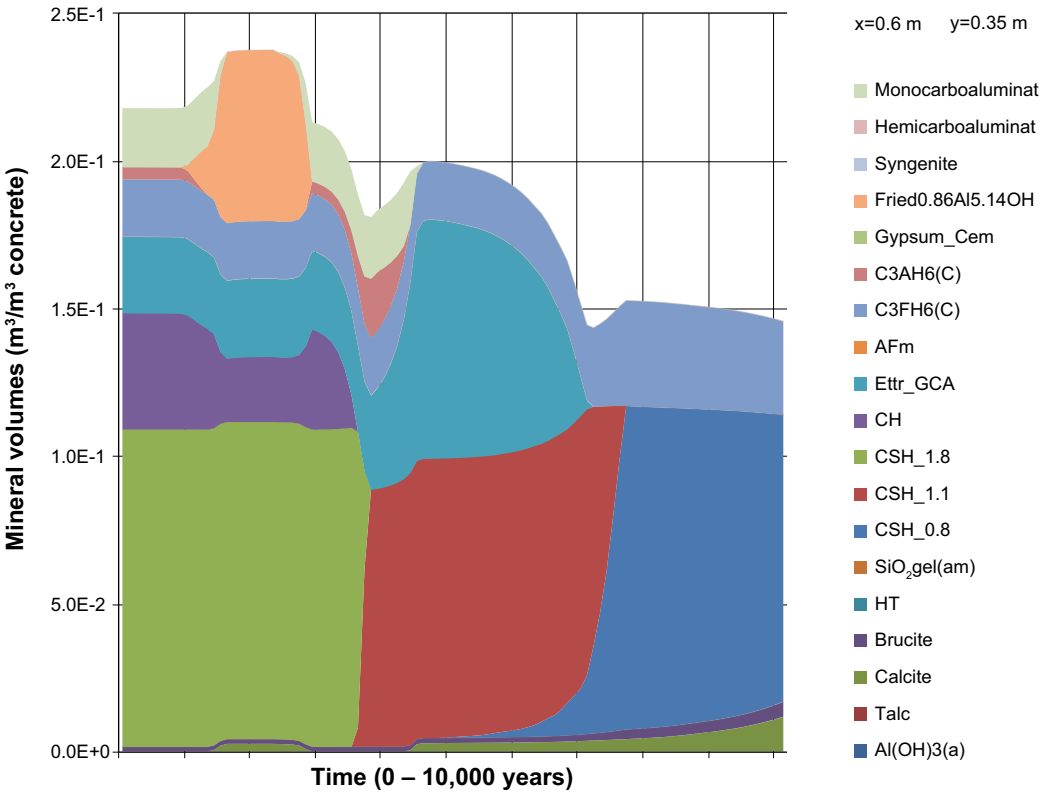

Figure E-7. *The change of mineral volumes in concrete over time at position AE, case Large11.*

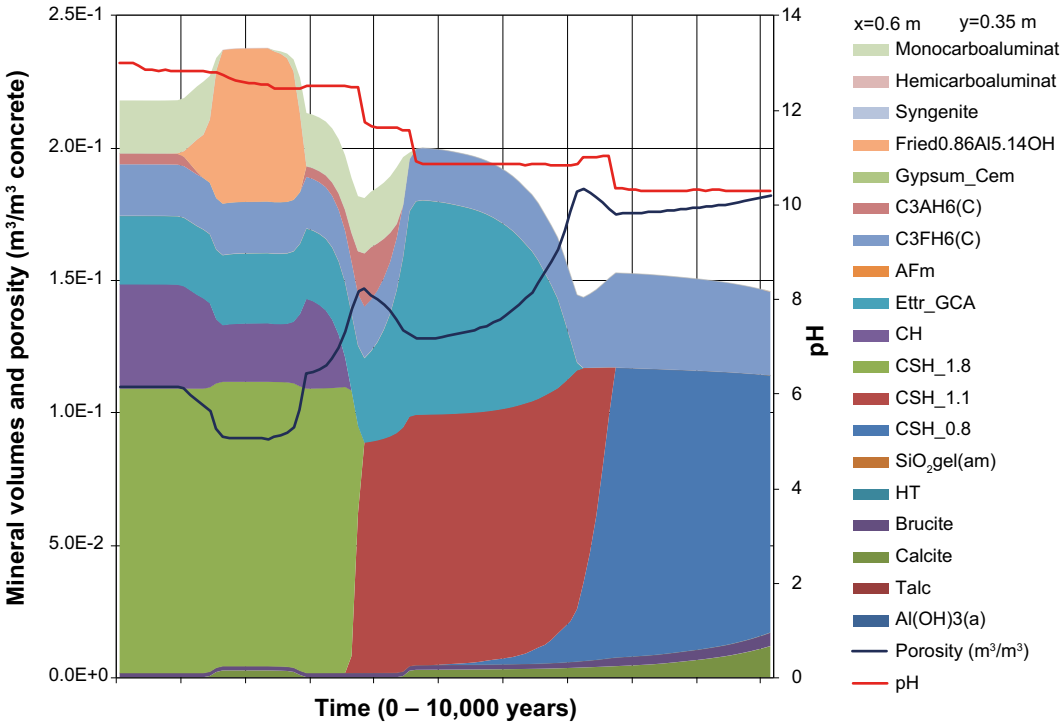

Figure E-8. *The change of mineral volumes and porosity in concrete over time at position AE, case Large11. The evolution of pH with time is also indicated.*

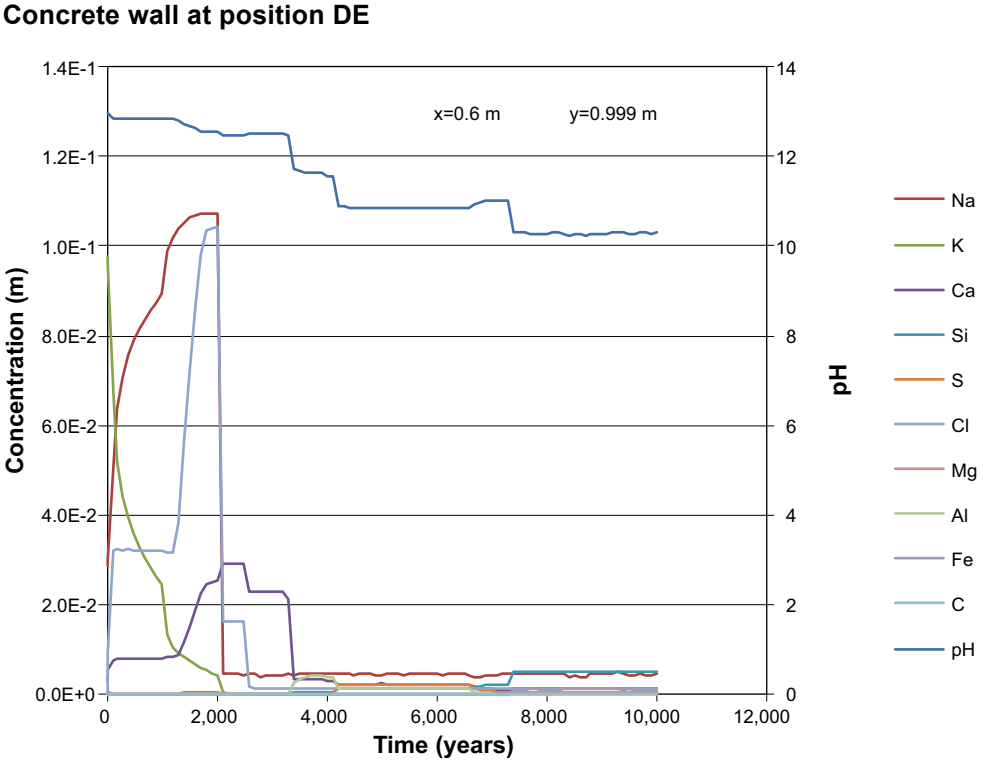

Figure E-9. *The development of the concentration of dissolved components in concrete pore water over time (during the first 10,000 years) at position DE (1 mm from an open fracture), case Large11. Units (mol/kg pore water).*

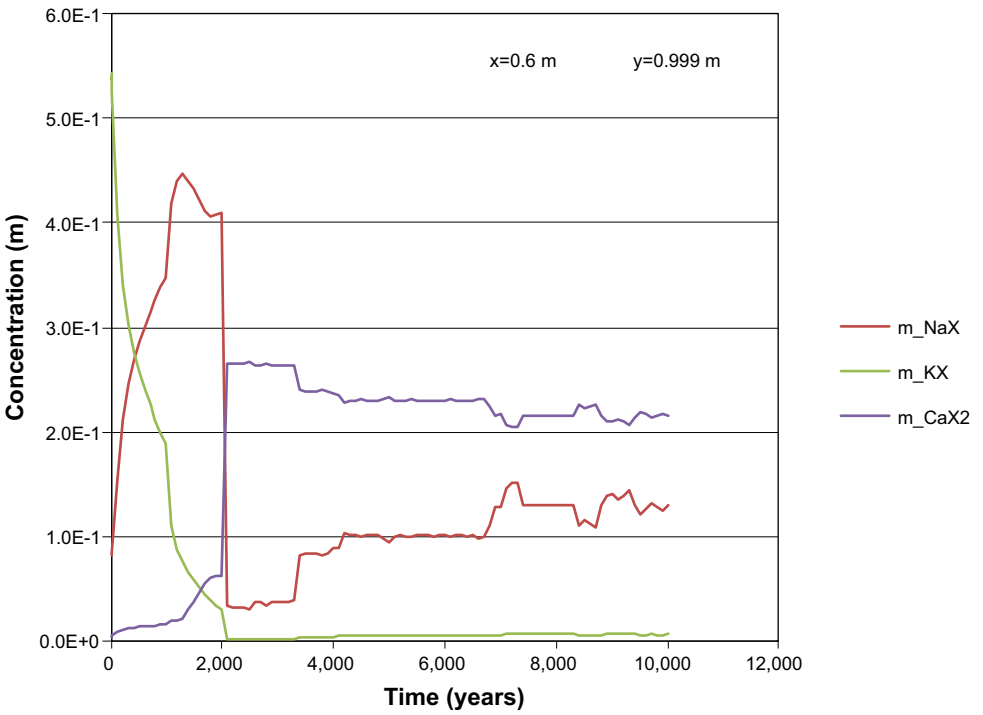

Figure E-10. *The development of the concentration of ion exchange species in concrete over time (during the first 10,000 years) at position DE (1 mm from an open fracture), case Large11. Units (mol/kg pore water).*

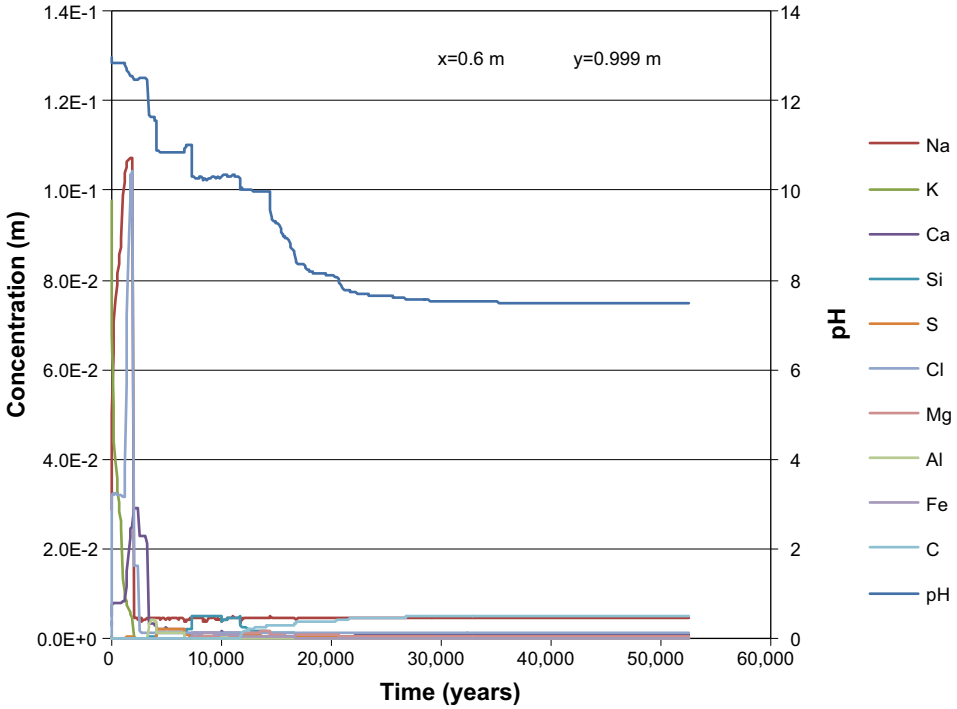

Figure E-11. *The development of the concentration of dissolved components in concrete pore water over time (during the first 52,600 years) at position DE (1 mm from an open fracture), case Large11. Units (mol/kg pore water).*

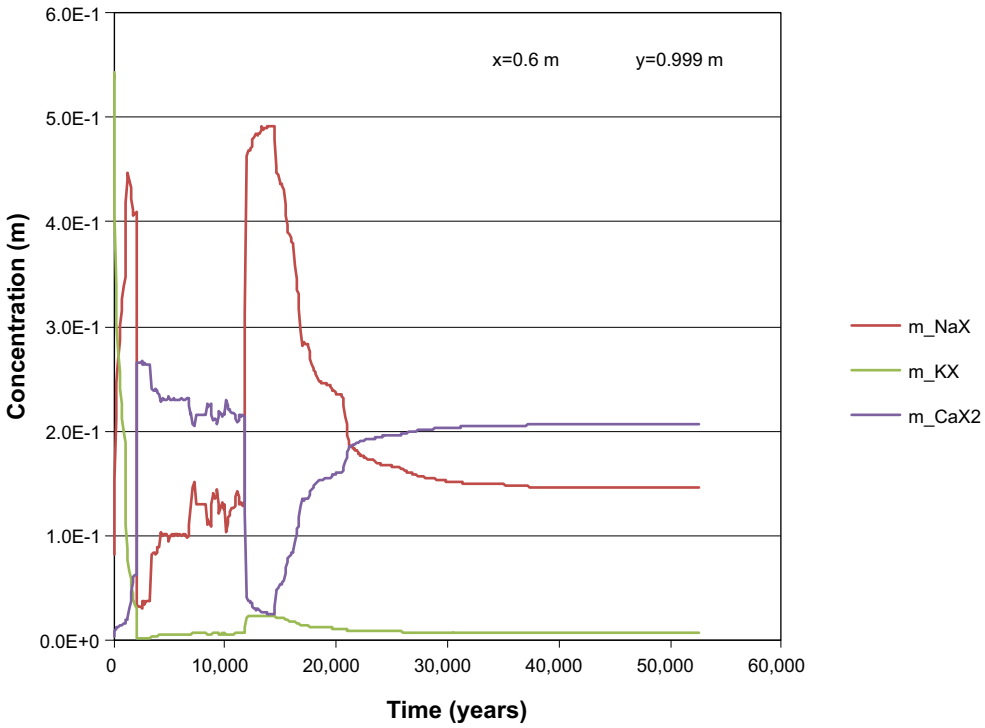

Figure E-12. *The development of the concentration of ion exchange species in concrete over time (during the first 52,600 years) at position DE (1 mm from an open fracture), case Large11. Units (mol/kg pore water).*

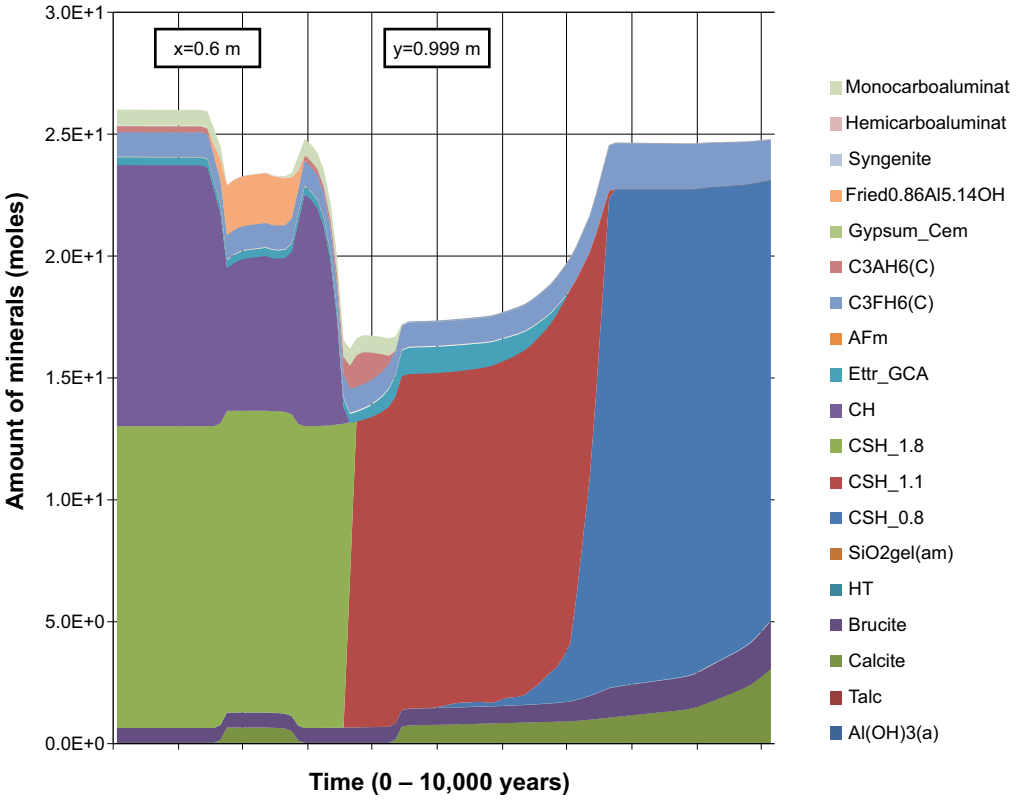

Figure E-13. *The amount of minerals in concrete over time at position DE (1 mm from an open fracture), case Large11. Units (mol/kg pore water).*

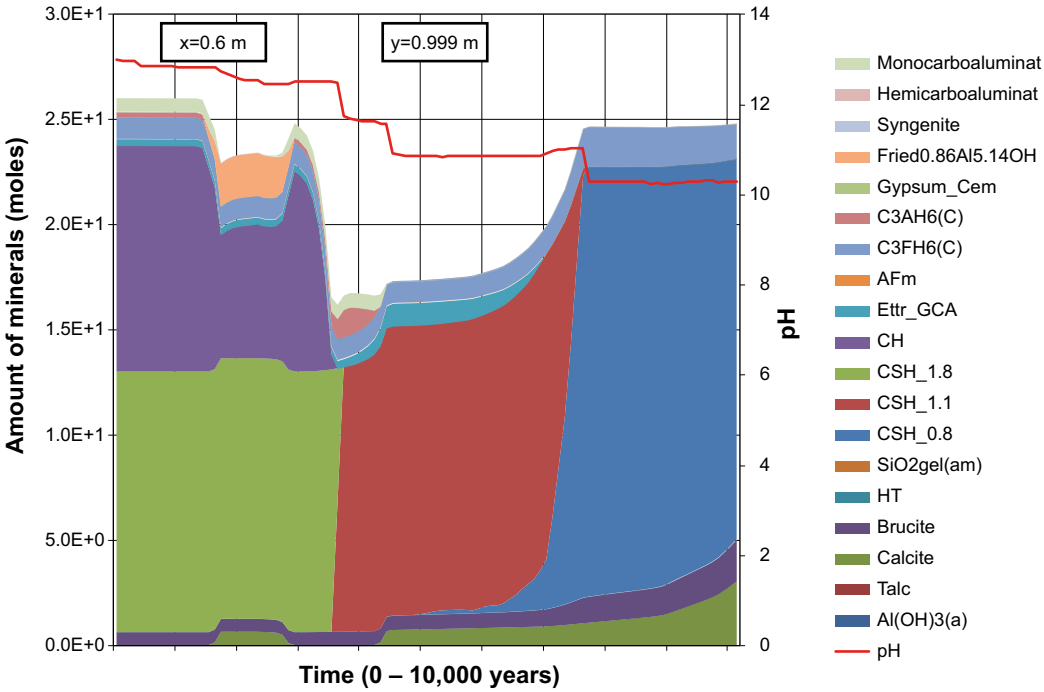

Figure E-14. *The amount of minerals in concrete over time at position DE (1 mm from an open fracture), case Large11. The evolution of pH with time is also indicated. Units (mol/kg pore water).*

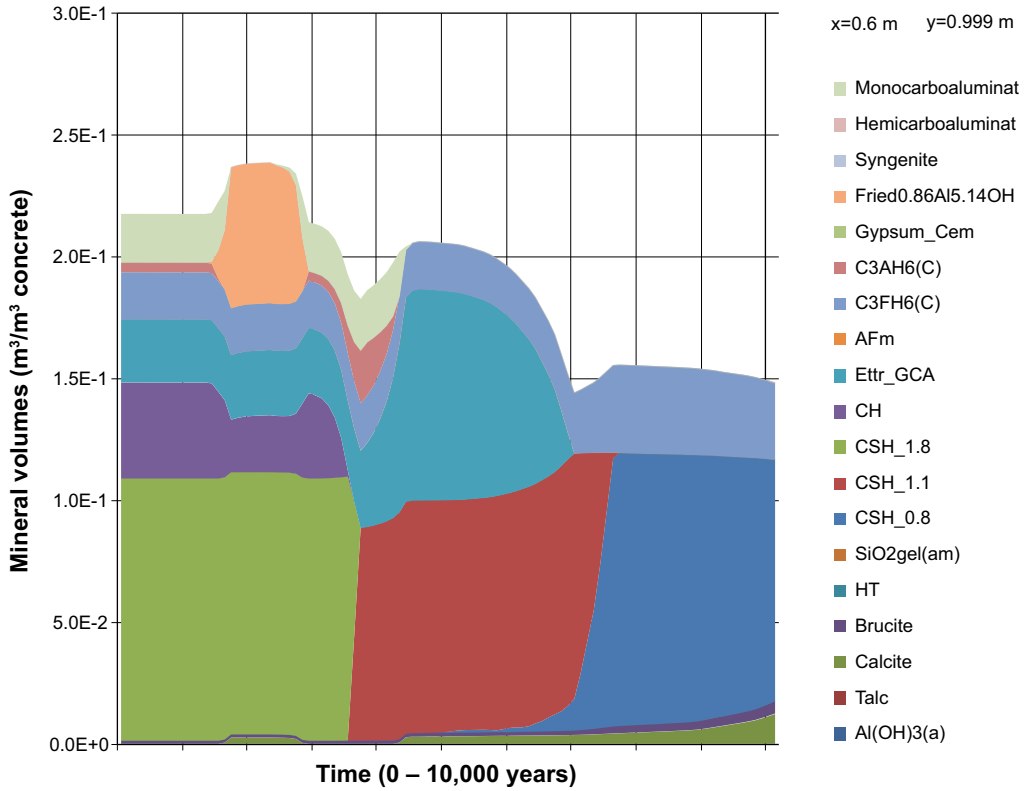

Figure E-15. *The change of mineral volumes in concrete over time at position DE (1 mm from an open fracture), case Large11.*

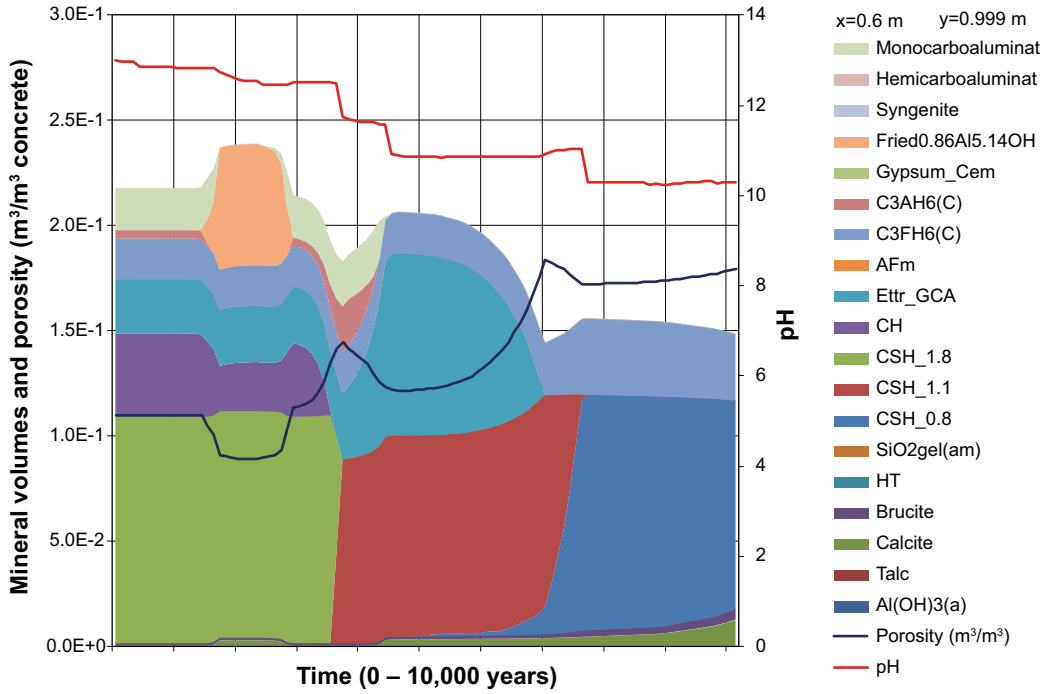

Figure E-16. *The change of mineral volumes and porosity in concrete over time at position DE (1 mm from an open fracture), case Large11. The evolution of pH with time is also indicated.*

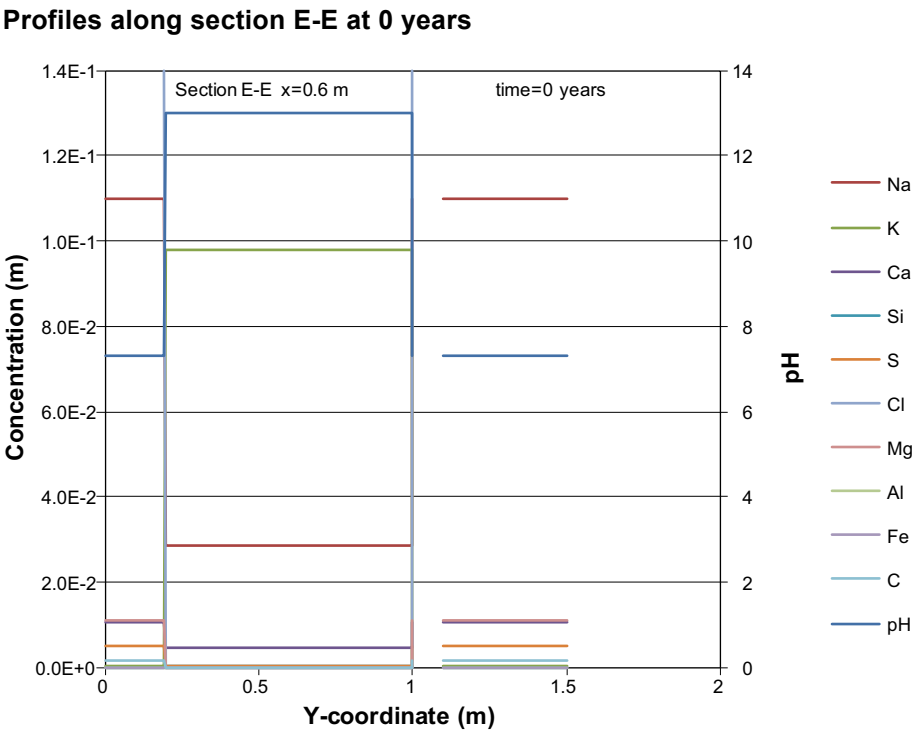

Figure E-17. *Concentration profiles of dissolved components in concrete pore water along the vertical Section E-E at time 0 years, case Large11. Units (mol/kg pore water).*

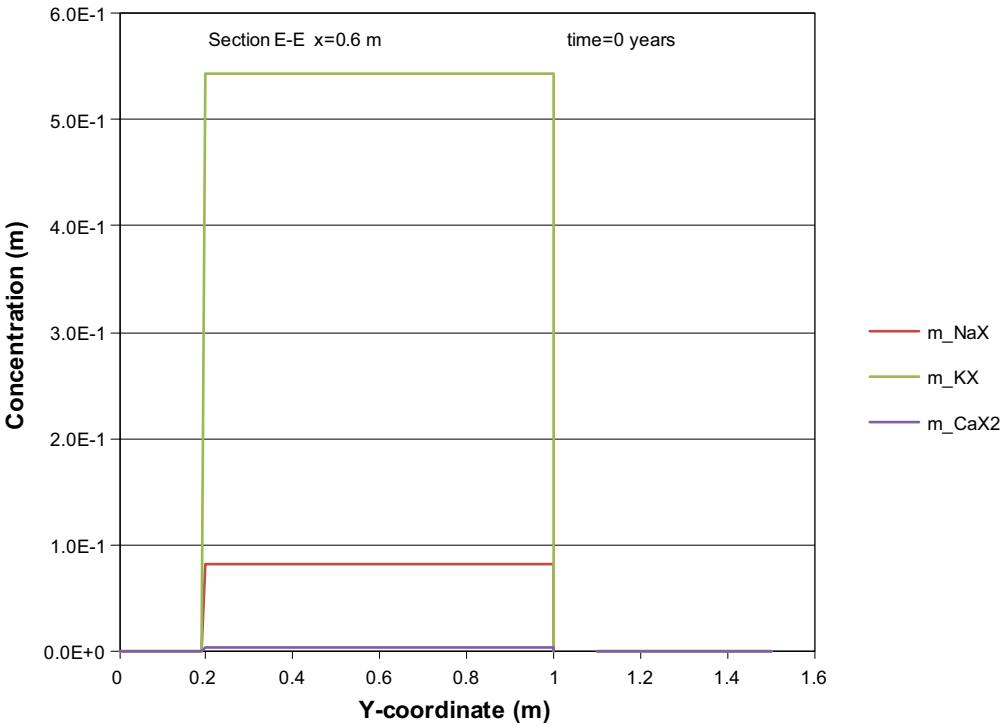

Figure E-18. *The assembly of ion exchange species in concrete along the vertical Section E-E at time 0 years, case Large11. Units (mol/kg pore water).*

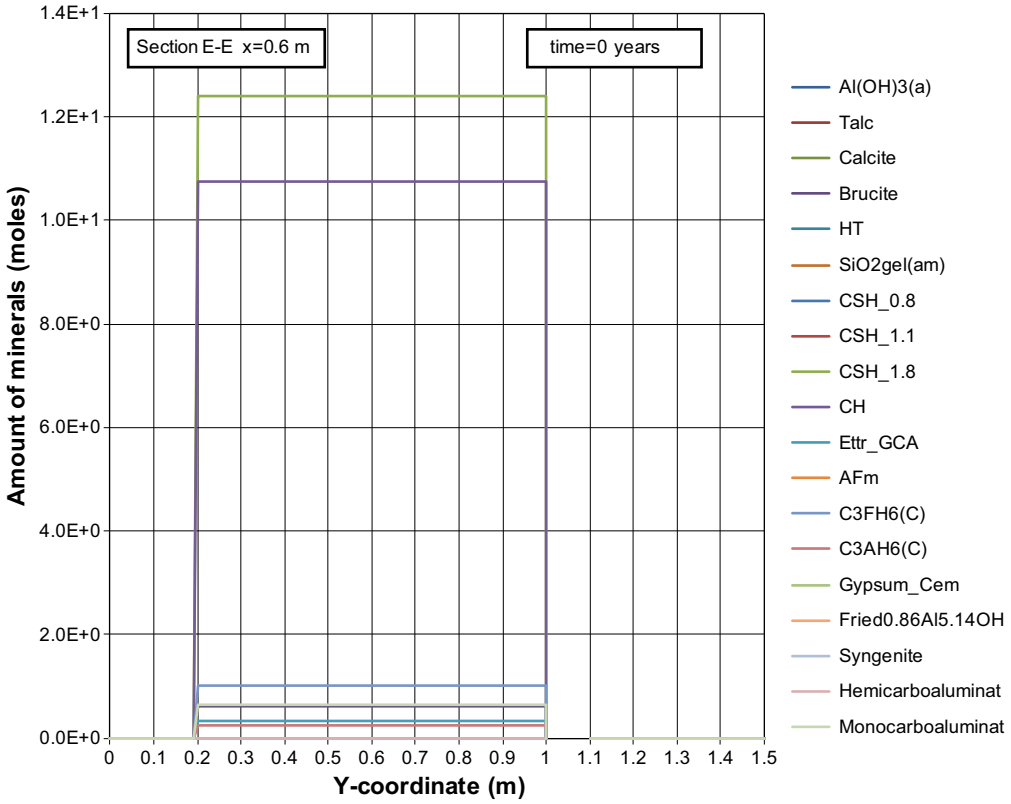

Figure E-19. *The mineral composition in concrete along the vertical Section E-E at time 0 years, case Large11. Units (mol/kg pore water).*

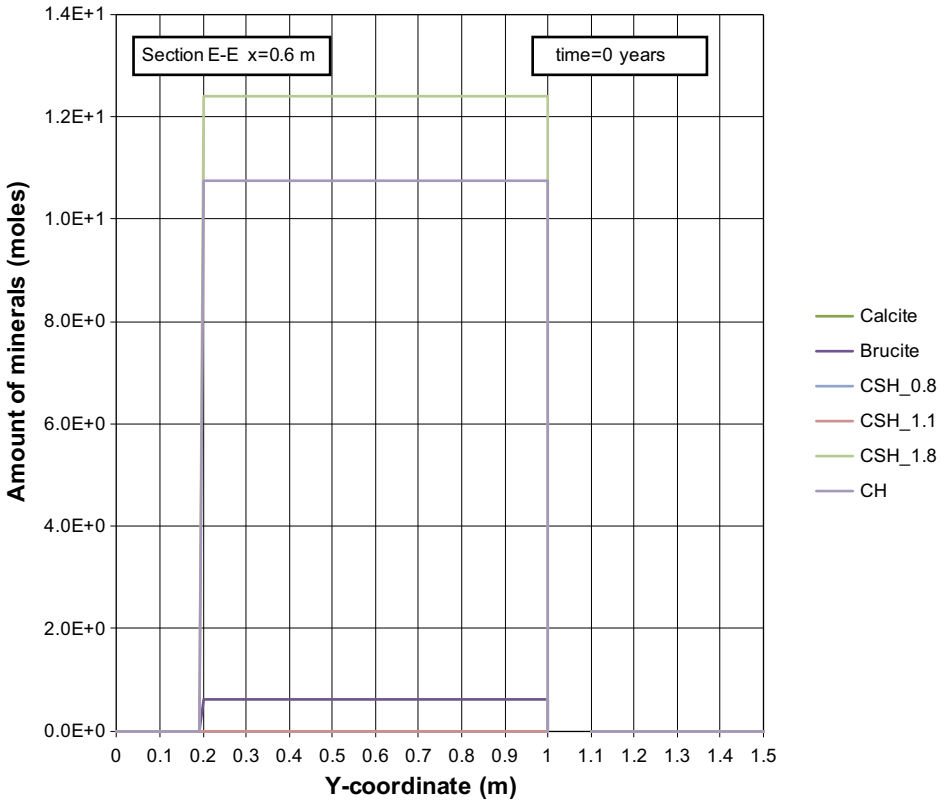

Figure E-20. *The mineral composition in concrete along the vertical Section E-E at time 0 years, case Large11. Units (mol/kg pore water).*

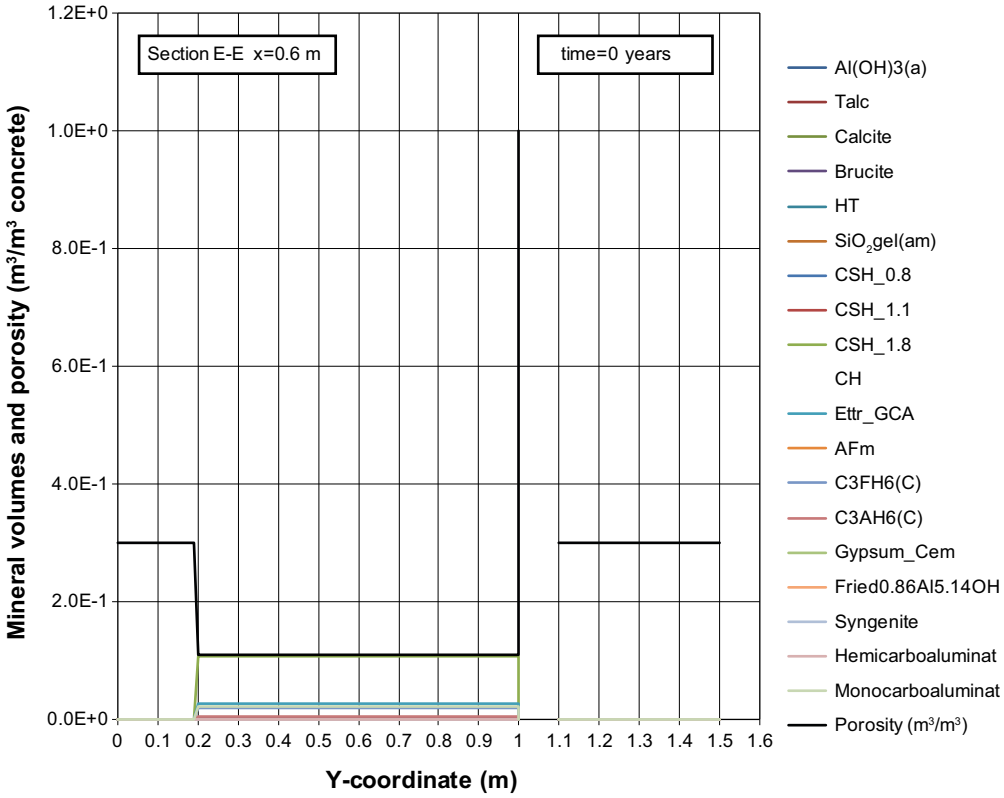

Figure E-21. *Mineral composition in concrete and calculated porosity along the vertical Section E-E at time 0 years, case Large11.*

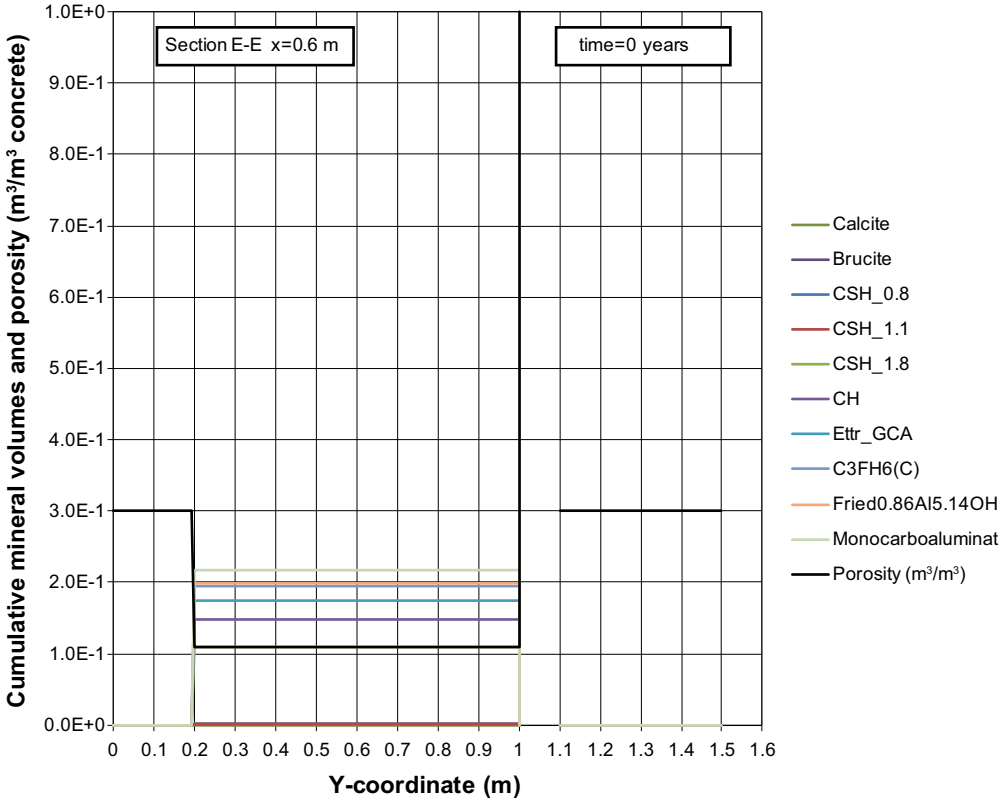

Figure E-22. *Cumulative representation of the mineral composition in concrete and calculated porosity along the vertical Section E-E at time 0 years, case Large11.*

Profiles along section E-E at 100 years

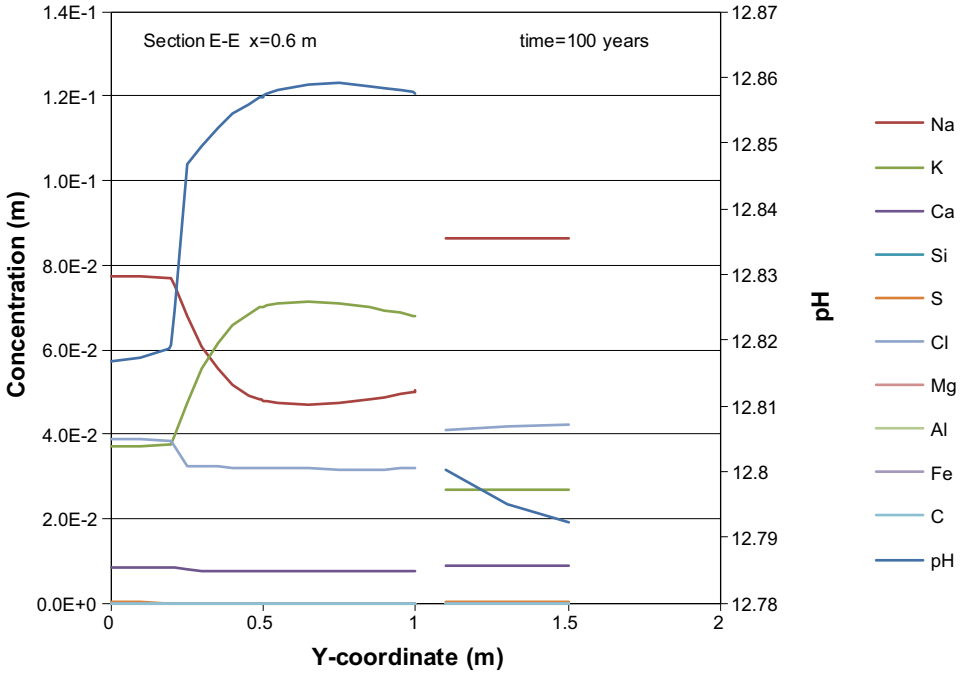

Figure E-23. *Concentration profiles of dissolved components in concrete pore water along the vertical Section E-E at time 100 years, case Large11. Units (mol/kg pore water).*

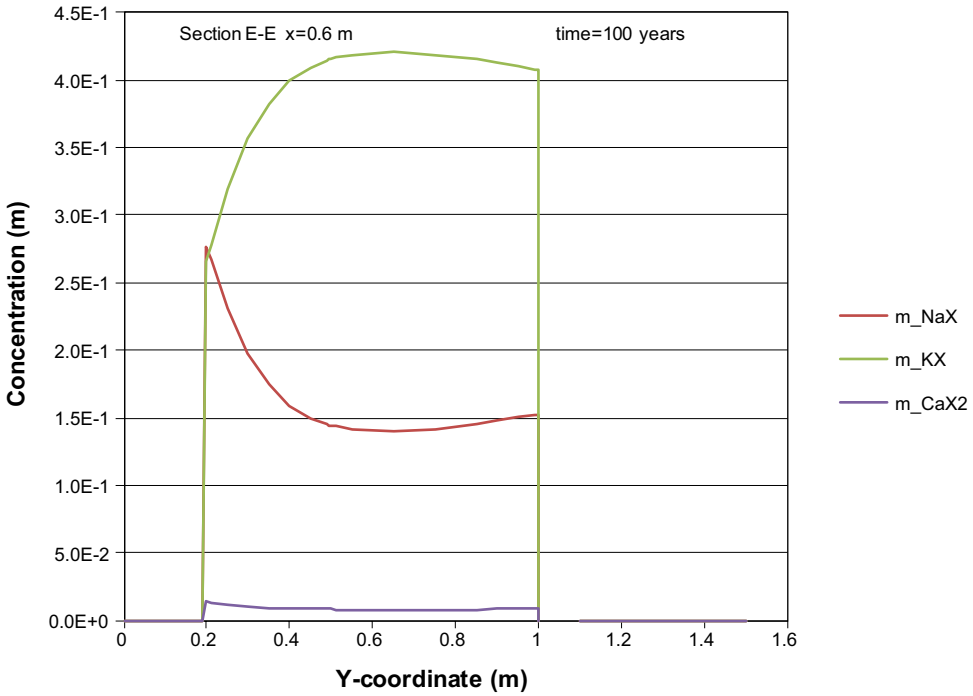

Figure E-24. *The assembly of ion exchange species in concrete along the vertical Section E-E at time 100 years, case Large11. Units (mol/kg pore water).*

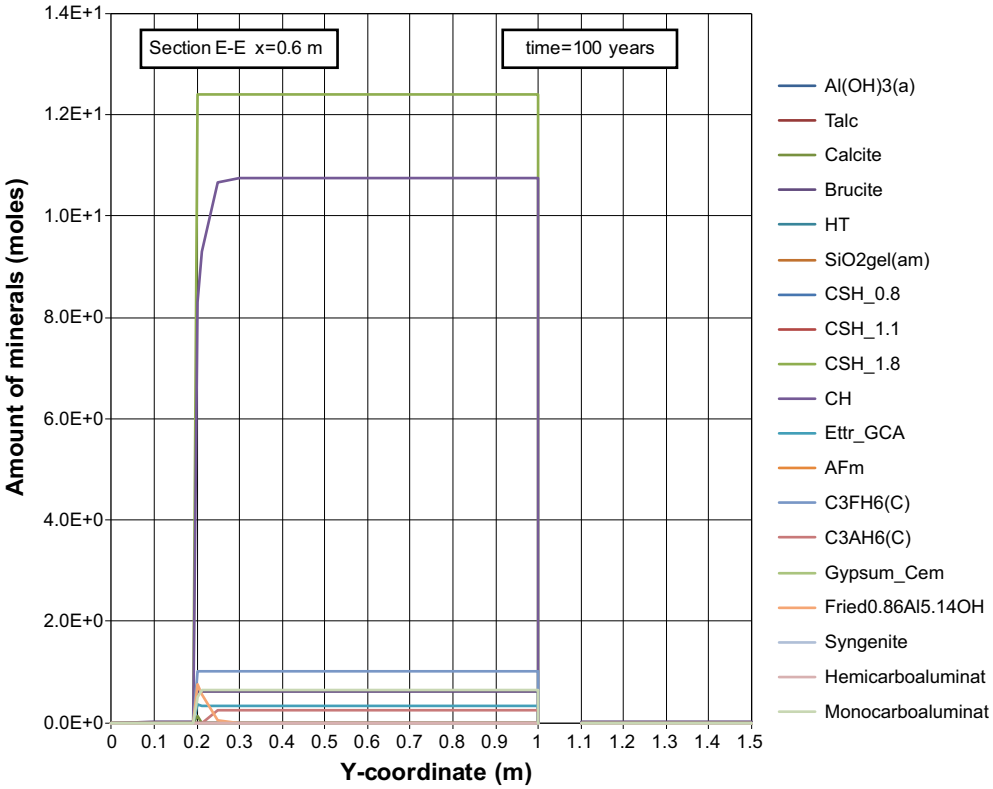

Figure E-25. *The mineral composition in concrete along the vertical Section E-E at time 100 years, case Large11. Units (mol/kg pore water).*

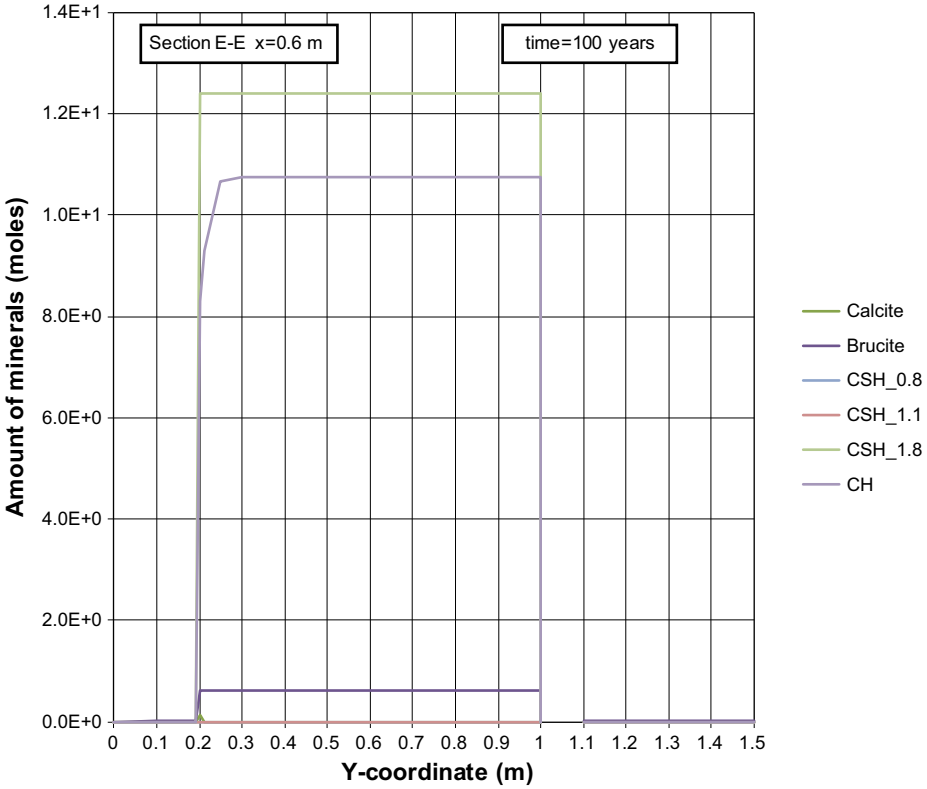

Figure E-26. *The mineral composition in concrete along the vertical Section E-E at time 100 years, case Large11. Units (mol/kg pore water).*

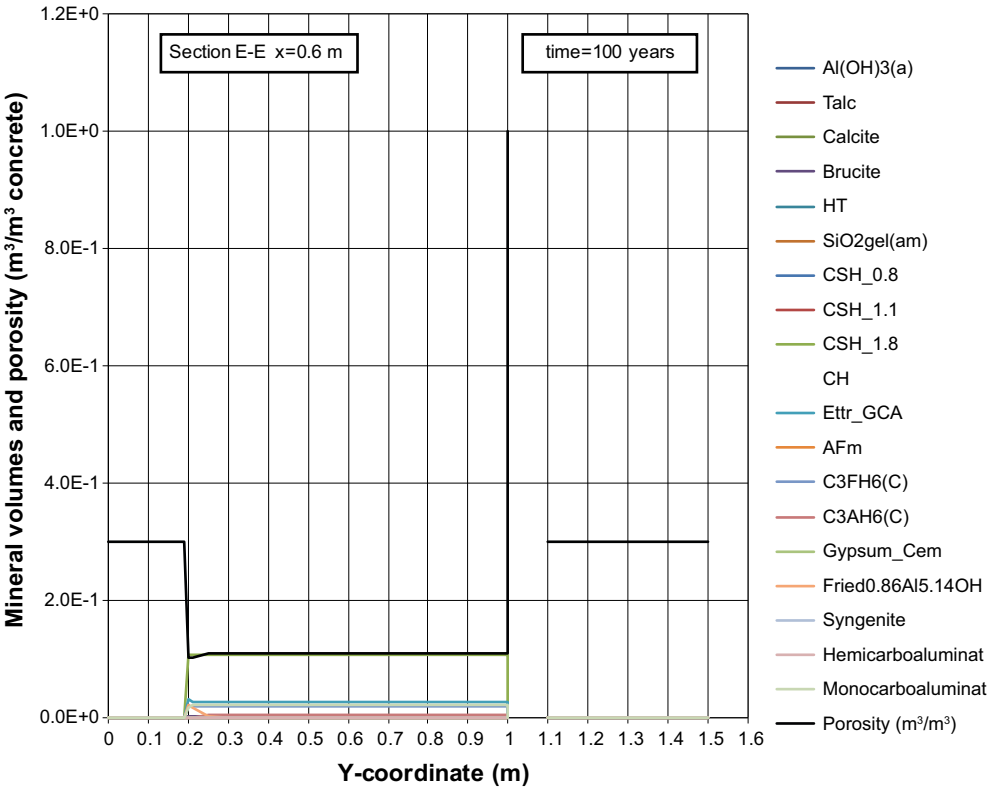

Figure E-27. *Mineral composition in concrete and calculated porosity along the vertical Section E-E at time 100 years, case Large11.*

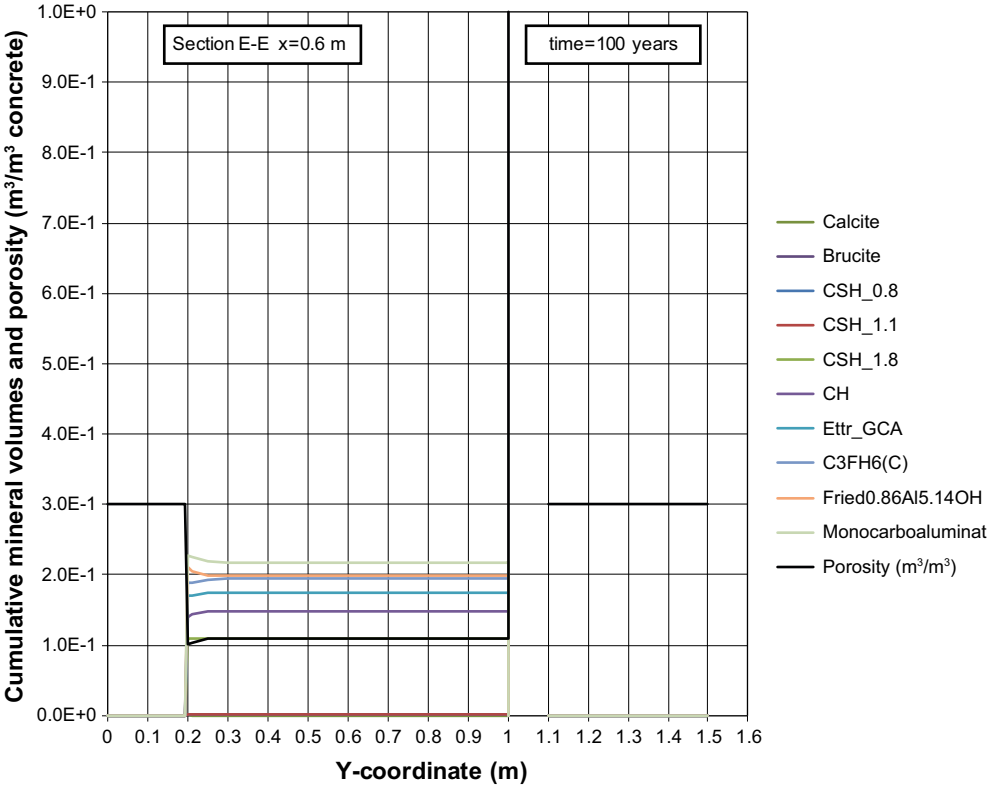

Figure E-28. *Cumulative representation of the mineral composition in concrete and calculated porosity along the vertical Section E-E at time 100 years, case Large11.*

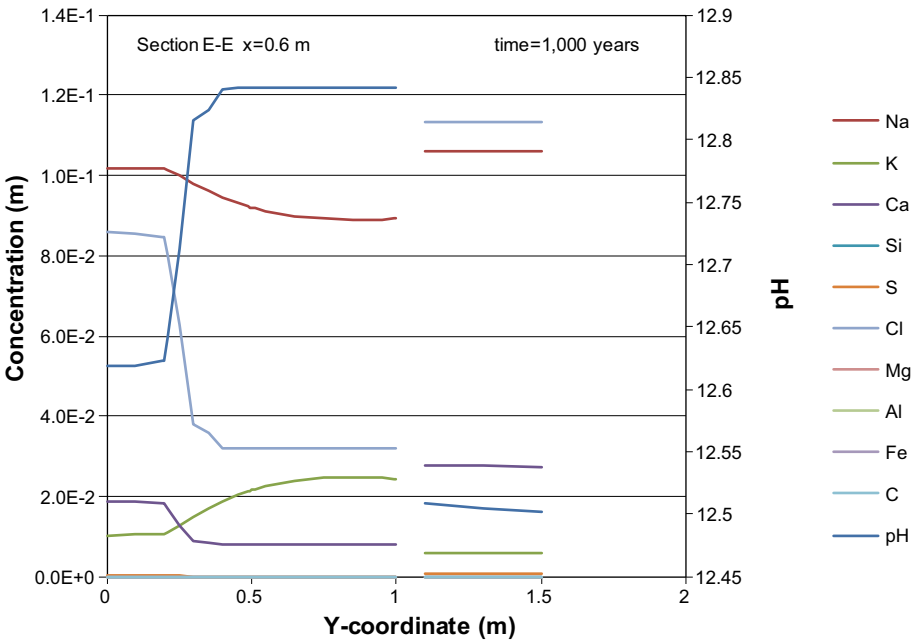

Figure E-29. *Concentration profiles of dissolved components in concrete pore water along the vertical Section E-E at time 1,000 years, case Large11. Units (mol/kg pore water).*

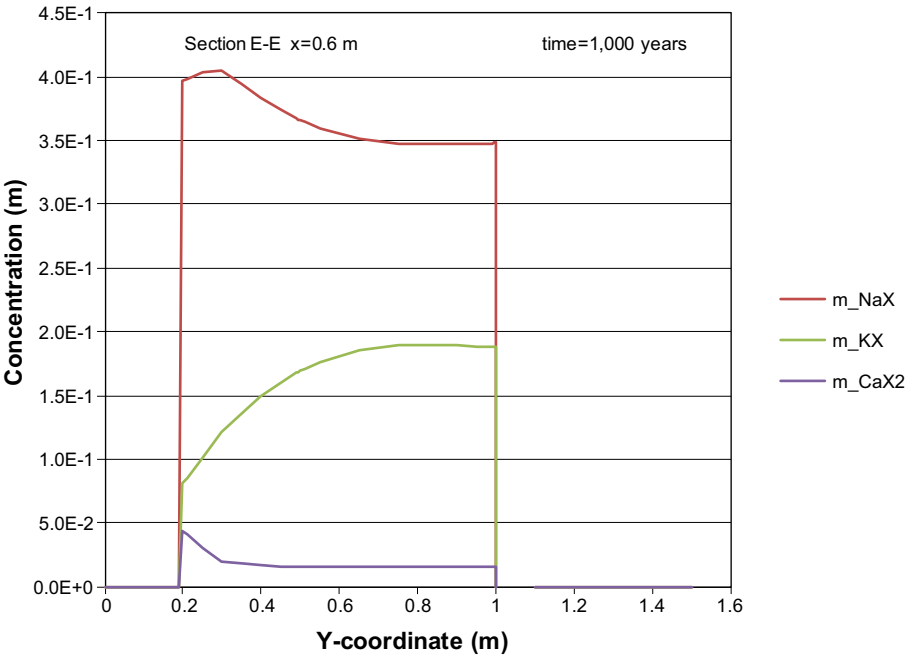

Figure E-30. *The assembly of ion exchange species in concrete along the vertical Section E-E at time 1,000 years, case Large11. Units (mol/kg pore water).*

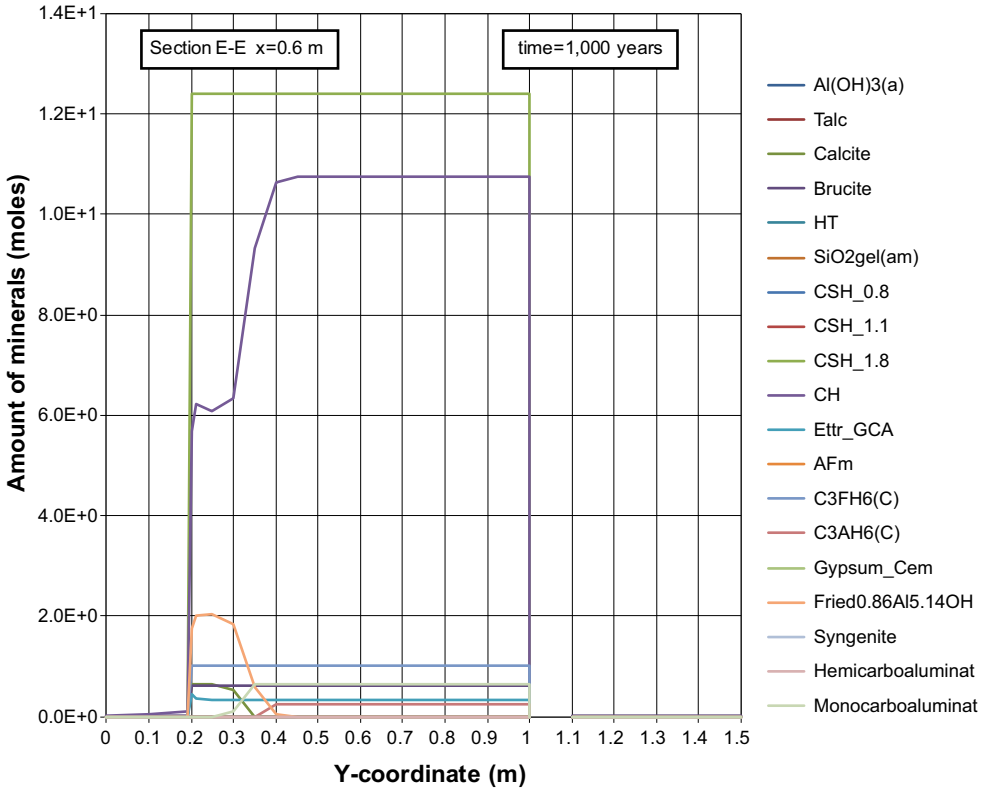

Figure E-31. *The mineral composition in concrete along the vertical Section E-E at time 1,000 years, case Large11. Units (mol/kg pore water).*

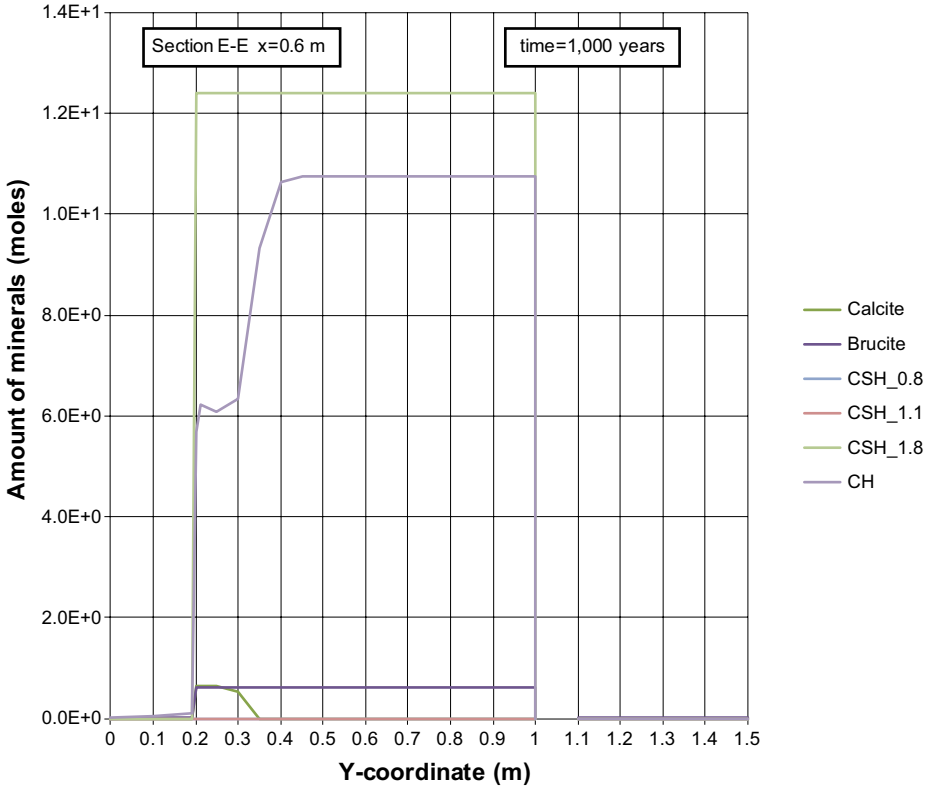

Figure E-32. *The mineral composition in concrete along the vertical Section E-E at time 1,000 years, case Large11. Units (mol/kg pore water).*

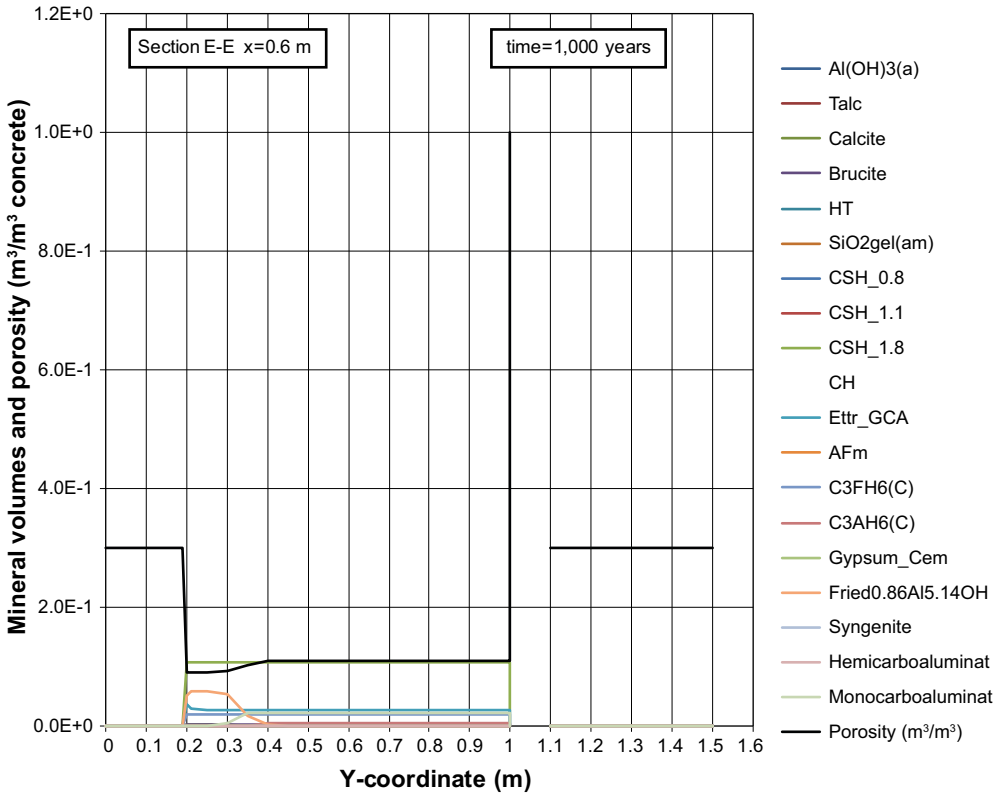

Figure E-33. *Mineral composition in concrete and calculated porosity along the vertical Section E-E at time 1,000 years, case Large11.*

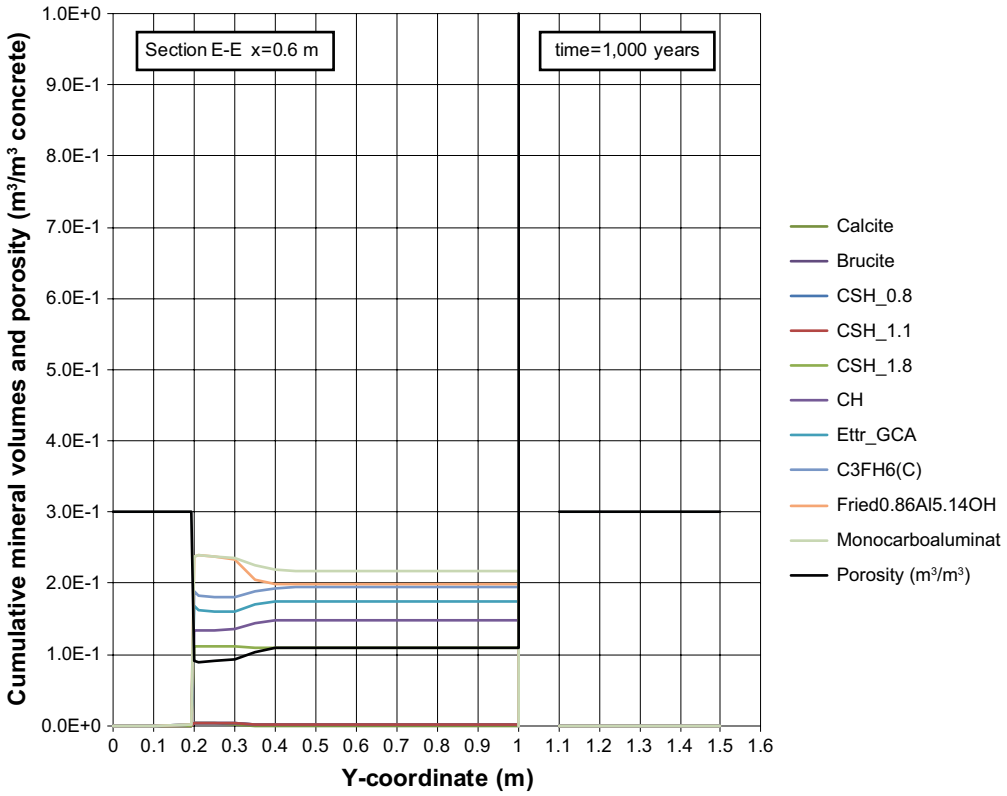

Figure E-34. *Cumulative representation of the mineral composition in concrete and calculated porosity along the vertical Section E-E at time 1,000 years, case Large11.*

Profiles along section E-E at 2,000 years

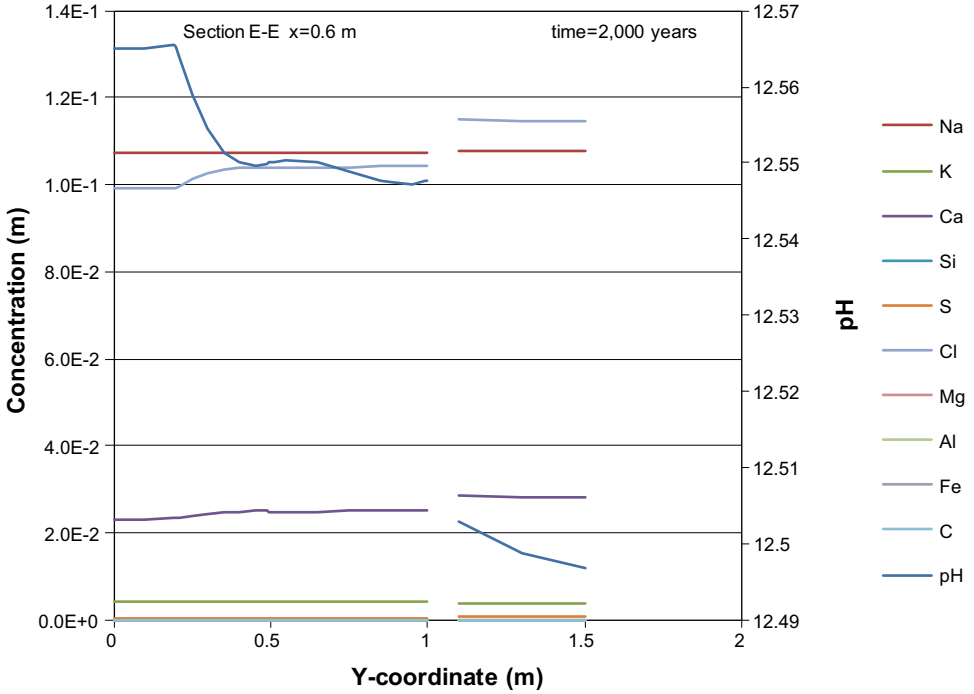

Figure E-35. *Concentration profiles of dissolved components in concrete pore water along the vertical Section E-E at time 2,000 years, case Large11. Units (mol/kg pore water).*

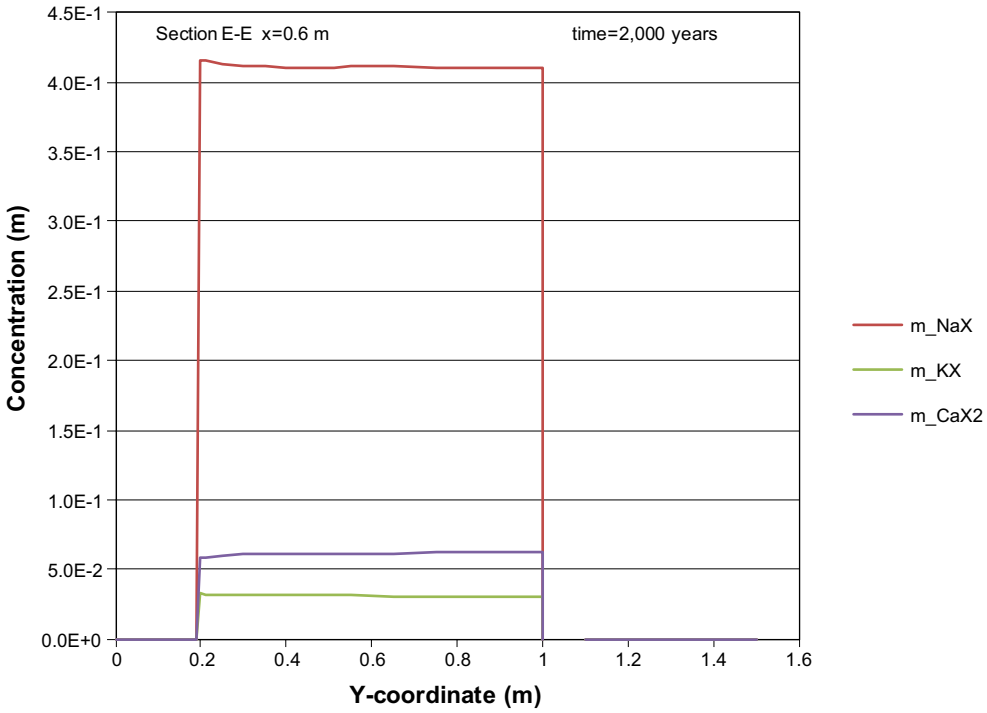

Figure E-36. *The assembly of ion exchange species in concrete along the vertical Section E-E at time 2,000 years, case Large11. Units (mol/kg pore water).*

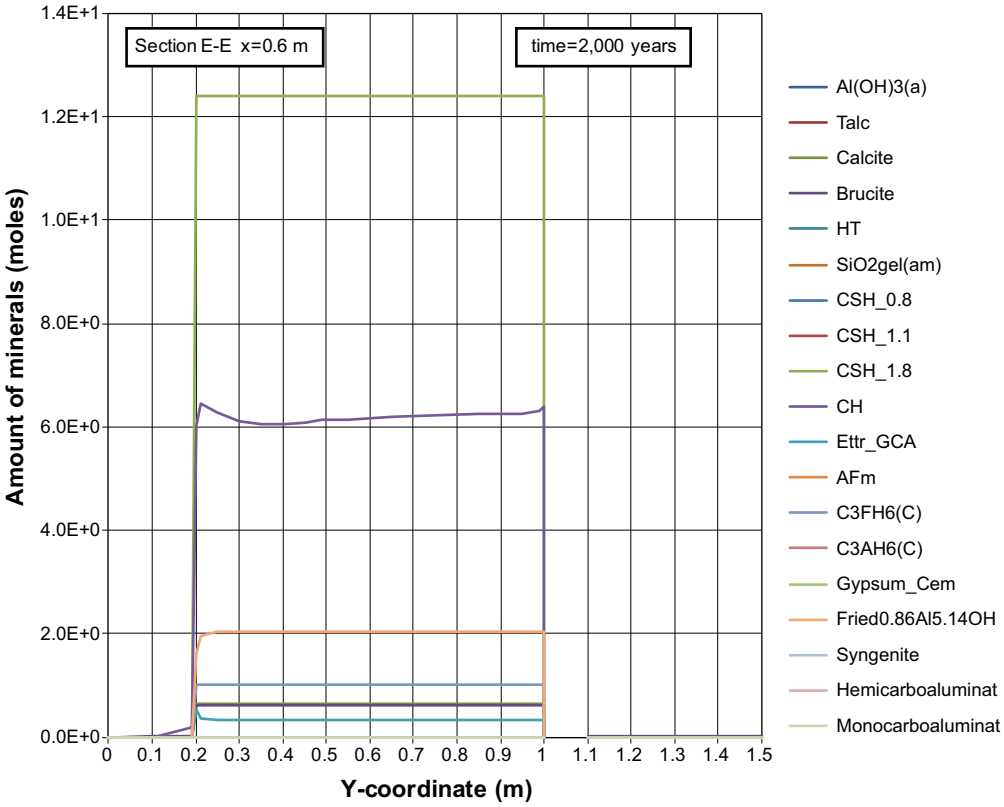

Figure E-37. *The mineral composition in concrete along the vertical Section E-E at time 2,000 years, case Large11. Units (mol/kg pore water).*

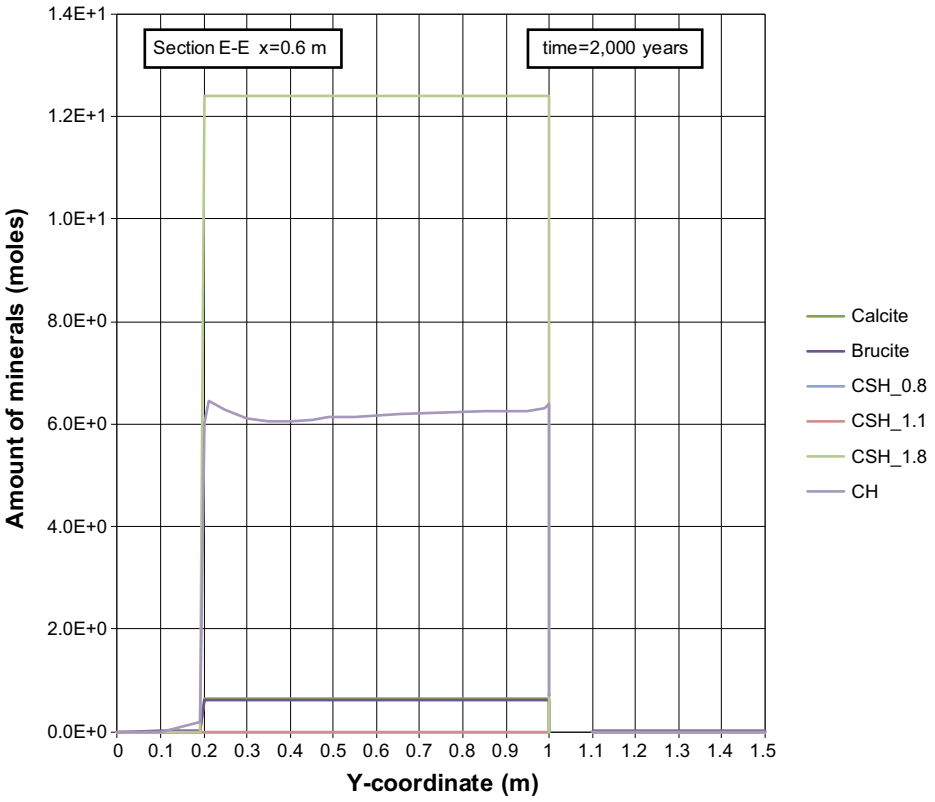

Figure E-38. *The mineral composition in concrete along the vertical Section E-E at time 2,000 years, case Large11. Units (mol/kg pore water).*

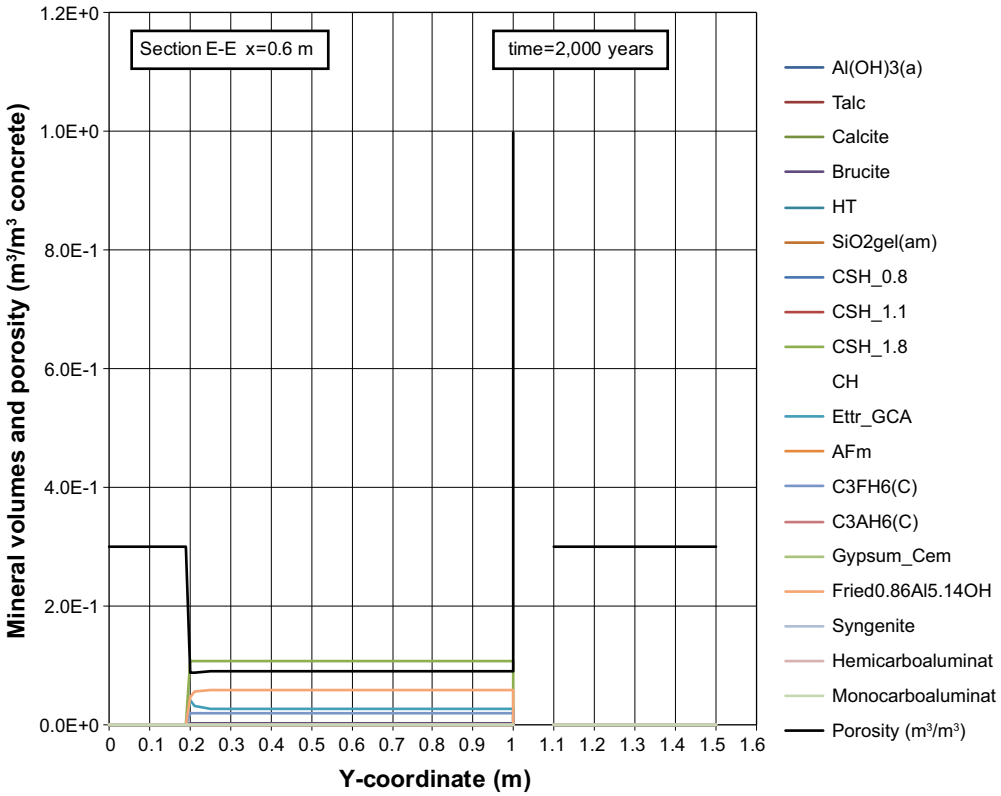

Figure E-39. *Mineral composition in concrete and calculated porosity along the vertical Section E-E at time 2,000 years, case Large11.*

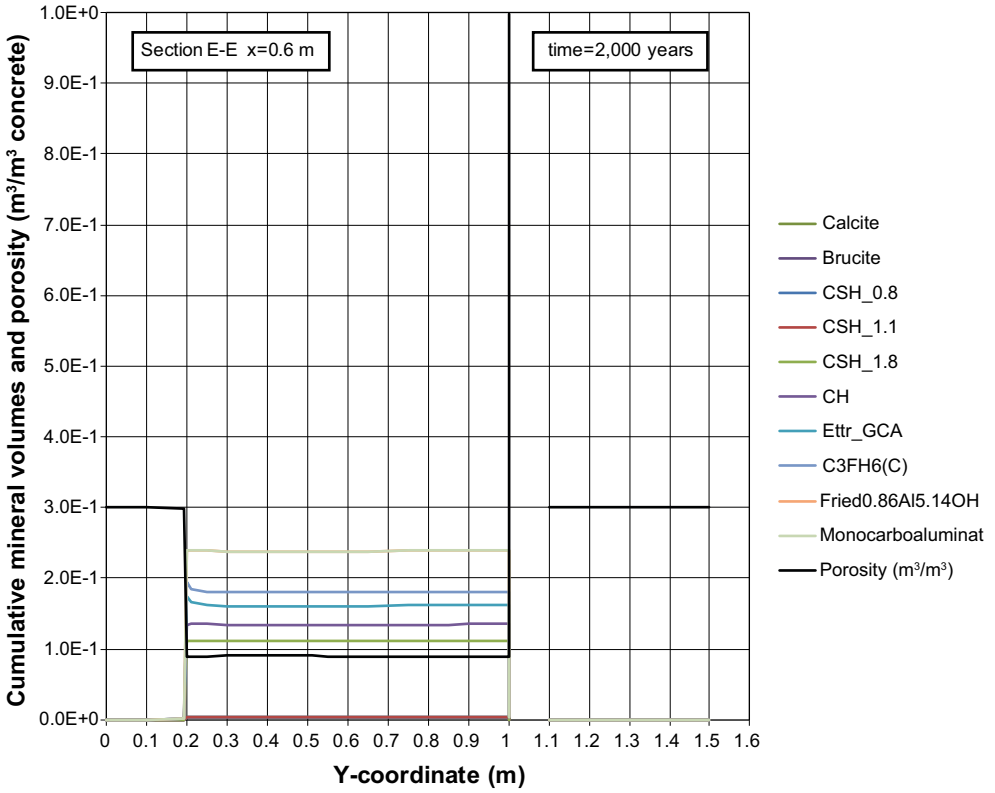

Figure E-40. *Cumulative representation of the mineral composition in concrete and calculated porosity along the vertical Section E-E at time 2,000 years, case Large11.*

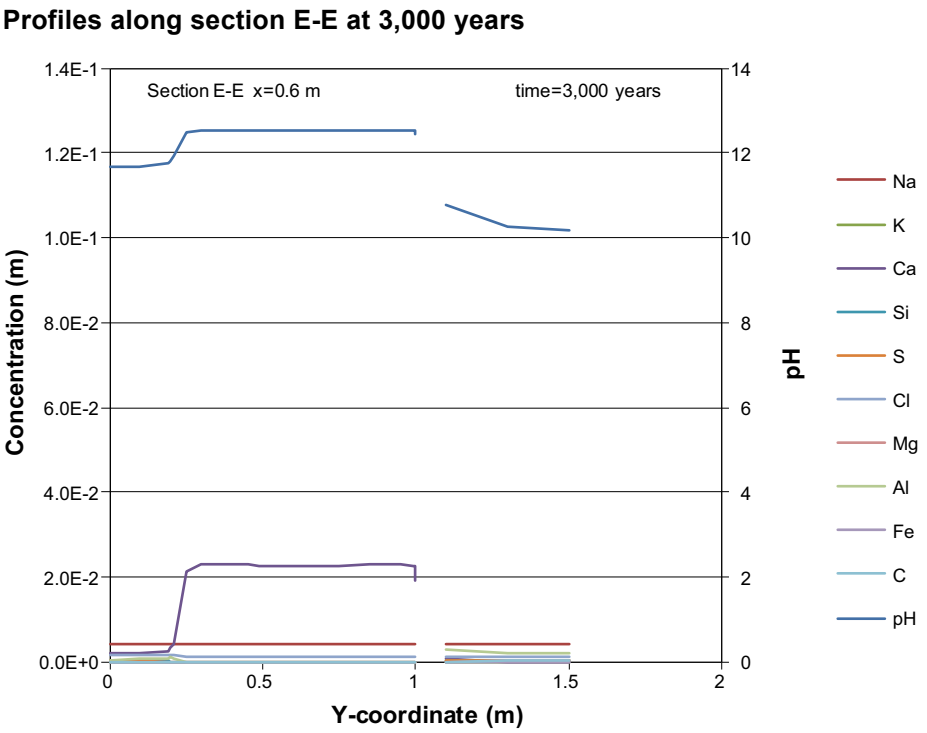

Figure E-41. *Concentration profiles of dissolved components in concrete pore water along the vertical Section E-E at time 3,000 years, case Large11. Units (mol/kg pore water).*

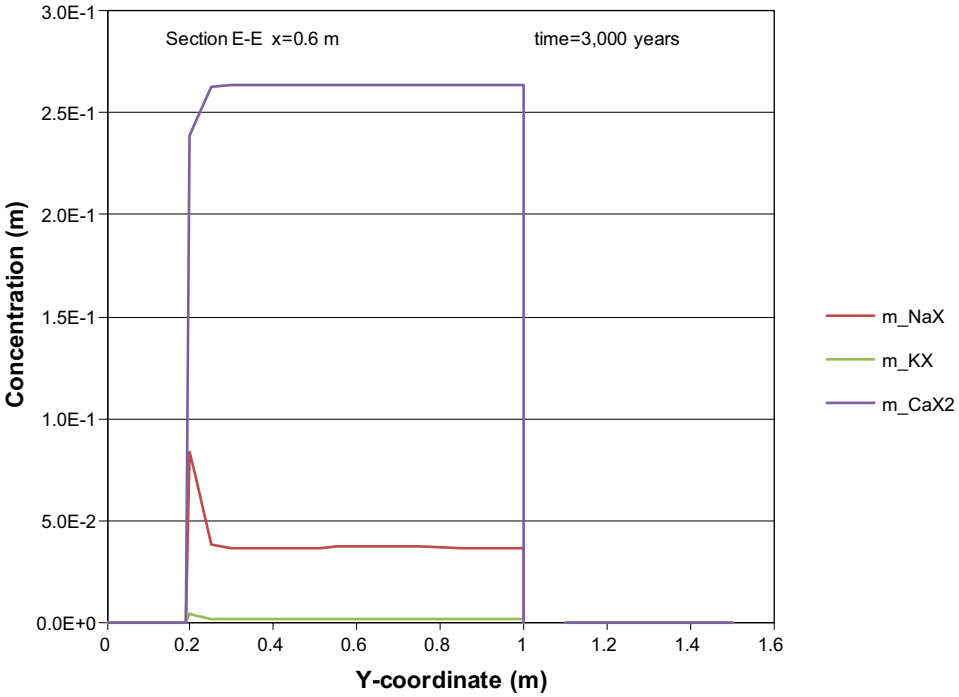

Figure E-42. *The assembly of ion exchange species in concrete along the vertical Section E-E at time 3,000 years, case Large11. Units (mol/kg pore water).*

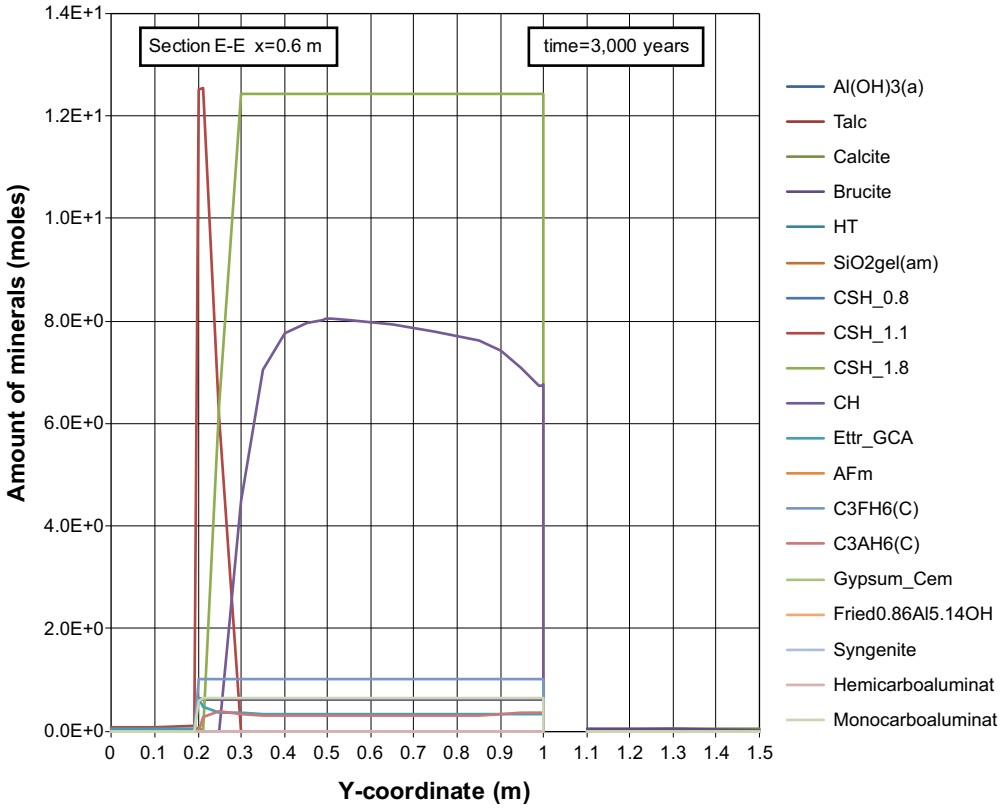

Figure E-43. *The mineral composition in concrete along the vertical Section E-E at time 3,000 years, case Large11. Units (mol/kg pore water).*

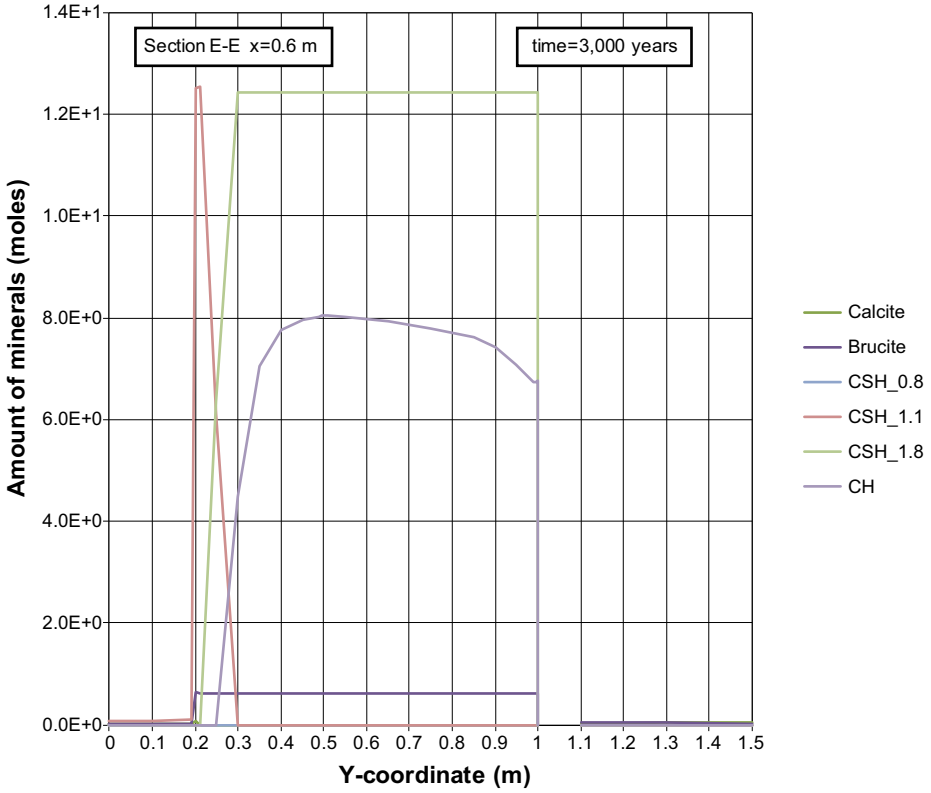

Figure E-44. *The mineral composition in concrete along the vertical Section E-E at time 3,000 years, case Large11. Units (mol/kg pore water).*

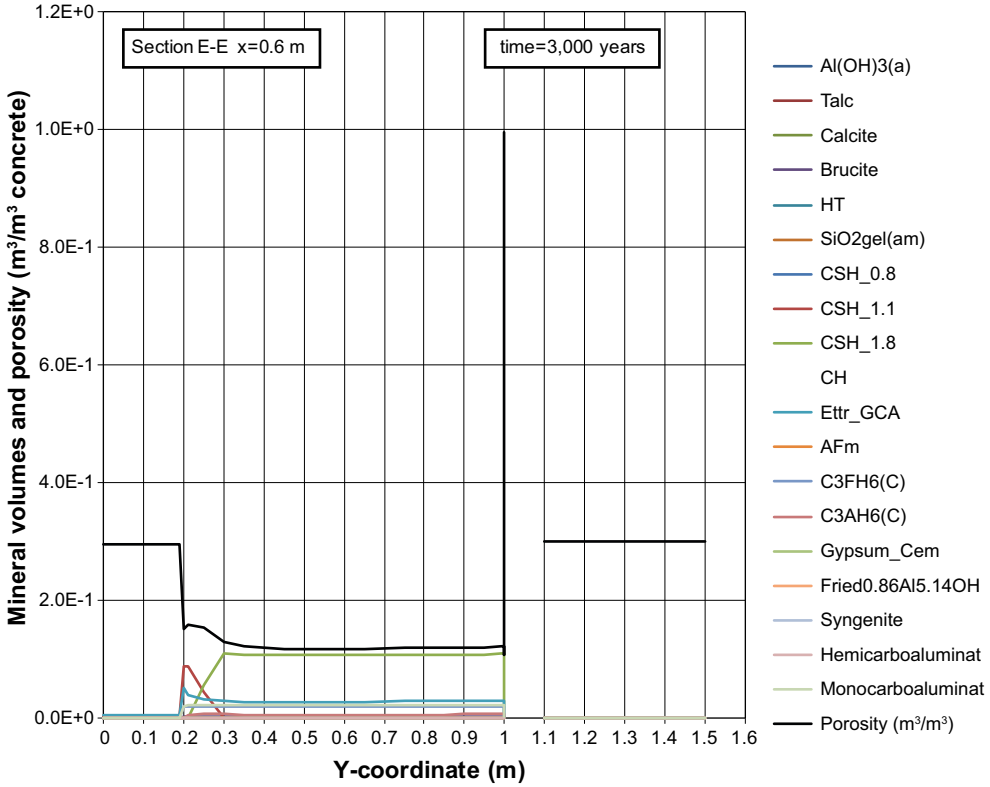

Figure E-45. *Mineral composition in concrete and calculated porosity along the vertical Section E-E at time 3,000 years, case Large11.*

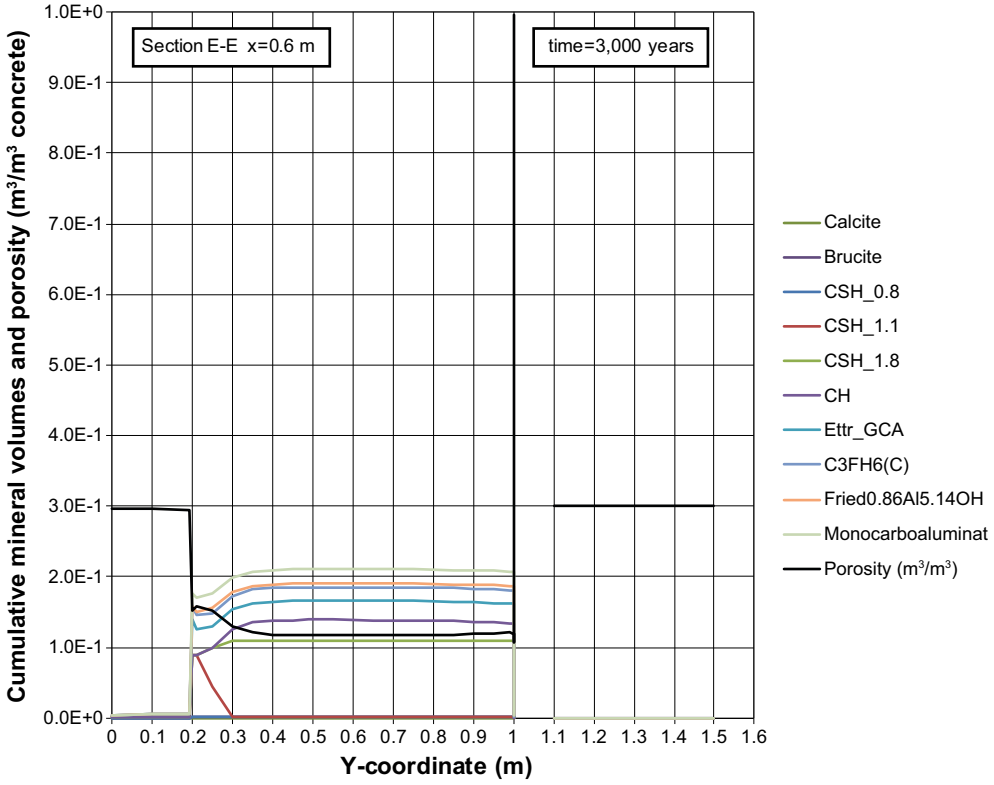

Figure E-46. *Cumulative representation of the mineral composition in concrete and calculated porosity along the vertical Section E-E at time 3,000 years, case Large11.*

Profiles along section E-E at 5,000 years

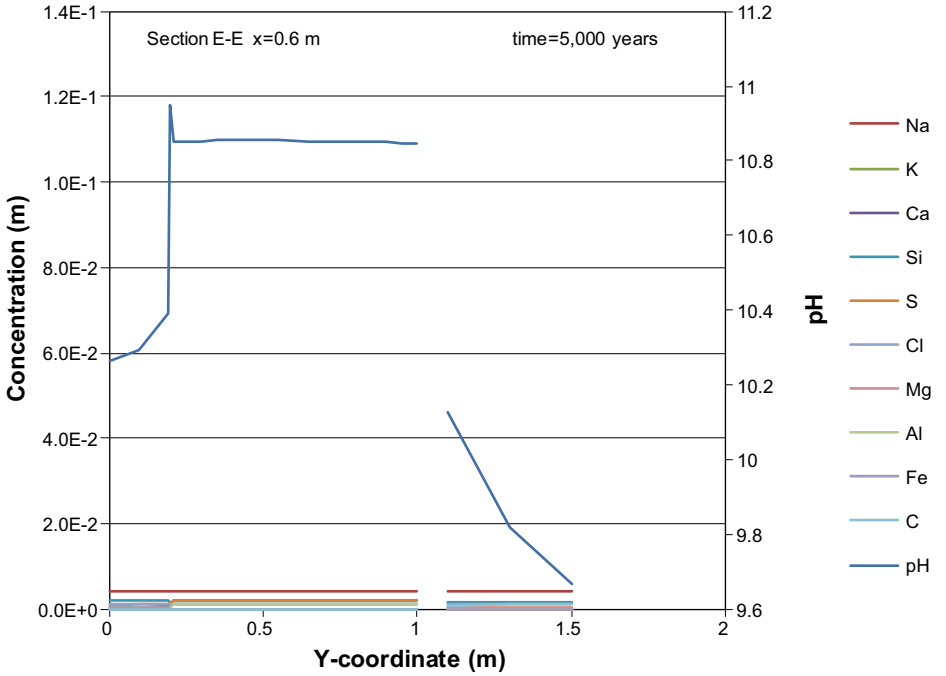

Figure E-47. *Concentration profiles of dissolved components in concrete pore water along the vertical Section E-E at time 5,000 years, case Large11. Units (mol/kg pore water).*

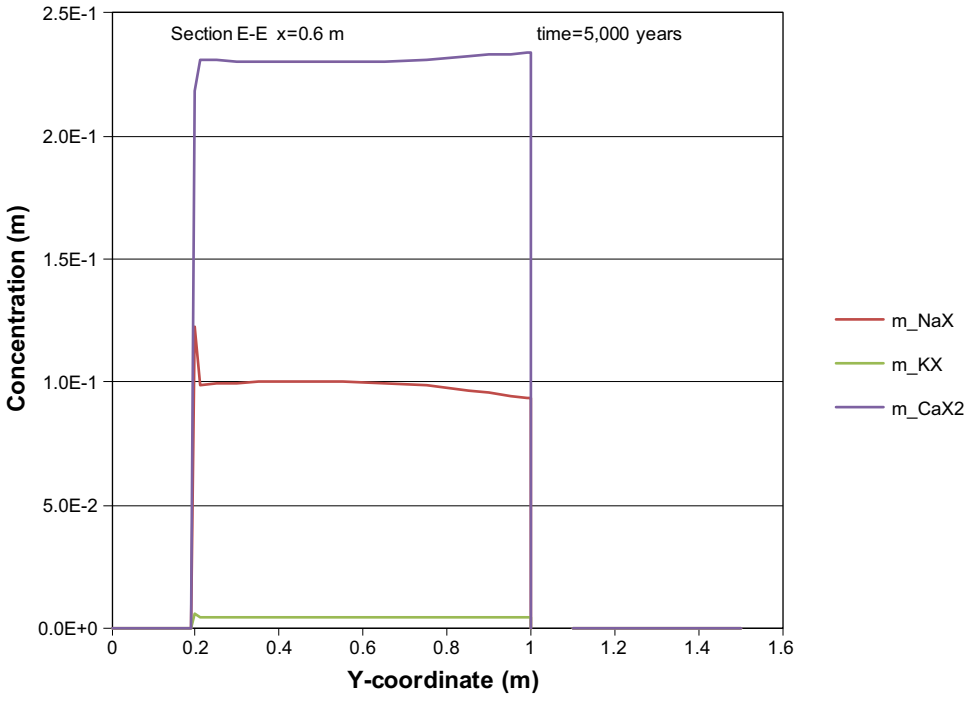

Figure E-48. *The assembly of ion exchange species in concrete along the vertical Section E-E at time 5,000 years, case Large11. Units (mol/kg pore water).*

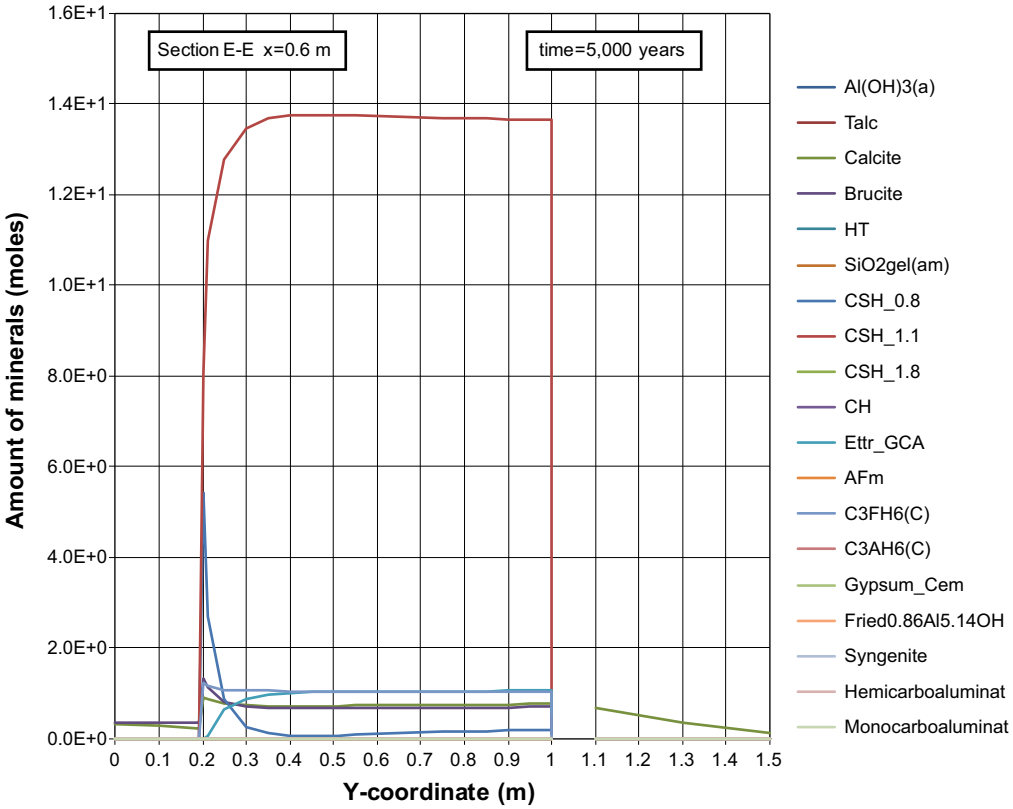

Figure E-49. *The mineral composition in concrete along the vertical Section E-E at time 5,000 years, case Large11. Units (mol/kg pore water).*

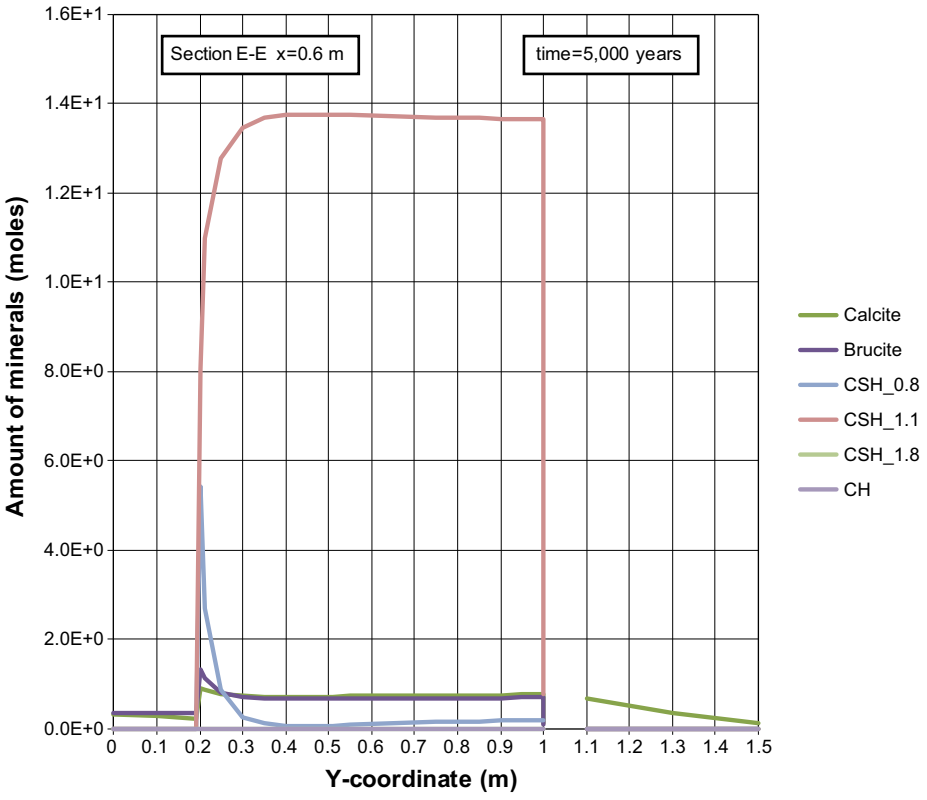

Figure E-50. *The mineral composition in concrete along the vertical Section E-E at time 5,000 years, case Large11. Units (mol/kg pore water).*

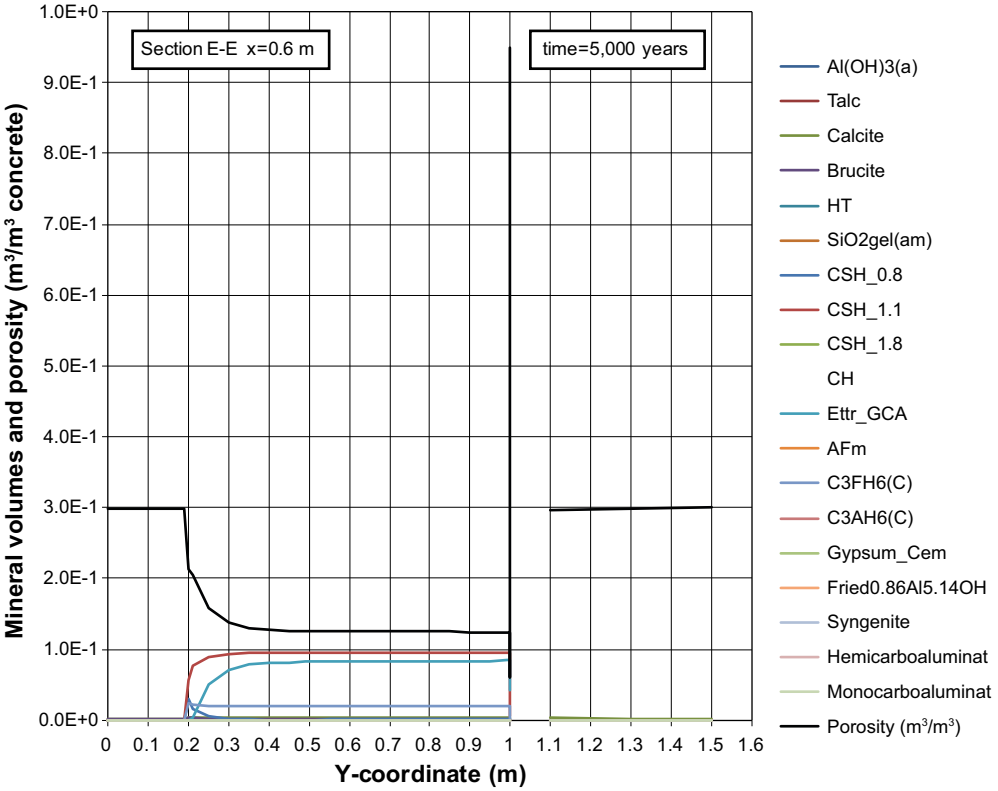

Figure E-51. *Mineral composition in concrete and calculated porosity along the vertical Section E-E at time 5,000 years, case Large11.*

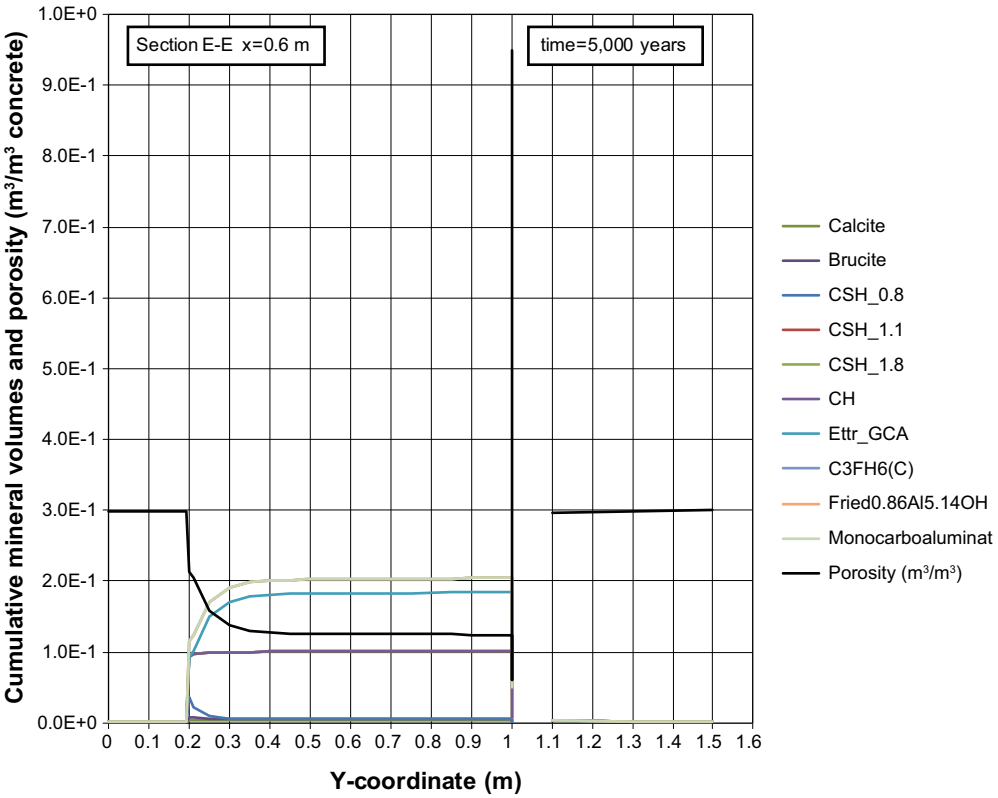

Figure E-52. *Cumulative representation of the mineral composition in concrete and calculated porosity along the vertical Section E-E at time 5,000 years, case Large11.*

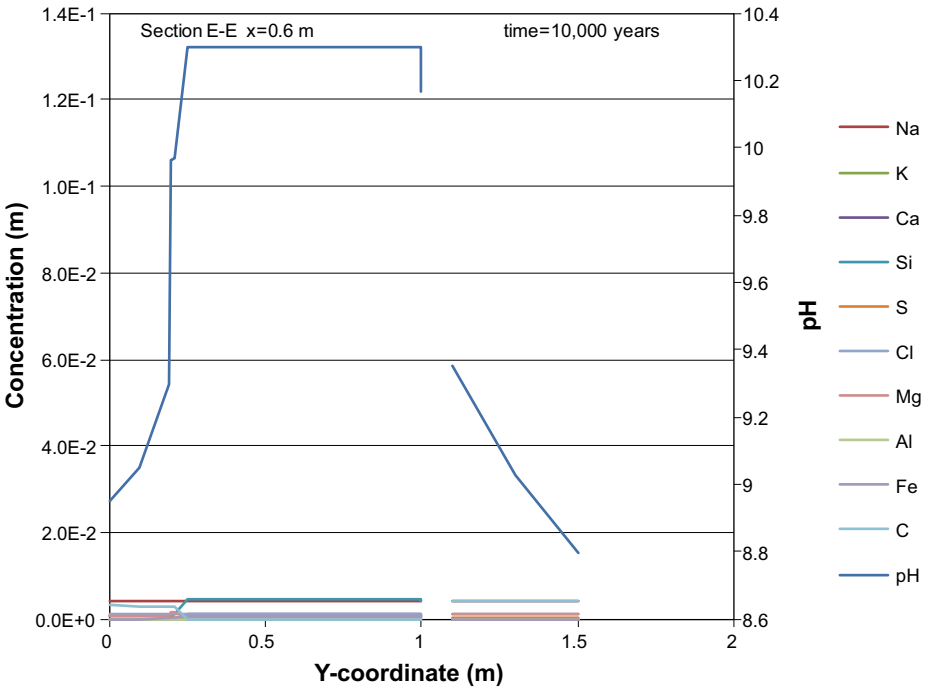

Figure E-53. *Concentration profiles of dissolved components in concrete pore water along the vertical Section E-E at time 10,000 years, case Large11. Units (mol/kg pore water).*

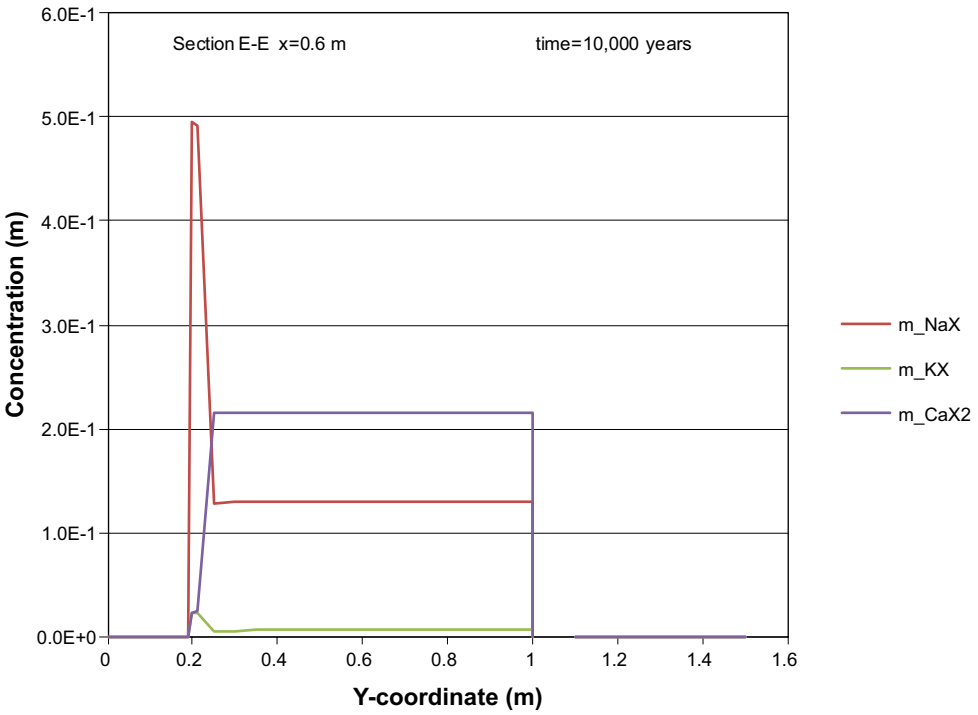

Figure E-54. *The assembly of ion exchange species in concrete along the vertical Section E-E at time 10,000 years, case Large11. Units (mol/kg pore water).*

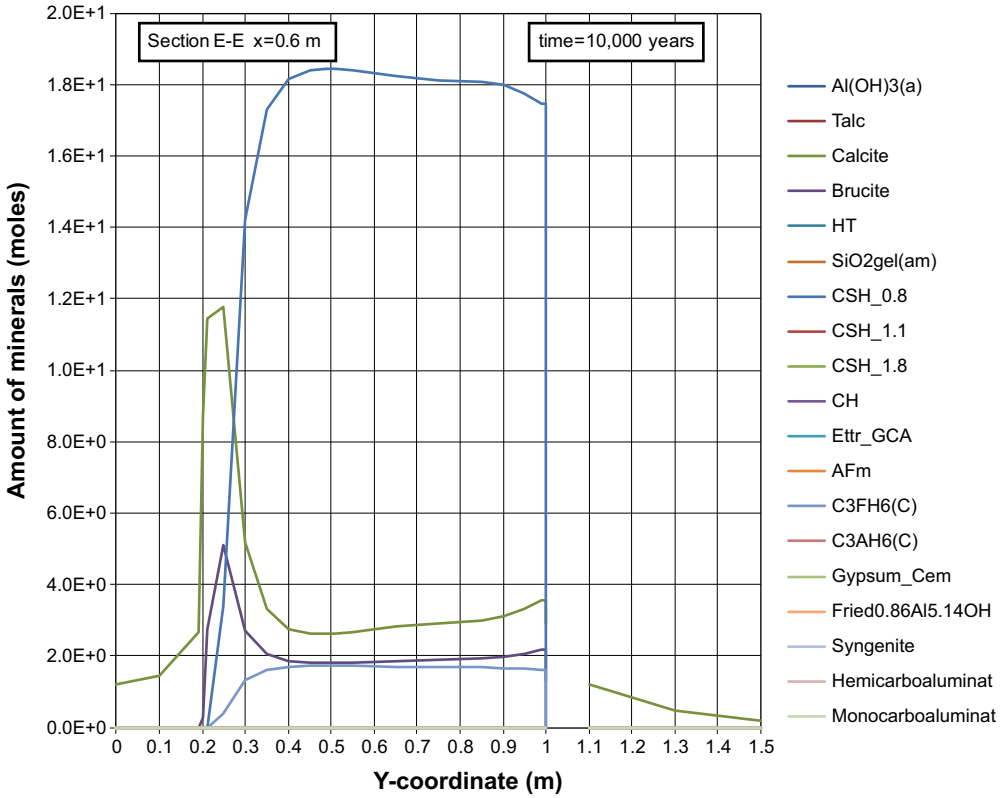

Figure E-55. *The mineral composition in concrete along the vertical Section E-E at time 10,000 years, case Large11. Units (mol/kg pore water).*

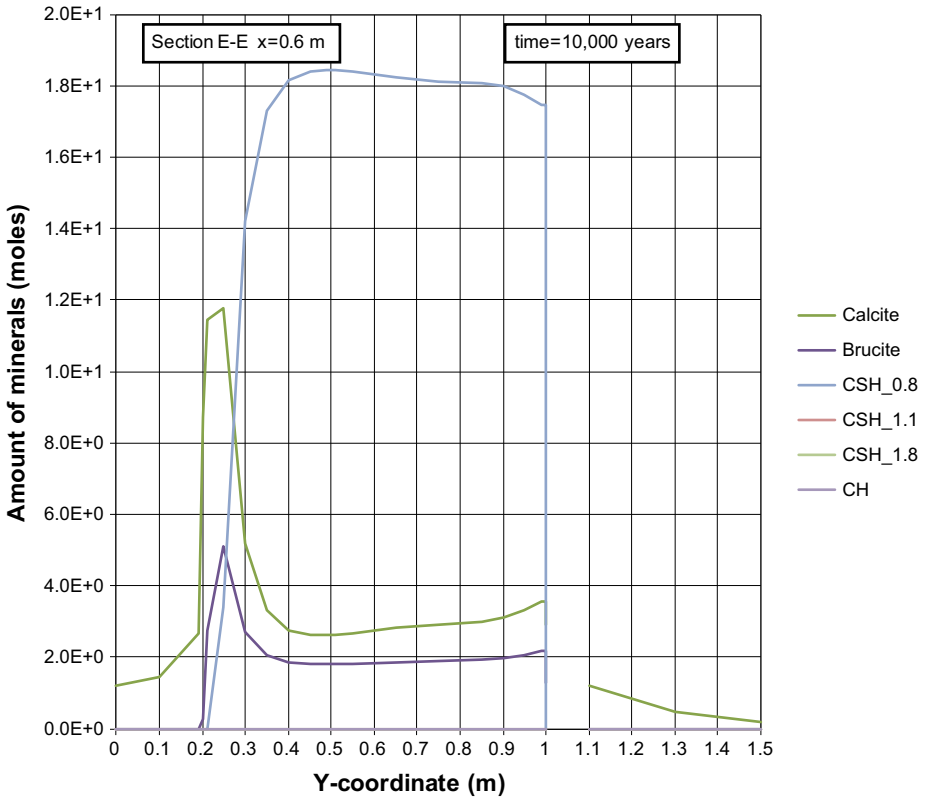

Figure E-56. *The mineral composition in concrete along the vertical Section E-E at time 10,000 years, case Large11. Units (mol/kg pore water).*

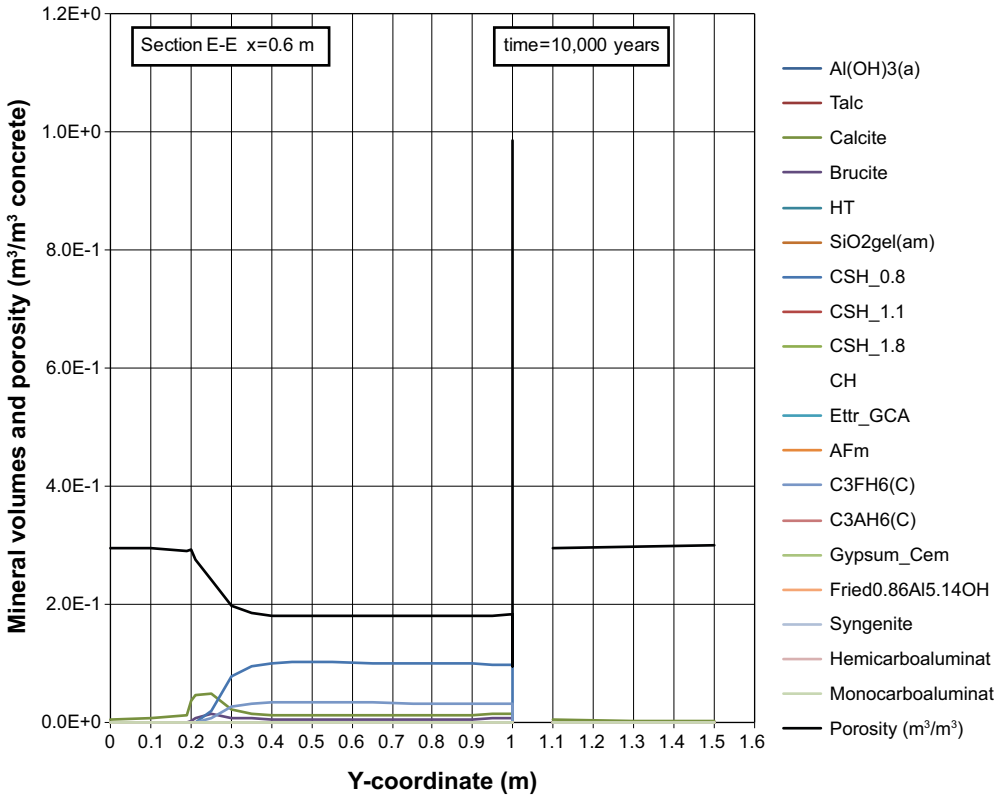

Figure E-57. *Mineral composition in concrete and calculated porosity along the vertical Section E-E at time 10,000 years, case Large11.*

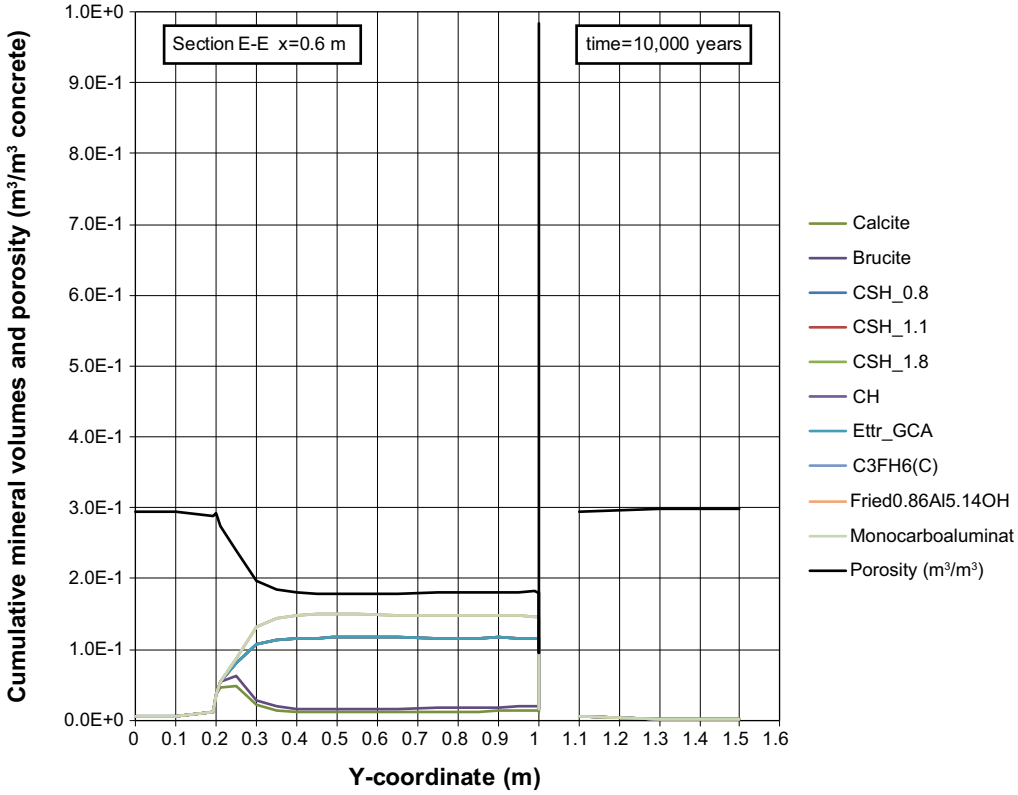

Figure E-58. *Cumulative representation of the mineral composition in concrete and calculated porosity along the vertical Section E-E at time 10,000 years, case Large11.*

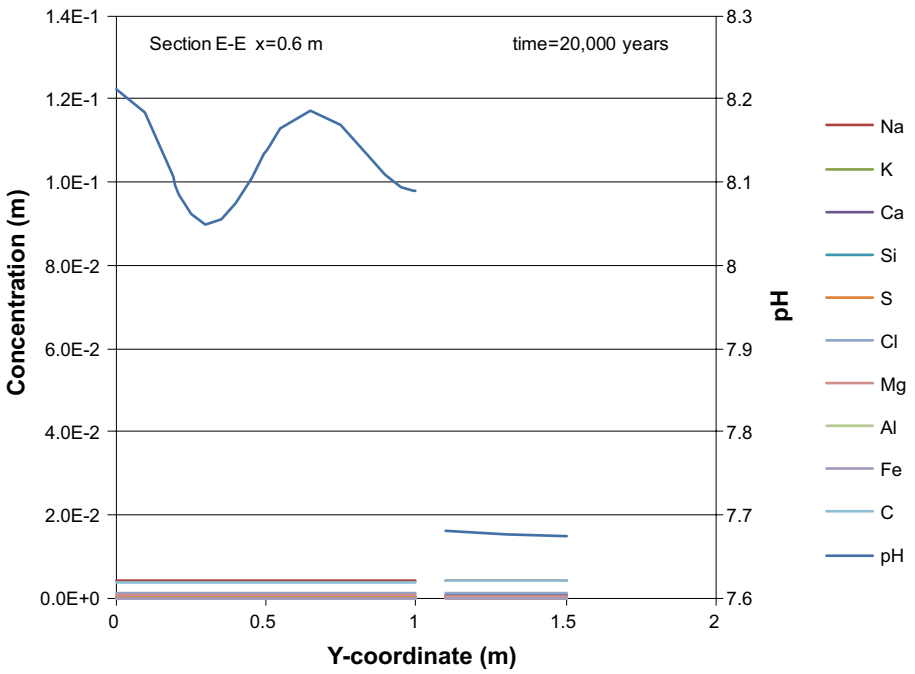

Figure E-59. *Concentration profiles of dissolved components in concrete pore water along the vertical Section E-E at time 20,000 years, case Large11. Units (mol/kg pore water).*

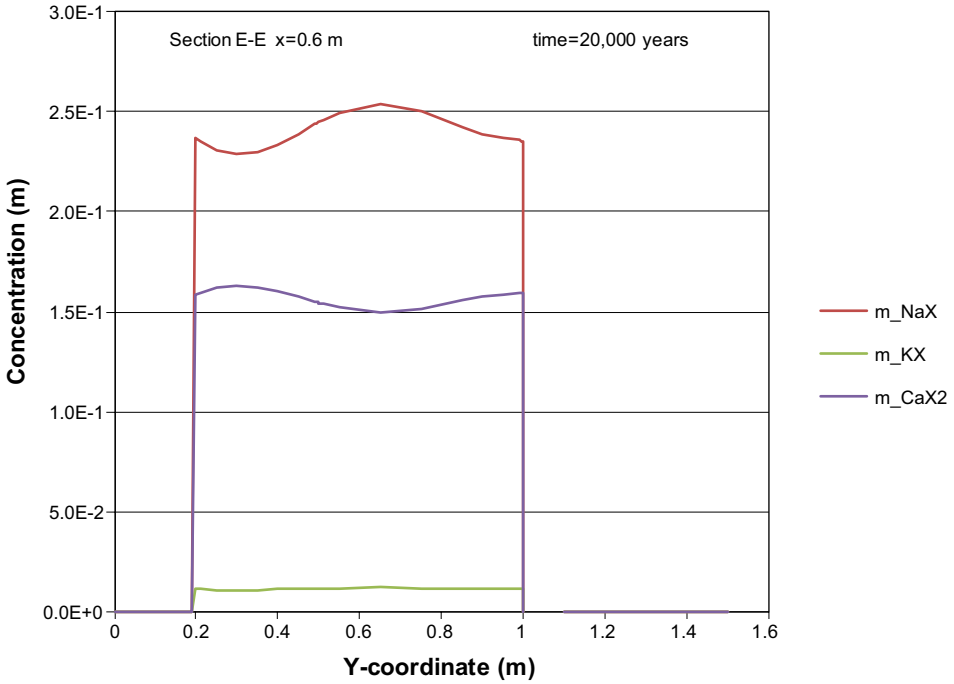

Figure E-60. *The assembly of ion exchange species in concrete along the vertical Section E-E at time 20,000 years, case Large11. Units (mol/kg pore water).*

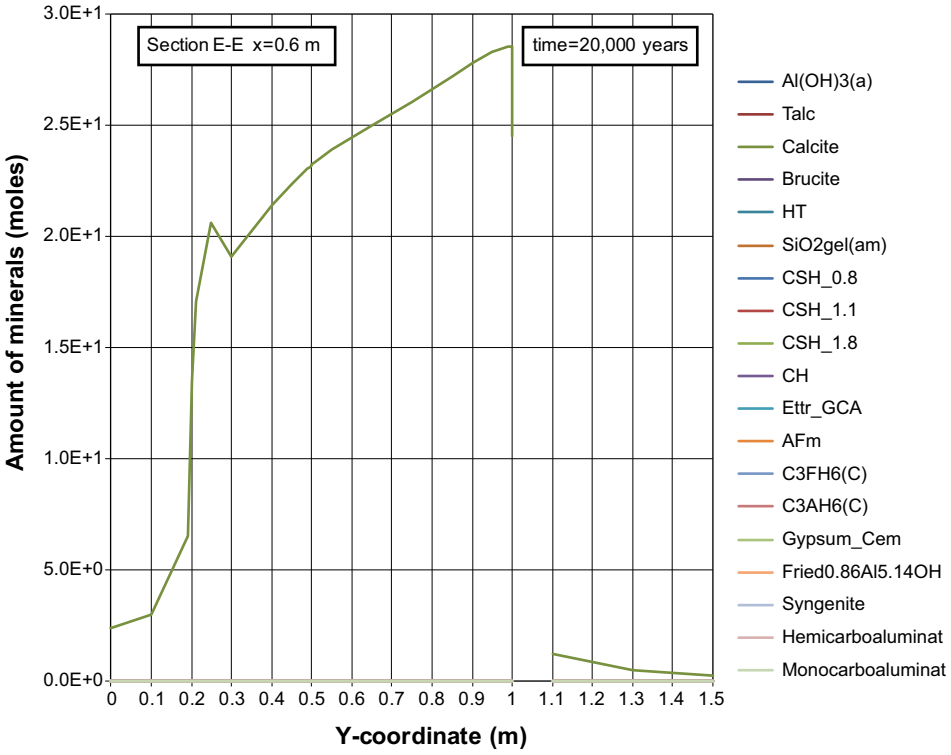

Figure E-61. *The mineral composition in concrete along the vertical Section E-E at time 20,000 years, case Large11. Units (mol/kg pore water).*

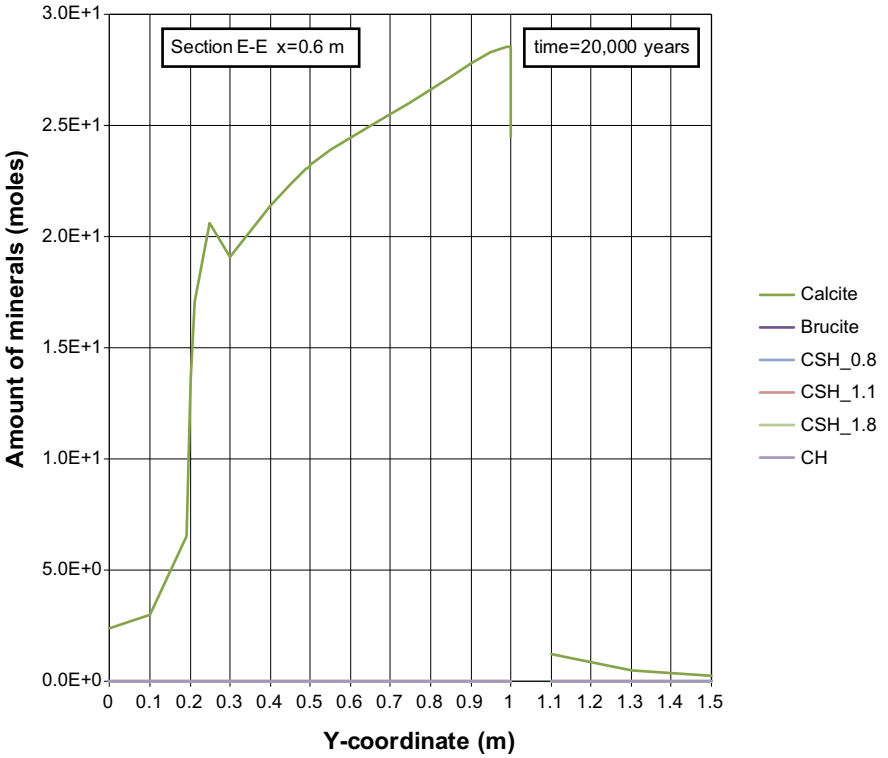

Figure E-62. *The mineral composition in concrete along the vertical Section E-E at time 20,000 years, case Large11. Units (mol/kg pore water).*

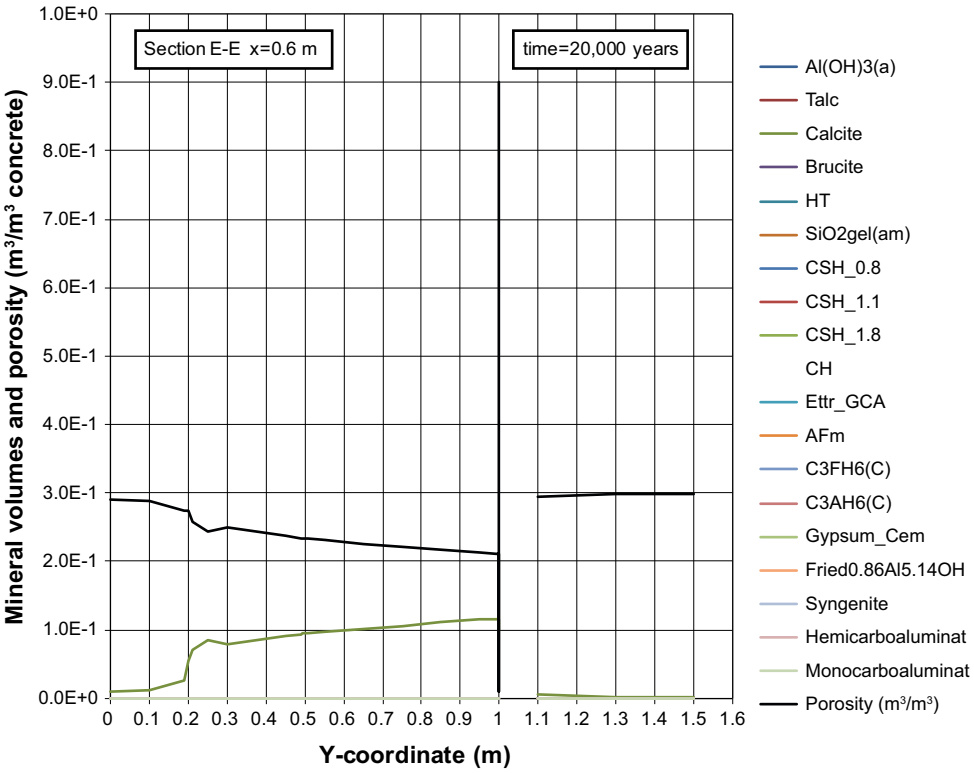

Figure E-63. *Mineral composition in concrete and calculated porosity along the vertical Section E-E at time 20,000 years, case Large11.*

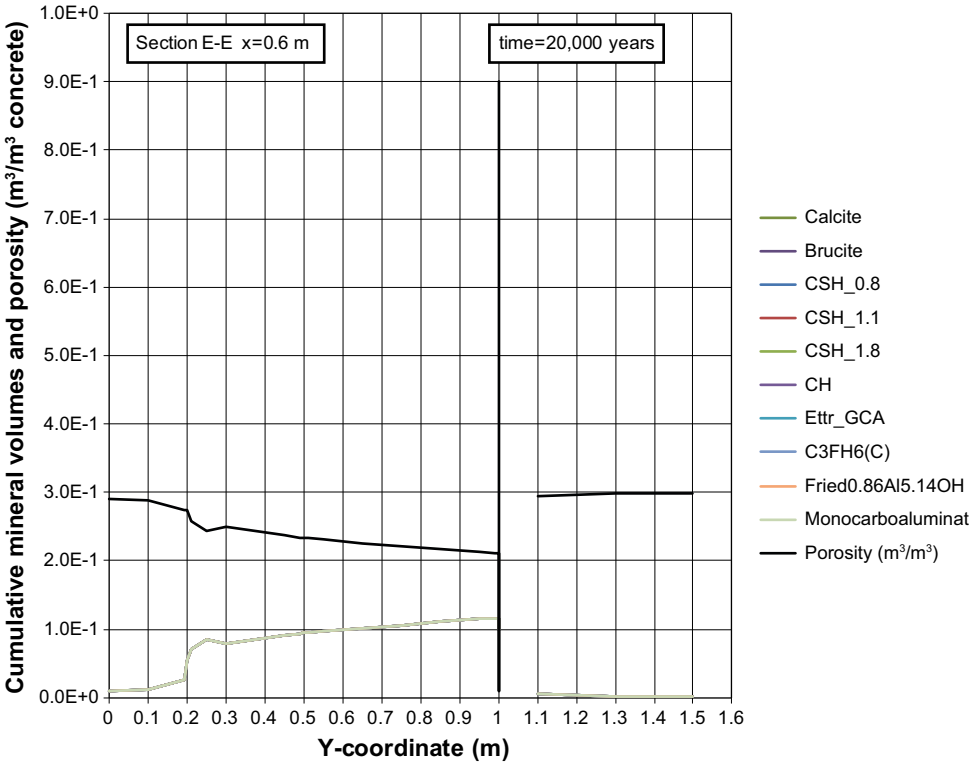

Figure E-64. *Cumulative representation of the mineral composition in concrete and calculated porosity along the vertical Section E-E at time 20,000 years, case Large11.*

Repair concrete at position AH

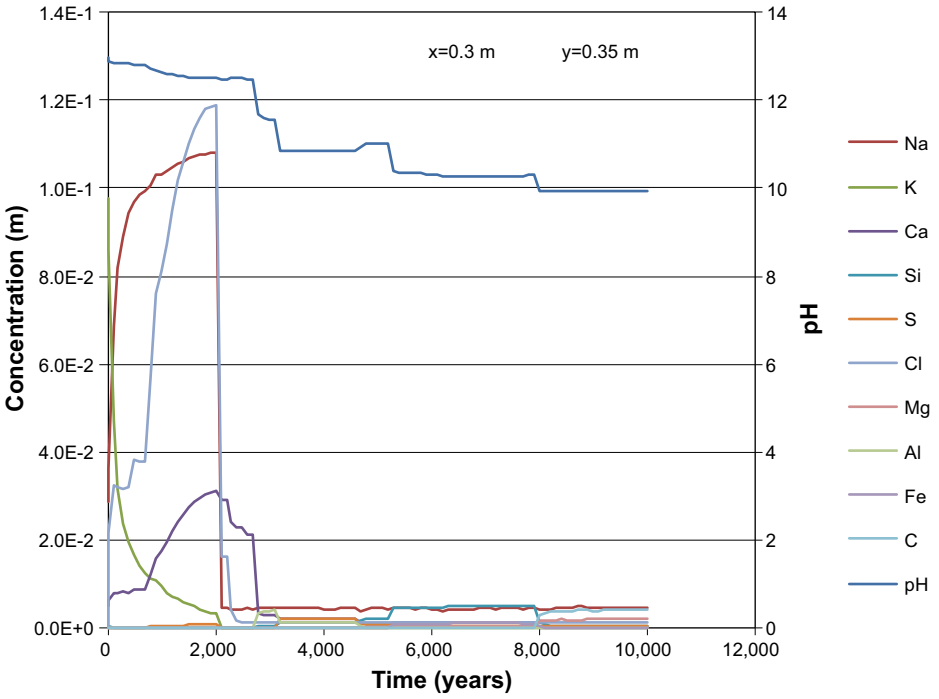

Figure E-65. *The development of the concentration of dissolved components in repair concrete pore water over time (during the first 10,000 years) at position AH, case Large11. Units (mol/kg pore water).*

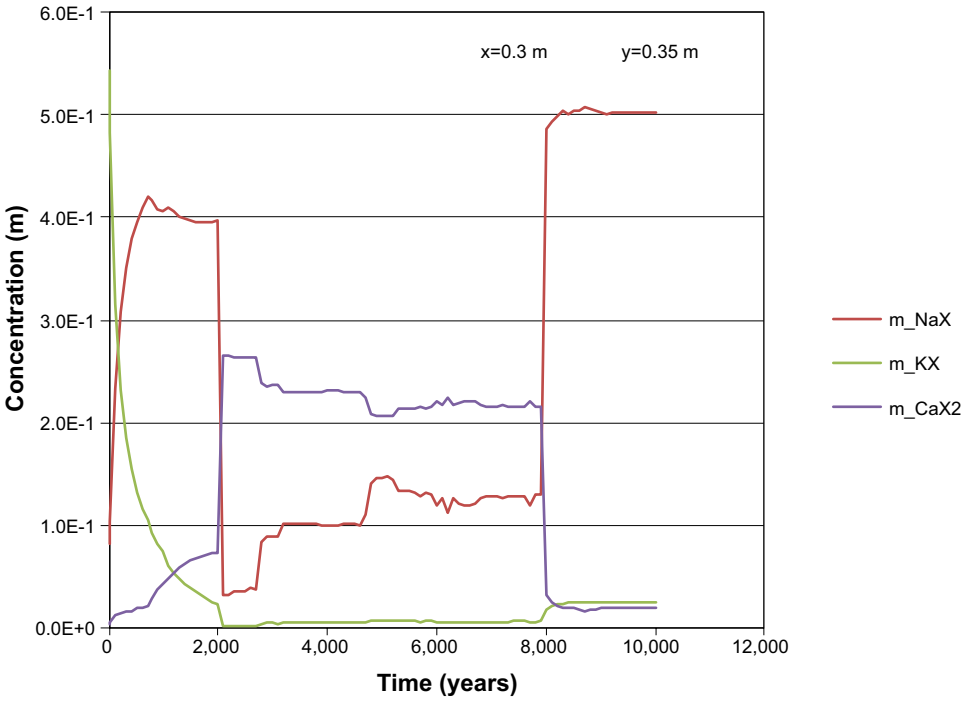

Figure E-66. *The development of the concentration of ion exchange species in repair concrete over time (during the first 10,000 years) at position AH, case Large11. Units (mol/kg pore water).*

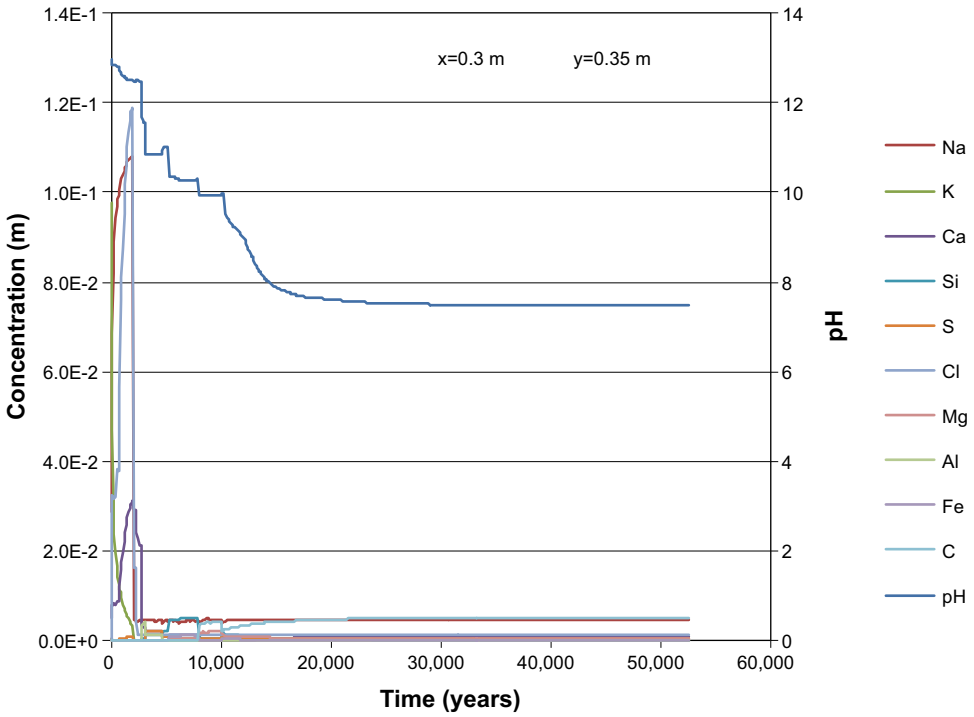

Figure E-67. *The development of the concentration of dissolved components in repair concrete pore water over time (during the first 52,600 years) at position AH, case Large11. Units (mol/kg pore water).*

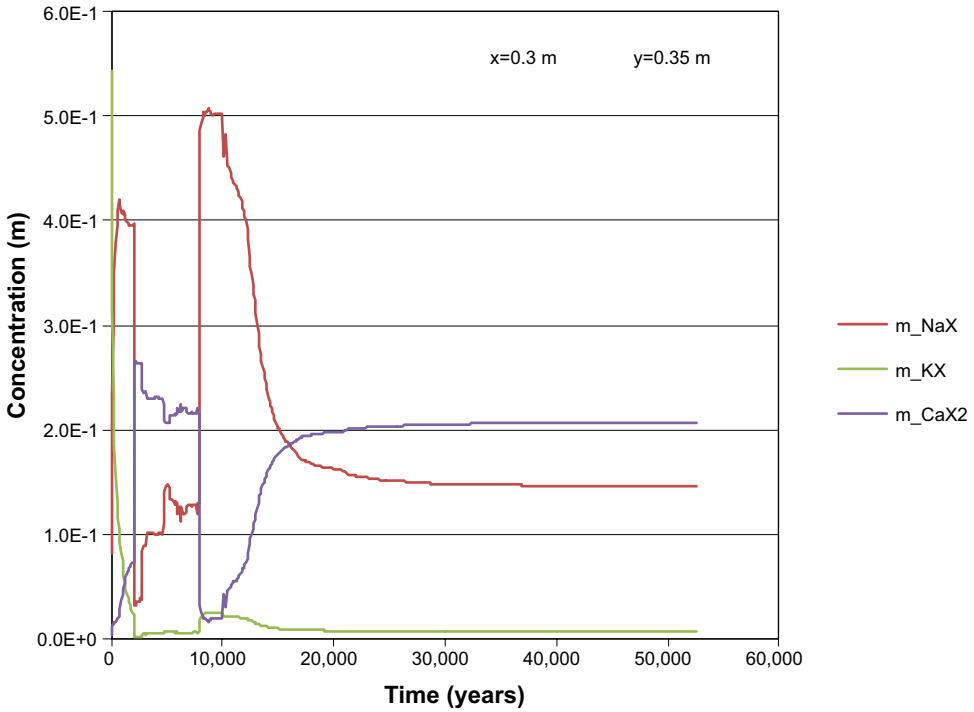

Figure E-68. *The development of the concentration of ion exchange species in repair concrete over time (during the first 52,600 years) at position AH, case Large11. Units (mol/kg pore water).*

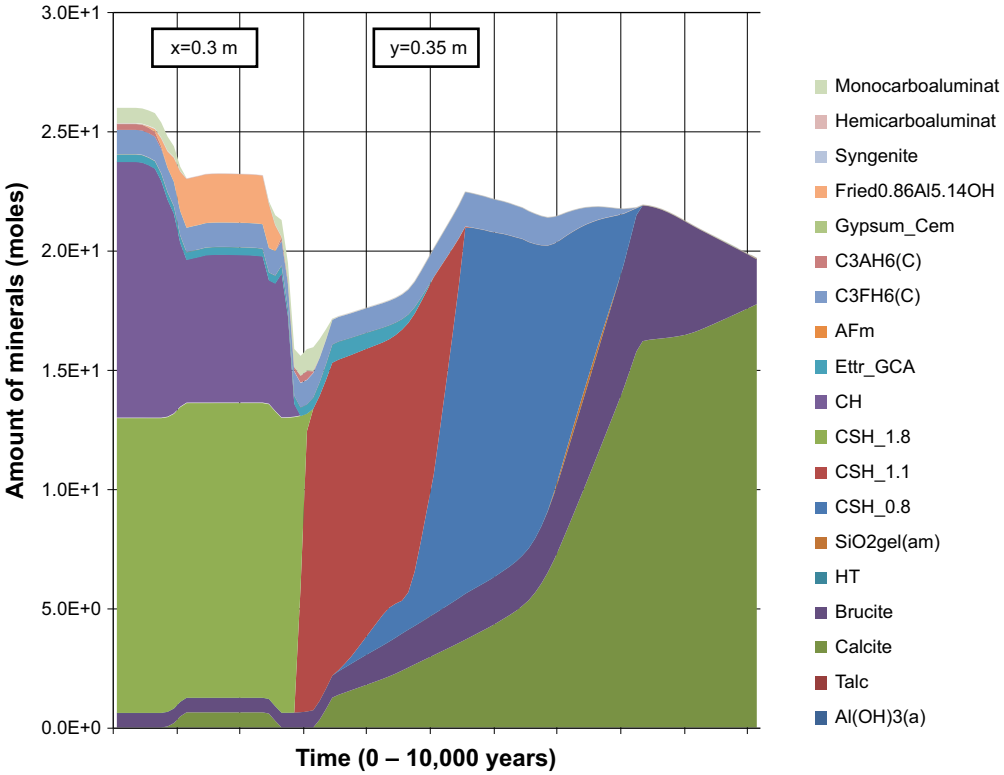

Figure E-69. *The amount of minerals in repair concrete over time at position AH, case Large11. Units (mol/kg pore water).*

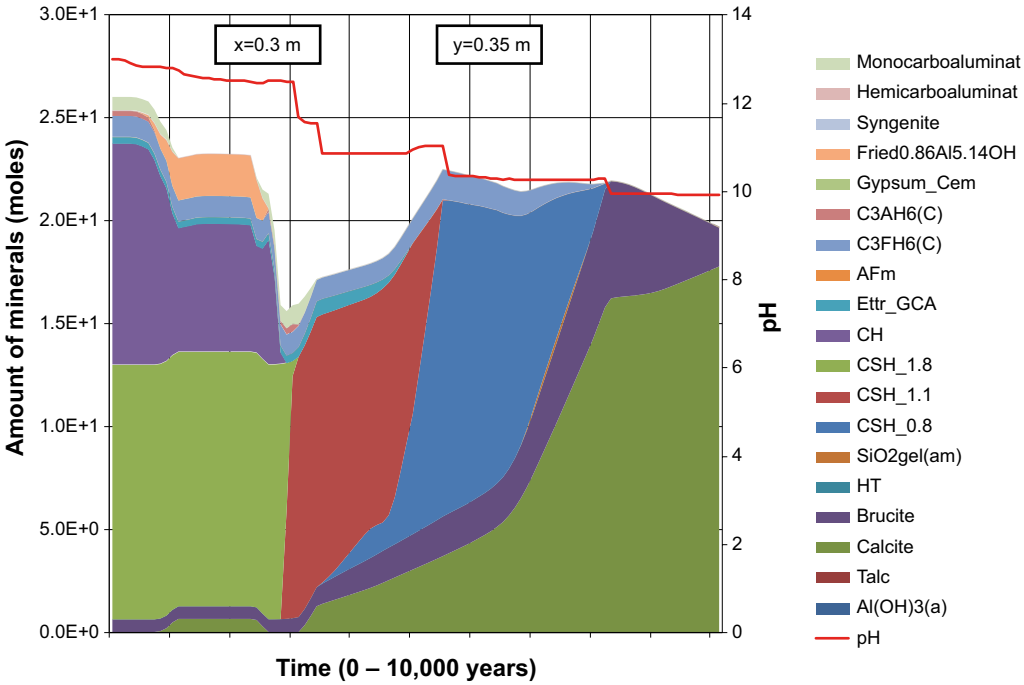

Figure E-70. *The amount of minerals in repair concrete over time at position AH, case Large11. The evolution of pH with time is also indicated. Units (mol/kg pore water).*

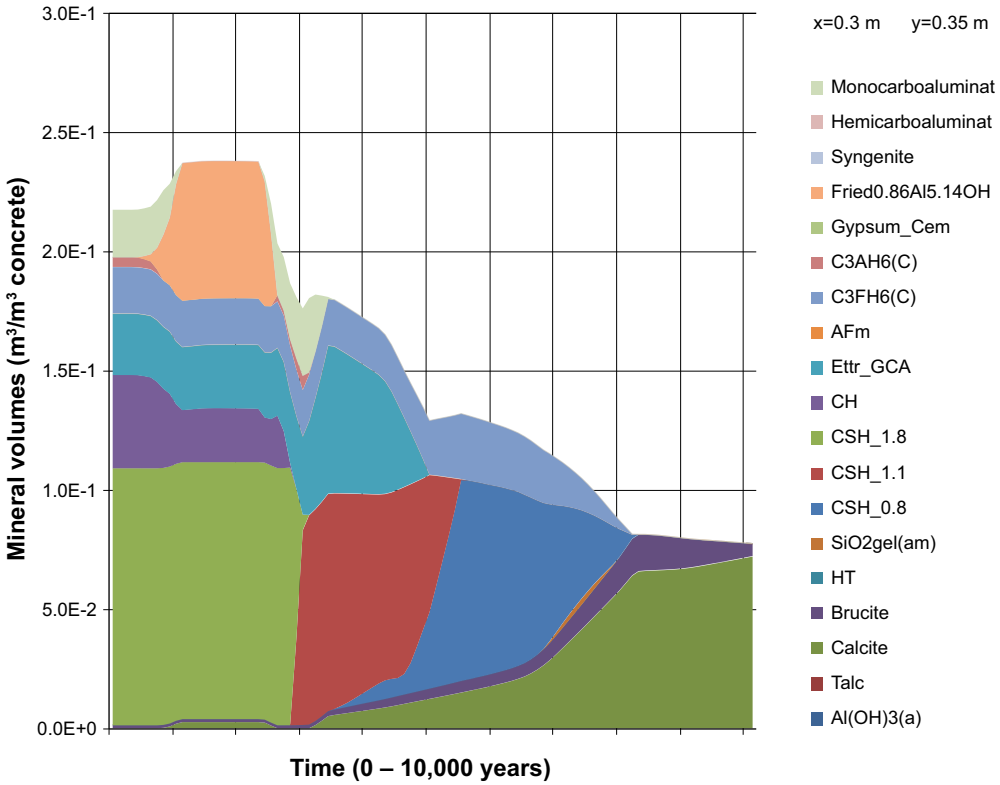

Figure E-71. *The change of mineral volumes in repair concrete over time at position AH, case Large11.*

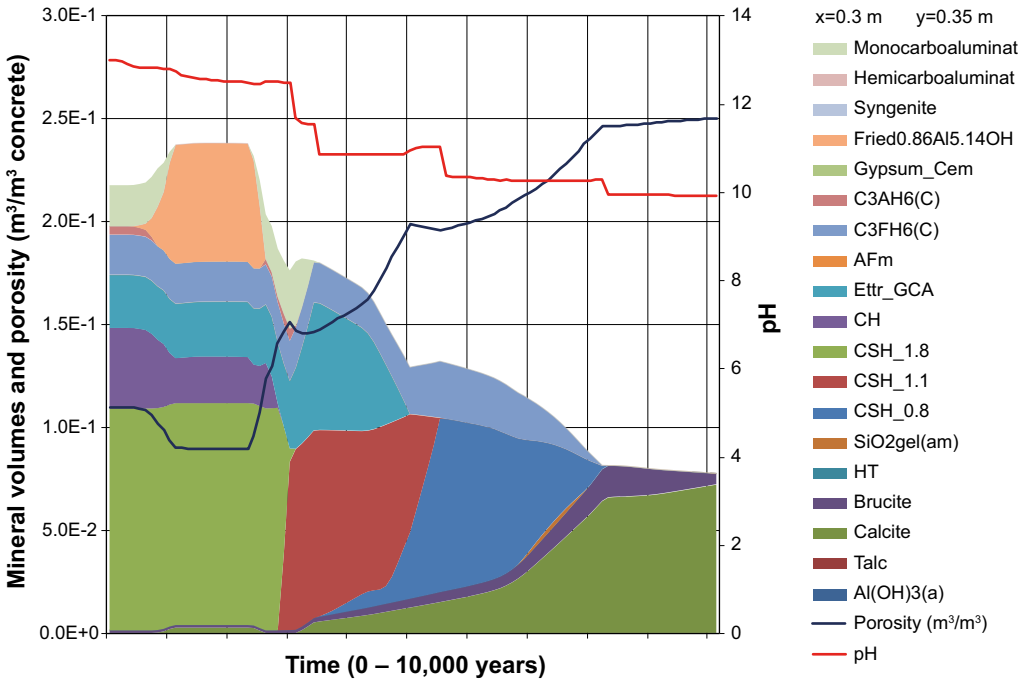

Figure E-72. *The change of mineral volumes and porosity in repair concrete over time at position AH, case Large11. The evolution of pH with time is also indicated.*

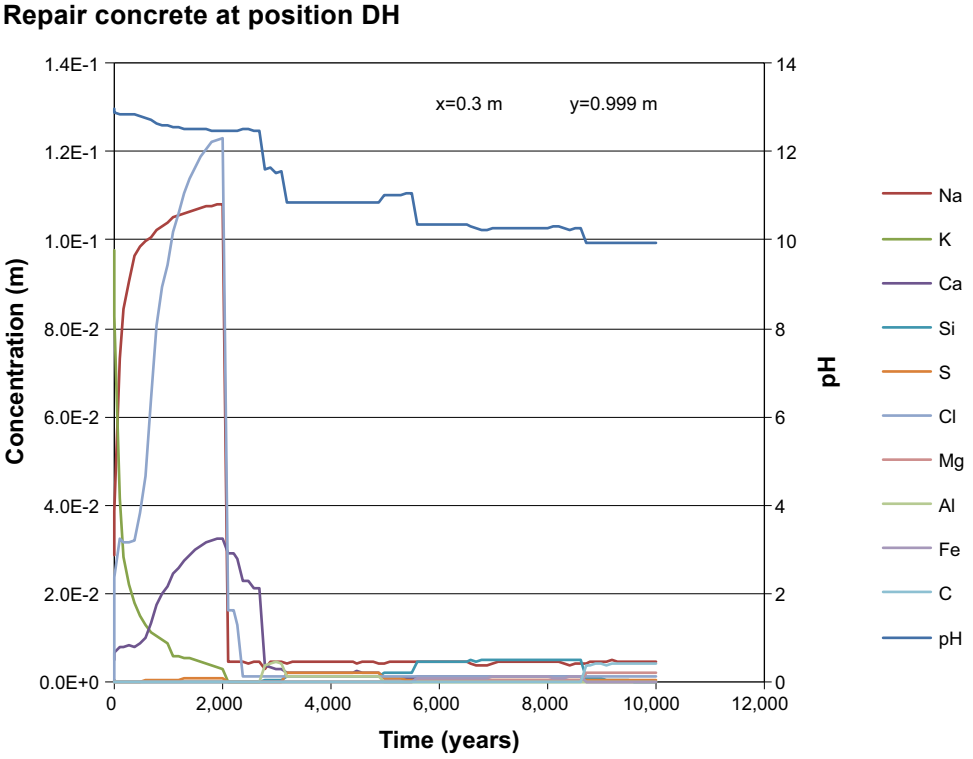

Figure E-73. *The development of the concentration of dissolved components in repair concrete pore water over time (during the first 10,000 years) at position DH, case Large11. Units (mol/kg pore water).*

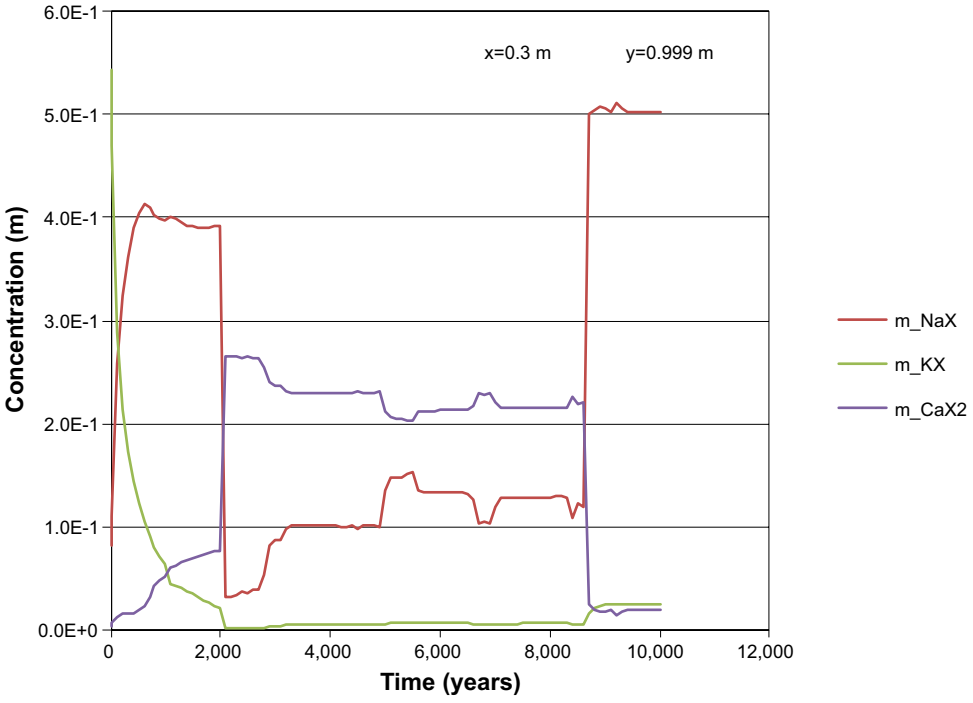

Figure E-74. *The development of the concentration of ion exchange species in repair concrete over time (during the first 10,000 years) at position DH, case Large11. Units (mol/kg pore water).*

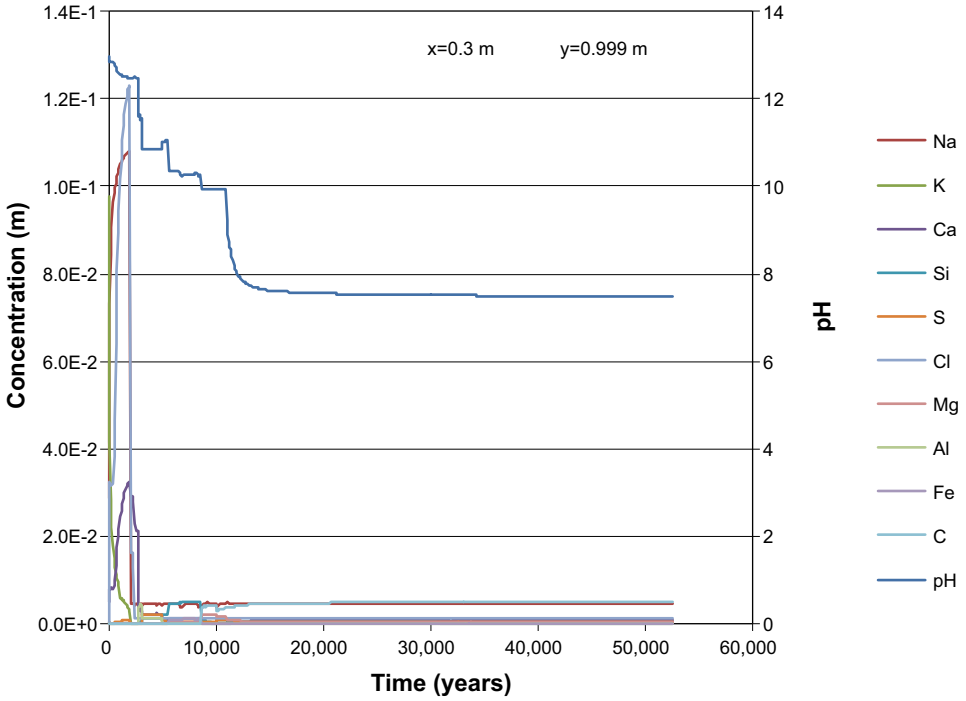

Figure E-75. *The development of the concentration of dissolved components in repair concrete pore water over time (during the first 52,600 years) at position DH, case Large11. Units (mol/kg pore water).*

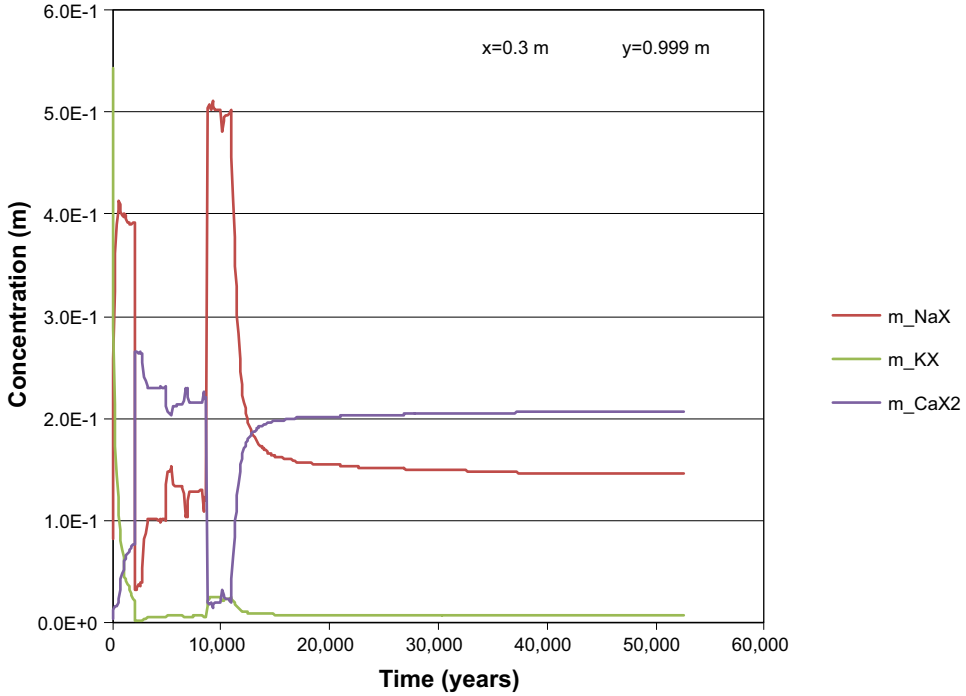

Figure E-76. *The development of the concentration of ion exchange species in repair concrete over time (during the first 52,600 years) at position DH, case Large11. Units (mol/kg pore water).*

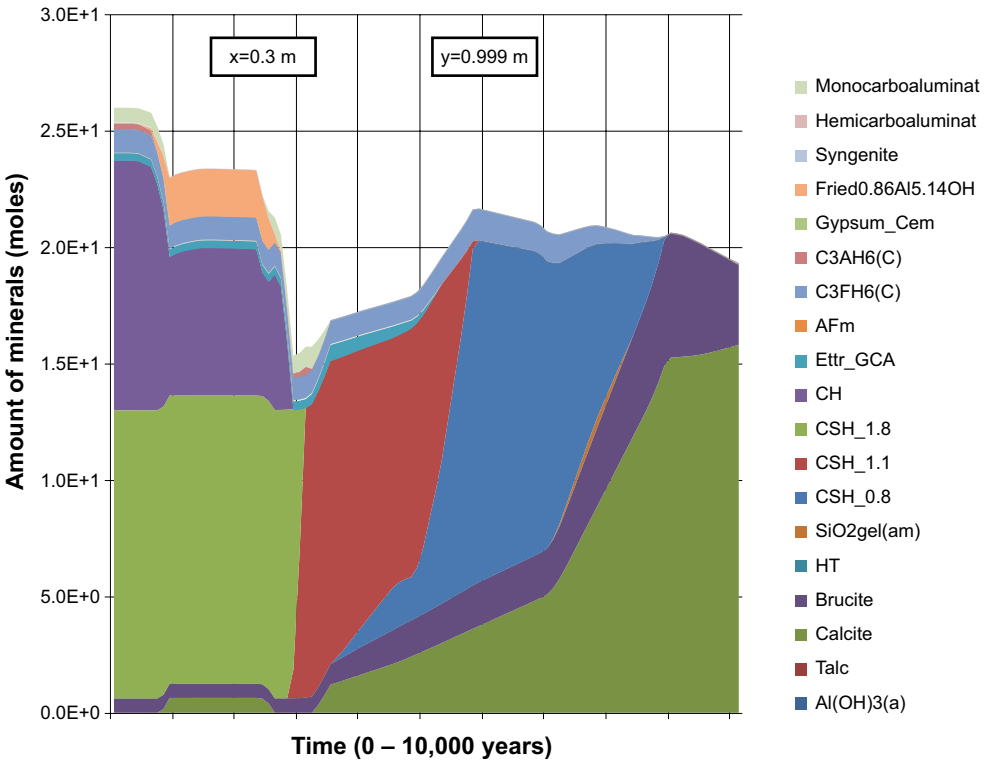

Figure E-77. *The amount of minerals in repair concrete over time at position DH, case Large11. Units (mol/kg pore water).*

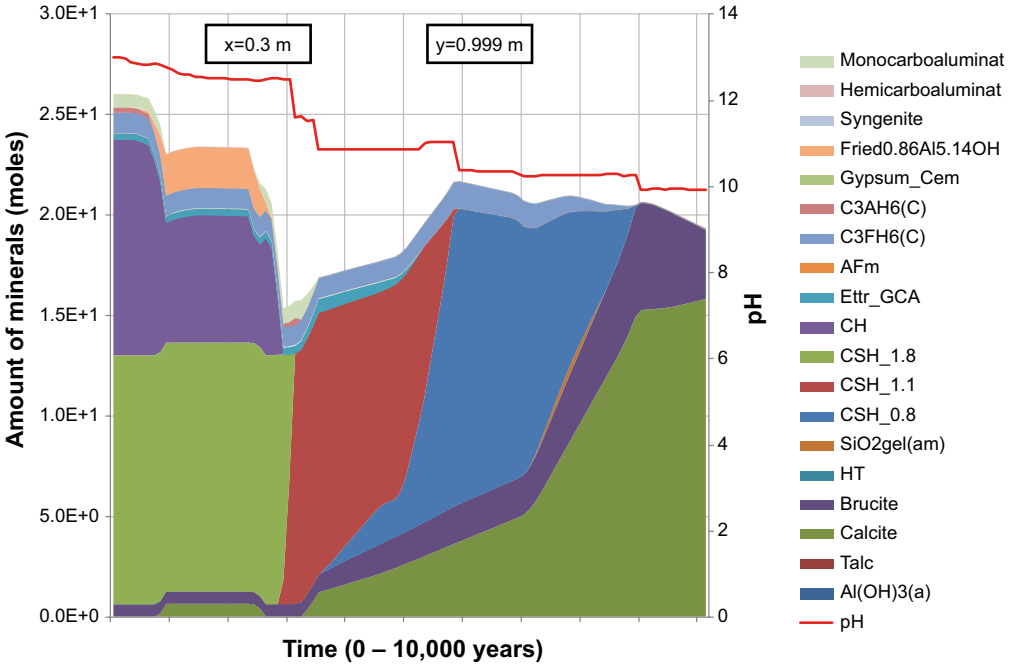

Figure E-78. *The amount of minerals in repair concrete over time at position DH, case Large11. The evolution of pH with time is also indicated. Units (mol/kg pore water).*

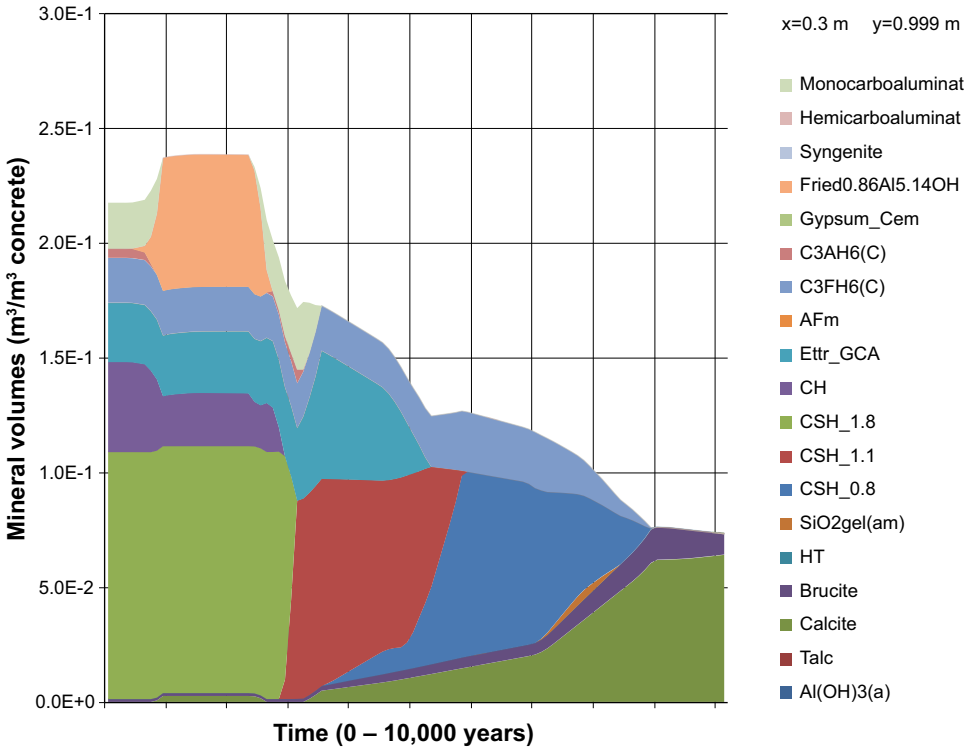

Figure E-79. *The change of mineral volumes in repair concrete over time at position DH, case Large11.*

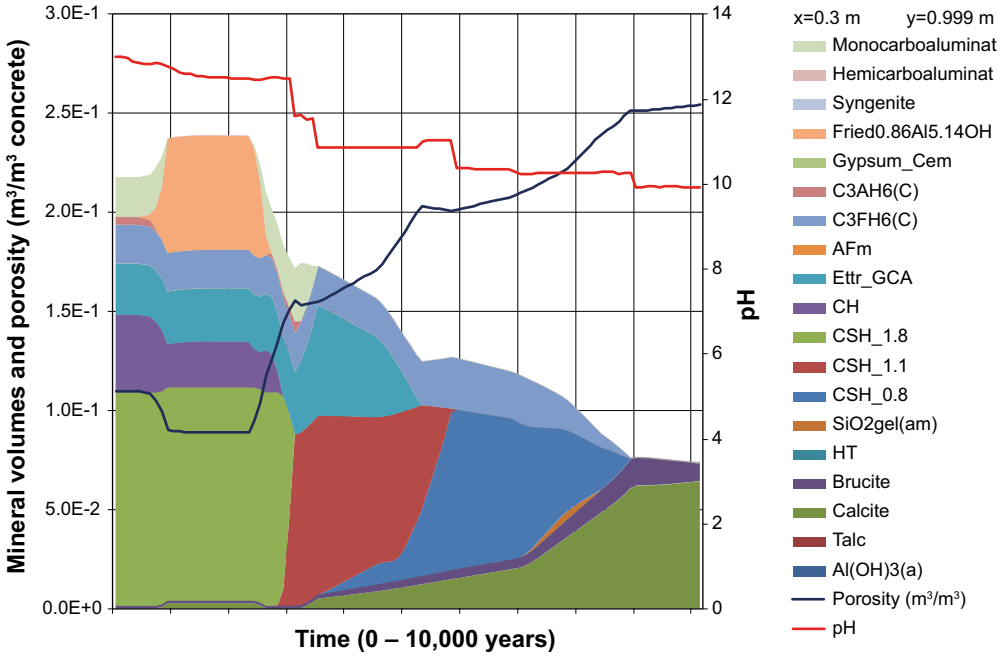

Figure E-80. *The change of mineral volumes and porosity in repair concrete over time at position DH, case Large11. The evolution of pH with time is also indicated.*

Appendix F

Results for Case Large12

Evolution over time at inspection point AE

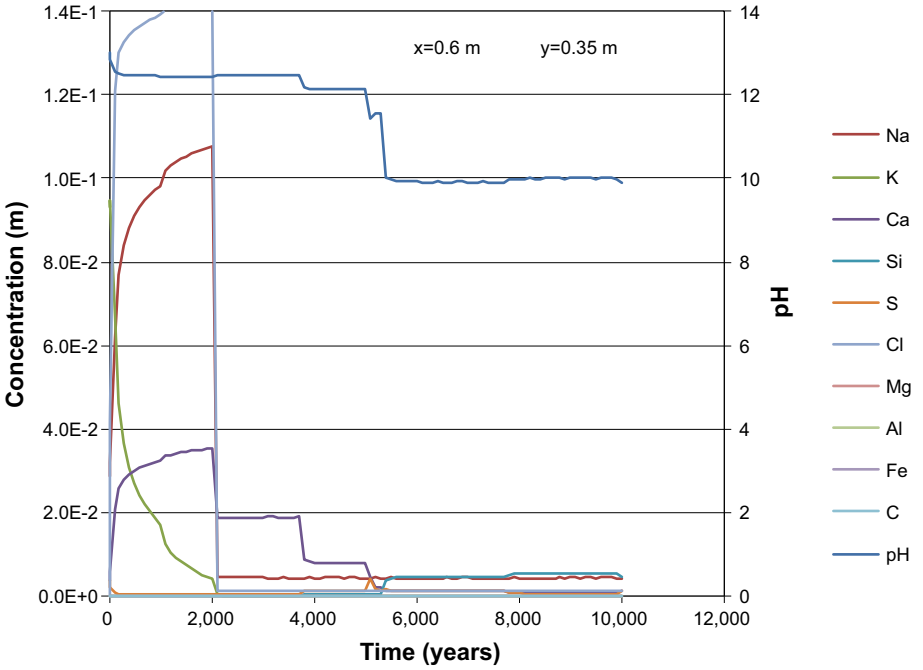

Figure F-1. *The development of the concentration of dissolved components in concrete pore water over time (during the first 10,000 years) at position AE, case Large12. Units (mol/kg pore water).*

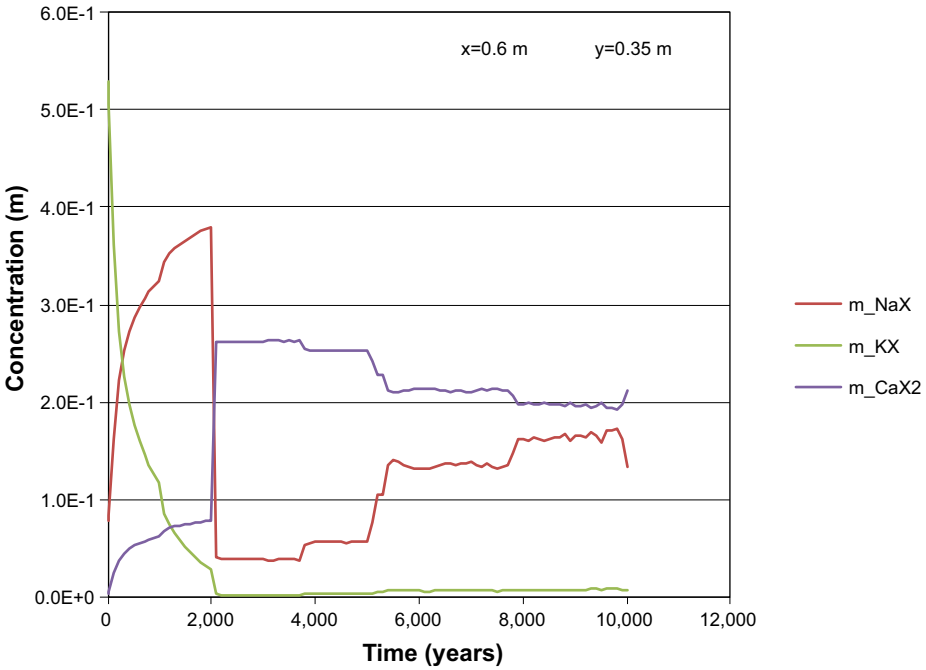

Figure F-2. *The development of the concentration of ion exchange species in concrete over time (during the first 10,000 years) at position AE, case Large12. Units (mol/kg pore water).*

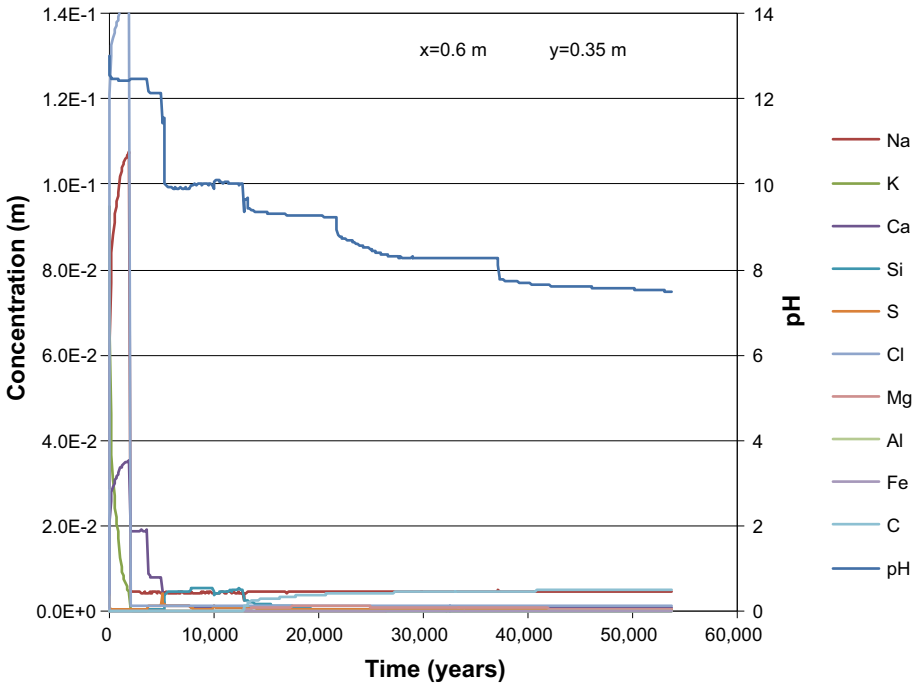

Figure F-3. *The development of the concentration of dissolved components in concrete pore water over time (during the first 53,800 years) at position AE, case Large12. Units (mol/kg pore water).*

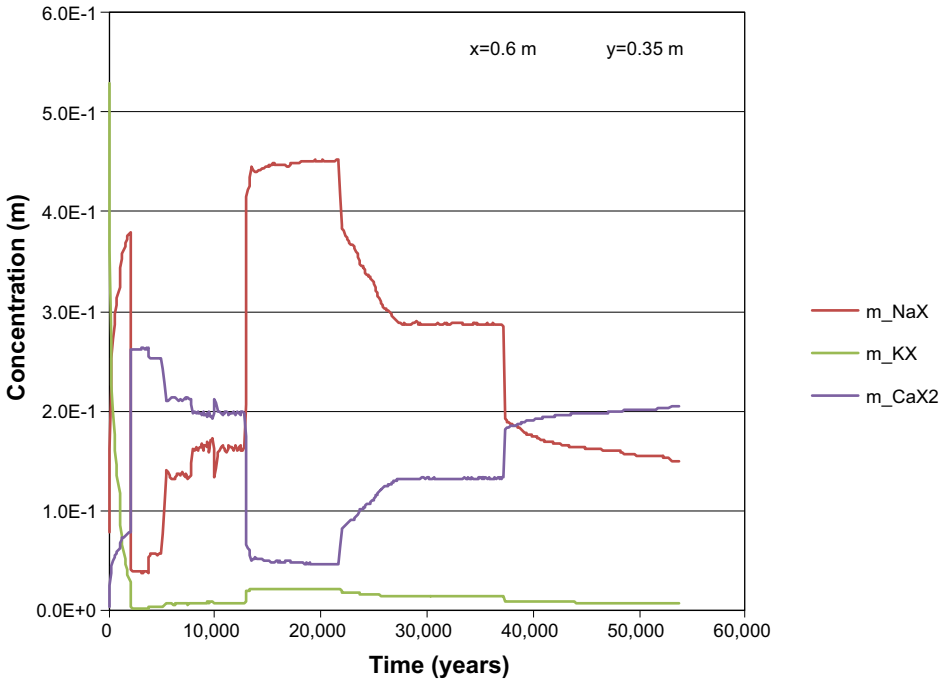

Figure F-4. *The development of the concentration of ion exchange species in concrete over time (during the first 53,800 years) at position AE, case Large12. Units (mol/kg pore water).*

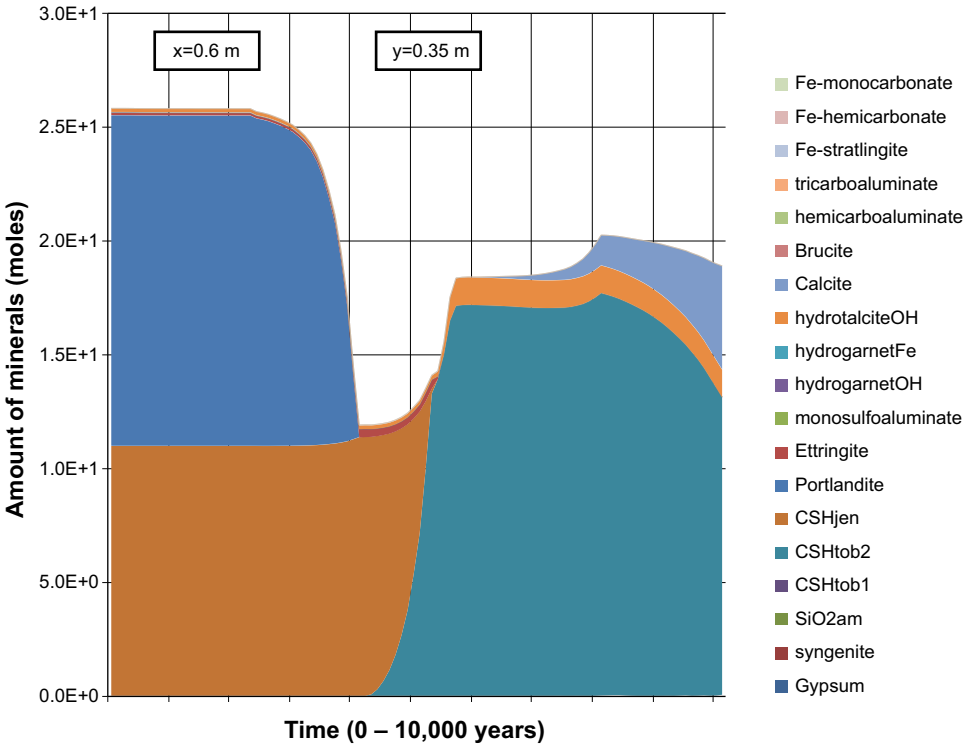

Figure F-5. *The amount of minerals in concrete over time at position AE, case Large12. Units (mol/kg pore water).*

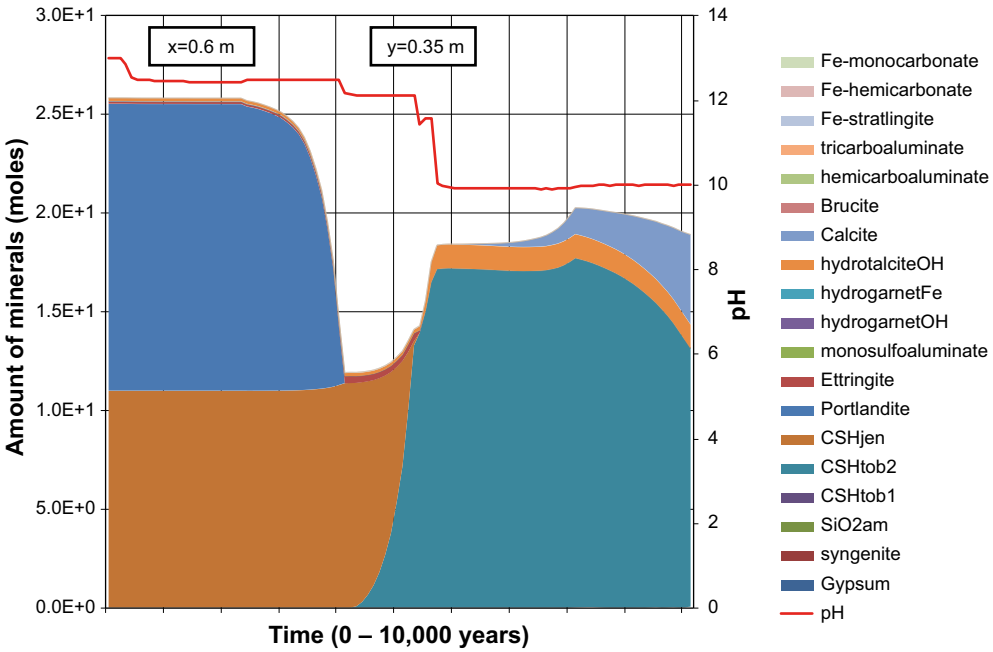

Figure F-6. *The amount of minerals in concrete over time at position AE, case Large12. The evolution of pH with time is also indicated. Units (mol/kg pore water).*

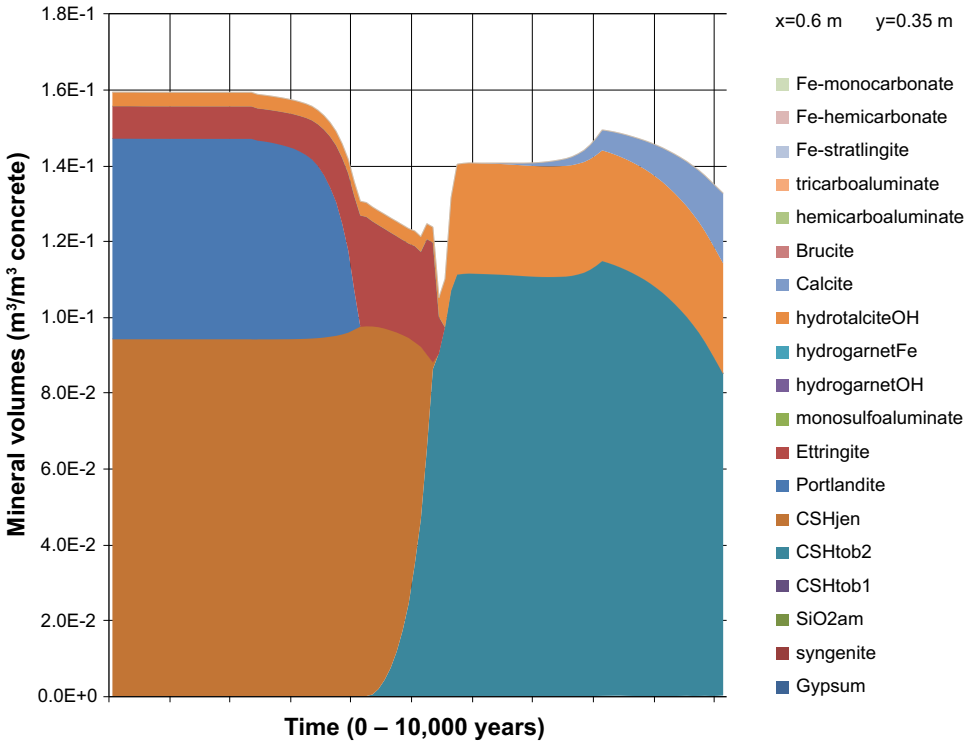

Figure F-7. *The change of mineral volumes in concrete over time at position AE, case Large12.*

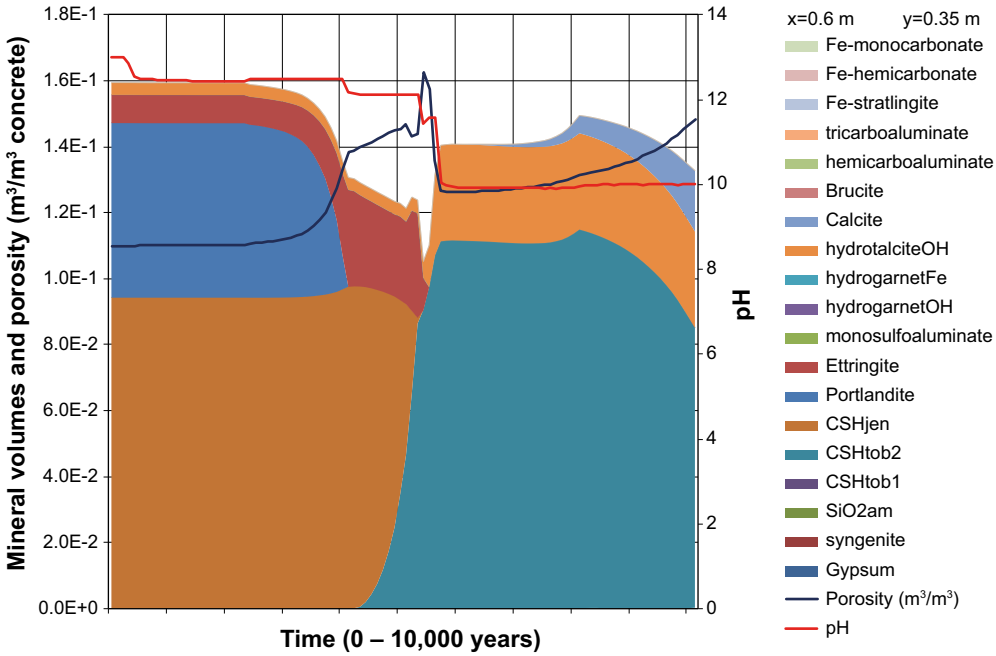

Figure F-8. *The change of mineral volumes and porosity in concrete over time at position AE, case Large12. The evolution of pH with time is also indicated.*

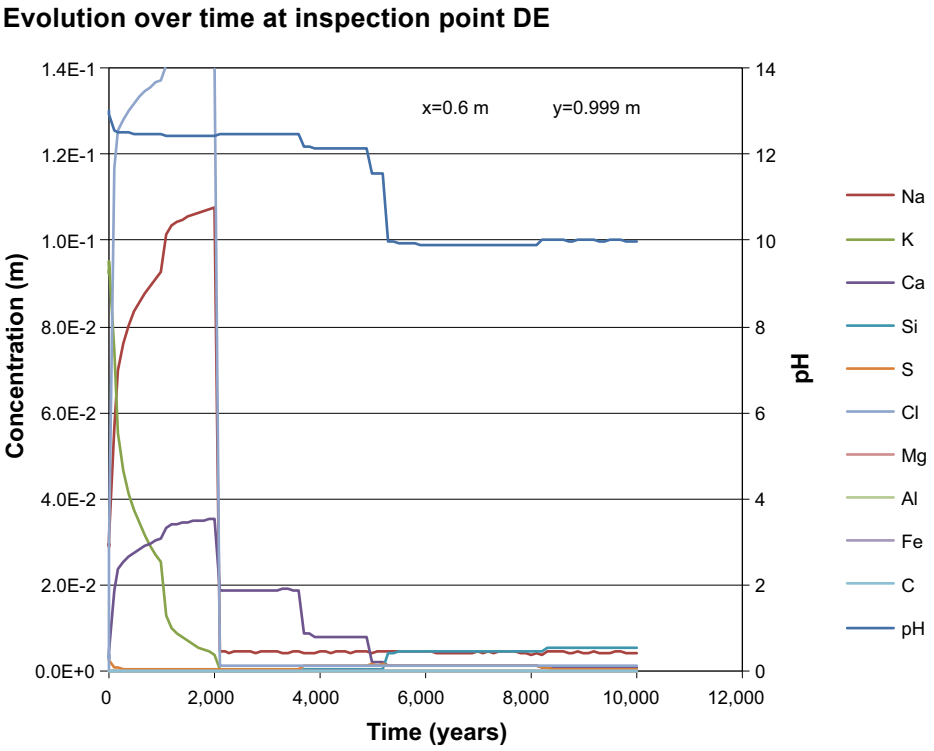

Figure F-9. *The development of the concentration of dissolved components in concrete pore water over time (during the first 10,000 years) at position DE (1 mm from an open fracture), case Large12. Units (mol/kg pore water).*

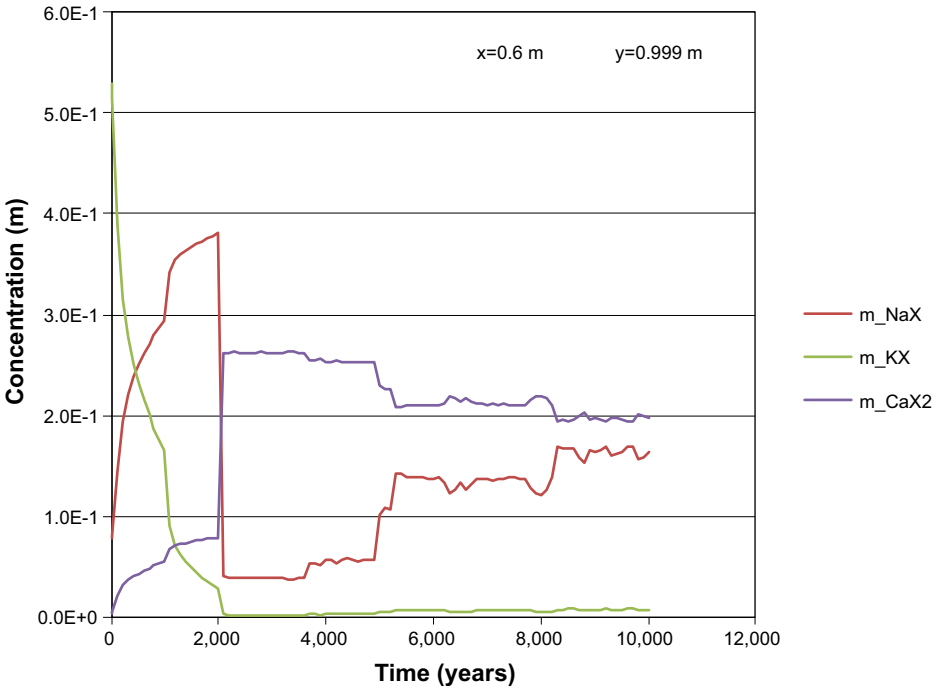

Figure F-10. *The development of the concentration of ion exchange species in concrete over time (during the first 10,000 years) at position DE (1 mm from an open fracture), case Large12. Units (mol/kg pore water).*

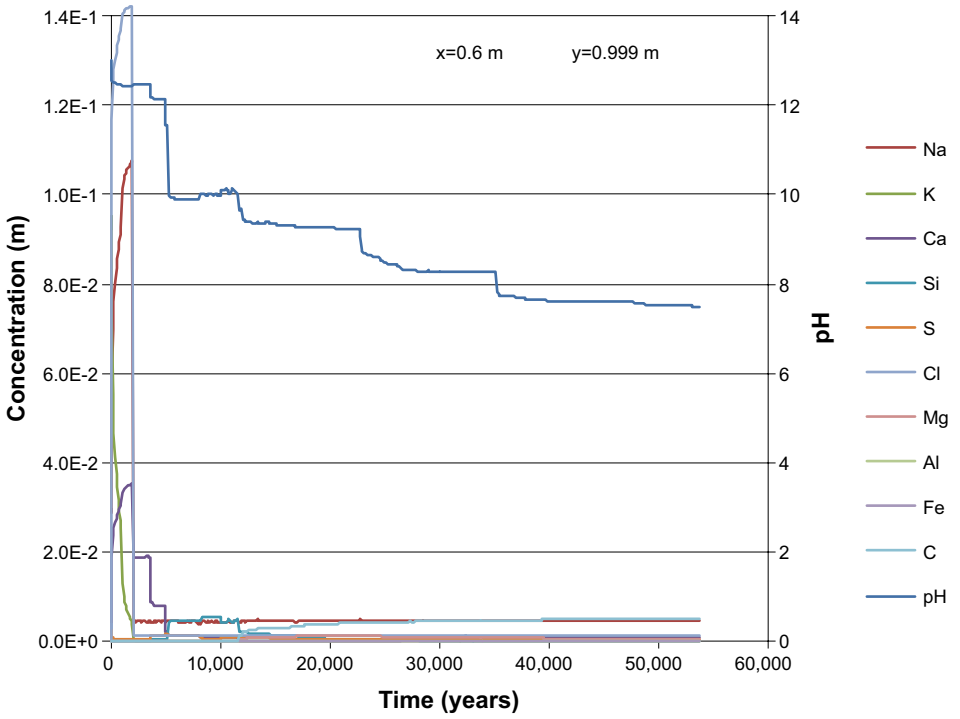

Figure F-11. *The development of the concentration of dissolved components in concrete pore water over time (during the first 53,800 years) at position DE (1 mm from an open fracture), case Large12. Units (mol/kg pore water).*

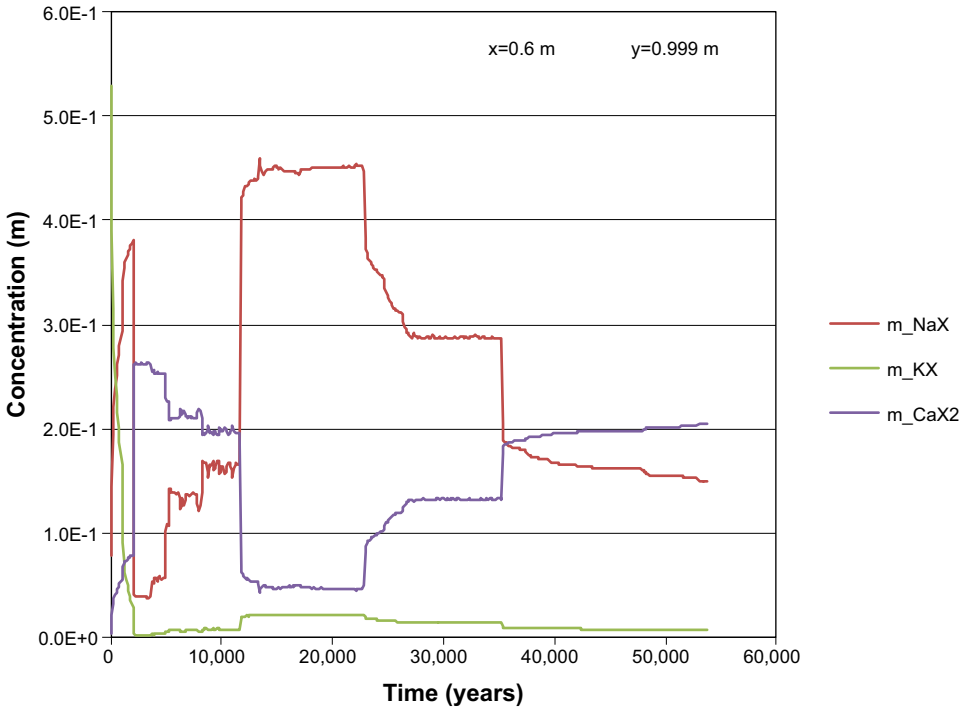

Figure F-12. *The development of the concentration of ion exchange species in concrete over time (during the first 53,800 years) at position DE (1 mm from an open fracture), case Large12. Units (mol/kg pore water).*

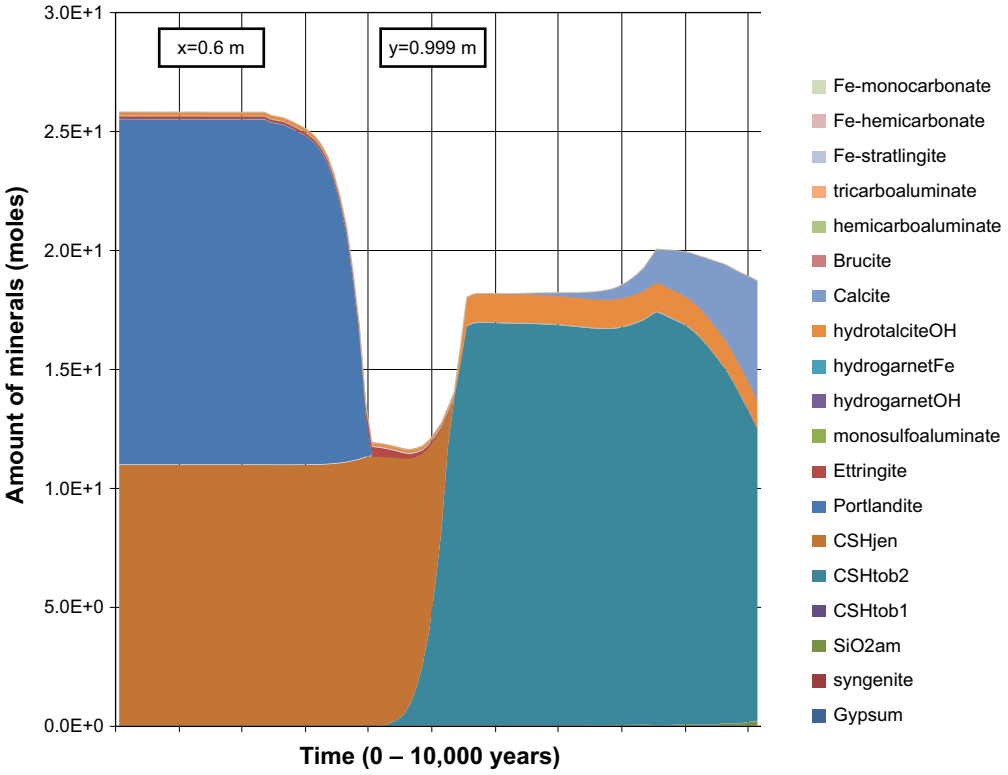

Figure F-13. *The amount of minerals in concrete over time at position DE (1 mm from an open fracture), case Large12. Units (mol/kg pore water).*

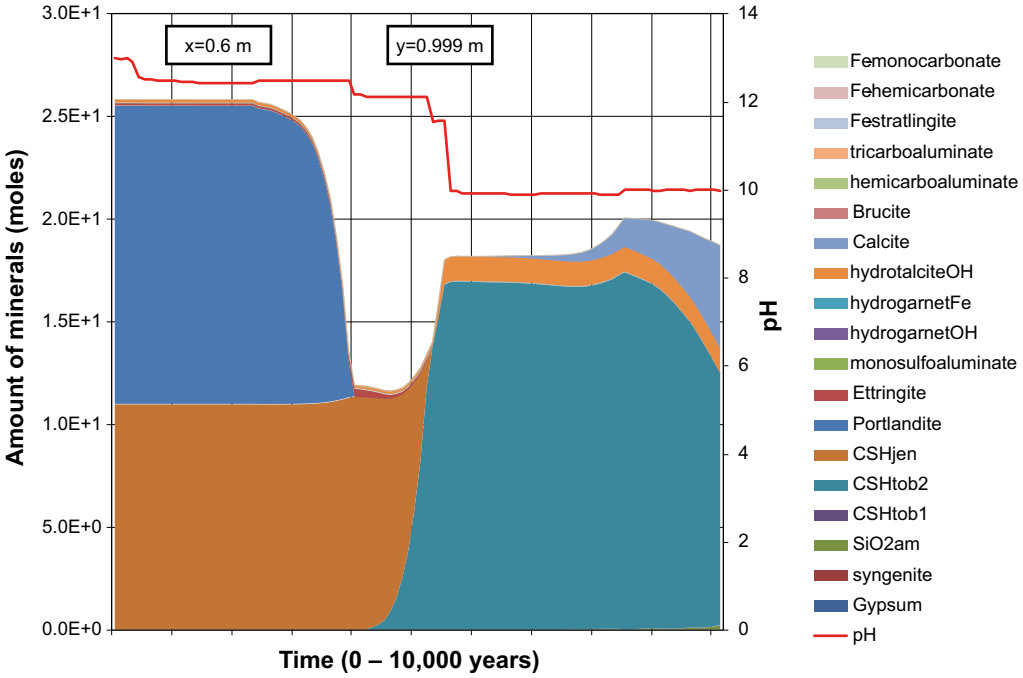

Figure F-14. *The amount of minerals in concrete over time at position DE (1 mm from an open fracture), case Large12. The evolution of pH with time is also indicated. Units (mol/kg pore water).*

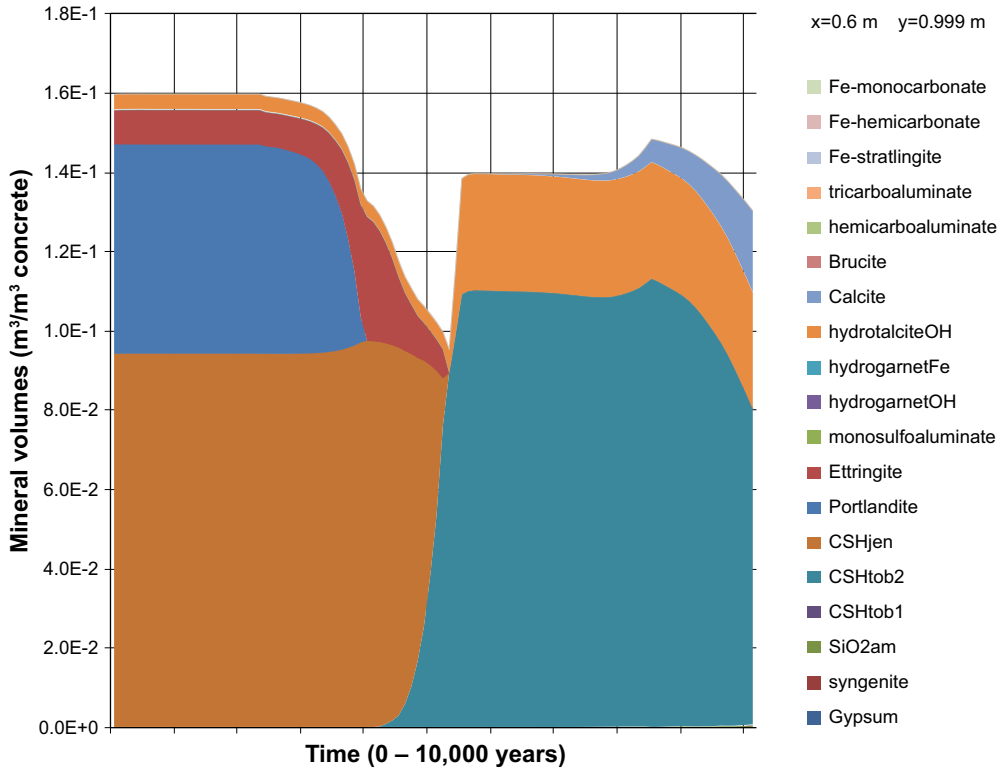

Figure F-15. *The change of mineral volumes in concrete over time at position DE (1 mm from an open fracture), case Large12.*

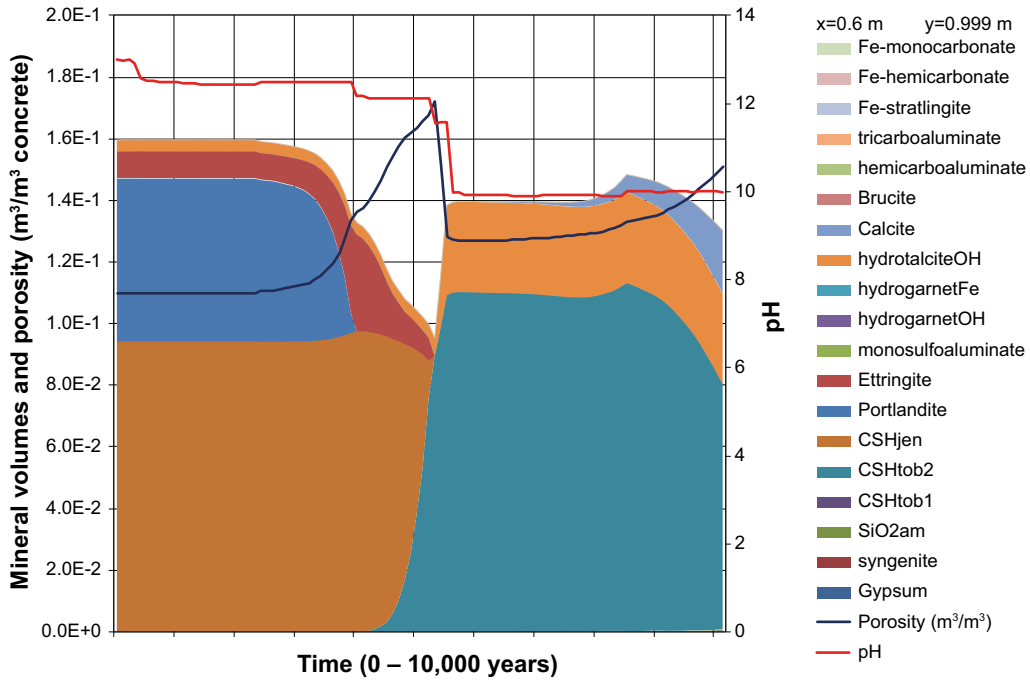

Figure F-16. *The change of mineral volumes and porosity in concrete over time at position DE (1 mm from an open fracture), case Large12. The evolution of pH with time is also indicated.*

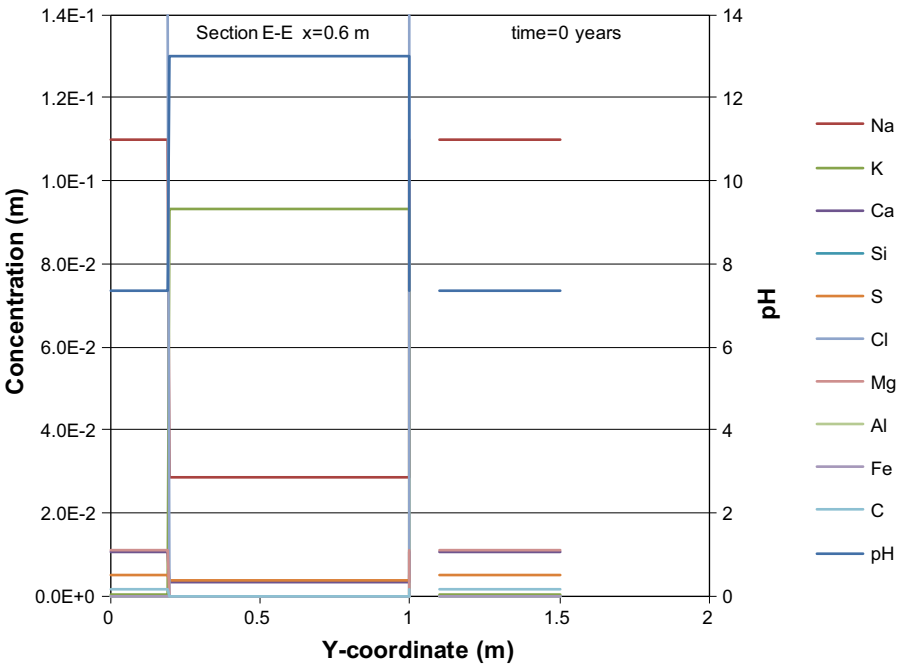

Figure F-17. *Concentration profiles of dissolved components in concrete pore water along the vertical Section E-E at time 0 years, case Large12. Units (mol/kg pore water).*

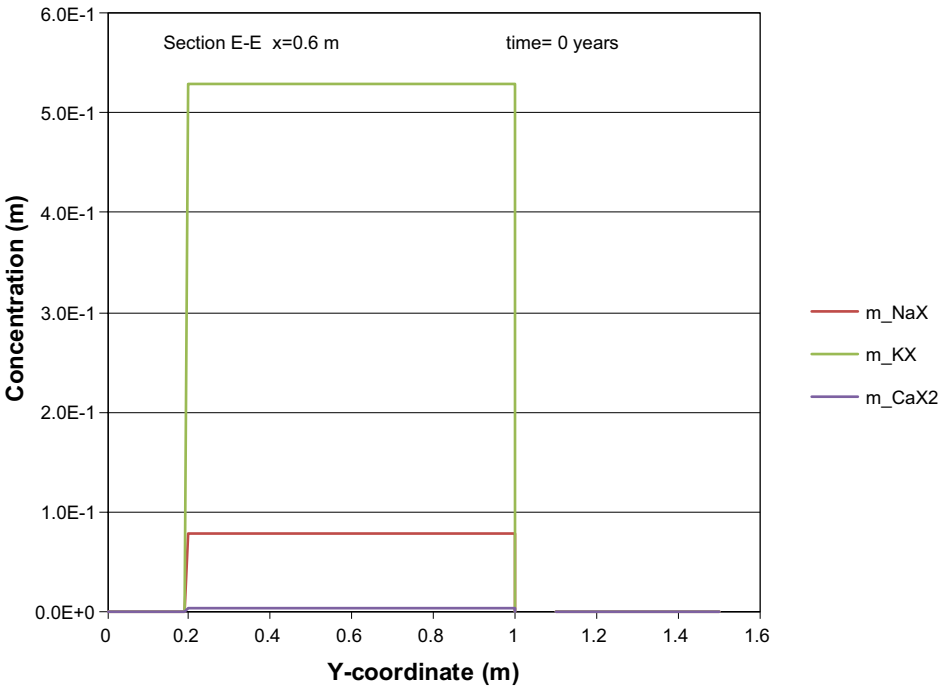

Figure F-18. *The assembly of ion exchange species in concrete along the vertical Section E-E at time 0 years, case Large12. Units (mol/kg pore water).*

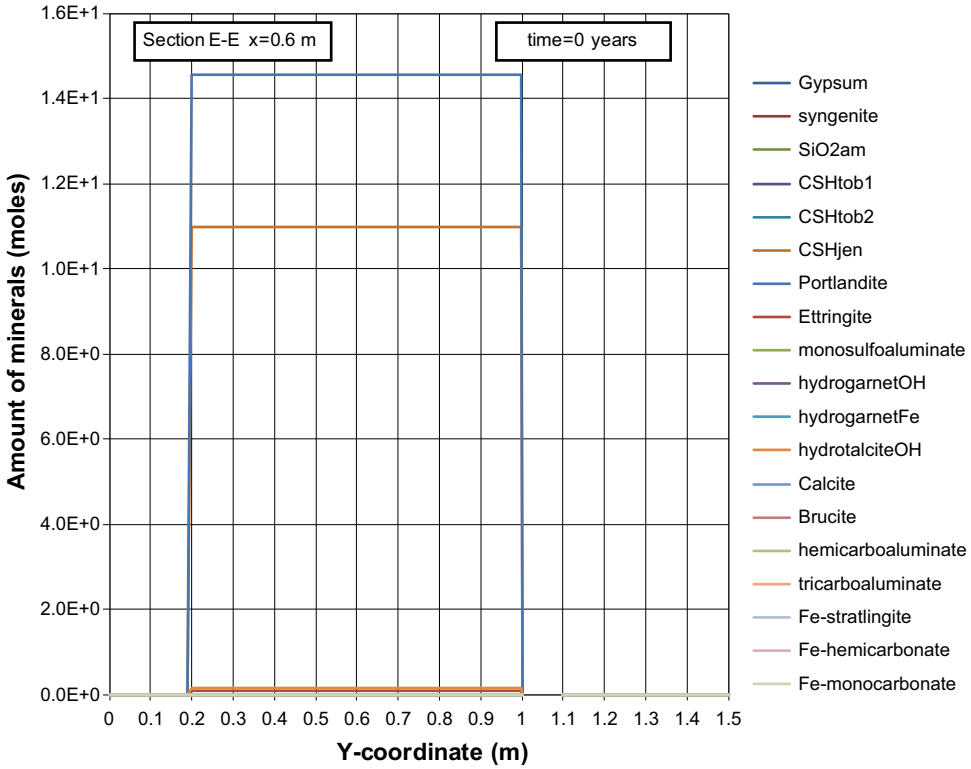

Figure F-19. *The mineral composition in concrete along the vertical Section E-E at time 0 years, case Large12. Units (mol/kg pore water).*

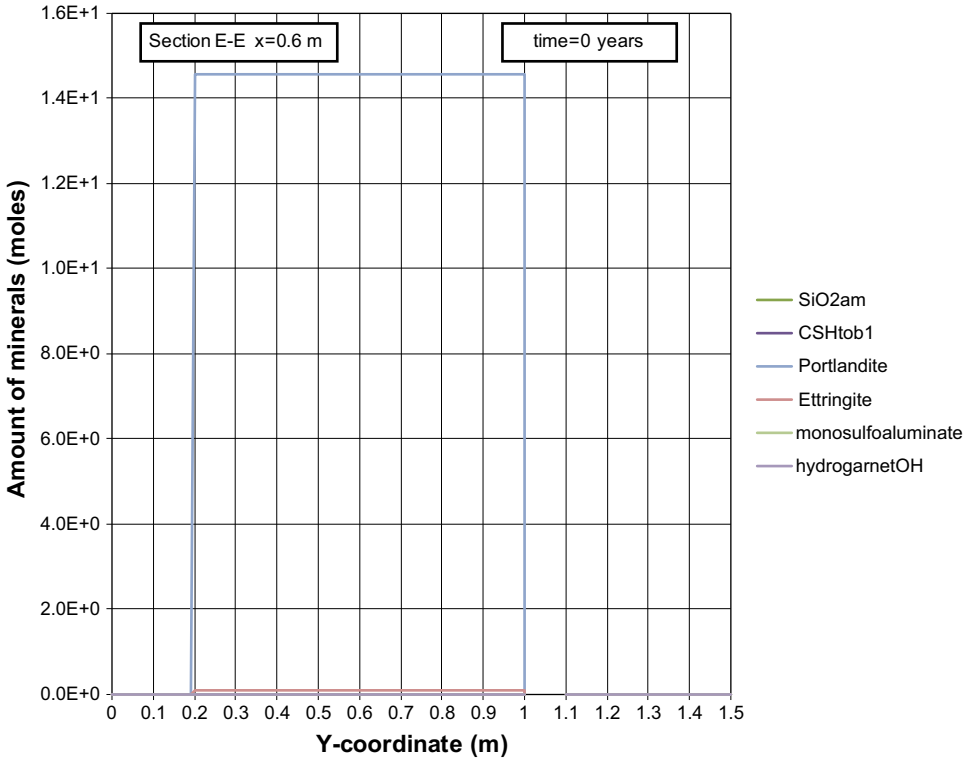

Figure F-20. *The mineral composition in concrete along the vertical Section E-E at time 0 years, case Large12. Units (mol/kg pore water).*

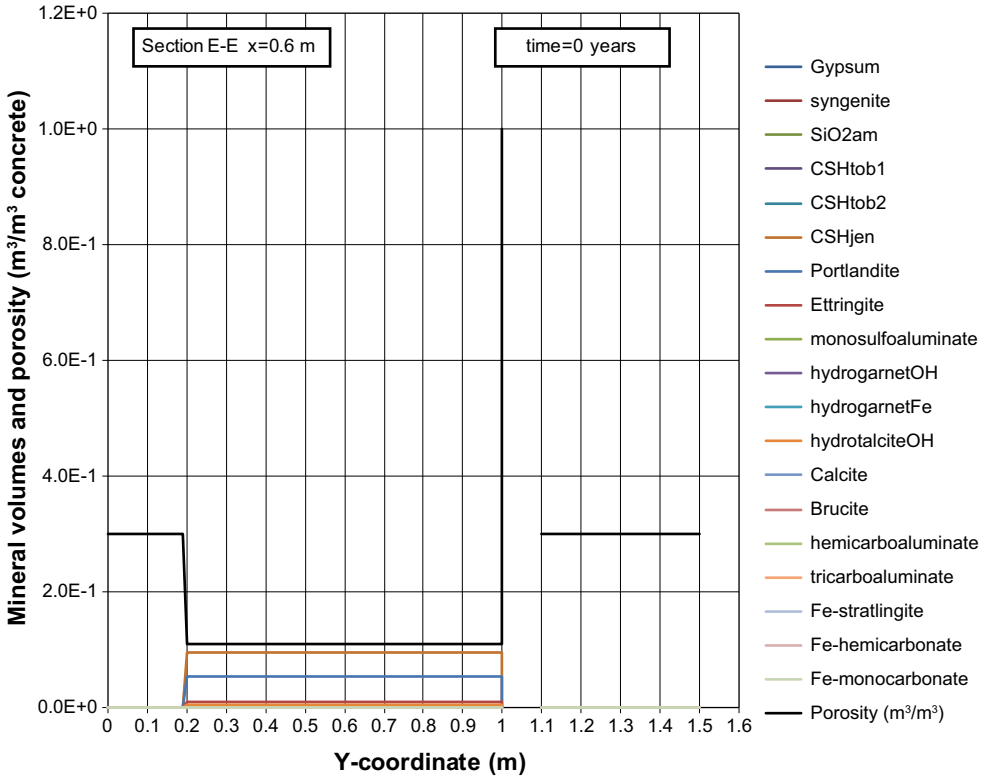

Figure F-21. *Mineral composition in concrete and calculated porosity along the vertical Section E-E at time 0 years, case Large12.*

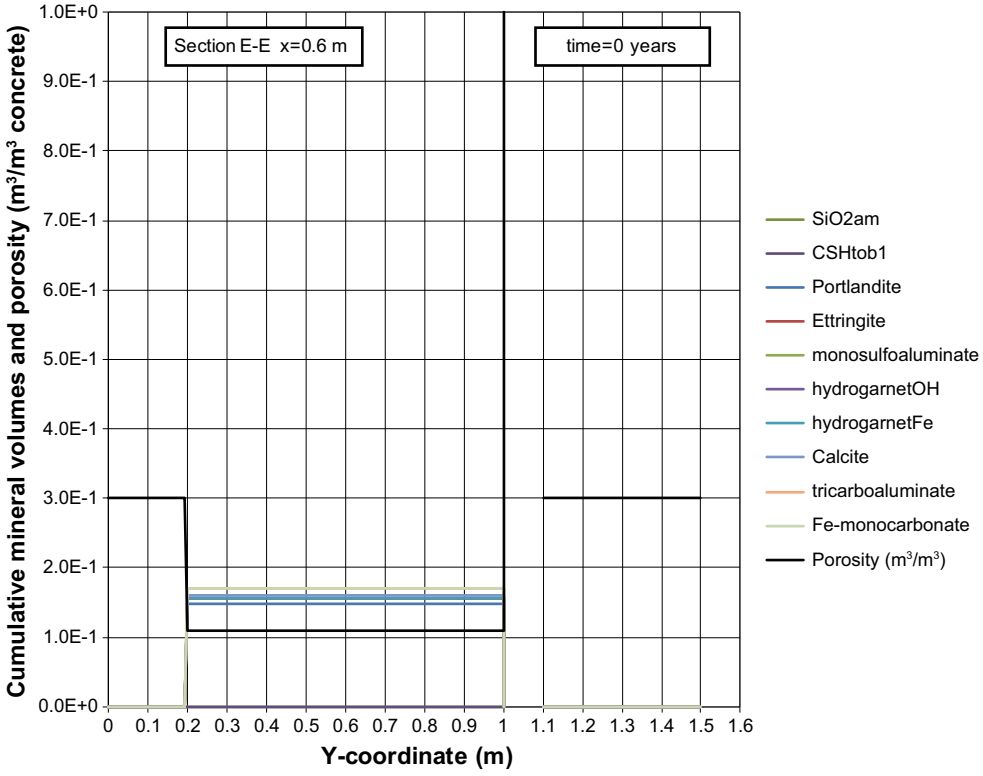

Figure F-22. *Cumulative representation of the mineral composition in concrete and calculated porosity along the vertical Section E-E at time 0 years, case Large12.*

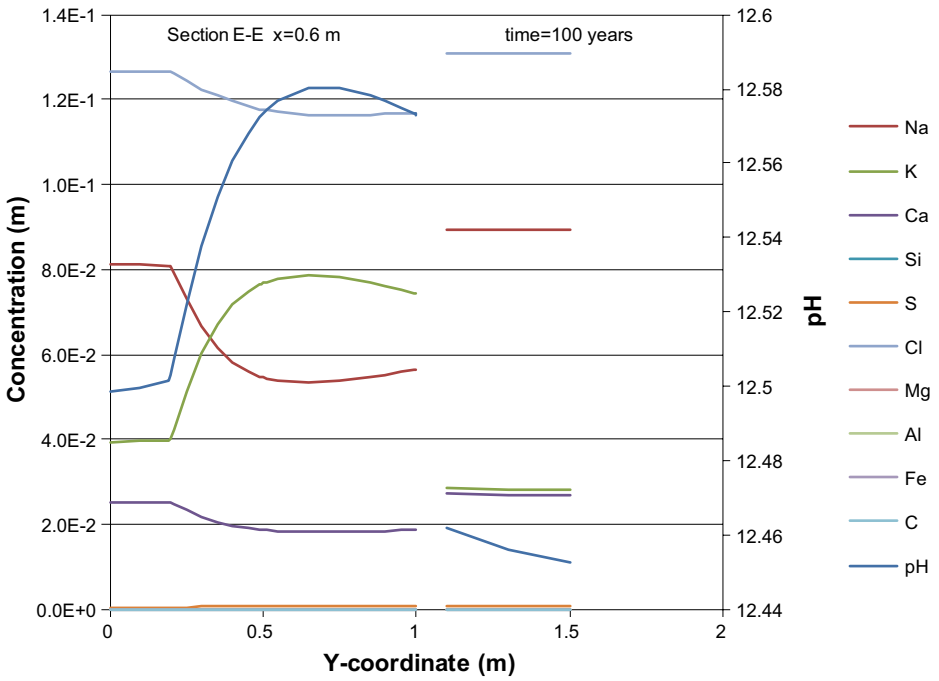

Figure F-23. *Concentration profiles of dissolved components in concrete pore water along the vertical Section E-E at time 100 years, case Large12. Units (mol/kg pore water).*

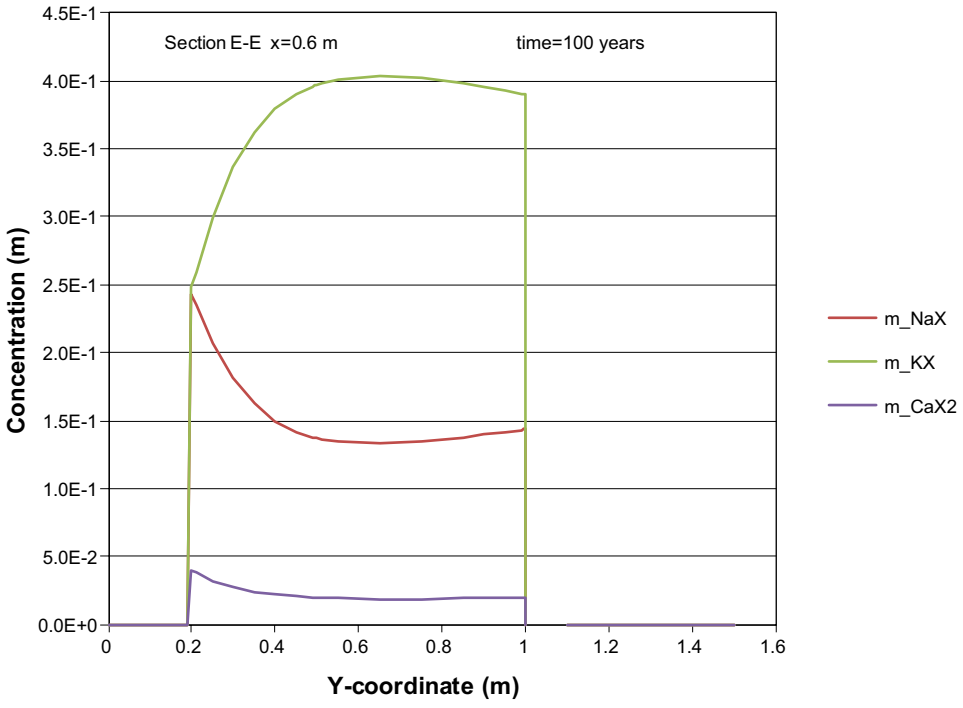

Figure F-24. *The assembly of ion exchange species in concrete along the vertical Section E-E at time 100 years, case Large12. Units (mol/kg pore water).*

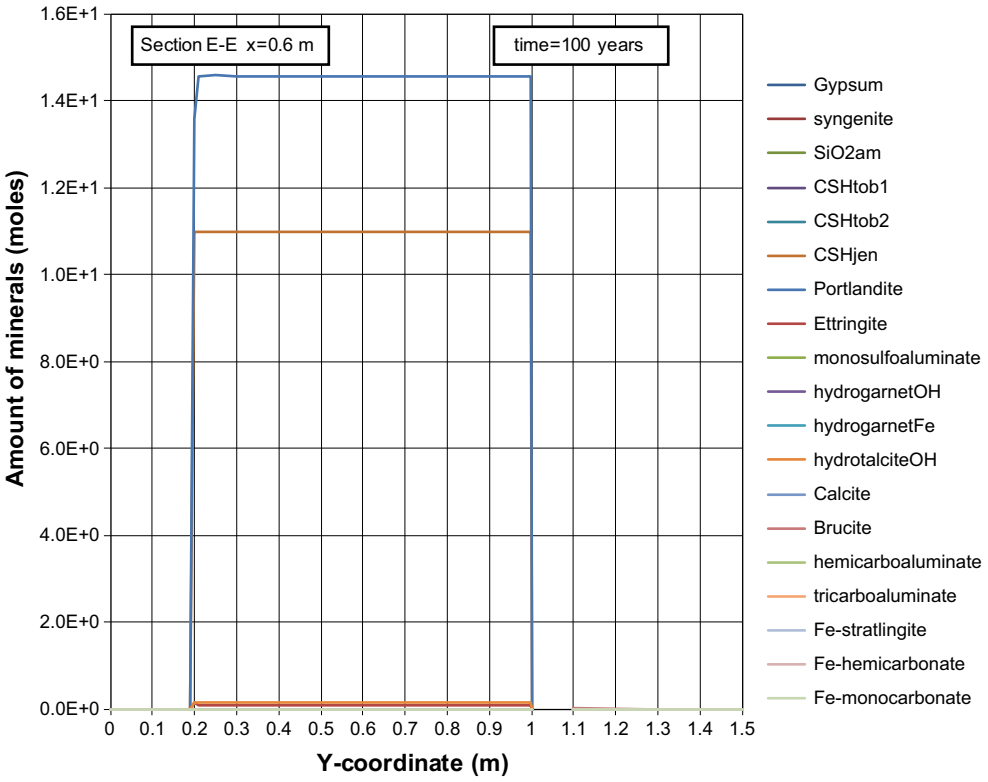

Figure F-25. *The mineral composition in concrete along the vertical Section E-E at time 100 years, case Large12. Units (mol/kg pore water).*

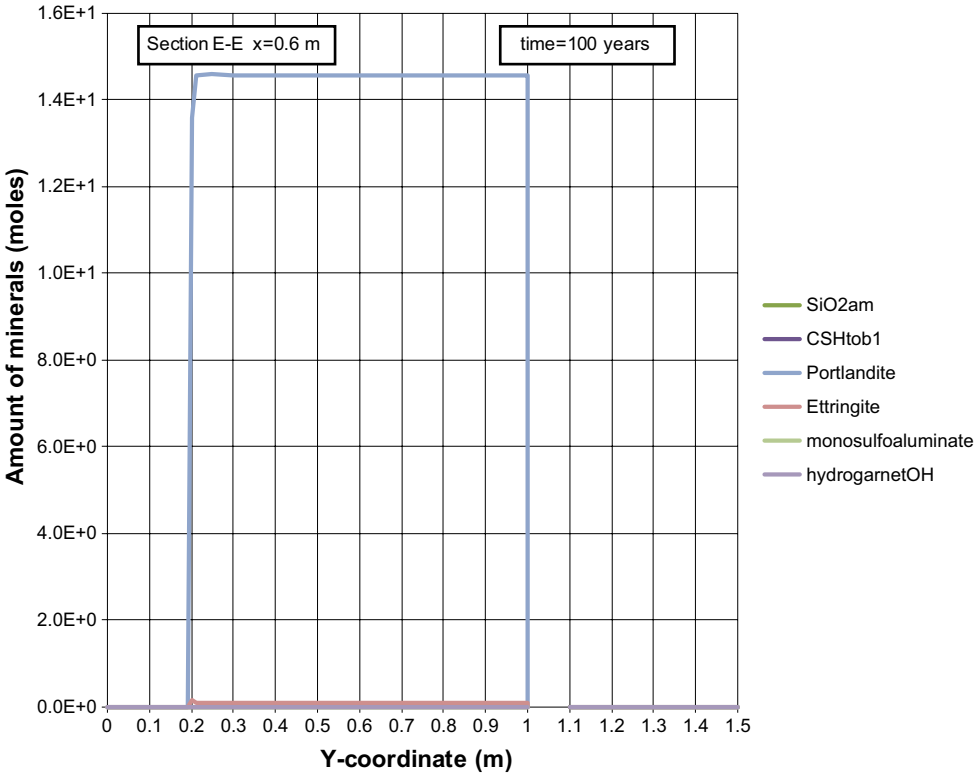

Figure F-26. *The mineral composition in concrete along the vertical Section E-E at time 100 years, case Large12. Units (mol/kg pore water).*

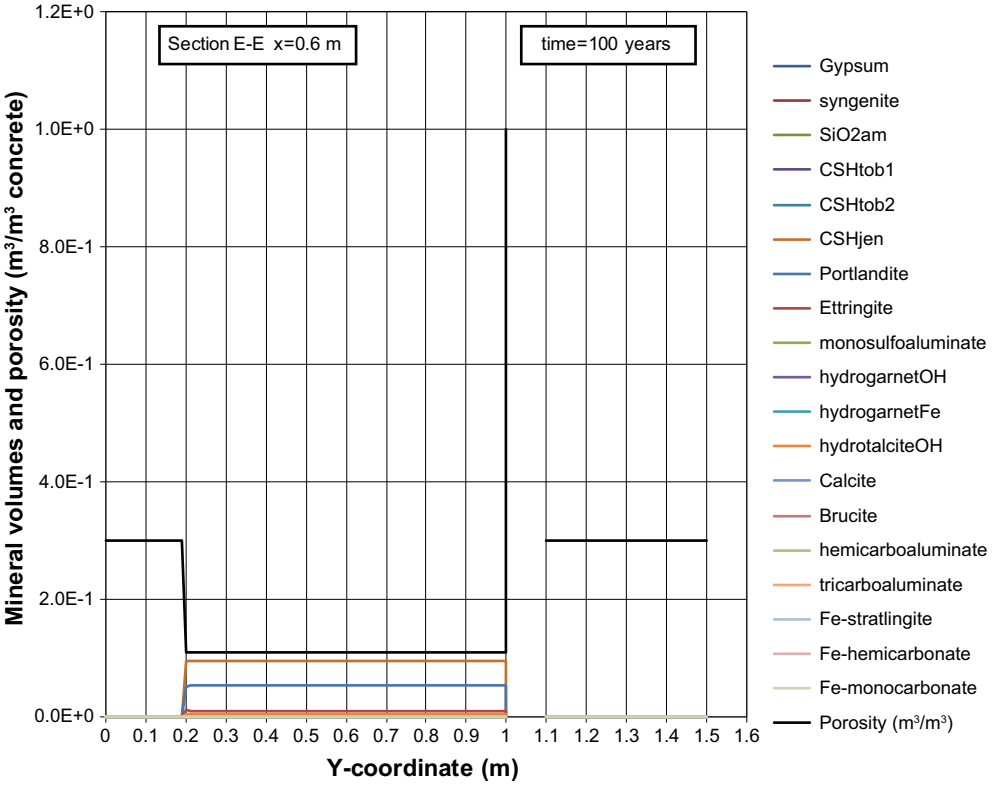

Figure F-27. *Mineral composition in concrete and calculated porosity along the vertical Section E-E at time 100 years, case Large12.*

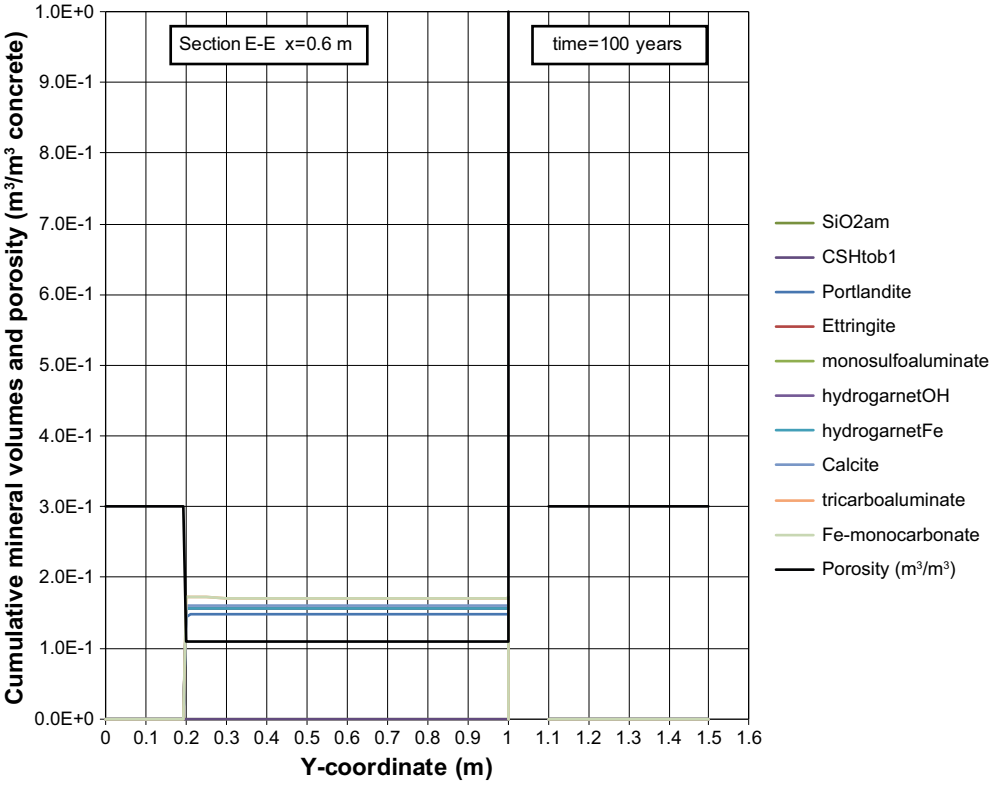

Figure F-28. *Cumulative representation of the mineral composition in concrete and calculated porosity along the vertical Section E-E at time 100 years, case Large12.*

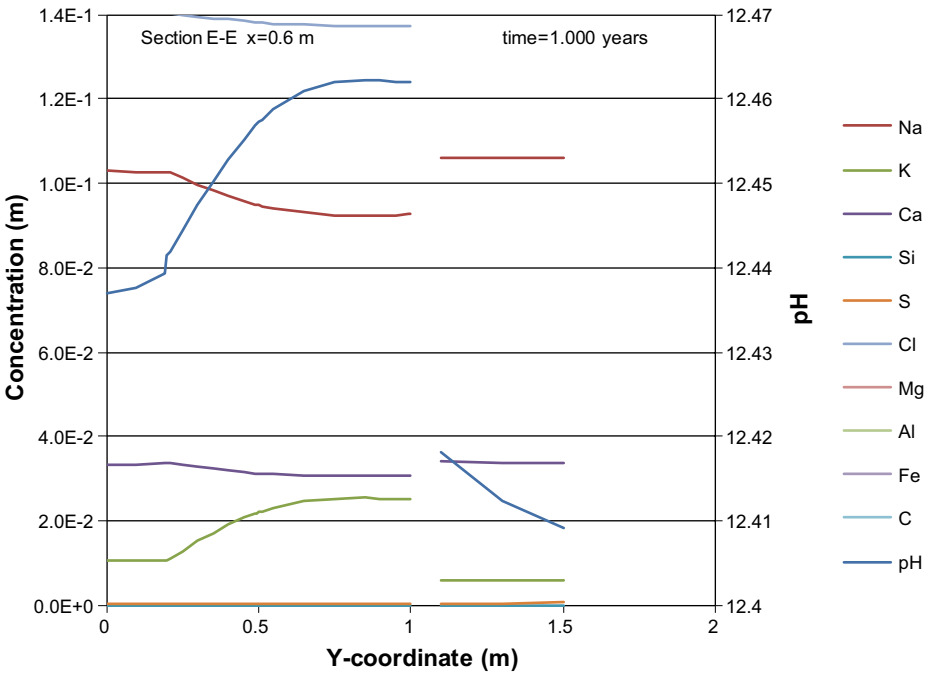

Figure F-29. *Concentration profiles of dissolved components in concrete pore water along the vertical Section E-E at time 1,000 years, case Large12. Units (mol/kg pore water).*

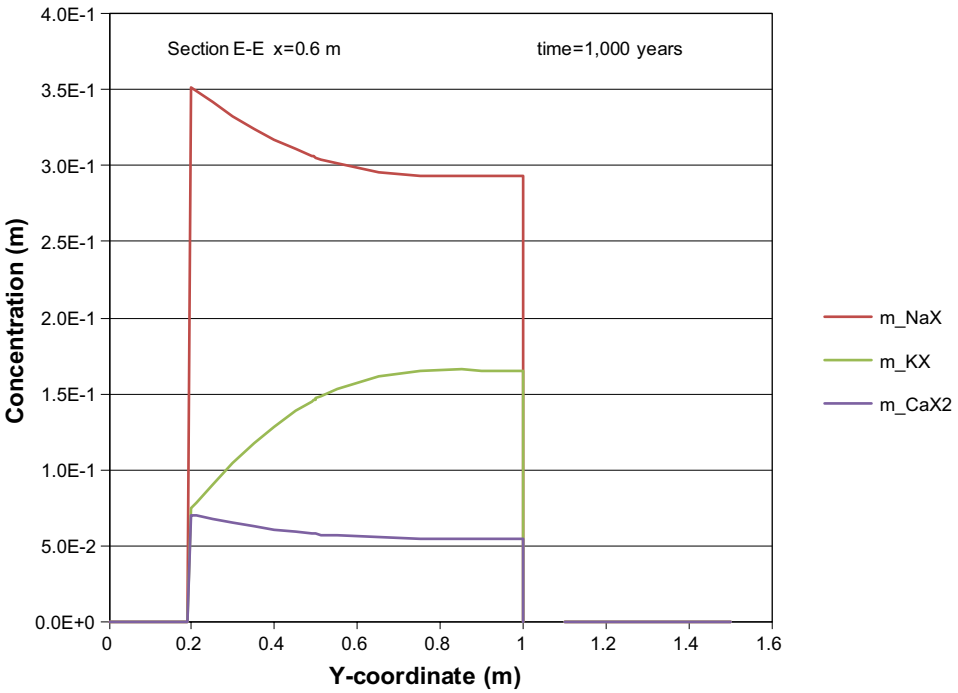

Figure F-30. *The assembly of ion exchange species in concrete along the vertical Section E-E at time 1,000 years, case Large12. Units (mol/kg pore water).*

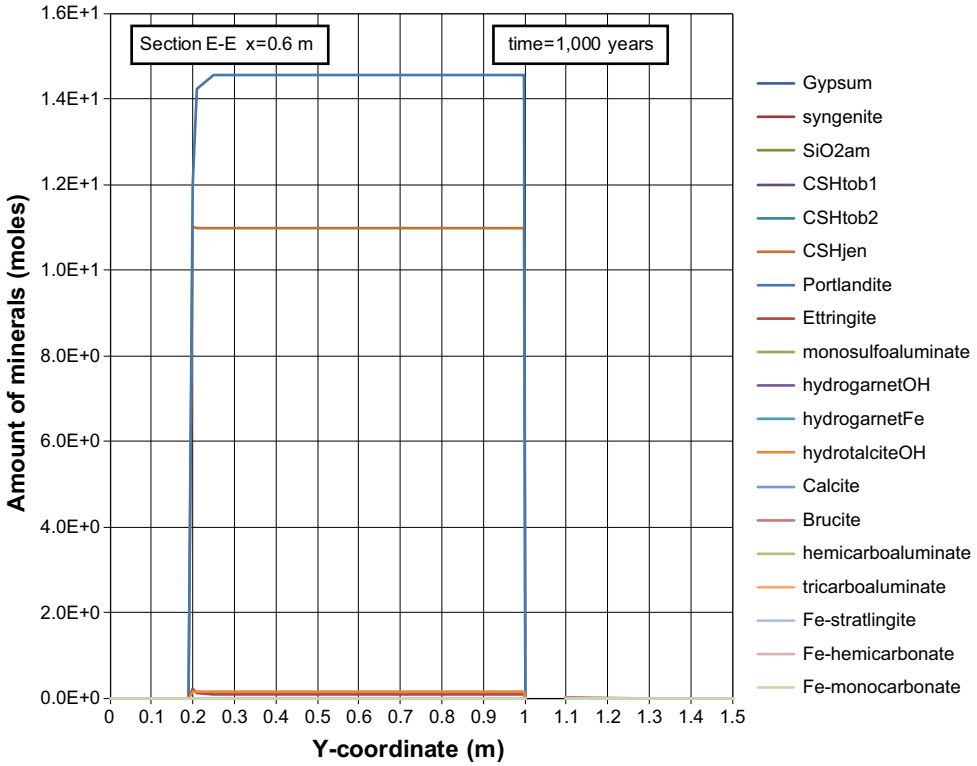

Figure F-31. *The mineral composition in concrete along the vertical Section E-E at time 1,000 years, case Large12. Units (mol/kg pore water).*

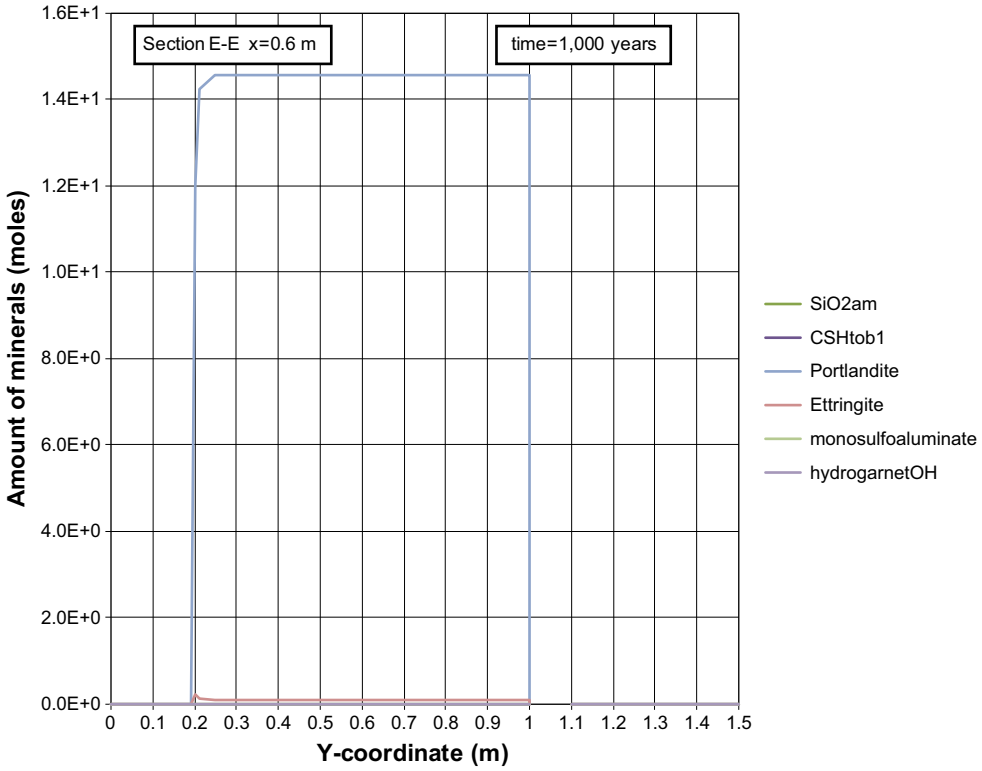

Figure F-32. *The mineral composition in concrete along the vertical Section E-E at time 1,000 years, case Large12. Units (mol/kg pore water).*

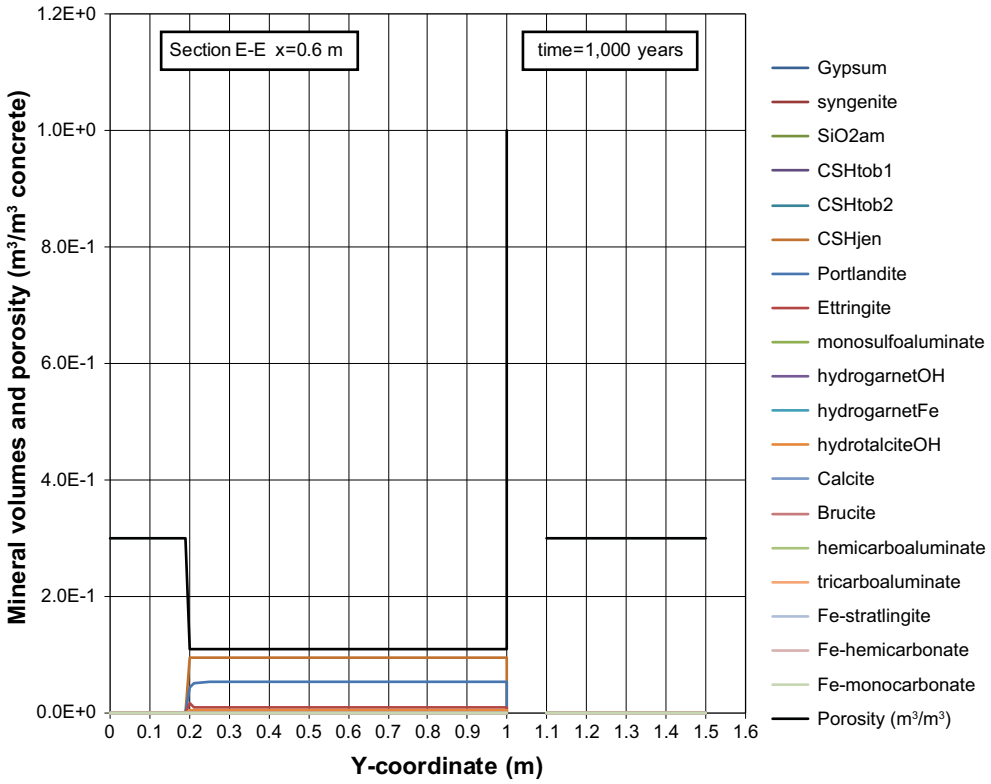

Figure F-33. *Mineral composition in concrete and calculated porosity along the vertical Section E-E at time 1,000 years, case Large12.*

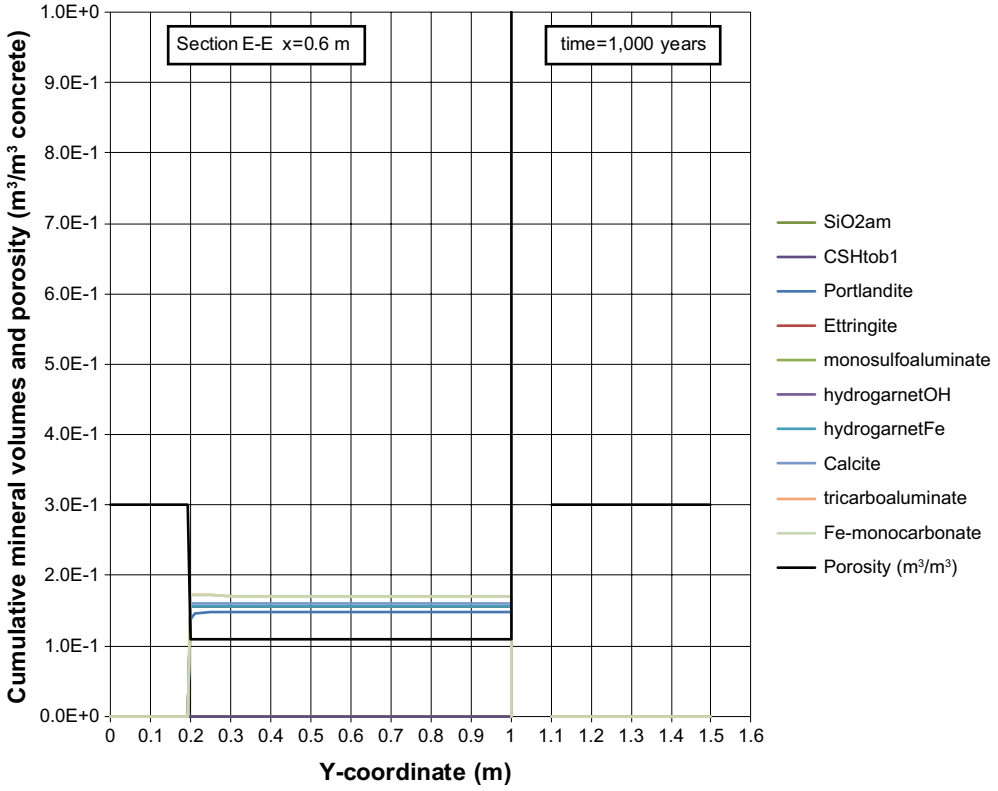

Figure F-34. *Cumulative representation of the mineral composition in concrete and calculated porosity along the vertical Section E-E at time 1,000 years, case Large12.*

Profiles along section E-E at 2,000 years

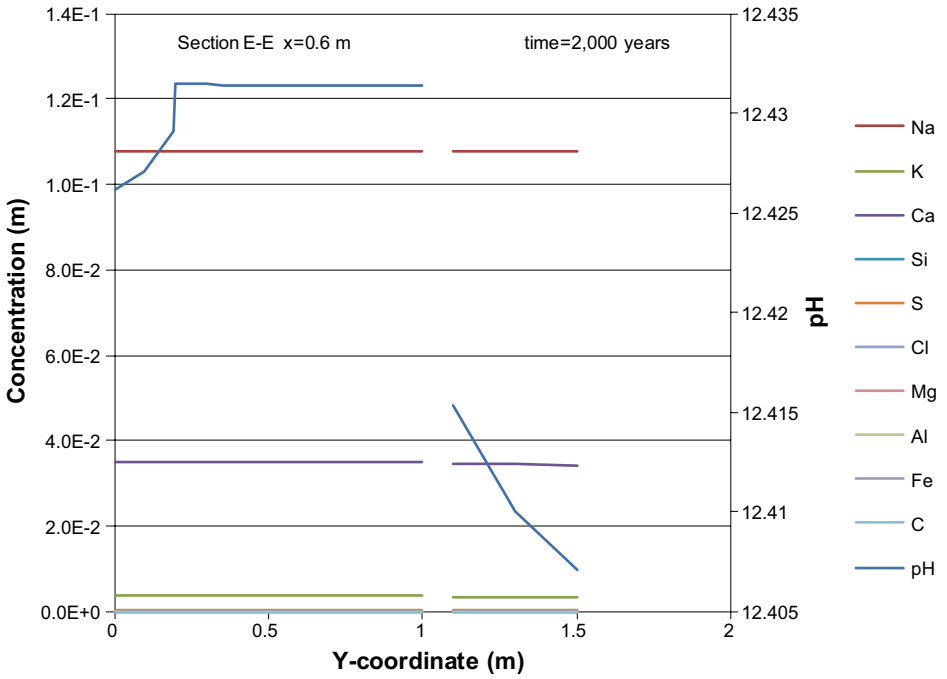

Figure F-35. *Concentration profiles of dissolved components in concrete pore water along the vertical Section E-E at time 2,000 years, case Large12. Units (mol/kg pore water).*

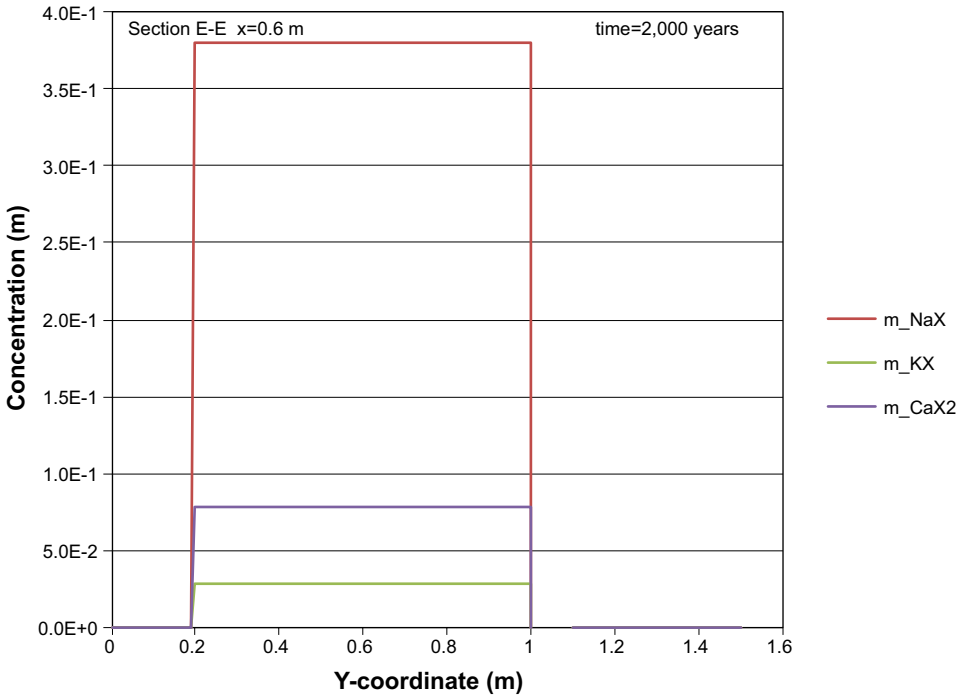

Figure F-36. *The assembly of ion exchange species in concrete along the vertical Section E-E at time 2,000 years, case Large12. Units (mol/kg pore water).*

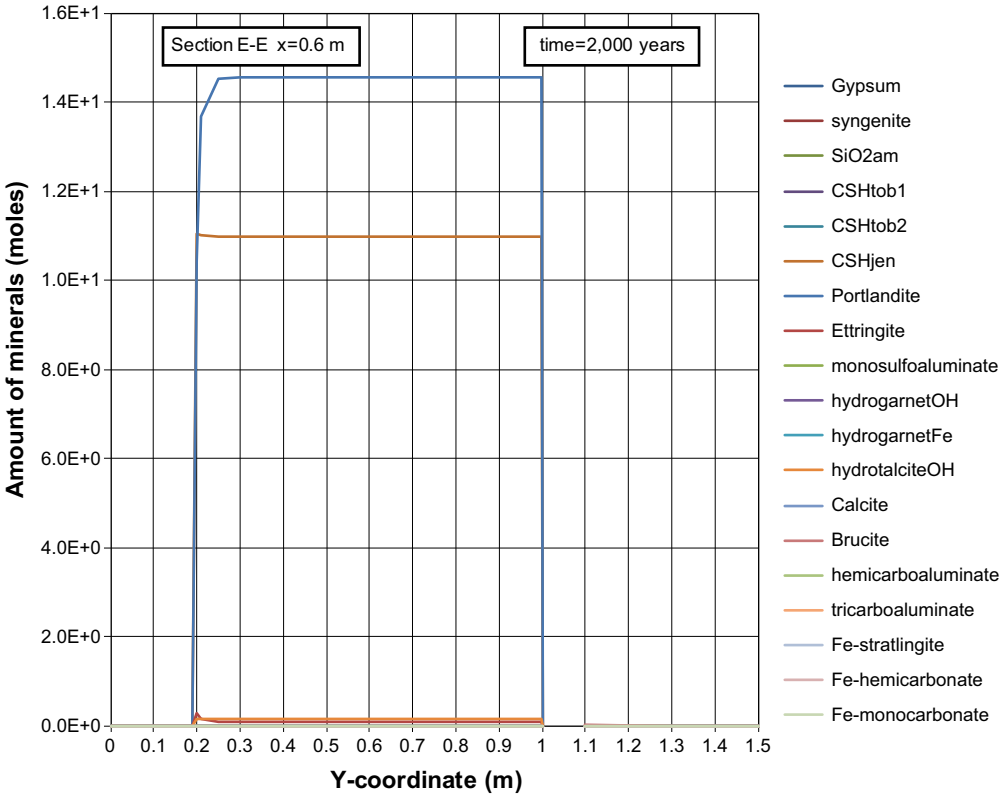

Figure F-37. *The mineral composition in concrete along the vertical Section E-E at time 2,000 years, case Large12. Units (mol/kg pore water).*

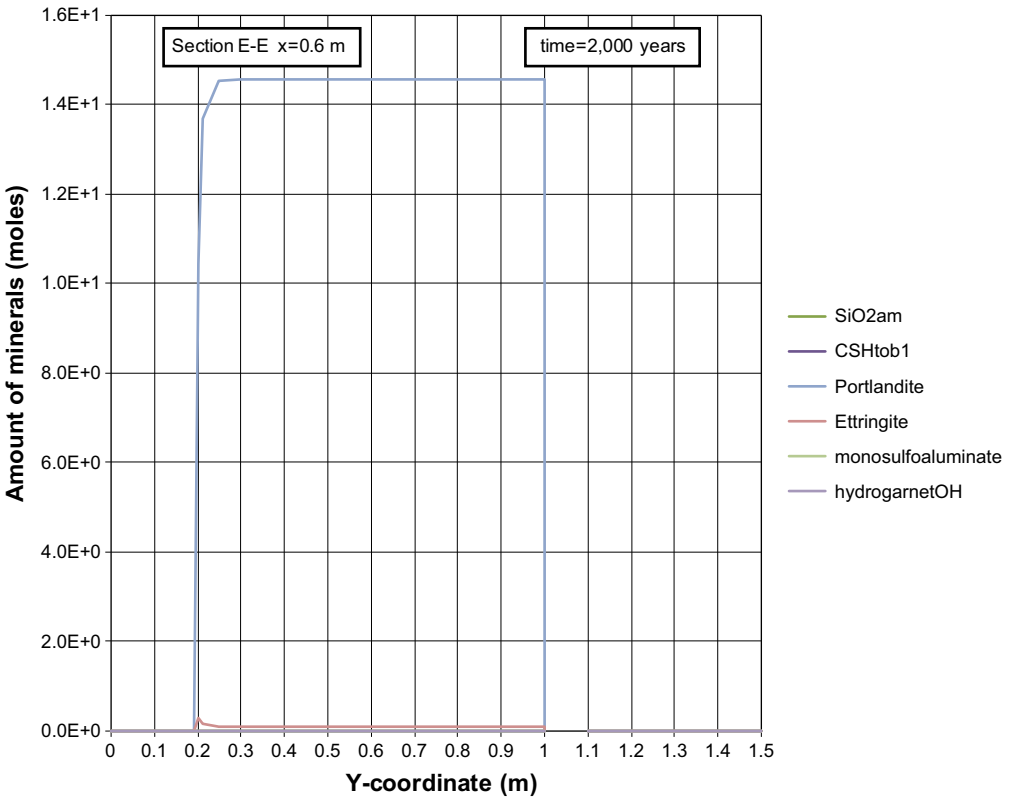

Figure F-38. *The mineral composition in concrete along the vertical Section E-E at time 2,000 years, case Large12. Units (mol/kg pore water).*

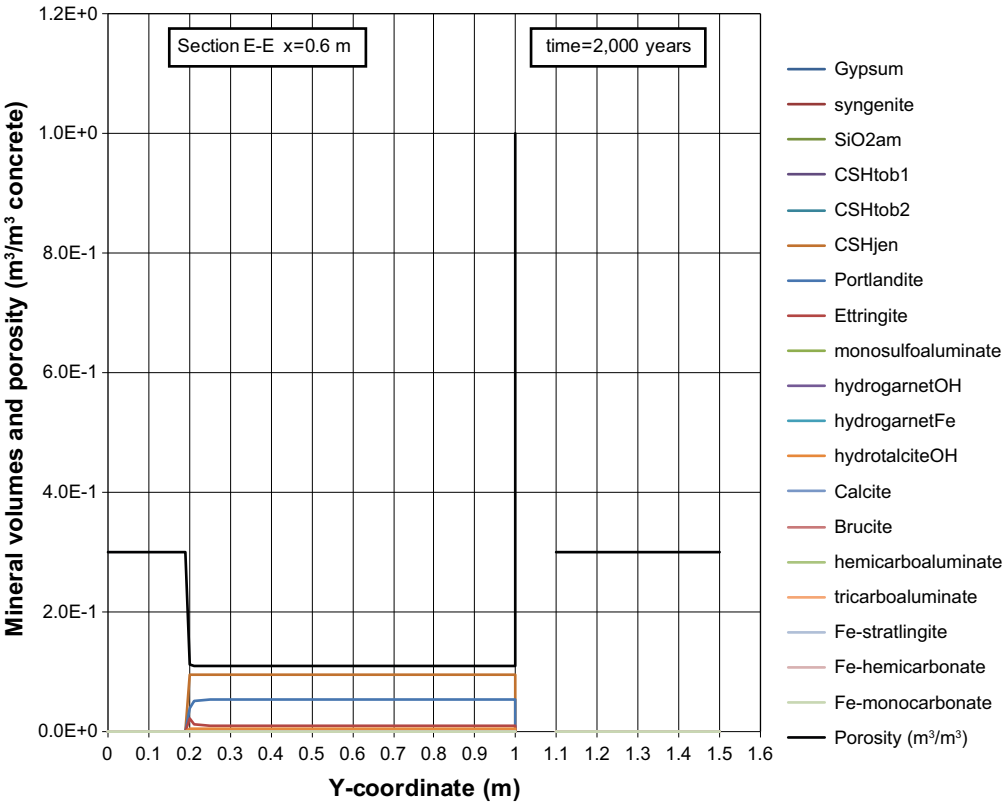

Figure F-39. *Mineral composition in concrete and calculated porosity along the vertical Section E-E at time 2,000 years, case Large12.*

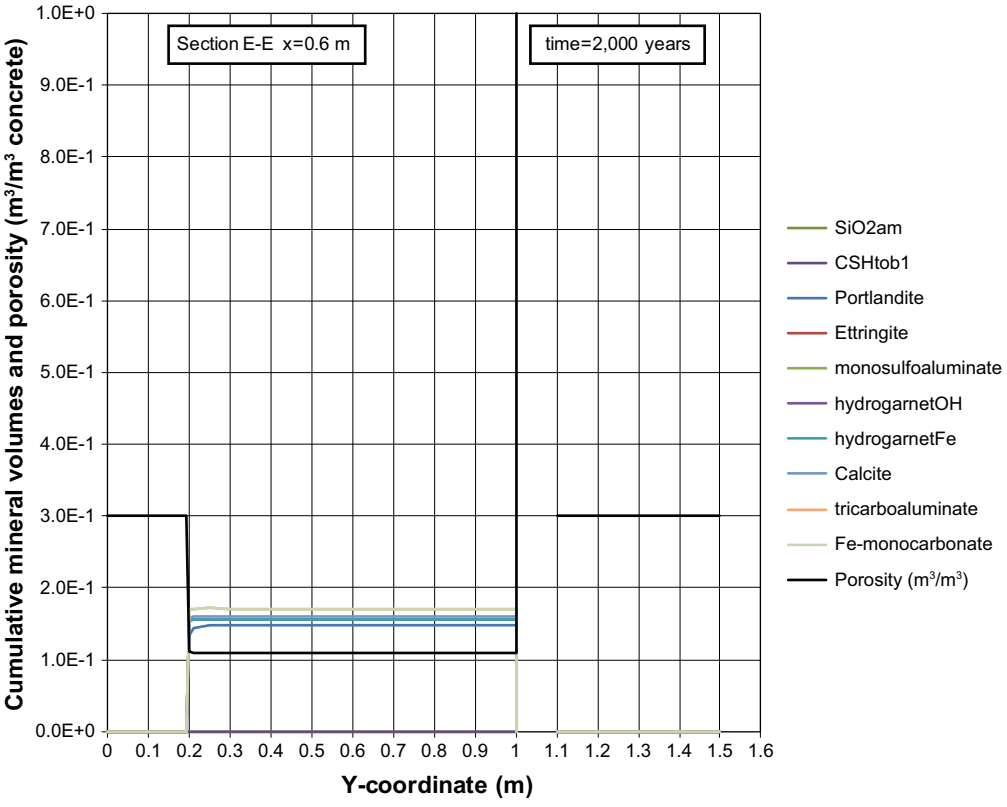

Figure F-40. *Cumulative representation of the mineral composition in concrete and calculated porosity along the vertical Section E-E at time 2,000 years, case Large12.*

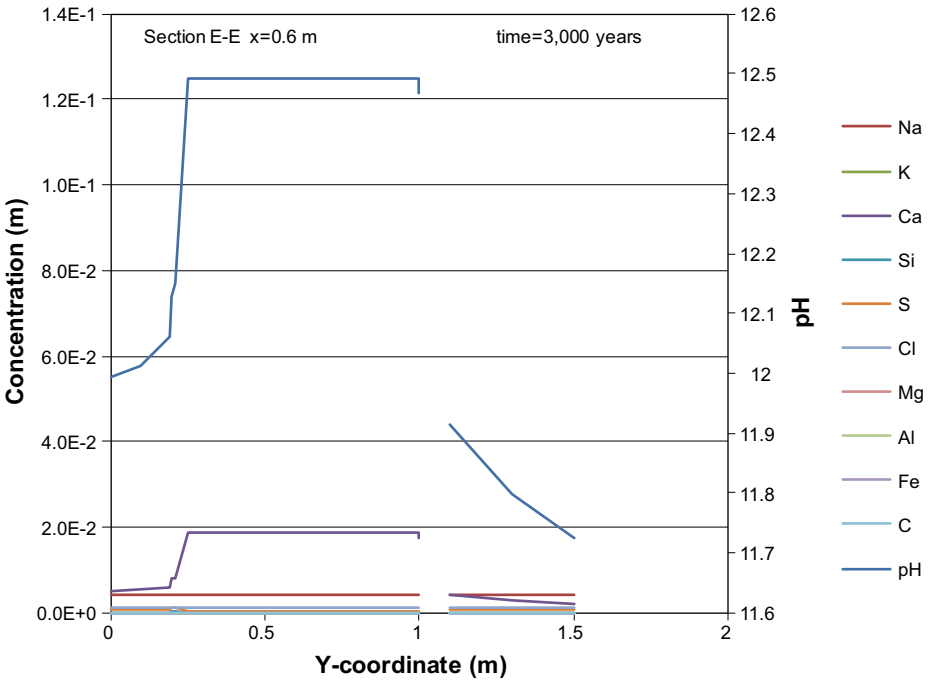

Figure F-41. *Concentration profiles of dissolved components in concrete pore water along the vertical Section E-E at time 3,000 years, case Large12. Units (mol/kg pore water).*

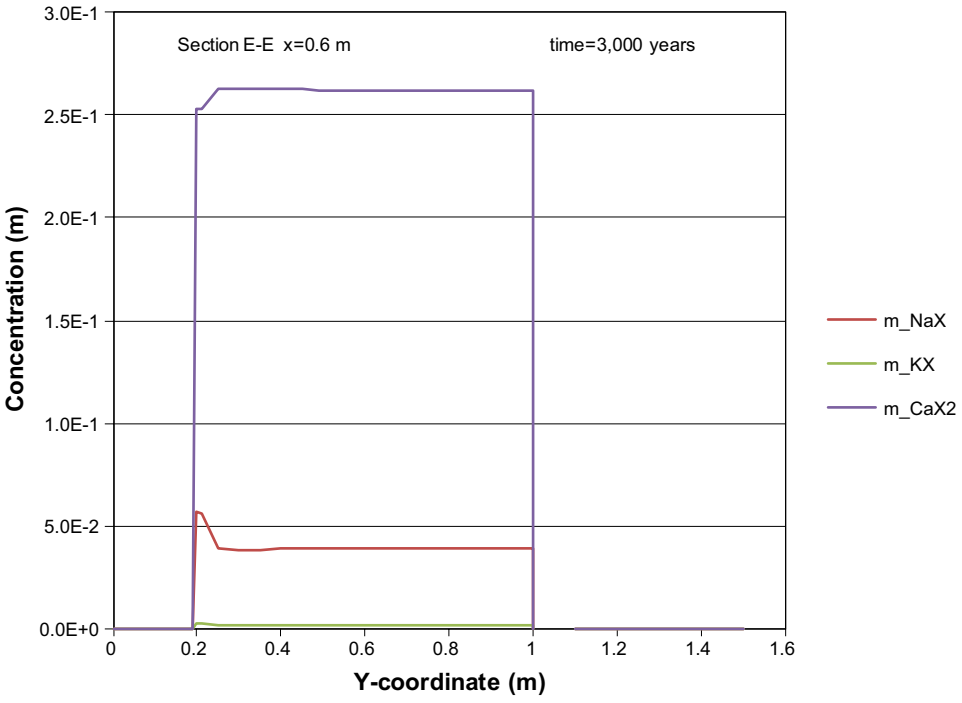

Figure F-42. *The assembly of ion exchange species in concrete along the vertical Section E-E at time 3,000 years, case Large12. Units (mol/kg pore water).*

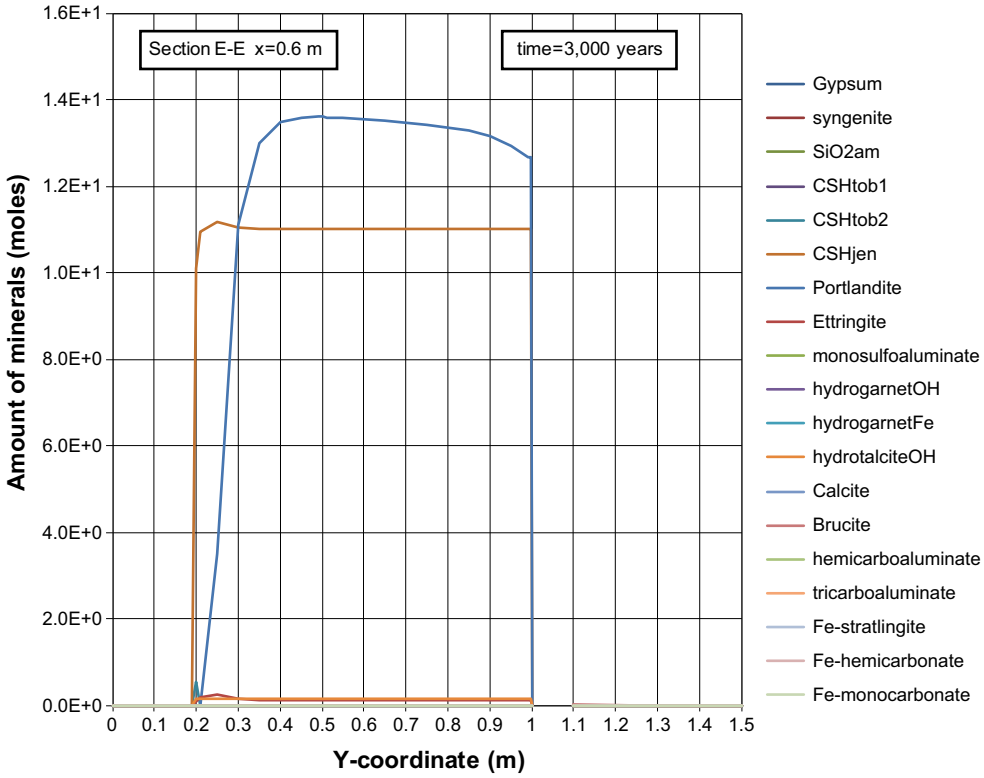

Figure F-43. *The mineral composition in concrete along the vertical Section E-E at time 3,000 years, case Large12. Units (mol/kg pore water).*

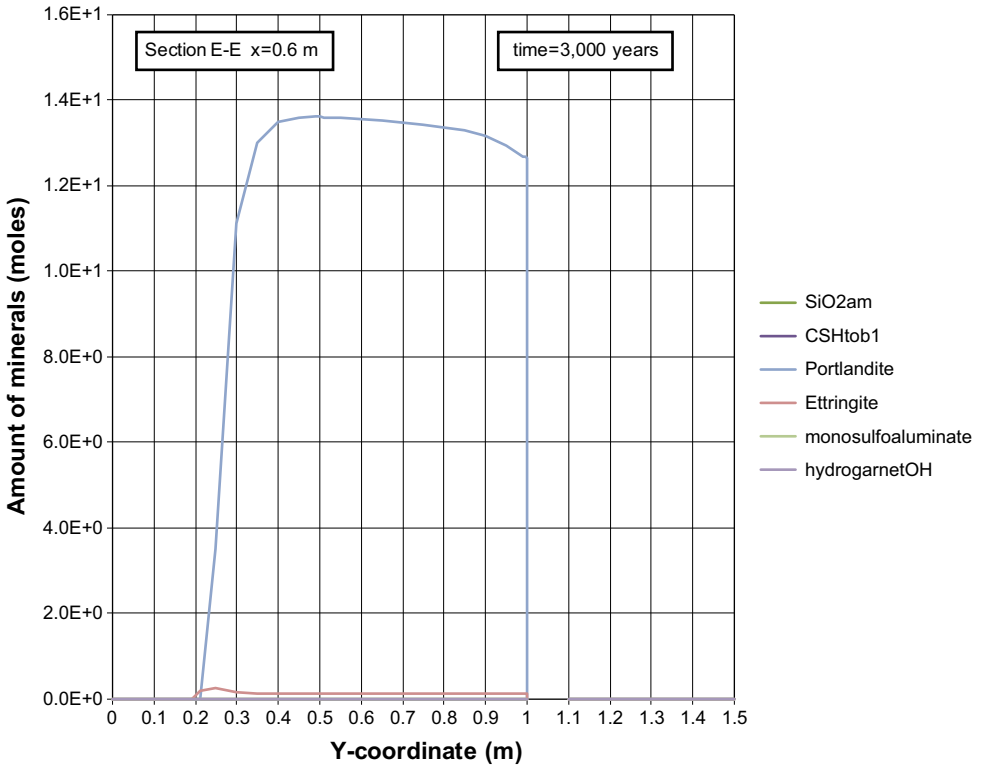

Figure F-44. *The mineral composition in concrete along the vertical Section E-E at time 3,000 years, case Large12. Units (mol/kg pore water).*

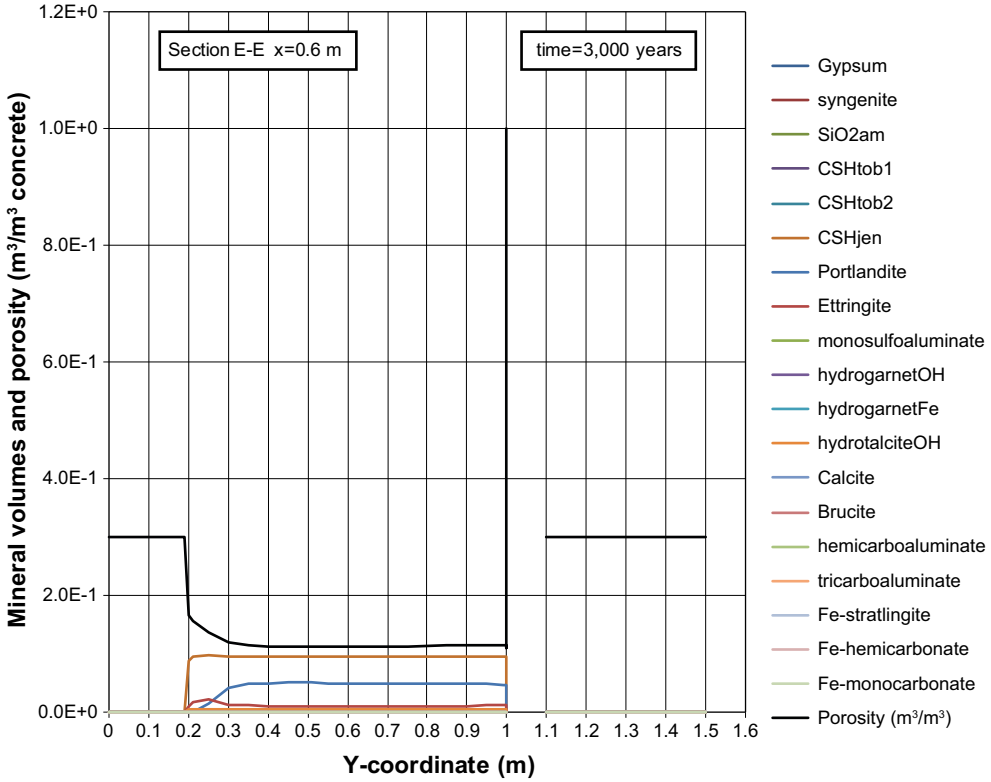

Figure F-45. *Mineral composition in concrete and calculated porosity along the vertical Section E-E at time 3,000 years, case Large12.*

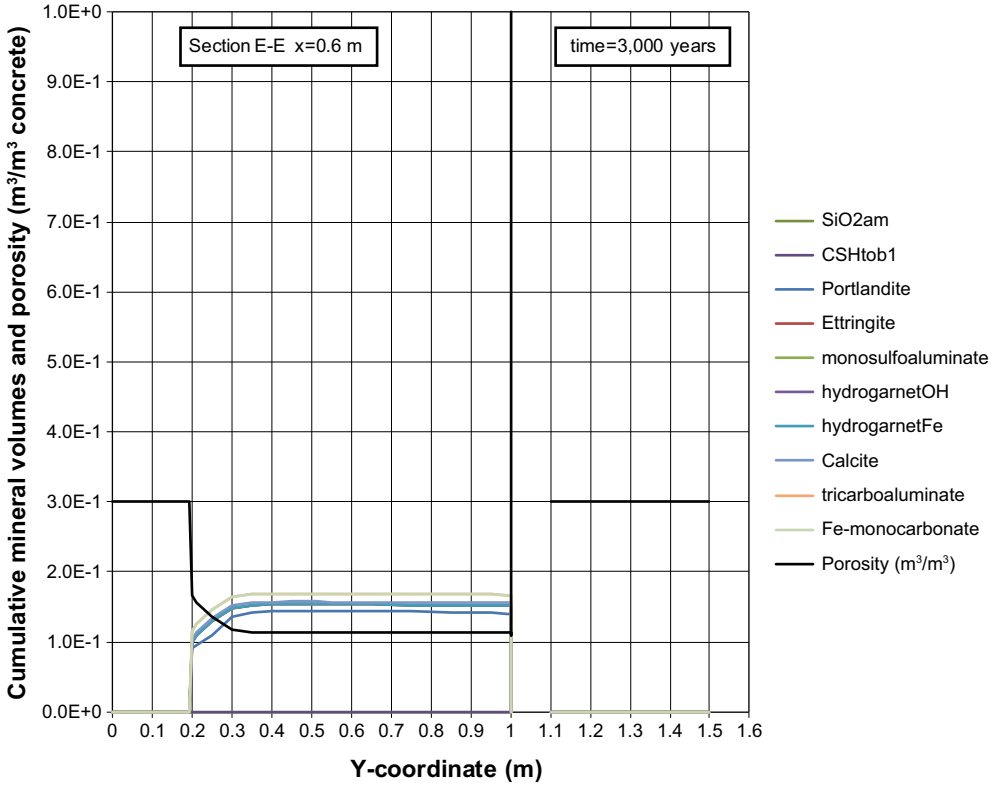

Figure F-46. *Cumulative representation of the mineral composition in concrete and calculated porosity along the vertical Section E-E at time 3,000 years, case Large12.*

Profiles along section E-E at 5,000 years

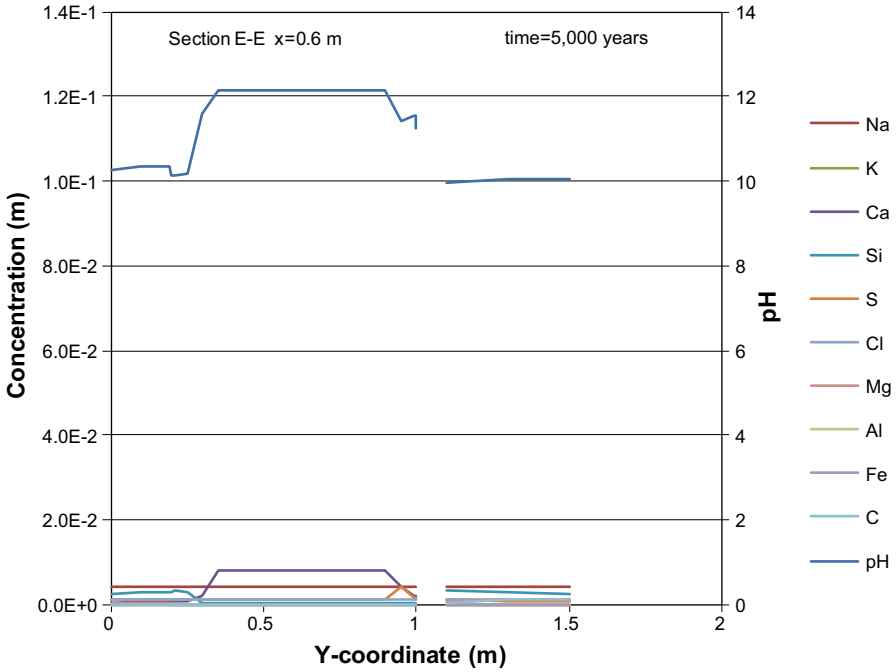

Figure F-47. *Concentration profiles of dissolved components in concrete pore water along the vertical Section E-E at time 5,000 years, case Large12. Units (mol/kg pore water).*

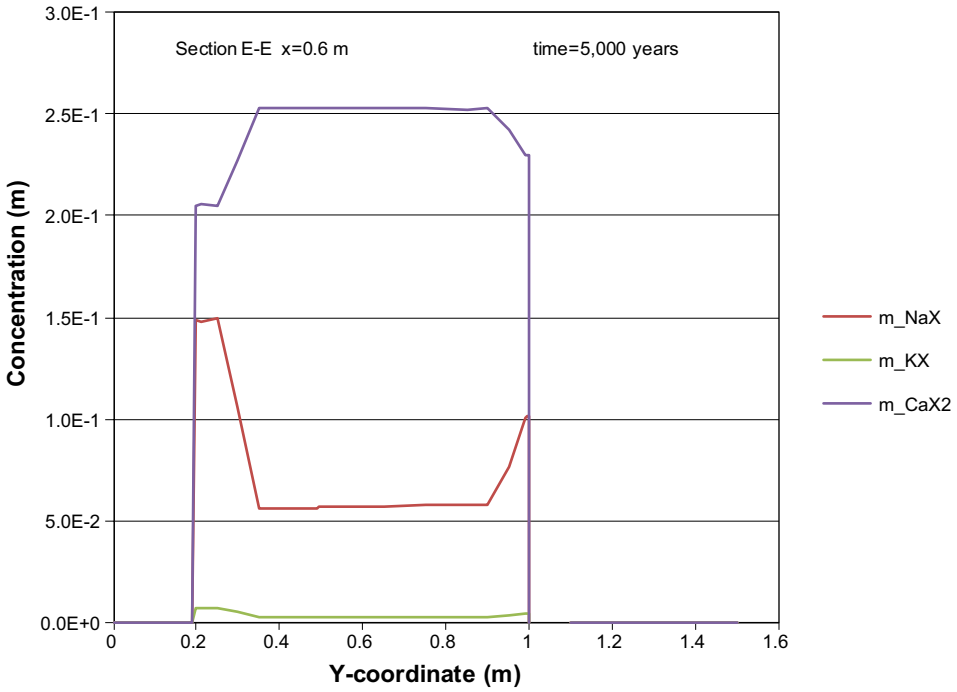

Figure F-48. *The assembly of ion exchange species in concrete along the vertical Section E-E at time 5,000 years, case Large12. Units (mol/kg pore water).*

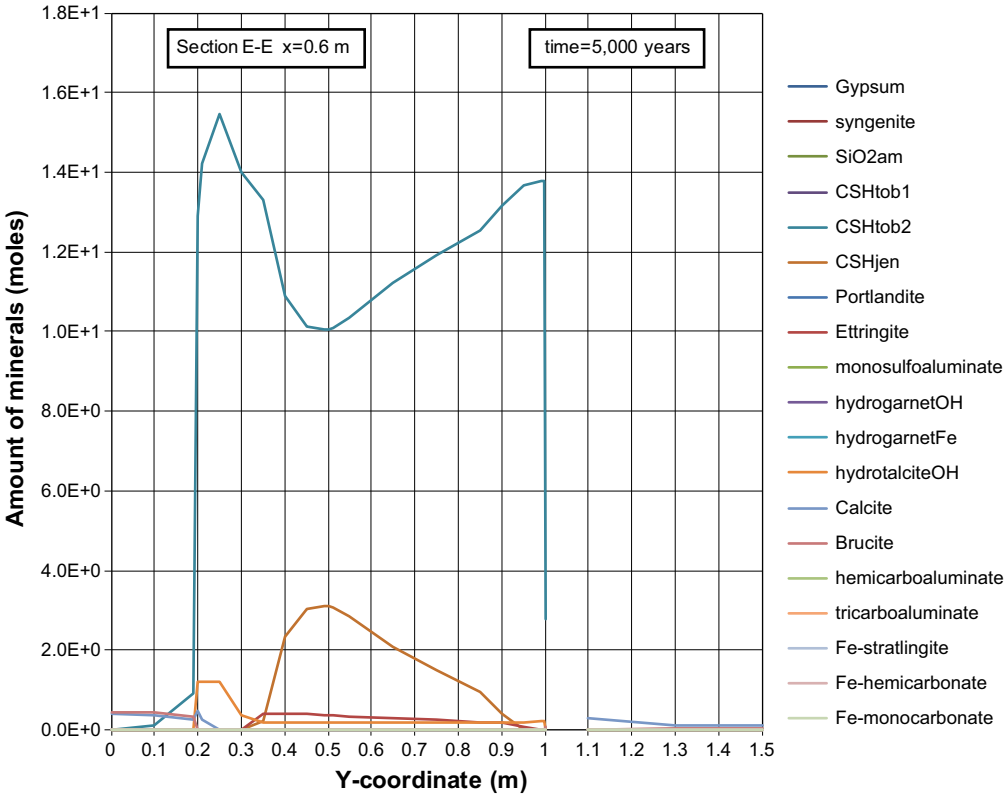

Figure F-49. *The mineral composition in concrete along the vertical Section E-E at time 5,000 years, case Large12. Units (mol/kg pore water).*

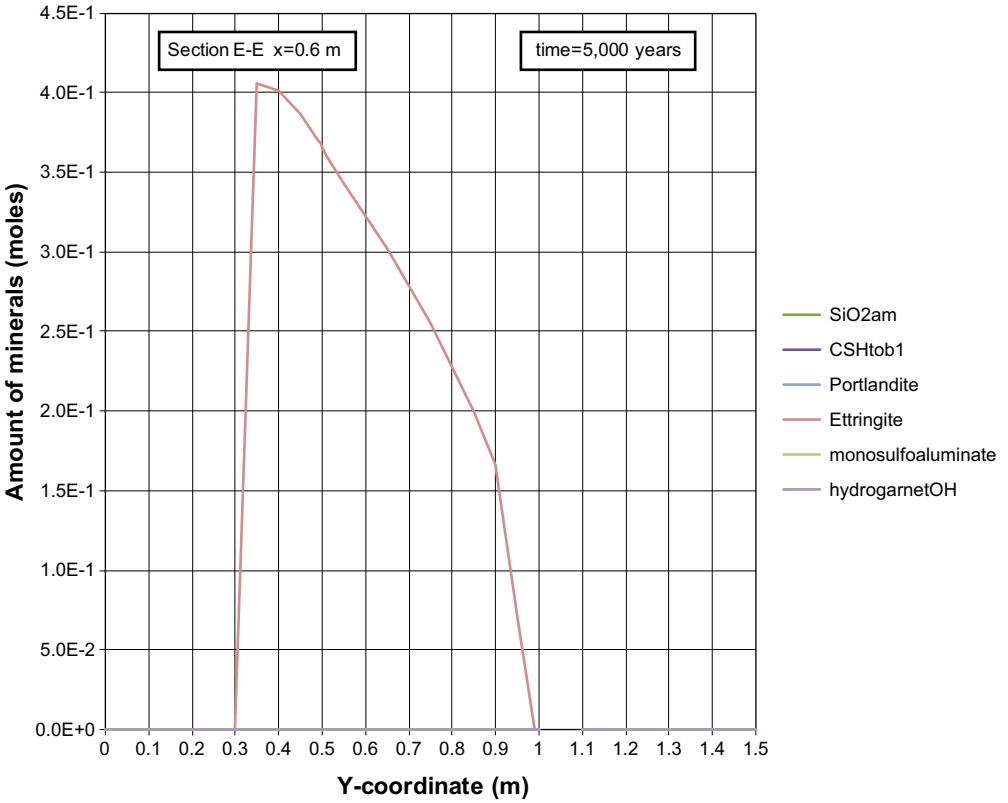

Figure F-50. *The mineral composition in concrete along the vertical Section E-E at time 5,000 years, case Large12. Units (mol/kg pore water).*

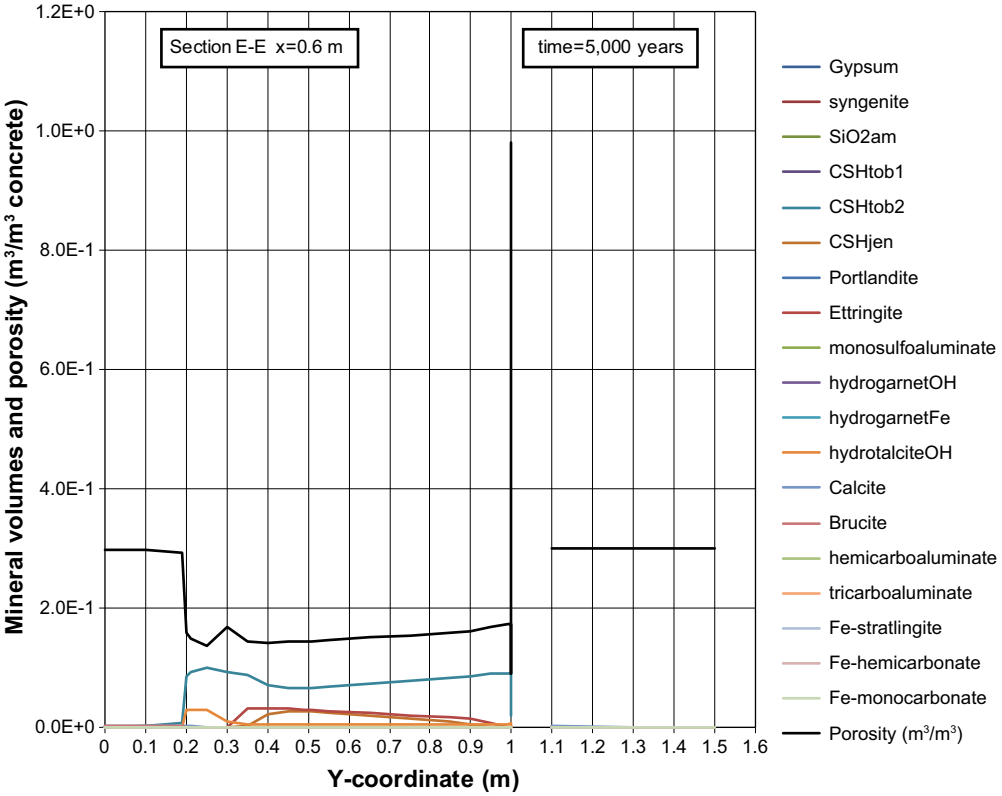

Figure F-51. *Mineral composition in concrete and calculated porosity along the vertical Section E-E at time 5,000 years, case Large12.*

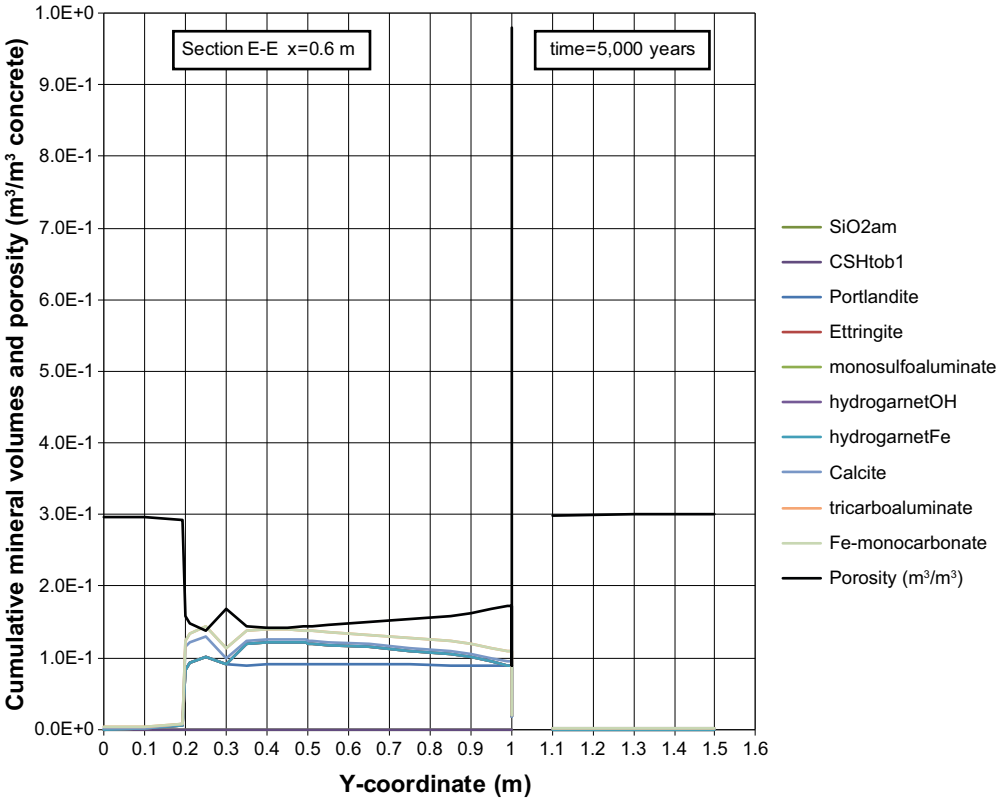

Figure F-52. *Cumulative representation of the mineral composition in concrete and calculated porosity along the vertical Section E-E at time 5,000 years, case Large12.*

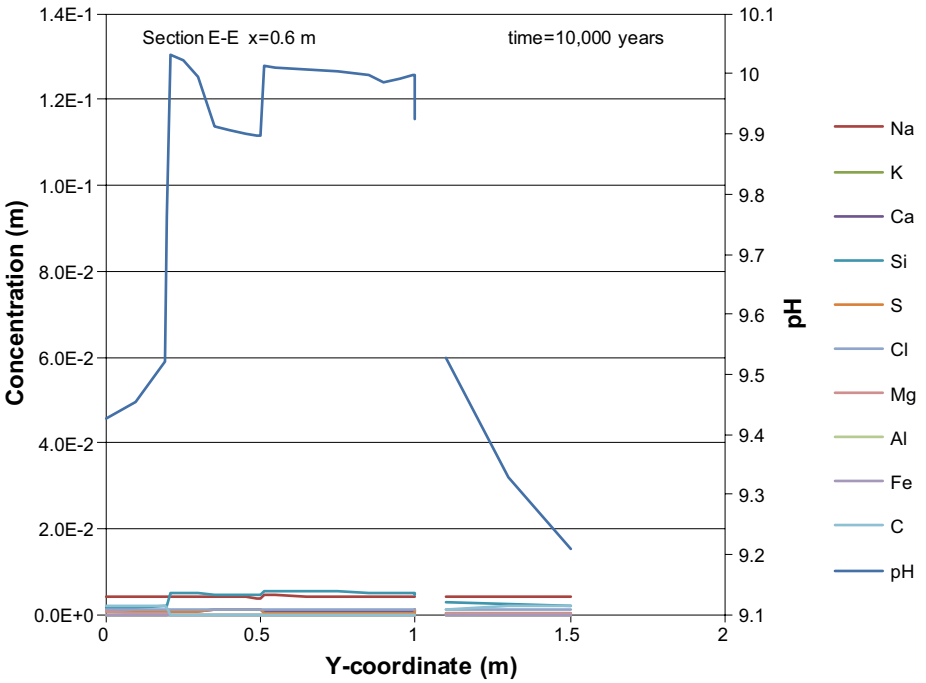

Figure F-53. *Concentration profiles of dissolved components in concrete pore water along the vertical Section E-E at time 10,000 years, case Large12. Units (mol/kg pore water).*

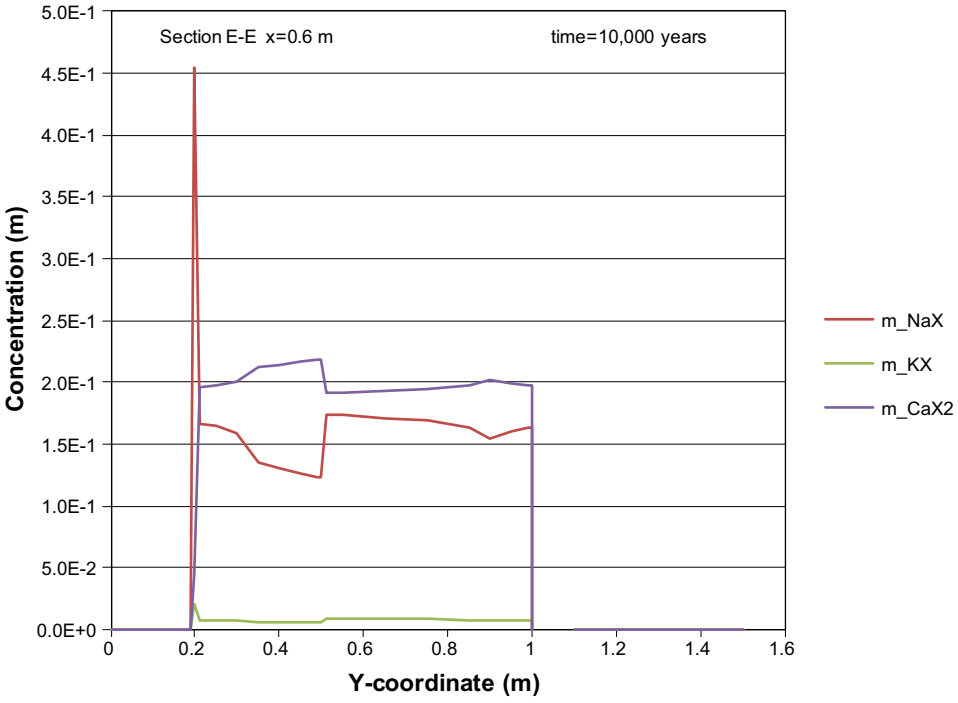

Figure F-54. *The assembly of ion exchange species in concrete along the vertical Section E-E at time 10,000 years, case Large12. Units (mol/kg pore water).*

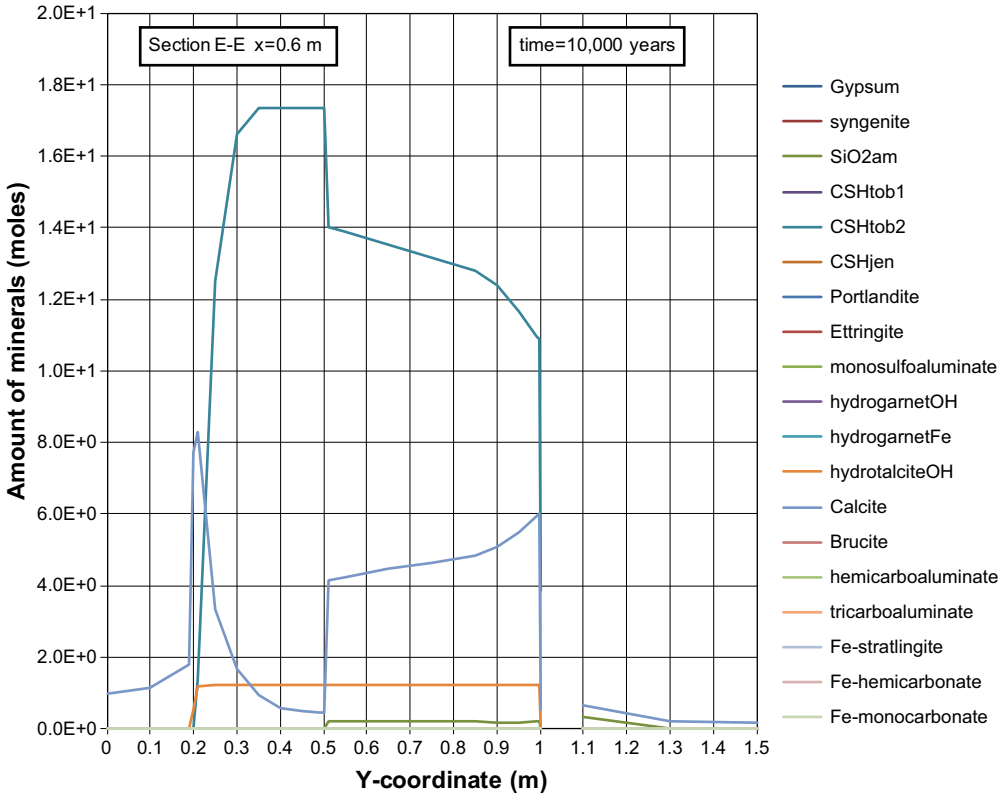

Figure F-55. *The mineral composition in concrete along the vertical Section E-E at time 10,000 years, case Large12. Units (mol/kg pore water).*

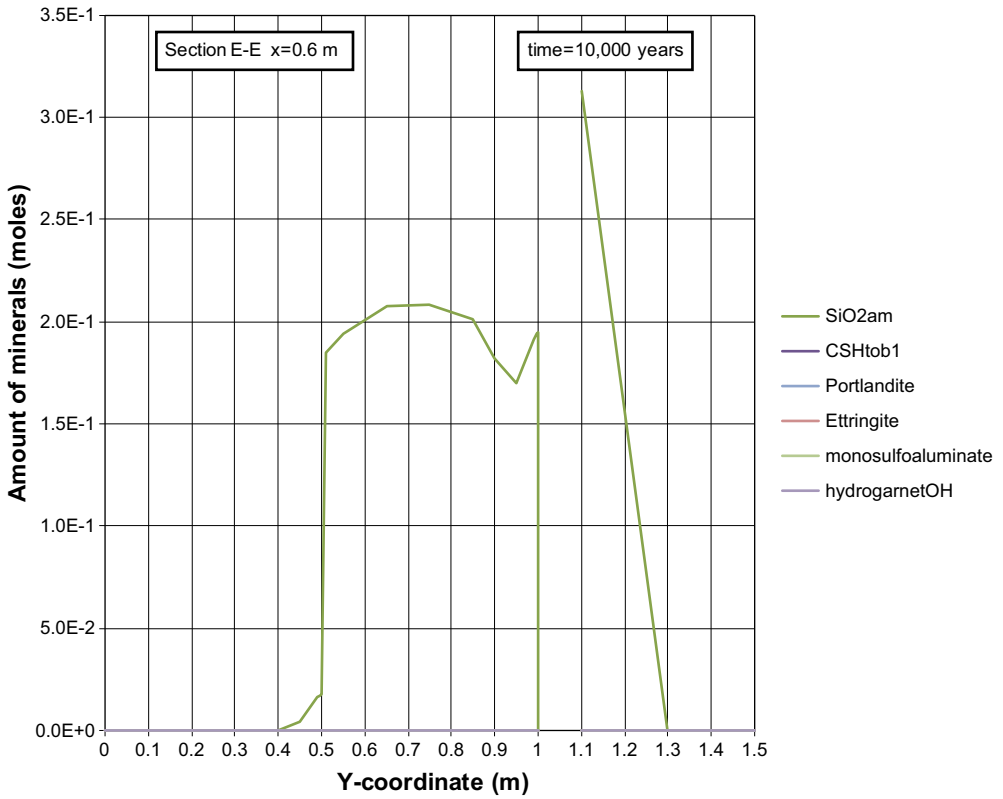

Figure F-56. *The mineral composition in concrete along the vertical Section E-E at time 10,000 years, case Large12. Units (mol/kg pore water).*

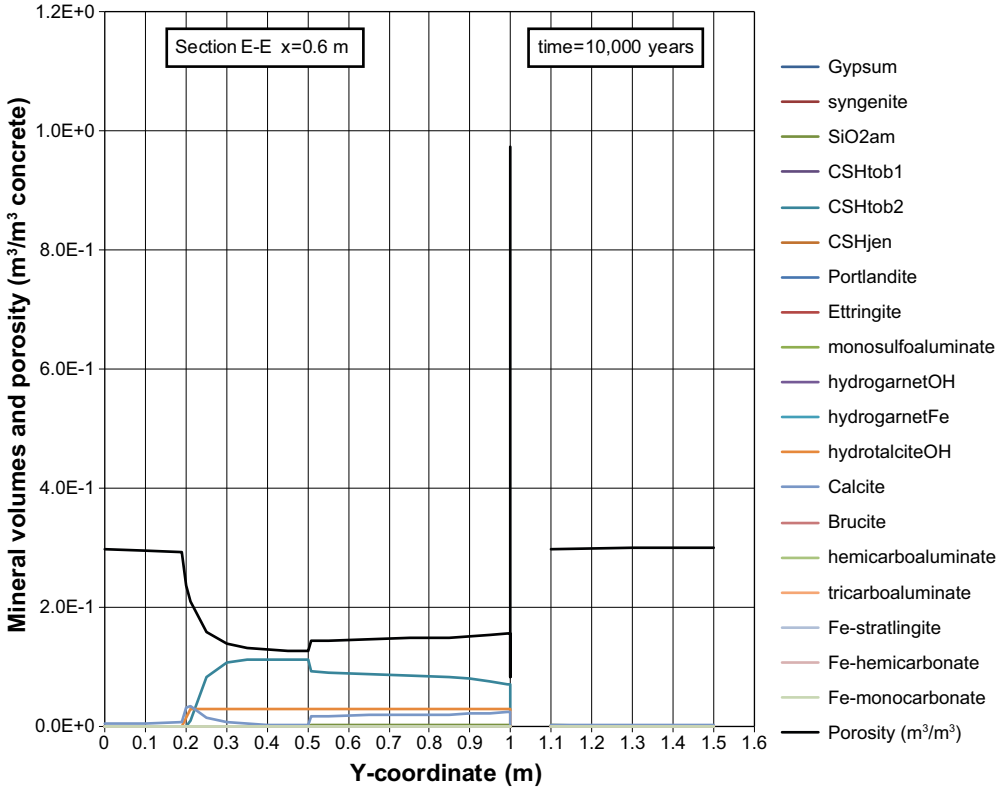

Figure F-57. *Mineral composition in concrete and calculated porosity along the vertical Section E-E at time 10,000 years, case Large12.*

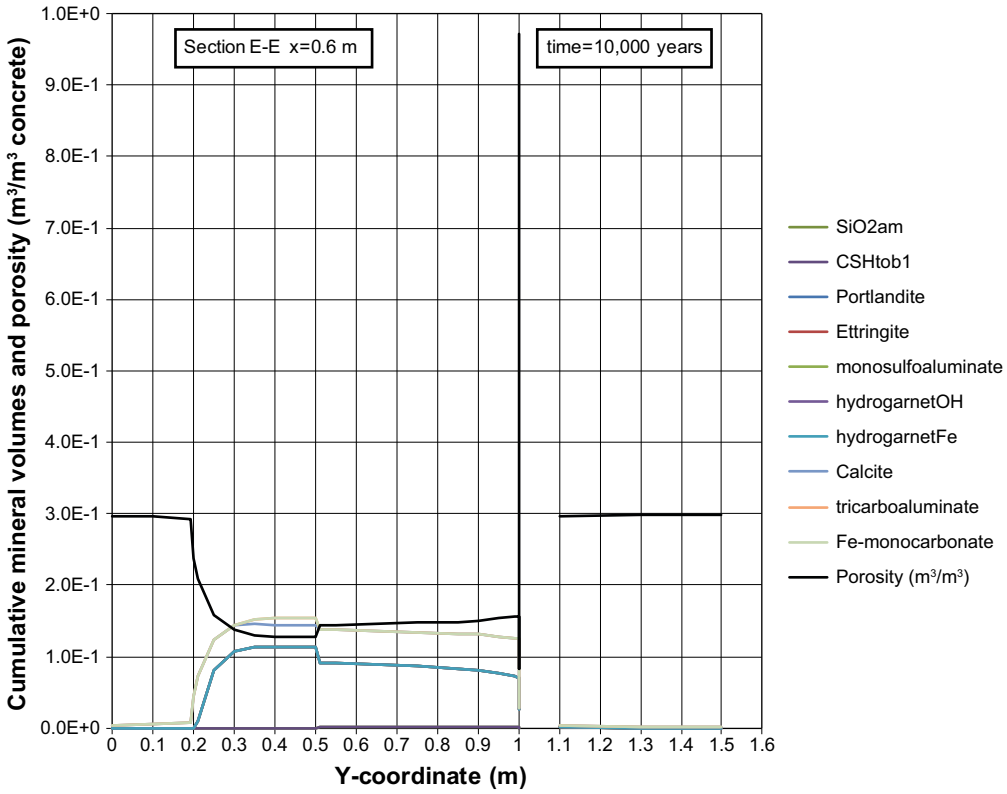

Figure F-58. *Cumulative representation of the mineral composition in concrete and calculated porosity along the vertical Section E-E at time 10,000 years, case Large12.*

Profiles along section E-E at 20,000 years

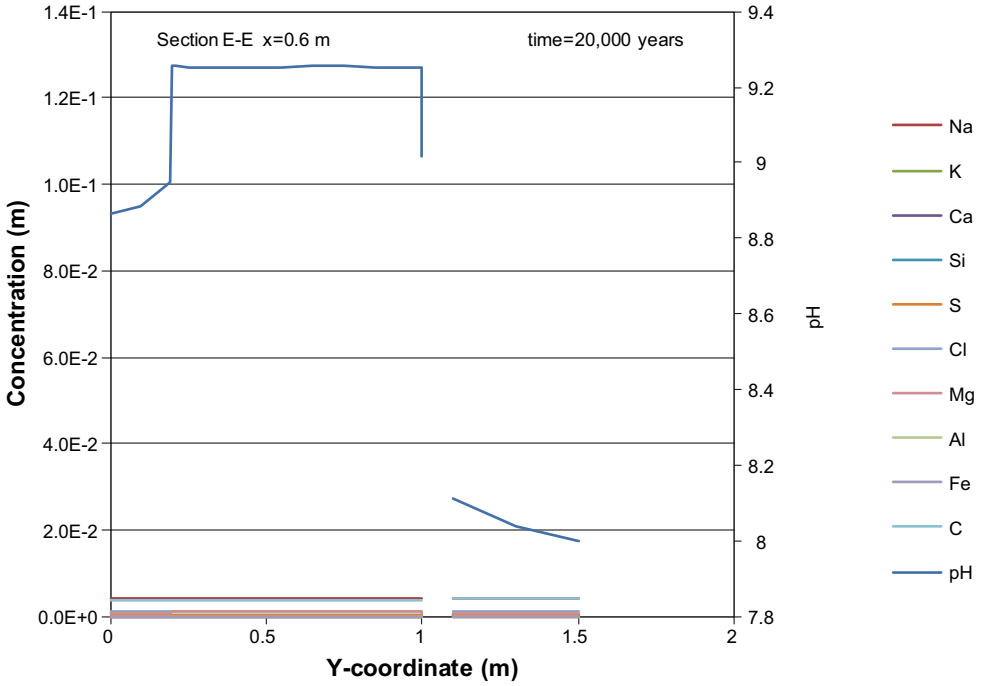

Figure F-59. *Concentration profiles of dissolved components in concrete pore water along the vertical Section E-E at time 20,000 years, case Large12. Units (mol/kg pore water).*

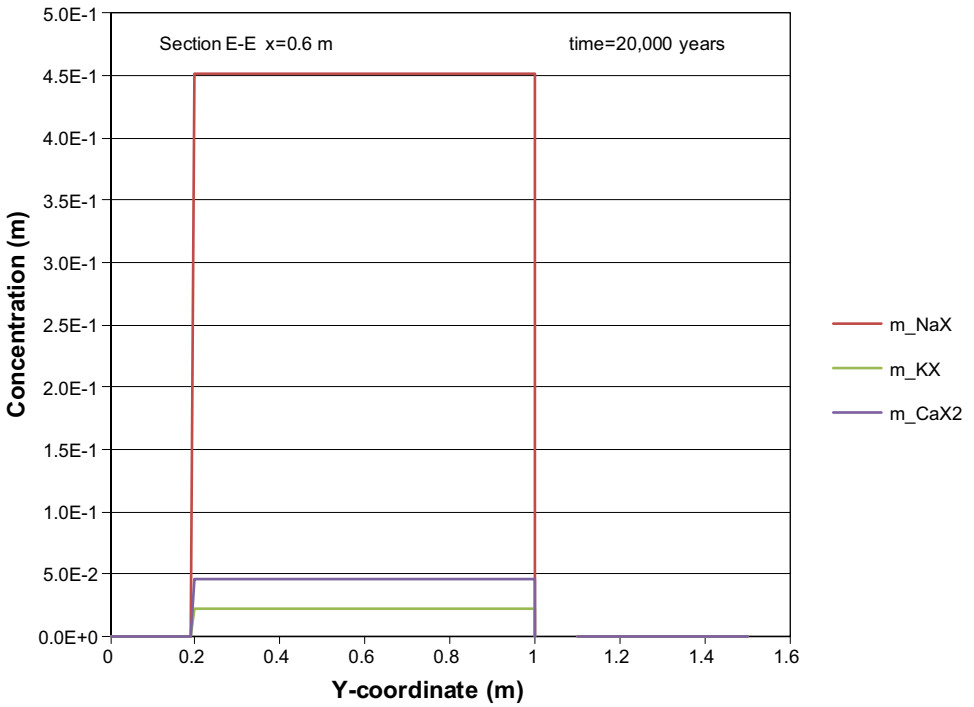

Figure F-60. *The assembly of ion exchange species in concrete along the vertical Section E-E at time 20,000 years, case Large12. Units (mol/kg pore water).*

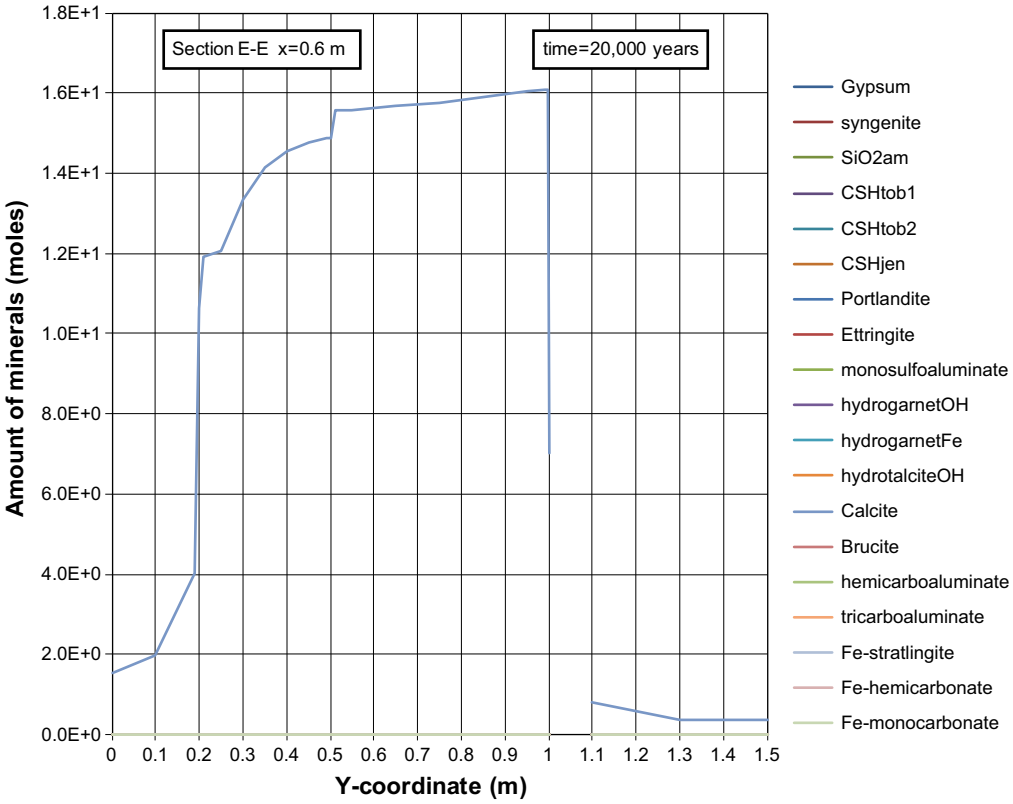

Figure F-61. *The mineral composition in concrete along the vertical Section E-E at time 20,000 years, case Large12. Units (mol/kg pore water).*

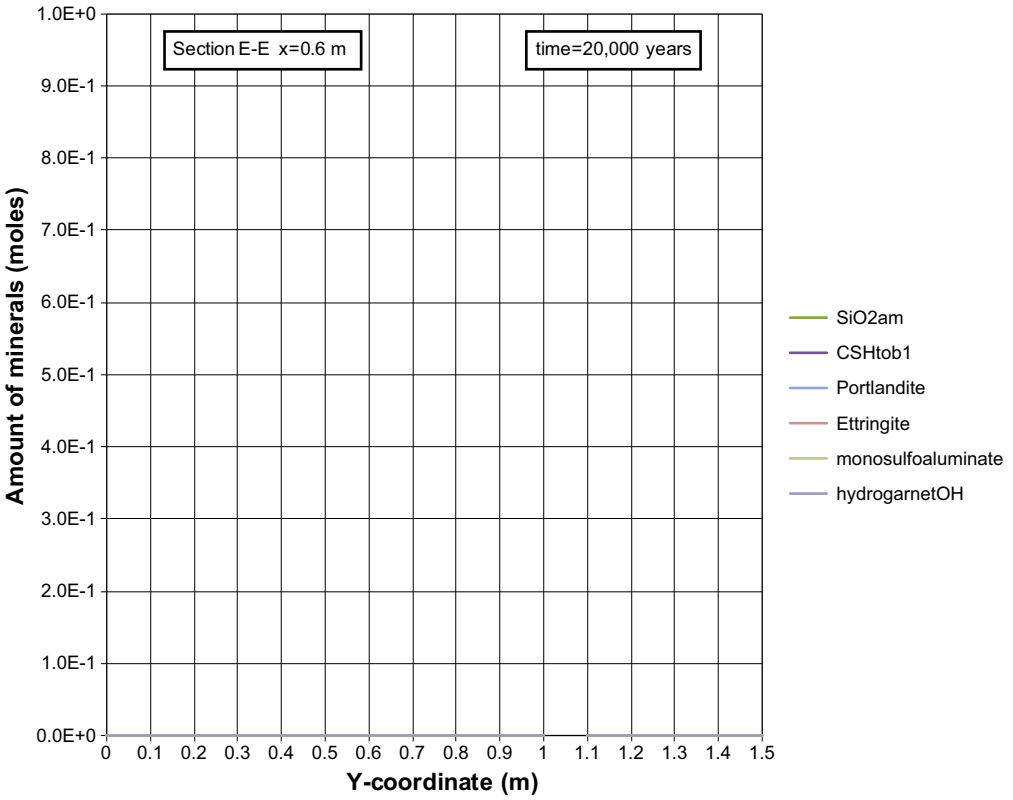

Figure F-62. *The mineral composition in concrete along the vertical Section E-E at time 20,000 years, case Large12. Units (mol/kg pore water).*

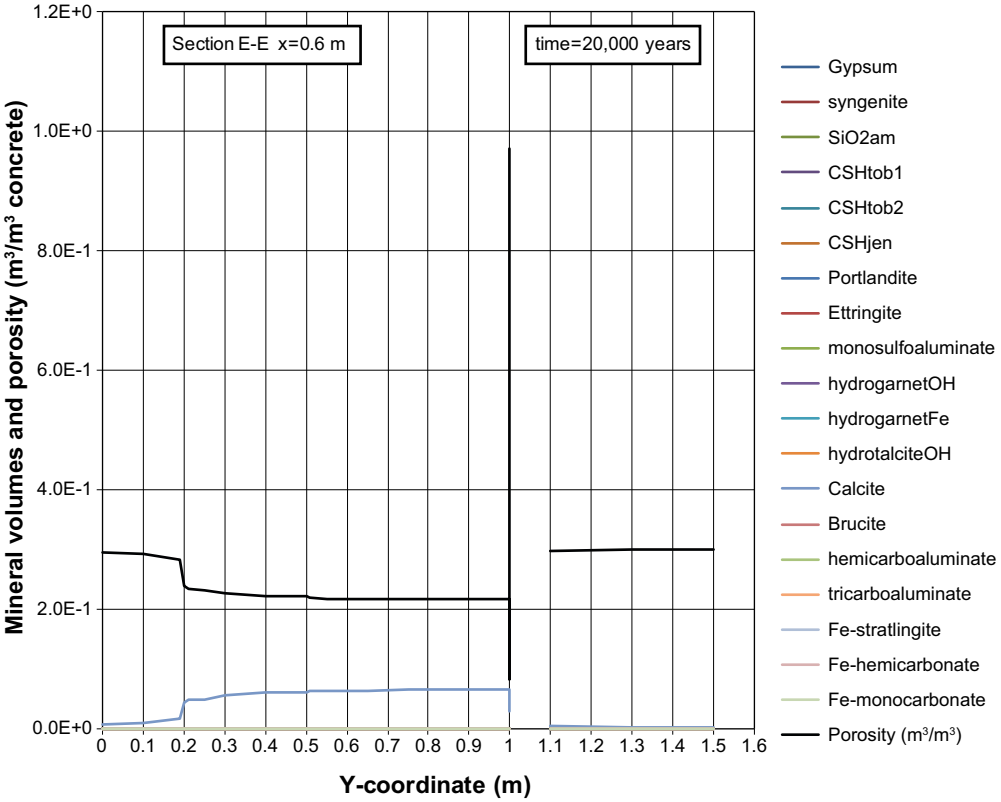

Figure F-63. *Mineral composition in concrete and calculated porosity along the vertical Section E-E at time 20,000 years, case Large12.*

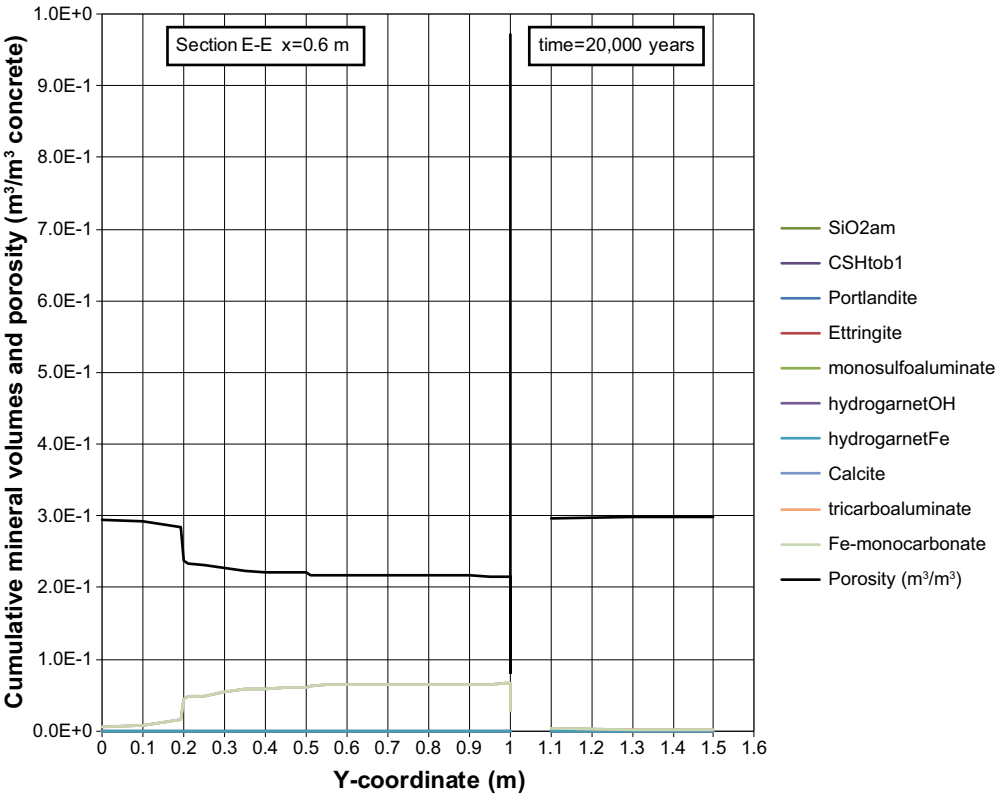

Figure F-64. *Cumulative representation of the mineral composition in concrete and calculated porosity along the vertical Section E-E at time 20,000 years, case Large12.*

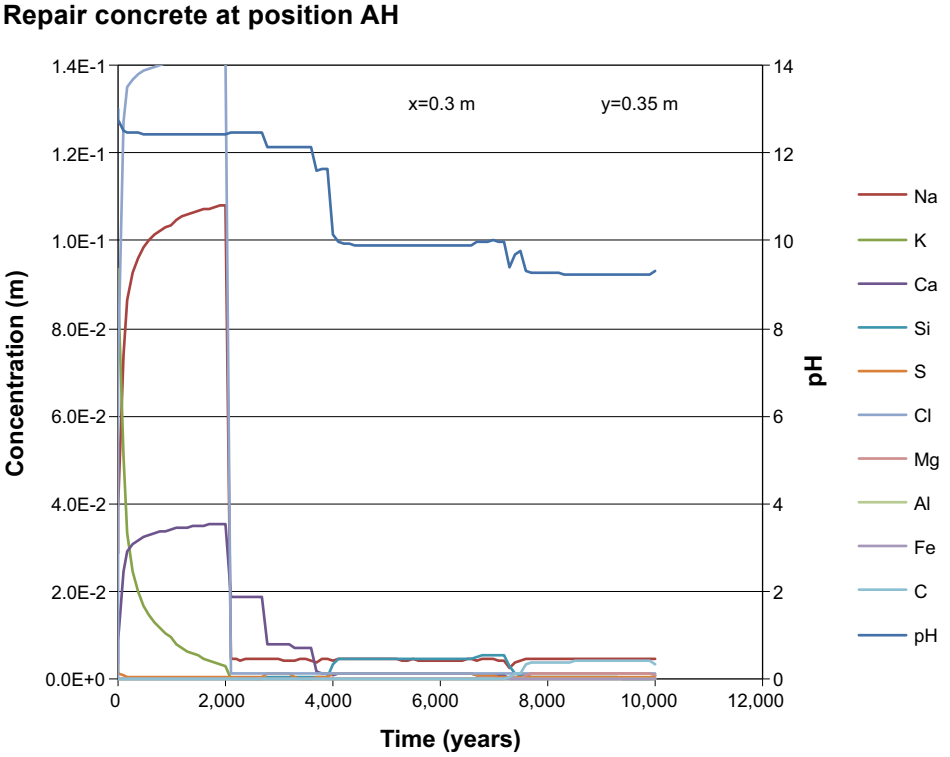

Figure F-65. *The development of the concentration of dissolved components in repair concrete pore water over time (during the first 10,000 years) at position AH, case Large12. Units (mol/kg pore water).*

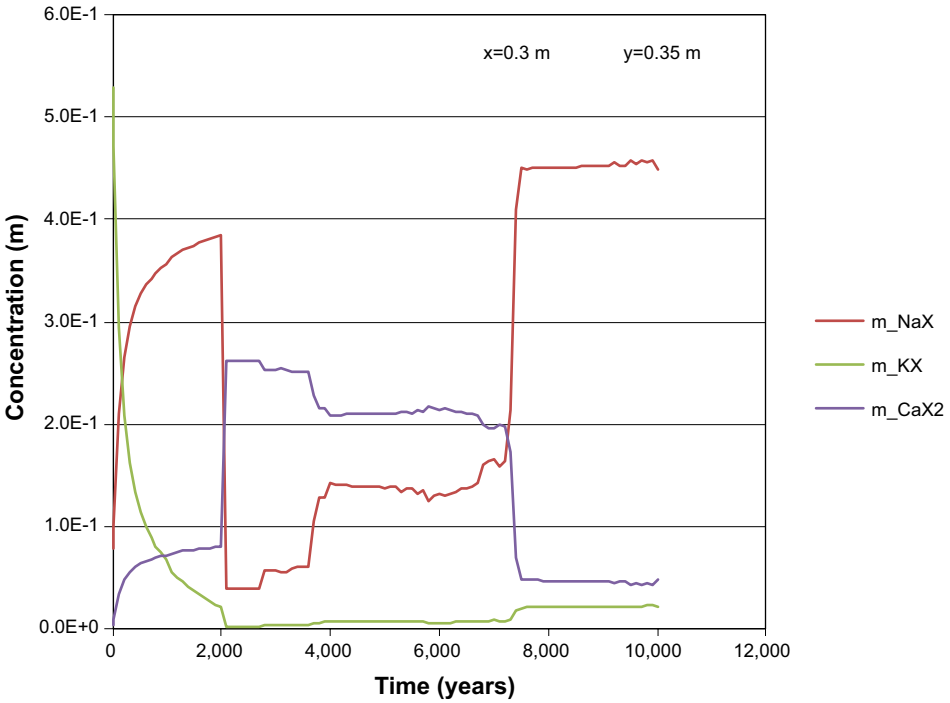

Figure F-66. *The development of the concentration of ion exchange species in repair concrete over time (during the first 10,000 years) at position AH, case Large12. Units (mol/kg pore water).*

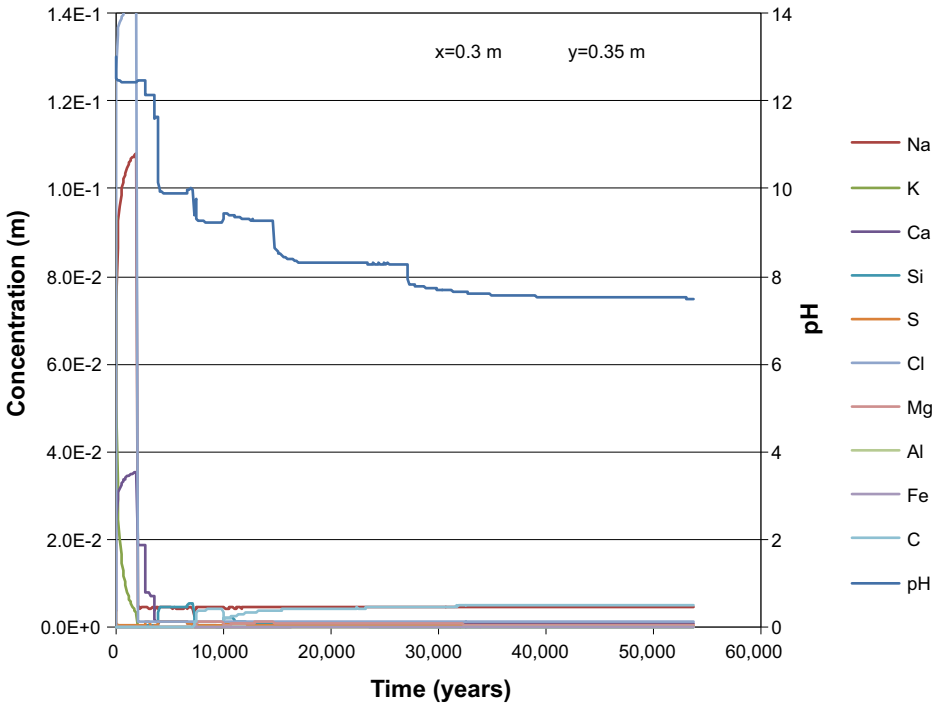

Figure F-67. *The development of the concentration of dissolved components in repair concrete pore water over time (during the first 53,800 years) at position AH, case Large12. Units (mol/kg pore water).*

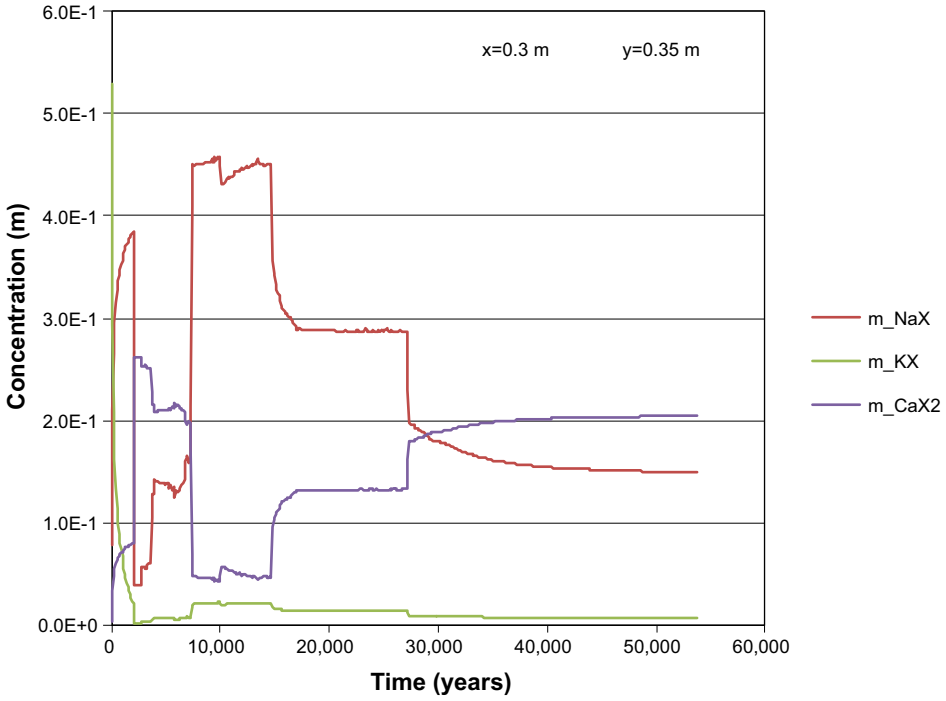

Figure F-68. *The development of the concentration of ion exchange species in repair concrete over time (during the first 53,800 years) at position AH, case Large12. Units (mol/kg pore water).*

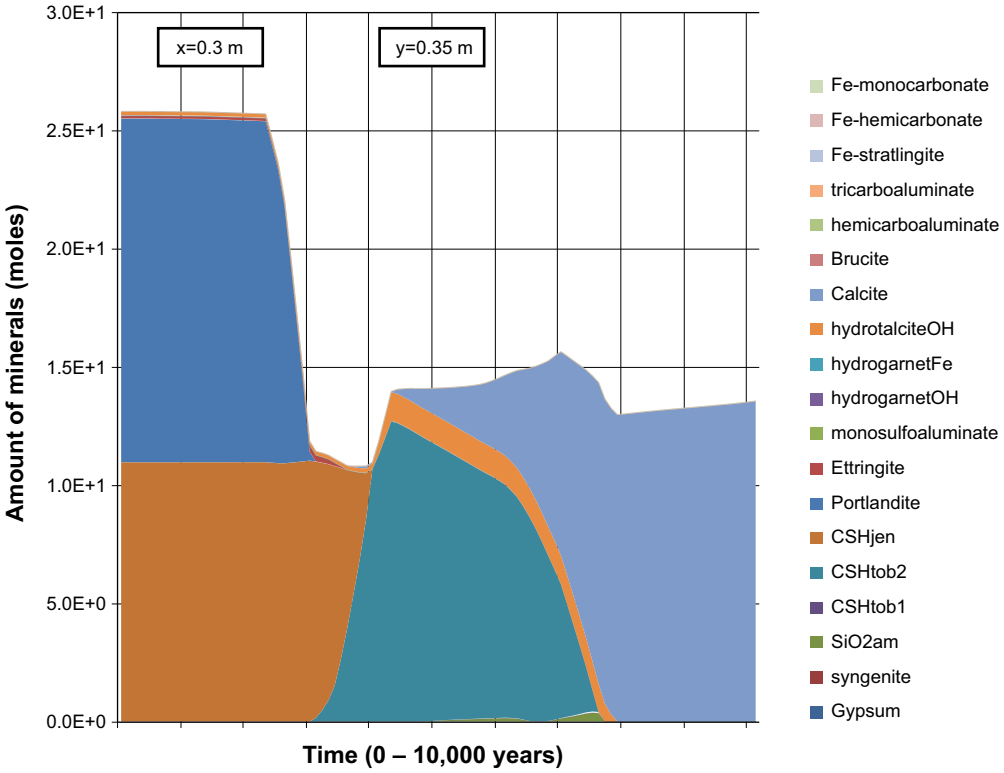

Figure F-69. *The amount of minerals in repair concrete over time at position AH, case Large12. Units (mol/kg pore water).*

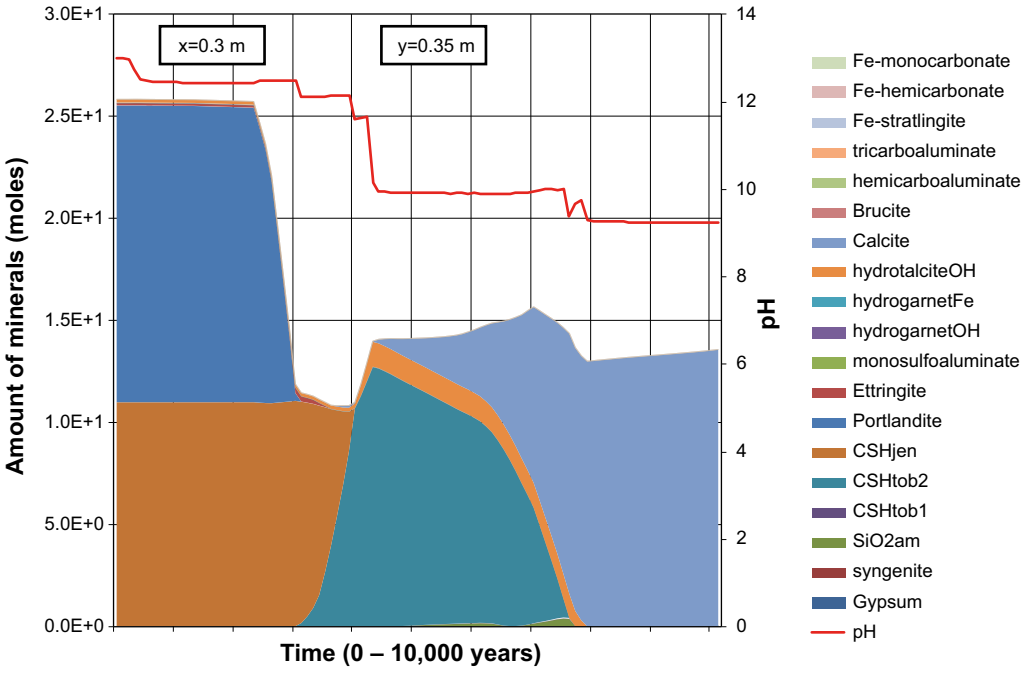

Figure F-70. *The amount of minerals in repair concrete over time at position AH, case Large12. The evolution of pH with time is also indicated. Units (mol/kg pore water).*

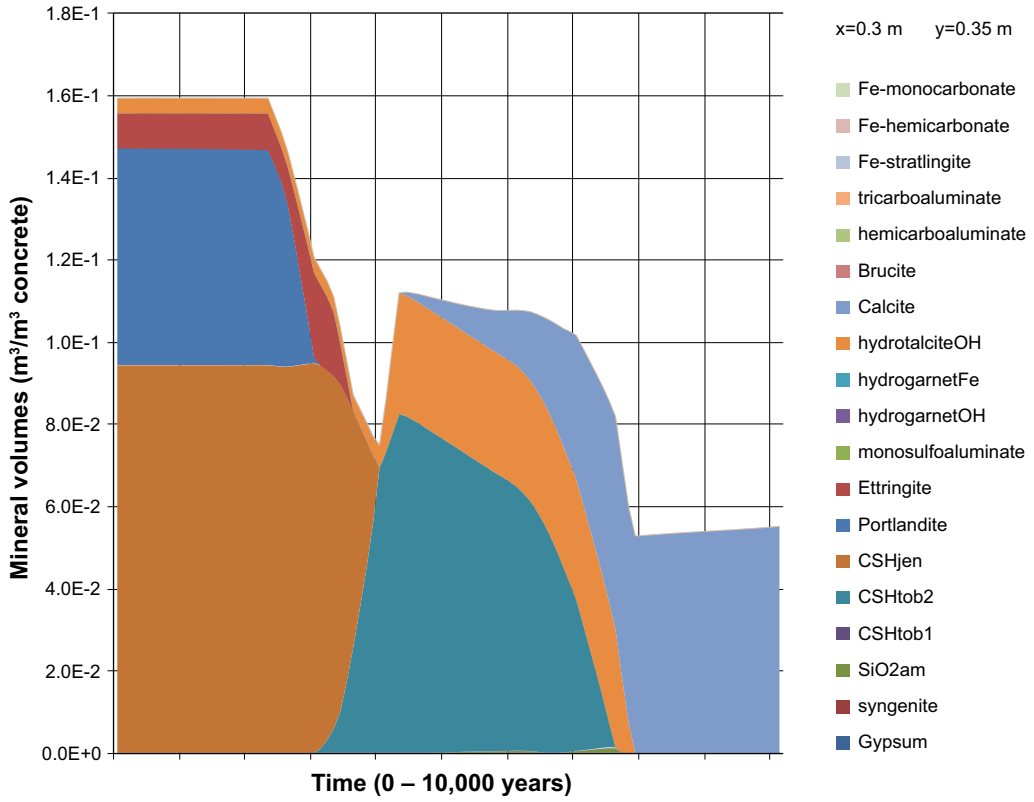

Figure F-71. *The change of mineral volumes in repair concrete over time at position AH, case Large12.*

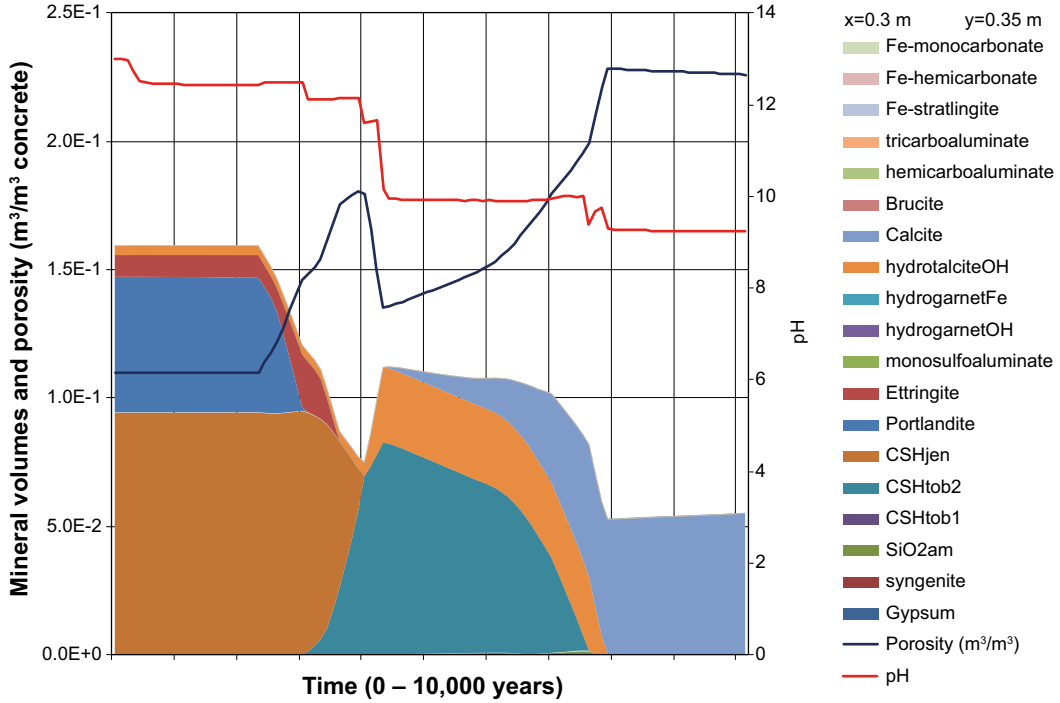

Figure F-72. *The change of mineral volumes and porosity in repair concrete over time at position AH, case Large12. The evolution of pH with time is also indicated.*

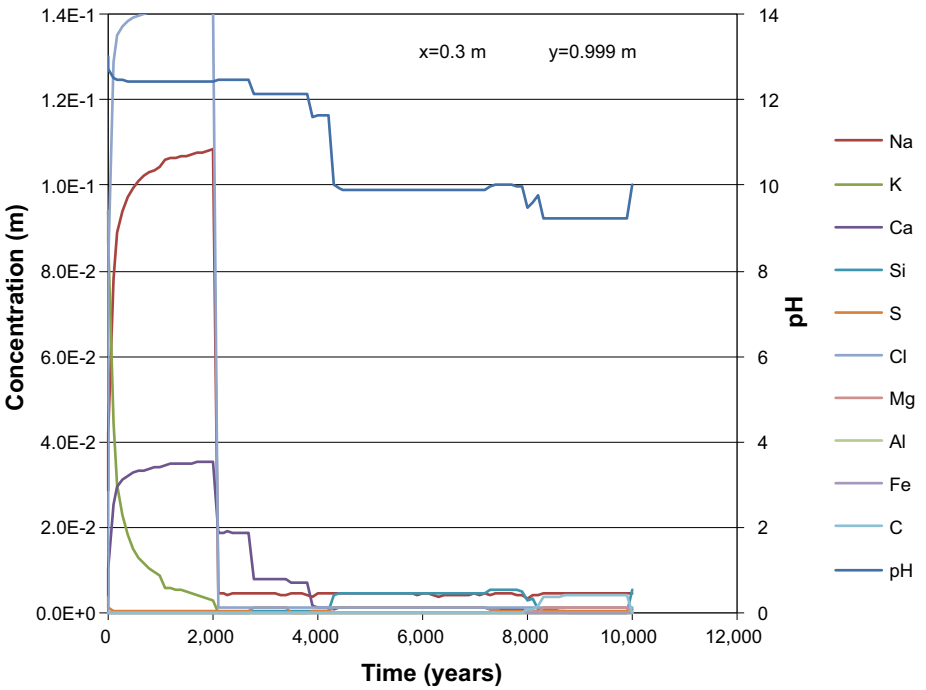

Figure F-73. *The development of the concentration of dissolved components in repair concrete pore water over time (during the first 10,000 years) at position DH, case Large12. Units (mol/kg pore water).*

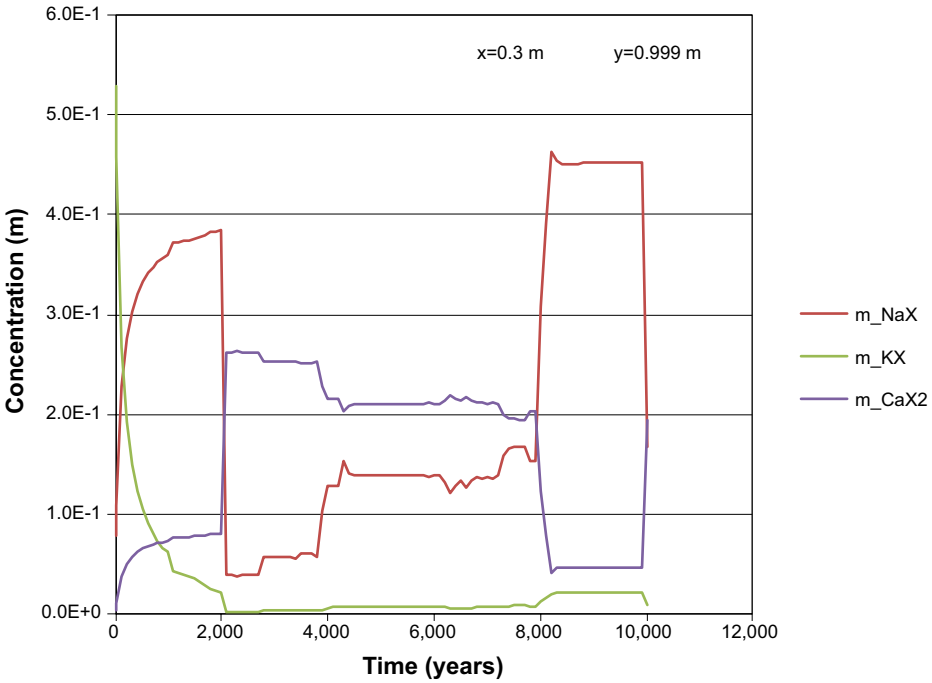

Figure F-74. *The development of the concentration of ion exchange species in repair concrete over time (during the first 10,000 years) at position DH, case Large12. Units (mol/kg pore water).*

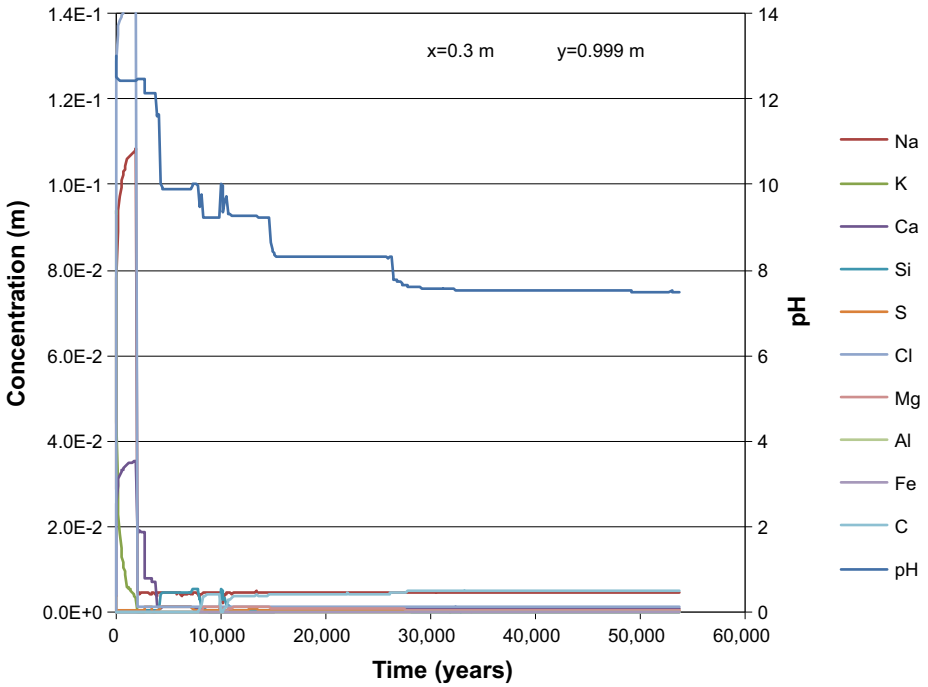

Figure F-75. *The development of the concentration of dissolved components in repair concrete pore water over time (during the first 53,800 years) at position DH, case Large12. Units (mol/kg pore water).*

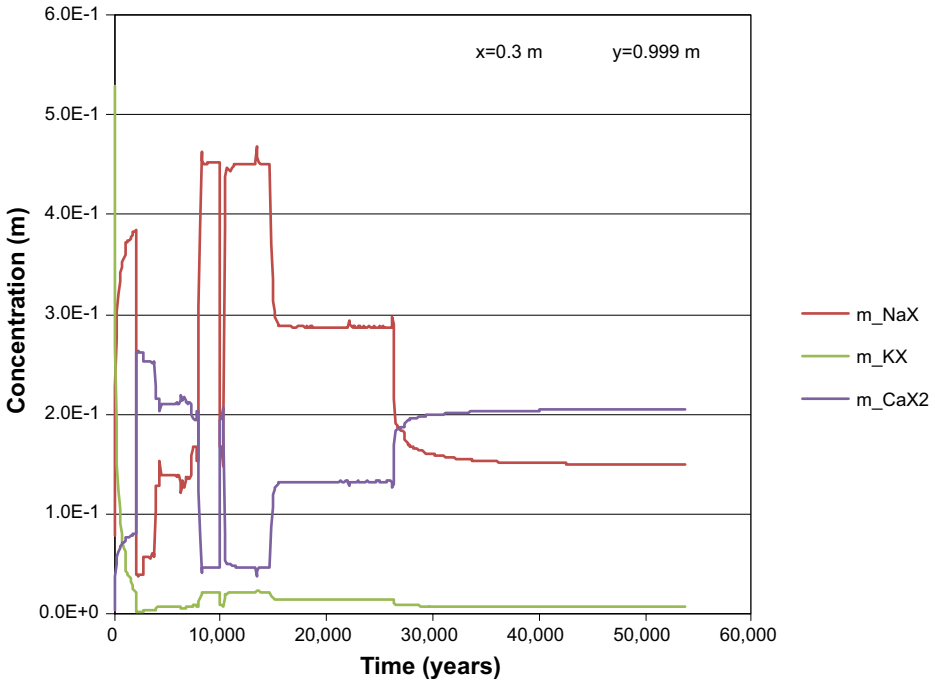

Figure F-76. *The development of the concentration of ion exchange species in repair concrete over time (during the first 53,800 years) at position DH, case Large12. Units (mol/kg pore water).*

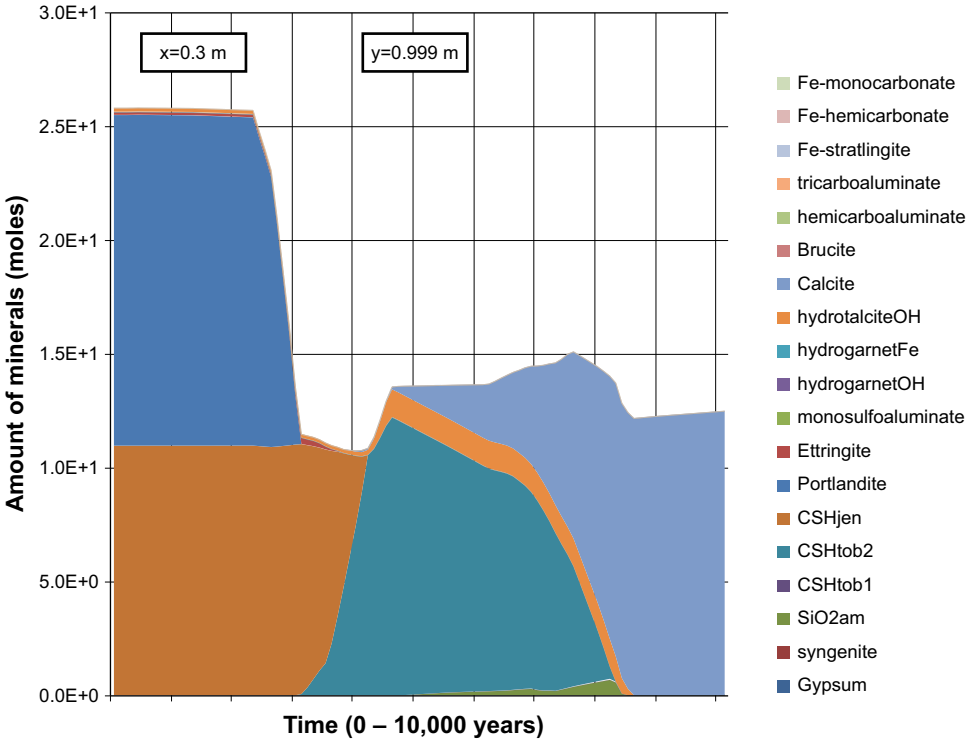

Figure F-77. *The amount of minerals in repair concrete over time at position DH, case Large12. Units (mol/kg pore water).*

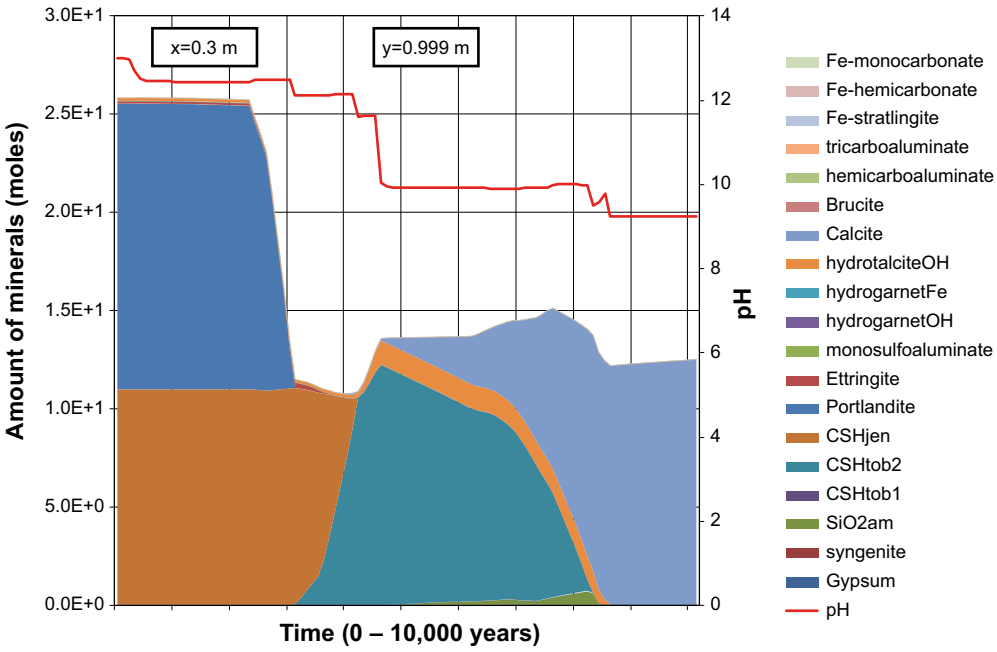

Figure F-78. *The amount of minerals in repair concrete over time at position DH, case Large12. The evolution of pH with time is also indicated. Units (mol/kg pore water).*

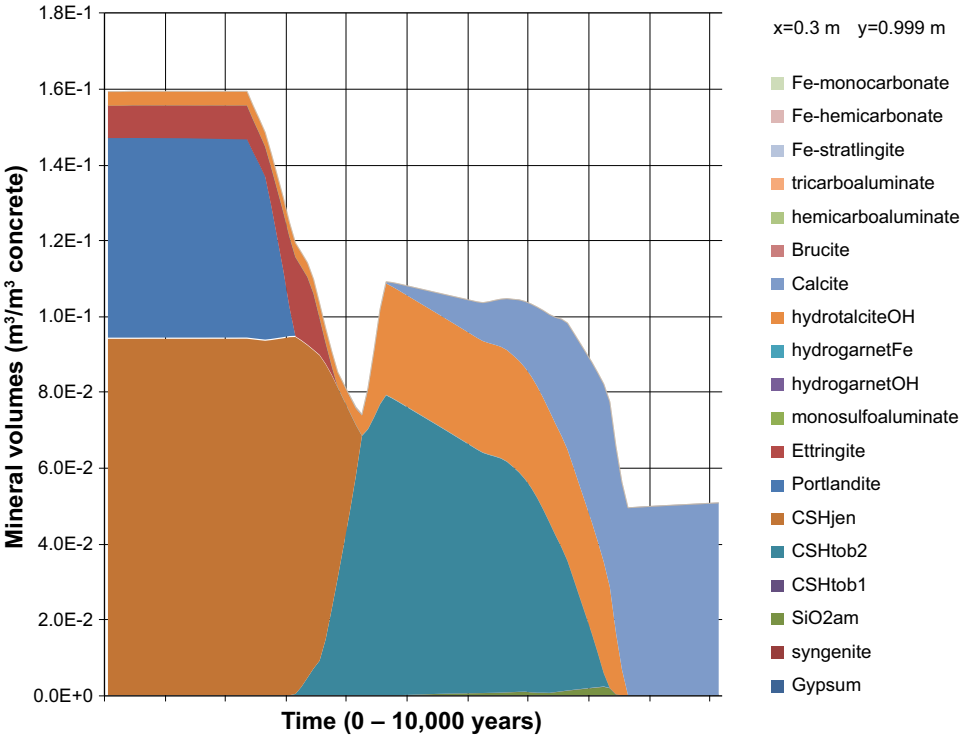

Figure F-79. *The change of mineral volumes in repair concrete over time at position DH, case Large12.*

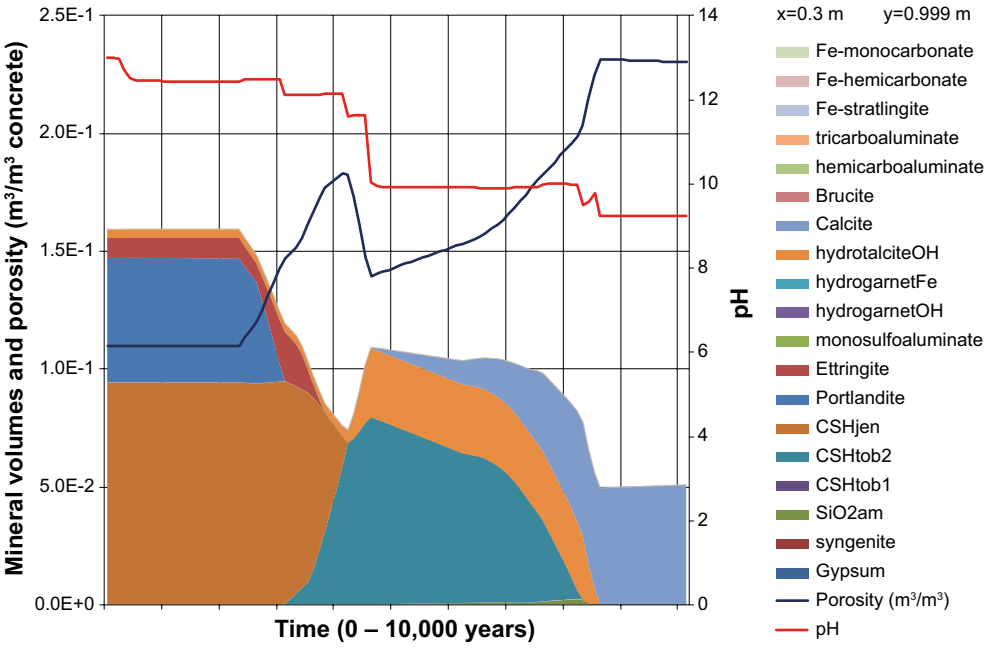

Figure F-80. *The change of mineral volumes and porosity in repair concrete over time at position DH, case Large12. The evolution of pH with time is also indicated.*

Results for Case Large9

Concrete wall at position AE

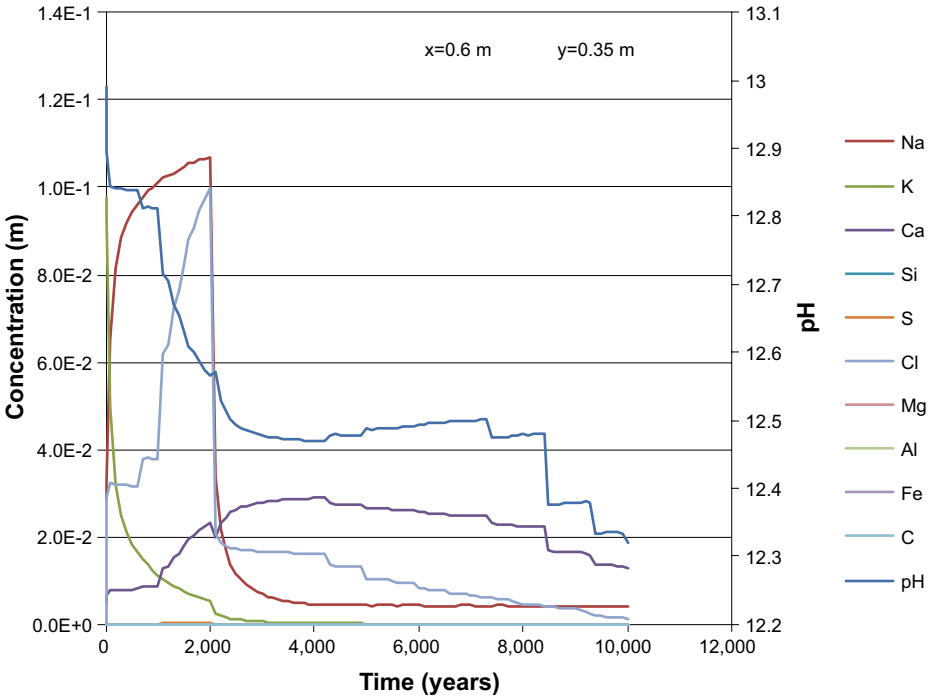

Figure G-1. *The development of the concentration of dissolved components in concrete pore water over time (during the first 10,000 years) at position AE, case Large9. Units (mol/kg pore water).*

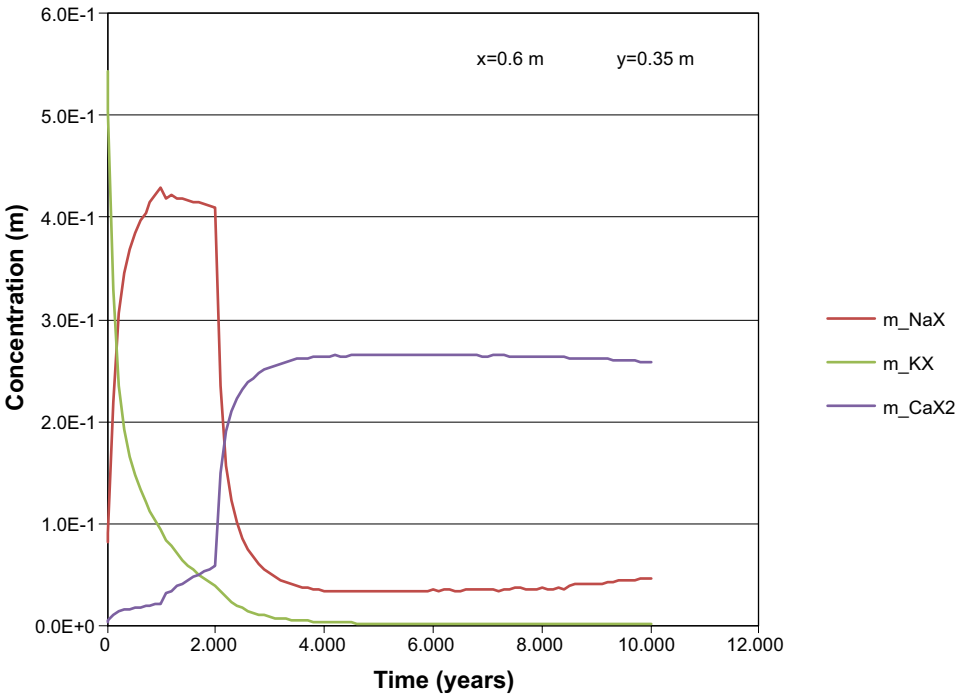

Figure G-2. *The development of the concentration of ion exchange species in concrete over time (during the first 10,000 years) at position AE, case Large9. Units (mol/kg pore water).*

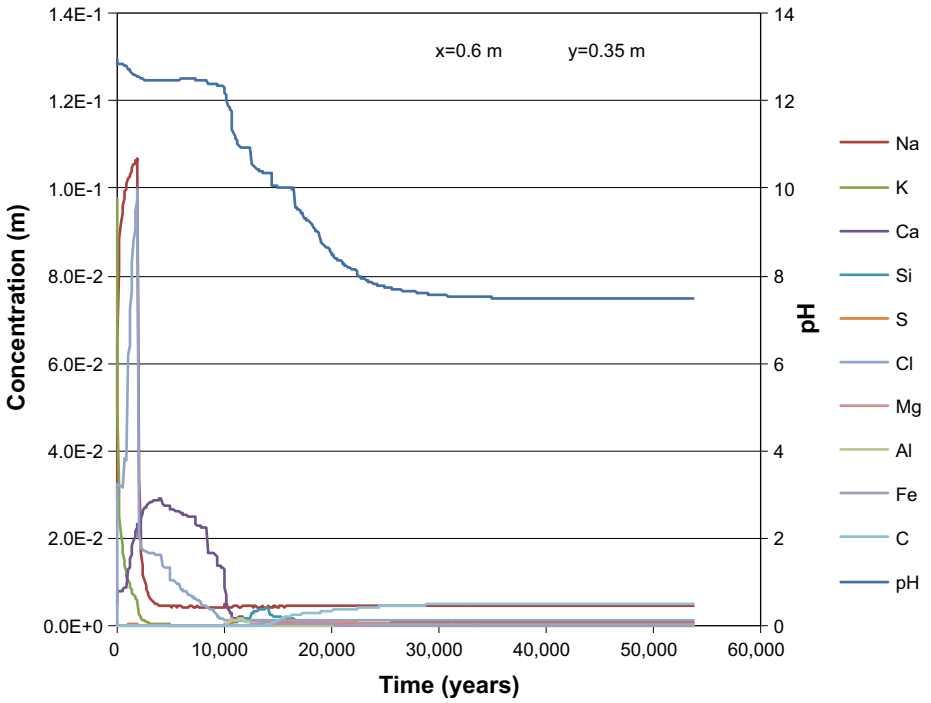

Figure G-3. *The development of the concentration of dissolved components in concrete pore water over time (during the first 53,800 years) at position AE, case Large9. Units (mol/kg pore water).*

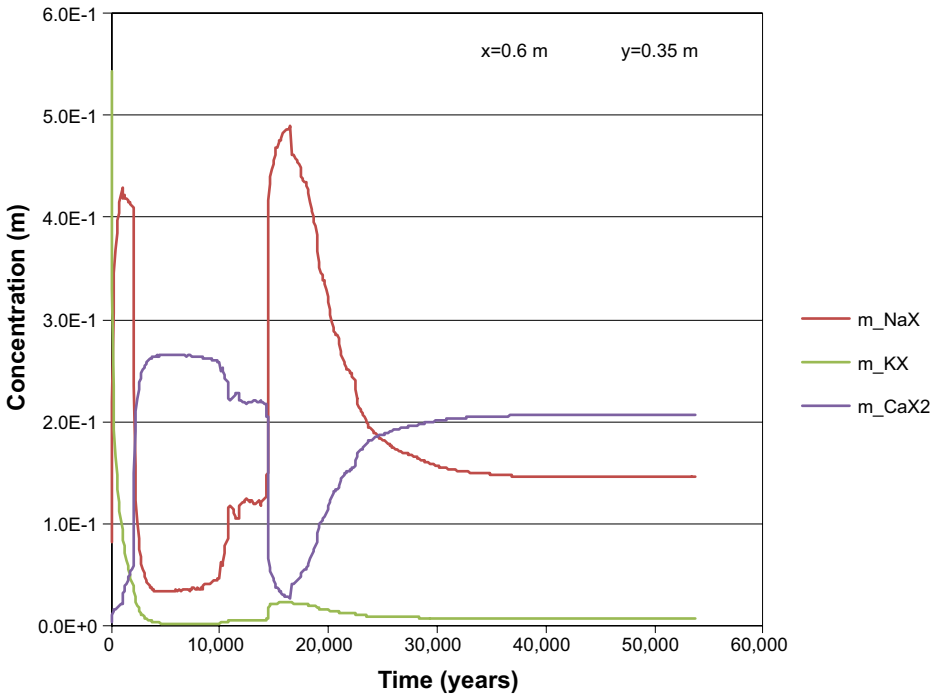

Figure G-4. *The development of the concentration of ion exchange species in concrete over time (during the first 53,800 years) at position AE, case Large9. Units (mol/kg pore water).*

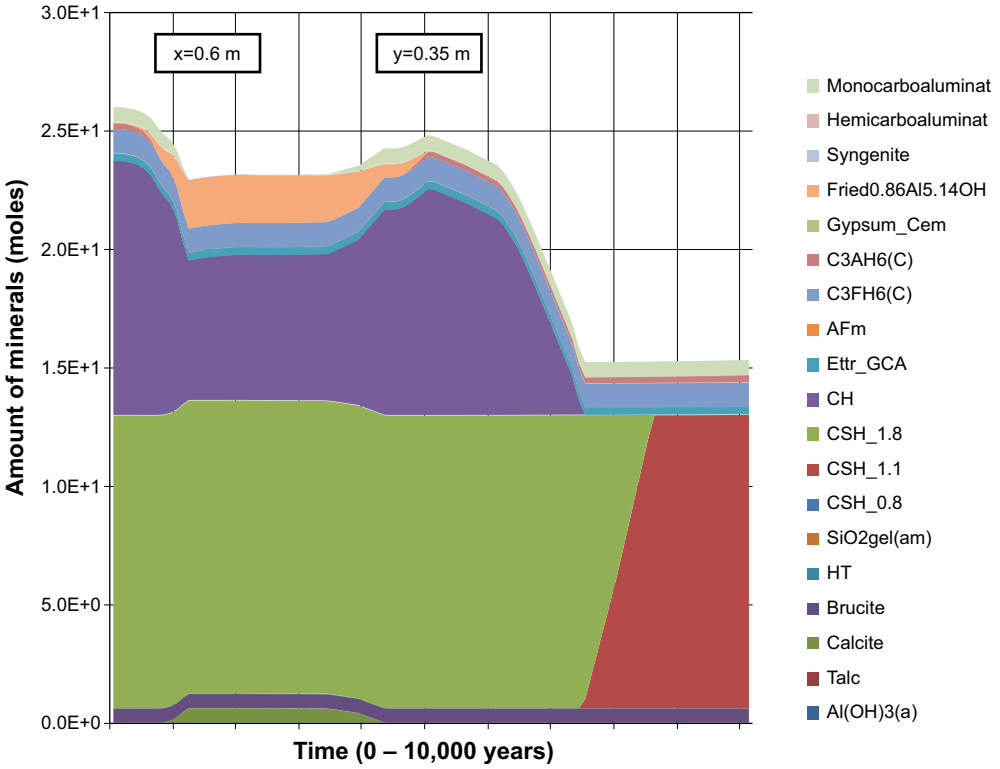

Figure G-5. *The amount of minerals in concrete over time at position AE, case Large9. Units (mol/kg pore water).*

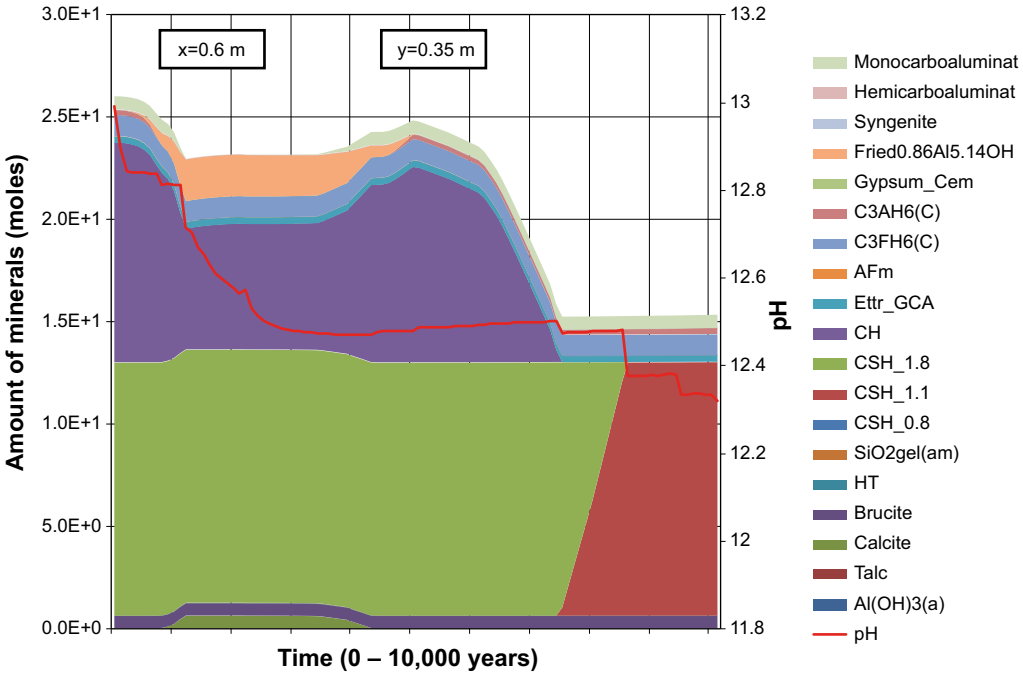

Figure G-6. *The amount of minerals in concrete over time at position AE, case Large9. The evolution of pH with time is also indicated. Units (mol/kg pore water).*

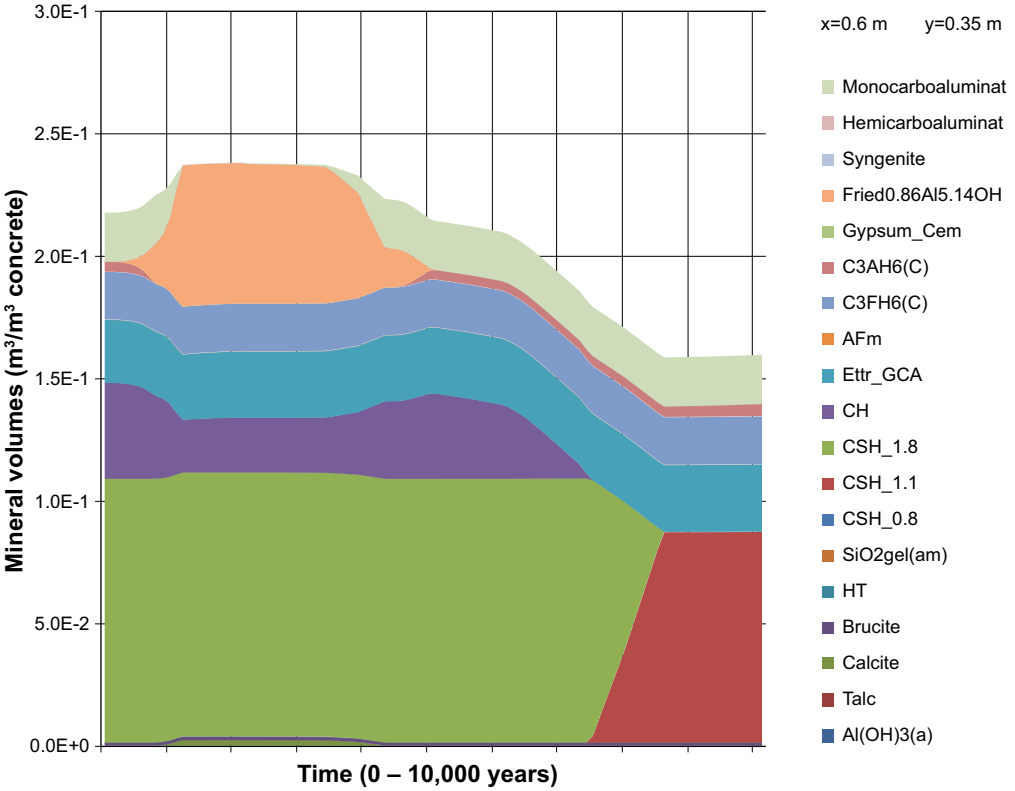

Figure G-7. *The change of mineral volumes in concrete over time at position AE, case Large9.*

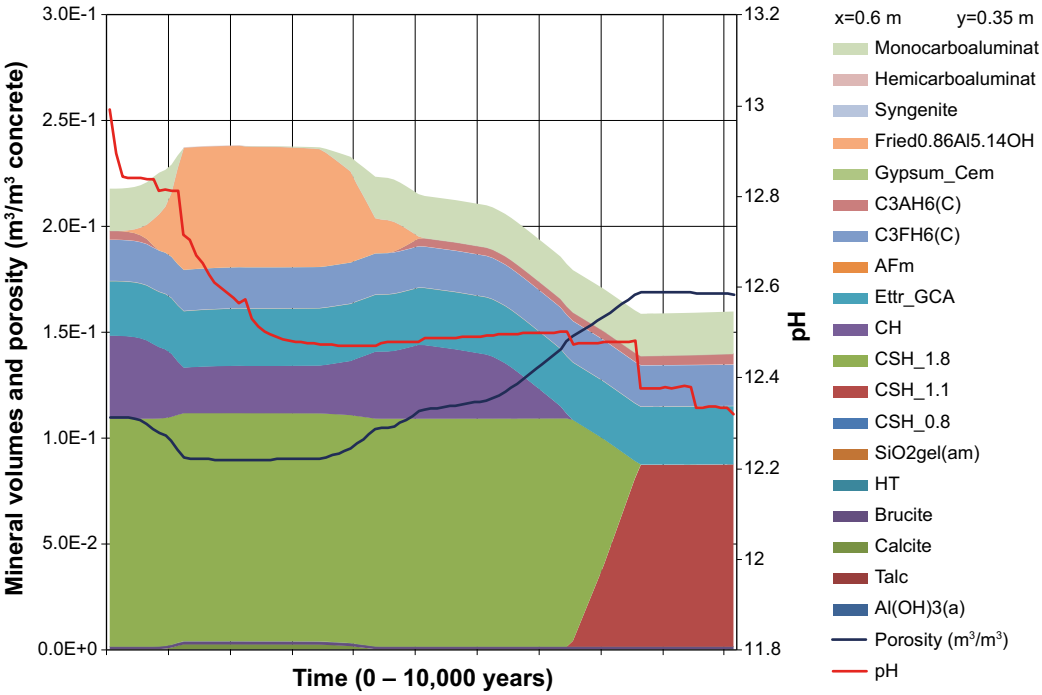

Figure G-8. *The change of mineral volumes and porosity in concrete over time at position AE, case Large9. The evolution of pH with time is also indicated.*

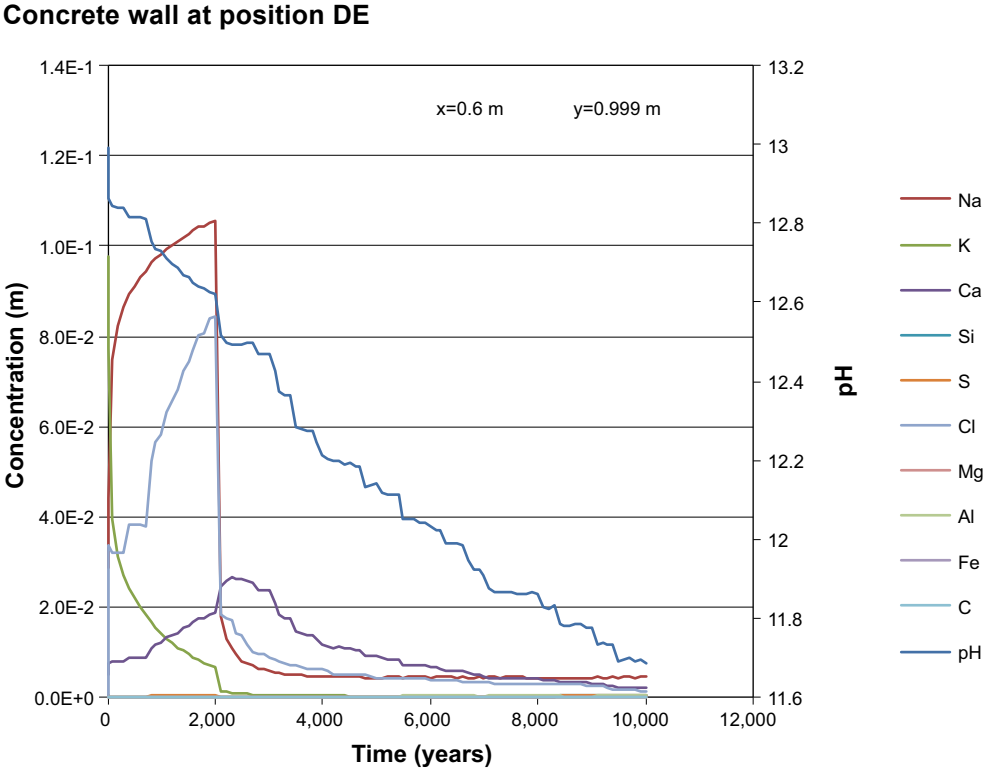

Figure G-9. *The development of the concentration of dissolved components in concrete pore water over time (during the first 10,000 years) at position DE (1 mm from an open fracture), case Large9. Units (mol/kg pore water).*

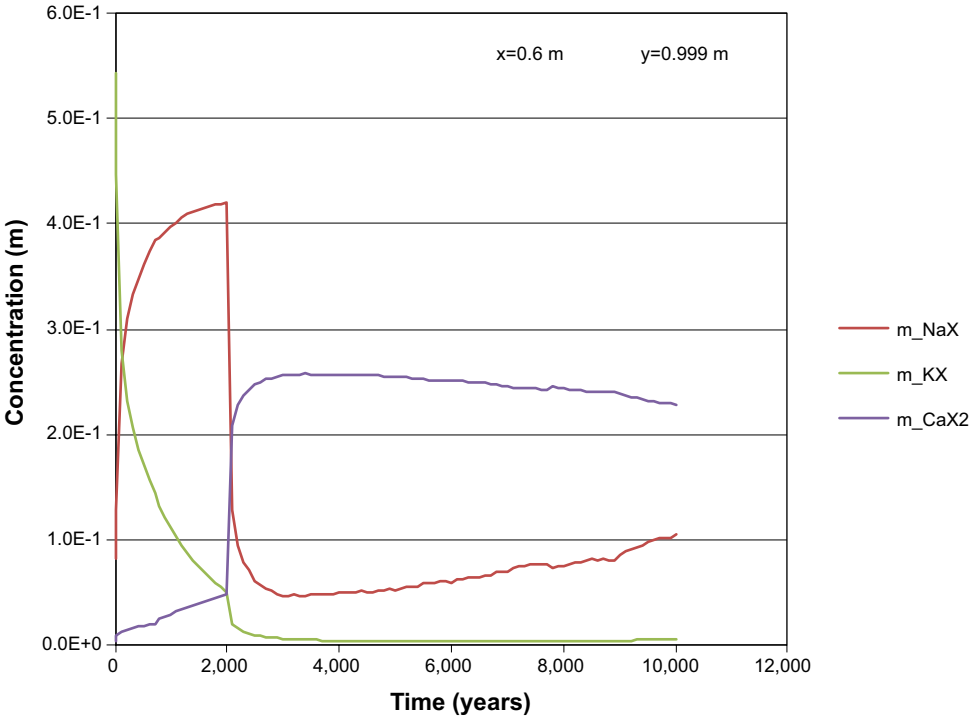

Figure G-10. *The development of the concentration of ion exchange species in concrete over time (during the first 10,000 years) at position DE (1 mm from an open fracture), case Large9. Units (mol/kg pore water).*

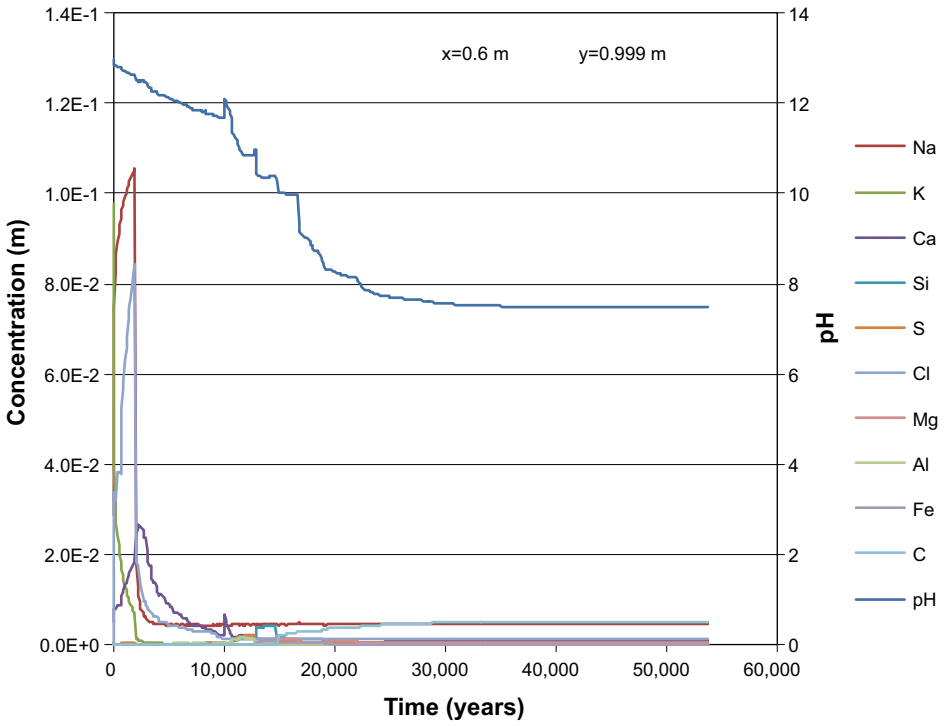

Figure G-11. *The development of the concentration of dissolved components in concrete pore water over time (during the first 53,800 years) at position DE (1 mm from an open fracture), case Large9. Units (mol/kg pore water).*

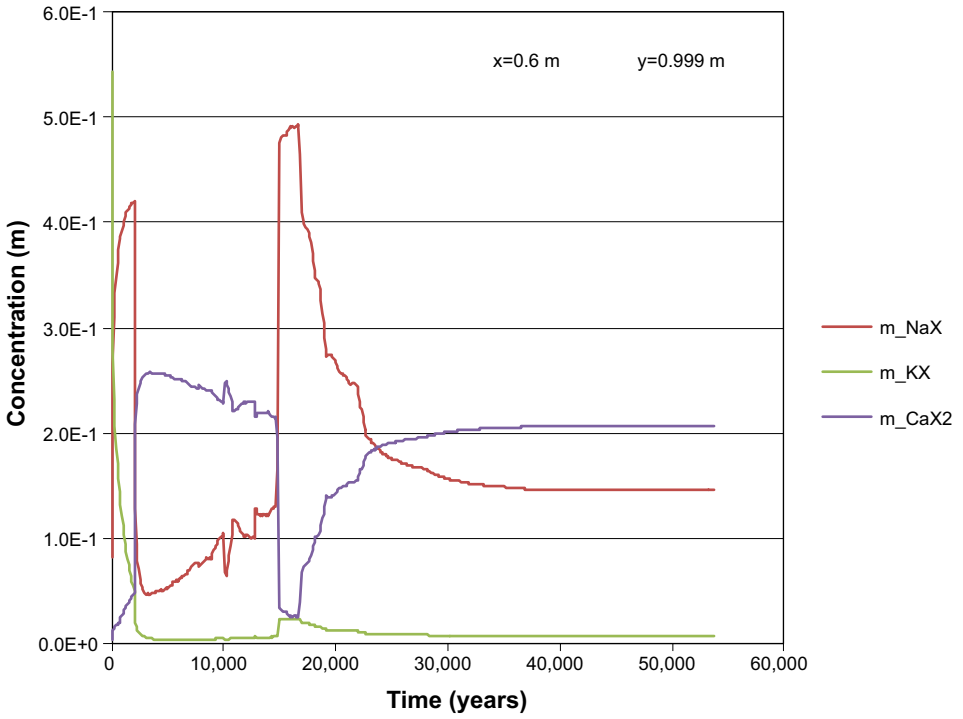

Figure G-12. *The development of the concentration of ion exchange species in concrete over time (during the first 53,800 years) at position DE (1 mm from an open fracture), case Large9. Units (mol/kg pore water).*

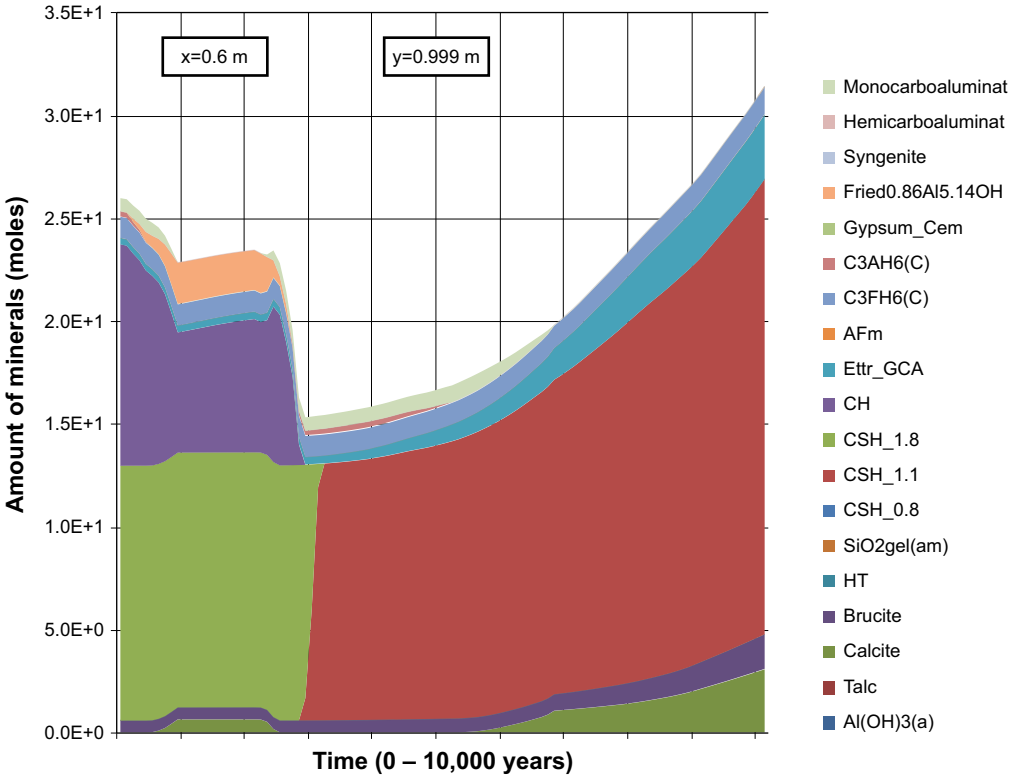

Figure G-13. *The amount of minerals in concrete over time at position DE (1 mm from an open fracture), case Large9. Units (mol/kg pore water).*

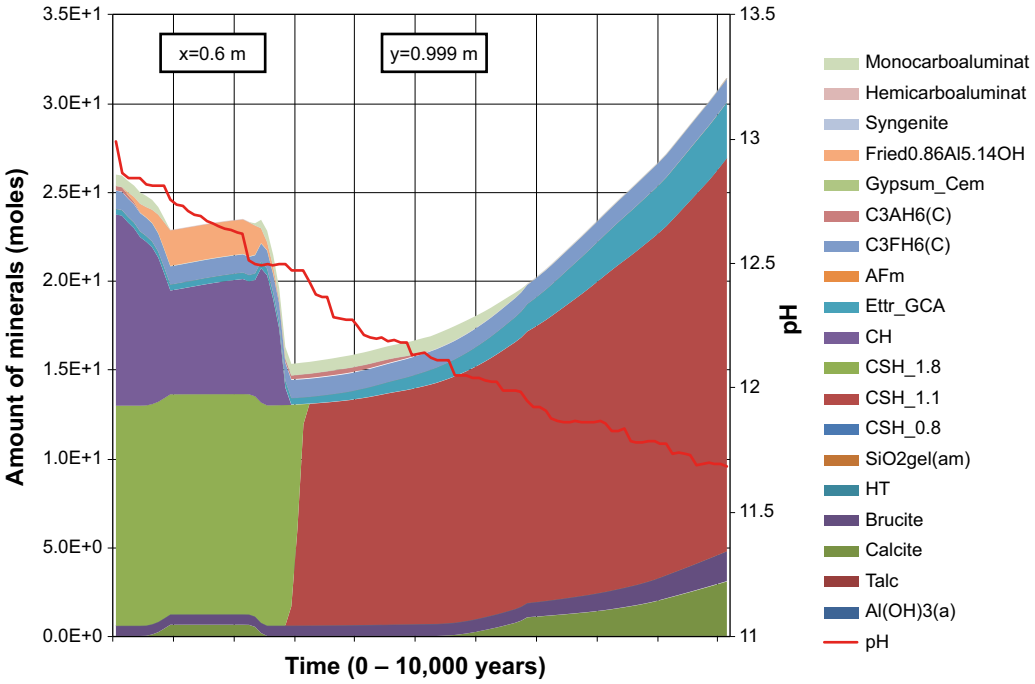

Figure G-14. *The amount of minerals in concrete over time at position DE (1 mm from an open fracture), case Large9. The evolution of pH with time is also indicated. Units (mol/kg pore water).*

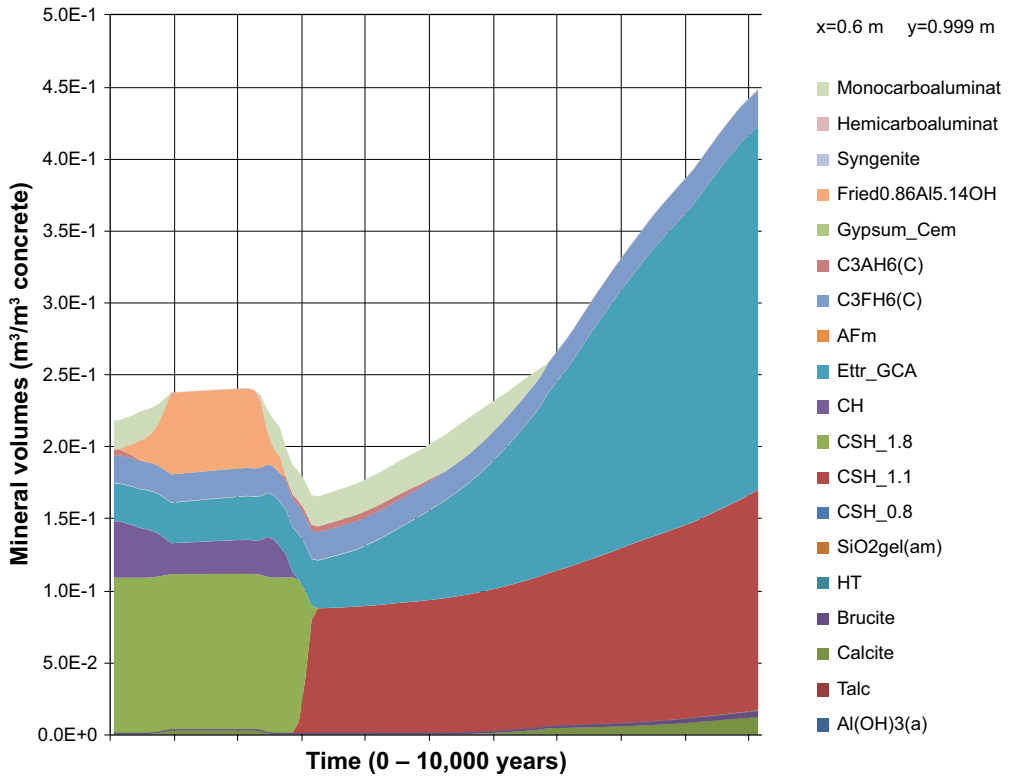

Figure G-15. *The change of mineral volumes in concrete over time at position DE (1 mm from an open fracture), case Large9.*

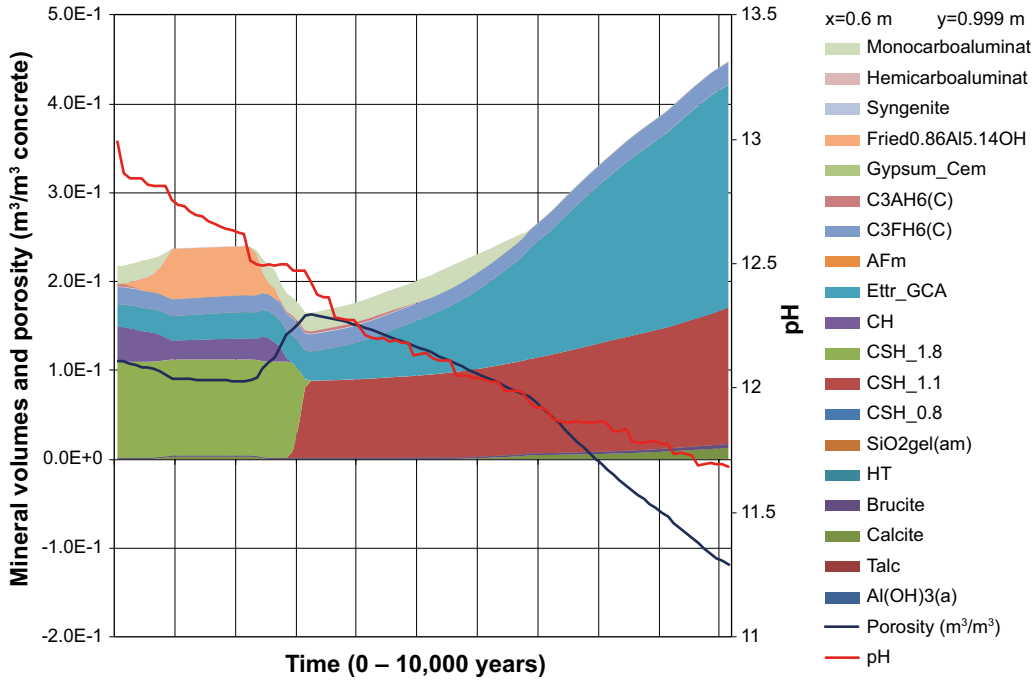

Figure G-16. *The change of mineral volumes and porosity in concrete over time at position DE (1 mm from an open fracture), case Large9. The evolution of pH with time is also indicated. The results indicate clogging of the porosity at 8,000 years giving an artificial negative value of the porosity.*

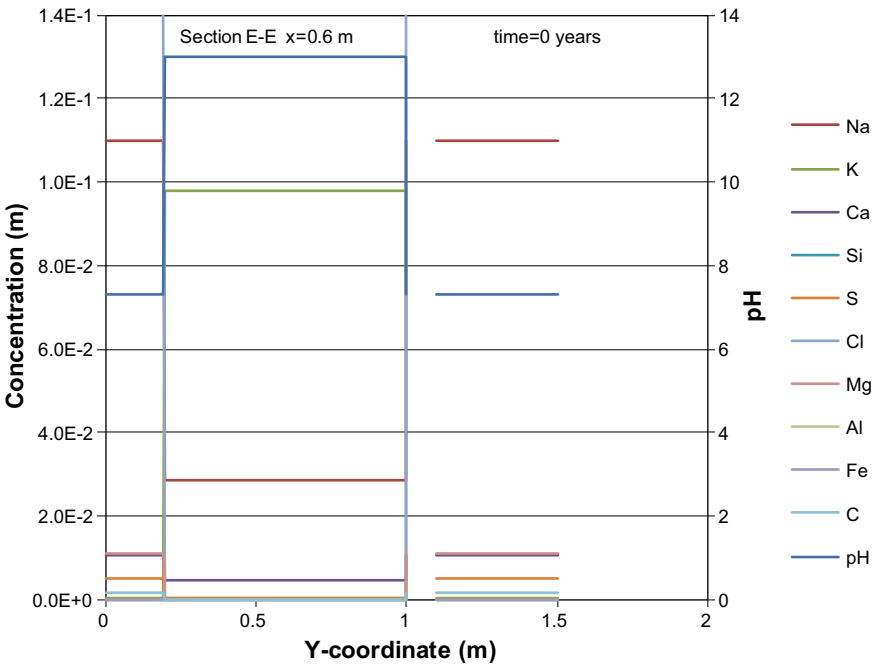

Figure G-17. *Concentration profiles of dissolved components in concrete pore water along the vertical Section E-E at time 0 years, case Large9. Units (mol/kg pore water).*

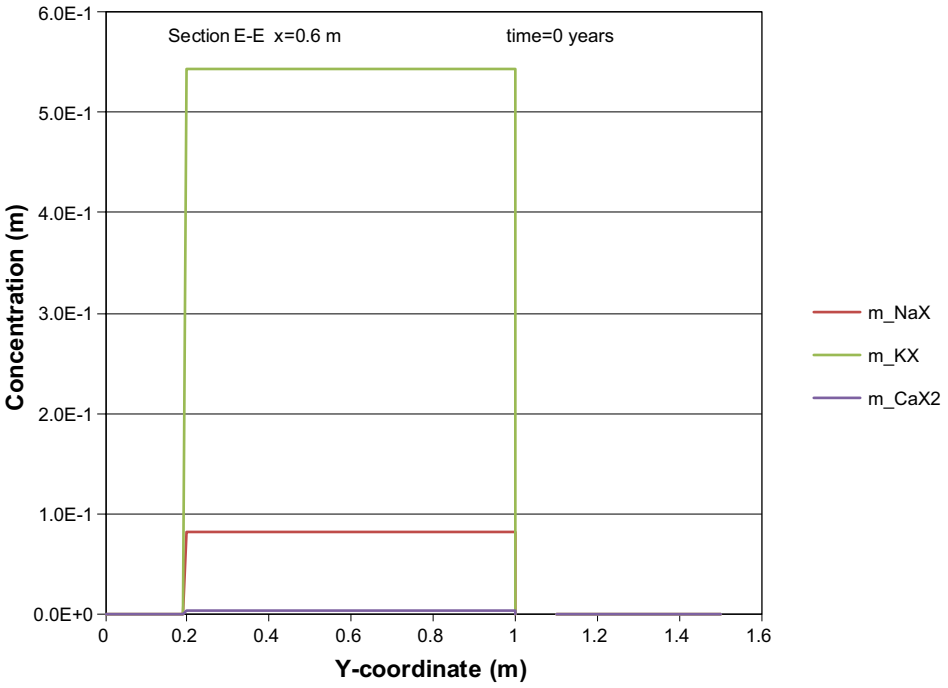

Figure G-18. *The assembly of ion exchange species in concrete along the vertical Section E-E at time 0 years, case Large9. Units (mol/kg pore water).*

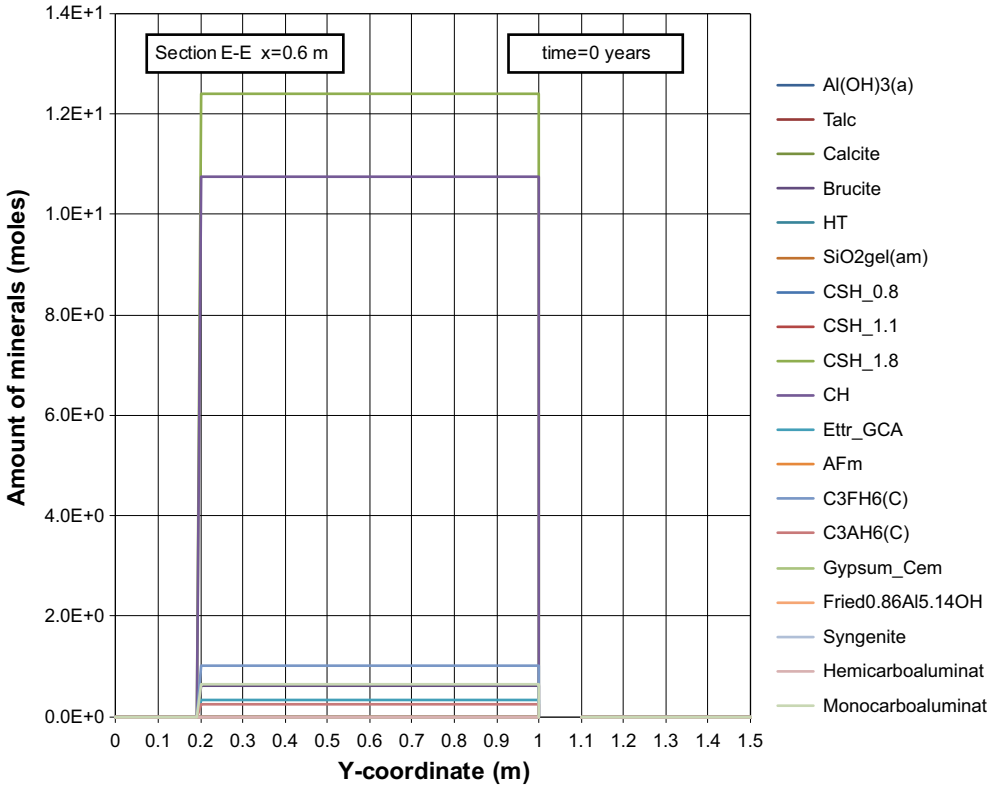

Figure G-19. *The mineral composition in concrete along the vertical Section E-E at time 0 years, case Large9. Units (mol/kg pore water).*

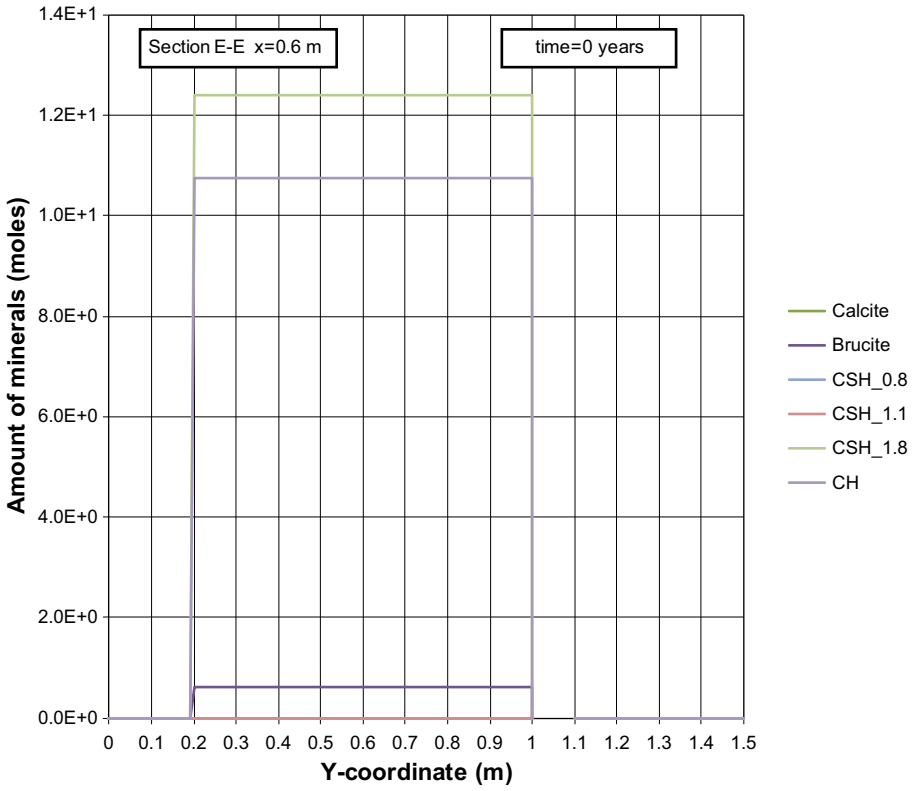

Figure G-20. *The mineral composition in concrete along the vertical Section E-E at time 0 years, case Large9. Units (mol/kg pore water).*

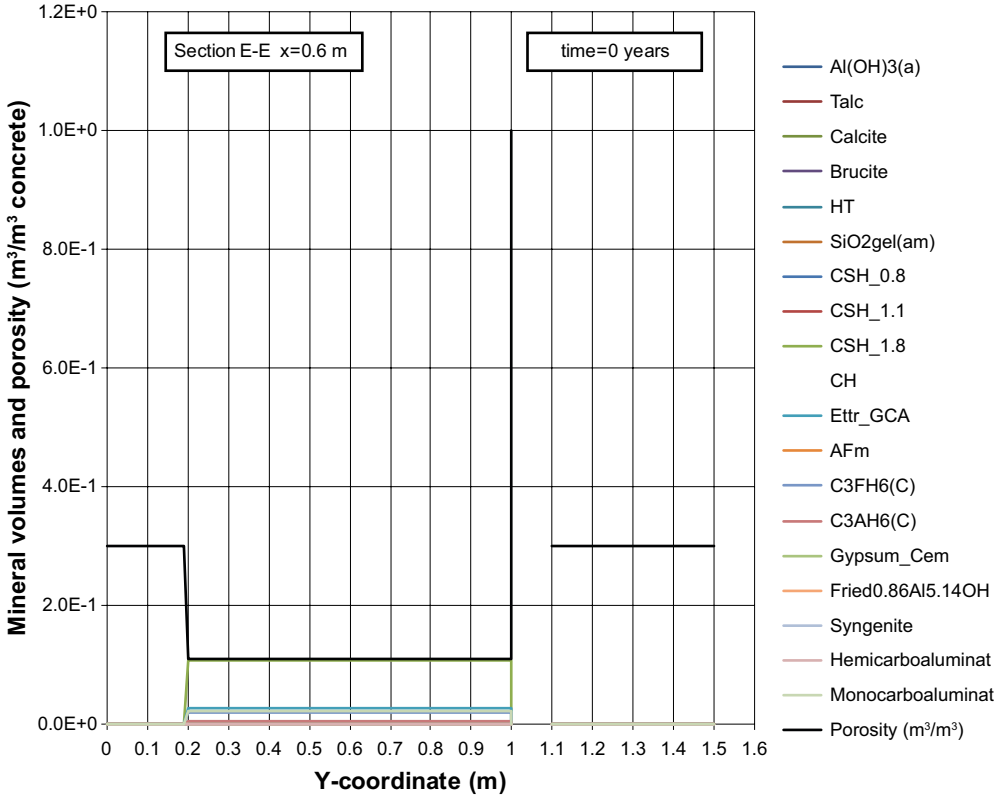

Figure G-21. *Mineral composition in concrete and calculated porosity along the vertical Section E-E at time 0 years, case Large9.*

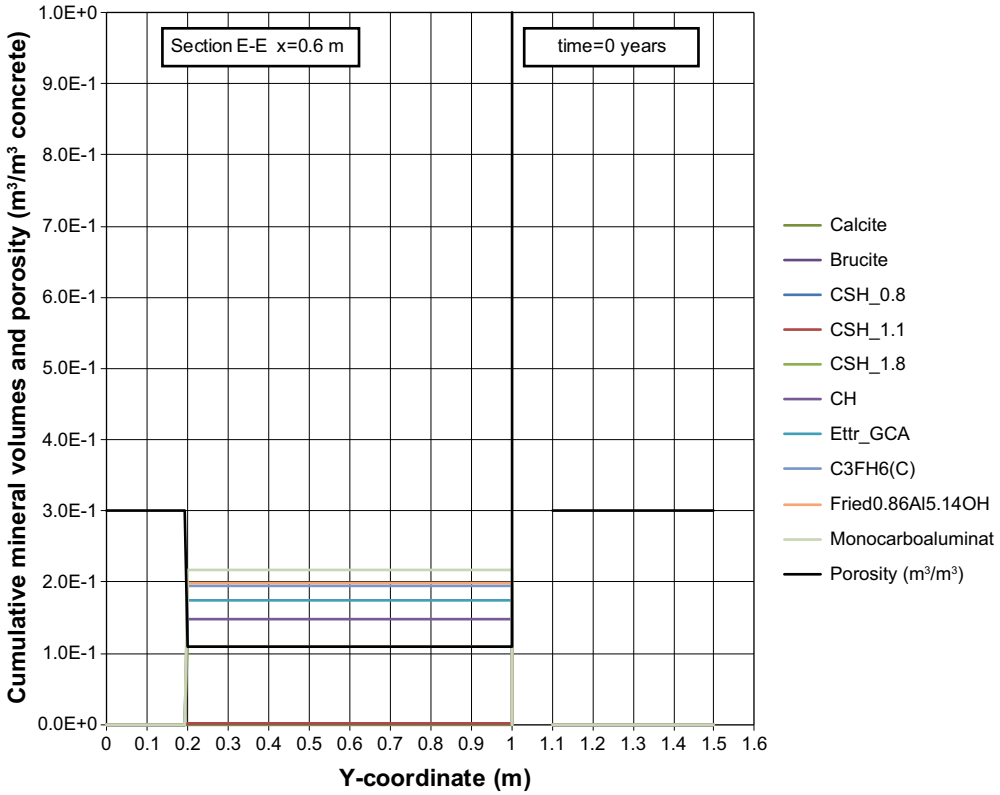

Figure G-22. *Cumulative representation of the mineral composition in concrete and calculated porosity along the vertical Section E-E at time 0 years, case Large9.*

Profiles along section E-E at 100 years

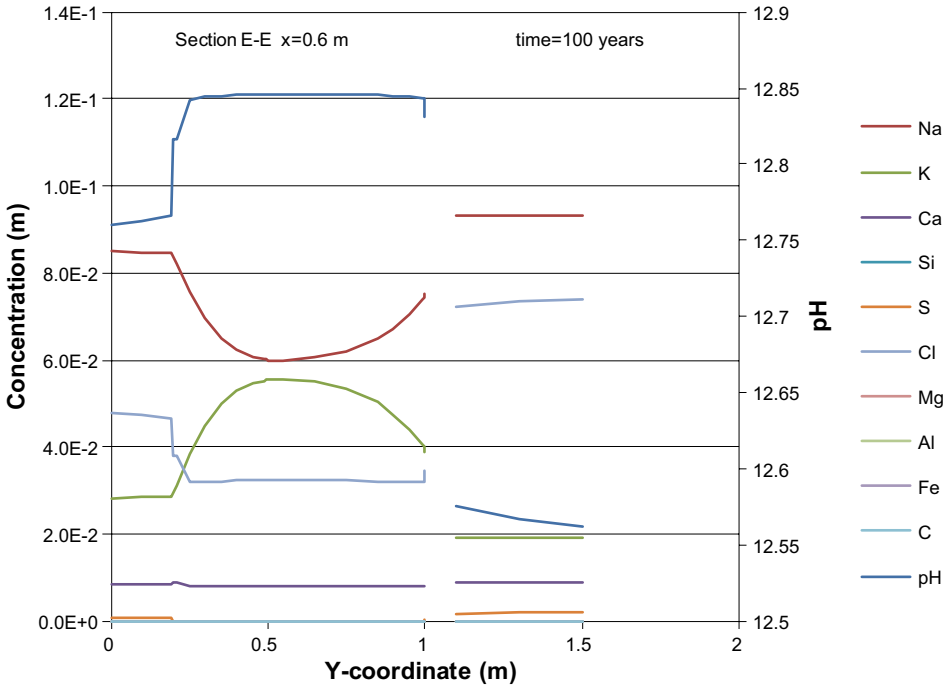

Figure G-23. *Concentration profiles of dissolved components in concrete pore water along the vertical Section E-E at time 100 years, case Large9. Units (mol/kg pore water).*

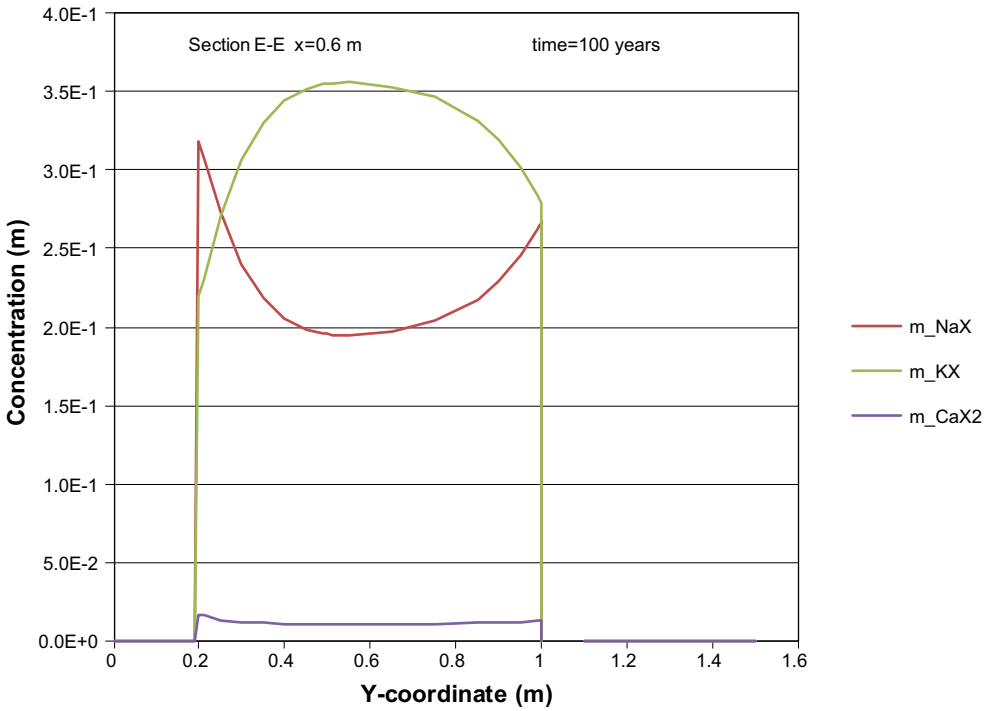

Figure G-24. *The assembly of ion exchange species in concrete along the vertical Section E-E at time 100 years, case Large9. Units (mol/kg pore water).*

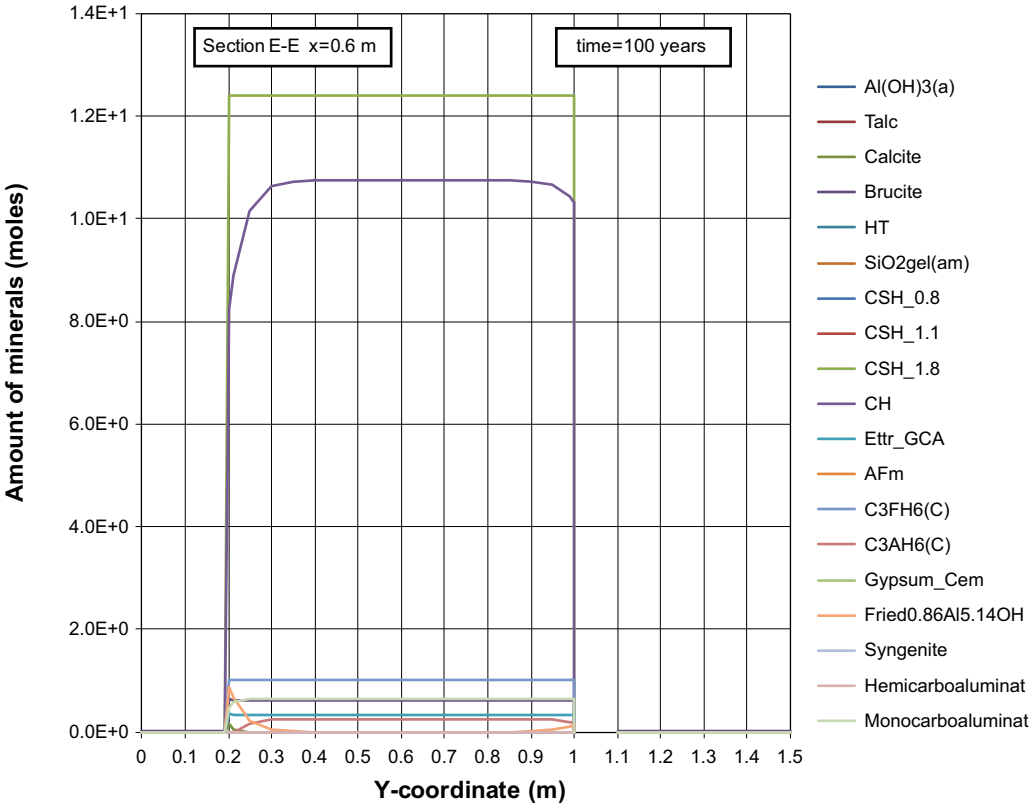

Figure G-25. *The mineral composition in concrete along the vertical Section E-E at time 100 years, case Large9. Units (mol/kg pore water).*

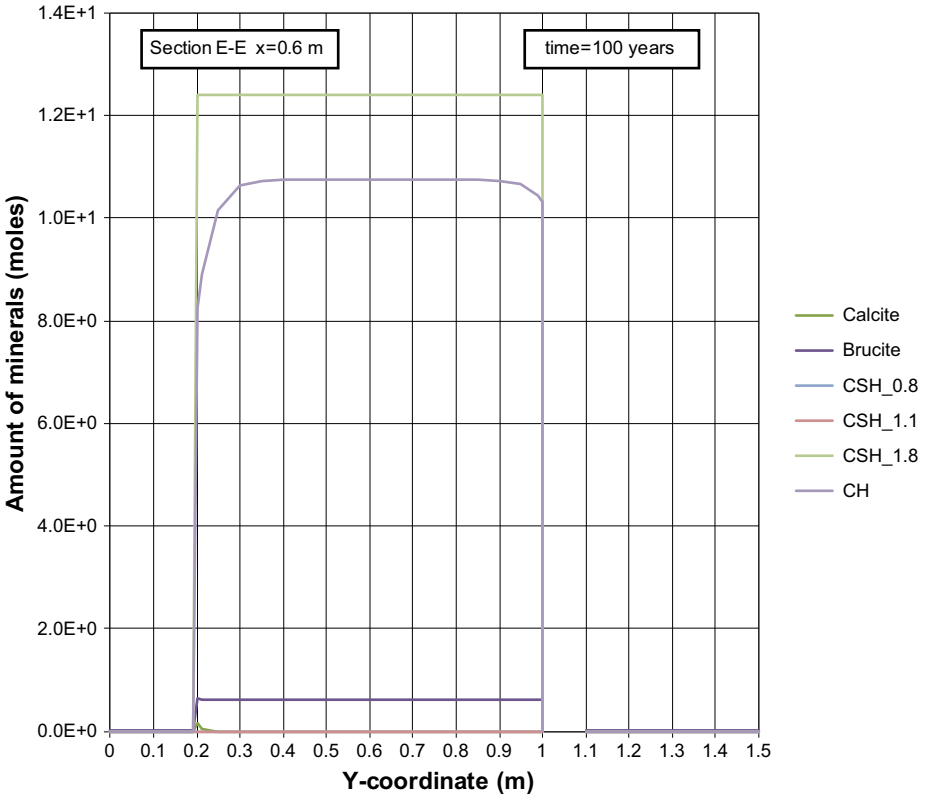

Figure G-26. *The mineral composition in concrete along the vertical Section E-E at time 100 years, case Large9. Units (mol/kg pore water).*

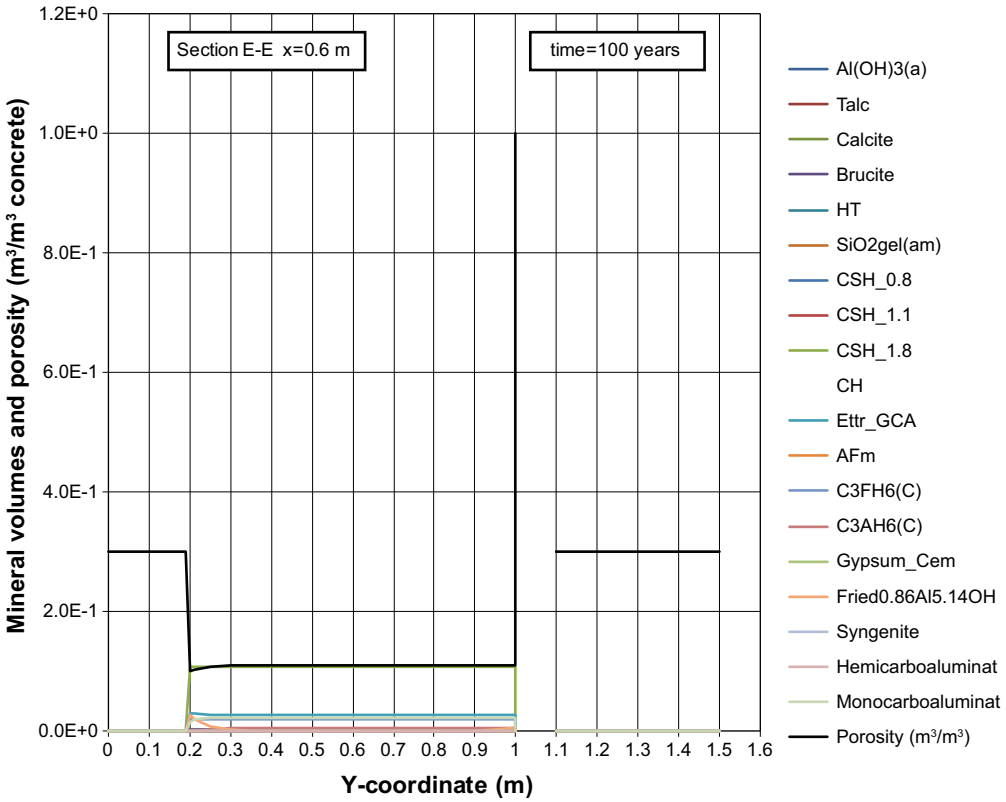

Figure G-27. *Mineral composition in concrete and calculated porosity along the vertical Section E-E at time 100 years, case Large9.*

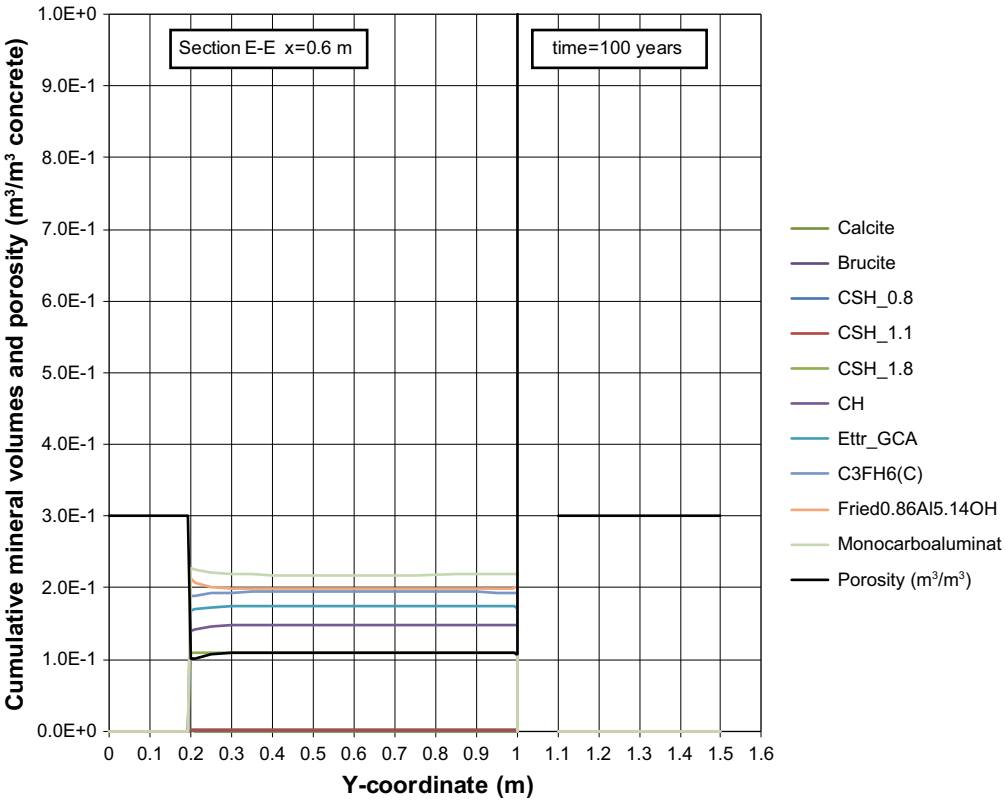

Figure G-28. *Cumulative representation of the mineral composition in concrete and calculated porosity along the vertical Section E-E at time 100 years, case Large9.*

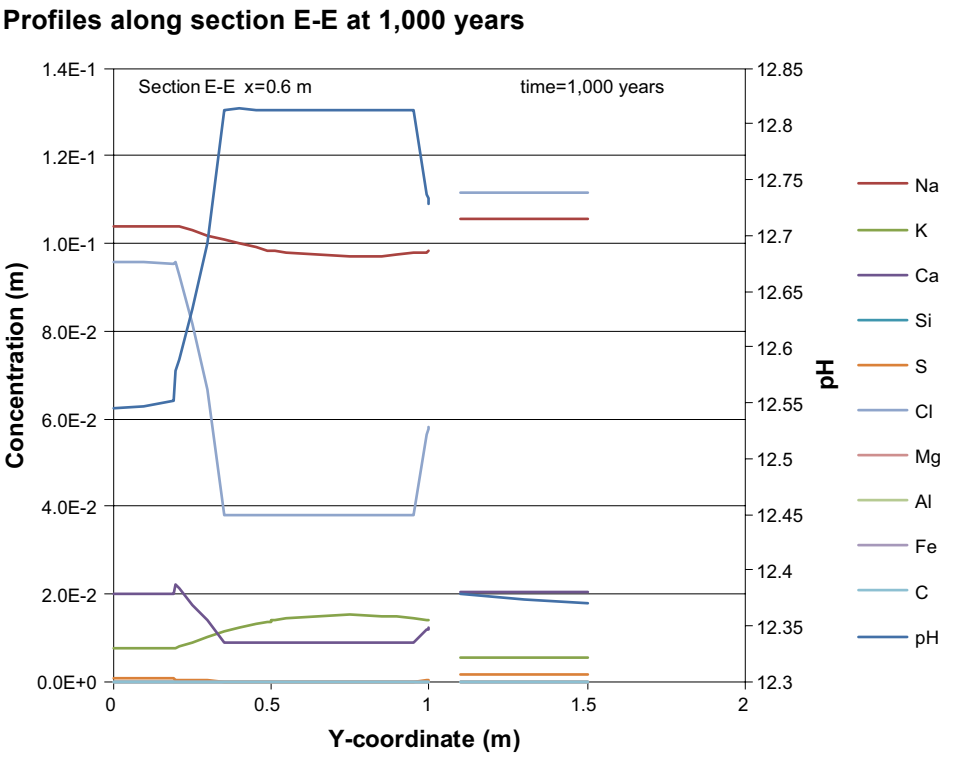

Figure G-29. *Concentration profiles of dissolved components in concrete pore water along the vertical Section E-E at time 1,000 years, case Large9. Units (mol/kg pore water).*

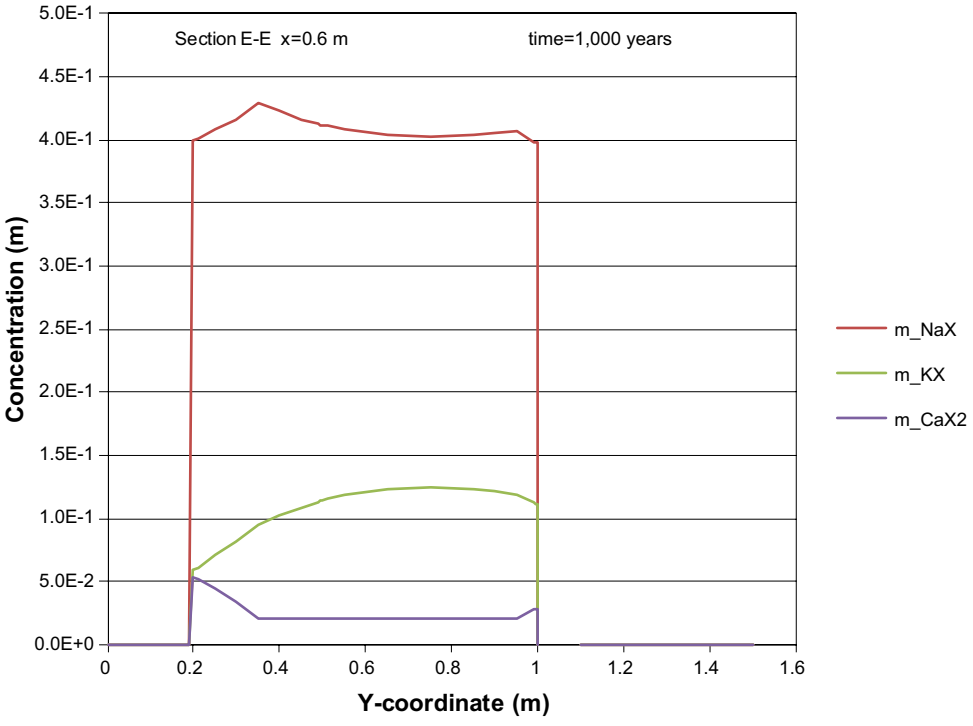

Figure G-30. *The assembly of ion exchange species in concrete along the vertical Section E-E at time 1,000 years, case Large9. Units (mol/kg pore water).*

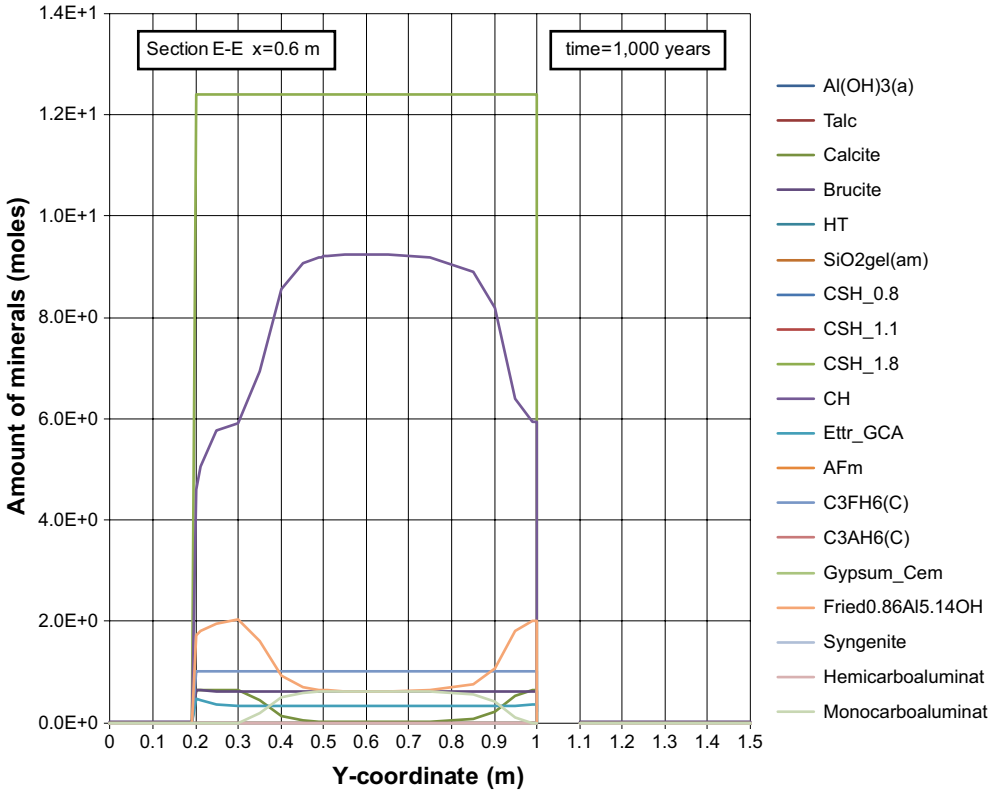

Figure G-31. *The mineral composition in concrete along the vertical Section E-E at time 1,000 years, case Large9. Units (mol/kg pore water).*

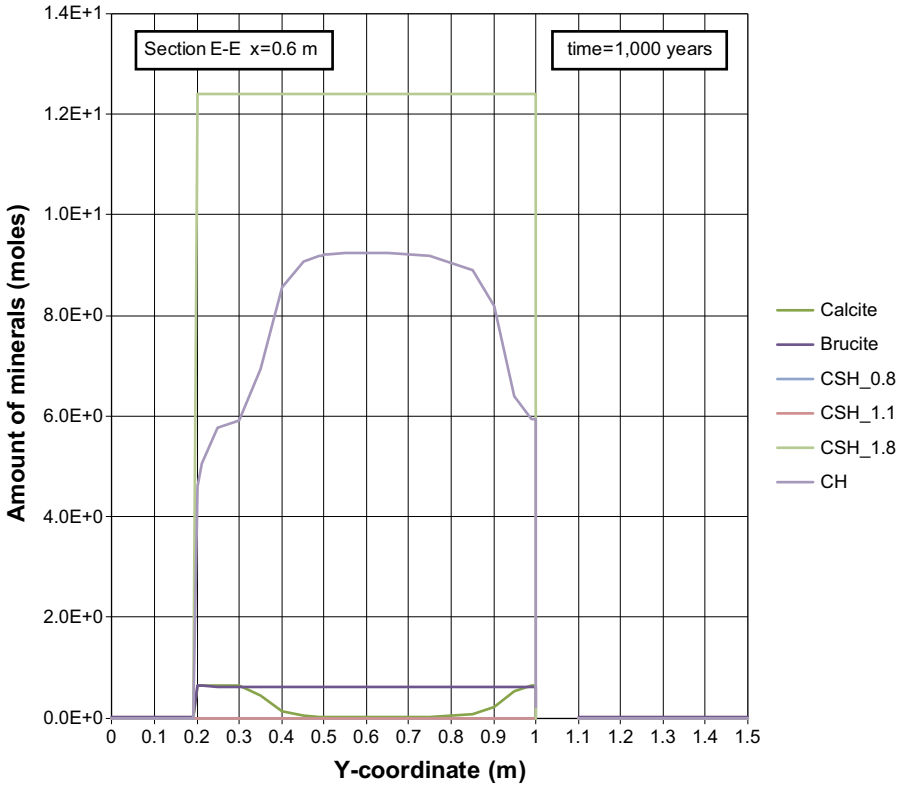

Figure G-32. *The mineral composition in concrete along the vertical Section E-E at time 1,000 years, case Large9. Units (mol/kg pore water).*

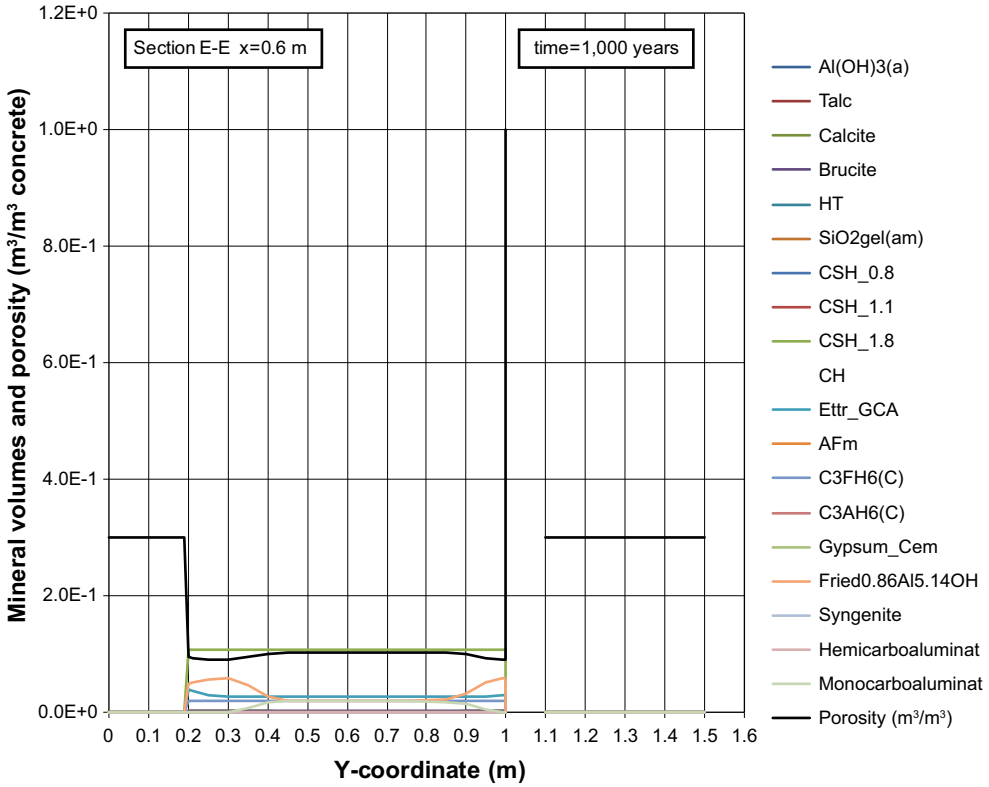

Figure G-33. *Mineral composition in concrete and calculated porosity along the vertical Section E-E at time 1,000 years, case Large9.*

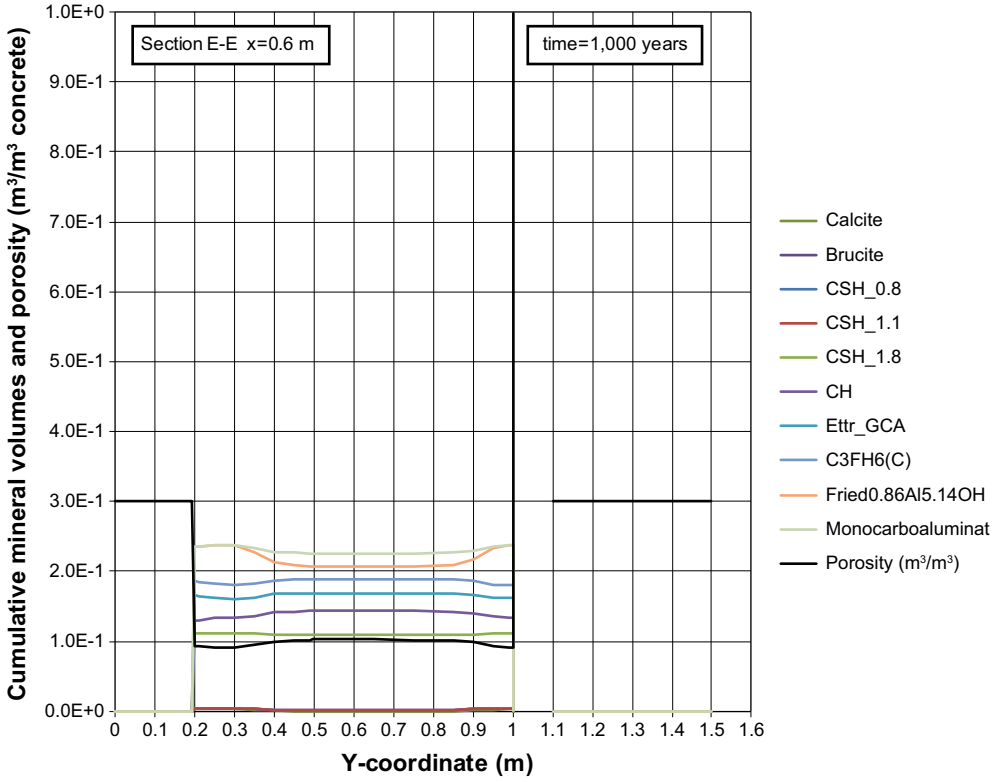

Figure G-34. *Cumulative representation of the mineral composition in concrete and calculated porosity along the vertical Section E-E at time 1,000 years, case Large9.*

Profiles along section E-E at 2,000 years

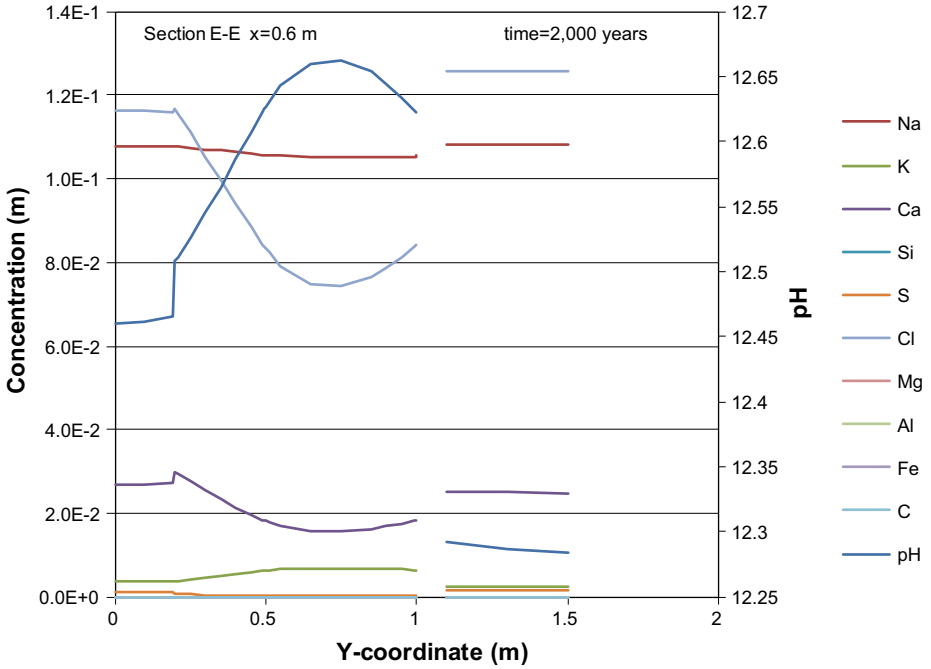

Figure G-35. *Concentration profiles of dissolved components in concrete pore water along the vertical Section E-E at time 2,000 years, case Large9. Units (mol/kg pore water).*

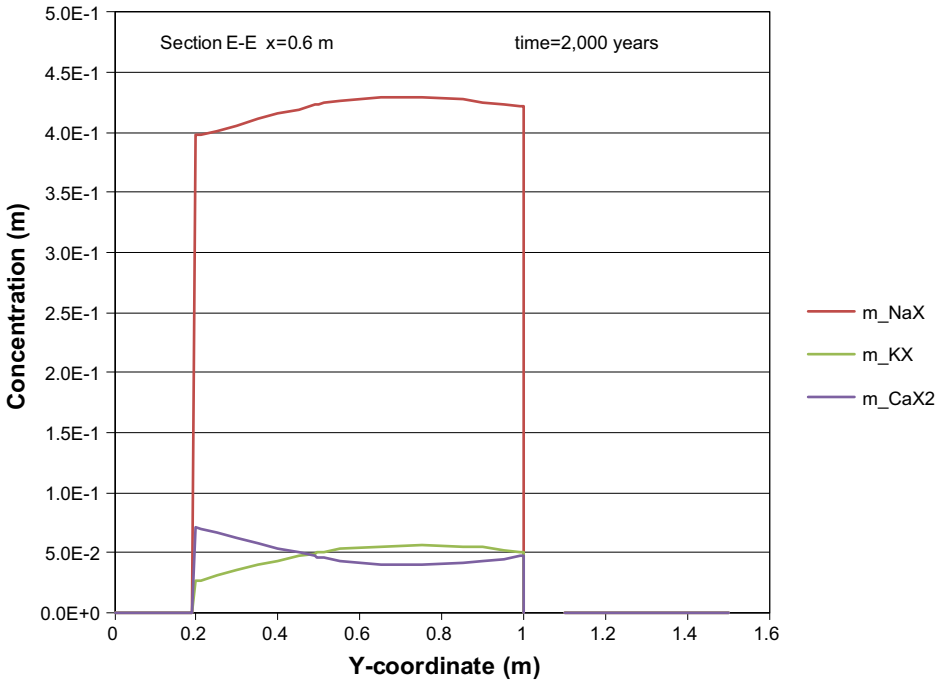

Figure G-36. *The assembly of ion exchange species in concrete along the vertical Section E-E at time 2,000 years, case Large9. Units (mol/kg pore water).*

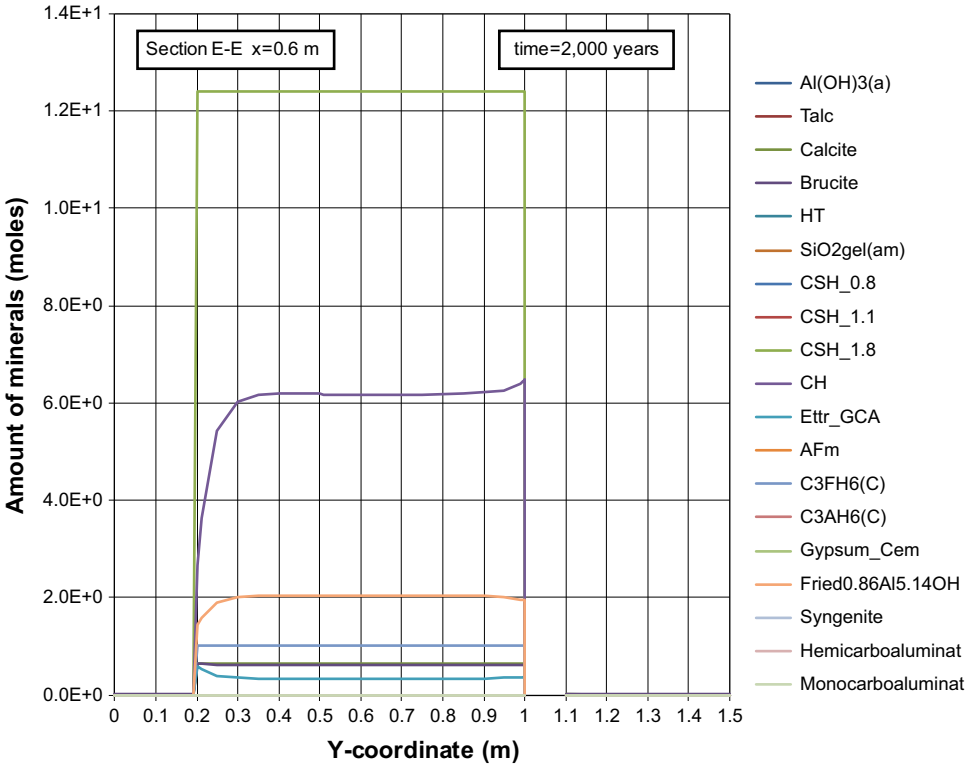

Figure G-37. *The mineral composition in concrete along the vertical Section E-E at time 2,000 years, case Large9. Units (mol/kg pore water).*

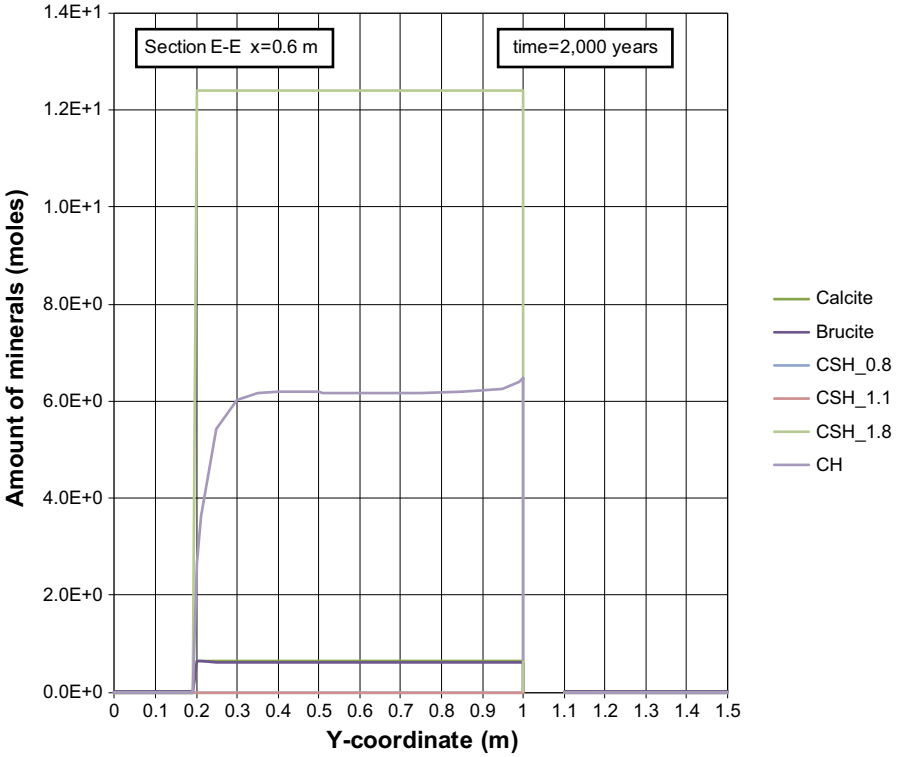

Figure G-38. *The mineral composition in concrete along the vertical Section E-E at time 2,000 years, case Large9. Units (mol/kg pore water).*

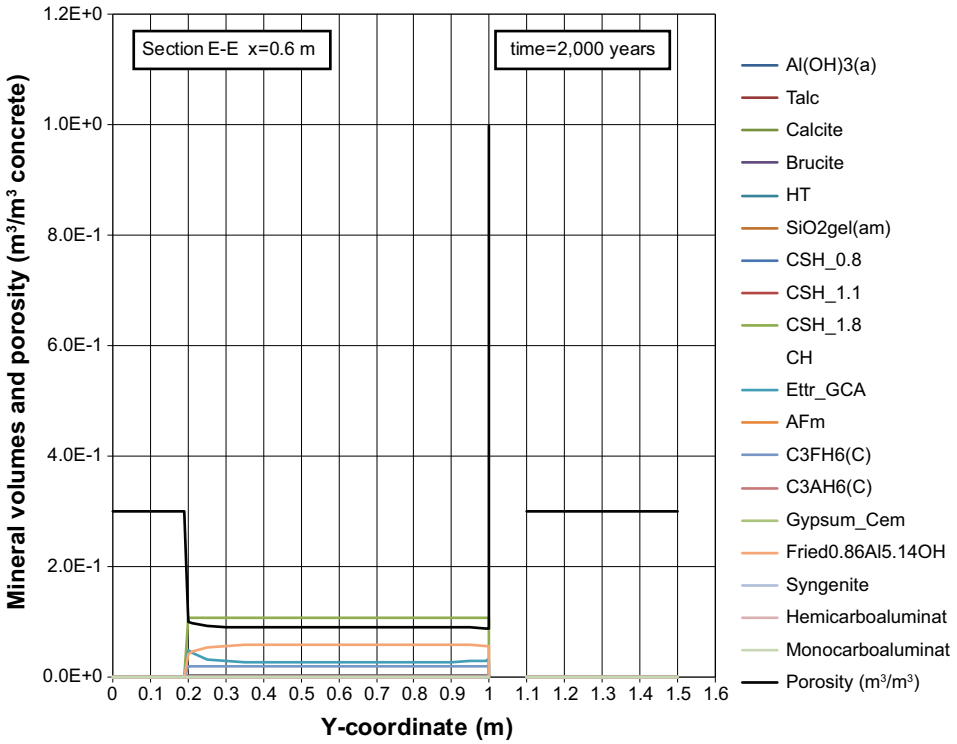

Figure G-39. *Mineral composition in concrete and calculated porosity along the vertical Section E-E at time 2,000 years, case Large9.*

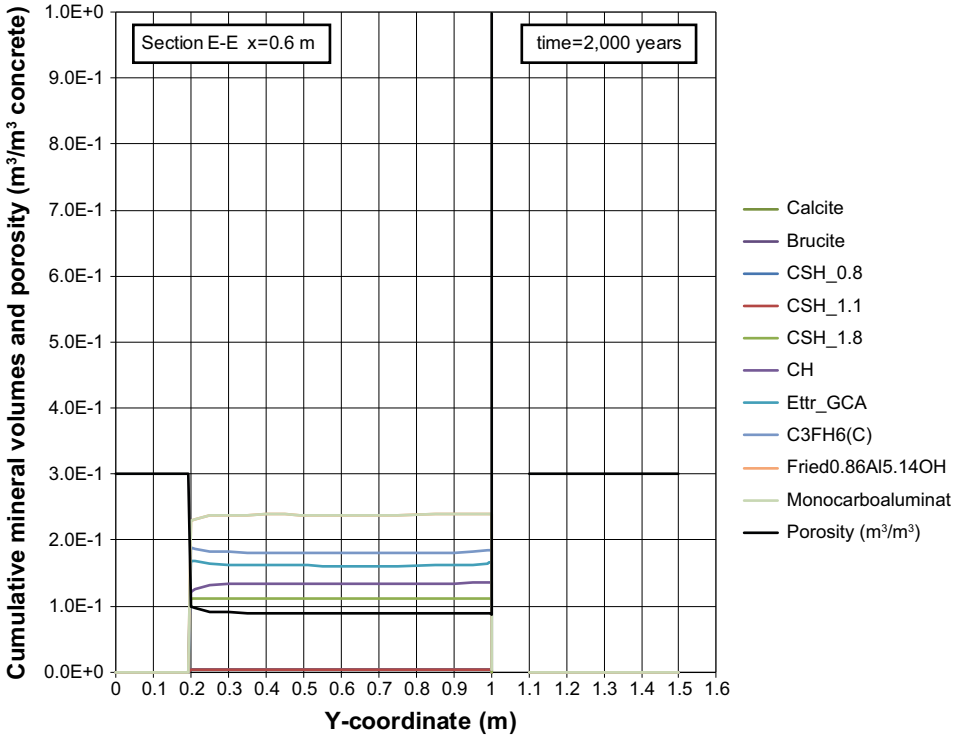

Figure G-40. *Cumulative representation of the mineral composition in concrete and calculated porosity along the vertical Section E-E at time 2,000 years, case Large9.*

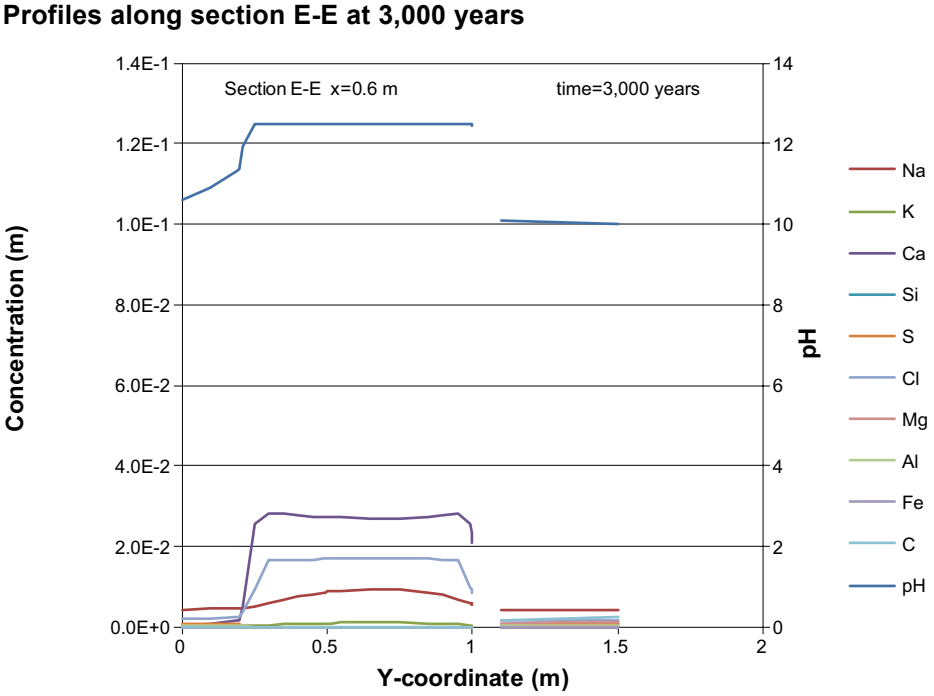

Figure G-41. *Concentration profiles of dissolved components in concrete pore water along the vertical Section E-E at time 3,000 years, case Large9. Units (mol/kg pore water).*

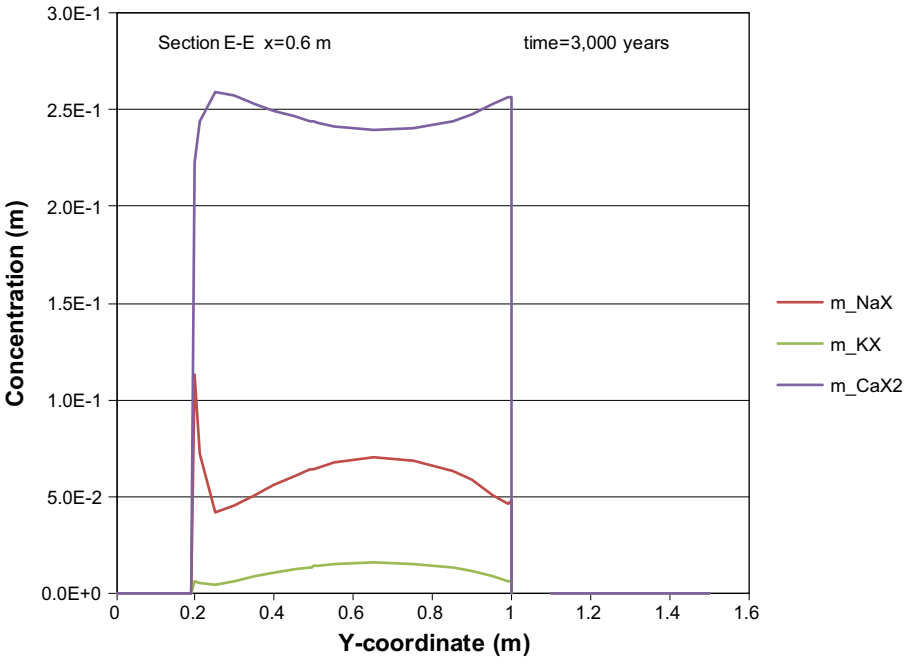

Figure G-42. *The assembly of ion exchange species in concrete along the vertical Section E-E at time 3,000 years, case Large9. Units (mol/kg pore water).*

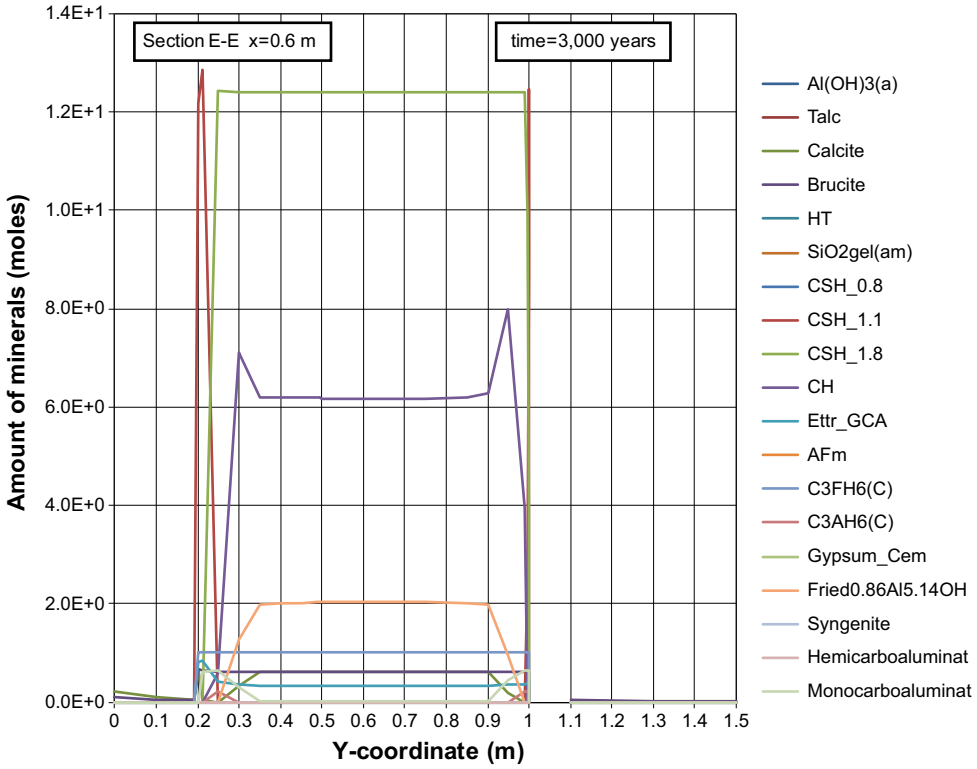

Figure G-43. *The mineral composition in concrete along the vertical Section E-E at time 3,000 years, case Large9. Units (mol/kg pore water).*

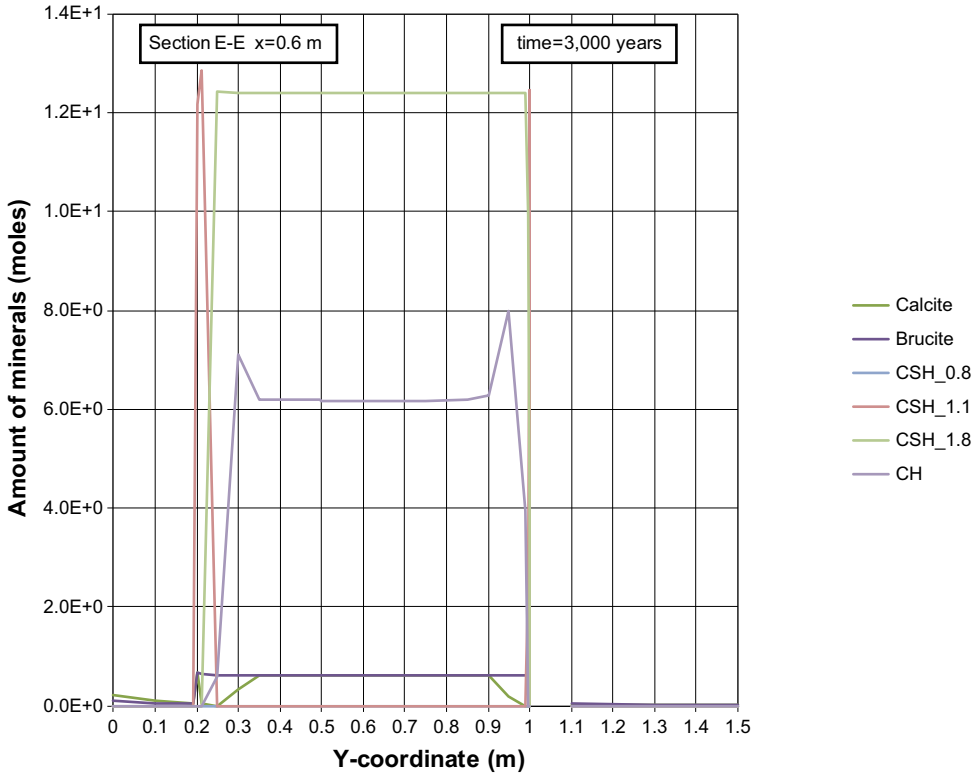

Figure G-44. *The mineral composition in concrete along the vertical Section E-E at time 3,000 years, case Large9. Units (mol/kg pore water).*

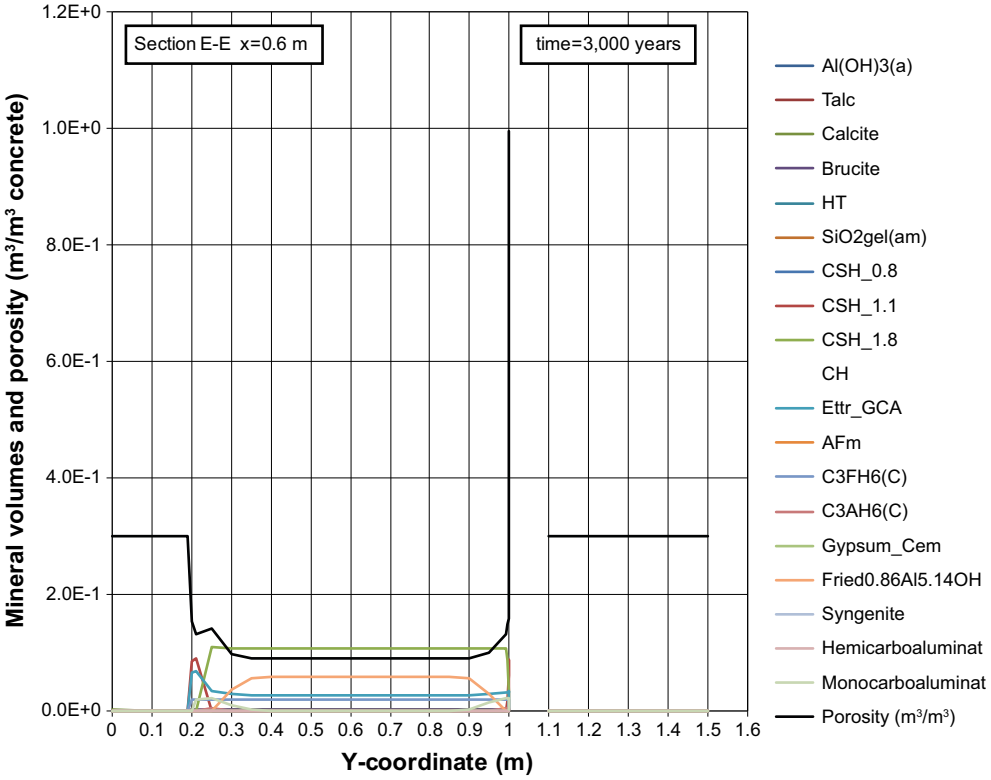

Figure G-45. *Mineral composition in concrete and calculated porosity along the vertical Section E-E at time 3,000 years, case Large9.*

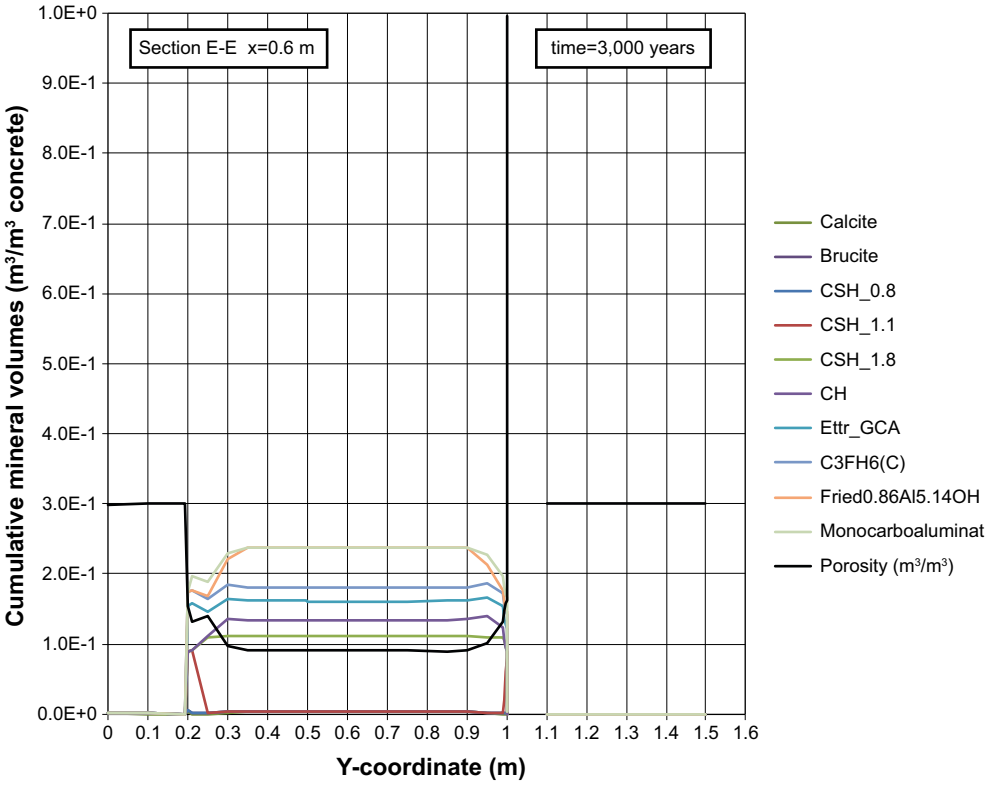

Figure G-46. *Cumulative representation of the mineral composition in concrete and calculated porosity along the vertical Section E-E at time 3,000 years, case Large9.*

Profiles along section E-E at 5,000 years

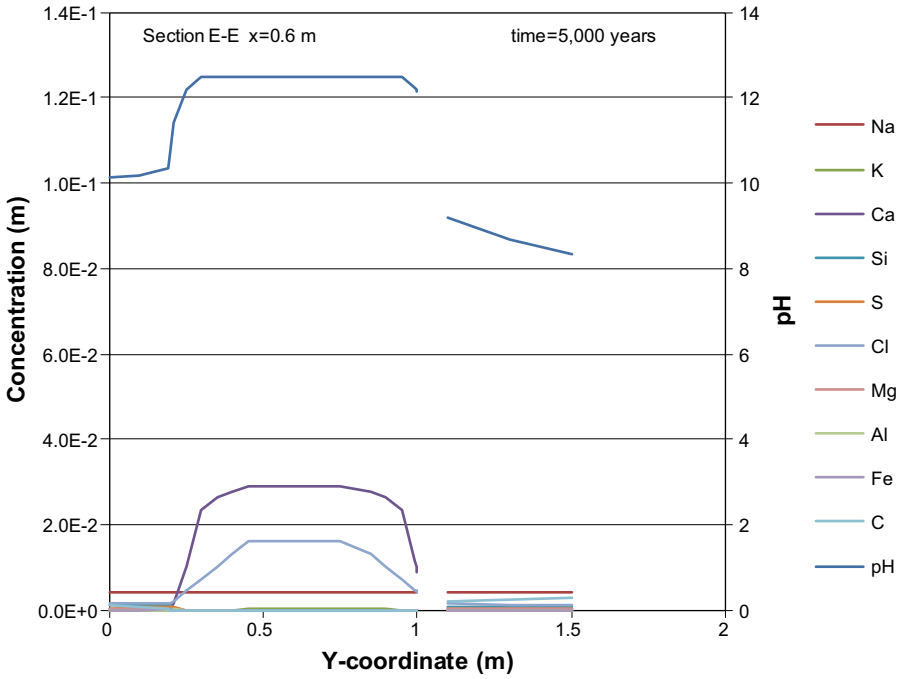

Figure G-47. *Concentration profiles of dissolved components in concrete pore water along the vertical Section E-E at time 5,000 years, case Large9. Units (mol/kg pore water).*

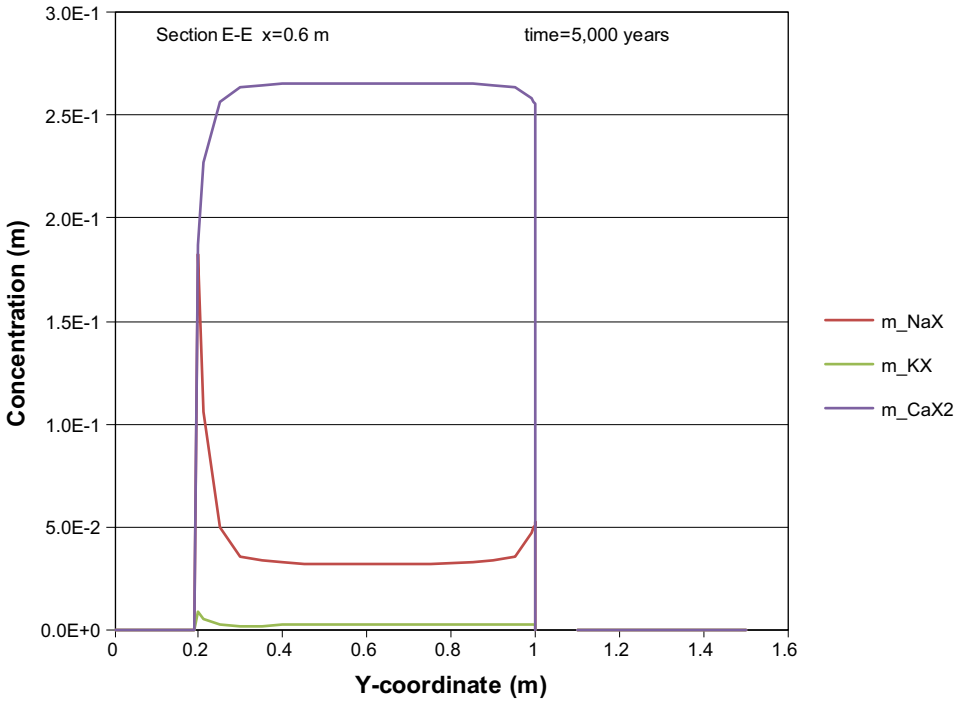

Figure G-48. *The assembly of ion exchange species in concrete along the vertical Section E-E at time 5,000 years, case Large9. Units (mol/kg pore water).*

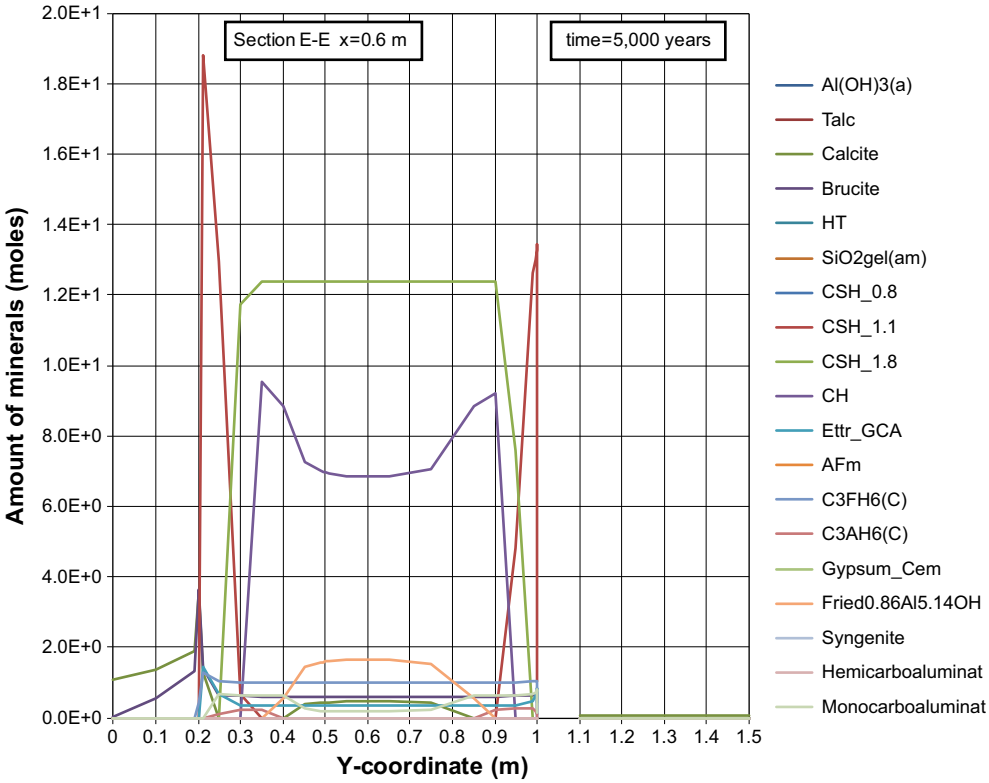

Figure G-49. *The mineral composition in concrete along the vertical Section E-E at time 5,000 years, case Large9. Units (mol/kg pore water).*

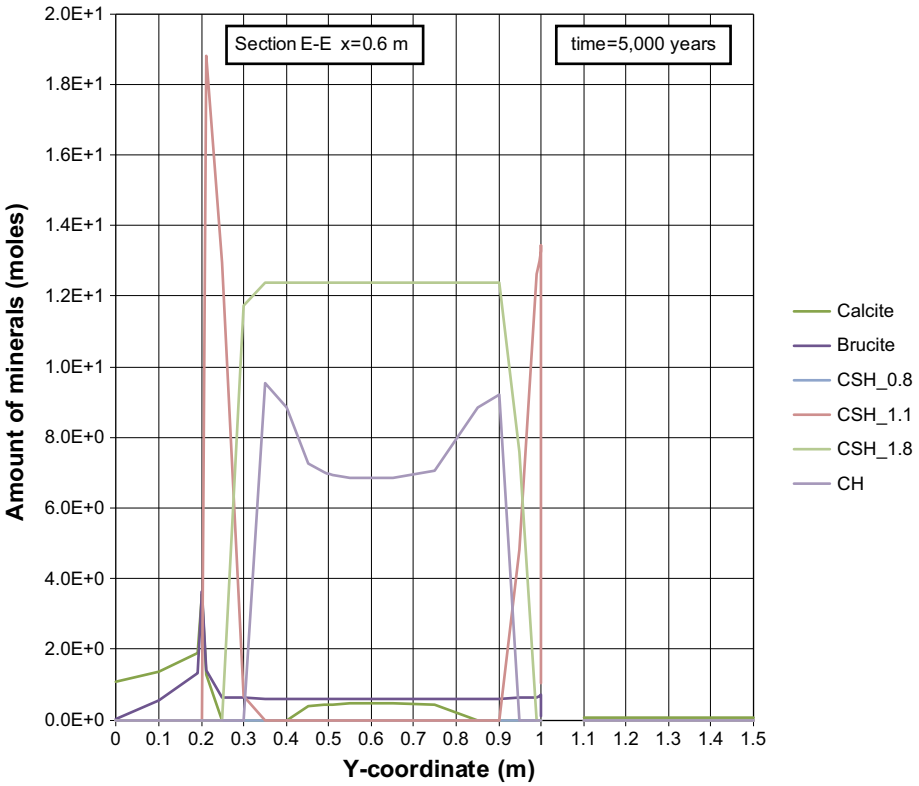

Figure G-50. *The mineral composition in concrete along the vertical Section E-E at time 5,000 years, case Large9. Units (mol/kg pore water).*

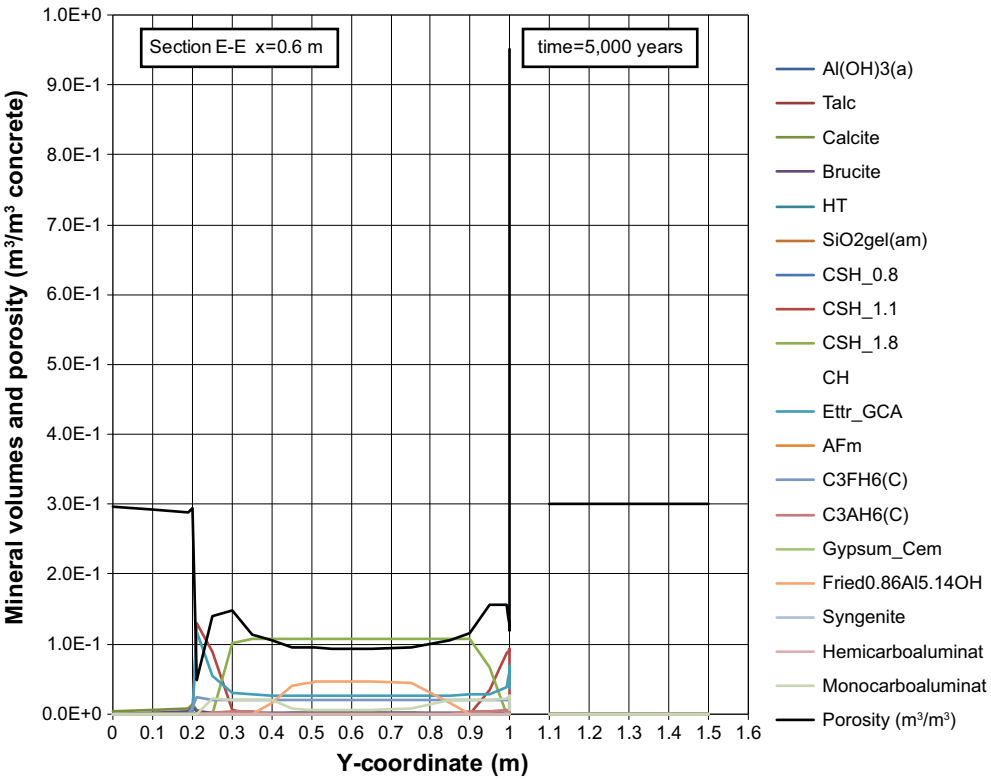

Figure G-51. *Mineral composition in concrete and calculated porosity along the vertical Section E-E at time 5,000 years, case Large9.*

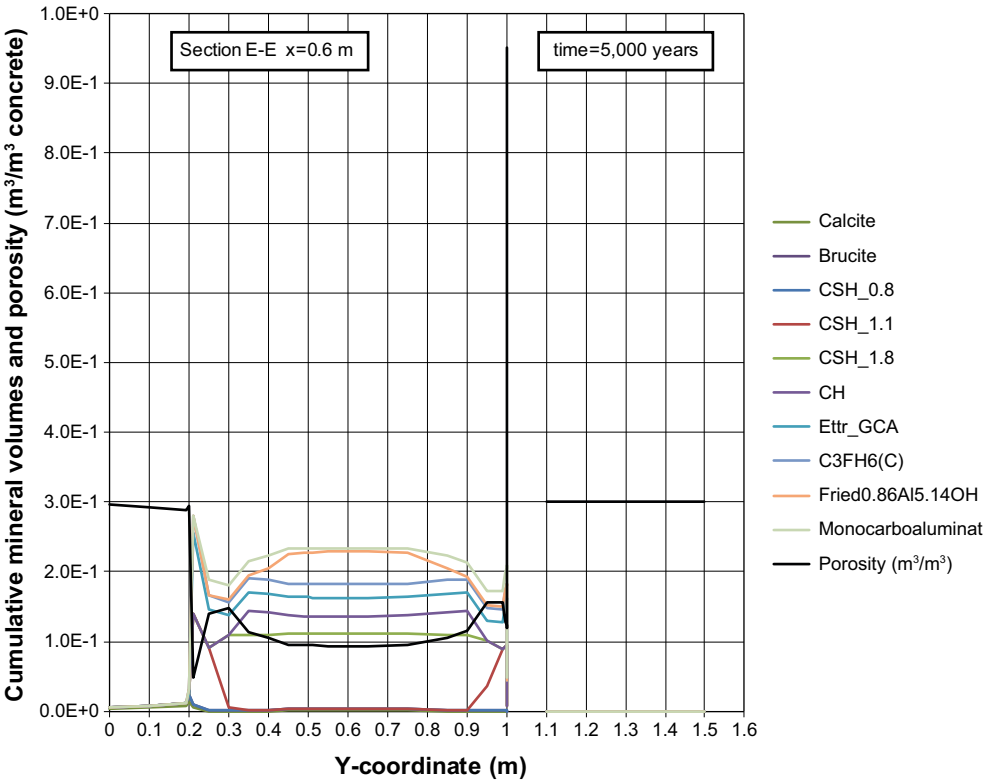

Figure G-52. *Cumulative representation of the mineral composition in concrete and calculated porosity along the vertical Section E-E at time 5,000 years, case Large9.*

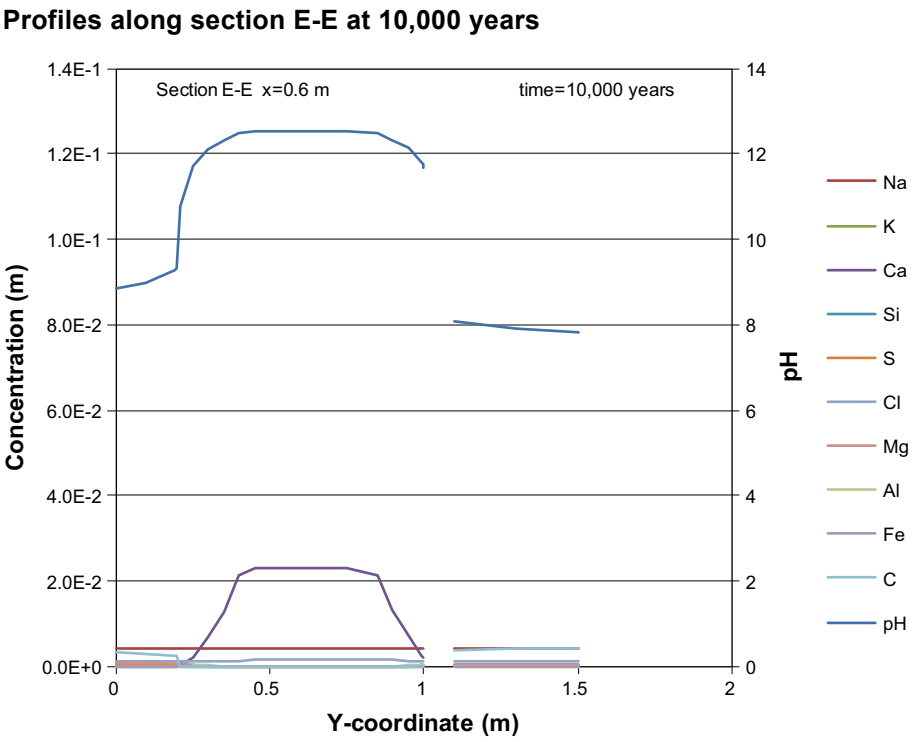

Figure G-53. *Concentration profiles of dissolved components in concrete pore water along the vertical Section E-E at time 10,000 years, case Large9. Units (mol/kg pore water).*

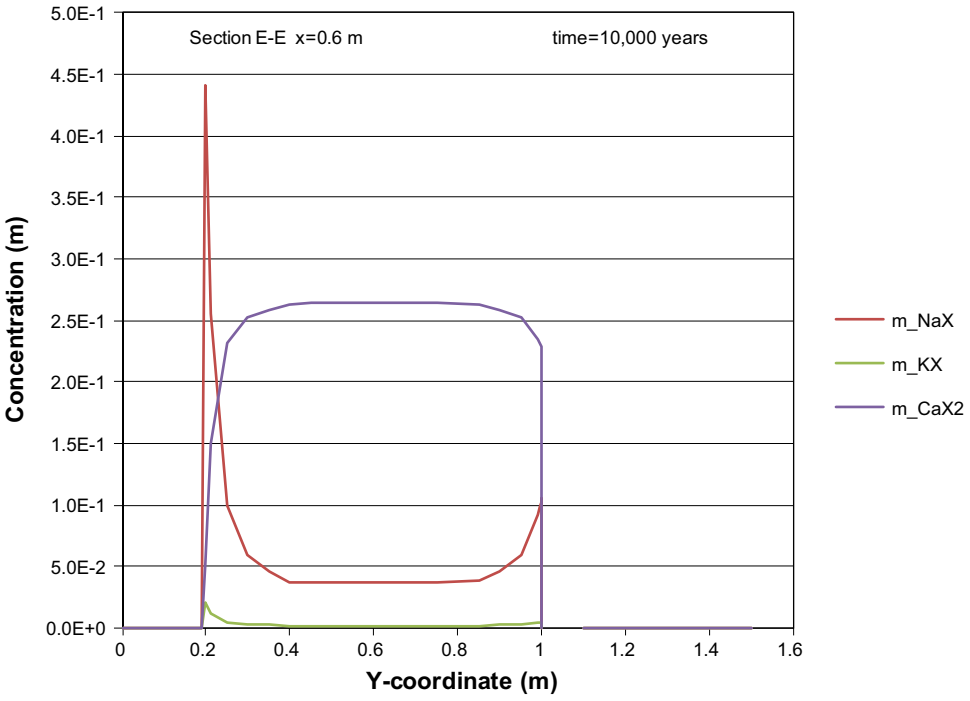

Figure G-54. *The assembly of ion exchange species in concrete along the vertical Section E-E at time 10,000 years, case Large9. Units (mol/kg pore water).*

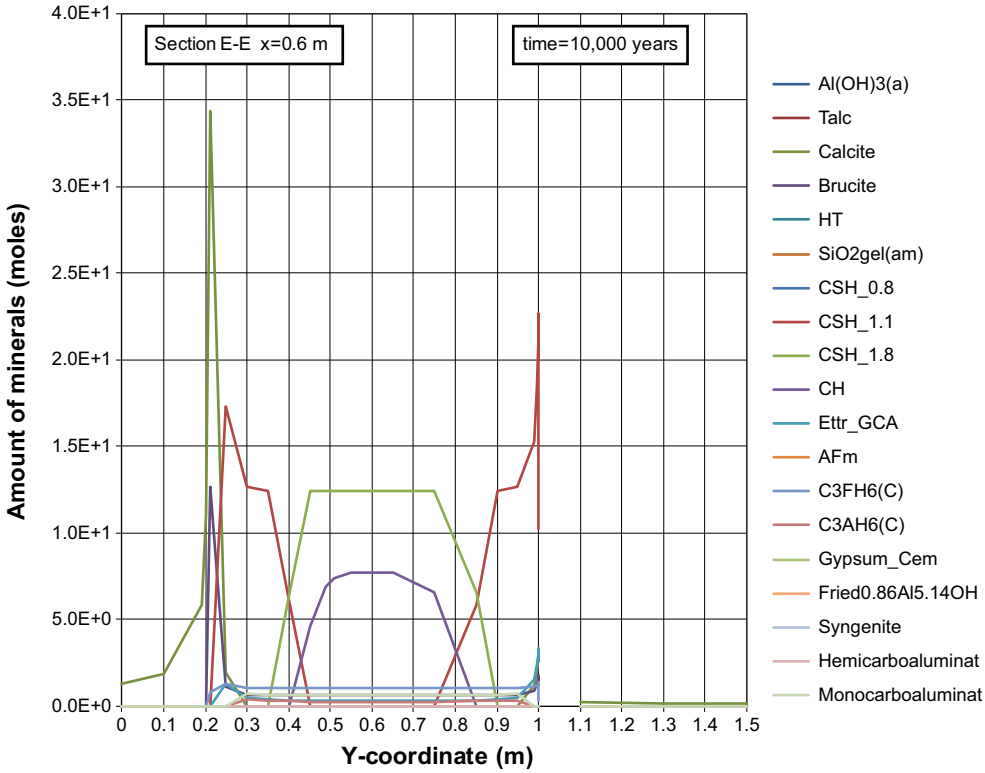

Figure G-55. *The mineral composition in concrete along the vertical Section E-E at time 10,000 years, case Large9. Units (mol/kg pore water).*

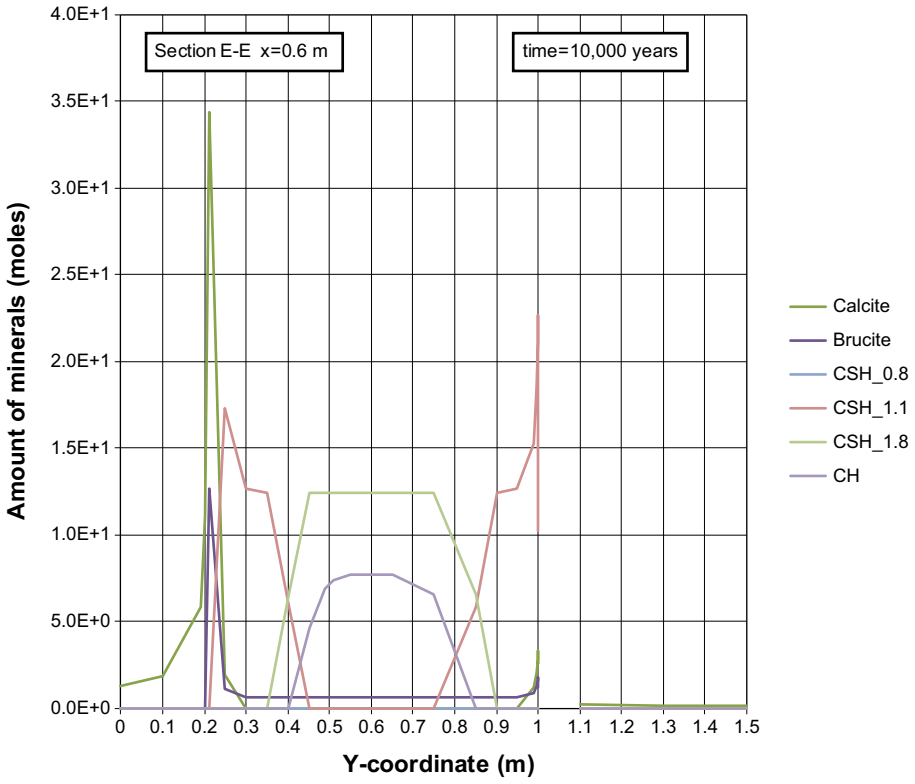

Figure G-56. *The mineral composition in concrete along the vertical Section E-E at time 10,000 years, case Large9. Units (mol/kg pore water).*

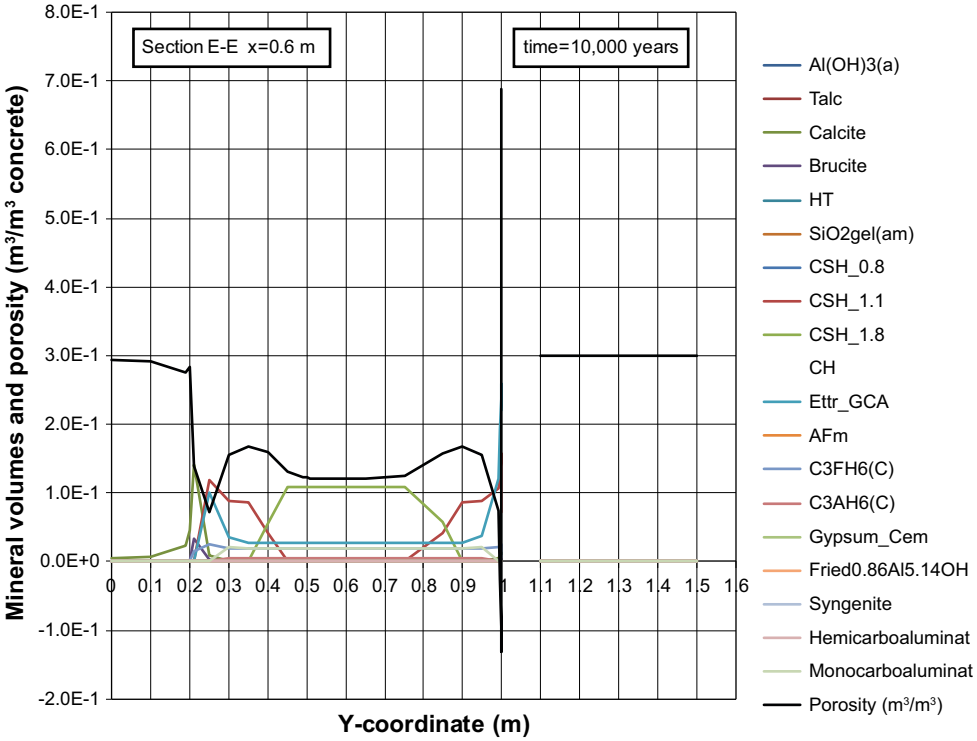

Figure G-57. *Mineral composition in concrete and calculated porosity along the vertical Section E-E at time 10,000 years, case Large9. The results indicate clogging of the thin fracture at y-coordinate ~1 m giving an artificial negative value of the porosity.*

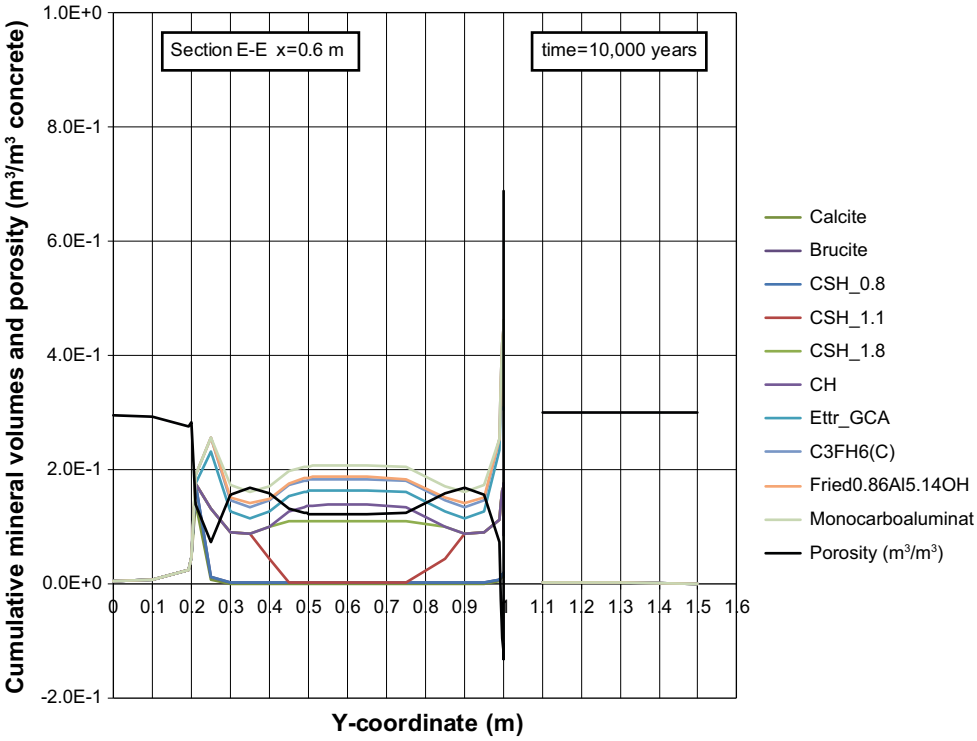

Figure G-58. *Cumulative representation of the mineral composition in concrete and calculated porosity along the vertical Section E-E at time 10,000 years, case Large9. The results indicate clogging of the thin fracture at y-coordinate ~1 m giving an artificial negative value of the porosity.*

Profiles along section E-E at 20,000 years

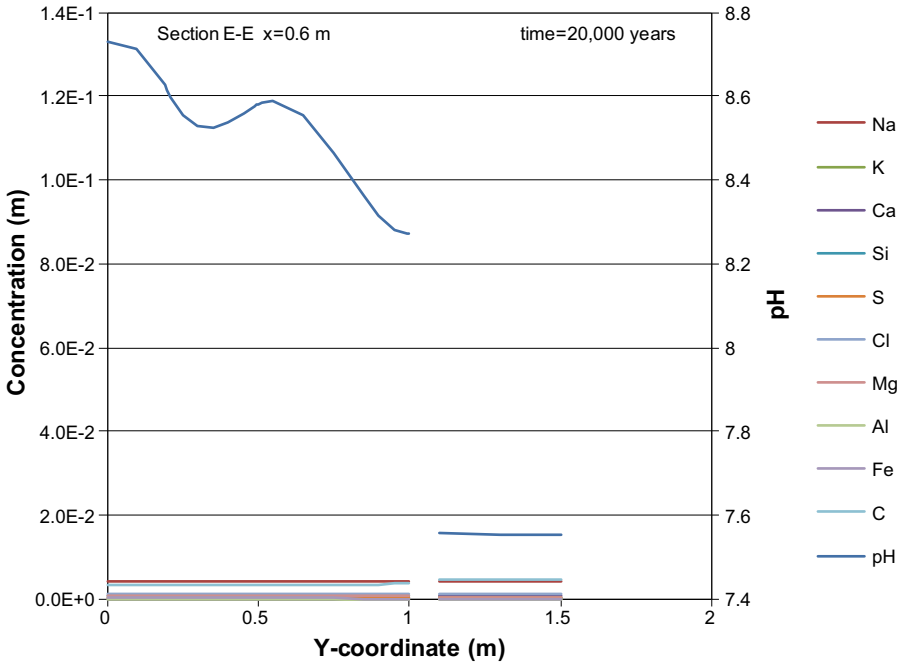

Figure G-59. *Concentration profiles of dissolved components in concrete pore water along the vertical Section E-E at time 20,000 years, case Large9. Units (mol/kg pore water).*

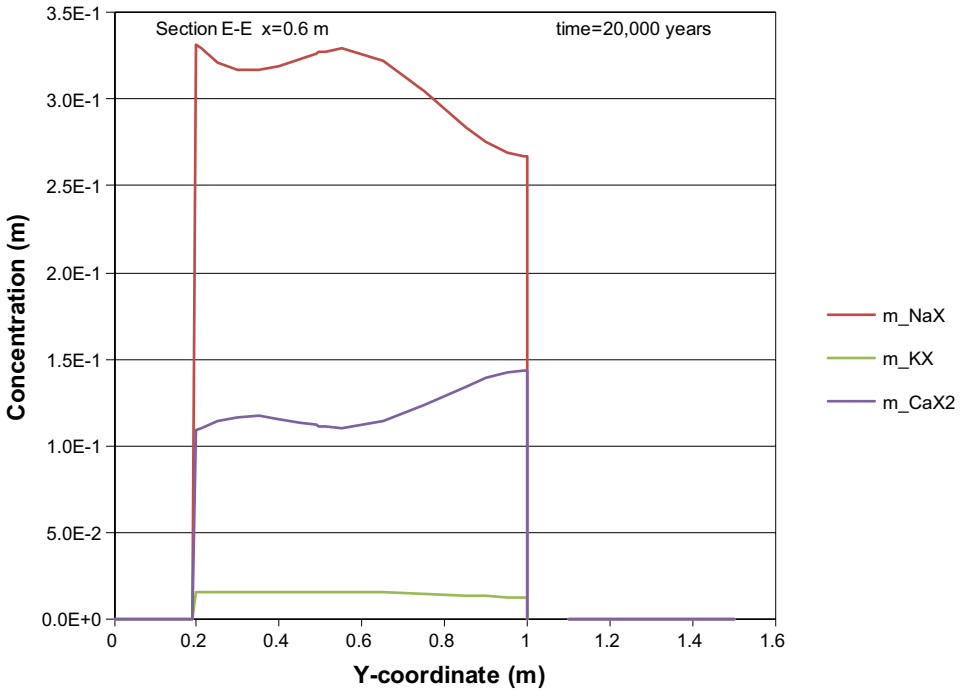

Figure G-60. *The assembly of ion exchange species in concrete along the vertical Section E-E at time 20,000 years, case Large9. Units (mol/kg pore water).*

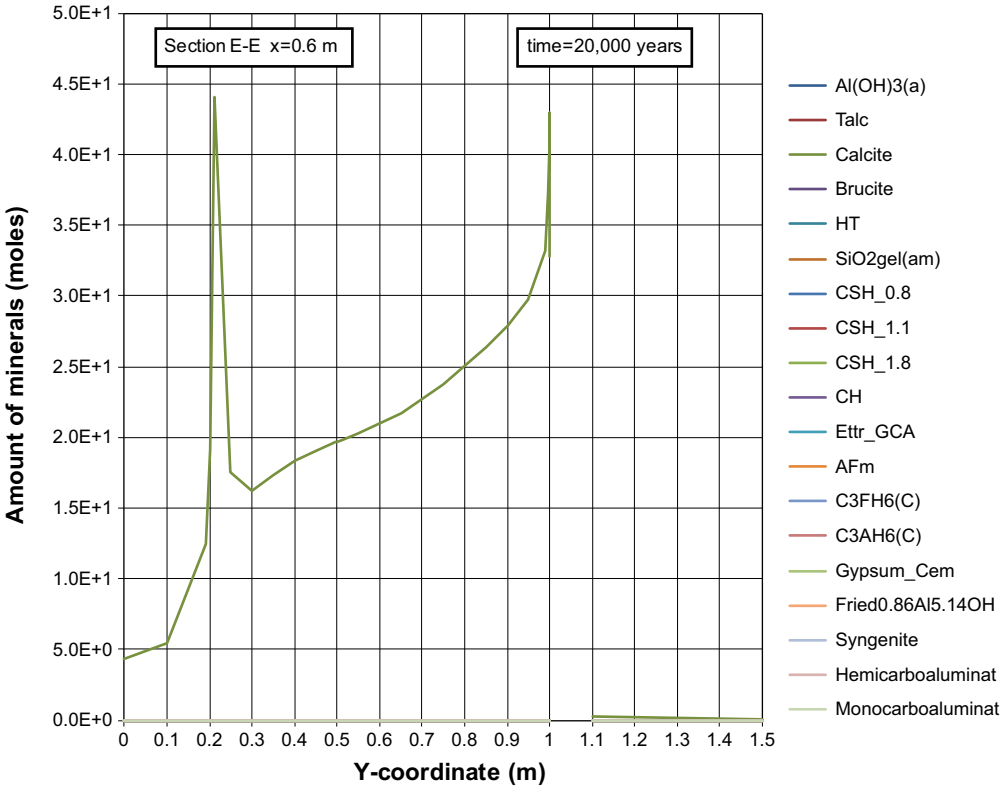

Figure G-61. *The mineral composition in concrete along the vertical Section E-E at time 20,000 years, case Large9. Units (mol/kg pore water).*

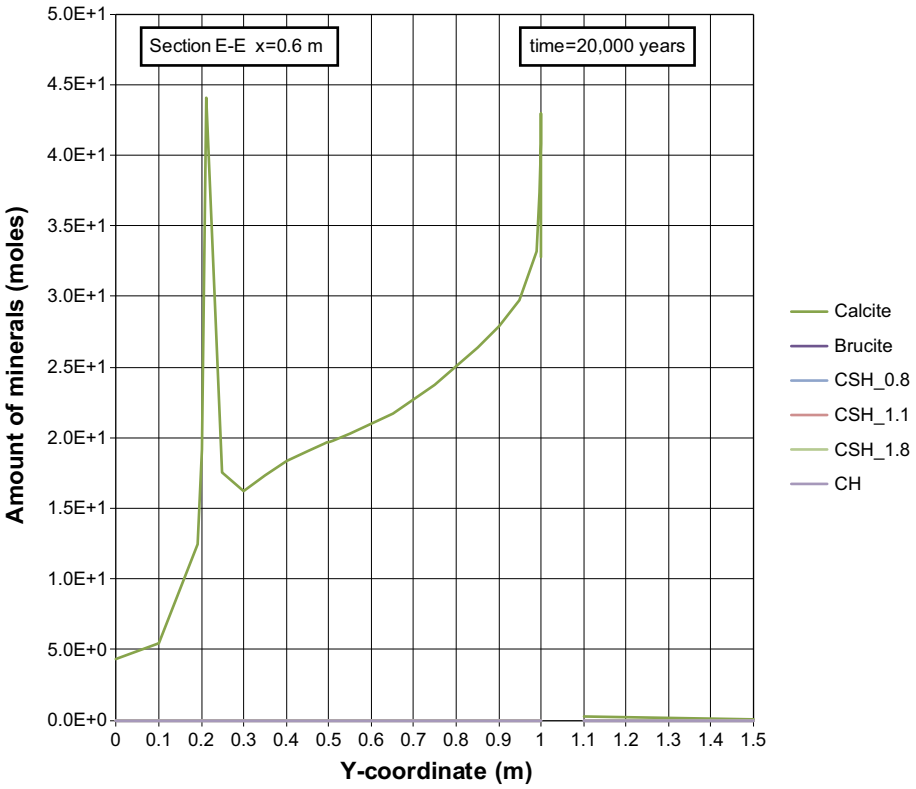

Figure G-62. *The mineral composition in concrete along the vertical Section E-E at time 20,000 years, case Large9. Units (mol/kg pore water).*

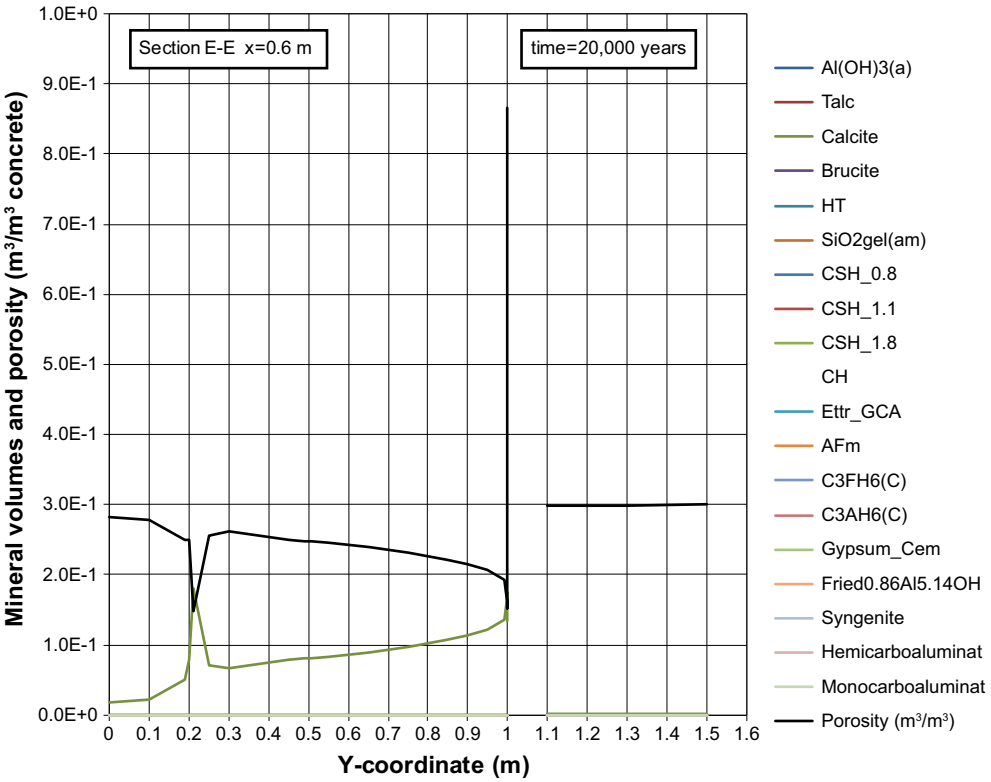

Figure G-63. *Mineral composition in concrete and calculated porosity along the vertical Section E-E at time 20,000 years, case Large9.*

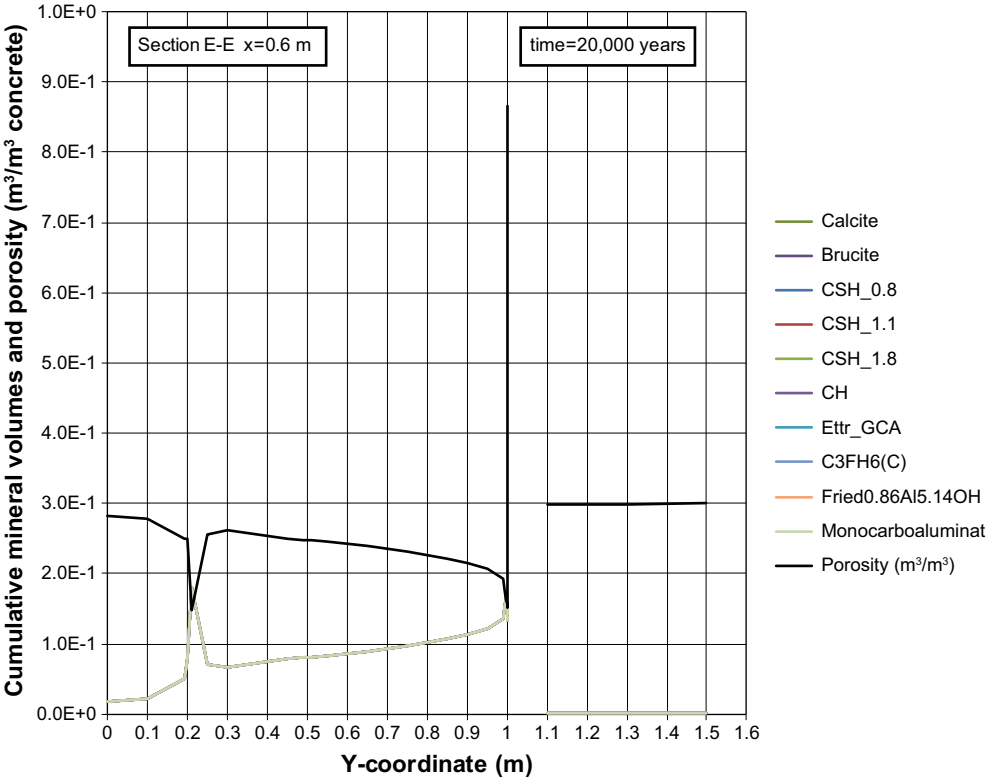

Figure G-64. *Cumulative representation of the mineral composition in concrete and calculated porosity along the vertical Section E-E at time 20,000 years, case Large9.*

Appendix H

Aqueous and mineral compositions assumed in the reactive transport modelling

Aqueous compositions assumed in the reactive transport modelling

Table H-1. Groundwater composition in SFR – Salt water period. Assumed as an initial condition in the Macadam backfill and as a boundary condition for the influx of groundwater during the initial period.

Parameter	Values as given in input	Units	Values as converted by program	Units	Values at equilibrium with minerals as calculated by program, c f. Table A-8	Units
pH	7.5	–	7.5	–	7.291	–
pe	–0.4	–	–0.4	–	–0.154	–
density	1.0	kg/l	1.0	kg/l	1.0	kg/l
temp	25.0	°C	25.0	°C	25.0	°C
HCO_3^-	100.	mg/l	$1.65\cdot10^{-3}$	mol/kg w	$1.61\cdot10^{-3}$	mol/kg w
S(+VI)	500.	mg/l	$5.25\cdot10^{-3}$	mol/kg w	$5.25\cdot10^{-3}$	mol/kg w
Cl	5,000.	mg/l	$1.42\cdot10^{-1}$	mol/kg w	$1.42\cdot10^{-1}$	mol/kg w
Na	2,500.	mg/l	$1.10\cdot10^{-1}$	mol/kg w	$1.10\cdot10^{-1}$	mol/kg w
K	20.	mg/l	$5.16\cdot10^{-4}$	mol/kg w	$5.16\cdot10^{-4}$	mol/kg w
Ca	430.	mg/l	$1.08\cdot10^{-2}$	mol/kg w	$1.08\cdot10^{-2}$	mol/kg w
Mg	270.	mg/l	$1.12\cdot10^{-2}$	mol/kg w	$1.12\cdot10^{-2}$	mol/kg w
Fe	0.0001	mg/l	$1.81\cdot10^{-9}$	mol/kg w	$1.81\cdot10^{-9}$	mol/kg w
H_4SiO_4	9.0545	mg/l	$9.50\cdot10^{-5}$	mol/kg w	$9.50\cdot10^{-5}$	mol/kg w

Table H-2. Groundwater composition in SFR – Fresh water period. Assumed as a boundary condition for the influx of groundwater in the long-term period.

Parameter	Values as given in input	Units	Values as converted by program	Units
pH	7.49	–	7.49	–
Pe	–0.4	–	–0.4	–
Density	1.0	kg/l	1.0	kg/l
Temp	25.0	°C	25.0	°C
HCO_3^-	300.	mg/l	$4.92\cdot10^{-3}$	mol/kg w
S(+VI)	50.	mg/l	$5.21\cdot10^{-4}$	mol/kg w
Cl	45.	mg/l	$1.27\cdot10^{-3}$	mol/kg w
Na	100.	mg/l	$4.35\cdot10^{-3}$	mol/kg w
K	4.	mg/l	$1.02\cdot10^{-4}$	mol/kg w
Ca	35.	mg/l	$8.74\cdot10^{-4}$	mol/kg w
Mg	9.	mg/l	$3.70\cdot10^{-4}$	mol/kg w
Fe	0.0001	mg/l	$1.79\cdot10^{-9}$	mol/kg w
H_4SiO_4	9.4384	mg/l	$9.83\cdot10^{-5}$	mol/kg w

Table H-3. Porewater composition in fresh construction concrete. Assumed as an initial condition in construction concrete and void.

Parameter	Values as given in input	units	Values as converted by program	Units	Values after equilibration with mineral phases and ion exchange (MinteqCem-2001)	Units	Values after equilibration with mineral phases and ion exchange (Cemdata07)	Units
pH	13.06 Initial guess, programme adjusts the pH to reach charge balance		13.62	–	12.965	–	12.994	–
pe	–0.6	–	–0.6	–	6.372	–	–4.43	–
density	1.0	kg/l	1.0	kg/l	1.0	kg/l	1.0	kg/l
temp	25.0	°C	25.0	°C	25.0	°C	25.0	°C
Na	96.03	mmol/l	$9.84\cdot10^{-2}$	mol/kg w	$2.67\cdot10^{-2}$	mol/kg w	$2.85\cdot10^{-2}$	mol/kg w
K	559.8	mmol/l	$5.74\cdot10^{-1}$	mol/kg w	$9.09\cdot10^{-2}$	mol/kg w	$9.32\cdot10^{-2}$	mol/kg w
Ca	0.9	mmol/l	$9.22\cdot10^{-4}$	mol/kg w	$5.20\cdot10^{-3}$	mol/kg w	$3.48\cdot10^{-3}$	mol/kg w
Mg	0.	mmol/l	0	mol/kg w	$1.58\cdot10^{-8}$	mol/kg w	$2.43\cdot10^{-8}$	mol/kg w
Cl	0.05	mmol/l	$5.12\cdot10^{-5}$	mol/kg w	$5.24\cdot10^{-5}$	mol/kg w	$5.55\cdot10^{-5}$	mol/kg w
S(+VI)	0.04	mmol/l	0	mol/kg w	$1.63\cdot10^{-5}$	mol/kg w	$3.65\cdot10^{-3}$	mol/kg w
Al	0.04	mmol/l	$4.10\cdot10^{-5}$	mol/kg w	$2.29\cdot10^{-4}$	mol/kg w	$5.80\cdot10^{-7}$	mol/kg w
Si	0.8	mmol/l	$4.10\cdot10^{-5}$	mol/kg w	$1.66\cdot10^{-5}$	mol/kg w	$4.58\cdot10^{-5}$	mol/kg w
Fe	0.0001	mmol/l	$8.20\cdot10^{-4}$	mol/kg w	$1.76\cdot10^{-4}$	mol/kg w	$6.0\cdot10^{-9}$	mol/kg w

Table H-4. Porewater composition in fresh concrete grout, assumed as an initial condition in concrete grout (only considered for 2BMA).

Parameter	Values as given in input	units	Values as converted by program (MinteqCem-2001)	Units	Values after equilibration with mineral phases and ion exchange (MinteqCem-2001)	Units
pH	13.06 Initial guess, programme adjusts the pH to reach charge balance		13.62	–	12.961	–
pe	–0.6	–	–0.6	–	–4.992	–
density	1.0	kg/l	1.0	kg/l	1.0	kg/l
temp	25.0	°C	25.0	°C	25.0	°C
Na	96.03	mmol/l	$9.84\cdot10^{-2}$	mol/kg w	$2.64\cdot10^{-2}$	mol/kg w
K	559.8	mmol/l	$5.74\cdot10^{-1}$	mol/kg w	$8.98\cdot10^{-2}$	mol/kg w
Ca	0.9	mmol/l	$9.22\cdot10^{-4}$	mol/kg w	$5.27\cdot10^{-3}$	mol/kg w
Mg	0.	mmol/l	0	mol/kg w	$1.60\cdot10^{-8}$	mol/kg w
Cl	0.05	mmol/l	$5.12\cdot10^{-5}$	mol/kg w	$5.16\cdot10^{-5}$	mol/kg w
S(+VI)	0.04	mmol/l	0	mol/kg w	$1.61\cdot10^{-5}$	mol/kg w
Al	0.04	mmol/l	$4.10\cdot10^{-5}$	mol/kg w	$2.24\cdot10^{-4}$	mol/kg w
Si	0.8	mmol/l	$4.10\cdot10^{-5}$	mol/kg w	$1.64\cdot10^{-5}$	mol/kg w
Fe	0.0001	mmol/l	$8.20\cdot10^{-4}$	mol/kg w	$1.72\cdot10^{-4}$	mol/kg w

Mineral phases assumed in the reactive transport modelling

The mineral assemblage differs between the two databases. Calcium is considered the most important component and the assumed start concentrations given as input data (portlandite + CSH-gel) have been adjusted to give the same total inventory of calcium.

Table H-5. Initial mineral content in construction concrete (start guesses in columns 2 and 4, and the composition after initial speciation by PHAST/PHREEQC in columns 3 and 5) for the two different databases. Units are in kmol/m^3 pore water.

Mineral	MinteqCem-2001 Values as given in input – Start guess	MinteqCem-2001 Values as calculated by program – After initial speciation	Cemdata07 Values as given in input – Start guess	Cemdata07 Values as calculated by program – After initial speciation
Portlandite	10.48	10.75	12.132	14.56
CSH_1.8	12.39	12.39	–	–
CSHjen	–	–	12.390	10.99
Ettringite/monosulfoaluminate	0.3241/ –	0.324/–	– / 0.9722	0.1107/–
C3AH6(C)/hydrogarnetOH	0.2424	0	0.2424	0
C3FH6(C)/hydrogarnetFe	1.02	1.02	1.02	1.02
Monocarboaluminate	–	0.2425	–	–
Calcite	0.6367	0.3942	0.6367	0
Brucite	0.6149	0.6149	0.6149	0
HydrogarnetSi	–	–	–	0.95
Thaumasite	–	–	–	0.318
HydrotalciteOH	–	–	–	0.154

Table H-6. Initial content in concrete grout (only considered in calculations for 2BMA). Start guesses are shown in column 2 and the composition after initial speciation by PHAST/PHREEQC is presented in column 3. Units are in kmol/m^3 pore water.

Mineral	MinteqCem-2001 Values as given in input – Start guess	MinteqCem-2001 Values as calculated by program – After initial speciation
Portlandite	3.158	3.431
CSH_1.8	3.733	3.734
Ettringite	0.09767	0.09761
C3AH6(C)	0.07305	0
C3FH6(C)	0.3072	0.3072
Monocarboaluminate		0.07312
Calcite	0.1918	0.1187
Brucite	0.1853	0.1853

Table H-7. Minerals allowed to precipitate (Construction concrete and concrete grout) for the two different databases.

Mineral	MinteqCem-2001	Cemdata07
Portlandite	Yes	Yes
CSH_1.8	Yes	–
CSH_1.1	Yes	–
CSH_0.8	Yes	–
CSHtob1	–	Yes
CSHtob2	–	Yes
CSHjen	–	Yes
Ettringite	Yes	Yes
Monosulfoaluminate/Afm (monosulphate)	Yes	Yes
Fe-ettringite	–	Yes
Fe-monosulfate	–	Yes
C3AH6(C)/hydrogarnetOH	Yes	Yes
C3FH6(C)/hydrogarnetFe	Yes	Yes
hydrotalciteFe	–	Yes
Calcite	Yes	Yes
Brucite	Yes	Yes
Gypsum	Yes	Yes
SiO2gel(am)	Yes	Yes
Friedelsalt	Yes	–
Fried1.96Al4.04OH	Yes	–
Fried1.42Al4.58OH	Yes	–
Fried1.34Al4.66OH	Yes	–
Fried1.04Al4.96OH	Yes	–
Fried0.88Al5.12OH	Yes	–
Fried0.86Al5.14OH	Yes	–
(CaO)3CaCl2:15H2O	Yes	–
Syngenite	Yes	Yes
Hemicarboaluminat	Yes	Yes
Monocarboaluminat	Yes	Yes
tricarboaluminate	–	Yes
Fe-hemicarbonate	–	Yes
Fe-monocarbonate	–	Yes
Thaumasite	Only for 2BMA	Yes
hydrotalciteOH[x)]	–	Yes
C2AH8	–	Yes
C2FH8	–	Yes
C4AH13	–	Yes
C4FH13	–	Yes
stratlingite	–	Yes
Fe-stratlingite	–	Yes
CAH10	–	Yes
hydrogarnetSi	–	Yes
hydrotalciteC	–	Yes
Al(OH)3am	–	Yes
Fe(OH)3mic	–	Yes

[x)] The mineral is misspelled (hydrotaliceOH) in the database, corrected to hydrotalciteOH in this report.

Table H-8. Minerals allowed to precipitate (Macadam and void) for the two different databases.

Mineral	MinteqCem-2001	Cemdata07
Portlandite	Yes	Yes
CSH_1.8	Yes	–
CSH_1.1	Yes	–
CSH_0.8	Yes	–
CSHtob1	–	Yes
CSHtob2	–	Yes
CSHjen	–	Yes
Ettringite	Yes	Yes
monosulfoaluminate/Afm	Yes	Yes
Fe-ettringite	–	Yes
Fe-monosulfate	–	Yes
C3AH6(C)/hydrogarnetOH	Yes	Yes
C3FH6(C)/hydrogarnetFe	Yes	Yes
hydrotalciteFe	–	Yes
Calcite	Yes	Yes
Brucite	Yes	Yes
Gypsum	Yes	Yes
SiO2gel(am)	Yes	Yes
Friedelsalt	Yes	–
Fried1.96Al4.04OH	Yes	–
Fried1.42Al4.58OH	Yes	–
Fried1.34Al4.66OH	Yes	–
Fried1.04Al4.96OH	Yes	–
Fried0.88Al5.12OH	Yes	–
Fried0.86Al5.14OH	Yes	–
(CaO)3CaCl2:15H2O	Yes	–
Syngenite	Yes	Yes
Hemicarboaluminat	Yes	Yes
Monocarboaluminat	Yes	Yes
tricarboaluminate	–	Yes
Fe-hemicarbonate	–	Yes
Fe-monocarbonate	–	Yes
Thaumasite	Only for 2BMA	Yes
hydrotalciteOH[x)]	–	Yes
C2AH8	–	Yes
C2FH8	–	Yes
C4AH13	–	Yes
C4FH13	–	Yes
stratlingite	–	Yes
Fe-stratlingite	–	Yes
CAH10	–	Yes
hydrogarnetSi	–	Yes
hydrotalciteC	–	Yes
Al(OH)3am	–	Yes
Fe(OH)3mic	–	Yes

[x)] The mineral is misspelled (hydrotaliceOH) in the database, corrected to hydrotalciteOH in this report.